

Contrast Agents for MRI

Experimental Methods

New Developments in NMR

Editor-in-Chief:

William S. Price, *Western Sydney University, Australia*

Series Editors:

Sharon Ashbrook, *University of St Andrews, UK*

Bruce Balcom, *University of New Brunswick, Canada*

István Furó, *Industrial NMR Centre at KTH, Sweden*

Masatsune Kainosho, *Tokyo Metropolitan University, Japan*

Maili Liu, *Chinese Academy of Sciences, Wuhan, China*

Titles in the Series:

- 1: Contemporary Computer-Assisted Approaches to Molecular Structure Elucidation
- 2: New Applications of NMR in Drug Discovery and Development
- 3: Advances in Biological Solid-State NMR
- 4: Hyperpolarized Xenon-129 Magnetic Resonance: Concepts, Production, Techniques and Applications
- 5: Mobile NMR and MRI: Developments and Applications
- 6: Gas Phase NMR
- 7: Magnetic Resonance Technology: Hardware and System Component Design
- 8: Biophysics and Biochemistry of Cartilage by NMR and MRI
- 9: Diffusion NMR of Confined Systems: Fluid Transport in Porous Solids and Heterogeneous Materials
- 10: NMR in Glycoscience and Glycotechnology
- 11: Fast NMR Data Acquisition: Beyond the Fourier Transform
- 12: Cross-relaxation and Cross-correlation Parameters in NMR: Molecular Approaches
- 13: Contrast Agents for MRI: Experimental Methods

How to obtain future titles on publication:

A standing order plan is available for this series. A standing order will bring delivery of each new volume immediately on publication.

For further information please contact:

Book Sales Department, Royal Society of Chemistry, Thomas Graham House, Science Park, Milton Road, Cambridge, CB4 0WF, UK

Telephone: +44 (0)1223 420066, Fax: +44 (0)1223 420247

Email: booksales@rsc.org

Visit our website at www.rsc.org/books

Contrast Agents for MRI Experimental Methods

Edited by

Valérie C. Pierre

University of Minnesota, USA

Email: pierre@umn.edu

Matthew J. Allen

Wayne State University, USA

Email: mallen@chem.wayne.edu



New Developments in NMR No. 13

Print ISBN: 978-1-78262-447-9

PDF eISBN: 978-1-78801-014-6

EPUB eISBN: 978-1-78801-254-6

ISSN: 2044-253X

A catalogue record for this book is available from the British Library

© The Royal Society of Chemistry 2018

All rights reserved

Apart from fair dealing for the purposes of research for non-commercial purposes or for private study, criticism or review, as permitted under the Copyright, Designs and Patents Act 1988 and the Copyright and Related Rights Regulations 2003, this publication may not be reproduced, stored or transmitted, in any form or by any means, without the prior permission in writing of The Royal Society of Chemistry or the copyright owner, or in the case of reproduction in accordance with the terms of licences issued by the Copyright Licensing Agency in the UK, or in accordance with the terms of the licences issued by the appropriate Reproduction Rights Organization outside the UK. Enquiries concerning reproduction outside the terms stated here should be sent to The Royal Society of Chemistry at the address printed on this page.

Whilst this material has been produced with all due care, The Royal Society of Chemistry cannot be held responsible or liable for its accuracy and completeness, nor for any consequences arising from any errors or the use of the information contained in this publication. The publication of advertisements does not constitute any endorsement by The Royal Society of Chemistry or Authors of any products advertised. The views and opinions advanced by contributors do not necessarily reflect those of The Royal Society of Chemistry which shall not be liable for any resulting loss or damage arising as a result of reliance upon this material.

The Royal Society of Chemistry is a charity, registered in England and Wales, Number 207890, and a company incorporated in England by Royal Charter (Registered No. RC000524), registered office: Burlington House, Piccadilly, London W1J 0BA, UK, Telephone: +44 (0) 207 4378 6556.

For further information see our web site at www.rsc.org

Printed in the United Kingdom by CPI Group (UK) Ltd, Croydon, CR0 4YY, UK

Preface

The field of contrast agents for magnetic resonance imaging (MRI) has progressed by leaps and bounds over the last few decades, from metal complexes to responsive and targeted probes that enable multicolor imaging with remarkable resolution and sensitivity. Along the way, our understanding of the richness of the coordination chemistry of lanthanide and transition metals has grown tremendously, as has our ability to manipulate chemical and physical parameters to achieve new types of contrast. The complexity of the interactions of metal complexes and nanoparticles with biological systems and the uniqueness of their pharmacological properties is now widely appreciated.

As this field progresses quickly, the breadth of the techniques used in the synthesis and characterization of contrast agents can seem overwhelming. This book is not a classical review of the literature; many excellent reviews and books exist that serve that purpose. Rather, our intention is for this book to serve as a benchtop companion for chemists, physicists, and biologists. Throughout this book, different techniques that are used in the field of contrast agents for MRI are described. The strengths and limitations of the techniques are discussed together with a summary of the information that those techniques can and cannot provide and descriptions of how to interpret data. This book is intended not only for those working on the design, synthesis, and evaluation of contrast agents, but also on their medical and biological applications. It is intended for students, postdoctoral scholars and researchers working in the lab, and also for those writing manuscripts and grant applications. Throughout its chapters, this book provides information that is intended to help in the design of contrast agents to fill specific needs and guides readers through synthesis, characterization, evaluation, and determination of the chemical, physical, and biological properties of new contrast agents.

The first chapter of this book discusses the synthesis and characterization of metal-based contrast agents. Ligand choice affects not only the contrast-enhancing ability of an agent but also its thermodynamic stability and kinetic inertness, which are paramount to the safety profiles of probes. Those studies are also discussed in the first chapter. Subsequent chapters detail the techniques relevant to specific classes of contrast agents: Gd^{III}-based contrast agents (Chapter 2), chemical exchange saturation transfer agents (Chapter 3), nanoparticle-based contrast agents (Chapter 4), transition-metal based T_1 -shortening contrast agents (Chapter 5), and fluorine probes (Chapter 6). In each chapter, the principles underlying that class of contrast agent and the physical experiments uniquely suited to their studies are described. The book finishes with a chapter focused on biological and pharmacological experiments that are key to evaluating the potential of contrast agents for use *in vivo*.

This book would not have been possible without substantial contributions from the world-renowned experts who authored the chapters. To each of them, we offer our most sincere and largest possible thank you! We are especially indebted to Susan A. White, who downloaded, reviewed, and edited every single reference of this book. We also gratefully acknowledge Dr Sylvie Pailloux, who contributed to the editing of a few subchapters. Both of us thank our research groups for their patience as we spent time editing the book. More than anything, we are incredibly grateful for our families for their unwavering support throughout this journey.

To the reader, we hope this book will guide you through your own journey into the future of contrast agents for MRI.

Valérie C. Pierre and Matthew J. Allen

Contents

Chapter 1	General Synthetic and Physical Methods	1
	<i>Quyen N. Do, James S. Ratnakar, Zoltán Kovács, Gyula Tircsó, Ferenc Krisztián Kálmán, Zsolt Baranyai, Ernő Brücher and Imre Tóth</i>	
1.1	Ligand Synthesis and Characterization	1
1.1.1	Relationships between Ligand Structure and Complex Properties	1
1.1.2	Ligand Design for MRI Contrast Agents	5
1.1.3	Synthetic Methods	15
1.1.4	Purification and Characterization of Ligands	27
1.2	Synthesis and Characterization of Metal Complexes	32
1.2.1	Preparation of Metal Complexes	32
1.2.2	Characterization of Metal Complexes	34
1.3	Stability of Metal Complexes	40
1.3.1	Introduction	40
1.3.2	Equilibrium Constants Used to Characterize Metal–Ligand Interactions	41
1.3.3	Equilibrium Models	46
1.3.4	Physicochemical Methods for Characterizing Metal–Ligand Interactions	51
1.3.5	Stabilities of Gadolinium Complexes: Selected Examples	69
1.3.6	Acknowledgements	74
1.4	Lability of Metal Complexes	75
1.4.1	Introduction	75
1.4.2	Dissociation Kinetics of Metal Chelates	76

1.4.3	Methods for Kinetic Studies	81
1.4.4	Decomplexation Reactions near Physiological Conditions	82
1.4.5	Effect of Ligand Structure on the Inertness of Gadolinium Complexes	88
1.4.6	Acknowledgements	95
	Notes and References	95
Chapter 2	Gadolinium-based Contrast Agents	121
	<i>Lothar Helm, Janet R. Morrow, Christopher J. Bond, Fabio Carniato, Mauro Botta, Mihály Braun, Zsolt Baranyai, Rosa Pujales-Paradela, Martín Regueiro-Figueroa, David Esteban-Gómez, Carlos Platas-Iglesias and Timothy J. Scholl</i>	
2.1	General Theory of the Relaxivity of Gadolinium-based Contrast Agents	122
2.1.1	Definition of Relaxivity	122
2.1.2	Theory of Inner-sphere Relaxivity	124
2.1.3	Theory of Outer-sphere Relaxivity	127
2.2	Measuring Longitudinal (T_1) and Transverse (T_2) Relaxation Times	128
2.2.1	General Experimental Method to Measure T_1	128
2.2.2	General Experimental Method to Measure T_2	132
2.3	NMRD Profiles: Theory, Acquisition, and Interpretation	135
2.3.1	Acquisition of NMRD Profiles	135
2.3.2	Theory and Interpretation of NMRD Profiles	136
2.4	Measuring Water Coordination Numbers (q)	139
2.4.1	Hydration: Inner- <i>Versus</i> Outer-Sphere Water Ligands	139
2.4.2	Oxygen-17 NMR Spectroscopy	139
2.4.3	Luminescence Spectroscopy	142
2.4.4	Electron Nuclear Double Resonance	149
2.4.5	Single Crystal X-ray Diffraction	151
2.4.6	Extended X-ray Absorbance Fine Structure Spectroscopy	151
2.5	Measuring Rotational Correlation Times (τ_R)	153
2.5.1	Fit of NMRD Profiles	154
2.5.2	Debye–Stokes Equation	156
2.5.3	Oxygen-17 $1/T_1$ NMR Spectroscopy	156
2.5.4	Deuterium-NMR Spectroscopy	157

2.5.5	Carbon-13-NMR Spectroscopy	158
2.5.6	Hydrogen-NMR Longitudinal Relaxation Rates (Curie Mechanism)	161
2.6	Measuring Water Residence Times (τ_M)	164
2.6.1	Variable Temperature Oxygen-17-NMR Spectroscopy	164
2.6.2	Variable Temperature Hydrogen-NMR Spectroscopy	169
2.6.3	$1/T_1$ Hydrogen-NMRD Profiles	170
2.6.4	Temperature Dependence of Proton Relaxivity	171
2.7	Measuring the Concentration of Gadolinium	174
2.7.1	Importance of Accurate Measurements	174
2.7.2	Mineralization Monitored by NMR Relaxometry	175
2.7.3	Metal Analysis with Plasma Techniques	177
2.7.4	High-Resolution NMR Technique: Bulk Magnetic Susceptibility	180
2.7.5	Complexometry	182
2.8	Relaxometric Titrations	187
2.8.1	Determination of the Binding Parameters: E- and M-titrations	188
2.8.2	The Enhancement Factor ϵ^*	192
2.8.3	Experimental Procedure	194
2.9	Computational Methods	196
2.9.1	Molecular Mechanics and Molecular Dynamics Simulations	196
2.9.2	Semi-empirical Calculations	198
2.9.3	Density Functional Theory and <i>Ab Initio</i> Methods	198
2.9.4	Basis Sets and Relativistic Effects	203
2.9.5	Solvent Effects	205
2.9.6	Practical Aspects and Selected Examples	207
2.9.7	Software	214
2.9.8	Acknowledgements	214
2.10	Acquiring Phantom Images	215
2.10.1	Image Formation in MRI	215
2.10.2	MRI Pulse Sequences	222
2.10.3	Effect of T_1 and T_2 on Image Contrast	224
2.10.4	Measurement of T_1 and T_2 Time Constants by MRI	225
2.10.5	Field-strength Dependencies	228
	References	229

Chapter 3	Chemical Exchange Saturation Transfer (CEST) Contrast Agents	243
	<i>Giuseppe Ferrauto, Silvio Aime, Michael T. McMahon, Janet R. Morrow, Eric M. Snyder, Alex Li and Robert Bartha</i>	
3.1	General Theory of CEST Agents	244
3.1.1	General Introduction to CEST Contrast	244
3.1.2	Theoretical and Practical Considerations about CEST Agents	247
3.1.3	Practical Considerations for CEST Experiments	251
3.1.4	Classification of CEST Agents	253
3.1.5	Selected Applications of CEST and PARACEST Agents	257
3.2	Acquisition of CEST Spectra	263
3.2.1	Instrumentation and Sample Conditions for Collecting Z-Spectra to Characterize CEST Contrast	263
3.2.2	Pulse Sequences Utilized for Collecting Z-Spectra	263
3.2.3	Data Post-processing and Analysis	265
3.2.4	Acknowledgements	266
3.3	Determining q for CEST Complexes	267
3.3.1	Oxygen-17 NMR Spectroscopy for CEST Agents	267
3.3.2	Other Techniques for Gadolinium-based Complexes That Also Apply to CEST Agents	269
3.4	Determining Proton Exchange Rates (k_{ex})	274
3.4.1	Introduction to Proton Exchange	274
3.4.2	Linewidth Measurement for Assessing Exchange Rate	274
3.4.3	WEX Experiments for Assessing Exchange Rate	275
3.4.4	QUEST and QUESP Experiments for Assessing Exchange Rate	275
3.4.5	Acknowledgements	279
3.5	Preparation and Characterization of Paramagnetic Micelles and Liposomes	280
3.5.1	Routes to Enhance the Sensitivity of CEST Agents	280
3.5.2	Preparation and Characterization of Paramagnetic CEST Micelles	281

<i>Contents</i>	xi
3.5.3 Preparation and Characterization of Paramagnetic CEST Liposomes	286
3.5.4 Preparation and Characterization of Other Paramagnetic CEST Nanosystems	293
3.5.5 Preparation and Characterization of Cell-based Paramagnetic CEST Agents	296
3.5.6 CEST Readout of Binding Interactions	302
3.6 Acquiring CEST MR Phantom Images	304
3.6.1 B_0 Field Correction	304
3.6.2 B_1 Field Corrections	306
3.6.3 Continuous Wave Saturation	306
3.6.4 Practical Considerations	306
3.6.5 Field-strength Dependencies	309
References	309
Chapter 4 Iron-oxide Nanoparticle-based Contrast Agents	318
<i>Dimitri Stanicki, Luce Vander Elst, Robert N. Muller, Sophie Laurent, Delphine Felder-Flesch, Damien Mertz, Audrey Parat, Sylvie Begin-Colin, Geoffrey Cotin, Jean-Marc Greneche, Ovidiu Ersen, Benoit Pichon, Vlad Socoliuc, Victor Kuncser, Rodica Turcu, Ladislau Vékás, Paula Foster and Robert Bartha</i>	
4.1 General Theory of the Relaxivity of Particulate Contrast Agents	319
4.1.1 General Introduction to Iron Oxide Nanoparticles	319
4.1.2 Mechanisms of Relaxation of Iron Oxide Nanoparticles	322
4.1.3 Acknowledgements	330
4.2 Synthesis of Iron Oxide Nanoparticles	331
4.2.1 Mechanism of Formation	331
4.2.2 Methods for the Preparation of Magnetic Nanoparticles	332
4.2.3 Acknowledgements	338
4.3 Coatings for Iron Oxide Nanoparticles	339
4.3.1 Standard Coatings for Iron Oxide Nanoparticles	339
4.3.2 Effects of Coatings and Anchoring Groups on Magnetic Properties of Nanoparticles	353
4.3.3 Effects of Coatings on Relaxivity	356

4.4	Characterizing Functionalized Iron Oxide Nanoparticles	362
4.4.1	Characterization of the Iron Oxide Core of Functionalized Nanoparticles	363
4.4.2	Characterization Techniques for Nanoparticle Coatings	383
4.5	Magnetic Characterization	391
4.5.1	Magnetic Parameters of Iron Oxide Nanoparticles of Interest to MRI	391
4.5.2	Magnetism at the Nanoscale with Applications to Iron Oxide Nanoparticles	394
4.5.3	Characterization Techniques of Iron Oxide Nanoparticles for MRI	401
4.5.4	Acknowledgements	426
4.6	Acquiring Phantom Images with Nanoparticles	427
4.6.1	Contrast in T_2 - and T_2^* -weighted MRI	427
4.6.2	Contrast in T_1 -weighted MRI and Magnetic-field-strength Dependencies	429
	Notes and References	430
Chapter 5	Transition Metal-based T_1 Contrast Agents	448
	<i>Rosa Pujales-Paradela, Martín Regueiro-Figueroa, David Esteban-Gómez and Carlos Platas-Iglesias</i>	
5.1	Differences and Similarities Between Gd^{III} and Transition Metal Complexes	448
5.1.1	Historical Perspective	448
5.1.2	Similarities and Differences between the Coordination Chemistry of Gd^{III} , Mn^{II} , and Fe^{III}	449
5.1.3	Contributions to 1H Relaxivity and Interpretation of NMRD Profiles	453
5.1.4	Characterizing Manganese and Iron Complexes	461
5.1.5	Computational Methods	463
5.2	Determining Effective Magnetic Moment (μ_{eff})	465
5.2.1	Bulk Magnetic Susceptibility (BMS) Shifts	468
5.2.2	Superconducting Quantum Interference Device (SQUID) Measurements	469
5.3	Measuring q for Transition Metal Complexes	471
5.4	Acknowledgements	473
	Notes and References	473

<i>Contents</i>	xiii
Chapter 6 Fluorine-based Contrast Agents	479
<i>Emma Stares, Junsung Rho, Eric T. Ahrens, Paula Foster, Alex Li and Robert Bartha</i>	
6.1 Compositions for Fluorine-19 MRI Molecular Imaging Applications	479
6.1.1 Fluorine-19 MRI Probes	479
6.1.2 Perfluorocarbons (PFCs)	481
6.1.3 Emulsion Formulations for Imaging	487
6.1.4 Acknowledgements	490
6.2 Acquiring Fluorine-19 Phantom Images	491
6.2.1 Fluorine-19 Imaging	491
6.2.2 Complications of ¹⁹ F Imaging: Chemical Shift Dispersion and Multiple Peaks	492
Notes and References	493
Chapter 7 Standard Biological and <i>in vivo</i> Methods	499
<i>Tang Tang, Angeliqye Y. Louie, Eric M. Gale, Peter Caravan, Christian T. Farrar and Boris Keil</i>	
7.1 Cell Toxicity, Binding, and Uptake	499
7.1.1 Introduction and Biological Characterization of Molecular Imaging Agents	499
7.1.2 Cytotoxicity	501
7.1.3 Cell Binding	518
7.1.4 Cell Uptake	527
7.2 Distribution, Metabolism, Pharmacokinetics, and Toxicity	536
7.2.1 Rationale for Measuring Distribution, Metabolism, Pharmacokinetics, and Toxicity	536
7.2.2 Routes of Administration	537
7.2.3 Dose and Exposure	539
7.2.4 Distribution in Tissue	539
7.2.5 Pharmacokinetics and Elimination	544
7.2.6 Metabolism	552
7.2.7 Toxicity	553
7.3 Practical Aspects of Contrast-enhanced Preclinical MRI	559
7.3.1 When to Image: Molecular Probe Clearance	559
7.3.2 How to Image: MRI Methods for Probe Quantification	561

7.3.3	Where to Image: Magnetic Field Strength and Contrast Agent Relaxivity	565
7.3.4	Physiological Monitoring and Image Gating	565
7.3.5	Image Reconstruction and Probe Quantification	567
7.3.6	MRI Radio-frequency Coils	568
	Notes and References	575

Subject Index	585
----------------------	------------

CHAPTER 1

General Synthetic and Physical Methods

QUYEN N. DO,^a JAMES S. RATNAKAR,^b ZOLTÁN KOVÁCS,^{*b}
GYULA TIRCSÓ,^{*c} FERENC KRISZTIÁN KÁLMÁN,^c
ZSOLT BARANYAI,^c ERNŐ BRÜCHER^c AND IMRE TÓTH^c

^a Department of Radiology, University of Texas Southwestern Medical Center, Dallas, TX 75390, USA; ^b Advanced Imaging Research Center, University of Texas Southwestern, Dallas, TX 75390, USA; ^c Department of Inorganic and Analytical Chemistry, Faculty of Science and Technology, University of Debrecen, H-4010 Debrecen, Hungary
*Email: zoltan.kovacs@utsouthwestern.edu; gyula.tircso@science.unideb.hu

1.1 Ligand Synthesis and Characterization

QUYEN N. DO, JAMES S. RATNAKAR AND ZOLTÁN KOVÁCS*

1.1.1 Relationships between Ligand Structure and Complex Properties

Gd^{III}-based contrast agents for MRI are used in approximately 30% of MRI exams.¹ Although the FDA-approved contrast agents are among the safest drugs on the market, their core, the Gd^{III} ion, has a 50% lethal dose, (LD₅₀) around 0.1–0.2 mmol kg⁻¹.² Therefore, for medical diagnostic applications, Gd^{III} ions must be chelated by ligands to prevent the metal ion from being

released. Administration of complexes with insufficient kinetic inertness can result in the debilitating disease nephrogenic systemic fibrosis (NSF), deposition of metal in the brain, or other issues.³⁻⁵ To develop safe and efficient Gd^{III}-based (Chapter 2) and lanthanide-based CEST agents (Chapter 3) for MRI, it is important to understand the role of the ligand in determining the relaxivity, thermodynamic stability, and kinetic inertness of complexes. The fundamentals described in this chapter are intended to assist with the design of future imaging agents for MRI.

Ligands play a critical role not only in reducing the toxicity of metal ions, but also in optimizing the parameters that determine the relaxivity or CEST-enhancing ability of metal complexes. These parameters include the number of inner-sphere water molecules (q), the residence lifetime of coordinated inner-sphere water molecules (τ_M), and the rotational correlation time (τ_R). Chelators sometimes contain moieties for biosensing or reactive functionalities as points of attachment for targeting vectors. All chelators currently used in clinically approved contrast agents for MRI are octadentate ligands based either on the open-chain ligand diethylenetriaminepentaacetic acid (DTPA) or the macrocyclic ligand 1,4,7,10-tetraazacyclododecane-1,4,7,10-tetraacetic acid (DOTA) (Figure 1.1). Most reported responsive and bifunctional ligands are also derivatives of these two chelators. With both of these ligands, the ninth coordination site of Gd^{III} is occupied by a rapidly exchanging water molecule that transfers the paramagnetic relaxation effect of the metal ion to the pool of bulk water. Properties of ligands, such as total basicity (sum of the protonation constants), basicity of the first protonation site, preorganization, and rigidity, influence the thermodynamic stability and kinetic behavior of the resulting metal complexes.

The bonding in lanthanide complexes is predominantly ionic, and coordination geometries are largely determined by the steric bulk of the ligands. Because Ln^{III} ions are considered to be hard Lewis acids, they favor hard donor atoms, such as fluoride, oxygen, and, to a lesser extent, nitrogen. Ln^{III} ions typically have coordination numbers of eight or nine, and they can form stable complexes with ligands that have matching denticities. Ln^{III} ions form relatively stable complexes with ligands that enable the formation of five-membered chelate rings; ligands that form six-membered chelate rings are far less stable.⁶⁻¹²

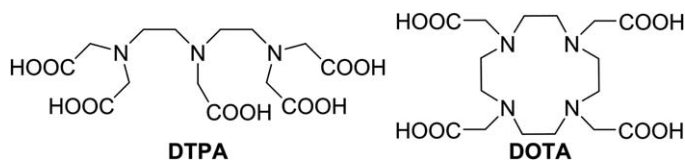


Figure 1.1 The two standard ligand scaffolds of clinically used Gd^{III} complexes: DTPA and DOTA.

The thermodynamic stability of a complex is expressed as the equilibrium constant written for the reaction between the free metal ion and the fully deprotonated ligand [eqn (1.1)].^{13–15}



The stability constant of the complex, K_{LnL} , is defined as follows:

$$K_{\text{LnL}} = \frac{[\text{LnL}]}{[\text{Ln}][\text{L}]} \quad (1.2)$$

In aqueous solution, the ligand can be fully or partially protonated depending on both the pH of the solution and the protonation constants (basicity) of the ligand. The formation of the metal complex is thus essentially a competition between protons and the metal ion for the donor sites of the ligand. Consequently, the true stability of a complex at a given pH is determined by its conditional stability constant, $K_{\text{LnL}}^{\text{C}}$, which takes into account the protonation of the ligand. Thus, for the formation of a lanthanide chelate with one inner-sphere water molecule, the stability of the complex is characterized by the following equilibrium.



$$K_{\text{LnL}}^{\text{C}} = \frac{[\text{LnL}]}{[\text{Ln}][\text{L}]_{\text{total}}} = \frac{[\text{LnL}]}{[\text{Ln}][\text{L}]\alpha_{\text{H}}} = \frac{K_{\text{LnL}}}{\alpha_{\text{H}}} \quad (1.4)$$

In eqn (1.4), $[\text{L}]_{\text{total}}$ is the total concentration of the free and protonated ligand species that are not bound to the lanthanide ion, and α_{H} is the total or equilibrium ligand concentration ratio.^{14–17} α_{H} is expressed using the $[\text{H}^+]$ and the protonation constants of the ligand as:

$$\alpha_{\text{H}} = 1 + K_1[\text{H}^+] + K_1K_2[\text{H}^+]^2 + K_1K_2 \dots K_n[\text{H}^+]^n \quad (1.5)$$

For polyaminopolycarboxylate ligands, there is a nearly linear relationship between the basicity of the ligand, determined in terms of the sum of the protonation constants, $\Sigma \log K_i$, and the stability of the corresponding Gd^{III} complexes (Figure 1.2). Deviations were reported for ligands that do not form five-membered chelate rings, for ligands that have non-coordinating peripheral groups that undergo protonation, and for non-polyaminocarboxylate ligands. For DTPA- and DOTA-type ligands, more basic ligands tend to form complexes with higher stabilities.^{15,16}

According to the chelate effect, metal complexes with polydentate ligands are more stable than similar complexes with the same number of monodentate ligands. Macrocyclic ligands with the same number of donor atoms as linear ligands tend to be even more stable; this is known as the macrocyclic effect.^{6,18–20} The chelate effect is driven by entropy because the number of particles increases as ligands displace coordinated water molecules

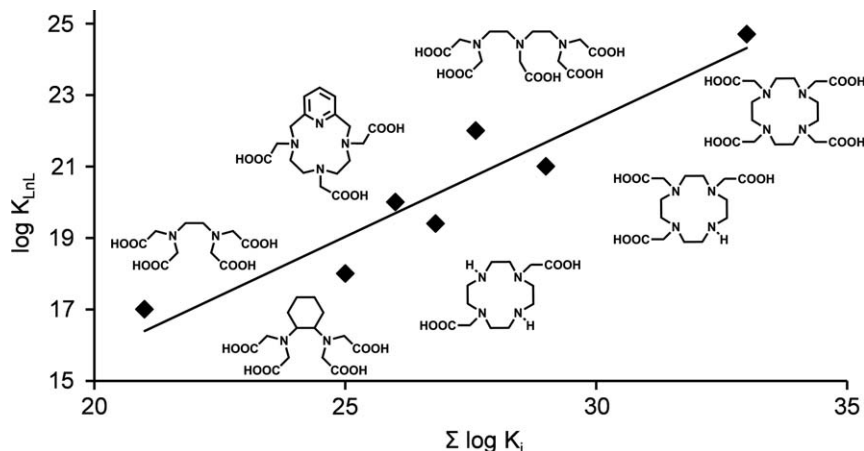


Figure 1.2 Linear correlation between the stability of the Gd^{III} complexes and the total basicity of the ligands for common polyaminopolycarboxylates. The graph is based on stability constant data reported in ref. 16.

during complex formation. There is also an enthalpic contribution to the formation of metal complexes that can be significant for some systems.^{9,21} The origin of the macrocyclic effect is at least partially due to the increased preorganization of macrocyclic ligands relative to their linear analogues.^{6,22} Therefore, less energy is needed for macrocyclic ligands to convert into the final conformation of the complex. A preorganized ligand is one whose metal-free conformation is similar to that of the metal-bound one.^{23–26} Preorganized ligands undergo minimal reorganization upon complex formation. Such ligands are important in the design of improved lanthanide-based contrast agents for MRI.²³ Conformational preorganization is often achieved with rigid ligands.^{7,27} Here, the term rigid is not limited to molecules that exist in a single minimum conformational energy. Ligands that are conformationally restricted by structural modification, most commonly either by hydrogen-bonding, by the introduction of bulky substituents, or by fusing of an aromatic or small aliphatic ring to the ligand backbone, are also rigid.^{26,27} Polyazamacrocyclic ligands with pendant coordinating side arms, such as DOTA, are less pre-organized than cryptands, spherands, and coronands, which have nearly identical conformations in the free and bound states. Nevertheless, in spite of the larger work required to convert DOTA-type ligands from their free conformations into the final metal complexes, $[\text{Ln}(\text{DOTA})]^-$ complexes are more stable than corresponding cryptand complexes. The high stabilities observed for polyazamacrocyclic ligands with acetate pendant arms are largely owing to the steric efficiency of the carboxylate groups. The carboxylate C-atom is sp^2 hybridized with a trigonal planar geometry and the oxygens are not bonded to protons. Thus, upon coordination, carboxylates create minimal steric crowding around metal ions.⁷

If a ligand is preorganized in a conformation that is not favorable to the formation of a metal complex, then the stability of the latter will be low regardless of the basicity of the ligand. This is the case for dicyclohexyl DOTA, whose lanthanide complexes are about an order of magnitude less stable than their corresponding DOTA analogues because the cyclen ring of dicyclohexyl DOTA cannot adapt the square [3333] conformation.²⁸

The basicity and rigidity of a ligand also influence the kinetic inertness (lability) of the resulting metal complexes. Flexible open chain ligands such as ethylenediaminetetraacetic acid (EDTA) and DTPA form complexes with Ln^{III} ions rapidly. Rigid open chain ligands form complexes more slowly. In such cases, the kinetics for the formation of La^{III} -CDTA (CDTA = cyclohexanediaminetetraacetic acid) indicate the rapid formation of a protonated intermediate in which La^{III} is coordinated only by the acetate groups of the ligand. The final complex is formed upon rearrangement and concomitant deprotonation of the intermediate.²⁹ Lanthanide chelates of DOTA, 3,6,9,15-tetraazabicyclo[9.3.1]pentadeca-1(15),11,13-triene-3,6,9-triacetic acid (PCTA), and several other DOTA derivatives form *via* an analogous mechanism involving mono- or di-protonated intermediates. For these ligands, the rate-determining step for the formation of the metal complex involves deprotonation of the protonated intermediate. This step is followed by a rapid rearrangement in which the metal ion moves into the cavity of the ligand.^{30,31} Because the rearrangement requires the removal of the last proton from the ligand, the rate constant for the base-catalyzed rearrangement of the protonated intermediates, k_{OH} , is inversely proportional to the $\log K_{\text{a}}$ of the most basic nitrogen of the macrocycle (Figure 1.3).^{30,32}

1.1.2 Ligand Design for MRI Contrast Agents

Ligands fulfill two main roles in Gd^{III} -based contrast agents for MRI: maximizing relaxivity and minimizing dissociation. The r_1 and r_2 relaxivities (in units of $\text{mM}^{-1} \text{s}^{-1}$) characterize the shortening effect of a contrast agent on the T_1 (longitudinal) and T_2 (transverse) relaxation times of the protons of bulk water (see Chapter 2.1). Relaxivity is influenced by a number of factors, and in this section the factors that can be modified by rational ligand design are briefly reviewed. The relaxation rate enhancement (shortening of the T_1 and T_2 relaxation times) of ^1H nuclei of the bulk water by Gd^{III} complexes originates from time-fluctuating dipolar interactions between the unpaired electrons of the Gd^{III} ion and the ^1H nuclear spins. Relaxivity has three components (inner-sphere, outer-sphere, and second-sphere) for Gd^{III} complexes that have at least one inner-sphere molecule of water. The inner-sphere contribution to relaxivity tends to be the most important and accounts for about 50–60% of the total relaxivity of most Gd^{III} complexes. A complete theoretical description is provided in Chapter 2.1. The inner-sphere relaxivity (r_i , $i = 1$ for longitudinal or 2 for transverse) is determined by a complex interplay of several parameters, such as the number of inner-sphere water molecules (q), the bound-water residence lifetime (τ_{M} , the

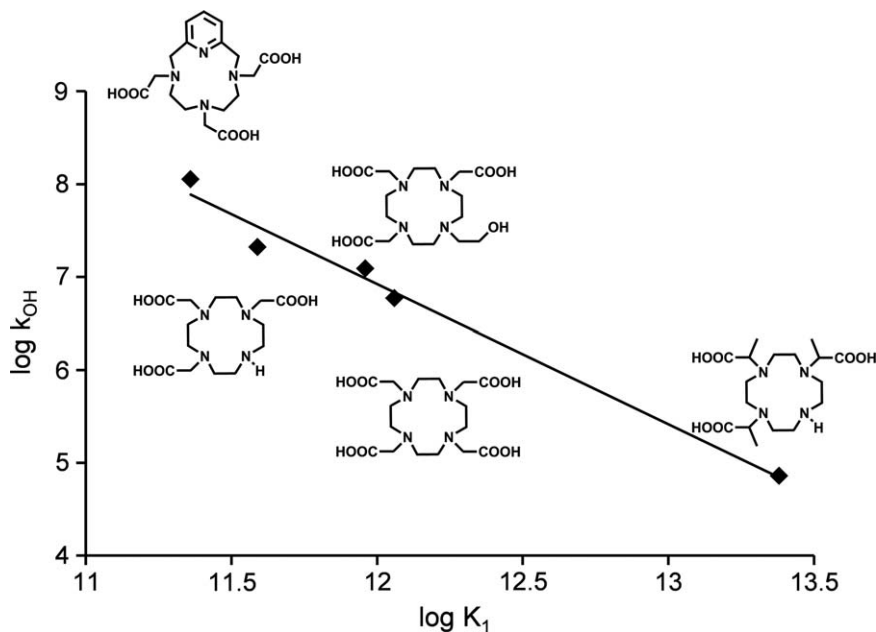


Figure 1.3 The linear dependence of the rearrangement rate of the intermediate (expressed as $\log k_{\text{OH}}$) on the basicity of the first protonation site ($\log K_1$) for Gd^{III} complexes of some 12-membered macrocyclic ligands. The graph is based on formation kinetic data reported in ref. 30 and 32.

inverse of the exchange rate, k_{ex}), the distance between the Gd^{III} ion and the protons of the inner-sphere water molecule (r_{H}), the rotational correlation time (τ_{R} , the inverse of the tumbling rate of the complex), and the electronic relaxation times (T_{1e} and T_{2e}) of the metal ion.

Of these parameters, only q , τ_{R} , and τ_{M} can be optimized reliably by ligand design. The inner-sphere contribution increases linearly with the number of inner-sphere water molecules. Lanthanide ions in general have a coordination number of eight or nine in aqueous media. The number of inner-sphere water molecules is determined by the denticity of the ligand (number of donor atoms), the steric properties of the ligand, and the size of the lanthanide ion. All clinically approved contrast agents for MRI have eight donor atoms and one inner-sphere water molecule. Ligands with fewer than eight donor atoms often form Gd^{III} complexes with two or three inner-sphere water molecules. These complexes have higher relaxivities than complexes with one inner-sphere water molecule, but the kinetic inertness of complexes with fewer donor atoms is usually lower than that of monohydrated chelates. These include the hydroxypyridinone-based tripodal chelates, which have high relaxivities and near-optimal water-exchange rates at some magnetic field strengths.³³ Although kinetically labile, these complexes are highly stable and are minimally influenced by physiologically relevant cations or anions.^{33–37} Some ligand systems with seven donor atoms form lanthanide complexes with satisfactory kinetic inertness. In particular, lanthanide

chelates of PCTA and 6-amino-6-methylperhydro-1,4-diazepinetetraacetic acid (AAZTA) and their derivatives are more inert than DTPA derivatives.^{30,38}

At the clinically relevant fields of 1.5 to 3 T, relaxivity will largely be determined by τ_M and τ_R (see Chapter 2.1). For low-molecular-weight complexes, such as $[\text{Gd}(\text{DOTA})]^-$ and $[\text{Gd}(\text{DTPA})]^{2-}$, inner-sphere relaxivity is limited by τ_R . An increase in τ_R has a strongly field-dependent effect on inner-sphere relaxivity with a maximum value that is dependent on τ_M and is usually around 1.5 T. Between 0.5 and 3 T, the gain in relaxivity is quite significant even when τ_M is not optimal. However, the effect levels off at higher fields, and above 3 T, r_1 decreases with increasing τ_R . At 9.4 T, the optimal τ_R is around 400 ps, corresponding to the tumbling rate of medium-sized rigid molecules.^{15,39,40}

In practice, slowing the tumbling rate is usually achieved by binding Gd^{III} complexes covalently or non-covalently to macromolecules, such as polymers, dendrimers, proteins, viral capsids, gold and silica nanoparticles, or nanodiamonds, or by incorporating them into self-assembling systems.^{15,39,41–58} A large number of Gd^{III} -based agents have been developed in which the Gd^{III} complex is covalently linked to a high-molecular-weight scaffold with free amino groups on the surface.^{43,59,60} The synthesis involves the functionalization of amino groups with an amine-reactive bifunctional ligand (Figure 1.4)^{61–63} followed by complexation with Gd^{III} ions.^{44,58}

In addition to the peptide-coupling or protein-labeling functional groups shown in Figure 1.4, the azide–alkyne Huisgen cycloaddition reaction, commonly referred to as click chemistry, can also be used to functionalize biomolecules, polymers, and nanoparticles with metal complexes.^{64–66} Several copper-catalyzed azide–alkyne cycloadditions as well as copper-free bifunctional chelators have been reported that contain alkyne or azide functionalities (Figure 1.5). This approach requires a complementary functional group to be synthesized into the targeting vector but offers site-selective labeling and mild reaction conditions.^{67–81}

Noncovalent interactions have also been explored to form supramolecular adducts with slow tumbling rates. Such systems include micelles and liposomes formed with Gd^{III} complexes with one or more hydrophobic tails. These systems offer the additional benefits of being able to accumulate in

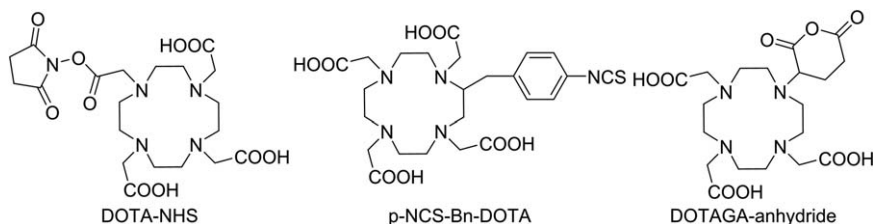


Figure 1.4 DOTA-NHS and *p*-NCS-benzyl DOTA are commonly used amine reactive bifunctional ligands. DOTAGA-anhydride is a bifunctional derivative of DOTA with a carboxylic anhydride functionality.

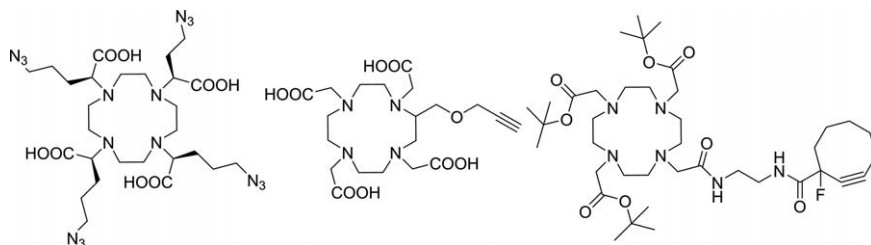


Figure 1.5 Bifunctional chelators for click-chemistry-based conjugations.

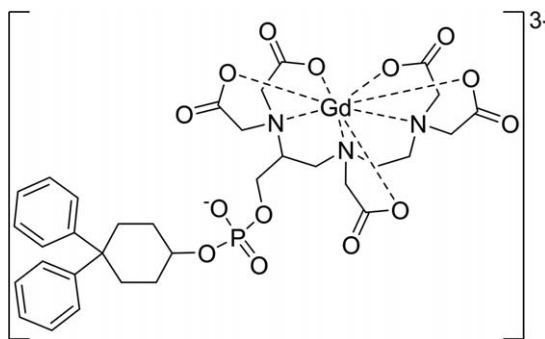


Figure 1.6 Structure of Gadofosveset (also known as Vasovist, Ablavar, and MS-325).

tumors and delivering a large payload of Gd^{III} -based contrast agents to target sites. Similar approaches have been utilized to form CEST micelle agents (Chapter 3.5.2).

When a noncovalent interaction leading to a longer value of τ_{R} involves specific binding of a Gd^{III} complex to a particular target protein, the effect is known as receptor-induced magnetization enhancement.^{82–84} Relaxation enhancement only occurs where the target receptor is present, thereby improving target-to-background ratios. One of the most successful adaptations of this concept exploits the reversible noncovalent binding of a complex to serum albumin.⁸³ Reversible binding confines the agent in the intravascular space (blood pool), increases its relaxivity, and results in high-quality vasculature angiographic images.^{85,86} The first clinically approved blood-pool agent that binds non-covalently to albumin is gadofosveset (Ablavar) (Figure 1.6). The diphenylcyclohexyl group of this DTPA-based ligand was designed to bind human serum albumin. The reversible, non-covalent binding of the complex to albumin results in favorable pharmacokinetics because the complex has increased retention in blood. Yet, it is efficiently eliminated by the kidneys as a low-molecular-weight molecule when not interacting with albumin.

While albumin is an ideal target because of its abundance and binding properties, the receptor-induced magnetization enhancement strategy is not limited to this protein. Several other Gd^{III} -based agents have been developed

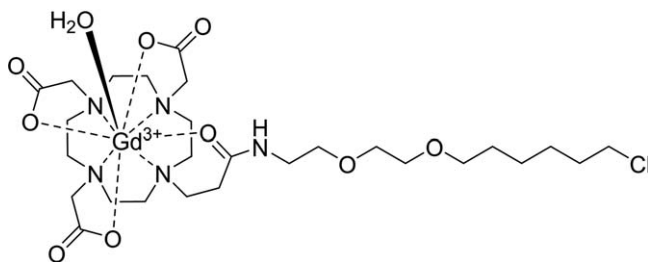


Figure 1.7 Gd^{III} complex with a chloroalkane functional group designed for conjugation to HaloTagged proteins.

that bind to other specific proteins.^{87–89} The majority of these complexes contain peptide-targeting vectors, but peptoid, DNA aptamer, and small-molecule inhibitor conjugates have also been reported.^{62,90–92} In general, the concept of receptor-induced magnetization enhancement is based on reversible binding. In some cases, however, a covalent bond can form between a complex and a protein. For example, derivatives of $[\text{Gd}(\text{DOTA})]^-$ with chloroalkane targeting moieties designed to interact with HaloTagged fusion proteins covalently bind their target protein (Figure 1.7). The HaloTag used to attach various labels to fusion proteins is a mutant bacterial haloalkane dehalogenase modified to form an ester between a chloroalkane and a specific Asp residue in the hydrophobic tunnel of a target protein. As a result of this conjugation, r_1 of the contrast agent increases from 3.8 to 22.0 $\text{mM}^{-1} \text{s}^{-1}$ at 1.5 T.

For slowly tumbling Gd^{III} complexes, τ_{M} , the residence lifetime of an inner-sphere water molecule, also influences relaxivity (see Chapter 2.1). Based on Solomon–Bloembergen–Morgan theory, the optimal value of τ_{m} is field-dependent, but should be between 10 and 50 ns for a Gd^{III} complex to achieve maximum inner-sphere relaxivity at clinically relevant fields. Typical polyaminopolycarboxylate-based monohydrated Gd^{III} complexes have longer than optimal water residence lifetimes (τ_{M} around 200 ns), although some derivatives have faster water-exchange rates.⁹³ Unlike with Gd^{III} -based contrast agents, contrast agents for chemical exchange saturation transfer (CEST) require slow water-exchange rates (see Chapter 3.1).⁹⁴

The water-exchange rates of lanthanide complexes are influenced by both the steric and electronic properties of ligands.^{15,95,96} Monohydrated Gd^{III} chelates generally have a dissociative water-exchange mechanism in which bound water dissociates before incoming water binds.⁹³ In these complexes, the exchange rate can be increased by increasing the steric crowding around the exchange site, which is known as steric compression.⁹⁷ This crowding can be achieved by inserting an extra methylene group into the polyamine backbone or the sidearm of the ligand, or by substituting the carboxylate groups with bulkier phosphonates.^{15,95,96} Backbone substitution and increased negative charge also increase the water-exchange rate, although to a smaller degree.^{95,96,98,99} Furthermore, steric compression around the site of

water coordination can be different in different isomers. Lanthanide complexes of DOTA and similar ligand derivatives often exist in two interconverting diastereomeric isomers, one of which is square antiprismatic (SAP with an N4/O4 twist angle of approximately 39°) and the other twisted square antiprismatic (TSAP with a twist angle of around -29°).^{100–102} In lanthanide complexes of DOTA-type ligands, the tetraazacyclododecane ring adopts a square conformation [3333]. All four ethylene groups have gauche conformations. Depending on the sign of the N–C–C–N torsion angle in the five-membered chelate rings, the conformation of each macrocyclic ethylene group is left-handed (λ , negative N–C–C–N torsion angle) or right-handed (δ , positive N–C–C–N torsion angle). The entire macrocyclic ring can have either a ($\lambda\lambda\lambda\lambda$) or a ($\delta\delta\delta\delta$) conformation in the complex. The helicity of the ligand pendant arms in the complex can be clockwise (Δ , positive N–C–C–O torsion angle) or counterclockwise (Λ , negative N–C–C–O torsion angle). Thus, two enantiomeric pairs of diastereoisomers exist, of which the $\Delta(\lambda\lambda\lambda\lambda)$ and $\Lambda(\delta\delta\delta\delta)$ enantiomeric pairs adopt the SAP geometry, and the $\Lambda(\lambda\lambda\lambda\lambda)$ and $\Delta(\delta\delta\delta\delta)$ enantiomeric pairs adopt the TSAP geometry.^{103,104} The basal N4 and capped O4 squares are closer to each other in the SAP isomer than in the TSAP one, making the former more compact.

The inner-sphere water molecule occupies a capping position above the O4 square and experiences less steric compression in the more compact structure of the SAP isomer. Consequently, the bound-water residence lifetime is nearly two orders of magnitude longer in the SAP isomer than in the TSAP isomer.^{105,106} Normally, these isomers interconvert by arm rotation ($\Lambda \leftrightarrow \Delta$) and ring inversion [$(\lambda\lambda\lambda\lambda) \leftrightarrow (\delta\delta\delta\delta)$], forming an equilibrium mixture.¹⁰² The SAP/TSAP ratio depends on the size of the Ln^{III} ion, the position of the steric bulk on the ligand, and other factors, including solvent and temperature.^{101,107–111} For sterically non-demanding ligand systems, larger (lighter) lanthanide ions prefer the TSAP geometry, and the SAP isomer is preferred by the smaller (heavier) lanthanides. Towards the end of the lanthanide series starting from Er^{III}, the TSAP geometry without an inner-sphere molecule of water becomes the dominant structure. Alpha substitution of the acetate sidearms increases the ratio of the TSAP isomer.^{109,110,112} Interestingly, the isomer ratio for the rigid DOTA derivative (SSSS)-(SSSS)-M4DOTMA (Figure 1.8) shows the opposite trend than that observed for [Ln(DOTA)][−] complexes: the lighter lanthanides (from Ce^{III} to Sm^{III}) almost exclusively exist in the SAP conformation, and the heavier ions prefer the TSAP geometry (Figure 1.9). The preference of SAP geometry by the early lanthanides in this case is explained by a repulsion that arises between the methyl groups present on both the sidearms and the cyclen backbone, leading to the destabilization of the more compact SAP geometry.¹¹¹ This example demonstrates the feasibility of stabilizing one isomer *via* the incorporation of steric bulk.^{113,114}

This strategic placement of bulk can be achieved by chiral substitution on the alpha carbon of the acetate side arms and on the carbon atoms of the

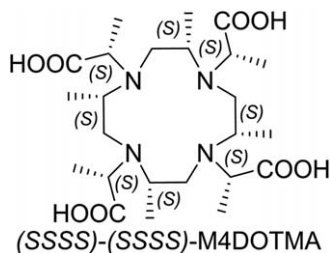


Figure 1.8 The extremely rigid polymethylated DOTA derivative forms SAP complexes with the early lanthanides.

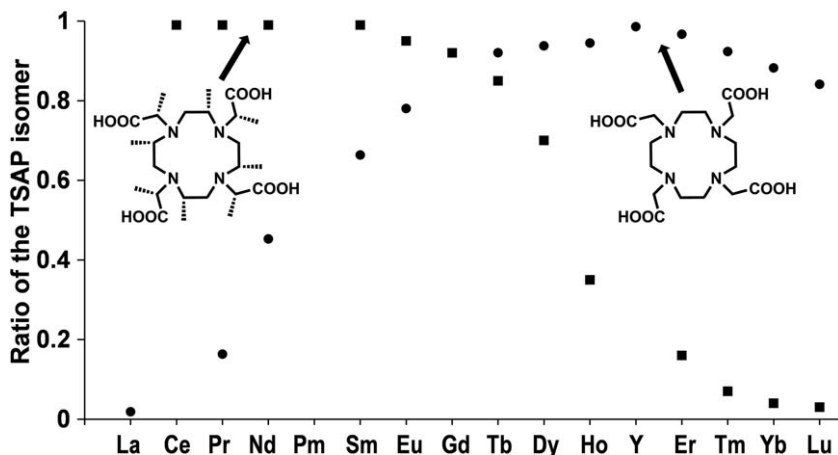


Figure 1.9 Ratio of the TSAP isomer in lanthanide complexes of DOTA and (SSSS)-(SSSS)-M4DOTMA.

macrocyclic backbone. An *RRRR* configuration of the acetate alpha carbons bearing a methyl substituent generates the Λ pendant arm helicity, and an *SSSS* configuration leads to the Δ helicity. The conformation of the macrocyclic ring can also be locked with a single nitrobenzyl group.¹¹⁵ The Eu^{III} and Gd^{III} complexes of the (*S*)-(*SSSS*) and (*S*)-(*RRRR*) diastereomers of 2-(*p*-nitrobenzyl)-DOTMA exclusively adopt the TSAP (*S*)-(*SSSS*) and SAP (*S*)-(*RRRR*) geometries, respectively (Figure 1.10). Notably, the τ_{M} value for the TSAP (*S*)-(*SSSS*) isomer is one order of magnitude lower than that of the SAP (*S*)-(*RRRR*) isomer.

Because the interaction between the Ln^{III} ion and the bound water is predominantly ionic in character, the water-exchange rate is influenced by the electron deficiency around the lanthanide ion. Indeed, negatively charged carboxylates tend to increase water-exchange rates compared with neutral coordinating groups. It has been demonstrated that in Gd^{III} complexes of derivatives of DOTA in which a single coordinating sidearm was

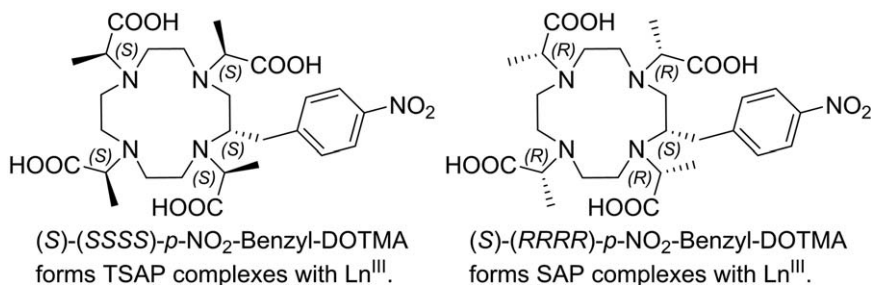


Figure 1.10 Structures of the (S)-(SSSS) and SAP (S)-(RRRR) diastereoisomers of *p*-NO₂-benzyl-DOTMA.

varied, the water-exchange rate decreases in the following order: phosphonate, phenolate > substituted acetate > acetate > hydroxamate > sulfonamide > amide, pyridyl, imidazole.^{116,117}

Consecutive substitution of amides in place of carboxylates increase τ_M roughly three- to four-fold with each substitution. The exchange rate of the inner-sphere water in lanthanide DOTAM complexes is about three orders of magnitude slower than the corresponding complexes of DOTA.⁹⁴ The exchange rate in these tetraamide chelates can further be fine-tuned by adjusting the charge and polarity of the sidearms.^{94,95} The values of τ_M in lanthanide tetraamides are strongly dependent on the size of the lanthanide ion, with a maximum value for Eu^{III}.¹¹⁸ As a result of the slow water-exchange kinetics and the favorable magnetic properties of Eu^{III} (negligible paramagnetic relaxation enhancement), [Eu(DOTA)]⁻ tetraamide complexes are effective chemical exchange saturation transfer agents (see Chapter 3.1).⁹⁴

Beyond the ability of a ligand to influence inner-sphere contributions to relaxivity, ligands also influence the contributions of second-sphere water molecules. If a ligand contains functional groups such as phosphonates and amides that can form strong hydrogen bonds, the contribution from the second-sphere water to relaxivity can be significant (see Chapter 2.1.3). Second-sphere water molecules are those that form hydrogen-bonds with the ligand on the hydrophilic side of the complex. Molecular dynamics simulations suggest that the residence lifetime of second-sphere water for Gd^{III} complexes of polyaminopolycarboxylate ligands is between 20 and 25 ps.¹¹⁹ For these complexes, second-sphere contributions to relaxivity are negligible because these residence lifetime values are too short for Gd^{III} to efficiently relax the protons of the second-sphere water.¹¹⁹ Polar groups such as phosphonates can stabilize the second coordination sphere, which increases the second-sphere relaxivity. For instance, [Gd(DOTP)]⁵⁻ (DOTP is 1,4,7,10-tetraazacyclododecane-1,4,7,10-tetramethylenephosphonic acid), which does not have inner-sphere water, has a slightly higher relaxivity than [Gd(DOTA)]⁻ because the negatively charged phosphonate groups in [Gd(DOTP)]⁵⁻ lead to a structured second hydration shell in which the hydrogen-bonded water molecules have relatively long residence lifetimes

(56 ps). This long residence lifetime combined with the anisotropy of the second-sphere hydration shell (it is on the hydrophilic side of the complex) can adequately account for the relaxivity of $[\text{Gd}(\text{DOTP})]^{5-}$ at low magnetic fields.¹¹⁹

A related Gd^{III} complex with extended, non-coordinating phosphonate groups attached to DOTA *via* amide bonds displays pH-sensitive relaxivity. The value of τ_{M} in this tetraamide complex is extremely long, yet its relaxivity increases from 3.8 to 9.8 $\text{mM}^{-1} \text{s}^{-1}$ as the pH goes from 8 to 6.^{120,121} This pH range corresponds to the protonation of the phosphonate groups. The pH-sensitive relaxivity of this complex is likely due to the modulation of the inner- and second-sphere water exchange processes by protonation of the phosphonates. Second-sphere contributions to relaxivity cannot be controlled as predictably as those arising from inner-sphere contributions, largely because the number and residence lifetime of water composing the second coordination sphere is not well defined. Nevertheless, it was demonstrated that high relaxivity agents can rationally be designed and constructed by simultaneous optimization of τ_{M} , τ_{R} , and the second-sphere organization (Figure 1.11).^{88,116,117}

The design platform in Figure 1.11 was based on the well-established DOTA framework containing an albumin-binding moiety linked to a cyclen backbone either *via* an α -substituted acetate or acetamide sidearm. Analysis of the parameters that affect inner-sphere relaxivity revealed that the two amide sidearms slow the water-exchange rate, and that this effect can be overcome by the incorporation of a phosphonate or phenolate sidearm. Another important observation is that the relaxivity of complexes with sidearms that contain two carboxylates per arm have substantial second-sphere contributions.

The development of new ligand systems for applications in MRI has remained an active area of research with major focuses on high relaxivity, targeted, and responsive agents. The main goal of targeted contrast agents is to deliver a large payload of paramagnetic centers to a target site.^{50,87,88,91,122–130} Targeting is often combined with an amplification strategy in an attempt to overcome the low sensitivity of MRI.⁵⁶ Despite progress, the disparity between the detection limit of the best T_1 -shortening agents (10–100 μM) and the concentration of target biomolecules, such as cell surface receptors (often in the nM range), remains a challenge.^{125,131,132}

Responsive contrast agents are designed to have relaxivity or CEST effect that is dependent on a triggering molecule or event, such as the presence of a specific biomarker, a physiological process, a metabolite, an ion, pH, redox potential, temperature, or enzyme activity. The design of such probes is based on the modulation of one or more parameters that influence either relaxivity or the CEST effect (including q , τ_{M} , and τ_{R}). Responsive probes based on contrast agents for CEST MRI offer some advantages over Gd^{III} complexes because Gd^{III} -based T_1 -shortening agents cannot be completely silent, even when they are turned off. In addition, changes in relaxivity in response to environmental stimuli are often only modest. With contrast agents for CEST

Gd^{III} deposition also strongly imply that open chain agents have lower stability *in vivo* than the macrocyclic ones.^{2,144,145} These reports are in agreement with *in vivo* Gd^{III} retention and *in vitro* dissociation kinetic data.¹⁴⁶ The amounts of Gd^{III} released from clinically approved agents in human serum at 37 °C over several days decreases in the following order: DTPA bis(amide)s > DTPA and sidearm substituted DTPA > backbone substituted DTPA >> macrocyclic agents.¹⁴³ Thus, it appears that the *in vivo* stability of lanthanide-based contrast agents is determined both by their thermodynamic stability and their kinetic inertness. From a ligand design point of view, the kinetic inertness can in general be improved by lowering the basicity and increasing the rigidity of the ligand.^{147,148}

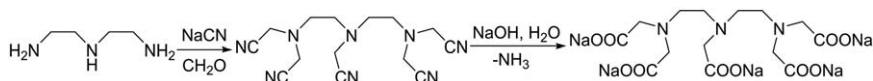
1.1.3 Synthetic Methods

This section focuses on general synthetic methods and selected reactions that are potentially useful to a wide range of readers. For more details, please refer to the following reviews on the synthesis of Gd^{III}-based contrast agents for MRI.^{16,61,62,149–164}

1.1.3.1 DTPA and its Derivatives

[Gd(DTPA)]²⁻ was the first clinically approved contrast agent for MRI. Six approved agents are based on the same open chain ligand. Diethylenetriamine is a commercially available, inexpensive starting material for the synthesis of various N-substituted derivatives of DTPA. Pentaalkylation of diethylenetriamine and backbone-substitution of diethylenetriamine derivatives is fairly straightforward (Scheme 1.1). The parent ligand DTPA was originally prepared by reacting diethylene triamine with formaldehyde and sodium cyanide in the presence of NaOH.¹⁶⁵ Under these basic conditions, the cyanomethyl intermediate instantaneously hydrolyses to give the final product and ammonia.

On a small scale, it is more convenient to introduce the acetate sidearms on a polyamine backbone with chloroacetate in basic aqueous solutions or with haloacetic acid esters (*tert*-butyl bromoacetate) in an organic solvent, such as acetonitrile or dimethylformamide (DMF), in the presence of an inorganic (for example, K₂CO₃) or organic (for example, diisopropylethylamine) base.^{166–168} The use of esters that are reactive towards nucleophilic acyl substitution, such as methyl or ethyl, can result in a competitive side reaction involving the formation of six-membered lactams between the acetate sidearm and backbone NH present in partially alkylated



Scheme 1.1 Synthesis of DTPA by cyanomethylation.

intermediates.^{169–171} For example, the desired pentamethyl ester of DTPA could not be isolated when methyl bromoacetate was used as the alkylating agent. To suppress lactam formation, it is imperative that either a bulky ester, such as *tert*-butyl, or reactive alkylating functionalities, such as triflate, be used.¹⁶⁹ A lactam ring can also form in the intramolecular condensation between a free carboxylate and NH, and syntheses should be designed to avoid such intermediates.¹⁷² The ethyl ester of DTPA can be obtained by the acid-catalyzed esterification of the free acid. Ammonolysis of the pentaethyl ester affords DTPA pentaamide in good yields.¹⁷³

Selective functionalization strategies of diethylenetriamine exploit the reactivity difference between primary and secondary amines. The more reactive primary amino groups can be protected in various forms, such as phthalimido,^{174–177} *tert*-butyl carbamate,^{172,178–181} trifluoroacetamide,¹⁸² or *p*-toluenesulfonamide,¹⁸³ offering convenient access to selectively functionalized derivatives of DTPA. Starting from these compounds, derivatives in which the secondary N-atom is selectively protected can be obtained using protecting groups such as benzyl, *tert*-butoxycarbonyl or benzyloxycarbonyl, which can be removed with different conditions (Figure 1.12).^{81,184–189} 4-Benzyl diethylenetriamine is a valuable intermediate in the synthesis of various macrocyclic ligands, including selectively protected 1,4,7,10-tetraazacyclododecane derivatives.^{183,190}

A number of DTPA analogs have been reported to have at least one pendant arm other than acetate. DTPA-bis(anhydride) (Figure 1.13) is a versatile intermediate for the synthesis of bis- and mono-amide derivatives as well as for the conjugation of DTPA to peptides and other biomolecules. Commercially available or easily prepared by the action of acetic anhydride or isobutyl chloroformate on DTPA in the presence of pyridine or triethylamine,^{191–195} this compound reacts readily with two equivalents of a primary or secondary amine in DMF, dimethylsulfoxide, or water to afford the bisamides.^{196–201}

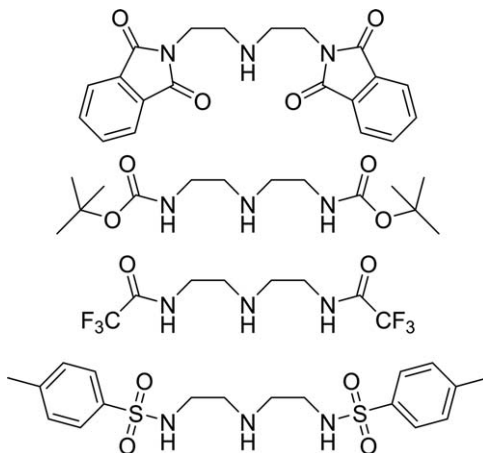


Figure 1.12 Selectively protected diethylenetriamine derivatives.

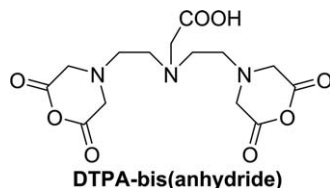
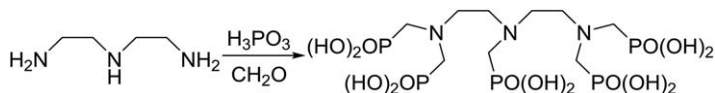


Figure 1.13 Chemical structure of DTPA-bisanhydride.



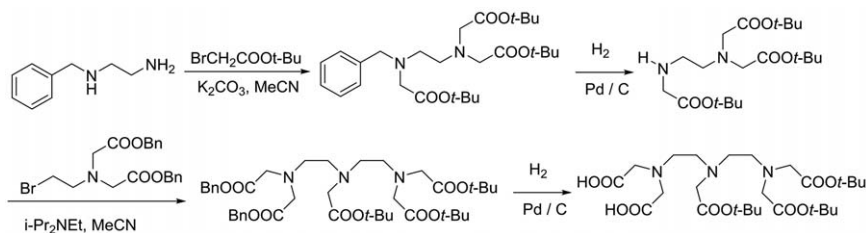
Scheme 1.2 Synthesis of diethylenetriamine pentamethylenephosphonic acid.

DTPA bis(amides) form neutral complexes with Gd^{III} , thereby affording lower osmolality solutions than $[\text{Gd}(\text{DTPA})]^{2-}$. There are two Gd^{III} -containing DTPA bisamide chelates among the approved contrast agents (Omniscan and OptiMARK). Unfortunately, these agents are strongly implicated in the development of the disease NSF. It is also possible to obtain DTPA monoamides when excess DTPA bisanhydride is used, but the product of such reactions is usually a mixture of the monoamides and bisamides, which can be challenging to separate.^{99,202} The monomethyl and monopropyl amide was also prepared through the mixed anhydride of DTPA formed with isobutyl chloroformate followed by ion-exchange purification.^{99,203} The pentamethylamide was prepared from the *N*-hydroxysuccinimidyl (NHS) ester of DTPA, prepared *in situ* by reacting DTPA bisanhydride with hydroxysuccinimide, dicyclohexylcarbodiimide, and 4-dimethylaminopyridine.⁹⁹

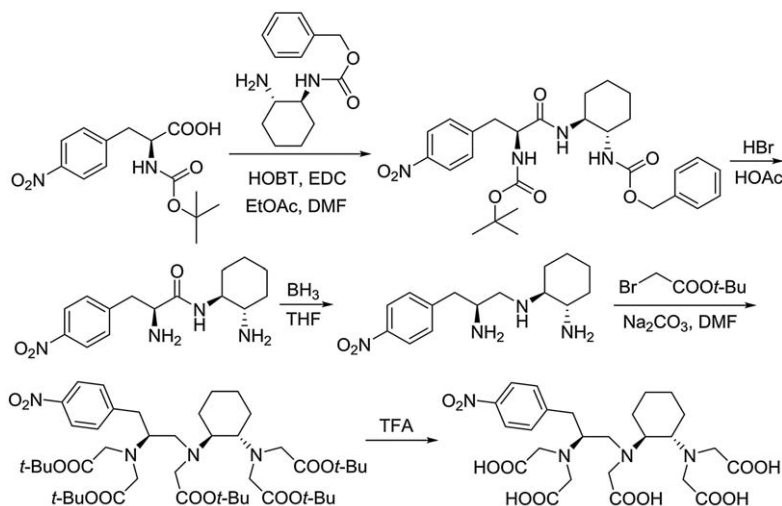
Methylenephosphonate and phosphinate derivatives of diethylenetriamine are usually synthesized in a Mannich-related reaction (the Kabachnik–Fields reaction) with formaldehyde and an appropriate phosphorus compound (H_3PO_3 , phosphite, or phosphinate esters) (Scheme 1.2).^{204,205} Diethylenetriamine penta(methylenephosphonic acid) has been prepared by reacting the triamine with formaldehyde and orthophosphorous acid in strongly acidic solution.²⁰⁶

For special purposes the diethylenetriamine backbone itself can be built from suitable precursors. The *tert*-butyl or benzyl esters of *N*-(2-bromoethyl)-iminodiacetic acid are useful reagents to introduce two or one iminodiacetic acid units by alkylating a mono- or di-amine starting material, most commonly a suitably protected ethylenediamine or amino acid derivative.^{80,99,169,207–218} For example, DTPA derivatives with orthogonally protected carboxylate groups have been synthesized by alkylating a suitably functionalized ethylenediamine triacetic acid ester with a derivative of *N*-bromoethyl-iminodiacetic acid (Scheme 1.3).

DTPA derivatives bearing substituents on a carbon atom of the triamine backbone are usually synthesized through amide derivatives made from



Scheme 1.3 Synthesis of DTPA with orthogonally protected carboxylate groups.



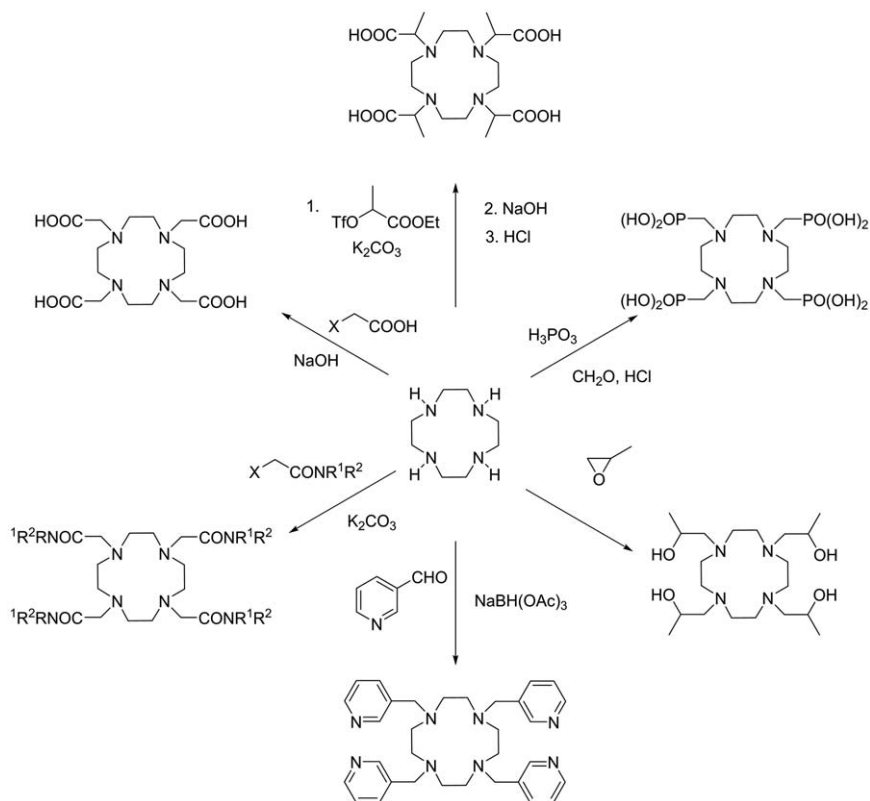
Scheme 1.4 Synthesis of backbone-substituted derivatives of DTPA.

amino acids. Methyl esters of amino acids condense with ethylenediamine or 1,2-propylenediamine to form an amide when the diamine is used as a solvent. The large excess of the diamine speeds up the reaction and suppresses bisamide formation. The amide is reduced to the amine, usually with BH_3 -tetrahydrofuran.^{98,167,219–221} However, when the use of excess diamine is not feasible (for example, due to limited availability) or when the amide formation with the diamine is too slow (*e.g.* for steric reasons), activated amino acid esters or a peptide coupling agent can be used to form an amide bond between a protected amino acid and a selectively mono-protected or functionalized diamine.^{171,222} This latter approach was used for the synthesis of bifunctional DTPA derivatives with a cyclohexyl rigidified backbone.^{170,223} This methodology is outlined in Scheme 1.4 showing the synthesis of one of the four stereoisomers of 2-(*p*-nitrobenzyl)-*trans*-cyclohexyl-DTPA starting from *N*-*tert*-butoxycarbonyl *L*-*p*-nitrophenylalanine. Alternatively, the amino acid methyl ester can be alkylated followed by ammonolysis and reduction of the amide groups.²²⁴

1.1.3.2 DOTA and its Derivatives

The macrocyclic chelator DOTA is superior to the linear DTPA for biomedical applications in every respect except for complex formation kinetics with lanthanide ions. The parent cyclic tetramine (1,4,7,10-tetraazacyclododecane, cyclen) was first prepared by the reduction of the cyclic diamide 1,4-ditosyl-6,11-dioxo-1,4,7,10-tetraazacyclododecane obtained by the condensation of ethylenediamine and the tosyl-protected ethylenediamine *N,N'*-diacetic acid chloride.²²⁵ Shortly thereafter, it was also obtained by the general cyclization method of Richman and Atkins.^{226,227} The original procedure reported by Richman and Atkins in 1974 employed the disodium salt of an *N*-tosylated polyamine and an appropriately protected bis-alkylating agent containing two leaving groups, such as tosyl, bromide, or mesyl. The reaction is usually performed in DMF. Surprisingly, high dilution conditions are not required because the restriction of the rotational freedom of the open-chain reactants by the bulky *p*-toluenesulfonyl groups favors macrocyclization over polymerization. Cations such as Na⁺ or K⁺ present in the reaction mixture do not induce a template effect.^{226,228} The tosyl group is usually cleaved with hot sulfuric acid.²²⁹ The scope of this methodology is somewhat limited by the harsh conditions necessary to remove the tosyl protecting groups. However, the use of other protective groups has been reported, including 2-nitrophenylsulfonyl, β-trimethylsilylethanesulfonyl, and diethoxyphosphoryl, which are easier to remove than tosyl.^{230–233} It was shown later that it is not necessary to use the preformed salts because the tosylamide can be deprotonated *in situ* with K₂CO₃ or Cs₂CO₃.²²⁹ Other variants include the use of LiOH as a base and running the reaction in a two-phase system with phase-transfer catalysts.^{234,235} Another modification uses tritosylated diethanolamine and tosylamide mono sodium salt as starting materials and microwave irradiation in DMF. Interestingly, under microwave irradiation, macrocyclization is slightly favored over the formation of ditosyl piperazine, affording tetratosyl cyclen in about a 52% yield.²³⁶ However, the Richman–Atkins procedure is not amenable for scale-up, and consequently, several specific synthetic approaches were developed that are more convenient for industrial-scale production.^{237–241}

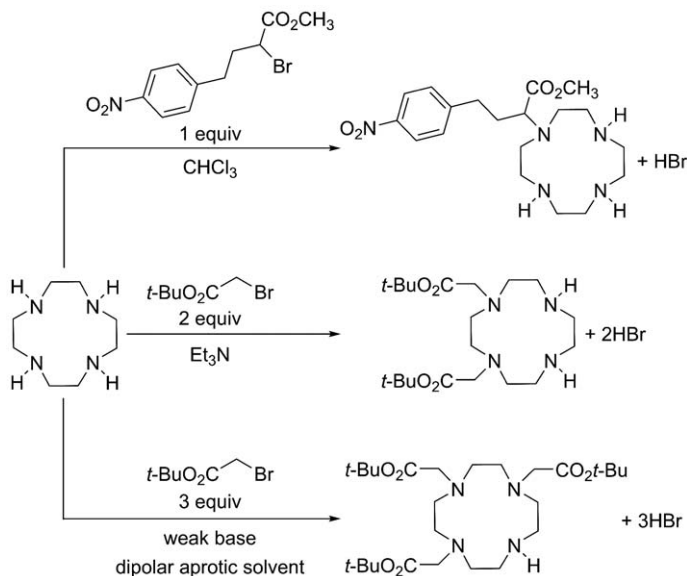
Cyclen can be easily tetraalkylated with a variety of alkylating agents (Scheme 1.5).^{105,112,242–246} By far, DOTA is the most significant cyclen derivative. It is usually prepared by reacting cyclen with four equivalents of bromo- or, more preferably, chloro-acetic acid in basic aqueous solution.^{246–248} The pH of the reaction mixture is maintained above 10 with the addition of NaOH. The [Gd(DOTA)][−] complex (gadoteric acid, sold as the meglumine salt under the trade names Dotarem, Artirem, or Dotagita) is possibly the safest MR agent in clinical practice today.²⁴⁹ Tetraamide derivatives of DOTA have received a considerable amount of attention because their lanthanide complexes have markedly different exchange and kinetic properties from the corresponding DOTA chelates. Certain lanthanide complexes of DOTA tetraamides have found application in MRI as CEST



Scheme 1.5 Selected reactions for the tetrafunctionalization of cyclen.

agents (see Chapter 3).⁹⁴ DOTA tetraamides are usually synthesized by alkylating cyclen with bromo- or chloroacetyl amides in a dipolar aprotic solvent, most commonly acetonitrile or DMF in the presence of a base such as K_2CO_3 or *i*-Pr₂NEt. Alternatively, tetraamide derivatives of DOTA can be prepared starting from DOTA and activating the carboxylates with a peptide coupling agent (such as benzotriazole-1-yl-oxy-tris(dimethylamino)-phosphonium hexafluorophosphate or 2-(1*H*-benzotriazole-1-yl)-1,1,3,3-tetramethyluronium hexafluorophosphate followed by treatment with an amine. This latter approach can be useful when the haloacetyl amides are not available, but the yields can be less than satisfactory and the isolation and purification of the product can be difficult, especially when the product tetraamide is water soluble.⁹⁴

A number of tetrasubstituted derivatives of cyclen with methylenephosphonate and phosphinate sidearms have been reported.^{242,250–262} The most important is DOTP, whose Tm^{III} complex is a popular *in vivo* shift reagent for MRI.^{263,264} DOTP is prepared by reacting cyclen with excess phosphoric acid and formaldehyde in a strongly acid solution.²⁴²



Scheme 1.6 Direct mono-, bi-, and trifunctionalization of cyclen.

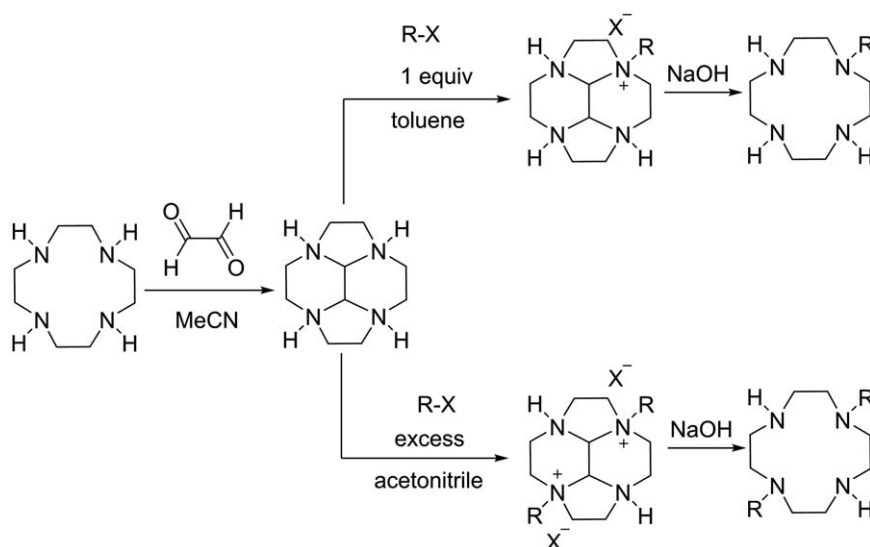
Selective functionalization of cyclen is particularly important because mono-, bi-, and tri-functionalized cyclen-based intermediates are frequently used in the synthesis of responsive and bifunctional derivatives. There are many reported synthetic routes to selectively *N*-functionalize cyclen. These routes have been described in several excellent reviews,^{16,151–153} and this section focuses on only the most versatile methodologies (Scheme 1.6).

Interestingly, cyclen displays some preference for selective monoalkylation with certain alkylating agents in nonpolar, aprotic solvents, such as chloroform, in the absence of base. Yields in the range of 70 to 80% have been reported for some alkylating agents; however, purification using flash chromatography was necessary to remove over-alkylated derivatives.²⁶⁵ In the presence of weak bases, such as Et_3N , NaHCO_3 , or NaOAc , selective 1,4-bis- and 1,4,7-tris-alkylations were observed with various alkylating agents, such as *tert*-butyl bromoacetate, benzyl bromide, or chloroacetamides.^{266,267} The products are often isolated as monohydrobromide or chloride salts from which free bases can be liberated. The regioselectivity in these reactions arises from the formation of monoprotonated products that lower the nucleophilicity of unalkylated *N*-atoms.

Based on this approach, several procedures have been published for the synthesis of DO3A-tris(*t*-Bu ester), which is one of the most useful selectively functionalized derivatives of cyclen.²⁶⁸ For small-scale (<2 g) syntheses, cyclen can be reacted with three equivalents of *tert*-butyl bromoacetate in acetonitrile in the presence of sodium bicarbonate or Et_3N . The fully deprotonated DO3A-*t*-Bu ester is obtained after column chromatography.^{267,269–272} On a larger scale (<100 g) DO3A-*t*-Bu can be prepared

without the need for chromatographic purification by alkylating cyclen with three equivalents of *tert*-butyl bromoacetate using NaOAc as a base in dimethylacetamide.^{273–275} The product is crystallized from the reaction mixture as the monohydrobromide salt. It can be deprotonated with aqueous potassium hydroxide and extracted into hexanes or ether. Removal of the solvent yields the free base as an oil that solidifies upon standing.²⁶⁸ Other esters of DO3A have also been prepared this way.^{276,277}

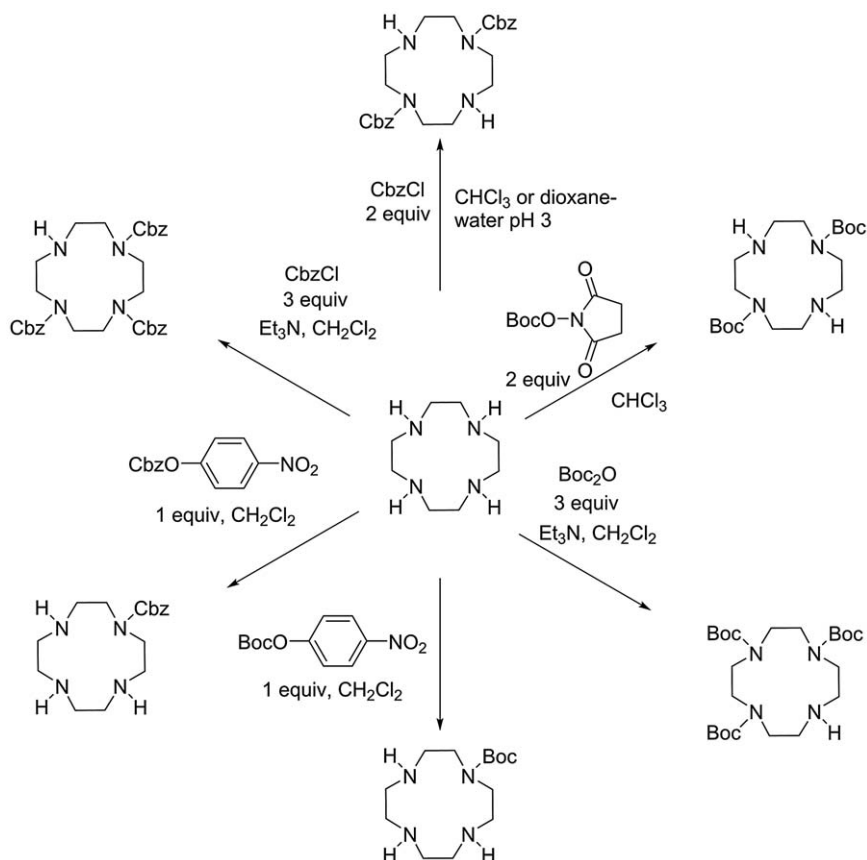
The synthesis of partially functionalized cyclen derivatives by direct regioselective alkylation is extremely attractive because it can shorten the synthesis of cyclen-based ligands with mixed sidearms. However, regioselectivity is never 100%, and therefore the products usually need to be purified by chromatography. In addition, direct regioselective functionalization of cyclen is somewhat limited in scope because it works only with a few alkylating agents. With a few exceptions, 1,7-disubstituted derivatives usually are not accessible by this approach. These limitations prompted the development of selective protection-functionalization-deprotection strategies that provide access to cyclen derivatives that cannot be synthesized by direct functionalization. The topic has been reviewed before and, therefore, only two conceptually different approaches are described here. Cyclen can easily be converted with glyoxal into a tetracyclic bisaminal (perhydro-3,6,9,12-tetraazacyclopenteno[1,3-*f,g*]acenaphthylene) that reacts with various alkylating agents to form mono- or 1,7-bis-quaternary salts, depending on the reaction conditions. These can be hydrolyzed with aqueous sodium hydroxide or deprotected with hydrazine monohydrate, hydroxylamine, ethylenedi-amine, or *o*-phenylenediamine to produce mono- or 1,7-bisalkylated derivatives in excellent yields.^{278–281} Mono- and 1,7-bisbenzyl cyclen can be obtained this way, and these are potentially useful intermediates (Scheme 1.7).



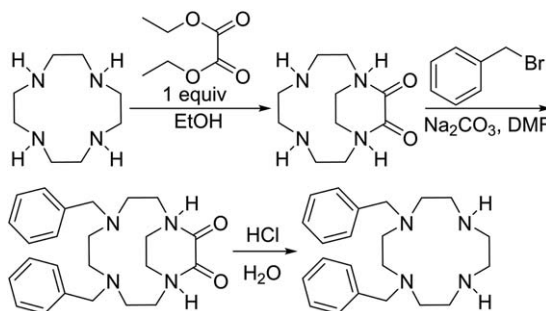
Scheme 1.7 Mono- and bis-functionalization of cyclen *via* its bisaminal derivative.

A versatile, selective functionalization of cyclen is based on the adaptation of orthogonal protection strategies used in peptide synthesis and involves the protection of one, two, or three macrocyclic N-atoms in the form of selectively cleavable carbamates. Since the introduction of benzyloxycarbonyl,²⁸² carbamate-type protecting groups have been successfully used in peptide synthesis. Benzyloxycarbonyl can be cleaved using catalytic hydrogenolysis and forms a useful orthogonal pair with the acid-labile *tert*-butoxycarbonyl and *tert*-butyl ester functionalities. Depending on the reagents and reaction conditions, cyclen can be selectively protected on one, two (1,7-bis), or three N-atoms, as illustrated in Scheme 1.8.^{283–289} The remaining N atoms can be functionalized or protected. 1,7-Bis-DO2A-*t*-Bu ester, a convenient starting material for mixed sidearm ligands, is usually prepared from 1,7-bis(benzyloxycarbonyl) cyclen.^{285,290}

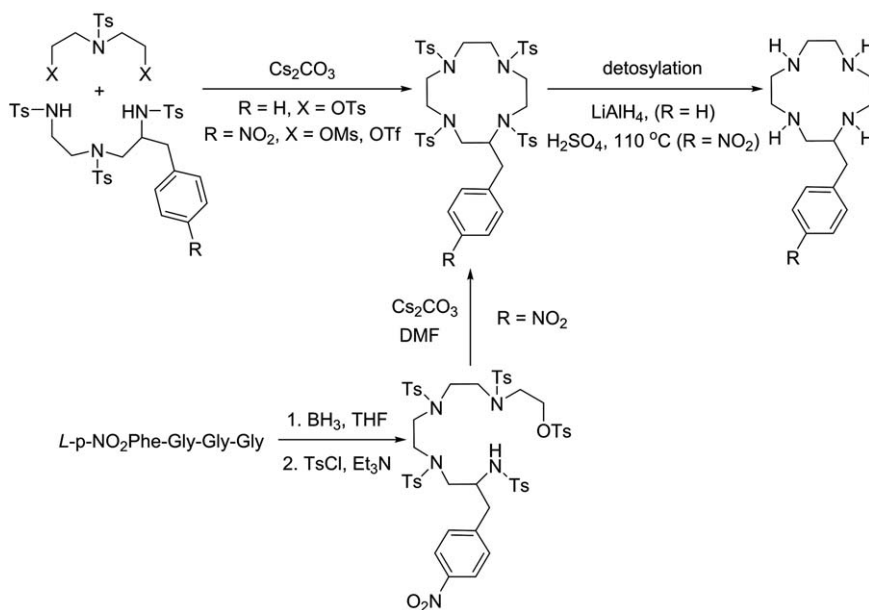
Selective 1,4-protection of cyclen is more challenging than 1,7-functionalization. A general synthetic route to 1,4-substituted cyclen proceeds through cyclenoxamide, accessible from cyclen in excellent yield, as shown in Scheme 1.9.²⁹¹



Scheme 1.8 Synthetic routes to protected derivatives of cyclen (Cbz = carboxybenzyl or benzyloxycarbonyl, Boc = *tert*-butoxycarbonyl).



Scheme 1.9 Synthetic route to 1,4-bisfunctionalized derivatives of cyclen *via* cyclenoxamide.



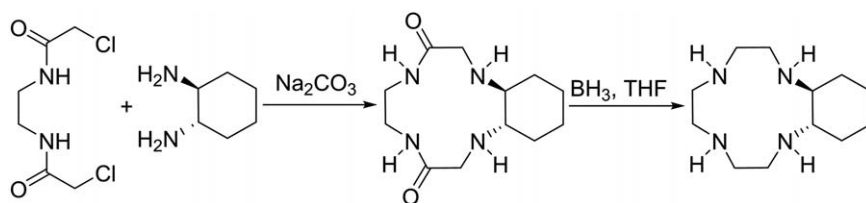
Scheme 1.10 Synthetic route to backbone-functionalized cyclen derivatives using the Richman-Atkins cyclization.

Backbone-substituted 1,4,7,10-tetraazacyclododecanes constitute an important class of cyclen derivatives. Bifunctional cyclen-based ligands, such as the widely used *p*-isothiocyanatobenzyl DOTA, have a reactive functionality attached to the macrocyclic backbone to avoid interference with the metal-binding face of the ligand. Backbone modification is also used to rigidify the resulting complex.

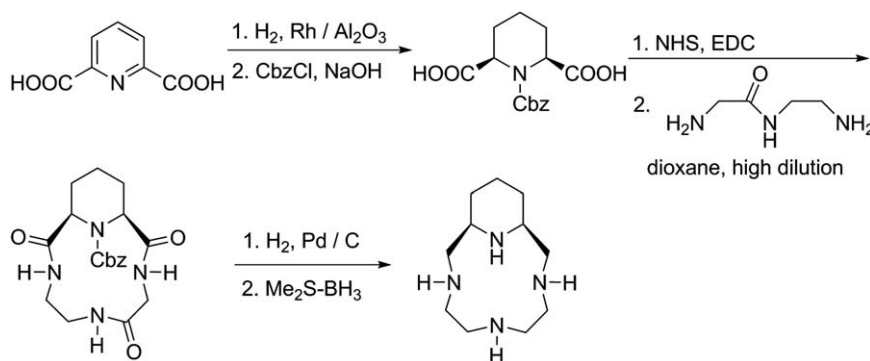
The Richman-Atkins cyclization remains one of the most versatile routes to polyaza macrocycles and can easily be adapted to synthesize backbone-substituted cyclen (Scheme 1.10). Good yields of the tetratosylated benzyl

and nitrobenzyl cyclen were achieved in bimolecular [3 + 1] or intramolecular [4 + 0] cyclization using mesyl, tosyl, or triflate as leaving groups and Cs_2CO_3 as a base.^{292–295} The nitrobenzyl derivative was desotylated with hot sulfuric acid. However, H_2SO_4 treatment of the benzyl derivative led to the formation of sulfonated side products, which were circumvented by deprotection with lithium aluminum hydride. Benzyl-functionalized cyclen was nitrated with $\text{HNO}_3/\text{H}_2\text{SO}_4$ to produce nitrobenzyl cyclen in about 60% yield.²⁹⁵

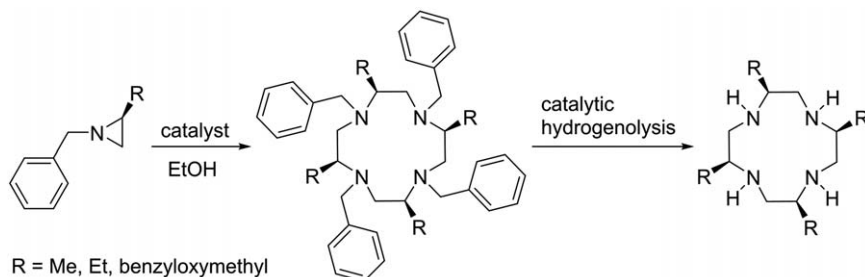
Backbone-functionalized cyclen can be synthesized *via* cyclic amide derivatives (Scheme 1.11). *p*-Nitrobenzylcyclen was obtained by alkylating *p*-nitrobenzyl ethylenediamine with ethylenediamine bis(bromoacetamide) to produce the cyclic diamide.²⁹⁶ Alternatively, macrocyclic amides were synthesized by acylating *p*-nitrobenzyl ethylenediamine or *N*-(2-aminoethyl)-*p*-nitrophenylalaninamide with a BOC-protected disuccinimidyl ester in dioxane to produce the cyclic products in about 40% yield (Scheme 1.12). These cyclizations lack the beneficial effect of the tosyl that favors macrocyclization, and therefore, they require the use of high dilution. The lower yields compared to the Richman–Atkins protocol are due to the formation of polymeric side products. The macrocyclic amide derivatives were reduced to amines with BH_3 –tetrahydrofuran or RED-Al.³⁰² Both the dialkylation and diacylation methodologies have been extended for the syntheses of



Scheme 1.11 Synthesis of backbone-functionalized cyclen *via* cyclic amide derivatives using dialkylation.



Scheme 1.12 Synthetic route to backbone-functionalized cyclen *via* cyclic amide derivatives using diacylation.



Scheme 1.13 Synthetic route to backbone-substituted cyclen *via* the tetramerization of aziridines.

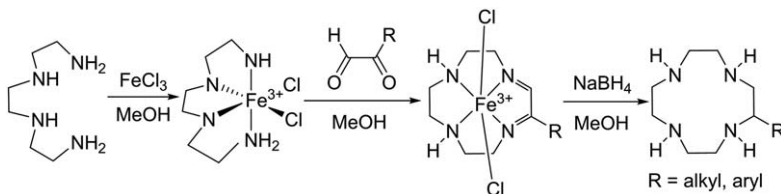
derivatives of cyclen that have a cyclohexane²⁹⁸ or piperidine ring²⁹⁹ fused into the tetraazacyclododecane macrocycle.

An interesting and unusual route to cyclen and its backbone-substituted derivatives involve the cyclotetramerization of benzyl aziridines (Scheme 1.13). *N*-Benzylaziridine leads to good yields of *N*-tetrabenzyl cyclen when heated in ethanol in the presence of a catalytic amount of *p*-toluenesulfonic acid.³⁰⁰ It was shown that C-substituted benzylaziridines as well as a few other *N*-substituted aziridine derivatives tetramerize to produce tetraazacyclododecane derivatives under the right conditions. Yields are usually low and the products require extensive purification, but the reaction offers access to backbone substituted cyclen derivatives that would be difficult to obtain by other routes. The ring opening can be brought about by various catalysts, including *p*-toluenesulfonic acid, anodic oxidation, $\text{BF}_3 \cdot \text{Et}_2\text{O}$, Cu^{II} salts, and trialkyl aluminum compounds.^{301–304} Chiral *N*-benzylaziridines, bearing a substituent on the carbon atom in position 2, undergo ring opening at the primary carbon. The resulting tetramer retains the configuration of the monomer at the secondary carbon.^{305–307}

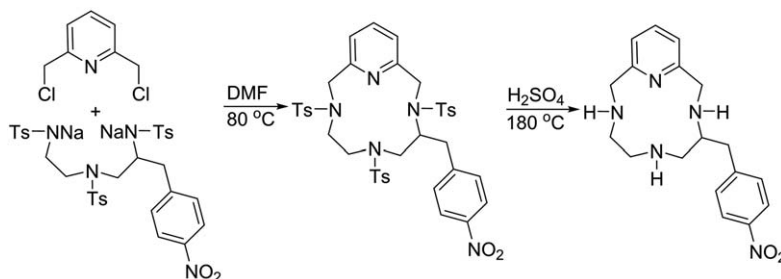
Finally, another route to obtain backbone-substituted cyclen involves Fe^{III} -templated condensation of glyoxals with the Fe^{III} complex of triethylenetetramine followed by reduction of the unsaturated intermediate with sodium borohydride (Scheme 1.14).^{308,309}

1.1.3.3 PCTA and AAZTA

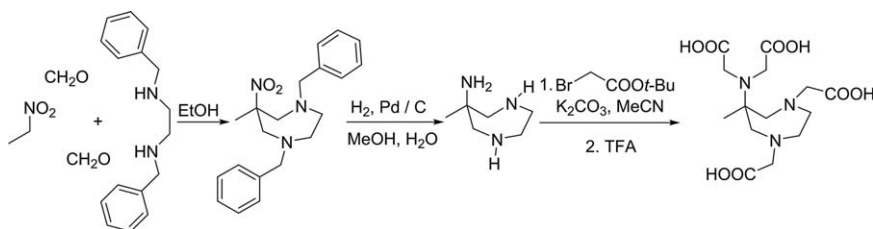
The two heptadentate ligands PCTA and AAZTA form complexes with lanthanide ions that contain two inner-sphere molecules of water. These complexes have more favorable formation and water-exchange kinetics than the corresponding DOTA complexes and maintain sufficiently high thermodynamic stability and kinetic inertness for *in vivo* applications. PCTA contains a pyridine ring fused to a cyclen ring and can be considered to be a rigidified DO3A analog.³⁰ The parent macrocycle cyclen as well as backbone-substituted derivatives can be synthesized using the Richman–Atkins methodology (Scheme 1.15).^{310–313}



Scheme 1.14 Fe^{III}-templated synthetic route to backbone-functionalized cyclen.



Scheme 1.15 Richman-Atkins synthesis of derivatives of pycnen.



Scheme 1.16 Synthesis of 6-amino-6-methylperhydro-1,4-diazepine tetraacetic acid (AAZTA).

AAZTA and its derivatives can be considered as crossover ligands between the open-chain ligands EDTA and DTPA and macrocyclic ligands such as DOTA or NOTA (1,4,7-triazacyclononane-*N,N',N''*-triacetic acid).³¹⁴ Although AAZTA has lower denticity than DTPA or DOTA, the stability of the Ln^{III} complexes of AAZTA is comparable to that of [Ln(DTPA)]²⁻ complexes.¹⁶ The seven-membered cyclic triamine 6-amino-6-methylperhydro-1,4-diazepine can be prepared using a nitro-Mannich reaction³¹⁵ starting from *N,N'*-dibenzylethylenediamine, nitromethane, and formaldehyde (Scheme 1.16).^{314,316}

1.1.4 Purification and Characterization of Ligands

1.1.4.1 Isolation and Purification

DTPA, DOTA, and derivatives of those ligands can be purified by standard techniques used in organic chemistry; however, these compounds are quite

hydrophilic, which can make purification challenging. Crystallization from aqueous solutions is a convenient and efficient way of purification of large quantities of ligands. Chelators such as DTPA, DOTA, or DOTP can successfully be crystallized as free acids.^{242,247,317} Crystallization, however, does not always result in salt-free preparations, in which case, unwanted cations and anions can be removed by ion-exchange chromatography. The purification of DOTA is an example of how the combination of crystallization and ion-exchange chromatography can be used to obtain a high-quality product.³¹⁸ DOTA is usually synthesized by alkylating cyclen with chloroacetic acid in the presence of NaOH and is isolated by acidifying the reaction mixture below pH 3.²⁴⁷ The product that precipitates at low pH contains varying amounts of HCl and has an approximate composition of DOTA · 2HCl when isolated at pH 0.5 or DOTA · HCl at around pH 3. Below pH 3, the ligand is positively charged, and when loaded onto a strongly acidic cation exchange resin, protonated ligand binds to the resin, enabling the anions to be removed with repeated washings. The ligand can be eluted by treating the ion exchange column with a solution of ammonium hydroxide because DOTA is negatively charged above pH 4. To remove undesirable cations, excess ammonia is removed and the product is loaded on an anion exchange column. The cations are removed with washing and the product is recovered by treating the resin with a dilute solution of formic acid.³¹⁸

A general anion-exchange chromatographic method has been reported for the purification of large amounts (up to 10 g) of *p*-nitrobenzyl-backbone-substituted DTPA ligands.³¹⁹ The crude products obtained by the acid hydrolysis of the penta-*tert*-butyl esters were loaded on a cation-exchange resin, eluted with ammonium hydroxide, and recovered by removing the water and ammonia. The products were loaded onto the chloroacetate form of AG1 anion-exchange resin, which is prepared by treating the hydroxide form of the resin with a solution of ClCH₂CO₂H (1 M). The column was washed with water to remove impurities that were not bound to the resin. Finally, the products were recovered by washing the column with a linear gradient of aqueous ClCH₂CO₂H (from 0.0 to 1.0 M). Chloroacetic acid was chosen because it is a stronger acid than formic acid, which failed to elute DTPA from the resin. ClCH₂CO₂H was removed from the desired products by extracting the aqueous solutions with ether.

On a smaller scale, gel filtration chromatography³²⁰ with Sephadex G-10 medium can be conveniently used for desalting. Analytically pure samples of most ligands can be obtained by preparative high-performance liquid chromatography (HPLC) on a C18 reversed-phase column using a linear gradient of water and acetonitrile containing trifluoroacetic acid, HCl, or some other buffer (0.1 to 0.3%).³²¹ An integrated HPLC-mass spectrometry platform composed of an HPLC system, detectors, columns, and mobile phases has been developed for the purification of DOTA-based targeted diagnostic and therapeutic agents.³²²

1.1.4.2 Characterization of Ligands

The identity and purity of polyaminopolycarboxylate ligands are established by standard analytical techniques. Reverse-phase HPLC and ion-exchange chromatography are the preferred methods for assays because these methods are more sensitive than spectrophotometric and titrimetric techniques when a quality detector is used. Relatively simple polyaminopolycarboxylates, such as EDTA, DTPA, or DOTA, lack an easily detectable chromophore, and although HPLC methods based on the spectroscopic detection of the carboxylates (195–220 nm) have been developed,³¹⁸ the ligands are often complexed with Cu^{II} or Fe^{III} in a sample pretreatment step for easier detection in the UV–visible region of the electromagnetic spectrum.³²³ Derivatives with an aromatic chromophore, such as bifunctional chelators with a benzyl linker, can be detected around 250–280 nm.²²³

Other detection methods not limited by the lack of chromophores, such as evaporative light scattering, charged aerosol, or refractive index detection, have also been used in the analysis of derivatives of DTPA and DOTA. In particular, the extremely sensitive (ng to pg) evaporative light scattering detection³²⁴ works well in the characterization of conjugates of DOTA. Backbone substitution on DTPA and DOTA introduces an asymmetric center, and the stereochemistry has a significant influence on the *in vivo* stability of the resulting complexes.²²³ It is, therefore, important to determine the enantiomeric purity of such bifunctional ligands. Several chiral chromatographic methods have been explored for the chiral discrimination of the *S* and *R* enantiomers of nitrobenzyl–DOTA. A reversed-phase cyclodextrin-based column was found to give satisfactory separation of the two enantiomers of nitrobenzyl–DOTA, but chiral derivatization of the *p*-aminobenzyl derivatives with Marfey's reagent followed by chromatography on a C18 reversed-phase column failed to discriminate the resulting diastereomers.²⁹⁴

In a laboratory setting, elemental analysis is a satisfactory and cost-effective way of determining the composition of samples and provides useful information for the chelation reaction because the apparent molecular weight of polyaminopolycarboxylate ligands is usually much higher than the formal molecular weight due to protonation, water content, and inorganic salts.

NMR spectroscopy is a valuable tool for studying conformational, protonation and exchange processes of ligands. ¹H-NMR spectroscopy has been used extensively to study the protonation schemes of various polyaminopolycarboxylate ligands. In general, protonation of a functional group results in deshielding of the adjacent protons and, consequently, leads to a downfield shift of the resonance signal. The magnitude of the protonation shift depends on factors such as the nature of the protonated atom, its position relative to the observed proton, and the mole fraction of the protonated and deprotonated species at a given pH (assuming fast exchange). Therefore, the identity of the protonation sites can be established from the pH-dependence of the chemical shifts of the ¹H or ¹³C nuclei of the ligand

(NMR titration).^{325–331} ^1H -NMR studies of DTPA demonstrated that the first protonation occurred on the central nitrogen atom but the second protonation led to the formation of a di-protonated species in which only the two terminal nitrogen atoms were protonated.^{331–333} The NMR spectra of relatively rigid macrocyclic ligands such as DOTA and its derivatives are often more challenging to interpret owing to slow exchange processes.^{334–336} Below pH 1, the ^1H -NMR spectrum of DOTA has two broad acetate and four ethylene signals. At higher pH values (up to around 10), the spectrum consists of two broad peaks at 3.6 and 3.3 ppm assigned to the acetate and the ethylene protons, respectively, indicating faster molecular dynamics. The observed protonation shifts reflect the peculiar protonation scheme of this ligand (Figure 1.14).

At low pH, DOTA exists in its rigid, hexaprotonated form, $[\text{H}_6\text{DOTA}]^{2+}$, in which all four carboxylates and two nitrogen atoms that are *trans* to one other are protonated (the fully protonated form would be $[\text{H}_8\text{DOTA}]^{4+}$). Around pH 2, the two acetates attached the two protonated N-atoms deprotonate and, concomitantly, form strong H-bonds with the protonated nitrogens. At around pH 4 to 5, the acetate groups not participating in H-bonding undergo deprotonation. The prevalence of di-protonation at two macrocyclic N-atoms *trans* to one other in the pH range of 2 to 10 is a characteristic feature of DOTA and other cyclen-based ligands, and it influences the formation and dissociation kinetics of the metal complexes.

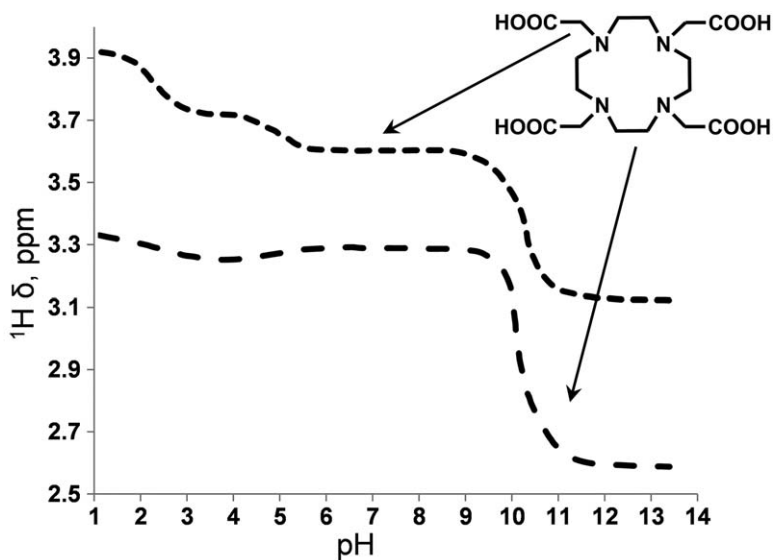


Figure 1.14 The pH-dependence of the ^1H chemical shifts of the acetate and macrocyclic protons of DOTA.³³⁴ Adapted with permission from J. F. Desreux, E. Merciny and M. F. Loncin, *Inorg. Chem.*, 1981, 20, 987. Copyright (1981) American Chemical Society.

Two-dimensional NMR techniques, such as homonuclear correlation spectroscopy (COSY), exchange spectroscopy (EXSY), nuclear Overhauser effect spectroscopy (NOESY), and heteronuclear multiple quantum coherence (HMQC) spectroscopy, have given helpful insights into the fluxional behavior of DOTA and related ligands.^{306,336} The parent compound DOTA exhibits relatively fast dynamic processes at room temperature, except at low pH. However, substitution on the sidearm alpha carbon or on the macrocyclic backbone decelerates these dynamic processes. For example, variable-temperature NMR studies revealed that *p*-nitrophenyl substitution on the alpha carbon of one acetate sidearm slows the rotation of the arms of the ligand.¹¹³ Tetramethyl substitution on the macrocyclic backbone gives rise to two slowly exchanging species with elongated geometries where the methyl substituents are positioned either close to or away from the acetate sidearms, as evidenced by HMQC spectroscopy, COSY, and EXSY.³⁰⁶ Furthermore, NaOD or KOD might not be suitable bases to adjust pH when performing NMR titrations with DOTA and related ligands because Na⁺ and K⁺ can form weak complexes with these chelators and have an appreciable effect on the NMR spectra.³³⁶

The protonation constants of the ligands and the thermodynamic stability constants of their complexes are usually determined by pH-potentiometry. This technique is described in detail in Section 1.3.

1.2 Synthesis and Characterization of Metal Complexes

QUYEN N. DO, JAMES S. RATNAKAR AND ZOLTÁN KOVÁCS*

1.2.1 Preparation of Metal Complexes

In comparison to ligand synthesis, preparation of the complexes is relatively simple. The use of high-purity ligands with a known composition facilitates the synthesis, purification, and characterization of the resulting complexes. Therefore, purification and complete characterization of the ligand, including molecular weight determination prior to complexation, is highly recommended. The optimal conditions will largely depend on the structure of the ligand: in general, macrocyclic chelators may require harsher conditions for successful complexation than linear ones. To avoid toxicity problems or incorrect physical or chemical measurements, appropriate care must be taken to ensure that the desired complex is fully formed and that no uncomplexed metal or intermediary species remain. The most important factors to be optimized include the solvent, pH, temperature, reaction time, and the metal ion source.

Water is the most commonly used solvent. However, complexation can be performed in organic solvents such as methanol or acetonitrile if there are solubility concerns with either the reactants or products. pH is one of the most important parameters to be considered. On one hand, the ligand needs to be at least partially deprotonated to interact with metal ions. In addition, the formation of DOTA-like complexes proceeds through a protonated intermediate with a base-catalyzed rearrangement as the rate-determining step of complex formation. On the other hand, above pH 6, lanthanide ions start to hydrolyze, forming undesirable hydroxo-bridged polynuclear clusters and nanoparticles, and this hydrolysis slows the formation of the complex. Thus, the optimal pH is around 5 for linear ligands and is somewhat more basic, around 6, for macrocyclic chelators. However, the optimal pH might be different for individual ligands⁵⁷⁷ and speciation diagrams calculated using the pK_a values of the ligand and the $\log K$ values of the complex and its protonated species should be consulted to determine the dominant species at a given pH. Because the formation of a complex is accompanied by the release of protons from the ligand, pH is kept in the desirable range by the addition of an inorganic base such as NaOH or by the use of buffers or weak organic bases such as pyridine.^{578,579} The progress of complexation can be monitored by the rate of change of pH. The time and temperature necessary to achieve full complexation depends on the nature of the ligand. Flexible open chain ligands such as EDTA or DTPA form lanthanide complexes nearly instantaneously at room temperature, but rigid macrocyclic ligands often require several days at elevated temperature.⁵⁸⁰ In most cases, the metal and ligand are in equimolar amounts, although excess metal can also be employed to ensure complete complexation of the ligand.^{581,582} The ligand is

rarely used in large excess except for in radiopharmaceutical preparations. Lanthanide salts like chlorides, trifluoromethanesulfonates, and acetates are convenient metal sources, but they generate an additional three equivalents of inorganic salts that might be a limitation for some applications where high osmolality is undesirable (*e.g.* liposomal encapsulation).⁵⁷⁹ Metal oxides (Gd_2O_3), hydroxides ($\text{Gd}(\text{OH})_3$), or carbonates (Gd_2CO_3) can be used in place of chlorides, and the use of these starting materials will afford salt-free complexes if the ligand does not contain extra acid.^{198,348,482,529,583–588} These starting materials work best when the ligand is in its protonated form and can be used in an equimolar ratio or in large excess followed by the removal of the undissolved oxide and the dissolved but uncomplexed metal. Complexations with metal oxides are relatively slow, and they are usually performed by refluxing the reaction mixture. The complexation is faster with lanthanide hydroxides, which should be freshly prepared by reacting the chlorides with NaOH followed by thorough washing with water.⁴⁸² The final chelate preparations often contain a slight excess of ligand (1–5%) to suppress dissociation of the complex.

Uncomplexed lanthanide ions are toxic, and their presence interferes with most physicochemical or biological applications of the complex. In a laboratory setting, a colorimetric test with a metal indicator such as xylol orange or Arsenazo III can be used to check for the presence of uncomplexed metal in solution.^{588–593} This can be done visually as a qualitative test. For example, the change of yellow color to pink in a buffered aqueous solution of xylol orange provide a visual indication of the presence of uncomplexed Gd^{III} ions in the micromolar range of concentration. The test also can be performed as a quantitative spectrophotometric method to determine the concentration of the free metal.⁵⁸⁹ An analytical HPLC method has also been developed for the detection of uncomplexed Gd^{III} in samples of ionic chelates ($\text{Gd}^{\text{III}}\text{EDTA}$, $\text{Gd}^{\text{III}}\text{DTPA}$, and $\text{Gd}^{\text{III}}\text{DOTA}$).⁵⁹⁴ It uses a second ligand (cyclohexanediaminetetraacetic acid, CDTA, in a buffered mobile phase) that forms a complex with uncomplexed Gd^{III} but does not equilibrate or react with the sample. $\text{Gd}^{\text{III}}\text{CDTA}$ can be separated from any of the other complexes using a C18 reversed-phase column equipped with a fluorescence detector (280 nm excitation and 310 nm emission wavelengths).

If a solution tests positive for uncomplexed metal then extra ligand can be added until complete complexation is achieved. If this is not a viable option, for example, due to unavailability of the ligand, then the uncomplexed metal must be removed. This removal can be done using several methods. The most common one is to raise the pH of the reaction mixture to about 8–9. The solution can then be centrifuged or filtered through a 0.2 mm syringe filter to remove precipitated hydroxide. Another frequently used method involves treating the complex solution with a chelating resin, Chelex 100 for example, at pH 6.^{581,582} Uncomplexed metal ions bind to the available iminodiacetic acid moieties on the resin, and filtration of the resin followed by washing with water results in a solution with only metal complexes.

Other methods that remove inorganic salts include dialysis, ion exchange, and gel filtration, each of them having their own advantages and limitations. Dialysis in a laboratory setting is performed against water with commercially available dialysis tubing or dialysis cassettes with the appropriate molecular-weight cutoff. Dialysis is a membrane separation process: small metal ions pass freely through the membrane, and larger molecules cannot cross. The advantage of this technique is that it does not use organic solvents and the equipment setup is minimal. Commercially available Sephadex desalting columns are well-suited to removing salts and other small molecular weight impurities from lanthanide chelate-macromolecule conjugates.

Purification of lanthanide complexes can be done *via* a wide range of methods. Crystallization is a rapid and cost effective method of purification. Depending on the ligand structure, charge, and counter ion, lanthanide chelates have been crystallized from water, methanol, ethanol, and water/alcohol or water/acetone mixtures. However, crystallization is not always successful. Alternatively, complexes can be purified using preparative HPLC, which removes inorganic salts and other unwanted impurities.⁵⁹⁵ Occasionally, it might be easier to purify the lanthanide complex than the free ligand by HPLC. In general, it is a good idea to characterize the complex *via* analytical HPLC prior to purification on a large-scale HPLC system. Symmetry C18 or Delta-Pak C4 columns are two examples of column families that are designed for rapid scaling. Semi-preparative or preparative HPLC purification is most often done using a reversed-phase C18 column. Inorganic salts can be removed with 100% water, followed by a linear gradient of 0–95% acetonitrile to elute the complex. Other solvent systems, such as water/methanol can also be used. The addition of acids, such as or trifluoroacetic acid or hydrochloric acid (0.1%), to solvent systems can improve the eluting peak shape. Ion-exchange resins can also be used to remove salts.

1.2.2 Characterization of Metal Complexes

Characterization of a metal complex starts with the analysis of its metal content. For biomedical applications, dosage is often determined based on metal content. Therefore, excess inorganic salts, ligands, and water present in the samples can increase the apparent molecular weight. The Gd^{III} content is typically measured using inductively coupled plasma atomic emission spectroscopy (ICP-AES) or inductively coupled plasma mass spectrometry (ICP-MS) (see Chapter 2.7 for details).

Lanthanide chelates of DOTA, DTPA, and related ligands exist as mixtures of interconverting coordination isomers. As described earlier, the water-exchange rates of these forms can be dramatically different, and so their ratio in the mixture can influence relaxivity. Therefore, it is fundamentally important to study the structure and interconversion of these coordination isomers. NMR spectroscopy is ideally suited for these studies. Because the dipolar field induced by paramagnetic Ln^{III} ions (other than the isotropic Gd^{III} ion) is distance- and direction-dependent, the structures of complexes

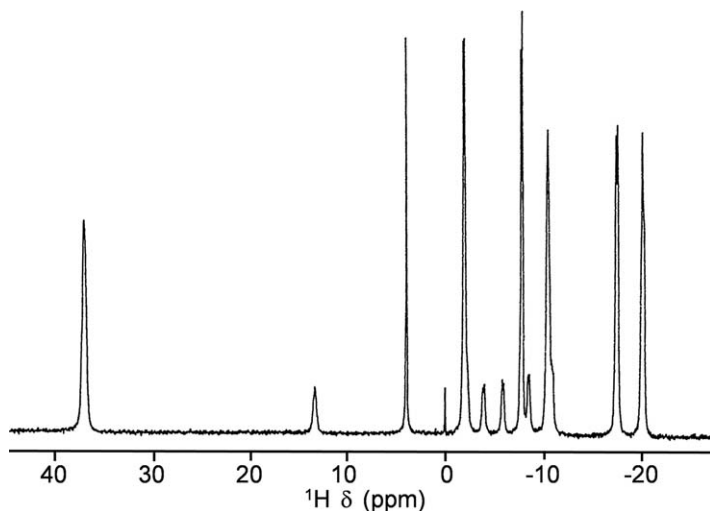


Figure 1.15 ^1H -NMR spectrum at 90 MHz of $[\text{Eu}(\text{DOTA})]^-$ (0.1 M in D_2O , pH 7) showing the presence of two isomers.¹⁰¹

Adapted with permission from S. Aime, M. Botta, M. Fasano, M. P. M. Marques, C. F. G. C. Geraldes, D. Pubanz and A. E. Merbach, *Inorg. Chem.*, 1997, **36**, 2059. Copyright (1997) American Chemical Society.

can be determined from the pseudo-contact shifts of the ^1H -nuclei of ligands.^{27,94,147,337,338} Yb^{III} is commonly used for this purpose because it induces large paramagnetic shifts with negligible line broadening, which facilitates the interpretation of NMR data. With lanthanide complexes of DOTA and related ligands, structural differences between SAP and TSAP isomers lead to dramatically different paramagnetic shifts of the axial protons of the macrocyclic ethylene bridge (H4 protons). The axial protons of the TSAP isomer lie farther away from the lanthanide ion and are not as shifted on a ^1H -NMR spectrum. For $[\text{Eu}(\text{DOTA})]^-$, the axial protons for the SAP isomer usually reside in the 31–38 ppm region, and the TSAP isomer protons are in the region of 10–14 ppm (Figure 1.15).¹⁰¹ For Eu^{III} -DOTAGly₄-based complex, the TSAP axial protons usually are around 11 ppm, compared to the ~25 ppm for the SAP isomer. Integration of axial-proton ^1H -NMR peaks gives the isomeric ratio of the two species.

Occasionally, in the case of rigid chelators where interconversion between the two isomers is slow (several hours), it is possible to separate and characterize the different coordination isomers by HPLC. Separation of the SAP and TSAP isomers for $[\text{Ln}(\text{SSSS-SSSS-M4DOTMA})]^-$ (Figure 1.8) using HPLC has been reported.¹¹¹ The relative ratio of the two isomers was determined by the integration of the HPLC peaks. In this particular case, the interconversion was slow enough to enable NMR studies of the isomers.¹¹¹

The exchange processes involving coordination isomers are generally studied using variable-temperature NMR spectroscopy.^{339,340} At low temperatures, isomeric exchange slows, enabling the observation of relatively sharp peaks of the exchanging isomers. For example, $[\text{Eu}(\text{DTPA})]^{2-}$ gives rise

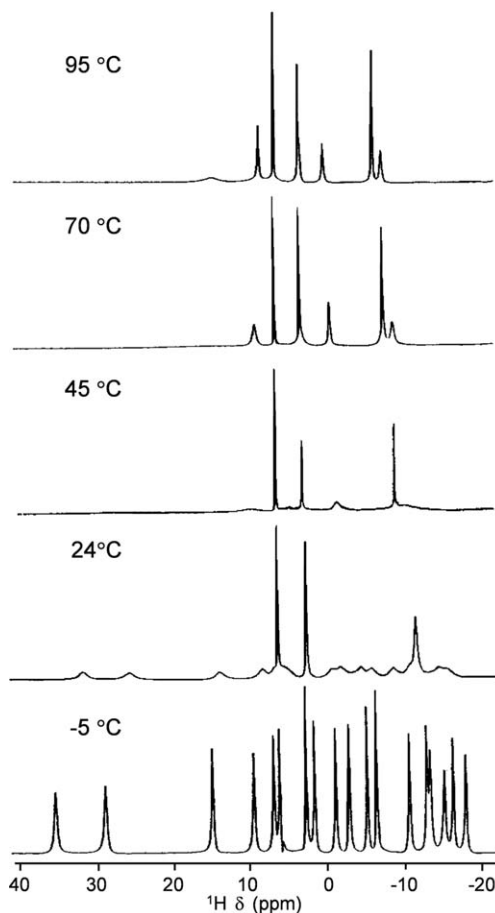


Figure 1.16 Temperature dependence of the ^1H -NMR spectrum of $[\text{Eu}(\text{DTPA})]^{2-}$ (0.2 M in D_2O at 270 MHz).

Reprinted from *Inorganica Chimica Acta*, Volume 177, S. Aime and M. Botta, Solution structure and dynamics of DTPA-Ln(III) complexes, 101–105, Copyright 1990, with permission from Elsevier.³⁴¹

to 18 proton chemical shifts that are observable at $-5\text{ }^\circ\text{C}$ but only seven at $95\text{ }^\circ\text{C}$. This difference indicates an exchange occurring between two species (Figure 1.16).³⁴¹ Variable-temperature ^{13}C - and ^{17}O -NMR spectroscopy has also been used to investigate the solution-phase structure of lanthanide complexes of DTPA and DTPA-bisamide.^{338,342} Variable-temperature NMR measurements enable determination of thermodynamic parameters that characterize exchange processes.^{339,342} Although useful, one-dimensional ^1H -NMR data of lanthanide complexes of polyaminopolycarboxylate-based ligands can be complicated, and it can be difficult to resolve individual peaks. Two-dimensional NMR techniques such as homonuclear correlation spectroscopy (COSY) and exchange spectroscopy (EXSY) are often useful in

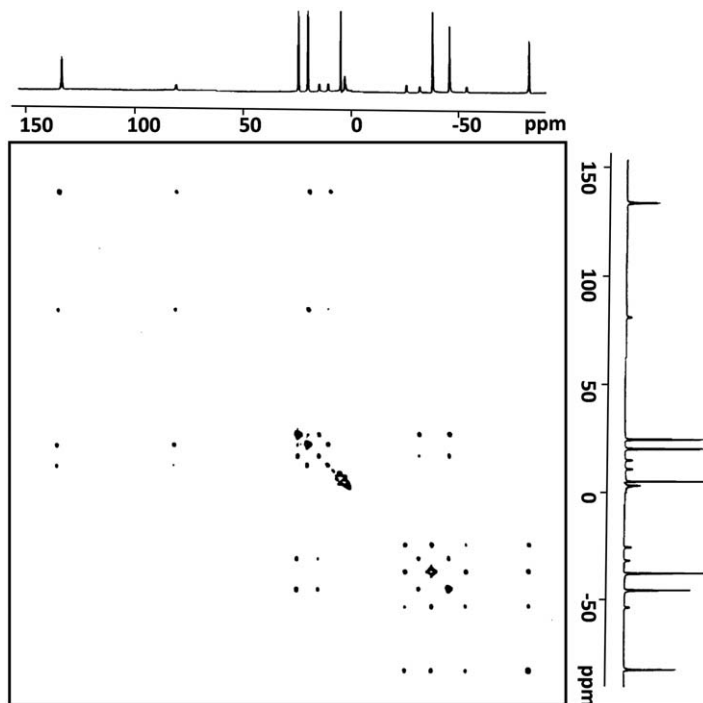


Figure 1.17 EXSY spectrum of $[\text{Yb}(\text{DOTA})]^-$ at 30 °C.¹⁰⁰
Adapted with permission from S. Aime, M. Botta and G. Ermondi, *Inorg. Chem.*, 1992, 31, 4291. Copyright (1992) American Chemical Society.

studying dynamic exchange processes and identifying exchanging species. For example, the reorientation of acetate sidearms and ring inversions can be studied with two-dimensional NMR techniques (Figure 1.17).^{100,343}

Two-dimensional NMR techniques such as COSY and EXSY can be used to assign specific resonances and are complimentary to the ^1H -NMR experiment.^{100,102,113} Two-dimensional NMR experiments offer the advantage of sampling of the entire exchange matrix in one experiment. However, because of the shortened T_1 of paramagnetic complexes, if $1/T_1 \gg k_{\text{ex}}$, the transverse magnetization can be decreased by T_1 relaxation before cross-peak intensity can accumulate. This problem can be at least partially eliminated by optimizing the mixing time.¹⁰² In variable-temperature, two-dimensional NMR experiments, the optimal mixing time must be determined at each temperature.

The presence of coordination isomers can also be studied using luminescence spectroscopy provided that the exchange is slow on the Ln^{III} emission time scale. If there is a large enough difference in the excited state lifetimes of the isomers, then the observed excitation peaks can be assigned to different species applying a time delay that is longer than the lifetime of the shorter-lived species (see Chapter 2.4.3). Alternatively, the

transition can be monitored at different emission wavelengths. If there is only one species present, then the excitation profile does not change. However, because different complexes might have different emission spectra, the dependence of the excitation profile on the emission wavelength is an indication of the presence of more than one species.³⁴⁴

Along with NMR data, X-ray crystal structures of lanthanide complexes are routinely obtained to study structural features in the solid state. Previously reported X-ray crystal structures of $[\text{Ln}(\text{DOTA})]^-$ complexes³⁴⁵ include those of Eu^{III} ,³⁴⁶ La^{III} ,³⁴⁷ Gd^{III} ,³⁴⁸ Lu^{III} ,³⁴⁹ Ce^{III} ,³⁵⁰ Pr^{III} ,³⁵⁰ Nd^{III} ,³⁵⁰ Dy^{III} ,³⁵⁰ and Tm^{III} .³⁵⁰ Although solid-state data are useful to understand structural differences between isomers, solution- and solid-state structures are not necessarily the same. In solution, the SAP and TSAP isomers coexist in equilibrium, with one often being dominant. However, in the solid state, complexes often adopt a single coordination geometry, which is not necessarily the dominant species in solution. For instance, ^1H -NMR solution studies show a 50 : 50 mix of TSAP/SAP isomers for $[\text{Nd}(\text{DOTA})]^-$, even though only SAP crystals can be grown.³⁵⁰ Preferential crystallization of the minor isomer indicates its coexistence with the major one in solution, even when its presence cannot be detected in solution. Complexes of DOTA-based ligands with bulky side arms preferentially crystallize as the TSAP isomers. Reported examples include $\text{La}(\text{DOTAAM})$ (DOTAAM = 1,4,7,10-tetrakis(2-carbamoyl ethyl)-1,4,7,10-tetraazacyclododecane),³⁵¹ $[\text{Eu}(\text{THP})]^{3+}$ (THP = 1,4,7,10-tetrakis(2-hydroxypropyl)-1,4,7,10-tetraazacyclododecane),³⁵² $\text{Gd}(\text{DO3MA})$ (DO3MA = (1*R*,4*R*,7*R*)- α,α',α'' -trimethyl-1,4,7,10-tetraazacyclododecane-1,4,7-triacetic acid),³⁵³ and $[\text{Yb}(\text{DOTPBz4})]^-$ (DOTPBz4 = 1,4,7,10-tetraazacyclododecane-1,4,7,10-tetrakis(methylenebenzylphosphinic acid)).³⁵⁴

The X-ray crystal structures of several Ln^{III} complexes of DTPA have also been reported: $\text{Ba}[\text{Nd}^{\text{III}}(\text{DTPA})(\text{H}_2\text{O})]$,³⁵⁵ $\text{Na}_2[\text{Gd}^{\text{III}}(\text{DTPA})(\text{H}_2\text{O})]$,³⁵⁶ $(\text{NH}_4)_2[\text{Gd}^{\text{III}}(\text{DTPA})(\text{H}_2\text{O})]$,³⁵⁷ and $(\text{guanidinium})_2[\text{Gd}^{\text{III}}(\text{DTPA})(\text{H}_2\text{O})]$.³⁵⁸ These structures display nine-coordinate metal ions bound to three nitrogen atoms and five carboxylate oxygen atoms of the DTPA ligand with the ninth coordination site occupied by a molecule of water. The coordination geometry is a distorted capped square antiprism. The solution structure deduced from the two-dimensional EXSY spectroscopy and lanthanide-induced relaxation enhancement of the ^{13}C -nuclei of the Nd^{III} - and Eu^{III} -complexes are consistent with the X-ray crystal structures.

Although the solid-state structures of numerous lanthanide complexes of DOTA- and DTPA-like ligands with different side arms have been reported, it is not an easy task to obtain an X-ray quality crystal of such compounds. The easiest way is often through slow evaporation of solvents. Occasionally, crystals are obtained from NMR tube samples that have been left standing on the lab bench for several days. Obtaining an X-ray quality single crystal, however, requires both laboratory skills and luck. Diffraction-quality crystals usually need to be 0.1–0.3 mm in each dimension. Water or aqueous solutions with miscible organic solvents are normally used for crystallization. Occasionally, X-ray quality crystals were obtained from an organic solvent such as methanol.¹⁹⁸

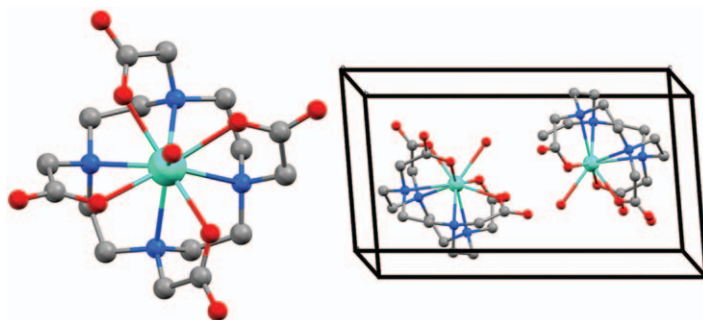


Figure 1.18 The crystal structure of sodium aqua-(1,4,7,10-tetrakis(carboxymethyl)-1,4,7,10-tetraazacyclododecane)-gadolinium tetrahydrate ($\text{Na}[\text{Gd}(\text{DOTA})] \cdot \text{H}_2\text{O}$) showing a top view of the complex on the left and the unit cell on the right (C grey, N blue, O red, and Gd green). The Na and H atoms and three non-inner-sphere water molecules are omitted for clarity. The images were generated using the Mercury software (version 3.9) provided by the Cambridge Crystallographic Data Centre (CCDC) (www.ccdc.cam.ac.uk). The CSD reference code and CCDC number associated with this crystal structure are JOPJIH01 and 1188960, respectively.

Binary solvent systems, where (1) the two liquids are miscible and (2) the compound is soluble in only one liquid but practically insoluble in the other, can afford good quality crystals. Diffusion methods require only a small amount of material; water and organic solvents such as acetone or ethanol are often good starting points.^{348,359} Regardless of the crystallization method, it might take several days or weeks to grow quality crystals.^{347,360,361} The crystal structures of several lanthanide complexes can be accessed free of charge from the Cambridge Crystallographic Data Centre (CCDC) (Figure 1.18). NMR and X-ray crystal information are often used supplementary to each other. It is often necessary to consider both crystal structure and NMR data to understand the complexity of the structure of lanthanide chelates.³⁶²

1.3 Stability of Metal Complexes

GYULA TIRCSÓ,* FERENC KRISZTIÁN KÁLMÁN, ZSOLT BARANYAI,
ZOLTÁN KOVÁCS, ERNŐ BRÜCHER AND IMRE TÓTH

1.3.1 Introduction

A large number of open-chain, macrocyclic, and hybrid complexes have been reported as diagnostic, therapeutic, and theranostic agents. Lanthanide and transition-metal ions, which are Lewis acids, are used in biological systems in the form of complexes that do not dissociate in the body because the non-complexed (“free”) metal ions tend to be toxic. These include paramagnetic lanthanides (Ln^{III}) and transition metal ions (including Mn^{II} , Fe^{III} , Fe^{II} , Co^{II} , and Ni^{II}) used in T_1 - or T_2 -shortening contrast agents or chemical exchange saturation transfer agents for MRI, and metals used in radio-pharmaceuticals, such as Cu^{II} , Ga^{III} , and In^{III} . Moreover, metal aqua ions readily hydrolyze at physiological pH forming metal hydroxides that can precipitate and are therefore not suitable for *in vivo* applications. The use of complexes in living systems necessitates the knowledge of their *in vitro* behavior. This behavior is generally characterized by physicochemical parameters such as stability constants, which in turn require knowledge of the protonation constants of the ligands, formation and dissociation rates of the complexes, and the structures of the complexes. The majority of these data are usually collected *in vitro*, but they are relevant to *in vivo* applications largely because biofluids (often referred to as competitive biological media) contain endogenous ligands and metal ions at concentrations that compete with the components of the administered complexes. Thus, knowledge of solution speciation and stability *in vitro* enables prediction of the *in vivo* fate of complexes and can yield useful information for the design of contrast agents.

Several reviews, book chapters, and books have been devoted to the physicochemical methods used to assess and refine the thermodynamic (stability) data that characterize the complexes that serve as contrast agents for MRI, including calorimetry, pH-potentiometry, and UV-visible and luminescence spectroscopies.^{363–365} In particular, there are reviews and book chapters summarizing the thermodynamic data for an extraordinarily large number of Gd^{III} complexes formed with linear and macrocyclic ligands.^{156,366–368} Detailed information on the factors affecting the stability of the complexes, such as the charge of the metal ion, hardness and softness of the metal ion and the ligand, the number of donor atoms, and the chelate and macrocyclic effects, have been discussed in numerous publications.^{369–372} Information regarding the programs used to determine stability constants^{373,374} and perform model calculations^{375–379} is also available. In fact, the speciation diagrams generated from the stability constants provide a useful pictorial overview of the different species present in multi-component systems. This is nearly impossible to do just by looking at the numerical

values of the stability constants alone. Thus, instead of discussing these data again, this chapter describes the constants that are used to characterize the strength of metal–ligand interactions and summarizes the selection of a proper equilibrium model for a given system. Additionally, more problematic cases are described that require extra attention owing to the complications associated with slow formation of complexes or the formation of stable complexes. This information is targeted at scientists interested in collecting high quality and reliable equilibrium data. The selected examples in this chapter are based on published data for Gd^{III} - (in some cases Eu^{III} -, which is used occasionally because of its luminescent properties), Cu^{II} -, and Mn^{II} -based systems.

1.3.2 Equilibrium Constants Used to Characterize Metal–Ligand Interactions

Acid-dissociation constants (K_a) of the ligands (Lewis bases) are important physicochemical parameters that are frequently determined in the first step of equilibrium studies because they must be known to quantify the competition between metal ions and protons for the ligand, that is, to determine stability constants. Ligands used in biomedical applications tend to possess several basic sites, often referred to as polydentate chelators, and therefore, several protonated species can exist in solutions of these ligands. Each species can be characterized by protonation equilibria and constants corresponding to given equilibria. Stepwise equilibria are defined by the addition of a single proton at a time [eqn (1.6) and (1.7)].



$$K_i^H = \frac{[\text{H}_i\text{L}^+]}{[\text{H}_{i-1}\text{L}][\text{H}^+]} \quad (1.7)$$

where $i = 1, 2, \dots, n$; and $[\text{H}^+]$, $[\text{H}_{i-1}\text{L}]$, and $[\text{H}_i\text{L}^+]$ are the equilibrium concentrations of H^+ , H_{i-1}L , and H_iL^+ , respectively. Note that protonation constants are the inverse of acid-dissociation constants (K_a).

The equilibrium constant for the formation of H_nL^{n+} from $n\text{H}^+$ and L (formation of n th protonation species) is known as the overall protonation constant [β_{01n} , eqn (1.8) and (1.9)];



$$\beta_{01n} = \frac{[\text{H}_n\text{L}^{n+}]}{[\text{L}][\text{H}^+]^n} \quad (1.9)$$

The total (net) basicity of a ligand, β_{01n} , is also used for comparative purposes when comparing the complexation properties of structurally

similar ligands. For instance, in the case of ethylenediaminetetraacetic acid (EDTA), the value of β_{014} is often used for this purpose, but for DOTA and its derivatives, the product of the first two protonation constants β_{012} is frequently used for the same reason.

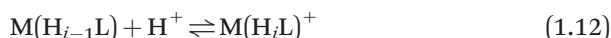
The formation equilibria of metal–ligand complexes are characterized by their stability constants, as defined by eqn (1.10) and (1.11):



$$K_{ML} = \frac{[ML]}{[M][L]} \quad (1.11)$$

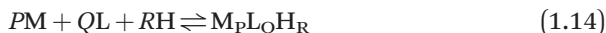
where $[ML]$, $[M]$, and $[L]$ are the equilibrium concentrations of the complex, the metal ion, and the deprotonated ligand, respectively.

Because most ligands used in contrast agents are multidentate, one or more donor atoms in the complex can be protonated at low pH. The complex might also exhibit acidic character, which in turn might lead to the coordination of hydroxide anions to produce ternary (also called mixed-ligand) complexes of the composition $M(H_{i-1}L)$ or $M(L)(OH)$. Protonated complexes are symbolized as $M(H_iL)$ and the protonation constants of such complexes are defined as in eqn (1.12) and (1.13):



$$K_{M(H_iL)} = \frac{[M(H_iL)^+]}{[M(H_{i-1}L)][H^+]} \quad (1.13)$$

where $i = 1, 2, \dots, n$; and $[H^+]$, $[M(H_{i-1}L)]$, and $[M(H_iL)^+]$ are the equilibrium concentrations of H^+ , $[M(H_{i-1}L)]$, and $M(H_iL)^+$, respectively. In practice, all of these constants are derived from the overall or cumulative equilibrium constants (β_{PQR}) defined by eqn (1.14) and (1.15). These are usually the ones calculated by fitting programs.



$$\beta_{PQR} = \frac{[M_P H_Q L_R]}{[M]^P [H]^Q [L]^R} \quad (1.15)$$

Importantly, direct comparison of stability constants of structurally diverse complexes might lead to incorrect conclusions about their stability because these comparisons do not consider the competition of the ligands between protons and metal ions, which might differ considerably from ligand to ligand. To account for the protonation of the ligand occurring simultaneously with complexation, conditional stability constants, $K_{M(L)}^c$, were

introduced. The term $K_{M(L)}^c$ reflects the apparent stability of a complex at a given pH [eqn (1.16)].³⁶³

$$K_{M(L)}^c = \frac{[ML]}{[M][L]_t} = \frac{[ML]}{[M][L]\alpha_H} \quad (1.16)$$

Where:

$$[L]_t = [L] + [HL] + [H_2L] + \dots + [H_nL] \quad (1.17)$$

$$\alpha_H = 1 + K_1[H^+] + K_1K_2[H^+]^2 + \dots + K_1K_2 \dots K_n[H^+]^n \quad (1.18)$$

Therefore:

$$K_{ML}^c = K_{ML}/\alpha_H \quad (1.19)$$

In complex biological systems, a ligand L might or might not be protonated or form complexes with endogenous metal ions such as Ca^{II} , Mg^{II} , Zn^{II} , and Cu^{II} . Likewise, complexed metal ions might or might not interact with endogenous ligands present in biological fluids, such as citrate, phosphate, or carbonate (denoted below as A, B, *etc.*). In addition, metal complexes can be protonated, and such protonated complexes can also form ternary complexes with endogenous ligands. By taking into account all of these possible equilibria, a more general conditional stability constant (K^*) can be defined as follows.

$$K^* = \frac{[ML]_t}{[M]_t[L]_t} = \frac{[ML]}{[M][L]} \frac{\alpha_{ML}}{\alpha_M\alpha_L} = K_{ML} \frac{\alpha_{ML}}{\alpha_M\alpha_L} \quad (1.20)$$

where:

$$[M]_t = [M] + [MA] + [MB] + \dots \quad (1.21)$$

$$[L]_t = [L] + [HL] + [H_2L] + \dots + [H_nL] + [Ca(L)] + [Ca(HL)] \\ + \dots + [ZnL] + [Zn(HL)] + \dots \quad (1.22)$$

$$[M(L)]_t = [M(L)] + [M(HL)] + [M(L)A] + [M(L)B] + \dots \quad (1.23)$$

$$\alpha_M = 1 + K_{MA}[A] + K_{MB}[B] + \dots \quad (1.24)$$

$$\alpha_L = 1 + K_1[H^+] + K_1K_2[H^+]^2 + \dots + K_1K_2 \dots K_n[H^+]^n + K_{Ca(L)}[Ca^{2+}] \\ + K_{CaH(L)}[H^+] + \dots \quad (1.25)$$

and

$$\alpha_{ML} = 1 + K_{M(HL)}[H^+] + K_{M(L)A}[A] + K_{M(L)B}[B] + \dots \quad (1.26)$$

The stability and protonation constants of complexes, the conditional stability constants (K^*), and the concentration of the non-complexed metal ion ($[M^{z+}]$) can be calculated using the protonation constants of the ligand. Concentration is often included when reporting studies of complexes because it is often assumed that the toxicity of metal complexes is related to the concentration of “free” metal ions released from complexes, which can be expressed as the pM value.

$$\text{pM} = -\log[M^{z+}] \quad (1.27)$$

where $[M^{z+}]$ is the concentration of non-complexed metal ion. The more stable the complex, the lower the concentration of non-complexed metal ion, and the higher the pM. The pM values for Gd^{III} complexes are calculated for the special condition as proposed by Raymond and co-workers: $[M]_t = 10^{-6}$ M, $[L]_t = 10^{-5}$ M, physiological concentration of $[\text{Ca}^{\text{II}}]$, $[\text{Zn}^{\text{II}}]$, and $[\text{Cu}^{\text{II}}]$, $\text{pH} = 7.4$.³⁸⁰ Under these conditions, ligands that do not form complexes with M^+ ions have a pM of 6.0. Tóth and co-workers suggested that pMn values could be calculated for complexes under slightly different conditions ($[\text{Mn}]_t = [\text{L}]_t = 10^{-5}$ M at $\text{pH} = 7.4$) because ten-fold excess of ligand is not used in the formulation of contrast agents.³⁸¹ Thus, the pM values calculated using these conditions appear to be much smaller (in the range of 5–10) than those of Gd^{III} complexes (values calculated for the commercially available contrast agents are >15).

Although it is relatively easy to calculate pM values because software [such as Make Equilibrium Diagrams Using Sophisticated Algorithms (Medusa) or Hyperquad Simulation and Speciation (Hyss)] exists for the calculation of species-distribution curves, there are two issues that must be addressed for the sake of clarity. According to the original definition proposed by Raymond in 1979, the pM value reflects the concentration of the non-complexed, albeit fully solvated, metal ions. The use of pM values can lead, in some instances, to erroneous conclusions, as highlighted by Meyer and co-workers.³⁷⁷ Amphoteric metal ions, such as those belonging to group 13 (Al^{III} , Ga^{III} , or In^{III}), are typical examples of coordination compounds relevant to medical-imaging applications. These ions form hydroxido complexes near pH 7.4 (-ate complexes such as $[\text{Ga}(\text{OH})_4]^-$ that can exist at low concentrations). In the presence of ligands, high pM values can be computed for such systems, misleadingly suggesting a high metal-binding affinity for a ligand. It should be realized, however, that the competition of hydroxide anions for the metal ion can be so strong that the metal ion can be displaced from the ligand. It is obvious that the inefficiency of the chelator under such circumstances is overlooked if only the concentration of the aqua cation is considered as the only representative species of the non-complexed metal.

Conversely, in the absence of complexation (*i.e.* no affinity), the lower limiting pM value equals the total metal concentration chosen to perform the speciation calculation. To avoid confusion, the relative affinity criterion, denoted $A_{L/M}$, was introduced by Meyer and co-workers.³⁷⁷ Taking into account the fraction of all metallic species remaining unbound to the ligand

of interest (L), $A_{L/M}$ serves as a universal tool for the reliable assessment and comparison of the complexing power of any ligand [eqn (1.28)]. From a practical point of view, computation of relative affinities is performed in a straightforward manner using the Apparent Constant calculator implemented in the general speciation program Hyss2009, which is available free-of-charge from the Protonic Software website.³⁷⁵

$$A_{L/M} = -\log\left(\frac{\sum[M]_{\text{unbound}}}{[M]_{\text{tot}}}\right) = -\log\left(\frac{[M]_{\text{tot}} - \sum[M]_{\text{bound}}}{[M]_{\text{tot}}}\right) \quad (1.28)$$

Meyer and co-workers treated the problem of Ga^{III} complexation by calculating the speciation diagram for the $[\text{Ga}(\text{DOTA})]^-$ complex using published stability constants.³⁸² In spite of the high pGa value of 21.6, the radiolabeling of DOTA and DOTA-type ligands with ^{68}Ga is often problematic and results in relatively low radiochemical yields.³⁸³ Moreover, in some cases the radiolabeling of DOTA and DOTA-type ligands was found to proceed with higher radiochemical yields at lower pH, which is rather unusual (coordination complexes are usually less stable under acidic conditions). As seen in Figure 1.19, Ga^{III} is fully complexed by the ligand DOTA at pH 7.4 at millimolar concentrations $[\text{Ga}^{3+}]_{\text{total}} = 1 \times 10^{-4} \text{ M}$ and $[\text{Ligand}]_{\text{total}} = 1 \times 10^{-3} \text{ M}$. However, $[\text{Ga}(\text{DOTA})]^-$ does not form near pH 7.4 at the more dilute conditions used in labeling ($[\text{Ga}^{3+}]_{\text{total}} = 1 \times 10^{-9} \text{ M}$ and $[\text{Ligand}]_{\text{total}} = 1 \times 10^{-8} \text{ M}$). These data

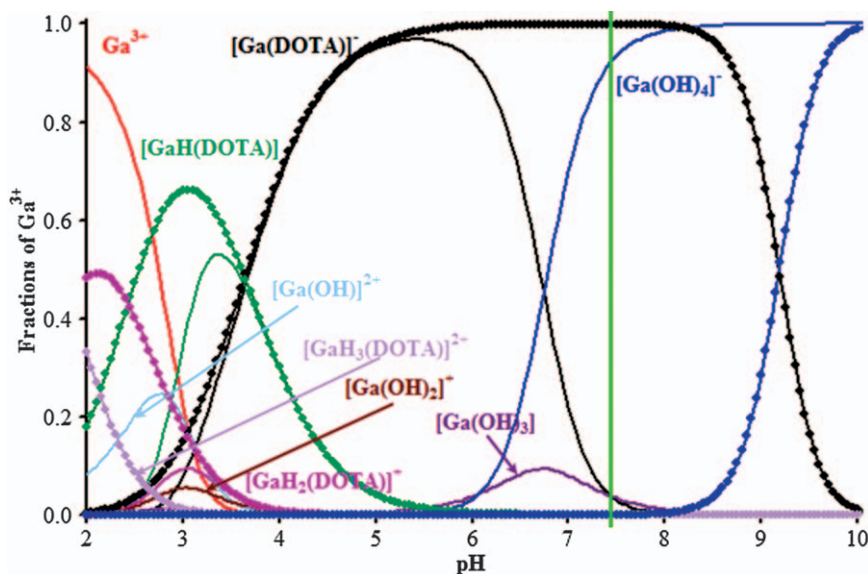


Figure 1.19 Speciation diagram (species distribution curves) for the $[\text{Ga}(\text{DOTA})]^-$ system in the pH range of 2–10 calculated using $[\text{Ga}^{\text{III}}] = 0.1 \text{ mM}$ and $[\text{DOTA}] = 1.0 \text{ mM}$ (lines with dots) and $[\text{Ga}^{\text{III}}] = 1 \text{ nM}$ and $[\text{DOTA}] = 10 \text{ nM}$ (lines without dots). Identical species are marked with the same color.

indicate that high dilutions can become problematic for radiolabeling experiments. This problem compounds itself onto the slow complexation rates that are often a bottleneck for complex formation for labeling macrocyclic ligands with short-lived radioisotopes.

1.3.3 Equilibrium Models

The first step in setting up a proper equilibrium model is a detailed investigation of the ligand, including the determination of its protonation constants and, potentially, a full characterization of the processes occurring at each protonation site. A difference between the real and estimated number of protonation steps or deviation from the actual values of the protonation constants of the ligand can significantly influence the calculated stability constants for the corresponding metal complexes. There are numerous practical methods for the determination of protonation constants in the pH range of 1.8–12.2. These methods include calorimetry, pH-potentiometry and other electrochemical methods, various spectrophotometric methods, and multinuclear NMR techniques. Problems can arise when the protonation constants of ligands do not fall into the pH range where the pH can be measured reliably with the use of combined glass electrode, for example with acidic protonation sites of phosphinates, basic protonation sites of ligands possessing phosphonate pendant arms, or basic nitrogen atoms of some cross-bridged macrocyclic polyamines.

This relationship between protonation and stability constants is demonstrated by the data reported for the first protonation constant of DOTA. This protonation constant is in the range of 10.14–12.72 and depends on the choice of the electrolyte used to set the ionic strength (the effect of the ionic strength on the protonation constants of the ligands is discussed in detail later). The reported values, however, differ by nearly 1 log unit, even for experiments performed with the same or similar ionic strengths. This discrepancy indicates the difficulty associated with the accurate measurement of such protonation constants. Performing pH-potentiometric titrations at high ligand concentrations (3.5–5.0 mM) helps resolve this problem because the equilibrium concentration of all the species present in solution are increased. Therefore, protonation and deprotonation cause larger effects that are more easily detectable by electrodes. When high concentrations are not practical, UV-visible spectroscopy or various NMR spectroscopic methods can be used as supporting techniques to determine pH values in samples from the total concentration of H^+ or OH^- ions ($c_{\text{analyte}} \ll c_{\text{H}^+}$ or OH^- and thus c_{analyte} can be neglected).^{384–386} Noszál and co-workers developed a method that relies on the readout of pH from the chemical shifts of a set of indicator molecules with known protonation constants and chemical shift dispersions in the same sample as the molecule of interest. The results obtained for two biguanidine drugs, metformin and phenformin, indicate that a set of eight indicator molecules enables the precise determination of large values of $\log K$ with high accuracy and precision.³⁸⁷

The protonation scheme of the ligands can be characterized using NMR spectroscopy, as was demonstrated for open-chain³³¹ or macrocyclic ligands.^{330,334} Spectrophotometric methods can be used to monitor protonation processes if the ligands contain chromophores close to the site of protonation and have measurable changes in their absorbance upon metal binding. For example, the protonation constants of a pyridine-based ligand were assigned using a combination of UV-visible and NMR spectroscopies.^{388,389}

Finally, before starting equilibrium studies, the nature of the electrolyte used to set ionic strength should be carefully considered. Salts such as KCl or KNO₃ have frequently been used in different concentrations to maintain ionic strength. The use of K⁺ salts is a convenient choice because K⁺ tends to form weaker complexes with ligands designed for MRI applications than Na⁺. However, the protonation constants (especially the log K_1^H) determined in the presence of K⁺ are lower than those obtained in the presence of the tetramethylammonium cation. Tetramethylammonium would be the best ion to maintain ionic strength because interactions between ligands and tetramethylammonium can be neglected. However, the evaluation of protonation constants can be challenging because protonation equilibria are shifted to more basic pH regimes without the interaction between the cation and the ligand.^{30,390–392} Thus, somewhat paradoxically, the advantages of using a salt that does not affect protonation of a ligand are outnumbered by the limitations of using one that weakly interacts with the ligand. However, it should be mentioned that the determination of a highly basic protonation constant ($pK_a \geq 12$) using NMR methods can be easily corrupted by the formation of Na⁺ or K⁺ complexes at high pH values, affecting chemical shifts. Nevertheless, to mimic *in vivo* conditions, characterization of ligands should be performed in a solution of NaCl (0.15 M). Despite some variability in the stability constants that results from differences in ionic strength, the use of NaCl does not translate into significant differences in the distribution of species because the values of protonation and stability constants are shifted in the same direction. Conditional constants and pM values measured at different ionic strengths are also usually similar for the same system.

The anions of the electrolyte can also have an effect on the outcome of characterization. For example, halogen ions are known to form stable complexes with In^{III}, Tl^{III}, and Bi^{III} ions, and thus their stability must be considered when calculating stability constants. The formation of these relatively weak complexes might actually aid the determination of stability constants because these complexes can compete with multidentate ligands at high concentrations, thereby shifting equilibria to higher pH values, where they can be followed by more common methods.^{393–396}

There are several metal ion and ligand properties that have to be considered to create a proper equilibrium model for a metal–chelate system: (i) the number of donor atoms, which is the denticity of the ligand; (ii) the coordination number of the metal ion; (iii) the type of donor atoms of the ligand; and (iv) the hard–soft character of the metal ions. Along the

lanthanide series, the coordination number of the +3 ions decreases from 9 to 8 with increasing atomic number.³⁹⁷ The coordination number of transition metals is often 6, for example, with Cu^{II}, Fe^{II}, and Fe^{III} complexes, but occasionally it can be 7, like with complexes of Mn^{II}.³⁹⁸ A comparison between the coordination number of the metal ion and the denticity of the ligand can yield useful conclusions: if the denticity is smaller than the coordination number, then the formation of ML₂ complexes, including the hydroxido species, is likely. This scenario was observed in the case of [Ln(EDTA)]⁻ complexes,^{399,400} where the formation of [Ln₂(EDTA)₃]⁶⁻ species was evidenced in addition to the presence of Ln(L) and Ln(L)₂. The existence of ternary species was confirmed by spectrophotometric method in the Nd^{III}-EDTA system. The Nd^{III} aqua ion has a low-intensity band at 427.3 nm in the absorption spectrum corresponding to a ²P_{1/2}-⁴I_{9/2} transition. This absorption is sensitive to the coordination environment of Nd^{III}, and changes in the coordination sphere lead to shifts in wavelength, making absorption spectroscopy a valuable tool to confirm the existence of different species in solution.^{401,402} In the [Ln₂(EDTA)₃]⁶⁻ complex, each Ln^{III} ion is coordinated separately to one EDTA ligand and the third EDTA ligand acts a bridge between the two [Ln(EDTA)]⁻ units by binding each metal ion *via* an iminodiacetate group. The Ce^{III} ion is also useful for spectrophotometric studies because its 4f^{*n*} → 4f^{*n*-1}5d¹ allowed transition provides a high intensity band in the UV region of the electromagnetic spectrum. This transition is red-shifted when the number of coordinated donor atoms increases.^{30,386,403-405} This transition has been used to obtain information about the structure of long-lived reaction intermediates involved in the formation of macrocyclic Ln^{III} complexes.

The formation of ternary complexes between contrast agents for MRI and endogenous ligands such as citrate, phosphate, and carbonate is an important issue because the formation of these complexes reduces the relaxation rate enhancement caused by paramagnetic complexes and can accelerate *in vivo* decomplexation of the agents.⁴⁰⁶⁻⁴⁰⁸ The ternary hydroxido complexes of metal chelates usually form under basic conditions and in several cases lead to precipitation of metal hydroxides. The presence of mixed-ligand complexes in equilibrium can be confirmed by ¹H-relaxometric methods by following the relaxation rate (1/*T*₁, where *T*₁ is the longitudinal relaxation time) of samples as a function of substrate concentration at a fixed pH, like with the Gd^{III} complexes of phosphinate derivatives of propylene diamine tetraacetic acid.⁴⁰¹ The data from those studies revealed a decrease of relaxivity in basic solutions. The formation of ternary complexes can also be followed by spectrophotometry, as in the case of [Cu(DOTAgly)(OH)]³⁻ and [Gd(PTDITA)]⁻ (Figure 1.20).^{148,389} When the formation of a ternary complex is favored, as is the case with complexes of tetra-, penta-, and hexa-dentate ligands with oxalate, malonate, citrate, or iminodiacetate,^{400,409-411} pH-potentiometric titrations can be used to obtain reliable data about their formation and stability. The advantage of stability data is that they enable modeling of complexation (calculation of speciation diagrams) over wide ranges of pH values and ligand concentrations.

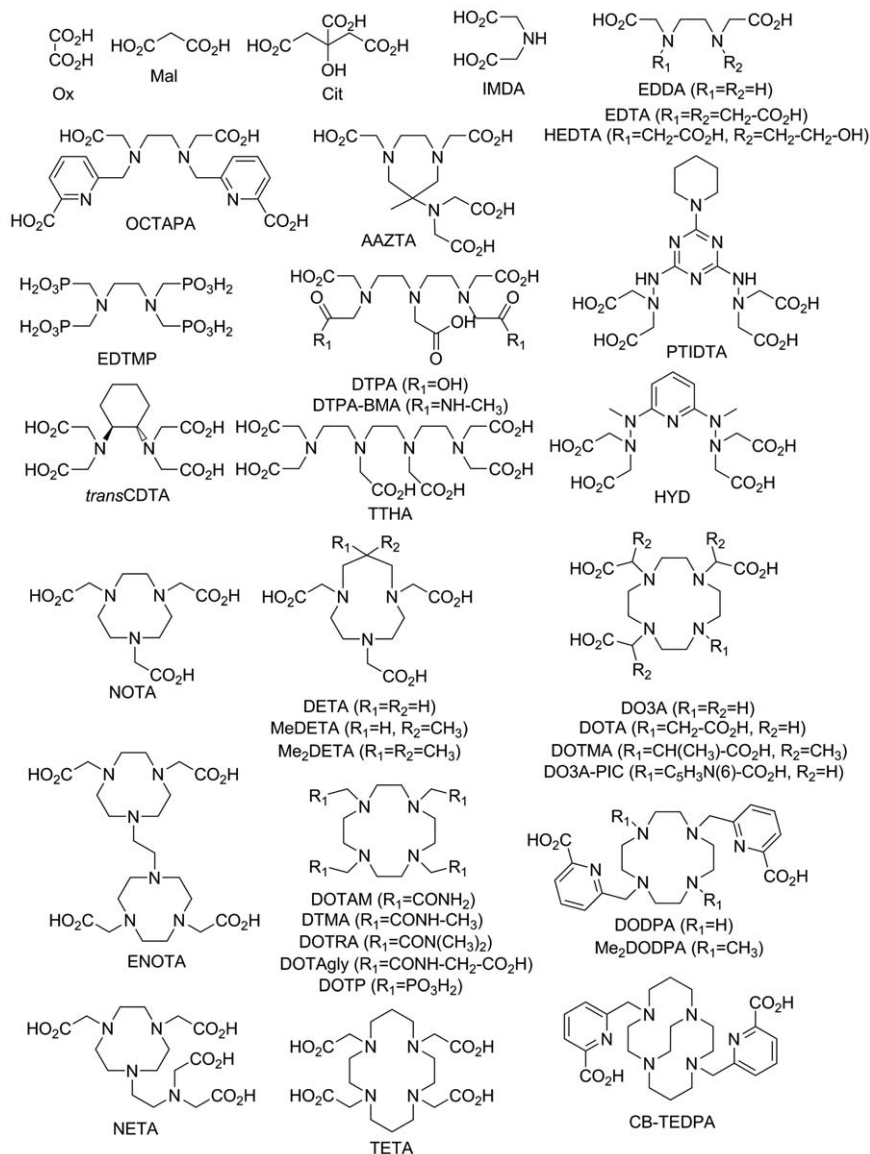


Figure 1.20 Structure of ligands described in the text.

When the potential denticity of a ligand is larger than the maximum coordination number of a metal ion, the formation of dinuclear and protonated complexes is possible. Ligands designed for applications relevant to MRI usually contain fewer donor atoms than the maximum coordination number of lanthanide ions; thus, the formation of stable dinuclear complexes in equilibrium is rare. However, the relatively small coordination numbers of transition metal ions relative to lanthanides enables the

existence of dinuclear species. Sometimes the formation of dinuclear complexes is the goal. For example, a chemical exchange saturation transfer agent candidate was reported to have a chemical exchange saturation transfer effect owing to the formation of a Cu^{II} -centered dinuclear species.⁴¹² In this respect, electron paramagnetic resonance spectroscopy is a useful technique to study equilibria involving Cu^{II} species, including dinuclear complexes.⁴¹³

High relaxivity of contrast agents for MRI is a desirable property that can be obtained, for example, by designing contrast agents that contain more than one paramagnetic metal ion. This design feature can be achieved by multiplying the coordinative site, resulting in a paramagnetic oligomer such as $(\text{Gd-AAZTA})_2$,⁴¹⁴ ditopic DO3A-based Mn^{II} complexes,⁴¹⁵ or $[\text{Mn}_2(\text{ENOTA})]$ (Figure 1.20).⁴¹⁶ Relatively flexible open chain ligands have higher propensities to form dinuclear complexes than rigid macrocyclic ligands.³⁹⁰ Furthermore, there is a special class of contrast agents for MRI designed to form dinuclear complexes with endogenous metal ions such as Ca^{II} , Cu^{II} , and Zn^{II} offering the possibility of determining the *in vivo* concentration of these ions.^{417–419} These responsive probes are composed of a unit to coordinate the paramagnetic metal ion and another moiety to selectively bind the other metal ion, thereby activating the probe.^{417–419} The characterization of these complexes has been performed with the techniques described earlier in this chapter.

Last but not least, the protonation of the metal chelates must be considered. Protonation of lanthanide(III)-polyaminopolycarboxylate complexes such as $[\text{Ln}(\text{DTPA})]^{2-}$ or $[\text{Ln}(\text{DOTA})]^-$ and their derivatives occurs at the carboxylic pendant arms. Because these carboxylates are coordinated to the metal ions, the values of these protonation constants are generally low.^{30,391} On the other hand, coordinated pendants such as phosphonates or amines have higher basicities, and therefore protonation is shifted to neutral or basic pH values. For example, $[\text{Gd}(\text{DOTP})]^{5-}$ has four protonation steps in the pH range of 4–8 related to the four phosphonate groups.⁴²⁰ Generally, the number of the protonation processes and the values of the protonation constants depend on denticity, the basicity of the donor atoms, and the coordination number of the metal ion. As mentioned above, protonation of transition-metal-ion complexes with DTPA- or DOTA-like ligands is also expected.³⁹⁰

In addition to the techniques mentioned above, NMR spectroscopy plays a role in the investigation of the equilibrium properties and confirmation of equilibrium models of metal chelates. Unfortunately, the study of paramagnetic metal complexes with NMR spectroscopy is often difficult or frequently impossible owing to line-broadening caused by paramagnetic metal ions. Therefore, in the case of lanthanides, diamagnetic or less paramagnetic surrogate ions such as Y^{III} , La^{III} , Lu^{III} , or Eu^{III} are often used. Similar approaches can be applied for the NMR studies of equilibria involving transition metal complexes: for example, the diamagnetic Zn^{II} ion can be substituted for paramagnetic Cu^{II} or Mn^{II} .^{401,421,422}

In summary, the following items should be considered when selecting an equilibrium model to study contrast agents for MRI: The equilibrium model

should be based on the formation of the ML species independently of the metal ion type. Furthermore, the presence of protonated $M(H_iL)$ species and ternary $ML(OH)_i$ hydroxo complexes should be assumed based on the denticity of the ligand and the coordination number of the metal ion. Protonation of ML complexes should be confirmed experimentally in samples containing the metal ion and ligand in a one-to-one ratio. Based on these data, the stability constants of ternary and dinuclear complexes can be determined by studying systems at various metal-to-ligand ratios.

1.3.4 Physicochemical Methods for Characterizing Metal–Ligand Interactions

Protonation and stability constants can be obtained from experimental data using various computer programs like HYPERQUAD, PSEQUAD, OPIUM, BEST, SUPERQUAD, and MINIQUAD. These equilibrium calculation programs are generally based on nonlinear least-squares fitting.^{257,374,423} Among them, the commercially available HYPERQUAD is one of the most widespread,³⁷⁵ in part because of the regular software updates and maintenance. Although some versions of HYPERQUAD are limited to fitting pH-potentiometric data, other versions can simultaneously fit data obtained by different techniques. The company that produces HYPERQUAD also offers other programs that treat data collected by other methods. These include HypSpec2014 for fitting spectrophotometric data, HypNMR for fitting NMR chemical shift data (limited to the fast-exchange regime), and HypDH for obtaining stability constants and enthalpies from calorimetric data.³⁷⁵ Programs such as PSEQUAD or OPIUM can simultaneously fit data obtained by potentiometry, UV–visible spectroscopy, 1H -relaxometry, and multinuclear NMR titrations.³⁷⁴ In addition to the software listed above, other programs are available for performing equilibrium calculations. Data obtained solely from UV–visible spectroscopy are often fit using SPECFIT/32TM, a sophisticated, multivariable data-analysis program for modeling and fitting equilibrium titration data.⁴²⁴ Analyses are also performed using SQUAD or the equilibrium routine of the ReactLab™ software.⁴²⁵ Multinuclear NMR data are frequently processed *via* HypNMR, PSEQUAD, or EQNMR.^{374,424,426–429}

Generation of speciation diagrams is useful in the design of equilibrium and kinetic experiments. Although such diagrams can be generated using data-fitting software within the concentration limits of the calculation, there are specifically designed programs that create speciation diagrams from the H^+L-M^{z+} equilibrium constants. These include the Medusa and HySS2009 freeware, which are also capable of handling redox equilibria and heterogeneous reactions.^{375,376}

In each case, calculations are performed assuming a chemical model involving equilibria between components: the metals (M), ligands (L), and protons (H^+), and complex species ($M_pL_qH_r^+$). These equilibria are characterized by the cumulative formation constants β_{pqr} [see eqn (1.14) and (1.15)]. The software uses the proposed equilibrium model to fit measured

data (titration volume, absorbance, or chemical shift) obtained from the concentrations of the components and the pH. During data fitting, the sum of squared residuals (the differences between the measured and calculated data) are minimized while values of β_{pqr} are varied. Some software programs calculate statistical data characterizing the goodness of fit (χ^2 or the standard deviation of fitted data) and the reliability of the estimated β_{pqr} constants. The infrastructure for computations that is commercially available enables calculations to be repeated with different equilibrium models within a few seconds, and the model that has the best statistical parameters is usually accepted.

The nature of the species involved in the equilibrium model should be supported by an independent method. For example, the formation of dinuclear species for Cu^{II} systems might be confirmed by electron paramagnetic resonance spectroscopy, mass spectrometry, or another analytical technique. Additionally, distribution curves for species can be compared: values calculated using the stability constants determined from one method can be compared with the absorbance values (for Cu^{II}), T_1 or $1/T_1$ values (for Mn^{II} or Gd^{III}), or NMR-signal intensity data (for diamagnetic complexes). In some cases, however, when the coordination number of the metal ion is smaller than the potential maximum denticity of the ligand, protonation can occur at a donor atom located far from the coordination environment of the metal ion. For such systems, it is best to fit simultaneously the data collected by multiple techniques. For instance, the stability of Cu^{II} complexes formed with macrocyclic ligands can be estimated reliably only when the formation of the first species occurs at fairly low pH values. These species can be followed by UV-visible spectroscopy as a function of acid concentration. Once the constant for the formation of the copper complex under acidic conditions has been determined, then the stepwise deprotonation of this species can be determined by pH-potentiometry or UV-visible spectroscopy as a function of pH.

Individual stability constants (K corresponding to a given equilibrium) can be calculated from the $\log \beta_{\text{pqr}}$ values and the related protonation and equilibrium constants. The standard deviations calculated for stability constants originate from random experimental error and reflect only a part of the total uncertainty. The true errors in the calculated equilibrium constants can be evaluated by comparison of constants obtained by different methods or in independent studies.

1.3.4.1 Experimental Methods

A wide range of experimental methods have been proposed for the determination of equilibrium constants. The relative simplicity, low cost, and wide availability of the pH-potentiometric titration has made it one of the most commonly used methods for the determination of protonation and stability constants of ligands and metal complexes. Importantly, equilibria involving ligands without protonation sites cannot be studied by

pH-potentiometry. The basicity of donor atoms and the competition reactions between metal ions and H^+ for coordination by donor groups both affect the concentration of H^+ . Hence, both protonation of ligands and complex formation influence pH.

The instrumentation necessary to perform pH-potentiometric titrations is relatively simple and generally includes glass and reference electrodes, or a combined electrode, a voltmeter or a pH-meter, and an automatic burette. To determine the relationship between the measured electromotive force or pH values and the volume of H^+ or OH^- added, both types of titration systems must be calibrated.

For potentiometric titrations, the electrode is calibrated by titrating a known amount of HCl or HNO_3 with a standardized solution of KOH, NaOH, or $(CH_4)_4NOH$ at constant ionic strength (for example, KCl, KNO_3 , NaCl, $(CH_4)_4NCl$, or $(CH_4)_4NNO_3$ electrolytes at 0.1 or 1.0 M). The relationship between the measured electromotive force and the concentration of H^+ is expressed by the Nernst equation:

$$E = E_0 + S \log [H^+] = E_0 + S \log \frac{K_W}{[OH^-]} \quad (1.29)$$

where the additive term E_0 contains the standard potential of the electrode system and the contribution of the liquid-junction potentials, S corresponds to the Nernstian slope, and K_W is the stoichiometric ionic product of water. The values of E_0 , S , and K_W can be calculated from the titration data pairs (volume of base (mL)–pH or electromotive force) of the calibration titration curve. Taking into account the contribution of H^+ and OH^- ions to the liquid-junction potentials, eqn (1.29) can be expressed in the following form:

$$E = E_0 + S \log [H^+] + j_1 [H^+] + j_2 \frac{K_W}{[H^+]}, \quad (1.30)$$

where j_1 and j_2 are the coefficients characterizing the contribution of H^+ and OH^- ions to the liquid-junction potentials in acidic and basic conditions, respectively. By using the related E_0 , S , j_1 , j_2 , and K_w values, the concentration of H^+ and pH are calculated from the electromotive force values obtained in the potentiometric titration experiments of ligands or ligands and metal ions.

For pH-potentiometric titrations, two or three standard buffer solutions are used for the calibration of the pH meter. The pH_a ($pH_a = -\log(H^+)_a$, where $(H^+)_a$ is the activity of the hydrogen ion), is expressed by:

$$pH_a = \frac{(E - E^0 - E_j)zF}{2.303RT} \quad (1.31)$$

where E , E^0 , and E_j are the measured electromotive force, standard potential, and sum of the liquid-junction potentials, respectively. If the sample contain salt, a constant ionic strength difference exists between the E_j of the

sample and the buffer solution. The difference between the measured pH_r and pH_a can be taken into account by the following equation:

$$\text{pH}_r = \text{pH}_a - \Delta E_j = \text{pH} + \log \gamma_{\pm} - \Delta E_j = \text{pH} + A = \text{p}K_w - \text{pOH} + A \quad (1.32)$$

where ΔE_j is the difference between the liquid-junction potentials of the sample and the buffer solutions, pH is $-\log[\text{H}^+]$, γ_{\pm} is the activity coefficient, A is a correction factor, and $\text{p}K_w$ is the stoichiometric water ionic product. The calibration of the electrode involves determining the pH-independent correction factor (A) and the stoichiometric water ionic product ($\text{p}K_w$).⁴³⁰ The correction factor (A) and the stoichiometric water ionic product ($\text{p}K_w$) are then used to obtain the concentration of H^+ from the pH_r values measured in the titration experiments of ligands or ligands and metal ions.

pH-potentiometric titrations can be used to determine the protonation constants of ligands and the protonation and stability constants of metal complexes. In these systems, equilibrium must be attained within a few seconds to minutes after the addition of the titrant. The metal-to-ligand concentration ratios are usually kept at 1:1. For some metal complexes, however, titrations are sometimes made with metal-to-ligand ratios of 2:1, 3:1, 1:2, or 1:3. The concentration of the ligand is generally kept in the range of 2–5 mM. Depending on the availability of the ligand, the volume of the sample is usually 3, 5, 6, 10, or 20 mL. The temperature of the samples must be kept constant during the titration (usually at 25 or 37 °C). Solutions are magnetically stirred with N_2 or Ar being bubbled through them to avoid the absorption of CO_2 during titrations. pH-potentiometric titrations are usually performed according to the calibration method described above in the pH range of 1.8–12.2.

Complex-formation reactions of polyaminopolycarboxylate-type macrocyclic ligands are generally too slow to monitor by direct pH-potentiometric titrations. Consequently, the stability constants of metal complexes of these macrocyclic ligands are often determined using an out-of-cell method. This is referred to as the batch method.⁴³¹ In this method, several separate samples are prepared in the pH range where complexation equilibria exist; each sample corresponds to a different point in the titration curve. The tightly closed samples are kept under an atmosphere of N_2 or Ar at 25 °C until equilibrium is reached. The time required to reach the equilibrium must first be confirmed by a supporting method, such as UV-visible spectroscopy for complexes of Cu^{II} and Ce^{III} , or by relaxometry for complexes of Mn^{II} or Gd^{III} . To obtain reliable stability constants, at least two or three parallel measurements should be performed.

The protonation and complexation properties of the ligands and the coordination of the metal ions can be studied by other techniques. If the metal ions and ligands have absorption bands in the UV-visible range of the electromagnetic spectrum, protonation and complexation can be monitored

by UV–visible spectrophotometry. In this technique, absorbance can be expressed by the Lambert–Beer law:

$$A = -\log \frac{I}{I_0} = \varepsilon lc \quad (1.33)$$

where I_0 and I are the intensity of the incident light before and after, respectively, the absorbing solution; ε is the molar absorptivity; l is the path length; and c is the concentration of the absorbing species. Because the observed absorbance includes contributions from the absorption of each absorbing species in a sample, the absorbance for each wavelength can be expressed by the following equation:

$$A = [L]_t + \sum x_i l \varepsilon_i \quad (1.34)$$

where $i = 0, 1, 2, \dots, n$; x_i is the molar fraction; l is the path length; and ε_i is the molar absorptivity of each involved species. The absorption bands of ligands generally occur in the UV–range. By taking into account of the total concentration ($[L]_t = [L] + [HL] + [H_2L] + \dots + [H_nL]$) and the protonation constants ($\alpha_H = 1 + K_1^H[H^+] + K_1^H K_2^H [H^+]^2 + \dots + K_1^H K_2^H \dots K_n^H [H^+]^n$) of the ligand, eqn (1.34) can be expressed as eqn (1.35). Note that the term l can be omitted if the same cuvette is used for all measurements.

$$A = \left[\frac{\varepsilon_L}{\alpha_H} + \frac{\varepsilon_{HL} K_1^H [H^+]}{\alpha_H} + \frac{\varepsilon_{H_2L} K_1^H K_2^H [H^+]^2}{\alpha_H} + \dots + \frac{\varepsilon_{H_nL} K_1^H K_2^H \dots K_n^H [H^+]^n}{\alpha_H} \right] [L]_t \quad (1.35)$$

The protonation constants and the molar absorptivity of each protonated species of the ligand can be calculated by fitting the electromotive force or pH and the absorbance values with eqn (1.35). Similarly, the formation, protonation, and structure of metal complexes can be determined from the absorption bands of the ligands, metal ions, or complexes obtained from spectrophotometric titrations.

Stability constants of complexes are usually determined pH-potentiometrically because of the relative simplicity and precision of the method. Sometimes, complexation equilibria exist in pH ranges that are not easily measured. In those cases, competition reactions can be used to shift of the complexation equilibrium into a measurable pH range. Competition reactions can be either metal- or ligand-based. The appropriate competition partner is selected based on three criteria: (i) the relative simplicity of the system, which involves minimizing the number of species present in the equilibrium; (ii) the ease of monitoring the competition reaction; and (iii) prior knowledge of the stoichiometry and stability of the complex formed with the competition partner.

Metal and ligand competition reactions are described by eqn (1.36) and (1.37).





Such competition reactions can be monitored using the absorption bands of the exchanging metal ions, ligands, or both by spectrophotometry or by relaxometry if there is a difference in relaxivity between the two complexes (ML and ML' or ML and M'L). For competition reactions that are monitored by the absorption band of M'L and ML', the total absorbance of the system can be expressed by eqn (1.38) and (1.39), assuming that the absorbance of ML, L, and L' can be neglected.

$$A = \frac{[\text{M}']_t (\varepsilon_{\text{M}'} + \varepsilon_{\text{M}'\text{L}} K_{\text{M}'\text{L}} [\text{L}])}{1 + K_{\text{M}'\text{L}} [\text{L}]} \quad (1.38)$$

$$A = \frac{[\text{L}']_t \varepsilon_{\text{M}'\text{L}} K_{\text{M}'\text{L}} [\text{M}]}{\alpha'_{\text{H}} + K_{\text{M}'\text{L}} [\text{M}]} \quad (1.39)$$

The stability constant of the metal complex ML can be calculated from the protonation constants of the ligands, the stability constants of the complexes formed with the competition partners, and the molar absorptivity of complexes by fitting the pH and absorbance of the systems. Note that the pH must be known because the protonation of the non-complexed ligand also affect the absorbance. The out-of-cell method is generally used for these reactions because competition reactions are often slow. The conditions of the competition reaction, including the concentration of each reactant, volume of samples, and wavelength, first need to be optimized by independent experiments. Note that the volume of the sample is generally limited by the pH measurements, the volume of the cuvette, or the availability and solubility of the ligand. To obtain reliable data, potentiometric or pH-potentiometric systems should be calibrated using the method described above to measure pH.

The optical properties of lanthanide complexes arise primarily from *f-f* electronic transitions. Perturbations of *f-f* transitions by coordinating donor atoms in Ln(L) tend to be small. Therefore, *f-f* transitions are usually characterized by small bandwidths and, due to their forbidden nature, low intensities ($\varepsilon \leq 10 \text{ M}^{-1} \text{ cm}^{-1}$).⁴³² Those transitions can nonetheless be used to monitor complex formation. For instance, the ${}^2P_{1/2}$ term of Nd^{III} is not split by crystal fields. Instead, the absorption bands corresponding to the ${}^2P_{1/2} \leftarrow {}^4I_{9/2}$ transitions (Nd(H₂O)₉; $\lambda = 427.3 \text{ nm}$) are shifted to longer wavelengths by the formation of Nd^{III} complexes. The ${}^2P_{1/2} \leftarrow {}^4I_{9/2}$ transitions of Nd^{III} can thus give information with respect to the number and crystal-field-strength of coordinating donor atoms.⁴³³ The ${}^5L_6 \leftarrow {}^7F_0$ transition of Eu^{III} in the range of 390–400 nm shows a similar sensitivity to ligand binding.⁴³⁴ Because the shielding of 5d electrons by the outer shells is weak, the 5d \leftarrow 4f transitions of Ln^{III} ions can also be used to study the formation of Ln(L) complexes. For instance, the 5d \leftarrow 4f transitions of Ce^{III}, Pr^{III}, and Tb^{III} ions

result in broad and intense absorption bands ($\varepsilon \leq 1000 \text{ M}^{-1} \text{ cm}^{-1}$) in the UV region of the electromagnetic spectrum.

All Ln^{III} ions luminesce unless they have valence electronic configurations of f^0 or f^{14} . The luminescence of $\text{Ln}(\text{L})$ complexes is most commonly characterized by spectrofluorometry, that is, by measuring the emission spectra that result from excitation at an absorption wavelength associated with an emissive transition. The formation of $\text{Ln}(\text{L})$ complexes can generally be followed by spectrofluorometry in the concentration range of 10^{-6} to 10^{-8} M .^{435,436} The relationships between the concentrations of species and the measured intensities is described by eqn (1.40).⁴³⁷

$$I = \sum_1^n I_0 \varepsilon_i c_i \varphi_i l \quad (1.40)$$

In eqn (1.40), I_0 is the intensity of the entering light, l is the path length of the cell, ε_i is the molar absorptivity of the species, c_i is the concentration of the species, and φ_i is the quantum yield of the species. Importantly, the presence of compounds that contain absorbing or fluorescent molecules might change the emission of $\text{Ln}(\text{L})$ owing to the inner-filter effect. The inner-filter effect refers to the absorbance or optical dispersion of light at the excitation or emission wavelength by a compound present in the sample.⁴³⁸

The luminescence properties of Eu^{III} (${}^7\text{F}_{0-4} \leftarrow {}^5\text{D}_0$) and Tb^{III} complexes (${}^7\text{F}_{0-6} \leftarrow {}^5\text{D}_4$) are often exploited to investigate the formation, structure, and number of inner-sphere water molecules in $\text{Ln}(\text{L})$ complexes (see Chapter 2.4.3).^{439,440} The stability constants of several Eu^{III} complexes were determined by monitoring the excitation spectra of Eu^{III} -ligand systems with laser-induced luminescence spectroscopy in the pH range of 2–7.⁴⁴¹ The intensities of the ${}^5\text{D}_0 \leftarrow {}^7\text{F}_0$ transitions of different Eu^{III} -ligand systems are shown in Figure 1.21. Note that the luminescence intensity increases with increasing pH owing to the formation of $\text{Eu}(\text{L})$. The measured luminescence intensity values can be expressed by the sum of the contribution of each species [eqn (1.41)].

$$I_{\text{meas}} = \sum_1^n I_i c_i \quad (1.41)$$

In eqn (1.41), I_i and c_i are the molar intensity and the concentration of the species i , respectively. The values of c_i of the different species can be expressed in terms of the related equilibrium constants (such as K_{EuL} and K_{EuHilL}). The stability and protonation constants of $\text{Eu}(\text{L})$ can thus be calculated from I_{meas} and pH if the total concentration of each component ($[\text{Eu}^{3+}]_{\text{tot}}$ and $[\text{L}]_{\text{tot}}$) and the protonation constants of the ligand (K_i^{H}) are known. This is usually performed with equilibrium calculation software, as detailed above.

Multinuclear NMR spectroscopy has been used since the late 1950s to determine protonation and stability constants. This technique has numerous advantages relative to other techniques. For instance, it can be applied

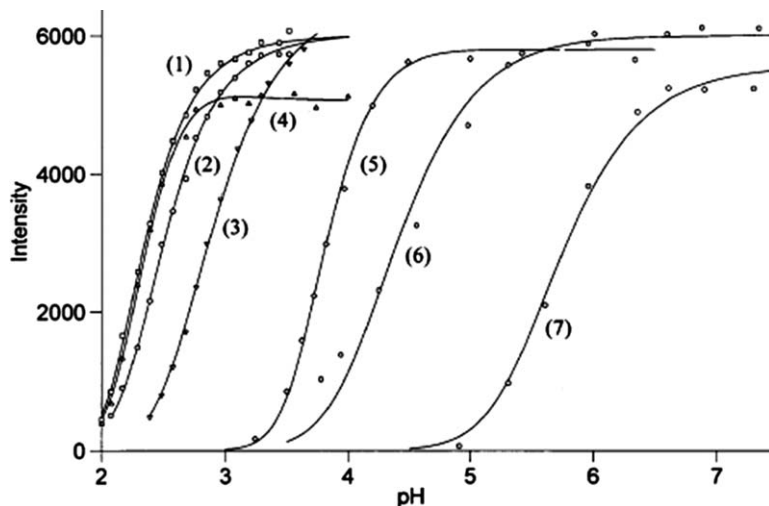


Figure 1.21 Intensities of the ${}^5D_0 \leftarrow {}^7F_0$ transitions of Eu^{III} complexes formed with DTPA (1), EDTA (2), HEDTA (3), DOTA (4), DOTRA (5), NOTA (6), and TETA (7). (1–5: $[\text{Eu}] = [\text{L}] = 2 \mu\text{M}$, 6: $[\text{Eu}] = [\text{NOTA}] = 10 \mu\text{M}$, 7: $[\text{Eu}] = [\text{TETA}] = 50 \mu\text{M}$, KCl (0.1 M), and 25°C). See Figure 1.20 for chemical structures of ligands. Adapted from ref. 441 with permission from The Royal Chemical Society.

to both acidic and basic solutions. pH can be determined by using the measured concentration of acid or base. It can also be determined with indicator molecules whose chemical shifts and protonation constants are known.³⁸⁷ NMR titration data can be used to determine the order of protonation of the donor atoms, that is, the protonation sequence of the ligand. NMR titration data can also be used to evaluate microconstants in cases of simultaneous or overlapping protonation equilibria.^{442–444} Advantageously, NMR titrations can be used to estimate protonation constants, even if ligands are not analytically pure.

When the pH-dependent acid–base equilibrium is fast on the NMR time scale, the chemical shift measured (δ_{obs}) is proportional to the chemical shifts of the HL and L species [eqn (1.42)]:

$$\delta_{\text{obs}} = \chi_{\text{HL}} \delta_{\text{HL}} + \chi_{\text{L}} \delta_{\text{L}} \quad (1.42)$$

In eqn (1.42), δ_{HL} and δ_{L} are the chemical shifts of the protonated and deprotonated ligand, respectively; and χ_{HL} and χ_{L} are the molar fractions of the protonated and deprotonated ligand, respectively. Molar fractions can be expressed in terms of protonation constants ($K_{\text{HL}} = [\text{HL}]/\{[\text{H}^+][\text{L}]\}$) and $[\text{H}^+]$ as follows:

$$\chi_{\text{HL}} = \frac{[\text{HL}]}{[\text{HL}] + [\text{L}]} = \frac{K_{\text{HL}}[\text{H}^+]}{1 + K_{\text{HL}}[\text{H}^+]} \quad (1.43)$$

Given that $\chi_{\text{HL}} + \chi_{\text{L}} = 1$, eqn (1.42) and (1.43) can be combined to give eqn (1.44), which is an equation that enables determination of K_{HL} by nonlinear, least-squares refinement.

$$\delta_{\text{obs}} = \frac{\delta_{\text{L}} + \delta_{\text{HL}}K_{\text{HL}}[\text{H}^+]}{1 + K_{\text{HL}}[\text{H}^+]} = \frac{\delta_{\text{L}} + \delta_{\text{HL}} \times 10^{\log K_{\text{HL}} - \text{pH}}}{1 + 10^{\log K_{\text{HL}} - \text{pH}}} \quad (1.44)$$

Although it is rare, slow exchange can sometimes be observed in protonation equilibria. This has been observed, for instance, in the protonation of DOTA-tetraamides or in the formation of the ternary hydroxido complex of $[\text{Ga}(\text{AAZTA})]^-$.^{394,445} In the case of slow exchange, separate peaks corresponding to the same proton are observed in the NMR spectra of the protonated and deprotonated forms of the species of interest. The ratio of $[\text{HL}]/[\text{L}]$ can then be calculated by the ratio of the integration of each peak. The concentrations of the protonated and deprotonated species can be calculated from this ratio and the total concentration of the ligand, $[\text{L}]_{\text{tot}}$. This, in turn, enables the determination of the protonation constants.

NMR spectroscopy is a good technique to determine protonation constants if the chemical exchange is slow enough that the signals for each species are resolved. For the multidentate ligands that are widely used in contrast agents for MRI, such as for macrocyclic systems, this condition is often satisfied, although the assignment of signals can be complicated. ^{13}C -NMR spectroscopy is usually limited by its low sensitivity. If applicable, NMR spectroscopy based on nuclei that are more sensitive than ^{13}C , such as ^{31}P and ^{19}F , is also viable for the determination of protonation constants. Similarly, equilibria of metal complexes can also be studied by monitoring the NMR signal of NMR-active metal isotopes. Detection of the metal ions can be useful in supporting data from ^1H -NMR titrations. Several metallic elements have $I = 1/2$ spin isotopes, such as Y, Cd, and Tl. Others that are quadrupolar with $I > 1/2$, such as Al, Ga, In, La, and Sc, can also be used in such experiments.⁴⁴⁵⁻⁴⁵⁰ An advantage of directly observing metal ions is an enabling of the determination of stability constants for mixed ligand complexes, such as $[\text{Tl}(\text{DOTA})(\text{CN})]^{2-}$.³⁹⁵ Quadrupolar nuclei are associated with broad signals that are sometimes immeasurable in non-symmetric species; therefore, only symmetric free aqua ions, such as $\text{Al}(\text{H}_2\text{O})_6^{3+}$, $\text{Al}(\text{OH})_4^-$, $\text{Ga}(\text{H}_2\text{O})_6^{3+}$, and $\text{Ga}(\text{OH})_4^-$, can be measured quantitatively. In most cases, $\text{M}(\text{L})$ complexes of these metals are difficult to detect. The further complication of NMR of metal nuclei is that the lone signal can be difficult to integrate. A standard, either internal or external, must therefore be used to determine the concentration of the metal species.

In general, NMR methods can be applied to diamagnetic complexes and many paramagnetic complexes. Gd^{III} complexes, however, cannot be investigated directly by ^1H -NMR spectroscopy because of the extreme line-broadening effect of the Gd^{III} ion. Complexes of Mn^{II} , Fe^{III} , or Gd^{III} can be studied through ^1H relaxometric studies by following the longitudinal (T_1) or transverse (T_2) relaxation times as a function of pH, exchanging metal, or

ligand concentration (see Chapters 2.1 and 5.1 for further reading on the relaxivities of Gd^{III} and transition metal complexes, respectively). Paramagnetic metal ions and their complexes often display significant differences in $r_{1\text{p}}$ and $r_{2\text{p}}$ relaxivities^{451–454} or the ratio of these relaxivities.⁴⁵⁵

The relaxivity of a sample containing paramagnetic species can be described as a weighted average of the contributions from $[\text{M}(\text{H}_2\text{O})_x]$ ($x = 6$ for Mn^{II} and 8 for Gd^{III}) and each of the metal-ion-containing species as described in eqn (1.45) (for $r_{1\text{p}}$).

$$r_{1,\text{obs}} = \chi_{\text{M}} r_{1\text{p},\text{M}} + \sum \chi_{\text{M}_p\text{H}_p\text{R}_p\text{L}_p} r_{1\text{p},\text{M}_p\text{H}_p\text{R}_p\text{L}_p} \quad (1.45)$$

In eqn (1.45), χ is the mole fraction of $[\text{M}(\text{H}_2\text{O})_x]$ and $\text{M}_p\text{H}_p\text{R}_p\text{L}_p$, $r_{1\text{p},\text{M}}$ is the molar relaxivity of the metal aqua ion ($7920 \text{ M}^{-1} \text{ s}^{-1}$ for Mn^{II} and $13\,170 \text{ M}^{-1} \text{ s}^{-1}$ for the Gd^{III} at 25°C and 20 MHz), and $r_{1\text{p},\text{M}_p\text{H}_p\text{R}_p\text{L}_p}$ is the molar relaxivity of the metal-ion-containing species. The formation constants of the metal complexes present in equilibrium can be determined from the protonation constants of each ligand species, which must be determined in advance by other methods. In the simplest case when complexes of 1:1 metal-to-ligand ratios are formed ($[\text{M}] = [\text{L}]$), this can be derived from eqn (1.46).

$$[\text{M}] = \frac{-A + \sqrt{A^2 + 4(\sum \beta_{\text{M}_p\text{H}_p\text{R}_p\text{L}_p} [\text{H}^+]^{\text{R}}) \cdot [\text{M}]_{\text{tot}} \cdot A}}{2 \sum \beta_{\text{M}_p\text{H}_p\text{R}_p\text{L}_p} [\text{H}^+]^{\text{R}}} \quad (1.46)$$

$$\text{where } A = 1 + \sum \beta_{\text{H}_p\text{R}_p\text{L}_p} [\text{H}^+]^{\text{R}}$$

The reliability of the method can be increased by performing titrations at different metal-to-ligand ratios in a wide range of pH values or by supplementing the ^1H -relaxometric data with pH-potentiometric data. The simultaneous fitting of data obtained by multiple methods enables an estimation of the relaxivity of the different species, including those present at low concentrations or that overlap other species in solution.^{120,456} One of the first examples of relaxometry to determine the stability of macrocyclic Gd^{III} complexes was for the study of triaza-triacetate macrocyclic ligands (Figure 1.22).⁴⁵⁷

1.3.4.2 Methods Relying on Separation

The determination of stability constants of metal complexes by separation techniques such as high-performance liquid chromatography,^{458,459} ion chromatography,⁴⁶⁰ and capillary electrophoresis^{461–464} has limitations. First, information is obtained from analyses performed on a series of similar samples with varying composition as in the out-of-cell (batch) method used in pH-potentiometry described above. Second, capillary electrophoresis requires relatively expensive instrumentation that is not widely available.^{460,465,466} These

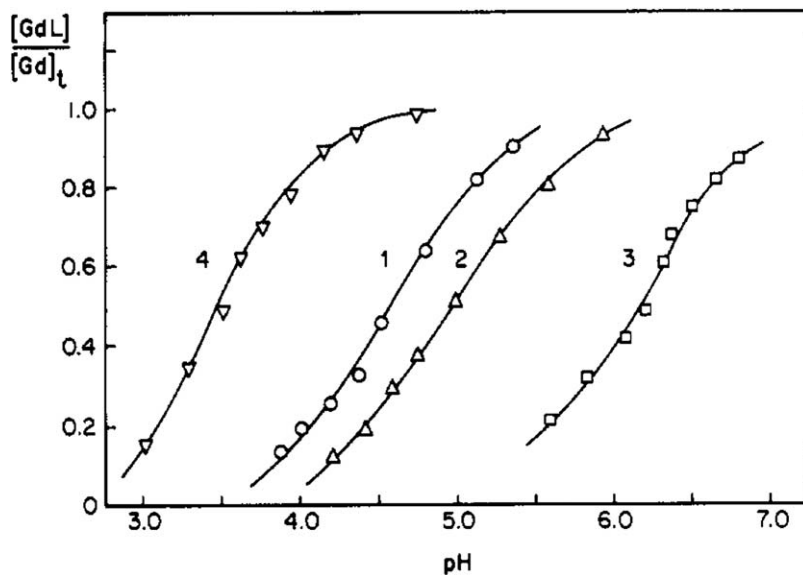


Figure 1.22 Extent of formation of [Gd(DETA)] (1), [Gd(MeDETA)] (2), [Gd(Me₂-DETA)] (3), and [Gd(NOTA)] (4) as a function of pH. Conditions: [Gd] = 1×10^{-3} M; [L] = 1.2×10^{-3} M (curves 1, 2, and 4) and [L] = 5×10^{-3} M (curve 3), 25 °C, KCl (0.1 M). Adapted with permission from E. Brucher, S. Cortes, F. Chavez and A. D. Sherry, *Inorg. Chem.*, 1991, **30**, 2092. Copyright (1991) American Chemical Society.⁴⁵⁷

techniques, however, generally have high separation efficiency and relatively high speed of analysis, and require much less compound than other techniques discussed above. In addition, these measurements can be automated.

Generally, in capillary electrophoresis, the components of a test solution are introduced into the capillary *via* hydrodynamic injection, which is the most widely used injection method. The components move along the capillary with different velocities when voltage is applied at the ends of the electrolyte-filled capillary (Figure 1.23). The velocities depend on the charges and ionic radii of the species, such that the components of the samples reach the detection zone at different time points. The qualitative characteristic of the signal is the migration time (μ). Quantitatively, the heights and areas of the peaks are proportional to the concentrations of the components.

Practically, capillary electrophoresis has only been applied to the determination of stability constants for the simplest systems, such as for labile metal complexes which form in 1:1 metal-to-ligand stoichiometries.^{467,468} In these cases, the metal ions are dissolved in the samples and the ligands are in the running buffer. Because the formation and dissociation of labile metal complexes is fast on the time scale of capillary electrophoresis, the resultant electrophoretic mobility (μ_{obs}) represents a weighted average of the electrophoretic mobility of the different species present in a sample

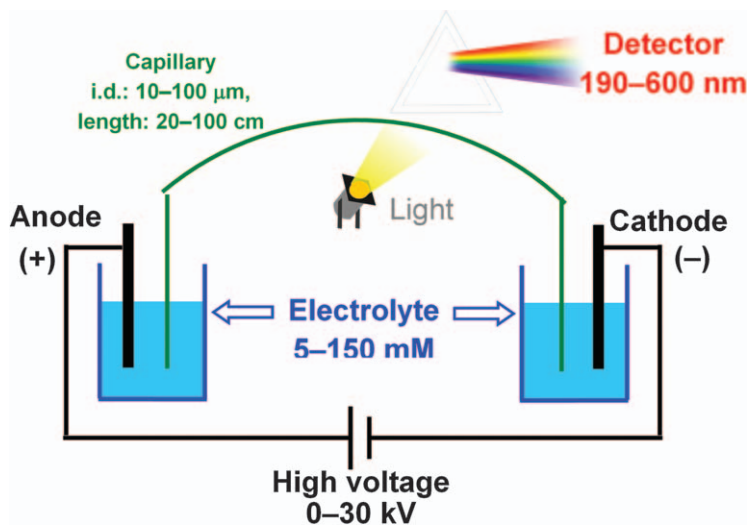


Figure 1.23 Experimental setup of capillary electrophoresis.

[eqn (1.47)]. Stability constants are obtained from monitoring the electrophoretic mobility shift of samples upon changing the concentration of the ligand in the buffer.

$$\mu_{\text{obs}} = x_{\text{ML}}\mu_{\text{ML}} + (1 - x_{\text{ML}})\mu_{\text{M}} = \frac{\mu_{\text{ML}}K_{\text{ML}}[\text{L}][\text{M}] + \mu_{\text{M}}[\text{M}]_t}{1 + K_{\text{ML}}[\text{L}]} \quad (1.47)$$

In eqn (1.47), μ_{M} and μ_{ML} are the electrophoretic mobility of the metal ion and the ML complex, respectively, and x_{ML} is the molar fraction of the complex. K_{ML} , μ_{M} , and μ_{ML} can be calculated from eqn (1.47) once the molar fraction of ML is expressed as a function of $[\text{M}]_t$ and K_{ML} (the stability constant of ML). These experiments require knowledge of $[\text{M}]_t$, which can be calculated by taking into account the injected volume of the test solution.

Measurements of stability constants become more straightforward when complexes remain intact, that is, when dissociation reactions of metal complexes are slow on the time scale of capillary electrophoresis experiments. In these cases, the peaks of the complexed and non-complexed ligands or metal ions are separated during electrophoresis.⁴⁶² For samples already at equilibrium, a mixture of metal and ligand is injected into the capillary to detect the concentrations of the metal and the ligand as well as the concentration of the complex. The stability constants can then be assessed from the areas of the peaks because the areas of the peaks are proportional to the concentrations of the different species. These calculations require the knowledge of the molar area values of different species, which must be separately determined in experiments performed under identical conditions.

Calculations of stability constants, however, become more complicated when several species are present in equilibrium, such as when both protonated ligands and complexes are present. In these cases, the conditions used for capillary electrophoresis, including buffer, pH, and temperature, must first be evaluated to avoid further complications of equilibrium calculations. Capillary electrophoresis can be used to evaluate the stabilities of complexes either by direct formation, ligand-exchange reactions (ligand competition), metal-exchange, and double-exchange. It has been applied, for example, to determine the stability and the formation and dissociation rates of $[\text{Ln}(\text{DOTA})]^-$ complexes.⁴⁶⁵

1.3.4.3 Other Less Common Methods

Calorimetry, including isothermal titration calorimetry and isothermal titration microcalorimetry, was among the first techniques used to characterize equilibria and determine protonation and stability constants in dilute solutions. This technique is based on the measurement of the amount of heat that evolves as a result of physical or chemical processes taking place in the sample.⁴⁶⁹ This technique yields both stability constants and standard enthalpy changes for the equilibria.⁴⁷⁰ This time-consuming method is mostly limited to complexes of 1 : 1 stoichiometry and with relatively small formation constants. In the case of stable complexes suitable for medical applications, calorimetry has no routine application, especially for macrocyclic ligands with slow rates of complex formation.

1.3.4.4 Speciation Diagrams (Equilibrium Distribution Curves)

Although the stability constants of metal–ligand systems are determined in equilibrium studies, the numbers alone cannot be used directly to visualize the chemical composition or speciation of solutions. The equilibrium constants characterizing a system—such as the protonation constants of ligands and the stability and protonation constants of complexes—enable calculation of the equilibrium distribution of a given system at any ratio of its components at any pH. Equilibria in solution are best illustrated by speciation diagrams, which are usually obtained by plotting the molar fraction of components or the logarithm of the equilibrium concentrations *versus* pH or the total concentration of a second component, while keeping the total concentration of other species constant. Calculations of distribution curves do not take a long time, mainly because they can be performed by computer programs like Medusa or HySS2009.^{375,376} However, distribution curves that characterize equilibrium systems are most meaningful in the concentration, metal-to-ligand ratio, and pH ranges in which the equilibrium constants were determined. The mathematical characterization of complex equilibria is not covered in this chapter. Interested readers are referred to other books and papers detailing this subject.^{6,364,471} In the following section, the

benefits of using equilibrium distribution curves will be demonstrated using selected examples.

The simplest species distribution curves are obtained when two-component systems related to stepwise protonation processes of ligands are studied. The distribution curves obtained by plotting the molar fraction of protonated ligand species *versus* pH provide an overview of the protonation processes. These speciation curves help define buffer ranges and enable rapid comparison of protonation constants obtained by different techniques, such as pH-potentiometry and NMR titrations. The curves can also be used to assign the protonation sequence of ligands and calculate the fractions of different forms present in solution as a result of microspeciation.

Three-component distributions are often important when studying contrast agents, and these distributions generally involve components of metal ions, ligands, and protons. Distribution curves are usually not complicated for these systems because the equilibrium models of potential contrast agents tend to be relatively simple. Usually, the metal complex, its protonated form, and, in some cases, a ternary hydroxide form are the predominant species over a wide pH range. The situation might become more complicated with dinuclear or ternary complexes because, in such cases, the obtained distribution curves can be misleading if they are calculated incorrectly.^{401,472} This problem is exemplified in Figure 1.24 for the $\text{Cu}^{\text{II}}:\text{TTHA}^{6-}:\text{H}^+$ system (Figure 1.20) in which Cu^{II} forms stable dinuclear complexes with TTHA^{6-} , even at one-to-one metal-to-ligand ratios. In this case, two different speciation diagrams can be calculated according to two different methods. The occurrence of a dinuclear complex is explained by the potential denticity of TTHA, which is ten, being higher than the maximum coordination number of Cu^{II} , which is six. The mismatch enables coordination of two metal ions per ligand. The distribution curves in Figure 1.24 were created from published data.⁴⁷³ The distribution in Figure 1.24(A) was obtained by plotting the fractions of Cu^{II} as a function of pH, resulting in several extrema in the pH range of 1–10. Based on this distribution, it appears that complex formation is complete at pH 2. However, the plot of the fraction of TTHA^{6-} *versus* pH in (B) reveals that TTHA^{6-} is not completely metallated in acidic samples because of the formation of stable dinuclear complexes.

A similar phenomenon is observed with $[\text{Gd}(\text{EDDA})]^+$ (Figures 1.20 and Figure 1.25) and in many other systems in which the ligand of interest has a lower number of donor atoms than the coordination number of the Ln^{III} ion (8 or 9).⁴⁷⁴ The Gd^{III} ion has a propensity to form ML_2 or ternary MLL' type complexes with the tetradentate EDDA^{2-} because the coordination number of the Gd^{III} (8 or 9) enables the coordination of two EDDA ligands. As shown in Figure 1.25(A), for this system, when a one-to-one metal-to-ligand ratio is used, the plot of EDDA^{2-} fractions *versus* pH shows that complex formation appears to be complete at pH 8. No non-complexed Gd^{III} appears to remain in solution after the formation of $[\text{Gd}(\text{EDDA})_2]^-$. The plot in Figure 1.25(B), however, shows that 10% of the Gd^{III} ions remain non-complexed in basic

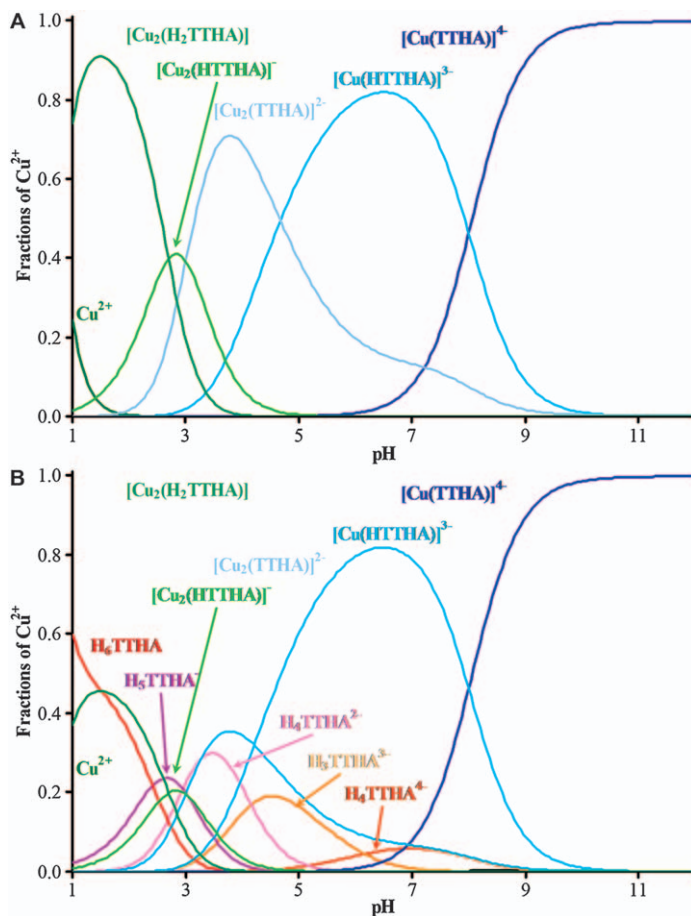


Figure 1.24 Distribution curves for $[\text{Cu}(\text{TTHA})]^{4-}$ ($[\text{Cu}^{\text{II}}] = [\text{TTHA}] = 1 \text{ mM}$). (A) Fraction of Cu^{II} versus pH and (B) fraction of TTHA versus pH. [$25 \text{ }^\circ\text{C}$ and $\text{KNO}_3 (0.1 \text{ M})$].

solutions as a result of the formation of a hydroxo species. Importantly, the speciation diagrams shown in Figure 1.25(A) and (B) were calculated using the protonation constants of EDDA^{2-} and the stability constants of the two complexes but omit metal-ion hydrolysis. These calculations assume that the non-complexed metal ions remain in solution as aqua ions, at least partially. However, hydrolysis of Gd^{III} does occur above pH 6, such that the actual equilibrium is shifted towards $\text{Gd}(\text{OH})_3$, which precipitates. The distribution curves in Figure 1.24(A) and (B) thus give a false picture of speciation. The speciation diagram shown in Figure 1.25(C) incorporates the hydrolysis constants of Gd^{III} .⁴⁷⁵ In this case, $\text{Gd}(\text{OH})_3$ precipitates at $\text{pH} > 7$. Equilibrium can be shifted toward the formation of complex by adding excess ligand that prevents the formation of $\text{Gd}(\text{OH})_3$. This system exemplifies some of the pitfalls in the interpretation of speciation diagrams.

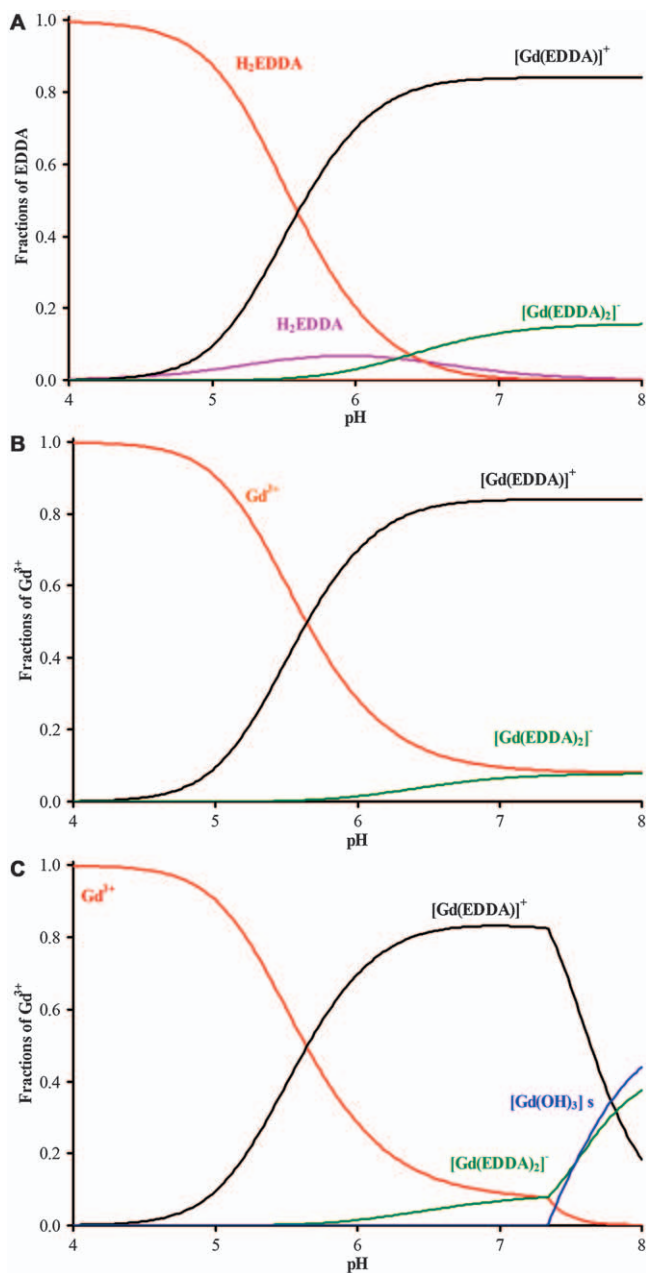


Figure 1.25 Distribution curves for $[\text{Gd}(\text{EDDA})]^+$ ($[\text{Gd}^{\text{III}}] = [\text{EDDA}] = 1 \text{ mM}$): (A) molar fraction of EDDA^{2-} versus pH, (B) and (C) molar fraction of Gd^{III} versus pH (25 °C and KNO_3 0.1 M). See text for details.

Four-component systems are of a great value in both equilibrium and kinetic investigations and provide many benefits in the study of metal complexes. In some cases, determination of stability constants of metal complexes cannot be performed by direct methods because complex formation is complete even under acidic conditions. In such cases, ligand or metal competition reactions are used to obtain equilibrium constants. These reactions are usually performed at constant pH by varying the concentration of only one component while keeping the total concentration of the other components constant.^{476,477} However, it is also possible to keep the concentrations of all components constant and vary the pH over a wide range of pH values. Ligands with large protonation constants (including many macrocyclic ligands) can be competed with less basic chelators (such as EDTA) in solutions of low pH because differences in protonation constants result in different conditional constants. The different conditional constants usually have different levels of dependence on pH. The large stability constants of Cu^{II} macrocyclic complexes are often determined by this method using EDTA or an EDTA-type ligand for competition.⁶ To determine stability constants by this method, the unknown system should be closely evaluated and compared to similar reported systems. This step is necessary to select the appropriate equilibrium systems for the determination of unknown constants.

The kinetic inertness of complexes is usually characterized by the rates of their metal- or ligand-exchange reactions. Some of these exchange reactions result in equilibrium instead of complete exchange, even in the presence of high excesses of competitors. In such cases, the equilibrium concentration of the species in each reaction can be calculated and taken into account using distribution curves.⁴⁷⁸

1.3.4.5 More Complicated Systems

Complicated equilibrium calculations can be used to draw conclusions about the fate of injected complexes using artificial plasma models. Because of the difficulties associated with handling many species at low concentrations, simplified models are often used. One study of a simplified plasma model involved 20 components, including the most abundant ligands in biology and essential metal ions.⁴⁰⁷ This study contained more than 300 species and was created to study the *in vivo* fate of the linear, neutral complex $\text{Gd}(\text{DTPA-BMA})$. The distribution calculations showed that $\sim 17\%$ of the intravenously injected complex dissociates at pH 7.4, Gd^{III} precipitates in the form of GdPO_4 , and non-complexed DTPA-BMA^{3-} binds to other metal ions, including Cu^{II} , Zn^{II} , and Ca^{II} .

1.3.4.6 Limitations

Because high thermodynamic stability is associated with many contrast agents for MRI, it is crucial to learn how to measure large equilibrium

constants. With the most trivial case of a protonated ligand being a weak acid, the reversible chemical reaction can be described by eqn (1.48) and (1.49).



$$K = \frac{[ML][H]^n}{[M][H_nL]} \quad (1.49)$$

In eqn (1.49), charges are omitted for clarity. For large stability constants, the value of K is large because the equilibrium is shifted to the right, thereby making $[M]$ and $[H_nL]$ small. However, the accuracy of analytical methods for detecting extremely small concentrations is limited, resulting in large uncertainties in measured equilibrium constants. The most accurate measurements are expected in cases of comparable concentrations of ML , M , and H_nL . The equilibrium can be tuned by adjusting pH, but there are at least two limitations to this experimental trick. The first is that the concept of pH is not valid in extremely acidic media. The second is that the accuracy of pH measurements below 2 is not good enough to detect the small contributions of ML formation to the overall acidity. An often-used strategy, if ligands or metals are compatible with such measurements, is to measure $[M]$, $[ML]$, or both by spectrophotometry or NMR spectroscopy. Unfortunately, high-resolution NMR spectroscopy cannot be used for Gd^{III} complexes because of large paramagnetic broadening effects. Nonetheless, NMR spectra can be obtained for complexes of analogous diamagnetic ions or some paramagnetic lanthanide ions, such as Ce^{III} and Eu^{III} . Most NMR laboratories have tunable probes for such measurements; however, the sensitivity and natural abundance of the nuclei first need to be known. Measurement of quantitative intensities, necessary to obtain concentrations for calculations of K , requires proper acquisition parameters because T_1 values might differ considerably between M and ML . Additionally, large chemical shift differences associated with lanthanide ions often require adjustment of the spectral window to encompass all signals.

Extremely stable complexes exist for which even extended pH ranges (for example, $-\log[H^+] < 0$) are not enough to shift equilibria to an optimal range of comparable concentrations of M and ML . In those situations, indirect measurements, also referred to as competition reactions, are used. In these experiments, secondary ligands (L') might compete for binding to metal ions, and secondary metal ions (M') compete for the ligand (L). Unfortunately, the competition method increases the experimental time because characterization of the subsystems, including the protonation constants of L' and stability constants of ML' and $M'L$, are needed for the evaluation of the stability constant of ML . Therefore, all of these values must be determined accurately in advance of studying ML . Some examples will be presented in the following section of this chapter. There are cases in which

multiple competitions enable estimation of large stability constants. For example, in the following reaction, Tl^{III} competes with H^+ and Na^+ , both present at high concentrations in a sample, and bromide competes with the DOTA ligand *via* the formation of relatively stable TlBr_3 . The stability constant of the $[\text{Tl}(\text{DOTA})]^-$ is expected to be in the range of 50–60 log units, which is too high to be determined directly. Under acidic conditions and in the presence of large concentrations of NaBr , however, the stability constant can be determined according to eqn (1.50).³⁹⁵



Finally, kinetics cannot be ignored during the study of equilibria. Reversible equilibrium reactions might be slow, and the time required to reach equilibrium might be long, from minutes to months. For slow reactions, separated samples using the batch or out-of-cell method need to be prepared using sample holders that keep the system intact during the long experiment. Samples prepared in duplicates representing the extremes of the conditions in the batch samples, for instance at high and low pH or concentration of exchanging metal or ligand, must be measured periodically to ensure that the equilibrium in the samples is attained.

1.3.5 Stabilities of Gadolinium Complexes: Selected Examples

Published stability constants for a same metal complex can differ by several orders of magnitude depending on the experimental methods and conditions used as well as on the equilibrium models used for the fitting. There is no single method and set of conditions to follow to obtain good values; rather, the examples presented below are meant to help readers avoid selecting unsuitable methods for the determination of stability constants.

The challenges associated with the determination of stability constants of complexes with linear ligands differ from those of complexes with macrocyclic ligands. For linear complexes, the difficulty comes in choosing the correct methodology and equilibrium model for data fitting. For complexes with multidentate macrocyclic ligands, the preferred pH-potentiometry techniques can lead to erroneous results. As highlighted above, pH-potentiometry can only be used to determine equilibrium constants reliably for reactions that occur in the pH range of 1.8–12.2.

The complex $[\text{Cu}(\text{DO3A})]^-$ exemplifies how the choice of the equilibrium model for data fitting can influence the determination of the stability constants.⁴⁷⁹ A stability constant of $\log K([\text{Cu}(\text{DO3A})]^-) = 23.1$ is calculated if $[\text{Cu}(\text{DO3A})]^-$, $[\text{Cu}(\text{HDO3A})]$, and $[\text{Cu}(\text{H}_2\text{DO3A})]^+$ are the only copper macrocyclic species considered. However, $\log K([\text{Cu}(\text{DO3A})]^-) = 26.49$ if the triprotonated species $[\text{Cu}(\text{H}_3\text{DO3A})]^{2+}$ is also included in the model. Similarly, for a system containing Cu^{II} and DO3A-PIC^{4-} , a stability constant $\log K([\text{Cu}(\text{DO3A-PIC})]^{2-}) = 22.32$ can be calculated from pH-potentiometric

titration data if the only species considered are $[\text{Cu}(\text{DO3A-PIC})]^{2-}$, $[\text{Cu}(\text{HDO3A-PIC})]^{-}$, and $\text{Cu}(\text{H}_2\text{DO3A-PIC})$. Such a fitting yields an acceptable fitting parameter.⁴⁸⁰ The same data can also be fitted by including the $[\text{Cu}(\text{H}_3\text{DO3A-PIC})]^{+}$ species in the model. Including this triprotonated species worsens the fitting parameter and increases the standard deviation on the concentration of each species calculated during the fitting (by nearly three log units). These differences do not necessarily mean that either model is incorrect (although this is one of the possibilities that should be considered). As seen from the species distribution curves calculated under the conditions applied in the study, it is evident that the problem is that the experimental conditions lead to an absence of non-complexed metal ions at the beginning of the titration. In other words, the system was out of the range of pH-potentiometry. Therefore, this approach cannot distinguish the formation of $[\text{Cu}(\text{H}_3\text{DO3A-PIC})]^{+}$ followed by its deprotonation (a two steps process) from the one-step formation of the diprotonated complex $\text{Cu}(\text{H}_2\text{DO3A-PIC})$ from Cu^{II} and the protonated ligand. This problem was resolved with a UV-visible titration that indicated the complete formation of $[\text{Cu}(\text{H}_3\text{DO3A-PIC})]^{+}$ at pH 1.75. Deprotonation of the triprotonated species to form $\text{Cu}(\text{H}_2\text{DO3A-PIC})$ occurs in the pH range of 1–2.

Similar differences can be found for most Gd^{III} complexes. Table 1.1 contains maximum and minimum stability constants and pGd values of some of the most widely studied Gd^{III} complexes. These data highlight the large differences in stability constants reported for each complex. These differences are largely the result of the equilibrium models used for data fitting as well as the different experimental techniques employed (pH-potentiometric and UV-visible methods). The speciation diagrams for $[\text{Gd}(\text{DTPA})]^{2-}$ reveal that complexation is expected to be complete near pH 2.5 and that only 10% of Gd^{III} is present in solution in non-complexed form at pH 2.0, the starting point of most pH titrations. This case is an example when another supporting method must be considered to ensure that the stability constants calculated from pH-potentiometry are reliable. For Gd^{III} complexes, relaxometry is one of the best methods to check speciation in

Table 1.1 Extreme values of the stability constants of $[\text{Gd}(\text{EDTA})]^{-}$, $[\text{Gd}(\text{DTPA})]^{2-}$, and $[\text{Gd}(\text{DOTA})]^{-}$ determined by various methods.

Complex	log <i>K</i>	pGd ^a	Method	Ref.
$[\text{Gd}(\text{EDTA})]^{-}$	16.28	14.6	pH-potentiometric titration	481
$[\text{Gd}(\text{EDTA})]^{-}$	17.70	15.9	UV-visible spectroscopy	482
$[\text{Gd}(\text{DTPA})]^{2-}$	20.73	18.3	pH-potentiometric titration	481
$[\text{Gd}(\text{DTPA})]^{2-}$	23.01	19.6	pH-potentiometric titration	165,483
$[\text{Gd}(\text{DOTA})]^{-}$	22.10	17.5	kinetic	334,484
$[\text{Gd}(\text{DOTA})]^{-}$	27.00	21.0	pH-potentiometric titration	392,485

^aCalculated using the approach suggested by Raymond and co-workers (pH = 7.4, $[\text{Gd}] = 1 \mu\text{M}$, and $[\text{L}] = 10 \mu\text{M}$);³⁸⁰ NaClO_4 (0.5 M) and 25 °C from ref. 481; $(\text{CH}_3)_4\text{NCl}$ (0.1 M) and 25 °C from ref. 482; KCl (0.1 M) and 25 °C from ref. 165; KCl (0.1 M) and 25 °C from ref. 483; NaCl (1.0 M) and 25 °C from ref. 386; NaCl (1.0 M) and 25 °C from ref. 484; $(\text{CH}_3)_4\text{NNO}_3$ (0.1 M) and 25 °C from ref. 392; $(\text{CH}_3)_4\text{NNO}_3$ (0.1 M) and 25 °C from ref. 485.

solution. Relaxometry can sometimes be used as a standalone technique for determining stability constants.⁴⁵⁷

There are other examples of open-chain Gd^{III} complexes for which even larger ranges of stability constants have been reported. For instance, the octadentate ligand OCTAPA (Figure 1.20) is often considered in radiochemistry for sequestering radioisotopes of Y^{III} , In^{III} , and Lu^{III} .⁴⁸⁶ It was also evaluated as a ligand for Gd^{III} for MRI applications.⁴⁸⁷ The stability constant of the Gd^{III} complex as determined by pH-potentiometry is $\log K([\text{Gd}(\text{OCTAPA})]^-) = 15.1$, whereas the stability constant for $[\text{Y}(\text{OCTAPA})]^-$ was reported to be 18.3.⁴⁸⁸ Furthermore, the stability of $[\text{Lu}(\text{OCTAPA})]^-$ was determined by competition titration with EDTA to be 20.08. The large difference between the stability constants of the complexes formed with intermediately sized Ln^{3+} ions (Gd^{III}) and smaller ones (Lu^{III}) suggests that OCTAPA could be used to separate Ln^{III} ions.⁴⁸⁹ A later study that used multiple methods, including ^1H -relaxometric and competition titrations with TTHA^{6-} , demonstrated that this is not the case. There is little difference between the stability of the Gd^{III} and Lu^{III} OCTPA complexes; the stability constant of $[\text{Gd}(\text{OCTAPA})]^-$ is 20.23–20.39, which is in agreement with other reports.^{477,488} The speciation diagrams calculated from the reported pH-potentiometry data⁴⁸⁷ and the ^1H -relaxometric titration data (Figure 1.26) indicate that the complexation of $[\text{Gd}(\text{OCTAPA})]^-$ is complete at pH 1.75. Thus, pH-potentiometry alone is not sufficient for studying this system. Instead, precise determination of speciation in solution requires that data from both pH-potentiometry and ^1H -relaxometry be treated simultaneously.

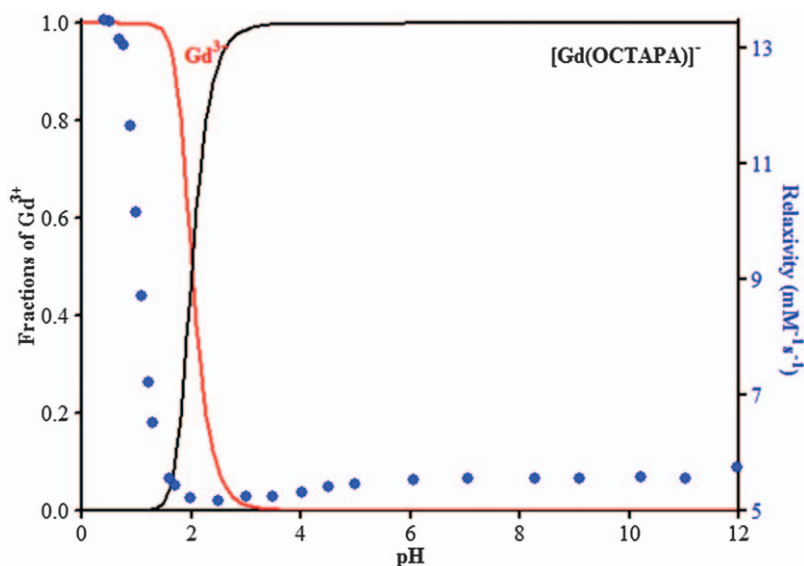


Figure 1.26 Species distribution curves and relaxivity values (blue dots as measured at 25 °C and 20 MHz) as a function of pH calculated from data published in ref. 477 and 487.

A similar situation was found with EDTMP (Figure 1.20), a linear tetra-phosphonate ligand. The $^{153}\text{Sm}^{\text{III}}$ complex of EDTMP is used in the palliation of pain associated with metastatic bone cancer. The stability constants reported for the Gd^{III} complex of EDTMP vary widely between 14.87 [$T = 37\text{ }^\circ\text{C}$, NaCl (0.15 M)]⁴⁹⁰ and 21.80 [$T = 25\text{ }^\circ\text{C}$, KCl (0.1 M)].⁴⁹¹ Even larger differences were reported for the stability constants of $[\text{Y}(\text{EDTMP})]^{5-}$ they vary between $\log K = 11.11$ and 19.18.⁴⁹² The first value was measured by pH-potentiometry [$T = 25\text{ }^\circ\text{C}$, KCl (0.10 M)];⁴⁹³ the second by competition with Cu^{II} in the presence of citrate monitored by UV-visible spectrophotometry [$T = 25\text{ }^\circ\text{C}$, NaCl (0.15 M)].⁴⁹² The reported stability constants for the Ho^{III} complex of EDTMP vary by as much as 8.5 orders of magnitude.^{490,491} These examples highlight the importance of the supportive data when determining the stability constants of complexes.

For macrocyclic systems, the problems of selecting the correct method and appropriate equilibrium model are compounded by the relatively slow kinetics of formation and dissociation. A final in-cage macrocyclic complex forms *via* a stable protonated, out-of-cage intermediate and its subsequent deprotonation followed by or concerted with structural rearrangements.^{31,494} The absorption spectra of $[\text{Ce}(\text{DOTA})]^-$ shown in Figure 1.27 exemplify this stepwise binding.

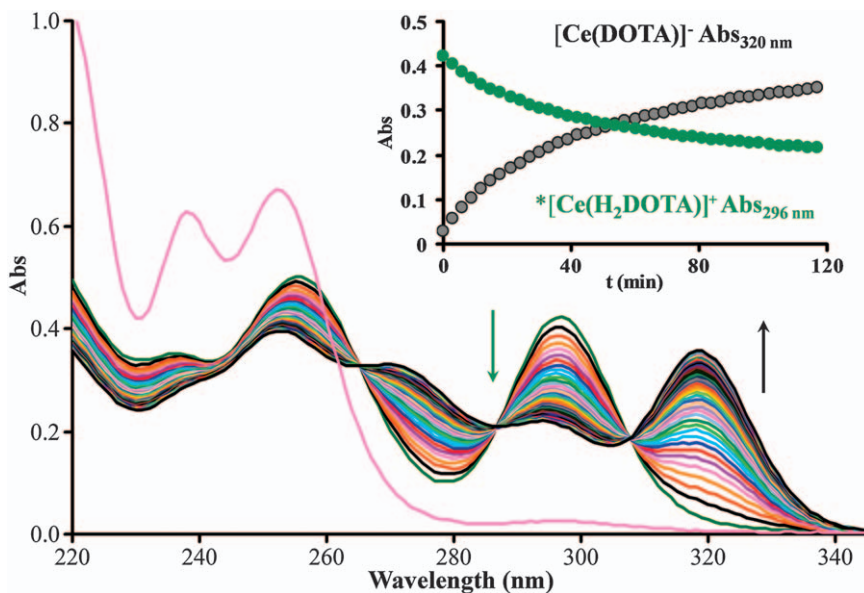


Figure 1.27 Absorption spectra of Ce^{III} (aq) and the formation of $\text{Ce}^{\text{III}}\text{DOTA}$ with time. The insert shows the absorbance at 296 nm (λ_{max} characteristic for the reaction intermediate) and 320 nm (λ_{max} characteristic for $[\text{Ce}(\text{DOTA})]^-$) as a function of time. Experimental conditions: $[\text{Ce}^{\text{III}}] = [\text{DOTA}] = 1.0\text{ mM}$, $\text{pH} = 4.46$, $l = 0.874\text{ cm}$, $[\text{NaCl}] = 0.15\text{ M}$, and $25\text{ }^\circ\text{C}$.

As depicted in Figure 1.27, the formation of $[\text{Ce}(\text{DOTA})]^-$ is a slow process that can be monitored by UV-visible spectrophotometry. The formation of $[\text{Ln}(\text{DOTA})]^-$ complexes takes place *via* the formation of a stable diprotonated $*[\text{Ln}(\text{H}_2\text{DOTA})]^+$ intermediate that must deprotonate to form the final $[\text{Ln}(\text{DOTA})]^-$ complex. Water molecules act as Brønsted bases and OH^- ions assist the deprotonation in the rate-determining step.^{31,495} Addition of Ce^{III} to H_xDOTA results in the immediate formation of the diprotonated $*[\text{Ce}(\text{H}_2\text{DOTA})]^+$, which is characterized by two new absorption bands at 260 and 296 nm. With time, the intensities of these absorption bands decrease, whereas the intensities of the absorption bands of the final $[\text{Ce}(\text{DOTA})]^-$ complex at 275 and 320 nm increase. The formation of $[\text{Ce}(\text{DOTA})]^-$ is fairly slow even at pH 4.46, and complete complexation requires a long time (6–12 weeks) at room temperature depending on the acidity of the samples (Figure 1.27). The most reliable experiments require the preparation of duplicate samples of the most acidic and most basic intermediates such that their absorbance (Ce^{III} and Eu^{III}), luminescence (Eu^{III} and Tb^{III}), or relaxivity (Gd^{III}) can be recorded as a function of time. One issue with this protocol is that the rates of complex formation depend on the size of the metal ions; data obtained using Ce^{III} might not be valid for Yb^{III} complexes.

The kinetics of complex formation is also a function of the ligand and its donor atoms (acetates in DOTA *versus* amides in DOTAM). For systems with slow kinetics of complexation, samples must be tightly sealed in vials so as to ensure that no solvent evaporates during the equilibration time. Sealed ampoules are preferable. For Ce^{III} complexes, photocatalytic oxidation of the metal to Ce^{IV} by visible light should also be considered. Such oxidation renders long-term studies with Ce^{III} complexes that require long equilibration times difficult to perform.⁴⁹⁶ Thus, it is easier to study Gd^{III} complexes and record in duplicate their relaxivity as a function of time. In this manner, reliable equilibrium data can be obtained with Gd^{III} even for slowly forming systems such as those involving DOTA^{31,494} or DOTAM^{404,445} if all of the suggestions in this chapter are taken into account. Several methods have been reported for determining stability constants of $[\text{Ln}(\text{DOTA})]^-$ complexes. These methods include direct techniques such as pH-potentiometry,⁴⁸⁵ capillary electrophoresis,⁴⁶⁵ and luminescence spectroscopy,⁴⁴¹ and indirect techniques, such as competitions titrations monitored by UV-visible spectroscopy.⁴³¹

Competition reactions can be used to determine the stability constants of macrocyclic complexes. However, the rates of complex formation are further decreased in the presence of competing partners, such as metal ions or ligands. These competitors reduce the concentration of the reaction intermediate ($*[\text{Ln}(\text{H}_2\text{DOTA})]^+$), thereby increasing the time necessary to reach equilibrium. The structure of the ligand might also affect the time required for equilibration and the determination of stability constants. For instance, the steric hindrance caused by the methyl groups in DOTMA slows the rate of complex formation by nearly two orders of magnitude. Similar decreases in rates of formation are found for some dipicolinates derived from cyclen

(DODPA and Me2DODPA, Figure 1.20).^{112,476} Moreover, in some cases, such as for dipicolinate derivatives of rigid, cross-bridged macrocycles like CB-TEDPA (Figure 1.20), there is no suitable method for the determination of stability constants because the Ln^{III} complexes of these ligands form and dissociate extremely slowly at room temperature.⁴⁹⁷ Computational methods such as density functional theory or quantitative structure–property relationships modeling might be useful when experimental determination of the stability constants is not feasible. Computational methods can also facilitate the design of experiments to measure stability constants.^{498–501}

1.3.6 Acknowledgements

The authors thank the Hungarian Scientific Research Fund (NKFIH K-120224 project). The writing of this book chapter was supported by the János Bolyai Research Scholarship of the Hungarian Academy of Sciences (G.T. and F.K.K.), the EU and co-financed by the European Regional Development Fund under the project GINOP-2.3.2-15-2016-00008 as well as the COST CA15209 “European Network on NMR Relaxometry” Action. Special thanks go to Prof. Michel Meyer (ICMUB, Dijon, France) for sharing the information concerning apparent constant and for reviewing the corresponding part in the chapter. F.K.K. and G.T. are also thankful for support from the Le Studium – Loire Valley Institute for Advanced Studies.

1.4 Lability of Metal Complexes

GYULA TIRCSÓ,* ZSOLT BARANYAI, FERENC KRISZTIÁN KÁLMÁN,
ZOLTÁN KOVÁCS, ERNŐ BRÜCHER AND IMRE TÓTH

1.4.1 Introduction

Kinetic inertness is one of the most important parameters to predict the *in vivo* safety of metal complexes because the products of dissociation, the released metal ion and ligand, are potentially toxic. No metal–ligand complex has unlimited thermodynamic stability. Generally, the receiving biological media of a diagnostic or therapeutic agent contains a large number of compounds that can serve as ligands and many metal ions that can interact with the components of the administered agents. Therefore, biofluids are competitive media. Thus, metal complexes considered for *in vivo* use must be highly inert to prevent transmetallation or transchelation. High levels of inertness are required both for safety and for targeting purposes to ensure that intact complex is delivered to a target organ or tissue. Therefore, physico-chemical characterization of complexes intended for medical diagnosis and therapy should include kinetic studies, and knowledge of dissociation rates is particularly important.

Kinetic inertness is a better predictor of the safety of metal-based contrast agents than thermodynamic stability constants. This statement can be rationalized because complexes are expected to dissociate if any thermodynamic force for the dissociation exists. However, this does not necessarily mean that equilibrium is attained rapidly. Dissociation can be slow enough to enable safe applications of metal complexes with relatively lower thermodynamic stability constants. It is therefore important to know the expected rate of release of metal ions and ligands in living systems. Various approaches have been reported to characterize the kinetic inertness of metal complexes depending on their mechanism of dissociation. The mechanism is different for complexes formed with linear and macrocyclic ligands. Moreover, the rates of dissociation of complexes with linear ligands are usually faster than those incorporating macrocyclic ones. It should be emphasized, however, that the rates of dissociation of macrocyclic complexes are largely influenced by the size of the macrocycle. Rates of dissociation are faster when the macrocycle is either much smaller or much larger than the metal ion.

Dissociation of linear complexes is often catalyzed by other endogenous metal ions such as Cu^{II} via a mechanism that involves direct interaction between the complex and the exchanging metal ion. For Gd^{III} complexes of various 9- to 13-membered macrocyclic triaza and tetraza ligands, acid-assisted decomplexation is the most important pathway leading to the release of Gd^{III} . Owing to these differences, the inertness of linear complexes is usually studied in metal-exchange reactions with biologically essential transition metal ions such as Cu^{II} and Zn^{II} or with other Ln^{III} ions such as Eu^{III} and Tb^{III} . The inertness of macrocyclic complexes, on the other hand, is normally evaluated by the acid-catalyzed dissociation of the complex.

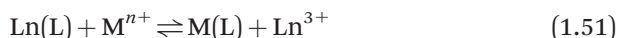
The effect of biogenic ligands on the rates of dissociation has not been studied as much as dissociation catalyzed by metal ions. However, some studies indicate that the inertness of some neutral Gd^{III} complexes formed with linear ligands might be negatively affected by the presence of bioligands. Thus, the effect of these endogenous ligands needs to be considered in the design of new ligands for biomedical applications. The goal of this section is to present an overview of reported methods for obtaining dissociation kinetic data. Structural features of the ligands that influence dissociation kinetics are also summarized. These data are intended to aid in the design of inert complexes for future applications.

1.4.2 Dissociation Kinetics of Metal Chelates

Metal complexes used as contrast agents in MRI should stay intact *in vivo* to avoid the dissociation of toxic metal ions. The half-life ($t_{1/2}$) of the excretion of small molecular weight lanthanide complexes through healthy human kidneys is about 1.5 hours.³⁶⁶ Therefore, 12 hours after intravenous administration, less than 1% of common contrast agents is expected to remain in the body. The retention times of complexes *in vivo* are lengthened in patients with compromised kidney functions, which increases the possibility of the contrast agent dissociating *in vivo*.

The *in vivo* dechelation of metal complexes can occur when endogenous metal ions—specifically Ca^{II} , Zn^{II} , or Cu^{II} —compete with the paramagnetic metal ion for the chelating ligand or when endogenous ligands—such as citrate, phosphate, or carbonate—compete with the chelating ligand for the paramagnetic metal ion. The dissociation mechanisms of metal complexes do not differ fundamentally from each other, and the dissociation pathways shown below for the lanthanide complexes can also be adapted to other complexes.

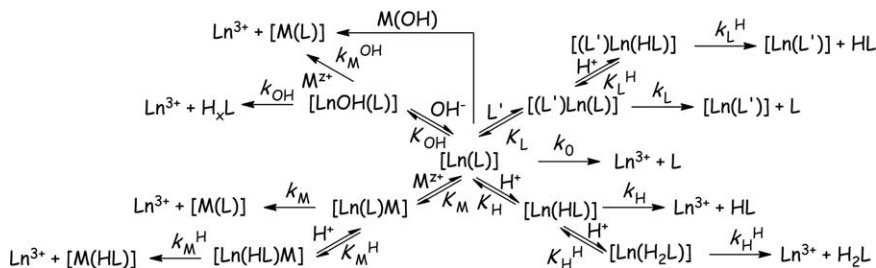
The kinetic inertness of a lanthanide complex is characterized by its rate of exchange with competing metal ions, often Cu^{II} or Zn^{II} , as indicated by eqn (1.51).



The stability constants of lanthanide complexes formed with endogenous ligands are generally orders of magnitude smaller than those of contrast agents. The mechanisms of ligand-exchange reactions are often associative and include the formation of ternary intermediate complexes. In this mechanism, some of the donor atoms of the exchanging ligand coordinate to the competing metal ion and others coordinate to the lanthanide ion. Overall ligand-exchange reactions are described by eqn (1.52).



Metal-exchange reactions can proceed through several pathways (Scheme 1.17). One such pathway is the exchanging metal-assisted mechanism, which involves direct attack of the metal ion at the complex, resulting



Scheme 1.17 Possible reaction mechanisms for the dissociation of Ln^{III} complexes (charges of complexes are omitted for clarity).

in the formation of a dinuclear intermediate, $[\text{Ln}(\text{L})\text{M}]$. In this intermediate, the functional groups of the ligand transfer stepwise from the Ln^{III} ion to the exchanging metal ion. Another possible mechanism involves the spontaneous or proton-assisted dissociation of the Ln^{III} ion from the complex followed by the reaction between the free ligand and the exchanging metal ion. The protonated complex can also be attacked by the exchanging metal ion resulting in a dinuclear protonated intermediate that dissociates to the exchanging metal complex and the Ln^{III} ion. Hydroxide-assisted pathways rarely play important roles in exchange reactions.

To obtain information regarding the kinetic inertness of metal complexes, metal-exchange reactions are frequently studied using at least 10-fold excess of the exchanging metal ion at different pH values. Under these conditions, reactions can be treated as pseudo-first-order processes, and thus, observed rate constants, k_{obs} , are also pseudo-first-order. In the presence of a large excess of the exchanging metal ion, the rate of exchange reactions can be expressed by eqn (1.53), where k_{obs} is the pseudo-first-order rate constant and $[\text{Ln}(\text{L})]_{\text{t}}$ is the total concentration of the Ln^{III} complex.

$$-\frac{d[\text{Ln}(\text{L})]_{\text{t}}}{dt} = k_{\text{obs}}[\text{Ln}(\text{L})]_{\text{t}} \quad (1.53)$$

Considering all the possible pathways shown in Scheme 1.17, the concentration of $\text{Ln}(\text{L})$ can be given as the sum of the concentrations of all species comprising both L and M.

$$[\text{Ln}(\text{L})]_{\text{t}} = [\text{LnL}] + [\text{Ln}(\text{HL})] + [\text{Ln}(\text{H}_2\text{L})] + [\text{Ln}(\text{OH})(\text{L})] + [\text{Ln}(\text{L})\text{M}(\text{OH})] \\ + [\text{Ln}(\text{L})\text{M}] + [\text{Ln}(\text{HL})\text{M}] + [\text{Ln}(\text{L})\text{L}'] + [\text{Ln}(\text{HL})\text{L}'] \quad (1.54)$$

Eqn (1.53) and (1.54) can be combined to give the following rate equation:

$$-\frac{d[\text{Ln}(\text{L})]_{\text{t}}}{dt} = k_{\text{obs}}[\text{Ln}(\text{L})]_{\text{t}} = k_0[\text{Ln}(\text{L})] + k_{\text{H}}[\text{Ln}(\text{HL})] + k_{\text{H}}^{\text{H}}[\text{Ln}(\text{H}_2\text{L})] \\ + k_{\text{OH}}[\text{Ln}(\text{OH})(\text{L})] + k_{\text{M}}^{\text{OH}}[\text{Ln}(\text{L})\text{M}(\text{OH})] + k_{\text{M}}[\text{Ln}(\text{L})\text{M}] \\ + k_{\text{M}}^{\text{H}}[\text{Ln}(\text{HL})\text{M}] + k_{\text{L}}[\text{Ln}(\text{L})\text{L}'] + k_{\text{L}}^{\text{H}}[\text{Ln}(\text{HL})\text{L}'] \quad (1.55)$$

The rate constants in eqn (1.55) characterize the rate of the spontaneous (k_0), proton-assisted (k_H and k_H^H), hydroxide-assisted (k_{OH}), hydroxide-metal-assisted (k_M^{OH}), metal-assisted (k_M), proton-metal-assisted (k_M^H), ligand-assisted (k_L), and proton-ligand-assisted (k_L^H) pathways.

Taking into account the different reaction pathways shown in Scheme 1.17 and the equations determining the $K_{Ln(HL)}$, $K_{Ln(H_2L)}$, $K_{Ln(OH)(L)}$, $K_{Ln(L)M(OH)}$, $K_{Ln(L)M}$, $K_{Ln(HL)M}$, $K_{Ln(L)(L')}$, and $K_{Ln(HL)(L')}$ equilibrium constants, the pseudo-first-order rate constant (k_{obs}) can be expressed by eqn (1.56):

$$k_{obs} = \frac{k_0 + k_1[H^+] + k_2[H^+]^2 + k_3[M^{n+}] + k_4[M^{n+}][H^+] + k_5[OH^-] +}{1 + K_{Ln(HL)}[H^+] + K_{Ln(H_2L)}[H^+]^2 + K_{Ln(L)M}[M^{n+}] + K_{Ln(HL)M}[M^{n+}][H^+] +} \\ \frac{+ k_6[M^{n+}][OH^-] + k_7[L'] + k_8[L'][H^+]}{+ K_{Ln(OH)(L)}[OH^-] + K_{Ln(L)M(OH)}[M^{n+}][OH^-] + K_{Ln(L)(L')}[L'] + K_{Ln(HL)(L')}[L'][H^+]} \quad (1.56)$$

In eqn (1.56), $K_{LnHL} = [Ln(HL)]/\{[Ln(L)][H^+]\}$, $K_{Ln(H_2L)} = [Ln(H_2L)]/\{[Ln(HL)][H^+]\}$, $K_{Ln(L)M} = [Ln(L)M]/\{[Ln(L)][M]\}$, $K_{Ln(HL)M} = [Ln(HL)M]/\{[Ln(HL)][M]\}$, $K_{Ln(OH)(L)} = [Ln(OH)(L)]/\{[Ln(L)][OH^-]\}$, $K_{Ln(L)M(OH)} = [Ln(L)M(OH)]/\{[Ln(L)][M(OH)]\}$, $K_{Ln(L)(L')} = [Ln(L)(L')]/\{[Ln(L)][L']\}$, $K_{Ln(HL)(L')} = [Ln(HL)(L')]/\{[Ln(HL)][L']\}$, $k_1 = k_H K_{Ln(HL)}$, $k_2 = k_H^H K_{Ln(HL)}$, $k_3 = k_M K_{Ln(L)M}$, $k_4 = k_M^H K_{Ln(HL)M}$, $k_5 = k_{OH} K_{Ln(OH)(L)}$, $k_6 = k_M^{OH} K_{Ln(L)M(OH)}$, $k_7 = k_L K_{Ln(L)(L')}$, and $k_8 = k_L^H K_{Ln(HL)(L')}$. Eqn (1.56) takes into account all of the rational dissociation pathways and provides a general description for dissociation rates.

Kinetic data of slowly dissociating (macrocyclic) complexes can be obtained by performing dissociation reactions under conditions where the concentration of the complex is high (~ 0.1 M) but the exchanging metal ion (for example, Cu^{II}) or its labile complex is present at a much lower concentration (pseudo-first-order conditions). Under these conditions, the rate of decomplexation (rate of formation of a CuL complex) can be followed by UV-visible spectrophotometry and expressed as follows:

$$-\frac{d[GdL]_t}{dt} = \frac{d[CuL]_t}{dt} = k_{obs}[GdL]_t, \quad \text{where } k_{obs} = \frac{\Delta Abs}{\Delta t(\epsilon_{[Cu(L)]} - \epsilon_{Cu^{2+}})[GdL]_t} \quad (1.57)$$

In eqn (1.57), $[Gd(L)]_t$ and $[Cu(L)]_t$ are the total concentrations of the $Gd(L)$ and $Cu(L)$ complexes, and k_{obs} is the pseudo-first-order rate constant. The formation rates of $Cu(L)$ complexes can be calculated from the slope of the absorbance *versus* time curves by accessing the concentration of $Cu(L)$ complexes at various time points. The method requires knowledge of the molar absorptivity coefficients of the Cu^{II} or $Cu(A)$ (where A is a ligand that binds Cu^{II} in a labile complex) and the $Cu(L)$ complexes. This approach enables the rapid determination of the dissociation kinetic parameters;

however, it also requires a relatively large amount of the complex Gd(L), even when micro-cuvettes are used.

Despite numerous publications describing the determination of rate constants (k_0) characterizing the spontaneous dissociation of metal chelates, there is no well-tested theory that satisfactorily interprets the molecular mechanism of this dissociation pathway. Based on the rate equations established by metal- or ligand-exchange reactions, the effect of the spontaneous pathway on the overall dissociation of a given complex must be independent of pH and of the concentrations of the exchanging partners. Analogously to the decay of radionuclides, spontaneous dissociation can be regarded as a monomolecular decay in which several coordinative bonds are broken simultaneously, a process that is induced by the fast internal motions of the molecule. These internal motions can be accelerated by molecular collisions with, for instance, solvent molecules. As expected, increasing the temperature increases the rate of spontaneous dissociation. Theoretically, spontaneous dissociation of GdL complexes could potentially be associated with the auto-dissociation of water, which results in the formation of H^+ and OH^- ions, which in turn could induce decomplexation. Because this process would be independent of pH, it is unlikely.

The k_0 value of metal complexes is generally small, and therefore accurate determination of k_0 can be challenging. For example, the spontaneous dissociation of $[Gd(DOTA)]^-$ was first determined to be $<5 \times 10^{-8} s^{-1}$, which is within the limits of the experimental error.⁴⁸⁴ This value was later refined to be $(5 \pm 2) \times 10^{-10} s^{-1}$.³¹ Almost a decade later, the value of k_0 was re-determined for $[Gd(DOTA)]^-$ to be $(6.7 \pm 0.4) \times 10^{-11} s^{-1}$.⁴⁰⁸ For accurate determination of k_0 , the kinetic inertness of a complex should be investigated at neutral or slightly basic conditions, where the role of proton-catalyzed dissociation is negligible or comparable with that of spontaneous dissociation. Considering that k_0 for $[Gd(DOTA)]^-$ is near $10^{-10} s^{-1}$, the half-life of such a reaction would be nearly 200 years, give or take a few decades. This timescale demonstrates why it is necessary to study the kinetic properties of the macrocyclic metal chelates in acidic conditions, where the relatively fast proton-assisted pathway is the major dissociation pathway. Under these conditions, the value of k_0 is frequently calculated to be zero or to have a negative value with large error, thus accounting for the discrepancies in the values of k_0 reported for $[Gd(DOTA)]^-$. Although spontaneous dissociation rates of open-chain Ln^{III} complexes are orders of magnitude faster than those of macrocyclic complexes, k_0 can be neglected in most cases.³⁹¹

Complexes of ligands having highly basic donor groups, such as phosphonates or amines, can be protonated over a wide pH range. Frequently, investigation of kinetic inertness is performed in acidic solutions, where the basic donor groups are protonated. In these systems, k_0 characterizes the spontaneous dissociation of the protonated species $Ln(H_xL)$, which means that information regarding dissociation of the completely deprotonated form, $Ln(L)$, cannot be obtained from these measurements.^{386,502} The presence of an OH^- -assisted pathway in the exchange reaction of a complex can prevent

the evaluation of k_0 because OH^- -assisted dissociation becomes the dominant reaction pathway when the concentration of H^+ decreases.^{401,477,503}

Proton-assisted dissociation of metal complexes requires the formation of a protonated intermediate that can be either a thermodynamically stable species in the given pH range or a kinetically active but directly undetectable minor intermediate. The protonation of complexes usually occurs at pendant arms when they are dissociated from the metal ion. Following protonation, the proton from the pendant arm transfers to a nitrogen donor atom of the ligand backbone, which eventually leads to the dissociation of the metal ion from the complex. Proton transfer is generally a slow process because of the electrostatic repulsion between positively charged Ln^{III} ions and protons. The complexes formed between lanthanide ions and macrocyclic ligands are relatively inert to proton-assisted dissociation owing to the rigid structure of the coordination cavity. Proton-assisted dissociation of open-chain complexes is several orders of magnitude faster.^{30,386,391,403,404,407,484,504–509}

Because of their high kinetic inertness, the dissociation reactions of macrocyclic complexes can in practice only be investigated in acidic or highly acidic conditions. Because macrocyclic lanthanide complexes are not stable thermodynamically in highly acidic solutions, their dissociation can be studied without the use of exchanging metal ions or ligands.^{31,250,386,403,404,477,484,510} The determination of the rate constants (k_1 and k_2) characterizing the proton-assisted pathways is relatively straightforward. In some cases, however, the rate constants k_1 and k_2 cannot be determined from the kinetic data because the metal-exchange reaction involves competing metal- or hydroxide-assisted pathways. In such cases, an alternative method must be found to characterize the proton-assisted pathway independently. These alternative methods might require performing dissociation reactions under acidic conditions or ligand-exchange reactions in an appropriately chosen pH range.^{477,503,511}

The metal-assisted pathways (k_{M} and k_{M}^{H}) play an important role in the metal-exchange reactions of complexes with flexible open-chain ligands but can be neglected in the dissociation of rigid macrocyclic complexes. In metal-assisted pathways, the formation of a relatively stable dinuclear intermediate is essential as it enables the donor atoms of the ligand to be transferred in a stepwise fashion to the incoming metal ion. Higher stabilities of dinuclear intermediates correlate with larger rate constants (k_{M}), which characterize metal-assisted dissociation. The direct interaction of the exchanging metal ion becomes important at pH values where the extent of proton- and metal-assisted dissociation are similar. Thus, the metal-assisted pathway is the dominant one for transmetalation under physiological conditions.^{388,507,512} The exchanging metal ion can also interact with the protonated complex forming a protonated dinuclear intermediate.^{391,506}

The hydroxide-assisted and hydroxide-metal-assisted pathways (k_{OH} and k_{M}^{OH}) rarely play a role in the exchange reactions of metal complexes. Nevertheless, the strength of the interactions between metal ions and coordinating ligands can be weakened by the coordination of a hydroxide ion

due to a decrease of electrostatic attraction, resulting in faster dissociation.⁴⁰¹ When Cu^{II} is used as the exchanging metal ion, the dissociation of the complex depends on the concentrations of both OH^- and Cu^{II} .^{477,503} The kinetic activity of $[\text{Cu}(\text{OH})]^+$ is greater than that of the Cu^{II} aqua ion in substitution reactions.⁵¹³

The rates of ligand-exchange reactions of contrast agents for MRI are rarely investigated. However, some data have been published on the role of ligand-exchange reactions in the dissociation of clinically approved and potential MR contrast agents. These studies revealed that the exchanging ligands can directly attack both the deprotonated and protonated form of the metal complex (k_{L} and k_{L}^{H}), forming ternary intermediates.⁵¹¹ Small endogenous ligands such as citrate, carbonate, or phosphate accelerate *in vivo* dissociation because the formation of ternary complexes between the contrast agents and these ligands eventually leads to the release of Gd^{III} ions.^{407,514} These results demonstrate that the fast dissociation of ternary complexes formed with endogenous ligands can contribute to the *in vivo* dissociation of contrast agents. Previously, the dissociation assisted by endogenous metal ions was thought to be the most important dissociation pathway in spite of the low plasma concentration of these ions.

Last but not least, the protonation and stability constants of the intermediates formed during exchange reactions ($K_{\text{Ln}(\text{HL})}$, $K_{\text{Ln}(\text{H}_2\text{L})}$, $K_{\text{Ln}(\text{OH})(\text{L})}$, $K_{\text{Ln}(\text{L})\text{M}(\text{OH})}$, $K_{\text{Ln}(\text{L})\text{M}}$, $K_{\text{Ln}(\text{HL})\text{M}}$, $K_{\text{Ln}(\text{L})(\text{L}^')}$, and $K_{\text{Ln}(\text{HL})(\text{L}^')}$) often cannot be calculated because the concentrations of these complexes are low and their kinetic activity is high. With the exception of the protonated metal chelates, the independent determination of these constants is not possible because most of these intermediates are short-lived, reactive species. Values of $K_{\text{Ln}(\text{HL})}$ and $K_{\text{Ln}(\text{H}_2\text{L})}$ can be determined separately and are often used as fixed constants in the calculations of kinetic parameters.

1.4.3 Methods for Kinetic Studies

Several methods have been proposed to characterize the kinetic inertness of Gd^{III} complexes. These include optical methods such as UV-visible spectrophotometry,⁵¹⁵ luminescence spectroscopy, and luminescence-life-time measurements,⁵⁰⁴ direct NMR methods, T_1 or T_2 relaxometry,^{408,516} capillary electrophoretic methods,⁵¹⁷ high-performance liquid chromatography methods, and inductively coupled plasma atomic emission spectrometry or inductively coupled plasma mass spectrometry coupled with other separation techniques.^{518–520} Among these methods, UV-visible spectrophotometry is the most widespread owing to the availability of the instrument and applicability of the technique to a broad range of reaction times. Stopped-flow UV-visible spectrophotometry can be used for fast reactions, whereas conventional UV-visible spectrophotometry is applicable for reactions occurring on time scales of a few minutes to a few days. The rates of slow reactions can be followed by periodically measuring the absorbance of samples over a period of months. However, it should be kept in mind that these methods are limited to the

study of complexes (or products of dissociation) that absorb either in the UV or in the visible range of the electromagnetic spectrum. Because this is often not the case for Gd^{III} complexes, Cu^{II} is usually used as a ligand scavenger when studying metal-exchange reactions; Cu^{II} usually rapidly forms complexes with ligands released from contrast agents. The ligand-to-metal charge transfer transitions of Cu^{II} complexes typically have strong absorptions in the UV-visible range of the electromagnetic spectrum. Thus, the dissociation of the $\text{Ln}(\text{L})$ complexes can be monitored indirectly by measuring the formation of the CuL complexes.

Studying the dissociation reactions of Eu^{III} complexes is another option. Because Eu^{III} has a nearly identical radius to Gd^{III} , Eu^{III} and Gd^{III} complexes are expected to have similar dissociation kinetics. The absorption bands of Eu^{III} that form broad shoulders in the range of 220 to 300 nm enable direct measurement of dissociation rates. Direct NMR (^1H -NMR spectra of La^{III} , Y^{III} , Eu^{III} , and Lu^{III} complexes) and relaxation techniques (T_1 or T_2 relaxometry) can be used to monitor reactions occurring on the half hour or longer time scales. This technique is more appropriate for slower reactions because each data points require seconds to tens of seconds (for the relaxation techniques) to be acquired. Experimental methods that can be used at moderately acidic or higher pH ranges, such as the ones based on capillary electrophoresis or high-performance liquid chromatography, are routinely used for studying dissociation reactions near physiological conditions as well as in more complex media such as artificial fluids that mimic biofluids or serum.

1.4.4 Decomplexation Reactions near Physiological Conditions

The kinetic stabilities of complexes are routinely characterized by the rates of their dissociation, k_{d} , first order-rate constants measured in HCl (0.1 M) or by the rates of transmetallation reactions occurring with Zn^{II} , Cu^{II} , or Eu^{III} ions in the pH range of 3 to 6 (25 °C and 1.0 M KCl).^{507,512,521} Unfortunately, the rate constants obtained under such conditions cannot be directly used to estimate the kinetic behavior of complexes close to physiological conditions (pH 7.4, 37 °C, and 0.15 M NaCl). To understand and describe the kinetic properties of metal complexes, the rates of dissociation reactions should be studied as close as possible to physiologically relevant pH and other biological conditions.

It is generally assumed that dechelation of metal complexes in biological fluids takes place *via* transmetallation reactions with Zn^{II} and Cu^{II} . The formation of dinuclear complex intermediates is essential for metal exchange. Dechelation can also occur *via* ligand exchange reactions, whereby an endogenous ligand displaces the chelating agent of the Gd^{III} complex. Phosphate ions compete with the aminopolycarboxylate ligands for Gd^{III} in the presence of ZnCl_2 or CuCl_2 to yield the insoluble GdPO_4 (GdPO_4 : $K_{\text{sp}} = 10^{-20.53}$ at 37 °C in 0.15 M NaCl).⁴⁰⁷ In the absence of these metal salts,

dissociation reactions do not proceed. The rate-determining step of transmetallation and ligand-exchange reactions is dissociation of the metal followed by fast reactions of the released metal ion and ligand with the exchanging ligand or metal ion, respectively.

Dissociation reactions of macrocyclic Gd^{III} complexes occur mainly *via* proton-assisted pathways.^{408,507,512,521} Dissociation reactions of Gd^{III} complexes formed with derivatives of DTPA are affected by citrate, phosphate, and bicarbonate ions, which form labile ternary intermediates at physiological conditions.^{407,408} The kinetic properties of the complexes formed with other Ln^{III} ions and Y^{III} are similar to those observed for Gd^{III} complexes.²⁵³

Several methods have been proposed to characterize the kinetic inertness of Gd^{III} complexes close to physiological conditions. These include (i) relaxometric;⁵²² (ii) spectrophotometric;^{407,408} and (iii) high-performance liquid chromatography,^{523,524} inductively coupled plasma atomic emission spectroscopy,⁵²⁴ inductively coupled plasma mass spectrometry,⁵²³ and capillary electrophoresis^{407,525,526} measurements.

(i) Relaxometric Measurements

One relaxometric method determines the rates of dechelation of Gd^{III} complexes by the rate of formation of insoluble GdPO_4 .⁵²² In phosphate buffer at pH 7 and 37 °C, non-complexed Gd^{III} , released from Gd^{III} complexes in the presence of Zn^{II} , forms GdPO_4 , which precipitates from solution. This results in a decrease of the relaxation rate of the solution. The experimental setup of this method is shown in Figure 1.28. The ratios of the relaxation rates measured at time t and at the start ($t = 0$) of the reaction $[R_1^{\text{P}}(t)/R_1^{\text{P}}(t = 0)]$ for $[\text{Gd}(\text{DOTA})]^-$, $[\text{Gd}(\text{EOB-DTPA})]^{2-}$, $[\text{Gd}(\text{DTPA})]^{2-}$, and $\text{Gd}(\text{DTPA-BMA})$ are shown in Figure 1.29.

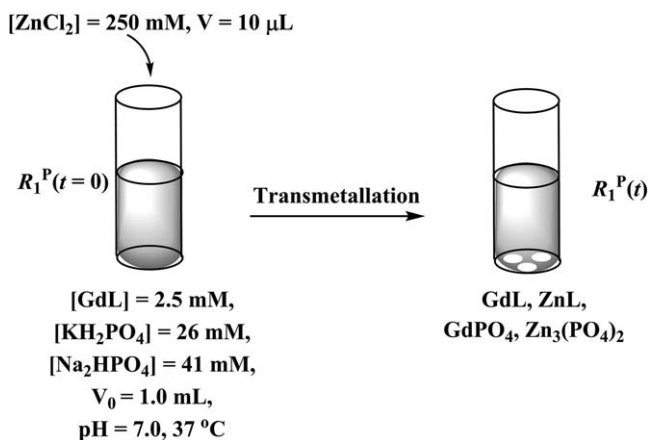


Figure 1.28 Experimental set up of the relaxometric measurements.

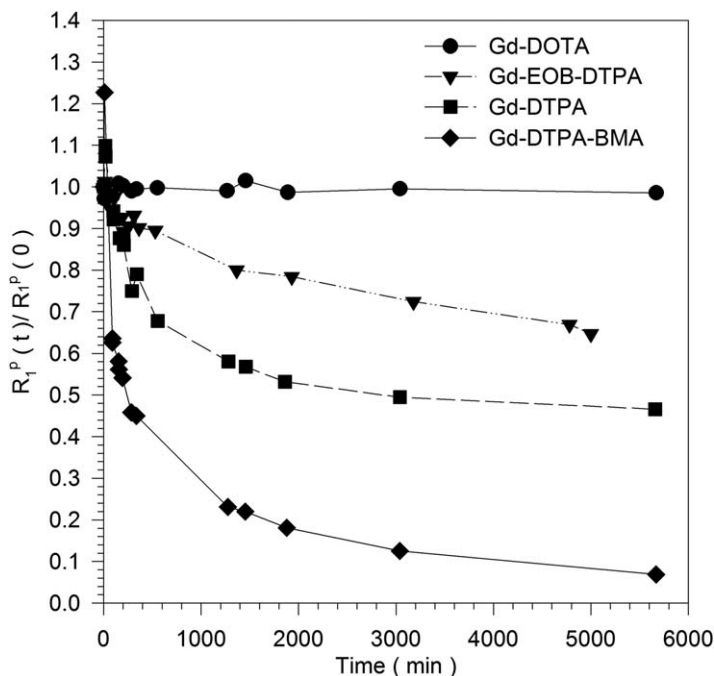


Figure 1.29 $R_1^P(t)/R_1^P(t=0)$ ratio values for $[\text{Gd}(\text{DOTA})]^-$, $[\text{Gd}(\text{EOB-DTPA})]^{2-}$, $[\text{Gd}(\text{DTPA})]^{2-}$, and $\text{Gd}(\text{DTPA-BMA})$ as a function of time.

This method enables rapid comparison of different complexes, but it cannot be used for kinetic studies because $\text{Zn}_3(\text{PO}_4)_2$ precipitate also forms during the reaction, decreasing the concentration of Zn^{II} over time. Additionally, an excess of phosphate increases the dissociation rates of Gd^{III} complexes owing to the phosphate-assisted mechanism.^{407,408} Importantly, the kinetic properties of macrocyclic Gd^{III} complexes cannot be compared with this method because the relaxation rates of solutions of macrocyclic complexes do not change over time (Figure 1.29).

(ii) **Spectrophotometric Measurements**

Because of the broad and the intense absorption bands ($\epsilon \geq 1000 \text{ M}^{-1} \text{ cm}^{-1}$) of Cu^{II} complexes in the UV range of the electromagnetic spectrum, transmetallation reactions between Gd^{III} and Cu^{II} can be monitored by spectrophotometry at nearly physiological conditions.^{407,408} This experimental set up is shown in Figure 1.30. Example absorbance *versus* time plots for the reaction of $\text{Gd}(\text{DTPA-BMA})$ with Cu^{II} at 25 and 37 °C in the presence of endogenous ions are shown in Figure 1.31.

In Figure 1.31, the absorbance *versus* time curves are straight lines for about 7 minutes at 37 °C, after which time the absorbance values increase more rapidly because the formation of GdPO_4 precipitate

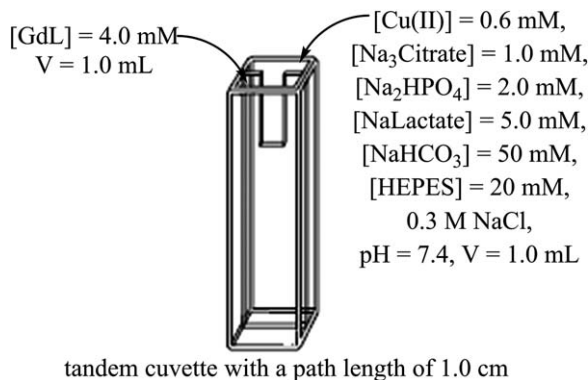


Figure 1.30 Experimental set up of the spectrophotometric measurements.

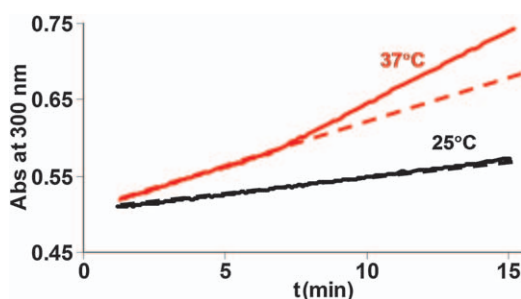


Figure 1.31 Absorbance versus time curves for the reaction of Gd(DTPA-BMA) with Cu^{II} at 25 °C and 37 °C. ([Gd(L)] = 2.0 mM, [Cu^{II}] = 0.3 mM, [Citrate] = 0.5 mM, [Na-lactate] = 2.5 mM, [Na₂HPO₄] = 1.0 mM, [NaHCO₃] = 25 mM, pH = 7.4, 4-(2-hydroxyethyl)-1-piperazineethanesulfonic acid (HEPES) = 0.02 M, and NaCl = 0.15 M).

Adapted with permission from Z. Baranyai, E. Brücher, F. Uggeri, A. Maiocchi, I. Tóth, M. András, A. Gáspár, L. Zékány and S. Aime, *Chem.—Eur. J.*, 2015, **21**, 4789. Copyright © 2015 Wiley-VCH Verlag GmbH & Co. KGaA, Weinheim.

scatters light. In this case, the excess citrate is not enough to prevent the formation of GdPO_{4(s)}. From the slope of the straight lines, the k_d first-order rate constants characterizing the dissociation of the Gd(L) can be calculated using eqn (1.57), where ΔAbs is the increase of the absorbance during a time Δt ; $[\text{Gd(L)}]_t$ is the total concentration of Gd(L); ε_{Cu} and ε_{CuL} are the molar absorptivities of $[\text{Cu}(\text{Cit})\text{H}_{-1}]^{2-}$ and the Cu(L) complex formed in the transmetallation reactions, respectively (e.g. $[\text{Cu}(\text{Cit})\text{H}_{-1}]^{2-}$: $\varepsilon_{\text{Cu}(\text{Cit})\text{H}_{-1}} = 921 \text{ M}^{-1} \text{ cm}^{-1}$ and $[\text{Cu}(\text{DTPA-BMA})]^-$: $\varepsilon_{\text{CuL}} = 3293 \text{ M}^{-1} \text{ cm}^{-1}$ at 300 nm). The k_d values obtained for the dissociation of Gd(DTPA-BMA) at 25 and 37 °C are $1.2 \times 10^{-5} \text{ s}^{-1}$ ($t_{1/2} = 15.9 \text{ h}$) and $3.8 \times 10^{-5} \text{ s}^{-1}$ ($t_{1/2} = 5.1 \text{ h}$), respectively.⁴⁰⁷ The spectrophotometric method enables determination of dissociation rates of metal complexes at nearly physiological conditions. Moreover, the

contribution of the different endogenous ions, including citrate, phosphate, carbonate, and lactate, to the dissociation rates of metal complexes can be determined by following the reactions in the presence of different concentrations of the ions of interest.

(iii) **High-performance Liquid Chromatography (HPLC), Inductively Coupled Plasma Atomic Emission Spectroscopy (ICP-AES), Inductively Coupled Plasma Mass Spectrometry (ICP-MS), and Capillary Electrophoresis (CE) Measurements**

Several experiments were performed with sensitive analytical methods to determine the kinetic inertness and the amount of Gd^{III} released in the dissociation reactions of Gd^{III} -based contrast agents for MRI in human samples.^{407,523–526} The biodistribution of Omniscan was studied with inductively coupled plasma atomic emission spectroscopy (ICP-AES) and high-performance liquid chromatography (HPLC) methods in the blood and fecal samples of patients with severe renal insufficiency. The results indicated that ICP-AES and HPLC methods are suitable for detection of Gd^{III} in biological samples. Moreover, there was no evidence of metabolism of the chelator or transmetallation of Omniscan in samples collected seven days after the administration of the Gd^{III} -based contrast agent.⁵²⁴

The dissociation rates of all marketed Gd^{III} -based contrast agents for MRI were examined at pH 7.4 and 37 °C in human serum samples.⁵²³ In these experiments, serum was spiked with Gd^{III} complexes to obtain a final concentration of 1 mmol L⁻¹. The assay mixtures were stored at 37 °C in closed vials. The samples were analyzed by HPLC-ICP-MS before the start of the incubation, 8 hours after the start, and after 1, 2, 3, 4, 5, 6, 7, 9, 11, 13, and 15 days of incubation. The results indicated that the dissociation of Gd^{III} -based contrast agents took place with the release of Gd^{III} in human serum samples. Macrocyclic Gd^{III} complexes showed higher kinetic inertness than the linear ones after 15 days at 37 °C in human plasma and in the presence of elevated phosphate levels (10 mM).⁵²⁴ In some experiments, the possible products of transmetallation of Gd^{III} -based contrast agents have been examined by capillary electrophoresis.^{407,525,526} In the blood plasma of healthy volunteers, the products of transmetallation reactions of $[\text{Gd}(\text{DTPA})]^{2-}$ with Cu^{II} , Zn^{II} , and Fe^{III} could not be detected using capillary electrophoresis–electrospray ionization time-of-flight mass spectroscopy.^{525,526} However, the dissociation of $\text{Gd}(\text{DTPA-BMA})$ and the formation of $[\text{Ca}(\text{DTPA-BMA})]^-$ in serum samples spiked with Omniscan (2 mM) at pH 7.4 and 37 °C was detected by micellar electrokinetic capillary chromatography measurements.⁴⁰⁷

1.4.4.1 Model Calculations

To assess the amount of Gd^{III} released in body fluids, the equilibrium, kinetic, and pharmacokinetic properties of Gd^{III} -based contrast agents must

be taken into account. Gd^{III} complexes are administered intravenously in doses of 0.1–0.3 $\text{mmol Gd}^{\text{III}} \text{ kg}^{-1}$ body weight. These Gd^{III} complexes are distributed rapidly in the extracellular space of the body and the elimination occurs primarily through the kidneys *via* glomerular filtration. The half-life of elimination is generally 1.3–1.6 hours in patients with normal kidney function.^{527,528} In patients with severe renal insufficiency, the rate of glomerular filtration is slow, and the half-life of elimination of Gd^{III} complexes can be in the range of 30–90 hours. During such a long residence time, Gd^{III} complexes might partially dissociate, with release and subsequent accumulation of Gd^{III} .⁵²⁹ The extent of release of Gd^{III} can be expressed by the stability constants of different complexes formed in body fluids. Considering the known stability constants, the equilibrium of competition reactions can be predicted between Gd^{III} and endogenous metal ions, in particular, Cu^{II} , Zn^{II} , and Ca^{II} , for a ligand.

Importantly, the amount of non-complexed Gd^{III} accumulating in the body is strongly influenced by the rate of dissociation and the rate of glomerular filtration. The latter is much faster for patients with normal kidney function than those with end-stage renal disease.¹ To predict the amount of the Gd^{III} released in the body fluids of patients with normal kidney function and with renal insufficiency, an open two-compartment model was developed by considering the equilibrium and the kinetic and the pharmacokinetic properties of Gd^{III} complexes (Figure 1.32).⁴⁰⁷

In Figure 1.32, $k_{\text{int}} = k_{-\text{int}} = \ln 2 / t_{1/2\alpha}$, $k_{\text{el}} = \ln 2 / t_{1/2\beta}$. The rate constants k_{int} , k_{el} , and k_{d} characterize the distribution, elimination, and dissociation, respectively, of Gd^{III} complexes. The half-lives of distribution ($t_{1/2\alpha}$) and elimination ($t_{1/2\beta}$) are 0.062 and 1.28 h, respectively. The rate constant k_{f}

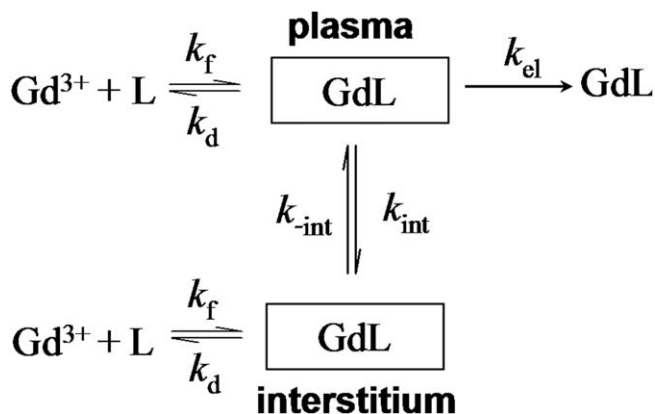


Figure 1.32 The distribution (k_{int}), dissociation (k_{d}), and elimination (k_{el}) of Gd^{III} complexes.

Adapted with permission from Z. Baranyai, E. Brücher, F. Uggeri, A. Maiocchi, I. Tóth, M. András, A. Gáspár, L. Zékány and S. Aime, *Chem.—Eur. J.*, 2015, **21**, 4789. Copyright © 2015 Wiley-VCH Verlag GmbH & Co. KGaA, Weinheim.

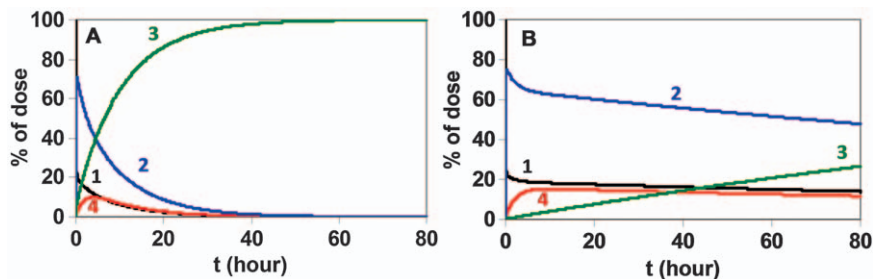


Figure 1.33 The distribution, elimination, and dissociation of Gd(DTPA-BMA) in subjects with normal kidney function (A) and with renal insufficiency (B). The amounts of Gd(L) in plasma (1) and the interstitium (2) and the amounts of eliminated gadolinium as Gd(L) (3) or dissociated Gd^{III} (4). The dose of the Omniscan was 0.1 mmol kg^{-1} body weight, the distribution volume was 0.25 L kg^{-1} body weight, and the volume of the plasma was taken 3.5 L ($k_{\text{int}} = 3.1 \times 10^{-3} \text{ s}^{-1}$, $k_{\text{el}} = 1.5 \times 10^{-4} \text{ s}^{-1}$ (normal kidney function), $k_{\text{el}} = 5.6 \times 10^{-5} \text{ s}^{-1}$ (renal insufficiency), $k_{\text{f}} = 1.1 \times 10^{-4} \text{ s}^{-1}$, and $k_{\text{d}} = 2.1 \times 10^{-5} \text{ s}^{-1}$). Adapted with permission from Z. Baranyai, E. Brücher, F. Uggeri, A. Maiocchi, I. Tóth, M. András, A. Gáspár, L. Zékány and S. Aime, *Chem.—Eur. J.*, 2015, **21**, 4789. Copyright © 2015 Wiley-VCH Verlag GmbH & Co. KGaA, Weinheim.

corresponds to the reformation of Gd^{III} complexes, and this rate constant can be calculated from the relationship $K_e = k_{\text{f}}/k_{\text{d}}$. The equilibrium constant K_e can be calculated from the dissociation equilibrium.

The time dependence of the concentration of Gd(DTPA-BMA) has been simulated during its distribution in the vascular and interstitial spaces, and the elimination from the extracellular space of patients with normal renal function and with renal insufficiency. The simulation was performed by taking into account the rates of distribution and elimination determined by the pharmacokinetic studies, the rates of reformation and the dissociation obtained by the equilibrium and kinetic studies, as well as all the possible pathways of distribution, dissociation, and elimination shown in Figure 1.32. The data obtained are shown in Figure 1.33.

The data calculated for patients with normal kidney function using this the model (Figure 1.33A) are in agreement with clinical observations, indicating that about 95% of the contrast agent is eliminated from the body of patients with normal kidney function in about 48 hours.^{530,531} The open, two-compartment model enables calculation of the amount of the metal ion released from any metal complexes in the body of patients with different levels of renal insufficiency.

1.4.5 Effect of Ligand Structure on the Inertness of Gadolinium Complexes

As outlined above, a variety of kinetic methods are available to study and characterize the kinetic properties of complexes relevant to MRI. The best

approach would be the comparison of the dissociation kinetic parameters obtained at or near physiological conditions. However, because the amount of such data is limited, the rate of acid-catalyzed dissociation is normally used for comparison.

The structure of ligands—including the nature and number of the donor atoms, geometry, preorganization, and rigidity—affects the thermodynamic and kinetic parameters of complexes formed with the ligands. Prior to data analysis, modifications applied to basic ligand structures should be defined. Common ligand structures relevant to MRI include open-chain (also known as linear or acyclic chelators), tripodal and macrocyclic ligands, and ligands consisting of both acyclic and cyclic units (for example, AAZTA, NETA, NPTA, and DEPA).^{299,532–537} Ligands are modified for various reasons, such as lowering the overall charge of the complex, incorporating a chemically reactive group for linking or targeting purposes, or accelerating the rate of complex formation. These changes to the structures of ligands require consideration because they can induce changes to the properties of their corresponding complexes, including changes in equilibrium, formation and dissociation kinetics, and relaxivity.

Modification of ligand structures might be performed either on the sidearm of the ligands^{78,172,207,293,297,538–548} or on the backbone of the ligand (Figure 1.34).^{70,114,313,549} Modifications made to the backbone of the ligands are often preferable because they maintain or improve the inertness of the resulting complexes. This increase in inertness is expected given that demetallation of complexes requires structural rearrangements. These rearrangements tend to proceed more slowly for complexes formed

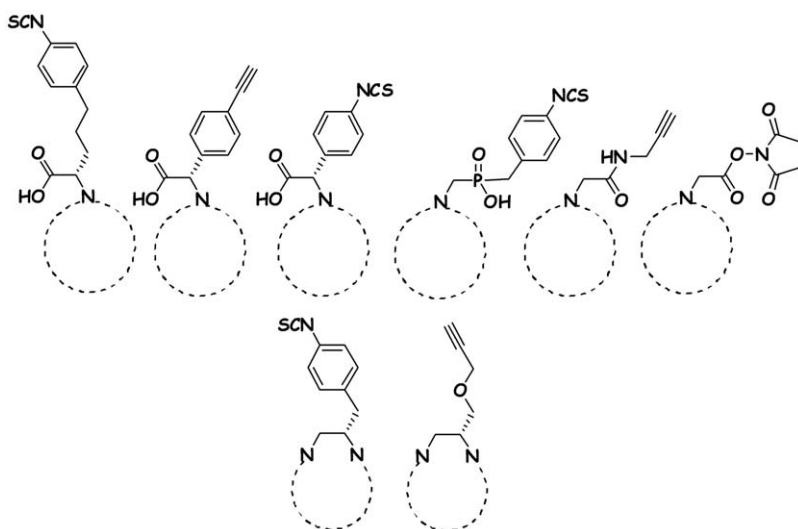


Figure 1.34 Structural fragments appearing in bifunctional ligands with some examples of arm-functionalization (upper row) and backbone-functionalization (lower row).

with more constrained ligands, and backbone modifications usually rigidify ligands.

1.4.5.1 Complexes of Open-chain and Hybrid Ligands

The first marketed contrast agent for MRI was $[\text{Gd}(\text{DTPA})]^{2-}$ in the early 1980s (Figure 1.35).⁵⁵⁰ The rates of acid- ($k_1 = 0.58 \text{ M}^{-1} \text{ s}^{-1}$) and metal-ion-catalyzed dissociation ($k_3^{\text{Cu(II)}} = 0.93 \text{ M}^{-1} \text{ s}^{-1}$, $k_3^{\text{Zn(II)}} = 0.056 \text{ M}^{-1} \text{ s}^{-1}$ and $k_3^{\text{Eu(III)}} = 4.9 \times 10^{-4} \text{ M}^{-1} \text{ s}^{-1}$) were evaluated by studying the metal-exchange reactions of $[\text{Gd}(\text{DTPA})]^{2-}$ occurring with Zn^{II} , Cu^{II} , and Eu^{III} ions.⁵⁰⁷ From these data, it is evident that among the metal ions available *in vivo*, Cu^{II} has the greatest catalytic effect on the dissociation of $[\text{Gd}(\text{DTPA})]^{2-}$. The rate constants of acid- and Cu^{II} -catalyzed dissociation are often comparable, and the dissociation *via* Zn^{II} generally occurs one to two orders of magnitude slower than the reaction catalyzed by Cu^{II} . This trend holds for nearly all open-chain contrast agents for MRI. The removal of the central acetate

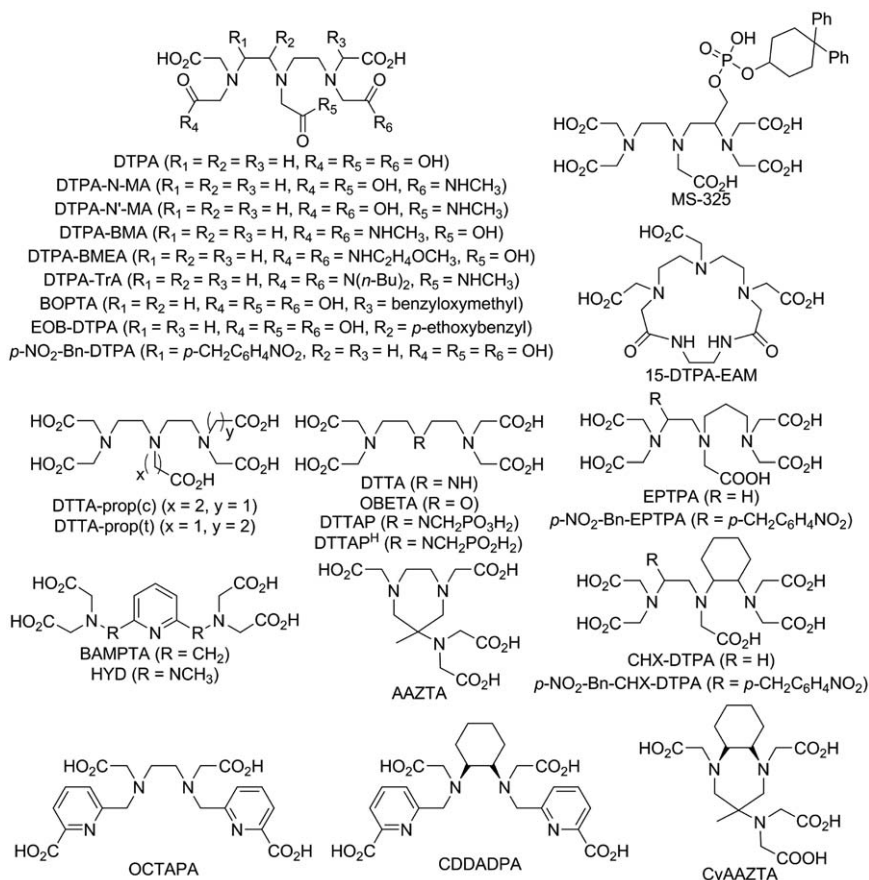


Figure 1.35 Structures of linear and hybrid ligands discussed in the text.

(DTTA),^{551,552} replacement of the central nitrogen atom with oxygen (OBETA),^{514,553} and substitution of more basic phosphonate (DTTAP) or phosphinate groups (DTTAP^{Ph}) for the central carboxylate increase the lability of the Gd^{III} complexes (see Figure 1.35 for ligand structures). For complexes of these modified ligands, k_1 is $(3-6) \times 10^3$ times greater than that of the parent [Gd(DTPA)]²⁻.⁵⁵⁴

Replacing the acetate arm attached to the central nitrogen with a pyridine nitrogen, such as in the pyridine-based DTTA derivatives with an extra methoxy or triazole ring systems, yields relatively inert Ln^{III} complexes (Table 1.2). The inertness of these derivatives is comparable to that of [Gd(DTPA)]²⁻. This observations indicates that the loss of inertness due to removing a single acetate arm can be compensated by rigidifying the molecule.^{388,555-558}

Replacing one or two carboxylates by amides, such as in DTPA-NMA, DTPA-N'MA, DTPA-BMA, and DTPA-BMEA, yields charge-neutral Gd^{III} contrast agents that lower the osmotic pressure of the injectable solutions (see Figure 1.35 for ligand structures). These complexes are, however, less inert than [Gd(DTPA)]²⁻. Moreover, these modifications further increase the dissociation rate of the Gd^{III} complex in the presence of bioligands. The rate of dissociation is somewhat slower for Gd^{III}-DTPA-tris(amides) derivatives compared to Gd(DTPA-BMA) because the rates of acid- and metal-ion-assisted dissociation are slower for the tris-amide ligands. The rates of acid-catalyzed dissociation are also slower for 15-membered macrocyclic ligands such as 15-DTPA-EAM (Figure 1.35). Dissociation is also slower for Gd^{III} complexes of propionates derivatives of DTPA and for derivatives incorporating a propylene diamine chain as opposed to the ethylene diamine one of DTPAs.

The second generation of commercially available contrast agents, including the liver-specific agents [Gd(BOPTA)]²⁻ and [Gd(EOB-DTPA)]²⁻ and the albumin binding MS-325, each have modifications on their side arms or backbone relative to the parent ligand. As a result of these changes, the Gd^{III} complexes are more inert: $k_1 = 0.41$, 0.12 , and $0.029 \text{ M}^{-1} \text{ s}^{-1}$ for [Gd(BOPTA)]²⁻, [Gd(EOB-DTPA)]²⁻, and [Gd(MS-325)]³⁻, respectively. [Gd(MS-325)]³⁻ (Ablavar) is the most inert commercially available linear-based contrast agent.

Gd^{III} complexes of the cyclohexanediamine derivative of DTPA likely have slower rates of dissociation than [Gd(DTPA)]²⁻. This speculation is based on the limited number of a studies reported with the Y^{III} analogue. Because Y^{III} and Gd^{III} have similar sizes, the corresponding complexes are expected to have similar dissociation rates. The methods used to obtain the kinetic data of these Y^{III} complexes, however, only yield conditional rate constants. Thus, data obtained this way can be used to make conclusions only for systems investigated by the same method. Nevertheless, these studies indicate that complexes of rigidified DTPA derivatives CHX-DTPA, CHX-A, and CHX-B dissociate 200, 300, and 3000 times more slowly than [Y(DTPA)]²⁻ (Figure 1.35).⁵⁷² These studies also reveal that the incorporation of methyl or nitrobenzyl groups on the backbone of DTPA slows the dissociation of the corresponding complexes.⁵⁷²

Table 1.2 Rate constants characterizing the acid-catalyzed dissociation of Gd^{III} complexes.

Complex	k_1 (M ⁻¹ s ⁻¹)	Ref.	Complex	k_1 (M ⁻¹ s ⁻¹)	Ref.
[Gd(DTPA)] ²⁻	0.58	507	[Gd(DO3A)]	2.3×10^{-3} , 2.6×10^{-3} , 1.2×10^{-2}	479,564
[Gd(OBETA)] ⁻	7.8	514,553	[Gd(DO3A-SA)]	0.86	564
[Eu(BAMPTA)] ⁻	0.17	555	[Gd(AE-DO3A)]	0.18	565
[Gd(HYD)] ⁻	0.85	388	[Gd(DMAE-DO3A)]	0.043	565
[Gd(BOPTA)] ²⁻	0.41	391	[Eu(PCTA)]	5.08×10^{-4}	30
[Gd(EOB-DTPA)] ²⁻	0.16	509	[Gd(<i>p</i> -NO ₂ -Bn-PCTA)]	1.75×10^{-4}	313
[Gd(MS-325)] ³⁻	2.9×10^{-2}	559	[Gd(TRITA)] ⁻	0.35	566
[Gd(DTTA-Nprop(t))] ²⁻	48	508	[Gd(BT-DO3A)]	2.8×10^{-5}	567
[Gd(DTPA-N-MA)]	1.5	512	[Gd(HP-DO3A)]	6.4×10^{-4} , 2.6×10^{-4}	505,567
[Gd(DTPA-N'-MA)] ⁻	1.6	512	[Eu(DO3A-Pic)] ⁻	1.56×10^{-3}	508
[Gd(DTPA-BMA)]	12.7	512	[Ce(DO3A-Nprop)] ^{- a}	7.3×10^{-3}	508
[Gd(DTPA-BMEA)]	8.6	560	[Gd(DO3AP)] ²⁻	2.8×10^{-3}	568
[Gd(DTPA-TrA)] ⁺	0.40	506	[Y(DO3AP ^{ABn})] ⁻	1.02×10^{-3}	569
[Gd(DTTAP)] ³⁻	3.38×10^3	554	[Y(DO3AP ^{Pra})] ⁻	4.4×10^{-3}	569
[Gd(DTTAP ^{Ph})] ²⁻	1.6×10^3	554	[Eu(DO3AP ^{Pra})] ²⁻	1.03×10^{-4}	504
[Gd(15-DTPA-EAM)]	0.12	561	[Gd(DOTPMB)] ⁻	4.0×10^{-4}	250
[Gd(OCTAPA)]	11.8	477	[Eu(DO3AM ^{n-Bu})]	2.1×10^{-6}	570
[Gd(CDDADPA)]	1.6×10^{-2}	562	[Gd(DOTAMA)]	2.6×10^{-6}	403
[Gd(AAZTA)] ⁻	1.05	532	[Gd(DOTAMAP)]	2.1×10^{-3}	403
[Gd(CyAAZTA)] ⁻	6.2×10^{-3}	38	[Eu(DTMA)] ³⁺	5.6×10^{-7}	404
[Gd ₃ (TCAS) ₂] ⁷⁻	8.1×10^{-3}	563	[Eu(DOTA-(gly) ₄)] ⁻	8.1×10^{-6}	148
[Gd(DOTA)] ⁻	8.4×10^{-6} , 1.8×10^{-6}	408,484	[Eu(PCTA-(gly) ₃)] ⁻	1.7×10^{-5}	571

^aOnly data corresponding to Ce^{III} is available, and based on known trends, data concerning Gd^{III} complexes are expected to be more favorable.

CDDADPA and CyAAZTA are derivatives of the octadentate ligand OCTAPA and the hexadentate ligand AAZTA (Figure 1.35).^{38,562} $[\text{Gd}(\text{CDDADPA})]^-$ is among the most inert Gd^{III} complexes incorporating a linear ligand. Its dissociation rate is 1 to 3 orders of magnitude slower than that of the clinically approved $\text{Gd}(\text{DTPA-BMA})$, $\text{Gd}(\text{DTPA-BMEA})$, $[\text{Gd}(\text{DTPA})]^{2-}$, $[\text{Gd}(\text{MS-325})]^{3-}$, $[\text{Gd}(\text{BOPTA})]^{2-}$, and $[\text{Gd}(\text{EOB-DTPA})]^{2-}$. $[\text{Gd}(\text{CyAAZTA})]^-$ also displays slow dissociation rate relative to other bisaquated ($q = 2$) complexes. High kinetic inertness was observed for a trinuclear Gd^{III} complex of thiacaalix[4]arene-*p*-tetrasulfonate (TCAS) in which three Gd^{III} ions are chelated by two TCAS ligands.⁵⁶³ The k_1 value for $[\text{Gd}_3(\text{TCAS})_2]^{7-}$ ($8.1 \times 10^{-3} \text{ M}^{-1} \text{ s}^{-1}$) compares favorably to that of approved contrast agents, and is similar to that of $[\text{Gd}(\text{CyAAZTA})]^-$, although it is still faster than that of macrocyclic contrast agents.

1.4.5.2 Complexes of Macrocyclic Ligands

The forefather of macrocyclic-based contrast agents, $[\text{Gd}(\text{DOTA})]^-$, is the most inert contrast agent. The kinetic inertness of this complex originates from the rigid, preorganized structure of the ligand. Gd^{III} and other metal ions are deeply buried in the coordination cage defined by the four macrocyclic nitrogen atoms and four carboxylate oxygen atoms. The coordination sphere of Gd^{III} in $[\text{Gd}(\text{DOTA})]^-$ is inaccessible to other ligands, except for the one inner-sphere water molecule, which is essential to relaxivity. The cavity of the ligand can be occupied by an exchanging metal ion only when the Gd^{III} ion leaves. Thus, complexes of DOTA and DOTA-type ligands dissociate *via* acid-catalyzed pathways and competing metal ions or bioligands do not accelerate dissociation rates (Figure 1.36).^{148,403,404,408,479,484,505,564,565,567} Thus, the kinetic inertness of DOTA-type complexes is often characterized only by the rates of acid-catalyzed dissociation. $[\text{Gd}(\text{DOTA})]^-$ is the gold standard when comparing the inertness of Ln^{III} complexes.

Gd^{III} complexes formed with derivatives of DOTA tend to remain inert even when the coordination environment of the metal ion is affected by the nature of donor atoms. When one sidearm is removed completely as in the case of $\text{Gd}(\text{DO3A})$, however, the rate of acid-catalyzed dissociation increases dramatically by a factor of $\sim 10^4$.^{479,564} Data published on a sulfonamide-based pH sensor and a pH-responsive chelate possessing an aminoethyl sidearm indicate that the rate constant of acid-catalyzed dissociation increases with modifications to DO3A. This should be considered when using the DO3A platform to design responsive contrast agents.^{564,565}

DO3A type ligands can be rendered more inert by incorporating a pyridine moiety, which rigidifies the macrocycle, as in PCTA. A detailed dissociation kinetic study involving several Ln^{III} complexes of PCTA demonstrated that this rigidification slows dissociation relative to DO3A ($k_1 = 5.1 \times 10^{-4} \text{ M}^{-1} \text{ s}^{-1}$ for $\text{Eu}(\text{PCTA})$).³⁰ Other studies including various bifunctional and rigidified derivatives of PCTA confirm these results.^{313,573–575} Ln^{III} complexes of the bifunctional *p*-NO₂-Bn-PCTA chelator have similar dissociation kinetics as

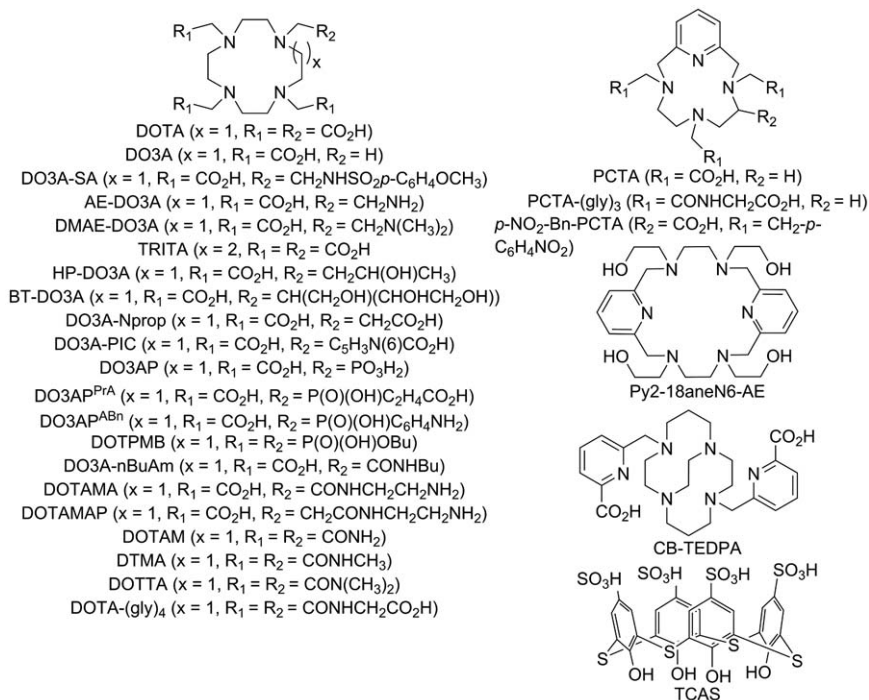


Figure 1.36 Structures of macrocyclic ligands discussed in the text.

those of complexes formed by the parent PCTA ligand. This indicates that the attachment of the *p*-nitrobenzyl substituent to the rigid PCTA backbone has little effect on rates of dissociation.³¹³ Although the kinetic inertness of complexes of heptadentate ligands can be increased by rigidifying the ligand backbone, they remain more labile than $[\text{Gd}(\text{DOTA})]^-$.

Octadentate DOTA-type ligands obtained by enlargement of the macrocycle or replacement of one or more acetates with moieties containing alcohols or amines are more labile than $[\text{Gd}(\text{DOTA})]^-$. Replacing one carboxylate group by an acetamide does not affect the dissociation kinetic properties of the resulting complexes.^{403,570} However, replacing an acetamide arm by a propionamide arm decreases the rate of acid-catalyzed dissociation of Ln(L) complexes by three order of magnitude.⁴⁰³ Gd^{III} complexes of macrocyclic ligands possessing an alcohol have somewhat higher rates of acid-catalyzed dissociation than Gd^{III} chelates of DOTA-monoamides.

Replacement of all four acetate sidearms in DOTA by acetamides leads to DOTA-tetraamides that are capable of inducing contrast *via* chemical exchange saturation transfer (see Chapter 3.1). Lanthanide complexes of DOTA-tetraamides are the most inert complexes of all DOTA-type ligands studied to date. The exceptional kinetic inertness of Ln^{III} complexes formed with DOTA-tetraamides can be rationalized in terms of the low basicity of the

amide oxygen of DOTAM compared to the carboxylate oxygen of DOTA. Protonation and subsequent proton transfer to a ring nitrogen occurs is unlikely. The amide functionally offers another approach to fine tune the kinetic inertness of the resulting complexes because the nature of the amide group (primary, secondary, or tertiary) can also affect the rates of dissociation. Among the DOTA-tetraamides, the dimethylamide complexes have the highest kinetic inertness because the methyl groups hinder the transfer of protons to ring nitrogens, slowing dissociation.^{105,404}

Lanthanide chemical exchange saturation transfer agents based on the 3,6,10,13-tetra-aza-1,8(2,6)-dipyridinacyclotetradecaphane macrocyclic platform containing four hydroxyethyl pendant arms were found to be extraordinarily inert.⁵⁷⁶ The rates of acid-catalyzed dissociation of complexes formed with Ln^{III} ions were not quantitatively evaluated in this study because the complexes were so inert that the extent of dissociation of the [Eu(L)]³⁺ complex in competitive media (e.g. 1 M HCl) over a period of months at room temperature was negligible as studied by ¹H-NMR spectroscopy. Another astonishingly high kinetic inertness was observed for Ln^{III} complexes formed with a rigid cross-bridged cyclam derivative containing two picolinate pendant arms. This complex does not undergo dissociation under harsh conditions, such as 2 M HCl; under these conditions, no release of metal ion was detected for at least 5 months.⁴⁹⁷ The absence of a bound water molecule in this complex, however, prevents its application as a *T*₁-shortening contrast agent. Regardless, this compound demonstrates the possibility to further rigidify macrocyclic ligands and increase the kinetic inertness of Ln^{III} complexes.

1.4.6 Acknowledgements

The authors thank the Hungarian Scientific Research Fund (K-120224 project). The writing of this book chapter was supported by the János Bolyai Research Scholarship of the Hungarian Academy of Sciences (G.T. and F.K.K.), the EU and co-financed by the European Regional Development Fund under the project GINOP-2.3.2-15-2016-00008 as well as the COST CA15209 “European Network on NMR Relaxometry” Action. F.K.K. and G.T. are also thankful for support from the Le Studium – Loire Valley Institute for Advanced Studies. Special thanks go to Prof. Dr Sophie Laurent for granting access to Figure 1.29.

Notes and References

1. S. Aime and P. Caravan, *J. Magn. Reson. Imaging*, 2009, **30**, 1259.
2. J. Ramalho, R. C. Semelka, M. Ramalho, R. H. Nunes, M. AlOabady and M. Castillo, *Am. J. Neuroradiol.*, 2016, **37**, 1192.
3. M. Port, J.-M. Idée, C. Medina, C. Robic, M. Sabatou and C. Corot, *Biomaterials*, 2008, **21**, 469.
4. H. S. Thomsen and P. Marckmann, *Eur. J. Radiol.*, 2008, **66**, 180.

5. S. K. Morcos, *Eur. J. Radiol.*, 2008, **66**, 175.
6. A. E. Martell and R. D. Hancock, *Metal Complexes in Aqueous Solutions*, Springer, New York, 1996.
7. R. D. Hancock and A. E. Martell, *Chem. Rev.*, 1989, **89**, 1875.
8. G. R. Choppin, Annals of the 8th Annual Symposium of the ACIESP, 1983, **1**, 24.
9. J.-C. G. Bünzli, *Acc. Chem. Res.*, 2006, **39**, 53.
10. F. S. Richardson, *Chem. Rev.*, 1982, **82**, 541.
11. E. G. Moore, A. P. S. Samuel and K. N. Raymond, *Acc. Chem. Res.*, 2009, **42**, 542.
12. S. Cotton, *Lanthanide and Actinide Chemistry*, Wiley, Chichester, U.K., 2006, ch. 4, pp. 35–60.
13. A. E. Martell and M. Calvin, *Chemistry of the Metal Chelate Compounds*, Prentice, New York, 1952.
14. G. Swarzenbach and H. A. Flaschka, *Complexometric Titrations*, Methuen Young Books, London, 2nd edn, 1969.
15. V. Kubiček and É. Tóth, *Adv. Inorg. Chem.*, 2009, **61**, 63.
16. *The Chemistry of Contrast Agents in Medical Magnetic Resonance Imaging*, ed. A. Merbach, L. Helm and É. Tóth, Wiley, Chichester, U.K., 2nd edn, 2013.
17. A. D. Sherry, P. Caravan and R. E. Lenkinski, *J. Magn. Reson. Imaging*, 2009, **30**, 1240.
18. R. D. Hancock and A. E. Martell, *Comments Inorg. Chem.*, 1988, **6**, 237.
19. K. B. Yatsimirskii, *Theor. Exp. Chem.*, 1980, **16**, 28.
20. D. K. Cabbiness and D. W. Margerum, *J. Am. Chem. Soc.*, 1969, **91**, 6540.
21. V. Vallet, U. Wahlgren and I. Grenthe, *J. Am. Chem. Soc.*, 2003, **125**, 14941.
22. B. L. Haymore, J. D. Lamb, R. M. Izatt and J. J. Christensen, *Inorg. Chem.*, 1982, **21**, 1598.
23. C. A. Chang, Y.-L. Liu, C.-Y. Chen and X.-M. Chou, *Inorg. Chem.*, 2001, **40**, 3448.
24. D. J. Cram, T. Kaneda, R. C. Helgeson, S. B. Brown, C. B. Knobler, E. Maverick and K. N. Trueblood, *J. Am. Chem. Soc.*, 1985, **107**, 3645.
25. B. W. Parks, R. D. Gilbertson, J. E. Hutchison, E. R. Healey, T. J. R. Weakley, B. M. Rapko, B. P. Hay, S. I. Sinkov, G. A. Broker and R. D. Rogers, *Inorg. Chem.*, 2006, **45**, 1498.
26. R. D. Hancock, D. L. Melton, J. M. Harrington, F. C. McDonald, R. T. Gephart, L. L. Boone, S. B. Jones, N. E. Dean, J. R. Whitehead and G. M. Cockrell, *Coord. Chem. Rev.*, 2007, **251**, 1678.
27. V. Jacques, D. Gilsoul, V. Comblin and J. F. Desreux, *J. Alloys Compd.*, 1997, **249**, 173.
28. K. Kumar, *J. Alloys Compd.*, 1997, **249**, 163.
29. G. A. Nyssen and D. W. Margerum, *Inorg. Chem.*, 1970, **9**, 1814.
30. G. Tircsó, Z. Kovács and A. D. Sherry, *Inorg. Chem.*, 2006, **45**, 9269.
31. É. Tóth, E. Brücher, I. Lázár and I. Tóth, *Inorg. Chem.*, 1994, **33**, 4070.
32. K. Kumar and M. F. Tweedle, *Inorg. Chem.*, 1993, **32**, 4193.

33. K. N. Raymond and V. C. Pierre, *Bioconjugate Chem.*, 2005, **16**, 3.
34. V. C. Pierre, M. Melchior, D. M. J. Doble and K. N. Raymond, *Inorg. Chem.*, 2004, **43**, 8520.
35. D. M. J. Doble, M. Melchior, B. O'Sullivan, C. Siering, J. Xu, V. C. Pierre and K. N. Raymond, *Inorg. Chem.*, 2003, **42**, 4930.
36. V. C. Pierre, M. Botta, S. Aime and K. N. Raymond, *J. Am. Chem. Soc.*, 2006, **128**, 5344.
37. V. C. Pierre, M. Botta, S. Aime and K. N. Raymond, *Inorg. Chem.*, 2006, **45**, 8355.
38. A. Vágner, E. Gianolio, S. Aime, A. Maiocchi, I. Tóth, Z. Baranyai and L. Tei, *Chem. Commun.*, 2016, **52**, 11235.
39. L. Helm, *Future Med. Chem.*, 2010, **2**, 385.
40. L. Helm, *Chimia*, 2011, **65**, 696.
41. S. Aime, M. Botta and E. Terreno, *Adv. Inorg. Chem.*, 2005, **57**, 173.
42. C. S. Bonnet and É. Tóth, in *Ligand Design in Medicinal Inorganic Chemistry*, ed. T. Storr, Wiley, Chichester, U.K., 2014, ch. 12, pp. 321–354.
43. A. Bumb, M. W. Brechbiel and P. Choyke, *Acta Radiol.*, 2010, **51**, 751.
44. J. Tang, Y. Sheng, H. Hu and Y. Shen, *Prog. Polym. Sci.*, 2013, **38**, 462.
45. L. Zhao, A. Shiino, H. Qin, T. Kimura and N. Komatsu, *J. Nanosci. Nanotechnol.*, 2015, **15**, 1076.
46. L. M. Manus, D. J. Mastarone, E. A. Waters, X.-Q. Zhang, E. A. Schultz-Sikma, K. W. MacRenaris, D. Ho and T. J. Meade, *Nano Lett.*, 2010, **10**, 484.
47. L. F. Vistain, M. W. Rotz, R. Rathore, A. T. Preslar and T. J. Meade, *Chem. Commun.*, 2016, **52**, 160.
48. L. Moriggi, C. Cannizzo, E. Dumas, C. R. Mayer, A. Ulianov and L. Helm, *J. Am. Chem. Soc.*, 2009, **131**, 10828.
49. F. Carniato, L. Tei, M. Cossi, L. Marchese and M. Botta, *Chem. – Eur. J.*, 2010, **16**, 10727.
50. A. Accardo, D. Tesauro, L. Aloj, C. Pedone and G. Morelli, *Coord. Chem. Rev.*, 2009, **253**, 2193.
51. S. Qazi, L. O. Liepold, M. J. Abedin, B. Johnson, P. Prevelige, J. A. Frank and T. Douglas, *Mol. Pharm.*, 2013, **10**, 11.
52. M. F. Ferreira, B. Mousavi, P. M. Ferreira, C. I. O. Martins, L. Helm, J. A. Martins and C. F. G. C. Geraldés, *Dalton Trans.*, 2012, **41**, 5472.
53. M. Allen, J. W. M. Bulte, L. Liepold, G. Basu, H. A. Zywicke, J. A. Frank, M. Young and T. Douglas, *Magn. Reson. Med.*, 2005, **54**, 807.
54. H. Kobayashi and M. W. Brechbiel, *Mol. Imaging*, 2003, **2**, 1.
55. M. A. Bruckman, X. Yu and N. F. Steinmetz, *Nanotechnology*, 2013, **24**, 462001.
56. S. Aime, D. D. Castelli, S. G. Crich, E. Gianolio and E. Terreno, *Acc. Chem. Res.*, 2009, **42**, 822.
57. C.-H. Huang and A. Tsourkas, *Curr. Top. Med. Chem.*, 2013, **13**, 411.
58. M. Botta and L. Tei, *Eur. J. Inorg. Chem.*, 2012, **2012**, 1945.

59. M. R. Longmire, M. Ogawa, P. L. Choyke and H. Kobayashi, *Wiley Interdiscip. Rev.: Nanomed. Nanobiotechnol.*, 2014, **6**, 155.
60. H. Kobayashi and M. W. Brechbiel, *Curr. Pharm. Biotechnol.*, 2004, **5**, 539.
61. L. Lattuada, A. Barge, G. Cravotto, G. B. Giovenzana and L. Tei, *Chem. Soc. Rev.*, 2011, **40**, 3019.
62. L. M. De León-Rodríguez and Z. Kovacs, *Bioconjugate Chem.*, 2008, **19**, 391.
63. C. Bernhard, M. Moreau, D. Lhenry, C. Goze, F. Boschetti, Y. Rousselin, F. Brunotte and F. Denat, *Chem. – Eur. J.*, 2012, **18**, 7834.
64. D. Zeng, B. M. Zeglis, J. S. Lewis and C. J. Anderson, *J. Nucl. Med.*, 2013, **54**, 829.
65. M. Wang, Y. Yuan and G. Liang, *Curr. Mol. Imaging*, 2012, **1**, 87.
66. J. E. Moses and A. D. Moorhouse, *Chem. Soc. Rev.*, 2007, **36**, 1249.
67. J. Notni and H.-J. Wester, *Chem. – Eur. J.*, 2016, **22**, 11500.
68. S. Knör, A. Modlinger, T. Poethko, M. Schottelius, H.-J. Wester and H. Kessler, *Chem. – Eur. J.*, 2007, **13**, 6082.
69. E. Kriemen, E. Ruf, U. Behrens and W. Maison, *Chem. – Asian J.*, 2014, **9**, 2197.
70. C. Vanasschen, N. Bouslimani, D. Thonon and J. F. Desreux, *Inorg. Chem.*, 2011, **50**, 8946.
71. C. Wängler, M. Schäfer, R. Schirmacher, P. Bartenstein and B. Wängler, *Bioorg. Med. Chem.*, 2011, **19**, 3864.
72. M. Jauregui, W. S. Perry, C. Allain, L. R. Vidler, M. C. Willis, A. M. Kenwright, J. S. Snaith, G. J. Stasiuk, M. P. Lowe and S. Faulkner, *Dalton Trans.*, 2009, 6283.
73. M. Colombo and A. Bianchi, *Molecules*, 2010, **15**, 178.
74. S. El Habnoui, B. Nottelet, V. Darcos, B. Porsio, L. Lemaire, F. Franconi, X. Garric and J. Coudane, *Biomacromolecules*, 2013, **14**, 3626.
75. M. Suchý, M. Milne, A. X. Li, N. McVicar, D. W. Dodd, R. Bartha and R. H. E. Hudson, *Eur. J. Org. Chem.*, 2011, 6532.
76. N. J. Baumhover, M. E. Martin, S. G. Parameswarappa, K. C. Kloepping, M. S. O'Dorisio, F. C. Pigge and M. K. Schultz, *Biorg. Med. Chem. Lett.*, 2011, **21**, 5757.
77. M. K. Schultz, S. G. Parameswarappa and F. C. Pigge, *Org. Lett.*, 2010, **12**, 2398.
78. P. Verwilst, S. V. Eliseeva, S. Carron, L. V. Elst, C. Burtea, G. Dehaen, S. Laurent, K. Binnemans, R. N. Muller, T. N. Parac-Vogt and W. M. De Borggraeve, *Eur. J. Inorg. Chem.*, 2011, **2011**, 3577.
79. T. L. Mindt, C. Müller, F. Stuker, J.-F. Salazar, A. Hohn, T. Mueggler, M. Rudin and R. Schibli, *Bioconjugate Chem.*, 2009, **20**, 1940.
80. L. N. Goswami, L. Ma, S. Chakravarty, Q. Cai, S. S. Jalisatgi and M. F. Hawthorne, *Inorg. Chem.*, 2013, **52**, 1694.
81. J. M. Bryson, W.-J. Chu, J.-H. Lee and T. M. Reineke, *Bioconjugate Chem.*, 2008, **19**, 1505.

82. R. B. Lauffer, *Magn. Reson. Med.*, 1991, **22**, 339.
83. P. Caravan, N. J. Cloutier, M. T. Greenfield, S. A. McDermid, S. U. Dunham, J. W. M. Bulte, J. C. Amedio, Jr., R. J. Looby, R. M. Supkowski, W. D. Horrocks, Jr., T. J. McMurry and R. B. Lauffer, *J. Am. Chem. Soc.*, 2002, **124**, 3152.
84. K. Hanaoka, K. Kikuchi, T. Terai, T. Komatsu and T. Nagano, *Chem. – Eur. J.*, 2008, **14**, 987.
85. R. B. Clarkson, Blood-Pool MRI Contrast Agents: Properties and Characterization, in *Contrast Agents I: Magnetic Resonance Imaging*, ed. W. Krause, Springer, Heidelberg, 2002, pp. 201–235.
86. M. Goyen, *Radiography*, 2007, **13**, e85.
87. P. Caravan, *Acc. Chem. Res.*, 2009, **42**, 851.
88. P. Caravan and Z. Zhang, *Eur. J. Inorg. Chem.*, 2012, **2012**, 1916.
89. L. M. De León-Rodríguez, A. Ortiz, A. L. Weiner, S. Zhang, Z. Kovacs, T. Kodadek and A. D. Sherry, *J. Am. Chem. Soc.*, 2002, **124**, 3514.
90. W. Xu and Y. Lu, *Chem. Commun.*, 2011, **47**, 4998.
91. L. M. De León-Rodríguez, A. Lubag, D. G. Udugamasooriya, B. Proneth, R. A. Brekken, X. Sun, T. Kodadek and A. D. Sherry, *J. Am. Chem. Soc.*, 2010, **132**, 12829.
92. P. L. Anelli, I. Bertini, M. Fragai, L. Lattuada, C. Luchinat and G. Parigi, *Eur. J. Inorg. Chem.*, 2000, **2000**, 625.
93. L. Helm and A. E. Merbach, *Chem. Rev.*, 2005, **105**, 1923.
94. S. Viswanathan, Z. Kovacs, K. N. Green, S. J. Ratnakar and A. D. Sherry, *Chem. Rev.*, 2010, **110**, 2960.
95. B. N. Siriwardena-Mahanama and M. J. Allen, *Molecules*, 2013, **18**, 9352.
96. S. Aime, M. Botta, M. Fasano and E. Terreno, *Acc. Chem. Res.*, 1999, **32**, 941.
97. R. Ruloff, É. Tóth, R. Scopelliti, R. Tripier, H. Handel and A. E. Merbach, *Chem. Commun.*, 2002, 2630.
98. S. Laurent, F. Botteman, L. V. Elst and R. N. Muller, *Magn. Reson. Mater. Phys., Biol. Med.*, 2004, **16**, 235.
99. S. Laurent, L. V. Elst, F. Botteman and R. N. Muller, *Eur. J. Inorg. Chem.*, 2008, **2008**, 4369.
100. S. Aime, M. Botta and G. Ermondi, *Inorg. Chem.*, 1992, **31**, 4291.
101. S. Aime, M. Botta, M. Fasano, M. P. M. Marques, C. F. G. C. Geraldès, D. Pubanz and A. E. Merbach, *Inorg. Chem.*, 1997, **36**, 2059.
102. S. Hoelt and K. Roth, *Chem. Ber.*, 1993, **126**, 869.
103. L. Di Bari, G. Pescitelli, A. D. Sherry and M. Woods, *Inorg. Chem.*, 2005, **44**, 8391.
104. D. Parker, R. S. Dickins, H. Puschmann, C. Crossland and J. A. K. Howard, *Chem. Rev.*, 2002, **102**, 1977.
105. S. Aime, A. Barge, J. I. Bruce, M. Botta, J. A. K. Howard, J. M. Moloney, D. Parker, A. S. de Sousa and M. Woods, *J. Am. Chem. Soc.*, 1999, **121**, 5762.
106. F. A. Dunand, S. Aime and A. E. Merbach, *J. Am. Chem. Soc.*, 2000, **122**, 1506.

107. K. J. Miller, A. A. Saherwala, B. C. Webber, Y. Wu, A. D. Sherry and M. Woods, *Inorg. Chem.*, 2010, **49**, 8662.
108. M. P. C. Campello, S. Lacerda, I. C. Santos, G. A. Pereira, C. F. G. C. Geraldes, J. Kotek, P. Hermann, J. Vaněk, P. Lubal, V. Kubíček, É. Tóth and I. Santos, *Chem. – Eur. J.*, 2010, **16**, 8446.
109. J. P. André, E. Brücher, R. Kiraly, R. A. Carvalho, H. Mäcke and C. F. G. C. Geraldes, *Helv. Chim. Acta*, 2005, **88**, 633.
110. M. Woods, S. Aime, M. Botta, J. A. K. Howard, J. M. Moloney, M. Navet, D. Parker, M. Port and O. Rousseaux, *J. Am. Chem. Soc.*, 2000, **122**, 9781.
111. A. C. L. Opina, M. Strickland, Y.-S. Lee, N. Tjandra, R. A. Byrd, R. E. Swenson and O. Vasalatiy, *Dalton Trans.*, 2016, **45**, 4673.
112. S. Aime, M. Botta, Z. Garda, B. E. Kucera, G. Tircso, V. G. Young and M. Woods, *Inorg. Chem.*, 2011, **50**, 7955.
113. S. Aime, M. Botta, G. Ermondi, E. Terreno, P. L. Anelli, F. Fedeli and F. Uggeri, *Inorg. Chem.*, 1996, **35**, 2726.
114. M. Woods, Z. Kovacs, R. Kiraly, E. Brücher, S. Zhang and A. D. Sherry, *Inorg. Chem.*, 2004, **43**, 2845.
115. B. C. Webber and M. Woods, *Inorg. Chem.*, 2012, **51**, 8576.
116. S. Dumas, V. Jacques, W.-C. Sun, J. S. Troughton, J. T. Welch, J. M. Chasse, H. Schmitt-Willich and P. Caravan, *Invest. Radiol.*, 2010, **45**, 600.
117. V. Jacques, S. Dumas, W.-C. Sun, J. S. Troughton, M. T. Greenfield and P. Caravan, *Invest. Radiol.*, 2010, **45**, 613.
118. S. Zhang, K. Wu and A. D. Sherry, *J. Am. Chem. Soc.*, 2002, **124**, 4226.
119. A. Borel, L. Helm and A. E. Merbach, *Chem. – Eur. J.*, 2001, **7**, 600.
120. F. K. Kálmán, M. Woods, P. Caravan, P. Jurek, M. Spiller, G. Tircsó, R. Király, E. , Brücher and A. D. Sherry, *Inorg. Chem.*, 2007, **46**, 5260.
121. S. Zhang, K. Wu and A. D. Sherry, *Angew. Chem., Int. Ed.*, 1999, **38**, 3192.
122. C. F. G. C. Geraldes and S. Laurent, *Contrast Media Mol. Imaging*, 2009, **4**, 1.
123. A. M. Morawski, G. A. Lanza and S. A. Wickline, *Curr. Opin. Biotechnol.*, 2005, **16**, 89.
124. X. Chen, *Theranostics*, 2011, **1**, 28.
125. S. Iwaki, K. Hokamura, M. Ogawa, Y. Takehara, Y. Muramatsu, T. Yamane, K. Hirabayashi, Y. Morimoto, K. Hagiwara, K. Nakahara, T. Mineno, T. Terai, T. Komatsu, T. Ueno, K. Tamura, Y. Adachi, Y. Hirata, M. Arita, H. Arai, K. Umemura, T. Nagano and K. Hanaoka, *Org. Biomol. Chem.*, 2014, **12**, 8611.
126. L. Frullano, C. Wang, R. H. Miller and Y. Wang, *J. Am. Chem. Soc.*, 2011, **133**, 1611.
127. A. H.-H. Leung, J. Jin, S. Wang, H. Lei and W.-T. Wong, *Bioconjugate Chem.*, 2014, **25**, 1112.
128. Z. Zhou, M. Qutaish, Z. Han, R. M. Schur, Y. Liu, D. L. Wilson and Z.-R. Lu, *Nat. Commun.*, 2015, **6**, 7984.
129. G. H. Lee, Y. Chang and T.-J. Kim, *Eur. J. Inorg. Chem.*, 2012, **2012**, 1924.
130. D. Artemov, *J. Cell. Biochem.*, 2003, **90**, 518.

131. K. Hanaoka, A. J. M. Lubag, A. Castillo-Muzquiz, T. Kodadek and A. D. Sherry, *Magn. Reson. Imaging*, 2008, **26**, 608.
132. E. Terreno, D. D. Castelli, A. Viale and S. Aime, *Chem. Rev.*, 2010, **110**, 3019.
133. S. Viswanathan, S. J. Ratnakar, K. N. Green, Z. Kovacs, L. M. De León-Rodríguez and A. D. Sherry, *Angew. Chem., Int. Ed.*, 2009, **48**, 9330.
134. H. S. Thomsen, *Acta Radiol.*, 2016, **57**, 515.
135. H. S. Thomsen, *Acta Radiol.*, 2016, **57**, 643.
136. E. Kanal and M. F. Tweedle, *Radiology*, 2015, **275**, 630.
137. R. J. McDonald, J. S. McDonald, D. F. Kallmes, M. E. Jentoft, D. L. Murray, K. R. Thielen, E. E. Williamson and L. J. Eckel, *Radiology*, 2015, **275**, 772.
138. A. Radbruch, L. D. Weberling, P. J. Kieslich, O. Eidel, S. Burth, P. Kickingereeder, S. Heiland, W. Wick, H.-P. Schlemmer and M. Bendszus, *Radiology*, 2015, **275**, 783.
139. T. Kanda, T. Fukusato, M. Matsuda, K. Toyoda, H. Oba, J. Kotoku, T. Haruyama, K. Kitajima and S. Furui, *Radiology*, 2015, **276**, 228.
140. T. Kanda, K. Ishii, H. Kawaguchi, K. Kitajima and D. Takenaka, *Radiology*, 2014, **270**, 834.
141. T. Kanda, H. Oba, K. Toyoda and S. Furui, *Am. J. Neuroradiol.*, 2016, **37**, E1.
142. J. Ramalho, M. Castillo, M. AlObaidy, R. H. Nunes, M. Ramalho, B. M. Dale and R. C. Semelka, *Radiology*, 2015, **276**, 836.
143. M. F. Tweedle, E. Kanal and R. Muller, *Appl. Radiol.*, 2014, **43**(Suppl), 1.
144. P. Robert, X. Violas, S. Grand, S. Lehericy, J.-M. Idée, S. Ballet and C. Corot, *Invest. Radiol.*, 2016, **51**, 73.
145. N. Murata, L. F. Gonzalez-Cuyar, K. Murata, C. Fligner, R. Dills, D. Hippe and K. R. Maravilla, *Invest. Radiol.*, 2016, **51**, 447.
146. A. A. P. Kartamihardja, T. Nakajima, S. Kameo, H. Koyama and Y. Tsushima, *Br. J. Radiol.*, 2016, **89**, 20160509.
147. V. Comblin, D. Gilsoul, M. Hermann, V. Humblet, V. Jacques, M. Mesbahi, C. Sauvage and J. F. Desreux, *Coord. Chem. Rev.*, 1999, **185–186**, 451.
148. Z. Baranyai, E. Brücher, T. Iványi, R. Király, I. Lázár and L. Zékány, *Helv. Chim. Acta*, 2005, **88**, 604.
149. H. Gries, Extracellular MRI Contrast Agents Based on Gadolinium, in *Contrast Agents I: Magnetic Resonance Imaging*, ed. W. Krause, Springer, Heidelberg, 2002, pp. 1–24.
150. E. Pérez-Mayoral, J. Soler-Padrós, V. Negri, S. Cerdán and P. Ballesteros, *Molecules*, 2007, **12**, 1771.
151. N. Cakić, S. Gündüz, R. Rengarasu and G. Angelovski, *Tetrahedron Lett.*, 2015, **56**, 759.
152. M. Suchý and R. H. E. Hudson, *Eur. J. Org. Chem.*, 2008, **29**, 4847.
153. F. Denat, S. Brandès and R. Guillard, *Synlett*, 2000, **2000**, 561.
154. L. Frullano and P. Caravan, *Curr. Org. Synth.*, 2011, **8**, 535.

155. S. Laurent, C. Henoumont, L. V. Elst and R. N. Muller, *Eur. J. Inorg. Chem.*, 2012, **2012**, 1889.
156. E. Brücher, Z. Baranyai and G. Tircsó, *The Future of Biomedical Imaging: Synthesis and Chemical Properties of the DTPA and DOTA Derivative Ligands and Their Complexes*, in *Biomedical Imaging: The Chemistry of Labels, Probes and Contrast Agents*, ed. M. Braddock, Royal Society of Chemistry, Cambridge, U.K., 2012, ch. 5.2, pp. 208–260.
157. H. U. Rashid, M. A. U. Martines, J. Jorge, P. M. de Moraes, M. N. Umar, K. Khan and H. U. Rehman, *Biorg. Med. Chem.*, 2016, **24**, 5663.
158. M. D. Bartholomä, *Inorg. Chim. Acta*, 2012, **389**, 36.
159. S. Liu, *Adv. Drug Delivery Rev.*, 2008, **60**, 1347.
160. S. Liu and D. S. Edwards, *Bioconjugate Chem.*, 2001, **12**, 7.
161. J. A. Bender, N. A. Meanwell and T. Wang, *Tetrahedron*, 2002, **58**, 3111.
162. R. Delgado, V. Félix, L. M. P. Lima and D. W. Price, *Dalton Trans.*, 2007, 2734.
163. I. Lukeš, J. Kotek, P. Vojtišek and P. Hermann, *Coord. Chem. Rev.*, 2001, **216–217**, 287.
164. P. Niedziałkowski, D. Zarzecznańska and T. Ossowski, *Pol. J. Chem.*, 2008, **82**, 1175.
165. A. E. Frost, *Nature*, 1956, **178**, 322.
166. S. Laurent, L. V. Elst, S. Houzé, N. Guérit and R. N. Muller, *Helv. Chim. Acta*, 2000, **83**, 394.
167. J. C. Amedio, Jr., P. J. Bernard, M. Fountain and G. V. Wagenen, Jr., *Synth. Commun.*, 1999, **29**, 2377.
168. H. Sajiki, K. Y. Ong, S. T. Nadler, H. E. Wages and T. J. McMurry, *Synth. Commun.*, 1996, **26**, 2511.
169. I. F. Pickersgill and H. Rapoport, *J. Org. Chem.*, 2000, **65**, 4048.
170. M. W. Brechbiel and O. A. Gansow, *J. Chem. Soc., Perkin Trans. 1*, 1992, 1173.
171. C. W. Grote, D. J. Kim and H. Rapoport, *J. Org. Chem.*, 1995, **60**, 6987.
172. D. A. Westerberg, P. L. Carney, P. E. Rogers, S. J. Kline and D. K. Johnson, *J. Med. Chem.*, 1989, **32**, 236.
173. D. Burdinski, J. Lub, J. A. Pikkemaat, D. M. Jalón, S. Martial and C. D. P. Ochoa, *Dalton Trans.*, 2008, 4138.
174. G. Sosnovsky and J. Lukszo, *Z. Naturforsch.*, 1986, **41b**, 122.
175. S. Teramae, T. Osako, S. Nagatomo, T. Kitagawa, S. Fukuzumi and S. Itoh, *J. Inorg. Biochem.*, 2004, **98**, 746.
176. C. Y. Ng, R. J. Motekaitis and A. E. Martell, *Inorg. Chem.*, 1979, **18**, 2982.
177. C. Miranda, F. Escartí, L. Lamarque, M. J. R. Yunta, P. Navarro, E. García-España and M. L. Jimeno, *J. Am. Chem. Soc.*, 2004, **126**, 823.
178. A. S. Malamas, E. Jin, Q. Zhang, J. Haaga and Z.-R. Lu, *Pharm. Res.*, 2015, **32**, 3029.
179. F. Silva, M. P. C. Campello, L. Gano, C. Fernandes, I. C. Santos, I. Santos, J. R. Ascenso, M. J. Ferreira and A. Paulo, *Dalton Trans.*, 2015, **44**, 3342.

180. J. C. Lukesh, III, K. A. Andersen, K. K. Wallin and R. T. Raines, *Org. Biomol. Chem.*, 2014, **12**, 8598.
181. A. Makino, E. Hara, I. Hara, E. Ozeki and S. Kimura, *Langmuir*, 2014, **30**, 669.
182. M. C. O'Sullivan and D. M. Dalrymple, *Tetrahedron Lett.*, 1995, **36**, 3451.
183. S. W. Kohl, K. Kuse, M. Hummert, H. Schumann, C. Mügge, K. Janek and H. Weißhoff, *Z. Naturforsch.*, 2007, **62b**, 397.
184. D. S. Kopchuk, D. E. Pavlyuk, I. S. Kovalev, G. V. Zyryanov, V. L. Rusinov and O. N. Chupakhin, *Can. J. Chem.*, 2016, **94**, 599.
185. Y.-M. Zhang, D.-C. Chang, J. Zhang, Y.-H. Liu and X.-Q. Yu, *Bioorg. Med. Chem.*, 2015, **23**, 5756.
186. S. O. Kang, V. W. Day and K. Bowman-James, *Inorg. Chem.*, 2010, **49**, 8629.
187. A. Blum, J. Böttcher, B. Sammet, T. Luksch, A. Heine, G. Klebe and W. E. Diederich, *Bioorg. Med. Chem.*, 2008, **16**, 8574.
188. S. Koščová, M. Buděšínský and J. Hodačová, *Collect. Czech. Chem. Commun.*, 2003, **68**, 744.
189. M. P. Hay, F. B. Pruijn, S. A. Gamage, H. D. S. Liyanage, M. S. Kovacs, A. V. Patterson, W. R. Wilson, J. M. Brown and W. A. Denny, *J. Med. Chem.*, 2004, **47**, 475.
190. J. Sienkiewicz, E. Goss and A. Stanczak, *Pol. J. Chem.*, 1990, **64**, 77.
191. D. J. Hnatowich, W. W. Layne and R. L. Childs, *Appl. Radiat. Isot.*, 1982, **33**, 327.
192. C. H. Paik, P. R. Murphy, W. C. Eckelman, W. A. Volkert and R. C. Reba, *J. Nucl. Med.*, 1983, **24**, 932.
193. G. E. Krejcarek and K. L. Tucker, *Biochem. Biophys. Res. Commun.*, 1977, **77**, 581.
194. W. C. Eckelman, S. M. Karesh and R. C. Reba, *J. Pharm. Sci.*, 1975, **64**, 704.
195. F. E. Armitage, D. E. Richardson and K. C. P. Li, *Bioconjugate Chem.*, 1990, **1**, 365.
196. W. P. Cacheris and S. C. Quay, Chelate Compositions, WO1990003804 A1, 19 April 1990.
197. F. Botteman, G. M. Nicolle, L. V. Elst, S. Laurent, A. E. Merbach and R. N. Muller, *Eur. J. Inorg. Chem.*, 2002, **2002**, 2686.
198. M. S. Konings, W. C. Dow, D. B. Love, K. N. Raymond, S. C. Quay and S. M. Rocklage, *Inorg. Chem.*, 1990, **29**, 1488.
199. S. Aime, F. Benetollo, G. Bombieri, S. Colla, M. Fasano and S. Paoletti, *Inorg. Chim. Acta*, 1997, **254**, 63.
200. Y.-M. Wang, T.-H. Cheng, G.-C. Liu and R.-S. Sheu, *J. Chem. Soc., Dalton Trans.*, 1997, 833.
201. S. W. A. Bligh, A. H. M. S. Chowdhury, D. Kennedy, C. Luchinat and G. Parigi, *Magn. Reson. Med.*, 1999, **41**, 767.
202. M. S. Ardestani, A. J. Arabzadeh, Z. Heidari, A. Hosseinzadeh, H. Ebrahimi, E. Hashemi, M. Mosayebnia, M. Shafiee-Alavidjeh,

- A. Alavi, M. H. Babaei, A. Rahmim, S. E. S. Ebrahimi and M. Amanlou, *J. Radioanal. Nucl. Chem.*, 2010, **283**, 447.
203. A. D. Sherry, W. P. Cacheris and K.-T. Kuan, *Magn. Reson. Med.*, 1988, **8**, 180.
204. G. Keglevich and E. Bálint, *Molecules*, 2012, **17**, 12821.
205. K. Moedritzner and R. R. Irani, *J. Org. Chem.*, 1966, **31**, 1603.
206. R. M. Cigala, M. Cordaro, F. Crea, C. De Stefano, V. Fracassetti, M. Marchesi, D. Milea and S. Sammartano, *Ind. Eng. Chem. Res.*, 2014, **53**, 9544.
207. M. A. Williams and H. Rapoport, *J. Org. Chem.*, 1993, **58**, 1151.
208. P. L. Anelli, F. Fedeli, O. Gazzotti, L. Lattuada, G. Lux and F. Rebasti, *Bioconjugate Chem.*, 1999, **10**, 137.
209. J. C. Amedio, G. Van Wagenen, Jr. and G. Zavlin, *Synth. Commun.*, 2000, **30**, 3755.
210. S. Quici, M. Cavazzini, G. Marzanni, G. Accorsi, N. Armaroli, B. Ventura and F. Barigelletti, *Inorg. Chem.*, 2005, **44**, 529.
211. J. Costa, É. Tóth, L. Helm and A. E. Merbach, *Inorg. Chem.*, 2005, **44**, 4747.
212. K.-H. Choi, Y.-D. Hong, M.-S. Pyun and S.-J. Choi, *Bull. Korean Chem. Soc.*, 2006, **27**, 1194.
213. G. A. Rolla, L. Tei, M. Fekete, F. Arena, E. Gianolio and M. Botta, *Bioorg. Med. Chem.*, 2011, **19**, 1115.
214. G. Dehaen, S. V. Eliseeva, K. Kimpe, S. Laurent, L. V. Elst, R. N. Muller, W. Dehaen, K. Binnemans and T. N. Parac-Vogt, *Chem. – Eur. J.*, 2012, **18**, 293.
215. G. B. Giovenzana, C. Guanci, S. Demattio, L. Lattuada and V. Vincenzi, *Tetrahedron*, 2014, **70**, 4809.
216. S.-Y. Lee, Y. D. Hong, H.-S. Kim and S.-J. Choi, *Nucl. Med. Biol.*, 2013, **40**, 424.
217. S. Achilefu, R. R. Wilhelm, H. N. Jimenez, M. A. Schmidt and A. Srinivasan, *J. Org. Chem.*, 2000, **65**, 1562.
218. K. A. Deal and M. J. Welch, *J. Med. Chem.*, 1997, **40**, 3986.
219. M. W. Brechbiel, O. A. Gansow, R. W. Atcher, J. Schlom, J. Esteban, D. E. Simpson and D. Colcher, *Inorg. Chem.*, 1986, **25**, 2772.
220. M. W. Brechbiel and O. A. Gansow, *Bioconjugate Chem.*, 1991, **2**, 187.
221. C. H. Cummins, E. W. Rutter, Jr. and W. A. Fordyce, *Bioconjugate Chem.*, 1991, **2**, 180.
222. M. W. Brechbiel, O. A. Gansow, C. G. Pippin, R. D. Rogers and R. P. Planalp, *Inorg. Chem.*, 1996, **35**, 6343.
223. C. Wu, H. Kobayashi, B. Sun, T. M. Yoo, C. H. Paik, O. A. Gansow, J. A. Carrasquillo, I. Pastan and M. W. Brechbiel, *Bioorg. Med. Chem.*, 1997, **5**, 1925.
224. S. M. Quadri and H. Mohammadpour, *Bioorg. Med. Chem. Lett.*, 1992, **2**, 1661.
225. H. Stetter and K.-H. Mayer, *Chem. Ber.*, 1961, **94**, 1410.
226. J. E. Richman and T. J. Atkins, *J. Am. Chem. Soc.*, 1974, **96**, 2268.

227. T. J. Atkins, J. E. Richman and W. F. Oettle, *Org. Synth.*, 1978, **58**, 86.
228. V. Martí-Centelles, M. D. Pandey, M. I. Burguete and S. V. Luis, *Chem. Rev.*, 2015, **115**, 8736.
229. I. Lázár, *Synth. Commun.*, 1995, **25**, 3181.
230. M. I. Burguete, B. Escuder, S. V. Luis, J. F. Miravet and M. Querol, *Tetrahedron Lett.*, 1998, **39**, 3799.
231. J.-M. Siaugue, F. Segat-Dioury, A. Favre-Réguillon, C. Madic, J. Foos and A. Guy, *Tetrahedron Lett.*, 2000, **41**, 7443.
232. L. Qian, Z. Sun, M. P. Mertes and K. B. Mertes, *J. Org. Chem.*, 1991, **56**, 4904.
233. R. C. Hoye, J. E. Richman, G. A. Dantas, M. F. Lightbourne and L. S. Shinneman, *J. Org. Chem.*, 2001, **66**, 2722.
234. N. G. Lukyanenko, S. S. Basok and L. K. Filonova, *J. Chem. Soc., Perkin Trans. 1*, 1988, 3141.
235. J. M. Wilson, F. Giordani, L. J. Farrugia, M. P. Barrett, D. J. Robins and A. Sutherland, *Org. Biomol. Chem.*, 2007, **5**, 3651.
236. B. Jebasingh and V. Alexander, *Synth. Commun.*, 2006, **36**, 653.
237. G. R. Weisman and D. P. Reed, *J. Org. Chem.*, 1996, **61**, 5186.
238. G. Hervé, H. Bernard, N. L. Bris, J.-J. Yaouanc, H. Handel and L. Toupet, *Tetrahedron Lett.*, 1998, **39**, 6861.
239. D. P. Reed and G. R. Weisman, *Org. Synth.*, 2002, **78**, 73.
240. P. S. Athey and G. E. Kiefer, *J. Org. Chem.*, 2002, **67**, 4081.
241. F. Denat, R. Tripier, F. Boschetti, E. Espinosa and R. Guillard, *ARKIVOC*, 2006, **2006**, 212.
242. I. Lázár, D. C. Hrnčir, W.-D. Kim, G. E. Kiefer and A. D. Sherry, *Inorg. Chem.*, 1992, **31**, 4422.
243. R. D. Hancock, M. S. Shaikjee, S. M. Dobson and J. C. A. Boeyens, *Inorg. Chim. Acta*, 1988, **154**, 229.
244. Y. Habata, F. Osaka and S. Yamada, *J. Heterocycl. Chem.*, 2006, **43**, 157.
245. R. Katakya, K. E. Matthes, P. E. Nicholson, D. Parker and H.-J. Buschmann, *J. Chem. Soc., Perkin Trans. 2*, 1990, 1425.
246. H. Stetter and W. Frank, *Angew. Chem., Int. Ed. Engl.*, 1976, **15**, 686.
247. J. F. Desreux, *Inorg. Chem.*, 1980, **19**, 1319.
248. D. Buffel, R. Ganorkar, J. Burt and X. Boi, Process for Producing 1,4,7,10-Tetraazacyclododecane-1,4,7,10-tetraacetic Acid and Complexes Thereof, WO2014/114664 A1, 2014.
249. C. U. Herborn, E. Honold, M. Wolf, J. Kemper, S. Kinner, G. Adam and J. Barkhausen, *Invest. Radiol.*, 2007, **42**, 58.
250. L. Burai, R. Király, I. Lázár and E. Brücher, *Eur. J. Inorg. Chem.*, 2001, **2001**, 813.
251. Z. Kotková, G. A. Pereira, K. Djanashvili, J. Kotek, J. Rudovský, P. Hermann, L. V. Elst, R. N. Muller, C. F. G. C. Geraldés, I. Lukeš and J. A. Peters, *Eur. J. Inorg. Chem.*, 2009, **2009**, 119.
252. I. Lazar, A. D. Sherry, R. Ramasamy, E. Brucher and R. Kiraly, *Inorg. Chem.*, 1991, **30**, 5016.

253. K. P. Pulukkody, T. J. Norman, D. Parker, L. Royle and C. J. Broan, *J. Chem. Soc., Perkin Trans. 2*, 1993, 605.
254. X. Li, S. Zhang, P. Zhao, Z. Kovacs and A. D. Sherry, *Inorg. Chem.*, 2001, **40**, 6572.
255. E. Cole, D. Parker, G. Ferguson, J. F. Gallagher and B. Kaitner, *J. Chem. Soc., Chem. Commun.*, 1991, 1473.
256. D. Parker, K. Pulukkody, T. J. Norman, A. Harrison, L. Royle and C. Walker, *J. Chem. Soc., Chem. Commun.*, 1992, 1441.
257. J. Rohovec, M. Kývala, P. Vojtíšek, P. Hermann and I. Lukeš, *Eur. J. Inorg. Chem.*, 2000, **2000**, 195.
258. J. Rohovec, P. Vojtíšek, P. Hermann, J. Mosinger, Z. Žák and I. Lukeš, *J. Chem. Soc., Dalton Trans.*, 1999, 3585.
259. M. Försterová, Z. Jandurová, F. Marques, L. Gano, P. Lubal, J. Vaněk, P. Hermann and I. Santos, *J. Inorg. Biochem.*, 2008, **102**, 1531.
260. G. A. Pereira, L. Ball, A. D. Sherry, J. A. Peters and C. F. G. C. Geraldles, *Helv. Chim. Acta*, 2009, **92**, 2532.
261. C. F. G. C. Geraldles, A. D. Sherry, I. Lázár, A. Miseta, P. Bogner, E. Berenyi, B. Sumegi, G. E. Kiefer, K. McMillan, F. Maton and R. N. Muller, *Magn. Reson. Med.*, 1993, **30**, 696.
262. W. D. Kim, G. E. Kiefer, J. Huskens and A. D. Sherry, *Inorg. Chem.*, 1997, **36**, 4128.
263. N. Bansal, M. J. Germann, V. Seshan, G. T. Shires, III, C. R. Malloy and A. D. Sherry, *Biochemistry*, 1993, **32**, 5638.
264. A. D. Sherry, *J. Alloys Compd.*, 1997, **249**, 153.
265. W. J. Kruper, Jr., P. R. Rudolf and C. A. Langhoff, *J. Org. Chem.*, 1993, **58**, 3869.
266. C. Li and W.-T. Wong, *J. Org. Chem.*, 2003, **68**, 2956.
267. C. Li and W.-T. Wong, *Tetrahedron*, 2004, **60**, 5595.
268. B. Jagadish, G. L. Brickert-Albrecht, G. S. Nichol, E. A. Mash and N. Raghunand, *Tetrahedron Lett.*, 2011, **52**, 2058.
269. A. Adhikari, A. Datta, M. Adhikari, K. Chauhan, K. Chuttani, S. Saw, A. Shukla and A. K. Mishra, *Mol. Pharm.*, 2014, **11**, 445.
270. J. Tanwar, A. Datta, A. K. Tiwari, S. Chaturvedi, H. Ojha, M. Allard, N. K. Chaudary, M. Thirumal and A. K. Mishra, *Dalton Trans.*, 2011, **40**, 3346.
271. P. Srivastava, A. K. Tiwari, N. Chadha, K. Chuttani and A. K. Mishra, *Eur. J. Med. Chem.*, 2013, **65**, 12.
272. F. Fuge, M. Weiler, J. Gätjens, T. Lammers and F. Kiessling, *Tetrahedron Lett.*, 2013, **54**, 918.
273. N. Raghunand, G. P. Guntle, V. Gokhale, G. S. Nichol, E. A. Mash and B. Jagadish, *J. Med. Chem.*, 2010, **53**, 6747.
274. O. Axelsson and A. Olsson, Synthesis of Cyclen Derivatives, WO/2006/112723, 2006.
275. H.-Y. Hu, N.-H. Lim, D. Ding-Pfennigdorff, J. Saas, K. U. Wendt, O. Ritzeler, H. Nagase, O. Plettenburg, C. Schultz and M. Nazare, *Bioconjugate Chem.*, 2015, **26**, 383.

276. B. Wängler, C. Beck, U. Wagner-Utermann, E. Schirrmacher, C. Bauer, F. Rösch, R. Schirrmacher and M. Eisenhut, *Tetrahedron Lett.*, 2006, **47**, 5985.
277. L. S. Karfeld, S. R. Bull, N. E. Davis, T. J. Meade and A. E. Barron, *Bioconjugate Chem.*, 2007, **18**, 1697.
278. J. Rohovec, R. Gyepes, I. Císařová, J. Rudovský and I. Lukeš, *Tetrahedron Lett.*, 2000, **41**, 1249.
279. F. Oukhatar, M. Beyler and R. Tripier, *Tetrahedron*, 2015, **71**, 3857.
280. W. C. Baker, M. J. Choi, D. C. Hill, J. L. Thompson and P. A. Petillo, *J. Org. Chem.*, 1999, **64**, 2683.
281. M. Le Baccon, F. Chuburu, L. Toupet, H. Handel, M. Soibinet, I. Déchamps-Olivier, J.-P. Barbier and M. Aplincourt, *New J. Chem.*, 2001, **25**, 1168.
282. M. Bergmann and L. Zervas, *Ber. Dtsch. Chem. Ges.*, 1932, **65**, 1192.
283. L. M. De León-Rodríguez, Z. Kovacs, A. C. Esqueda-Oliva and A. D. Miranda-Olvera, *Tetrahedron Lett.*, 2006, **47**, 6937.
284. Z. Kovacs and A. D. Sherry, *J. Chem. Soc., Chem. Commun.*, 1995, 185.
285. Z. Kovacs and A. D. Sherry, *Synthesis*, 1997, 759.
286. A. M. Skwierawska, *Tetrahedron Lett.*, 2008, **49**, 6308.
287. S. Brandès, C. Gros, F. Denat, P. Pullumbi and R. Guillard, *Bull. Soc. Chim. Fr.*, 1996, **133**, 65.
288. E. Kimura, S. Aoki, T. Koike and M. Shiro, *J. Am. Chem. Soc.*, 1997, **119**, 3068.
289. J. S. Prasad, F. J. Okuniewicz, E. J. Delaney and D. D. Dischino, *J. Chem. Soc., Perkin Trans. 1*, 1991, 3329.
290. L. E. Hopper and M. J. Allen, *Tetrahedron Lett.*, 2014, **55**, 5560.
291. F. Bellouard, F. Chuburu, N. Kervarec, L. Toupet, S. Triki, Y. Le Mest and H. Handel, *J. Chem. Soc., Perkin Trans. 1*, 1999, 3499.
292. M. H. Ansari, M. Ahmad and K. A. Dicke, *Bioorg. Med. Chem. Lett.*, 1993, **3**, 1067.
293. M. K. Moi, C. F. Meares and S. J. DeNardo, *J. Am. Chem. Soc.*, 1988, **110**, 6266.
294. O. Renn and C. F. Meares, *Bioconjugate Chem.*, 1992, **3**, 563.
295. M. L. Garrity, G. M. Brown, J. E. Elbert and R. A. Sachleben, *Tetrahedron Lett.*, 1993, **34**, 5531.
296. A. K. Mishra, J. F. Gestin, E. Benoist, A. Faivre-Chauvet and J. F. Chatal, *New J. Chem.*, 1996, **20**, 585.
297. T. J. McMurry, M. Brechbiel, K. Kumar and O. A. Gansow, *Bioconjugate Chem.*, 1992, **3**, 108.
298. J. F. Desreux, M. F. Tweedle, P. C. Ratsep, T. R. Wagler and E. R. Marinelli, Preparation of Hepatobiliary Tetraazamacrocyclic Magnetic Resonance Contrast Agents, US5358704 A, 1994.
299. H.-S. Chong, K. Garmestani, L. H. Bryant, Jr., D. E. Milenic, T. Overstreet, N. Birch, T. Le, E. D. Brady and M. W. Brechbiel, *J. Med. Chem.*, 2006, **49**, 2055.
300. G. R. Hansen and T. E. Burg, *J. Heterocycl. Chem.*, 1968, **5**, 305.

301. R. Kossai, J. Simonet and G. Dauphin, *Tetrahedron Lett.*, 1980, **21**, 3575.
302. S. Cornier and C. Wymore, Process for Preparing Cyclic Oligomers of N-Substituted Aziridines, US 3828023, 1974.
303. M. Căproiu, C. Florea, C. Galli, A. Petride and H. Petride, *Eur. J. Org. Chem.*, 2000, 1037.
304. C. Drăghici, C. Florea, C. Galli, A. Petride and H. Petride, *ARKIVOC*, 2002, **2002**, 109.
305. P. L. Anelli, A. Beltrami, M. Franzini, P. Paoli, P. Rossi, F. Uggeri and M. Virtuani, *Inorg. Chim. Acta*, 2001, **317**, 218.
306. R. S. Ranganathan, R. K. Pillai, N. Raju, H. Fan, H. Nguyen, M. F. Tweedle, J. F. Desreux and V. Jacques, *Inorg. Chem.*, 2002, **41**, 6846.
307. S. Tsuboyama, K. Tsuboyama, I. Higashi and M. Yanagita, *Tetrahedron Lett.*, 1970, **11**, 1367.
308. C. D. Edlin, S. Faulkner, D. Parker and M. P. Wilkinson, *Chem. Commun.*, 1996, 1249.
309. C. M. Reid, C. Ebikeme, M. P. Barrett, E.-M. Patzewitz, S. Müller, D. J. Robins and A. Sutherland, *Bioorg. Med. Chem. Lett.*, 2008, **18**, 2455.
310. H. Stetter, W. Frank and R. Mertens, *Tetrahedron*, 1981, **37**, 767.
311. J. Costa and R. Delgado, *Inorg. Chem.*, 1993, **32**, 5257.
312. F. Dioury, E. Guéné, A. Di Scala-Roulleau, C. Ferroud, A. Guy and M. Port, *Tetrahedron Lett.*, 2005, **46**, 611.
313. G. Tircsó, E. T. Benyó, E. H. Suh, P. Jurek, G. E. Kiefer, A. D. Sherry and Z. Kovács, *Bioconjugate Chem.*, 2009, **20**, 565.
314. S. Aime, L. Calabi, C. Cavallotti, E. Gianolio, G. B. Giovenzana, P. Losi, A. Maiocchi, G. Palmisano and M. Sisti, *Inorg. Chem.*, 2004, **43**, 7588.
315. A. Noble and J. C. Anderson, *Chem. Rev.*, 2013, **113**, 2887.
316. E. M. Elemento, D. Parker, S. Aime, E. Gianolio and L. Lattuada, *Org. Biomol. Chem.*, 2009, **7**, 1120.
317. B. H. J. Bielski and M. J. Thomas, *J. Am. Chem. Soc.*, 1987, **109**, 7761.
318. D. Buffel, X. Boi and J. Pype, Process for Purifying 1,4,7,10-Tetraazacyclododecane-1,4,7,10-tetraacetic Acid, WO2015/117911 A1, 2015.
319. M. W. Brechbiel, P. M. Beitzel and O. A. Gansow, *J. Chromatogr. A*, 1997, **771**, 63.
320. J. Porath and P. Flodin, *Nature*, 1959, **183**, 1657.
321. A. Hamplová, T. Křížek, V. Kubíček, Z. Bosáková and P. Coufal, *J. Sep. Sci.*, 2010, **33**, 658.
322. V. Humblet, P. Misra and J. V. Frangioni, *Contrast Media Mol. Imaging*, 2006, **1**, 196.
323. M. Sillanpää and M.-L. Sihvonen, *Talanta*, 1997, **44**, 1487.
324. T. H. Mourey and L. E. Oppenheimer, *Anal. Chem.*, 1984, **56**, 2427.
325. N. A. Kostromina, *Russ. Chem. Rev.*, 1973, **42**, 261.
326. C. Frassinetti, S. Ghelli, P. Gans, A. Sabatini, M. S. Moruzzi and A. Vacca, *Anal. Biochem.*, 1995, **231**, 374.
327. G. R. Choppin, S. A. Khan and G. C. Levy, *Spectrosc. Lett.*, 1980, **13**, 205.
328. J. L. Sudmeier and C. N. Reilly, *Anal. Chem.*, 1964, **36**, 1698.

329. J. L. Sudmeier and C. N. Reilley, *Anal. Chem.*, 1964, **36**, 1707.
330. C. F. G. C. Geraldes, M. C. Alpoim, M. P. M. Marques, A. D. Sherry and M. Singh, *Inorg. Chem.*, 1985, **24**, 3876.
331. P. Letkeman and A. E. Martell, *Inorg. Chem.*, 1979, **18**, 1284.
332. P. Letkeman, *J. Chem. Educ.*, 1979, **56**, 348.
333. R. J. Kula and D. T. Sawyer, *Inorg. Chem.*, 1964, **3**, 458.
334. J. F. Desreux, E. Merciny and M. F. Loncin, *Inorg. Chem.*, 1981, **20**, 987.
335. D. A. Keire and M. Kobayashi, *Bioconjugate Chem.*, 1999, **10**, 454.
336. É. Csajbók, I. Bányai and E. Brücher, *Dalton Trans.*, 2004, 2152.
337. J. Ren, S. Zhang, A. D. Sherry and C. F. G. C. Geraldes, *Inorg. Chim. Acta*, 2002, **339**, 273.
338. J. A. Peters, *Inorg. Chem.*, 1988, **27**, 4686.
339. M. P. M. Marques, C. F. G. C. Geraldes, A. D. Sherry, A. E. Merbach, H. Powell, D. Pubanz, S. Aime and M. Botta, *J. Alloys Compd.*, 1995, **225**, 303.
340. S. P. Babailov, P. V. Dubovskii and E. N. Zapolotsky, *Polyhedron*, 2014, **79**, 277.
341. S. Aime and M. Botta, *Inorg. Chim. Acta*, 1990, **177**, 101.
342. C. F. G. C. Geraldes, A. M. Urbano, M. A. Hoefnagel and J. A. Peters, *Inorg. Chem.*, 1993, **32**, 2426.
343. V. Jacques and J. F. Desreux, *Inorg. Chem.*, 1994, **33**, 4048.
344. M. Albin, W. D. Horrocks, Jr. and F. J. Liotta, *Chem. Phys. Lett.*, 1982, **85**, 61.
345. N. Viola-Villegas and R. P. Doyle, *Coord. Chem. Rev.*, 2009, **253**, 1906.
346. M.-R. Spirlet, J. Rebizant, J. F. Desreux and M.-F. Loncin, *Inorg. Chem.*, 1984, **23**, 359.
347. S. Aime, A. Barge, F. Benetollo, G. Bombieri, M. Botta and F. Uggeri, *Inorg. Chem.*, 1997, **36**, 4287.
348. C. A. Chang, L. C. Francesconi, M. F. Malley, K. Kumar, J. Z. Gougoutas, M. F. Tweedle, D. W. Lee and L. J. Wilson, *Inorg. Chem.*, 1993, **32**, 3501.
349. S. Aime, A. Barge, M. Botta, M. Fasano, J. D. Ayala and G. Bombieri, *Inorg. Chim. Acta*, 1996, **246**, 423.
350. F. Benetollo, G. Bombieri, L. Calabi, S. Aime and M. Botta, *Inorg. Chem.*, 2003, **42**, 148.
351. J. R. Morrow, S. Amin, C. H. Lake and M. R. Churchill, *Inorg. Chem.*, 1993, **32**, 4566.
352. K. O. A. Chin, J. R. Morrow, C. H. Lake and M. R. Churchill, *Inorg. Chem.*, 1994, **33**, 656.
353. S. I. Kang, R. S. Ranganathan, J. E. Emswiler, K. Kumar, J. Z. Gougoutas, M. F. Malley and M. F. Tweedle, *Inorg. Chem.*, 1993, **32**, 2912.
354. S. Aime, A. S. Batsanov, M. Botta, J. A. K. Howard, D. Parker, K. Senanayake and G. Williams, *Inorg. Chem.*, 1994, **33**, 4696.
355. J. J. Stezowski and J. L. Hoard, *Isr. J. Chem.*, 1984, **24**, 323.
356. H. Gries and H. Miklautz, *Physiol. Chem. Phys. Med. NMR*, 1984, **16**, 105.
357. M. B. Inoue, M. Inoue and Q. Fernando, *Inorg. Chim. Acta*, 1995, **232**, 203.

358. R. Ruloff, T. Gelbrich, E. Hoyer, J. Sieler and L. Beyer, *Z. Naturforsch.*, 1998, **53b**, 955.
359. F. Avecilla, J. A. Peters and C. F. G. C. Geraldés, *Eur. J. Inorg. Chem.*, 2003, **2003**, 4179.
360. G. H. Stout and L. H. Jensen, *X-Ray Structure Determination: A Practical Guide*, Wiley, New York, 2nd edn, 1989.
361. P. Vojtišek, P. Cígler, J. Kotek, J. Rudovský, P. Hermann and I. Lukeš, *Inorg. Chem.*, 2005, **44**, 5591.
362. J. Vipond, M. Woods, P. Zhao, G. Tircsó, J. Ren, S. G. Bott, D. Ogrin, G. E. Kiefer, Z. Kovacs and A. D. Sherry, *Inorg. Chem.*, 2007, **46**, 2584.
363. A. Ringbom, *Complexation in Analytical Chemistry (Chemical Analysis)*, Wiley, New York, 1963.
364. M. T. Beck and I. Nagypál, *Chemistry of Complex Equilibria, Translation*, ed. D. R. Williams and D. A. Durham, Ellis Horwood Series in Inorganic Chemistry, Halsted Press, Chichester, UK, 1990.
365. G. H. Nancollas and M. B. Tomson, *Pure Appl. Chem.*, 1982, **54**, 2675.
366. E. Brücher, G. Tircsó, Z. Baranyai, Z. Kovács and A. D. Sherry, in *The Chemistry of Contrast Agents in Medical Magnetic Resonance Imaging*, ed. A. Merbach, L. Helm and É. Tóth, Wiley, Chichester, U.K., 2nd edn, 2013, ch. 4, pp. 157–208.
367. A. Bianchi, L. Calabi, F. Corana, S. Fontana, P. Losi, A. Maiocchi, L. Paleari and B. Valtancoli, *Coord. Chem. Rev.*, 2000, **204**, 309.
368. G. Anderegg, F. Arnaud-Neu, R. Delgado, J. Felcman and K. Popov, *Pure Appl. Chem.*, 2005, **77**, 1445.
369. F. Dwyer and D. Mellor, *Chelating Agents and Metal Chelates*, Academic Press, New York, 1964.
370. *Coordination Chemistry of Macrocyclic Compounds*, ed. G. Melson, Plenum Press, New York, 1979.
371. J.-L. Burgot, *Ionic Equilibria in Analytical Chemistry*, Springer, New York, 2012.
372. P. Caravan, J. J. Ellison, T. J. McMurry and R. B. Lauffer, *Chem. Rev.*, 1999, **99**, 2293.
373. A. E. Martell and R. J. Motekaitis, *Determination and Use of Stability Constants*, Wiley-VCH, New York, 2nd edn, 1992.
374. *Computational Methods for the Determination of Formation Constants*, ed. D. J. Leggett, Springer, New York, 1985.
375. *Stability Constants*, Protonic Software. <http://www.HYPERQUAD.co.uk> (last accessed 2017).
376. *Chemical Equilibrium Diagrams*, School of Chemical Science and Engineering, KTH, Stockholm, Sweden, 2013. <https://www.kth.se/en/che/medusa/> (last accessed 2017).
377. L. Alderighi, P. Gans, A. Ienco, D. Peters, A. Sabatini and A. Vacca, *Coord. Chem. Rev.*, 1999, **184**, 311.
378. G. Eriksson, *Anal. Chim. Acta*, 1979, **112**, 375.
379. N. Ingri, W. Kakolowicz, L. G. Sillén and B. Warnqvist, *Talanta*, 1967, **14**, 1261.

380. K. N. Raymond and C. J. Carrano, *Acc. Chem. Res.*, 1979, **12**, 183.
381. B. Drahoš, J. Kotek, P. Hermann, I. Lukeš and É. Tóth, *Inorg. Chem.*, 2010, **49**, 3224.
382. M. Meyer, N. Rollet, T.-H. Vu, S. Brandes and P. Gans, *Acta Int. Symp. Metal Complexes*, 2016, **6**, 9.
383. V. Kubiček, J. Havlíčková, J. Kotek, G. Tircsó, P. Hermann, É. Tóth and I. Lukeš, *Inorg. Chem.*, 2010, **49**, 10960.
384. C. F. G. C. Geraldes, A. D. Sherry and W. P. Cacheris, *Inorg. Chem.*, 1989, **28**, 3336.
385. M. P. Campello, M. Balbina, I. Santos, P. Lubal, R. Ševčík and R. Ševčíková, *Helv. Chim. Acta*, 2009, **92**, 2398.
386. F. K. Kálmán, Z. Baranyai, I. Tóth, I. Bányai, R. Király, E. Brücher, S. Aime, X. Sun, A. D. Sherry and Z. Kovács, *Inorg. Chem.*, 2008, **47**, 3851.
387. G. Orgován and B. Noszál, *J. Pharm. Biomed. Anal.*, 2011, **54**, 958.
388. C. S. Bonnet, S. Laine, F. Buron, G. Tircso, A. Pallier, L. Helm, F. Suzenet and É. Tóth, *Inorg. Chem.*, 2015, **54**, 5991.
389. Z. Baranyai, L. Tei, G. B. Giovenzana, F. K. Kálmán and M. Botta, *Inorg. Chem.*, 2012, **51**, 2597.
390. A. E. Martell and R. M. Smith, *Critical Stability Constants*, Plenum Press, New York, 1974.
391. Z. Baranyai, Z. Pálinkás, F. Uggeri and E. Brücher, *Eur. J. Inorg. Chem.*, 2010, **2010**, 1948.
392. R. Delgado and J. J. R. F. da Silva, *Talanta*, 1982, **29**, 815.
393. É. Csajbók, Z. Baranyai, I. Bányai, E. Brücher, R. Király, A. Müller-Fahrnow, J. Platzek, B. Radüchel and M. Schäfer, *Inorg. Chem.*, 2003, **42**, 2342.
394. Z. Baranyai, F. Uggeri, A. Maiocchi, G. B. Giovenzana, C. Cavallotti, A. Takács, I. Tóth, I. Bányai, A. Bényei, E. Brucher and S. Aime, *Eur. J. Inorg. Chem.*, 2013, **2013**, 147.
395. T. Fodor, I. Bányai, A. Bényei, C. Platas-Iglesias, M. Purgel, G. L. Horváth, L. Zékány, G. Tircsó and I. Tóth, *Inorg. Chem.*, 2015, **54**, 5426.
396. J. Blixt, J. Glaser, P. Solymosi and I. Tóth, *Inorg. Chem.*, 1992, **31**, 5288.
397. S. A. Cotton, *C. R. Chim.*, 2005, **8**, 129.
398. N. N. Greenwood and A. Earnshaw, *Chemistry of the Elements*, Elsevier Butterworth-Heinemann, Oxford, 2nd edn, 1997.
399. E. Brücher, R. Király and I. Nagypál, *J. Inorg. Nucl. Chem.*, 1975, **37**, 1009.
400. E. Brücher, R. Király and I. Tóth, *Inorg. Nucl. Chem. Lett.*, 1976, **12**, 167.
401. G. Tircsó, F. K. Kálmán, R. Pál, I. Bányai, T. R. Varga, R. Király, I. Lázár, L. Québatte, A. E. Merbach, É. Tóth and E. Brücher, *Eur. J. Inorg. Chem.*, 2012, **2012**, 2062.
402. K. B. Yatsimirskii, N. K. Davidenko, N. A. Kostromina and T. V. Ternovaya, *Teoret. Eksperiment. Khimiya*, 1965, **1**, 100.
403. L. Tei, Z. Baranyai, L. Gaino, A. Forgács, A. Vágner and M. Botta, *Dalton Trans.*, 2015, **44**, 5467.

404. A. Pasha, G. Tircsó, E. T. Benyó, E. Brücher and A. D. Sherry, *Eur. J. Inorg. Chem.*, 2007, **2007**, 4340.
405. E. Brücher and L. Zékány, *J. Inorg. Nucl. Chem.*, 1981, **43**, 351.
406. L. Burai, V. Hietapelto, R. Király, É. Tóth and E. Brücher, *Magn. Reson. Med.*, 1997, **38**, 146.
407. Z. Baranyai, E. Brücher, F. Uggeri, A. Maiocchi, I. Tóth, M. András, A. Gáspár, L. Zékány and S. Aime, *Chem. – Eur. J.*, 2015, **21**, 4789.
408. Z. Baranyai, Z. Pálkás, F. Uggeri, A. Maiocchi, S. Aime and E. Brücher, *Chem. – Eur. J.*, 2012, **18**, 16426.
409. S. Verma and M. C. Saxena, *Proc. Indian Acad. Sci., Chem. Sci.*, 1987, **99**, 217.
410. P. Thakur, J. L. Conca and G. R. Choppin, *J. Solution Chem.*, 2012, **41**, 599.
411. C. J. Leggett and M. P. Jensen, *J. Solution Chem.*, 2013, **42**, 2119.
412. K. Du and T. D. Harris, *J. Am. Chem. Soc.*, 2016, **138**, 7804.
413. N. V. Nagy, T. Szabó-Plánka, G. Tircsó, R. Király, Z. Árkosi, A. Rockenbauer and E. Brücher, *J. Inorg. Biochem.*, 2004, **98**, 1655.
414. E. Gianolio, K. Ramalingam, B. Song, F. Kalman, S. Aime and R. Swenson, *Inorg. Chem. Commun.*, 2010, **13**, 663.
415. R. Artali, Z. Baranyai, M. Botta, G. B. Giovenzana, A. Maspero, R. Negri, G. Palmisano, M. Sisti and S. Tollari, *New J. Chem.*, 2015, **39**, 539.
416. E. Balogh, Z. He, W. Hsieh, S. Liu and É. Tóth, *Inorg. Chem.*, 2007, **46**, 238.
417. R. Trokowski, J. Ren, F. K. Kálmán and A. D. Sherry, *Angew. Chem., Int. Ed.*, 2005, **44**, 6920.
418. W.-H. Li, S. E. Fraser and T. J. Meade, *J. Am. Chem. Soc.*, 1999, **121**, 1413.
419. E. L. Que, E. Gianolio, S. L. Baker, A. P. Wong, S. Aime and C. J. Chang, *J. Am. Chem. Soc.*, 2009, **131**, 8527.
420. A. D. Sherry, J. Ren, J. Huskens, E. Brücher, É. Tóth, C. F. C. G. Geraldes, M. M. C. A. Castro and W. P. Cacheris, *Inorg. Chem.*, 1996, **35**, 4604.
421. G. Tircsó, A. Bényei, E. Brücher, A. Kis and R. Király, *Inorg. Chem.*, 2006, **45**, 4951.
422. A. Forgács, L. Tei, Z. Baranyai, I. Tóth, L. Zékány and M. Botta, *Eur. J. Inorg. Chem.*, 2016, **2016**, 1165.
423. P. Gans, A. Sabatini and A. Vacca, *Talanta*, 1996, **43**, 1739.
424. *Pioneering Instrumentation for Transient Kinetics & Spectroscopy*, TgK Scientific Ltd., 2017. <http://www.hi-techsci.com> (last accessed 2017).
425. *ReactLabTM*, Jplus Consulting: Multivariate Analytical Technologies, 2017. <http://jplusconsulting.com/> (last accessed 2017).
426. H. Gampp, M. Maeder, C. J. Meyer and A. D. Zuberbühler, *Talanta*, 1985, **32**, 95.
427. H. Gampp, M. Maeder, C. J. Meyer and A. D. Zuberbühler, *Talanta*, 1985, **32**, 257.
428. C. Frassinetti, L. Alderighi, P. Gans, A. Sabatini, A. Vacca and S. Ghelli, *Anal. Bioanal. Chem.*, 2003, **376**, 1041.

429. M. J. Hynes, *J. Chem. Soc., Dalton Trans.*, 1993, 311.
430. H. M. Irving, M. G. Miles and L. D. Pettit, *Anal. Chim. Acta*, 1967, **38**, 475.
431. É. Tóth and E. Brücher, *Inorg. Chim. Acta*, 1994, **221**, 165.
432. R. D. Peacock, The Intensities of Lanthanide $f \leftrightarrow f$ Transitions, in *Rare Earths: Structure and Bonding*, ed. J. D. Dunitz, P. Hemmerich, R. H. Holm, J. A. Ibers, C. K. Jørgensen, J. B. Neilands, D. Reinen and R. J. P. Williams, Springer, Berlin, 1975, vol. 22, pp. 83–122.
433. N. A. Kosztromina, *Zh. Neorg. Khim.*, 1974, **19**, 665.
434. G. Geier, U. Karlen and A. von Zelewsky, *Helv. Chim. Acta*, 1969, **52**, 1967.
435. W. D. Horrocks, Jr. and D. R. Sudnick, *Acc. Chem. Res.*, 1981, **14**, 384.
436. W. D. Horrocks, Jr., *Methods Enzymol.*, 1993, **226**, 495.
437. J. R. Lakowicz, *Principles of Fluorescence Spectroscopy*, Springer, New York, 3rd edn, 2006.
438. M. van de Weert and L. Stella, *J. Mol. Struct.*, 2011, **998**, 144.
439. *Lanthanide Probes in Life, Chemical and Earth Sciences: Theory and Practice*, ed. J.-C. G. Bünzli and G. R. Choppin, Elsevier, Amsterdam, 1989.
440. W. D. Horrocks, Jr. and D. R. Sudnick, *J. Am. Chem. Soc.*, 1979, **101**, 334.
441. S. L. Wu and W. D. Horrocks, Jr., *J. Chem. Soc., Dalton Trans.*, 1997, 1497.
442. K. Ósz, G. Lente and C. Kállay, *J. Phys. Chem. B*, 2005, **109**, 1039.
443. Z. Szakács, M. Kraszni and B. Noszál, *Anal. Bioanal. Chem.*, 2004, **378**, 1428.
444. B. Noszál and Z. Szakács, *J. Phys. Chem. B*, 2003, **107**, 5074.
445. Z. Baranyai, I. Bányai, E. Brücher, R. Király and E. Terreno, *Eur. J. Inorg. Chem.*, 2007, **2007**, 3639.
446. E. Farkas, T. Fodor, F. K. Kálmán, G. Tirsoó and I. Tóth, *React. Kinet., Mech. Catal.*, 2015, **116**, 19.
447. M. Pniok, V. Kubíček, J. Havlíčková, J. Kotek, A. Sabatie-Gogová, J. Plutnar, S. Huclier-Markai and P. Hermann, *Chem. – Eur. J.*, 2014, **20**, 7944.
448. R. Kerdjoudj, M. Pniok, C. Alliot, V. Kubíček, J. Havlíčková, F. Rösch, P. Hermann and S. Huclier-Markai, *Dalton Trans.*, 2016, **45**, 1398.
449. R. Garcia, V. Kubíček, B. Drahoš, L. Gano, I. C. Santos, P. Campello, A. Paulo, É. Tóth and I. Santos, *Metallomics*, 2010, **2**, 571.
450. A. Bodor, I. Tóth, I. Bányai, Z. Szabó and G. T. Hefter, *Inorg. Chem.*, 2000, **39**, 2530.
451. P. Caravan, C. T. Farrar, L. Frullano and R. Uppal, *Contrast Media Mol. Imaging*, 2009, **4**, 89.
452. M. Rohrer, H. Bauer, J. Mintorovitch, M. Requardt and H.-J. Weinmann, *Invest. Radiol.*, 2005, **40**, 715.
453. L. O. Morgan and A. W. Nolle, *J. Chem. Phys.*, 1959, **31**, 365.
454. S. H. Koenig and R. D. Brown, III, *Magn. Reson. Med.*, 1984, **1**, 478.
455. J. King and N. Davidson, *J. Chem. Phys.*, 1958, **29**, 787.

456. G. Tircsó, Z. Garda, F. K. Kálmán, Z. Baranyai, I. Pócsi, G. Balla and I. Tóth, *J. Inorg. Biochem.*, 2013, **127**, 53.
457. E. Brucher, S. Cortes, F. Chavez and A. D. Sherry, *Inorg. Chem.*, 1991, **30**, 2092.
458. *Handbook of HPLC*, ed. D. Corradini and T. M. Phillips, Chromatographic Science Series, CRC Press, Boca Raton, 2nd edn, 2011, vol. 101.
459. D. Kretschy, G. Koellensperger and S. Hann, *Metallomics*, 2011, **3**, 1304.
460. M. Wacker and A. Seubert, *J. Anal. At. Spectrom.*, 2014, **29**, 707.
461. *Handbook of Capillary Electrophoresis Applications*, ed. H. Shintani and J. Polonský, Chapman & Hall, London, 1997.
462. C. A. Chang, C.-Y. Chen and H.-Y. Chen, *J. Chin. Chem. Soc.*, 1999, **46**, 519.
463. J. Petit, V. Geertsen, C. Beaucaire and M. Stambouli, *J. Chromatogr. A*, 2009, **1216**, 4113.
464. V. V. Sursyakova, G. V. Burmakina and A. I. Rubaylo, *J. Coord. Chem.*, 2017, **70**, 431.
465. X. Zhu and S. Z. Lever, *Electrophoresis*, 2002, **23**, 1348.
466. *Chromatography: Fundamentals and Applications of Chromatography and Related Differential Migration Methods, Part A: Fundamentals and Techniques*, ed. E. Heftmann, Journal of Chromatography Library, Elsevier, Amsterdam, 6th edn, 2004, vol. 69A.
467. X. Cahours, P. Morin and M. Dreux, *Chromatographia*, 1998, **48**, 739.
468. R. Kautenburger and H. P. Beck, *J. Chromatogr. A*, 2007, **1159**, 75.
469. G. Bianchini, L. Fabbrizzi and P. Paoletti, *J. Chem. Soc., Dalton Trans.*, 1975, 1036.
470. R. O'Brien, B. Z. Chowdhry and J. E. Ladbury, Isothermal Titration Calorimetry of Biomolecules, in *Protein-Ligand Interactions: Hydrodynamics and Calorimetry*, ed. S. E. Harding and B. Z. Chowdhry, Practical Approach Series, Oxford University Press, Oxford, 2001, ch. 10, pp. 263–288.
471. I. Nagypál and M. T. Beck, *J. Phys. Chem.*, 1980, **84**, 722.
472. Z. Baranyai, Complexation Properties of the Triaza, Tetraaza and Diaza-tetraoxa Macrocyclic Ligands Containing Acetyl-glycinate Functional Groups. Kinetic Behaviour of Lanthanide(III)–DOTA-tetraamide Derivative Complexes, Ph.D Thesis, University of Debrecen, Debrecen, Hungary, 2007.
473. L. Harju, *Anal. Chim. Acta*, 1970, **50**, 475.
474. L. C. Thompson, *J. Inorg. Nucl. Chem.*, 1962, **24**, 1083.
475. P. Djurdjević, R. Jelić, L. Joksović, I. Lazarević and M. Jelikić-Stankov, *Acta Chim. Slov.*, 2010, **57**, 386.
476. A. Rodríguez-Rodríguez, Z. Garda, E. Ruscsák, D. Esteban-Gómez, A. de Blas, T. Rodríguez-Blas, L. M. P. Lima, M. Beyler, R. Tripiier, G. Tircsó and C. Platas-Iglesias, *Dalton Trans.*, 2015, **44**, 5017.
477. F. K. Kálmán, A. Végh, M. Regueiro-Figueroa, É. Tóth, C. Platas-Iglesias and G. Tircsó, *Inorg. Chem.*, 2015, **54**, 2345.

478. Z. Jászberényi, I. Bányai, E. Brücher, R. Király, K. Hideg and T. Kálai, *Dalton Trans.*, 2006, 1082.
479. H.-Z. Cai and T. A. Kaden, *Helv. Chim. Acta*, 1994, 77, 383.
480. M. Regueiro-Figueroa, E. Ruscák, L. Fra, G. Tircsó, I. Tóth, A. de Blas, T. Rodríguez-Blas, C. Platas-Iglesias and D. Esteban-Gómez, *Eur. J. Inorg. Chem.*, 2014, **2014**, 6165.
481. T. F. Gritmon, M. P. Goedken and G. R. Choppin, *J. Inorg. Nucl. Chem.*, 1977, **39**, 2021.
482. K. Kumar, C. A. Chang, L. C. Francesconi, D. D. Dischino, M. F. Malley, J. Z. Gougoutas and M. F. Tweedle, *Inorg. Chem.*, 1994, **33**, 3567.
483. R. Harder and S. Chaberek, *J. Inorg. Nucl. Chem.*, 1959, **11**, 197.
484. X. Wang, T. Jin, V. Comblin, A. Lopez-Mut, E. Merciny and J. F. Desreux, *Inorg. Chem.*, 1992, **31**, 1095.
485. S. Aime, P. L. Anelli, M. Botta, F. Fedeli, M. Grandi, P. Paoli and F. Uggeri, *Inorg. Chem.*, 1992, **31**, 2422.
486. E. W. Price, J. F. Cawthray, G. A. Bailey, C. L. Ferreira, E. Boros, M. J. Adam and C. Orvig, *J. Am. Chem. Soc.*, 2012, **134**, 8670.
487. N. Chatterton, C. Gateau, M. Mazzanti, J. Pécaut, A. Borel, L. Helm and A. Merbach, *Dalton Trans.*, 2005, 1129.
488. E. W. Price, J. F. Cawthray, M. J. Adam and C. Orvig, *Dalton Trans.*, 2014, **43**, 7176.
489. A. Roca-Sabio, M. Mato-Iglesias, D. Esteban-Gómez, É. Tóth, A. de Blas, C. Platas-Iglesias and T. Rodríguez-Blas, *J. Am. Chem. Soc.*, 2009, **131**, 3331.
490. J. M. Wagener and N. V. Jarvis, *S. Afr. J. Chem.*, 1995, **48**, 85.
491. M. I. Kubechnik, I. M. Dyatlova, T. Y. Medbet, Y. F. Begulin and V. V. Gidorenko, *Proc. Acad. Sci. USSR*, 1967, **175**, 621.
492. F. K. Kálmán, R. Király and E. Brücher, *Eur. J. Inorg. Chem.*, 2008, **2008**, 4719.
493. G. C. de Witt, P. M. May, J. Webb and G. Hefter, *Inorg. Chim. Acta*, 1998, **275-276**, 37.
494. E. Brücher, G. Laurency and Z. Makra, *Inorg. Chim. Acta*, 1987, **139**, 141.
495. L. Burai, I. Fábrián, R. Király, E. Szilágyi and E. Brücher, *J. Chem. Soc., Dalton Trans.*, 1998, 243.
496. B. Chouchene, T. B. Chaabane, L. Balan, E. Giro, K. Mozet, G. Medjahdi and R. Schneider, *Beilstein J. Nanotechnol.*, 2016, **7**, 1338.
497. A. Rodríguez-Rodríguez, D. Esteban-Gómez, R. Tripier, G. Tircsó, Z. Garda, I. Tóth, A. de Blas, T. Rodríguez-Blas and C. Platas-Iglesias, *J. Am. Chem. Soc.*, 2014, **136**, 17954.
498. A. Rodríguez-Rodríguez, M. Regueiro-Figueroa, D. Esteban-Gómez, R. Tripier, G. Tircsó, F. K. Kálmán, A. C. Bényei, I. Tóth, A. de Blas, T. Rodríguez-Blas and C. Platas-Iglesias, *Inorg. Chem.*, 2016, **55**, 2227.
499. S. Vukovic, B. P. Hay and V. S. Bryantsev, *Inorg. Chem.*, 2015, **54**, 3995.
500. V. P. Solov'ev, A. Y. Tsivadze and A. A. Varnek, *Macrocyclics*, 2012, **5**, 404.

501. R. Svetlitski, A. Lomaka and M. Karelson, *Separ. Sci. Technol.*, 2006, **41**, 197.
502. M. P. Placidi, M. Botta, F. K. Kálmán, G. E. Hagberg, Z. Baranyai, A. Krenzer, A. K. Rogerson, I. Tóth, N. K. Logothetis and G. Angelovski, *Chem. – Eur. J.*, 2013, **19**, 11644.
503. Z. Pálinkás, A. Roca-Sabio, M. Mato-Iglesias, D. Esteban-Gómez, C. Platas-Iglesias, A. de Blas, T. Rodríguez-Blas and É. Tóth, *Inorg. Chem.*, 2009, **48**, 8878.
504. P. Táborský, I. Svobodová, P. Lubal, Z. Hnatejko, S. Lis and P. Hermann, *Polyhedron*, 2007, **26**, 4119.
505. K. Kumar, C. A. Chang and M. F. Tweedle, *Inorg. Chem.*, 1993, **32**, 587.
506. Z. Jászberényi, É. Tóth, T. Kálai, R. Király, L. Burai, E. Brücher, A. E. Merbach and K. Hideg, *Dalton Trans.*, 2005, 694.
507. L. Sarka, L. Burai and E. Brücher, *Chem. – Eur. J.*, 2000, **6**, 719.
508. E. Balogh, R. Tripier, P. Fousková, F. Reviriego, H. Handel and É. Tóth, *Dalton Trans.*, 2007, 3572.
509. L. Burai, E. Brücher, R. Király, P. Solymosi and T. Víg, *Acta Pharm. Hung.*, 2001, **70**, 89.
510. L. M. P. Lima, C. V. Esteves, R. Delgado, P. Hermann, J. Kotek, R. Ševčíková and P. Lubal, *Eur. J. Inorg. Chem.*, 2012, **2012**, 2533.
511. Z. Pálinkás, Z. Baranyai, E. Brücher and B. Rózsa, *Inorg. Chem.*, 2011, **50**, 3471.
512. L. Sarka, L. Burai, R. Király, L. Zékány and E. Brücher, *J. Inorg. Biochem.*, 2002, **91**, 320.
513. D. W. Margerum, B. A. Zabin and D. L. Janes, *Inorg. Chem.*, 1966, **5**, 250.
514. R. Negri, Z. Baranyai, L. Tei, G. B. Giovenzana, C. Platas-Iglesias, A. C. Bényei, J. Bodnár, A. Vágner and M. Botta, *Inorg. Chem.*, 2014, **53**, 12499.
515. C. A. Chang and Y.-L. Liu, *J. Chin. Chem. Soc.*, 2000, **47**, 1001.
516. E. M. Gale, I. P. Atanasova, F. Blasi, I. Ay and P. Caravan, *J. Am. Chem. Soc.*, 2015, **137**, 15548.
517. J. Künemeyer, L. Terborg, S. Nowak, C. Brauckmann, L. Telgmann, A. Albert, F. Tokmak, B. K. Krämer, A. Günzel, G. A. Wiesmüller and U. Karst, *Electrophoresis*, 2009, **30**, 1766.
518. P. Hajós, D. Lukács, E. Farsang and K. Horváth, *J. Chromatogr. Sci.*, 2016, **54**, 1752.
519. U. Lindner, J. Lingott, S. Richter, W. Jiang, N. Jakubowski and U. Panne, *Anal. Bioanal. Chem.*, 2015, **407**, 2415.
520. L. Beuvier, C. Bresson, A. Nonell, L. Vio, N. Henry, V. Pichon and F. Chartier, *RSC Adv.*, 2015, **5**, 92858.
521. P. Wedeking, K. Kumar and M. F. Tweedle, *Magn. Reson. Imaging*, 1992, **10**, 641.
522. S. Laurent, L. V. Elst, C. Henoumont and R. N. Muller, *Contrast Media Mol. Imaging*, 2010, **5**, 305.
523. T. Frenzel, P. Lengsfeld, H. Schirmer, J. Hütter and H.-J. Weinmann, *Invest. Radiol.*, 2008, **43**, 817.

524. P. T. Normann, P. Joffe, I. Martinsen and H. S. Thomsen, *J. Pharm. Biomed. Anal.*, 2000, **22**, 939.
525. J. Künnemeyer, L. Terborg, S. Nowak, L. Telgmann, F. Tokmak, B. K. Krämer, A. Günzel, G. A. Wiesmüller, J. Waldeck, C. Bremer and U. Karst, *Anal. Chem.*, 2009, **81**, 3600.
526. L. Telgmann, C. A. Wehe, J. Künnemeyer, A.-C. Bülter, M. Sperling and U. Karst, *Anal. Bioanal. Chem.*, 2012, **404**, 2133.
527. H. J. Weinmann, M. Laniado and W. Mützel, *Physiol. Chem. Phys. Med. NMR*, 1984, **16**, 167.
528. A. Spinazzi, V. Lorusso, G. Pirovano and M. Kirchin, *Acad. Radiol.*, 1999, **6**, 282.
529. G. Schuhmann-Giampieri and G. Krestin, *Invest. Radiol.*, 1991, **26**, 975.
530. M. Van Wagoner and D. Worah, *Invest. Radiol.*, 1993, **28**, S44.
531. M. VanWagoner, M. O'Toole, D. Worah, P. T. Leese and S. C. Quay, *Invest. Radiol.*, 1991, **26**, 980.
532. Z. Baranyai, F. Uggeri, G. B. Giovenzana, A. Bényei, E. Brücher and S. Aïme, *Chem. – Eur. J.*, 2009, **15**, 1696.
533. H.-S. Chong, D. E. Milenic, K. Garmestani, E. D. Brady, H. Arora, C. Pfiester and M. W. Brechbiel, *Nucl. Med. Biol.*, 2006, **33**, 459.
534. H.-S. Chong, S. Mhaske, M. Lin, S. Bhuniya, H. A. Song, M. W. Brechbiel and X. Sun, *Bioorg. Med. Chem. Lett.*, 2007, **17**, 6107.
535. H.-S. Chong, H. A. Song, S. Lim, K. Macrenaris, X. Ma, H. Lee, P. Bui and T. Meade, *Bioorg. Med. Chem. Lett.*, 2008, **18**, 2505.
536. H.-S. Chong, H. A. Song, N. Birch, T. Le, S. Lim and X. Ma, *Bioorg. Med. Chem. Lett.*, 2008, **18**, 3436.
537. H.-S. Chong, S. Lim, K. E. Baidoo, D. E. Milenic, X. Ma, F. Jia, H. A. Song, M. W. Brechbiel and M. R. Lewis, *Bioorg. Med. Chem. Lett.*, 2008, **18**, 5792.
538. J. Rudovský, P. Hermann, M. Botta, S. Aïme and I. Lukeš, *Chem. Commun.*, 2005, 2390.
539. D. Parker, *Chem. Soc. Rev.*, 1990, **19**, 271.
540. L. L. Chappell, B. E. Rogers, M. B. Khazaeli, M. S. Mayo, D. J. Buchsbaum and M. W. Brechbiel, *Bioorg. Med. Chem.*, 1999, **7**, 2313.
541. L. L. Chappell, D. Ma, D. E. Milenic, K. Garmestani, V. Venditto, M. P. Beitzel and M. W. Brechbiel, *Nucl. Med. Biol.*, 2003, **30**, 581.
542. K. D. Brandt, K. E. Schnobrich and D. K. Johnson, *Bioconjugate Chem.*, 1991, **2**, 67.
543. S. J. Kline, D. A. Betebenner and D. K. Johnson, *Bioconjugate Chem.*, 1991, **2**, 26.
544. K.-P. Eisenwiener, P. Powell and H. R. Mäcke, *Bioorg. Med. Chem. Lett.*, 2000, **10**, 2133.
545. J. F. W. Keana and J. S. Mann, *J. Org. Chem.*, 1990, **55**, 2868.
546. C. Szíjjártó, E. Pershagen and K. E. Borbas, *Dalton Trans.*, 2012, **41**, 7660.
547. M. Tropiano, C. J. Record, E. Morris, H. S. Rai, C. Allain and S. Faulkner, *Organometallics*, 2012, **31**, 5673.

548. L. Frullano, C. Catana, T. Benner, A. D. Sherry and P. Caravan, *Angew. Chem., Int. Ed.*, 2010, **49**, 2382.
549. J. P. L. Cox, A. S. Craig, I. M. Helps, K. J. Jankowski, D. Parker, M. A. W. Eaton, A. T. Millican, K. Millar, N. R. A. Beeley and B. A. Boyce, *J. Chem. Soc., Perkin Trans. 1*, 1990, 2567.
550. C. de Haën, *Top. Magn. Reson. Imaging*, 2001, **12**, 221.
551. L. Moriggi, C. Cannizzo, C. Prestinari, F. Berrière and L. Helm, *Inorg. Chem.*, 2008, **47**, 8357.
552. S. Silvério, S. Torres, A. F. Martins, J. A. Martins, J. P. André, L. Helm, M. I. M. Prata, A. C. Santos and C. F. G. C. Geraldes, *Dalton Trans.*, 2009, 4656.
553. Z. Baranyai, M. Botta, M. Fekete, G. B. Giovenzana, R. Negri, L. Tei and C. Platas-Iglesias, *Chem. – Eur. J.*, 2012, **18**, 7680.
554. J. Kotek, F. K. Kálmán, P. Hermann, E. Brücher, K. Binnemans and I. Lukeš, *Eur. J. Inorg. Chem.*, 2006, **2006**, 1976.
555. L. Pellegatti, J. Zhang, B. Drahos, S. Villette, F. Suzenet, G. Guillaumet, S. Petoud and É. Tóth, *Chem. Commun.*, 2008, 6591.
556. S. L. C. Pinho, H. Faneca, C. F. G. C. Geraldes, J. Rocha, L. D. Carlos and M.-H. Delville, *Eur. J. Inorg. Chem.*, 2012, **2012**, 2828.
557. C. S. Bonnet, F. Buron, F. Caillé, C. M. Shade, B. Drahoš, L. Pellegatti, J. Zhang, S. Villette, L. Helm, C. Pichon, F. Suzenet, S. Petoud and É. Tóth, *Chem. – Eur. J.*, 2012, **18**, 1419.
558. F. Caillé, C. S. Bonnet, F. Buron, S. Villette, L. Helm, S. Petoud, F. Suzenet and É. Tóth, *Inorg. Chem.*, 2012, **51**, 2522.
559. P. Caravan, C. Comuzzi, W. Crooks, T. J. McMurphy, G. R. Choppin and S. R. Woulfe, *Inorg. Chem.*, 2001, **40**, 2170.
560. G. L. Rothermel, Jr., E. N. Rizkalla and G. R. Choppin, *Inorg. Chim. Acta*, 1997, **262**, 133.
561. K.-Y. Choi, K. S. Kim and J. C. Kim, *Polyhedron*, 1994, **13**, 567.
562. G. Tircsó, M. Regueiro-Figueroa, V. Nagy, Z. Garda, T. Garai, F. K. Kálmán, D. Esteban-Gómez, É. Tóth and C. Platas-Iglesias, *Chem. – Eur. J.*, 2016, **22**, 896.
563. N. Iki, E. Boros, M. Nakamura, R. Baba and P. Caravan, *Inorg. Chem.*, 2016, **55**, 4000.
564. A. Takács, R. Napolitano, M. Purgel, A. C. Bényei, L. Zékány, E. Brücher, I. Tóth, Z. Baranyai and S. Aime, *Inorg. Chem.*, 2014, **53**, 2858.
565. Z. Baranyai, G. A. Rolla, R. Negri, A. Forgács, G. B. Giovenzana and L. Tei, *Chem. – Eur. J.*, 2014, **20**, 2933.
566. E. Balogh, R. Tripier, R. Ruloff and É. Tóth, *Dalton Trans.*, 2005, 1058.
567. É. Tóth, R. Király, J. Platzek, B. Radüchel and E. Brücher, *Inorg. Chim. Acta*, 1996, **249**, 191.
568. P. Táborský, P. Lubal, J. Havel, J. Kotek, P. Hermann and Ivan Lukeš, *Collect. Czech. Chem. Commun.*, 2005, **70**, 1909.
569. M. Försterová, I. Svobodová, P. Lubal, P. Táborský, J. Kotek, P. Hermann and I. Lukeš, *Dalton Trans.*, 2007, 535.

570. F. A. Rojas-Quijano, G. Tircsó, E. T. Benyó, Z. Baranyai, H. T. Hoang, F. K. Kálmán, P. K. Gulaka, V. D. Kodibagkar, S. Aime, Z. Kovács and A. D. Sherry, *Chem. – Eur. J.*, 2012, **18**, 9669.
571. F. A. Rojas-Quijano, E. T. Benyó, G. Tircsó, F. K. Kálmán, Z. Baranyai, S. Aime, A. D. Sherry and Z. Kovács, *Chem. – Eur. J.*, 2009, **15**, 13188.
572. T. J. McMurry, C. G. Pippin, C. Wu, K. A. Deal, M. W. Brechbiel, S. Mirzadeh and O. A. Gansow, *J. Med. Chem.*, 1998, **41**, 3546.
573. Y. Lin, A. Favre-Réguillon, S. Pellet-Rostaing and M. Lemaire, *Tetrahedron Lett.*, 2007, **48**, 3463.
574. M. Port, C. Corot and T. Gautheret, Compounds Comprising a Biological Target Recognizing Part, Coupled to a Signal Part Capable of Complexium Gallium, WO 2007/042504, 2007.
575. F. Dioury, C. Ferroud, A. Guy and M. Port, *Tetrahedron*, 2009, **65**, 7573.
576. G. Castro, M. Regueiro-Figueroa, D. Esteban-Gómez, R. Bastida, A. Macías, P. Pérez-Lourido, C. Platas-Iglesias and L. Valencia, *Chem. – Eur. J.*, 2015, **21**, 18662.
577. W. A. P. Breeman, M. de Jong, T. J. Visser, J. L. Erion and E. P. Krenning, *Eur. J. Nucl. Med. Mol. Imaging*, 2003, **30**, 917.
578. S. Laurent, T. N. Parac-Vogt, K. Kimpe, C. Thirifays, K. Binnemans, R. N. Muller and L. V. Elst, *Eur. J. Inorg. Chem.*, 2007, **2007**, 2061.
579. J. F. Desreux and D. Gilsoul, Chemical Synthesis of Paramagnetic Complexes, in *Trends in Contrast Media*, ed. H. Thomsen, R. N. Muller and R. F. Mattrey, Springer-Verlag, Berlin, 1999, pp. 161–168.
580. J. Vipond, M. Woods, P. Zhao, G. Tircsó, J. Ren, S. G. Bott, D. Ogrin, G. E. Kiefer, Z. Kovacs and A. D. Sherry, *Inorg. Chem.*, 2007, **46**, 2584.
581. S. Y. Yoon and H. B. Lim, *Bull. Korean Chem. Soc.*, 2012, **33**, 3665.
582. P. Lebdušková, P. Hermann, L. Helm, É. Tóth, J. Kotek, K. Binnemans, J. Rudovský, I. Lukeš and A. E. Merbach, *Dalton Trans.*, 2007, 493.
583. Y. Inomata, T. Sunakawa and F. S. Howell, *J. Mol. Struct.*, 2003, **648**, 81.
584. M. Magerstädt, O. A. Gansow, M. W. Brechbiel, D. Colcher, L. Baltzer, R. H. Knop, M. E. Girton and M. Naegele, *Magn. Reson. Med.*, 1986, **3**, 808.
585. S. K. Sarkar, R. E. Rycyna, R. E. Lenkinski, H. A. Solleveld and L. B. Kinter, *Magn. Reson. Med.*, 1991, **17**, 328.
586. C. F. G. C. Geraldés, A. M. Urbano, M. C. Alpoim, A. D. Sherry, K.-T. Kuan, R. Rajagopalan, F. Maton and R. N. Muller, *Magn. Reson. Imaging*, 1995, **13**, 401.
587. H.-J. Weinmann, R. C. Brasch, W.-R. Press and G. E. Wesbey, *Am. J. Roentgenol.*, 1984, **142**, 619.
588. D. J. Averill, J. Garcia, B. N. Siriwardena-Mahanama, S. M. Vithanarachchi and M. J. Allen, *J. Vis. Exp.*, 2011, **53**, e2844.
589. A. Barge, G. Cravotto, E. Gianolio and F. Fedeli, *Contrast Media Mol. Imaging*, 2006, **1**, 184.
590. H. Rohwer, N. Collier and E. Hosten, *Anal. Chim. Acta*, 1995, **314**, 219.
591. H. Rohwer and E. Hosten, *Anal. Chim. Acta*, 1997, **339**, 271.

592. T. N. Nagaraja, R. L. Croxen, S. Panda, R. A. Knight, K. A. Keenan, S. L. Brown, J. D. Fenstermacher and J. R. Ewing, *J. Neurosci. Methods*, 2006, **157**, 238.
593. S. B. Sawin, *Talanta*, 1961, **8**, 673.
594. K. Kumar, K. V. Sukumaran and M. F. Tweedle, *Anal. Chem.*, 1994, **66**, 295.
595. D. D. Dischino, E. J. Delaney, J. E. Emswiler, G. T. Gaughan, J. S. Prasad, S. K. Srivastava and M. F. Tweedle, *Inorg. Chem.*, 1991, **30**, 1265.

CHAPTER 2

Gadolinium-based Contrast Agents

LOTHAR HELM,^{*a} JANET R. MORROW,^{*b}
CHRISTOPHER J. BOND,^b FABIO CARNIATO,^c
MAURO BOTTA,^{*c} MIHÁLY BRAUN,^d ZSOLT BARANYAI,^e
ROSA PUJALES-PARADELA,^f MARTÍN REGUEIRO-FIGUEROA,^f
DAVID ESTEBAN-GÓMEZ,^f CARLOS PLATAS-IGLESIAS^{*f} AND
TIMOTHY J. SCHOLL^{*g}

^a Ecole Polytechnique Fédérale de Lausanne, Institute of Chemical Sciences and Engineering, BCH, 1015 Lausanne, Switzerland; ^b University at Buffalo, State University of New York, Department of Chemistry, Amherst, NY 14260, USA; ^c Dipartimento di Scienze e Innovazione Tecnologica, Università del Piemonte Orientale “Amedeo Avogadro”, 15121 Alessandria, Italy; ^d Isotope Climatology and Environmental Research Centre (ICER), Institute for Nuclear Research, Hungarian Academy of Sciences, H-4026 Debrecen, Hungary; ^e Department of Inorganic and Analytical Chemistry, Faculty of Science and Technology, University of Debrecen, H-4010 Debrecen, Hungary; ^f Centro de Investigaciones Científicas Avanzadas (CICA) and Departamento de Química Fundamental, Universidade da Coruña, 15008 A Coruña, Spain; ^g Medical Biophysics and Robarts Research Institute, Western University, London, N6A 3K7 ON, Canada
^{*}Email: lothar.helm@epfl.ch; jmorrow@buffalo.edu; mauro.botta@uniupo.it; carlos.platas.iglesias@udc.es; tscholl@robarts.ca

2.1 General Theory of the Relaxivity of Gadolinium-based Contrast Agents

LOTHAR HELM

2.1.1 Definition of Relaxivity

Gd^{III}-based contrast agents for MRI influence image contrast by increasing the relaxation rates of the nuclear spins of the hydrogen nuclei of water.¹ The acceleration of spin relaxation—longitudinal relaxation, $1/T_1$, as well as transverse relaxation, $1/T_2$ —is generated by fluctuating local magnetic fields that are produced by the electron spin of the paramagnetic gadolinium ion.² The increase of relaxation owing to the paramagnetic compound, $1/T_{i,p}$, adds to the diamagnetic relaxation, $1/T_{i,d}$, giving the observed relaxation rates, $1/T_{i,obs}$.^{3–5}

$$\frac{1}{T_{i,obs}} = \frac{1}{T_{i,d}} + \frac{1}{T_{i,p}} \quad \text{with } i = 1, 2 \quad (2.1)$$

In the case of dilute paramagnetic solutions, the paramagnetic term $1/T_{i,p}$ is proportional to the concentration of the paramagnetic species, in this case the gadolinium ion, [Gd].

$$\frac{1}{T_{i,p}} = r_i[\text{Gd}] \quad \text{with } i = 1, 2 \quad (2.2)$$

The concentration is usually given in units of millimolar ($\text{mM} = \text{mmol L}^{-1}$). The constant of proportionality, r_i , is called relaxivity and has the units of $\text{mM}^{-1} \text{s}^{-1}$. Because this chapter focuses on ¹H or proton relaxation, r_1 and r_2 are called longitudinal and transverse proton relaxivity, respectively. Proton relaxivity reflects the ability of a compound to enhance relaxation and is therefore a direct measure for its efficiency as contrast agent.

It should be stressed that relaxivity always refers to the concentration of paramagnetic centers, *i.e.* [Gd]. If a compound incorporates more than one Gd^{III}, the relaxation enhancement per molecule or per particle can be obtained by multiplying the relaxivity with the number of gadolinium ions per molecule or per particle. The “per gadolinium” definition of relaxivity avoids ambiguities, for example, if the exact number of ions per species is not known. The concentration of Gd^{III} can in general be determined experimentally even after digestion of the species or particles (see Chapter 2.7).

A plot of observed relaxation, $1/T_{i,obs}$, as a function of [Gd] should result in a straight line with a slope of r_i . Deviation from a straight line indicates that the paramagnetic species experience a concentration-dependent transformation, such as the formation of aggregates or precipitation, which is not always easily observable. In the case of compound aggregation, such as the formation of dimers or trimers, nonlinearity of relaxivity as a function of

concentration can be used to determine equilibrium constants for the formation of the aggregates.^{6,7}

The magnetic field produced by an electron spin decreases with the distance from a paramagnetic ion, and hence only water molecules close to paramagnetic ions will experience relaxation enhancement. The strongest influence will be on water molecules in direct contact with a paramagnetic ion, so-called inner-sphere water molecules (Figure 2.1). The relaxation enhancement of inner-sphere water molecules is transmitted to the bulk of the solution by chemical exchange. Water molecules outside the first coordination sphere, but in the vicinity of the paramagnetic species, will also experience relaxation enhancement, although to a lesser extent. It is therefore common to separate the total paramagnetic relaxation enhancement into inner-sphere water, $(1/T_{i,p})^{\text{IS}}$, and outer-sphere water, $(1/T_{i,p})^{\text{OS}}$, contributions.

$$\frac{1}{T_{i,p}} = (1/T_{i,p})^{\text{IS}} + (1/T_{i,p})^{\text{OS}} \quad \text{with } i = 1, 2 \quad (2.3)$$

In a similar way, proton relaxivities can be separated into inner- and outer-sphere contributions.

$$r_i = r_i^{\text{IS}} + r_i^{\text{OS}} \quad \text{with } i = 1, 2 \quad (2.4)$$

In the following sections, standard theoretical descriptions for $(1/T_{i,p})^{\text{IS}}$ and $(1/T_{i,p})^{\text{OS}}$ will be presented with the parameters that influence them. To obtain values for these parameters from experimental relaxivities, relaxation rates are commonly measured as a function of the Larmor frequency of the proton, ν_1 , which is linked to the static magnetic field B_0 by $\nu_1 = \gamma_1 B_0 / 2\pi$. More details regarding these measurements, nuclear magnetic relaxation dispersion (NMRD) profiles, are presented in Section 2.3.

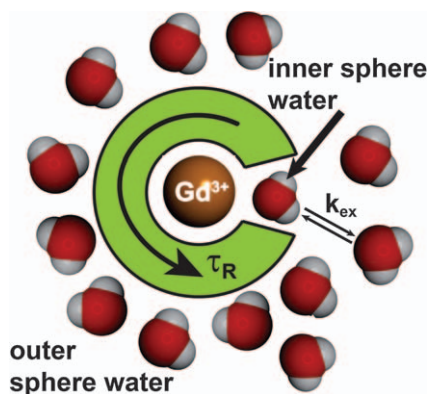


Figure 2.1 Inner- and outer-sphere water molecules around a Gd^{III} complex.

2.1.2 Theory of Inner-sphere Relaxivity

Inner-sphere contributions to observed water-proton relaxation enhancement, $(1/T_{i,p})^{\text{IS}} = r_i^{\text{IS}}[\text{Gd}]$, result from chemical exchange of coordinated water protons with those of the bulk. This relationship represents a two-site exchange, which has been described by Luz and Meiboom⁸ and Swift and Connick⁹ in the case of dilute paramagnetic species as follows:

$$\left(\frac{1}{T_{1,p}}\right)^{\text{IS}} = \frac{cq}{55.56} \frac{1}{T_{1m} + \tau_m} \quad (2.5)$$

$$\left(\frac{1}{T_{2,p}}\right)^{\text{IS}} = \frac{cq}{55.56} \frac{1}{\tau_m} \frac{T_{2m}^{-1}(T_{2m}^{-1} + \tau_m^{-1}) + \Delta\omega_m^2}{(T_{2m}^{-1} + \tau_m^{-1})^2 + \Delta\omega_m^2} \quad (2.6)$$

In these equations, c is the molal concentration (mol kg^{-1}) of gadolinium; q is the number of inner-sphere water molecules (hydration number); τ_m is the residence time of an inner-sphere water molecule; T_{1m} and T_{2m} are the longitudinal and transverse proton relaxation times of bound water, respectively; and $\Delta\omega_m$ is the ^1H chemical shift difference between the bound-water and bulk-water resonances (in the absence of chemical exchange). The residence time of inner-sphere water is linked to the water-exchange rate constant, k_{ex} , by eqn (2.7).

$$\tau_m = k_{\text{ex}}^{-1} \quad (2.7)$$

The concentration factor $cq/55.56$ is equal to the mole fraction of inner-sphere water molecules, P_m . In dilute aqueous solutions, the molal concentration is equal to the molar concentration (mol L^{-1}). The inner-sphere relaxivities are therefore given by eqn (2.7) and (2.8).

$$r_1^{\text{IS}} = 1.80 \times 10^{-5} \frac{q}{T_{1m} + \tau_m} \quad (2.8)$$

$$r_2^{\text{IS}} = 1.80 \times 10^{-5} \frac{q}{\tau_m} \frac{T_{2m}^{-1}(T_{2m}^{-1} + \tau_m^{-1}) + \Delta\omega_m^2}{(T_{2m}^{-1} + \tau_m^{-1})^2 + \Delta\omega_m^2} \quad (2.9)$$

The relaxation of nuclear spins in compounds with a paramagnetic center is governed by the hyperfine interaction between the electron spin and the nuclear spin. The “classical theory” describing the nuclear spin relaxation was developed in the 1950s and 1960s and is now called the “modified Solomon–Bloembergen–Morgan” or SBM theory.^{10–13} This theory is based on several rather constringent assumptions that are described later in this chapter; however, SBM theory has the immense advantage of leading to analytical equations that enable fitting of experimental data. Paramagnetic contributions to the relaxation of bound nuclear spins are described by the sum of contributions from dipole–dipole (DD), scalar (SC), and the Curie

(Cu) mechanisms.¹⁴ For ¹H spin relaxation of water molecules in the inner-sphere of Gd^{III}, the scalar coupling constant A/\hbar is small and $1/T_i^{\text{SC}}$ can be neglected.^{15,16} Furthermore, the contribution from Curie relaxation to longitudinal relaxation is much smaller than the dipolar contribution, $1/T_1^{\text{Cu}} \ll 1/T_1^{\text{DD}}$, and, therefore, can be neglected. However, the Curie contribution to transverse relaxation increases with the square of the resonance frequency, ω_{I} , and, therefore, can be important at high magnetic fields [eqn (2.16)].

$$\frac{1}{T_{\text{im}}} = \frac{1}{T_i^{\text{DD}}} + \frac{1}{T_i^{\text{SC}}} + \frac{1}{T_i^{\text{Cu}}} \quad \text{with } i = 1, 2 \quad (2.10)$$

The individual relaxation terms are given by eqn (2.11)–(2.16).

$$\frac{1}{T_1^{\text{DD}}} = \frac{2}{15} \frac{\gamma_1^2 g^2 \mu_{\text{B}}^2}{r_{\text{IS}}^6} S(S+1) \left(\frac{\mu_0}{4\pi}\right)^2 \left[7 \frac{\tau_{\text{c}2}}{1 + \omega_{\text{S}}^2 \tau_{\text{c}2}^2} + 3 \frac{\tau_{\text{c}1}}{1 + \omega_{\text{I}}^2 \tau_{\text{c}1}^2} \right] \quad (2.11)$$

$$\frac{1}{T_1^{\text{SC}}} = \frac{2S(S+1)}{3} \left(\frac{A}{\hbar}\right)^2 \left(\frac{\tau_{\text{e}2}}{1 + \omega_{\text{S}}^2 \tau_{\text{e}2}^2}\right) \quad (2.12)$$

$$\frac{1}{T_1^{\text{Cu}}} = \frac{2}{5} \left(\frac{\mu_0}{4\pi}\right)^2 \frac{\omega_{\text{I}}^2 \mu_{\text{B}}^4 \mu_{\text{eff}}^4}{(3k_{\text{B}}T)^2 r_{\text{IS}}^6} \left(\frac{3\tau_{\text{Cu}}}{1 + \omega_{\text{I}}^2 \tau_{\text{Cu}}^2}\right) \quad (2.13)$$

$$\frac{1}{T_2^{\text{DD}}} = \frac{1}{15} \frac{\gamma_1^2 g^2 \mu_{\text{B}}^2}{r_{\text{IS}}^6} S(S+1) \left(\frac{\mu_0}{4\pi}\right)^2 \left[13 \frac{\tau_{\text{c}2}}{1 + \omega_{\text{S}}^2 \tau_{\text{c}2}^2} + 3 \frac{\tau_{\text{c}1}}{1 + \omega_{\text{I}}^2 \tau_{\text{c}1}^2} + 4\tau_{\text{c}1} \right] \quad (2.14)$$

$$\frac{1}{T_2^{\text{SC}}} = \frac{S(S+1)}{3} \left(\frac{A}{\hbar}\right)^2 \left(\frac{\tau_{\text{e}2}}{1 + \omega_{\text{S}}^2 \tau_{\text{e}2}^2} + \tau_{\text{e}1}\right) \quad (2.15)$$

$$\frac{1}{T_2^{\text{Cu}}} = \frac{1}{5} \left(\frac{\mu_0}{4\pi}\right)^2 \frac{\omega_{\text{I}}^2 \mu_{\text{B}}^4 \mu_{\text{eff}}^4}{(3k_{\text{B}}T)^2 r_{\text{IS}}^6} \left(4\tau_{\text{Cu}} + \frac{3\tau_{\text{Cu}}}{1 + \omega_{\text{I}}^2 \tau_{\text{Cu}}^2}\right) \quad (2.16)$$

In eqn (2.11) to (2.16), S is the electron spin; γ_1 is the nuclear gyromagnetic ratio; g is the electron g factor; μ_{B} is the Bohr magneton; r_{IS} is the nuclear-spin–electron-spin distance; ω_{I} and ω_{S} are the nuclear and electron Larmor frequencies, respectively, in units of rad s^{-1} ; and A/\hbar is the scalar coupling constant. The different correlation times in these equations describe the time fluctuations of the interactions and are given by eqn (2.17)–(2.19):

$$\frac{1}{\tau_{\text{ci}}} = \frac{1}{\tau_{\text{R}}} + \frac{1}{\tau_{\text{m}}} + \frac{1}{T_{\text{ie}}} \quad \text{with } i = 1, 2 \quad (2.17)$$

$$\frac{1}{\tau_{\text{ei}}} = \frac{1}{\tau_{\text{m}}} + \frac{1}{T_{\text{ie}}} \quad \text{with } i = 1, 2 \quad (2.18)$$

$$\frac{1}{\tau_{\text{Cu}}} = \frac{1}{\tau_{\text{R}}} + \frac{1}{\tau_{\text{m}}} \quad (2.19)$$

where $\tau_R = 1/(6D_R)$ is the rotational correlation time, D_R is the rotational diffusion coefficient, and T_{ie} are the longitudinal ($i = 1$) and transverse ($i = 2$) electron spin relaxation times.

Electron spin relaxation depends strongly on the metal ion. For pure S spins like Gd^{III} ($S = 7/2$) and Mn^{II} or Fe^{III} ($S = 5/2$), electron spin relaxation is dominated by zero-field-splitting (ZFS) interactions.¹⁷ In an environment with cubic symmetry like in an octahedral complex (for example, $[Mn(H_2O)_6]^{2+}$), static ZFS cancels and only a transient ZFS exists due to temporal distortions of symmetry. The electron spin relaxation is then given by the approximate equations developed by Bloembergen and Morgan:¹⁸

$$\left(\frac{1}{T_{1e}}\right)^{ZFS} = \frac{2}{50} (4S(S+1)-3)\Delta^2 \left(\frac{\tau_v}{1 + \omega_S^2 \tau_v^2} + \frac{4\tau_v}{1 + 4\omega_S^2 \tau_v^2} \right) \quad (2.20)$$

$$\left(\frac{1}{T_{2e}}\right)^{ZFS} = \frac{1}{50} (4S(S+1)-3)\Delta^2 \left(3\tau_v + \frac{5\tau_v}{1 + \omega_S^2 \tau_v^2} + \frac{2\tau_v}{1 + 4\omega_S^2 \tau_v^2} \right) \quad (2.21)$$

The correlation time τ_v is for the modulation of the transient ZFS, and Δ^2 is the mean squared amplitude of the ZFS in frequency units.

The correlation times used in eqn (2.17)–(2.21) are temperature-dependent. The temperature dependence is described by Arrhenius behavior (τ_R, τ_v)

$$\tau = \tau^{298} \exp\left\{ \frac{-E_a}{R} \left(\frac{1}{298} - \frac{1}{T} \right) \right\} \quad (2.22)$$

or by Eyring behavior (τ_m , respectively k_{ex})

$$k_{ex} = \frac{1}{\tau_m} = k_{ex}^{298} \frac{T}{298} \exp\left\{ \frac{-\Delta H^\ddagger}{R} \left(\frac{1}{298} - \frac{1}{T} \right) \right\} = \frac{k_B T}{h} \exp\left\{ \frac{\Delta S^\ddagger}{R} - \frac{\Delta H^\ddagger}{RT} \right\} \quad (2.23)$$

As already mentioned, SBM theory is based on several assumptions. First, SBM theory is based on the validity of the Redfield theory to the nuclear spin and electron spin systems. The second major assumption is that electron spin relaxation is uncorrelated with molecular reorientation. The third assumption is that the electron spin system is dominated by Zeeman interaction and ZFS can be treated as a perturbation. The fourth assumption is the point-dipole approximation, which treats the electron spin as a point dipole located at the nucleus of the metal ion. In addition to these major assumptions, several others are used to obtain the equations presented above.^{10,12} General treatments of the nuclear spin relaxation due to paramagnetic metal ions have been developed by the groups of Kowalewski,^{19–21} Sharp,²² and Fries.^{23,24}

2.1.3 Theory of Outer-sphere Relaxivity

The outer-sphere contribution to relaxivity has its origin in the interaction between the electron spin of the paramagnetic ion and nuclei of water molecules not in the inner-coordination sphere of the paramagnetic ion. Outer-sphere water molecules can be divided into two groups: (1) a few molecules that form hydrogen bonds with charged groups of the chelating ligand or with inner-sphere water molecules, and (2) other water molecules diffusing freely close to the chelate. Hydrogen-bound water molecules are commonly called second-sphere water.²⁵

The increase of relaxation rate generated by second-sphere water molecules can be described using the same equations as for inner-sphere water.^{26,27} The longitudinal relaxivity of second-sphere water, r_1^{SS} , is given by

$$r_1^{SS} = 1.80 \times 10^{-5} \frac{q_{SS}}{T_{1m}^{SS} + \tau_m^{SS}} \quad (2.24)$$

where q_{SS} is the number of second-sphere water molecules, τ_m^{SS} is the residence time of water in the second sphere, and T_{1m}^{SS} is the relaxation time of water in the second sphere, which is normally described using only dipolar relaxation. Due to relatively weak binding, τ_m^{SS} is short and is often the effective correlation time for dipolar relaxation. The distance between second-sphere water protons and the paramagnetic center, r_{SS} , is not well known and is often fixed to a “reasonable value”. In most data treatments, people do not consider second-sphere water molecules specifically but include second-sphere contributions with outer-sphere contributions.

The dipolar relaxation of freely diffusing outer-sphere water molecules is commonly described by a model developed by Ayant,²⁸ Freed,^{29,30} and others.^{31,32} The model is based on interaction-free diffusion of particles:

$$\left(\frac{1}{T_{1,p}}\right)^{OS} = \frac{32\pi}{405} \left(\frac{\mu_0}{4\pi}\right)^2 \frac{N_A[M]}{dD} \gamma_I^2 \gamma_S^2 \hbar^2 S(S+1) [3J_1^{OS}(\omega_I) + 7J_2^{OS}(\omega_S)] \quad (2.25)$$

$$J_k^{OS}(\omega) = \text{Re} \left\{ \frac{1 + z/4}{1 + z + 4z^2/9 + z^3/9} \right\} \quad (2.26)$$

$$z = \sqrt{i\omega\tau + \tau_D/T_{ke}} \quad \tau_D = d^2/D; \quad k = 1, 2$$

where N_A is Avogadro's number, d is the closest distance of approach of the nuclear spin I and the electron spin S , D is the diffusion coefficient for relative translational diffusion, $[M]$ is the molar concentration of the paramagnetic ion, and τ_D is the correlation time for the relative translational diffusion. The relative translational diffusion coefficient is described by the sum of the self-diffusion coefficients of the complex bearing the electron spin (D_S) and the water molecules bearing the proton nuclear spin (D_I):

$$D = D_I + D_S \quad (2.27)$$

Because water molecules diffuse much faster than the relatively large complexes, D is close to the self-diffusion coefficient of water.

2.2 Measuring Longitudinal (T_1) and Transverse (T_2) Relaxation Times

LOTHAR HELM

Modern nuclear magnetic resonance (NMR) is in general performed by exciting nuclear spin systems *via* a short high-frequency pulse or a sequence of pulses. The response of the system, the free induction decay (FID), is then Fourier transformed and an NMR spectrum is obtained. In the simplest experiment, a single pulse disturbs nuclear magnetization that is at equilibrium and aligned along the external magnetic field, by convention along the z -axis. During the pulse, magnetization is induced in a plane perpendicular to that axis, the xy -plane. After the excitation, the perturbed nuclear spin system returns back to equilibrium as characterized by two relaxation times: T_1 and T_2 . The longitudinal relaxation time T_1 describes the buildup of the z -component of the nuclear magnetization. The transverse relaxation time T_2 describes the decay of the nuclear magnetization in the xy -plane toward zero.^{33–35} The behavior of the nuclear magnetization is described by the phenomenological equations developed by Bloch.

Relaxation times, or more commonly relaxation rates $1/T_1$ and $1/T_2$, measured for the water hydrogen nuclear spin (^1H , protons) provide information regarding dynamics and molecular interactions of paramagnetic compounds with the solvent, for example, water. In the following sections, the experimental methods used to measure T_1 and T_2 are described with a special emphasis on the ^1H spins of water. Other NMR experiments like ^{17}O -nuclear magnetic relaxation and chemical shift enable the acquisition of specific information regarding, for instance, rotational correlation times and water-exchange rate constants of Gd^{III} complexes (see Sections 2.5 and 2.6, respectively).^{5,36}

2.2.1 General Experimental Method to Measure T_1

The most commonly used method to measure longitudinal relaxation times, T_1 , is the inversion-recovery experiment.^{37,38} The method is based on the two pulse sequence $[\pi]-\tau_i-[\pi/2]$ -AQ, where $[\pi]$ and $[\pi/2]$ are 180 and 90° pulses, respectively, and AQ means acquisition of the FID. The sequence is repeated for 10 to 20 different values of the delay τ_i (Figure 2.2). The inversion-recovery method is robust as long as the delays τ encompass the range of $0.01T_1$ to $\sim 3T_1$ and the repetition time between the applications of the pulse sequence is longer than $5T_1$.³⁸ Setting the exact pulse lengths for the 180 and 90° pulses is not crucial but will lead to smaller variations of the recorded FIDs.

The recovery of the z -magnetization after the perturbation is given by eqn (2.28).

$$M_z(\tau) = M_z(\infty) [1 - A \exp(-\tau/T_1)] \quad (2.28)$$

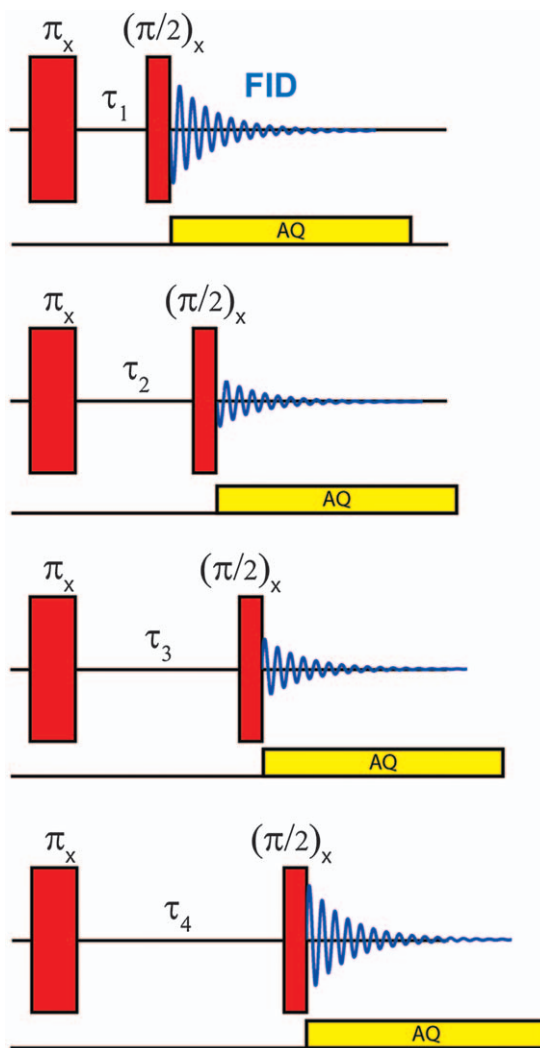


Figure 2.2 Inversion-recovery experiment to measure longitudinal relaxation $1/T_1$.

The z -magnetization $M_z(\tau)$ at a delay τ is proportional to the integral or the height of the resonance line in the NMR spectrum (Figure 2.3). Therefore, the magnetization M_z in eqn (2.28) can be replaced by the height, h , or the integral of the resonance signal. The relaxation rate is obtained by fitting eqn (2.28) to the experimental data using the three parameters: $1/T_1$, $M_z(\infty)$, and A (Figure 2.4). The equilibrium magnetization $M_z(\infty)$ is given by the magnetization measured at $\tau \geq 5T_1$, and A is equal to 2 for a perfect setting of the π pulse lengths.

In the special case of measuring the T_1 of water protons of solutions containing paramagnetic compounds, the following advice with respect to

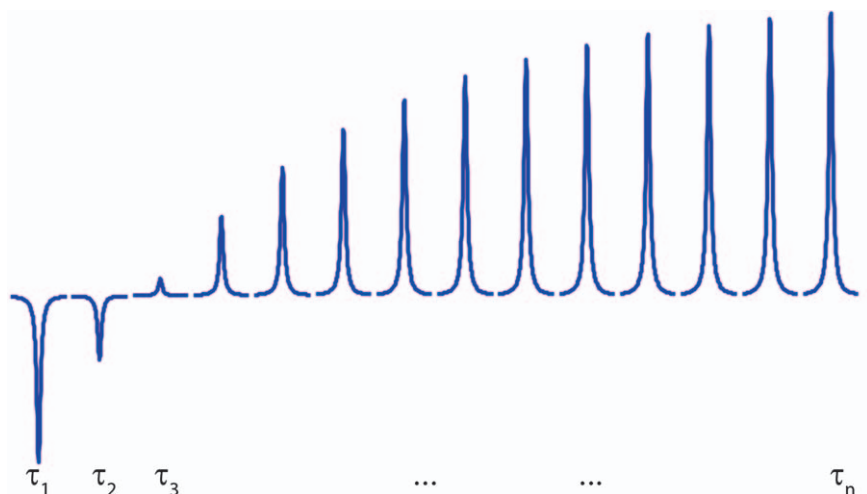


Figure 2.3 NMR signal as a function of the delay τ between the π and the $\pi/2$ pulses.

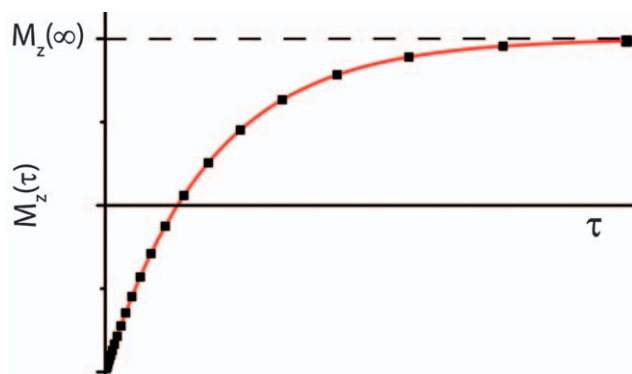


Figure 2.4 Magnetization M_z as function of τ .

radiation damping, FID *versus* spectrum, choice of delays, and ^{17}O -longitudinal relaxation should be considered.

2.2.1.1 Radiation Damping

If a sample consists essentially of water, a strong ^1H -NMR signal is often observed. With modern high-field NMR spectrometers this situation leads to the problem of radiation damping.^{39–41} Several remedies can be considered to avoid erroneous T_1 values due to this phenomenon. The simplest remedy is detuning the NMR probe. By decreasing the quality factor, Q , considerably, radiation damping can be avoided by conserving a high signal-to-noise ratio. The detuning leads to longer π and $\pi/2$ pulses, which are not problematic if

relaxation times are not too short (not shorter than 1 ms). Another method to avoid radiation damping is decreasing the sample volume by filling the sample solution into a capillary tube that is placed into an ordinary 5 mm NMR tube. Short pulses and sufficient signal-to-noise ratios can be obtained with the capillary method. A positive aspect of the capillary method is the relatively small amount of solution needed for the experiments; its limitation is the longer time needed for temperature stabilization compared to not using a capillary tube. The same “capillary effect” can be obtained by using ordinary 5 mm NMR tubes placed inside 10 mm NMR tubes and using the decoupling coil of a multinuclear 10 mm NMR probe. It should be noted that radiation damping plays no role at low magnetic fields, for example, those used in field cycling instruments and low-resolution permanent magnet systems.

2.2.1.2 FID Versus Spectrum

Because the NMR spectrum of a dilute aqueous solution of a paramagnetic compound shows essentially only one strong resonance, inversion recovery can be used either on the FID or on the spectrum obtained by Fourier transform. On low-resolution instruments like fast-field cycling relaxometers or permanent magnet systems, such as the Bruker minispec, the FID method is commonly applied. On high-resolution high-field NMR spectrometers, the experimental routines to measure T_1 normally apply to spectra. Data processing is often simplified by setting the resonance frequency on the water proton resonance.

2.2.1.3 Choice of Delays τ

As mentioned above, the longest τ values should be about $3T_1$. The shortest value is commonly chosen to be 1 to 5% of T_1 . Control of instrument stability can be achieved by increasing τ to the maximum value followed by a decrease to the shortest value. Any change in temperature or sample composition appearing during the T_1 experiment should show up in a scatter of data points.

2.2.1.4 Measuring ^{17}O -Longitudinal Relaxation

Measuring T_1 of the ^{17}O -NMR signal of water is as easy as the measurement of T_1 of ^1H spins. Owing to the lower gyromagnetic ratio of ^{17}O spins and the low natural abundance of the ^{17}O isotope, radiation damping is no concern. The low signal intensity needs accumulation of several hundreds of FID to obtain a decent signal-to-noise ratio. This is, however, not a major problem because T_1 values are short, $T_1 < 7$ ms at room temperature, and the experimental sequence can be repeated more than 25 times per second.

2.2.2 General Experimental Method to Measure T_2

The transverse relaxation rate $1/T_2$ is in principle linked to the width of the Lorentzian NMR resonance line by:

$$\frac{1}{T_2} = \pi\nu_{1/2} \quad (2.29)$$

where $\nu_{1/2}$ is the full width at half height (Figure 2.5). However, inhomogeneity of the static magnetic field, ΔB_0 , induces broadening of the resonance line, and the observed linewidth is:

$$\nu_{1/2}^{\text{obs}} = \frac{1}{\pi T_2^*} = \frac{1}{\pi T_2} + \frac{\gamma \Delta B_0}{2\pi} \quad (2.30)$$

Unless $1/T_2 \gg \gamma \Delta B_0/2$ (γ is the gyromagnetic ratio), obtaining transverse relaxation from linewidth is precluded by magnetic field inhomogeneity. Therefore, transverse relaxation is often measured using a spin-echo method.³³ The intensities of sequences of spin-echoes generated by the pulse sequence $[\pi/2]-\tau-[\pi]-\tau$ -AQ decays as:

$$M_{x,y}(2\tau) = M_{x,y}(\infty) [\exp(-2\tau/T_2 - 2/3\gamma^2 G^2 D \tau^3)] \quad (2.31)$$

where D is the self-diffusion coefficient and G is the gradient of the magnetic field. Assuming a magnetic-field gradient of $G = 47 \mu\text{T m}^{-1}$ (corresponding to a broadening of the ^1H resonance line of 10 Hz in a 5 mm NMR tube) and a self-diffusion coefficient of $D = 2.3 \times 10^{-9} \text{ m}^2 \text{ s}^{-1}$ (water at 25 °C), the contribution due to diffusion can be estimated to be $2/3\gamma^2 G^2 D \approx 0.24 \text{ s}^{-3}$.

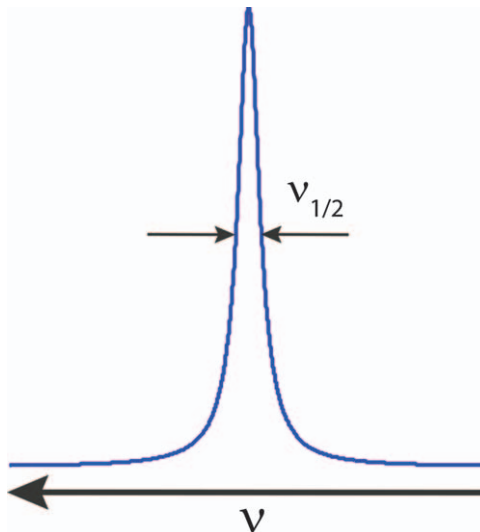


Figure 2.5 Lorentzian resonance line showing full width at half height $\nu_{1/2}$.

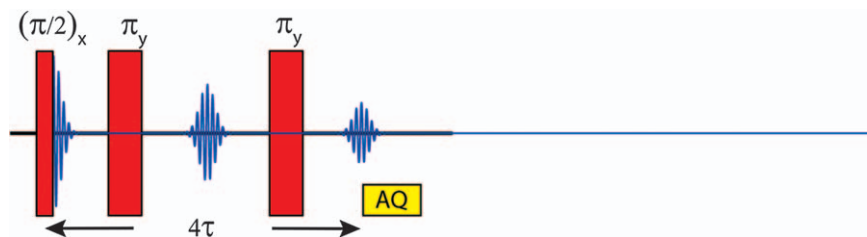


Figure 2.6 CPMG spin-echo pulse sequence to measure transverse relaxation $1/T_2$.

The contribution due to diffusion can be neglected if $\tau \ll 1$ s (assuming $1/T_2 > 1$ s $^{-1}$). The mostly applied spin-echo variant is the Carr–Purcell–Meiboom–Gill (CPMG) sequence. In this sequence, a 90° phase shift between the $\pi/2$ pulse and the π pulse is introduced. Moreover, only even echoes are used, which enables partial compensation of mis-settings of the π pulses (Figure 2.6).

Signal accumulation can be performed in repeating the basic pulse sequence. Attention should be paid to wait at least $\sim 5T_1$ between repetitions of the $\pi/2$ pulses. The need for this wait arises because in many paramagnetic systems, $T_1 \gg T_2$ and the relaxation delay can be relatively long.

Instead of increasing the delay τ , a series of echoes can be created by using a short delay τ and repeating the π pulses $2n$ times (Figure 2.7). Sampling even echoes enables recording of the exponential decay of $M_{x,y}$ in one shot, and the relaxation delay only has to be applied between the pulse trains. Furthermore, τ can be chosen to be relatively short (for example, 1 ms) allowing the diffusion contribution to be neglected in case of inhomogeneous magnetic fields [eqn (2.32)].

$$M_{x,y}(t) = M_{x,y}(\infty) [\exp(-t/T_2 - 1/3\gamma^2 G^2 D \tau^2 t)] \quad (2.32)$$

The echo height or integral measured at time t is proportional to the magnetization in the xy -plane, $M_{x,y}$. If the diffusion contribution can be neglected, $M_{x,y}$ decreases exponentially (Figure 2.8), and $1/T_2$ can be obtained by fitting eqn (2.33) using the two parameters $1/T_2$ and $M_{x,y}(\infty)$.

$$M_{x,y}(t) = M_{x,y}(\infty) \exp(-t/T_2) \quad (2.33)$$

In case of fast transverse relaxation leading to short T_2 values, the multi-echo CPMG variant (Figure 2.7) leads to short τ values ($\tau \ll 1$ ms) that can become of the order of the lengths of the π pulses. In that case, relaxation during the pulse, which can be different from relaxation in the absence of high-frequency irradiation, can no longer be neglected. Using a three-pulse variant and changing τ (Figure 2.6) leads, in that case, to more reliable results. If instruments with low-resolution permanent magnets are used to measure T_2 , the variant creating a long echo train (Figure 2.7) is preferred to allow short τ and, therefore, neglecting of the diffusion contribution [eqn (2.32)].

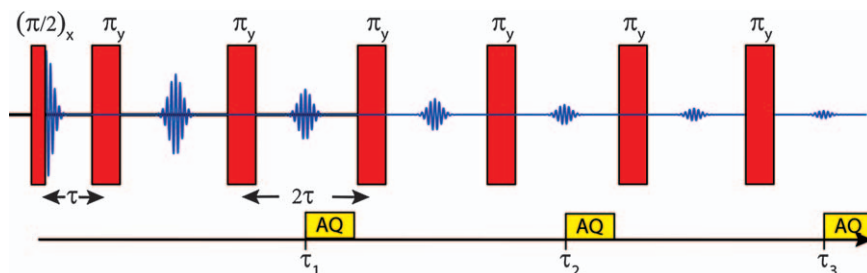


Figure 2.7 CPMG sequence to create a spin echo train.

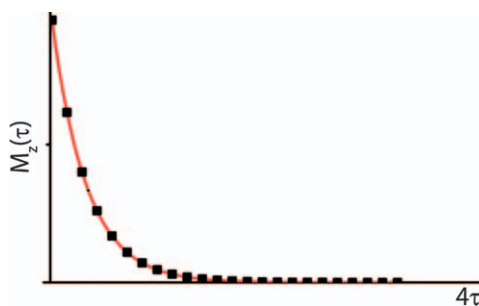


Figure 2.8 Magnetization $M_{x,y}$ as a function of the delay τ .

The decay of the echoes in a CPMG pulse train experiment (Figure 2.7) can depend on τ in case of chemical exchange.^{42–45} In the slow pulsing limit, $\tau \rightarrow 0$ or more precisely $1/\tau \gg k_{\text{ex}}$, the measured decay constant $1/T_2$ is equal to the value obtained by linewidth as defined by Swift and Connick⁹ for exchanging systems.⁴⁵

2.3 NMRD Profiles: Theory, Acquisition, and Interpretation

LOTHAR HELM

2.3.1 Acquisition of NMRD Profiles

To optimize MRI contrast agents, it is essential to link observed relaxation enhancement, expressed as relaxivity, to structural and dynamical parameters like distances and correlation times (described in Chapter 2.1). Even the “simple” SBM theory includes many parameters that enter the equations and influence r_1 . Information regarding some of the parameters can be obtained by independent measurements. An example is q , the number of inner-sphere water molecules (see Chapter 2.4) or t_R , the rotational correlation time (Chapter 2.5). With respect to these multiple variables, one method to obtain information involves the measurement of relaxivity as a function of a physical variable, like temperature or applied static magnetic field, B_0 . The nuclear spin relaxation as a function of the applied static magnetic field, which is proportional to the Larmor frequency ν_1 , is called nuclear magnetic relaxation dispersion (NMRD). Measuring r_1 over the wide range of magnetic fields from 10^{-4} to 10 T enables relaxation mechanisms to be separated. A graph showing the relaxation rate or the relaxivity as a function of Larmor frequency or magnetic field is commonly called an NMRD profile. Due to the variation of the field over five orders of magnitude, a logarithmic plot is normally shown (Figure 2.10). Nuclear spin relaxation rates cannot be measured across a range that spans from near the magnetic field of the Earth up to 10 or 20 T using a single instrument. Therefore, magnetic fields are generally divided into three regions:

- (i) Very low fields from the field of the Earth to about 1 T (or $\nu_1 = \sim 40$ MHz).
- (ii) Mid fields from 0.5 to 2 T ($\nu_1 = \sim 20$ to ~ 80 MHz).
- (iii) High fields above 3 T ($\nu_1 \geq 130$ MHz).

In the very low field region, which covers more than three orders of magnitude of magnetic field, the general techniques to measure relaxation rates as described in Section 2.2 cannot be used. This is primarily owing to the low signal-to-noise ratio of NMR signals at those low fields. At low magnetic fields, fast field cycling relaxometers are generally used. Fast field cycling can be achieved either by shuttling a sample mechanically between different magnetic fields^{46,47} or by changing the magnetic field rapidly.^{48–50} In both systems, signal detection is accomplished at the same, relatively high magnetic field. This detection enables an automatic measurement of relaxation over a wide range of magnetic fields without the need to retune the probes. In general, in this case, variations of the inversion-recovery technique are used to measure longitudinal relaxation rates.^{50,51}

In the mid-field region, either instruments equipped with fixed-field permanent magnets or with variable-field electromagnets can be used. Relaxation rates at different magnetic fields are acquired point-by-point generally using the standard inversion-recovery method (see Section 2.2.1). Instruments for low- and mid-field relaxation measurements tend to be of low resolution and do not distinguish between ^1H spin resonances with different chemical shifts. Because in an aqueous solution of Gd^{III} complexes the detected NMR signal is >99% owing to the water protons, the lack of spectral resolution is not a problem, and the measured relaxation is that of water protons.

At magnetic fields at or above 3 T, normal high-resolution NMR instruments or MRI scanners equipped with cryomagnets need to be used. For each magnetic field, a dedicated instrument must be used. Inversion-recovery sequences are applied to measure $1/T_1$. High-resolution NMR instruments enable measurement of the relaxation of water protons and, in principle, of other signals present in the NMR spectrum. As mentioned in Section 2.2, radiation damping can influence the results on high-field NMR instruments and, therefore, should be avoided.

In all cases, sample temperature must be carefully controlled because it influences dynamic processes related to relaxation. Relying only on the temperature setting of the instrument can be unreliable; the actual sample temperature should therefore be measured using an independent device.⁵²

2.3.2 Theory and Interpretation of NMRD Profiles

The theoretical description of NMRD profiles of aqueous solutions of Gd^{III} complexes is generally based on SBM theory for inner-sphere contributions and Freed–Ayant theory for outer-sphere contributions (see Section 2.1). As mentioned above, the Freed–Ayant and especially the SBM theories are based on stringent assumptions. NMRD profiles of solutions of small Gd^{III} complexes (for example, $[\text{Gd}(\text{DOTA})(\text{H}_2\text{O})]^-$ or $[\text{Gd}(\text{DTPA})(\text{H}_2\text{O})]^{2-}$) can be well-described by the SBM theory.⁵³ Nonlinear, least-squares fitting of experimental data enables parameters to be obtained like rotational correlation time τ_R , zero-field splitting parameters Δ^2 and τ_v , and water-exchange rate constants k_{ex} .

The SBM theory is not able to fit NMRD profiles measured on macromolecular compounds like dendrimers or protein-bound Gd^{III} -based complexes. For these systems, deviations between experimental and calculated relaxivities appear, notably in the Larmor frequency range around 1 MHz. Furthermore, for macromolecular complexes, fitted parameters and especially those related to electron spin relaxation are not reliable. Fitting full NMRD profiles of macromolecular systems requires more elaborate theoretical models like those developed by the groups of Kowalewski^{10,12} and Fries and Belorizki.^{24,54,55} However, these models do not result in analytical equations, making the fitting of experimental data tedious.

Independently of the model used to fit the experimental NMRD profiles, qualitative information can be obtained by visually inspecting relaxivity data.

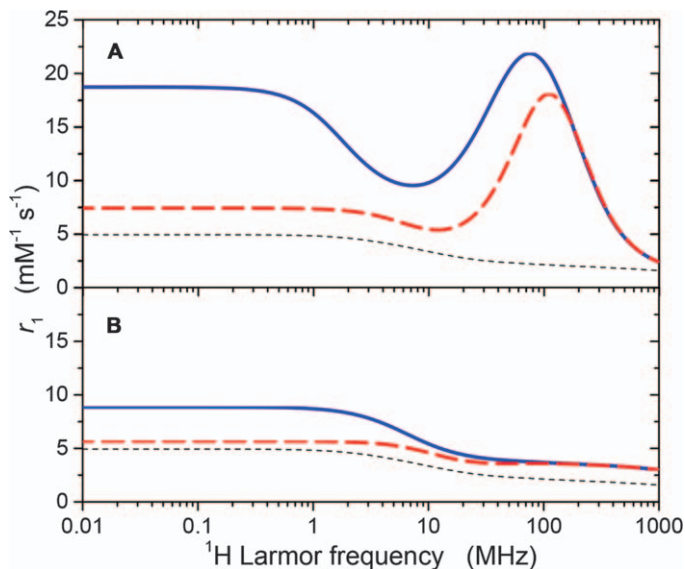


Figure 2.9 NMRD profiles as a function of electron spin relaxation [eqn (2.22) and (2.23)], $\tau_v = 10 \text{ ps}$, blue: $\Delta^2 = 0.5 \times 10^{20} \text{ s}^{-2}$, red: $\Delta^2 = 2.0 \times 10^{20} \text{ s}^{-2}$ and rotational correlation time (A) $\tau_R = 1 \text{ ns}$ (B) $\tau_R = 50 \text{ ps}$. The dotted lines show outer-sphere relaxation r_1^{OS} .

Reprinted from Elsevier Books, S. Aime, M. Botta, E. Terreno, *Advances in Inorganic Chemistry*, 173–237, Copyright 2005, with permission from Elsevier.

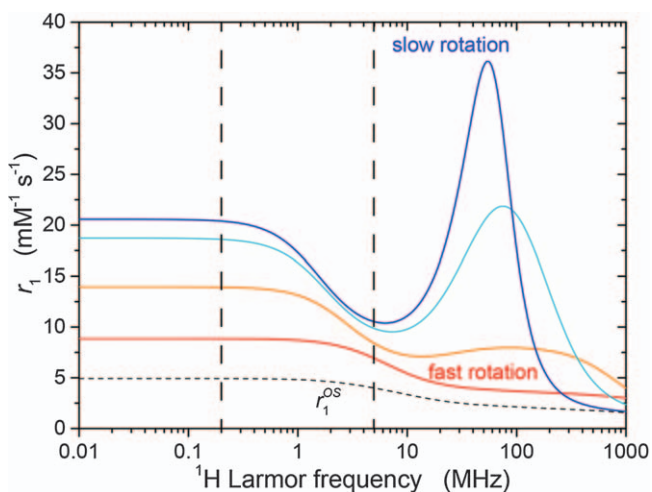


Figure 2.10 NMRD profiles as a function of rotational motion: fast rotation, short τ_R ; slow rotation, long τ_R . The outer-sphere r_1^{OS} contribution is shown as a dashed line.

All NMRD profiles of Gd^{III} complexes in aqueous solution show a relaxation plateau at Larmor frequencies below 0.1 MHz (see Figure 2.9). The relaxivity values measured in this range depend on the electron spin relaxation of Gd^{III} and on the rotational correlation time. In that region, faster electron spin relaxation and faster molecular rotation lead to lower r_1 values.

In the frequency range between 0.2 and 6 MHz, r_1 decreases with increasing ν . This decrease originates from the dispersion around ω_{S} , $\tau_{\text{c2}}/(1 + \omega_{\text{S}}^2\tau_{\text{c2}}^2)$ [eqn (2.11)]. The correlation time τ_{c2} is dominated either by fast rotation (small τ_{R}) or fast electron-spin relaxation (small $T_{2\text{e}}$) [eqn (2.19)]. Residence times, τ_{m} , are normally too long to influence τ_{c2} . For slowly rotating compounds, $\tau_{\text{R}} \gg T_{2\text{e}}$, and in that case, r_1 is governed by transverse electron spin relaxation. At low magnetic fields, the SBM theory is mostly prone to errors especially in the part describing electron spin relaxation. This source of error is the main reason for the failure of the theory to describe NMRD profiles correctly at frequencies below several MHz.

At frequencies above 6 to 8 MHz, r_1 is dominated by the dispersion around ω_{I} , $\tau_{\text{c1}}/(1 + \omega_{\text{I}}^2\tau_{\text{c1}}^2)$ [eqn (2.11)]. In this region, except for fast-rotating small complexes, a maximum of relaxivity is observed (Figure 2.10). The increase of r_1 at frequencies below ν^{max} is due to the decrease with frequency of the longitudinal electron spin relaxation $1/T_{1\text{e}}$ [eqn (2.19) and (2.22)]. At higher frequencies, the frequency-independent rotational correlation time τ_{R} starts to govern τ_{c1} . This dominance of τ_{R} leads to the decrease of r_1 at frequencies $\nu \gg 1/(2\pi\tau_{\text{c1}})$. Therefore, slowly rotating complexes generally show lower relaxivities at high magnetic fields ($\nu > 300$ MHz, Figure 2.10) than faster rotating compounds.

At frequencies above 8 to 10 MHz, relaxivities depend mainly on longitudinal electron spin relaxation and rotational motion (Figure 2.9).¹³ At these magnetic fields, the Bloembergen–Morgan equation for $1/T_{1\text{e}}$ [eqn (2.22)] describes its field dependence more or less correctly.^{56,57} The SBM theory can therefore be used to fit the high-frequency part of NMRD profiles and to obtain information on the rotational motion of complexes.^{6,58} Depending on the molecular structure of the complexes, internal motion, anisotropic motion, or both need to be considered.^{59–61}

2.4 Measuring Water Coordination Numbers (q)

JANET R. MORROW* AND CHRISTOPHER J. BOND

2.4.1 Hydration: Inner- Versus Outer-Sphere Water Ligands

The protons of water molecules directly coordinated to a Gd^{III} ion relax more effectively than those of water molecules that are not coordinated (see Section 2.1). Thus, the identification of inner-sphere water molecules in Gd^{III} complexes is important in the design of T_1 -shortening contrast agents for MRI. This sub-chapter describes methods to determine the number of bound water molecules in Gd^{III} and related Ln^{III} complexes. A related discussion in Chapter 3.3 describes analogous methods for chemical exchange saturation transfer agents. As these techniques are discussed, it is important to keep in mind that aqueous chemistry of metal ion complexes can be complicated. The interpretation of the number of bound waters, q , can be affected by the presence of ligand conformers and hydration isomers. Second-sphere interactions with metal cations are not well-defined and can influence, sometimes significantly, these measurements. Many of the techniques discussed below involve replacing the Gd^{III} ion by another lanthanide, such as Dy^{III} , Eu^{III} , or Tb^{III} . Most of the time, swapping lanthanide ions is synthetically facile; analogues of different lanthanide ions can provide information regarding the Gd^{III} complex of interest. However, it should be noted that in some cases, the number of inner-sphere water molecules, q , can change across the lanthanide series due to the lanthanide contraction. If possible, experiments to determine the number of inner-sphere water molecules should be supplemented by additional methods to identify speciation and structural complications.

2.4.2 Oxygen-17 NMR Spectroscopy

For Gd^{III} complexes, q can be obtained from variable-temperature ^{17}O -NMR studies as described in Section 2.6.1. These studies enable determination of both q and the rate constant for the exchange of bound and bulk water, k_{ex} .^{62–65} The best practice is to combine the values of q obtained from variable-temperature ^{17}O -NMR experiments with data from fitting of NMRD profiles to generate q for Gd^{III} complexes (Section 2.3.2).

Alternatively, Ln^{III} ions that are not strong relaxation agents can be used in lieu of Gd^{III} . Because of the similarity of the coordination chemistry of the trivalent lanthanide ions, in most cases, one can readily replace one lanthanide ion by another with minimal changes to the structure of the lanthanide complex. It should be noted, however, that in some cases, the lanthanide contraction can cause a decrease in the value of q across the lanthanide series.

^{17}O -NMR studies in ^{17}O -enriched water, and in particular, the ^{17}O chemical shift of water in the presence of a paramagnetic complex, is one of

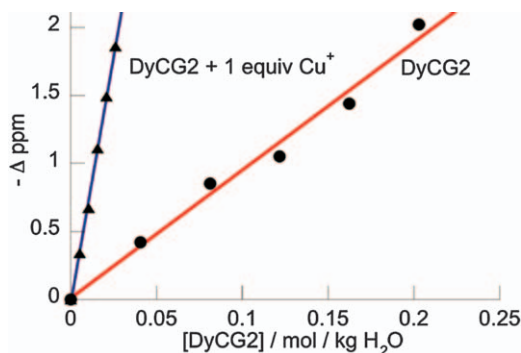


Figure 2.11 Plot of the dysprosium-induced shift (DIS) of the ^{17}O -signal of H_2O (in ppm) versus DyCG2 in the absence (red) and presence (blue) of one equivalent of Cu^{I} . Spectra were acquired at room temperature in a buffered solution (4-(2-hydroxyethyl)-1-piperazineethanesulfonic acid, 20 mM, pH 7) at an ^{17}O -Lamor frequency of 67.8 MHz.⁶⁹ Adapted with permission from E. L. Que, E. Gianolio, S. L. Baker, A. P. Wong, S. Aime and C. J. Chang, *J. Am. Chem. Soc.*, 2009, 131, 8527. Copyright (2009) American Chemical Society.

the most widely used methods to estimate the number of bound molecules of water in paramagnetic Ln^{III} complexes other than Gd^{III} .^{66–68} The paramagnetic metal ion modulates the chemical shift and also the linewidth of the ^{17}O resonance of inner-sphere water.^{62–64} For most Ln^{III} complexes, water exchange is sufficiently rapid on the NMR timescale to produce a single ^{17}O resonance, although complexes often need to be heated to temperatures as high as 80 °C to ensure that exchange is rapid. In the case of fast water exchange, the ^{17}O resonance appears at a frequency that is a weighted average of bound and bulk water.

For ^{17}O NMR shift experiments, typically the Dy^{III} ion is used as a surrogate for Gd^{III} .^{66–68} Dy^{III} , which has the largest Bleaney coefficient ($C_J = -100$, Table 3.4) gives large paramagnetically shifted ^{17}O resonances without producing unduly large line widths, two substantial advantages for the accurate determination of chemical shift. It should be noted that because Gd^{III} has a Bleaney coefficient of 0 (Table 3.4), it broadens but does not shift resonances. Hence, lanthanide-induced shifts cannot be used to determine the q of Gd^{III} complexes. An advantage of monitoring ^{17}O -NMR spectra rather than ^1H -NMR spectra is that the ^{17}O resonances of outer-sphere water do not appreciably experience a paramagnetic shift. Studies have shown that the ^{17}O chemical shift correlates to the number of inner-sphere waters bound to Dy^{III} , although a good correlation is limited to certain types of complexes, mostly polyaminocarboxylate-based. As shown in Figure 2.11, when the dysprosium-induced shift (DIS) is plotted as a function of the concentration of complex, the slope of the line is proportional to the number of bound molecules of water, q , multiplied by the ^{17}O shift for each bound water [eqn (2.34)].^{66,69} Typically, this type of determination is calibrated using a

Dy^{III} standard such as the aquo ion, [Dy(H₂O)₉]³⁺, for which $q=9$ or [Dy(DTPA)]²⁻ for which $q=1$. An example of data obtained for a q -based responsive Gd^{III} contrast agent for copper is shown in Figure 2.11.

$$\text{DIS} = \frac{q\Delta[\text{Dy}(\text{agent})_n(\text{H}_2\text{O})_q]}{[\text{H}_2\text{O}]} \quad (2.34)$$

The contributions to the observed ¹⁷O chemical shift (δ_{obs}) are given by eqn (2.35).⁶⁷ The bulk magnetic susceptibility term (δ_{γ}) does not require a chemical interaction; in spherical compartments, this contribution is nil. The term δ_{M} is the shift of the bound water due to the paramagnetic or hyperfine contribution. P_{m} is the molar ratio (Ln^{III}/H₂O), a term that accounts for averaging of the ¹⁷O resonance of bulk water with that from bound water, and q is the number of inner-sphere water molecules.

$$\delta_{\text{obs}} = \delta_{\gamma} + q(P_{\text{m}}\delta_{\text{M}}) \quad (2.35)$$

$$\Delta = \frac{\delta_{\text{obs}} - \delta_{\gamma}}{P_{\text{m}}} = q\delta_{\text{dia}} + q\delta_{\text{c}} + q\delta_{\text{pc}} \quad (2.36)$$

As shown in eqn (2.36), the lanthanide-induced shift of a coordinated water (Δ) arises from three types of contributions, which include: (1) the diamagnetic contribution (δ_{dia}), (2) the through-space or pseudocontact shift (δ_{pc}), and (3) the through-bond or contact shift (δ_{c}).⁷⁰ The diamagnetic term, which arises from binding of the metal ion, can be approximated by use of a diamagnetic lanthanide ion, such as La^{III}, Lu^{III}, or Y^{III}. This term is typically small in magnitude in comparison to paramagnetic contributions and can generally be neglected. The pseudocontact shift arises from a through-space interaction of the magnetic moments of the unpaired electrons and the ¹⁷O-nucleus. This contribution depends on the distance separating the ¹⁷O nucleus of water from the lanthanide ion and the relative orientation of the nucleus with respect to the principal magnetic susceptibility tensor. The contact shift arises from delocalization of unpaired electron spin density on the ¹⁷O nucleus of water from bonding interactions.⁷¹⁻⁷³

The breakdown of Δ into different paramagnetic contributions raises questions. What is the relative importance of the contact and pseudo-contact contributions to the ¹⁷O NMR chemical shift? Does each contribution vary according to the type of coordination site of bound water? These factors can complicate the correlation of a shift difference with q . For many Dy^{III} complexes, however, the ¹⁷O contact contributions to the paramagnetic shift are dominant (>85%), given that the oxygen of water is directly bound to Dy^{III}. The predominance of contact contributions to the ¹⁷O-paramagnetic shift appears to hold as long as q is two or greater. Notably, most contrast agents

have values of q in the range of 1 to 2. In addition, if water is bound along the principal axis of magnetic susceptibility, the pseudo-contact shift contribution to the ^{17}O -resonance can be substantial. In this case, q might not match that determined by other methods, such as luminescence, thus limiting the accuracy of the technique. In the best case, q can be determined with an error of ± 0.2 waters.⁶⁷ However, not all Dy^{III} complexes give such good agreement between ^{17}O -NMR and luminescence methods.⁶⁶

2.4.2.1 Practical Concerns

The determination of the number of inner-sphere water molecules by Dy^{III} -induced ^{17}O -NMR shifts requires relatively high concentrations of complex (5–100 mM) and is thus more appropriate for complexes that are highly soluble. However, experiments can be run in a 50 μL capillary tube to minimize sample volume. In some cases, it is necessary to heat solutions to 70–80 $^{\circ}\text{C}$ to ensure rapid water exchange. Notably, some Ln^{III} complexes exchange water so slowly that distinct ^{17}O -NMR resonances for bound and bulk water are observed. Such slow water exchange, on the order of 10^3 s^{-1} , is atypical for a good Gd^{III} -based contrast agent, but useful for a chemical exchange saturation transfer agent. This topic is covered further in Chapter 3.3.

2.4.3 Luminescence Spectroscopy

Studies involving lanthanide luminescence are some of the most powerful for characterization of the solution chemistry of lanthanide-containing complexes. Insight can be gained into the number of bound molecules of water, symmetry of the complex, number of isomeric forms in solution, ligand ionization, and extent of dimerization.^{74–78} This topic has been reviewed,^{79–82} and only a brief introduction will be given to cover methods pertinent to measurement of q and characterization of solution chemistry.

Of the members of the lanthanide series, Tb^{III} and Eu^{III} ions are the most highly luminescent. These two lanthanide ions emit in the visible region and have long luminescence lifetimes that range from microseconds to milliseconds, depending on the coordination sphere. The long lifetimes and emission in the visible region of the spectrum make it feasible to monitor steady-state and time-resolved luminescence on moderately priced fluorospectrometers. As described below, time-resolved studies are useful for measurement of q . Unfortunately, Gd^{III} does not share the favorable luminescence properties of Eu^{III} and Tb^{III} . Gd^{III} luminesces in the UV region with luminescence lifetimes that are not sufficiently affected by bound water to enable determination of values of q .⁸³ However, the similarity of the coordination chemistry of the trivalent lanthanide ions and the close proximity of Gd to Tb and Eu in the periodic table suggest that Eu^{III} or Tb^{III} complexes are reasonable surrogates for Gd^{III} -containing complexes. It should be noted, however, that due to the lanthanide contractions, there could be

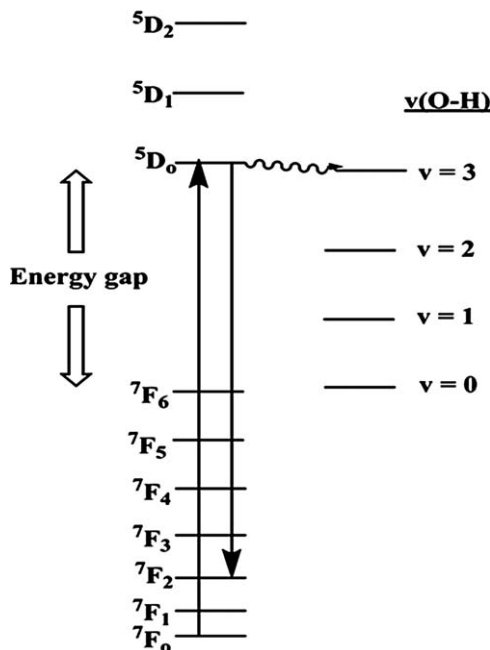


Figure 2.12 Energy level diagram for Eu^{III} (left) showing how OH oscillators lead to radiationless decay of luminescence.

some discrepancies in the number of inner-sphere water molecules determined by luminescence lifetime for a Eu^{III} or Tb^{III} complex and the number determined by NMR spectroscopy for the analogous Gd^{III} or Dy^{III} complex.

A brief background in the photophysics of Ln^{III} ions is given here. The 4f valence orbitals of Ln^{III} ions are shielded from the environment and their energies are not substantially affected by ligand fields.⁸¹ Because there is little covalency in bonding to ligands, bonds between the lanthanide ion and its ligands are considered to be primarily electrostatic in character. Thus, even upon complexation with ligands, the atomic properties of the lanthanide are retained. The isolation of the f-orbitals results in nearly line-like absorption and emission spectral peaks that are attributed to f-f transitions. Magnetic dipole f-f transitions are Laporte (parity) allowed but spin forbidden; electric dipole f-f transitions are Laporte and spin forbidden.^{84,85} Furthermore, electric dipole transitions are much weaker in lanthanides ($\epsilon \approx 0.1 \text{ M}^{-1} \text{ cm}^{-1}$) than in transition metals, meaning magnetic dipole transitions can often be observed.^{86,87} The resulting low molar absorptivity ($\epsilon < 1 \text{ M}^{-1} \text{ cm}^{-1}$) and low photoluminescence quantum yields ($\theta \approx 1.9 \times 10^{-2}$) are typical in experiments that use direct excitation of Ln^{III} ions.

The energy levels of Eu^{III} are shown in Figure 2.12.^{76,80,83} In Eu^{III}, the six f electrons give rise to a 7F_0 ground state. The other levels in the ground state manifold are aligned according to increasing values for the J number from 7F_0 at lowest energy to 7F_6 at the highest energy. The lowest-energy emissive

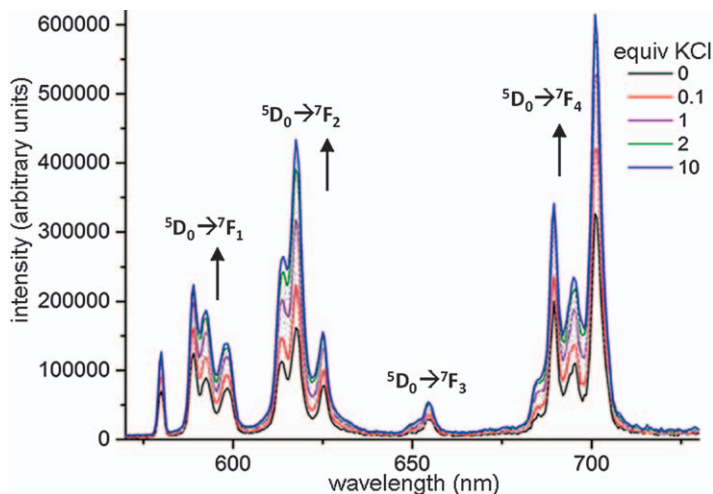


Figure 2.13 Emission spectra of Eu(L1) in methanol with excitation at 290 nm. Arrows show an increase in intensity upon addition of KCl.⁸⁸ Adapted with permission from A. K. R. Junker, M. Tropiano, S. Faulkner and T. J. Sørensen, *Inorg. Chem.*, 2016, 55, 12299. Copyright (2016) American Chemical Society.

state is 5D_0 , from which most luminescence is observed. Emission from this state to the different levels of the 7F manifold produces multiple emission bands, most notably $^5D_0 \rightarrow ^7F_1$, $^5D_0 \rightarrow ^7F_2$, $^5D_0 \rightarrow ^7F_3$, and $^5D_0 \rightarrow ^7F_4$, as shown in Figures 2.12 and 2.13.⁸⁸ For the majority of Eu^{III} complexes, the $^5D_0 \rightarrow ^7F_2$ emission band is the most intense and is thus most easily monitored. Each of these bands can be split by crystal-field interactions to produce the observed fine structure as shown in Figure 2.13. Notably, the $^5D_0 \rightarrow ^7F_0$ transition is between two energy levels that are not degenerate and thus not split by crystal fields. This means that each distinct Eu^{III} species in solution should give rise to a distinct emission (or excitation) peak.^{76,89–91} These transitions are useful for studying solution-phase chemistry, as described below.

Lanthanide luminescence is partially quenched by vibronic coupling to OH and NH oscillators, as shown in Figure 2.12. Both the number of oscillators close to the first coordination sphere and the R parameter influence this vibronic quenching. The number of vibrational quanta between ΔE is represented by the R parameter. When the value of R is higher, the rate of vibronic coupling will be lower and the emission quenching will be less accentuated.

$$R = \frac{\Delta E}{\hbar\omega} = \frac{\Delta E}{\hbar\omega} \sqrt{\frac{\mu}{k}} \quad (2.37)$$

In eqn (2.37), ΔE is the energy gap between the emitting state and the higher energy J state of the ground multiplet (Eu^{III} : $^5D_0 \rightarrow ^7F_6 = 12000 \text{ cm}^{-1}$

and Tb^{III} : ${}^5\text{D}_4 \rightarrow {}^7\text{F}_0 = 15\,000\text{ cm}^{-1}$), $\hbar\omega$ is the oscillator vibrational quantum, the oscillator μ is the reduced mass, and κ is the oscillator force constant.^{83,92}

A general rule is that quenching is most efficient for lanthanide ions with an energy gap that is a low integral value of the vibronic energy of the OH oscillators.⁸³ Eu^{III} and Tb^{III} have relatively large energy gaps and are moderately quenched by bound water, whereas the near-IR-emitting Ln^{III} ions that have lower energy gaps are more effectively quenched by water and are thus less luminescent. This quenching by OH oscillators can be turned into a useful method to estimate the number of bound water molecules, q . Early work by Horrocks and co-workers showed that the luminescence lifetime of Eu^{III} could be correlated to the number of bound waters in the solid-state structures of the complexes.^{93–95}

In eqn (2.38), q_{M} is related to the difference in the luminescence lifetime in H_2O compared to D_2O . In this case, the D_2O measurements are made to estimate the effect of the OH quenching. The OD oscillator energy is much larger and does not couple as readily to the luminescence emission, giving an estimate of the natural lifetime of the particular Eu^{III} -containing complex. The excited-state life time in water and heavy water are represented by $\tau_{\text{H}_2\text{O}}$ and $\tau_{\text{D}_2\text{O}}$. Parker revised these equations to include exchangeable NH oscillators of amides in the term k_{XH} , which represents the rate constant for the depopulated lanthanide excited state in water.^{77,96} The effect of additional oscillators—including XH from amines (γn_{NH}) or alcohols (βn_{OH}) and NH from the number of amide oscillators in which the amide carboxylic oxygen ($n_{\text{O}=\text{CNH}}$) is in the first coordination sphere of lanthanides, and the contributions from outer-sphere water molecules (α)—is depicted by eqn (2.39).⁷⁷

$$q_{\text{M}} = A[(1/\tau_{\text{H}_2\text{O}} - 1/\tau_{\text{D}_2\text{O}}) - k_{\text{XH}}] \quad (2.38)$$

$$k_{\text{XH}} = \alpha + \beta n_{\text{OH}} + \gamma n_{\text{NH}} + \delta n_{\text{O}=\text{CNH}} \quad (2.39)$$

In eqn (2.38), A represents the sensitivity of the lanthanide to the vibronic quenching, which varies from one metal to another. For Eu^{III} , the original value of A of 1.05 water molecules \cdot ms was re-evaluated to 1.2 water molecules \cdot ms with $\alpha = 0.25\text{ ms}^{-1}$ by Beeby.⁷⁷ The contribution to the deactivation of the ${}^5\text{D}_0$ excited state by each oscillator gives $\beta = 0.44\text{ ms}^{-1}$ and $\gamma = 0.99\text{ ms}^{-1}$. The accepted equation for the determination of q from the luminescence lifetimes of Eu^{III} complexes is as follows:

$$q_{\text{Eu}} = 1.2[(1/\tau_{\text{H}_2\text{O}} - 1/\tau_{\text{D}_2\text{O}}) - 0.25 - 0.075x] \quad (2.40)$$

For Tb^{III} complexes, A is 5 water molecules \cdot ms and $\alpha = 0.06\text{ ms}^{-1}$, leading to eqn (2.41) for the determination of q from the luminescence lifetimes of Tb^{III} complexes.

$$q_{\text{Tb}} = [(1/\tau_{\text{H}_2\text{O}} - 1/\tau_{\text{D}_2\text{O}}) - 0.06] \quad (2.41)$$

Uncertainties in these measurements derive from the ill-defined second-sphere contribution, which is generally established from Eu^{III} -containing

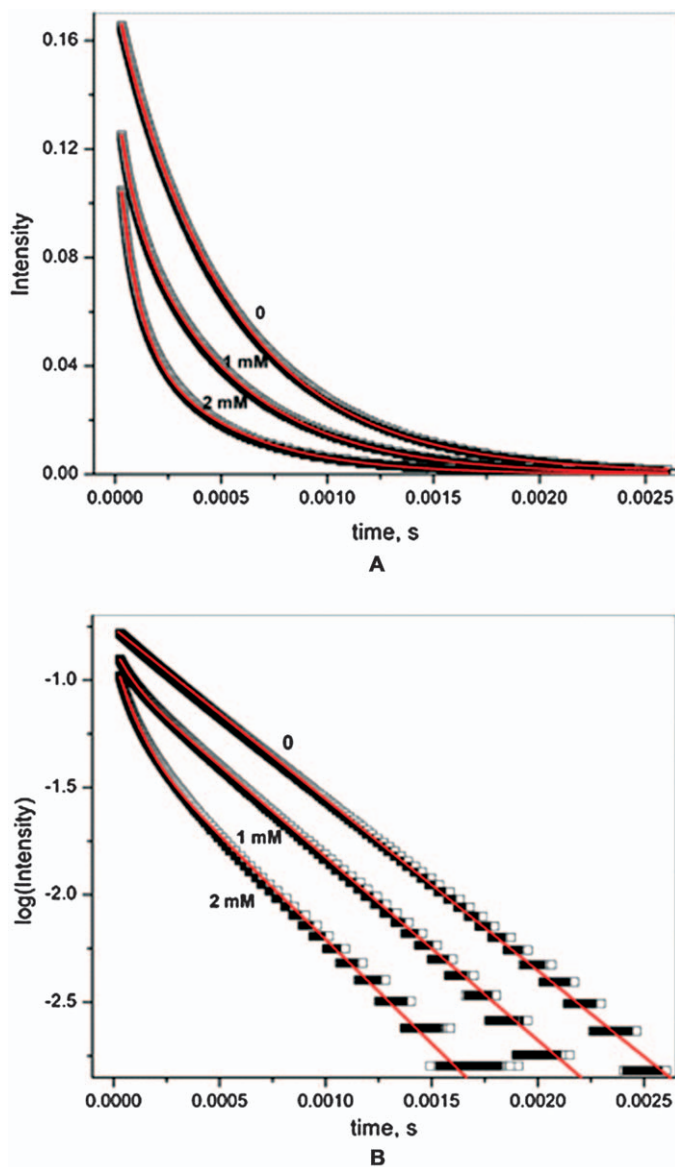


Figure 2.14 Time-resolved intensity decays at 579.22 nm for 1.0 mM $\text{Eu}(\text{CF}_3\text{SO}_3)_3$ in the presence of 0, 1.0, and 2.0 mM $(\text{CH}_4)_4\text{NOH}$ in 80% dimethylsulfoxide. Red lines show fitting to a single-exponent curve for decay in the absence of added base and to a two-exponent curve for decays in the presence of added base. A = linear scale, B = semilogarithmic scale.

Adapted from ref. 101 with permission from The Royal Society of Chemistry.

complexes with $q = 0$. Second-sphere contributions should be considered only if H/D exchange occurs within the experimental time scale. The contribution for Tb^{III}, 0.09 ms⁻¹, is less than that for Eu^{III}, 1.2 ms⁻¹. In each case, all oscillators are considered to be at the same distance from the metal ion.

Importantly, any process that gives rise to quenching of the excited state, whether it be OH oscillators or not, will affect the luminescence lifetime and the calculation of q . These processes include back-energy or electron-transfer processes. The distance between luminescence-quenching OH oscillators and Ln^{III} ions also affects the efficiency of quenching, but there is no established correction for different geometries or coordination numbers. Nonintegral values of q arise from these variations and also from the presence of isomers that have different numbers of bound waters.

The presence of multiple isomers from different hydration states or bound-water environments is a complicating feature in Ln^{III} solution chemistry that can be investigated using luminescence methods.⁹⁷⁻⁹⁹ Theoretically, each luminescent Ln^{III} complex gives rise to a distinct lifetime as long as the species are not interconverting rapidly on the luminescence timescale.¹⁰⁰ However, unless the lifetimes are different and each species is present in comparable amounts, it is difficult to resolve the luminescence-decay of each species by fitting to multi-exponential decays.⁹⁸ An example of the lifetime data for two different Eu^{III} complexes fit to a bi-exponential function is shown in Figure 2.14.¹⁰¹ Similar luminescence lifetimes, however, might result in an average lifetime value. This problem can be addressed in part by identification of multiple Eu^{III} species by monitoring the ⁷F₀ → ⁵D₀ transition using visible-absorbance or excitation spectroscopy. These experiments are described below.

Lanthanide luminescence can be produced by direct excitation of lanthanide f-f transitions or by using an antenna to sensitize luminescence *via* an organic chromophore.^{81,91} Ligand-sensitized luminescence of Ln^{III} ions is common; however, given that contrast agents do not typically contain organic dyes attached as antennae, ligand sensitization is generally not an option. Direct excitation of Ln^{III} ions has the advantage of being amenable to any Ln^{III} complex, regardless of whether or not there is an organic dye. However, owing to the low absorptivity and quantum yields of Ln^{III}-ion-based luminescence, direct excitation of f-f transitions is often carried out with a tunable laser.⁹⁸ This is especially true for low-intensity excitation bands such as the ⁷F₀ → ⁵D₀ transitions described below. An alternative to using a laser is excitation of the more intense Eu^{III}-based transitions in the UV region at 394 or 250 nm, excitations that are feasible on some fluorometers.^{88,102,103}

Direct excitation spectroscopy of Eu^{III} complexes is useful for determining speciation, pH-induced changes, and dimerization. When used in combination with lifetime data, direct excitation can be used for distinguishing between inner-sphere and outer-sphere ligands. In particular, the ⁷F₀ → ⁵D₀ excitation band of Eu^{III} features a transition between two levels that are both

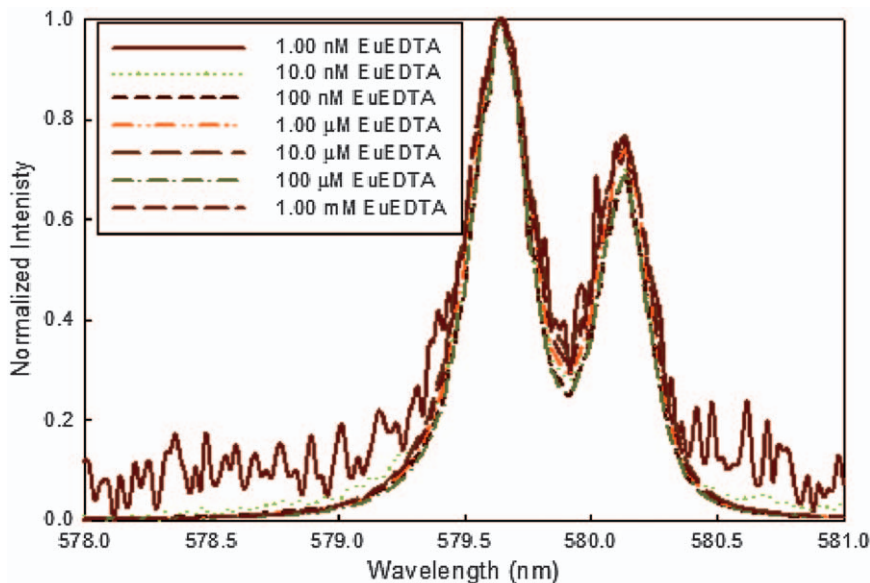


Figure 2.15 The ${}^7F_0 \rightarrow {}^5D_0$ excitation spectrum of Eu(EDTA) at different concentrations showing two different excitation peaks attributed to hydration isomers.⁹⁸

Adapted with permission from C. M. Andolina, W. G. Holthoff, P. M. Page, R. A. Mathews, J. R. Morrow and F. V. Bright, *Appl. Spectrosc.*, 2009, 63, 483. Copyright © 2009 Society for Applied Spectroscopy.

nondegenerate and, thus, not split by ligand fields. Each species in solution can thus be anticipated to produce a distinct excitation peak. For example, the excitation spectrum of $[\text{Eu}(\text{EDTA})]^-$ is shown in Figure 2.15.⁹⁸ The two distinct peaks in this spectrum most likely correspond to two different isomers that differ by hydration number. Excitation of either peak, however, gives rise to the same luminescence lifetime as expected if the conversion between the two isomers was rapid on the luminescence timescale. Other examples of the usefulness of excitation spectroscopy include monitoring changes in the coordination sphere upon binding of small anionic ligands such as carbonate, phosphate, alkoxides, or hydroxide to explain their effect on a contrast agent. For example, the value of q decreases from 1.2 to 0.1 for an Eu^{III} complex that binds to citrate, consistent with replacement of the bound water.^{104,105}

Instead of using a tunable laser system, the ${}^7F_0 \rightarrow {}^5D_0$ transition can be monitored using UV–visible spectroscopy. For example, the absorbance due to the ${}^7F_0 \rightarrow {}^5D_0$ transition has been used to monitor hydration states of Eu^{III} complexes as a function of temperature or pressure.^{65,106,107} Notably, the wavelengths of these absorbance peaks are close (<0.5 nm difference), so that most UV–visible spectrometers do not have adequately fine resolution for these experiments. An alternative method, if the Eu^{III} complex has a

sensitizing ligand, is to monitor the ${}^5D_0 \rightarrow {}^7F_0$ emission peak.^{84,88} For this method, a high-resolution monochromator must be used to resolve closely spaced emission peaks.

2.4.3.1 Practical Concerns

Relatively inexpensive fluorimeters can be used to study emission spectra of either Eu^{III} or Tb^{III} by excitation into one of the transitions in the UV, which have relatively large extinction coefficients.⁸⁸ Time-resolved data can also be collected on these instruments.^{102,103} Direct excitation spectroscopy requires a laser system that either has a dye or a master oscillator power oscillator for tuning the wavelength with high ($>0.2 \text{ cm}^{-1}$) resolution.⁹⁸ UV-visible spectrometers also require better than average resolution for monitoring sharp f-f transitions.^{65,107} A long path length cuvette (5–10 cm) is also useful for monitoring low-intensity absorbance bands of Ln^{III} complexes.

2.4.4 Electron Nuclear Double Resonance

Electron nuclear double resonance (ENDOR) spectroscopy is one of the few techniques that can be used to measure q directly on a Gd^{III} complex. The advantage is thus that other Ln^{III} analogs need not be prepared and studied as surrogates for the Gd^{III} complex of interest. Further advantages of ENDOR spectroscopy include the small sample size (mL) and the ability to examine the effect of proteins on q . In certain cases, estimates of the distance between Gd^{III} and the proton or oxygen of water can also be obtained.¹⁰⁸

ENDOR spectroscopy uses pulsed electron paramagnetic resonance (EPR) spectroscopy methods to monitor the electronic spin transitions of Gd^{III} while the radiofrequency pulse is swept through the nuclear spin transition frequencies (Figure 2.16, left panel).^{108,109,111,112} Different types of pulsed EPR experiments can be used, but Mims, which uses an electron spin echo pulse sequence, is the most common. Experiments are carried out at 7–9 K, a low temperature that can affect q , and typically in methanol–water mixtures that form a glass. This medium is potentially a concern because the interactions between methanol and the Gd^{III} ion can also affect q . Studies have shown, however, that water interacts more strongly with Gd^{III} than methanol: the likelihood of water coordination in aqueous solutions containing up to 30% molar concentration of methanol is 85–90%.¹¹⁰

Generally, ENDOR experiments are carried out at field strengths from 30 to 95 GHz. Because Gd^{III} has seven unpaired electrons, seven transitions for the ground state can be observed. Of these, the $+1/2$ to $-1/2$ is the most commonly monitored one given that this transition is generally the most intense and gives the narrowest linewidth. Other transitions ($\pm 3/2$ to $1/2$; $5/2$ to $3/2$; and $7/2$ to $5/2$) are split and broadened by ligand-field interactions; they give broad featureless lines that can be subtracted with background.¹¹¹ A three-pulse ESE field-sweep spectrum of a Gd^{III} complex is shown in Figure 2.16 with the central peak arising from the $+1/2$ to $-1/2$ electron spin

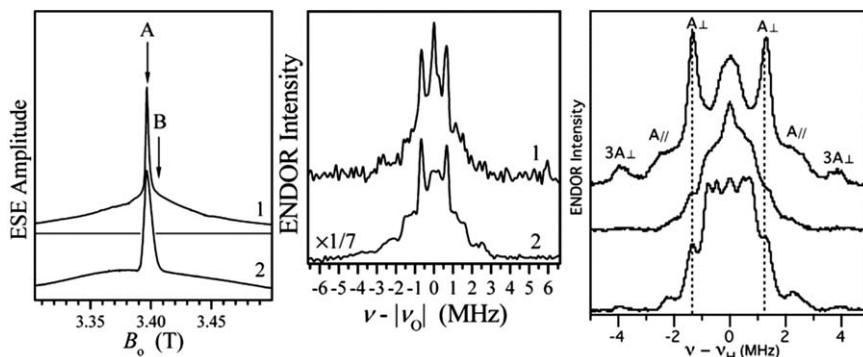


Figure 2.16 Left: Electron spin echo (ESE) field-sweep spectrum of a 1 mM solution of a Gd^{III} complex. Middle: Traces 1 and 2 are, respectively, the ^{17}O Mims ENDOR spectra of MS-325 and Gd aquo complex recorded at $B_0 = 3.3966$ T. Right: Mims ENDOR spectrum of $[\text{Gd}(\text{H}_2\text{O})_8]^{3+}$ (top), MS-325 (middle), and Gd(HP-DO3A) (bottom).^{111,112} Adapted with permission from A. M. Raitsimring, A. V. Astashkin, D. Baute, D. Goldfarb and P. Carvan, *J. Phys. Chem. A*, 2004, 108, 7318. Copyright (2004) American Chemical Society and with permission from P. Caravan, A. V. Astashkin and A. M. Raitsimring, *Inorg. Chem.*, 2003, 42, 3972. Copyright (2003) American Chemical Society.

transition. ENDOR spectra are typically taken at two field strengths; that of the $1/2$ to $-1/2$ transition and one just removed from the transition.

Proton ENDOR has been reported as a method to determine q of Gd^{III} -based contrast agents.^{108,109,112} The proton ENDOR spectrum shows the hyperfine coupling tensor appearing as A(parallel) and A(perpendicular) values in the spectrum. This is shown for $\text{Gd}(\text{H}_2\text{O})_9$ in Figure 2.16 (right) along with two other contrast agents containing a single inner-sphere water molecule.¹¹¹ Importantly, this signal intensity is proportional to the number of protons with identical proton–metal distances.¹¹² The near linear relationship between numbers of equivalent protons and hyperfine signal intensity is a strength of the pulsed Mims-ENDOR experiment. If the shapes of the hyperfine tensors change, the spectra can be integrated for accurate measurements and the spectra can be simulated. A complicating feature, however, is that ligand protons other than water also show coupling. A common method to account for coupling is to run ENDOR experiments both in H_2O /methanol and in D_2O /methanol. Experiments in D_2O remove couplings from exchangeable protons, enabling the identification of water protons. Notably, the components of the hyperfine tensor can be used to obtain information about the distance of the water protons from the Gd^{III} ion.¹¹²

The hyperfine coupling observed in an ENDOR experiment is a powerful tool to determine whether a contrast agent loses its inner-sphere water molecules upon interaction with protein.¹⁰⁹ Loss of hyperfine coupling signals a loss of inner-sphere water molecules upon protein binding.

This technique has been used to study the basis for changes in relaxivity of a series of Gd^{III} -based contrast agents in the presence and absence of human serum albumin.¹⁰⁹

^{17}O -ENDOR spectroscopy of Gd^{III} complexes has the advantage of eliminating the uncertainty associated with non-water protons. ^{17}O -ENDOR experiments are reported at high field strength, typically 93 and 130 GHz.^{110,111} Experiments are carried out in frozen solutions with isotopically enriched ^{17}O -labeled water and methanol/water ratios of 1 : 1. The number of coordinated water molecules is determined from the amplitude of the ^{17}O -ENDOR lines as shown for the Gd^{III} aquo complex and for the contrast agent MS-325 in Figure 2.16.

2.4.4.1 Practical Concerns

Because the instruments needed for this technique are relatively uncommon, collaborations are usually necessary to perform experiments at multiple field strengths. Furthermore, experiments are conducted in frozen solutions that are usually a mixture of water and methanol. Nonetheless, these measurements yield accurate data about q as well as water oxygen and proton distances from Gd^{III} , another parameter that affects relaxivity (Section 2.1.2).

2.4.5 Single Crystal X-ray Diffraction

Single crystal structures are the gold standard for identifying coordinated water molecules in the solid state.¹¹³ The solution methods described above are usually referenced with respect to crystallographic data.¹¹⁴ For analysis by this method, crystals of the complex must be grown, and for certain types of complexes this is difficult (Section 1.2). However, modern diffractometers enable data to be collected on relatively small crystals of size ($\leq 1 \text{ mm}^3$). Metal–oxygen bond lengths of inner-sphere water are readily determined from X-ray diffraction data on single crystals of small molecules.

One must always keep in mind the caveat that the ligand coordination sphere observed in solid-state structures can be different from that in solution. A compound that crystallizes is generally poorly soluble and might not represent all species in solution. In particular, under conditions that mimic those in blood, metal complexes can ionize to give hydroxide or change the protonation state of the complex. Alternatively, metal complexes might exchange inner-sphere water for anions such as carbonate or phosphate.

2.4.6 Extended X-ray Absorbance Fine Structure Spectroscopy

Extended X-ray absorbance fine structure (EXAFS) spectroscopy is another method for determining the structure of compounds. One of the advantages of the EXAFS method is that compounds need not be in a single crystalline

form. EXAFS experiments are useful for metalloproteins or for extended solids that do not readily crystallize.¹¹⁵ For small molecular contrast agents, the structure is typically determined by crystallography, not by EXAFS spectroscopy. One should keep in mind that the accuracy of the EXAFS technique is substantially lower for lanthanide ions than for transition metal ions. As such, this technique has an inherent uncertainty in the value of q it is used to determine. Nonetheless, EXAFS is a useful tool for the study of Gd^{III}-based contrast agents that are not simple coordination complexes, such as those that are incorporated into nanotubes.¹¹⁶

2.5 Measuring Rotational Correlation Times (τ_R)

FABIO CARNIATO AND MAURO BOTTA*

Clinically approved Gd-based contrast agents and a number of functionalized derivatives of these agents based on the diethylenetriaminepentaacetic acid (DTPA) and 1,4,7,10-tetraazacyclododecane-1,4,7,10-tetraacetic acid (DOTA) ligands exist as monohydrated ($q=1$) complexes with molecular weights of ~ 550 – 900 Da, corresponding to rotational correlation times, τ_R , of about 60–120 ps at room temperature.^{117,118} The typical residence time, τ_M , of the coordinated water molecule in this class of polyaminopolycarboxylate complexes falls in the range 50–600 ns, whereas the longitudinal electronic relaxation time, T_{1e} , is of the order of ~ 1 ns at 0.5 T.^{117–119} Thus, it is clear from eqn (2.17) (Section 2.1.2) that, for magnetic fields above 0.5 T ($\nu \geq 20$ MHz), the overall correlation time τ_{ci} is largely dominated by the rotational correlation time, whereas both the water-exchange process and electronic relaxation play minor or negligible roles. These relationships have long been known, as well as the concept that the relaxivity of low-molecular-weight Gd^{III} chelates is determined primarily by rotational dynamics (τ_R), particularly in the high field region.⁶¹ This dominance of rotational dynamics is illustrated by the well-known linear dependence of r_1 on the molecular mass of Gd^{III} complexes endowed with the same hydration number q .¹¹⁸ Similarly, the value of τ_R presents a linear correlation with molecular mass for small Gd^{III} complexes (Figures 2.17 and 2.18). Therefore, a rough estimate of τ_R can be obtained based on the molecular mass of a complex and on preliminary knowledge (or an estimate from the r_1 value) of the state of hydration of the complex. This information might be of use in determining initial estimates of the properties of a

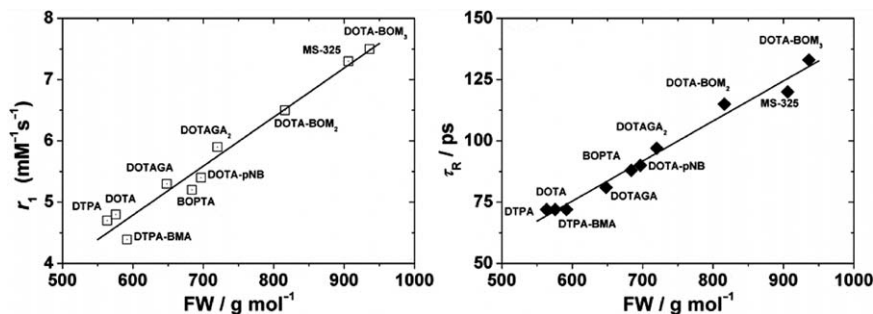


Figure 2.17 Left: Plot of r_1 (0.5 T and 25 °C) for monoqua polyaminocarboxylate Gd^{III} complexes (Figure 2.18) versus molecular weight. The correlation coefficient R of the best fit line is 0.984. Right: Plot of the corresponding rotational correlation times, evaluated from the NMRD profiles, as a function of molecular weight. The correlation coefficient R of the best fit line is 0.991.

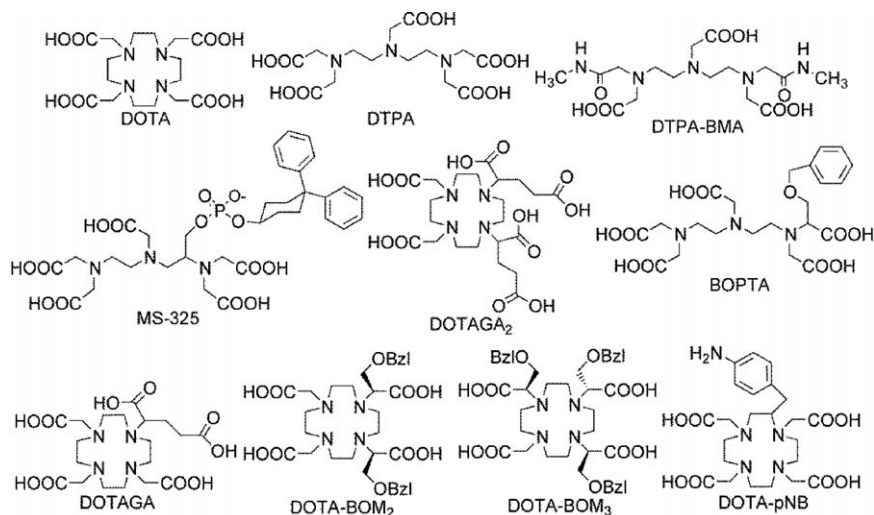


Figure 2.18 Chemical structure of the ligands in Figure 2.17.

complex, assuming control exists in preventing aggregation or the occurrence of anisotropic molecular tumbling.⁵

However, as previously pointed out, it is not easy to obtain a precise and independent assessment of the value of τ_R with the aim of facilitating the analysis of NMRD profiles.⁵ Instead, most of the reported τ_R values were obtained through the analysis of ¹H-NMRD profiles. Possible experimental approaches for the determination of τ_R are briefly described below, with reference to reported model cases or to measurements made in our laboratory.

2.5.1 Fit of NMRD Profiles

The most convenient and accurate procedure for obtaining values of τ_R is by fitting experimental NMRD profiles. This method is particularly useful in the case of small Gd^{III} complexes where contributions to inner-sphere relaxivity are dominated (or strongly influenced) by τ_R . As described in Sections 2.1 and 2.3, r_1 is dependent on a large number of molecular parameters (in addition to the applied magnetic field), making accurate assessment of any one parameter impossible from a dispersion profile that is as featureless as those that characterize rapidly tumbling Gd^{III} chelates. Therefore, it is standard practice to reduce the number of adjustable parameters by fixing as many parameters as possible to values that are typical, physically reasonable, or independently obtained with other experimental techniques. For example, with regards to the outer-sphere contribution, the diffusion coefficient D is often assumed to be $2.24 \times 10^{-5} \text{ cm}^2 \text{ s}^{-1}$ at 25 °C, and the maximum approach distance d is often taken to be equal to the molecular radius, *i.e.* about 3.7–4.0 Å. Similarly, the hydration number q is usually known, can be measured experimentally (see Chapter 2.4), or can be

Table 2.1 Best-fit parameters of the NMRD profile of $[\text{Gd}(\text{BOPTA})(\text{H}_2\text{O})]^-$ (298 K) obtained fixing the parameters r_{GdH} and d to different values. Other parameters were set as follows: $q = 1$; $\tau_{\text{M}} = 250$ ns; $D = 2.24 \times 10^{-5} \text{ cm}^2 \text{ s}^{-1}$.

Parameters	$r_{\text{GdH}} = 3.0 \text{ \AA}$		$r_{\text{GdH}} = 3.1 \text{ \AA}$	
	$d = 3.7 \text{ \AA}$	$d = 4.0 \text{ \AA}$	$d = 3.7 \text{ \AA}$	$d = 4.0 \text{ \AA}$
$\Delta^2 (10^{19} \text{ s}^{-2})$	4.0 ± 0.1	3.7 ± 0.1	3.3 ± 0.1	3.2 ± 0.2
$^{298}\tau_{\text{V}} (\text{ps})$	28 ± 0.2	27 ± 0.3	32 ± 0.4	27 ± 0.6
$^{298}\tau_{\text{R}} (\text{ps})$	70 ± 0.3	88 ± 0.2	77 ± 0.8	92 ± 0.9

estimated on the basis of chemical considerations and of the relaxivity. The metal-ion–water–proton distance, r_{GdH} , appears to be independent of the chemical nature of the chelate and is typically set in the range 3.0–3.1 Å.¹¹⁷

In general, the parameter τ_{M} does not influence NMRD profiles, except in special cases (slow exchange conditions: $\tau_{\text{M}} \geq T_{1\text{M}}$).¹²⁰ For most of Gd^{III} complexes with ligands that are derivatives of DOTA and DTPA, the τ_{M} value falls in the range 1–350 ns, and therefore, it is longer than τ_{R} and T_{ic} [eqn (2.17) in Section 2.1.2]. Under such conditions, the fit of an NMRD profile can be carried out using the parameters Δ^2 , τ_{V} , and τ_{R} taken to be adjustable. The data in Figure 2.17 were obtained using this procedure. One must be aware that calculated values of τ_{R} appreciably depend on the choice of the r_{GdH} value (as well as that of d) because the inner-sphere relaxation rate depends roughly on the ratio $\tau_{\text{R}}/r_{\text{GdH}}$.⁶ Table 2.1 reports the values of the best-fit parameters obtained from the analysis of the NMRD profile of $[\text{Gd}(\text{BOPTA})(\text{H}_2\text{O})]^-$ using different values of the parameters r_{GdH} and d .

A more accurate and reliable procedure consists of the measurement of ^1H -NMRD profiles at different temperatures (in the range of ~ 5 –39 °C) and ^{17}O -NMR R_2 and shift ($\Delta\omega$) data as a function of temperature, followed by a simultaneous fitting procedure.⁶³ More specifically, the simultaneous fitting of data from multiple techniques enables obtaining a more accurate estimate of the electronic relaxation parameters together with a detailed assessment of the exchange process of the coordinated water (^{17}O R_2) and of the hydration state of the Gd complex (^{17}O $\Delta\omega$). Recently, the advantages associated with the simultaneous fitting have been discussed in detail, and it was demonstrated that the calculated parameters are more reliable and accurate with simultaneous fitting of data from multiple techniques.¹²¹

As discussed in Section 2.3.2, caution is required when assessing τ_{R} for slowly tumbling systems because of the inadequacy of Solomon–Bloembergen–Morgan theory, particularly at low magnetic fields (Section 2.3.2). In these cases, there is a need to obtain r_1 data at high frequencies, where τ_{R} plays a dominant role in τ_{ci} . However, reliable values are extracted only for τ_{R} values <10 ns, otherwise r_1 becomes insensitive to this parameter. Finally, in the case of Gd^{III} complexes conjugated through flexible linking groups to macromolecular substrates or nanosystems, incorporated into micelles or liposomes, or contained in inclusion compounds with cyclodextrins, local rotational motion is superimposed on the overall rotation of the macromolecular system. In these cases motion, it is necessary

to consider the presence of two rotational correlation times: local (τ_{RL}) and global (τ_{RG}).¹²²

2.5.2 Debye–Stokes Equation

Using Debye–Stokes theory, it is possible to obtain an estimated value of τ_{R} for spherical complexes, provided that the microviscosity (η) and the molecular radius (r_{eff}) are known. If it assumed the molecule is a sphere of radius r_{eff} in a continuous medium of viscosity η , the following equation provides τ_{R} :

$$\tau_{\text{R}} = 4\pi\eta r_{\text{eff}}^3 / 3k_{\text{B}}T \quad (2.42)$$

Such a model correctly describes the experimental observations that the correlation time increases for larger molecules, for increased viscosities, or with decreasing temperature.¹²³ However, microviscosity can differ greatly from the experimentally accessible macroscopic viscosity, and the radius is often difficult to estimate. Although this equation appears attractive for its relative simplicity, the results are not accurate for small molecules, for which the calculated values of τ_{R} are too large and represent only an estimation of an upper limit. One reason for this equation leading to only rough estimates is that the parameter η , which refers to the rotational microviscosity, can differ substantially from the experimental data of the macroscopic viscosity of the solution. It has been proposed to modify the equation with the expression $\tau_{\text{R}} = (4\pi\eta r_{\text{eff}}^3 / 3k_{\text{B}}T)f$, where f represents the microviscosity factor, which depends on the ratio of the radius of the solvent and of the solute ($f = 0.163$ for pure liquids). When the solute molecules are much larger than those of the solvent, as for proteins in water, f tends to one and eqn (2.42) can be used.¹²⁴ However, despite its relative simplicity and ease of use, this is an oversimplified model that does not enable accurate values needed for the analysis of the relaxometric properties of small paramagnetic complexes of Gd^{III} or Mn^{II} .

In recent years, pulsed-field gradient spin echo diffusion $^1\text{H-NMR}$ spectroscopy has been used to determine the size and the rotational correlation time of small to large molecules. In the case of lanthanide(III) chelates, data can be obtained for the corresponding Y^{III} , La^{III} , or Lu^{III} diamagnetic complexes. Using pulsed-field gradient spin echo diffusion $^1\text{H-NMR}$ spectroscopy, the translational self-diffusion coefficients D of the diamagnetic metal chelates can be calculated.¹²⁵ For spherical molecules, the coefficient D is related to the hydrodynamic radius r_{eff} via the Stokes–Einstein equation [eqn (2.43)]. Using eqn (2.42) and (2.43), τ_{R} can be calculated from r_{eff} .¹²⁵

$$D = k_{\text{B}}T / 6\pi\eta r_{\text{eff}} \quad (2.43)$$

2.5.3 Oxygen-17 $1/T_1$ NMR Spectroscopy

If the Gd^{III} -based complexes contain one or more water molecules in their inner coordination sphere, then the rotational correlation time can be

extracted from the analysis of the temperature dependence of the ^{17}O longitudinal relaxation time.⁶³ The ^{17}O $1/T_1$ of the Gd^{III} -bound water molecules is determined by the quadrupolar mechanism [eqn (2.44)] and by the dipolar contribution [eqn (2.45)], according to the following equations:⁵

$$\frac{1}{T_1^{\text{Q}}} = \frac{3\pi^2}{10} \left(\frac{2I+3}{I^2(2I-1)} \right) \chi^2 (1 + \eta^2/3) \left[0.2 \left(\frac{\tau_{\text{R}}}{1 + \omega_1^2 \tau_{\text{R}}^2} \right) + 0.8 \left(\frac{\tau_{\text{R}}}{1 + 4\omega_1^2 \tau_{\text{R}}^2} \right) \right] \quad (2.44)$$

$$\frac{1}{T_1^{\text{DD}}} = \frac{2}{15} \left(\frac{\gamma_{\text{O}}^2 g^2 \mu_{\text{B}}^2}{r_{\text{GdO}}^6} \right) S(S+1) \left(\frac{\mu_0}{4\pi} \right)^2 \left[7 \left(\frac{\tau_{\text{c2}}}{1 + \omega_{\text{S}}^2 \tau_{\text{c1}}^2} \right) + 3 \left(\frac{\tau_{\text{c1}}}{1 + 4\omega_1^2 \tau_{\text{c2}}^2} \right) \right] \quad (2.45)$$

In eqn (2.44) and (2.45), I denotes the nuclear spin, χ^2 is the quadrupolar coupling constant, η is the asymmetry parameter, and r_{GdO} is the Gd–O distance of the coordinated water molecules. In an experiment, longitudinal relaxation rates are measured on high-field NMR spectrometers at different temperatures over the range of ~ 275 – 355 K. The rotational correlation time, τ_{R} , is assumed to have exponential temperature dependence [eqn (2.46)] with value τ_{R}^{298} at 298.15 K and activation energy E_{R} :

$$\tau_{\text{R}} = \tau_{\text{R}}^{298} \exp \left[\frac{E_{\text{R}}}{R} \left(\frac{1}{T} - \frac{1}{298.15} \right) \right] \quad (2.46)$$

For the measurements, fairly concentrated aqueous solutions are used (ideally, >10 – 15 mM), containing H_2^{17}O enrichment (2–10%). The longitudinal relaxation times are obtained with the inversion recovery experiment (Section 2.2.1). Normally, a simultaneous least-squares fitting of ^{17}O -NMR ($1/T_1$ and $1/T_2$) and ^1H -NMRD data is performed.⁶³

The main problem associated with this approach is the unknown values of the term $\sqrt{\chi^2(1 + \eta^2/3)}$ and of the Gd–O distance in solution. Quite often, the hypothesis is made that both parameters have a negligible variation within different Gd complexes. Therefore, the value for pure water (7.58 MHz) often is used for $\sqrt{\chi^2(1 + \eta^2/3)}$ and r_{GdO} is set to 2.5 Å. The obvious and important advantage of the method is that the measurement is directly performed on a solution of the Gd^{III} complex without the need to prepare derivatives with different Ln^{III} cations, as in deuterium or carbon-13 NMR spectroscopy (Sections 2.5.4 and 2.5.5). In addition, from reported studies, the values of the rotational correlation time obtained are consistent and reliable for Gd^{III} complexes that are structurally similar but differ in size.

2.5.4 Deuterium-NMR Spectroscopy

Another method to determine τ_{R} is based on ^2H -NMR relaxation data measured on high-resolution NMR spectrometers of diamagnetic

lanthanide(III) complexes (La^{III}, Lu^{III}, or Y^{III}). For this purpose, ligands are selectively (in most cases; *e.g.* methylene of an acetate group) or fully (occasionally) deuterated. After complexation with a Ln^{III} ion, measurements of ²H longitudinal relaxation rates in aqueous solution are performed that enable calculation of the rotational correlation times.^{126,127} Like ¹⁷O, deuterium is a quadrupolar nucleus with relaxation largely dominated by quadrupolar interactions that have a direct dependence on τ_R [eqn (2.47)]. The measurement and analysis of ²H $1/T_1$ relaxation rates represents an effective method to estimate the rotational motion of metal complexes.

$$\frac{1}{T_1^Q} = \frac{3}{40} \left(\frac{e^2 q Q}{\hbar} \right)^2 \left(1 + \frac{\eta^2}{3} \right) \left[\frac{\tau_R}{1 + \omega^2 \tau_R^2} + \frac{4\tau_R}{1 + 4\omega^2 \tau_R^2} \right] \quad (2.47)$$

In eqn (2.47), ω is the resonance frequency of ²H, and the term $(e^2 q Q/\hbar)$ represents the quadrupolar coupling constant with a value that shows dependence on the bond length C–²H and on the degree of hybridization. For a C_{sp³}–²H bond, the value of the quadrupolar term has been reported to be close to 170 kHz.¹²⁷ The asymmetry parameter η contains information about the environment surrounding the nucleus (deviation from axial symmetry), and for deuterium the value is close to zero. If the measurements are performed at 7.05 T ($\omega = 2.92 \times 10^8$ rad s⁻¹), the extreme narrowing condition ($\omega\tau_R \ll 1$) is met for values of rotational correlation times lower than ~ 1 –2 ns. Thus, the simplified equation [eqn (2.48)] can be used for low molecular weight Ln^{III} chelates:

$$\frac{1}{T_1^Q} = \frac{3}{8} \left(\frac{e^2 q Q}{\hbar} \right)^2 \tau_R \quad (2.48)$$

A possible problem with this method is the low sensitivity of the ²H nucleus that requires either isotopic labeling of ligands or the use of highly concentrated solutions. The values of $1/T_1$ and, therefore, the calculated τ_R values for ²H in samples of the La^{III} complexes of deuterated ligands were found to be dependent on the concentration of the complex for concentrations varying between 4 and 200 mM. Extrapolation of the curves to the concentration used in the NMRD measurements (~ 1 –2 mM) provided estimated values comparable with those calculated from the NMRD profiles.²⁷

2.5.5 Carbon-13-NMR Spectroscopy

Another procedure that uses experimental data obtained on high-resolution NMR spectrometers is based on the measurement of $1/T_1$ and nuclear Overhauser enhancement (NOE) values of protonated ¹³C nuclei of ligands in diamagnetic complexes, namely La^{III}, Lu^{III}, or Y^{III}. The approach is similar to that illustrated in the previous section for deuterium, but has the advantage of not requiring isotopic substitutions (and hence laborious synthetic steps) thanks to the greater NMR sensitivity of ¹³C compared to

that of ^2H . The procedure requires recording of the ^{13}C -NMR spectrum of a relatively concentrated solution of a diamagnetic complex, selection of one or more well-resolved peaks attributable to CH or CH_2 groups of the ligand, and measurement of T_1 and NOE values using standard methods.¹²⁸

Generally, for ^{13}C nuclei, dipolar interactions with nearby protons represent the dominant relaxation mechanism, especially when the carbon is directly bonded to one or more hydrogen atoms. However, because other relaxation mechanisms can contribute, it is necessary to extract the component of the total relaxation rate (R_1^T) due to dipolar interaction (R_1^{DD}). This is possible by means of the measurement of the nuclear Overhauser enhancement:

$$R_1^{\text{DD}} = \frac{\eta}{\eta_{\text{max}}} R_1^T \quad (2.49)$$

where η_{max} is the maximum possible NOE (~ 1.988). From the experimental values of η and R_1^T , R_1^{DD} can be derived, enabling the correlation time to be obtained through eqn (2.50):

$$R_1^{\text{DD}} = \left(\frac{\mu_0}{4\pi}\right)^2 \frac{N}{10} \hbar^2 \gamma_C^2 \gamma_H^2 \frac{\tau_R}{r_{\text{CH}}^6} \left[\frac{1}{1 + (\omega_H - \omega_C)^2 \tau_R^2} + \frac{3}{1 + (\omega_C)^2 \tau_R^2} + \frac{6}{1 + (\omega_H + \omega_C)^2 \tau_R^2} \right] \quad (2.50)$$

where N is the number of directly bonded protons on each carbon, r_{CH} is the C–H bond length ($\sim 1.08 \text{ \AA}$), and the other parameters have their usual meanings (physical constants).¹²⁹ If the reasonable assumption is made that r_{CH} is constant for sp^3 protonated carbon atoms in different molecules, then a standard value can be used for the internuclear C–H distance to calculate τ_R from eqn (2.50). Under extreme narrowing conditions ($\omega^2 \tau_R^2 \ll 1$) the equation simplifies to eqn (2.51):

$$R_1^{\text{DD}} = \left(\frac{\mu_0}{4\pi}\right)^2 N \hbar^2 \gamma_C^2 \gamma_H^2 \frac{\tau_R}{r_{\text{CH}}^6} \quad (2.51)$$

The simplified equation can be used in the case of measurements performed on low-molecular-weight complexes with τ_R values below ~ 80 ps at magnetic field strengths ≤ 11.75 T.

This procedure has been applied to obtain an independent evaluation of τ_R and reduce the number of parameters for the analysis of the NMRD profiles. For example, in the case of $[\text{La}(\text{DOTA})]^-$ and $[\text{La}(\text{DTPA})]^{2-}$, τ_R values of 73 ± 4 ps were calculated from data measured at 9.4 T for 0.06 M solutions, in good agreement with those evaluated afterwards from the NMRD profiles.¹²⁸ Similarly, ^{13}C $1/T_1$ measurements were used to obtain a reasonably accurate value of τ_R for the complex $\text{La}(\text{BP2A})^+$ (Figure 2.19), using a 40 mM solution (containing a small amount of D_2O for field locking).

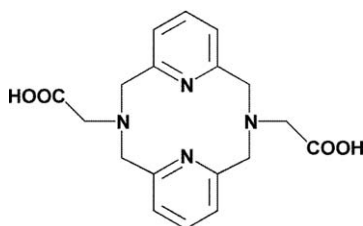


Figure 2.19 The polyazamacrocyclic ligand BP2A.

Table 2.2 Rotational correlation time, τ_R , of $\text{La}(\text{BP2A})^+$ determined at 25 °C from ^{13}C -NMR R_1 and η data at 11.7 T.¹³⁰

Carbon	N	R_1^T (s^{-1})	η	R_1^{DD} (s^{-1})	τ_R (ps)
4-py	1	4.33	0.56	1.22	54
3,5-py	1	3.65	0.79	1.45	64
py- $\text{CH}_2\text{-N}$	2	5.33	1.20	3.22	71

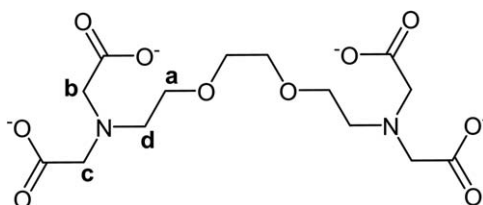


Figure 2.20 The ligand EGTA with the labeling scheme.

^{13}C spin-lattice relaxation rates and η factors were measured for all carbon atoms in the complex with this polyazamacrocyclic ligand that contain a pyridine moiety (Table 2.2). Finally, the average τ_R value of 64 ± 8 ps was used to fit the NMRD profile.¹³⁰

The application of the procedure is now illustrated in detail for the case of the determination of the rotational correlation time for the diamagnetic $\text{La}(\text{EGTA})^-$ complex (Figure 2.20).

The experimental ^{13}C $1/T_1$ and η data were acquired on a 500 MHz NMR spectrometer (11.7 T) for an aqueous solution of the complex at neutral pH and 25 °C. First, a 0.08 M solution was prepared by dissolving $\text{La}(\text{EGTA})^-$ in water at pH 7.2. An aliquot (550 μL) of this solution was transferred into a 5 mm NMR tube to which was added D_2O (50 μL) for magnetic field locking. The ^{13}C -longitudinal relaxation times of the methylene groups of the complex (a–d, Figure 2.20) were recorded using the standard inversion recovery sequence with 16 τ values in the range 0.1–1.5 s, with a repetition time of 1.5 s ($>5T_1$).

The nuclear Overhauser enhancement factors, η , were determined using standard procedures, *i.e.* by comparing the intensities of a noise-decoupled

Table 2.3 Rotational correlation time, τ_R , of $[\text{La}(\text{EGTA})]^-$ determined at 25 °C from ^{13}C -NMR R_1 and η data at 11.7 T.

Carbon	N	R_1^T (s^{-1})	η	R_1^{DD} (s^{-1})	τ_R (ps)
CH_2 (a)	2	5.00	1.30	3.27	86
CH_2 (b, c)	2	3.85	1.30	2.55	65
CH_2 (d)	2	5.25	1.31	3.46	92

spectrum and of the corresponding gated decoupled spectrum. About 1000 scans were accumulated for each experiment, corresponding to a total time of 1.5 hours. The use of a waiting period of $\sim 8\text{--}10 T_1$ (^{13}C) is advisable to obtain accurate NOE factors. Exploiting as a reference the signals of CD_3CN , of which a small aliquot (5 μL) was added to the starting solution, the integrals of the peaks were compared and the NOE factors calculated according to the following expression:

$$\eta_{\text{obs}} = \frac{I - I_0}{I_0} \quad (2.52)$$

where I is the area of the signal that experiences the full Overhauser enhancement and I_0 is the area of the peak free of NOE effect.³⁴ The experimental $1/T_1$ and η data and the values of R_1^{DD} and τ_R calculated with eqn (2.50) are reported in Table 2.3.

The average value of the rotational correlation time, $\langle \tau_R \rangle = 81 \pm 14$ ps, is larger than that obtained from the simultaneous fitting of EPR, ^{17}O -NMR, and NMRD data for $\text{Gd}(\text{EGTA})^-$ (58 ± 6 ps).¹³¹ As noted above, however, the correlation time evaluated from NMRD profiles depends on the choice of the parameters of the outer-sphere contribution. In the published study of Aime and co-workers, the values of 3.6 Å and $2.0 \times 10^{-5} \text{ cm}^2 \text{ s}^{-1}$ were used for the parameters d and D . By fixing these parameters to the values of 4.0 Å and $2.24 \times 10^{-5} \text{ cm}^2 \text{ s}^{-1}$, a τ_R value of 85 ps is obtained, in excellent agreement with the ^{13}C -NMR results for $\text{La}(\text{EGTA})^-$.

2.5.6 Hydrogen-NMR Longitudinal Relaxation Rates (Curie Mechanism)

The variable-field measurement of proton longitudinal relaxation rate for most paramagnetic lanthanide ions other than Gd^{III} can be an additional means to extract the molecular rotational correlation time by exploiting the Curie mechanism.¹⁴ This contribution originates from the dipolar interaction between the nucleus and the static electron magnetic moment that results from the partial polarization of the electrons by an applied magnetic field. In general, the two dominant mechanisms of inner-sphere contribution to the longitudinal relaxation rate of paramagnetic lanthanide ions characterized by short electronic relaxation times are represented by the

dipolar (R_1^{DD}) and Curie (R_1^{Cu}) terms.¹³² For Ln^{III} ions such as Tb^{III}, Dy^{III}, Ho^{III}, Tm^{III}, and Yb^{III}, these terms are given by:

$$\frac{1}{T_1^{\text{DD}}} = \frac{2}{15} \left(\frac{\mu_0}{4\pi} \right)^2 \gamma_I^2 \mu_B^2 g_j^2 J(J+1) \frac{1}{r_{\text{CH}}^6} \left[\frac{3\tau_{\text{c1}}}{1 + \omega_I^2 \tau_{\text{c1}}^2} + \frac{7\tau_{\text{c2}}}{1 + \omega_S^2 \tau_{\text{c2}}^2} \right] \quad (2.53)$$

$$\frac{1}{T_1^{\text{Cu}}} = \frac{2}{5} \left(\frac{\mu_0}{4\pi} \right)^2 \frac{\gamma_I^2 B_0^2 \mu_B^4 g_j^4 J^2 (J+1)^2}{(3k_B T)^2 r_{\text{IS}}^6} \left[\frac{3\tau_{\text{Cu}}}{1 + \omega_I^2 \tau_{\text{Cu}}^2} \right] \quad (2.54)$$

in which g_j and J are the Landé factor and the total spin quantum number of the Ln^{III} ion, r_{IS} is the distance between the Ln^{III} ion and the observed nucleus, B_0 is the applied magnetic field, k_B is the Boltzmann constant, and T is the temperature. The correlation time of the dipolar contribution (τ_{ci}) is largely dominated by the electronic relaxation time T_{ie} . The Curie term depends on the square of the applied magnetic field and hence becomes significant at high fields only (>2 T). Furthermore the Curie term depends on τ_{Cu} ($1/\tau_{\text{Cu}} = 1/\tau_{\text{R}} + 1/\tau_{\text{M}}$) that, at least for low-to-medium molecular weight Ln^{III} chelates, coincides with rotational correlation time. By measuring R_1 at a variety of magnetic field strengths, particularly at corresponding high Larmor frequencies (~200–600 MHz), it is possible to obtain an accurate estimate of τ_{R} after fixing r_{IS} to a reasonable value (3.0–3.1 Å). For example, this procedure was applied in the case of a series of Dy-DTPA derivatives for which the ¹H R_1 data were measured between 0.47 and 18.8 T and analyzed to obtain fairly accurate τ_{R} values.¹³³

Analogously, if a Ln^{III} complex contains a sensitive NMR nucleus X (for example, X = ¹⁹F or ³¹P) at a well-defined distance from the paramagnetic ion, the same procedure can be applied using X instead of the ¹H water signal.^{132,134} In these conditions, in which the chemical exchange process is absent, $\tau_{\text{Cu}} = \tau_{\text{R}}$, but the Ln–X distance is generally not known *a priori*, and must be treated as a fitting parameter. A thorough study was recently reported using ¹⁹F magnetic relaxation data over a field range of 4.7 to 16.5 T on a series of Ln^{III} complexes containing a CF₃ reporter group.¹³²

A clear advantage of this method is the speed of the T_1 measurements and the use of dilute solutions, ~1 mM, of the same order of magnitude as those used for the NMRD profiles of the Gd^{III} complexes. A potential limitation of this method is the need to have access to a sufficient number of NMR spectrometers operating at different (high) fields.

A number of experimental approaches are available to obtain a reliable assessment of the rotational correlation time. There are differences in the accuracy of the results and in the simplicity of the procedures, both in regards to the implementation of the experiment and the data analysis. Methods based on relaxometric measurements (Sections 2.5.1 and 2.5.6) of the bulk water proton signal in the presence of paramagnetic solutes require only dilute solutions (~1–10 mM), whereas those based on ²H- and ¹³C-NMR experiments on diamagnetic complexes need more concentrated solutions

(~50 mM). These latter methods and the ^{17}O -NMR method can be carried out on a single NMR spectrometer. The ^1H -relaxometric measurements, however, require either a field-cycling spectrometer (NMRD) or access to a series of spectrometers operating at high magnetic fields (Section 2.5.6).

It is worth pointing out that values of τ_{R} obtained with different procedures are not strictly identical. ^{17}O -NMR measurements describe the rotation of the Gd–oxygen vector of the coordinated water (τ_{RO}) while NMRD profiles or ^1H -relaxometric experiments that exploit the Curie mechanism provide information regarding the Gd–hydrogen vector of the coordinated water (τ_{RH}). The value of τ_{RH} might be different from τ_{RO} . The internal motion of the bound water molecule in lanthanide(III) complexes has been analyzed for a tetraamide derivative of DOTA, and that study concluded that τ_{RH} is shorter than τ_{RO} by a factor of about 1.5. In general, it is considered that the ratio of the two correlation times falls in the range $0.65 \leq \tau_{\text{RH}}/\tau_{\text{RO}} \leq 1$.^{5,134} Finally, ^2H - and ^{13}C -NMR measurements provide values of τ_{R} that should be similar to τ_{RO} , provided that local internal motions are absent and that tumbling is isotropic.

2.6 Measuring Water Residence Times (τ_M)

FABIO CARNIATO AND MAURO BOTTA*

It is a well-established concept that the exchange process of metal-bound water molecules plays a fundamental role in determining the efficiency of contrast agents for MRI (Section 2.1).¹³⁵ Therefore, optimization of water-exchange rates ($k_{\text{ex}} = 1/\tau_M$) is necessary to achieve high efficiencies (relaxivity). Optimal τ_M values are rather short for T_1 -shortening agents, roughly between 1 and 100 ns for low molecular weight Gd^{III} or Mn^{II} complexes. On the other hand, fairly long values ($\sim 10^{-6}$ – 10^{-3} s) are required when the contrast enhancement is achieved using CEST agents (Chapter 3.1). Thus, these two classes of probes require water-exchange optimization in opposite directions: fast rates for T_1 -shortening agents and slow rates for CEST agents.¹³⁶

The water-exchange rates measured for Ln^{III} complexes cover a considerably wide range of values over more than six orders of magnitude, from 10^9 to 10^3 s^{-1} , thus enabling their use in different applications.¹¹⁹ In most cases, the k_{ex} values of Ln^{III} complexes are obtained using NMR techniques. In particular, accurate procedures are based on the analysis of the temperature dependence of transverse relaxation rates, R_2 , of ^{17}O -enriched water measured by variable-temperature ^{17}O -NMR spectroscopy.⁶⁴

In this section, four NMR procedures are described that enable the evaluation of the parameter $\tau_M = 1/k_{\text{ex}}$ for Gd^{III} -based contrast agents.

2.6.1 Variable Temperature Oxygen-17-NMR Spectroscopy

NMR spectroscopy is a suitable technique to investigate dynamic phenomena because the exchange process markedly influences NMR parameters, in particular chemical shift and relaxation. Water exchange between a paramagnetic metal site and bulk water falls into the category of the exchange between two sites with different populations and relaxation times. For this situation, the chemical shift of the solvent in the paramagnetic solution, ω_p , referred to a diamagnetic reference, ω_d , takes the following dependence on τ_M :⁶³

$$\Delta\omega_p = \omega_p - \omega_d = \frac{p_M}{\tau_M^2} \frac{\Delta\omega_M}{(R_{2M} + \tau_M^{-1})^2 + (\Delta\omega_M)^2} + \Delta\omega_{\text{OS}} \quad (2.55)$$

$$\Delta\omega_M = \frac{g_L \mu_B S(S+1)BA}{3k_B T} \frac{1}{\hbar} \quad (2.56)$$

In eqn (2.55), p_M is the molar fraction of bound water molecules, $\Delta\omega_M$ is the chemical shift difference between the paramagnetic site and the diamagnetic site, R_{2M} is the transverse nuclear relaxation rate of the bound

water ^{17}O , and $\Delta\omega_{\text{OS}}$ is the outer-sphere contribution. Typically, it is assumed that the parameter $\Delta\omega_{\text{OS}}$ is proportional to $\Delta\omega_{\text{M}}$ through an empirical constant, $\Delta\omega_{\text{OS}} = C_{\text{OS}}\Delta\omega_{\text{M}}$. In eqn (2.56), g_{L} is the isotropic Landé g -factor, B the magnetic field strength, S the electron spin, and A/\hbar the hyperfine coupling constant.

In analogy with the chemical shift, the relaxation rates of the solvent nuclei are enhanced by exchange with solvent molecules in a paramagnetic site. In particular, the transverse relaxation rate enhancement

$$R_{2\text{p}} = R_{2}^{\text{obs}} - R_{2\text{d}} \quad (2.57)$$

depends on both τ_{M} and $\Delta\omega_{\text{M}}$ because a difference in chemical shift, particularly large in the case of a paramagnetic site, is a source of line broadening. The expression that connects $R_{2\text{p}}$ to τ_{M} and $\Delta\omega_{\text{M}}$ is the following:⁶³

$$R_{2\text{p}} = \frac{p_{\text{M}} R_{2\text{M}}^2 + R_{2\text{M}} \tau_{\text{M}}^{-1} + (\Delta\omega_{\text{M}})^2}{\tau_{\text{M}} (R_{2\text{M}} + \tau_{\text{M}}^{-1})^2 + (\Delta\omega_{\text{M}})^2} + R_{2\text{OS}} \quad (2.58)$$

In the absence of exchange $\tau_{\text{M}}^{-1} = 0$, $R_{2\text{p}} = 0$. Under the condition of fast water exchange $\tau_{\text{M}}^{-1} \gg R_{2\text{M}}$, however, $R_{2\text{p}} = p_{\text{M}}/R_{2\text{M}}$, as is the case for the longitudinal relaxation rates of most low-molecular-weight Gd^{III} -based contrast agents.

Unlike ^1H -nuclear spin where the dipolar interaction dominates the relaxation, for ^{17}O the most important contribution to transverse relaxation is the scalar term, $R_{2\text{sc}}$, because oxygen is directly bound to Gd^{III} :

$$R_{2\text{M}} = \frac{1}{T_{2\text{M}}} \cong R_{2\text{sc}} = \frac{S(S+1)}{3} \left(\frac{A}{\hbar}\right)^2 \left(\tau_{\text{e1}} \frac{\tau_{\text{e2}}}{1 + \omega_{\text{S}}^2 \tau_{\text{e2}}^2}\right) \cong \frac{S(S+1)}{3} \left(\frac{A}{\hbar}\right)^2 \tau_{\text{e1}} \quad (2.59)$$

$$\frac{1}{\tau_{\text{ei}}} = \frac{1}{\tau_{\text{M}}} + \frac{1}{T_{\text{ei}}} \quad \text{where } i = 1, 2 \quad (2.60)$$

In eqn (2.59) and (2.60), the reciprocal of the correlation time τ_{ei} is the sum of a frequency-independent term ($k_{\text{ex}} = 1/\tau_{\text{M}}$) and of the frequency-dependent longitudinal [$1/T_{1\text{e}}$; eqn (2.20) in Section 2.1.2] or transverse [$1/T_{2\text{e}}$; eqn (2.21) in Section 2.1.2] electron-spin relaxation rate.

In the event the isotropic shift is small to the point of being negligible, eqn (2.58) assumes a particularly simple form, identical to that for $R_{1\text{p}}$ in eqn (2.5) (Section 2.1.2):

$$R_{2\text{p}} = \frac{p_{\text{M}}}{T_{2\text{M}} + \tau_{\text{M}}} \quad (2.61)$$

By increasing the temperature, τ_{M} decreases (the rate of exchange increases) and $T_{2\text{M}}$ increases, so that the temperature-dependence of $R_{2\text{p}}$ is dictated by the dominant term in the denominator of eqn (2.61). In the case

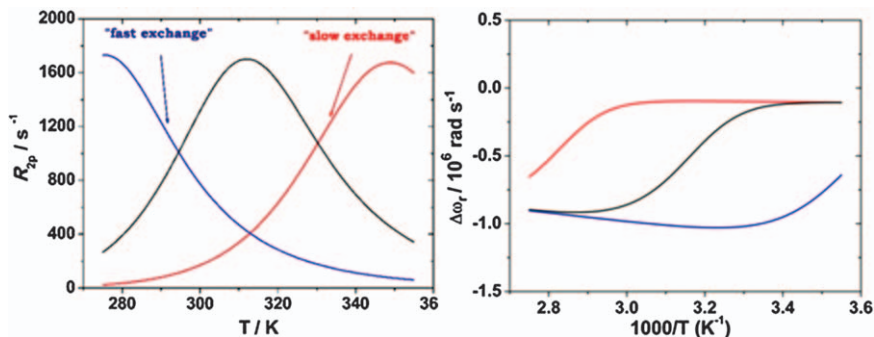


Figure 2.21 Calculated temperature dependence of ^{17}O -transverse relaxation rate (left) and of reduced ^{17}O -chemical shift (right) at 11.74 T of a 25 mM solution of a $q=1$ Gd^{III} complex with $\tau_{\text{M}}^0=3$ μs and $\Delta H^\ddagger=52$ kJ mol^{-1} (red); $\tau_{\text{M}}^0=30$ ns and $\Delta H^\ddagger=40$ kJ mol^{-1} (blue); $\tau_{\text{M}}^0=0.3$ μs and $\Delta H^\ddagger=48$ kJ mol^{-1} (black). The other parameters have been set to the following values: $\Delta^2=2\times 10^{19}$ s^{-2} , $\tau_{\text{V}}^0=15$ ps, $E_{\text{V}}=1$ kJ mol^{-1} , $A/\hbar=-3.6\times 10^6$ rad s^{-1} , $C_{\text{OS}}=0.1$.

of short τ_{M} , τ_{M} is negligible and therefore $R_{2\text{p}}$ decreases with increasing temperature. Conversely, in the opposite case of slow exchange, τ_{M} becomes predominant and $R_{2\text{p}}$ increases with the temperature increase. Often there is a maximum in the curves of $R_{2\text{p}}$ as a function of temperature, indicating the transition from a slow-exchange to a fast-exchange region (Figure 2.21). The inflection point in the temperature-dependence of $\Delta\omega_{\text{M}}$, corresponding to the maximum in the $R_{2\text{p}}$ curve, also signals the changeover between fast and slow exchange regions.⁶³

Typically, it is assumed that the variation with temperature of the exchange rate, k_{ex} , of water molecules in the inner-sphere of Gd^{III} follows the Eyring equation [eqn (2.62)]:

$$\tau_{\text{M}}^{-1} = k_{\text{ex}} = \frac{k_{\text{B}}T}{h} \exp\left(\frac{\Delta S^\ddagger}{R} - \frac{\Delta H^\ddagger}{RT}\right) = \frac{k_{\text{ex}}^0 T}{298.15} \exp\left[\frac{\Delta H^\ddagger}{R} \left(\frac{1}{298.15} - \frac{1}{T}\right)\right] \quad (2.62)$$

where ΔS^\ddagger and ΔH^\ddagger are the entropy and enthalpy of activation for the exchange process and k_{ex}^0 is the rate of exchange at 298.15 K. In addition to the exchange lifetime, the electronic relaxation times T_{ie} have temperature dependence through the τ_{V} parameter, *i.e.* the correlation time associated with the modulation of the zero-field splitting interaction. Commonly, τ_{V} is assumed to vary with temperature following an exponential behavior, where τ_{V}^0 is the value of τ_{V} at 298 K and E_{V} the activation energy:

$$\tau_{\text{V}} = \tau_{\text{V}}^0 \exp\left[\frac{E_{\text{V}}}{R} \left(\frac{1}{T} - \frac{1}{298.15}\right)\right] \quad (2.63)$$

Often, experimental data are expressed conveniently as reduced transverse relaxation rates and chemical shifts, R_{2r} and $\Delta\omega_r$, defined as in eqn (2.64) and (2.65).

$$1/T_{2r} = R_{2r} = R_{2p}/p_M \quad (2.64)$$

$$\Delta\omega_r = \Delta\omega_p/p_M \quad (2.65)$$

Data are plotted as $\ln R_{2r}$ and $\Delta\omega_r$ versus $1000/T$, and a simultaneous least-squares fitting procedure is performed to extract the parameters that describe the water-exchange kinetics. The adjustable parameters are k_{ex}^0 , ΔH^\ddagger , A/\hbar , Δ^2 , τ_V^0 , and E_V . The electronic relaxation parameters, Δ^2 and τ_V , can be estimated from analysis of $^1\text{H-NMRD}$ profiles or, preferably, by carrying out a global analysis of $^1\text{H-}$ and $^{17}\text{O-NMR}$ data. The hyperfine coupling constant, in the case of Gd^{III} complexes, normally takes values ranging from -3.0×10^6 to $-4.0 \times 10^6 \text{ rad s}^{-1}$, whereas the value of E_V is often fixed to 1.0 kJ mol^{-1} . For the $^{17}\text{O-chemical shift}$ data, the parameter C_{Os} must be considered; its value is small and is typically between 0 and 0.3. Finally, the hydration state q of the complex must be known or evaluated independently because it defines the value of p_M .

As an example, $^{17}\text{O-NMR}$ experimental data measured at 11.4 T for the complex $[\text{Gd}(\text{OBETA})(\text{H}_2\text{O})_2]^-$ (Figure 2.22) and the corresponding curves calculated with the best-fit parameters are shown in Figure 2.23.¹³⁷

From the experimental point of view, the procedure is analogous to that described in Section 2.7.4 for the bulk magnetic susceptibility shift measurement. Two separate solutions are added to a 5 mm NMR co-axial tube: in the outer compartment, an aqueous solution containing the paramagnetic species and a small amount of *tert*-butyl alcohol (1 wt %), D_2O (10 wt %), and H_2^{17}O (5 wt %), and in the inner compartment a corresponding diamagnetic solution (1 wt % *tert*-butyl alcohol, 10 wt % D_2O , and 5 wt % H_2^{17}O). The concentration of the aqueous solutions of the Gd^{III} complexes should not be lower than about 10 mM, preferably around 20–30 mM. This concentration ensures R_2^{obs} and ω_p values will be higher than those of the corresponding diamagnetic solution, and thus the experiment will provide accurate data.

The chemical shift and the full width at half peak height of the $^{17}\text{O-NMR}$ water peak are measured for both the diamagnetic and paramagnetic solutions at each temperature in the range of $\sim 278\text{--}350 \text{ K}$. The

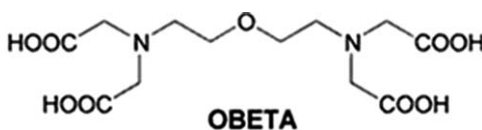


Figure 2.22 Chemical structure of OBETA.

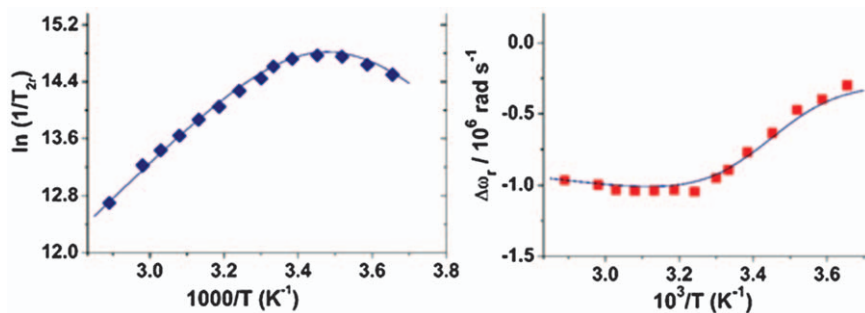


Figure 2.23 Temperature dependence of the (left) ^{17}O -reduced relaxation rates and (right) reduced chemical shifts for $[\text{Gd}(\text{OBETA})(\text{H}_2\text{O})_2]^-$ at 11.74 T. The lines through the experimental data are calculated using the following best-fit parameters: $\tau_{\text{M}}^0 = 74$ ns, $\Delta H^\ddagger = 40.5$ kJ mol $^{-1}$, $\Delta^2 = 4.9 \times 10^{19}$ s $^{-2}$, $\tau_{\text{V}}^0 = 12$ ps, $E_{\text{V}} = 1$ kJ mol $^{-1}$, $A/\hbar = -3.1 \times 10^6$ rad s $^{-1}$, $C_{\text{OS}} = 0.2$.¹³⁷ Reprinted with permission from R. Negri, Z. Baranyai, L. Tei, G. B. Giovenzana, C. Platas-Iglesias, A. C. Bényei, J. Bodnár, A. Vágner and M. Botta, *Inorg. Chem.*, 2014, 53, 12499. Copyright (2014) American Chemical Society.

reduced chemical shifts values, $\Delta\omega_{\text{r}}$, can be calculated using the following equation:

$$\Delta\omega_{\text{r}} = \frac{1}{p_{\text{M}}} (\Delta_{17\text{O}} - \Delta_{1\text{H}}) \times \omega_{17\text{O}}^0 \times 2\pi \quad (2.66)$$

where $p_{\text{M}} = q[\text{Gd}^{\text{III}}]/55.6$, $\Delta_{17\text{O}}$ is the chemical shift difference (ppm) of the water ^{17}O -NMR peak in the spectra of the diamagnetic and paramagnetic solutions, $\Delta_{1\text{H}}$ is the chemical shift difference of the ^1H -NMR resonance of *tert*-butyl alcohol in the paramagnetic and diamagnetic solutions, and $\omega_{17\text{O}}^0$ is the ^{17}O -NMR Larmor frequency (67.8 MHz at 11.74 T). Taking into account the $\Delta_{1\text{H}}$ parameter enables subtraction of the contribution of magnetic susceptibility to chemical shift.

^{17}O -transverse relaxation rates can be measured either by the Carr-Purcell-Meiboom-Gill technique or, more easily and quickly, by measuring the full width at half peak height of the water resonance:

$$\frac{1}{T_{2\text{r}}} = \frac{(\text{FWHM}_{\text{p}} - \text{FWHM}_{\text{d}})}{p_{\text{M}}} \times 3.14 \quad (2.67)$$

Diamagnetic aqueous solutions have line widths of about 17–90 Hz over the temperature range 10–70 °C and, therefore, contributions of the magnetic field inhomogeneity to the bandwidth can be safely neglected.

2.6.2 Variable Temperature Hydrogen-NMR Spectroscopy

The method described above is the best approach to obtain reliable and accurate kinetic parameters of water exchange. However, it requires the use of rather concentrated solutions, generally of the order of 20–30 mM and at least >5 mM, to ensure the acquisition of accurate and reproducible data. Sometimes, these concentrations might be higher than the solubility limits of the complexes. Recently, it has been shown that water-exchange rates can be extracted by measuring the temperature-dependence of the ^1H -NMR transverse relaxation rates of bulk water.¹³⁸ This approach is particularly suitable for measurements in the case of lanthanide ions other than Gd^{III} for which low concentrations have a particularly negative impact on the accuracy of ^{17}O -NMR data.

It should be noted that it is preferable to perform measurements at pH values close to neutral where prototropic exchange coincides with the exchange of the whole water molecule. Due to acid- or base-catalyzed processes, proton exchange might become faster than water exchange in acidic or basic environments.¹³⁹ Moreover, unlike with ^{17}O -NMR spectroscopy, the contributions of outer-sphere relaxation cannot be neglected during analysis of ^1H -NMR data.

The paramagnetic contribution to transverse relaxation, $1/T_{2p}$, is generally described as the sum of two components, inner-sphere and outer-sphere [eqn (2.68)]:

$$\frac{1}{T_{2p}} = \left(\frac{1}{T_{2p}}\right)^{\text{IS}} + \left(\frac{1}{T_{2p}}\right)^{\text{OS}} \quad (2.68)$$

The inner-sphere term is given by eqn (2.6) (Section 2.1.2), which contains $1/T_{2m}$, the transverse proton relaxation rate of the bound water molecule. This latter term, as detailed in Section 2.1.2, represents the sum of three contributions: dipole–dipole (DD), scalar coupling (SC), and Curie (Cu) mechanisms:

$$\frac{1}{T_{2m}} = \frac{1}{T_2^{\text{DD}}} + \frac{1}{T_2^{\text{SC}}} + \frac{1}{T_2^{\text{Cu}}} \quad (2.69)$$

Each of these contributions is expressed by eqn (2.14)–(2.16) (Section 2.1.2), and the relative correlation times that describe the time fluctuations of the interactions are described by eqn (2.17)–(2.19) (Section 2.1.2). The outer-sphere component represents the sum of the dipolar and Curie relaxation rates:

$$\left(\frac{1}{T_{2p}}\right)^{\text{OS}} = \left(\frac{1}{T_{2\text{DD}}}\right)^{\text{OS}} + \left(\frac{1}{T_{2\text{Cu}}}\right)^{\text{OS}} \quad (2.70)$$

Details regarding the dipole–dipole relaxation, as developed by Freed,³⁰ and the Curie contribution, described by Fries,¹⁴⁰ can be found elsewhere.¹³⁸

The ^1H -paramagnetic chemical shift ($\Delta\omega_p$) is a function of the shift due to the water molecule present in the inner-sphere ($\Delta\omega_m$) of the metal ion and the shift of water molecules in the second coordination sphere ($\Delta\omega_{\text{OS}}$), according to an expression analogous to eqn (2.55). ^1H -NMR transverse relaxation rates and chemical shifts of two $q=2$ Dy^{III} complexes were measured as a function of temperature and fitted using the full set of equations. The obtained exchange rate constants and activation parameters are similar to the values previously calculated from ^{17}O -NMR measurements,¹⁴¹ supporting the hypothesis that accurate k_{ex} values can be obtained using variable-temperature ^1H -NMR measurements. In conclusion, the ^1H -NMR transverse relaxation and shift measurements provide accurate and reliable results, but because of the uncertainties in the evaluation of the outer-sphere contributions to chemical shifts, the ^{17}O -NMR procedure should be preferred for the determination of water-exchange rate constants if complexes are sufficiently soluble.

2.6.3 $1/T_1$ Hydrogen-NMRD Profiles

In the previous sections, the dual role of τ_M was highlighted: it contributes to the correlation time associated with the time fluctuation of the dipolar interaction [eqn (2.17), Section 2.1.2], and it controls the efficiency of the transmission of the paramagnetic contribution from the metal site to the bulk solvent [eqn (2.5), Section 2.1.2]. Generally, the NMRD profiles are not affected by the value of this parameter because the overall correlation time τ_C is largely dominated by τ_R and often the condition $\tau_M \gg \tau_R$ or T_{1c} occurs. For the same reason, T_{1M} assumes values much greater than τ_M , and therefore r_1^{IS} is not significantly influenced by the rate of water exchange. With respect to eqn (2.5) (Section 2.1.2), two limiting cases might occur:

- (a) $\tau_M \ll T_{1M}$. This situation defines the “fast exchange” condition where r_1^{IS} is not limited by slow water exchange.
- (b) $\tau_M \geq T_{1M}$. In the “intermediate/slow exchange” condition, r_1^{IS} can be limited by the long residency lifetime.

For the clinically available Gd^{III} -based contrast agents and related low-molecular weight derivatives, the fast exchange condition generally applies, and thus, detailed information regarding k_{ex} cannot be obtained from the analysis of NMRD profiles. Only in the case of complexes characterized by values of τ_M of the order of microseconds can the water-exchange lifetime represent a limiting factor for r_1 . This effect was observed for the first time in the case of the neutral complex GdDTPA-BMA .¹⁴² Following the replacement of two carboxylates of DTPA with two carboxoamide groups, τ_M increased from ~ 0.3 ns to 2.2 μs (298 K).⁶³ In this case, τ_M becomes comparable to T_{1M} , resulting in an r_1 nearly 10% lower than that of $[\text{GdDTPA}]^{2-}$ at 20 MHz and 298 K. So, for Gd^{III} chelates characterized by values of τ_M longer than ~ 2 μs , τ_M can be estimated with reasonable accuracy from the analysis of NMRD

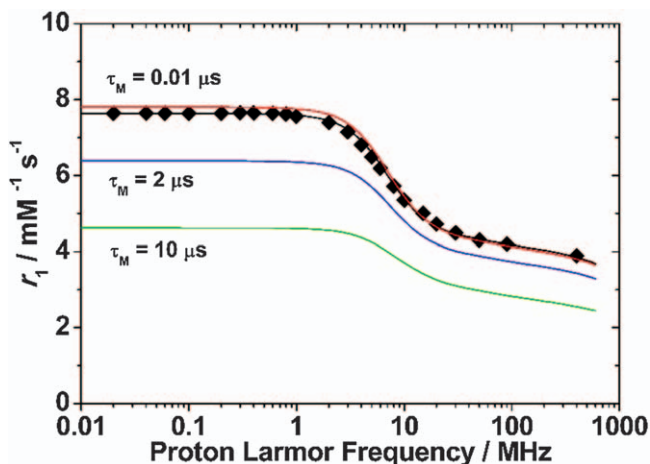


Figure 2.24 NMRD profile of $[\text{GdDTPA}]^{2-}$ at 298 K. The curve through the experimental data is calculated using the following best-fit parameters: $\Delta^2 = 2 \times 10^{19} \text{ s}^{-2}$, $\tau_v = 22 \text{ ps}$, $\tau_R = 65 \text{ ps}$, $\tau_M = 0.3 \text{ }\mu\text{s}$, $q = 1$, $r = 3.0 \text{ \AA}$, $a = 4.0 \text{ \AA}$, and $D = 2.24 \times 10^{-5} \text{ cm}^2 \text{ s}^{-1}$. The red, blue, and green curves are calculated NMRD profiles showing the effect of varying τ_M .

profiles provided that it is possible to acquire an independent assessment of τ_R . The effects of increasing values of τ_M on NMRD profiles are shown in Figure 2.24.

On the other hand, for slowly tumbling systems, T_{1M} can be more than one order of magnitude shorter and the intermediate/slow exchange requirement is more easily satisfied for the water residency time to become a limiting factor. Attenuation of relaxivity owing to long values of τ_M is particularly pronounced in the range 10–60 MHz and tends to strongly attenuate at higher fields.^{122,143} Moreover, in nanosized systems, τ_R is of the order of a few or several ns, and thus τ_M contributes appreciably to τ_C . When these conditions are met, the rate of water exchange can be assessed from the analysis of NMRD profiles with accuracy. This approach has been used to obtain values of τ_M covering over three orders of magnitude from the simultaneous fitting of variable-temperature NMRD profiles of a series of albumin-bound Gd^{III} complexes.¹⁴⁴

In conclusion, when particular conditions are met, the water residency time, τ_M , can be estimated from the fit of NMRD profiles. However, caution should be used, limiting the number of adjustable parameters, making accurate predictions of some of them, and possibly by performing a simultaneous fitting of profiles measured at different temperatures.

2.6.4 Temperature Dependence of Proton Relaxivity

Useful information regarding water-exchange rates can be obtained from analysis of the temperature-dependence of relaxivity, measured at a single

frequency. This information can be of a purely qualitative nature (conditions of slow, intermediate, or fast exchange) or quantitative, related to the evaluation of the value of k_{ex}^0 and ΔH^\ddagger . The factors determining the temperature dependence of r_1 are known. Outer-sphere relaxivity increases with decreasing temperature as a consequence of the increase of T_{ic} and τ_{D} , the correlation time for the relative translational diffusion ($\tau_{\text{D}} = a^2/D$). The variation of r_1^{IS} with temperature depends on the relative values of $T_{1\text{M}}$ and τ_{M} , which are inversely dependent on temperature [eqn (2.5), Chapter 2.1.2].

In the fast-exchange regime ($\tau_{\text{M}} < T_{1\text{M}}$) the observed behavior is dictated by $T_{1\text{M}}$ and decreases with decreasing temperature because of the lengthening of τ_{C} (longer τ_{R} and T_{ic}). This situation is common for many complexes of Gd^{III} characterized by low molecular weights or fast molecular tumbling rates, for which relaxivity is limited essentially by τ_{R} . A typical example, concerning a complex of Gd^{III} with a monoamide derivative of DOTA (L^1 ; Figure 2.25) is reported in Figure 2.26.

In the example in Figure 2.26, relaxivity was measured at neutral pH over the range 277 to 334 K. From the fitting of the NMRD profile at 298 K, good estimates of the parameters Δ^2 ($3.8 \times 10^{19} \text{ s}^{-2}$), τ_{V} (11 ps), and τ_{R} (79 ps) were obtained.¹⁴⁵ A set of other parameters can be fixed to standard values: $q = 1$, $r = 3.0 \text{ \AA}$, $a = 4.0 \text{ \AA}$, $D = 2.24 \times 10^{-5} \text{ cm}^2 \text{ s}^{-1}$. The parameters τ_{V} , τ_{R} , and D are assumed to follow an exponential law [eqn (2.63)] given by the activation energies E_{V} , E_{R} , and E_{D} . The water-residency time follows Eyring-type behavior [eqn (2.63)]. It is possible to fit the temperature dependence of r_1 using adjustable parameters: τ_{M} , $\Delta H_{\text{M}}^\ddagger$, E_{V} , E_{R} , and E_{D} . The best-fit parameters are in excellent agreement with those evaluated by ^{17}O -NMR transverse relaxation measurements. Relaxivity increases with decreasing temperature because of the increase of both inner- and outer-sphere contributions (Figure 2.26). This complex is in an intermediate-exchange regime ($\tau_{\text{M}} = 0.96 \text{ \mu s}$ at 298 K) and at temperatures below $\sim 285 \text{ K}$, τ_{M} becomes longer than $T_{1\text{M}}$ and $r_{1\text{P}}^{\text{IS}}$ decreases.

In the slow-exchange regime ($\tau_{\text{M}} \geq T_{1\text{M}}$), outer- and inner-sphere contributions show a different trend relative to the fast-exchange regime. While $r_{1\text{P}}^{\text{OS}}$ increases with decreasing temperature, r_1^{IS} decreases with decreasing

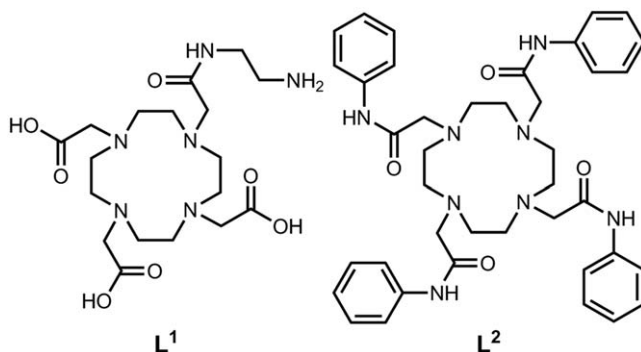


Figure 2.25 Chemical structures of monoamide derivative of DOTA (L^1) and the tetraamide-derivative of DOTA (L^2).

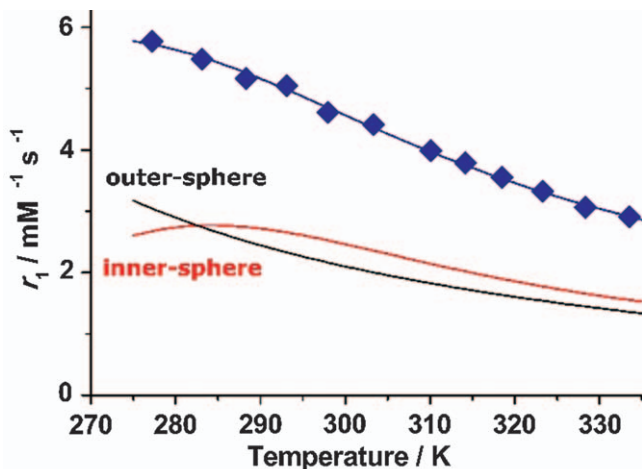


Figure 2.26 r_1 as a function of temperature for $[\text{GdL}^1]$ at neutral pH. The curve through the experimental data is calculated using the following best-fit parameters: $\tau_M = 0.96 \mu\text{s}$, $\Delta H_M^\ddagger = 34 \text{ kJ mol}^{-1}$, $E_V = 2 \text{ kJ mol}^{-1}$, $E_R = 17 \text{ kJ mol}^{-1}$, $E_D = 20 \text{ kJ mol}^{-1}$. The red and black curves are calculated inner- and outer-sphere contributions to relaxivity.

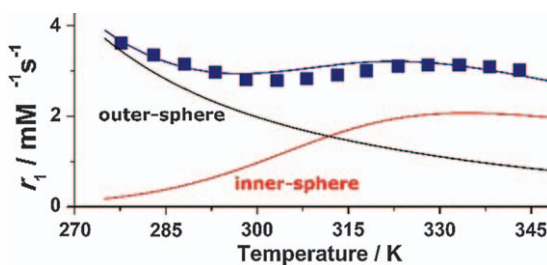


Figure 2.27 r_1 as a function of temperature for $[\text{GdL}^2]$ at neutral pH. The curve through the experimental data was calculated using the best-fit parameters given in the text and by fixing the following parameters, obtained from analysis of the NMRD profile: Δ^2 ($2.0 \times 10^{19} \text{ s}^{-2}$), τ_V (8 ps), τ_R (110 ps), $q = 1$, $r = 3.0 \text{ \AA}$, $a = 4.2 \text{ \AA}$, and $D = 2.24 \times 10^{-5} \text{ cm}^2 \text{ s}^{-1}$. The red and black curves represent calculated inner- and outer-sphere contributions to relaxivity.

temperature, and the two terms eventually cancel each other because of the progressive increase of the water residency time.¹²⁰ An example is provided by the macrocyclic cationic Gd^{III} complex (GdL^2) whose dependency of r_1 on temperature is shown in Figure 2.27. In this case, the rate of water exchange is so slow that the condition $\tau_M \geq T_{1M}$ holds for temperatures up to $\sim 340 \text{ K}$, where r_1^{IS} reaches a broad peak before decreasing at higher temperatures. In fact, $r_1^{\text{IS}} < r_1^{\text{OS}}$ for $T < 310 \text{ K}$ and the overall relaxivity is strongly limited by the slow rate of exchange over a wide range of temperatures. The data were analyzed as in the previous example and provided the following results: $\tau_M = 16 \mu\text{s}$, $\Delta H_M^\ddagger = 50.7 \text{ kJ mol}^{-1}$, $E_V = 2 \text{ kJ mol}^{-1}$, $E_R = 15 \text{ kJ mol}^{-1}$, and $E_D = 23 \text{ kJ mol}^{-1}$.

2.7 Measuring the Concentration of Gadolinium

MIHÁLY BRAUN, ZSOLT BARANYAI, FABIO CARNIATO AND MAURO BOTTA*

2.7.1 Importance of Accurate Measurements

The importance of the parameter relaxivity, r_1 , to assess the ability of a paramagnetic complex to act as an MRI contrast agent by enhancing the relaxation rate of solvent water protons is well-established. As described in Section 2.1, the relaxivity of a Gd^{III} chelate is dictated by the strength of the dipolar interaction between the metal center and the proximate water protons. The paramagnetic effect is propagated to the bulk solvent through: (i) the exchange of the inner-sphere water molecules, the exchange of its protons only ($k_{\text{ex}} = 1/\tau_{\text{M}}$), or both; (ii) the exchange of water molecules hydrogen bonded to polar groups of the ligand, the exchange of mobile hydrogens on the ligand, or both; and (iii) the diffusion near the metal chelate of outer-sphere water molecules.¹¹⁷ A number of structural, dynamic, and electronic factors contribute to determine the relaxivity of a given Gd^{III} chelate, whereby two identical relaxivity values must be associated with two complexes characterized by the same hydration state and similar rotational dynamics and rate of water exchange.¹¹⁸ Then, though only qualitatively, it is often possible to obtain from the measured value of r_1 a preliminary estimation of: (a) the hydration state of the complex q ; (b) the rotational correlation time τ_{R} (or information regarding the occurrence of molecular association or self-assembly); and (c) the possible role of a sizeable second-sphere contribution; as well as (d) an indication of the presence of a long lifetime of the coordinated water that limits relaxivity.

For all of these reasons, it is evident that relaxivity needs to be determined with a good level of accuracy. In turn, this requirement translates into the need to accurately measure both the concentration of Gd^{III} and the values of T_1 (or T_2) of the solution. We must therefore prepare the metal complex and make sure that the complexation is complete, *i.e.* there is no excess of uncomplexed Gd^{III} ions or, likewise, an excess of ligand. In the former case, we might observe a relaxivity that changes over time and with the pH, owing to slow formation and precipitation of hydroxo-species (r_1 decreases for $\text{pH} > \sim 7-8$).¹⁴⁶ Moreover, in the presence of uncomplexed Gd^{III} ions, relaxivity is often greater than the real value because of the contribution of $[\text{Gd}(\text{H}_2\text{O})_8]^{3+}$ species ($r_1 = 13 \text{ mM}^{-1} \text{ s}^{-1}$ at 25°C and 0.5 T). On the other hand, an excess of free ligand could favor the formation of ternary complexes, mixed species, or outer-sphere complexes.

In the following sections of this chapter, the most common methods for determining the concentration of solutions of Gd^{III} complexes are described based on widely available instrumentation in chemical laboratories. These procedures entail the use of four main experimental techniques: (a) NMR

relaxometry; (b) inductively coupled plasma (ICP) spectroscopy; (c) high-resolution NMR spectroscopy; and (d) complexometry.

2.7.2 Mineralization Monitored by NMR Relaxometry

The procedure is based on the complete de-coordination of Gd^{III} from a ligand occurring in a strongly acidic solution and leading to the formation of the aquo ion $[\text{Gd}(\text{H}_2\text{O})_8]^{3+}$, with a relaxivity value that is known with precision (Figure 2.28). Many Gd^{III} complexes are labile at acidic pH values, as can be observed by measuring relaxivity as a function of pH. Typically, dissociation is complete at pH values below two, where only the aquo ion is present in solution.

A general experimental procedure can be outlined as follows:

- (i) Carry out three accurate determinations of the ^1H longitudinal water proton relaxation rate (R_1^{obs}) on 1 mL of $\sim 0.5\text{--}1.5$ mM aqueous solutions of a complex at a given pH, temperature, and frequency.
- (ii) Prepare three new identical solutions by adding 300 μL of the starting solution to 300 μL of HNO_3 (65%) in three 1.0 mL glass vials (Figure 2.28). After gentle centrifugation of the resulting solutions (1500 rpm, 2 min), leave the vials to stand for about an hour. This treatment ensures that all Gd^{III} is solubilized as aquo ions.

The R_1 values (R_1^*) are then measured for each of the new solutions and the mean value of concentration of Gd^{III} in the starting solution is calculated using eqn (2.71), which applies at 25 $^\circ\text{C}$ and 20 MHz, where r_1^{A} (13.99 $\text{mM}^{-1}\text{s}^{-1}$) is the relaxivity of the aquo ion under identical experimental conditions and $R_1^{\#}$ (0.51 s^{-1}) is the relaxation rate of the diamagnetic solution [1:1 H_2O and HNO_3 (65%)].

$$[\text{Gd}] = [(R_1^* - R_1^{\#})/r_1^{\text{A}}] \times 2 \quad (2.71)$$

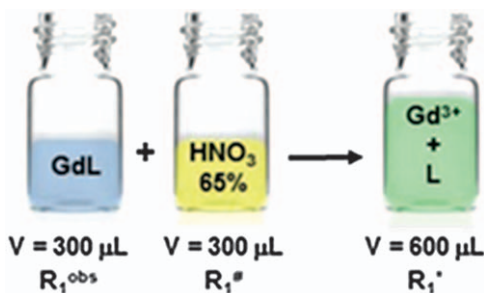


Figure 2.28 Schematic representation of a typical set-up for the relaxometric method. Colors have been added to highlight the addition of two solutions.

Finally, the relaxivity, r_1 ($\text{mM}^{-1} \text{s}^{-1}$; 20 MHz; 25 °C), is obtained from the observed relaxation rates, R_1^{obs} , by using eqn (2.72), where 0.38 is the relaxation rate of an identical solution without the paramagnetic metal ions and $[\text{Gd}]$ is given by eqn (2.71).

$$r_1 = \frac{R_1^{\text{obs}} - 0.38}{[\text{Gd}]} \quad (2.72)$$

Identical results are obtained using HCl (35%) instead of HNO_3 (65%) for the mineralization. In this case, and for any other strong acid, the correct value of r_1^{A} and $R_1^{\#}$ must be employed (Table 2.4). Note that different values of r_1^{A} and $R_1^{\#}$ must be used if the measurements are performed at another magnetic field. Also note that R_1 and r_1 values are temperature-dependent, hence the importance of controlling temperature during the measurements.

As an example, the experimental data obtained for a solution of $[\text{Gd}(\text{DTPA})(\text{H}_2\text{O})]^{2-}$ at 25 °C, pH = 7.2, and 20 MHz is described. The starting solution has an R_1^{obs} of 23.90 s^{-1} . After the addition of HNO_3 (65%), the mean R_1^* measured for the resulting solution is 35.01 s^{-1} , which corresponds to a concentration of Gd^{III} ions of 2.51 mM. Then, using eqn (2.72), a relaxivity for the complex can be calculated, $r_1 = 4.72 \text{ mM}^{-1} \text{ s}^{-1}$:

$$r_1 = (23.90 - 0.38) / [2.51 \times 2] = 4.72 \quad (2.73)$$

An accurate value of the concentration of a solution of $[\text{Gd}(\text{H}_2\text{O})_8]^{3+}$ is necessary to obtain the value of r_1^{A} . Hydrated Gd^{III} salts are commercially available. An acidic stock aqueous solution of Gd^{III} is easily prepared with a concentration that can be precisely obtained by ICP determination (Section 2.7.3) or complexometric titration, *e.g.* with ethylenediamine tetraacetic acid (Section 2.7.5).

The relaxometric procedure provides fairly accurate results, although some precautions must be taken into consideration to avoid major errors:

- For complexes characterized by a high kinetic inertia, such as $[\text{Gd}(\text{DOTA})(\text{H}_2\text{O})]^-$ and similar macrocyclic derivatives, it is necessary to mix the starting solution and the acid in an ampoule that, once sealed, is heated at 120 °C for a few hours (preferably overnight). This treatment ensures the complete formation of the aqua ion.
- The relaxivity can have a pronounced dependence on pH (and on magnetic field strength and temperature). Therefore, it is essential to accurately control the pH value of the starting solution and always associate the calculated r_1 value to a given value of pH, temperature, and B_0 (or ν).¹⁴⁷

Table 2.4 Standard data measured at 20 MHz and 25 °C.

Acid	r_1^{A} ($\text{mM}^{-1} \text{s}^{-1}$) at 20 MHz and 25 °C	$R_1^{\#}$ (s^{-1})
HNO_3 (65%)	13.99	0.51
HCl (37%)	13.70	0.50
H_2O	13.50	0.38

- (c) Preferably, the concentration of the starting solution should be around 0.5–1.0 mM or higher, but certainly greater than 0.1 mM to avoid inaccurate or unreliable results.

2.7.3 Metal Analysis with Plasma Techniques

The concentration of gadolinium in a sample solution can be determined with high precision by inductively coupled plasma optical emission spectroscopy (ICP-OES), microwave plasma atom emission spectrometry (MP-AES), or inductively coupled plasma mass spectrometry (ICP-MS).

2.7.3.1 Methods

ICP-OES is a widely used analytical technique in which a peristaltic pump delivers a sample into a nebulizer that produces a mist of fine droplets called an aerosol.^{148,149} The fine aerosol is introduced into an argon plasma. The temperature of argon plasma is close to 10 000 K. The atomization process consists of several steps (*e.g.* desolvation, melting, and dissociation) and results in excited atoms and ions. The emitted radiation of the plasma is used for the analysis. The high temperature of inductively coupled argon plasma enables use of lines emitted by the excited Gd^{+*} ions. These have over 400 emission lines in the plasma; however, only a few are appropriate for quantitative analysis (Table 2.5).¹⁵⁰ Moreover, the presence of interfering elements should be considered during the selection of lines for the analysis.

Replacement of inductively coupled argon plasma with microwave-induced nitrogen plasma was a great challenge in the field of emission spectroscopy. The first commercially available MP-AES instrument appeared in 2011 (MP-AES 4100).¹⁵¹ The technique has similar features to the ICP-OES. Even though the temperature of microwave nitrogen plasma is lower, gadolinium can be measured using emission lines of Gd^{+*} ions similar to those of ICP-OES. Nevertheless, because of the lower temperatures, the spectral interferences are different.

The most sensitive analytical method available is ICP-MS in which the charged ions produced by inductively coupled argon plasma are analyzed by mass spectrometry.¹⁵² The mass spectrometer sorts the ions according to their mass to charge ratios. Three types of mass spectrometers are normally coupled with ICP, *i.e.* sector field, time-of-flight, and quadrupole, with the latter being the most commonly used. The Gd^+ ion in the ground state is usually detected with an electron multiplier. With ICP-MS analysis of Gd^{III} samples, two main types of interference must be considered: (i) isobaric interference, associated with isotopes of different elements with identical mass (*e.g.* ^{156}Gd and ^{156}Dy ; ^{158}Gd and ^{158}Dy ; and ^{160}Gd and ^{160}Dy) and (ii) polyatomic interference, due to the formation of polyatomic ions with the same mass/charge ratio (*e.g.* ^{155}Gd : $^{138}\text{Ba}^{16}\text{O}^1\text{H}^+$, $^{137}\text{Ba}^{18}\text{O}^+$, $^{136}\text{Ba}^{18}\text{O}^1\text{H}^+$, $^{139}\text{La}^{16}\text{O}^+$, and $^{138}\text{Ce}^{16}\text{O}^1\text{H}^+$).¹⁵³

Table 2.5 Comparison of the main characteristics of the elemental analysis techniques.

	ICP-OES	MP-AES	ICP-MS
Sample introduction	Pneumatic nebulizer		
Plasma	Argon	Nitrogen	Argon
Sample volumes	5–10 mL	5–10 mL	1–2 mL
Dissolved solids in solution	0–20%	0–10%	0–0.4%
Concentration range	0.05–100 mg L ⁻¹	0.05–100 mg L ⁻¹	0.001–1000 µg L ⁻¹
Method development and operation	Skill required	Easy	Skill required
Operating costs	Medium	Low	High
	Wavelengths (nm)		Gd ⁺ isotopes (natural abundance)
	342.246 ^a	342.247 ^a	155 (14.80%)
	335.048	376.839	156 (20.47%)
	336.224	385.097	157 (15.65%) ^a
	335.863	379.637	158 (24.86%)
	358.496	335.047	160 (21.86%)

^aWavelengths and isotopes with minimal interferences.

2.7.3.2 Sample Preparation

In the case of water-soluble Gd^{III} complexes, such as those relevant as potential MRI contrast agents, sample preparation is relatively simple. A known amount by weight of a compound is dissolved and diluted to a predetermined volume with double deionized water. The resulting final concentration should have a value within the working range of the applied method. The application of the procedure can be illustrated in the case of the determination of the concentration of two solutions of Gd^{III} chelates. Aqueous solutions of GdDOTA and GdDTPA (~5 mmol L⁻¹) were prepared by dilution with double deionized water of the commercially available contrast agent solutions Dotarem[®] (Guerbet) and Magnevist[®] (Bayer-Schering Pharma). Because the approximate concentration of the starting solutions (5 mmol L⁻¹) is above the working range of the three ICP techniques discussed here, a 200-fold dilution of the samples was made using double deionized water. The concentration of Gd in the samples was determined by MP-AES with the use of a 10 000 mg L⁻¹ Gd calibration standard solution (CPAChem). With 10 mg L⁻¹ being the upper limit of the linear working range of MP-AES for Gd, we prepared calibration standards containing 2, 4, 6, 8, and 10 mg L⁻¹ of Gd. In a first step, a 1000 mg L⁻¹ Gd solution was prepared by pipetting 5 mL of a 10 000 mg L⁻¹ standard into a 50 mL volumetric flask. Then, after the addition of 1 mL of 65% (m/m) nitric acid, the solution was adjusted to the final volume with double deionized water. Calibration standards were prepared from this solution by dilution of 0.1, 0.2, 0.3, 0.4, and 0.5 mL to 50 mL in volumetric flasks containing 1 mL of 65% (m/m) nitric acid.

2.7.3.3 Measurements

Data collection is discussed using the example described above. The measurements were performed on an Agilent 4100 MP-AES instrument. The intensity of emission lines of Gd were measured at 335.047, 342.247, 376.839, 379.637, and 385.097 nm wavelengths. The intensity at 342.247 nm was recorded for the standard solutions with Gd concentrations of 2, 4, 6, 8, and 10 mg L⁻¹ and used for obtaining a calibration curve, as shown Figure 2.29.

The concentration ([Gd]_d) of the two diluted solutions of GdDOTA and GdDTPA (in mg L⁻¹) is then calculated using the following expression (eqn (2.74)):

$$[\text{Gd}]_d = \frac{\text{Intensity} + 908.7}{9910} \quad (2.74)$$

where 908.7 and 9910 are the intersection and the slope of the calibration curve, respectively. Finally, the concentration of the initial GdDOTA and GdDTPA solutions in mmol L⁻¹ is calculated by considering the atomic weight of Gd (157.25) and the dilution (200-fold) of our samples ([Gd] = 200 × [Gd]_d(mg L⁻¹)/157.25; Table 2.6).

The results of the measurements performed at different wavelength are comparable (Table 2.6). Spectral interferences or matrix effects did not play a role during these measurements. The sensitivity of the method allows performing the analysis on highly diluted samples. Normally, the temperature of plasma is high enough to decompose the organic matrix, which therefore has no influence on the results. However, in the case of more complex matrices (*e.g.* blood, serum, urine, or brain tissue) or when the results of the direct measurements differ from those of the mineralized samples, sample pretreatment becomes necessary (*e.g.* microwave-assisted acid digestion with

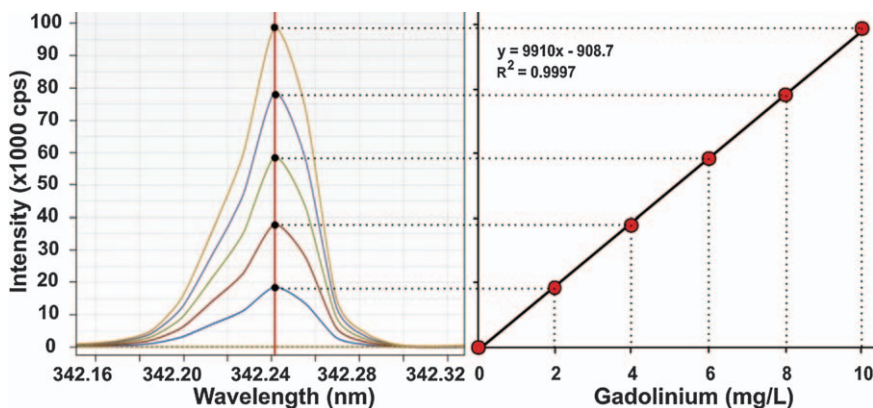


Figure 2.29 Calibration curve for determination of Gd concentration.

concentrated nitric acid and hydrogen peroxide at 200–220 °C and 20–100 bar in closed Teflon reaction vessels).

2.7.4 High-Resolution NMR Technique: Bulk Magnetic Susceptibility

A paramagnetic lanthanide ion interacts with the nuclei of the atoms of a coordinated ligand and is able to cause a measurable shift (Δ) in the nuclear resonance frequencies of these nuclei. This effect is referred to as lanthanide-induced chemical shift.^{68,154} The overall shift is expressed generally in terms of four additive contributions: the diamagnetic (Δ_d), the contact (Δ_c), the pseudocontact (Δ_p), and the bulk magnetic susceptibility (Δ_χ) shifts [eqn (2.75)]:

$$\Delta = \Delta_d + \Delta_c + \Delta_p + \Delta_\chi \quad (2.75)$$

The diamagnetic term corresponds to the coordination shift. On ¹H-NMR resonances, it is normally upfield, quite small, and negligible. The contact, or Fermi, term depends on the delocalization of unpaired electron density on the substrate nuclei and is therefore particularly relevant for atoms directly coordinated to the metal ion or in their close proximity. The dipolar or pseudocontact term depends on the spatial proximity of the nucleus to the paramagnetic ion and on the anisotropy of the magnetic susceptibility tensor. The Δ_χ shift arises from the variation in bulk magnetic susceptibility associated with the presence of a paramagnetic ion in solution. The effect is identical for all nuclei of the sample, and therefore it is effectively deleted when an NMR spectrometer is frequency-locked. It is this contribution that is measured to derive an accurate value of the concentration of a paramagnetic species in solution.¹⁵⁵

Bulk magnetic susceptibility shift is measured by using the well-established Evans method in which the bulk magnetic susceptibility shift of an inert molecule (*tert*-butyl alcohol, dioxane, or any other substrate that is not involved in some type of chemical interaction with the paramagnetic species) is measured in the presence of the paramagnetic solute on a standard NMR spectrometer.¹⁵⁶ In the most common experimental procedure, the measurement is carried out using a 5 mm co-axial NMR tube containing two separate solutions. Typically, an aqueous solution containing the paramagnetic species and a small amount of *tert*-butyl alcohol (1 wt %) and D₂O (10 wt %) is placed in the outer co-axial NMR tube, while a corresponding diamagnetic solution (1 wt % *tert*-butyl alcohol and 10 wt % D₂O) is introduced in the inner co-axial tube (Figure 2.30). The difference between the chemical shift values for the ¹H-NMR peak of the inert compound in the two compartments corresponds to Δ_χ (in ppm) that, to a good approximation, is expressed by eqn (2.76), where c is the concentration of the paramagnetic solution in mol L⁻¹, s is a parameter related to the shape of the NMR tube and its position relative to the magnetic field ($s = 1/3$ for a

Table 2.6 Concentrations of solutions of [GdDOTA]⁻ and [GdDTPA]²⁻ determined by MP-AES at different wavelengths.^a

Wavelength (nm)	GdDOTA (mmol/L)	± SD	GdDTPA (mmol/L)	± SD
335.047	5.20	0.04	5.22	0.05
342.247	5.23	0.03	5.26	0.04
376.839	5.20	0.05	5.23	0.04
379.637	5.23	0.04	5.23	0.04
385.097	5.17	0.06	5.14	0.05
Average	5.21	0.02	5.22	0.04

^aSD, standard deviation.

cylinder parallel to the main field), T is the absolute temperature, and μ_{eff} is the effective magnetic moment in Bohr magnetons, which for Gd^{III} assumes the value of 7.94.¹⁵⁷

$$\Delta_{\chi} = \frac{4\pi cs}{T} \left(\frac{\mu_{\text{eff}}}{2.84} \right)^2 \times 10^3 \quad (2.76)$$

The dependence of Δ_{χ} on concentration makes its value, easily measured with good accuracy on modern NMR spectrometers, a convenient, relatively easy, and accurate means to determine the concentration of a solution of a Gd^{III} complex. In turn, knowledge of concentration enables acquisition of a precise value of relaxivity by measuring the relaxation rate R_1 of the same solution. It is worth noting that this approach is particularly sensitive for metal ions with high effective magnetic moments, such as Gd^{III}. Indicatively, this procedure can be applied to solutions of Gd^{III} complexes with concentrations between ~0.5 and 150 mM.¹⁵⁵ On spectrometers operating at higher magnetic fields, more dilute solutions are measured more accurately because the greater line broadening makes the procedure less accurate for higher concentrations.

Alternatively, the measurement of the bulk magnetic susceptibility shift could also be carried out using two distinct NMR tubes (3 or 5 mm) for the diamagnetic aqueous solution (1 wt % *tert*-butyl alcohol and 10 wt% D₂O) and the solution with the paramagnetic species, respectively.

As an example, experimental data is presented that was obtained in the determination of the concentration of an aqueous solution at neutral pH of [Gd(DOTA)(H₂O)]⁻. In detail, 188 μL of the GdDOTA solution was mixed with H₂O (10 μL), D₂O (20 μL), and *tert*-butyl alcohol (2 μL). The corresponding diamagnetic solution contains H₂O (198 μL), D₂O (20 μL), and *tert*-butyl alcohol (2 μL). The ¹H-NMR spectrum is recorded at 298 K with a spectrometer operating at 11.74 T (500 MHz). A frequency shift (Δ_{χ}) of 234 Hz (0.47 ppm) is measured for the CH₃ resonances of *tert*-butyl alcohol in the paramagnetic solution contained in the outer tube. By applying eqn

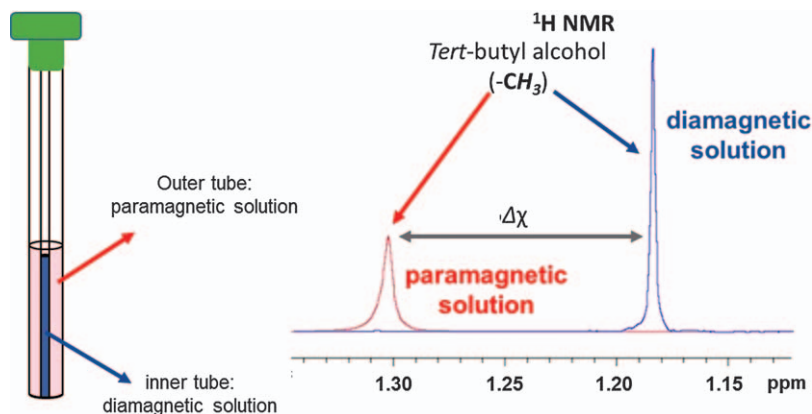


Figure 2.30 Evaluation of the bulk magnetic susceptibility shift of a paramagnetic solution by using the Evans NMR method.

(2.76) and correcting for the dilution of the starting solution, a concentration of 4.9 mM is calculated for the GdDOTA solution.

2.7.5 Complexometry

The concentration of uncomplexed metal ions (M^{n+}) in solutions can be determined with standard complexometric titrations by following the ML complex formation reaction between the M^{n+} ion (analyte) and the ligand (L; titrant) described by eqn (2.77) and (2.78), where K_{ML} , $[M^{n+}]$, $[L]$, and $[ML]$ are the stability constant of the ML complex, the concentration of the metal ion, the concentration of the ligand, and the concentration of the complex ML, respectively.



$$K_{ML} = \frac{[ML]}{[M^{n+}][L]} \quad (2.78)$$

The aim of a complexometric titration is the determination of the volume of the titrant (L) that contains a number of moles (or equivalents) equal to the number of moles (or equivalents) of the analyte (M^{n+}) in the initial solution to be analyzed.

2.7.5.1 Ligand Selection

This volumetric technique of analysis is relatively simple, useful, and accurate but has some requirements: (i) known stoichiometry of the reaction with M^{n+} ; (ii) fast complex formation at room temperature;

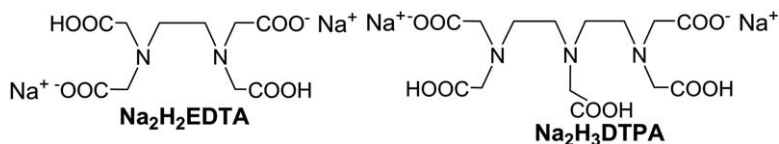


Figure 2.31 The formula of Na₂H₂EDTA and Na₂H₃DTPA.

(iii) complexation equilibrium strongly shifted towards product formation (stable complexes characterized by high K_{ML} values); and (iv) ease of detection of the equivalence point (large change in the concentration of free M^{n+} ions). These conditions are fulfilled by Na₂H₂EDTA and Na₂H₃DTPA, whose use as titrants for Gd^{III} ions is well established (Figure 2.31).¹⁵⁸

2.7.5.2 Indicator Selection

Complexometric titrations can be monitored with complexometric indicators, which are organic dyes able to coordinate M^{n+} ions.¹⁵⁸ The free and complexed forms of the indicator have different colors. The color change indicates that the indicator has been displaced by the titrant L (L = EDTA or DTPA) from the metal cations in solution, *i.e.* that the endpoint of the titration has been reached [eqn (2.79)]:



color *a* colorless colorless color *b*

Two general characteristics are important in choosing the appropriate indicator: (i) the stability of the $\text{M}nd$ complex must be high enough to allow observation of the color of the $\text{M}nd$ species even at low metal-ion concentrations and (ii) the stability of $\text{M}nd$ must be lower than that of the complexes MEDTA or MDTPA to ensure complete displacement of the metal ion from the $\text{M}nd$ complex (*e.g.* $\log K_{\text{Ln}(\text{EDTA})} = 15\text{--}19$, $\log K_{\text{Ln}nd} \leq 11$; $\log K_{\text{Ln}(\text{DTPA})} = 19\text{--}23$, $\log K_{\text{Ln}nd} \leq 15$).¹⁵⁹ Typical complexometric indicators for the determination of Gd^{III} and other Ln^{III} ions that satisfy these requirements are *xylene orange* ($\log K_{\text{GdL}} = 5.8$),^{160–165} *eriochrome black T* ($\log K_{\text{GdL}} = 11.4$),^{166,167} and *arsenazo III* ($\log \beta_{\text{Gd2L2}} = 80.5$)^{168–170} (Figure 2.32).¹⁵⁸

2.7.5.3 Factors Affecting the Complexometric Titration

The selectivity of the ligands EDTA or DTPA for Gd^{III} or other Ln^{III} ions is influenced by a number of intrinsic and extrinsic factors. The most relevant are the following:

- (i) pH. It affects the formation of the $\text{Ln}nd$, $\text{Ln}(\text{EDTA})$, and $\text{Ln}(\text{DTPA})$ complexes and the hydrolysis of the metal ions (*e.g.* precipitation of $\text{Ln}(\text{OH})_3$).^{158,171}

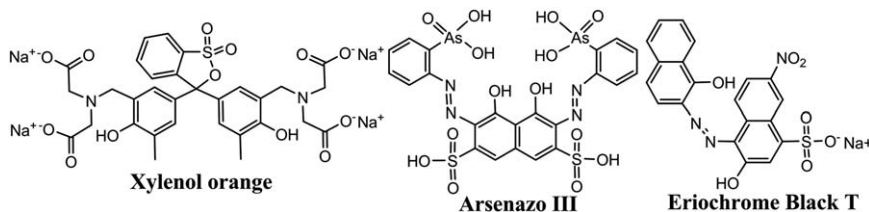


Figure 2.32 The most common complexometric metal indicators of Ln^{III} ions.¹⁵⁸

- (ii) Buffer. It might interact with the Ln^{III} ions favoring the formation of Ln–buffer complexes (acetic acid: $\log K_{\text{Gd}} = 2.16$; citric acid: $\log K_{\text{Gd}} = 6.87$; formic acid: $\log K_{\text{LaF}} = 1.11$).^{172–174}
- (iii) Interfering metal ions. These might form complexes with the ligand L leading to extra consumption of the titrant. The effect can be removed by addition of an appropriate masking agent able to form a complex with the interfering metal ions (e.g. 3,5-disulfo-pyrocatechol with Al^{III} , dithiocarbamate with Zn^{II} , and CN^- with 3d cations), by changing the oxidation state (e.g. reduction of Fe^{III} to Fe^{II} with ascorbic acid), and by formation of a precipitate (e.g. Ba^{II} can be precipitated using SO_4^{2-}).¹⁵⁸

Therefore, careful adjustment of pH and temperature, knowledge of the exact concentration of the background electrolyte, and correct selection of the buffer are all required to achieve a precise complexometric determination of Gd^{III} ions.

2.7.5.4 Experimental Procedures

According to a common experimental procedure, the complexometric titration of Gd^{III} (or other Ln^{III} ions) stock solutions is performed with 25 mL of analyte ($[\text{Ln}^{\text{III}}] = 0.2\text{--}20\text{ mM}$) in the presence of 3–4 mM urotropine buffer (~three drops of a 40% solution; urotropine $\text{p}K_{\text{a}} = 4.89$),¹⁷⁵ and xylenol orange indicator (~six drops of a 0.5% solution). As titrant, a 0.01 M solution of $\text{Na}_2\text{H}_2\text{EDTA}$ is typically used. The pH is adjusted in the range 5.8–6.0 by stepwise addition of concentrated HCl and KOH or NaOH solutions. Because the complex formation reaction between the Ln^{III} ions and $\text{Na}_2\text{H}_2\text{EDTA}$ results in the release of H^+ ions, the pH of the analyte solution must be carefully checked and corrected with the addition of two–three drops of the urotropine solution during the experiment. The endpoint of the titration is signaled by a color change from red to yellow (a steady yellow color must be achieved).¹⁷⁶ The experimental setup of the experiment is illustrated in Figure 2.33. By using this procedure and a visual detection of the endpoint, ~1–100 mg of Ln^{III} ions can be determined in the starting solution.¹⁵⁸

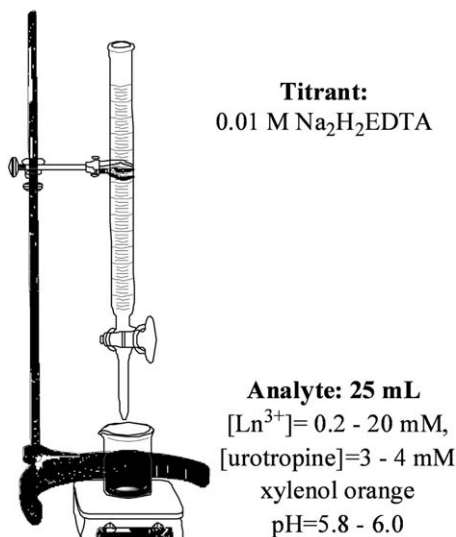


Figure 2.33 Experimental set up of a complexometric titration.

2.7.5.5 Other Methods

To decrease the detection limit of the procedure, instrumental methods like amperometric titrations,¹⁷⁷ high-frequency titrations,¹⁷⁸ and $^1\text{H-NMR}$ relaxometric titrations¹⁷⁹ have been proposed to follow the complexation of Ln^{III} cations with $\text{Na}_2\text{H}_2\text{EDTA}$ (or $\text{Na}_3\text{H}_2\text{DTPA}$) as the titrant. Using a complexometric indicator, the reaction of complex formation between the Ln^{III} ions and $\text{Na}_2\text{H}_2\text{EDTA}$ (or $\text{Na}_3\text{H}_2\text{DTPA}$) can be monitored with high sensitivity by spectrophotometry owing to the different absorption spectra and molar absorptivity of the free indicator and the LnInd complexes. The detection limit of the spectrophotometric titration was found to be $\sim 20 \mu\text{g}$ Ln_2O_3 .^{168,180-184}

To standardize a spectrophotometric titration, a new procedure has been developed for the determination of uncomplexed Gd^{III} ions in solutions of Gd complexes using xylene orange as an indicator.¹⁸⁴ Using this method, the concentration of uncomplexed Gd^{III} ions is directly proportional to the ratio of the absorption maxima ($[\text{Gd}^{\text{III}}] \propto (\text{Abs}^{573}/\text{Abs}^{433})$) of the GdInd complex (573 nm) and of the free xylene orange indicator (433 nm) in 50 mM acetate buffer solution ($[\text{xylene orange}] = 16 \mu\text{M}$; $\text{pH} = 5.8$). The color of the xylene orange indicator in the absence and presence of Gd^{III} ions is shown in Figure 2.34. The concentration of uncomplexed Gd^{III} ion has been calculated from the $\text{Abs}^{573}/\text{Abs}^{433}$ versus $[\text{Gd}^{\text{III}}]$ calibration curve obtained over the 0–50 mM concentration range. The detection limit of this spectrophotometric measurement is 3 mM.¹⁸⁴

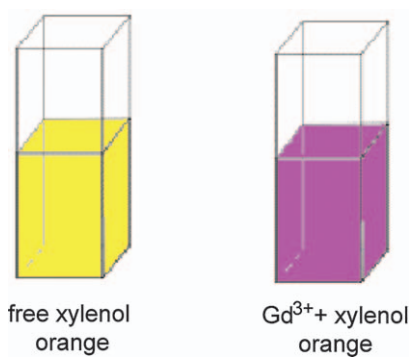


Figure 2.34 The colour of the xylene orange indicator in the absence and presence of Gd^{3+} ions.

2.8 Relaxometric Titrations

FABIO CARNIATO AND MAURO BOTTA*

Commercially available, Gd^{III} -based contrast agents for MRI are low-molecular-weight, hydrophilic complexes that, after intravenous administration, distribute into intravascular and extracellular spaces. They are characterized by high water solubilities, lack of tissue specificities, high thermodynamic stabilities, and favorable safety profiles.¹¹⁷ However, clinically used Gd^{III} -based probes have only a moderate ability to induce contrast because of their low relaxivity. In the search for strategies to increase their efficiency, rotational dynamics represents a key factor determining the relaxivity of small Gd^{III} complexes.^{61,118} Therefore, different approaches have been devised to slow rotation (*i.e.* increase τ_{R}) of paramagnetic complexes through conjugation to large substrates. Furthermore, systems have been developed in which several Gd^{III} chelates are linked to different macromolecular scaffolds or incorporated into nanoparticles. Examples of these systems include protein-bound complexes, polymers, dendrimers, micelles, liposomes, and a variety of inorganic nanoparticles. These nanoprobe enable a relatively large number of Gd^{III} ions to accumulate in sites of interest, thus enhancing the sensitivity of the MRI.^{122,185}

An alternative route to increase τ_{R} has been pursued through the formation of noncovalent interactions between suitably functionalized complexes and slowly tumbling substrates. A clear and distinct advantage of this approach is that the structural integrity of the complex is preserved and so it can be excreted in the free form (as a monomer), thereby minimizing toxicological problems associated with the use of covalently bound conjugates.¹⁸⁶ In addition, the binding constant K_{A} can be modulated to some extent because it depends on the physicochemical properties of the targeting group. Human serum albumin has been the focus of most studies regarding the formation of adducts with Gd^{III} chelates bearing hydrophobic pendant groups for angiographic applications.^{117,186} Other alternative routes to the formation of slowly tumbling adducts have relied on host-guest interactions between complexes with pendant hydrophobic functional groups and cyclodextrins and polycyclodextrins (polycyclodextrins average molecular weight $\approx 6\text{--}130$ kDa).¹⁴³

In all of these cases, a relevant requisite is the occurrence of a high binding affinity because observed relaxation enhancement in blood serum depends on the relaxivity of the free (r_1^{f}) and bound (r_1^{b}) complexes and on the molar fraction of the contrast agent in the supramolecular adduct. Consequently, for preliminary *in vitro* evaluations, it is of considerable interest and importance to determine binding parameters: the affinity constant K_{A} , the number of equivalent and independent binding sites n , and the relaxivity of the supramolecular adduct r_1^{b} . In this chapter, an effective relaxometric method is described that is based on the proton relaxation enhancement effect.

2.8.1 Determination of the Binding Parameters: E- and M-titrations

The relaxivity of a paramagnetic specie changes following binding with a substrate mainly because of the pronounced lengthening of τ_R as the rapidly rotating Gd^{III} complex (or ion) tumbles more slowly upon formation of the supramolecular adduct. Rotational correlation time is generally the most important factor that influences relaxivity of supramolecular complexes, although the relaxivity enhancement of a bound complex also depends on several other factors, including the number of bound water molecules, the rate of water-exchange of bound water with the bulk, and the degree of rotational mobility of the complex in the bound form (Section 2.1).

The proton relaxation enhancement technique is a nonseparative methodology through which binding parameters can be assessed by measuring and analyzing variations in NMR relaxation rates of water protons between the bound and free paramagnetic substrate [eqn (2.80)].¹⁸⁷

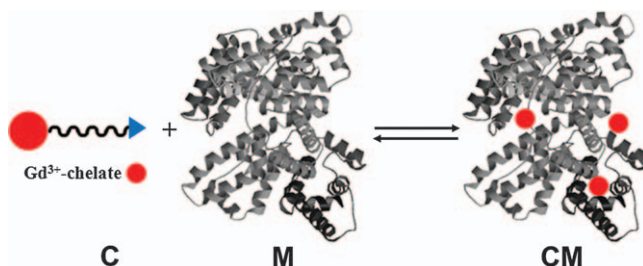


Assuming a reversible binding interaction between a paramagnetic complex (C) and a macromolecule (M), as schematically shown in Scheme 2.1 in the case where only a single class of equivalent binding sites is involved, the association constant can be expressed as follows:

$$K_A = \frac{[CM]}{[C]_f[M]_f} = \frac{[CM]}{([C]_t - [CM])([nM]_t - [CM])} \quad (2.81)$$

where $[C]_t$ ($[C]_t = [C]_f + [CM]$) and $[nM]_t$ represent the total molar concentration of the paramagnetic species and of the equivalent and independent binding sites on the macromolecule, respectively.

In an aqueous solution of a Gd^{III} complex C in the presence of the macromolecule M that interact with each other, the measured longitudinal water proton relaxation rate (R_1^{obs}) represents the sum of the relaxation rates of the unbound or free complex, R_1^f ; of the bound complex, R_1^b ; and of the



Scheme 2.1 Binding equilibrium between a Gd^{III} complex C and a macromolecule M with $n=3$.

macromolecule (diamagnetic contribution), R_1^M . The relationship between relaxation rate and relaxivity [eqn (2.2), Section 2.1.1] results in eqn (2.82):

$$R_1^{\text{obs}} = (r_1^f[C]_f + r_1^b[CM]) \times 1000 + R_1^M \quad (2.82)$$

The combination of eqn (2.81) and (2.82) gives an expression that correlates the experimental R_1^{obs} data to the binding parameters K_A and n :

$$R_1^{\text{obs}} = \frac{(K_A[C]_t + K_A[nM]_t + 1) - ((K_A[C]_t + K_A[nM]_t + 1)^2 - 4K_A^2[C]_t[nM]_t)^{1/2}}{2K_A} - (r_1^b - r_1^f + r_1^f[C]_t) \times 1000 + R_1^M \quad (2.83)$$

The complete experimental procedure for relating K_A to R_1^{obs} involves two relaxometric titrations, carried out at well-defined values of frequency and temperature. These two titrations are commonly referred to as “E” (direct) and “M” (reverse) titrations.¹⁸⁷ In these experiments, the concentration of one species (C or M) is kept constant and the concentration of the other is changed.

E titrations consist of the addition of increasing amounts of M and measurement of longitudinal relaxation rates, R_1^{obs} . During the course of the titration, changes of R_1^{obs} are measured at a fixed proton Larmor frequency and plotted as a function of the added species. R_1^{obs} increases with the concentration of M (and thus of the fraction of bound complex) and approaches an asymptotic value, which depends on r_1^b , following a binding isotherm (Figure 2.35). To ensure a high fraction of bound complex at the end of the titration, a diluted starting solution of the paramagnetic complex is used, typically corresponding to a $[C]_t$ value of about 0.2 mM. In addition, using a low $[C]_t$ causes the effect of possible additional low-affinity binding sites on the observed relaxation rate to be small.

Titration curves do not necessarily tend to asymptotic values. This tendency depends on the concentration dependence of the diamagnetic term R_1^M . In the case of the formation of inclusion complexes with cyclodextrin or polycyclodextrins, the diamagnetic term varies only marginally with concentration in the range of values normally used (~ 0 –10 mM), and this value can be considered constant. With this value assumed to be constant, the corresponding titration curves show well-defined asymptotic plateaus. On the other hand, the R_1^M value of human serum albumin varies with concentration, and therefore this value must be taken into account. This concentration effect is visible in the quasi-linear increase of R_1^{obs} at the end of titrations in the simulated binding curves in Figure 2.35. Thus, it is advisable to measure the values of R_1^M of the protein solution as a function of concentration and subtract them from the experimental data of the E titration.

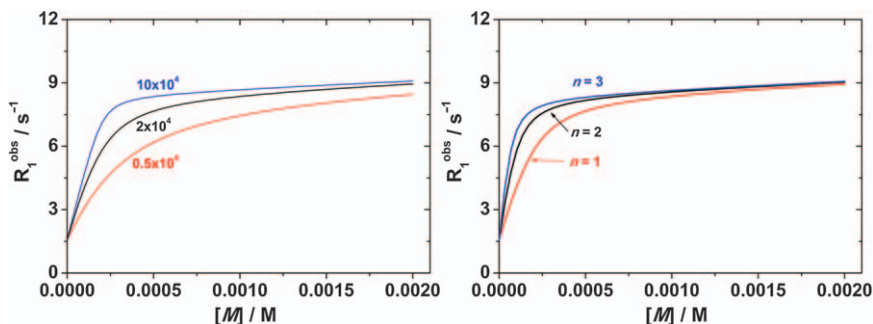


Figure 2.35 Calculated E titration curves of a 0.2 mM solution of a Gd^{III} complex with human serum albumin at 20 MHz and 298 K. Left: effect of increasing binding strength on the observed longitudinal relaxation rate [$K_{\text{A}} = 0.5 \times 10^4 \text{ M}^{-1}$ (lower curve); $2 \times 10^4 \text{ M}^{-1}$ (middle curve); and $1 \times 10^5 \text{ M}^{-1}$ (upper curve)]. The other parameters are: $n = 1$; $r_1^{\text{f}} = 6.0 \text{ mM}^{-1} \text{ s}^{-1}$; $r_1^{\text{b}} = 40 \text{ mM}^{-1} \text{ s}^{-1}$. Right: effect of the different number of equivalent binding sites n on the E-titration curve ($K_{\text{A}} = 2 \times 10^4 \text{ M}^{-1}$; $r_1^{\text{f}} = 6.0 \text{ mM}^{-1} \text{ s}^{-1}$; $r_1^{\text{b}} = 40 \text{ mM}^{-1} \text{ s}^{-1}$).

Quantitative analysis of an E titration in terms of eqn (2.83) provides an accurate estimation of the relaxivity of Gd^{III} chelates (r_1^{b}) bound to high-affinity sites and of the term nK_{A} . In general, accurate and independent evaluation of K_{A} and n is not possible with this procedure because the method is not sufficiently sensitive to n , particularly when K_{A} is small. Often, data relative to interactions with human serum albumin are fitted to a 1:1 binding isotherm ($n = 1$) despite the presence of multiple affinity sites on human serum albumin. Although this is an approximation, it enables accurate values of r_1^{b} to be obtained and the fraction of bound complex to be estimated from well-defined experimental conditions.

It is worth highlighting that the same approach can be applied to investigate the formation of ternary complexes of Gd^{III} chelates of high hydration state ($q > 1$) with oxyanions (for example, oxalate, carbonate, phosphate, fluoride, and acetate). The difference lies in the decreases in R_1 with the concentration of the oxyanion because the ternary complex is formed by displacing water molecules of the inner-coordination sphere, therefore decreasing relaxivity.¹⁸⁸

A better approach to independently evaluate n and K_{A} involves the execution and data analysis of an M titration in which a solution with a given concentration of the macromolecule is titrated with increasing amounts of the Gd^{III} complex. In the case where there is a single class of binding sites with high affinity, the increase of R_1^{obs} following the addition of the paramagnetic complex is almost linear up to the point where the interaction sites are completely saturated (Figure 2.36). After this point, the concentration of unbound complex in solution increases gradually, and therefore there is a change in the slope of the curves as consequence of the difference of relaxivity between the bound and unbound forms of the complex. An

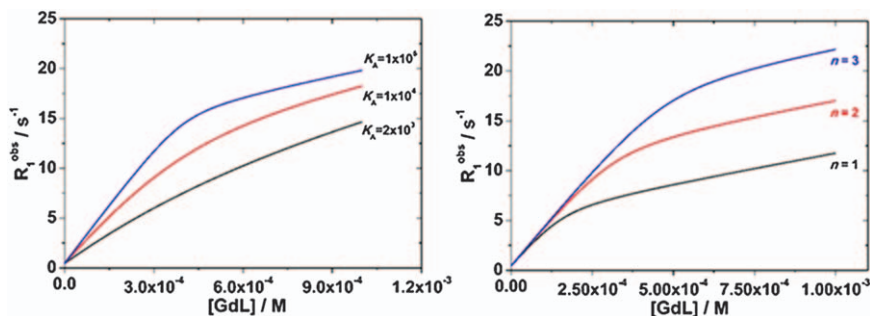


Figure 2.36 Calculated M titration curves of a solution of human serum albumin with a Gd^{III} complex at 20 MHz and 298 K. Left: effect of the binding strength [$K_A = 2 \times 10^3 \text{ M}^{-1}$ (lower curve); $1 \times 10^4 \text{ M}^{-1}$ (middle curve); and $1 \times 10^5 \text{ M}^{-1}$ (upper curve)]. The other parameters are: [human serum albumin] = 0.2 mM; $n = 2$; $r_1^f = 6.0 \text{ mM}^{-1} \text{ s}^{-1}$; and $r_1^b = 40 \text{ mM}^{-1} \text{ s}^{-1}$. Right: effect of different numbers of equivalent binding sites n on M-titration curves ([human serum albumin] = 0.16 mM; $K_A = 5 \times 10^4 \text{ M}^{-1}$; $r_1^f = 6.0 \text{ mM}^{-1} \text{ s}^{-1}$; and $r_1^b = 40 \text{ mM}^{-1} \text{ s}^{-1}$).

interesting feature of this titration data is that the $[\text{C}]_f/[\text{M}]_t$ ratio at the inflection point enables n to be approximated. The value of K_A can be determined through fitting the experimental data measured at $[\text{C}]_f$ values lower than the inflection point and by fixing n and r_1^b (obtained from an E titration).

It can be difficult to identify the inflection point when there are binding sites of low affinity on a macromolecule that induce changes in R_1^{obs} after saturation of the high-affinity sites. A similar situation occurs when the metal complex has a low affinity for the macromolecule (see the lower curve of Figure 2.36, left). In these cases, it is convenient to use a graphical method, known as a Scatchard plot, for extracting the parameters of the binding system.¹⁸⁹ Scatchard plots are useful for assessing the number of binding sites on a receptor (e.g. a protein or guest molecule) and the affinity of each site, even if more than one class of site exists. The experimental parameters used for a Scatchard plot are the concentration of unbound complex, $[\text{C}]_f$, and the average number of metal complexes bound to a receptor, r , at a given concentration of macromolecule at equilibrium. The formal definition of r is shown in eqn (2.84):

$$r = \frac{[\text{C}]_b}{[\text{M}]_t} = \sum_{i=1}^J \frac{n_i [\text{C}]_f K_{Ai}}{1 + [\text{C}]_f K_{Ai}} \quad (2.84)$$

It follows that the Scatchard plot, $r/[\text{C}]_f$ versus r , is linear for systems that have one identical and independent set of sites. An example of a system with two classes of binding sites on the same macromolecule is shown in Figure 2.37.

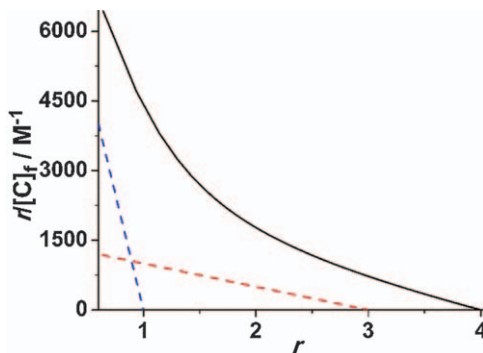


Figure 2.37 Calculated Scatchard plot for the interaction of a complex with a macromolecule presenting two classes of binding sites with different affinities. Strong site (dotted blue line): $n = 1$ and $K_A = 1 \times 10^4$; weak site (dotted red line): $n = 3$ and $K_A = 5 \times 10^2$.

To organize data in the form of a Scatchard plot, it is convenient to rearrange eqn (2.82) to show the dependence of the concentration of the bound complex on R_1^{obs} :

$$[C]_b = \frac{r_1^f [C]_t 1000 - R_1^{\text{obs}} + R_1^M}{(r_1^b) 1000} \quad (2.85)$$

Eqn (2.85) enables calculation of the values of r and $[C]_f$.

It is worth highlighting two issues concerning the Scatchard plot. The Scatchard plot obtained from data of a proton relaxation enhancement titration provides detailed information for the class of sites for which the value of r_1^b is known. This limitation restricts analyses to high-affinity sites because they are the only ones for which r_1^b can be accurately determined by this procedure. In addition, a pronounced scattering of the experimental data is observed in Scatchard plots obtained from proton relaxation enhancement measurements. Scattering is particularly an issue when the concentration of an unbound complex is small, that is, for low values of r and for complexes with high affinity for the macromolecule of interest.

2.8.2 The Enhancement Factor ε^*

There is another way to use the experimental data of the relaxometric titrations, which is based on the definition of enhancement factor.¹⁸⁷ Because this method is common in the literature, a short summary is provided here. The increase of relaxation rate observed upon addition of a macromolecule in a solution of a Gd^{III} complex can be expressed in terms of the enhancement factor ε^* :

$$\varepsilon^* = \frac{R_{1p}^*}{R_{1p}} = \frac{(R_1^{\text{obs}} - R_1^{\circ})^*}{(R_1^{\text{obs}} - R_1^{\circ})} \quad (2.86)$$

The asterisk indicates the presence of the macromolecule in the aqueous solution of the Gd^{III} complex. The enhancement factor can assume values from one (absence of interactions) to the upper limit of $\varepsilon^{\text{b}} = R_{1\text{p}}^{\text{b}}/R_{1\text{p}}$ when the metal complex is completely bound (large excess of macromolecule). Because the observed relaxation rate is a linear combination of the bound and unbound rates [eqn (2.87)], it follows that the enhancement factor can be described using eqn (2.88).

$$R_{1\text{p}}^* = \chi^{\text{f}} R_{1\text{p}} + \chi^{\text{b}} R_{1\text{p}}^{\text{b}} \quad (2.87)$$

$$\varepsilon^* - 1 = \chi^{\text{b}}(\varepsilon^{\text{b}} - 1) \quad (2.88)$$

The determination of the binding parameters K_{A} and n from the mass action law follows:

$$K_{\text{A}} = \frac{[\text{CM}]}{[\text{C}]_{\text{f}}[\text{M}]_{\text{f}}} = \frac{[\text{CM}]}{([\text{C}]_{\text{t}} - [\text{CM}])([\text{nM}]_{\text{t}} - [\text{CM}])} \quad (2.89)$$

$$\varepsilon^* = \chi^{\text{b}} \varepsilon^{\text{b}} + (1 - \chi^{\text{b}}) = \frac{[\text{CM}]}{[\text{C}]_{\text{t}}} \varepsilon^{\text{b}} + \frac{[\text{C}]_{\text{t}} - [\text{CM}]}{[\text{C}]_{\text{t}}} \quad (2.90)$$

The combination of eqn (2.89) and (2.90) yields eqn (2.91), which enables the nonlinear fitting of experimental data:

$$\varepsilon^* = (\varepsilon^{\text{b}} - 1) \times \frac{(K_{\text{A}}[\text{C}]_{\text{t}} + K_{\text{A}}[\text{nM}]_{\text{t}} + 1) - ((K_{\text{A}}[\text{C}]_{\text{t}} + K_{\text{A}}[\text{nM}]_{\text{t}} + 1)^2 - 4K_{\text{A}}^2[\text{C}]_{\text{t}}[\text{nM}]_{\text{t}})^{1/2}}{2K_{\text{A}}[\text{C}]_{\text{t}}} + 1 \quad (2.91)$$

The experimental procedure to obtain the data necessary to use eqn (2.91) requires measurement of the enhancement factor ε^* through the two distinct E and M titrations. In the first case, a rectangular hyperbola is obtained describing the change of ε^* as $[\text{M}]_{\text{t}}$ increases (Figure 2.38). The treatment of the obtained binding isotherm yields the value of ε^{b} and the product nK_{A} .

In the second titration, the behavior of ε^* is monitored at a fixed concentration of the macromolecule by changing the metal complex concentration. The results can be expressed in the form of a Scatchard plot:

$$\frac{r}{[\text{C}]_{\text{f}}} = nK_{\text{A}} - rK_{\text{A}} \quad (2.92)$$

The value of r can be calculated from the value of ε^{b} evaluated from the E titration (eqn (2.93)). In the same way, the concentration of unbound complex, $[\text{C}]_{\text{f}}$, can be derived from the total concentration of the complex, $[\text{C}]_{\text{t}}$ (eqn (2.94)).

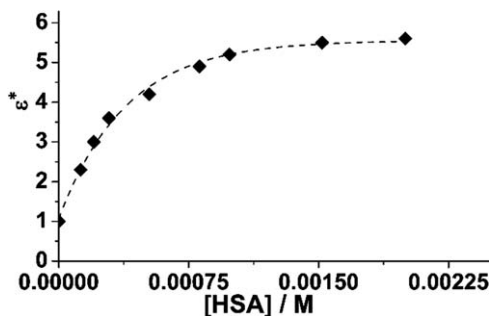


Figure 2.38 Proton relaxation enhancement E titration of a Gd^{III} complex with human serum albumin. From the obtained rectangular hyperbola, ϵ^{b} and nK_{A} can be obtained using eqn (2.91).

$$r = \frac{(\epsilon^* - 1)[\text{C}]_{\text{t}}}{(\epsilon^{\text{b}} - 1)[\text{M}]_{\text{t}}} \quad (2.93)$$

$$[\text{C}]_{\text{f}} = \left(1 - \frac{\epsilon^* - 1}{\epsilon^{\text{b}} - 1}\right) [\text{C}]_{\text{t}} \quad (2.94)$$

By plotting $r/[\text{M}]_{\text{f}}$ versus r , a straight line is obtained with an x -axis intercept that is equal to n and with a slope equal to $-K_{\text{A}}$.

2.8.3 Experimental Procedure

As an example, this section considers the binding interaction of a lipophilic Gd^{III} complex with human serum albumin. The experimental procedure consists of carrying out E and M titrations. During the experiments, it is important to ensure constant values of temperature (298 or 310 K) and pH.

In the first titration, human serum albumin ($\sim 1\text{--}5$ mg) is added to a dilute aqueous solution of the paramagnetic complex. A starting volume of 1 mL containing a concentration of $\sim 0.1\text{--}0.2$ mM of the Gd^{III} chelate is recommended. Before beginning the titration, the concentration of the starting solution should be assessed by one of the procedures described in Section 2.7. After the measurement of R_1 of the starting solution, the protein is added *via* stepwise additions. The total amount of human serum albumin added is often in the range of 60 to 100 mg. The observed longitudinal relaxation rate is plotted as a function of the protein concentration. For a good definition of the binding isotherm, it is advisable to measure more values of R_1 in the initial part of the titration (at low protein concentrations) instead of the asymptotic end of the curve. If the interaction of interest involves an inclusion complex with cyclodextrin or polycyclodextrin, then stepwise additions by weight are not viable because the small amounts added at each interval will be associated with large error. In this case, it is convenient to

prepare a stock solution containing the cyclodextrin with a concentration close to its solubility value and the complex (*e.g.* 0.15 mM). The R_1 value of this solution corresponds to the end point of the titration. By mixing different volumes (decreasing) of this solution with a solution of an identical concentration of the complex (increasing volumes), values of R_1 can be measured that correspond to decreasing concentrations of the substrate to complete the titration curve.

In the M titration method, a solution of the protein (~ 0.1 – 0.2 mM) is titrated with increasing concentrations of the paramagnetic complex (up to about 10 times the fixed concentration of the protein). The observed relaxation rate is plotted as a function of the concentration of the Gd^{III} complex.

Proton relaxation enhancement is the method of choice when the substrate interacting with the macromolecule is a paramagnetic species. Nevertheless, alternative strategies such as equilibrium dialysis, ultrafiltration, and ultracentrifugation are also available for investigating the binding interactions of metal chelates.^{190–192} Equilibrium dialysis and ultrafiltration are separative methods that make use of a membrane or a filter of suitable size to enable the separation and subsequent quantitative analysis of the unbound substrate. A few reports provide comparison between the results obtained for the same systems using both equilibrium dialysis and proton relaxation enhancement.^{126,191,193} In these cases, the agreement is broad and satisfying. Furthermore, it should be noted that the proton relaxation enhancement method enables evaluation of weak association constants that are otherwise not detectable using the equilibrium dialysis approach.

2.9 Computational Methods

ROSA PUJALES-PARADELA, MARTÍN REGUEIRO-FIGUEROA,
DAVID ESTEBAN-GÓMEZ AND CARLOS PLATAS-IGLESIAS*

The rational design of Gd^{III}-based contrast agents with predetermined properties requires relating the structural features of the complexes with the microscopic physicochemical parameters that describe their relaxivities. Computational methods are a powerful tool to obtain information regarding the structure and dynamics of Gd^{III} complexes in solution. Theoretical studies provide insight at the molecular level for important properties of Gd^{III} complexes that are difficult to access with experimental techniques (*i.e.* fast dynamic processes that cannot be followed by NMR spectroscopy). In principle, the complete set of computational approaches can be applied to investigate Gd^{III} complexes, including: (i) molecular mechanics (MM) and classical molecular dynamics (MD) simulations; (ii) semi-empirical calculations; and (iii) density function theory (DFT) and *ab initio* methods. This section provides an overview of different computational approaches that can be applied to the characterization of Gd^{III}-based contrast agents. Basic foundations and practical aspects are presented for each methodology, which might be interesting for experimentalists that wish to employ computational studies in parallel to experimental work.

2.9.1 Molecular Mechanics and Molecular Dynamics Simulations

The use of MM methods to investigate Gd^{III} complexes is not straightforward owing to the lack of parametrization of high-coordination lanthanide compounds in commonly available force fields. A force field is a mathematical expression that relates the energy of the system and the coordinates of its particles. Many force fields with different degrees of sophistication have been reported, but a general expression of a common force field is given by eqn (2.95):^{194,195}

$$E = \sum_{\text{bonds}} K_r (r - r_{\text{eq}})^2 + \sum_{\text{angles}} K_\theta (\theta - \theta_{\text{eq}})^2 + \sum_{\text{dihedrals}} \frac{V_n}{2} [1 + \cos(n\theta - \gamma)] + \sum_{i < j} \left[\frac{A_{ij}}{r_{ij}^{12}} - \frac{B_{ij}}{r_{ij}^6} + \frac{q_i q_j}{\epsilon r_{ij}} \right] \quad (2.95)$$

As observed in eqn (2.95), bond stretching and bending are represented by harmonic potentials, where r_{eq} and θ_{eq} represent the distances and angles, respectively, at equilibrium. The torsional energy associated with changes in dihedral angles is often expressed by cosine functions, with ϕ being the dihedral angle and γ the phase; V_n determines the height of the potential

energy barrier; and n is the multiplicity, which refers to the number of minima or maxima between 0 and 2π . The last term describes the interactions of nonbonded atoms, including the repulsive and Van der Waals interactions—expressed by a 12-6 Lennard–Jones potential—and Coulombic interactions.

The application of MM methods to Gd^{III} complexes requires careful parametrization of force fields. Cosentino, Villa, and co-workers developed a parameter set within the TRIPOS force fields for Gd^{III} complexes with cyclen-based ligands containing amidic, alcoholic, and phosphinic oxygen atoms.^{196–199} This force field was developed by fitting empirical potentials to *ab initio* potential energy surfaces (PES) calculated at the Hartree–Fock level. MM calculations employing this force field were subsequently applied to investigate the structure and dynamics of responsive Gd^{III} -based contrast agents.^{198,200} A set of parameters consistent with the chemistry at Harvard macromolecular mechanics (CHARMM)²⁰¹ force field was also determined for $[\text{Gd}(\text{DOTA})]^-$.²⁰² The parameters for Gd^{III} within the framework of the assisted model building with energy refinement (AMBER)²⁰³ force field were published and a range of macrocyclic and nonmacrocyclic complexes were investigated using MM and classical MD simulations.^{204–207}

Molecular dynamics simulations provide a dynamical trajectory of a system with N particles by integration of Newton's equations of motion [eqn (2.96)]:

$$F_i = m_i a_i = m_i \frac{d^2 r_i}{dt^2} = - \frac{\partial}{\partial r_i} E(r_1, r_2 \dots r_N) \quad (2.96)$$

where $E(r_1, r_2 \dots r_N)$ is the potential energy of the system that depends on the coordinates of its N particles. Thus, Newton's equations of motion relate the derivative of the potential energy and the changes in position as a function of time. No analytical solution exists to the equations of motion that must be solved using numerical integration algorithms. Thus, to perform a classical MD simulation, one needs to choose an appropriate force field, an integration algorithm (which should conserve energy and momentum), and the initial conditions. Often MD calculations use periodic boundary conditions, that is, the simulation box is surrounded by an infinite number of replicas of itself, but only N atoms inside the main box are considered explicitly.

MD simulations based on force fields have the advantage of being orders of magnitude faster than *ab initio* MD simulations, thus, enabling handling of systems composed of thousands of atoms that reach simulation times up to the microsecond timescale. The main limitation of MD simulations is that they do not provide information about the electronic structure of the system and cannot model reactions involving bond formation and breaking or electron transfer. Furthermore, the applicability of the force field is generally limited to compounds having a similar nature to those used for parametrization.

Classical MD simulations have been shown to provide relevant information about some of the parameters that control the ^1H relaxivities of Gd^{III}

complexes. Radial distribution functions calculated along the MD trajectories provide information on the distances between Gd^{III} ions and the oxygen (r_{GdO}) and hydrogen (r_{GdH}) atoms of coordinated water molecules, which affect the ¹⁷O- and ¹H-longitudinal relaxation times of the coordinated water molecules. Furthermore, the residence time of second-sphere water molecules in polyaminocarboxylate complexes was estimated to be 20–25 ps using classical MD simulations, which also provided access to the outer-sphere contributions to ¹H relaxivity.²⁰⁵ Additionally, rotational correlation times (τ_{R}) can be extracted from the time evolution of an appropriate vector, providing that the simulation time is long enough (τ_{R} values of small Gd^{III} complexes are in the range of 100 ps). Other studies used classical MD trajectories to calculate quadrupole coupling constants and hyperfine coupling constants, which affect longitudinal ¹⁷O-NMR relaxation rates and transverse ¹⁷O-NMR relaxation rates and chemical shifts, respectively.²⁰⁸ Typically, the snapshots obtained from classical MD simulations were analyzed with DFT to obtain the target parameters and to assess dynamic effects in aqueous solutions.^{15,209}

2.9.2 Semi-empirical Calculations

Semi-empirical methods are the simplest class of electronic structure (quantum chemical) methods that involve integral approximations and parametrization to simplify calculations.²¹⁰ These simplifications reduce accuracy but make calculations suitable to treat large molecules. The most popular semi-empirical methods are based on the modified neglect of diatomic overlap (MNDO) introduced at the end of the 1970s.^{211,212} Parametrization of Gd^{III} was carried out for several of these semi-empirical models (PM3 and RM1)^{213,214} and the Sparkle/AM1,²¹⁵ Sparkle/PM3,²¹⁶ Sparkle/PM6,²¹⁷ and Sparkle/PM7²¹⁸ variants, which have been implemented in the molecular orbital package (MOPAC).²¹⁹ The Sparkle model considers lanthanide trications to be +3 charged with closed-shell inert-gas electron density, without angular steric properties. The model is justified by the contracted nature of the 4f orbitals and the predominantly ionic character of the Gd^{III}-ligand bonds.

Semi-empirical approaches have been used in a limited number of Gd^{III} systems and therefore require careful testing and evaluation by comparison with experimental data or high-level calculations.²²⁰ However, the low computational cost of these calculations makes them a useful tool for handling large systems (above several hundreds of atoms) or for preliminary investigations of the conformational space of small Gd^{III} complexes that will be optimized afterwards at a higher computational level.

2.9.3 Density Functional Theory and *Ab Initio* Methods

The description of the electronic structure of Gd^{III}-based contrast agents for MRI is essential to an understanding of their physicochemical properties

and therefore to aid in developing applications in many technological fields. The experimental work performed with potential Gd^{III}-based contrast agents and the analogues containing other Ln^{III} ions provides a wide range of information on relationships between structure and the parameters governing the relaxivity. However, theoretical investigations performed on this kind of systems are behind experimental knowledge. The reasons for this delay are likely related to some difficulties associated with the quantum chemical treatment of Gd^{III} and other Ln^{III} ions, including: (i) the presence of unpaired 4f electrons; (ii) the importance of relativistic effects; (iii) the multi-configurational character of the wavefunctions of ground and excited states of the lanthanides; and (iv) the importance of spin-orbit coupling.

Electronic structure methods rely on several approximations to simplify the solution of the Schrödinger equation. The first of such approximations is the Born–Oppenheimer approximation, which separates the nuclear and electronic motions on the basis of their different masses. Even in the case of light atoms such as the hydrogen atom, the mass of the nucleus is ~1800 times greater than that of the electron so nuclei movement is slow compared to electrons. Thus, neglecting the kinetic energy term of nuclei, the molecular electronic Hamiltonian for a system with N electrons and M nuclei can be written as eqn (2.97) (in atomic units):

$$H_{\text{BO}} = -\frac{1}{2} \sum_{i=1}^N \nabla_i^2 - \sum_{\alpha} \sum_i^N \frac{Z_A}{|r_i - R_A|} + \sum_i^N \sum_{j < i}^N \frac{1}{|r_i - r_j|} + \sum_A^M \sum_{B < A}^M \frac{Z_A Z_B}{|R_A - R_B|} \quad (2.97)$$

In eqn (2.97), the first term represents the electron kinetic energy and the remaining three terms account for the nuclear–electron attraction, electron–electron repulsion, and nuclear–nuclear repulsion, respectively. The molecular N -electron Hamiltonian can be used in the time-independent Schrödinger equation, which describes the motion of electrons in the field of fixed nuclei [eqn (2.98)]:

$$\hat{H}_{\text{BO}} \Psi^{\text{elec}}(x_1, x_2 \dots x_N; R_A, R_B \dots R_M) = E \Psi^{\text{elec}}(x_1, x_2 \dots x_N; R_A, R_B \dots R_M) \quad (2.98)$$

In eqn (2.98), $\Psi^{\text{elec}}(x_i; R_i)$ is the electronic wave function, which depends only parametrically on the positions of the nuclei, and E is the electronic energy. Thus, the Born–Oppenheimer approximation leads to the concept of potential energy surface that describes the energy of the system in terms of the nuclear positions. It is important to note that in eqn (2.98), x_i denotes both the spatial and spin degrees of freedom. Molecular orbital theory expresses ψ as a combination of a set of normalized and orthogonal molecular orbitals ($\psi_1, \psi_2, \dots, \psi_N$). Because $\psi(x_1, x_2, \dots, x_N)$ must be antisymmetric, that is, the function must change sign if two identical particles are interchanged,

a convenient form of describing ψ is using a Slater determinant of the form in eqn (2.99):

$$\Psi(x_1, x_2 \dots x_N) = \frac{1}{\sqrt{N!}} \begin{vmatrix} \psi_1(x_1) & \psi_2(x_1) & \dots & \psi_N(x_1) \\ \psi_1(x_2) & \psi_2(x_2) & \dots & \psi_N(x_2) \\ \vdots & \vdots & \ddots & \vdots \\ \psi_1(x_N) & \psi_2(x_N) & \dots & \psi_N(x_N) \end{vmatrix} \quad (2.99)$$

The determinant is constructed by representing all possible assignments of electron i to all single-electron functions in each row. Hartree–Fock theory uses the variational principle in which the energy of the exact wavefunction serves as a lower bound to the energies calculated for a set of orthonormal orbitals.

DFT methods are based on the Hohenberg–Kohn theorem,²²¹ which states that all molecular electronic properties can be calculated if the electron density of the system is known. Although the exact form of all the components of the functional (a function of a function) that gives the energy from the electron density is not known, available functionals often provide an accurate description of many chemical properties. The Kohn–Sham formulation of DFT starts by considering a system of noninteracting N electrons. The electron density associated with a single Slater determinant representing a system of N noninteracting electrons is given by eqn (2.100):

$$\rho(r) = \int \sum_i^N |\psi_i(x)|^2 ds \quad (2.100)$$

Here, x represents the three space variables and the spin variable, and the integration is performed over the spin variable s . The Kohn–Sham equations derived from the Hohenberg–Kohn theorem may be written as eqn (2.101):^{222,223}

$$\left[-\frac{\nabla^2}{2} + v_{\text{eff}}(r) \right] \Psi_i(x) = \varepsilon_i \Psi_i(x) \quad (2.101)$$

The term v_{eff} is an effective potential that has a functional form with respect to the electron density $\rho(r)$ described by eqn (2.102):

$$v_{\text{eff}}(r) = - \sum_A \frac{Z_A}{|r - R_A|} + \int \frac{\rho(r')}{|r - r'|} dr' + v_{\text{XC}}(r) \quad (2.102)$$

The exchange correlation potential is defined as the functional derivative of the exchange correlation energy with respect to the density, as shown in eqn (2.103):

$$v_{\text{XC}}(r) = \frac{\delta E_{\text{XC}}[\rho]}{\delta \rho(r)} \quad (2.103)$$

The energy in Kohn–Sham theory is expressed as the sum of five different terms that, except for the nuclear–nuclear repulsion term V_{NN} , are all functions of the electron density ρ , as shown in eqn (2.104):

$$E[\rho] = V_{\text{NN}} + T_{\text{s}}[\rho] + V_{\text{eN}}[\rho] + J[\rho] + E_{\text{XC}}[\rho] \quad (2.104)$$

The noninteracting kinetic energy is obtained from the Kohn–Sham orbitals *via* eqn (2.105):

$$T_{\text{s}}[\rho] = -\frac{1}{2} \sum_i^N \langle \psi_i | \nabla^2 | \psi_i \rangle \quad (2.105)$$

Thus, the exchange correlation functional may be redefined to cover the part of the kinetic energy that is not included in $T_{\text{s}}[\rho]$ in the form of eqn (2.106):

$$E_{\text{XC}}[\rho] = E'_{\text{XC}}[\rho] + T[\rho] - T_{\text{s}}[\rho] \quad (2.106)$$

The Kohn–Sham equations are one-electron equations that can be solved iteratively, just like the Hartree–Fock equations. Electron correlation is incorporated with the exchange correlation potential $v_{\text{XC}}(r)$, whose form is unknown. Usually $E_{\text{XC}}[\rho]$ is separated in two parts, denoted as the exchange and correlation parts, which account for the interactions between electrons with the same spin and different spin, respectively.

The different functionals available for application to molecular systems can be divided into six classes: (i) functionals based on the local density approximation (LDA) that depend on the value of the electron density at any given point in space $\rho(r)$; (ii) functionals based on the generalized gradient approximation (GGA) that depend not only on the value of the electron density but also on its gradient $\nabla\rho(r)$; (iii) meta-GGA functionals that depend on the electron density, its gradient, and the kinetic energy density; (iv) hybrid functionals that can be divided into hybrid GGA and hybrid meta-GGA functionals and include a mixture of Hartree–Fock exchange with DFT exchange–correlation; (v) double-hybrid functionals that include nonlocal correlation effects through second-order perturbation treatment (*i.e.* MP2); and (vi) long-range corrected functionals that use a short term to include the DFT exchange interaction and a second term to account for long-range interactions.²²⁴ Some common density functionals are listed in Table 2.7.

In general, DFT methods provide a clear improvement over Hartree–Fock calculations without a dramatic increase of the computational cost. Given the broad range of functionals available in most computational packages, it is important to search the literature and select a functional that has been shown to perform well for similar problems and systems. Some studies have shown that functionals using the LDA approximation often predict too short Gd–ligand bonds and binding energies that are too high,²³⁸ and thus they are not recommended to investigate solution structures of Gd^{III}-based contrast agents. GGA functionals were also found to perform poorly compared to

Table 2.7 Some density functionals commonly used in molecular calculations.^a

Type	Functional	Exchange	Correlation	Ref.
GGA	PBE	PBE	PBE	225
	BLYP	B88	LYP	226, 227
	BP86	B88	P86	226, 228
	mPWLYP	mPW	LYP	227, 229
Hybrid	PBE0 (25%) ^a	PBE	PBE	230
	B3LYP (20%) ^a	B88	LYP	227, 231
	B3PW91 (20%) ^a	B88	PW91	226, 232
Meta-GGA	TPSS	TPSS	TPSS	233
	M06-L	Minnesota	Minnesota	234
Hybrid Meta-GGA	TPSSh (10%) ^a	TPSS	TPSS	233
	M06 (27%) ^a	Minnesota	Minnesota	235
	M06-2X (54%) ^a	Minnesota	Minnesota	235
Long-range corrected DFs	CAM-B3LYP	B3LYP including long-range corrections using the Coulomb attenuating method		224
	LC- ω PBE	Long-range corrected version of PBE		236
	DFT-D3	Conventional DFs including Grimme's empirical dispersion		237

^aThe % of Hartree–Fock exchange is indicated within parenthesis.

hybrid-GGA, meta-GGA, and hybrid meta-GGA functionals, and thus they should not be used to obtain accurate geometries of Gd^{III} complexes. The popular B3LYP functional was also found to provide larger deviations of Gd–N distances compared to meta-GGA (TPSS) and hybrid meta-GGA functionals (TPSSh, M06).²³⁹

In spite of the successful application of DFT to investigate many chemical problems, one should bear in mind the multiconfigurational character of Ln^{III} complexes due to the presence of quasi-degenerate ground states and low-lying excited states. Thus, Hartree–Fock and DFT are clearly not well suited to treat some specific chemical problems in Gd^{III}-based complexes, for example, magnetic properties. In such cases, multiconfigurational methods, such as the complete active space self-consistent field (CASSCF) and multireference configuration interaction (MRCI) methods, are necessary.²⁴⁰ CASSCF calculations have been applied in the past to relatively small Ln^{III} complexes, including Gd^{III} derivatives.^{241,242} However, the increasing computational power enables application of high-level *ab initio* wave function techniques to systems of practical relevance.²⁴³ For instance, CASSCF calculations have been applied to investigate the zero field splitting parameters of Gd^{III} complexes relevant as contrast agents for MRI.²⁴⁴ The CASSCF method divides orbitals into three different subspaces: (i) internal orbitals that are occupied in each Slater determinant; (ii) active orbitals that have varying occupations and thus are described by all possible Slater determinants (configuration state functions) that can be generated by

distributing N electrons in the M active orbitals; and (iii) virtual orbitals that are empty in all Slater determinants. Thus, in the case of Gd^{III} complexes ($4f^7$ configuration) the active space normally includes seven electrons in seven orbitals, which can be abbreviated as CAS(7,7). CASSCF provides qualitatively correct reference wavefunctions that can be employed for a subsequent treatment of dynamic correlation using second order multiconfigurational perturbation theory (*i.e.* CASPT2 or NEVPT2).^{245–249}

2.9.4 Basis Sets and Relativistic Effects

The molecular orbitals $\psi_1, \psi_2, \dots, \psi_N$ in eqn (2.99) are normally expressed in terms of a set of predefined functions known as basis functions χ_k described by eqn (2.107):

$$\Psi_i = \sum_k c_{ki} \chi_k \quad (2.107)$$

The coefficients of the molecular orbitals c_{ki} are determined using the self-consistent field (SCF) method. Most computational packages perform their calculations using Gaussian basis sets with the form described in eqn (2.108):

$$\chi_{\alpha, l_x, l_y, l_z}(z, y, z) = N \sum_{i=1}^n d_{ik} x^{l_x} y^{l_y} z^{l_z} e^{-\alpha r^2} \quad (2.108)$$

In eqn (2.108), $l_x + l_y + l_z = l$ determines the shape of the orbital, and α is the exponent that controls the width of the orbital. Large α values result in tight functions, and small α values give diffuse functions. n is the degree of contraction of the basis function, that is, the number of primitive functions composing the basis function. The d_{ik} coefficients are called contraction coefficients. Some program packages, in particular the ADF code,²⁵⁰ use Slater-type orbitals rather than Gaussian functions. Slater-type orbitals present $e^{-\alpha r}$ terms instead of the $e^{-\alpha r^2}$ dependence of Gaussian functions. Some programs (*i.e.* CPMD)²⁵¹ use plane waves that depend on e^{ikr} and are particularly useful to model periodic boundary conditions.

An important issue in the computational treatment of Gd^{III} complexes and other systems containing heavy elements is the inclusion of relativistic effects²⁵² because high nuclear charges have a strong influence on the shape and energy of the valence orbitals in heavy element systems.²⁵³ The importance that relativistic effects have for heavy elements can be understood by the following reasoning: The ground state energy of a 1s electron bound to a nucleus of charge $+Z$ equals $-Z^2/2$ atomic units, which corresponds to a kinetic energy of $+Z^2/2 = 1/2mv^2$, where m is the electron mass and v is the speed of the electron. The electron mass equals one atomic unit, and thus the average electron velocity at the nonrelativistic limit would be $v = Z$ atomic units. The speed of light in atomic units is $c = 137.036$, and therefore, for heavy nuclei, the electron velocities approach a substantial fraction of the

speed of light. The main consequences of relativity on the atomic orbitals of heavy elements are on radial contraction and energetic stabilization of the s and p shells, spin-orbit splitting, and radial expansion and energetic destabilization of the outer d and f shells.

Two different approaches have been developed to account for relativistic effects in systems containing heavy elements such as Gd^{III} complexes: (i) all-electron relativistic approaches and (ii) relativistic effective core potentials (RECP) that can be either pure scalar or include spin-orbital effects. The most widely used approximation for quantum chemical treatment of Gd^{III} complexes (and complexes of other Ln^{III} ions) is the RECP approach. RECP calculations explicitly treat only the chemically relevant valence electrons, and relativistic effects are implicitly accounted for by a proper adjustment of free parameters in the valence model Hamiltonian.²⁵⁴ Besides including the most important relativistic effects, the RECP approach also serves to decrease the computational cost so that calculations on relatively large Gd^{III} complexes become practical. Three different classes of RECPs and associated basis sets have been proposed for Gd^{III} and the other lanthanides: (1) the averaged relativistic RECPs with a [Xe] core and spin-orbit operators of Ross and co-workers;²⁵⁵ (2) the shape-consistent RECPs of Cundari and Stevens;²⁵⁶ and (3) the energy-consistent RECPs and associated basis sets of Dolg (Stuttgart–Cologne pseudopotentials).^{257–261} Two different core definitions have been developed for the latter RECPs: “large-core” in which the 4f electrons are included in the core and “small-core”, which treats the four, five, and six shell electrons explicitly. Both large-core and small-core pseudopotentials were developed to be used in *ab initio* molecular dynamics simulations in combination with plane wave basis sets.²⁶²

Large core RECPs take advantage of the fact that 4f orbitals do not significantly contribute to chemical bonding due to their limited radial extension as compared to the 5d and 6s shells. As a result of including the 4f electrons in the core, calculations of Gd^{III} complexes are conducted in a pseudo-singlet state, that is, as if the complex had a closed-shell configuration. This treatment of the 4f electrons simplifies calculations considerably so that geometry optimizations of relatively large systems become feasible. Large-core calculations sometimes overestimate the bond distances of the metal coordination environment compared to their small-core counterparts.^{263–265} However, in other instances both approaches were found to provide similar Gd–donor distances in complexes with polyaminocarboxylate ligands.²⁶⁶ Two different basis sets were derived for the energy-consistent small-core RECPs: a (14s13p10d8f6g)/[6s6p5d4f3g] atomic natural orbital (ANO) Gaussian valence basis set²⁶⁷ and a Gaussian (14s13p10d8f6g)/[10s8p5d4f3g] valence basis set using a segmented contraction scheme.²⁶⁸ Recent computational studies of Gd^{III} complexes found that DFT calculations with the latter basis set converge in some cases to a state with an unphysical electron spin density.²⁶⁹

The use of RECPs might not be appropriate for the treatment of some specific problems that can be better addressed by all-electron relativistic

approaches.^{270,271} The Douglas–Kroll–Hess (DKH) transformation-based methods^{272–274} and zero order regular approximation (ZORA)^{275–277} methods are the most widely tested and used all-electron relativistic approaches. Different studies showed that the ZORA and DKH approaches often provide results of similar quality.^{265,278} In some specific cases, relativistic all-electron calculations provide better results than RECP calculations, for instance, in the case of lanthanide mercaptobenzothiazolyl complexes, for which pseudopotential calculations led to a strong overestimation of the Ln–S bond lengths compared to all-electron relativistic calculations (up to 0.5 Å).²⁷⁹

Different basis sets have been proposed to be used for Gd^{III} and other lanthanides together with scalar relativistic Hamiltonians, including the Slater-type scalar relativistic all-electron basis sets for ZORA calculations included in the Amsterdam density functional code,²⁵⁰ the atomic natural orbital (ANO-RCC) basis set of Roos and co-workers for use with the DKH2 Hamiltonian,²⁸⁰ the DKH adapted basis set of Dolg,²⁸¹ and the SARC²⁸² and SARC2²⁸³ basis sets of Neese developed for use with both the DKH2 or ZORA approaches.

The use of RECP methods to model Gd^{III} complexes relevant as contrast agents for MRI requires a basis set to describe the ligand atoms. Generally the use of polarized valence double- ξ (*i.e.* 6-31G(d) and cc-pVDZ) or polarized valence triple- ξ (6-311G(d), 6-311G(d,p), cc-pVTZ or TZVP) basis sets provide similar bond distances of the Gd^{III} coordination environment.²³⁹ The use of diffuse functions generally does not significantly influence the quality of the calculated structures, although it is advisable to test the effect of diffuse functions when dealing with high negative charges. Non-polarized basis sets (3-21G, 6-31G or 6-311G) were found to provide artificially short bond distances of the metal coordination environment.²³⁹ Nonrelativistic basis sets should not be used in relativistic calculations (*i.e.* DKH or ZORA).

The program packages commonly used to perform quantum chemical calculations store internally the most common basis sets that can be indicated using appropriate keywords. Alternatively, basis sets can be specified in the input file using formats that vary from one package to another. Basis sets can be obtained from the original publications or from different databases (*i.e.* basis set exchange),^{284,285} which often provide basis sets and effective core potentials using formats suitable for different program packages. Alternatively, some groups offer their basis sets and ECPs in personal webpages (*i.e.* Stuttgart/Cologne ECPs²⁸⁶ or Sadler's basis sets for calculations of NMR properties).²⁸⁷

2.9.5 Solvent Effects

Due to their specific application in MRI, generally computational studies of Gd^{III}-based contrast agents aim at obtaining information regarding the structure and properties of the complexes in solution. Furthermore, potential candidates for Gd^{III}-based contrast agents are often complexes with

polyaminopolycarboxylate ligands having concentrated charge densities, so that solvent effects often have an important impact on the properties of the complex. Two different approaches have emerged to take into account solvent effects in quantum chemical calculations of Gd^{III} complexes: cluster calculations and the continuum models of solvation. Cluster calculations are performed using model clusters that explicitly include a second hydration shell.²⁸⁸ These calculations enable optimization of the energy minima and transition states required to study water-exchange reactions. Additionally, cluster calculations provide information regarding the second-sphere solvation shell,²⁸⁹ which provides an important contribution to the relaxivity of certain Gd^{III} complexes.^{26,106}

The main limitation of cluster calculations is that adding extra solvent molecules increases the computational cost and the number of minimum energy structures. Alternatively, bulk solvent effects can be considered with the aid of a continuum model. Two main types of continuum solvation models are available, the conductor-like screening model (COSMO) of Klamt and co-workers^{290,291} and the polarizable continuum model (PCM) of Tomasi.²⁹² In both variants, the cavity occupied by the solute is surrounded by apparent charges that polarize it as it would do a surrounding solvent. In the COSMO approximation the dielectric constant of the medium is changed from the specific finite value characteristic of each solvent to $\epsilon = \infty$, which corresponds to that of a conductor. On the other hand, the PCM approach calculates the magnitude of these apparent charges by considering that the molecule is surrounded by a polarizable continuum of the appropriate dielectric constant. The cavity containing the solute is often constructed with a series of interlocking spheres with appropriate radii that have to be parametrized. Thus, one should keep in mind that the results obtained with continuum models are strongly dependent on the model used to describe the solute cavity. Another limitation of continuum models of solvation is that they cannot account for specific solvent–solute interactions, which can be particularly important for charged solutes. Geometry optimizations using the PCM model were found to provoke a significant shortening of the Gd^{III}–N distances in complexes with polyaminocarboxylate ligands and a slight elongation of the Gd^{III}–O distances.²⁹³ The structures optimized in solution generally present a better agreement with reference crystallographic data than those optimized in the gas phase.

A strategy to overcome the limitations of continuum models is to use mixed cluster–continuum models that explicitly include a few second-sphere water molecules with bulk solvent effects being considered with a continuum model. In particular, the inclusion of a few water molecules involved in hydrogen-bonding interactions with the coordinated water molecule was found to be crucial to an accurate calculation of Gd^{III}–O_{water} distances (Figure 2.39),¹⁶ which decrease in the presence of explicit second-sphere water molecules while approaching the experimental Gd^{III}–O_{water} distance observed by X-ray crystallography.

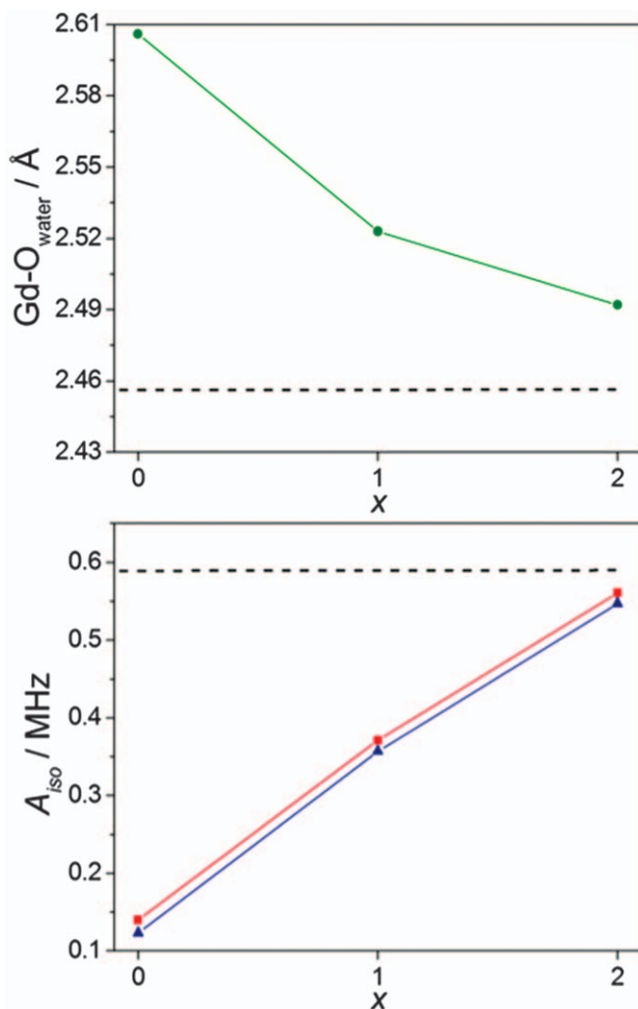


Figure 2.39 Bond distance of the coordinated water molecule ($\text{Gd-O}_{\text{water}}$) and ^{17}O hyperfine coupling constant (A_{iso}) calculated for the $[\text{Gd}(\text{DOTA})\text{-(H}_2\text{O)}]^- \cdot x\text{H}_2\text{O}$ systems using the TPSSh functional. Geometries were obtained using a polarized continuum approach and a large-core RECP, while A_{iso} values were computed using small-core (red squares) or all-electron DKH2 calculations (blue triangles). Dashed lines represent the experimental values.

2.9.6 Practical Aspects and Selected Examples

Figure 2.40 provides a schematic representation of a typical procedure used for the computational investigation of a Gd^{III} complex. The application of any computational method requires generating a collection of reasonable starting geometries that can be subsequently optimized using a method with a low computational cost. These methods might include MM,

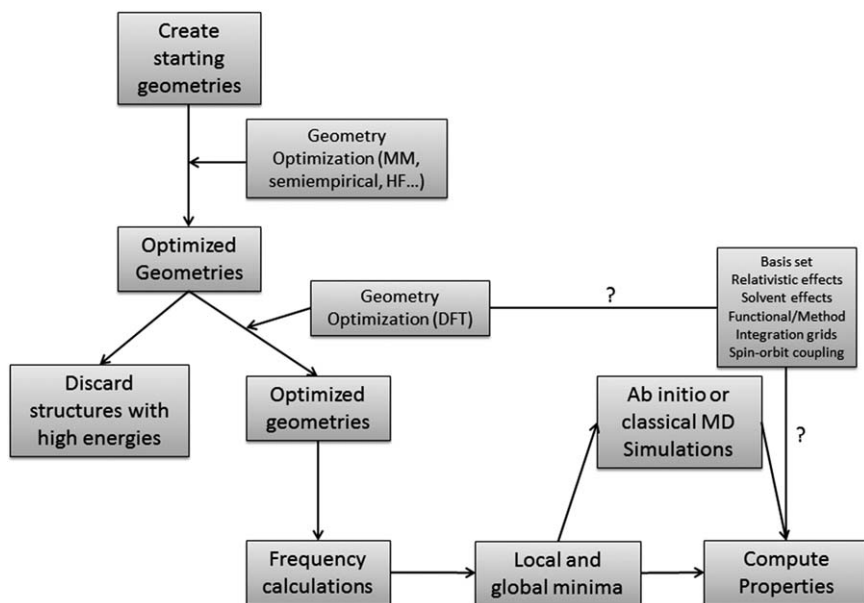


Figure 2.40 Flow chart showing a typical procedure for the characterization of a Gd^{III} complex using computational methods.

semi-empirical calculations, or Hartree–Fock or DFT calculations, likely using a large-core RECP and a small basis set to describe the ligand atoms (*i.e.* 3-21G or STO-3G). These geometry optimizations generate a number of reasonable structures for the system of interest, enabling the discarding of structures endowed with high energies. The remaining geometries (presumably local energy minima at the selected computational level) are then optimized at a higher computational level. This preliminary conformational screening is of critical importance to locate the global energy minima for the system of interest and perhaps other energy minima of chemical importance. At this point, it is also important to emphasize that any experimental information available for the concerned system should be considered to aid obtaining meaningful results (for example, structural information from X-ray or NMR data or the number of coordinated water molecules obtained with luminescence measurements). The investigation of conformational space is simpler for systems that have been extensively characterized by using experimental means. This is the case for Gd^{III} complexes with DOTA-like ligands, which are known to exist in solution in the form of two different diastereoisomers providing either square antiprismatic (SAP) or twisted square antiprismatic (TSAP) coordination geometries.²⁹⁴

Once the conformational space of the system has been screened, the relevant molecular geometries can be optimized using a higher computational level. The computational level selected at this stage should take into account a number of factors and will depend on the size of the system, the

computational resources available, and the precedents found in the literature. Generally DFT is the method of choice at this point because it often provides good molecular geometries of the complexes at a reasonable computational cost, providing that hybrid-GGA, meta-GGA, or hybrid meta-GGA functionals are employed. The large-core approximation usually provides reasonable results at a much smaller computational cost than small-core calculations. The computational time required to perform a geometry optimization depends on different factors, such as the number of basis functions used, the time required to achieve convergence of the SCF procedure and the number of geometries required to complete the optimization.²⁹⁵ Nevertheless, a rough estimate is that a geometry calculation using the small-core approach takes ~15 times more computational time than a similar optimization using the large-core approximation.²³⁹ Besides the selection of an RECP or an all-electron basis set for the metal ion (for DKH2 or ZORA calculations), an appropriate basis set should be selected to describe the ligand atoms. As a general rule, the best combination of method and basis set should be selected that considers the size of the system and the computational resources available. Another factor that might be important in DFT calculations is the use of an adequate (large enough) integration grid for numerical integration.

Geometry optimizations proceed by minimizing the energy of the system with respect to the nuclear coordinates, eventually leading to energy minima on the potential energy surface. At energy minima, the first derivatives of the energy and the forces are zero. However, the nature of the optimized geometries as true local energy minima should be confirmed in a subsequent frequency calculation. Molecular frequencies depend on the second derivative of the energy with respect to the nuclear coordinates. Besides providing the vibrational frequencies of the system, which can be compared to those obtained from IR or Raman spectra, frequency calculations also provide the zero point energies and thermal corrections required to obtain entropies and enthalpies. This set of data enables a comparison of the computational results with experimental data, for instance to analyze the population of different isomers in solution. Frequency calculations are also required to characterize transition states (saddle points) on the potential energy surface, which are characterized by one imaginary frequency.

The slow electron spin relaxation of Gd^{III} complexes often prevents the observation of any signals in their high-resolution NMR spectra. Thus, structural information about Gd^{III} complexes in solution is normally obtained using the NMR spectra of other Ln^{III} ions that present similar coordination properties. For instance, the conformational properties of Ln^{III} complexes with cyclen-based ligands have been extensively studied. In some cases, these studies provided not only the relative populations of the SAP and TSAP isomers, but also experimental values for the energy barriers and mechanisms characterizing the SAP and TSAP interconversion process.^{296,297} This is the case of the [Ln(DTMA)(H₂O)]³⁺ complexes, for which experimental and computational data are available for Ln=Eu and Lu,

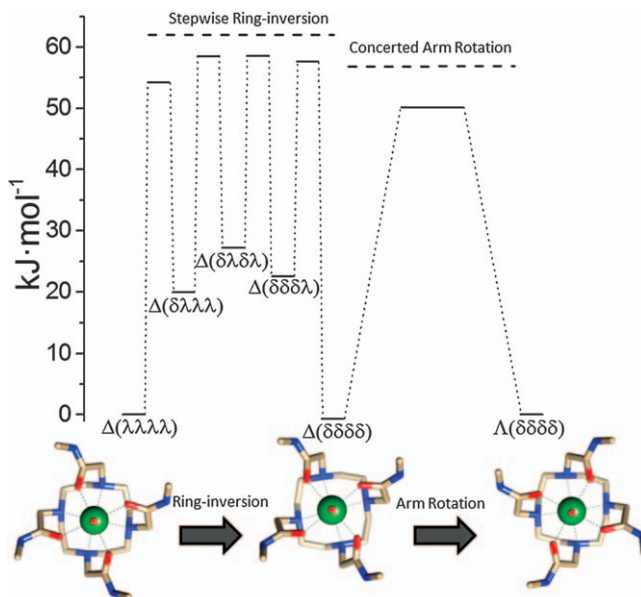


Figure 2.41 Energy profile obtained for the ring inversion and arm rotation processes in $[\text{Lu}(\text{DTMA})(\text{H}_2\text{O})]^{3+}$ calculated with DFT (B3LYP/LCRECP/6-31G(d)). The dashed horizontal lines represent the experimental values determined for the Eu^{III} analogue.

respectively.^{298,299} The SAP to TSAP interconversion (Figure 2.41) might proceed either through the inversion of the macrocyclic cyclen ring, whose conformation changes from $(\delta\delta\delta\delta)$ to $(\lambda\lambda\lambda\lambda)$, or *vice versa*, or by rotation of the four pendant arms of the ligand (either in a single step or by stepwise rotation of each pendant arm). DFT calculations performed on the $[\text{Ln}(\text{DTMA})(\text{H}_2\text{O})]^{3+}$ system using the large-core approximation provided a number of local energy minima that corresponded to different conformations of the cyclen ring (Figure 2.41). Among these local energy minima, those with the lowest energy correspond to the expected SAP and TSAP forms, and other minimum energy structures correspond to intermediates responsible for the stepwise inversion of each of the four five-membered chelate rings formed due to the coordination of the cyclen moiety. The different energy minima are connected by transition states in which the $\text{H}_2\text{C}-\text{CH}_2$ cyclen groups present eclipsed conformations. Furthermore, the SAP and TSAP isomers can be interconverted following a simultaneous rotation of the four pendant arms of the ligand. The transition states obtained with DFT provide activation free energies in good agreement with the experimental values while providing a detailed picture of the interconversion mechanism at the molecular level.

The molecular geometries obtained from the careful exploration of the conformational space might be subsequently employed to calculate different properties. These subsequent calculations might require using a different

method, basis set, or both with respect to those used in the previous optimization steps. In some cases, dynamic effects might have an important role in the property to be computed; DFT-based molecular dynamics simulations based on the Car–Parrinello approach³⁰⁰ might offer a straightforward access to dynamic processes occurring on the picosecond time-scale. Furthermore, the use of metadynamics to escape free-energy minima enables exploration of free-energy profiles along high-dimensional reaction coordinates, giving access to processes occurring on the time scale of hundreds of nanoseconds, like water-exchange reactions.³⁰¹ Trajectories obtained from molecular dynamics studies can be subsequently used to compute different properties, such as ¹H and ¹⁷O hyperfine coupling constants.³⁰² The isotropic ¹⁷O hyperfine coupling constants $A/\hbar = 2\pi A_{\text{iso}}$ that govern ¹⁷O-NMR chemical shifts and transverse relaxation rates can be obtained using DFT and the relationship in eqn (2.109):²²³

$$A_{\text{iso}} = \frac{4\pi}{3S} \beta_e \beta_N g_e g_N \rho^{\alpha-\beta}(R_N) \quad (2.109)$$

In eqn (2.109), β_N and β_e are the nuclear and Bohr magnetons, respectively; g_N and g_e are nuclear and free-electron g values, respectively; S is the total electron spin; and $\rho^{\alpha-\beta}(R_N)$ represents the difference between majority spin (α) and minority spin (β) densities at the position of the nucleus N . The calculation of A_{iso} requires an explicit description of the 4f electrons of Gd^{III}, preventing the use of the large-core approximation. As for the Gd–O_{water} distances, the explicit inclusion of a few second-sphere water molecules was found to be crucial to obtain A_{iso} values in good agreement with the experimental values (see the example of [Gd(DOTA)(H₂O)][−] in Figure 2.39). Furthermore, the use of the small-core approximation of relativistic DKH2 calculations gave nearly identical results.²⁹⁴ A similar approach provided an A_{iso} value of 0.42 MHz for [Gd(HP-DO3A)(H₂O)], while the average value obtained from the analysis of a 23 ps Car–Parrinello trajectory was 0.45 MHz.³⁰³ The two approaches give calculated values in excellent agreement with the experiment (0.46 MHz).⁵³

Although DFT calculations have been successful for the investigation of many chemical problems relevant to Gd^{III} complexes, some studies have revealed limitations. For instance, the calculation of zero-field splitting parameters of Gd^{III} complexes with DFT methods was found to be particularly problematic. The electronic ⁸S ground state of the Gd^{III} ion is characterized by an electronic spin state $S = 7/2$, which implies that the degeneracy of the magnetic sublevels $M_S = \pm 7/2, \pm 5/2, \pm 3/2$, and $\pm 1/2$ is broken in the absence of any applied magnetic field due to zero-field splitting effects.²⁴⁴ The phenomenological ZFS Hamiltonian contains the nine components of the 3×3 D -tensor, and can be expressed as eqn (2.110):³⁰³

$$\hat{H}_{\text{ZFS}} = \hat{\mathbf{S}}\mathbf{D}\hat{\mathbf{S}} \quad (2.110)$$

Taking a coordinate system that diagonalizes the \mathbf{D} tensor allows writing the ZFS Hamiltonian in terms of the usual axial and rhombic ZFS parameters D and E , expressed by eqn (2.111)–(2.113):

$$\hat{H}_{ZFS} = D \left(\hat{S}_z^2 - \frac{1}{3} \hat{S}^2 \right) + E (\hat{S}_x^2 - \hat{S}_y^2) \quad (2.111)$$

$$D = D_{zz} - \frac{1}{2} (D_{xx} + D_{yy}) \quad (2.112)$$

$$E = \frac{1}{2} (D_{xx} - D_{yy}) \quad (2.113)$$

The ZFS energy can be calculated from the values of the axial and rhombic ZFS parameters according to eqn (2.114):

$$\Delta = \sqrt{\frac{2}{3} D^2 + 2E^2} \quad (2.114)$$

The ZFS parameters of [Gd(HP-DO3A)(H₂O)] were calculated using different functionals along the trajectories of Car-Parrinello molecular dynamics simulations. These studies concluded that hybrid functionals significantly overestimate the magnitude of the splitting. Subsequent work found similar trends for different Gd^{III}-based model systems and complexes, such as [Gd(DOTA)(H₂O)]⁻ and [Gd(DTPA)(H₂O)]²⁻. Post-Hartree-Fock wave function methods based on the CASSCF approach provided more systematic and accurate results than DFT methods, which failed to reproduce experimental data and presented strong functional dependence. This discrepancy is illustrated in Figure 2.42, which provides a comparison between the absolute D values computed for the [GdF₆]³⁻ model system using CASSCF calculations and the pure and hybrid PBE and PBE0 functionals.²⁴⁴ In this example, the

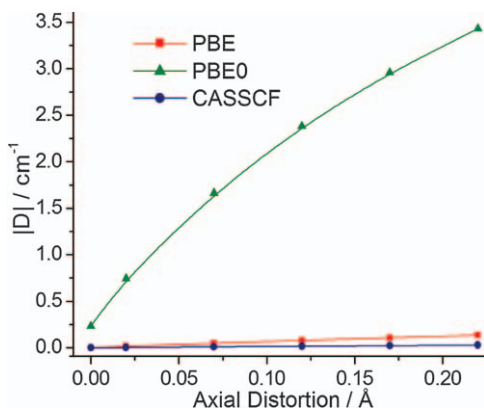


Figure 2.42 ZFS of GdF₆³⁻ under axial distortion computed using DFT methods and CASSCF calculations (data taken from ref. 244).

Table 2.8 Non-exhaustive list of the major program packages used for computational studies (in alphabetical order).

Program	Purpose and comments	Website	Ref.
ADF	DFT calculations of molecules with heavy atoms using all-electron STO basis sets	https://www.scm.com/	250
AMBER	Classical (MM) and QM/MM MD simulations	http://ambermd.org/	304
CPMD	Plane wave/pseudopotential implementation of DFT for <i>ab initio</i> MD	http://cpmd.org/	305
DALTON	General purpose package. Includes a linear-scaling Hartree–Fock and DFT code suitable for large molecular systems	http://www.daltonprogram.org/	306
GAUSSIAN	General purpose package for electronic structure calculations	http://gaussian.com/	307
GAMESS	General <i>ab initio</i> quantum chemistry package	http://www.msg.ameslab.gov/GAMESS/	308
GROMACS	Classical MD simulations	http://www.gromacs.org/	309
JAGUAR	<i>Ab initio</i> quantum chemical program specialized in molecular systems of medium and large size (focusing on DFT and MP2)	https://www.schrodinger.com/jaguar	310
MOLCAS	Multiconfigurational methods across the periodic table	http://www.molcas.org/	311
MOLPRO	General purpose (Hartree–Fock, DFT, coupled-cluster and multi-reference wave function methods)	http://www.molpro.net/	312
NWChem	General purpose. Supports both Gaussian and Plane wave basis sets as well as MM and QM/MM simulations	http://www.nwchem-sw.org/index.php/Main_Page	313
ORCA	General purpose tool for quantum chemistry with emphasis on open-shell molecules	https://orcaforum.cec.mpg.de/	314
SPARTAN	General purpose program that provides a rather wide range of methods from MM to post- Hartree–Fock wave function methods	https://www.wavefun.com/products/windows/Spartan16/win_spartan.html	315
TURBOMOLE	Quantum chemical calculations (DFT, MP2, coupled cluster methods) including MD	http://turbomole.com/	316

PBE0 functional overestimates the magnitude of the ZFS by several orders of magnitude, and this effect is much smaller for PBE, which predicts an opposite sign for the axial ZFS parameter D. This example showcases that, in spite of the successful application of DFT to a wide variety of problems, DFT has some limitations that might be overcome by post-Hartree–Fock methods.²⁴⁴

2.9.7 Software

Enormous progress has been made on the software and hardware required for the computational characterization of metal complexes, including classical and *ab initio* molecular dynamics, DFT methods and post-Hartree–Fock *ab initio* methods. A wide range of computational packages is available to perform these calculations, either commercial or free. Some of these program packages are conceived for a general-purpose application, providing access to a wide range of methods (Table 2.8). Other programs are specialized with respect to specific methods, such as molecular dynamics. Each program has its own strengths and weaknesses, and thus it is important to assess whether a given program is suitable to address a particular chemical problem. Other factors that are relevant when selecting one program or another include user friendliness, price, and availability.

2.9.8 Acknowledgements

The authors thank Ministerio de Economía y Competitividad (CTQ2013-43243-P and CTQ2015-71211-REDT) for generous financial support.

2.10 Acquiring Phantom Images

TIMOTHY J. SCHOLL

2.10.1 Image Formation in MRI

Magnetic resonance imaging is a modality that forms images of the spatial distribution of properties related to protons within a sample. These properties include local density, mobility, or the ability of their magnetic dipole moments to interact with the electromagnetic fields present from other nuclei in their vicinity (*i.e.*, T_1 -shortening or spin-lattice relaxation and T_2 -shortening or spin-spin relaxation). This range of properties leads to a large palette of possible contrasts for magnetic resonance images. For example, T_1 -weighted MRI contrast highlights portions of the sample with short T_1 values as bright voxels and T_2 weighting produces bright image voxels corresponding to long T_2 values. The type of image contrast is controlled by the details of image acquisition (pulse sequence) and choice of imaging parameters available within that sequence.

2.10.1.1 Magnetization and Relaxation

For an ensemble of protons, their magnetic dipole moments will be randomly oriented in space, and such ensembles have no net magnetization. The introduction of a static magnetic field, \mathbf{B}_0 , will cause these magnetic moments to precess around the local direction of the magnetic field at the Larmor frequency, given by the Larmor equation:

$$\omega_0 = \gamma \mathbf{B}_0 \quad (2.115)$$

where γ is a nuclear property of the proton known as the gyromagnetic ratio ($2.675 \times 10^8 \text{ rad s}^{-1} \text{ T}^{-1}$ for protons) related to its magnetic dipole moment. By convention, the z-axis of a Cartesian coordinate system is chosen to be along \mathbf{B}_0 . As the moments of the protons in the sample precess, a net magnetization develops in the direction of \mathbf{B}_0 by longitudinal (T_1) relaxation of the protons. That is to say, after introduction of the magnetic field, the distribution of precessing spins is slightly skewed in the direction of the magnetic field. However, complete relaxation of the nuclear spins is impossible due to the thermal energy associated with the finite temperature, T , of the sample. At thermal equilibrium, the magnitude of the longitudinal magnetization, M_0 of the sample is given by

$$M_0(x, y, z) = \frac{\rho_0(x, y, z) \gamma^2 \hbar^2}{4kT} \mathbf{B}_0 \quad (2.116)$$

where ρ_0 is the local spin (*i.e.*, proton) density.

The evolution of the magnetization, \mathbf{M} , is described by the Bloch equation:³¹⁷

$$\frac{d\mathbf{M}}{dt} = \gamma \mathbf{M} \times \mathbf{B}_0 + \frac{1}{T_1} (M_0 - M_z) \hat{\mathbf{z}} - \frac{1}{T_2} (M_x \hat{\mathbf{x}} + M_y \hat{\mathbf{y}}) \quad (2.117)$$

(Here $\hat{\mathbf{x}}$, $\hat{\mathbf{y}}$, and $\hat{\mathbf{z}}$ are unit vectors in the three Cartesian directions.) The first term after the equals sign describes the Larmor precession of the magnetization around the magnetic field; the second term governs the relaxation of the magnetization along \mathbf{B}_0 , which recovers at a rate characterized by the spin–lattice relaxation time constant, T_1 ; and the term containing T_2 describes the decay of the transverse components of \mathbf{M} , M_x and M_y .

The time evolution of the z-component of the magnetization depends only on T_1 , which governs spin–lattice relaxation. The longitudinal magnetization, M_z , asymptotically approaches the thermal equilibrium magnetization, M_0 , as:

$$M_z = M_0 + (M_{z0} - M_0) e^{-t/T_1} \quad (2.118)$$

assuming the initial magnetization at $t=0$ is given by M_{z0} . For the case where the initial longitudinal magnetization is zero (*i.e.*, after an excitation pulse tipping all the magnetization into the transverse plane), the recovery of magnetization is given by eqn (2.119).

$$M_z(t) = M_0(1 - e^{-t/T_1}) \quad (2.119)$$

Solutions for the transverse components of the magnetization are more complicated because their evolution is coupled by the Bloch equation. They are traditionally combined into a single quantity, M_{xy} , represented by a complex number made up of the x - and y -components of \mathbf{M} :

$$M_{xy}(t) = M_x(t) + iM_y(t) = M_{xy0} e^{-i\omega t} e^{-t/T_2} \quad (2.120)$$

Here, $M_{xy0} \equiv M_x(t=0) + iM_y(t=0)$ defines the initial transverse magnetization after excitation. If the initial conditions are assumed to be $M_x(0) + iM_y(0) = M_0$, then application of Euler's formula yields:

$$M_{xy}(t) = M_0(\cos \omega t - i \sin \omega t) e^{-t/T_2} \quad (2.121)$$

Therefore, the transverse magnetization is a vector rotating at the Larmor frequency, ω , in the xy -plane with an exponentially decreasing magnitude characterized by the spin–spin T_2 value. As this rotation is occurring, the longitudinal magnetization is growing asymptotically to the thermal equilibrium.

2.10.1.2 Gradients and k-Space

In addition to the main (static) magnetic field, which produces sample magnetization, an electromagnetic (or radiofrequency) field, \mathbf{B}_1 , that

matches the Larmor frequency is also required to produce a magnetic resonance image. The purpose of B_1 is to perturb (excite) the longitudinal magnetization away from the z-axis so that the resulting precession in the transverse plane can be measured by the detection coils. For NMR experiments, this perturbation is all that is required; however, to spatially encode the location of the excited magnetization, a third hardware component is required: the magnetic gradient fields, G .

Gradient fields are produced by an independent system of three electromagnets that can add a linearly varying magnetic field to modulate a spatially uniform static field in one or more of three orthogonal (Cartesian) directions. Because the uniform main magnetic field, $B_0 = B_0 \hat{z}$, is oriented along the axis of bore of the scanner, the total magnetic field along the z-axis at any time, t , and position (x, y, z) is given by

$$B_z(x, y, z, t) = B_0 + G_x(t)x + G_y(t)y + G_z(t)z \quad (2.122)$$

where $G_x = \frac{dB_z}{dx}$, $G_y = \frac{dB_z}{dy}$, and $G_z = \frac{dB_z}{dz}$. Under the control of the gradients, the Larmor frequency, $\omega = \gamma B_z$, becomes spatially and temporally dependent, and the equation for M_{xy} must be modified to include this dependence:

$$M_{xy}(t) = M_{xy0} e^{-i\omega t} e^{-t/T_2} = M_{xy0} e^{-i\gamma B_0 t} e^{-i\gamma \int_0^t (G_x(t)x + G_y(t)y + G_z(t)z) dt} e^{-t/T_2} \quad (2.123)$$

Here, the accumulated phase, ϕ , of the transverse magnetization at time t is the sum of phases from the main magnetic field and the gradient fields:

$$\phi = \gamma \left(B_0 t + \int_0^t (G_x(t)x + G_y(t)y + G_z(t)z) dt \right) \quad (2.124)$$

The precessing transverse magnetization is detected as a voltage induced in a receiving antenna, known as a radio-frequency coil. This coil is often the same radio-frequency hardware used to excite the longitudinal magnetization. The magnetic resonance signal received by the radio-frequency coil depends on several factors, including details of the radio-frequency coil geometry and the spatial distribution of M_{xy} ; however, in its simplest form, the MR signal at any time t is proportional to the integral over the entire distribution of M_{xy} :

$$S(t) \propto \omega_0 \iiint M_{xy}(x, y, z, t) dx dy dz \quad (2.125)$$

The factor ω_0 arises from induction of the voltage in the radio-frequency coil and is often omitted. Therefore, the signal equation is equal to

$$S(t) \propto \iiint M_{xy0} e^{-i\gamma B_0 t} e^{-i\gamma \int_0^t (G_x(t)x + G_y(t)y + G_z(t)z) dt} e^{-t/T_2} dx dy dz \quad (2.126)$$

Signals acquired from MRI systems are demodulated by the resonant frequency $\omega_0 = \gamma B_0$, and the exponential function $e^{-i\gamma B_0 t}$ can be dropped from the signal equation to yield:

$$S(t) \propto \iiint M_{xy0} e^{-i\gamma \int_0^t (G_x(t)x + G_y(t)y + G_z(t)z) dt} e^{-t/T_2} dx dy dz \quad (2.127)$$

Likewise, the exponential function e^{-t/T_2} governs spin-spin relaxation, affecting only signal magnitude and not localization, can be omitted for simplicity.

The simplest method for acquiring an MR image is to select only a finite portion or “slice” of the longitudinal magnetization of the sample. This is known as “slice selection”. The resulting two-dimensional distribution of precessing spins is then spatially encoded by manipulating the gradient field. In principle, this slice can be of arbitrary thickness and location and be in any plane. As an example, the excited transverse magnetization, $M_{\text{slice}}(x, y)$ in a slice parallel to the xy -plane centered at z_0 , with thickness Δz , integrated along the z -direction is given by:

$$M_{\text{slice}}(x, y) = \int_{z_0 - \frac{\Delta z}{2}}^{z_0 + \frac{\Delta z}{2}} M_{xy0}(x, y, z) dz \quad (2.128)$$

The resulting signal equation can be reduced to a two-dimensional integration over x and y :

$$S(t) \propto \iint M_{xy0} e^{-i\gamma \int_0^t (G_x(t)x + G_y(t)y) dt} dx dy \quad (2.129)$$

This equation is often rewritten in terms of the quantities:

$$k_x(t) = \frac{\gamma}{2\pi} \int_0^t G_x dt \quad \text{and} \quad k_y(t) = \frac{\gamma}{2\pi} \int_0^t G_y dt \quad (2.130)$$

These quantities are positional variables in a space known as k -space. k -Space describes the spatial frequency content of the imaged object and is related to image space *via* Fourier transformations. Written in terms of k -space variables, k_x and k_y , the signal equation becomes:

$$S(k_x, k_y) \propto \iint M_{\text{slice}}(x, y) e^{-i2\pi k_x(t)x} e^{-i2\pi k_y(t)y} dx dy \quad (2.131)$$

where the time dependence is implicit in the spatial frequencies $k_x(t)$ and $k_y(t)$. This expression can be interpreted to mean that for the implementation of linear encoding gradients, the signal $S(k)$ represents the Fourier transform of the magnetization and, hence, the spin density, ρ_0 . In other words, the spin density is Fourier-encoded by the linear gradients, in this example, along the x - and y -axes. Therefore, the distribution of spin density

in the sample, $\rho_0(x,y,z)$, integrated from $(z_0 - \Delta z/2)$ to $(z_0 + \Delta z/2)$ is obtained by taking the inverse Fourier transform of $S(k)$:

$$\int_{z_0 - \frac{\Delta z}{2}}^{z_0 + \frac{\Delta z}{2}} \rho_0(x,y,z) dz \propto \iint S(k_x, k_y) e^{+i2\pi k_x x} e^{+i2\pi k_y y} dk_x dk_y \quad (2.132)$$

In MRI, image reconstruction is the process of converting acquired k -space data into image data by application of a discrete inverse Fourier transformation, in this example, a two-dimensional transformation. The center region of k -space, represented by small values of k_x and k_y , determines the low spatial frequency data, overall image brightness and signal-to-noise ratio. The exact center of k -space ($k_x = k_y = 0$) represents the total transverse magnetization excited in the slice, and, as such, it contains the highest signal in the entire space.

2.10.1.3 Image Formation

The process of image formation for MRI can be roughly broken down into a number of sequential steps: longitudinal magnetization relaxation of the sample, volume selection and excitation, transverse magnetization and relaxation, spatial encoding, and signal acquisition. These steps are repeated multiple times to fill k -space. Finally, an MR image is formed or reconstructed by inverse Fourier transformation.

2.10.1.4 Slice Selection

Spin-lattice relaxation of a sample results in the accrual of longitudinal magnetization, as described above. For two-dimensional imaging, a slab of this magnetization known as a slice is chosen. This selection is accomplished by applying a slice-selecting gradient along an axis perpendicular to the plane of the desired slice (z -axis, for example). This produces a linear variation of Larmor frequencies for transverse magnetization excited in that region. Slice-only excitation is achieved by application of an appropriate radio-frequency pulse (\mathbf{B}_1 field) with an apparent frequency content that closely matches only the range of Larmor frequencies contained within the slice. The frequency of the radio-frequency pulse is chosen to match the Larmor frequency ($F_{z_0} = \gamma/2\pi(B_0 + G_z z_0)$) of the center of the slice at $z = z_0$. Because each slice has a finite extent (Δz), the range of frequencies, ΔF , within that slab is related to the slice-selective gradient by:

$$\Delta F = \gamma/2\pi G_z \Delta z \quad (2.133)$$

which must be uniformly excited by the \mathbf{B}_1 field. This excitation is ideally accomplished by application of a \mathbf{B}_1 field at the resonant frequency for the center of the slice, which is amplitude-modulated by a sinc function:

$$B_1(t) = A \frac{\sin(\Delta F \pi t)}{\Delta F \pi t} \sin F_{z_0} \quad (2.134)$$

where A is an amplitude determined by radio-frequency-coil parameters and the desired excitation (flip) angle. The term ΔF is known as the transmit bandwidth of the radio-frequency pulse. An ideal sinc function has uniform frequency content over the bandwidth ΔF and no frequency content outside that band. However, in practice, the sinc function undergoes apodization to limit the number of side lobes. Thus, temporal width is reduced, reducing spatial selectivity to a minor extent. The use of stronger slice-selective gradients produces a greater range in Larmor frequencies after excitation, and in principle, improves spatial selectivity for a given radio-frequency pulse.

2.10.1.5 Spatial Encoding

The sample is considered to be made up of a matrix of volume elements, known as voxels, which are three-dimensional analogs of pixels in a two-dimensional image. Spatial encoding is the process of imprinting the MR signal with information so that the signal can be localized to individual voxels. This localization is accomplished by application of gradients to frequency encode and phase encode in the two remaining directions after slice selection (for this example, using the G_x and G_y gradients).

The k -space variables k_x and k_y can be controlled within k -space because they are the time integrals of their respective gradients to systematically acquire k -space signal data. For typical MRI imaging sequences, k -space is acquired in Cartesian fashion, one k -space line at a time. After slice excitation using the G_z gradient and an appropriate radio-frequency pulse, the G_y gradient is applied for a fixed time interval, Δt , which causes the transverse magnetization to accrue a changing phase along the y -direction of the slice:

$$\phi(y) = \gamma \int_0^{\Delta t} G_y y \, dt \quad (2.135)$$

This accruing of a changing phase is known as phase encoding, and G_y is the phase-encoding gradient in this example. Subsequently, the G_x gradient is turned on during signal acquisition by the receiving coil so that the frequency of the acquired signal varies linearly along the x -axis of the signal. This is known as frequency encoding, and by analogy G_x is the frequency-encoding gradient.

A pulse sequence is a series of instructions to the hardware controlling the gradient and radio-frequency systems to specify the gradient axes and temporal waveforms for spatial encoding and synchronize their timing with application of radio-frequency excitation and subsequent reception. As mentioned previously, k -space data are typically acquired as one line of k -space at a time oriented along one of the Cartesian axes. This systematic acquisition is accomplished by repeated application of the phase-encoding gradient followed by the frequency-encoding gradient to control the

sampling path through k -space after slice selection. The result is a systematic path for acquisition of the MR signal throughout the k -space matrix.

Before the k -space trajectories can be specified, several parameters must be chosen by the user. This includes phase- and frequency-encode directions, image field-of-view (FOV), and the desired spatial resolution. FOV_x and FOV_y determine the spatial imaging extent along the x - and y -directions, respectively. These can be different lengths, but they are practically limited by the volume of \mathbf{B}_0 homogeneity and the extent of gradient linearity. Field-of-view is inversely related to the sample spacing of k -space along that direction so that:

$$\text{FOV}_x = \frac{1}{\Delta k_x} \quad \text{and} \quad \text{FOV}_y = \frac{1}{\Delta k_y} \quad (2.136)$$

For a given field-of-view, image resolution is determined by the number of voxels, N_x and N_y , along those two directions. This collection of voxels is known as the imaging matrix. The image resolution along the i th axis is given by FOV_i/N_i .

Therefore, the image resolution along the i th axis is calculated as:

$$\frac{\text{FOV}_i}{N_i} = \frac{1}{N_i \Delta k_i} = \frac{1}{2k_{i\max}} \quad (2.137)$$

where $2k_{i\max}$ is the total extent of k -space along the i th Cartesian direction and is sometimes known as the k -space field-of-view, k_{FOV} . Increasing k_{FOV_x} , k_{FOV_y} , or both decreases the image voxel size along that dimension. This decreasing of voxel size is achieved by increasing the image matrix size in that direction (N_x and N_y). Decreasing the sample spacing of k -space increases the field-of-view in image space along that direction. The center of k -space contains information about the gross image shape and contains the majority of image signal-to-noise ratio and contrast. The periphery of k -space contains information related to the finest image details and sharp edges.

After all k -space has been acquired by a pulse sequence, a two-dimensional image can be constructed from the k -space data by a two-dimensional inverse Fourier transformation. This process can be generalized from two-dimensional to three-dimensional imaging. Instead of slice selection, an extended volume is excited by a low-amplitude gradient along the z -axis, for example. Spatial information along this axis is encoded by the addition of another phase-encoding gradient to the pulse sequence in addition to the two-dimensional phase- and frequency-encoding gradients. This requires a third k -space dimension, k_z , which is the time integral of the z -axis gradient:

$$k_z(t) = \frac{\gamma}{2\pi} \int_0^t G_z dt \quad (2.138)$$

A three-dimensional Fourier transformation is used to reconstruct the resulting three-dimensional data set in image space.

2.10.2 MRI Pulse Sequences

A pulse sequence is a set of instructions for the MRI hardware controlling the generation and timing of the radio-frequency and gradient pulses that are used to acquire imaging data. There are two general families of MRI pulse sequences known as spin echo and gradient-recalled-echo sequences.³¹⁸ Spin-echo sequences use a train of radio-frequency pulses to create a series of signal echoes whose signal intensities can be measured. Gradient-recalled-echo sequences use a single radio-frequency excitation pulse followed by gradient pulse to produce signal echoes. In general, spin-echo sequences require longer acquisition times but produce images with better quality than gradient-recalled-echo sequences.

2.10.2.1 Spin-echo Sequences

For spin-echo sequences, the entire longitudinal magnetization is excited into the transverse plane by a 90° radio-frequency pulse. The transverse magnetization simultaneously begins to dephase *via* spin-spin interactions (T_2) and magnetic-field inhomogeneities (T_2^*) as the longitudinal magnetization begins to recover (T_1). A 180° radio-frequency pulse is applied at a time equal to half the echo time (TE). This 180° pulse begins the process of rephasing of the transverse magnetization, which is complete at the echo time. The resulting echo, often referred to as a Hahn echo, is acquired as a frequency-encoded signal.³¹⁹ In the simplest implementation of a spin-echo sequence, one line of k -space is acquired per Hahn echo. The sequence can employ an echo train consisting of several 180° refocusing pulses spaced by the echo time for a single 90° radio-frequency excitation. This incorporation of several pulses permits the acquisition of a larger number of k -space lines per sequence repetition time (TR), decreasing image acquisition time, and is known as a fast spin-echo sequence. However, dephasing of transverse magnetization that is related to random spin-spin interactions or diffusion is not recoverable, and each refocused echo is reduced in amplitude by an amount governed by T_2 . The use of long echo train lengths with short echo times reduces image acquisition times at the expense of image blurring and reduced contrast. This combination has a larger effect on T_1 -weighted and proton-density images, restricting long echo train lengths to fewer than eight echoes. Fast spin-echo sequences are usually employed for rapid acquisition of images with T_2 -weighting.

2.10.2.2 Gradient-Recalled-Echo Sequences

Gradient-recalled-echo sequences employ a single radio-frequency excitation pulse and omit the formation of a Hahn echo.³¹⁸ Instead, the transverse magnetization during free induction decay is rapidly dephased by application of a brief pulse of the frequency-encoding gradient, immediately followed by a second pulse with opposite polarity for rephasing. Because the

gradients cannot refocus dephasing due to field inhomogeneity or susceptibility mismatches, gradient-focused echoes have echo amplitudes governed by T_2^* decay. Therefore, echo times must be much shorter than for spin-echo sequences. The ability to use short echo times is possible because gradient pulses have shorter durations than 180° radio-frequency pulses, producing reduced minimum echo times for gradient-recalled-echo sequences.

MRI acquisition consists of multiple repetitions of a pulse sequence containing periods of longitudinal magnetization growth, radio-frequency excitation, spatial encoding, and generation of signal echoes for acquisition. For every pulse sequence, there are several parameters that define this intricate interplay of waveforms and the acquisition of the NMR signal. These parameters include the sequence repetition time (TR), the echo time (TE), and radio-frequency flip angles (α). Gradient-recalled-echo imaging can be divided into two cases depending upon the choice of sequence repetition time.

2.10.2.2.1 Gradient-recalled-echo Imaging ($TR \gg T_2$). When a gradient-recalled-echo sequence is set up with a long repetition time compared with the spin-spin relaxation time, the transverse magnetization will completely decay before the next radio-frequency excitation. However, the sequence repetition time is still typically shorter than the spin-lattice relaxation time, T_1 , and as a result, longitudinal magnetization is not fully recovered to its initial value given by thermal equilibrium, M_0 , prior to the next sequence repetition. As a result, a new steady-state magnetization, M_{ss} , is reached after several sequence repetition times, which is given by the Ernst Equation:

$$M_{ss} = M_0 \frac{1 - e^{-TR/T_1}}{1 - e^{-TR/T_1} \cos \alpha} \quad (2.139)$$

This new steady-state magnetization is maximized for given values of the sequence repetition time and T_1 by the Ernst angle, $\alpha = \cos^{-1}[\exp(-TR/T_1)]$. Compared with spin-echo imaging using 90 and 180° radio-frequency pulses to achieve maximum signal intensity for Hahn echoes, the radio-frequency excitation pulses for gradient-recalled-echo sequences are much smaller than 90° . For most imaging, the largest signal intensities are produced for flip angles in the range of 40 to 50° that produce T_1 -weighting. However, tissue contrast is often improved at larger angles. For example, the contrast between white and gray matter is maximized for $60^\circ \leq \alpha \leq 80^\circ$.

2.10.2.2.2 Fast Gradient-Recalled-Echo Imaging ($TR < T_2$). For this case, when the sequence repetition time is shorter than T_2 , the transverse magnetization, M_{xy} , does not fully decay before the next radio-frequency excitation pulse. As a result, both the longitudinal magnetization, M_z , and the remaining M_{xy} contribute to the signal in the next sequence repetition,

leading to a complicated steady-state magnetization. Therefore, the signal intensity for fast gradient-recalled-echo imaging is also dependent on T_2 in addition to flip angle, sequence repetition time, and T_1 . Gradient-recalled-echo sequences can be classified as either coherent (refocused) or incoherent (spoiled), depending on how they deal with the residual transverse magnetization.

Transverse magnetization remaining from a previous sequence repetition can interact with the next excitation radio-frequency pulse, producing Hahn or partial echoes that add to the free-induction decay. These interactions are known as transverse coherences. For incoherent (spoiled) gradient-recalled-echo sequences, transverse coherences are eliminated by the application of radio-frequency or gradient spoiling. For radio-frequency spoiling, the phase of the radio-frequency carrier for the excitation pulse is systematically changed from one sequence repetition to the next. Gradient spoiling is accomplished by pulsing the slice-select or frequency-encoding gradient before the end of each sequence repetition with variable amplitude. Spoiling leads to images with either T_1 - or proton-density-weighting. Alternatively, the sequence can include additional rewinding gradient pulses to completely refocus the transverse magnetization before the end of each sequence repetition. In addition, the phase of each excitation pulse is alternated between 0 and 180° for successive sequence repetition times. Variations of this method lead to a large subfamily of refocused gradient-recalled-echo sequences with mixed T_1 - and T_2 -weighted contrast depending on sequence parameters.

An important difference between spin-echo and gradient-recalled-echo sequences is the inability of gradient refocusing to rephase transverse magnetization affected by magnetic field inhomogeneities leading to T_2^* decay of the echo amplitudes. As a result, gradient-recalled-echo sequences are sensitive to sharp changes in magnetic susceptibility. For gradient-recalled-echo sequences with long echo times, there can be almost complete signal loss in vicinities such as air–tissue interfaces. Spin-echo sequences are more immune to these artifacts. Nevertheless, the T_2^* -sensitivity of gradient-recalled-echo sequences is useful for functional MRI, where T_2^* -weighted contrast is sensitive to differences in blood oxygen levels for assessment of brain activity. Other important applications of T_2^* -weighted gradient-recalled-echo sequences include the detection of cerebral microbleeds in stroke patients and perfusion mapping of cerebral blood flow and volume.

2.10.3 Effect of T_1 and T_2 on Image Contrast

Magnetic resonance images are regional representations of three basic properties of protons associated with water molecules found in tissue. These include proton density, spin–lattice or longitudinal relaxation time (T_1), and spin–spin or transverse relaxation time (T_2). Different tissues have different proton densities and exhibit different T_1 and T_2 relaxation. Tissues with short T_1 values such as fat, fatty bone marrow, or those enhanced by

paramagnetic contrast agents have brighter contrast in T_1 -weighted images. Fluids and tissue with high free-water content have long T_2 values and appear bright in T_2 -weighted images. Particular combinations of signal repetition times, echo times, and flip angles produce image contrast that is largely determined by one of these three properties leading to T_1 -weighted, T_2 -weighted, and proton-density-weighted images.

Anatomy is often best depicted using T_1 -weighting. The addition of paramagnetic contrast agents that increase spin-lattice relaxation of nearby tissues can help enhance pathologies. However, T_2 -weighted images typically produce the best contrast to highlight disease because higher water content is usually found in tissues involved with many pathological processes. Consequently, increased brightness is produced in the vicinity of those tissues. Proton-density weighted MR images are usually used to depict anatomy, but can also be useful for delineation of disease.

Repetition and echo times are key parameters that influence image contrast for MRI. Precise values for these times depend on the choice of pulse sequence and tissues under investigation. The use of short sequence repetition times, particularly with T_1 -weighted images, will highlight tissues with innate fast spin-lattice relaxation or tissues with enhanced relaxation as a result of the presence of a contrast agent. Long repetition times enable discrimination of tissues by their spin-lattice relaxation times. Specifying long echo times sensitizes images to tissues or fluids with longer values of T_2 , particularly for T_2 -weighted imaging. For a combination of long sequence repetition time and short echo time, no distinction can be made between longitudinal magnetization recovery and transverse magnetization decay, and the resulting images will have contrast dominated by proton density. Approximate values for repetition times (TR), echo times (TE), and flip angles (α) used for achieving these image contrasts at clinical field strengths are shown in Table 2.9 for spin-echo and gradient-recalled-echo sequences.

2.10.4 Measurement of T_1 and T_2 Time Constants by MRI

Quantitative MRI involves the regional measurement of tissue parameters including relaxation time constants, T_1 and T_2 , as well as proton density. Disease can be characterized and segmented based on comparison with healthy tissue. Although examination of T_1 - and T_2 -weighted imaging can point to local pathological conditions, subtle differences between vendor pulse sequences and hardware as well as sequence parameter prescription can lead to variations in image contrast that cloud image interpretation, particularly across imaging centers. The use of quantitative MRI for tissue segmentation can reduce this problem by acquisition of physical tissue properties that are less subject to differences in pulse sequence and hardware. As acquisition strategies for quantitative MRI become more efficient, the use of this technique has increased in both research and clinical settings. For example, early tumor progression in the brain has been examined using T_1 and T_2 mapping. Quantitative MRI has been used for brain tissue

Table 2.9 Approximate values for repetition times (T_R), echo times (T_E), and flip angles (α) used for achieving image contrasts at clinical field strengths.

Spin echo Contrast	T_R (ms)	T_E (ms)	α (°)	Gradient echo Contrast	T_R (ms)	T_E (ms)	α (°)
T_1 -weighted	<750	<40	90	T_1 -weighted	<50	<10	>50
T_2 -weighted	>2000	>75	90	T_2 -weighted	>100	>30	<40
Proton-density-weighted	>2000	<40	90	Proton-density-weighted	>100	<10	<40

segmentation to assess neurological diseases, such as those associated with brain atrophy. Myocardial edema can be assessed with non-contrast-enhanced quantitative MRI following reperfusion after ischemia.

The spin-echo pulse sequence is the gold standard for T_1 and T_2 mapping.³²⁰ For T_1 measurement, the spin-echo sequence is combined with inversion recovery. A preparatory 180° radio-frequency pulse is used to invert the longitudinal magnetization, M_0 , after which it begins to relax. Later, the spin-echo sequence, beginning with a 90° radio-frequency pulse, is used to measure longitudinal magnetization. The interval between the 180 and 90° radio-frequency pulses is known as the inversion time, TI . Two implementations of the spin-echo with inversion recovery method are widely used in clinical imaging. Short inversion time inversion recovery (STIR) and fluid-attenuated inversion-recovery (FLAIR) sequences are frequently used to null signals from fat and cerebral spinal fluid, respectively.

The spin-echo with inversion recovery sequence is repeated for a range of inversion time values to acquire a set of images that can be analyzed to produce inversion recovery curves that can be analyzed on a pixel-by-pixel basis to extract regional T_1 values. Signal recovery data as a function of inversion time is fit by an exponential recovery function:

$$S(TI) = A(1 - Be^{-t/T_1}) \quad (2.140)$$

This formulation assumes perfect spoiling of the transverse magnetization prior to each subsequent excitation. Although reliable, this is a time-consuming process. The pulse sequence is repeated for a range of inversion times, with a maximum value of three to four times the expected T_1 value for best accuracy. Furthermore, the sample needs to be fully relaxed prior to inversion, leading to long sequence repetition times equal to approximately five T_1 times.

Impetus for clinical T_1 mapping of brain tissue has led to the development of several faster methods including the Look-Locker and variable-flip-angle methods. The Look-Locker method³²¹ prepares the longitudinal magnetization with an inverse pulse, θ . However, instead of acquiring a single sample on the inversion recovery curve, a train of N regularly-spaced (τ), low-angle (α), radio-frequency pulses interspersed with rapid gradient-recalled-echo readout are employed to sample the relaxing magnetization.

The resulting signal after the n th sampling pulse is described by eqn (2.141).³²⁰

$$S_n = \sin \alpha M_n e^{-T_D/T_2^*} \quad (2.141)$$

T_D is the delay between the sampling pulse, α , and the readout.

Functions, M_n and F are given by:

$$M_n = M_0 [F + (\cos \alpha E_2)^{n-1}(Q - F)] \quad (2.142)$$

and:

$$F = (1 - E_2)/(1 - \cos \alpha E_2) \quad (2.143)$$

where:

$$Q = \frac{F \cos \theta \cos \alpha E_r E_1 [1 - (\cos \alpha E_2)^{N-1}] + \cos \theta E_1 (1 - E_r) - E_1 + 1}{1 - \cos \theta \cos \alpha E_r E_1 (\cos \alpha E_2)^{N-1}} \quad (2.144)$$

Finally:

$$E_1 = e^{-TI/T_1} \quad (2.145)$$

$$E_2 = e^{-\tau/T_1} \quad (2.146)$$

$$E_r = e^{-t_r/T_1} \quad (2.147)$$

and:

$$t_r = TR - TI - (N - 1)\tau \quad (2.148)$$

The Look-Locker method is sensitive to \mathbf{B}_1 field inhomogeneities because it assumes perfect radio-frequency pulses with negligible duration. This sensitivity can be reduced for larger choices of τ .

The variable-flip-angle method is capable of mapping spin-lattice relaxation in all three spatial dimensions within a clinically feasible time.³²² This method uses two or more spoiled gradient-recalled-echo scans prescribed with the same sequence-repetition-time and echo-time parameters but with different flip angles, α_n . The signal for the n th scan is given by eqn (2.149).

$$S_n = \frac{PD(1 - e^{-TR/T_1}) \sin \alpha_n}{1 - \cos \alpha_n e^{-TR/T_1}} \quad (2.149)$$

This formulation assumes perfect spoiling of the transverse magnetization prior to excitation for the next sequence repetition. Relative to the Look-Locker method, the variable-flip-angle method is sensitive to \mathbf{B}_1 field inhomogeneities, and a field map is typically acquired as well as a proton-density-weighted image to improve accuracy.

The benchmark method for T_2 mapping employs a single-echo spin-echo pulse sequence that is repeated with a set of echo times varied from a few to

hundreds of milliseconds. A 90° radio-frequency excitation pulse is used with a long sequence repetition time to eliminate T_1 -weighting. Mapping times can be decreased by multi-echo spin-echo imaging or the use of T_2 -prepared balanced-steady-state-free-precession methods.^{323,324}

The signal intensity of a balanced-steady-state-free-precession sequence acquired after spin inversion and a magnetization-preparation pulse of $\alpha/2$ is well approximated by a longitudinal relaxation curve with an apparent relaxation time, T_1^* , that depends on T_1 , T_2 , and flip angle. This sequence can be used to map both T_1 and T_2 by fitting T_1^* curves acquired at different flip angles with theoretical response curves.

2.10.5 Field-strength Dependencies

Spin-lattice relaxation and spin-spin relaxation times are important parameters for MRI protocols. These parameters depend on a host of factors such as temperature, tissue type, pH, and magnetic field strength. Because the density of protons varies little between different tissues, *in vivo* imaging derives contrast from differences in predominantly T_1 and T_2 values among tissues and pathologies of tissue such as tumors and inflammation. As clinical field strengths increase, this has an important effect on relaxation and tissue contrast. Measurement of relaxation as a function of magnetic field is known as nuclear magnetic relaxation dispersion (NMRD). NMRD measurements of spin-lattice and spin-spin interactions show that there is a larger change in relaxation for T_1 of tissues than for T_2 , with T_1 values for different tissues growing and converging as a function of field strength.

Some of the earliest measurements of T_1 relaxation of tissue were *ex vivo* measurements of rodent and later human tissue samples.^{325–327} Early T_1 -dispersion measurements were made by magnetizing samples in an NMR magnet and then applying a 180° inversion pulse before rapidly transporting the sample to the fringe field for relaxation.³²⁷ The sample is then returned to the magnet, and the remaining magnetization sampled by a 90° excitation pulse and acquisition of the resulting free induction decay. This process is repeated as the relaxation time is varied logarithmically from short intervals to several expected T_1 values to build up a T_1 decay curve. The shuttle times for these systems are relatively slow, and this becomes a serious systematic error for measurements at low fields where T_1 values are short. NMRD measurements for field strengths below 1 T are typically acquired using fast magnetic field-cycling relaxometry (Section 2.2.1).⁵¹ In this method, samples are magnetized at a high magnetic field strength (~ 1 T), and then the magnetic field is rapidly ramped down to a lower field strength for a short duration of relaxation before the magnetic field is cycled to the acquisition field strength, where the remaining magnetization is sampled as a free induction decay after a 90° radio-frequency pulse. The magnetic field can be ramped from full field strength (1 T) to ~ 0.25 mT in less than 5 ms. This ability to rapidly change field strength facilitates accurate measurement of

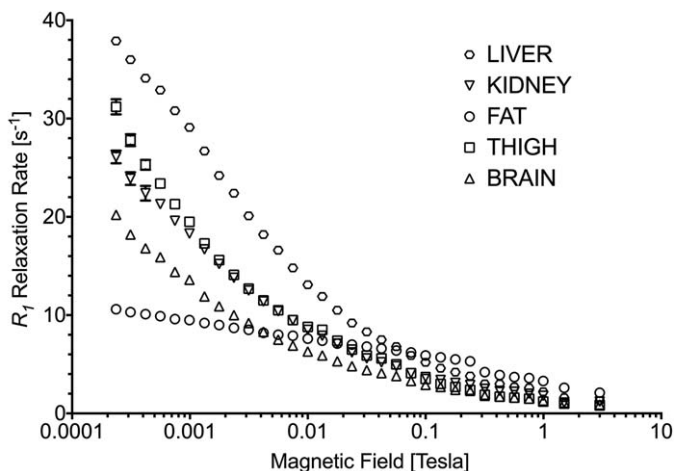


Figure 2.43 Field dependence of spin–lattice relaxation of tissues.

samples with fast spin–lattice relaxation with the possibility of precise temperature control because the sample remains stationary during the measurement.

The relaxation of water protons in tissue is predominantly a result of interactions at the interfaces of cytoplasmic proteins.^{328,329} It has been shown that a small number of water-binding sites with efficient relaxation-inducing properties comprising less than 1% of the interface area are responsible for almost all of the observed relaxation. Binding of water to proteins reduces the molecular motion of the water molecules. A full discussion of relaxation theory applied to this situation is found in Section 2.1. In general, for liquids, spin–lattice and spin–spin relaxation rates ($1/T_1$ and $1/T_2$, respectively) vary differently with magnetic field strength. At low fields, these rates are nearly equal. For larger field strengths, $1/T_1$ approaches zero and $1/T_2$ approaches approximately 0.3 times the low-field value of $1/T_1$. This situation holds for semi-solids such as tissues. NMRD data for rodent tissues illustrate the field dependence of spin–lattice relaxation up to the clinical field strength of 3 T (Figure 2.43).

Dispersion of T_1 is evident for almost all tissue types. At fields greater than 3 T, spin–lattice relaxation rates for different tissues converge to zero. This means that although high-field MRI is capable of producing images of exquisite detail, particularly in the brain, image contrast between tissue types is often limited in comparison to images acquired at lower field strengths.

References

1. *Contrast Agents I: Magnetic Resonance Imaging*, ed. W. Krause, *Topics in Current Chemistry*, Vol. 221, Springer, Heidelberg, 2002.
2. D. Canet, *Adv. Inorg. Chem.*, 2005, 57, 3.

3. R. B. Lauffer, *Chem. Rev.*, 1987, **87**, 901.
4. S. Aime, M. Botta, M. Fasano and E. Terreno, *Chem. Soc. Rev.*, 1998, **27**, 19.
5. É. Tóth, L. Helm and A. Merbach, *Relaxivity of Gadolinium(III) Complexes: Theory and Mechanism, in The Chemistry of Contrast Agents in Medical Magnetic Resonance Imaging*, ed. A. Merbach, L. Helm and É. Tóth, Wiley, Chichester, 2nd ed., 2013, Chapter 2, pp. 25–81.
6. H. Jaccard, P. Miéville, C. Cannizzo, C. R. Mayer and L. Helm, *J. Biol. Inorg. Chem.*, 2014, **19**, 145.
7. A. Fontes, S. Karimi, L. Helm, M. Yulikov, P. M. Ferreira and J. P. André, *Eur. J. Inorg. Chem.*, 2015, 1579.
8. Z. Luz and S. Meiboom, *J. Chem. Phys.*, 1964, **40**, 2686.
9. T. J. Swift and R. E. Connick, *J. Chem. Phys.*, 1962, **37**, 307.
10. J. Kowalewski, L. Nordenskiöld, N. Benetis and P.-O. Westlund, *Prog. Nucl. Magn. Reson. Spectrosc.*, 1985, **17**, 141.
11. L. Banci, I. Bertini and C. Luchinat, *Nuclear and Electron Relaxation: the Magnetic Nucleus-Unpaired Electron Coupling in Solution*, VCH, Weinheim, 1991.
12. J. Kowalewski, D. Kruk and G. Parigi, *Adv. Inorg. Chem.*, 2005, **57**, 41.
13. L. Helm, *Prog. Nucl. Magn. Reson. Spectrosc.*, 2006, **49**, 45.
14. M. Gueron, *J. Magn. Reson.*, 1975, **19**, 58.
15. O. V. Yazyev, L. Helm, V. G. Malkin and O. L. Malkina, *J. Phys. Chem. A*, 2005, **109**, 10997.
16. D. Esteban-Gómez, A. de Blas, T. Rodríguez-Blas, L. Helm and C. Platas-Iglesias, *ChemPhysChem*, 2012, **13**, 3640.
17. M. Rubinstein, A. Baram and Z. Luz, *Mol. Phys.*, 1971, **20**, 67.
18. N. Bloembergen and L. O. Morgan, *J. Chem. Phys.*, 1961, **34**, 842.
19. N. Benetis, J. Kowalewski, L. Nordenskiöld, H. Wennerström and P.-O. Westlund, *Mol. Phys.*, 1983, **48**, 329.
20. T. Nilsson and J. Kowalewski, *Mol. Phys.*, 2000, **98**, 1617.
21. D. Kruk, T. Nilsson and J. Kowalewski, *Phys. Chem. Chem. Phys.*, 2001, **3**, 4907.
22. N. Schaeffle and R. Sharp, *J. Magn. Reson.*, 2005, **176**, 160.
23. S. Rast, P. H. Fries, E. Belorizky, A. Borel, L. Helm and A. E. Merbach, *J. Chem. Phys.*, 2001, **115**, 7554.
24. P. H. Fries and E. Belorizky, *J. Chem. Phys.*, 2007, **126**, 204503.
25. M. Botta, *Eur. J. Inorg. Chem.*, 2000, 399.
26. K. I. Hardcastle, M. Botta, M. Fasano and G. Digilio, *Eur. J. Inorg. Chem.*, 2000, 971.
27. J. Kotek, P. Lebdušková, P. Hermann, L. Vander Elst, R. N. Muller, C. F. G. C. Geraldes, T. Maschmeyer, I. Lukeš and J. A. Peters, *Chem.—Eur. J.*, 2003, **9**, 5899.
28. Y. Ayant, E. Belorizky, P. Fries and J. Rosset, *J. Phys.*, 1977, **38**, 325.
29. L.-P. Hwang and J. H. Freed, *J. Chem. Phys.*, 1975, **63**, 4017.
30. J. H. Freed, *J. Chem. Phys.*, 1978, **68**, 4034.
31. C. F. Polnaszek and R. G. Bryant, *J. Chem. Phys.*, 1984, **81**, 4038.

32. C. C. Lester and R. G. Bryant, *J. Phys. Chem.*, 1990, **94**, 2843.
33. T. C. Farrar and E. D. Becker, *Pulse and Fourier Transform NMR: Introduction to Theory and Methods*, Academic Press, New York, 1971.
34. M. L. Martin, G. J. Martin and J.-J. Delpuech, *Practical NMR Spectroscopy*, Heyden, London, 1980.
35. J. Keeler, *Understanding NMR Spectroscopy*, Wiley, Singapore, 2nd ed., 2010.
36. F. A. Dunand, L. Helm and A. E. Merbach, *Adv. Inorg. Chem.*, 2003, **54**, 1.
37. R. L. Vold, J. S. Waugh, M. P. Klein and D. E. Phelps, *J. Chem. Phys.*, 1968, **48**, 3831.
38. A. D. Bain, *J. Magn. Reson.*, 1990, **89**, 153.
39. W. S. Warren, S. L. Hammes and J. L. Bates, *J. Chem. Phys.*, 1989, **91**, 5895.
40. X.-a. Mao, J.-x. Guo and C.-h. Ye, *Chem. Phys. Lett.*, 1994, **222**, 417.
41. M. P. Augustine, *Prog. Nucl. Magn. Reson. Spectrosc.*, 2002, **40**, 111.
42. A. Allerhand and H. S. Gutowsky, *J. Chem. Phys.*, 1964, **41**, 2115.
43. A. Allerhand and E. Thiele, *J. Chem. Phys.*, 1966, **45**, 902.
44. J. P. Carver and R. E. Richards, *J. Magn. Reson.*, 1972, **6**, 89.
45. D. G. Davis, M. E. Perlman and R. E. London, *J. Magn. Reson. B*, 1994, **104**, 266.
46. S. Wagner, T. R. J. Dinesen, T. Rayner and R. G. Bryant, *J. Magn. Reson.*, 1999, **140**, 172.
47. A. G. Redfield, *Magn. Reson. Chem.*, 2003, **41**, 753.
48. F. Noack, *Prog. Nucl. Magn. Reson. Spectrosc.*, 1986, **18**, 171.
49. R. Kimmich and E. Anoardo, *Prog. Nucl. Magn. Reson. Spectrosc.*, 2004, **44**, 257.
50. G. Ferrante and S. Sykora, *Adv. Inorg. Chem.*, 2005, **57**, 405.
51. E. Anoardo, G. Galli and G. Ferrante, *Appl. Magn. Reson.*, 2001, **20**, 365.
52. C. Ammann, P. Meier and A. E. Merbach, *J. Magn. Reson.*, 1982, **46**, 319.
53. S. Laurent, L. Vander Elst and R. N. Muller, *Contrast Media Mol. Imaging*, 2006, **1**, 128.
54. P. H. Fries, G. Ferrante, E. Belorizky and S. Rast, *J. Chem. Phys.*, 2003, **119**, 8636.
55. E. Belorizky, P. H. Fries, L. Helm, J. Kowalewski, D. Kruk, R. R. Sharp and P.-O. Westlund, *J. Chem. Phys.*, 2008, **128**, 052315.
56. E. Belorizky and P. H. Fries, *Phys. Chem. Chem. Phys.*, 2004, **6**, 2341.
57. P. H. Fries, *Eur. J. Inorg. Chem.*, 2012, **2012**, 2156.
58. L. Moriggi, A. Aebischer, C. Cannizzo, A. Sour, A. Borel, J.-C. G. Bünzli and L. Helm, *Dalton Trans.*, 2009, 2088.
59. F. A. Dunand, É. Tóth, R. Hollister and A. E. Merbach, *J. Biol. Inorg. Chem.*, 2001, **6**, 247.
60. G. M. Nicolle, É. Tóth, K.-P. Eisenwiener, H. R. Mäcke and A. E. Merbach, *J. Biol. Inorg. Chem.*, 2002, **7**, 757.
61. P. Caravan, *Chem. Soc. Rev.*, 2006, **35**, 512.
62. K. Adzhamli, E. Toth, M. P. Periasamy, S. H. Koenig, A. E. Merbach and M. D. Adams, *Magn. Reson. Mater. Phys., Biol. Med.*, 1999, **8**, 163.

63. D. H. Powell, O. M. N. Dhubhghaill, D. Pubanz, L. Helm, Y. S. Lebedev, W. Schlaepfer and A. E. Merbach, *J. Am. Chem. Soc.*, 1996, **118**, 9333.
64. L. Helm, G. M. Nicolle and A. E. Merbach, *Adv. Inorg. Chem.*, 2005, **57**, 327.
65. N. Graepi, D. H. Powell, G. Laurenczy, L. Zékány and A. E. Merbach, *Inorg. Chim. Acta*, 1995, **235**, 311.
66. M. C. Alpoim, A. M. Urbano, C. F. G. C. Geraldés and J. A. Peters, *J. Chem. Soc., Dalton Trans.*, 1992, 463.
67. K. Djanashvili and J. A. Peters, *Contrast Media Mol. Imaging*, 2007, **2**, 67.
68. J. A. Peters, J. Huskens and D. J. Raber, *Prog. Nucl. Magn. Reson. Spectrosc.*, 1996, **28**, 283.
69. E. L. Que, E. Gianolio, S. L. Baker, A. P. Wong, S. Aime and C. J. Chang, *J. Am. Chem. Soc.*, 2009, **131**, 8527.
70. C. F. G. C. Geraldés and C. Luchinat, *Met. Ions Biol. Syst.*, 2003, **40**, 513.
71. I. Bertini and C. Luchinat, *NMR of Paramagnetic Molecules in Biological Systems*, The Benjamin/Cummings Publishing Company, Inc., Menlo Park, CA, 1986.
72. I. Bertini, C. Luchinat, G. Parigi and R. Pierattelli, *ChemBioChem*, 2005, **6**, 1536.
73. I. Bertini, P. Turano and A. J. Vila, *Chem. Rev.*, 1993, **93**, 2833.
74. G. R. Choppin and D. R. Peterman, *Coord. Chem. Rev.*, 1998, **174**, 283.
75. W. D. Horrocks Jr. and M. Albin, *Lanthanide Ion Luminescence in Coordination Chemistry and Biochemistry*, in *Progress in Inorganic Chemistry*, Vol. 31, ed. S. J. Lippard, Wiley, Hoboken, NJ, 1984, pp. 1–104.
76. W. D. Horrocks Jr. and D. R. Sudnick, *Acc. Chem. Res.*, 1981, **14**, 384.
77. A. Beeby, I. M. Clarkson, R. S. Dickins, S. Faulkner, D. Parker, L. Royle, A. S. de Sousa, J. A. G. Williams and M. Woods, *J. Chem. Soc., Perkin Trans. 2*, 1999, 493.
78. D. Parker, *Chem. Soc. Rev.*, 2004, **33**, 156.
79. J. R. Morrow and C. M. Andolina, *Spectroscopic Investigations of Lanthanide Ion Binding to Nucleic Acids*, in *Interplay between Metal Ions and Nucleic Acids*, ed. A. Sigel, H. Sigel and R. K. O. Sigel, *Metal Ions in Life Sciences 10*, Springer, Dordrecht, The Netherlands, 2012, pp. 171–199.
80. J.-C. G. Bünzli, *Acc. Chem. Res.*, 2006, **39**, 53.
81. S. V. Eliseeva and J.-C. G. Bünzli, *Chem. Soc. Rev.*, 2010, **39**, 189.
82. *Luminescence of Lanthanide Ions in Coordination Compounds and Nanomaterials*, ed. A. De Bettencourt-Dias, Wiley, West Sussex, U.K., 2014.
83. G. Stein and E. Würzberg, *J. Chem. Phys.*, 1975, **62**, 208.
84. D. Parker, R. S. Dickins, H. Puschmann, C. Crossland and J. A. K. Howard, *Chem Rev.*, 2002, **102**, 1977.
85. D. Parker and J. A. G. Williams, *J. Chem. Soc., Dalton Trans.*, 1996, 3613.
86. S. Cotton, *Lanthanide and Actinide Chemistry*, Wiley, West Sussex, England, 2006, Chapter 5, pp. 61–88.
87. J.-C. G. Bünzli and G. R. Choppin, *Lanthanide Probes in Life, Chemical and Earth Sciences: Theory and Practice*, Elsevier, New York, 1989.

88. A. K. R. Junker, M. Tropiano, S. Faulkner and T. J. Sørensen, *Inorg. Chem.*, 2016, **55**, 12299.
89. M. Albin and W. D. Horrocks Jr., *Inorg. Chem.*, 1985, **24**, 895.
90. S. T. Frey and W. D. Horrocks Jr., *Inorg. Chim. Acta*, 1995, **229**, 383.
91. W. D. Horrocks Jr., G. F. Schmidt, D. R. Sudnick, C. Kittrell and R. A. Bernheim, *J. Am. Chem. Soc.*, 1977, **99**, 2378.
92. N. Sabbatini, M. Guardigli and I. Manet, *Antenna Effect in Encapsulation Complexes of Lanthanide Ions*, in *Handbook on the Physics and Chemistry of Rare Earths*, Vol. 23, Elsevier, North Holland, Amsterdam, 1996.
93. W. D. Horrocks Jr. and D. R. Sudnick, *Science*, 1979, **206**, 1194.
94. W. D. Horrocks Jr. and D. R. Sudnick, *J. Am. Chem. Soc.*, 1979, **101**, 334.
95. R. M. Supkowski and W. D. Horrocks Jr., *Inorg. Chim. Acta*, 2002, **340**, 44.
96. R. S. Dickins, D. Parker, A. S. de Sousa and J. A. G. Williams, *Chem. Commun.*, 1996, 697.
97. S. Amin, D. A. Voss Jr., W. D. Horrocks Jr., C. H. Lake, M. R. Churchill and J. R. Morrow, *Inorg. Chem.*, 1995, **34**, 3294.
98. C. M. Andolina, W. G. Holthoff, P. M. Page, R. A. Mathews, J. R. Morrow and F. V. Bright, *Appl. Spectrosc.*, 2009, **63**, 483.
99. R. M. Supkowski and W. D. Horrocks Jr., *Inorg. Chem.*, 1999, **38**, 5616.
100. W. D. Horrocks Jr., V. K. Arkle, F. J. Liotta and D. R. Sudnick, *J. Am. Chem. Soc.*, 1983, **105**, 3455.
101. I. Sánchez-Lombardo, C. M. Andolina, J. R. Morrow and A. K. Yatsimirsky, *Dalton Trans.*, 2010, **39**, 864.
102. J. H. S. K. Monteiro, A. de Bettencourt-Dias, I. O. Mazali and F. A. Sigoli, *New J. Chem.*, 2015, **39**, 1883.
103. A. Mishra, P. Fousková, G. Angelovski, E. Balogh, A. K. Mishra, N. K. Logothetis and É. Tóth, *Inorg. Chem.*, 2008, **47**, 1370.
104. J. Hammell, L. Buttarazzi, C.-H. Huang and J. R. Morrow, *Inorg. Chem.*, 2011, **50**, 4857.
105. R. S. Dickins, S. Aime, A. S. Batsanov, A. Beeby, M. Botta, J. I. Bruce, J. A. K. Howard, C. S. Love, D. Parker, R. D. Peacock and H. Puschmann, *J. Am. Chem. Soc.*, 2002, **124**, 12697.
106. E. Balogh, M. Mato-Iglesias, C. Platas-Iglesias, É. Tóth, K. Djanashvili, J. A. Peters, A. de Blas and T. Rodríguez-Blas, *Inorg. Chem.*, 2006, **45**, 8719.
107. F. Yerly, F. A. Dunand, É. Tóth, A. Figueirinha, Z. Kovács, A. D. Sherry, C. F. G. C. Geraldés and A. E. Merbach, *Eur. J. Inorg. Chem.*, 2000, 1001.
108. A. V. Astashkin, A. M. Raitsimring and P. Caravan, *J. Phys. Chem. A*, 2004, **108**, 1990.
109. S. G. Zech, W.-C. Sun, V. Jacques, P. Caravan, A. V. Astashkin and A. M. Raitsimring, *ChemPhysChem*, 2005, **6**, 2570.
110. A. M. Raitsimring, A. V. Astashkin, D. Baute, D. Goldfarb, O. G. Poluektov, M. P. Lowe, S. G. Zech and P. Caravan, *ChemPhysChem*, 2006, **7**, 1590.

111. A. M. Raitsimring, A. V. Astashkin, D. Baute, D. Goldfarb and P. Carvan, *J. Phys. Chem. A*, 2004, **108**, 7318.
112. P. Caravan, A. V. Astashkin and A. M. Raitsimring, *Inorg. Chem.*, 2003, **42**, 3972.
113. D. Parker, H. Puschmann, A. S. Batsanov and K. Senanayake, *Inorg. Chem.*, 2003, **42**, 8646.
114. S. Aime, A. Barge, J. I. Bruce, M. Botta, J. A. K. Howard, J. M. Moloney, D. Parker, A. S. de Sousa and M. Woods, *J. Am. Chem. Soc.*, 1999, **121**, 5762.
115. J. E. Penner-Hahn, *Coord. Chem. Rev.*, 2005, **249**, 161.
116. Q. Ma, M. Jebb, M. F. Tweedle and L. J. Wilson, *J. Mater. Chem. B*, 2013, **1**, 5791.
117. P. Caravan, J. J. Ellison, T. J. McMurry and R. B. Lauffer, *Chem. Rev.*, 1999, **99**, 2293.
118. S. Aime, M. Botta and E. Terreno, *Adv. Inorg. Chem.*, 2005, **57**, 173.
119. B. N. Siriwardena-Mahanama and M. J. Allen, *Molecules*, 2013, **18**, 9352.
120. A. L. Thompson, D. Parker, D. A. Fulton, J. A. K. Howard, S. U. Pandya, H. Puschmann, K. Senanayake, P. A. Stenson, A. Badari, M. Botta, S. Avedano and S. Aime, *Dalton Trans.*, 2006, 5605.
121. J. A. Peters, *Contrast Media Mol. Imaging*, 2016, **11**, 160.
122. M. Botta and L. Tei, *Eur. J. Inorg. Chem.*, 2012, 1945.
123. T. L. James, *Nuclear Magnetic Resonance in Biochemistry: Principles and Applications*, Academic Press, New York, 1975, pp. 38–40.
124. L. Vander Elst, S. Laurent, H. M. Bintoma and R. N. Muller, *Magn. Reson. Mater. Phys., Biol. Med.*, 2001, **12**, 135.
125. J. Henig, É. Tóth, J. Engelmann, S. Gottschalk and H. A. Mayer, *Inorg. Chem.*, 2010, **49**, 6124.
126. L. Vander Elst, F. Maton, S. Laurent, F. Seghi, F. Chapelle and R. N. Muller, *Magn. Reson. Med.*, 1997, **38**, 604.
127. T. K. Hitchens and R. G. Bryant, *J. Phys. Chem.*, 1995, **99**, 5612.
128. S. Aime, M. Botta and G. Ermondi, *J. Magn. Reson.*, 1991, **92**, 572.
129. D. Neuhaus and M. P. Williamson, *The Nuclear Overhauser Effect in Structural and Conformational Analysis*, Wiley-VCH, New York, 2nd ed., 2000.
130. W. D. Kim, G. E. Kiefer, F. Maton, K. McMillan, R. N. Muller and A. D. Sherry, *Inorg. Chem.*, 1995, **34**, 2233.
131. S. Aime, A. Barge, A. Borel, M. Botta, S. Chemerisov, A. E. Merbach, U. Müller and D. Pubanz, *Inorg. Chem.*, 1997, **36**, 5104.
132. K. H. Chalmers, E. De Luca, N. H. M. Hogg, A. M. Kenwright, I. Kuprov, D. Parker, M. Botta, J. I. Wilson and A. M. Blamire, *Chem.—Eur. J.*, 2010, **16**, 134.
133. L. Vander Elst, A. Roch, P. Gillis, S. Laurent, F. Botteman, J. W. M. Bulte and R. N. Muller, *Magn. Reson. Med.*, 2002, **47**, 1121.
134. F. A. Dunand, A. Borel and A. E. Merbach, *J. Am. Chem. Soc.*, 2002, **124**, 710.
135. S. Aime, M. Botta, M. Fasano and E. Terreno, *Acc. Chem. Res.*, 1999, **32**, 941.

136. A. D. Sherry and Y. Wu, *Curr. Opin. Chem. Biol.*, 2013, **17**, 167.
137. R. Negri, Z. Baranyai, L. Tei, G. B. Giovenzana, C. Platas-Iglesias, A. C. Bényei, J. Bodnár, A. Vágner and M. Botta, *Inorg. Chem.*, 2014, **53**, 12499.
138. S. Karimi, L. Tei, M. Botta and L. Helm, *Inorg. Chem.*, 2016, **55**, 6300.
139. S. Aime, A. Barge, M. Botta, D. Parker and A. S. De Sousa, *J. Am. Chem. Soc.*, 1997, **119**, 4767.
140. C. Vigouroux, E. Belorizky and P. H. Fries, *Eur. Phys. J. D*, 1999, **5**, 243.
141. S. Karimi and L. Helm, *Inorg. Chem.*, 2016, **55**, 4555.
142. S. Aime, M. Botta, M. Fasano, S. Paoletti, P. L. Anelli, F. Uggeri and M. Virtuani, *Inorg. Chem.*, 1994, **33**, 4707.
143. S. Aime, M. Botta, M. Fasano, S. G. Crich and E. Terreno, *Coord. Chem. Rev.*, 1999, **185–186**, 321.
144. S. Dumas, V. Jacques, W.-C. Sun, J. S. Troughton, J. T. Welch, J. M. Chasse, H. Schmitt-Willich and P. Caravan, *Invest. Radiol.*, 2010, **45**, 600.
145. L. Tei, G. Gugliotta, Z. Baranyai and M. Botta, *Dalton Trans.*, 2009, 9712.
146. S. Aime, M. Botta, S. G. Crich, G. Giovenzana, R. Pagliarin, M. Sisti and E. Terreno, *Magn. Reson. Chem.*, 1998, **36**, S200.
147. M. Botta, S. Aime, A. Barge, G. Bobba, R. S. Dickins, D. Parker and E. Terreno, *Chem.—Eur. J.*, 2003, **9**, 2102.
148. *Inductively Coupled Plasma Emission Spectroscopy, Part 1: Methodology, Instrumentation, and Performance*, ed. P. W. J. M. Boumans, *Chemical Analysis*, Vol. 90, Wiley, New York, 1987.
149. *Inductively Coupled Plasma Emission Spectroscopy, Part 2: Applications and Fundamentals*, ed. P. W. J. M. Boumans, *Chemical Analysis*, Vol. 90, Wiley, New York, 1987.
150. NIST Atomic Spectra Database Lines Form [Online]. http://physics.nist.gov/PhysRefData/ASD/lines_form.html (last accessed 2017).
151. W. Li, P. Simmons, D. Shrader, T. J. Herrman and S. Y. Dai, *Talanta*, 2013, **112**, 43.
152. R. Thomas, *Practical Guide to ICP-MS: a Tutorial for Beginners*, CRC Press, Baton Rouge, 3rd ed., 2013.
153. T. W. May and R. H. Wiedermeyer, *At. Spectrosc.*, 1998, **19**, 150.
154. S. Aime, M. Botta, M. Fasano and E. Terreno, Chemical Shift and Relaxation Reagents in NMR, in *Encyclopedia of Spectroscopy and Spectrometry*, ed. J. C. Lindon, G. E. Tranter and D. W. Koppenaal, Elsevier, Amsterdam, 3rd ed., 2017, pp. 195–202.
155. D. M. Corsi, C. Platas-Iglesias, H. van Bekkum and J. A. Peters, *Magn. Reson. Chem.*, 2001, **39**, 723.
156. D. F. Evans, *J. Chem. Soc.*, 1959, 2003.
157. S. C.-K. Chu, Y. Xu, J. A. Balschi and C. S. Springer Jr., *Magn. Reson. Med.*, 1990, **13**, 239.
158. G. Schwarzenbach, H. Falschka, *Complexometric Titrations*, Methuen, London, 2nd English ed., 1969, pp. 194–199.

159. R. M. Smith, A. E. Martell and R. J. Motekaitis, *NIST Critically Selected Stability Constants of Metal Complexes Database, version 8.0 for Windows, NIST Standard Reference Database 46*, National Institute of Standards and Technology, Gaithersburg, MD, 2004. <https://www.nist.gov/srd/nist46> (last accessed 2017).
160. J. Kinnunen and B. Wennerstrand, *Chemist-Analyst*, 1957, **46**, 92.
161. G. W. C. Milner and J. W. Edwards, *Anal. Chim. Acta*, 1958, **18**, 513.
162. V. Patrovsky, *Collect. Czech. Chem. Commun.*, 1959, **24**, 3305.
163. G. S. Tereshin and I. V. Tananaev, *Zhur. Anal. Khim.*, 1962, **17**, 526.
164. S. J. Lyle and M. M. Rahman, *Talanta*, 1963, **10**, 1177.
165. K. V. Yatsimirsky, N. A. Kostromina, Z. A. Seka, N. K. Davidenko, E. E. Kriss and V. J. Ermolenko, *Khimiya Kompleksnikh Redkozemel Nihk Elementov*, Nauova Dumka, Kiev, 1966.
166. H. Flaschka, *Mikrochim. Acta*, 1955, 55.
167. B. Satyanarayana, K. L. Omprakash, A. V. C. Pal and M. L. N. Reddy, *Indian J. Chem.*, 1987, **26A**, 710.
168. J. S. Fritz, R. T. Oliver and D. J. Pietrzyk, *Anal. Chem.*, 1958, **30**, 1111.
169. A. F. Kuteinikov and V. M. Brodskay, *Zavodsk. Lab.*, 1962, **22**, 792.
170. B. Buděšínský, *Talanta*, 1968, **15**, 1063.
171. C. F. Baes Jr. and R. E. Mesmer, *The Hydrolysis of Cations*, Wiley, New York, 1976.
172. R. S. Kolat and J. E. Powell, *Inorg. Chem.*, 1962, **1**, 293.
173. Z. Baranyai, Z. Pálinkás, F. Uggeri, A. Maiocchi, S. Aime and E. Brücher, *Chem.—Eur. J.*, 2012, **18**, 16426.
174. C. F. F. Lopes, K. Iha, E. A. Neves and M. E. V. Suárez-Iha, *J. Coord. Chem.*, 1996, **40**, 27.
175. A. P. Cooney, M. Crampton and P. Golding, *J. Chem. Soc., Perkin Trans. 2*, 1986, 835.
176. I. Sajó, *Komplexometria*, Műszaki Könyvkiadó, Budapest, 1973.
177. M. Kobayashi and A. Iwase, *Yamagata Daigaku Kiyo*, 1960, **5**, 301.
178. R. Hara and P. W. West, *Anal. Chim. Acta*, 1956, **14**, 280.
179. A. Schlüter and A. Weiss, *Anal. Chim. Acta*, 1978, **99**, 157.
180. V. M. Peshkova, M. I. Gromova, I. P. Efimov and A. V. Chenko, *Vest. Mosk. Univ., Ser. 2: Khim.*, 1961, 59.
181. V. M. Peshkova, M. I. Gromova and N. M. Aleksandrova, *Zhur. Analit. Khim.*, 1962, **17**, 218.
182. I. P. Efimov and V. M. Ivanov, *Zhur. Analit. Khim.*, 1960, **15**, 750.
183. K. Tonosaki and M. Otomo, *Bull. Chem. Soc. Japan*, 1962, **35**, 1683.
184. A. Barge, G. Cravotto, E. Gianolio and F. Fedeli, *Contrast Media Mol. Imaging*, 2006, **1**, 184.
185. A. J. L. Villaraza, A. Bumb and M. W. Brechbiel, *Chem. Rev.*, 2010, **110**, 2921.
186. S. Aime, M. Botta, M. Fasano and E. Terreno, Protein-Bound Metal Chelates, in *The Chemistry of Contrast Agents in Medical Magnetic Resonance Imaging*, ed. A. E. Merbach and É. Tóth, Wiley, Chichester, 2001, Chapter 5, pp. 193–242.

187. R. A. Dwek, *Nuclear Magnetic Resonance (N.M.R.) in Biochemistry: Applications to Enzyme Systems*, Clarendon Press, Oxford, 1973, pp. 174–284.
188. V. C. Pierre, M. Botta, S. Aime and K. N. Raymond, *Inorg. Chem.*, 2006, **45**, 8355.
189. G. Scatchard, *Ann. N. Y. Acad. Sci.*, 1949, **51**, 660.
190. J. D. Wright, F. D. Boudinot and M. R. Ujhelyi, *Clin. Pharmacokinet.*, 1996, **30**, 445.
191. J. Barré, J. M. Chamouard, G. Houin and J. P. Tillement, *Clin. Chem.*, 1985, **31**, 60.
192. L. H. Cohen, Plasma Protein-Binding Methods in Drug Discovery, in *Optimization in Drug Discovery: In Vitro Methods*, ed. Z. Yan and G. W. Caldwell, Humana, Totowa, NJ, 2004, Chapter 8, pp. 111–122.
193. S. K. Larsen, B. G. Jenkins, N. G. Memon and R. B. Lauffer, *Inorg. Chem.*, 1990, **29**, 1147.
194. M. A. González, *Collection SFN*, 2011, **12**, 169.
195. K. Vanommeslaeghe, O. Guvench and A. D. MacKerell Jr., *Curr. Pharm. Des.*, 2014, **20**, 3281.
196. A. Villa, U. Cosentino, D. Pitea, G. Moro and A. Maiocchi, *J. Phys. Chem. A*, 2000, **104**, 3421.
197. U. Cosentino, G. Moro, D. Pitea, A. Villa, P. C. Fantucci, A. Maiocchi and F. Uggeri, *J. Phys. Chem. A*, 1998, **102**, 4606.
198. U. Cosentino, D. Pitea, G. Moro, G. A. A. Saracino and A. Villa, *Phys. Chem. Chem. Phys.*, 2009, **11**, 3943.
199. M. Clark, R. D. Cramer III and N. Van Opdenbosch, *J. Comput. Chem.*, 1989, **10**, 982.
200. D. Bini, M. Gregori, U. Cosentino, G. Moro, A. Canales, A. Capitoli, J. Jiménez-Barbero and L. Cipolla, *Carbohydr. Res.*, 2012, **354**, 21.
201. K. Vanommeslaeghe, E. Hatcher, C. Acharya, S. Kundu, S. Zhong, J. Shim, E. Darian, O. Guvench, P. Lopes, I. Vorobyov and A. D. MacKerell Jr., *J. Comput. Chem.*, 2010, **31**, 671.
202. E. S. Henriques, M. Bastos, C. F. G. C. Geraldés and M. J. Ramos, *Int. J. Quantum Chem.*, 1999, **73**, 237.
203. J. Wang, R. M. Wolf, J. W. Caldwell, P. A. Kollman and D. A. Case, *J. Comput. Chem.*, 2004, **25**, 1157.
204. F. Yerly, A. Borel, L. Helm and A. E. Merbach, *Chem.—Eur. J.*, 2003, **9**, 5468.
205. A. Borel, L. Helm and A. E. Merbach, *Chem.—Eur. J.*, 2001, **7**, 600.
206. F. Yerly, K. I. Hardcastle, L. Helm, S. Aime, M. Botta and A. E. Merbach, *Chem.—Eur. J.*, 2002, **8**, 1031.
207. G. M. Nicolle, F. Yerly, D. Imbert, U. Böttger, J.-C. Bünzli and A. E. Merbach, *Chem.—Eur. J.*, 2003, **9**, 5453.
208. O. V. Yazyev and L. Helm, *Eur. J. Inorg. Chem.*, 2008, 201.
209. O. V. Yazyev and L. Helm, *J. Chem. Phys.*, 2006, **125**, 054503.
210. W. Thiel, *WIREs Comput. Mol. Sci.*, 2014, **4**, 145.
211. M. J. S. Dewar and W. Thiel, *J. Am. Chem. Soc.*, 1977, **99**, 4899.

212. M. J. S. Dewar and W. Thiel, *J. Am. Chem. Soc.*, 1977, **99**, 4907.
213. J. P. McNamara, S. D. Berrigan and I. H. Hillier, *J. Chem. Theory Comput.*, 2007, **3**, 1014.
214. M. A. M. Filho, J. D. L. Dutra, H. L. B. Cavalcanti, G. B. Rocha, A. M. Simas and R. O. Freire, *J. Chem. Theory Comput.*, 2014, **10**, 3031.
215. R. O. Freire, G. B. Rocha and A. M. Simas, *Inorg. Chem.*, 2005, **44**, 3299.
216. R. O. Freire, N. B. da Costa Jr., G. B. Rocha and A. M. Simas, *J. Chem. Theory Comput.*, 2007, **3**, 1588.
217. R. O. Freire and A. M. Simas, *J. Chem. Theory Comput.*, 2010, **6**, 2019.
218. J. D. L. Dutra, M. A. M. Filho, G. B. Rocha, R. O. Freire, A. M. Simas and J. J. P. Stewart, *J. Chem. Theory Comput.*, 2013, **9**, 3333.
219. J. Stewart, *MOPAC2016*, Stewart Computational Chemistry, Colorado Springs, CO, USA [Online], 2016. <http://OpenMOPAC.net> (last accessed October 2016).
220. M. Seitz and N. Alzakhem, *J. Chem. Inf. Model.*, 2010, **50**, 217.
221. W. Kohn and L. J. Sham, *Phys. Rev.*, 1965, **140**, A1133.
222. A. C. Tsepis, *Coord. Chem. Rev.*, 2014, **272**, 1.
223. F. Neese, *Coord. Chem. Rev.*, 2009, **253**, 526.
224. T. Yanai, D. P. Tew and N. C. Handy, *Chem. Phys. Lett.*, 2004, **393**, 51.
225. J. P. Perdew, K. Burke and M. Ernzerhof, *Phys. Rev. Lett.*, 1996, **77**, 3865.
226. A. D. Becke, *Phys. Rev. A*, 1988, **38**, 3098.
227. C. Lee, W. Yang and R. G. Parr, *Phys. Rev. B*, 1988, **37**, 785.
228. J. P. Perdew, *Phys. Rev. B*, 1986, **33**, 8822.
229. C. Adamo and V. Barone, *J. Chem. Phys.*, 1998, **108**, 664.
230. C. Adamo and V. Barone, *J. Chem. Phys.*, 1999, **110**, 6158.
231. A. D. Becke, *J. Chem. Phys.*, 1993, **98**, 5648.
232. J. P. Perdew, K. Burke and Y. Wang, *Phys. Rev. B*, 1996, **54**, 16533.
233. J. Tao, J. P. Perdew, V. N. Staroverov and G. E. Scuseria, *Phys. Rev. Lett.*, 2003, **91**, 146401.
234. Y. Zhao and D. G. Truhlar, *J. Chem. Phys.*, 2006, **125**, 194101.
235. Y. Zhao and D. G. Truhlar, *Theor. Chem. Acc.*, 2008, **120**, 215.
236. O. A. Vydrov and G. E. Scuseria, *J. Chem. Phys.*, 2006, **125**, 234109.
237. L. Goerigk and S. Grimme, *Phys. Chem. Chem. Phys.*, 2011, **13**, 6670.
238. L. Petit, A. Borel, C. Daul, P. Maldivi and C. Adamo, *Inorg. Chem.*, 2006, **45**, 7382.
239. A. Roca-Sabio, M. Regueiro-Figueroa, D. Esteban-Gómez, A. de Blas, T. Rodríguez-Blas and C. Platas-Iglesias, *Comp. Theor. Chem.*, 2012, **999**, 93.
240. J. Paulovč, F. Cimpoesu, M. Ferbinteanu and K. Hirao, *J. Am. Chem. Soc.*, 2004, **126**, 3321.
241. G. Hong, F. Schautz and M. Dolg, *J. Am. Chem. Soc.*, 1999, **121**, 1502.
242. J. Kuta and A. E. Clark, *Inorg. Chem.*, 2010, **49**, 7808.
243. D. Aravena, M. Atanasov and F. Neese, *Inorg. Chem.*, 2016, **55**, 4457.
244. S. Khan, A. Kubica-Misztal, D. Kruk, J. Kowalewski and M. Odellius, *J. Chem. Phys.*, 2015, **142**, 034304.

245. K. Andersson, P.-Å. Malmqvist, B. O. Roos, A. J. Sadlej and K. Wolinski, *J. Phys. Chem.*, 1990, **94**, 5483.
246. K. Andersson, P.-Å. Malmqvist and B. O. Roos, *J. Chem. Phys.*, 1992, **96**, 1218.
247. C. Angeli, R. Cimiraglia, S. Evangelisti, T. Leininger and J.-P. Malrieu, *J. Chem. Phys.*, 2001, **114**, 10252.
248. C. Angeli, R. Cimiraglia and J.-P. Malrieu, *Chem. Phys. Lett.*, 2001, **350**, 297.
249. C. Angeli, R. Cimiraglia and J.-P. Malrieu, *J. Chem. Phys.*, 2002, **117**, 9138.
250. G. T. Velde, F. M. Bickelhaupt, E. J. Baerends, C. F. Guerra, S. J. A. van Gisbergen, J. G. Snijders and T. Ziegler, *J. Comput. Chem.*, 2001, **22**, 931.
251. D. Marx and J. Hutter, *Ab Initio Molecular Dynamics: Basic Theory and Advanced Methods*, Cambridge University Press, Cambridge, 2009.
252. *Relativistic Methods for Chemists*, ed. M. Barysz and Y. Ishikawa, *Challenges and Advances in Computational Chemistry and Physics*, Vol. 10, Springer, Dordrecht, The Netherlands, 2010.
253. P. Pykkö, *Chem. Rev.*, 1988, **88**, 563.
254. H. Stoll, B. Metz and M. Dolg, *J. Comput. Chem.*, 2002, **23**, 767.
255. R. B. Ross, S. Gayen and W. C. Ermler, *J. Chem. Phys.*, 1994, **100**, 8145.
256. T. R. Cundari and W. J. Stevens, *J. Chem. Phys.*, 1993, **98**, 5555.
257. M. Dolg, H. Stoll, A. Savin and H. Preuss, *Theor. Chim. Acta*, 1989, **75**, 173.
258. M. Dolg, H. Stoll and H. Preuss, *J. Chem. Phys.*, 1989, **90**, 1730.
259. J. Yang and M. Dolg, *Theor. Chem. Acc.*, 2005, **113**, 212.
260. A. Weigand, X. Cao, J. Yang and M. Dolg, *Theor. Chem. Acc.*, 2010, **126**, 117.
261. M. Hülsen, A. Weigand and M. Dolg, *Theor. Chem. Acc.*, 2009, **122**, 23.
262. R. Pollet, C. Clavaguéra and J.-P. Dognon, *J. Chem. Phys.*, 2006, **124**, 164103.
263. B. Kvamme, M. C. F. Wander and A. E. Clark, *Int. J. Quant. Chem.*, 2009, **109**, 2474.
264. L. Maron and O. Eisenstein, *J. Phys. Chem. A*, 2000, **104**, 7140.
265. D. Guillaumont, *J. Phys. Chem. A*, 2004, **108**, 6893.
266. Z. Baranyai, M. Botta, M. Fekete, G. B. Giovenzana, R. Negri, L. Tei and C. Platas-Iglesias, *Chem.—Eur. J.*, 2012, **18**, 7680.
267. X. Cao and M. Dolg, *J. Chem. Phys.*, 2001, **115**, 7348.
268. X. Cao and M. Dolg, *J. Mol. Struct.: THEOCHEM*, 2002, **581**, 139.
269. A. S. Ivanov and V. S. Bryantsev, *Eur. J. Inorg. Chem.*, 2016, 3474.
270. C. van Wüllen, *J. Comput. Chem.*, 1999, **20**, 51.
271. M. Reiher, *Theor. Chem. Acc.*, 2006, **116**, 241.
272. B. A. Hess, *Phys. Rev. A*, 1986, **33**, 3742.
273. G. Jansen and B. A. Hess, *Phys. Rev. A*, 1989, **39**, 6016.
274. M. Barysz and A. J. Sadlej, *J. Mol. Struct.: THEOCHEM*, 2001, **573**, 181.
275. E. van Lenthe, A. Ehlers and E.-J. Baerends, *J. Chem. Phys.*, 1999, **110**, 8943.

276. E. van Lenthe, E.-J. Baerends and J. G. Snijders, *J. Chem. Phys.*, 1993, **99**, 4597.
277. E. van Lenthe, E.-J. Baerends and J. G. Snijders, *J. Chem. Phys.*, 1994, **101**, 9783.
278. G. Hong, M. Dolg and L. Li, *Chem. Phys. Lett.*, 2001, **334**, 396.
279. A. F. Shestakov and N. S. Emelyanova, *J. Mol. Struct.: THEOCHEM.*, 2010, **954**, 124.
280. B. O. Roos, R. Lindh, P.-Å. Malmqvist, V. Veryazov, P.-O. Widmark and A. C. Borin, *J. Phys. Chem. A*, 2008, **112**, 11431.
281. M. Dolg, *J. Chem. Theory Comput.*, 2011, **7**, 3131.
282. D. A. Pantazis and F. Neese, *J. Chem. Theory Comput.*, 2009, **5**, 2229.
283. D. Aravena, F. Neese and D. A. Pantazis, *J. Chem. Theory Comput.*, 2016, **12**, 1148.
284. K. L. Schuchardt, B. T. Didier, T. Elsethagen, L. Sun, V. Gurumoorthi, J. Chase, J. Li and T. L. Windus, *J. Chem. Inf. Model.*, 2007, **47**, 1045.
285. D. Feller, *J. Comput. Chem.*, 1996, **17**, 1571.
286. Stuttgart/Cologne energy-consistent (ab initio) pseudopotentials [Online]. <http://www.tc.uni-koeln.de/PP/index.en.html>, (last accessed October 2016).
287. S. P. A. Sauer, Basis Sets for Calculations of NMR Properties [Online]. <https://sites.google.com/site/spasauer/basis-sets>, (last accessed October 2016).
288. H. Erras-Hanauer, T. Clark and R. van Eldik, *Coord. Chem. Rev.*, 2003, **238–239**, 233.
289. M. Mato-Iglesias, E. Balogh, C. Platas-Iglesias, É. Tóth, A. de Blas and T. R. Blas, *Dalton Trans.*, 2006, 5404.
290. A. Klamt and G. Schüürmann, *J. Chem. Soc., Perkin Trans. 2*, 1993, 799.
291. F. Eckert and A. Klamt, *AIChE J.*, 2002, **48**, 369.
292. J. Tomasi, B. Mennucci and R. Cammi, *Chem. Rev.*, 2005, **105**, 2999.
293. U. Cosentino, A. Villa, D. Pitea, G. Moro, V. Barone and A. Maiocchi, *J. Am. Chem. Soc.*, 2002, **124**, 4901.
294. C. Platas-Iglesias, *Eur. J. Inorg. Chem.*, 2012, 2023.
295. S. F. Sousa, E. S. Carvalho, D. M. Ferreira, I. S. Tavares, P. A. Fernandes, M. J. Ramos and J. A. N. F. Gomes, *J. Comput. Chem.*, 2009, **30**, 2752.
296. M. Purgel, Z. Baranyai, A. de Blas, T. Rodríguez-Blas, I. Bányai, C. Platas-Iglesias and I. Tóth, *Inorg. Chem.*, 2010, **49**, 4370.
297. S. Aime, M. Botta, M. Fasano, M. P. M. Marques, C. F. G. C. Geraldès, D. Pubanz and A. E. Merbach, *Inorg. Chem.*, 1997, **36**, 2059.
298. F. A. Dunand, R. S. Dickins, D. Parker and A. E. Merbach, *Chem.—Eur. J.*, 2001, **7**, 5160.
299. L. M. P. Lima, A. Lecointre, J.-F. Morfin, A. de Blas, D. Visvikis, L. J. Charbonnière, C. Platas-Iglesias and R. Tripier, *Inorg. Chem.*, 2011, **50**, 12508.
300. R. Car and M. Parrinello, *Phys. Rev. Lett.*, 1985, **55**, 2471.
301. R. Pollet, N. N. Nair and D. Marx, *Inorg. Chem.*, 2011, **50**, 4791.

302. A. Lasoroski, R. Vuilleumier and R. Pollet, *J. Chem. Phys.*, 2013, **139**, 104115.
303. R. Boča, *Coord. Chem. Rev.*, 2004, **248**, 757.
304. R. Salomon-Ferrer, D. A. Case and R. C. Walker, *WIREs Comput. Mol. Sci.*, 2013, **3**, 198.
305. CPMD [Online]. <http://www.cpmd.org/> (last accessed 2017), *Copyright IBM Corp 1990-2015*, Copyright MPI für Festkörperforschung Stuttgart 1997-2001.
306. K. Aidas, C. Angeli, K. L. Bak, V. Bakken, R. Bast, L. Boman, O. Christiansen, R. Cimiraglia, S. Coriani, P. Dahle, E. K. Dalskov, U. Ekström, T. Enevoldsen, J. J. Eriksen, P. Ettenhuber, B. Fernández, L. Ferrighi, H. Fliegl, L. Frediani, K. Hald, A. Halkier, C. Hättig, H. Heiberg, T. Helgaker, A. C. Hennum, H. Hettema, E. Hjertenæs, S. Høst, I.-M. Høyvik, M. F. Iozzi, B. Jansík, H. J. A. Jensen, D. Jonsson, P. Jørgensen, J. Kauczor, S. Kirpekar, T. Kjærgaard, W. Klopper, S. Knecht, R. Kobayashi, H. Koch, J. Kongsted, A. Krapp, K. Kristensen, A. Ligabue, O. B. Lutnæs, J. I. Melo, K. V. Mikkelsen, R. H. Myhre, C. Neiss, C. B. Nielsen, P. Norman, J. Olsen, J. M. H. Olsen, A. Osted, M. J. Packer, F. Pawłowski, T. B. Pedersen, P. F. Provasi, S. Reine, Z. Rinkevicius, T. A. Ruden, K. Ruud, V. V. Rybkin, P. Sałek, C. C. M. Samson, A. S. de Merás, T. Saue, S. P. A. Sauer, B. Schimmelpfennig, K. Sneskov, A. H. Steindal, K. O. Sylvester-Hvid, P. R. Taylor, A. M. Teale, E. I. Tellgren, D. P. Tew, A. J. Thorvaldsen, L. Thøgersen, O. Vahtras, M. A. Watson, D. J. D. Wilson, M. Ziolkowski and H. Ågren, *WIREs Comput. Mol. Sci.*, 2014, **4**, 269.
307. M. J. Frisch, G. W. Trucks, H. B. Schlegel, G. E. Scuseria, M. A. Robb, J. R. Cheeseman, G. Scalmani, V. Barone, B. Mennucci, G. A. Petersson, H. Nakatsuji, M. Caricato, X. Li, H. P. Hratchian, A. F. Izmaylov, J. Bloino, G. Zheng, J. L. Sonnenberg, M. Hada, M. Ehara, K. Toyota, R. Fukuda, J. Hasegawa, M. Ishida, T. Nakajima, Y. Honda, O. Kitao, H. Nakai, T. Vreven, J. A. Montgomery Jr., J. E. Peralta, F. Ogliaro, M. Bearpark, J. J. Heyd, E. Brothers, K. N. Kudin, V. N. Staroverov, R. Kobayashi, J. Normand, K. Raghavachari, A. Rendell, J. C. Burant, S. S. Iyengar, J. Tomasi, M. Cossi, N. Rega, J. M. Millam, M. Klene, J. E. Knox, J. B. Cross, V. Bakken, C. Adamo, J. Jaramillo, R. Gomperts, R. E. Stratmann, O. Yazyev, A. J. Austin, R. Cammi, C. Pomelli, J. W. Ochterski, R. L. Martin, K. Morokuma, V. G. Zakrzewski, G. A. Voth, P. Salvador, J. J. Dannenberg, S. Dapprich, A. D. Daniels, Ö. Farkas, J. B. Foresman, J. V. Ortiz, J. Cioslowski and D. J. Fox, *Gaussian 09, Revision D.01*, Gaussian Inc., Wallingford, CT, 2013.
308. M. W. Schmidt, K. K. Baldridge, J. A. Boatz, S. T. Elbert, M. S. Gordon, J. H. Jensen, S. Koseki, N. Matsunaga, K. A. Nguyen, S. Su, T. L. Windus, M. Dupuis and J. A. Montgomery Jr., *J. Comput. Chem.*, 1993, **14**, 1347.
309. M. J. Abraham, T. Murtola, R. Schulz, S. Páll, J. C. Smith, B. Hess and E. Lindahl, *SoftwareX*, 2015, **1-2**, 19.

310. A. D. Bochevarov, E. Harder, T. F. Hughes, J. R. Greenwood, D. A. Braden, D. M. Philipp, D. Rinaldo, M. D. Halls, J. Zhang and R. A. Friesner, *Int. J. Quantum Chem.*, 2013, **113**, 2110.
311. F. Aquilante, J. Autschbach, R. K. Carlson, L. F. Chibotaru, M. G. Delcey, L. D. Vico, I. F. Galván, N. Ferré, L. M. Frutos, L. Gagliardi, M. Garavelli, A. Giussani, C. E. Hoyer, G. L. Manni, H. Lischka, D. Ma, P. Å. Malmqvist, T. Müller, A. Nenov, M. Olivucci, T. B. Pedersen, D. Peng, F. Plasser, B. Pritchard, M. Reiher, I. Rivalta, I. Schapiro, J. Segarra-Martí, M. Stenrup, D. G. Truhlar, L. Ungur, A. Valentini, S. Vancoillie, V. Veryazov, V. P. Vysotskiy, O. Weingart, F. Zapata and R. Lindh, *J. Comput. Chem.*, 2016, **37**, 506.
312. H.-J. Werner, P. J. Knowles, G. Knizia, F. R. Manby and M. Schütz, *WIREs Comput. Mol. Sci.*, 2012, **2**, 242.
313. M. Valiev, E. J. Bylaska, N. Govind, K. Kowalski, T. P. Straatsma, H. J. J. Van Dam, D. Wang, J. Nieplocha, E. Apra, T. L. Windus and W. A. de Jong, *Comput. Phys. Commun.*, 2010, **181**, 1477.
314. F. Neese, *WIREs Comput. Mol. Sci.*, 2012, **2**, 73.
315. *Spartan'16*, Wavefunction Inc., Irvine, CA.
316. F. Furche, R. Ahlrichs, C. Hättig, W. Klopper, M. Sierka and F. Weigend, *WIREs Comput. Mol. Sci.*, 2014, **4**, 91.
317. F. Bloch, *Phys. Rev.*, 1946, **70**, 460.
318. M. Markl and J. Leupold, *J. Magn. Reson. Imaging*, 2012, **35**, 1274.
319. E. L. Hahn, *Phys. Rev.*, 1950, **80**, 580.
320. N. Stikov, M. Boudreau, I. R. Levesque, C. L. Tardif, J. K. Barral and G. B. Pike, *Magn. Reson. Med.*, 2015, **73**, 514.
321. D. C. Look and D. R. Locker, *Rev. Sci. Instrum.*, 1970, **41**, 250.
322. E. K. Fram, R. J. Herfkens, G. A. Johnson, G. H. Glover, J. P. Karis, A. Shimakawa, T. G. Perkins and N. J. Pelc, *Magn. Reson. Imaging*, 1987, **5**, 201.
323. S. C. L. Deoni, B. K. Rutt and T. M. Peters, *Magn. Reson. Med.*, 2003, **49**, 515.
324. P. Schmitt, M. A. Griswold, P. M. Jakob, M. Kotas, V. Gulani, M. Flentje and A. Haase, *Magn. Reson. Med.*, 2004, **51**, 661.
325. S. H. Koenig, R. D. Brown III, D. Adams, D. Emerson and C. G. Harrison, *Invest. Radiol.*, 1984, **19**, 76.
326. S. H. Koenig and R. D. Brown III, *Magn. Reson. Med.*, 1984, **1**, 437.
327. R. G. Bryant, D. A. Mendelson and C. C. Lester, *Magn. Reson. Med.*, 1991, **21**, 117.
328. S. H. Koenig, *Acad. Radiol.*, 1996, **3**, 597.
329. S. H. Koenig and R. D. Brown III, *Invest. Radiol.*, 1985, **20**, 297.

CHAPTER 3

Chemical Exchange Saturation Transfer (CEST) Contrast Agents

GIUSEPPE FERRAUTO,^a SILVIO AIME,^{*a}
MICHAEL T. McMAHON,^{*b,c} JANET R. MORROW,^{*d}
ERIC M. SNYDER,^d ALEX LI^e AND ROBERT BARTHA^{*e,f}

^a Molecular Imaging Center, Department of Molecular Biotechnologies and Health Sciences, University of Torino, 10126 Torino, Italy; ^b The Russell H. Morgan Department of Radiology and Radiological Science, Division of MR Research, The Johns Hopkins University School of Medicine, MD 21205, USA; ^c F. M. Kirby Research Center for Functional Brain Imaging, Kennedy Krieger Institute, Baltimore, MD 21205, USA;

^d University at Buffalo, State University of New York, Department of Chemistry, Amherst, NY 14260, USA; ^e Robarts Research Institute, University of Western Ontario, London, Ontario N6A 3K7, Canada;

^f Departments of Medical Biophysics, Medical Imaging, and Psychiatry, University of Western Ontario, London, Ontario N6A 3K7, Canada

*Email: silvio.aime@unito.it; mtmemaho@gmail.com; jmorrow@buffalo.edu; rbartha@robarts.ca

3.1 General Theory of CEST Agents

GIUSEPPE FERRAUTO AND SILVIO AIME*

3.1.1 General Introduction to CEST Contrast

Currently used clinical contrast agents for MRI are able to generate contrast in MR images by inducing changes in bulk longitudinal or transverse water relaxation times (T_1 and T_2), or both. The class of chemical exchange saturation transfer (CEST) agents differs from these established agents because CEST agents act by transferring saturated magnetization to the bulk water signal *via* exchangeable protons on the agents or water molecules. By applying a proper radiofrequency irradiation field, the resonance of exchangeable protons is directly saturated. Through chemical exchange, the saturated spins are transferred to the bulk water, thus causing a decrease of the water signal intensity, which is the source of the signal in the corresponding MR images.

The possibility of exploiting CEST as a new modality to generate contrast in an MR image was demonstrated for the first time by Ward, Aletras, and Balaban in 2000.¹ In general, a CEST agent is a molecule (diamagnetic or paramagnetic) or a macromolecular or supramolecular system (*e.g.* polymers, dendrimers, liposomes, or cells) containing exchangeable protons resonating at a frequency different from the bulk water protons such that they may be properly saturated by the application of a radiofrequency field. The resulting negative contrast arises from the transfer of the saturated magnetization to the bulk water resonance by the underlying chemical exchange process (Figure 3.1A–C).^{2–6}

The basic principles for the generation of a CEST contrast in a ^1H -MR image involve the signal of exchangeable CEST protons that resonate at a frequency different from the bulk water protons (Figure 3.1D left). By being directly saturated using a proper radiofrequency irradiation (Figure 3.1D middle), the saturation can be transferred to the bulk water through the chemical exchange of the protons (Figure 3.1D right). In this way, the signal of the CEST exchangeable protons is totally saturated whereas the signal from the bulk water proton is slightly attenuated (Figure 3.1D right). This attenuation triggers a darkening of the MR image signal intensity in the region in which the CEST agents are distributed, thus creating contrast relative to images acquired in the absence of the saturation of the exchangeable protons.^{2–6}

Notably, the concentration of the CEST mobile protons is generally low, in the μM – mM range, and is much lower than the one of the bulk water protons, which can reach 111 M. Because the irradiation time (t_{sat}) is longer than the residence lifetime (τ_{M}) of the mobile protons on the CEST molecule (*i.e.* $t_{\text{sat}} \gg \tau_{\text{M}} = 1/k_{\text{ex}}$, where k_{ex} is the exchange rate), each exchanging saturated proton is replaced by a non-saturated water proton, which is in turn saturated. Therefore, if: (i) CEST protons have a sufficiently fast

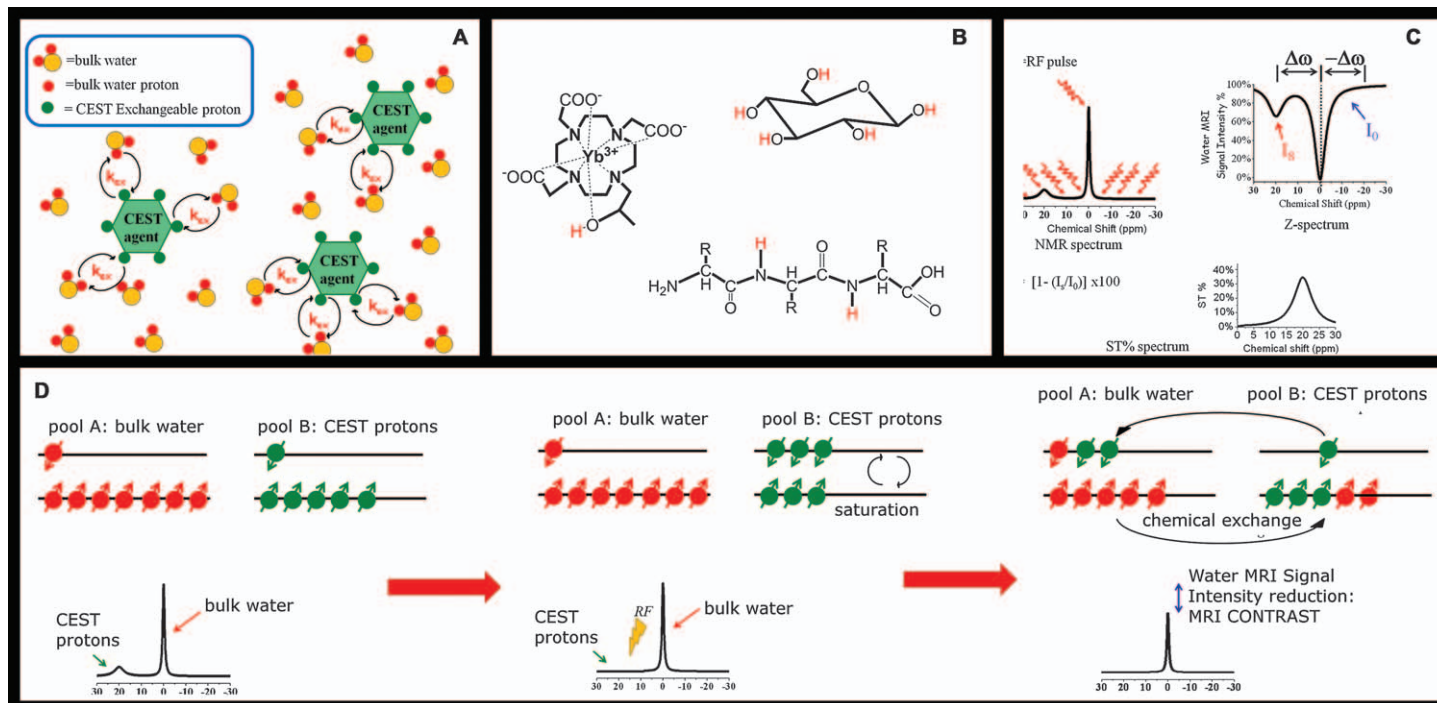


Figure 3.1 (A) Scheme of a generic CEST probe with protons in chemical exchange with bulk water protons. (B) Some representative CEST molecules (red Hs are exchangeable protons). (C) $^1\text{H-NMR}$, Z, and saturation transfer (ST)% spectra of a specimen containing a CEST molecule. (D) Mechanism of generation of CEST contrast. Left: two proton pools (bulk water and CEST proton pools). Middle: radiofrequency pulse saturates CEST resonance. Right: saturated CEST protons are transferred to bulk water through chemical exchange. The net result is a decrease of the MRI water signal intensity with consequent generation of contrast in the MR image.

exchange rate (τ_M in the millisecond range) and (ii) the saturation time is long enough (in the order of seconds), then the saturation transfer to the bulk water becomes sufficient to generate enough contrast in the resulting images.^{2–6} Therefore, the CEST modality enables the detection of molecules containing exchangeable protons at millimolar and even sub-millimolar concentrations by investigating their indirect effect on the intense bulk-water resonance *via* signal amplification.^{7,8}

Another important feature of CEST agents is that the contrast they induce can be switched on and off at will simply by changing the radiofrequency of irradiation. Because the contrast generated by CEST agents is frequency-encoded, CEST molecules with exchangeable groups displaying different NMR chemical shifts can be simultaneously detected in the same MR image. This means that if there are two or more CEST molecules present in the same region, the radiofrequency irradiation offset can be chosen to identify specific molecules. By assigning a given color to each contrast molecule, multicolor ^1H -MR imaging can be obtained. This feature can be attractive for the *in vivo* detection of different agents co-localized in the same region. This is particularly relevant in the field of cell tracking, where frequency coding might offer the opportunity to aid in the development of cell-based therapies.^{9–14} Furthermore, because a CEST agent can contain more than one pool of exchangeable protons, responsive agents can enable ratiometric imaging of physio-pathological parameters, such as pH, temperature, or enzyme activity, independently from the knowledge of the actual concentration of the probe simply by comparing the saturation transfer (ST) effect associated to the different sets of exchanging protons.^{15–21}

The main limitation of CEST contrast agents is their intrinsic low sensitivity, which has to some extent hampered the translation of this class of contrast agents to uses *in vivo*. To have a detectable CEST signal, millimolar concentrations of equivalent exchanging protons are necessary. Many attempts to overcome this limitation have been pursued to exploit the great potential of these agents in molecular and cellular imaging experiments. In particular, three strategies have been considered: (i) designing structures with a high number of exchanging protons endowed with optimal k_{ex} ,^{22–24} (ii) exploiting nano-carriers able to deliver a high number of MRI contrast agents to biological targets,^{12,25–29} and (iii) using compartmentalized water molecules in liposomes or cells as sources of CEST signal.^{24,30,31} An overview of highly sensitive CEST probes—including micelles, lipoCEST, and cells as CEST—is reported in Section 3.5.

Experimentally, the potential of a CEST agent is commonly assessed by recording their Z- and ST-spectra (Section 3.2).^{2–6,25} The Z-spectrum reports on how the ^1H water MR signal intensity decreases upon changing the offset of the irradiation frequency (Figure 3.1C upper right). The signal intensity of the ^1H of water reaches zero when the offset is set at the absorption of ^1H water resonance (direct saturation). As described above, the exchanging CEST protons also decrease the water signal because of the transfer of saturated magnetization. When the chemical shift of the exchanging proton

pool is close to that of bulk water, the CEST effect creates an asymmetry of the absorption centered at 0 ppm (bulk water is usually defined as 0 ppm in CEST experiments). In such a case, a quantitative CEST study is typically carried out by acquiring two images, one with irradiation at the CEST offset ($\Delta\omega$) and one at the opposite offset ($-\Delta\omega$). Comparison of the two images yields the percentage CEST effect, as determined in eqn (3.1):

$$\text{Saturation Transfer (ST \%)} = \left(1 - \frac{MS(\Delta\omega)}{MS(-\Delta\omega)}\right) \times 100 \quad (3.1)$$

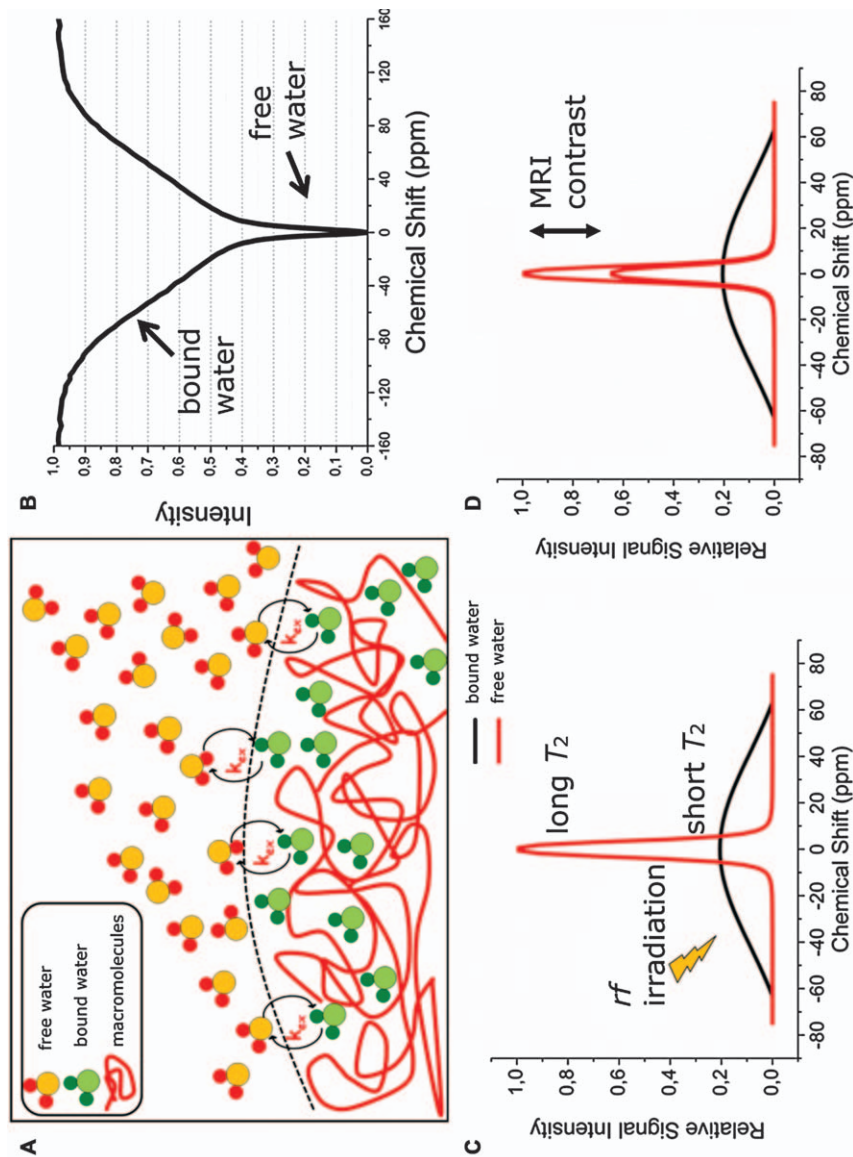
where $MS(\Delta\omega)$ and $MS(-\Delta\omega)$ are the magnetic resonance (MR) signal intensity of the bulk water protons upon applying the saturation radio-frequency field at $\Delta\omega$ and $-\Delta\omega$, respectively. The ST-spectrum reports the ST% values *versus* the irradiation frequency (Figure 3.1C bottom).

Endogenously occurring CEST contrast can arise from amide functionalities; this is called amide proton transfer.^{6,32} In amide proton transfer imaging, endogenous mobile proteins and peptides in tissues can be detected *via* saturation of all the amide protons present in peptides.^{6,32} This imaging technique gives information about the soluble protein content, an important biomarker of many diseases, such as cancer.³³ Other endogenous CEST reporters include glycosaminoglycans³⁴ and glucose.^{35,36}

Endogenous CEST is analogous to magnetization transfer contrast, a contrast that is based on the irradiation of resonances of protons belonging to immobilized, semi-solid macromolecules, such as bound proteins and membranes, and to water molecules that are tightly bound to macromolecules and that they are not normally visible by MRI because of their short T_2 relaxation times (bandwidth > 10 kHz, Figure 3.2A). Upon application of the radiofrequency irradiation at a chemical shift far from the bulk water resonance, the saturated protons may enter the free bulk water proton pool (bandwidth < 20 Hz), thus transferring their saturated magnetization to the free water protons (Figure 3.2A). The net effect is a decrease in the MR visible signal and consequently the generation of contrast in regions in which immobilized water molecules or proteins are present (Figure 3.2B–D).^{37,38} Magnetization transfer contrast implies that proton saturation occurs over a large bandwidth (*e.g.* 50 kHz), whereas in conventional CEST detection, only one specific resonance is saturated.

3.1.2 Theoretical and Practical Considerations about CEST Agents

The contrast in a CEST experiment is the result of a complex interplay of many parameters. It relies on the application of a proper radiofrequency field on-resonance with the exchangeable protons to saturate the NMR signal of the CEST molecule. If this field is sufficiently strong and applied for a sufficiently long time to allow multiple exchange events, partial saturation of the bulk water proton signal is expected, thereby generating contrast.



Different mathematical models have been developed to describe the dynamic process of CEST and to help in the proper setting of the experiment. Among these models, the two-pool model based on a series of Bloch–McConnell–Thompson equations is the simplest.^{3,4,39} The first pool is represented by the bulk water protons spins (water) and the second one by a small exchangeable pool of protons on the contrast molecule (CEST). The basic condition that must be satisfied for CEST to avoid coalescence of the two NMR peaks is that the shift difference between the two protons pools ($\Delta\omega$) must be higher than their exchange rate (k_{ex}), (*i.e.* $\Delta\omega \geq k_{\text{ex}}$). The relative concentration of the two pools is vastly different (up to ~ 111 M for water protons *versus* millimolar for the CEST exchangeable protons). The exchange between those two pools enables the transfer of null magnetization from the saturated CEST protons to the detected water protons, thus yielding a net signal decrease at the resonance of the latter. In other words, by applying a radiofrequency pulse at the $\Delta\omega$ frequency offset corresponding to the resonance of the mobile protons of the CEST agent, the longitudinal magnetization (M_z^{CEST}) of these protons is saturated. Because of the chemical exchange with water protons, the bulk water signal (M_z^{water}) also becomes partially saturated. The decrease of the water signal intensity during the irradiation time is given by eqn (3.2), in which M_0^{water} is the equilibrium longitudinal magnetization of bulk water protons at $t=0$, R_1^{water} is the water-proton longitudinal relaxation rate, and k^{water} is the chemical exchange rate.

$$M_{z(t)}^{\text{water}} = M_0^{\text{water}} \left[\frac{R_1^{\text{water}}}{R_1^{\text{water}} + k^{\text{water}}} + \frac{k^{\text{water}}}{R_1^{\text{water}} + k^{\text{water}}} e^{-(R_1^{\text{water}} + k^{\text{water}})t} \right] \quad (3.2)$$

After the application of the radiofrequency pulse, the magnetization decreases reaching a steady-state value at $t = \infty$ according to eqn (3.3).

$$M_{z(\infty)}^{\text{water}} = M_0^{\text{water}} \left(\frac{R_1^{\text{water}}}{R_1^{\text{water}} + k^{\text{water}}} \right) \quad (3.3)$$

Figure 3.2 Magnetization transfer contrast effect. (A) Two water pools are present in tissue, namely free bulk water and water molecules bound to macromolecules. The two pools are in an exchanging regime. (B) Representative Z-spectrum of tissue showing the presence of the two water components. The free water (long T_2) has a narrow dip in the Z-spectrum (a few ppm), whereas the bound water has a broad dip (hundreds of ppm). Both signals are centered at the same frequency (0 ppm). (C) In the magnetization transfer contrast experiment, the radiofrequency field of saturation is set to a chemical shift far from the bulk water resonance. (D) The bound water resonance is directly saturated whereas, through chemical exchange, the bulk water resonance is saturated. This saturation generates contrast in the MR image. Note: the signal of bound water is normally not detectable in the NMR spectrum because it is broad.

Therefore, under steady-state conditions, the saturation transfer (ST_{∞}) follows eqn (3.4):

$$ST_{\infty} = \frac{M_0^{\text{water}} - M_{z(\infty)}^{\text{water}}}{M_0^{\text{water}}} = \frac{k^{\text{water}}}{R_1^{\text{water}} + k^{\text{water}}} \quad (3.4)$$

The ST value ranges between 0 and 1 depending on the relative values of R_1^{water} and k^{water} . Note that because the ST% effect is linear with the bulk water longitudinal relaxation time ($T_1 = 1/R_1$), ST% is expected to strongly decrease in the presence of a paramagnetic complex.

The exchange rate k^{water} is related to the k^{CEST} and the molar fraction of the CEST proton spins. The latter is given by the product of the concentration of the CEST agent and the number of its magnetically equivalent mobile protons (n), which in dilute aqueous solutions can be represented by eqn (3.5).

$$k^{\text{water}} = k^{\text{CEST}} \frac{[\text{CEST spins}]}{[\text{Water spins}]} = k^{\text{CEST}} \frac{n[\text{CEST agent}]}{111.2} \quad (3.5)$$

The number n is different for the various classes of CEST agents. For paramagnetic CEST complexes or diamagnetic molecules such as sugars, n is usually small. Conversely, it is substantially greater for nano-sized systems, such as liposomes.

From eqn (3.4), it is apparent that ST_{∞} can be increased by increasing the exchange rate between the two proton pools up to their coalescence ($\Delta\omega \approx k^{\text{water}}$). Because $\Delta\omega$ depends on the magnetic field, greater contrast can be obtained at higher B_0 . Two assumptions have been made in the above model, (i) no direct saturation effect on bulk water is considered (*i.e.* no spillover effect) and (ii) the magnetization of the mobile protons of the CEST probe is completely saturated by the B_1 field. These assumptions are usually satisfied for paramagnetic CEST agents where $\Delta\omega$ is large. On the other hand, for diamagnetic CEST agents, where $\Delta\omega$ is small, both spillover and incomplete saturation are usually observed.

A more accurate quantification of the CEST effect has been recently developed by Sun and co-workers.³² In this model, the spillover effect (σ) and the saturation efficiency (α) are included as fundamental parameters to be considered for the quantification of the CEST effect. According to this model, ST_{∞} can be calculated by applying eqn (3.6)–(3.9), where α is the saturation efficiency and σ is the spillover factor.

$$ST_{\infty} = \frac{\alpha k^{\text{water}} [1 - (\sigma/\sigma_{\text{max}})]}{R_1^{\text{water}} + k^{\text{water}}} \quad (3.6)$$

$$\alpha = \frac{\omega_2^2}{\omega_2^2 + pq} \quad \text{where } \omega_2^2 = 2\pi B_1; \quad (3.7)$$

$$p = R_2^{\text{CEST}} - \left(k^{\text{water}} \times \frac{k^{\text{CEST}}}{R_2^{\text{water}}} \right) \quad (3.8)$$

$$q = R_1^{\text{CEST}} - \left(k^{\text{water}} \times \frac{k^{\text{CEST}}}{R_2^{\text{water}}} \right) \quad (3.9)$$

The maximum saturation efficiency of the CEST exchangeable protons ($\alpha = 1$) is reached when $pq \ll \omega_2^2$. The maximum value of the spillover factor for specific parameters involved in the ST experiment is σ_{max} . In the absence of spillover the term $1 - \sigma/\sigma_{\text{max}} = 1$; in presence of the maximum spillover, it is equal to 0, and the ST effect is completely eliminated. Consequently, a more accurate equation describing the ST time evolution is given by eqn (3.10):

$$\text{ST}_{(t)} = \frac{\alpha k^{\text{water}} [1 - (\sigma/\sigma_{\text{max}})]}{R_1^{\text{water}} + k^{\text{water}}} \times (1 - e^{-(R_1^{\text{water}} + k^{\text{water}})t}) \quad (3.10)$$

3.1.3 Practical Considerations for CEST Experiments

CEST MRI contrast agents have several advantages over conventional T_1 - and T_2 -shortening probes. First, with CEST contrast agents, the contrast can be switched on or off by applying the radiofrequency irradiation field. As opposed to relaxation-based MR image acquisition, in CEST MRI, the acquisition of pre-contrast images before injection of contrast agent is not necessary because such an image can be acquired either with no irradiation or with the radiofrequency irradiation field set at a frequency not corresponding to the absorption of the exchanging protons. Furthermore, it is possible to design contrast agents with distinct sets of exchanging protons to visualize multiple agents simultaneously. This task is not possible using T_1 - or T_2 -shortening probes because they act directly on the relaxation times of bulk water and the effects of different relaxation agents are additive, making it impossible to distinguish between the contribution of the different contrast agents. Finally, CEST agents can be employed in ratiometric protocols to quantify parameters of interest in the microenvironment of the CEST agents without knowing the actual concentration of the probe.

The main limitation of CEST contrast agents is their low sensitivity, which is lower than those of T_1 - and T_2 -shortening probes. This issue has been extensively studied, and several solutions have been proposed. Briefly, because ST% is proportional to the k_{ex} and the number of exchangeable protons, the proposed solutions rely on the manipulation of these two parameters.

3.1.3.1 Parameters Affecting the ST% Effect

The main parameters influencing the ST% appear in eqn (3.11) and (3.12).

$$\text{ST}\% = 1 - \frac{M_z}{M_0} = \frac{k_{\text{ex}} \times f_{\text{CEST}}}{R_1^w + k_{\text{ex}} \times f_{\text{CEST}}} (1 - e^{-t_{\text{sat}}(R_1^w + k_{\text{ex}} \times f_{\text{CEST}})}) \quad (3.11)$$

$$f_{\text{CEST}} = \frac{n[\text{CA}]}{2[\text{H}_2\text{O}_{\text{bulk}}]}, \text{ i.e. the molar fraction of CEST protons} \quad (3.12)$$

- (1) **Exchange Rate.** CEST efficiency is directly proportional to k_{ex} . The higher the value of k_{ex} , the higher ST%. However, the exchange rate cannot be increased indefinitely because it will eventually lead to coalescence between the CEST and bulk water signals. The condition $\Delta\delta > k_{\text{ex}}$ must be maintained at all times. Furthermore, the maximum ST% effect is achieved when $k_{\text{ex}} = 2\pi B_1$ (Figure 3.3A), which means that fast exchanging systems require high-intensity saturation fields (B_1). Higher B_1 values correspond to (i) a higher specific absorption

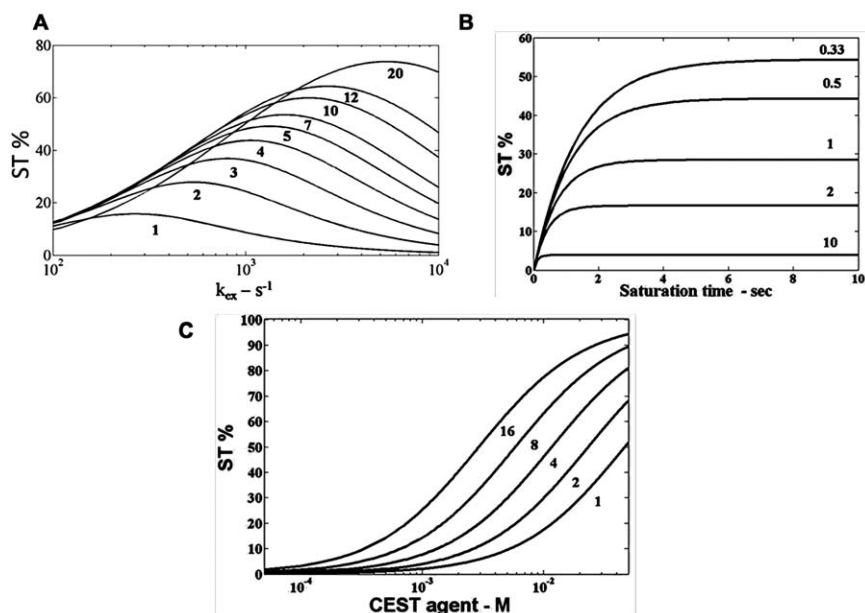


Figure 3.3 (A) k_{ex} dependence of ST% calculated at the B_1 amplitudes reported in the figure (from 1 to 20 μT). In systems with faster k_{ex} , it is necessary to use higher B_1 fields to reach the maximum ST% effect. (B) Simulated ST% dependence on the duration of the saturation B_1 field at the different R_1 (of bulk water) values reported in the plot. The ST% effect (at steady-state) is directly proportional to bulk-water T_1 . Steady-state is reached faster when bulk water T_1 is short. (C) Simulated ST% dependence on the molar concentration of the CEST agent calculated using an increasing number (from 1 to 16) of magnetically equivalent mobile protons. A higher number of equivalent mobile protons equates to a lower concentration of the agent needed to have a detectable ST% signal.³ Adapted with permission from E. Terreno, D. D. Castelli and S. Aime, *Contrast Media Mol. Imaging*, 2010, 5, 78. Copyright © 2010 John Wiley & Sons, Ltd.

Table 3.1 Relationship between the number of mobile protons and the relative sensitivity of various classes of CEST agents.

Mobile protons	Sensitivity	Chemical system
< 10	mM	Low MW molecules
10^3	μM	Macromolecules
10^6	nM	Nanoparticles
10^6 – 10^9	nM–pM	Liposomes
10^{12}	<pM	Cells

rate, *i.e.* tissue heating, and (ii) a strong direct saturation of water signal with less CEST effect.

- (2) **Longitudinal Relaxation Rate of the Bulk Water Protons.** The ST% is directly proportional to the T_1 of bulk water protons: longer T_1 times correspond to higher ST% in the steady state (Figure 3.3B). From eqn (3.11), the steady-state condition is met when both bulk water R_1 and k_{ex} are fast [eqn (3.13)].

$$e^{-t^{\text{sat}}(R_1^{\text{bw}} + k_{\text{ex}}^{\text{CEST}}) f_{\text{CEST}}} = 0 \quad (3.13)$$

- (3) **Number of Equivalent CEST Protons.** The attainable ST% is directly proportional to the molar fraction of CEST protons. This number is determined from the concentration of the CEST contrast agent and the number of equivalent protons present in the CEST probe (Figure 3.3C). It has been shown that increasing the number of exchanging protons is the most effective way to increase the sensitivity of CEST agents. The number of mobile protons present in different classes of CEST agents and their relative sensitivity threshold are reported in Table 3.1.
- (4) **Experimental Parameters of Irradiation Time, Power, Sequence and Magnetic Strength.** Experimental parameters strongly affect the ST% effect. The analysis of sequences normally employed for CEST-MRI acquisition is presented in Sections 3.2 and 3.4.

3.1.4 Classification of CEST Agents

Different ways of classifying CEST agents have been proposed. In one classification based on the magnetic properties of the agent, CEST agents are divided into either diamagnetic CEST (diaCEST) and paramagnetic CEST (paraCEST) agents (Figure 3.4A).^{2,3,5,6} DiaCEST agents are molecules and supramolecular adducts (*e.g.* sugars and polypeptides) characterized by relatively small $\Delta\omega$ values. Conversely, paraCEST agents are molecules and supramolecular adducts containing a paramagnetic ion that endows the systems with large $\Delta\omega$ terms. The paramagnetic metal ion is either a lanthanide (*e.g.* Tm^{III} , Yb^{III} , and Eu^{III}) or a transition metal (*e.g.* Fe^{II} and Co^{III}). In general, the chemical shifts of the exchanging protons of diaCEST compounds, such as hydroxyl, amine, amide, and imino groups, are not farther than 10 ppm from water. Conversely, paraCEST agents can show

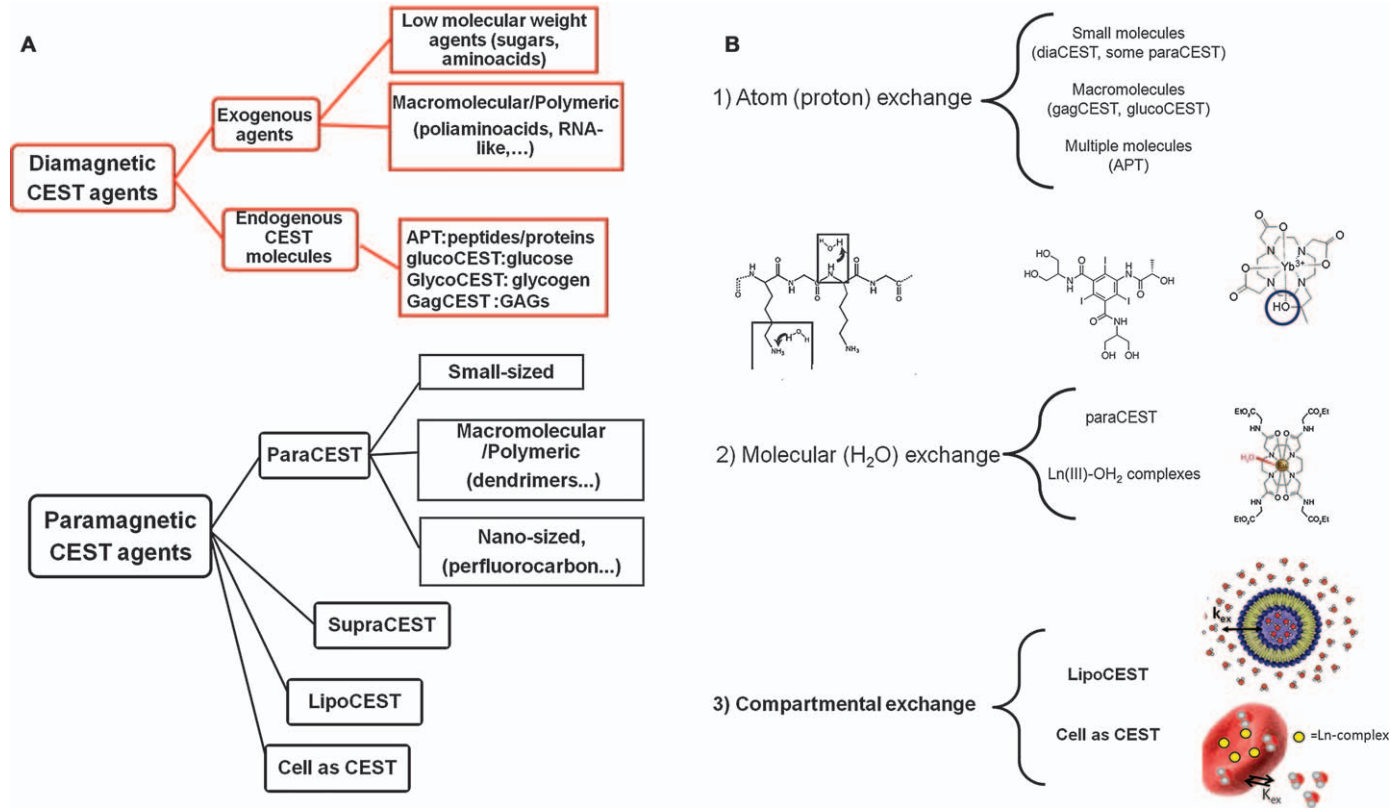


Figure 3.4 Two classifications of CEST agents based (A) on the magnetic properties and (B) on the exchange mechanism.

larger shifts, up to hundreds of ppm, with the advantages of (i) eliminating any interference with the background signal eventually present *in vivo* and (ii) exploiting much larger k_{ex} values before reaching coalescence.

The members of both classes can be further classified into subsets, mainly on the basis of molecular size, physicochemical characteristics, endogenous occurrence, and type of molecular constructs. For example, diaCEST agents can be divided into three groups, namely (i) low molecular weight agents, (ii) macromolecular agents, and (iii) endogenous agents (endoCEST).

Low-molecular-weight CEST agents include small molecules containing mobile protons, such as sugars, amino acids, small peptides, nucleosides, purine and pyrimidine bases, barbituric acid and derivatives, imino acids, and imidazoles. As exogenous agents, some iodinated X-ray contrast media with exchangeable amide protons such as Iopamidol, Iopromide, and Iodixanol have also been shown to act as CEST MRI contrast agents.^{40,41} In general, the chemical shift of mobile protons of this class ranges from ~ 0.8 ppm (OH groups of sugars) to $\sim 6\text{--}7$ ppm (some NH groups in heterocyclic compounds). Recently, McMahon and co-workers reported systems based on anthranilic acid analogs as diamagnetic CEST contrast agents.^{42,43} Such systems have shifts up to ~ 11 ppm because of intramolecular H-bonding in the plane of the aromatic ring. For diamagnetic systems, low-intensity ($B_1 < 3 \mu\text{T}$) and long irradiation time (>2 s) saturation fields are required for an efficient ST effect to occur.

Macromolecular diaCEST agents include macromolecules endowed with pseudo-equivalent mobile protons, such as polyaminoacids (*e.g.* poly-lysine or poly-glutamate), poly-uridilic acid, and dendrimers. The chemical shifts and exchanging properties of such groups are similar to those reported above for the monomeric species. Consequently, low-intensity radio-frequency fields and long saturation times are required for imaging with these agents. Finally, endoCEST agents are diamagnetic molecules naturally occurring in living organisms and include glucose, glycogen, glycosaminoglycans, proteoglycans, and proteins. Specific names have often been proposed, such as glucoCEST for glucose,^{35,36} glycoCEST for glycogen,⁴⁴ gagCEST for glycosaminoglycans,³⁴ and amide proton transfer for proteins.³⁷ Similar properties to diaCEST agents are observed with this class of compounds, and the *in vivo* abundance of such molecules necessary to determine the relative sensitivity threshold is noteworthy.

Analogous to diaCEST agents, paramagnetic CEST agents can also be classified in four sub-sets, namely (i) low-medium molecular weight paraCEST agents, (ii) supraCEST, (iii) lipoCEST, and (iv) cell-CEST agents. ParaCEST agents consist of small-to-medium sized coordination complexes containing a paramagnetic metal center, such as a lanthanide or a transition metal ion, in which the metal ion is chelated by a linear or a macrocyclic ligand. The mobile CEST protons belong either to the ligands (OH or NH groups) or to water molecules coordinated to the metal ions. The first example of this class of CEST agents was reported by Sherry and co-workers

in 2001. It was the tri-positively charged Eu^{III} macrocyclic complex $[\text{Eu-DOTA-4AmCE}]^{3+}$, which has a metal-bound water molecule that exchanges slowly with bulk water on the NMR timescale.⁴⁵

A large number of paraCEST agents have been developed for different applications.^{5,6,45} Many are macrocyclic tetra-amide derivatives of DOTA. Such coordination cages ensure a high kinetic inertness of the metal complexes, whereas the presence of a tri-positively charged lanthanide ion yields sufficiently slow water exchange rates. Furthermore, the overall geometry of the metal complex leads to large chemical shifts of the coordinated water protons, up to hundreds of ppm depending on the metal ion. As opposed to diaCEST molecules, paraCEST complexes provide good ST% in the presence of high-intensity ($B_1 > 6 \mu\text{T}$, up to 10 s of μT) and short saturation times (<2 s).

The intensity of the presaturation field is strongly related to the exchange rate of the mobile protons (k_{ex}). For example, for the protons of amide groups that exchange relatively slowly (k_{ex} of about 200 Hz at physiological pH), medium intensity saturation fields are enough to obtain optimal CEST signal. On the contrary, in the fast-exchanging Ln(III)-bound water protons (k_{ex} up to 2×10^5 Hz), intense presaturation fields are necessary. Therefore, paraCEST agents with a fast k_{ex} are not the preferred systems because their efficient saturation requires the application of saturation fields that are not compatible with *in vivo* experiments (high saturation fields lead to high specific absorption rate effects).

As for diaCEST agents, the sensitivity of paraCEST agents can be significantly enhanced with polymeric systems containing a large numbers of equivalent paraCEST units. Representative examples are micelles or dendrimers. A more detailed discussion of such agents is given later in this section. Another sub-set of paramagnetic CEST agents includes non-covalent supramolecular adducts between a paramagnetic shift reagent and a diamagnetic macromolecular substrate (supraCEST agents) that acts as source of mobile protons. The first reported example of such an agent was the adduct of $[\text{Tm-HDOTP}]^{4-}$ (a shift reagent) with cationic poly-arginine oligomers, the latter being the source of the exchanging protons. The large number of equivalent protons present in such structures lead to their high sensitivity (visualization of CEST contrast with micromolar concentration of $[\text{Tm-HDOTP}]^{4-}$).^{3,5,25}

The third and fourth sub-sets of paramagnetic CEST agents are the lipo- and cell-CEST agents.^{25,26,30,31} These two classes are strongly related. Both liposomes and cells are constituted of phospholipidic bilayers that separate inner and outer water compartments. When a paramagnetic shift reagent is loaded inside the inner compartment, the resonance of intra-liposomal or intra-cellular water protons is shifted with respect to the extra-liposomal or extra-cellular resonance. The inner-water resonance can be saturated and, because intra- and extra-compartmental water pools are in slow-to-intermediate exchange with each other, the saturation can be transferred to the bulk (extra-compartmental) water pool, thereby generating CEST

contrast. The advantage of both of these classes of paraCEST agents is that a large amount of equivalent proton scans be selectively saturated: 10^6 – 10^9 for liposomes, depending on the size, and, in principle, $\sim 10^{12}$ for red blood cells. The resulting CEST systems are thus highly sensitive (picomolar range for lipoCEST and the sub-picomolar range for cell-CEST). Because of the intermediate-to-slow exchange of protons, an efficient Z-spectrum acquisition requires low-to-medium intensity (*e.g.* $B_1 = 3 \mu\text{T}$) and short (irradiation time = 2 s) saturation pulses. A detailed description of nano- and micro-sized CEST systems (*e.g.* lipo- and cell-CEST) is presented later in Section 3.5.

Van Zijl and co-workers proposed another classification of CEST agents based instead on the exchange mechanism.² This classification includes three main classes: atom (proton)-, molecular-, and compartmental exchange-based CEST molecules (Figure 3.4B). In systems belonging to the first group (proton-exchange-based), a single proton of the molecule is involved in the chemical exchange with bulk water protons. Most of the diaCEST compounds (*e.g.* glucose), as well as several paraCEST probes (*e.g.* Yb-HPDO3A) belong to this class, as do supraCEST agents. The second group, molecular-exchange-based CEST agents, includes systems where an entire molecule is involved in the chemical exchange with bulk water. In these paraCEST complexes, such as $[\text{Eu-DOTA}(\text{Gly})_4]^-$, the coordinated water molecules exchange with bulk water to provide the CEST effect. In these agents, the molecular exchange rate is generally faster than the proton exchange rate. The last group, compartment-exchange-based CEST agents, includes those systems in which the chemical exchange of water protons occurs through a membrane, either artificial or natural. LipoCEST and cell-CEST agents are part of this group because the membranes modulate the intra-compartmental exchange.

3.1.5 Selected Applications of CEST and PARACEST Agents

A number of CEST agents and their *in vivo* applications have been reported. CEST agents have been shown to be particularly useful for as responsive agents, *i.e.* as probes that report on changes of a given parameter of the environment in which they distribute, such as pH, temperature, enzymatic activity, or concentration of metabolites;^{15,46,47} and as multi-tasking agents by exploiting frequency-encoding specificity as in the case of multicolor cell labeling.^{9,10} *In vivo* applications of responsive agents need to address the lack of knowledge of the concentration of the agent in the body. This issue can be addressed either by using molecules containing two or more sets of exchangeable proton pools or by using two or more CEST agents displaying the same biodistribution. In both cases, the ST% effect generated by the different proton pools has to be affected to a different extent by the parameter of interest (*e.g.* a different pH-responsiveness).

One of the most investigated families of paraCEST agents incorporates Ln^{III} complexes of HPDO3A (where Ln is different from Gd^{III} , La^{III} , Pm^{III} , or Lu^{III}). These molecules are analogous to Gd-HPDO3A , a clinically approved

MRI contrast agent. Such complexes have been demonstrated to be well-tolerated by cells, even at high intracellular concentrations.^{30,48,49}

3.1.5.1 Use of Ln-HPDO3A Probes as Responsive CEST Agents

In solution, these complexes are present as a pair of diastereoisomers, one with square antiprismatic (SAP) and one with twisted square antiprismatic (TSAP) geometry (Figure 3.5A).⁵⁰ The chemical shift of the resonances of the exchangeable OH protons of SAP and TSAP isomers is often quite different. In the case of the Yb^{III} complexes, the chemical shifts of OH protons are 71 and 99 ppm at 20 °C (Figure 3.5B). The chemical shifts of the hydroxyl protons of Yb-HPDO3A are sensitive to temperature. In fact, between 20 and 37 °C, the resonance frequencies switch from 99 to 88 ppm and from 72 to 64.3 ppm for the two isomers. Because the chemical shift does not depend on concentration, the exact temperature of the microenvironment of the agent can be determined by the Z-spectra.

The exchange rates of the two OH protons also have different pH dependencies and, consequently, different ST% (Figure 3.5C). The two diastereoisomers have the same *in vivo* biodistribution and thus maintain their relative concentration ratio. On this basis, the two OH proton resonances can be used to determine pH ratiometrically. From eqn (3.14), the pH can be calculated from the ratio of the relative SAP and TSAP ST% values (Figure 3.5D). Accordingly, the chemical shift can be used to determine temperature whereas ratiometric measurement of ST% provides the pH. Importantly, both parameters are determined without knowing the concentration of the probe.

$$\text{Ratio} = \frac{(\text{ST})_{\text{poolA}}(1 - (\text{ST})_{\text{poolB}})}{(\text{ST})_{\text{poolB}}(1 - (\text{ST})_{\text{poolA}})} \quad (3.14)$$

Yb-HPDO3A has been used to measure extravascular and extracellular pH in mice bearing subcutaneous melanoma tumors.¹⁵ This probe enabled mapping of the pH of the tumor with high spatial resolution. Maps of pH have been obtained for tumors at different development stages. These studies demonstrated that during tumor progression, there is an increase in pH heterogeneity rather than an overall pH change (Figure 3.6).¹⁵ Unfortunately, the potential clinical translation of Yb-HPDO3A has been questioned because the proton exchange rate of the complex is too fast and requires too high B_1 intensities, resulting in high specific absorption rate effects.⁵¹

3.1.5.2 Use of Ln-HPDO3A Probes as Labeling CEST Agents for Multicolor MR Imaging

Ln-HPDO3A complexes have also been investigated for cell labeling experiments. Such complexes can be efficiently loaded inside cells *via* different

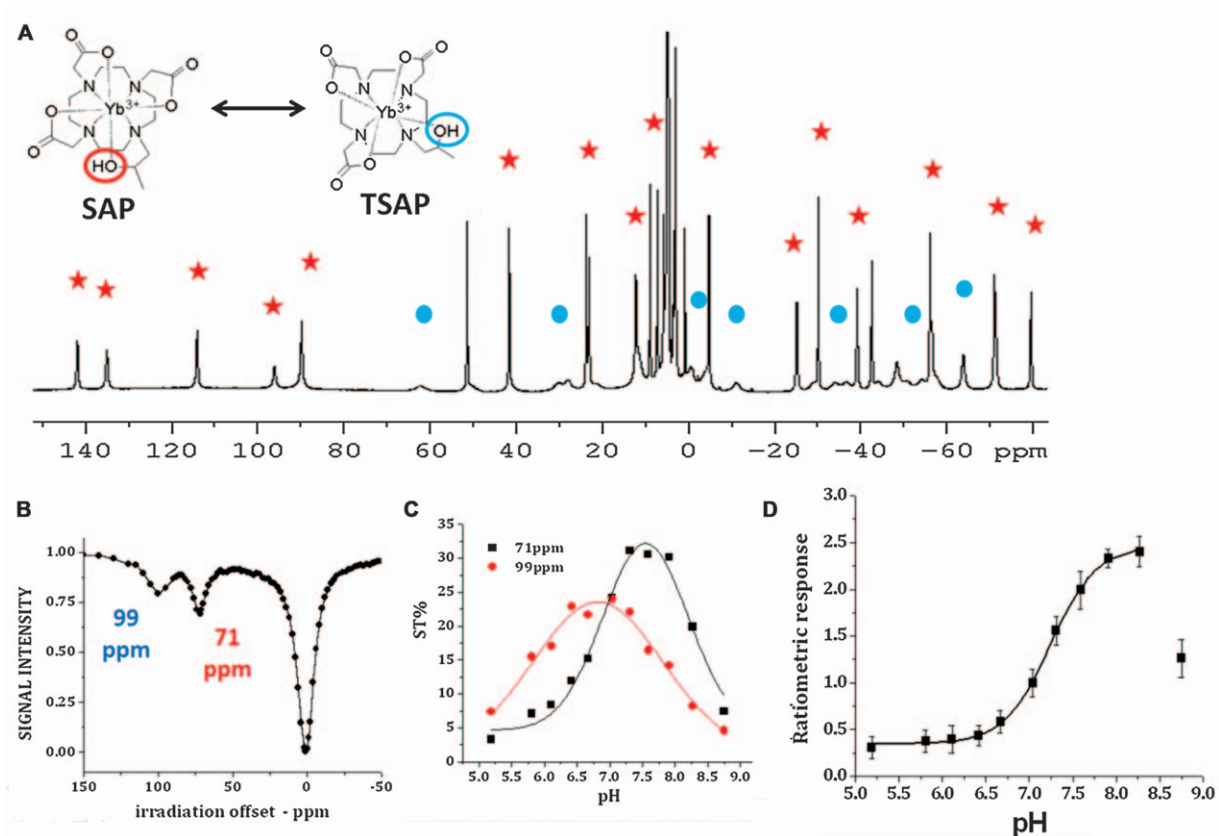


Figure 3.5 (A, top) Chemical structure of Yb-HPDO3A (two isomers, SAP and TSAP). (A, bottom) $^1\text{H-NMR}$ spectrum of Yb-HPDO3A, showing the presence of the two isomers. (B) Z-spectrum of Yb-HPDO3A (pH 7.4, 20 °C, $B_0 = 7\text{ T}$, $B_1 = 24\ \mu\text{T}$) showing the presence of two exchangeable hydroxyl groups (SAP in red and TSAP in blue). (C) ST% versus pH for the hydroxyl protons of the two isomers. (D) Ratiometric curve.

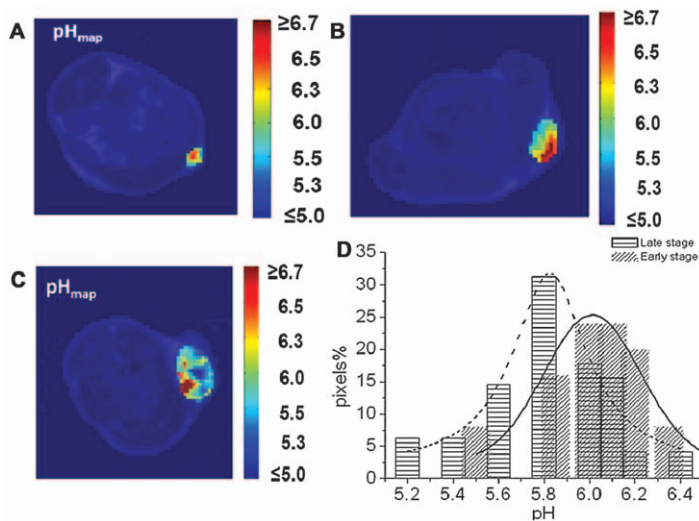


Figure 3.6 Representative pH maps of melanoma tumors at (A) early, (B) middle, and (C) late development stages. (D) Voxel-by-voxel pH distribution in the tumor region of early and late tumors.¹⁵ Adapted with permission from D. Delli Castelli, G. Ferrauto, J. C. Cutrin, E. Terreno and S. Aime, *Magn. Reson. Med.*, 2014, **71**, 326. © 2013 Wiley Periodicals, Inc.

techniques, such as electroporation, macropinocytosis, and hypotonic swelling, without affecting cell morphology or physiology.^{48,49,52,53} In this way, labeled cells can be administered and detected *in vivo* using MRI. By changing the metal center, it is possible to change both the resonance of the hydroxyl protons of the Ln-HPDO3A probe and the magnetic and thus contrastographic properties of such molecules. The entire family of paramagnetic Ln-HPDO3A molecules has been investigated, and Eu- and Yb-HPDO3A are often selected for simultaneous application.

In the Z-spectrum, Yb-HPDO3A contains two CEST signals at 72 and 99 ppm (Figure 3.7A). Eu-HPDO3A has only one signal at 20 ppm (Figure 3.7B). This signal is the contribution of both SAP and TSAP isomers with resonances that are not separable from each other. *Ex vivo* labeling of two cell types, macrophages and melanoma cells, with the two probes enables visualization of the distribution of each cell type *in vivo*.⁹ The use of false colors makes it possible to detect regions in which cells are located, highlighting the regions in which both cell types are simultaneously present (Figure 3.7C and D). Such an approach has been applied for the labeling and visualization of neural stem cells and endothelial cells implanted in the brain of a rat after a stroke,¹⁰ thus providing a tool for understanding the dynamics of cellular interactions leading to the formation of *de novo* tissue (Figure 3.7E). Eu-HPDO3A has also been used for *ex vivo* labeling of immortalized mouse skeletal myoblasts and tracking the cells after implantation in a cardiac region.^{13,53} CEST contrast generated by

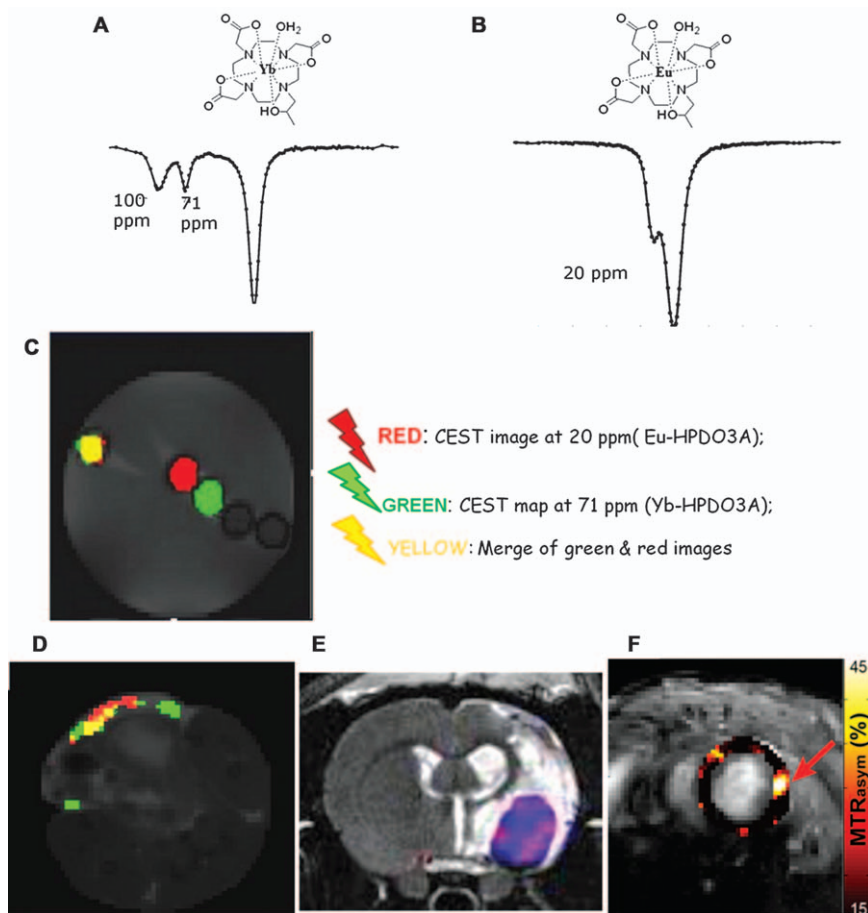


Figure 3.7 (A) Chemical structure and Z-spectrum of Eu-HPDO3A. (B) Chemical structure and Z-spectrum of Yb-HPDO3A. (C) False color map of a phantom containing glass capillaries loaded with Eu-labeled melanoma cells (red), Yb-labeled-macrophages (green), or a mixture of the two cell populations (yellow). Two capillaries loaded with non-labeled melanoma cells or macrophages have been added (uncolored). (D) Eu-labeled melanoma cells (red) and Yb-labeled-macrophages (green) localize after subcutaneous implantation in mice. (E) Eu-HPDO3A-labeled neural stem cells (blue) and Yb-HPDO3A-labeled endothelial cells (red) implanted in the brain of a rat after a stroke. (F) Eu-HPDO3A-labeled mouse skeletal myoblasts implanted in a murine cardiac region.

Adapted with permission from the following sources: G. Ferrauto, D. Delli Castelli, E. Terreno and S. Aime, *Magn. Reson. Med.*, 2013, **69**, 1703. © 2012 Wiley Periodicals, Inc.;⁹ F. J. Nicholls, W. Ling, G. Ferrauto, S. Aime and M. Modo, *Sci. Rep.*, 2015, **5**, 14597. Copyright © 2015, Rights Managed by Nature Publishing Group;¹⁰ and A. Pumphrey, Z. Yang, S. Ye, D. K. Powell, S. Thalman, D. S. Watt, A. Abdel-Latif, J. Unrrie, K. Thompson, B. Fornwalt, G. Ferrauto and M. Vandsburger, *NMR Biomed.*, 2016, **29**, 74. Copyright © 2015 John Wiley & Sons, Ltd.¹³

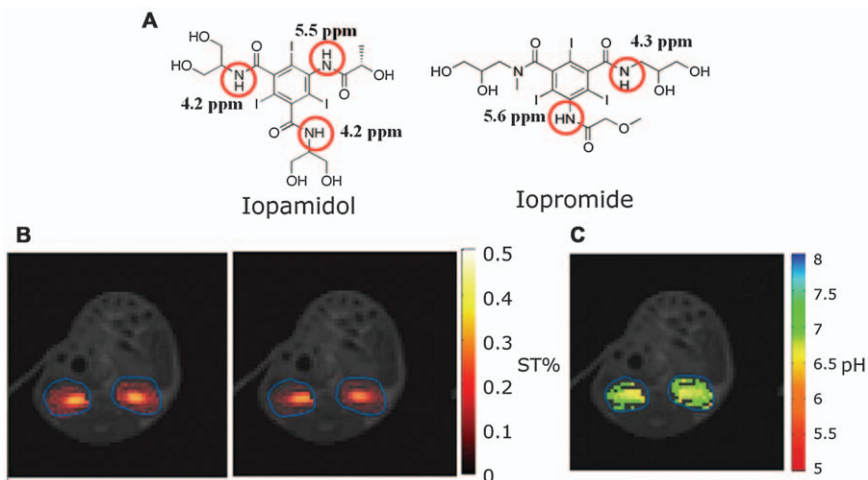


Figure 3.8 (A) Chemical structures of Iopamidol and Iopromide, showing exchangeable protons in red circles. (B) ST maps obtained after the intravenous injection of an Iopamidol (0.75 mg I g^{-1} by weight) bolus by irradiating the amide proton pools at 4.2 (left) and at 5.5 ppm (right). (C) pH map of kidney region obtained by applying the ratiometric method.⁵⁵ Adapted with permission from D. L. Longo, W. Dastrù, G. Digilio, J. Keupp, S. Langereis, S. Lanzardo, S. Prestigio, O. Steinbach, E. Terreno, F. Uggeri and S. Aime, *Magn. Reson. Med.*, 2011, 65, 202. © 2010 Wiley-Liss, Inc.

paramagnetic Eu-labeled cells has been demonstrated to be preserved in surviving cell grafts and eliminated in instances of cell rejection.⁵⁴

3.1.5.3 Use of Iodinated CT-contrast Agents as CEST Probes

Iodinated contrast media already commonly used in CT exams was also considered as CEST agents. The iodinated compounds are administrated at high doses and display good safety profiles. Importantly, the compounds contain several exchangeable protons per molecule, which have been exploited for the acquisition of CEST MR images. Most attention has been devoted to Iopamidol^{17,55} and Iopromide,^{40,56} which contain two types of amide protons that are useful for ratiometric assessment of pH (Figure 3.8A). These agents have been extensively tested on animal models for assessing the pH of extracellular space in tumors⁵⁶ as well as pH changes in the case of acute kidney injury (Figure 3.8B and C).^{17,55}

3.2 Acquisition of CEST Spectra

MICHAEL T. McMAHON

3.2.1 Instrumentation and Sample Conditions for Collecting Z-Spectra to Characterize CEST Contrast

To determine if a compound has favorable properties for detection *via* CEST imaging, the amount of signal loss must be quantified as a function of saturation frequency at an appropriate saturation field strength and set of offsets. This process is known as collecting a Z-spectrum. More precisely, the Z-spectrum is a plot of relative water saturation $S^{\Delta\omega}/S_0$ as a function of saturation frequency offset with respect to water ($\Delta\omega$). If other nuclei are used, the offset is set with respect to the bulk species of the nuclei, for example, xenon. This section describes the general procedure for determining if a compound is promising as a CEST agent, describes what to look for in Z-spectra, and provides some insights into common problems associated with this type of data collection.

Either an NMR spectrometer or an MRI scanner can be used to collect Z-spectra, with the scanner field strength being at least 1 T for paramagnetic agents and at least 3 T for diamagnetic, hyperpolarized, or liposomal agents. Traditionally, compounds are characterized at concentrations in the range of 10–100 mM at neutral pH and 37 °C in 10 mM phosphate-buffered saline. If an NMR spectrometer is used, ~350 μL of solution is required; however, if an MRI scanner is used, volumes as low as 40 μL will provide a reliable measurement of the Z-spectra in capillary tubes with diameters of 1–1.8 μm . Besides enabling the use of smaller volumes of sample, another advantage of MRI scanners over NMR spectrometers is that a wide number of samples or sample conditions can be screened at once. Because CEST contrast is sensitive to pH changes, it is often important to measure Z-spectra over a range of pH values to assess if a compound has potential to serve as a contrast agent. For hyperpolarized agents, screening is performed a little differently and is beyond the scope of this chapter. For more information on collecting Z-spectra of hyperpolarized agents, interested readers are referred to other sources.^{57–60}

3.2.2 Pulse Sequences Utilized for Collecting Z-Spectra

Either NMR or MRI pulse sequences can be used for collecting Z-spectra. The NMR sequence shown in Figure 3.9 is the simplest version, whereby a long (typically 1–3 s) continuous wave saturation pulse is inserted in front of a relatively short excitation pulse with the offsets of these pulses at different frequencies. For MRI scanners, which allow the use of multiple tube phantoms, multi-slice imaging sequences based on either gradient echoes or fast-spin echoes can be used.

Fast spin-echo sequences have the advantage of having low sensitivity to magnetic susceptibility gradients that are present with multiple-tube phantoms due to the interfaces between the tubes. These field gradients induce magnetic field (B_0) inhomogeneities that should be minimized by shimming. Generally for phantoms, the B_0 should be such that the range of frequencies encompassing the water signal should not vary by more than ± 600 Hz across an imaging slice and preferably varies by less than ± 100 Hz. To determine this range for a new agent, either an NMR spectra without saturation pulses or a point-resolved spectroscopy dataset is collected with a voxel geometry approximating the area of interest for the phantoms. Typical parameters for point-resolved spectroscopy are $T_R/T_E = 2000/20$, acquisition size = 8192, sweep width = 10 080 Hz, and number of acquisitions = 1. The width of the water peak after fast Fourier transformation and baseline correction is used to determine the range of B_0 inhomogeneities.

To collect Z-spectra using an NMR spectrometer, the frequency of the saturation pulse is incremented while the excitation pulse is fixed on the water frequency. The recycle delay after the $\pi/2$ excitation pulse should be in the range of 6–10 s as mentioned previously.⁶¹ As described in Figure 3.9, the range of frequencies depends on the type of CEST agent that is being screened. Diamagnetic agents typically have labile protons resonating between 0.1 and 6 ppm from water unless they have an intramolecular hydrogen bond.^{14,42,43,62} Diamagnetic agents with intramolecular-bond-shifted protons have labile protons that resonate as far as 12 ppm from water.¹⁴

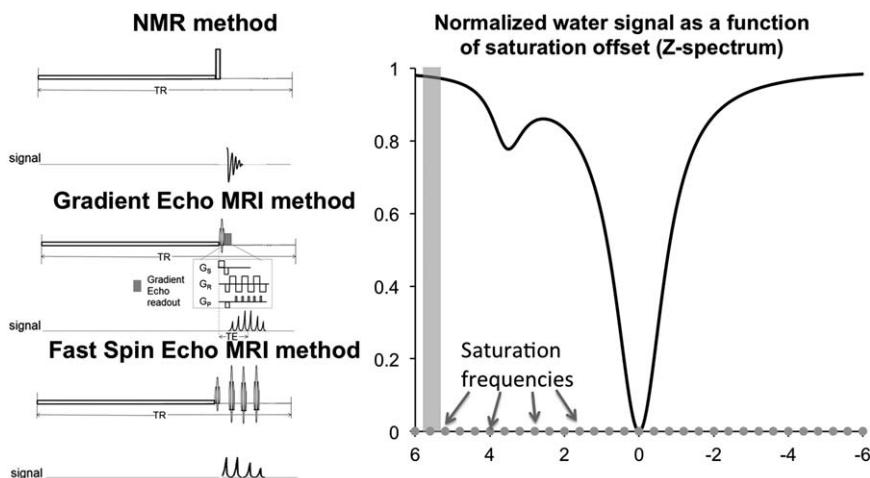


Figure 3.9 Pulse sequences and general acquisition strategy for collecting Z-spectra. For all sequences, saturation pulses: $\omega_1 \sim 1\text{--}12$ μT (diaCEST or lipoCEST) and 5–25 μT (paraCEST). Saturation pulse offset is incremented from 0.1–15 ppm from water (diaCEST) 0.1–30 ppm from water (lipoCEST) or 1–720 ppm from water (paraCEST). Excitation pulses have an offset centered on water.

For diamagnetic agents, contrast is typically expected to appear using a saturation pulse of 3 s and either 2 or 4 μT . If other parameters are used, the exchange is often too fast for detection. Liposomal agents have labile protons that resonate a little farther from water, but the same saturation conditions as used for diamagnetic agents should produce contrast with liposomal agents. Paramagnetic agents require large ranges of frequencies depending on the metal ion in the complex and the type of exchanging proton, for example, protons of coordinated water molecules or labile protons in NH, NH₂, or OH moieties. An example of the range of frequencies covered in paramagnetic samples can be found in the tabulation of the proton frequencies of water bound to a series of [Ln-DOTA(Gly)₄]⁻ complexes.⁶³ For paramagnetic CEST agents, contrast is typically expected to appear using a saturation pulse of 3 s and either 14 or 25 μT . These saturation parameters also will hold for the MRI experiments mentioned next.

For MRI-based data, it is necessary to correct Z-spectra for B_0 inhomogeneities. This correction process requires mapping the B_0 for each pixel. The method typically employed is termed water saturation shift reference (WASSR) mapping and involves collecting a set of images using one of the sequences in Figure 3.9 with a short (~ 200 – 500 ms), low-power ($B_1 \approx 0.5$ μT) saturation pulse incremented over the entire range of B_0 inhomogeneities found in the phantom, typically from -1 to 1 ppm from water.⁶⁴ Parameters that are typically used for collecting fast spin-echo water saturation shift reference images on a single slice are acquisition bandwidth = 50 kHz, slice thickness = 1 mm, $T_E = 6$ ms, $T_R/T_E = 1500/6$, echo train length = 16, field of view = 20 mm \times 20 mm, and matrix size = 128 \times 64. The signal is interpolated across the frequencies in the images to determine the water saturation shift reference absolute frequency maps and the error in these maps is typically <1 Hz for each pixel.⁶⁵ After collecting the water saturation shift reference maps, the CEST contrast images are collected using the same MRI sequence as for the water saturation shift reference images, and the same saturation conditions mentioned for NMR experiments. Using a 3 s saturation pulse, $T_R = 6$ s should produce nice contrast maps.

3.2.3 Data Post-processing and Analysis

To generate B_0 maps from the MRI datasets, the set of water saturation shift reference maps is pooled with the signal fit pixel-wise using Matlab, Interactive Data Language, or some other software. To fit the signal intensity ($S_{\text{exp}}(x,y)$) for each voxel, eqn (3.15) can be used.⁶⁵

$$S_{\text{exp}}(x,y) = \left\{ \eta^2 + \left[\frac{M_0(x,y)}{1 + \left(\frac{\omega_1(x,y)}{\Delta\omega(x,y) - \delta\omega_0(x,y)} \right)^2 \frac{T_1(x,y)}{T_2(x,y)}} \right]^2 \right\}^{1/2} \quad (3.15)$$

where η is the experimental noise; T_1 and T_2 are the longitudinal and transverse, respectively, relaxation times for water; M_0 is the normalized signal for the voxel; ω_1 is the saturation field strength; and $\delta\omega$ is the B_0 shift for the voxel.

Typically non-linear fitting functions are used (for example, lsqcurvefit) in Matlab with M_0 , $\delta\omega_0$, and $\left(\frac{T_1}{T_2}\omega_1^2\right)$ as free parameters. To save computational time, images can be masked using a signal-to-noise threshold prior to this fitting. This masking is done by estimating the experimental noise (η) by calculating the mean signal in a noise-only region of the images and retaining pixels with signal $>30 \eta$. A B_0 map is then prepared by plotting $\delta\omega_0(x,y)$ for each pixel. This step is unnecessary when using NMR spectrometers because the field should be sufficiently homogeneous for a single NMR tube to enable data processing.

The next step is to process the raw CEST images for calculation of CEST contrast and B_0 corrections. As was the case for water saturation shift reference images, the set of CEST images as a function of saturation frequency is pooled for each saturation field strength, and the signal is interpolated using a cubic-spline fitting to generate signal for intermediate frequencies. Saturation-transfer images are then corrected pixel-wise using the water saturation shift reference B_0 map using the expression in eqn (3.16).

$$\Delta\omega(x,y)_{\text{corrected}} = \Delta\omega(x,y) - \delta\omega_0(x,y) \quad (3.16)$$

The Z-spectra from individual tubes can be plotted using region-of-interest analyses with region-of-interest masks drawn and the mean intensity of the region-of-interest plotted as a function of corrected $\Delta\omega$. To quantify CEST contrast, the asymmetry in the magnetization transfer ratio (MTR_{asym}) is calculated using eqn (3.17):

$$\text{MTR}_{\text{asym}} = \frac{(S^{-\Delta\omega} - S^{+\Delta\omega})}{S^{-\Delta\omega}} \quad (3.17)$$

where $S^{+\Delta\omega}$ and $S^{-\Delta\omega}$ are the signal intensities with saturation at frequencies $\Delta\omega$ downfield and $\Delta\omega$ upfield, respectively, from the water-proton resonance frequency. These MTR_{asym} spectra are calculated to remove direct saturation of water, and they can be plotted for each tube using region-of-interest analysis.

3.2.4 Acknowledgements

The author was supported by a Maryland Stem Cell Research Fund grant, MSCRFI-2829.

3.3 Determining q for CEST Complexes

JANET R. MORROW* AND ERIC M. SNYDER

3.3.1 Oxygen-17 NMR Spectroscopy for CEST Agents

Unlike the Gd^{III} -based contrast agents for T_1 -weighted MRI discussed in Chapter 2, CEST agents do not require a water ligand for optimal contrast properties. All CEST agents must have a ligand proton that is in chemical exchange with protons in bulk water, but this exchangeable proton does not need to be on a water molecule directly coordinated to a metal ion. As discussed in Chapter 3.1, exchangeable protons for Ln^{III} ^{3,66–69} or transition metal ion-based ^{70–78} paraCEST agents include amide NH, alcohol OH, heterocyclic NH protons, and water (Figure 3.10). Regardless of the class of CEST agent, it is necessary that the resonances of these exchangeable protons are shifted away from the resonance of bulk water by the paramagnetic center and the exchange rate constants must be in a suitable range for CEST. In particular, rate constants for proton exchange must be no larger than the frequency difference between the proton resonance of the CEST agent and bulk water.⁷⁹ Rate constants for proton or water exchange on paraCEST agents typically are in the range of 10^2 to 10^4 s^{-1} .^{66,70} Thus, for water ligands to give rise to the CEST effect, exchange must be orders of magnitude slower than that of Gd^{III} -based T_1 -shortening contrast agents. Such slow water-exchange rate constants have been reported for Ln^{III} complexes that contain a macrocycle with neutral pendent groups, such as $[Eu(DOTAM)]^{3+}$ (Figure 3.10).^{80,81}

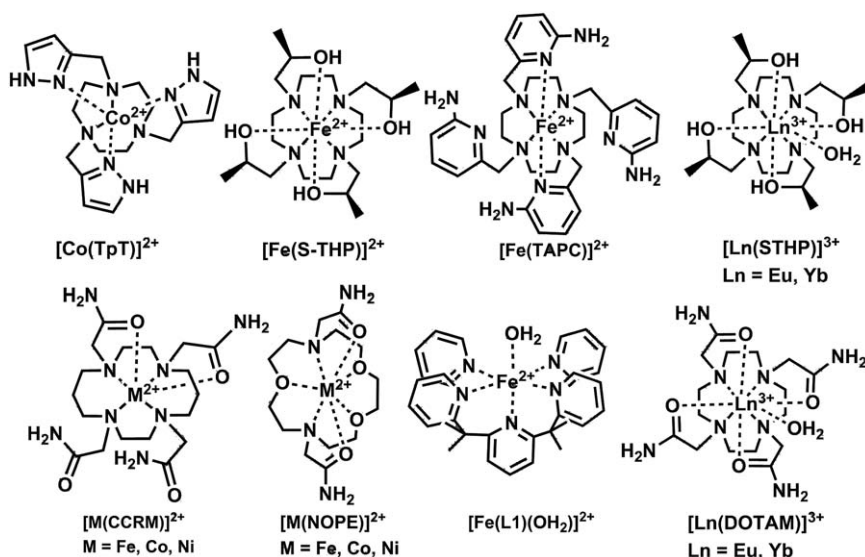


Figure 3.10 Selected transition-metal- and lanthanide-based paraCEST agents.

The $[\text{Eu-DOTAM}]^{3+}$ complex in Figure 3.10 has a single bound water ligand, as evidenced by luminescence spectroscopy studies (see Chapter 2.4.3 for a discussion on how to determine q by luminescence lifetimes of Eu^{III} and Tb^{III} complexes).⁸² There are two isomers, the twisted square antiprismatic and square antiprismatic forms, which coexist in solution for the Eu^{III} complex of DOTAM, as shown by $^1\text{H-NMR}$ spectroscopy⁸⁰ and by excitation of the $^7\text{F}_0 \rightarrow ^5\text{D}_0$ transition of Eu^{III} with luminescence spectroscopy.⁸² Many derivatives of the DOTAM ligand have been prepared and their Ln^{III} complexes have been studied as paraCEST agents.^{66,83–85}

For lanthanide-based complexes, and in the case of rapidly exchanging water, $^{17}\text{O-NMR}$ studies of Dy^{III} complexes might be used to determine q (see Chapter 2.4.2).^{86,87} However, for slowly exchanging systems, the situation is more complex. For $[\text{Eu-DOTAM}]^{3+}$, $^{17}\text{O-NMR}$ studies indicate that each of the two isomers produce distinct $^{17}\text{O-NMR}$ resonances.⁸⁸ This observation suggests that there is a distinct bound-water ^{17}O -resonance, consistent with a slow rate of water exchange. It is not feasible to count bound water molecules in this experiment, in part because studies were carried out in acetonitrile. In any case, measurement of the number of bound waters by integration would be challenging owing to the low intensity of the bound-water resonance in comparison to that of bulk water. Subsequent studies of an Eu^{III} complex of a DOTAM derivative by variable-temperature $^{17}\text{O-NMR}$ were used to measure the rate constant for water exchange (Figure 3.11).⁸⁹

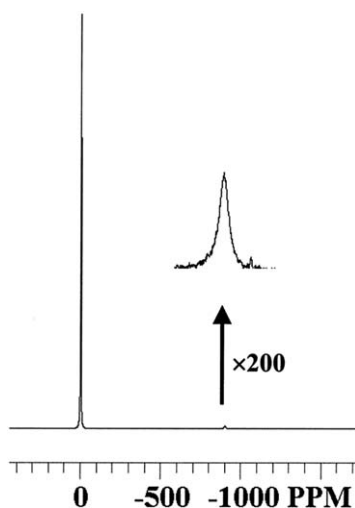


Figure 3.11 $^{17}\text{O-NMR}$ spectrum of $[\text{Eu-DOTAM}(\text{Gly})_4(\text{H}_2\text{O})]^-$ in aqueous solution (10% ^{17}O -enriched) at 25 °C, Eu^{III} concentration ≈ 0.1 M. The bulk water was used as the reference at 0 ppm.

Adapted with permission from S. Zhang, K. Wu, M. C. Biewer and A. D. Sherry, *Inorg. Chem.*, 2001, **40**, 4284 (ref. 89). Copyright 2001 American Chemical Society.

Only certain types of Ln^{III} complexes with a single bound water are known to give rise to the CEST effect through water exchange, and few transition metal complexes give rise to the CEST effect through water exchange.⁶⁶ This is attributed to the necessity of water ligand exchange being sufficiently slow to observe the CEST effect and the special characteristics of the water cavity in $[\text{Ln-DOTAM}]^{3+}$ complexes. To determine the number of water ligands for Ln^{III} -based paraCEST agents that have other types of ligand protons that produce a CEST effect, methods discussed in Chapter 2.4 might also be used.

Most reported transition metal-based paraCEST agents contain exchangeable protons on ligand donor groups, but not water (Figure 3.10).^{70,90} There is a single reported example of an Fe^{II} -based complex that has an exchangeable water ligand that gives rise to a CEST peak [$\text{Fe}(\text{L1})$ in Figure 3.10].⁷⁸ Structural studies of this complex demonstrate that there is a single water in the solid state, but no data is provided to determine the number of bound waters in solution. For transition-metal-based paraCEST agents, the study of q has similar considerations to those discussed for Ln^{III} complexes. Slowly exchanging water ligands should give rise to ^{17}O -NMR resonances that are distinct from bulk water, as observed for $[\text{Ln-DOTAM}]^{3+}$.⁸⁹ If the paraCEST agent is extremely soluble so that very high concentrations of complex (>100 mM) can be used, it might be feasible to integrate the peak from bound water and compare the integration to that of the peak from bulk water to estimate the number of bound water ligands. Such classic studies have been reported for the determination of the number of bound waters in simple metal salts under conditions where water exchange is slow.^{91,92}

Rapidly exchanging water ligands on paramagnetic complexes of transition metal ions produce a single ^{17}O -NMR resonance that is the weighted average of bulk and bound water. Under these conditions, variable-temperature ^{17}O -NMR measurements are useful for estimation of both the number of bound waters and the rate constant for exchange, as discussed in Chapters 2.4.2 and 2.6.2. Early variable-temperature ^{17}O -NMR studies of the Co^{II} aquo ion in solution were consistent with the presence of six coordinated waters with lifetime of 4.2×10^{-7} s.⁹³ Similar ^{17}O -NMR studies were also used to estimate numbers of water ligands and exchange rate of Fe^{II} and Ni^{II} aquo complexes.^{94,95} Studies on polyaminocarboxylate-based complexes of Fe^{II} gave detailed information regarding the rate constant and speciation for seven-coordinate complexes with a single coordinated water.⁹⁶ However, ^{17}O -NMR studies of Ni^{II} , Co^{II} , and Fe^{II} complexes with different ligands, geometries, and numbers of bound water molecules are lacking in the literature. These NMR spectroscopy studies remain to be further explored to characterize transition-metal-based paraCEST agents.

3.3.2 Other Techniques for Gadolinium-based Complexes That Also Apply to CEST Agents

Luminescence spectroscopy is perhaps the most useful tool for the determination of q in solution for Ln^{III} -based paraCEST agents.⁹⁷⁻⁹⁹ As

described in Chapter 2.4.3, excitation spectroscopy and luminescence lifetimes of Eu^{III} complexes are powerful tools for the study of solution chemistry and the determination of q .^{100–103} These methods have been used to show that the paraCEST agent, $[\text{Eu-DOTAM}]^{3+}$, has two isomers in solution and with a single coordinated water.⁸² However, even with luminescence methods, measurement of q is made challenging by poorly understood outer-sphere contributions to the quenching of luminescence. A particularly interesting example that shows the effect of both inner- and outer-sphere contributions to q was reported in the study of Eu^{III} -based paraCEST agents that contain alcohol pendant groups in complexes such as $[\text{Eu-STHP}]^{3+}$ (Figure 3.10).^{104–106} The $[\text{Eu-STHP}(\text{OH}_2)]^{3+}$ complex cation contains a nine-coordinate Eu^{III} ion in the solid state with all four alcohol pendant groups bound to Eu^{III} and a water ligand capping the twisted square prism formed by the macrocycle. In solution, however, the coordination chemistry is more complicated, as shown by direct-excitation luminescence studies. At neutral pH, luminescence lifetime data is consistent with a single bound water and four bound alcohol groups. In this analysis, alcohol OH oscillators are considered to be half as efficient in quenching luminescence as water, which contains two OH oscillators. A single excitation peak (${}^7\text{F}_0 \rightarrow {}^5\text{D}_0$) is observed at pH 6.3 (579.32 nm), suggesting that there is only a single species in solution under these conditions. However, at the more basic pH of 8.6, the complex ionizes by either deprotonation of the water ligand or one of the alcohols.¹⁰⁷ Consistent with the formation of a new ionized species, a second excitation peak is observed at 577.51 nm. Curiously, luminescence-lifetime studies show increased quenching; whereas, the expectation is that deprotonation should remove one of the OH oscillators and decrease the quenching of luminescence. Instead, q increases from 1.2 to 2.2 upon deprotonation of the complex, as if an additional water ligand was added to the coordination sphere. Most likely, there is an additional quenching contribution from second-sphere hydration that is promoted by deprotonation and the formation of new hydrogen bonding interactions. This data highlights the complexity of the interactions of the metal-ion coordination sphere in water.

The number of bound waters in Ln^{III} -based paraCEST agents is often modulated in the presence of biologically relevant anions that bind to the complexes. For example, addition of phosphate, carbonate, or citrate to $[\text{Eu-STHP}]^{3+}$ reduces q , as shown by luminescence-lifetime data, consistent with replacement of the water ligand with the anion (Table 3.2).¹⁰⁵ Anion binding can also be monitored by following changes in excitation or emission peaks because displacement of water ligands changes the coordination sphere. Changes in excitation or emission peaks as a function of the concentration of ligand are used to generate binding curves for anionic ligands. All of the anionic ligands in Table 3.2 are completely bound at the concentrations shown. Yet, q for $[\text{Eu}(\text{STHP})]^{3+}$ when fully bound to an anion is not close to zero, with the exception of citrate. The fact that q is not close to zero suggests that second-sphere contributions are not accurately counted.

Table 3.2 Luminescence lifetimes and q for a Eu^{III} paraCEST agent. All samples contain NaCl (0.100 M) and HEPES (0.100 M) at pH 7.2. Adapted with permission from J. Hammell, L. Buttarazzi, C.-H. Huang and J. R. Morrow, *Inorg. Chem.*, 2011, **50**, 4857 (ref. 105). Copyright 2011 American Chemical Society.

Complex	Excitation wavelength (nm)	Anion	[Anion] (mM)	$\tau_{\text{H}_2\text{O}}$ (ms)	$\tau_{\text{D}_2\text{O}}$ (ms)	q
Eu-STHP	579.36	Phosphate ^a	20	0.310	1.12	0.34
Eu-STHP	579.36	Monomethylphosphate ^a	20	0.298	1.03	0.41
Eu-STHP	579.36	Carbonate ^b	40	0.267	0.856	0.64
Eu-STHP	579.36	Acetate ^b	40	0.280	0.911	0.50
Eu-STHP	579.36	L-Lactate ^b	40	0.271	0.860	0.56
Eu-STHP	579.54	Citrate ^c	1.0	0.333	1.10	0.070

^aEu-STHP concentration 0.100 mM;

^bEu-STHP concentration 1.00 mM;

^cEu-STHP concentration 25 μM .

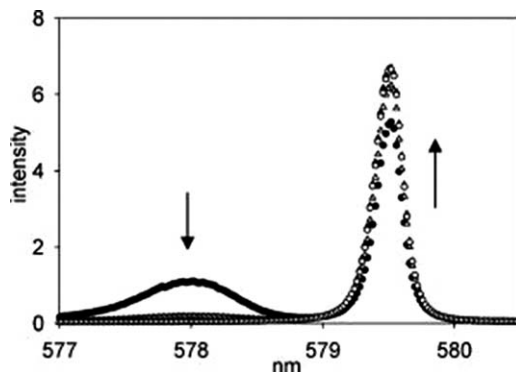


Figure 3.12 ${}^7\text{F}_0 \rightarrow {}^5\text{D}_0$ excitation spectra (${}^5\text{D}_0 \rightarrow {}^7\text{F}_2$ emission) of $[\text{Eu-STHP}]^{3+}$ (10.0 mM), buffer (20 mM), and NaCl (100 mM) with diethylphosphate [(●) 0 mM, (△) 10 mM, (▲) 20.0 mM, or (○) 30 mM] at pH 8.0 and 22 °C.¹⁰⁴ Adapted with permission from C.-H. Huang, J. Hammell, S. J. Ratnakar, A. D. Sherry and J. R. Morrow, *Inorg. Chem.*, 2010, **49**, 5963. Copyright 2010 American Chemical Society.

Alternatively, it is possible that the bound water is not completely displaced, and the anionic ligands bind in an outer-sphere mode.

This latter alternative is the case for binding of phosphate diesters to $[\text{Eu-STHP}]^{3+}$. The addition of phosphate esters such as diethylphosphate or bis-4-nitrophenylphosphate produces no change in the appearance of the ${}^7\text{F}_0 \rightarrow {}^5\text{D}_0$ excitation band nor of the lifetime of luminescence. However, binding of diethylphosphate is observed through a change in the pH dependence of the production of the 578 nm species in excitation luminescence studies (Figure 3.12) and also through a change in the pH dependence of the CEST spectrum.^{104,106} The dissociation constant for the outer-sphere diethylphosphate complex is 1.9 mM.¹⁰⁴ Similarly, there is

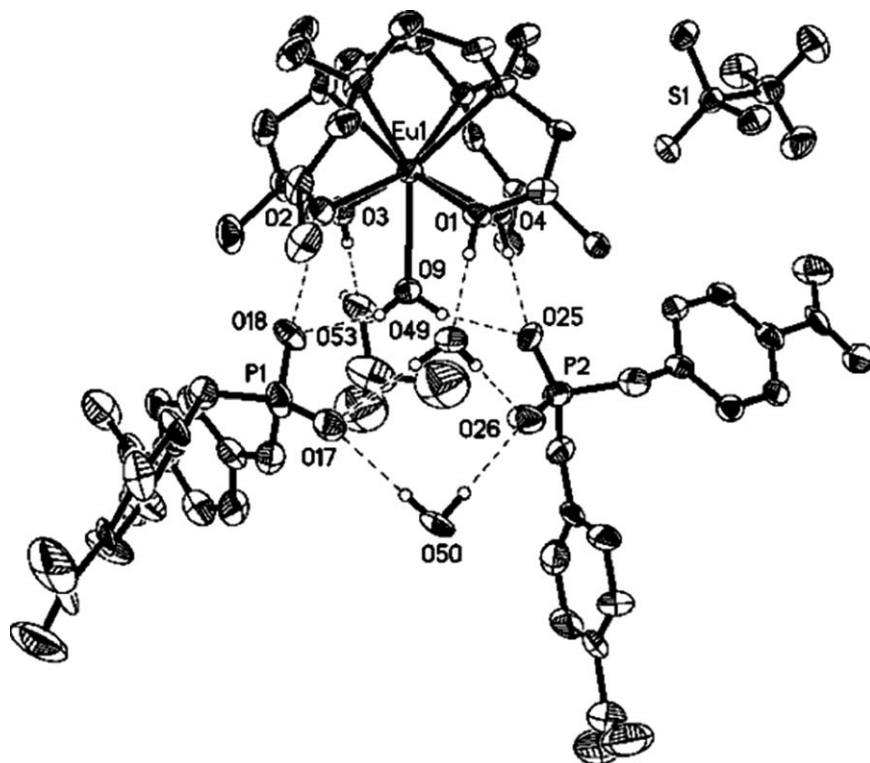


Figure 3.13 Ortep diagram (50% ellipsoids) of $[\text{Eu-STHP}(\text{OH})_2][(\text{O}_2\text{NPhO})_2\text{PO}_2]_2\text{-}[\text{CF}_3\text{SO}_3] \cdot 2\text{H}_2\text{O} \cdot i\text{-PrOH}$.¹⁰⁴ Adapted with permission from C.-H. Huang, J. Hammell, S. J. Ratnakar, A. D. Sherry and J. R. Morrow, *Inorg. Chem.*, 2010, **49**, 5963. Copyright 2010 American Chemical Society.

evidence of an outer-sphere interaction with the Yb^{III} analog.¹⁰⁴ $[\text{Yb-STHP}]^{3+}$ produces a CEST peak only at an acidic pH value of 3 (Figure 3.14). In the presence of two equivalents of diethylphosphate, the complex produces a CEST peak at pH 7.¹⁰⁴ The suppression of ionization is promoted by outer-sphere interactions. The crystal structure of the complex features the phosphate diester forming hydrogen bonds as a second-sphere ligand to the alcohols of $[\text{Eu-STHP}]^{3+}$ (Figure 3.13). Thus all three methods—X-ray diffraction, luminescence spectroscopy, and CEST imaging—are required to define the inner- and outer-sphere interactions of this paraCEST agent. This complexity in defining the coordination sphere would be difficult to resolve using a single technique (Figure 3.14).

An additional method for the determination of q for paraCEST agents is crystallography. This is discussed in greater detail in Chapter 2.4.5. For example, crystallographic studies of $[\text{Ln-DOTAM}]^{3+}$ complexes that are paraCEST agents showed that the series of complexes containing lanthanide ions

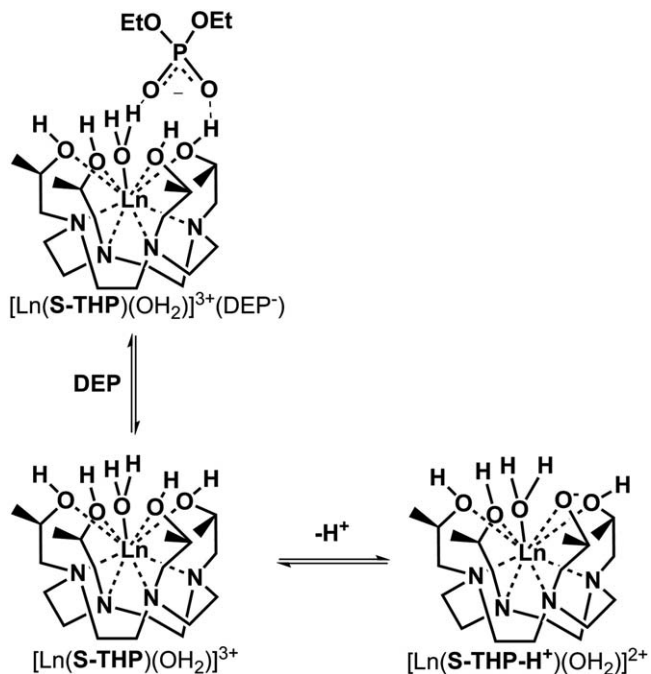


Figure 3.14 Hydrogen bonding of phosphate diester blocks ionization of $[\text{Ln-S-THP}(\text{OH}_2)]^{3+}$.¹⁰⁴ Adapted with permission from C.-H. Huang, J. Hammell, S. J. Ratnakar, A. D. Sherry and J. R. Morrow, *Inorg. Chem.*, 2010, **49**, 5963. Copyright 2010 American Chemical Society.

from Eu^{III} to Lu^{III} have a single bound water;¹⁰⁸ whereas the $[\text{La-DOTAM}]^{3+}$ complex has two bound waters,¹⁰⁹ as anticipated based on the larger ionic radius of La^{III} . Crystallographic studies to date have shown that transition metal-ion-based paraCEST agents, with one exception,⁷⁸ have no inner-sphere water.^{74,76}

3.4 Determining Proton Exchange Rates (k_{ex})

MICHAEL T. McMAHON

3.4.1 Introduction to Proton Exchange

Chemical exchange saturation transfer (CEST) MRI is a contrast mechanism that enables the amplified detection of low concentration solutes based on the exchange of their labile protons with water. To optimize pulse sequences and post-processing strategies for CEST imaging, it is important to quantitatively determine the exchange rates of protons associated with CEST contrast agents.

CEST has the requirement that proton exchange must occur with water or xenon exchange must occur with bulk xenon gas. These exchanges result in MRI contrast enhancement depending on several parameters, including concentration, T_1 and T_2 time constants, saturation time, saturation field strength, and the rate of exchange. Exchange rate is sensitive to changes in environment, such as temperature, pH, and ion concentration, and optimal exchange rates depend on the chemical shift with respect to water ($\Delta\omega$). Consequently, as described in Sections 3.1 and 3.2, CEST agents with large shifts have different rates for optimal contrast production to CEST agents with small shifts. The critical parameter of exchange rate can be measured using NMR spectroscopy or MRI. This section presents NMR- and MRI-compatible methods for measuring exchange rates to enable evaluation of prospective CEST agents. Notably, the methods discussed in Chapter 2.6 to determine the water residence time for Gd^{III} -based contrast agents can also be used for those paraCEST agents for which the CEST signal arises from a slowly exchanging coordinated water molecule.

3.4.2 Linewidth Measurement for Assessing Exchange Rate

The simplest method to measure exchange rates is by measuring the linewidth of the exchangeable solute protons (LW_s) because this parameter is known to be related to exchange rate from solute to water (k_{sw}) and T_2 relaxation through the following expression:^{110,111}

$$k_{\text{sw}} = \pi \cdot LW_s - 1/T_{2s} \quad (3.18)$$

To measure these linewidths, excite–detect NMR experiments can be performed, and linewidths can be determined through mixed Gaussian–Lorentzian deconvolution. This deconvolution is readily available on TopSpin and other NMR software, starting with 100% Lorentzian and adding Gaussian character to determine if the fit is improved. Typically, data is collected over a few pH values to determine the T_{2s} term, which dominates the expression for the slowest rates. This method is suitable for measuring solutes at high concentration (50–100 mM) with exchange rates with slow-to-moderate values ($k_{\text{sw}} < 1200 \text{ s}^{-1}$), conditions which are often too stringent to be practical.

3.4.3 WEX Experiments for Assessing Exchange Rate

Another NMR-based method that can be employed for measurement of exchange is the water-exchange (WEX) family of experiments.^{112–114} These sequences measure the magnetization transferred from water to solute, with the WEXII sequence shown in Figure 3.15.

By measuring magnetization transfer of the labile protons as a function of mixing time, the exchange rate to water (k_{sw}) can be quantified with the solute signal intensity (S_s) as a function of t_m given by eqn (3.19):^{112,115}

$$S_s(t_m) = \frac{k_{sw}S_{0s}}{k_{sw} + R_{1s} - R_{1w}} [e^{-R_{1w}t_m} - e^{-(k_{sw}+R_{1s})t_m}] \quad (3.19)$$

In eqn (3.19), S_{0s} is the equilibrium magnetization. This equation can be used provided the longitudinal relaxation rates ($1/T_1$) for water ($R_{1w} \sim 0.248 \text{ s}^{-1}$) and the agent ($R_{1s} \sim 0.71 \text{ s}^{-1}$) are known at the particular field strength (11.7 T). Typically water-exchange data are fit to eqn (3.19) using a Levenburg–Marquardt routine. The expression is normalized by setting $S_0 = 1$ to remove S_0 from the fitting. One of the challenges with this method, similar to the linewidth-based method, is sensitivity because exchangeable peaks are expected to be at low concentration. Additionally, peaks are broad for $k_{sw} < 400 \text{ s}^{-1}$. Furthermore, small changes in signal build-up tend to be difficult to detect for such k_{sw} , and the signal of the peak is also reduced owing to exchange with suppressed water protons. Therefore, the water-exchange family of sequences is applied over a narrow range of rates.

3.4.4 QUEST and QUESP Experiments for Assessing Exchange Rate

Unlike the previously mentioned NMR-based methods, saturation-transfer experiments can be used to assess exchange rates on a pixel-by-pixel basis in

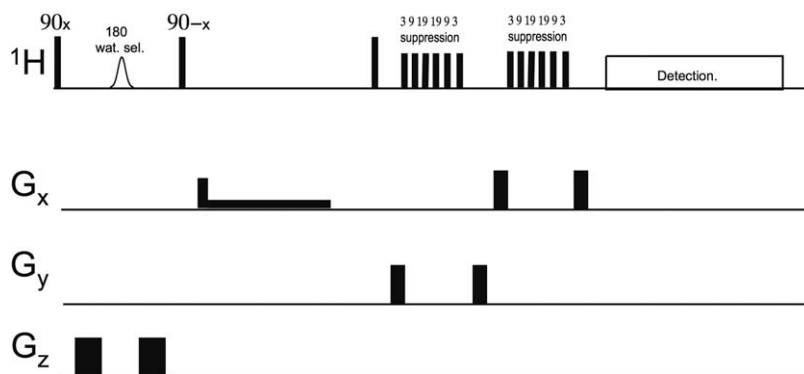


Figure 3.15 WEX II sequence for measuring exchange, including water selection, mixing, and 3-9-19 water suppression.

MR images. For two spins, water and a solute-labile proton, the transfer of signal loss from labile protons to water can be modeled using the Bloch equations, as described previously (Section 3.1.2):¹¹⁵

$$\frac{dM_{xs}}{dt} = -\Delta\omega_s M_{ys} - R_{2s} M_{xs} - k_{sw} M_{xs} + k_{ws} M_{xw} \quad (3.20)$$

$$\frac{dM_{ys}}{dt} = \Delta\omega_s M_{xs} + \omega_1 M_{zs} - R_{2s} M_{ys} - k_{sw} M_{ys} + k_{ws} M_{yw} \quad (3.21)$$

$$\frac{dM_{zs}}{dt} = -\omega_1 M_{ys} - R_{1s}(M_{zs} - M_{0s}) - k_{sw} M_{zs} + k_{ws} M_{zw} \quad (3.22)$$

$$\frac{dM_{xw}}{dt} = -\Delta\omega_w M_{yw} - R_{2w} M_{xw} + k_{sw} M_{xs} - k_{ws} M_{xw} \quad (3.23)$$

$$\frac{dM_{yw}}{dt} = \Delta\omega_w M_{xw} + \omega_1 M_{zw} - R_{2w} M_{yw} + k_{sw} M_{ys} - k_{ws} M_{yw} \quad (3.24)$$

$$\frac{dM_{zw}}{dt} = -\omega_1 M_{yw} - R_{1w}(M_{zw} - M_{0w}) + k_{sw} M_{zs} - k_{ws} M_{zw} \quad (3.25)$$

In eqn (3.20)–(3.25), $\omega_0 = \gamma B_0$ and $\omega_1 = \gamma B_1$; $\Delta\omega_s$ and $\Delta\omega_w$ are the chemical shift differences between the saturation pulse and the solute and water resonance frequencies, respectively; M_0 is the equilibrium magnetization; proton exchange between the two pools occurs with rates k_{sw} (solute to water) and k_{ws} (water to solute); and $k_{sw}M_{0s} = k_{ws}M_{0w}$ at equilibrium. With the assumption that solute protons instantaneously reach steady-state saturation, CEST contrast can be described as a function of saturation time (t_{sat}) and saturation field strength (ω_1) [eqn (3.26)].¹¹⁵

$$PTR = \frac{S_{0w} - S_w(t_{\text{sat}}, \alpha)}{S_{0w}} = \frac{k_{sw} \cdot \alpha \cdot x_{\text{CA}}}{R_{1w} + k_{sw} \cdot x_{\text{CA}}} [1 - e^{-(R_{1w} + k_{sw} \cdot x_{\text{CA}})t_{\text{sat}}}] \quad (3.26)$$

In eqn (3.26), x_{CA} is the fractional concentration of exchangeable protons of the contrast agent, t_{sat} is the saturation time, α is the saturation efficiency, and the term $k_{sw}x_{\text{CA}}$ accounts for back-exchange of saturated water protons to the solute. This back-exchange occurs when the exchange rate is fast, the concentration of exchangeable protons for the CEST agent is high, or both. Additionally, the water signal intensity depends on the pulse power ($\omega_1 = \gamma B_1$) via eqn (3.27):¹¹⁵

$$\alpha = \frac{\omega_1^2}{\omega_1^2 + pq}, \quad (3.27)$$

in which

$$p = R_{2s} + k_{sw} - k_{sw}^2 \cdot x_{\text{CA}} / (R_{2w} + k_{sw} \cdot x_{\text{CA}}) \quad (3.28)$$

and

$$q = R_{1s} + k_{sw} - k_{sw}^2 \cdot x_{CA} / (R_{1w} + k_{sw} \cdot x_{CA}) \quad (3.29)$$

In addition to the MTR_{asym} metric used for determining CEST contrast which was mentioned in Section 3.2, another important metric is the drop in water intensity due to direct saturation. This can be measured by applying a saturation pulse at the same frequency difference as water as the labile protons, but on the opposite side ($-\Delta\omega_{sw}$) of water (Section 3.1):

$$\text{Direct saturation} = \frac{S_{0w} - S_w^{-\Delta\omega_{sw}}(t_{\text{sat}}, \alpha)}{S_{0w}} \quad (3.30)$$

In eqn (3.30), S_0 and $S_w^{-\Delta\omega_{sw}}$ are the water signals without and with, respectively, saturation at $-\Delta\omega_{sw}$. This metric of direct saturation impacts whether or not the Dixon analytical expressions can be used to fit the saturation transfer data. The analytical expression developed by Dixon and co-workers to model the signal intensity as a function of $\frac{1}{\omega_1^2}$ during on-resonance saturation when k_{sw} is fast relative to the relaxation rates is given by eqn (3.31).¹¹⁶

$$\frac{M_z^{ss}}{M_0 - M_z^{ss}} = \frac{k_{sw}R_{1w}}{x_{CA}} \left(\frac{1}{k_{sw}^2} + \frac{1}{\omega_1^2} \right) \quad (3.31)$$

Eqn (3.31) can also be rearranged to a form that is convenient for plotting:¹¹⁷

$$\frac{\omega_1^2 M_z^{ss}}{M_0 - M_z^{ss}} = \frac{\omega_1^2 R_{1w}}{x_{CA} k_{sw}} + \frac{k_{sw} R_{1w}}{x_{CA}} \quad (3.32)$$

One MRI-based method to determine k_{sw} involves collecting the water signal as a function of saturation time at a single saturation field strength (quantification of exchange using saturation time, QUEST) and then fitting this MTR_{asym} data to the exponential term in eqn (3.26) or to the numerical solutions to eqn (3.20)–(3.25) if the direct saturation is too strong or if the exchange rate is faster than $\sim 500 \text{ s}^{-1}$.⁶¹ Data can be fit using a least squares nonlinear fitting routine. Numerical solutions to eqn (3.20)–(3.25) can be performed, for instance using the Matlab `expm` function,²³ and are typically solved using the initial conditions of $[0, 0, M_{0s}/M_{0w}, 0, 0, 1]$ for $[M_{xs}, M_{ys}, M_{zs}, M_{xw}, M_{yw}, M_{zw}]$, respectively. Pulse sequences for the QUEST experiment are shown in Figure 3.9 (Section 3.2). Typical lengths of saturation pulses are 0.5–10 s, with a 6 s recycle delay after the saturation pulse. Data are usually collected at a sufficiently strong saturation field strength ($\omega_1 \sim 3.6 \mu\text{T}$ for diamagnetic CEST agents) and at two frequencies [one on resonance with the exchangeable protons ($+\Delta\omega_{sw}$) and a second on the opposite side ($-\Delta\omega_{sw}$) of the water line]. This method requires precise knowledge of x_{CA} to obtain

reliable measurements of k_{sw} . Acquisition of this knowledge can be challenging for some samples and, as a result, can represent a problematic limitation. Consequently, this method is not widely used.

Another MRI-based method that is commonly used involves collecting the water signal as a function of saturation power at a single saturation length (quantification of exchange using saturation power, QUESP) and then fitting this data to eqn (3.26), (3.31), and (3.32) or to numerical solutions to eqn (3.20)–(3.25). Typical lengths of saturation pulses are 3–10 s, with a 3–6 s recycle delay after the saturation pulse. Data are often collected at two frequencies, one on resonance with the exchangeable protons ($+\Delta\omega_{sw}$), and a second on the opposite side ($-\Delta\omega_{sw}$) of the water line. For diamagnetic CEST agents, ω_1 is varied from ~ 1.2 to 12 μT generally, and for paramagnetic CEST agents, ω_1 is usually varied up to 20 μT or higher. The simplest approach to acquiring exchange rates from the resulting data involves plotting $\frac{1}{\text{MTR}_{\text{asym}}} \text{ versus } \frac{1}{\omega_1^2}$ and fitting the plot to eqn (3.31). This plot should be linear provided there is negligible direct water saturation. This strategy is referred to as Omega-plot fitting¹¹⁶ or LB-QUESP fitting.¹¹⁷ The x-axis intercepts in these plots are $-\frac{1}{k_{sw}^2}$ and enable determination of k_{sw} without knowledge of either the solute concentration or relaxation rates, making this method relatively straightforward. Unfortunately, the x-axis intercepts can be sensitive to small errors in measurements, particularly for faster k_{sw} ($>1000 \text{ s}^{-1}$).¹¹⁷ Therefore, caution should be applied when interpreting the results. For faster k_{sw} , it is better to plot $\frac{\omega_1^2}{\text{MTR}_{\text{asym}}} \text{ versus } \omega_1^2$ and use eqn (3.32) (HW QUESP fitting),¹¹⁷ then the ratio of the y-intercept and slope can be used to calculate k_{sw} . HW QUESP fitting does not work as well as LB QUESP for $k_{sw} < 300 \text{ s}^{-1}$, and this fitting method is challenged if there is non-negligible direct water saturation, as is often the case for measurements on diamagnetic CEST agents. As a result, for diamagnetic CEST agents, it is best to plot $\text{MTR}_{\text{asym}} \text{ versus } \omega_1^2$ and fit the data using a least squares nonlinear fitting routine to numerical solutions for eqn (3.20)–(3.25).⁶¹ This plot will produce the most precise results for diamagnetic CEST agents. There are six parameters to determine: k_{sw} , x_{CA} , R_{1s} , R_{2s} , R_{1w} , and R_{2w} . R_{1w} is typically allowed to be between 0.248 and 0.33 s^{-1} during the fitting. R_{2w} and R_{2s} are estimated by comparing the widths between simulations and experiment of the direct saturation and CEST contrast peaks in the Z-spectra at a single ω_1 and are typically $\sim 0.6 \text{ s}^{-1}$ and 39 s^{-1} , respectively. x_{CA} is known from the sample preparation, although this can also be measured using NMR and excite-detect measurements, as described in Section 3.4.2. Exchange rates in more complex spin systems can also be measured, although in these cases it is necessary to collect more frequency points to include all the labile proton frequencies and fit the data to three or larger pool Bloch equations.^{14,118}

Overall, QUESP-based methods have been the most applied techniques for measuring exchange rates for CEST agents and are recommended because of the broad range of rates that can be reliably determined using this method.

3.4.5 Acknowledgements

The author was supported by a Maryland Stem Cell Research Fund grant, MSCRFI-2829.

3.5 Preparation and Characterization of Paramagnetic Micelles and Liposomes

GIUSEPPE FERRAUTO AND SILVIO AIME*

3.5.1 Routes to Enhance the Sensitivity of CEST Agents

Since the development of the first CEST agents in 2000,¹ it was evident that the intrinsic low sensitivity of this class of probe could hinder translation to uses *in vivo*. To observe a detectable CEST signal, millimolar concentrations of equivalent exchanging protons are needed. In the last decade, a number of paraCEST agents have been synthesized, characterized, and applied to *in cellulo* and *in vivo* preclinical studies.^{2-6,24-26,119,120} These small molecules incorporate either a lanthanide or a paramagnetic transition metal ion. Optimizing the exchange rate and the chemical shift of the exchangeable protons of these paraCEST agents led to increased sensitivity. Nonetheless, because they contain only one or a few equivalent exchanging protons, detection thresholds did not decrease below the millimolar range.^{2-6,24-26,119,120} Multimeric assemblies of these complexes, such as dimers and tetramers, did not significantly improve the detection threshold of these agents on a per metal basis. In this context, enhancing the sensitivity of CEST probes required new systems with (i) optimum exchange rate of the protons responsible for the CEST signal and (ii) increased number of equivalent exchanging protons.

Sherry and co-workers investigated how k_{ex} can be optimized so as to increase the paraCEST effect.^{22,27,121} Generally, the CEST effect is larger for complexes with more rapid proton exchange, up until the point that increased k_{ex} leads to coalescence. Innovative chemical structures led to paraCEST agents with optimal proton-exchange rates. In these systems, the largest saturation transfer effects are reached using high B_1 presaturation power pulses. Unfortunately, high B_1 values correspond to large tissue energy deposition, which leads to undesired heating. This problem is called the specific absorption rate issue. It follows that the advantages of fast k_{ex} as a key factor to increase CEST sensitivity are intrinsically limited. Moreover, to maintain $\Delta\delta > k_{\text{ex}}$, which is necessary to observe CEST contrast, the frequency of the exchanging proton pool of fast-exchanging systems must be far from that of the protons of bulk water. Given these intrinsic limitations associated with k_{ex} , greater success in increasing the sensitivity of CEST has been reached with systems containing a large number of equivalent exchangeable protons. These include both nano-^{2-6,24-26,119,120,122,123} and micro-sized systems, such as (i) micelles,^{28,124,125} (ii) liposomes,^{24-26,29,126-130} (iii) dendrimers,^{118,131,132} (iv) silica nanoparticles,^{12,133} (v) viral capsids,¹³⁴ (vi) apoferritin,^{135,136} and (vii) cells.^{25,30,31}

Incorporating paramagnetic shift reagents into nanosystems is a powerful way to increase CEST sensitivity because the resulting agents have a large number of properly shifted exchangeable protons. Such nanosystems can be achieved either by encapsulation of small molecules in their cavity, *via*

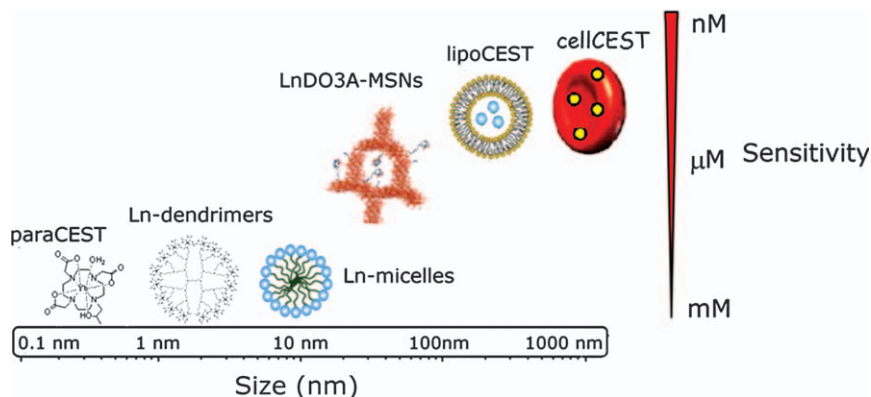


Figure 3.16 Sensitivity range of different nano- and micro-sized CEST probes. Sensitivity is in terms of [Ln^{III}]. Adapted ref. 12 with permission from The Royal Society of Chemistry.

surface conjugation, or both. The advantages of these systems are that (i) they are generally bio-compatible and cause limited side effects during *in vivo* application, (ii) their composition can be readily modified to modulate their biodistribution, and (iii) they can be synthesized with a variety of Ln^{III}- or transition-metal-based complexes as needed to tailor their CEST properties. A comparison of different nanosized CEST probes (in terms of size and sensitivity) is shown in Figure 3.16.

The sensitivity of a paraCEST agent is the minimum concentration of metal complex needed to obtain a detectable saturation transfer effect (ST% > 5%). Importantly, the number of exchangeable protons interacting with the metal center is substantially higher for mesoporous silica nanoparticle (MSN)-based agents, lipoCEST agents, and cell-as-CEST agents than for molecular paraCEST agents. It is this increase in the number of exchangeable protons that leads to the increased sensitivity of these nano- and micro-sized systems. In terms of targeted imaging, the structures of these agents enable them to carry a large number of paraCEST molecules and their associated mobile proton pools to sites of interest. They also lead to new exchangeable proton pools that can also act as CEST agent themselves, as in the case of lipoCEST, cell-as-CEST, MSN-CEST (see Section 3.1.4 for classification of CEST agents). In the following section, the preparation, characterization, and application of these systems are described.

3.5.2 Preparation and Characterization of Paramagnetic CEST Micelles

Paramagnetic CEST micelles are a relatively simple nanosized CEST system composed of micelles containing amphiphilic paraCEST agents.^{28,124} Typically, micelles are supramolecular assemblies of surfactant molecules in aqueous solution, in which the hydrophilic head region is in contact with the

aqueous solvent and the hydrophobic tail fills the system core. CEST micelles can consist of either 100% paramagnetic Ln^{III} complexes (with Ln^{III} ≠ La^{III}, Pm^{III}, Lu^{III}, or Gd^{III}) endowed with a hydrophobic (C₁₂–C₁₈) tail or a mixture of paramagnetic amphiphilic complexes with other phospholipidic components containing polyethylene glycol (PEG) moieties, such as DSPE-PEG2000-methoxy (Figure 3.17A). The phospholipid stabilizes the structure of the micelle by limiting the exchange of surfactants from micelles

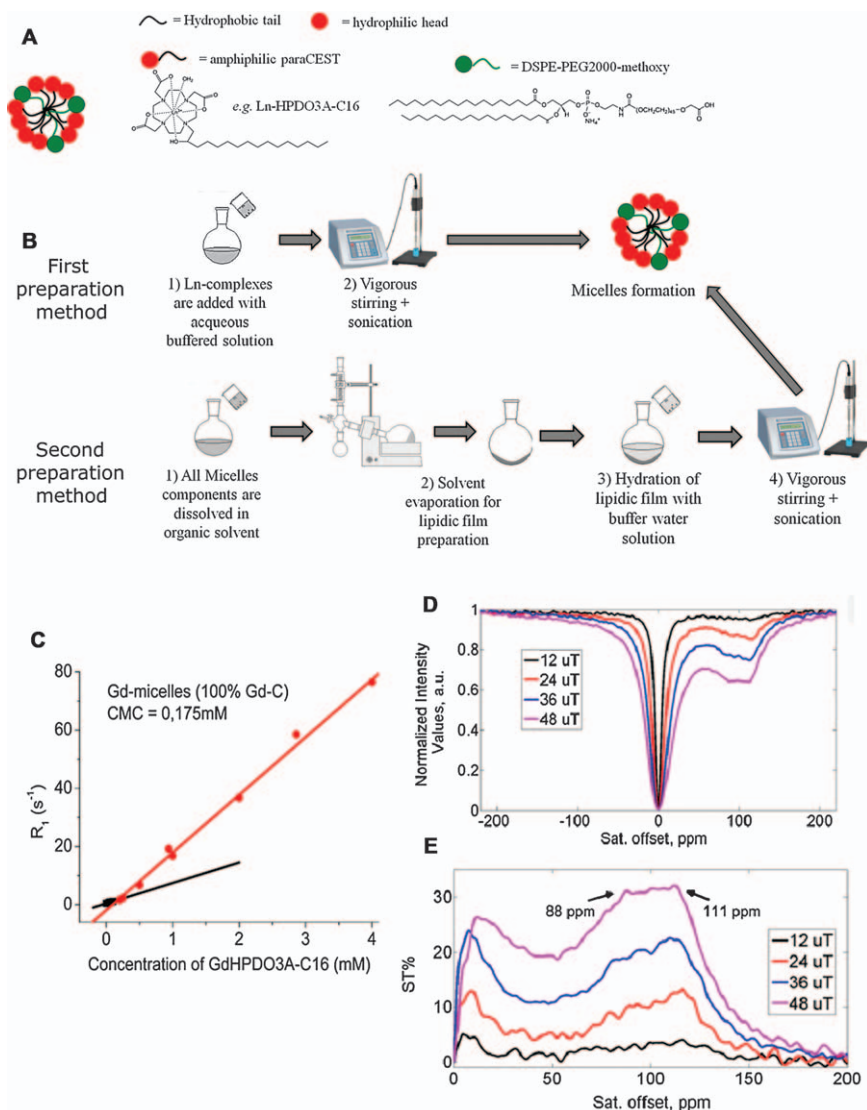


Figure 3.17 (A) Representative scheme of (mixed) micelles. (B) Schemes of micelle preparation. (C) Assessment of critical micelle concentration using relaxometry. (D) Z- and (E) ST-spectra of Yb-HPDO3A-C16-micelles.

to cells. In such mixed micelles, other phospholipidic components can be added, including fluorescent phospholipids for optical imaging or phospholipids functionalized for targeting. The preparation of paramagnetic micelles is relatively straightforward.¹³⁷ The assembly of amphiphilic Ln^{III} complexes into micelles in aqueous media is thermodynamically driven. Ln^{III} complexes functionalized with a single alkyl chain (C₁₂–C₂₀) added to a buffered aqueous solution result in micelles with an Ln^{III} concentration in the millimolar range. Vigorous stirring and sonication enhance the formation of micelles.

Another approach usually followed for the preparation of mixed micelles incorporating more than one component involves hydration of a thin lipid film composed of the components of the micelles (Figure 3.17B). This approach was followed for the synthesis of micelles incorporating amphiphilic Ln^{III} complexes and DSPE-PEG2000-methoxy polymer. Briefly, in the first step, defined amounts of the micelle components are dissolved in an organic solvent, most often chloroform or methanol, in a glass flask. The Ln^{III} complexes and PEG-containing phospholipids are generally used in an approximately 2 : 1–1 : 1 molar ratio. In the second step, the organic solvent is gently evaporated using a rotary evaporator. This results in the formation of a thin lipid film at the bottom of the flask. Next, the lipid film is hydrated with an aqueous buffer by gently heating and vortexing the resulting suspension. Typically, the buffer used is NaCl (0.15 M) and 4-(2-hydroxyethyl)-1-piperazineethanesulfonic acid (HEPES, 0.0038 M), at pH 7.4. In the last step, the micelle suspension is sonicated (for example, using a 20 kHz sonicator for three cycles of 1 min at 80% power) to facilitate the formation of nearly homogeneous micelles. Characterization of the resulting paramagnetic micelles include the determination of their structure, size, surface ζ -potential, and CEST properties. The hydrodynamic radius, polydispersity, and ζ -potential are typically measured by dynamic light scattering. The ζ -potential of micelles is used to predict their stability in suspension and propensity for coagulation, flocculation, or both.

The size of micelles strongly depends on its amphiphilic components. In general, longer alkyl chains result in larger micelles, with hydrodynamic radii ranging between 3 and 15 nm, as measured by dynamic light scattering. The ζ -potential also depends on the amphiphilic components, as well as on pH, temperature, and the medium used in the formation of the micelles. The presence of charged groups, either positive or negative, increases ζ -potential and, consequently, micelle stability. Alternatively, in the absence of charged groups, the ability to form suspensions of micelles and the stability of micelles can be increased *via* hydrogen bonding between PEG chains and water. Furthermore, the presence of PEG moieties on the outer surface of micelles prevents their uptake by macrophages, thereby increasing their half-lives in blood. It is worth noting that PEG generally increases the hydrodynamic radii of micelles.

The aggregation number of each micelle can be estimated from their hydrodynamic radius. For mono-component micelles, the number of

amphiphilic complexes (N_c) that form a micelle can be determined from eqn (3.33):²⁸

$$N_c = \frac{4\pi R^3}{3(27.4 + 26.9n) \times 10^{-3} \text{ nm}^3} \quad (3.33)$$

In eqn (3.33), R is the radius of the micelle, and n is the number of carbons in the aliphatic chain. The total number of exchanging groups present in the micelle, and thus the sensitivity of the CEST agent, can be calculated from N_c and the molar percentage of Ln^{III} complexes used for the preparation of micelles. Whereas the sensitivity of molecular paraCEST agents is in the millimolar range, that of micelle-based CEST agents is in the millimolar to micromolar range.

An important characteristic of micelles is their critical micellar concentration (CMC), which is the minimum concentration of surfactant needed to generate micelles. With paramagnetic systems, the critical micellar concentration can be assessed by relaxometric titrations, provided that the formation of micelles is accompanied by a change in the relaxation times.^{138,139} Because the amphiphilic Ln^{III} complexes used to form CEST micelles are often not sensitive enough for this measurement, micelles synthesized with the analogous Gd^{III} complexes should be used instead. In this experiment, longitudinal relaxation rates (R_1) at a fixed field are measured as a function of the concentration of the amphiphilic Gd^{III} complex. Because of the lengthening of τ_R , the relaxivity (r_{1p}) of the free complex is lower than that of the complex aggregated in micelles (Chapter 2.1.2). In a plot of R_1 versus $[\text{Gd}]$, this results in a break point, or two intersecting lines whose slopes are r_{1p} of the free and aggregated Gd^{III} complexes.¹³⁸ The critical micellar concentration corresponds to the intersection point of these two lines (Figure 3.17C). Note that if the critical micellar concentration is too low, the line corresponding to the free complex can be difficult, if not impossible, to observe. The critical micellar concentration can be similarly determined with 8-anilino-1-naphthalensulfonic acid, an anionic dye that has weak fluorescence in water but a strong one when embedded in the hydrophobic environments of the interior of the micelles. The formation of micelles leads to an increase in fluorescence intensity and a blue shift in the emission.²⁸

High-resolution $^1\text{H-NMR}$ can be used to obtain information about: (i) the coordination geometry and structural characteristics of complexes, (ii) the occurrence of more than one isomer of the Ln^{III} -complex and the relative abundances of each isomer, and (iii) the chemical shift of the exchangeable protons. The chemical structure and isomer ratios are usually assessed in D_2O . The chemical shift of the exchangeable protons is instead determined in H_2O .

The CEST properties of the micelles are primarily investigated by acquiring their Z-spectra (see Section 3.2).²⁸ These spectra report the percentage of saturation of the solvent water protons (y -axis) upon moving the off-set of the irradiating radiofrequency field (Figure 3.17D). Z-spectra can be acquired on

either high-resolution NMR spectrometers or MRI scanners. The magnetic field of the spectrometer plays a central role because it determines the frequency separation between the exchanging resonances. Generally, Z-spectra are recorded at high field (for example, 1–7 T). Different CEST sequences have been developed and optimized for this purpose; the most widely used being the rapid acquisition with relaxation enhancement (RARE) spin-echo sequence. The MRI sequence—in which the RARE factor, echo time, and repetition time are determined based on the T_2 of the sample—is preceded by a saturation scheme whose shape, amplitude, and duration are previously determined based on the sample to be analyzed. More detailed information about the proper choice of experimental parameters and fitting analysis tool are reported in Section 3.2. The extent of the CEST effect is calculated as:

$$\text{ST\%} = \left(1 - \frac{M_S}{M_0}\right) \times 100\% \quad (3.34)$$

where M_S is the intensity of the bulk-water signal after the irradiation at resonance ($\Delta\omega$) of the mobile proton pool and M_0 is the intensity of the bulk-water signal when the radiofrequency irradiation field is $-\Delta\omega$ (Figure 3.17D). Based on the Z-spectra, the k_{ex} of mobile protons can be calculated using the omega-plot method as reported by Sherry and co-workers (Section 3.4).¹¹⁶ Thus, by acquiring Z-spectra with variable presaturation pulse powers (6–48 μT), the CEST efficiency of micelles and the detection threshold can be assessed by measuring ST% at variable concentrations of micelles.

The toxicity of micelles is often evaluated *in vitro* with cell culture (see Chapter 7.1.2), as is the uptake of micelles by cells (see Chapter 7.1.4). Micelles are known to cause hemolysis of red blood cells (RBCs) when administered *in vivo* by intravenous injection. The extent of hemolysis caused by micelles can also be assessed *in vitro*. RBCs isolated from health donors' blood are diluted in buffer medium (PBS) and incubated in presence of micelles at variable concentration and incubation time. Upon centrifugation (2300 rpm for 8 min, room temperature) RBCs are pelleted and the amount of hemoglobin released in the supernatant is assessed by the spectrophotometric measurement at 413 nm, the Soret band of hemoglobin.⁴⁹ The number of lysed RBCs is assessed *via* the amount of released hemoglobin.

3.5.2.1 Example of Preparation of paraCEST-containing Micelles

Micelles are prepared by mixing Ln-HPDO3A-C16 (Ln = Yb or Gd) and DSPE-PEG2000-methoxy phospholipid at a 70/30 mol/mol ratio. The two components Ln-HPDO3A-C16 (7.2 mg, MW 680.6 g mol^{-1}) and DSPE-PEG-2000-methoxy (13 mg, MW 2805.54 g mol^{-1}) are dissolved in chloroform (3 mL), then transferred to a glass flask. Solvent is removed using a rotary evaporator (~ 2 h with rotation). The resulting lipid film is hydrated by using phosphate-buffered saline (PBS, 1 mL) while heating at 50 °C with either mechanical stirring or vortexing. The sample is then sonicated by using a

Table 3.3 Representative characteristics of Ln-HPDO3A-C16-micelles.

Membrane formulation	70% Yb-HPDO3A-C16 30% DSPE-PEG 2000-methoxy
Hydrodynamic radius	11.1 ± 0.5 (polydispersity index of 0.2) nm
Number of complexes (N_c) per micelle	~ 200 Yb complexes/micelle
Critical micellar concentration in PBS, 25 °C	0.08 mM (as assessed by R_1 relaxometric titration at 20 MHz, 25 °C, of Gd-HPDO3A-C16-micelles)
CEST peak(s) chemical shift	84 and 111 ppm
The CEST detection threshold for Yb-micelles	5 μ M in terms of [Yb-micelles] (irradiation time 2 s, $B_1 = 48 \mu$ T)
Cell viability	~ 60% (in murine macrophages, incubated for 18 h with 30 μ M Yb-micelles)
Hemolysis	~ 20% (in RBCs incubated for 15 min with 30 μ M Yb-micelles)

20 kHz sonicator (three cycles of 1 min, 80% power). The micelles are characterized using dynamic light scattering to determine hydrodynamic radius and ζ -potential. The critical micellar concentration is assessed as described above using the analogous complex Gd-HPDO3A-C16 by measuring the longitudinal relaxivity (r_{1p}) at 20 MHz and 25 °C in PBS as a function of Gd complex concentration. Standard characteristics of such CEST micelles are reported in Table 3.3.

3.5.3 Preparation and Characterization of Paramagnetic CEST Liposomes

The sensitivity of lipoCEST agents is in the picomolar range, a dramatic improvement over the millimolar sensitivity of molecular paraCEST.^{3,25,26,29} Liposomes are spherical vesicles composed of an aqueous core surrounded by a lipid bilayer membrane. The breakthrough in sensitivity of liposome-based CEST agents relies on the use of water molecules in the inner aqueous core of the liposome as the pool of exchangeable protons. The number of equivalent water protons for lipoCEST agents ranges from 10^6 (50 nm vesicles) to 10^9 (500 nm vesicles). Liposomes are highly biocompatible and extremely versatile vesicles; the external surface can be functionalized with a wide variety of chemicals, including targeting vectors or PEG chains for prolonging their blood half lifetime (PEGylated liposomes are sometimes referred to as stealth liposomes). As waters inside and outside the liposomal membrane are not monochromic, a paramagnetic lanthanide-based shift reagent must be entrapped in the cavity of the vesicle during liposome preparation.^{3,25,26,29} Different kinds of Ln^{III} complexes have been tested for this purpose. The most important characteristic of such complexes is the presence of one or more water molecules in the coordination sphere that are in rapid exchange with bulk intraliposomal water. The NMR resonance of the coordinated water molecule pool is highly shifted and, through the

occurring fast chemical exchange, all intraliposomal water molecules are affected, thus generating a shifted pool of water protons. This shifted pool is in slow-to-intermediate chemical exchange with extra-liposomal water, thus it can be exploited as a highly populated proton pool to be saturated and detected *via* a CEST response. The simplest route to entrap shift reagents in the liposome is to add them to the hydration solution during liposome preparation.^{3,25,26,29,128} Shift reagents entrapped inside of liposomes, or lipoCEST agents, can be prepared using different approaches.

The most common approach involves hydration of thin lipid films, followed by extrusion (Figure 3.18A).^{25,140} Briefly, in a first step, the membrane components, including the phospholipids and other surfactants, are dissolved in an organic solvent, usually chloroform, inside a flask. In the second step, the lipid film formation step, the organic solvent is evaporated with a rotary evaporator, resulting in the formation of a thin, homogenous layer of surfactants on the bottom of the flask. The third step is the hydration step. In this step, a buffered aqueous solution containing the paramagnetic shift reagent, such as Tm-HPDO3A, is poured into the flask to promote the self-assembly of the surfactants in a mixture of vesicles with different lamellarity. The fourth step is the extrusion step. Multilamellar large vesicles are extruded by passing through filters with decreasing pore size to yield small unilamellar vesicles. In the fifth and final dialysis step, small unilamellar vesicles are dialyzed against a buffer solution (typically NaCl 0.15 M, HEPES 3.8 mM, at pH 7.4) to remove the molecules that are not internalized inside the liposomes. Liposome hydrodynamic size and polydispersity are typically determined by dynamic light scattering. The particular characteristics, and thus the efficiency, of lipoCEST agents depend only on the properties of the paramagnetic shift reagent and the properties of the lipidic vesicles.

The first class of lipoCEST agents include spherical liposome with Ln-based shift reagents (Figure 3.18B) encapsulated inside the aqueous cavity (Figure 3.18C).^{25,29,126,128} The best shift reagents for water are paramagnetic lanthanide complexes with at least one coordinated water molecule, preferably placed along the main paramagnetic axis of the metal complex (Figure 3.18B). The chemical shift (δ) of the water protons in the presence of the paramagnetic shift reagent is the sum of three contributions:^{25,29,141}

$$\delta = \delta_{\text{DIA}} + \delta_{\text{HYP}} + \delta_{\text{BMS}} \quad (3.35)$$

where δ_{DIA} is the diamagnetic shift, which is often negligible, and δ_{HYP} is the hyperfine contribution to the shift. The hyperfine contribution requires a chemical interaction between the paramagnetic Ln^{III} ion and the water molecule. Such interactions can be through bonds (contact shifts) or through space (pseudocontact shifts). The term δ_{BMS} is the bulk magnetic susceptibility contribution to the shift; it does not require a chemical interaction. In spherical compartments, this contribution is nil ($\delta_{\text{BMS}} = 0$). Therefore, if k_{ex} between coordinated and liposomal water is fast enough

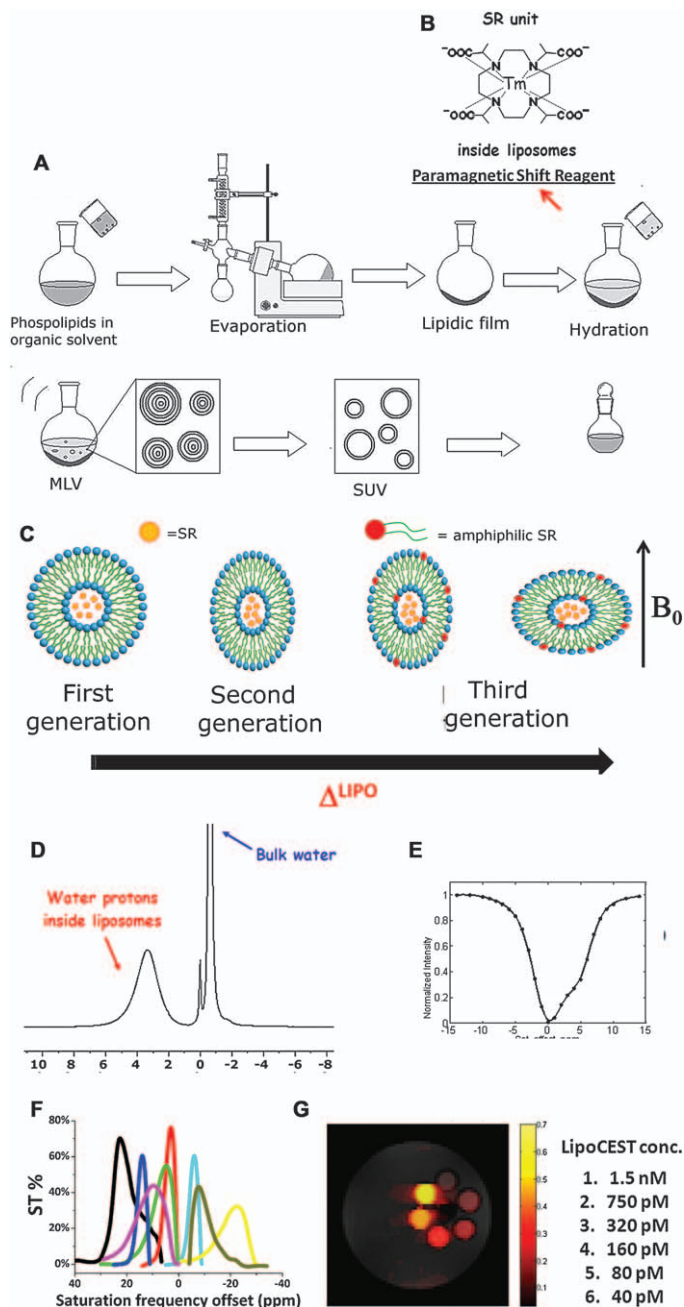


Figure 3.18 (A) Liposome preparation by using method of thin lipidic film hydration followed by extrusion; (B) representative paramagnetic Ln-based shift reagent (SR); (C) different generations of lipoCEST probes; (D) representative NMR spectrum of lipoCEST; (E) representative Z-spectrum of lipoCEST; (F) group of lipoCEST agents as multicolor CEST agents; and (G) example of detection threshold for spherical lipoCEST.

($k_{\text{ex}} >$ or $\gg \Delta\delta$), the chemical shift of the intraliposomal-water and bound-water resonances are given by the following equations:

$$\delta_{\text{intralipo water}} = \frac{[\text{H}_2\text{O}]_{\text{bound to SR}}}{[\text{H}_2\text{O}]_{\text{total}}} \times \delta_{\text{bound water}} \quad (3.36)$$

$$\delta_{\text{bound water}} = \delta_{\text{HYP}} = \delta_{\text{pseudo contact}} \propto \Delta\chi \times G \quad (3.37)$$

In eqn (3.36) and (3.37), $\Delta\chi$ is the magnetic anisotropy of the lanthanide complex and it is equal to

$$\Delta\chi = C_J \times A_0^2 \langle r^2 \rangle \quad (3.38)$$

G is a geometrical property of the Ln-complex and it is equal to:

$$G = \frac{3 \cos^2 \theta - 1}{r^3} \quad (3.39)$$

The term $\Delta\chi$ is the product of $A_0^2 \langle r^2 \rangle$; it depends on the crystal field and Bleaney's coefficient, C_J . Therefore, for isostructural Ln^{III} complexes, the shift of the coordinated water protons is dependent on Bleaney's coefficient. This term may be positive or negative, thus generating either up- or down-field shifts, and is a function of the lanthanide ion. For example, in the class of Ln-HPDO3A complexes, Tm^{III} has a positive value of C_J , thus Tm-lipoCEST yields a positive shift; conversely, Dy^{III} has a negative value of C_J , thus Dy-lipoCEST generates a negative shift (Table 3.4). Importantly, because Bleaney's coefficient of Gd^{III} is zero, Gd^{III}-containing liposomes cannot act as CEST agents. In principle, transition metal complexes, such as Fe^{II} or Co^{II} complexes, can be used for lipoCEST agents provided that the exchange rate of the coordinated water is fast enough.

Examples of a ¹H-NMR spectrum and a Z-spectrum of the first class of lipoCEST agents are shown in Figure 3.18D and E, respectively. For such systems, the detection threshold (ST > 5%) is reached when the concentration of the lipoCEST agent is in the high picomolar range (Figure 3.18G). Importantly, the exchange regime of lipoCEST water protons allows the use of B_1 values that are within the clinically safe specific absorption rate levels.

The choice of the shift reagent has been largely limited to Dy^{III} or Tm^{III} complexes of macrocyclic ligands, such as those shown in Figure 3.18B. These complexes often display an axial symmetry in addition to high thermodynamic stability and kinetic inertness, low cell toxicity, and high

Table 3.4 Effective magnetic moments (μ^{eff}) and Bleaney's constants (C_J) for paramagnetic Ln^{III} ions.

Ln	Pr	Nd	Eu	Gd	Tb	Dy	Ho	Er	Tm	Yb
μ^{eff}	3.62	3.68	3.4–3.6	7.9	9.7	10.6	10.6	9.6	7.6	4.5
C_J	–11	–42	4	0	–86	–100	–39	33	53	22

stability upon internalization inside cell endosomes.⁴⁸ Representative examples include complexes of the ligands DOTA, DOTMA, and HPDO3A (see Figure 1.36 in Chapter 1.4.4 for structures). Shift differences are also due to the geometric differences among the complexes, G , and in particular the angle between the $\text{Ln}^{\text{III}}\text{-}^1\text{H}$ vector and the main paramagnetic axis of the lanthanide. $[\text{Ln-DOTMA}]^-$ is more efficient than $[\text{Ln-DOTA}]^-$ and Ln-HPDO3A as a shift reagent.

As reported above, the efficiency of the CEST effect arises not only from the magnetic properties of the shift reagent but also from the characteristics of the liposome membrane. The saturation transfer effect, ST%, is influenced both by the number of exchanging equivalent protons and by their exchange rate, k_{ex} .^{3,25,26,29} In lipoCEST agents, k_{ex} can be modulated either by the liposome membrane permeability and by the size of the liposome [eqn (3.40) and Figure 3.19].

$$k_{\text{ex}} = P \times S/V = P \times 3/r \quad (3.40)$$

where P is the permeability of the liposome, S is the surface area of the liposome, V is the volume of the liposome, and r is the radius of the liposome.

The formulation of the phospholipidic membrane influences the efficiency of the lipoCEST agent. As a rule, saturated phospholipids generate tightly packed membranes with consequently slow water exchange and thus low CEST effects. Conversely, unsaturated phospholipids yield less tightly packed membranes with consequent faster water exchange (and thus large CEST effects). Cholesterol, which stiffens the membrane, can also modulate membrane rigidity and water exchange. The size of the vesicle also affects lipoCEST efficiency. Large lipoCEST contrast agents contain a larger number of water molecules and display a large saturation transfer effect compared to smaller vesicles. However, small lipoCEST contrast agents often also display a large CEST effect because of the large surface-to-volume ratios that result from the curvature of the liposome membrane, which results in an increased water-exchange rate. Hence, for a set fraction of intraliposomal water, smaller liposomes perform better, but for a fixed number of vesicles, larger liposomes might be more efficient.

One way to increase the sensitivity of spherical lipoCEST is to use neutral shift reagents with two water molecules coordinated to the metal center.¹⁴² This causes a large intraliposomal water chemical shift, and thus a highly efficient resulting lipoCEST agent. However, the thermodynamic stability of the complexes has to be considered as the release of metal ions might hamper their *in vivo* application.

The main limitation for *in vivo* applications of the first generation of lipoCEST agents, spherical lipoCEST agents, lies in the fact that the chemical shift of the intraliposomal water signal ranges from 4 to -4 ppm from the bulk water. This small shift is the consequence of the maximum concentration of shift reagent that can be loaded in the inner cavity of a vesicle as dictated by its osmolarity limits. At the maximum allowed concentration,

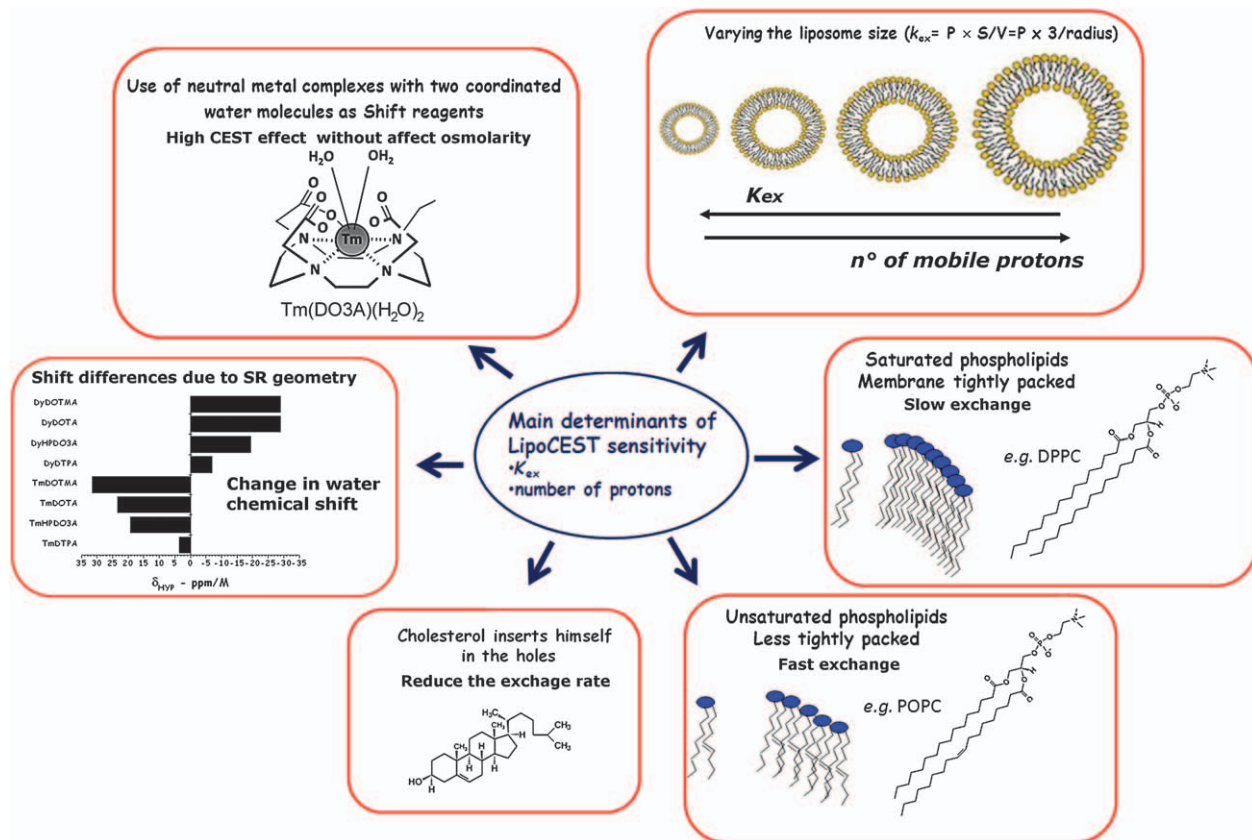


Figure 3.19 Main routes to enhance lipoCEST sensitivity by increasing k_{ex} , the number of mobile protons, or both.

Tm^{III} and Dy^{III} complexes of DOTA and DOTA-like ligands only yield 4 and -4 ppm shifts, respectively (Figure 3.18F). Thus, in a biological environment, such relatively small shift may lead to unwanted interferences with endogenous species that contain exchangeable protons.^{2,4,5}

To overcome this limitation, a second generation of lipoCEST agents has been developed (Figure 3.18C).^{3,5,25,26,29} In this second approach, the chemical shift of the intraliposomal water is moved farther away from the diamagnetic region by modifying the spherical shape of the liposomes. When shift reagents are entrapped in aspherical compartments, an additional contribution to the chemical shift of the water protons comes from the bulk magnetic susceptibility [BMS, eqn (3.35)]. BMS contributions to chemical shift may be larger than hyperfine contributions.

One way to generate aspherical vesicles involves modification of liposome shape by placing vesicles into a hypo-osmolar media.^{3,5,25,26,29} The effect of osmotic-driven changes of liposome shapes is reflected in the chemical shifts of the intravesicular protons. Upon increasing the osmotic pressure in the outer compartment, liposomes release water from the inner cavity until a new iso-osmolar condition between the two compartments is reached. The release of water causes the liposomes to lose their spherical shape and become discoidal, osmotically shrunken liposomes. As a result, the exchange rate of water across the liposomal membrane increases owing to the increase of the surface/volume ratio. Aspherical lipoCEST agents orient themselves in a magnetic field and the orientation is dependent on the magnetic anisotropy of the liposome membrane. The BMS shift is dependent on the concentration of the shift reagent in the liposomes ([SR]) and on the effective magnetic moment of the lanthanide ions:^{25,29,141}

$$\text{BMS} \propto [\text{SR}](\mu_{\text{eff}})^2 \quad (3.41)$$

The μ^{eff} values for lanthanides are reported in Table 3.4. Noticeably, Gd^{III}, Tb^{III}, Dy^{III}, Ho^{III}, Er^{III}, and Tm^{III} possess the highest μ^{eff} values. With lanthanide ions in osmotically shrunken liposomes, CEST signals from the intraliposomal water protons have been obtained with 15 ppm shifts.

Even more efficient third generation lipoCEST agents incorporate amphiphilic shift reagents in the liposome bilayer, for example with paramagnetic surfactants with polar head groups that contain metal complexes and apolar tails composed of two palmitic or stearic chains (Figure 3.18B).^{25,29} The orientation of such lipoCEST agents within a magnetic field, and thus the sign of the chemical shift, depends on the magnetic anisotropy induced by the incorporated shift reagents. In addition, the presence of shift reagents in the membrane increases the intraliposomal chemical shift values either from the hyperfine contribution or from the BMS effect. With these agents, chemical shifts up to 22 ppm have been reached. Finally, a further increase in the shift of intraliposomal water resonance can be achieved by increasing the concentration of the shift reagent in the liposomes. This task can be achieved through the encapsulation of

polymetallic, neutral complexes that increase the concentration of shift reagent units without affecting osmolarity.¹²⁷

With the strategies described above, it is possible to generate a large number of lipoCEST agents with unique encoded frequencies (Figure 3.18F). A group of agents with different frequencies enables multicolor CEST-MR imaging,^{3,9,10,12,25,26} which in turn enables the simultaneous detection of more than one epitope of interest *in vivo*. The first *in vivo* imaging with lipoCEST agents involved directly injecting the vesicles into different anatomical regions of healthy mice.^{25,29,143} By assigning a specific color to each lipoCEST agent *via* the irradiated frequency offsets, it was possible to assess their localization and the persistence of the contrast relative to wash-out. In addition, several *in vitro* applications of lipoCEST agents have been reported, demonstrating the suitability of lipoCEST agents: (i) as responsive agents sensitive to pH and ultrasound stimuli, (ii) as multimodal ¹H-MRI contrast agents, (iii) as multiparametric (T_1 - and T_2 -shortening, susceptibility, and CEST) agents when loaded with Gd^{III} complexes, and (iv) as targeting agents.

3.5.4 Preparation and Characterization of Other Paramagnetic CEST Nanosystems

In addition to liposomes and micelles, other nanosystems have been considered for the design of CEST-MRI contrast agents, namely: (i) silica nanoparticles,^{12,133} (ii) dendrimers,^{118,131,132} (iii) viral capsids,¹³⁴ (iv) apoferritin,^{135,136} (v) albumin-binding paraCEST agents,¹⁴⁴ and (vi) supramolecular assemblies based on paraCEST agents and polypeptide association.¹⁴⁵

Mesoporous silica nanoparticles (MSNs), including MCM-41 and SBA-15 silicas, are solid materials with mesoporous channels of pores sizes ranging between 2 and 10 nm that can be filled with drugs, bioactive molecules, or contrast agents.¹⁴⁶ The distinct properties of MSNs are their tunable mesoporosity, high surface areas ($>900 \text{ m}^2 \text{ g}^{-1}$), large pore volumes ($>0.9 \text{ cm}^3 \text{ g}^{-1}$), and high thermal stabilities. The chemical versatility and biocompatibility of MSNs have drawn attention from the scientific community for drug delivery and catalysis. They have also been evaluated as CEST probes by functionalizing MSNs with paramagnetic Ln-DO3A-like complexes (Figure 3.20A).¹²

Ln-DO3A complexes possess two water molecules in their inner-coordination sphere that, upon interacting with the silica surface, can be replaced by proximate silica OH groups. The result is a structure that mimics the CEST properties of Ln-HPDO3A complexes where the coordinating OH functionalities are the source of exchangeable protons. For this reason, a complex that normally does not display a CEST effect in solution, such as the fast water-exchanging Ln-DO3A becomes a CEST agent when bound to MSNs (Figure 3.20C). Interestingly, Ln-DO3A-MCM-41 systems display a CEST sensitivity in the micromolar range that is higher than that of LnHPDO3A molecules but with a smaller dipolar shift of the OH moieties. The properties of these CEST agents result from multiple, reversible interactions between

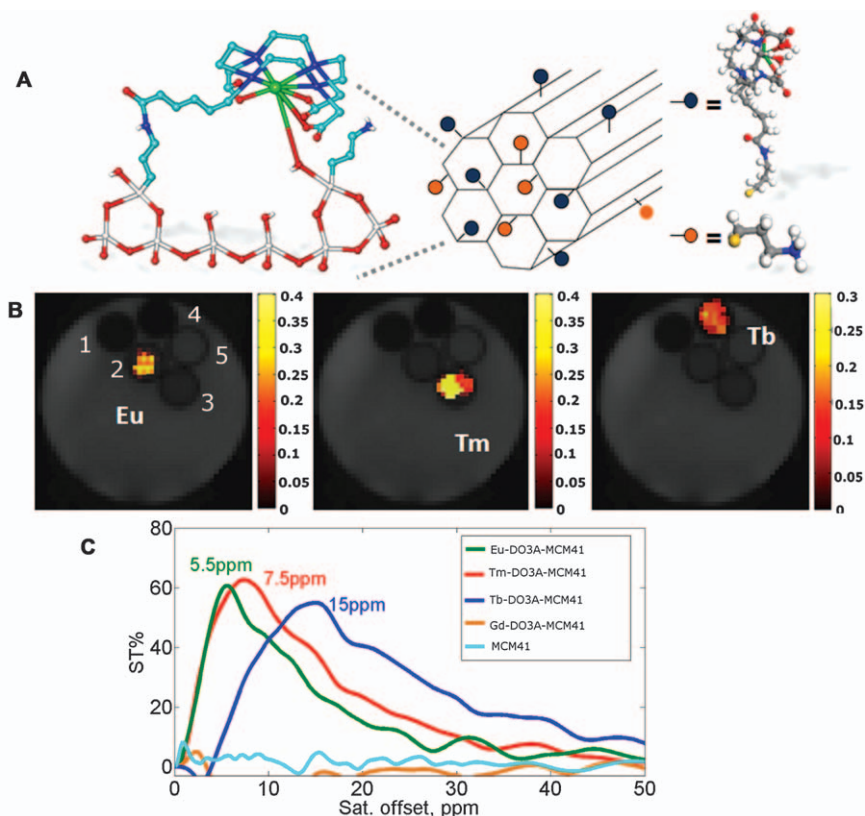


Figure 3.20 (A) Structure of MSNs functionalized with paramagnetic Ln-DO3A-like complexes. (B) ST_{map} at 5.5 ppm (*left*) at 7.5 ppm (*middle*) and at 15 ppm (*right*) of a phantom composed by glass capillaries filled with: (1) Gd-DO3A-MCM-41, (2) Eu-DO3A-MCM-41, (3) Tm-DO3A-MCM-41, (4) Tb-DO3A-MCM-41, (5) non-labeled MCM-41. (C) ST-spectra of different Ln-DO3A-MCM-41 nanoparticles.

Adapted from ref. 12 with permission from The Royal Society of Chemistry.

the paramagnetic metal ion and several silanol groups near the anchoring sites on the surface of MSNs. Furthermore, the fast prototropic exchange rates and weak binding interactions of the silanol groups might also contribute to the increased sensitivity of the lanthanide complex upon conjugation to MSNs.

MSNs are typically prepared by sol-gel procedures using block-copolymers according to the surfactant-assisted co-assembly method.¹⁴⁷ Tetraethoxysilane is used as a silicon precursor for nucleation. The first step of the synthesis involves aqueous acidic hydrolysis. It is in the second step, condensation, that the material forms with its unique structure. The sol-gel process is performed in the presence of the tensioactive hexadecyltrimethylammonium chloride with Pluronic F127 as a co-template. The interaction of the cationic micelles

with the negatively charged tetraethoxysilane triggers the formation of pores within the silica structure. After 3 h, the pH of the reaction mixture is increased to 9 so as to slow the condensation and polymerization of silica. Pluronic F127 slows the condensation process, thereby yielding spherical nanoparticles with diameters of $\sim 20\text{--}50$ nm. In the last step, the material is calcinated at 600°C to remove organic components. The silica surface is functionalized with amino groups by reaction with 3-aminopropyltriethoxysilane.¹² Then, neutral Ln^{III} complexes (where $\text{Ln}^{\text{III}} = \text{Eu}^{\text{III}}, \text{Tm}^{\text{III}}, \text{Tb}^{\text{III}},$ or Gd^{III}) of a DO3A derivative bearing a hexanoic acid pendant group are anchored to the MCM-41 silica surface by standard amide coupling. The physicochemical properties of the labeled silica nanoparticles, including their size, hydrodynamic radius, ζ -potential, and pore structure, can be determined using high-resolution transition electron microscopy, IR spectroscopy, dynamic light scattering, thermogravimetric analyses, and N_2 physisorption measurements. For CEST experiments, xanthan gum can be added to aqueous suspensions of Ln-DO3A-MCM-41 to stabilize the suspensions. The suspensions can be sonicated to prevent nanoparticle aggregation.

The saturation transfer spectra of four Ln-DO3A-MCM-41 materials ($\text{Ln}^{\text{III}} = \text{Eu}^{\text{III}}, \text{Gd}^{\text{III}}, \text{Tb}^{\text{III}},$ and Tm^{III}) and the control silica without anchored complexes (Figure 3.20B and C) showed that the chemical shift of the exchanging proton pool varies with the magnetic properties of the lanthanide ion. The signals arising from mobile proton pools of the Eu^{III} -, Tm^{III} -, and Tb^{III} -labeled silicas are 5.5, 7.5, and 15 ppm away, respectively, from the signal from bulk water.¹² The control silica containing no lanthanide complexes does not yield a CEST effect. Conversely, when Gd^{III} -DO3A was conjugated to silica particles, no CEST effect was observed because the Gd^{III} ion does not shift the OH proton signal through dipolar interaction ($C_J = 0$ for Gd^{III}). The sensitivity threshold of CEST MSNs is lower than that of the corresponding monomeric Ln-HPDO3A complexes. It is also better than other paramagnetic nanosystems, such as dendrimers and micelles.^{12,25,28} The sensitivity of CEST MSN is comparable to that of Ln complexes encapsulated in the inner core of small liposomes. The main characteristics of CEST MSNs are reported in Table 3.5.

Table 3.5 Representative characteristics of Tb-DO3A-MCM-41 MSNs.

Ln complex anchored to MSNs	Tb-DO3A derivative bearing a hexanoic acid pendant group
Size (transition electron microscopy)	20–50 nm
Hydrodynamic radius (dynamic light scattering)	80–100 nm
Pore diameter	2–3 nm
Number of Si-OH groups present on the surface of the functionalized silica (thermogravimetric analysis)	~ 2 Si-OH nm^{-2}
Ln^{III} concentration	0.05 mmol g^{-1}
Number of Ln^{III} chelates per particle	350
Saturation offset	15 ppm

Other nanosized systems have been investigated as CEST probes. These include dendrimers, viral capsids, apoferritin, perfluorocarbon droplets, albumin-binding paraCEST agents, and paraCEST agents in association with charged polypeptides. The sensitivity of these agents is not better than the corresponding monomeric Ln complexes. Therefore, these systems act only as carriers of paraCEST agents with sensitivity that is proportional to their number of Ln complexes.

3.5.5 Preparation and Characterization of Cell-based Paramagnetic CEST Agents

The high sensitivity of lipoCEST agents suggests that cells can also behave as containers for shift reagents. The membranes of both systems consist of semipermeable phospholipid bilayers that separate water into two compartments. In the case of red blood cells (RBC), the amount of water entrapped inside the cell is ~ 4 orders of magnitude greater than that contained inside a 100–150 nm wide liposome. Thus, RBC-based CEST are expected to be more sensitive than lipoCEST agents.²⁵ Furthermore, the anisotropic shape of biconcave RBCs renders them analogous to osmotically shrunken lipoCEST agents (Section 3.5.3).^{30,31} The two main features determining the sensitivity of lipoCEST agents are: (i) the dipolar shift of the intraliposomal water proton, which is in turn determined by the shift reagents, and (ii) the asymmetry of the liposomes. The latter also shifts the intraliposomal water protons by introducing a bulk magnetic susceptibility effect that is not present in spherical liposomes. Cell-CEST agents, RBCs labeled with paramagnetic shift reagents, exploits both of these effects. Consequently, the sensitivity of these CEST agents is extremely low (<1 pM).

To develop cell-CEST agents, paramagnetic shift reagents, usually lanthanide complexes, must be loaded inside cells.^{30,31} The internalization of the shift reagents depends on: (i) the charge, hydrophilicity/hydrophobicity ratio, and molecular weight of the shift reagent, (ii) the ability of the cells to internalize exogenous compounds by macropinocytosis or other mechanisms, and (iii) the cellular toxicity of the shift reagent. Ln-HPDO3A complexes (where Ln = Eu^{III}, Gd^{III}, Dy^{III}, Tm^{III}, or Yb^{III}) have been suggested as efficient shift reagents because they are small, hydrophilic, kinetically inert and thermodynamically stable. Moreover, they are well tolerated by cells even at high intracellular concentrations when distributed in the cell cytoplasm or entrapped in endosomes.^{9,48}

Shift reagents can be efficiently encapsulated inside RBCs following the hypotonic swelling procedure (Figure 3.21A).^{25,30,31,49} This labeling procedure can also be applied to other cell types that either grow in suspension or are adherent.^{10,13,53} It is based on the transient increase of cell permeability upon application of an osmotic shock. Briefly, cells are placed in a hypotonic medium that contains the shift reagent at as high a concentration as possible. Typically the osmolarity of the hypotonic medium is maintained at 160 mOsm L⁻¹ by addition of the corresponding amount of NaCl. RBCs are suspended and incubated in this medium for 30 min at 4 °C with gentle

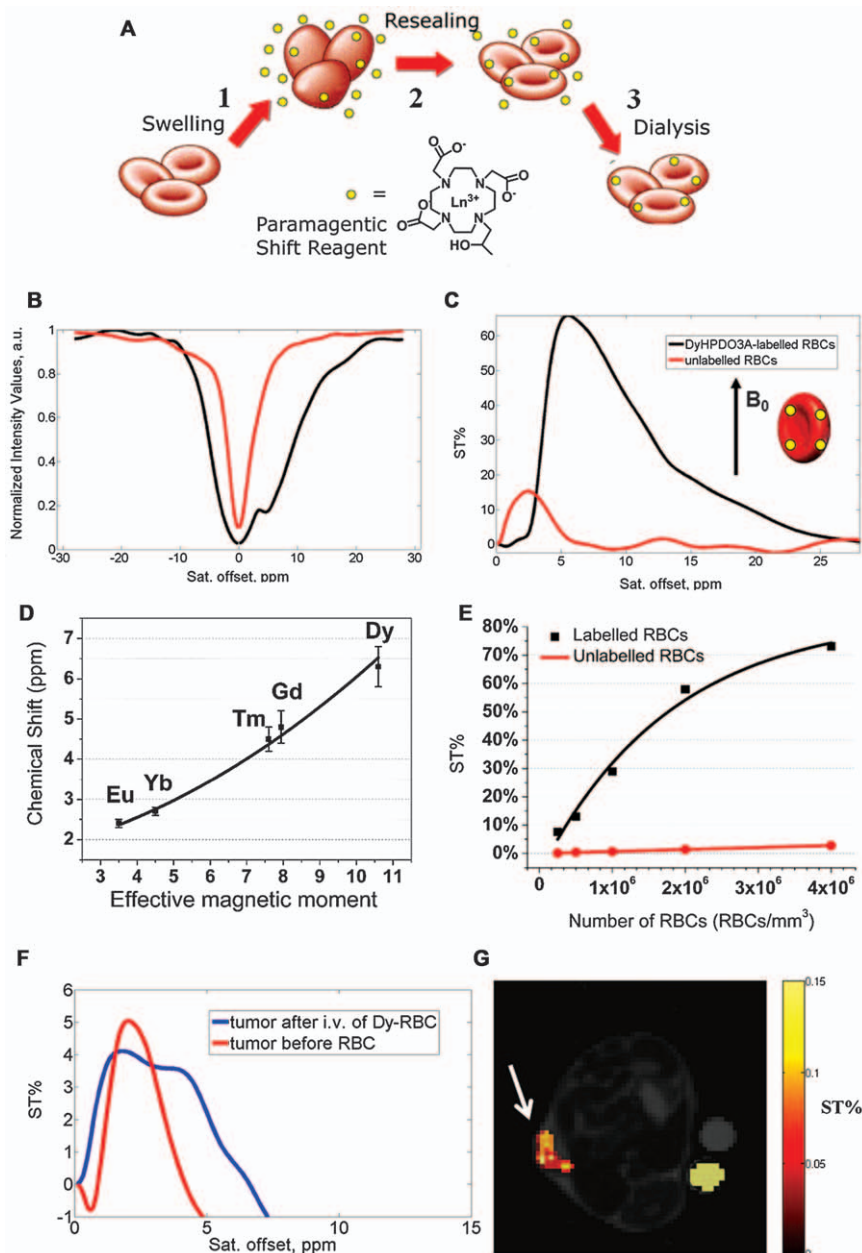
stirring. The osmolarity of the medium is then increased by slow addition over ~15 min at 4 °C of enough NaCl to increase the osmolarity of the medium to the physiological relevant 280 mOsm L⁻¹. Non-internalized shift reagent molecules are eliminated by washing of the suspension of RBCs using fresh PBS. This labeling procedure enables internalization of large amounts of Ln^{III} complexes inside RBCs (~3 × 10⁸ complexes/RBC, corresponding to an intracellular concentration of 4–5 mM).^{30,31,49} The number of internalized complexes can be determined by digesting the RBCs in concentrated nitric acid under microwave irradiation and determining the concentration of the lanthanide ion by ICP-MS (Chapter 2.7.3).

Different biological assays have been performed to verify potential deleterious effects on the morphology and physiology of RBCs. Typically, hemocromocytometric analysis can be used to assess mean corpuscular volume, red blood cell distribution width, mean hemoglobin content, mean corpuscular hemoglobin content, and hematocrit. Maintenance of the RBC biconcave morphology can be determined by optical and electron microscopy. Finally, functional assays can be performed to assess the RBCs': (i) deformability (by assessing the capability of RBCs to warp by passing through a 1–3 μm pore), (ii) osmotic fragility (by changing the osmolarity of the extracellular medium), and (iii) oxygen-binding capability (by acquiring O₂ saturation curves).

The Z-spectra of labeled and non-labeled RBCs in PBS (hematocrit < 55%) are shown in Figure 3.21B. For Dy-HPDO3A-loaded RBCs, an asymmetry centered at 6.5 ppm with a corresponding ST% value of ~65% is observed (Figure 3.21C). The Z-spectrum of non-labeled RBCs only has a small right-hand asymmetry 2–3 ppm downfield of the water resonance peak (Figure 3.21B). This peak is caused by the presence of a pool of exchanging protons, which are naturally present in erythrocytes. In the labeled RBCs, the large chemical shift of the intracellular water NMR signal observed is the result of both the asymmetric shape of the cell and of the presence of the paramagnetic shift reagent inside the cell. From a practical point of view, the best cell-CEST agents are obtained under the following conditions.

- The best hypotonic condition is at 160 mOsm L⁻¹. The efficiency of swelling decreases at higher osmolarity between 160–300 mOsm L⁻¹. This results in lower loadings of the shift reagents. Lower osmolarities (<140–160 mOsm L⁻¹) result in cell lysis.
- Neutral Ln complexes lead to higher concentrations of the shift reagent in the hypotonic swelling medium.
- Paramagnetic shift reagents with higher μ^{eff} values, such as Dy^{III}, Ho^{III}, and Tm^{III} complexes, create greater shifts (Figure 3.21D and Table 3.4 for the μ^{eff} of Ln^{III} ions).
- The incubation time and temperature must be optimized. A good compromise between cell viability and uptake efficiency is often 30 min of incubation at 4 °C followed by 15 min of re-incubation in isotonic medium at 4 °C.

The above conditions have been used to load RBCs with up to 3×10^8 Dy-HPDO3A/RBC, which corresponds to an intracellular concentration of 4–5 mM.³⁰ This system is highly sensitive with a detection threshold of $\sim 2.5 \times 10^5$ cells mm^{-3} . In a mouse, this value corresponds to $\sim 5\%$ of physiologically circulating RBCs (Figure 3.21E). The non-labeled RBCs did



not show a significant saturation transfer effect ($ST\% < 5\%$) at the specific frequency of the intracellular shifted water.

RBCs are fully retained in the vascular space and do not escape into the extravascular compartment. They can therefore be used to assess tumor vascular volume by CEST-MRI in a manner analogous to that reported for RBCs labeled with Gd^{III} complexes.^{30,49,148} A representative MR image of a mouse bearing a transplantable breast cancer tumor using a cell-CEST agent is shown in Figure 3.21G. The Z-spectrum of the tumor region shows the presence of a $ST\%$ maximum at 4 ppm upon the administration of Dy^{III} -loaded RBCs. The saturation transfer is not homogeneous in the tumor region, indicating heterogeneity in the distribution of blood vessels in the tumor (Figure 3.21F).

Further development of cell-CEST agents led to the design of lipoCEST-RBC aggregates that show promise as theranostic agents.^{25,31} The intracellular water signals can also be shifted by highly paramagnetic liposomes that bind tightly to cell surfaces (Figure 3.22A left). For instance, Dy -HPDO3A-containing cationic liposomes can be electrostatically anchored to the negatively charged membrane of RBCs. The Dy^{III} -loaded liposomes present on the cell surface trigger a shift of the intracellular water resonance by inducing BMS effects from the external side of the RBCs (Figure 3.22A right).

To yield a large BMS effect on the water signal of RBCs, careful design of the characteristics of the paramagnetic liposomes is important. Key factors to generate a large BMS effect are: (i) the use of large liposomes, (ii) the loading of a large content of paramagnetic complexes inside the liposomes, (iii) the choice of shift reagents endowed with high effective magnetic moments (Dy^{III} , for example), and (iv) the maximization of the number of liposomes anchored to the surface of RBCs (Figure 3.22B).³¹ Anchoring Dy^{III} -containing liposomes to the surface of RBCs results in two CEST signals.³¹ One arises from the protons of liposomal water (lipoCEST), and the other

Figure 3.21 (A) Scheme of labeling of RBCs by applying the hypotonic swelling procedure. RBCs are placed in a hypotonic solution in the presence of Ln-HPDO3A allowing internalization of the shift reagent (step 1). In the second step, the external medium is brought to an isotonic osmolarity, and the morphology of the cells is restored (resealing of the RBC, step 2). Finally, the lanthanide-loaded cells are washed with PBS to eliminate shift reagents that have not been internalized (step 3). (B) Z- and (C) ST-spectra of non-labeled (red) and Dy -HPDO3A-labeled (black) RBCs. (D) Relationship between μ^{eff} of the lanthanide and the chemical shift of CEST absorption. (E) Correlation between number of RBCs per mm^3 and $ST\%$ for Dy -HPDO3A-labeled (black) and non-labeled (red) cells. (F) ST-spectra of tumor region of interest before (red) and after intravenous administration of Dy^{III} -containing RBCs. (G) A saturation transfer map of a tumor region of interest after injection of Dy^{III} -containing RBCs.³⁰ Adapted with permission from G. Ferrauto, D. Delli Castelli, E. Di Gregorio, S. Langereis, D. Burdinski, H. Gröll, E. Terreno and S. Aime, *J. Am. Chem. Soc.*, 2014, **136**, 638. Copyright (2014) American Chemical Society.

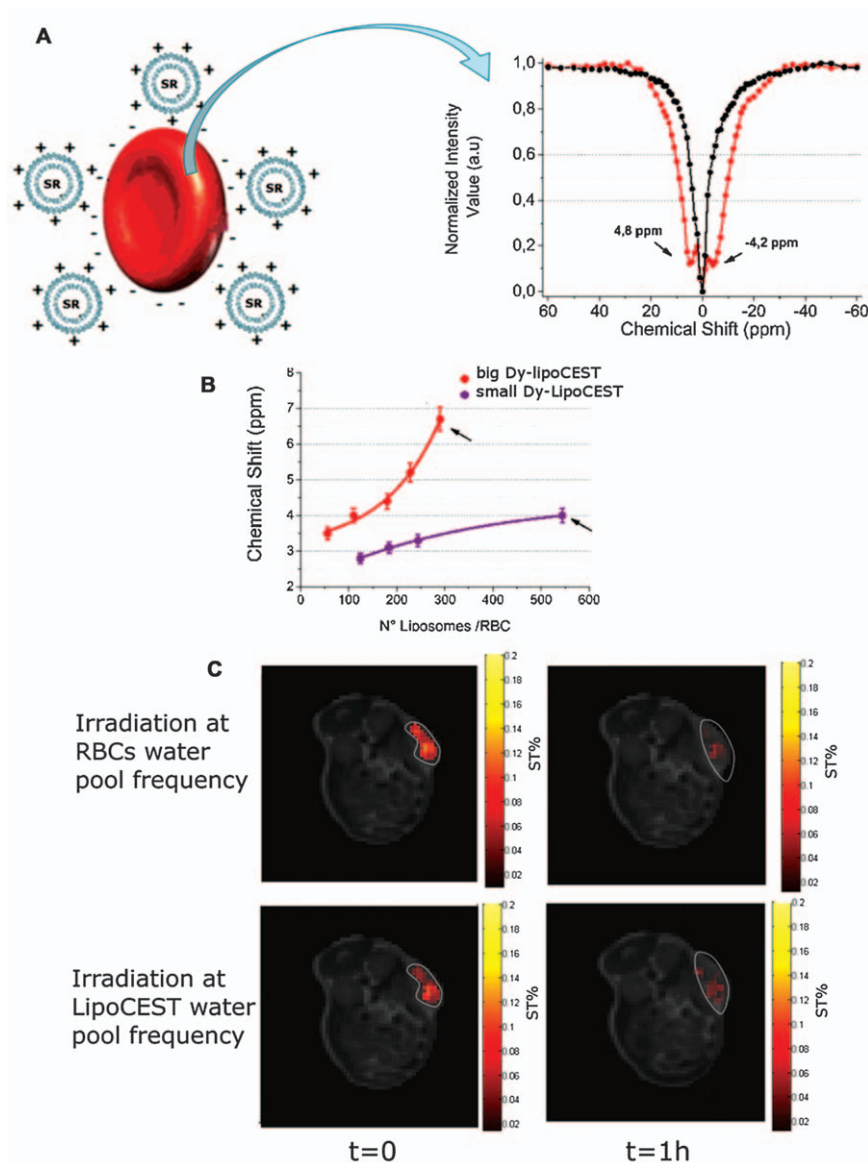


Figure 3.22 (A left): Scheme of interaction between RBCs and positively charged Dy^{III}-containing liposomes. (A right) Z-spectra of the assembly of Dy^{III}-containing liposomes and RBCs. (B) Variation of chemical shift as function of the number of liposomes anchored on the surface of RBCs for small and big Dy^{III}-containing liposomes. (C) CEST% map of tumor region upon administration of aggregates of Dy^{III}-containing liposomes and RBCs with radiofrequency irradiation offset at 3.2 ppm at $t=0$ (left top) and $t=1$ h (right top). CEST% map with radiofrequency irradiation offset at -4.2 ppm signal at $t=0$ (left bottom) and $t=1$ h (right bottom). The region of interest is circled with a white line.³¹ Adapted with permission from G. Ferrauto, E. Di Gregorio, S. Baroni and S. Aime, *Nano Lett.*, 2014, **14**, 6857. Copyright 2014 American Chemical Society.

from the shifted cytoplasmatic water protons of the RBC (cell-CEST). The lipoCEST signal has a negative chemical shift because it arises from the dipolar contribution of Dy^{III}-HPDO3A inside the spherical phospholipidic cavity. Conversely, the cell-CEST signal has a positive chemical shift because of the BMS effect induced by the Dy^{III}-containing liposomes anchored on the external surface of the RBCs. The positive cell-CEST-MRI effect of the Dy-liposome/RBC aggregates can be used to evaluate the vascular volume of the tumor because the aggregates are confined in the intravascular space. At the same time, the negative lipoCEST signal can be used to quantify the liposomes that are released in the tumor region. Immediately after *in vivo* administration of Dy^{III}-liposome/RBC aggregates, both the positive cellCEST and the negative lipoCEST effects are observed. Over time, the positive cellCEST signal decreases whereas the negative lipoCEST signal remains mostly constant. Thus, the vascular volume and the amount of liposomes that have detached from the RBCs and likely extravasated in the tumor extracellular matrix can be imaged simultaneously. The first is imaged from the positive CEST signal, the second from the negative signal. Furthermore, aggregation of lipoCEST to RBCs might also improve the circulation lifetime of liposomes.³¹

RBCs are not the only type of cell that can be used as cell-CEST agents. A wide variety of cells can be loaded with suitable shift reagents *via* different labeling techniques, such as electroporation, hypotonic swelling, macropinocytosis, phagocytosis, or receptor-mediated endocytosis. The choice of the labeling procedure depends on the biological application and on the complexes that are being internalized. Importantly, cytoplasmatic compartmentalization is strongly related to the labeling procedure.^{52,53} For this reason, hypotonic swelling and electroporation are preferred when endosomal compartmentalization is to be avoided. The localization of paramagnetic complexes in endosomes might induce unwanted signal broadening due to T_2 -shortening effects.

In conclusion, cell-CEST can be considered for a large portfolio of applications, including cell tracking and homing experiments. RBC-based cell-CEST can be used to report vascular volume and potentially for theranostic applications. As demonstrated with the lipoCEST/RBC aggregates, lipoCEST agents functionalized with a proper targeting vector might enable imaging of molecular targets on cellular membranes. Other cells can be also be labeled and used for cell tracking experiments, to localize the distribution of cells *in vivo*, and to monitor cells implanted *ex vivo*. The change in the chemical shift of the intracellular water signal can also be a marker of cell proliferation. Water chemical shift is a function of both the effective magnetic moment of the shift reagent and its intracellular concentration. Upon proliferation, as the cells divide, the intracellular concentration of the shift reagent decreases. This results in a decrease of intracellular water chemical shift and hence a shift in the CEST signal. CEST chemical shift can thus how many cell divisions have occurred post labeling. Finally, because the CEST effect is sensitive to the exchange rate of water across cellular membranes,

cell-CEST can also determine changes to membrane permeability and its relationship with pathological states.

3.5.6 CEST Readout of Binding Interactions

As discussed in Section 3.4.3, the performance of lipoCEST agents is a function of two parameters: (i) the absorption frequency of the water protons in the intraliposomal cavity and (ii) the exchange rate of water molecules across the liposomal membrane. Both parameters can be affected by the microenvironments in which lipoCEST agents are distributed. In particular, upon binding to a cell membrane, the shape of a lipoCEST agent is expected to change. In the presence of an ensemble of differently shaped liposomes, there will therefore be a dispersion of chemical shift values of the intravesicular water signal. This most often results in a broad band that decreases detection sensitivity. As a result, although lipoCEST agents display outstanding sensitivity *in vitro*, numerous *in vivo* targeting experiments have been unsuccessful. *In vitro* studies of the binding interactions of macromolecules with lipoCEST agents can give some insights into similar mechanisms occurring *in vivo*.²⁵ Such an example is shown in Figure 3.23.

Spherical lipoCEST agents can be functionalized with biotin moieties by introducing 2% biotinylated-PEG2000 in the phospholipid mixture. Such lipoCEST agents incorporating Tm-HPDO3A as the shift reagent display a

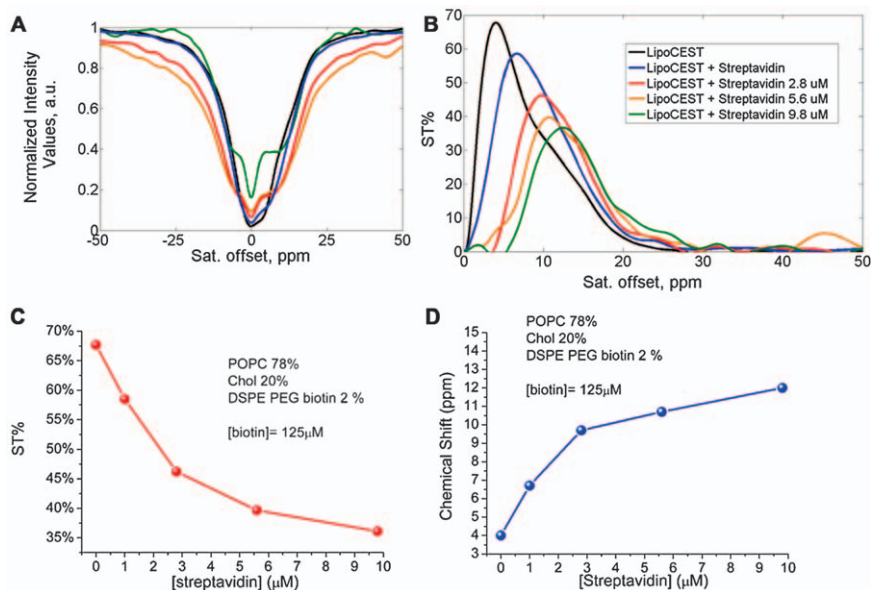


Figure 3.23 (A) Z- and (B) ST-spectra of biotin-containing lipoCEST agents with variable concentrations of streptavidin. (C) Variation of ST and (B) chemical shift of intracellular water as a function of the concentration of streptavidin.

water resonance at 4 ppm and a large CEST effect. Addition of streptavidin to the liposome suspension results in a change in the Z-spectrum, with a shift in the intraliposomal water chemical shift from 4 to 12 ppm. Further addition of streptavidin brought back the water chemical shift to 4 ppm. Changes in the water chemical shift arise from the bulk magnetic susceptibility (BMS) contribution. The change in the Z-spectrum observed suggests that initially, upon binding to the surface of the lipoCEST, streptavidin alters the architecture of the agent, creating an asymmetric liposome–streptavidin supramolecular system.²⁵ Further addition of streptavidin saturates all biotin receptors, the liposome returns to its spherical isotropic shape, and thus the chemical shift reverts back to 4 ppm (Figure 3.23). These results highlight the complexity of translating *in vitro* experiments with lipoCEST agents to *in vivo* targeted imaging.

3.6 Acquiring CEST MR Phantom Images

ALEX LI AND ROBERT BARTHA*

3.6.1 B_0 Field Correction

Following the synthesis of a new agent for chemical exchange saturation transfer,^{1,45,79,149,150} the agent is normally tested in phantoms to determine its behavior and properties with respect to imaging. Phantoms can be created in many sizes and shapes, depending on the goal of the study. NMR tubes are often chosen for testing in NMR spectrometers or imaging systems. When used in imaging systems, it is possible to reduce the amount of sample to 100–150 μL because it is only necessary to have enough sample in the tube that a cross-sectional image can be acquired. Larger phantoms can be used in imaging systems, to mimic the anatomy of a subject (for example, a mouse or a human), although the use of larger phantoms has the limitation that proportionally larger amounts of agent are required, increasing overall cost. The goals of testing CEST agents *in vitro* are: (1) to determine the chemical shifts of the exchangeable protons in the molecule, (2) to determine the magnitude of the CEST effect under specific conditions for each exchangeable proton, (3) to calibrate the effect of temperature, pH, or other external factors on the measured CEST effect, and (4) to determine the potential efficacy of the agent in biological systems. The last point is critical to evaluate the potential for translation of agents to animal models of disease, and ultimately to humans.

Accurate measurement of the CEST effect to evaluate various agents requires a homogeneous B_0 field within a sample. Homogeneity is relatively easily achieved in NMR spectrometers by shimming the magnetic field prior to acquisition of CEST spectra. A homogeneous B_0 across a phantom ensures that the CEST saturation pulses are affecting all isochromats within the sample as intended. When performing phantom experiments in high-field imaging systems with large samples, it is sometimes more difficult to ensure B_0 homogeneity across the entire sample. However, when using small samples combined with higher-order shimming, B_0 fields can be made highly uniform. Figure 3.24A shows an image of an NMR-tube phantom containing Tm-DOTAM-gly-lys-OH (10 mM, produced by Dr Robert Hudson and Dr Mojmír Suchý, Western University) obtained using an Agilent 9.4 Tesla 30 cm bore small animal MRI system with a 30 mm Agilent millipede radio frequency coil. The corresponding B_0 map is provided in Figure 3.24B. The image shows a homogeneous B_0 field across the phantom.

Similarly, Figure 3.25A shows the B_0 field acquired during a single acquisition of five different NMR test tube phantoms. In this example, significant variation in B_0 can be observed across the phantoms and within individual phantoms. Such variation requires the pixel-by-pixel correction of B_0 inhomogeneities using techniques that map B_0 . One such technique is water saturation shift referencing (WASSR),⁶⁴ which has been used for both

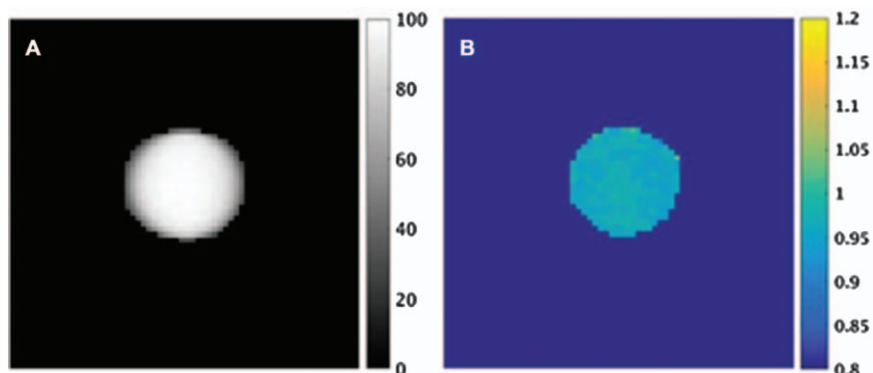


Figure 3.24 (A) T_2 -weighted magnetic resonance image of the cross section of an NMR tube containing Tm-DOTAM-gly-lys-OH (10 mM, produced by Dr Robert H. E. Hudson and Dr Mojmír Suchý, Western University).¹⁵¹ Images were acquired using a fast spin echo sequence ($TR=7$ s, $TE=7$ ms, echo train length = 32, field of view = 12.8 mm \times 12.8 mm, matrix = 64 \times 64). (B) Corresponding B_1 map obtained using the actual flip angle imaging gradient echo sequence ($TR=20$ ms, $TE=3.72$ and 5.24 ms, field of view = 12.8 mm \times 12.8 mm, matrix = 128 \times 128).

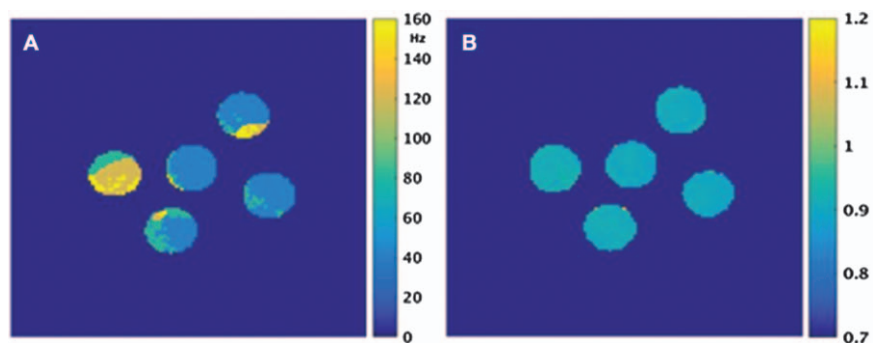


Figure 3.25 (A) A B_0 map obtained for a group of NMR tubes containing solutions of contrast agent. Variations in B_0 of up to 100 Hz are observed within and between phantoms. The B_0 map was obtained with the water saturation shift referencing technique (saturation power = 0.2 μ T, saturation pulse duration = 2 s, frequency range = -1.5 to 1.5 ppm, step = 0.1 ppm). (B) A B_1 map obtained with the actual flip angle sequence described in Figure 3.24 shows little variation in B_1 across the same phantoms using the volume millipede coil. No correction for B_1 variation is required under these circumstances.

in vitro and *in vivo* studies. With the water saturation shift referencing technique, the B_0 field is mapped using the same imaging sequence used to acquire CEST images but with a lower power and with shorter saturation pulses (a 0.2 μ T and 2 s pulse was used to produce the images in Figure 3.25). By applying the saturation pulse at frequencies around water, a CEST

spectrum is created that can be used to pinpoint the water frequency within each pixel. Using this information, a frequency shift can be applied to correct B_0 variation in the CEST maps.

3.6.2 B_1 Field Corrections

The CEST effect is dependent on the amplitude of the B_1 field used for saturation. It is possible to maximize the CEST effect for a particular pool of exchangeable spins based on their exchange rate using a specific amplitude of B_1 saturation.^{152,153} For this reason, it is critical to correct for or minimize B_1 inhomogeneities in phantom data prior to interpreting CEST spectra. CEST spectra can be corrected for B_1 inhomogeneities by calibrating the B_1 effect. However, in phantom studies and in studies of small regions of tissue,¹⁵⁴ calibrations are usually not required because variations in B_1 amplitude are relatively small. Therefore, it can be assumed that B_1 amplitude is constant throughout the phantom (Figure 3.25).

3.6.3 Continuous Wave Saturation

The use of continuous-wave radio-frequency saturation represents the most efficient means of generating CEST contrast (Figure 3.26). In phantoms, continuous-wave saturation is preferred over other saturation methods because issues related to power deposition are not normally limiting like they might be in animal models or humans. Continuous-wave saturation also produces a narrow excitation bandwidth that aids in frequency selection and reduces direct saturation of bulk water when applying saturation pulses near the frequency of bulk water. Saturation of bulk water is an important consideration for CEST agents with exchangeable protons that resonate within a few ppm of water, but less important for agents that have exchangeable protons with chemical shifts far from bulk water. Most high-field spectrometers and imaging systems are capable of continuous-wave saturation on the order of seconds. However, clinical MRI scanners are often restricted to pulse durations of hundreds of milliseconds, requiring the use of a pulsed saturation scheme.

A number of pulsed-saturation pulse sequences have been published for the generation of CEST contrast in images acquired on clinical MRI systems.^{152,155–162} Phantom requirements are the same for the testing of continuous-wave and pulsed-saturation imaging methods.

3.6.4 Practical Considerations

Temperature and pH are the most important variables that must be controlled during phantom measurements because these factors can greatly influence chemical-exchange rates and, as a result, contrast from CEST.^{149,154,159,163–166} Evaluation of CEST agents can be performed at room temperature, but if agents are being developed for use *in vivo*, the agents should be evaluated at 37 °C. Most NMR systems have built-in temperature

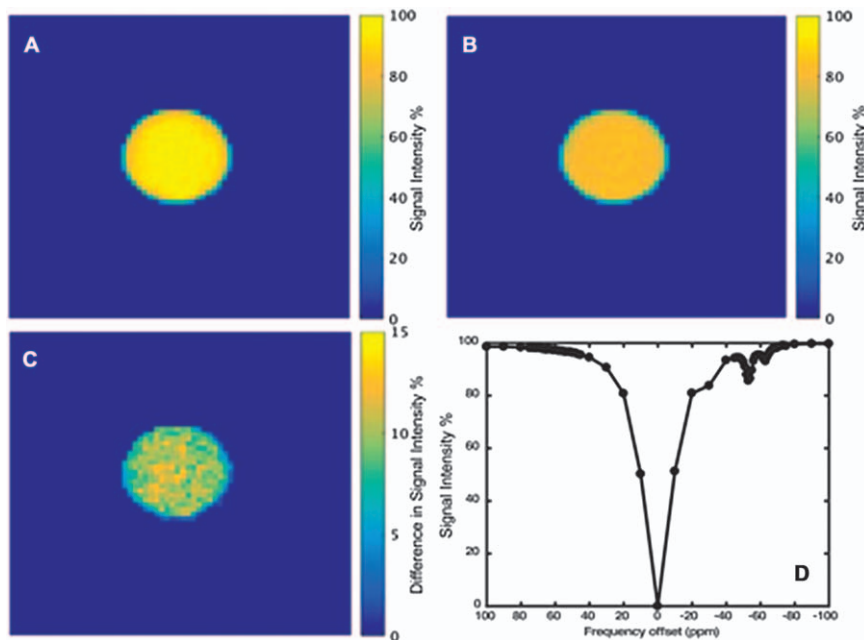


Figure 3.26 CEST continuous wave saturation in a sample of TM-DOTAM-lys-OH (15 mM and pH 7). Images were acquired using the same fast spin echo sequence described in Figure 3.24 with saturation frequencies ranging from -100 to 100 ppm in steps of 5 ppm, except between -40 and -70 ppm, where steps of 1 ppm were used. (A) Image acquired at a saturation frequency of 53 ppm. (B) Image acquired at a saturation frequency of -53 ppm. (C) The difference image obtained by subtracting the image in (B) from the image in (A). (D) The average CEST spectrum obtained for this sample showing two exchangeable protons at -53 and -63 ppm.

control. MRI systems often have integrated temperature control systems, although the effectiveness of these systems must be carefully monitored during each experiment. For example, the use of a hot-water blanket or blowing of warm air over a sample can be effective, but these methods of regulating temperature should be monitored closely to ensure temperature stability throughout an experiment. Similarly, the pH of the sample must also be controlled during imaging (Figure 3.27). Adjustments to pH can be made using standard techniques or by dissolving an agent in buffer. Care must be taken to ensure that the pH of a sample does not change over time.

Another critical consideration in assessing the efficacy of CEST agents for use *in vivo* is the influence of the macromolecule baseline on the observed contrast.¹⁵³ The macromolecule effect has been known for decades,¹⁶⁷ and this effect becomes important at the power levels required for some agents.¹⁵³ Large chemical shifts of exchanging protons from the bulk-water frequency are useful with respect to this consideration. Large frequency differences permit faster exchange rates to satisfy the slow-exchange limit,

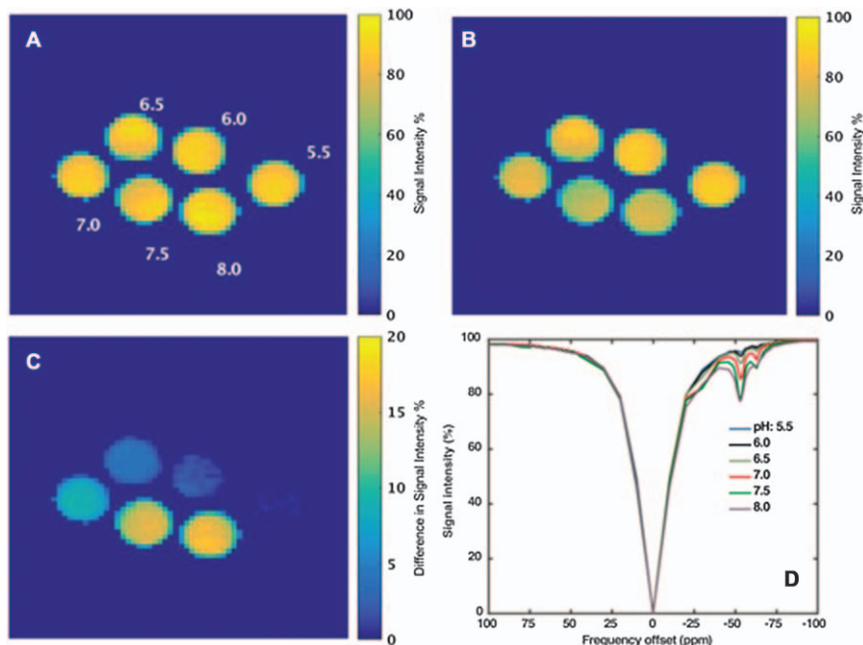


Figure 3.27 The effect of pH on the CEST effect. (A) Fast spin echo image ($TR = 7$ s, $TE = 7$ ms, echo train length = 32, field of view = 25.6 mm \times 25.6 mm, matrix = 128×128 , saturation frequency = 53 ppm) of a series of NMR-tube phantoms containing Tm-DOTAM-lys-OH (15 mM at 37°C). The solutions were adjusted to the pH value provided beside the phantom. (B) Fast spin echo image of the same phantoms acquired using a saturation frequency of -53 ppm. (C) The difference [between (A) and (B)] image shows greater signal change associated with the highest pH (8.0) compared to the lowest pH (5.5). (D) CEST spectra acquired as a function of pH. Spectra were obtained by selecting a region of interest within each vial and plotting the average CEST spectra for all pixels within that region.

ensuring that agents remain effective at influencing CEST (Section 3.1.1). However, the use of fast-exchange systems also requires higher saturation power. The use of high levels of saturation power has two important consequences: high levels of saturation power lead to large power deposition, and the high levels of saturation power cause saturation of exchangeable protons in endogenous macromolecules in tissues. Saturation of exchangeable spins in endogenous macromolecules leads to transfer of magnetization to the bulk water, essentially reducing the net magnetization of the bulk water available for the CEST agent to influence. The net result is a decrease in the detection sensitivity of the CEST agent.¹⁵³ Therefore, proper evaluation of the potential contrast from CEST agents should be made in phantoms that mimic *in vivo* macromolecule signals. Several macromolecule mimics have been reported, including bovine serum albumin,^{165,168} egg

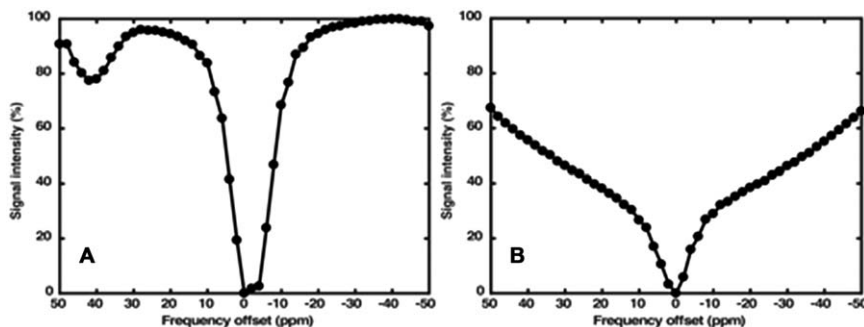


Figure 3.28 (A) CEST spectrum acquired from a phantom containing Eu-DOTAM-Gly-Phe (10 mM, pH 7, 37 °C).¹⁵¹ (B) CEST spectrum acquired from a phantom containing Eu-DOTAM-Gly-Phe (10 mM) and bovine serum albumin (5%) at pH 7 and 37 °C.

white,^{169,170} and tissue;⁶⁷ the preferred mimic depends on the conditions being studied. Figure 3.28 shows the result of combining a solution of Eu-DOTAM-gly-phe (10 mM) with bovine serum albumin (5%). The CEST peak visible at 42 ppm (Figure 3.28A) is not visible when combined with bovine serum albumin (Figure 3.28B) owing to the saturation from exchangeable protons on albumin.

3.6.5 Field-strength Dependencies

The CEST effect is field-strength dependent. Higher B_0 field strengths provide an advantage for CEST because they provide a greater separation between the chemical shift of the exchanging protons on the CEST agent and the protons of bulk water. Therefore, it is critical to test agents at field strengths that are the same as where they might be used. NMR spectrometers are commonly found with field strengths ranging from 9.4 T (400 MHz for proton) to 11.7 T (600 MHz for proton). Imaging systems for humans commonly range from 0.5 to 7 T, and animal imaging systems are typically 7 or 9.4 T. Development of CEST agents for animal use at 7 or 9.4 T should be evaluated using the same field strength. Similarly, agents designed for human use should be evaluated on lower-field-strength human imaging systems. Such systems are not typically designed to study samples as small as NMR tubes and therefore proper evaluation on such systems might require development of dedicated radio-frequency coils, pulse sequences, and the use of large phantoms to obtain optimal results.

References

1. K. M. Ward, A. H. Aletras and R. S. Balaban, *J. Magn. Reson.*, 2000, **143**, 79.
2. P. C. M. van Zijl and N. N. Yadav, *Magn. Reson. Med.*, 2011, **65**, 927.

3. E. Terreno, D. D. Castelli and S. Aime, *Contrast Media Mol. Imaging*, 2010, **5**, 78.
4. M. Zaiss and P. Bachert, *Phys. Med. Biol.*, 2013, **58**, R221.
5. S. Aime, D. D. Castelli, S. Geninatti Crich, E. Gianolio and E. Terreno, *Acc. Chem. Res.*, 2009, **42**, 822.
6. A. D. Sherry and M. Woods, *Annu. Rev. Biomed. Eng.*, 2008, **10**, 391.
7. H. Shinar, M. D. Battistel, M. Mandler, F. Lichaa, D. I. Freedberg and G. Navon, *Carbohydr. Res.*, 2014, **389**, 165.
8. K. W. Y. Chan, L. Jiang, M. Cheng, J. P. Wijnen, G. Liu, P. Huang, P. C. M. van Zijl, M. T. McMahon and K. Glunde, *NMR Biomed.*, 2016, **29**, 806.
9. G. Ferrauto, D. Delli Castelli, E. Terreno and S. Aime, *Magn. Reson. Med.*, 2013, **69**, 1703.
10. F. J. Nicholls, W. Ling, G. Ferrauto, S. Aime and M. Modo, *Sci. Rep.*, 2015, **5**, 14597.
11. M. T. McMahon, A. A. Gilad, M. A. DeLiso, S. M. Cromer Berman, J. W. M. Bulte and P. C. M. van Zijl, *Magn. Reson. Med.*, 2008, **60**, 803.
12. G. Ferrauto, F. Carniato, L. Tei, H. Hu, S. Aime and M. Botta, *Nanoscale*, 2014, **6**, 9604.
13. A. Pumphrey, Z. Yang, S. Ye, D. K. Powell, S. Thalman, D. S. Watt, A. Abdel-Latif, J. Unrine, K. Thompson, B. Fornwalt, G. Ferrauto and M. Vandsburger, *NMR Biomed.*, 2016, **29**, 74.
14. X. Yang, N. N. Yadav, X. Song, S. Ray Banerjee, H. Edelman, I. Minn, P. C. M. van Zijl, M. G. Pomper and M. T. McMahon, *Chem.—Eur. J.*, 2014, **20**, 15824.
15. D. Delli Castelli, G. Ferrauto, J. C. Cutrin, E. Terreno and S. Aime, *Magn. Reson. Med.*, 2014, **71**, 326.
16. S. J. Ratnakar, S. Viswanathan, Z. Kovacs, A. K. Jindal, K. N. Green and A. D. Sherry, *J. Am. Chem. Soc.*, 2012, **134**, 5798.
17. D. L. Longo, A. Busato, S. Lanzardo, F. Antico and S. Aime, *Magn. Reson. Med.*, 2013, **70**, 859.
18. E. Pérez-Mayoral, V. Negri, J. Soler-Padrós, S. Cerdán and P. Ballesteros, *Eur. J. Radiol.*, 2008, **67**, 453.
19. D. V. Hingorani, B. Yoo, A. S. Bernstein and M. D. Pagel, *Chem.—Eur. J.*, 2014, **20**, 9840.
20. V. R. Sheth, G. Liu, Y. Li and M. D. Pagel, *Contrast Media Mol. Imaging*, 2012, **7**, 26.
21. D. V. Hingorani, A. S. Bernstein and M. D. Pagel, *Contrast Media Mol. Imaging*, 2015, **10**, 245.
22. A. D. Sherry and Y. Wu, *Curr. Opin. Chem. Biol.*, 2013, **17**, 167.
23. D. E. Woessner, S. Zhang, M. E. Merritt and A. D. Sherry, *Magn. Reson. Med.*, 2005, **53**, 790.
24. E. Terreno, W. Dastrù, D. Delli Castelli, E. Gianolio, S. Geninatti Crich, D. Longo and S. Aime, *Curr. Med. Chem.*, 2010, **17**, 3684.
25. G. Ferrauto, D. Delli Castelli, E. Di Gregorio, E. Terreno and S. Aime, *Wiley Interdiscip. Rev.: Nanomed. Nanobiotechnol.*, 2016, **8**, 602.

26. D. D. Castelli, E. Terreno, D. Longo and S. Aime, *NMR Biomed.*, 2013, **26**, 839.
27. Y. Wu, M. Evbuomwan, M. Melendez, A. Opina and A. D. Sherry, *Future Med. Chem.*, 2010, **2**, 351.
28. O. M. Evbuomwan, G. Kiefer and A. D. Sherry, *Eur. J. Inorg. Chem.*, 2012, **2012**, 2126.
29. S. Aime, D. D. Castelli and E. Terreno, *Methods Enzymol.*, 2009, **464**, 193.
30. G. Ferrauto, D. Delli Castelli, E. Di Gregorio, S. Langereis, D. Burdinski, H. Grüll, E. Terreno and S. Aime, *J. Am. Chem. Soc.*, 2014, **136**, 638.
31. G. Ferrauto, E. Di Gregorio, S. Baroni and S. Aime, *Nano Lett.*, 2014, **14**, 6857.
32. J. Kim, Y. Wu, Y. Guo, H. Zheng and P. Z. Sun, *Contrast Media Mol. Imaging*, 2015, **10**, 163.
33. Y. Takayama, A. Nishie, M. Sugimoto, O. Togao, Y. Asayama, K. Ishigami, Y. Ushijima, D. Okamoto, N. Fujita, A. Yokomizo, J. Keupp and H. Honda, *Magn. Reson. Mater. Phys., Biol. Med.*, 2016, **29**, 671.
34. W. Ling, R. R. Regatte, G. Navon and A. Jerschow, *Proc. Natl. Acad. Sci. U. S. A.*, 2008, **105**, 2266.
35. K. W. Y. Chan, M. T. McMahon, Y. Kato, G. Liu, J. W. M. Bulte, Z. M. Bhujwalla, D. Artemov and P. C. M. van Zijl, *Magn. Reson. Med.*, 2012, **68**, 1764.
36. S. Walker-Samuel, R. Ramasawmy, F. Torrealdea, M. Rega, V. Rajkumar, S. P. Johnson, S. Richardson, M. Gonçalves, H. G. Parkes, E. Årstad, D. L. Thomas, R. B. Pedley, M. F. Lythgoe and X. Golay, *Nat. Med.*, 2013, **19**, 1067.
37. C. Bigot, G. Vanhoutte, M. Verhoye and A. Van der Linden, *NeuroImage*, 2014, **87**, 111.
38. D. Delli Castelli, G. Ferrauto, E. Di Gregorio, E. Terreno and S. Aime, *NMR Biomed.*, 2015, **28**, 1663.
39. K. Murase and N. Tanki, *Magn. Reson. Imaging*, 2011, **29**, 126.
40. B. F. Moon, K. M. Jones, L. Q. Chen, P. Liu, E. A. Randtke, C. M. Howison and M. D. Pagel, *Contrast Media Mol. Imaging*, 2015, **10**, 446.
41. D. L. Longo, F. Michelotti, L. Consolino, P. Bardini, G. Digilio, G. Xiao, P. Z. Sun and S. Aime, *Invest. Radiol.*, 2016, **51**, 155.
42. X. Yang, X. Song, Y. Li, G. Liu, S. Ray Banerjee, M. G. Pomper and M. T. McMahon, *Angew. Chem., Int. Ed.*, 2013, **52**, 8116.
43. X. Song, X. Yang, S. Ray Banerjee, M. G. Pomper and M. T. McMahon, *Contrast Media Mol. Imaging*, 2015, **10**, 74.
44. P. C. M. van Zijl, C. K. Jones, J. Ren, C. R. Malloy and A. D. Sherry, *Proc. Natl. Acad. Sci. U. S. A.*, 2007, **104**, 4359.
45. M. Woods, D. E. Woessner and A. D. Sherry, *Chem. Soc. Rev.*, 2006, **35**, 500.
46. B. Yoo and M. D. Pagel, *Front. Biosci., Landmark Ed.*, 2008, **13**, 1733.
47. Y. Li, V. R. Sheth, G. Liu and M. D. Pagel, *Contrast Media Mol. Imaging.*, 2011, **6**, 219.

48. E. Di Gregorio, E. Gianolio, R. Stefania, G. Barutello, G. Digilio and S. Aime, *Anal. Chem.*, 2013, **85**, 5627.
49. G. Ferrauto, E. Di Gregorio, W. Dastrù, S. Lanzardo and S. Aime, *Bio-materials*, 2015, **58**, 82.
50. D. Delli Castelli, M. C. Caligara, M. Botta, E. Terreno and S. Aime, *Inorg. Chem.*, 2013, **52**, 7130.
51. G. Rancan, D. Delli Castelli and S. Aime, *Magn. Reson. Med.*, 2016, **75**, 329.
52. E. Gianolio, R. Stefania, E. Di Gregorio and S. Aime, *Eur. J. Inorg. Chem.*, 2012, **2012**, 1934.
53. E. Di Gregorio, G. Ferrauto, E. Gianolio and S. Aime, *Contrast Media Mol. Imaging*, 2013, **8**, 475.
54. A. L. Pumphrey, S. Ye, Z. Yang, J. Simkin, J. C. Gensel, A. Abdel-Latif and M. H. Vandsburger, *Radiology*, 2017, **282**, 131.
55. D. L. Longo, W. Dastrù, G. Digilio, J. Keupp, S. Langereis, S. Lanzardo, S. Prestigio, O. Steinbach, E. Terreno, F. Uggeri and S. Aime, *Magn. Reson. Med.*, 2011, **65**, 202.
56. L. Q. Chen, C. M. Howison, J. J. Jeffery, I. F. Robey, P. H. Kuo and M. D. Pagel, *Magn. Reson. Med.*, 2014, **72**, 1408.
57. J. Döpfert, C. Witte, M. Kunth and L. Schröder, *Contrast Media Mol. Imaging*, 2014, **9**, 100.
58. J. Döpfert, C. Witte and L. Schröder, *ChemPhysChem*, 2014, **15**, 261.
59. T. K. Stevens, K. K. Palaniappan, R. M. Ramirez, M. B. Francis, D. E. Wemmer and A. Pines, *Magn. Reson. Med.*, 2013, **69**, 1245.
60. J. Zhang, W. Jiang, Q. Luo, X. Zhang, Q. Guo, M. Liu and X. Zhou, *Talanta*, 2014, **122**, 101.
61. M. T. McMahon, A. A. Gilad, J. Zhou, P. Z. Sun, J. W. M. Bulte and P. C. M. van Zijl, *Magn. Reson. Med.*, 2006, **55**, 836.
62. X. Yang, X. Song, S. Ray Banerjee, Y. Li, Y. Byun, G. Liu, Z. M. Bhujwala, M. G. Pomper and M. T. McMahon, *Contrast Media Mol. Imaging*, 2016, **11**, 304.
63. S. Zhang and A. D. Sherry, *J. Solid State Chem.*, 2003, **171**, 38.
64. M. Kim, J. Gillen, B. A. Landman, J. Zhou and P. C. M. van Zijl, *Magn. Reson. Med.*, 2009, **61**, 1441.
65. G. Liu, A. A. Gilad, J. W. M. Bulte, P. C. M. van Zijl and M. T. McMahon, *Contrast Media Mol. Imaging*, 2010, **5**, 162.
66. S. Viswanathan, Z. Kovacs, K. N. Green, S. J. Ratnakar and A. D. Sherry, *Chem. Rev.*, 2010, **110**, 2960.
67. T. K. Stevens, M. Milne, A. A. H. Elmehriki, M. Suchý, R. Bartha and R. H. E. Hudson, *Contrast Media Mol. Imaging*, 2013, **8**, 289.
68. T. Chauvin, S. Torres, R. Rosseto, J. Kotek, B. Badet, P. Durand and É. Tóth, *Chem.—Eur. J.*, 2012, **18**, 1408.
69. J. He, C. S. Bonnet, S. V. Eliseeva, S. Lacerda, T. Chauvin, P. Retailleau, F. Szeremeta, B. Badet, S. Petoud, É. Tóth and P. Durand, *J. Am. Chem. Soc.*, 2016, **138**, 2913.

70. S. J. Dorazio, A. O. Olatunde, P. B. Tsitovich and J. R. Morrow, *JBIC, J. Biol. Inorg. Chem.*, 2014, **19**, 191.
71. S. J. Dorazio and J. R. Morrow, *Inorg. Chem.*, 2012, **51**, 7448.
72. S. J. Dorazio, A. O. Olatunde, J. A. Sperry and J. R. Morrow, *Chem. Commun.*, 2013, **49**, 10025.
73. S. J. Dorazio, P. B. Tsitovich, K. E. Sifers, J. A. Sperry and J. R. Morrow, *J. Am. Chem. Soc.*, 2011, **133**, 14154.
74. A. O. Olatunde, C. J. Bond, S. J. Dorazio, J. M. Cox, J. B. Benedict, M. D. Daddario, J. A. Sperry and J. R. Morrow, *Chem.—Eur. J.*, 2015, **21**, 18290.
75. A. O. Olatunde, S. J. Dorazio, J. A. Sperry and J. R. Morrow, *J. Am. Chem. Soc.*, 2012, **134**, 18503.
76. P. B. Tsitovich, J. M. Cox, J. A. Sperry and J. R. Morrow, *Inorg. Chem.*, 2016, **55**, 12001.
77. P. B. Tsitovich, J. A. Sperry and J. R. Morrow, *Angew. Chem., Int. Ed.*, 2013, **52**, 13997.
78. I.-R. Jeon, J. G. Park, C. R. Haney and T. D. Harris, *Chem. Sci.*, 2014, **5**, 2461.
79. S. Zhang, M. Merritt, D. E. Woessner, R. E. Lenkinski and A. D. Sherry, *Acc. Chem. Res.*, 2003, **36**, 783.
80. S. Aime, A. Barge, M. Botta, A. S. De Sousa and D. Parker, *Angew. Chem., Int. Ed.*, 1998, **37**, 2673.
81. S. Zhang, P. Winter, K. Wu and A. D. Sherry, *J. Am. Chem. Soc.*, 2001, **123**, 1517.
82. S. Amin, D. A. Voss, Jr., W. D. Horrocks, Jr., C. H. Lake, M. R. Churchill and J. R. Morrow, *Inorg. Chem.*, 1995, **34**, 3294.
83. W. S. Fernando, A. F. Martins, P. Zhao, Y. Wu, G. E. Kiefer, C. Platas-Iglesias and A. D. Sherry, *Inorg. Chem.*, 2016, **55**, 3007.
84. F. Wojciechowski, M. Suchy, A. X. Li, H. A. Azab, R. Bartha and R. H. E. Hudson, *Bioconjugate Chem.*, 2007, **18**, 1625.
85. M. M. Ali, G. Liu, T. Shah, C. A. Flask and M. D. Pagel, *Acc. Chem. Res.*, 2009, **42**, 915.
86. M. C. Alpoim, A. M. Urbano, C. F. G. C. Geraldes and J. A. Peters, *J. Chem. Soc., Dalton Trans.*, 1992, **3**, 463.
87. K. Djanashvili and J. A. Peters, *Contrast Media Mol. Imaging*, 2007, **2**, 67.
88. F. A. Dunand, S. Aime and A. E. Merbach, *J. Am. Chem. Soc.*, 2000, **122**, 1506.
89. S. Zhang, K. Wu, M. C. Biewer and A. D. Sherry, *Inorg. Chem.*, 2001, **40**, 4284.
90. J. R. Morrow and P. B. Tsitovich, Transition Metal paraCEST Probes as Alternatives to Lanthanides, in *Chemical Exchange Saturation Transfer Imaging: Advances and Applications*, ed. M. T. McMahon, A. A. Gilad, J. W. M. Bulte and P. C. M. van Zijl, Pan Stanford/Singapore, 2017, Ch. 12, pp. 257–282.
91. S. F. Lincoln, *Coord. Chem. Rev.*, 1971, **6**, 309.

92. A. Fratiello, Nuclear Magnetic Resonance Cation Solvation Studies, in *Progress in Inorganic Chemistry: Inorganic Reaction Mechanisms: Part II*, ed. J. O. Edwards, Vol. 17, Wiley, Hoboken, NJ, 1972, pp. 57–92.
93. A. M. Chmelnick and D. Fiat, *J. Chem. Phys.*, 1967, **47**, 3986.
94. A. M. Chmelnick and D. Fiat, *J. Am. Chem. Soc.*, 1971, **93**, 2875.
95. R. E. Connick and D. Fiat, *J. Chem. Phys.*, 1966, **44**, 4103.
96. J. Maigut, R. Meier, A. Zahl and R. van Eldik, *Inorg. Chem.*, 2007, **46**, 5361.
97. W. D. Horrocks, Jr. and D. R. Sudnick, *Science*, 1979, **206**, 1194.
98. W. D. Horrocks, Jr. and D. R. Sudnick, *J. Am. Chem. Soc.*, 1979, **101**, 334.
99. S. Aime, A. Barge, J. I. Bruce, M. Botta, J. A. K. Howard, J. M. Moloney, D. Parker, A. S. de Sousa and M. Woods, *J. Am. Chem. Soc.*, 1999, **121**, 5762.
100. W. D. Horrocks, Jr. and M. Albin, Lanthanide Ion Luminescence in Coordination Chemistry and Biochemistry, in *Progress in Inorganic Chemistry*, ed. S. J. Lippard, Vol. 31, Wiley, Hoboken, NJ, 1984, pp. 1–104.
101. J. R. Morrow and C. M. Andolina, Spectroscopic Investigations of Lanthanide Ion Binding to Nucleic Acids, in *Interplay between Metal Ions and Nucleic Acids*, ed. A. Sigel, H. Sigel and R. K. O. Sigel, Vol. 10, Springer, Dordrecht, The Netherlands, 2012, Ch. 6, pp. 171–199.
102. *Luminescence of Lanthanide Ions in Coordination Compounds and Nanomaterials*, ed. A. de Bettencourt-Dias, Wiley, West Sussex, UK, 2014.
103. S. V. Eliseeva and J.-C. G. Bünzli, *Chem. Soc. Rev.*, 2010, **39**, 189.
104. C.-H. Huang, J. Hammell, S. J. Ratnakar, A. D. Sherry and J. R. Morrow, *Inorg. Chem.*, 2010, **49**, 5963.
105. J. Hammell, L. Buttarazzi, C.-H. Huang and J. R. Morrow, *Inorg. Chem.*, 2011, **50**, 4857.
106. C.-H. Huang and J. R. Morrow, *J. Am. Chem. Soc.*, 2009, **131**, 4206.
107. L. L. Chappell, D. A. Voss, Jr., W. D. Horrocks, Jr. and J. R. Morrow, *Inorg. Chem.*, 1998, **37**, 3989.
108. D. Parker, H. Puschmann, A. S. Batsanov and K. Senanayake, *Inorg. Chem.*, 2003, **42**, 8646.
109. S. Amin, J. R. Morrow, C. H. Lake and M. R. Churchill, *Angew. Chem., Int. Ed. Engl.*, 1994, **33**, 773.
110. H. S. Gutowsky, D. W. McCall and C. P. Slichter, *J. Chem. Phys.*, 1953, **21**, 279.
111. H. S. Gutowsky and A. Saika, *J. Chem. Phys.*, 1953, **21**, 1688.
112. S. Mori, C. Abeygunawardana, P. C. M. van Zijl and J. M. Berg, *J. Magn. Reson., Ser. B*, 1996, **110**, 96.
113. S. Mori, J. M. Berg and P. C. M. van Zijl, *J. Biomol. NMR*, 1996, **7**, 77.
114. P. C. M. van Zijl, J. Zhou, N. Mori, J.-F. Payen, D. Wilson and S. Mori, *Magn. Reson. Med.*, 2003, **49**, 440.
115. J. Zhou, D. A. Wilson, P. Z. Sun, J. A. Klaus and P. C. M. van Zijl, *Magn. Reson. Med.*, 2004, **51**, 945.
116. W. T. Dixon, J. Ren, A. J. M. Lubag, J. Ratnakar, E. Vinogradov, I. Hancu, R. E. Lenkinski and A. D. Sherry, *Magn. Reson. Med.*, 2010, **63**, 625.

117. E. A. Randtke, L. Q. Chen, L. R. Corrales and M. D. Pagel, *Magn. Reson. Med.*, 2014, **71**, 1603.
118. W. G. Lesniak, N. Oskolkov, X. Song, B. Lal, X. Yang, M. Pomper, J. Laterra, S. Nimmagadda and M. T. McMahon, *Nano Lett.*, 2016, **16**, 2248.
119. E. Vinogradov, A. D. Sherry and R. E. Lenkinski, *J. Magn. Reson.*, 2013, **229**, 155.
120. G. Liu, X. Song, K. W. Y. Chan and M. T. McMahon, *NMR Biomed.*, 2013, **26**, 810.
121. I. Hancu, W. T. Dixon, M. Woods, E. Vinogradov, A. D. Sherry and R. E. Lenkinski, *Acta Radiol.*, 2010, **51**, 910.
122. P. M. Winter, *Wiley Interdiscip. Rev.: Nanomed. Nanobiotechnol.*, 2012, **4**, 389.
123. M. T. McMahon and K. W. Y. Chan, Developing MR Probes for Molecular Imaging, in *Emerging Applications of Molecular Imaging to Oncology*, ed. M. G. Pomper and P. B. Fisher, *Advances in Cancer Research Series* Vol. 124, Academic Press, London, 2014, Ch. 9, pp. 297–327.
124. X. Zhu, S. Chen, Q. Luo, C. Ye, M. Liu and X. Zhou, *Chem. Commun.*, 2015, **51**, 9085.
125. S. Zhang, K. Zhou, G. Huang, M. Takahashi, A. D. Sherry and J. Gao, *Chem. Commun.*, 2013, **49**, 6418.
126. E. Terreno, D. Delli Castelli, C. Cabella, W. Dastrù, A. Sanino, J. Stancanello, L. Tei and S. Aime, *Chem. Biodiversity*, 2008, **5**, 1901.
127. E. Terreno, A. Barge, L. Beltrami, G. Cravotto, D. D. Castelli, F. Fedeli, B. Jebasingh and S. Aime, *Chem. Commun.*, 2008, 600.
128. S. Aime, D. Delli Castelli and E. Terreno, *Angew. Chem., Int. Ed.*, 2005, **44**, 5513.
129. E. Terreno, D. Delli Castelli, E. Violante, H. M. H. F. Sanders, N. A. J. M. Sommerdijk and S. Aime, *Chem.—Eur. J.*, 2009, **15**, 1440.
130. E. Terreno, C. Cabella, C. Carrera, D. Delli Castelli, R. Mazzon, S. Rollet, J. Stancanello, M. Visigalli and S. Aime, *Angew. Chem., Int. Ed.*, 2007, **46**, 966.
131. M. M. Ali, B. Yoo and M. D. Pagel, *Mol. Pharmaceutics*, 2009, **6**, 1409.
132. M. M. Ali, M. P. I. Bhuiyan, B. Janic, N. R. S. Varma, T. Mikkelsen, J. R. Ewing, R. A. Knight, M. D. Pagel and A. S. Arbab, *Nanomedicine (London, U. K.)*, 2012, **7**, 1827.
133. O. M. Evbuomwan, M. E. Merritt, G. E. Kiefer and A. D. Sherry, *Contrast Media Mol. Imaging.*, 2012, **7**, 19.
134. O. Vasalatiy, R. D. Gerard, P. Zhao, X. Sun and A. D. Sherry, *Bioconjugate Chem.*, 2008, **19**, 598.
135. O. Vasalatiy, P. Zhao, S. Zhang, S. Aime and A. D. Sherry, *Contrast Media Mol. Imaging*, 2006, **1**, 10.
136. S. Aime, L. Frullano and S. Geninatti Crich, *Angew. Chem., Int. Ed.*, 2002, **41**, 1017.
137. R. Straathof, G. J. Strijkers and K. Nicolay, Target-Specific Paramagnetic and Superparamagnetic Micelles for Molecular MR Imaging, in *In Vivo*

- NMR Imaging: Methods and Protocols*, ed. L. Schröder and C. Faber, *Methods in Molecular Biology Series 771*, Humana Press, New York, 011, Ch. 34, pp. 691–715.
138. G. M. Nicolle, É. Tóth, K.-P. Eisenwiener, H. R. Mäcke and A. E. Merbach, *J. Biol. Inorg. Chem.*, 2002, **7**, 757.
 139. F. Kielar, L. Tei, E. Terreno and M. Botta, *J. Am. Chem. Soc.*, 2010, **132**, 7836.
 140. G. Mulas, G. Ferrauto, W. Dastrù, R. Anedda, S. Aime and E. Terreno, *Magn. Reson. Med.*, 2015, **74**, 468.
 141. J. A. Peters, J. Huskens and D. J. Raber, *Prog. Nucl. Magn. Reson. Spectrosc.*, 1996, **28**, 283.
 142. B. Chahid, L. Vander Elst, J. Flament, F. Boumezbeur, C. Medina, M. Port, R. N. Muller and S. Lesieur, *Contrast Media Mol. Imaging*, 2014, **9**, 391.
 143. E. Terreno, D. D. Castelli, L. Milone, S. Rollet, J. Stancanello, E. Violante and S. Aime, *Contrast Media Mol. Imaging*, 2008, **3**, 38.
 144. M. M. Ali, M. Woods, E. H. Suh, Z. Kovacs, G. Tircsó, P. Zhao, V. D. Kodibagkar and A. D. Sherry, *JBIC, J. Biol. Inorg. Chem.*, 2007, **12**, 855.
 145. S. Aime, D. Delli Castelli and E. Terreno, *Angew. Chem., Int. Ed.*, 2003, **42**, 4527.
 146. Y. Chen, H. Chen and J. Shi, *Adv. Mater.*, 2013, **25**, 3144.
 147. K. Suzuki, K. Ikari and H. Imai, *J. Am. Chem. Soc.*, 2004, **126**, 462.
 148. E. Di Gregorio, G. Ferrauto, E. Gianolio, S. Lanzardo, C. Carrera, F. Fedeli and S. Aime, *ACS Nano*, 2015, **9**, 8239.
 149. S. Aime, A. Barge, D. Delli Castelli, F. Fedeli, A. Mortillaro, F. U. Nielsen and E. Terreno, *Magn. Reson. Med.*, 2002, **47**, 639.
 150. S. Aime, A. Barge, A. S. Batsanov, M. Botta, D. D. Castelli, F. Fedeli, A. Mortillaro, D. Parker and H. Puschmann, *Chem. Commun. (Cambridge, U. K.)*, 2002, 1120.
 151. M. Suchý, A. X. Li, R. Bartha and R. H. E. Hudson, *Bioorg. Med. Chem.*, 2008, **16**, 6156.
 152. P. Z. Sun, E. Wang, J. S. Cheung, X. Zhang, T. Benner and A. G. Sorensen, *Magn. Reson. Med.*, 2011, **66**, 1042.
 153. A. X. Li, R. H. E. Hudson, J. W. Barrett, C. K. Jones, S. H. Pasternak and R. Bartha, *Magn. Reson. Med.*, 2008, **60**, 1197.
 154. N. McVicar, A. X. Li, D. F. Gonçalves, M. Bellyou, S. O. Meakin, M. A. Prado and R. Bartha, *J. Cereb. Blood Flow Metab.*, 2014, **34**, 690.
 155. K. L. Desmond and G. J. Stanis, *Magn. Reson. Med.*, 2012, **67**, 979.
 156. H.-Y. Heo, C. K. Jones, J. Hua, N. Yadav, S. Agarwal, J. Zhou, P. C. M. van Zijl and J. J. Pillai, *J. Magn. Reson. Imaging*, 2016, **44**, 41.
 157. C. K. Jones, D. Polders, J. Hua, H. Zhu, H. J. Hoogduin, J. Zhou, P. Luijten and P. C. M. van Zijl, *Magn. Reson. Med.*, 2012, **67**, 1579.
 158. V. Khlebnikov, N. Geades, D. W. J. Klomp, H. Hoogduin, P. Gowland and O. Mougin, *Magn. Reson. Med.* [Online early access], DOI: 10.1002/mrm.26323, Published Online: July 25, 2016. <http://onlinelibrary.wiley.com/doi/10.1002/mrm.26323/full> (last accessed 2016).

159. P. Z. Sun, T. Benner, A. Kumar and A. G. Sorensen, *Magn. Reson. Med.*, 2008, **60**, 834.
160. Y. K. Tee, A. A. Khrapitchev, N. R. Sibson, S. J. Payne and M. A. Chappell, *J. Magn. Reson.*, 2012, **222**, 88.
161. E. S. Yoshimaru, E. A. Randtke, M. D. Pagel and J. Cárdenas-Rodríguez, *J. Magn. Reson.*, 2016, **263**, 184.
162. Z. Zu, K. Li, V. A. Janve, M. D. Does and D. F. Gochberg, *Magn. Reson. Med.*, 2011, **66**, 1100.
163. N. McVicar, A. X. Li, M. Suchý, R. H. E. Hudson, R. S. Menon and R. Bartha, *Magn. Reson. Med.*, 2013, **70**, 1016.
164. K. M. Ward and R. S. Balaban, *Magn. Reson. Med.*, 2000, **44**, 799.
165. A. X. Li, F. Wojciechowski, M. Suchy, C. K. Jones, R. H. E. Hudson, R. S. Menon and R. Bartha, *Magn. Reson. Med.*, 2008, **59**, 374.
166. S. Zhang, C. R. Malloy and A. D. Sherry, *J. Am. Chem. Soc.*, 2005, **127**, 17572.
167. R. M. Henkelman, X. Huang, Q.-S. Xiang, G. J. Stanisz, S. D. Swanson and M. J. Bronskill, *Magn. Reson. Med.*, 1993, **29**, 759.
168. K. J. Ray, J. R. Larkin, Y. K. Tee, A. A. Khrapitchev, G. Karunanithy, M. Barber, A. J. Baldwin, M. A. Chappell and N. R. Sibson, *NMR Biomed.*, 2016, **29**, 1624.
169. T. Wada, O. Togao, C. Tokunaga, R. Funatsu, K. Kobayashi and Y. Nakamura, *Radiol. Phys. Technol.*, 2016, **9**, 15.
170. A. O. Olatunde, J. M. Cox, M. D. Daddario, J. A. Sperry, J. B. Benedict and J. R. Morrow, *Inorg. Chem.*, 2014, **53**, 8311.

CHAPTER 4

Iron-oxide Nanoparticle-based Contrast Agents

DIMITRI STANICKI,^a LUCE VANDER ELST,^{a,b}
ROBERT N. MULLER,^{a,b} SOPHIE LAURENT,^{*a,b}
DELPHINE FELDER-FLESCH,^c DAMIEN MERTZ,^c
AUDREY PARAT,^c SYLVIE BEGIN-COLIN,^{*c} GEOFFREY COTIN,^c
JEAN-MARC GRENECHE,^d OVIDIU ERSEN,^c BENOIT PICHON,^c
VLAD SOCOLIUC,^c VICTOR KUNCSEK,^{*f} RODICA TURCU,^g
LADISLAU VÉKÁS,^{*c} PAULA FOSTER^{h,i} AND
ROBERT BARTHA^{*h,j}

^aLaboratory of NMR and Molecular Imaging, Department of General, Organic and Biomedical Chemistry, University of Mons, 19 7000, Mons, Belgium; ^bCMMI – Center for Microscopy and Molecular Imaging, 8 6041, Gosselies, Belgium; ^cIPCMS UMR Centre National de la Recherche Scientifique, 67034, Strasbourg, France; ^dIMMM UMR CNRS 6283 Université du Maine, 72085, Le Mans, France; ^eRomanian Academy-Timisoara Branch, Center for Fundamental and Advanced Technical Research, Lab. Magnetic Fluids, RO-300223, Timisoara, Romania; ^fNational Institute of Materials Physics, 077125, Bucharest-Magurele, Romania; ^gNational Institute R&D for Isotopic and Molecular Technologies, RO-400293, Cluj-Napoca, Romania; ^hRobarts Research Institute, University of Western Ontario, London, ON N6A 3K7, Canada; ⁱDepartment of Medical Biophysics, University of Western Ontario, London, ON N6A 3K7, Canada; ^jDepartments of Medical Imaging and Psychiatry, University of Western Ontario, London, ON N6A 3K7, Canada
*Email: Sophie.Laurent@umons.ac.be; Sylvie.Begin@ipcms.unistra.fr; vekas@acad-tim.tm.edu.ro; rbartha@robarts.ca

4.1 General Theory of the Relaxivity of Particulate Contrast Agents

DIMITRI STANICKI, LUCE VANDER ELST, ROBERT N. MULLER AND SOPHIE LAURENT*

4.1.1 General Introduction to Iron Oxide Nanoparticles

By reducing the size from bulk to the nanometer scale (<20 nm), ferrimagnetic iron oxide material acquires a magnetic property called superparamagnetism. When submitting superparamagnetic objects to an external magnetic field, their global magnetic moments align in the direction of the field. When the field is decreased to zero, however, the magnetic moment of the samples instantaneously returns to zero. Their magnetic properties and benign character led magnetic iron oxide nanoparticles to be extensively used in many biomedical applications, including magnetic resonance imaging (MRI). Some iron-oxide-based systems have been used clinically for the detection of hepatic or spleen anomalies. The emergence of areas such as cell tracking, magnetic hyperthermia, drug delivery, molecular imaging, and magnetic-particle imaging have encouraged researchers to pursue the development of efficient procedures to provide nanoparticles with specific desired properties. For example, to be used efficiently in biorelated applications, magnetic particles often must have specific magnetic properties, small size, narrow size distribution, specific surface functionality, and well-defined morphologies in addition to being nontoxic and biocompatible. Each of these characteristics can be achieved by the optimization of preparation processes.

The development of nanomaterials with interesting intrinsic properties has opened new exciting possibilities to solve unresolved challenges in several domains, such as medicine,¹⁻³ data storage,⁴ and catalysis.⁵ In particular, magnetic nanomaterials like iron oxide are widely exploited in biomedical applications as contrast agents for MRI, for drug delivery, and in hyperthermia.⁶⁻¹² The following characteristics are the main advantages of magnetic iron oxide nanostructures for such applications: a high concentration of superparamagnetic ions in a single unit; the ability to modulate size and surface as a function of desired applications; the possibility to couple active molecules on nanoparticle surfaces; biodegradability and biocompatibility; low toxicity for patients suffering from kidney disorders; and low price of production.

Despite these advantages, a challenging aspect of using iron oxide nanoparticles is that the morphology of the nanomaterials strongly influences their physicochemical properties and, in particular, their magnetic properties. Consequently, a difficulty of this field is the synthesis of magnetic nanoparticles with controlled diameters and size distributions. The colloidal instability and agglomeration of nanostructures in aqueous suspension

must also be carefully addressed. Because nanoparticle production is important, controlling the surface of nanoparticles is a challenge in the biomedical field.^{13,14}

Magnetite, $\text{FeO} \cdot \text{Fe}_2\text{O}_3$, and maghemite, $\gamma\text{-Fe}_2\text{O}_3$, exhibit inverse spinel structures with the general formula of AB_2X_4 , where A and B are cations and X are anions.¹⁵ Both of these materials adopt a face-centered cubic crystal-line structure. The inverse spinel structure of magnetite contains both ferric and ferrous ions. Thirty-two oxygen anions delimit a face-centered cubic unit cell in which the iron ions are located on eight tetrahedral sites surrounded by four oxygen ions and 16 octahedral sites surrounded by eight oxygen ions. The tetrahedral sites are exclusively occupied by ferric ions, whereas the octahedral sites are alternately occupied by ferrous and ferric ions (Figure 4.1). The composition of a unit cell of magnetite is thus $[\text{Fe}^{3+}]_{\text{tetrahedral}}[\text{Fe}^{3+}\text{Fe}^{2+}]_{\text{octahedral}}\text{O}_4$ or $\text{FeO} \cdot \text{Fe}_2\text{O}_3$. Because of superexchange-oxygen-mediated coupling, all the magnetic moments of the octahedral iron ions are aligned in a defined direction, and all magnetic moments of the tetrahedral iron ions are aligned in the opposite direction. Because ferric ions are equally distributed between octahedral and tetrahedral sites, they compensate for each other. Consequently, the resulting moment of a magnetite crystal arises solely from the uncompensated octahedral ferrous ions.

On the other hand, maghemite, which is the oxidized form of magnetite, is composed solely of trivalent iron ions. The oxidation of Fe^{II} to Fe^{III} creates vacancies in the octahedral sites. The formula of maghemite is $[\text{Fe}^{3+}]_{\text{tetrahedral}}[\text{Fe}^{3+}_{2/3}\text{V}_{1/3}]_{\text{octahedral}}\text{O}_4$.

Magnetic materials can be classified in two categories according to their response to an applied magnetic field: (1) “weak” magnetic materials, which are diamagnetic and paramagnetic, and (2) “strong” magnetic materials,

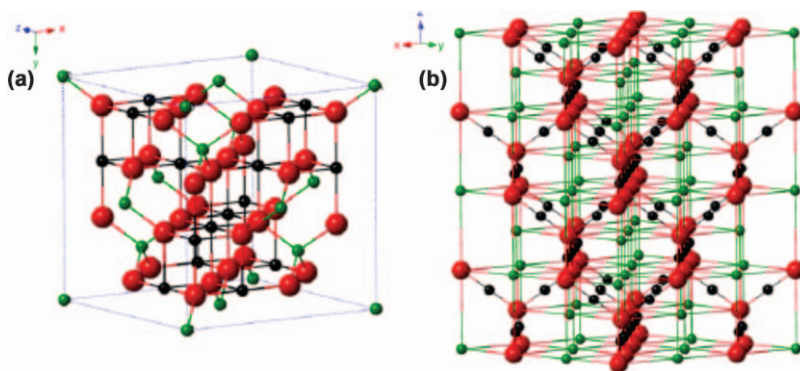


Figure 4.1 Inverse spinel structure of (a) magnetite and (b) maghemite (the black balls are Fe^{II} , the green balls are Fe^{III} , and the red balls are O^{2-}). Adapted with permission from W. Wu, Z. Wu, T. Yu, C. Jiang and W.-S. Kim, *Sci. Technol. Adv. Mater.*, 2015, **16**, 023501 (<https://creativecommons.org/licenses/by/3.0/>).

which include ferromagnetic, ferrimagnetic, and antiferromagnetic structures.

Magnetic materials are generally defined by three important parameters: their dipolar magnetic moment, their magnetization, and their magnetic susceptibility. The dipolar magnetic moment is defined as an expression of the vector magnitude resulting from the electron motion in atoms, or from the electron spin, leading to the formation of a magnetic field. The magnetic moment is represented by the vector μ . If an external magnetic field is applied on the material, magnetic moments tend to align in the same direction. This phenomenon creates a magnetization (M) defined as a magnetic moment per volume. The magnetic susceptibility, χ , is a constant value that indicates the magnetization level of a material when it is subjected to an external magnetic field.

Diamagnetic compounds are molecules that have zero orbital angular momentum, like Eu^{III} in the ground state, or contain no unpaired electrons, such as noble gases, diatomic gases, and most organic molecules. When an external magnetic field is applied, these substances induce a low opposite magnetization close to zero. Consequently, in this case, the magnetic susceptibility is negative.

Paramagnetic materials do not exhibit a spontaneous magnetization. If a magnetic field is applied, however, their spins will align in the direction parallel to the magnetic field. As a consequence, magnetization increases as a function of the intensity of the applied magnetic field. Paramagnetic materials have unpaired electrons. Examples include some transition metal salts, such as potassium chromium(III) sulfate dodecahydrate ($\text{KCr}(\text{SO}_4)_2 \cdot 12\text{H}_2\text{O}$), and some lanthanide ions, such as Gd^{III} .

In the absence of an external magnetic field, diamagnetic and paramagnetic compounds do not exhibit a permanent magnetization. Some other magnetic compounds, however, have a high magnetization state even without an external magnetic field. These compounds are either ferromagnetic, antiferromagnetic, or ferrimagnetic (Figure 4.2) and exhibit some particular magnetic properties.

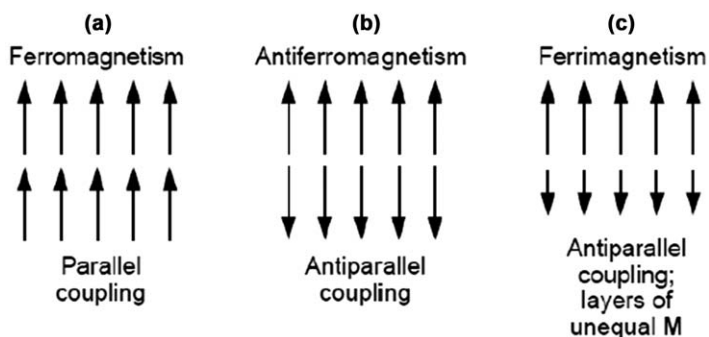


Figure 4.2 Schematic representations of (a) ferromagnetic, (b) antiferromagnetic, and (c) ferrimagnetic materials.

Ferromagnetism is the magnetism resulting from the alignment of permanent magnetic moments. In such materials, the magnetic moments are parallel to each other due to a strong interaction called ferromagnetic coupling.¹⁶ These materials display strong magnetization with an applied magnetic field and can retain magnetization when the external magnetic field is removed. This retention of magnetization is called magnetic remanence. Ferromagnetic materials can be considered to be permanent magnets.¹⁷

The electron spins of antiferromagnetic materials form a regular pattern with neighboring spins aligned in opposite directions. The resulting magnetization is lower than that of ferromagnetic compounds due to the interactions between spins.

As in antiferromagnetic materials, the electron spins of ferrimagnetic compounds are antiparallel. In ferrimagnetic compounds, however, the adjacent spins have different magnitudes and their magnetic moments are distributed in different subnetworks. The spontaneous magnetization of ferrimagnetic compounds stems from the unequal magnetization of spins.¹⁸

Most iron oxide material used as contrast agents for MRI are either magnetite or maghemite. Small crystals (4–15 nm diameter) of such materials are fully magnetized and have large magnetic moments. These nanocrystals are smaller than a magnetic domain and do not present magnetic remanence. They are thus called superparamagnetic nanoparticles.

Iron oxide nanoparticles can be classified into different categories according to their hydrodynamic size (see Section 4.4 for size measurement techniques): (1) ultrasmall superparamagnetic iron oxides (USPIO), which are characterized by a hydrodynamic diameter less than 50 nm: subsets of USPIO include very small particles of iron oxide (VSOP) that are between 7 and 9 nm wide and monocrystalline iron oxide nanoparticles (MION) that are between 10 and 30 nm wide; (2) superparamagnetic iron oxides (SPIO), which have a hydrodynamic diameter larger than 50 nm; and (3) micron-sized iron oxide particles (MPIO).

USPIO are single crystals usually embedded in a coating. SPIO, on the other hand, consist of several superparamagnetic cores distributed in a same nanosystem. Table 4.1 gives some examples of iron oxide nanoparticles together with their relaxivity (see Chapter 2.1 for a discussion of relaxivity) and their applications as contrast agents in MRI.

4.1.2 Mechanisms of Relaxation of Iron Oxide Nanoparticles

Relaxation induced by superparamagnetic iron oxide contrast agents cannot be described by a uniquely theoretical approach. The size, the distribution in size, and the morphological properties of the particles are all important parameters that need to be taken into account. In this section, the basic theory valid for USPIOs with diameters larger than 7.5 nm will first be described. The basic assumption of this model is that samples are composed of homogeneous dispersions of identically sized spherical iron oxide

Table 4.1 Examples of iron-oxide-based contrast agents. Data from S. Laurent, L. Vander Elst and R. N. Muller, Superparamagnetic Iron Oxide Nanoparticles for MRI, in *The Chemistry of Contrast Agents in Medical Magnetic Resonance Imaging*, ed. A. Merbach, L. Helm and É. Tóth, Wiley, 2nd edn, 2013, p. 427. © 2013 John Wiley & Sons, Ltd.

Short name/generic name/trade name	Iron oxide core diameter (TEM)/hydrodynamic diameter (PCS) coating	Relaxivity ($s^{-1} mM^{-1}$) (37 °C, 1.5 T)	Ref. (with some examples of MRI applications)
AMI-227	4–6 nm	$r_1 = 19.5$	19–23
Ferumoxtran	20–40 nm	$r_2 = 87.6$	
Sinerem [®] , Combidex [®]	Dextran		
SHU 555C	3–4 nm	$r_1 = 10.7$	20,23–26
Ferucarbotran	30 nm	$r_2 = 38$	
Supravist [®]	(17–46 nm) Carboxydextran		
NC100150	5–7 nm	$r_1 = 20$	20,21
Ferruglose PEG-feron	20 nm	$r_2 = 35$	
Clariscan [®]	Carbohydrate polyethyleneglycol	(0.47 T)	
Ferumoxytol	6.7 ± 0.4 nm	$r_1 = 15$	22,23,27,28
	30 ± 2 nm	$r_2 = 89$	
	Semi-synthetic carbohydrate (polyglucose sorbitol carboxymethyl ether)		
MION-46 I	4.5 ± 1.2 nm	$r_1 = 3.95$	21,29–34
	8–20 nm	$r_2 = 19.6$	
	Dextran		
VSOP-C184	4–5 nm	$r_1 = 14$	20,35–39
	7–9 nm	$r_2 = 33.4$	
	Citrate		
AMI-25	4.8–5.6 nm	$r_1 = 9.95$	19–22,25,29,30
Ferumoxide	80–150 nm	$r_2 = 158$	
Endorem [®] , Feridex [®]	Dextran		
SHU 555A	4.2 nm (3–5 nm)	$r_1 = 9.7$	19,21,24,25
Ferucarbotran	62 nm	$r_2 = 189$	
Resovist [®]	Carboxydextran		

nanocrystals. The relaxation induced by USPIOs with diameter smaller than 7.5 nm will then be discussed. The basic theory of USPIO can be adapted to structures of agglomerated SPIO particles.

Evaluating and understanding the efficiency of magnetic iron oxide nanosystems requires a theory describing the magnetic interactions between nanoparticles and water protons. Nuclear magnetic relaxation dispersion (NMRD) profiles, which describe the field dependence of the longitudinal proton relaxation rate, provide a powerful tool for evaluating the theory (see Chapter 2.3).^{40,41} Moreover, NMRD profiles are important for monitoring the quality of synthesized nanoparticles.⁴²

For superparamagnetic particles, inner-sphere contributions to relaxation are minor and outer-sphere contributions are dominant. The classical outer-sphere model provides longitudinal (R_1) and transverse (R_2) relaxation rates of water protons that diffuse near the unpaired electrons responsible for the magnetization of the particle.⁴³ The magnetic moments of superparamagnetic iron oxide nanoparticles are much larger than the electron moments but, at first approximation, are not qualitatively different. Curie relaxation⁴⁴ plays a central role in the reformulation of the basic theory and highlights the necessity to consider different time-scales. With respect to studying outer-sphere contributions, two parameters have to be examined separately: (1) the effect of water diffusion through the field inhomogeneities created by the time-averaged value of the particle magnetic moment—the dependence of this parameter on the external static field is governed by a Langevin function—and (2) the effect of the fluctuation of the magnetic moment itself.⁴⁵

This model fits well for the high-field part (>1 MHz) of NMRD profiles, but it fails to explain the low-field (<1 MHz) behavior characteristic of USPIO. The NMRD profiles of USPIO show a slight dispersion at low field below 1 MHz. This dispersion completely disappears for SPIO (Figure 4.3).⁴⁶ This behavior with respect to dispersions can be explained by considering the crystal anisotropy energy, which reflects the qualitative difference between superparamagnetic and paramagnetic compounds. Outer-sphere theory assumes an isotropic environment for unpaired electrons, a highly questionable assumption for superparamagnetic nanoparticles because an anisotropic field exists within such particles and forces the magnetic moment of the particle to align along the axes of easy magnetization.

The high magnetization of these compounds has a great influence on the surrounding water relaxation rate. The superparamagnetic relaxation phenomena are described by the Roch–Muller–Gillis model (also called RMG model or SPM model).^{46–48} This theory is based on the classical outer-sphere relaxation theory, but is extended to account for materials with a strong anisotropy. The relaxation induced by superparamagnetic nanoparticles is due to the coupling between the magnetic moments of water protons and the electron magnetic moments of particles. This modulation is caused by Néel relaxation (flipping of the magnetization vectors of particles from one easy axis to another), the diffusion of water protons, and the strength of the external magnetic field.

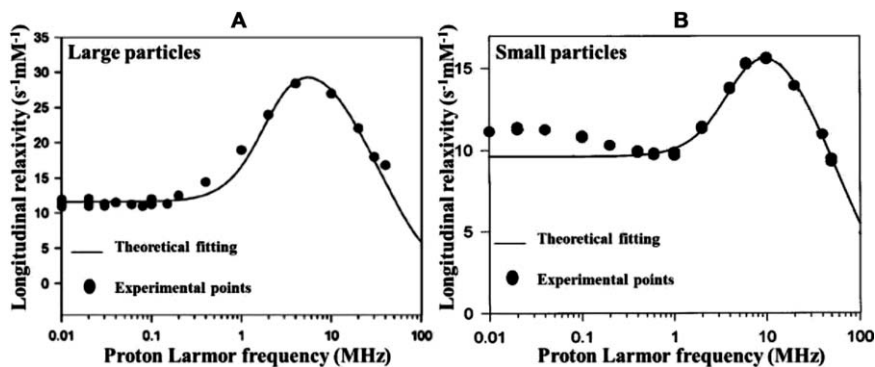


Figure 4.3 Nuclear magnetic relaxation dispersion profiles of suspensions of (A) large particles (Endorem[®]; $r = 15$ nm) and (B) small particles ($r = 5$ nm) as functions of proton Larmor frequency. The lines represent theoretical fits developed for large magnetic crystals.^{1,3} Adapted with permission from S. Laurent, D. Forge, M. Port, A. Roch, C. Robic, L. Vander Elst and R. N. Muller, *Chem. Rev.*, 2008, **108**, 2064. Copyright (2008) American Chemical Society.

4.1.2.1 Theory for Large Crystals and Particles with High Anisotropy

The anisotropy barrier is high for large crystals with a radius >7.5 nm. This high barrier induces locking of the magnetic moments of superparamagnetic materials on one anisotropy axis when high magnetic fields are applied. Depending on the strength of external magnetic field, three limiting cases can be described at low, high, and intermediate fields:

- (1) Low magnetic fields. At low magnetic fields magnetic moments can be easily moved from one anisotropy direction to another one, thereby causing drastic magnetic fluctuations on water diffusion in the vicinity of magnetic particles. In this case, the dipolar interactions between water protons and magnetic cores are modulated by the translational correlation time of the water molecules (τ_D) and the Néel relaxation time (τ_N). Both modulations define the global correlation time (τ_{CI}) with $\tau_D = r^2/D$, where r is the crystal radius and D is the diffusion constant [eqn (4.1)].

$$\frac{1}{\tau_{CI}} = \frac{1}{\tau_N} + \frac{1}{\tau_D} \quad (4.1)$$

The proton longitudinal (R_1) and the transversal (R_2) relaxation rates can in turn be expressed by the Freed spectral density [eqn (4.2)–(4.5)], where γ is the proton gyromagnetic ratio, μ is the electron magnetic moment, N_A is Avogadro's number, C corresponds to the molar

concentration of superparamagnetic particle, r is the crystal radius, and ω_I is the proton angular frequency.⁴⁹

$$R_1 = \frac{1}{T_1} = \frac{32\pi}{405000} \gamma^2 \mu^2 \left(\frac{N_A C}{r^3} \right) [10J_F(\omega_I, \tau_D, \tau_N)] \quad (4.2)$$

$$R_2 = \frac{1}{T_2} = \frac{32\pi}{405000} \gamma^2 \mu^2 \left(\frac{N_A C}{r^3} \right) [8J_F(\omega_I, \tau_D, \tau_N) + 2J_F(0, \tau_D, \tau_N)] \quad (4.3)$$

with

$$J_F(\omega_I, \tau_D, \tau_N) = R_e \left[\frac{1 + \frac{1}{4}\Omega^2}{1 + \Omega^2 + \frac{4}{9}\Omega + \frac{1}{9}\Omega^3} \right] \quad (4.4)$$

and

$$\Omega = i\omega_I \tau_D + \frac{\tau_D}{\tau_N} \quad (4.5)$$

- (2) High magnetic fields. At high magnetic fields, the magnetization vector aligns along one of the easy axes. In this case, the Néel relaxation time is relatively long due to the high anisotropy of the particles. Therefore, the modulation of their relaxation results solely from the diffusion of water protons. This modulation is described by the Ayant spectral density.⁵⁰ The relaxation rates can then be described using eqn (4.6)–(4.7).

$$R_1 = \frac{1}{T_1} = \frac{32\pi}{405000} \gamma^2 \mu^2 \left(\frac{N_A C}{r^3} \right) [9L^2(\alpha)J_A(\sqrt{2\omega_I \tau_D})] \quad (4.6)$$

$$R_2 = \frac{1}{T_2} = \frac{32\pi}{405000} \gamma^2 \mu^2 \left(\frac{N_A C}{r^3} \right) \left[\frac{9}{2}J_A(\sqrt{2\omega_I \tau_D}) + 6J_A(0) \right] \quad (4.7)$$

with

$$J_A(\mu) = \frac{1 + \frac{5\mu}{8} + \frac{\mu^2}{8}}{1 + \mu + \frac{\mu^2}{2} + \frac{\mu^3}{6} + \frac{4\mu^4}{81} + \frac{\mu^5}{81} + \frac{\mu^6}{648}} \quad (4.8)$$

- (3) Intermediate magnetic fields. The water relaxation induced by superparamagnetic particles at intermediate fields is modulated both by the low and the high field contributions. A linear combination of the equations with a Langevin function $[L(\alpha)]$ must be used to take into account the fact that the magnetization is divided into two parts: the first part is locked with the external magnetic field, and the second part is influenced by Néel relaxation [eqn (4.9) and (4.10)].

$$R_1 = \frac{1}{T_1} = \frac{32\pi}{405000} \gamma^2 \mu^2 \left(\frac{N_A C}{r^3} \right) \left\{ \left(\frac{L(\alpha)}{\alpha} \right) 21 J_F(\omega_I, \tau_D, \tau_N) \right. \\ \left. + 9 \left[1 - L^2(\alpha) - 2 \left(\frac{L(\alpha)}{\alpha} \right) \right] J_F(\omega_I, \tau_D, \tau_N) + 9 L^2(\alpha) J_A(\sqrt{2\omega_I \tau_D}) \right\} \quad (4.9)$$

$$R_2 = \frac{1}{T_2} = \frac{32\pi}{405000} \gamma^2 \mu^2 \left(\frac{N_A C}{r^3} \right) \left\{ \left(\frac{L(\alpha)}{\alpha} \right) 19.5 J_F(\omega_I, \tau_D, \tau_N) \right. \\ \left. + \left[1 - L^2(\alpha) - 2 \left(\frac{L(\alpha)}{\alpha} \right) \right] \frac{9}{2} [J_F(\omega_I, \tau_D, \tau_N) + 6 J_F(0, \tau_D, \tau_N)] \right. \\ \left. + L^2(\alpha) \left[\frac{9}{2} J_A(\sqrt{2\omega_I \tau_D}) + 6 J_A(0) \right] \right\} \quad (4.10)$$

In conclusion, for large crystals, relaxation is modulated differently depending on the strength of the external magnetic field. This theory predicts the evolution of water proton relaxation rate with magnetic field, as shown in Figure 4.4.

The RMG model enables a nearly perfect fitting of experimental data for large crystals (Figure 4.3A). However, this model does not fit well the dispersion profiles of particles with low anisotropy energies ($r < 7.5$ nm).

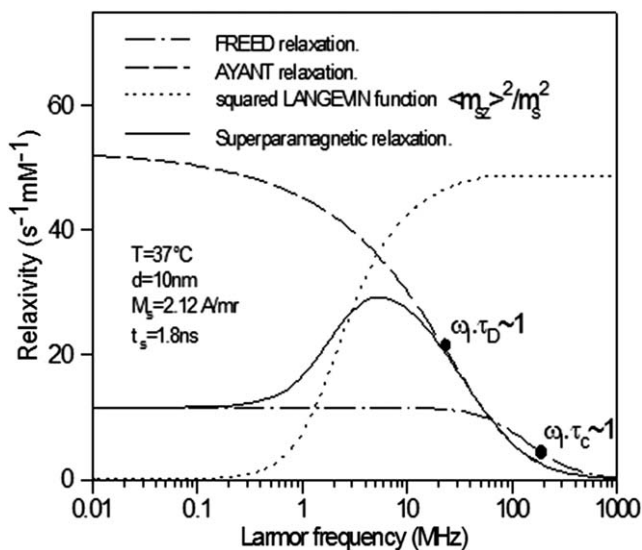


Figure 4.4 Contributions to proton relaxation in the simplified model for crystals of large anisotropy.¹³ Adapted with permission from S. Laurent, D. Forge, M. Port, A. Roch, C. Robic, L. Vander Elst and R. N. Muller, *Chem. Rev.*, 2008, **108**, 2064. Copyright (2008) American Chemical Society.

In these cases, experimental NMRD profiles have dispersions at low frequencies that do not agree with theoretical predictions. An example is shown in Figure 4.3B. For particles with relatively low anisotropies, an adaption of the RMG model thus had to be developed.

4.1.2.2 Theory for Small Crystals and Particles with Relatively Low Anisotropy

Small nanoparticles (particle radius <7.5 nm) have small anisotropic energy, and their magnetic moments can fluctuate between easy magnetization axes. A different model that incorporates the anisotropy energy as a quantitative parameter is thus needed to explain the superparamagnetic relaxation of small magnetic cores. Roch and co-workers developed an alternative method to include this parameter.^{13,46} This model reproduces the gradual vanishing of the low field dispersion through a linear combination of the rate for infinite and zero anisotropy energy, as described by eqn (4.11) and (4.12), where P is a weighting factor of the linear combination. The modified model enables a good interpretation of the relaxation for small particles (Figure 4.3B).

$$R_1 = \frac{1}{T_1} = \frac{32\pi}{405000} \gamma^2 \mu^2 \left(\frac{N_A C}{r^3} \right) \left\{ \left(\frac{L(\alpha)}{\alpha} \right) 21 P J_F(\omega_I, \tau_D, \tau_N) + 21(1-P) J_F(\omega_I, \tau_D, \tau_N) \right. \\ \left. + 9 \left[1 - L^2(\alpha) - 2 \left(\frac{L(\alpha)}{\alpha} \right) \right] J_F(\omega_I, \tau_D, \tau_N) + 9 L^2(\alpha) J_A(\sqrt{2\omega_I \tau_D}) \right\} \quad (4.11)$$

$$R_1 = \frac{1}{T_2} = \frac{32\pi}{405000} \gamma^2 \mu^2 \left(\frac{N_A C}{r^3} \right) \left\{ \left(\frac{L(\alpha)}{\alpha} \right) 19.5 J_F(\omega_I, \tau_D, \tau_N) \right. \\ \left. + \left[1 - L^2(\alpha) - 2 \left(\frac{L(\alpha)}{\alpha} \right) \right] \frac{9}{2} [J_F(\omega_I, \tau_D, \tau_N) \right. \\ \left. + 6 J_F(0, \tau_D, \tau_N) + L^2(\alpha) J_A \left[\frac{9}{2} J_A(\sqrt{2\omega_I \tau_D}) + 6 J_A(0) \right] \right\} \quad (4.12)$$

4.1.2.3 Nuclear Magnetic Relaxation Dispersion Profiles

As mentioned previously, NMRD profiles are an essential tool to evaluate the relaxometric properties of MRI contrast agents as a function of magnetic field (Chapter 2.3). The method enables rapid analysis of the properties of new contrast agents and can be exploited to monitor the reproducibility of nanoparticle synthetic protocols. The fitting of NMRD profiles with suitable theoretical models provides information about the magnetic crystals (Figure 4.5), such as their average radius (r), their saturation magnetization (M_s), their anisotropic energy (E_a) and their Néel relaxation times (τ_N).

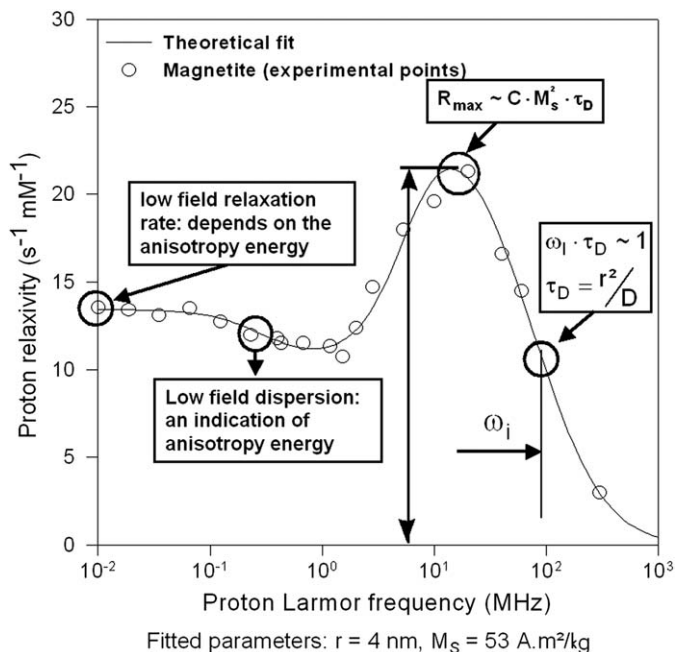


Figure 4.5 NMRD profile of magnetite particles in colloidal solution.¹³ Adapted with permission from S. Laurent, D. Forge, M. Port, A. Roch, C. Robic, L. Vander Elst and R. N. Muller, *Chem. Rev.*, 2008, **108**, 2064. Copyright (2008) American Chemical Society.

The NMRD profile is a function of several parameters.

- (1) Average radius (r): At high magnetic fields, the Ayant theory determines that the relaxation rates depend only on the diffusion correlation time (τ_D). The inflection point corresponds to the condition of $\omega_l \tau_D \gg 1$, where ω_l is the proton Larmor frequency. The diffusion correlation time is determined by the ratio of the square of crystal radius divided by diffusion constant ($\tau_D = r^2/D$), enabling estimations of average radii. An increase of crystal size modifies the position of the inflection point, moving it toward lower frequencies;
- (2) Saturation magnetization (M_s): At high magnetic fields, saturation magnetization is reached and can be estimated from the maximum relaxation rate using the relationship of $M_s \approx (R_{\max}/c\tau_D)^{1/2}$, where c and R_{\max} correspond to a constant and the maximum relaxation rate, respectively;
- (3) Crystal anisotropy energy (E_a): The dispersion observed at low magnetic fields provides information regarding the presence of crystals with low anisotropic energy. For materials with high anisotropic energy, no pitch dispersion is observed. The dispersion at low

- frequencies gives qualitative information about the magnitude of anisotropic energy of magnetic compounds in solution; and
- (4) Néel relaxation time (τ_N): The Néel relaxation time obtained from the theoretical fitting is an approximate value. It provides qualitative information in addition to the crystal size and the specific magnetization.

Magnetic and relaxometric measurements provide a thorough description of the physicochemical properties of iron oxide nanoparticles. It is important to note that the RMG model is based on the assumption that nanoparticle size is uniform and, consequently, the theoretical parameters extracted from the theoretical fitting are average values. However, in practice, size heterogeneity of magnetic crystals is often observed. If the size distribution is large or if the nanoparticle suspension contains agglomerated nanoparticles, the theoretical parameters calculated might not accurately represent the effective characteristics of the nanoparticle.

4.1.3 Acknowledgements

This work was performed with the financial support of the Fonds National pour la Recherche Scientifique (F.R.S.-FNRS), the FEDER, the Walloon Region, the COST Action TD1402, the Centre for Microscopy and Molecular Imaging (CMMI) supported by the European Regional Development Fund of the Walloon region, the ARC and UIAP programs.

4.2 Synthesis of Iron Oxide Nanoparticles

DIMITRI STANICKI, LUCE VANDER ELST, ROBERT N. MULLER AND SOPHIE LAURENT*

4.2.1 Mechanism of Formation

Because the physicochemical properties of superparamagnetic nanosystems depend on the homogeneity of samples, characterization of uniformity in size and composition is important (Section 4.4). Although absolutely monodisperse systems are rare outside of biology, systems are often considered to be monodisperse when the standard deviation in particle size is less than 5%.

The first model of nanoparticle formation was presented by LaMer in the 1950s (*i.e.* the LaMer and Dinegar model).⁵¹ This model describes the different mechanisms behind the synthetic process. This theory is based on nucleation-growth mechanisms and considers nucleation as the limiting step in the process. Typically, the diagrams presenting the evolution of the monomer concentration *versus* time (*i.e.* the LaMer diagram) can be divided into three stages as shown in Figure 4.6.⁵²

- In stage 1, the concentration of monomer increases until the nucleation concentration (C_{MIN}) is reached. At this minimal concentration, the system becomes heterogeneous, and solute molecules combine to produce small nuclei due to the collision of solute molecules in solution. Such nuclei are continuously being formed and dissolved.

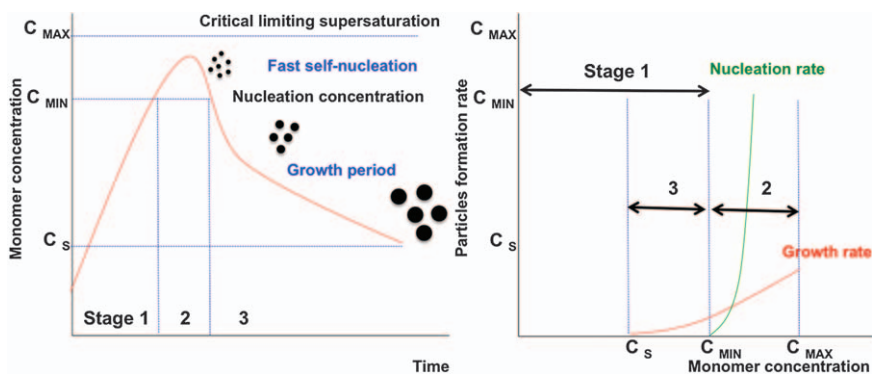


Figure 4.6 Nucleation and growth model according to LaMer's theory (left).⁵⁴ Comparison of nucleation and growth rates *versus* monomer concentration (right). Left: reprinted with permission from C. Hui, C. Shen, T. Yang, L. Bao, J. Tian, H. Ding, C. Li and H.J. Gao, *J. Phys. Chem. C*, 2008, **112**, 11336. Copyright (1950) American Chemical Society. Right: comparison of nucleation and growth rates *vs* monomer concentration (right), adapted from ref. 55.

The stability of the nuclei depends on the free-energy barrier (ΔG). If ΔG is high compared to the thermal energy (kT), the chance of forming such nuclei is negligible and no particles will form. However, if the free-energy barrier is low enough, the rate of nucleation tends to be infinite.

- During stage 2, nuclei formation partially reduces supersaturation, leading to a decrease of nucleation rate. When the critical limiting supersaturation (C_{MAX}) falls to C_{MIN} , particle growth replaces particle nucleation.
- If the system remains supersaturated, the growth of stable nuclei (stage 3) into discrete particles proceeds by diffusion of species from the solution to the nuclei.

This theory suggests that the synthesis of monodisperse nanoparticles requires a net separation of nucleation and growth.

4.2.2 Methods for the Preparation of Magnetic Nanoparticles

Due to their potential for use in a wide range of applications, numerous innovative protocols have been reported for the synthesis of iron oxide nanoparticles with control over size, shape, and composition. The many methods reported for the synthesis of nano-scaled magnetite include hydrothermal synthesis, sol-gel methods, micro-emulsion processes, and electrochemical or aerosol methods (Table 4.2). The most common ones are the coprecipitation method and the thermal decomposition of organo-metallic precursors.

4.2.2.1 Coprecipitation Method

Coprecipitation is the simplest and most efficient procedure to prepare iron oxide nanoparticles at the gram scale. In this method, nanoparticles are produced by mixing 2/1 stoichiometric mixtures of ferric and ferrous salts in alkaline medium [eqn (4.13)].



A complete precipitation of Fe_3O_4 occurs for pH values between 9 and 14 under a nonoxidizing, oxygen-free environment. The size and shape of the particles can be adjusted by the experimental conditions, including stoichiometry, pH, ionic strength, and temperature.^{53,54} In aqueous syntheses, coprecipitation is widely employed to obtain different ferrites (MFe_2O_4 , $M = Fe, Mn, Co, Mg, Zn, \text{ and } Ni$),⁵⁵ as shown in eqn (4.13). Although this procedure is fast, relatively easy to implement, and economical, it provides poorly crystalline particles that are characterized by a broad size distribution and that, consequently, requires size-sorting procedures to reduce polydispersity.

Better control over the properties of particles can be obtained by incorporating surfactants into the syntheses of particles. Small ferrites,

Table 4.2 Principal methods for the synthesis of iron oxide nanoparticles.

Synthetic method	Reaction time	Solvent	Surface capping molecule	Size distribution	Shape control	Yield
Coprecipitation	Minutes	Water	No	Broad	Not good	Medium
Thermal decomposition	Minutes–hours	High boiling apolar solvents	Yes	Very narrow	Very good	Medium
Polyol method	Hours	(Poly)glycol	Yes	Narrow–broad	Good	Medium
Microemulsion	Hours	Organic	Yes	Narrow	Good	Low
Laser pyrolysis	Seconds	Gas	No	Narrow	Good	High

including Fe_3O_4 , CoFe_2O_4 , and MnFe_2O_4 , were obtained using aminoalcohols such as isopropanolamine or diisopropanolamine⁵⁵ as the alkaline source. Such alkaline molecules act as complexing agents that control particle size during synthesis. These molecules also change the spin rearrangement at the surface (thinner magnetic “dead” layers), conferring better magnetic properties compared to synthesis in the absence of surfactants. Other surfactants, such as CTAB, PVP, or sodium cholate, were also shown to greatly influence mean size and size distribution.⁵⁶ Some solvents can also play the role of surfactants. For example, diethyleneglycol (DEG) can efficiently control the size and improve crystallinity of nanoparticles because of its high boiling point.^{57,58}

Stable colloids can be obtained by treating samples with acidic or alkaline medium, a process called peptisation. However, biomedical applications require stable particles in physiological conditions. The stability of magnetite colloids can be improved by performing the reaction in the presence of polymers such as dextran or polyacrylic acid.⁵⁴ Such processes often lead to the formation of particle clusters embedded within a polymeric matrix, which can be undesirable for certain applications.

4.2.2.2 Thermal Decomposition of Organometallic Precursors

USPIO with high monodispersity in both size and morphology can be synthesized by thermal decomposition of complexes of iron. Because these syntheses are performed at high temperatures ($<200\text{ }^\circ\text{C}$), nanoparticles prepared *via* this method exhibit high crystallinity and high saturation moments. Generally, the reaction is performed in the presence of surfactants, typically long-chain hydrophobic hydrocarbons, which guarantee near control over growth and good dispersibility of particles in nonpolar solvents, such as petroleum ether, dichloromethane, or tetrahydrofuran.

According to LaMer diagrams, the synthesis of monodisperse colloids through homogeneous nucleation requires a temporal separation of nucleation and growth steps. Initially, the concentration of monomers, which are the smallest subunits of the crystal, increases either by external addition or by *in situ* generation. In the case of thermal decomposition, the poly iron oxo clusters obtained from thermal degradation of organometallic complexes (intermediate species between the iron complexes and the final nanosized products) have been demonstrated to act as the smallest building blocks or monomers (Figure 4.7).⁵⁹

Experimentally, such separation between nucleation and growth steps can be achieved by the direct and fast injection of a solution of reagent into a hot solvent. In this process, referred to as a “hot injection”, the concentration of the precursor is rapidly raised above C_{MIN} , leading to instantaneous nucleation. Because the injected solution is at ambient temperature, the nucleation step is quickly quenched by the rapid cooling of the reaction mixture. The number of germs formed in solution will depend on the ease of formation of the monomers, which depends on the thermal stability of the

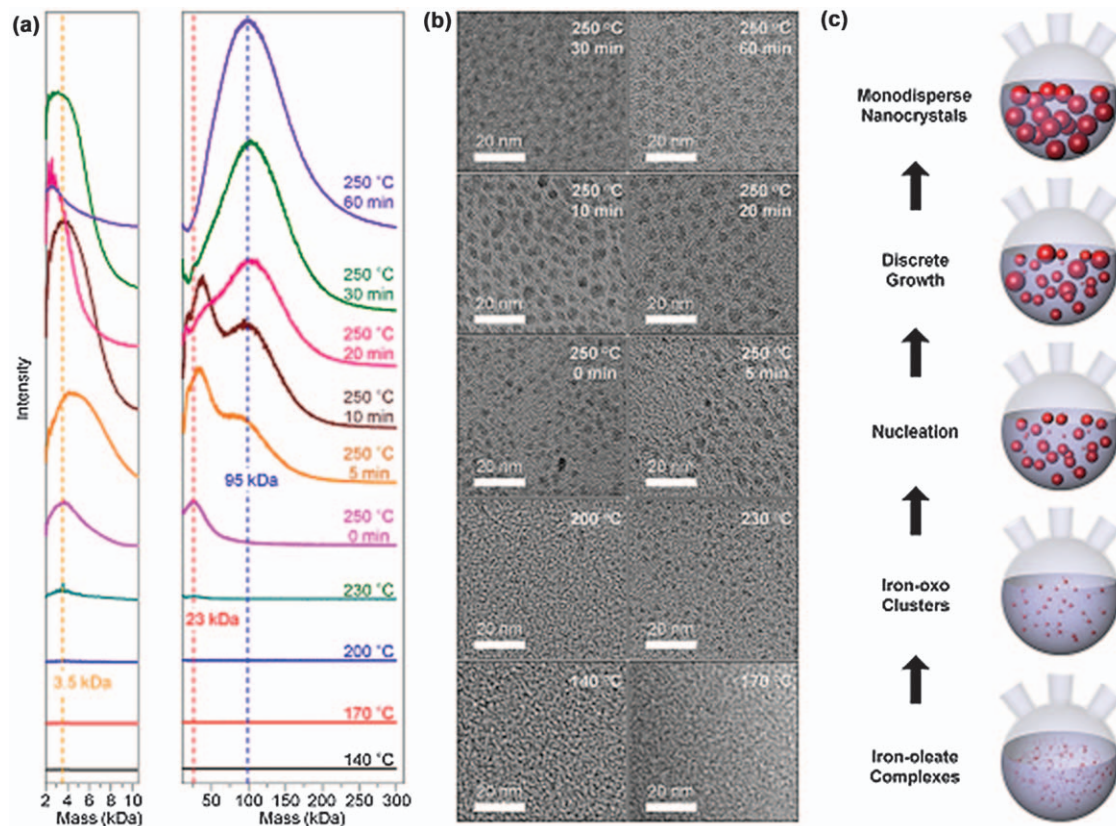


Figure 4.7 Mass spectra of sample aliquots drawn from a reaction during heating. For clarity, the spectra representing <10.5 kDa (left) and >11 kDa (right) have been plotted using different scales. (b) TEM images of the nanoclusters in the sample aliquots. (c) Schemes describing the formation mechanism proposed on the basis of the *ex situ* mass spectrometric measurements.⁵⁹ Adapted with permission from B. H. Kim, K. Shin, S. G. Kwon, Y. Jang, H.-S. Lee, H. Lee, S. W. Jun, J. Lee, S. Y. Han, Y.-H. Yim, D. H. Kim and T. Hyeon, *J. Am. Chem. Soc.*, 2013, **135**, 2407. Copyright 2013 American Chemical Society.

initial complexes in solution, the nature of the surfactant, and the influence of the solvent on stability.

In the thermal decomposition synthesis of nanoparticles, two strategies are used to vary the size of nanoparticles. The first one is referred to as “seed-mediated growth” and involves the addition of an iron precursor to pre-existing nuclei. In the second strategy, size is controlled by varying experimental parameters such as reaction time, temperature, ligand-to-precursor ratio, and solvent.^{60,61} As previously mentioned, the interactions among precursors, surfactants, and solvents influence the decomposition rate of iron(III)-containing precursors, consequently influencing the kinetics of the formation of monomers and nuclei.

Such synthetic processes can also control the shape of nanoparticles.⁶² For example, prismatic iron oxide nanostructures formed by the self-assembly of iron oxide nanoparticles were prepared using a low thermal decomposition of $[\text{Fe}(\text{CON}_2\text{H}_4)_6](\text{NO}_3)_3$.⁶³ The TG-DTA, FT-IR spectroscopic, and elemental analysis of the reaction indicated that *in situ* formation of cyanuric acid occurred during the decomposition of the iron-urea complexes, and that the urea also acted as the ligand for the formation of iron oxide nanoparticles. The synthesis of cubic particles has been thoroughly documented. Interestingly, the presence of halogen ions can favor the formation of cubic nanostructures.⁶⁴ In this case, when chloride or bromide ions are lacking, only spherical nanocrystals are observed. The halogens play a role in stabilizing the {100} facets of magnetic iron oxides but not in regulating the kinetics of thermolysis. Interestingly, chloride ions appeared as key inducers for the preparation of octapod nanostructures during the decomposition of iron oleate in octadecene. A proposed mechanism of forming octapod iron oxide nanoparticles is that the chloride ions are selectively bound to iron ions on the high-index facets (probably [311]) of iron oxide during the particle growth. Other examples of hybrid systems including $\text{Fe}_3\text{O}_4/\text{Au}$ (core-shell or dumbbell configuration), $\text{Fe}_3\text{O}_4/\text{GdO}$, and wüstite/magnetite (core-shell configuration; Figure 4.8) have also been reported.

Although high-temperature syntheses can produce highly crystalline and well-defined magnetic nanoparticles, it is important to note that some limitations are inherent to the technique: (1) With rare exceptions,⁶⁵ reported syntheses were performed at the hundreds-of-milligrams scale. The high temperatures and tedious procedures are likely to limit larger scale production. (2) Relatively expensive (and sometimes toxic) precursors are needed. (3) As-synthesized particles cannot be directly transferred to water because of the hydrophobic layer surrounding the nanoparticles (most often oleic acid). For such transfers to be possible, an additional step is required, consisting of either the addition of amphiphilic ligands, such as polymers, alkylammonium salts, or lipids,⁶⁶ or of exchange of the hydrophobic molecules by hydrophilic ones (Figure 4.9).⁶⁷ These procedures often employ small charged molecules (such as citric acid or tetramethyl ammonium hydroxide) or sophisticated architectures consisting of a strong anchoring

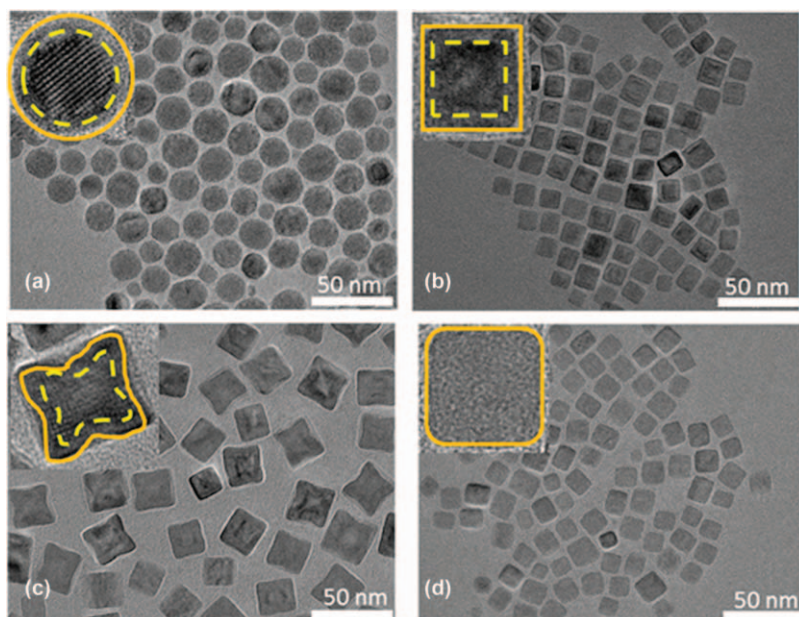


Figure 4.8 Transmission electron micrographs of nanoparticles: (a) NS19, (b) NC16, (c) NO24, and (d) oxNC16. Dashed lines indicate the Fe_{1-x}O core, and solid lines indicate the Fe_3-xO_4 shell. Insets show HRTEM images. Adapted with permission from A. Walter, C. Billotey, A. Garofalo, C. Ulhaq-Bouillet, J. Taleb, S. Laurent, L. Vander Elst, R. N. Muller, L. Lartigue, F. Gazeau, D. Felder-Flesch and S. Bégin-Colin, *Chem. Mater.*, 2014, 26, 5252. Copyright (2014) American Chemical Society.

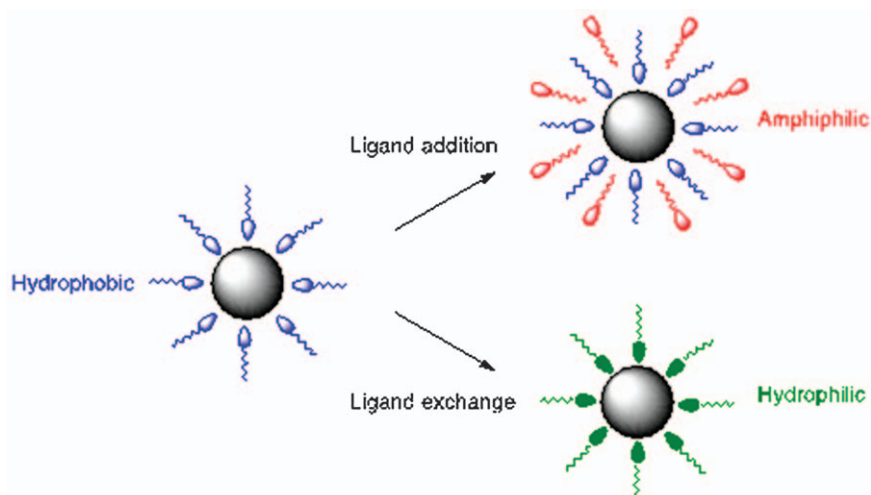


Figure 4.9 Schematic illustration of water-transfer procedure for USPIO obtained by thermal decomposition.

functional group (such as dopamine, carboxylic acid, phosphonate, or alkoxysilane) conjugated to a polymeric arm (often PEG).

4.2.3 Acknowledgements

This work was performed with the financial support of the Fonds National pour la Recherche Scientifique (F.R.S.-FNRS), the FEDER, the Walloon Region, the COST Action TD1402, the Centre for Microscopy and Molecular Imaging (CMMI) supported by the European Regional Development Fund of the Walloon region, the ARC and UIAP programs.

4.3 Coatings for Iron Oxide Nanoparticles

DELPHINE FELDER-FLESCHE, DAMIEN MERTZ, AUDREY PARAT AND SYLVIE BEGIN-COLIN*

One of the challenging components in the design of iron oxide nanoparticles for biomedical application is the coatings of nanoparticles. Biocompatible coatings at the surface of nanoparticles can perform different functions, such as enabling the conjugation of dyes for multimodal imaging, of targeting ligands for specific tissues or cells, or of therapeutic agents. The coatings of nanoparticles must also prevent agglomeration in physiological environments and enable desired biodistributions and elimination. The nature and steric hindrance of coatings can affect the fate of nanoparticles in biological systems, such as cellular uptake and accumulation, circulation, and clearance.⁶⁸ In the blood pool, nanoparticles are subjected to opsonization, the nonspecific fouling of plasma protein on the surface of nanoparticles and subsequent uptake by the reticuloendothelial system. Organic coatings and the anchoring of these coatings to the surface of nanoparticles have to be tailored to prevent opsonization of nanoparticles, avoid nonspecific interactions with components in the complex matrix, increase their ability to evade the reticuloendothelial system, and promote desired biodistribution and elimination. Ideally, the final average hydrodynamic sizes of functionalized nanoparticles should be in the range of 10–100 nm to have long blood-circulation times. The functionalization step, which involves anchoring the coating to the surface of nanoparticles, must be performed in such a way that the properties of both the nanoparticles and the coating are preserved while controlling the final nanoparticles hydrodynamic size. Certain coatings can also effectively prevent the dissolution and release of core materials that might cause toxicity.⁶⁹

The nature of bioactive coatings and coating strategies are critical aspects of biomedical applications involving nanoparticles. This section describes standard coatings and anchoring agents used with iron oxide nanoparticles and the effect of the coating on the magnetic properties relevant to the use of the nanoparticles as MRI contrast agents.

4.3.1 Standard Coatings for Iron Oxide Nanoparticles

Most coatings used for superparamagnetic iron oxide nanoparticles involve natural or synthetic polymers. Other molecules have also been developed for this purpose, including nonpolymeric coatings, dendrimers, dendrons, and silanes. Research into coatings has the potential to create advanced, biocompatible contrast agents for biomedical applications, including for *in vivo* diagnostic imaging. For instance, dendrimer-based organic-inorganic hybrids have the potential to target specific types of cells or organs, for either cell tracking or *in situ* drug delivery applications.

In addition to organic coatings, silica-based coatings have also been reported. Coatings of nonporous silica shells around iron oxide or other inorganic nanoparticles were initially developed with the aim of forming protective shells around the nanoparticles.⁷⁰ The possibility to coat or encapsulate plasmonic, magnetic, or luminescent nanoparticles with mesoporous silica shells^{71–73} generated interest in a range of applications related to catalysis, energy, and drug delivery. Mesoporous silica coatings of magnetic nanoparticles are attractive because of the synergy between the potential of porous silica for applications such as drug delivery and those of the magnetic core for application such as magnetic guidance, contrast enhancement in MRI, and magnetic hyperthermia. The ordered arrangement of pores, high surface area, and good loading capacity of the coating render mesoporous silica an interesting platform for drug delivery. A silica coating is particularly advantageous because it promotes chemical stability of the inorganic core, high dispersibility in aqueous solutions, and high biocompatibility of the resulting core–shell nanocomposites. Moreover, the silica surface can be modified by grafting alkoxysilanes that contain versatile chemical functionalization.

4.3.1.1 Nonpolymeric Surface: Adenosine Triphosphate

Adenosine triphosphate (ATP) is a promising candidate for surface engineering of iron oxide nanoparticles because the phosphate groups have a relatively strong affinity for the iron oxide surface and because ATP bears other functions enabling coupling to bioactive molecules. ATP is endogenous to living systems and consists of a purine base, a pentose sugar, and a triphosphate ester. Moreover, ATP has excellent biokinetics compared with polymeric materials.

Iron oxide nanoparticles coated with ATP have been modified with gluconic acid (Figure 4.10).⁷⁴ Such hybrids display reduced phagocytic uptake

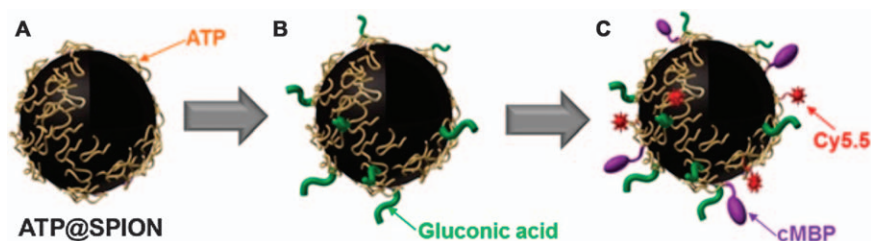


Figure 4.10 (A) Schematic diagram of the synthesis of (A) ATP-coated iron oxide nanoparticles, (B) gluconic-acid-functionalized ATP-coated iron oxide nanoparticles, and (C) the same particles labeled with Cy5.5 and cMet binding peptides.

Adapted with permission from C.-M. Lee, S.-J. Cheong, E.-M. Kim, S. T. Lim, Y. Y. Jeong, M.-H. Sohn and H.-J. Jeong, *J. Nucl. Med.*, 2013, 54, 1974. © by the Society of Nuclear Medicine and Molecular Imaging, Inc.

biodistribution and provide efficient active targeting properties for *in vivo* applications. For instance, iron oxide nanoparticles coated with ATP conjugated with gluconic and cMet-binding peptide enable multimodal imaging of U87MG tumors implanted in mice.

4.3.1.2 Dendrimers

Dendrimer-stabilized nanoparticles refer to nanostructures in which the nanoparticles are coated with multiple dendrimers. Iron oxide nanoparticles can be synthesized and simultaneously stabilized in the presence of dendrimers. For instance, stabilized ferromagnetic iron oxide nanoparticles were synthesized in the presence of carboxylated G4.5 polyamidoamine (PAMAM) dendrimers.⁷⁵ The carboxylated dendrimers provided a nucleation surface and passivating layer for the metal oxide surface. PAMAM dendrimers with other functionalities like amines or alcohols cannot stabilize iron oxide nanoparticles, thereby highlighting the role of electrostatic interactions in nanoparticle stabilization. Mammalian cells were successfully labeled with such magnetodendrimers through nonspecific membrane adsorption and subsequent intracellular localization in endosomes.⁷⁶ Magnetodendrimer incubated at doses as low as 1 mg iron mL⁻¹ enabled contrast enhancement in MRI without compromising cell viability or differentiation. Labeled neural stem cells could be detected *in vivo* by MRI 6 weeks after transplantation.

Dendrimer-assembled iron oxide nanoparticles are formed by dendrimers and pre-synthesized nanoparticles as a result of driving forces such as electrostatic interactions,⁷⁷ covalent bonding,⁷⁸ or the combination of different weak forces. Iron oxide nanoparticles have been assembled with multilayers of poly(glutamic acid) (PGA) and poly(L-lysine) (PLL), followed by addition of G5NH₂-FI (fluorescein isothiocyanate)-folic acid (FA) dendrimers.⁷⁹ The interlayers were then crosslinked using 1-ethyl-3-[3-dimethylaminopropyl]carbodiimide hydrochloride as a coupling agent, leading to covalent linkage between the hydroxy groups of iron oxide, the carboxy groups of PGA, the amino groups of PLL, and the dendrimers. The remaining amino groups of the dendrimers were acetylated to neutralize the surface charge. *In vivo* MRI showed that the signal intensity of tumor-bearing mice injected with targeted nanoparticles gradually decreased over 24 hours, whereas the signal intensity of tumor-bearing mice treated with nontargeted nanoparticles did not decrease significantly with time post-injection. This approach to the functionalization of magnetic nanoparticles can be modified for other small targeting molecules such as peptides or growth factors, thereby providing a general approach for *in vivo* detection of various biological systems by MRI.

Dendronized nanoparticles can be prepared *via* a grafting strategy. In this approach, the dendron is first synthesized in a step-by-step manner, similar to the conventional divergent approach used to synthesize dendrimers.^{80,81} Dendronized nanoparticles synthesized in this manner are able to transfect

antisense surviving oligodeoxynucleotides into human tumor cell lines, such as human breast and liver cancers.⁸² Composites of antisense-surviving-oligodeoxynucleotides, dendrimers, and iron oxide can penetrate tumor cells in 15 min, causing marked downregulation of the surviving gene as well as inhibition of protein synthesis and cell-growth in both dose- and time-dependent manners. These results showed that PAMAM-modified magnetic nanoparticles might represent a good system for gene delivery.

Dendronized iron oxide nanoparticles can also be prepared by direct grafting. In this approach, the functionalized nanoparticles are obtained through direct grafting of small hydrophilic dendrons on the iron oxide nanoparticle *via* phosphonate anchors. Such nanoparticles were demonstrated to be efficient contrast agents for MRI.^{83–85} Such nanoparticles have good colloidal properties and higher relaxivity than commercially available, polymer-functionalized nanoparticles. The choice of phosphonic acid as an anchor was justified by previous studies that evidenced a higher grafting rate and a stronger binding than those obtained with carboxylate anchors.^{86,87} Small-sized dendrons are preferable because they are discrete and monodisperse entities with size, hydrophilicity, molecular weight, and biocompatibility that can be tuned as a function of their generation.^{88–91}

4.3.1.3 Polymers

Biodegradable polymers used for functionalizing nanoparticles include polyorthoesters, polyanhydrides, polyamides, polyphosphazenes, and polyphosphoesters.⁹² Copolymers can also be used to synthesize particles with desired physical properties. Examples include copolymers of the above-mentioned polymers with hydrophilic polymers such as poly(ethylene glycol) (PEG), poly(ethylene oxide) (PEO), or poly(propylene oxide) (PPO). Polymer properties such as molecular weight, charge, branching, and stability have a great impact on the particle functions, including the mode of degradation, encapsulation efficiency, release rates, avoidance of protein binding, and cellular internalization (Tables 4.3 and 4.4).⁹³

Table 4.3 Advantages of different polymers for nanoparticle coating to enhance colloidal stability.

Synthetic polymers	Poly(ethylene glycol) (PEG) Improves biocompatibility, blood circulation time, and internalization efficiency
	Poly(vinylpyrrolidone) (PVP) Enhances blood circulation time and stabilizes colloidal suspensions
	Poly(vinyl alcohol) (PVA) Prevents coagulation of particles
	Poly(acrylic acid) (PAA) Increases stability and biocompatibility and helps in bioadhesion
	Poly(<i>N</i>-isopropylacryl amide) Enables thermosensitive drug delivery
Natural polymers	Dextran Enhances blood circulation lifetimes and stabilizes colloidal suspensions
	Gelatin Used as a gelling agent and as a hydrophilic and biocompatible emulsifier
	Chitosan Used as a nonviral gene delivery system that is biocompatible and hydrophilic

Table 4.4 Various organic shells, dendrimers, polymers, and combinations of polymer coatings for iron oxide nanoparticles (TEM = transmission electron microscopy; DLS = dynamic light scattering; HR = high resolution; XRD = X-ray diffraction; SEM = scanning electron microscopy; PCS = photon correlation spectroscopy; SMPS = scanning mobility particle sizer).

Coating	Diameter (nm) [technique used]	Application
Dextran	6.5 ± 1.2 [TEM], 39 ± 8 [DLS] 50 [DLS], 50–100 [TEM] 10 [TEM]	MRI contrast agent ¹⁰¹ Macrophage uptake ¹⁰² Bioassay agent ¹⁰³
Chitosan	10 [HRTEM], 21.2 [DLS] 10.3 [XRD], 8.1 [TEM] 10–20 [SEM]	Immunoassay, drug delivery agent, ¹⁰⁴ MRI contrast agent Bactericidal agents ¹⁰⁵ Tumor embolization agent ¹⁰⁶
Alginate	193.8 [DLS] 5–10 [TEM], 193.8–483.2 [DLS]	MRI contrast agent ¹⁰⁷ MRI contrast agent ¹⁰⁸
PVA	20 20–30 [TEM], 3.8 [XRD] 56.4 ± 4.1 [PCS] 21.6 ± 2.5 [PCS] 9 [TEM]	Drug delivery agents ¹⁰⁹ Cytotoxicity studies ¹¹⁰ Drug delivery agents ¹¹¹ MRI theranostics ¹¹² Drug delivery agents ¹¹³
Mannan	37.3 ± 5.6 [DLS] 46.2 ± 1.9 [DLS] 9–10 [TEM], 52 [DLS]	Drug delivery agents ¹¹⁴ MRI contrast agent ¹¹⁵ MRI theranostics ¹⁰⁴
PAMAM dendrimers	8.2 [XRD], 10 [TEM] 10 [TEM], 13.5–28.6 [DLS] 10 [DLS] 10–15 [TEM], 250–300 [DLS] 10 [TEM], 13 [DLS] 10.5 ± 0.5 [XRD], 9 ± 0.1 [TEM] 8.4 [SMPS] 84.0 ± 1.4 [HRTEM]	Drug delivery agents ¹¹⁶ MRI theranostics ¹¹⁷ Drug delivery agents ¹¹⁸ Magnetofection (gene delivery) ¹¹⁹ Drug delivery agents ¹²⁰ Immobilization of invertase ¹²¹ MRI contrast agent ¹²² Targeted tumor imaging ^{123,124}
Other dendrimers	9.5 ± 0.6 [TEM], 9.5 ± 1.0 [XRD] 11.5 [TEM, XRD] 5 [TEM], 16 [DLS] 7.6 ± 0.7 [TEM] 5.4 ± 1.2 [TEM]	MRI theranostics ¹²⁵ Multimodal imaging ⁸⁴ MRI contrast agent ¹²⁶ MRI contrast agent ¹²⁴ Self-assembly ⁷⁷
PVP	14 [TEM] 8–10 [TEM], 20–30 [DLS]	MRI contrast agent ¹²⁷ MRI contrast agent ¹²⁸
PEG	9, 19, 31 [TEM] 7 [XRD], 4.8 ± 2 [TEM], 15.7 ± 2 [DLS] 10.4 ± 0.8 [SEM], 61.7 ± 1.5 [DLS]	Magnetic hyperthermia agent ¹²⁹ MRI theranostics ¹³⁰ MRI contrast agent ¹³¹
PEG-co-tert-butyl methacrylate	10.1–24.3 [DLS]	MRI contrast agent ¹³²
PLGA	5 ± 1 [HRTEM]	MRI contrast agent ¹³³
PAA	8 ± 1 [HRTEM], 6.4 [XRD]	MRI contrast agent ¹³⁴

Surface chemistry plays a key role in governing the systemic circulation of nanoparticles. One of the major breakthroughs in this area was the discovery that nanoparticles coated with hydrophilic polymers such as PEG can resist serum protein adsorption and have prolonged systemic circulation.⁹⁴ Numerous variations of PEG and other hydrophilic polymers have been tested for improved circulation.⁹⁵ Surfaces covered with PEG are biocompatible; they are nonimmunogenic, non-antigenic, and protein resistant.⁹⁶ This is because PEG has uncharged hydrophilic residues and high surface mobility, leading to high steric exclusion.⁹⁷ Therefore, covalently immobilized PEG on surfaces of nanoparticles often improves their biocompatibility relative to nonfunctionalized nanoparticles. In addition, particles with PEG-modified surfaces can cross cell membranes *via* a nonspecific cellular uptake mechanism.⁹⁸ Poloxamers and poloxamines, which are block copolymers of PEO and PPO, have been extensively studied in this context.⁹⁹

A set of multifunctional and multicoordinating polymer ligands has been designed that is suitable for surface functionalization of iron oxide and potentially other magnetic nanoparticles to promote integration into biological systems.¹⁰⁰ The availability of several catechol groups in the same ligand enhances its affinity for the magnetic nanoparticles *via* the presence of multiple coordination sites, whereas hydrophilic and reactive groups promote colloidal stability in buffer and enable conjugation with biomolecules. The hybrid systems have compact hydrodynamic sizes and exhibit enhanced long-term colloidal stability over the pH range of 4–12 in the presence of excess electrolytes. Nanoparticles ligated with terminally reactive polymers have been coupled to target dyes and tested in live cell imaging with no measurable cytotoxicity. Finally, the resulting hydrophilic nanoparticles exhibit large and size-dependent relaxivity values.

4.3.1.4 Silane Coatings at Iron-Oxide Nanoparticle Surfaces

In 1980, Sagiv introduced the grafting of well-defined organosilane (octadecyltrichlorosilane, OTS) monolayers onto silica (SiO_2) surfaces.¹³⁵ Since then, the coating of various organosilanes on silicon or other metal oxide surfaces has generated broad interest in surface chemistry.^{136,137} The two main advantages of silanization at the surfaces of metal oxides relative to other coating methods are: (i) the chemical stability of the M–O–Si covalent bond and (ii) the availability of chemical end groups (*e.g.* NH_2 , COOH , and SH) at the extremity of silanes, enabling versatile functionalization of metal-oxide surfaces. Chemical functionalization of metal-oxide surfaces can be achieved by post-modification of a silane layer bearing a reactive end-group.¹³⁸ For example, amino-modified silanes were coupled to many different molecules, such as chromophores, fluorophores¹³⁹ or biomacromolecules¹⁴⁰ for imaging and sensing applications.

The features of the silanization at the surfaces of iron oxide nanoparticles are similar to the silanization on silica substrates. The organosilanes

typically used are trichloro- or trialkoxy-silanes denoted $R-Si-Cl_3$ and $R-Si-(OR')_3$, respectively, where R is an alkyl chain bearing any end-group function and R' is a methyl or an ethyl group. The mechanism involves a hydrolysis reaction of the silanes into silanols ($Si-OH$) catalyzed either in acidic or basic conditions. In a second step, a condensation occurs between $Si-OH$ and $Fe-OH$ at the iron oxide surface, resulting in the formation of $Fe-O-Si$ bonds. However, despite the numerous studies achieved in surface silanization, the precise mechanism of the formation of the silane layer remains elusive. Importantly, the presence of water molecules is a key factor influencing the formation of silane coatings. Water adsorbed on the silicon or metal-oxide surface and other parameters, such as the nature of the solvent, the type and concentration of silane, the temperature, and the reaction time, play key roles in the formation of silane coatings. These parameters can lead to cross-polymerized siloxane networks at metal-oxide surfaces.

Hydrolyzed silanes can bind surfaces of iron oxide nanoparticles *via* different methods because silanes can interact with the surface of iron oxide *via* chemisorption, physisorption, hydrogen bonding, or electrostatic interactions, followed by silane condensation.^{136,137,141,142} Figure 4.11 illustrates three different routes that might be involved with aminopropyltriethoxysilane (APTS) assembly at the surface of iron oxide nanoparticles. Route 1 corresponds to the ideal case in which the aminosilane molecules are bound to the $Fe-OH$ surface *via* $Fe-O-Si$ bonds, resulting in the formation of a pure monolayer of APTS that can condense laterally. Some studies performed on silica surfaces indicated that such true monolayers could be favored by reacting organosilanes in anhydrous apolar solvents (*e.g.* toluene, heptanes, or cyclohexane) in dilute conditions and short reaction times. In these cases, the expected monolayer thickness was less than 1 nm (0.7 nm), and the density was 2–4 silanes nm^{-2} .¹⁴¹

Beyond the difficulties associated with reproducing high-quality monolayers, an important limitation of silane monolayers is their low surface coverage, which can influence the colloidal stability of the resulting nanoparticles. Synthetic routes involving the formation of a polysiloxane layer (silane multilayer) around nanoparticles are often preferred because they can ensure more complete surface coverage and better colloidal and mechanical stability compared to nanoparticles coated with a monolayer approach. In route 2, only a fraction of the aminosilanes attach to the surface *via* the formation of $Fe-O-Si$ bonds as in route 1. A large fraction of the aminosilanes condenses directly onto neighboring silanes without binding to the surface of the nanoparticles. This condensation results in a multilayer cross-linked polysiloxane shell formed by the numerous $Si-O-Si$ bonds between aminosilane molecules. This route is one of the most commonly used. It is encountered when alkoxy-silane grafting is performed in polar or apolar solvents in the presence of water and with a high concentration of silanes ($\geq 1\%$).

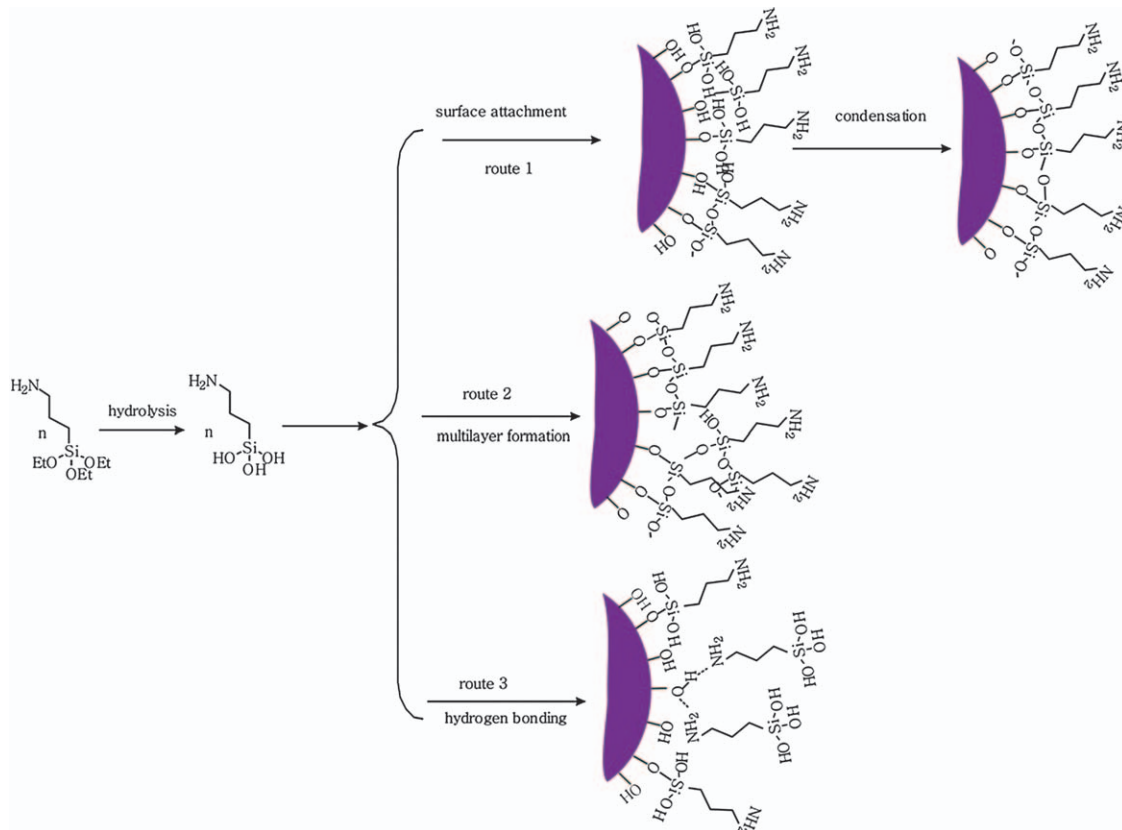


Figure 4.11 Scheme showing the different routes of amino silanization of the surface of iron oxide.¹⁴² Adapted with permission from Y. Liu, Y. Li, X.-M. Li and T. He, *Langmuir*, 2013, 29, 15275. Copyright (2013) American Chemical Society.

Route 3 describes the polysiloxane condensation associated with the reaction of amino-functionalized end groups with the surfaces of iron oxide nanoparticles. This case is encountered when the extremity of the silane can interact with the surface of the nanoparticle *via* hydrogen or electrostatic bonds.^{141,143} For routes 2 and 3, which yield polysiloxane shells, grafted APTS has a thicknesses of ~ 4.7 nm and densities of ~ 29 silanes nm^{-2} .¹⁴⁴ Carboxylate end groups analogues yield shell thicknesses of ~ 2.9 nm with densities of ~ 11 silanes nm^{-2} . These data suggest that the formation of polysiloxane shells is needed to stabilize iron oxide nanoparticles.

Given the relative simplicity of the procedure, grafting of silanes at the surfaces of iron oxide nanoparticles by the coprecipitation method has been evaluated for various applications. The coprecipitation of iron salts is one of the most straightforward methods to form magnetic iron oxide nanoparticles. Various applications were reported with APTS-coated iron oxide nanoparticles obtained by coprecipitation. For example, APTS was grafted onto magnetite nanoparticles prepared by coprecipitation in ethanol. The horseradish peroxidase enzyme was then adsorbed onto the particles to give biocatalytic iron oxide nanoparticle sensors.¹⁴⁵ In another example, PEG-silane was grafted in toluene onto iron oxide nanoparticles prepared by coprecipitation in aqueous basic conditions. The water-dispersible PEG-silanized nanoparticles behave as MRI contrast agents and enable MRI imaging of mice bearing tumors.¹⁴⁶ Polyglycerol-silane-coated iron oxide nanoparticles previously prepared by coprecipitation have also been reported for *in vivo* MRI applications.¹⁴⁷ In this work, the polyglycerol silane was synthesized by polymerization of glycidol groups by ring-opening anionic polymerization at the surface of iron oxide nanoparticles, affording highly stable ferrofluids that function as negative contrast agents for MRI.

An alternative to silanization of iron oxide nanoparticles synthesized by coprecipitation is silanization of thermally decomposed iron oxide nanoparticles. Although the silanization of nanoparticles synthesized by this method is relatively understudied, thermal decomposition is a choice method for the synthesis of iron oxide nanoparticles because it enables fine tuning of parameters such as morphology, crystallinity, and dispersity that cannot be achieved by the coprecipitation method (Section 4.2). Controlling the morphology and composition of iron oxide nanoparticles is crucial for their development as MRI contrast agents. The possibility to exchange silane ligands on ferrite nanoparticles prepared by thermal decomposition was demonstrated with oleic-acid-coated cobalt ferrite nanoparticles. This reaction was performed in hexane with acetic acid as a catalyst.¹⁴⁴

Numerous alkoxysilanes bearing various end-groups including amines, carboxylates, sulfur-containing functional groups, cyanate, and PEG were grafted on oleic-acid-capped nanoferrites. Despite the important advantages of efficacy and versatility, the main limitations of this method are the long reaction times (72 hours) and the high dilution conditions (0.2 mg mL^{-1} in nanoparticles). The silanization reaction time can be decreased to 5 hours at 50°C in toluene using ultrasound.¹⁴⁸ With the aim to improve the

silanization process of iron oxide nanoparticles synthesized by thermal decomposition, an efficient, facile and versatile protocol of silanization was developed.¹⁴⁹ In this method, highly monodisperse, hydrophobic, iron oxide nanoparticles (~11 nm diameter) obtained by the thermal decomposition method are efficiently dispersed in aqueous media. This process uses miscible solvents [EtOH/CHCl₃ (~3 : 1)] to ensure the efficient exchange of oleic acid bound at the surface of the nanoparticles by organosilanes with amine or carboxylate end groups. The hydrodynamic diameter of the silanized iron oxide nanoparticles thus obtained is below ~30 nm in aqueous solution, thereby demonstrating that these iron oxide nanoparticles are potentially suitable for *in vivo* applications. The advantages of this method relative to other silanization protocols are: (i) the shorter reaction times (4 versus 72 h); (ii) the cost-effectiveness because the process is carried out in concentrated conditions in affordable solvents, making use of commercially available silanes; and (iii) the use of mild conditions.

The water-dispersibility of silanized iron oxide nanoparticles is determined by the pH domains and the charge of the silane end-groups. Silanes with amino end groups stabilize iron oxide nanoparticles in ethanol or in acidified water (pH ≤ 5), whereas carboxylate silane end groups stabilize iron oxide nanoparticles in neutral and basic media (pH ≥ 5). MRI properties obtained with iron oxide nanoparticles bound with carboxylate-functionalized silanes thus demonstrate great potential as contrast agents for biomedical applications.

4.3.1.5 Nonporous Silica Coatings at Iron-Oxide Nanoparticle Surfaces

The coating of nonporous silica around magnetic nanoparticles dispersed in aqueous solution is mainly performed according to the Stöber process, often in a solution containing ethanol, water, and ammonia. In this approach, silica coatings are obtained by hydrolysis followed by the condensation of a sol-gel precursor such as tetraorthosilicate (TEOS). This sol-gel method was initially developed in the 1990s to coat ferro- and super-paramagnetic nanoparticles,^{150–152} metallic (*e.g.*, cobalt or gold) nanoparticles,^{153,154} and carbon nanotubes.¹⁵⁵ A main factor controlling the growth of silica shells is the concentration of the sol-gel precursor. Various studies have demonstrated that the thickness of the silica coating surrounding iron oxide nanoparticles previously prepared by coprecipitation can be tuned with good precision by adjusting the concentration of TEOS (Figure 4.12).^{156,157} The influence of shell thickness on relaxivity is described in Section 4.3.3.2.¹⁵⁶

An alternative to the Stöber process for coating hydrophobic magnetic nanoparticles prepared by thermal decomposition with silica is to use water-in-oil microemulsions, also referred to as reverse microemulsions. Water-in-oil microemulsions are surfactant-stabilized water nanodroplets dispersed in a water-immiscible organic solvent. They ensure the transfer of

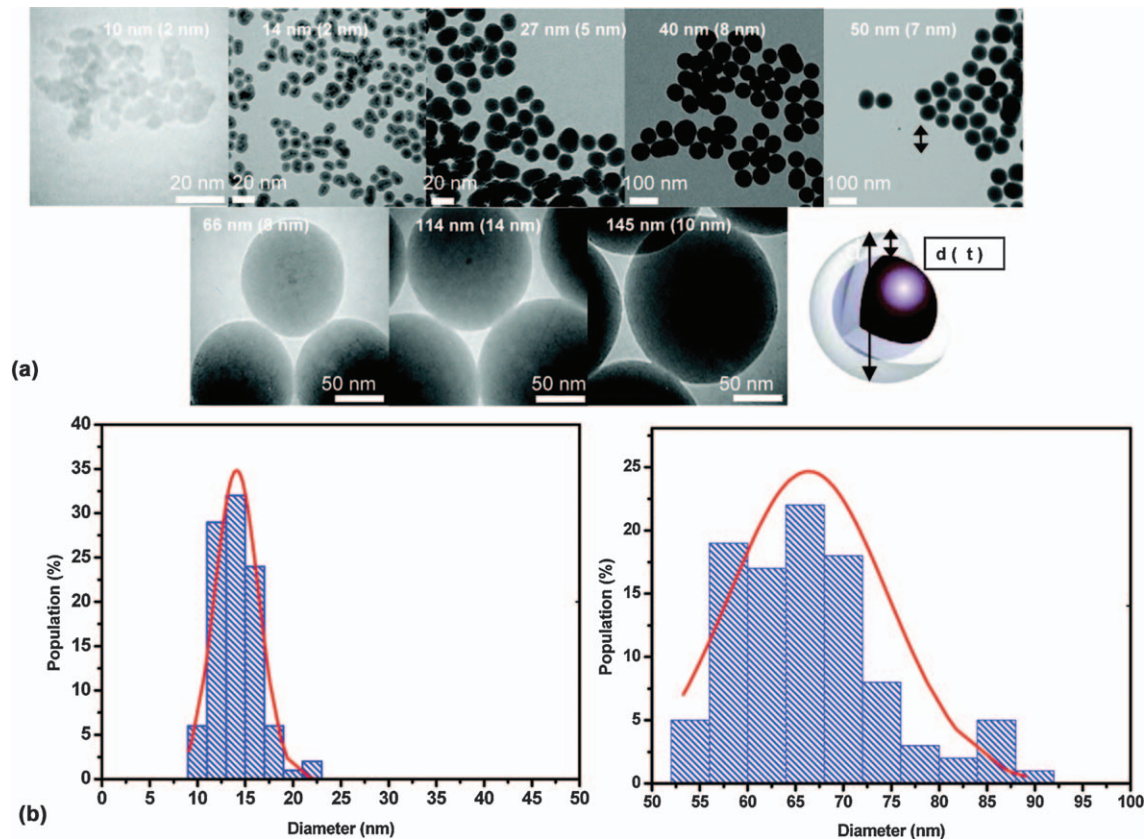


Figure 4.12 Silica-shell thickness around magnetic nanoparticles with different amounts of TEOS.¹⁵⁶ Adapted with permission from S. L. C. Pinho, G. A. Pereira, P. Voisin, J. Kassem, V. Bouchaud, L. Etienne, J. A. Peters, L. Carlos, S. Mornet, C. F. G. C. Geraldés, J. Rocha and M.-H. Delville, *ACS Nano*, 2010, 4, 5339. Copyright (2010) American Chemical Society.

hydrophobic nanoparticles to water droplets. The nonionic amphiphilic surfactant poly(5)oxyethylene-4-nonylphenyl-ether (IGEPAL) is one of the most efficient surfactants reported for reverse microemulsions. In this protocol, the water droplets act as confined nanoreactors that control the growth of the silica coating on the surface of the iron oxide nanoparticles. For example, oleic-acid-capped maghemite nanoparticles formed by thermal decomposition were uniformly capped with silica shells using a water-in-cyclohexane microemulsion.¹⁵⁸ That study demonstrated that the thickness of SiO₂ shells (1.8–30 nm) increases if higher concentrations of TEOS, longer aging time, or decreasing amounts of iron oxide nanoparticles are used. Hydrophobic cobalt ferrite (CoFe₂O₄) nanoparticles prepared by thermal decomposition and capped with a mixture of oleic acid and oleylamine can also be coated with silica *via* a water-in-cyclohexane microemulsion procedure in the presence of poly(5)oxyethylene-4-nonylphenyl-ether.¹⁵⁹ This synthesis yielded uniform core-shell nanoparticles with narrow size distributions. Additionally, the oleic acid and oleylamine surfactant layer was retained between the magnetic core and the silica shell after the sol-gel process and washing steps. Keeping this layer has important repercussions on the magnetic properties of the resulting core-shell magnetic composites, which will be detailed in Section 4.3.3.2.

Table 4.5 lists surfactants and solvents used to coat various nanomaterials with nonporous silica using water-in-oil microemulsions.⁷⁰ This table also reports the coating of nanocrystals that were synthesized *in situ* concomitantly with the sol-gel process, which will not be addressed in this book chapter.

Table 4.5 Nonporous silica coatings of various nanomaterials by water-in-oil microemulsions. Reproduced with permission from A. Guerrero-Martínez, J. Pérez-Juste and L. M. Liz-Marzán, *Adv. Mater.*, 2010, **22**, 1182. Copyright © 2010 WILEY-VCH Verlag GmbH & Co. KGaA, Weinheim, Germany.

Core nanoparticle	Surfactant/organic solvent
Ag ^a , Au ^a , Pd ^b , Fe-Pt ^b , Rh ^a CdS ^b , CdTe ^a , CdSe ^a , YF ₃ ^a Fe ₂ O ₃ [a,b], CoF ₂ O ₄ ^a , MnF ₂ O ₄ ^a	Igepal CO-520/cyclohexane
Au ^a	CTAB/chloroform
Au, Ag ^a Fe ₃ O ₄ ^b	CTAB/toluene
Au ^a	AOT/ <i>n</i> -heptane
CdS:Mn/ZnS ^b	
Fe ₃ O ₄ ^a CdS ^a , CdTe ^a	Triton X-100/cyclohexane
Fe ₃ O ₄ ^a	SDS/octane
Fe-Pt	Brij 52 or brij 56/iso-octane
Fe ₃ O ₄ ^b	Sodium decylbenzenesulfate/xylene

^aCoating of pre-synthesized nanocrystals.

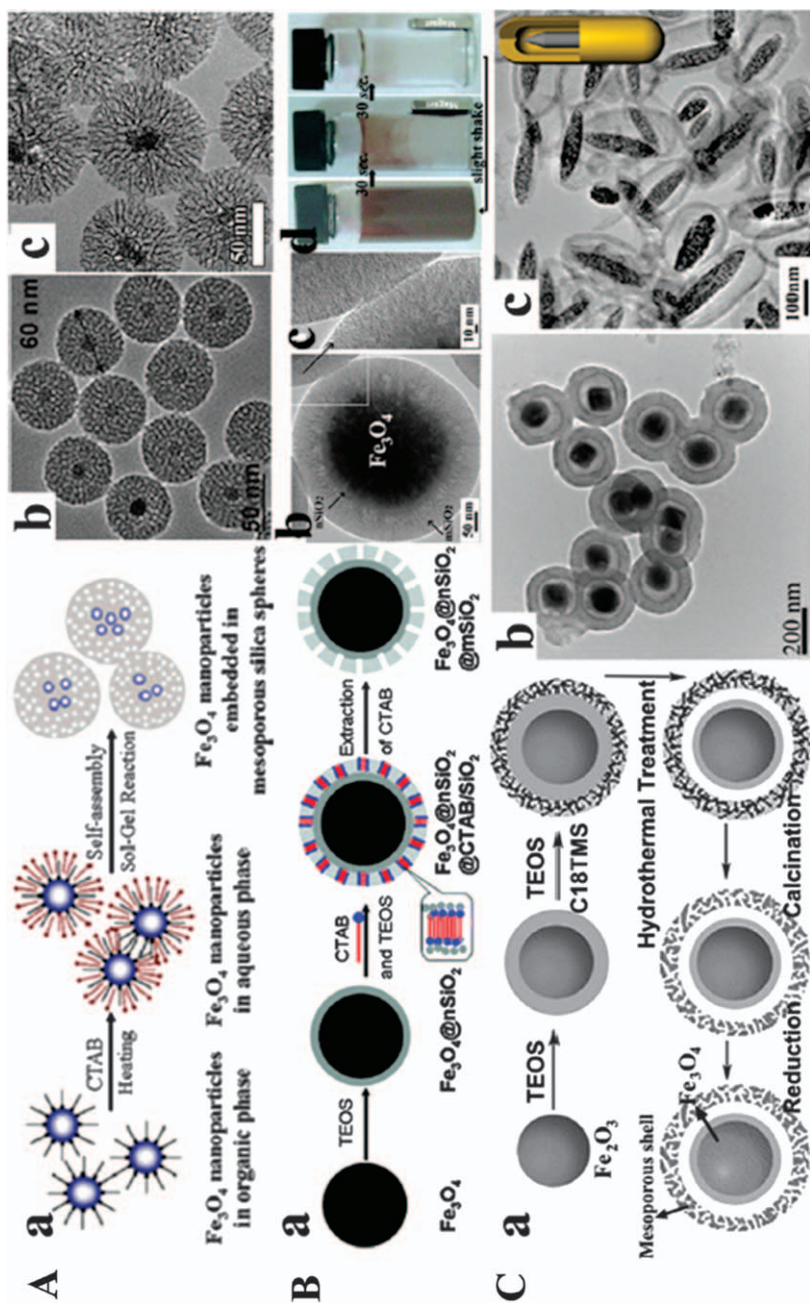
^bCoating of *in situ*-synthesized nanocrystals.

4.3.1.6 Mesoporous Silica Coatings on Iron Oxide Nanoparticle Surfaces

The mesostructures of mesoporous silica nanoparticles without an inorganic core are usually formed by the combination of amphiphilic molecules acting as organic templates (or directing agents) with sol-gel precursors such as TEOS. The first encapsulation of iron oxide nanoparticles by mesoporous shells was reported in 2006.¹⁶⁰ In this example, oleic-acid-capped magnetite nanoparticles previously synthesized by thermal decomposition and dispersed in chloroform were added to an aqueous solution of cetyltrimethylammonium bromide (CTAB). The CTAB surfactant dispersed the hydrophobic nanoparticles in water *via* van der Waals interactions between the alkyl chains of CTAB and oleic acid. The CTAB also acted as a structure-directing agent by forming templating micelles arranged in a hexagonal phase. Under aqueous, basic conditions and upon addition of TEOS precursor, mesoporous silica with ordered porous structure formed around the positively charged CTAB-coated iron oxide nanoparticles and around the templating micelles (Figure 4.13). In this work, several nanocrystals were coencapsulated within the mesoporous silica shells. Further improvements and optimization of this procedure led to a controlled design of mono-disperse-core@mesoporous-silica-shell nanocomposites.^{161,162}

An important feature of magnetic-core@mesoporous-silica-shell nanocomposites is the control of shell growth. Unlike nonporous silica where the concentrations of TEOS and iron oxide nanoparticles are the main parameters used to tune the thickness of silica, controlled growth of mesoporous silica shells is performed by adjusting the ratio between the amount of the magnetic core, the CTAB surfactant, and TEOS.¹⁶¹⁻¹⁶³ Adjusting this ratio is particularly important to achieve uniform syntheses. For example, if a large excess of CTAB is used, porous silica without magnetic cores will form as by-products.¹⁶¹ The effect of the thickness of the mesoporous silica shell on r_1 and r_2 relaxivities is discussed in Section 4.3.3.2. A limitation of coating magnetic cores with mesoporous silica is the presence, at the end of the sol-gel process, of CTAB surfactants within the pores.^{161,163} Given the notable cell toxicity of CTAB, it is necessary to remove this surfactant. Different procedures to remove CTAB have been attempted, including extractions with solutions of ammonium nitrate in ethanol or with acidic ethanolic solutions. The progress of these methods can be monitored by IR spectroscopy or zeta potential measurements. Calcination above 500 °C is not possible because this process changes the magnetic phase of maghemite and magnetite.

The pore size of these nanocomposites can also be controlled and modulated. This is a key parameter to enable the loading of large macromolecules, such as nucleic acids or proteins. N₂ isotherm adsorptions performed on silica-coated iron oxide nanoparticles formed using CTAB indicate that they often contain pore sizes in the range of 2–3 nm.^{161,163} Pore sizes can be increased to 6.1 nm with the use of 1,3,5-triisopropylbenzene/decane as



a pore swelling agent.¹⁶³ However, the synthesis of mesoporous silica shells around magnetic or plasmonic cores with pore sizes larger than 15–20 nm, which are needed for loading biological macromolecules, remains challenging.

4.3.2 Effects of Coatings and Anchoring Groups on Magnetic Properties of Nanoparticles

The functionalization of iron oxide nanoparticles is necessary because naked iron oxide nanoparticles are not stable at physiologically relevant pH values. Iron oxides have amphoteric hydroxide groups at their surface. Thus at high values of pH, deprotonation of some of these hydroxides causes a negative charge to build up on the surface of the nanoparticles. The opposite is observed at low pH. The pH at which the surface is charge neutral because the deprotonated and protonated hydroxides are balanced is called the isoelectric point. Near the isoelectric point, nonfunctionalized nanoparticles aggregate and flocculate in suspension. The isoelectric point of iron oxide is in the range 6.5–7.5 depending on the synthesis and purification methods. Therefore, functionalization of iron oxide nanoparticles is necessary for their use in biomedical applications.

Different coating strategies have been investigated to stabilize nanoparticles. Most research has aimed at optimizing the functionalization of iron oxide nanoparticles to optimize their colloidal stability, aggregation state, furtivity, cytotoxicity, and magnetic properties. For MRI, the preservation of the magnetic properties of the nanoparticles, and in particular the saturation magnetization, during functionalization is of great importance. Additionally, the coating molecules need to enable water diffusion near the magnetic core to maximize relaxivity. Another parameter in the design of coatings is the presence of functional groups for further anchoring of targeting or bioactive molecules to the surface of the nanoparticles. The anchor needs to be strong enough to avoid desorption and subsequent replacement

Figure 4.13 (A) Scheme showing the process to coat mesoporous silica shells around magnetic nanoparticles using CTAB; (B) mesoporous-silica-coated-multi-cores that were optimized in mesoporous-silica-coated single core; and (C) image of pore swelling using 1,3,5-triisopropylbenzene. Adapted with permission from Y. Wang and H. Gu, *Adv. Mater.*, 2015, 27, 576. Copyright © 2014 WILEY-VCH Verlag GmbH & Co. KGaA, Weinheim, Germany; J. Kim, J. E. Lee, J. Lee, J. H. Yu, B. C. Kim, K. An, Y. Hwang, C.-H. Shin, J.-G. Park, J. Kim and T. Hyeon, *J. Am. Chem. Soc.*, 2006, 128, 688. Copyright (2006) American Chemical Society;¹⁶⁰ J. Kim, H. S. Kim, N. Lee, T. Kim, H. Kim, T. Yu, I. C. Song, W. K. Moon and T. Hyeon, *Angew. Chem., Int. Ed.* 2008, 47, 8438. Copyright © 2008 WILEY-VCH Verlag GmbH & Co. KGaA, Weinheim, Germany; and *Journal of Colloid and Interface Science*, Volume 361, J. Zhang, X. Li, J. M. Rosenholm and H.-c. Gu, Synthesis and characterization of pore size-tunable magnetic mesoporous silica nanoparticles, 16–25, Copyright 2011, with permission from Elsevier.

of coating molecules by proteins that would induce aggregation and capture by the reticuloendothelial system.¹⁶⁴ Therefore, different anchoring ligands have been studied, including silanes, carboxylates, phosphonates, and catecholates.^{83,85,86,163–180}

Studies have been conducted on the strength of anchoring of molecules at the surfaces of nanoparticles and on the effect of anchoring groups on the magnetic properties of functionalized nanoparticles,^{86,171,172,181,182} but discrepancies exist among the published results. For example, some studies report a decrease of saturation magnetization after grafting molecules that contain phosphonates,^{172,183} but others report the opposite relationship.^{83,86} The colloidal stability of coated nanoparticles is often related to the anchoring strength of coatings, and contradictory results have been reported, in particular, when carboxylate anchoring groups are used. One explanation for these discrepancies is that the nanoparticles studied have different types of interactions between the anchoring groups and the iron oxide surfaces. These interactions might be purely electrostatic in nature, as shown in Figure 4.14, or involve monodentate, bidentate (chelate or bridging), or tridentate complexes at the surfaces of the nanoparticles.^{178,184} The strength of the anchoring and the effect of the anchoring group on the magnetic properties depend on the nature of the interactions.

At the nanoscale, spin-canting effects at the surfaces of nanoparticles or spin-glass-like behavior have been widely reported. These effects are mainly due to the presence of under-coordinated iron atoms at or near the surfaces of the nanoparticles and to the curvature of nanoparticles (Figure 4.15). These defects and spin-canting effects are present in varying amounts depending on the conditions used during the synthesis of the nanoparticles

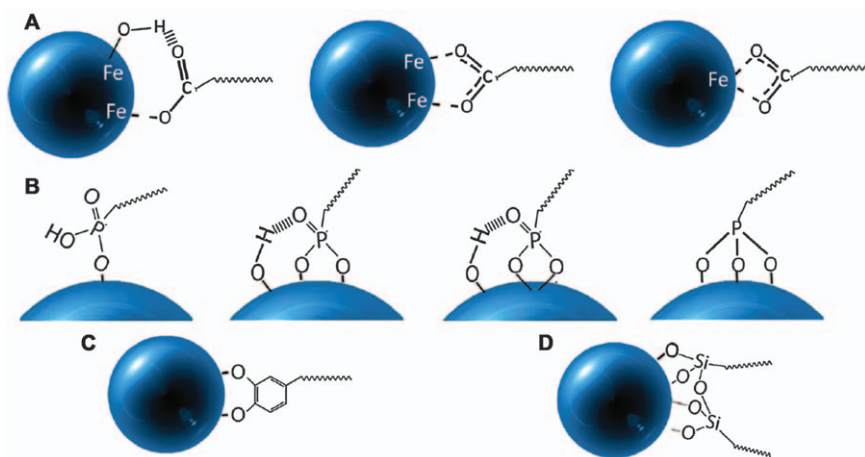


Figure 4.14 Possible surface interactions for different coupling agents: (A) carboxylates, (B) phosphonates, (C) catechol, and (D) silane. Adapted from ref. 382 with permission from The Royal Society of Chemistry.

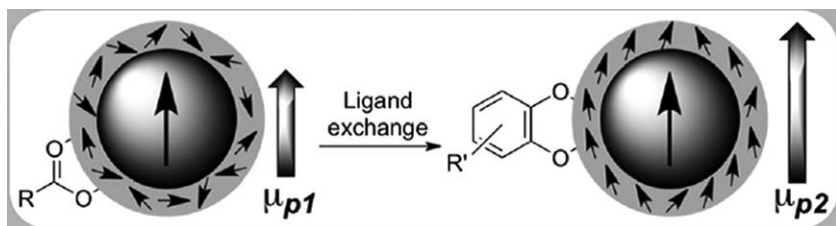


Figure 4.15 Influence of surface ligands on the overall magnetic moment (μ_p) of a superparamagnetic iron oxide nanoparticle. Canted surface spins are partially realigned upon exchange with strongly interacting catecholate ligands, *i.e.* $\mu_{p1} < \mu_{p2}$. Adapted from ref. 172 with permission from The Royal Society of Chemistry.

and on the size of the nanoparticles.^{61,185,186} These spin-canting effects and defects induce a decrease of the overall magnetization of nanoparticles compared to the bulk phase.^{187,188} However, surface complexes formed from anchoring groups can contribute to the preservation and, sometimes, enhancement of the saturation magnetization of nanoparticles (Figure 4.15).^{172,178,179} The covalent bonding of carboxylates partially reconstructs octahedral crystal-fields around surface iron sites.¹⁸⁹ For example, grafted dendrons bearing carboxylates or phosphonates as anchoring groups and the presence of phosphonates enhanced the saturation magnetization at the surfaces of iron oxide nanoparticles. This effect was attributed to surface phosphonate complexes in which the phosphonate oxygens take positions similar to those of oxygen atoms in bulk iron oxide, thereby keeping the symmetry and crystal field of the surface iron closer to that of the core. Consequently, the homogeneity of the crystal field reduces surface spin disorder.¹⁷² Similar results were observed with catecholate anchoring groups (Figure 4.15).¹⁹⁰

A decrease in surface spin canting is observed when the surface coatings strongly interact with iron atoms *via* bidentate or tridentate coordination. The type of interaction and the strength of bonding depend on the synthetic method used to form the iron oxide nanoparticles as well as on the grafting strategy.⁸³ Depending on the synthetic method, iron oxide nanoparticles can be either naked (as with the coprecipitation method) or coated with hydrophobic ligands, such as oleic acid (as with the thermal decomposition method). Different strategies have been reported for coating nanoparticles with bioactive molecules.^{83,164,170,176,177,191–195} Naked nanoparticles are often dispersible in water, and the nanoparticles can be either synthesized in the presence of molecules for grafting or synthesized prior to the grafting step.^{172,196,197} For nanoparticles coated with hydrophobic ligands, two strategies can be followed for grafting: (1) If the bioactive molecules and the nanoparticles are both soluble in organic solvents (generally polar), then the grafting molecules can be directly added to suspensions of the nanoparticles where they undergo ligand exchange.⁸³ In this strategy, the grafting step

often needs to be repeated to ensure that most of the hydrophobic ligands have been replaced. (2) Another strategy is to perform ligand exchange and phase transfer simultaneously by placing a water suspension of molecules at a suitable pH into contact with a suspension of nanoparticles in an apolar solvent (often hexane).^{83,170} During stirring, ligand exchange is accompanied by the transfer of nanoparticles from the organic phase to the aqueous phase.

Considering the numerous methods developed to synthesize iron oxide nanoparticles, the different molecules used for grafting, and the different grafting strategies, it is not surprising that surface complexes differ from one publication to another and, consequently, that the effect of the anchoring group on the bonding strength and magnetic properties differs. However, grafting *via* electrostatic interactions between anchoring groups and the surface of iron oxide nanoparticles consistently provides strong anchoring, as is the case for grafting performed in water suspensions or by ligand exchange and phase transfer processes.^{196–198} The presence of charge on both the nanoparticles and the grafting molecules favors the formation of surface interactions that are stronger than those formed *via* ligand exchange in organic solvents.⁸³

Moreover, for magnetite-based nanoparticles, the grafting step can also affect the composition of the nanoparticles. The presence of Fe^{II} at the surface of magnetite causes these particles to be sensitive to oxidation and, consequently, oxidizing grafting conditions can contribute to a decrease in the saturation magnetization of nanoparticles. This is predictable given that maghemite phase, the oxidized phase of magnetite, displays a lower saturation magnetization than magnetite.¹⁹⁹ Nevertheless, despite a slight oxidation of magnetite-based nanoparticles during their coating with phosphonated ligands, the saturation magnetization can be preserved due to the phosphonate surface complex inducing magnetic ordering of the surface.¹⁷² Finally, some particle etching has been observed with catecholate and citrate ligands modifying the shape of nanoparticles (Figure 4.16).¹⁷²

4.3.3 Effects of Coatings on Relaxivity

Anchoring agents influence the magnetic and colloidal properties of nanoparticles; as such, the nature of the coatings also influences contrast enhancement in magnetic resonance imaging. The parameters of nanoparticles relevant to contrast enhancement are the longitudinal (r_1) and transversal (r_2) relaxivities (see Chapter 2.1.1 and Section 4.1 for a description of relaxivity). A good T_2 -shortening contrast agent displays high values of r_2 and of r_2/r_1 , and these values are related to saturation magnetization and the nature of the coating on the nanoparticle.²⁰⁰ The type of coating has a strong influence on r_1 and r_2 : the accessibility of water to the magnetic core depends greatly on the characteristics of the coating, such as its chemical nature (polymer *versus* inorganic shell), hydrophilicity, hydrophobicity, thickness, and porosity.

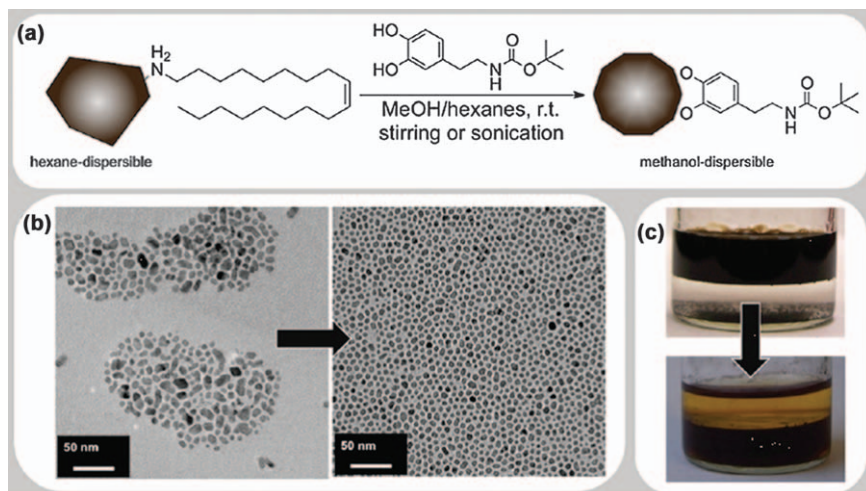


Figure 4.16 (a) Catechol-induced etching of oleylamine-stabilized iron oxide nanoparticles during ligand exchange; (b) transition emission microscopy micrographs before and after the exchange process; and (c) photos of the reaction mixture (hexane top phase and methanol bottom phase). Adapted from ref. 172 with permission from The Royal Society of Chemistry.

4.3.3.1 Functionalization by Polymers and Dendrons

Functionalization by polymers can influence the properties of nanoparticles and, in particular, those properties related to MRI. For example, transverse relaxivity, r_2 , decreases with increasing chain length or molecular weight of polymer coating.¹⁹¹ Hydrophobic polymers were found to lead to lower transverse relaxivity than hydrophilic ones.¹⁸¹ For example, nanoparticles with a core size of approximately 10 nm coated with poly(ethylene imine), a hydrophilic charged polymer, have large relaxivity values. Similar results were obtained for nanoparticles with core sizes greater than 30 nm.¹⁸¹

Functionalization of spherical superparamagnetic iron oxide nanoparticles with linear monophosphonates or with PEGylated monophosphonated dendrons of generation 1, 2, or 3 yielded dendritic nano-objects that were 15 to 30 nm in size. These nano-objects were stable in physiological media and displayed renal and hepatobiliary elimination.¹⁸² Nuclear magnetic relaxation dispersion profiles (NMRD, see Chapter 2.3 for details) and relaxivity measurements highlighted the influence of the molecular architecture on water diffusion close to the magnetic core and, consequently, on the relaxation properties of the nano-objects. NMRD profiles of the different suspensions (Figure 4.17) provided information about the diffusion of water molecules as a function of the composition of the organic coating. All the profiles displayed the characteristic shape of superparamagnetic nanoparticles. Because the size of the nanocrystals was similar for all samples, the profile maxima were similar for all of the functionalized

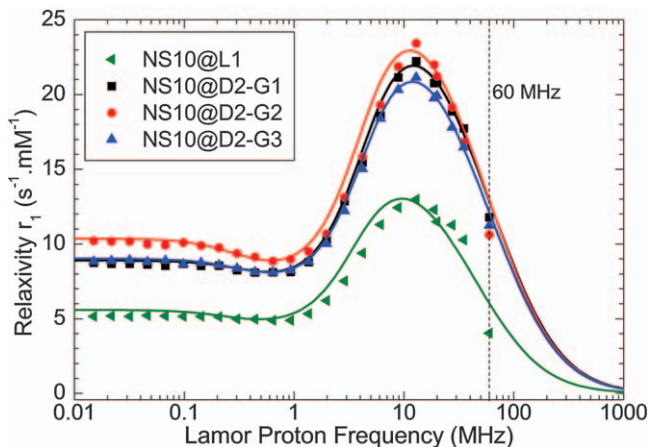


Figure 4.17 NMRD profiles of nanoparticles functionalized with the molecules L1, D2-G1, D2-G2, and D2-G3. Adapted from ref. 383 with permission from The Royal Society of Chemistry.

nanoparticles near 10 MHz. However, considerable differences in $r_{1\max}$ were observed between the nanoparticles functionalized with the linear molecules (NS10@L1 in Figure 4.17) and the nanoparticles coated with dendrimers (NS10@D2-G1, NS10@D2-G2, and NS10@D2-G3 in Figure 4.17).

The value of $r_{1\max}$ depends on water diffusion and is defined by $r_{1\max} = CM_s^2 \cdot \tau_D$, where M_s is the saturation magnetization of the magnetic core, τ_D is the diffusion coefficient of water, and C is a constant.²⁰¹ For the functionalized nanoparticles described in the previous paragraph, grafting small phosphonate dendrons to the surface of the superparamagnetic iron oxide nanoparticles does not affect their magnetic properties.⁸⁶ Therefore, the difference observed between $r_{1\max}$ values can be attributed only to the nature of the surface coating. At all frequencies studied, the $r_{1\max}$ value for the nanoparticles functionalized with linear molecules is lower than the value for the nanoparticles functionalized with dendrimers, regardless of the generation. These data indicate that water diffusion and circulation through the dendritic shell is more facile than through the linear organic layer. Those experimental data were fitted to extrapolate values of saturation magnetization (M_s) and radius (r).⁴⁷ The radius values agree quite well with the ones determined by transmission electron microscopy. However, the radius obtained by the fitting of the NMRD curves for the nanoparticles functionalized with linear polymers is slightly larger than the ones obtained for the dendronized nanoparticles. This difference suggests that the water molecules that are perturbed by the magnetic field of the nanoparticle circulate at a longer distance from the magnetic core in the case of the nanoparticles functionalized with linear polymers than in the case of the dendronized nanoparticles. This analysis was confirmed by the measured M_s values, which are smaller for the linear polymers derivatives, thereby confirming

that the water molecules are less perturbed by the magnetic field of the nanoparticles that have linear coatings.

4.3.3.2 Functionalization by Nonporous and Porous Silica Shells

For iron oxide nanoparticles covered by nonporous silica shells, r_1 and r_2 decrease as the silica shell thickness increases.¹⁵⁶ Figure 4.18 shows the evolutions of r_1 and r_2 as a function of the diameter of silica-coated iron oxide nanoparticles. The silica-coated nanoparticles were designed with a tunable diameter ranging from 14 to 145 nm with a 10 nm iron oxide core and a silica shell thickness from 2 to 67 nm. The data in the graph in the inset was acquired at 20 MHz and shows a decrease of r_1 at 25 °C with increasing thickness of silica. Indeed, r_1 dropped from 32 to 2 $\text{mM}^{-1} \text{s}^{-1}$ upon addition of a 7.5 nm silica shell (for $d = 25$ nm) (Figure 4.18, inset). At 500 MHz, r_1 had negligible values regardless of the shell thickness. A decrease of r_2 from 228 to 64 $\text{mM}^{-1} \text{s}^{-1}$ (500 MHz and 25 °C) was observed when the silica shell thickness was increased to 7.5 nm (for $d = 25$ nm). A similar trend was observed at 37 °C for r_1 and r_2 measured at 500 MHz. These results are caused by a decrease in the diffusion of water molecules close to the iron oxide cores with increasing thickness of nonporous silica shells. This behavior is consistent with an outer-sphere mechanism of

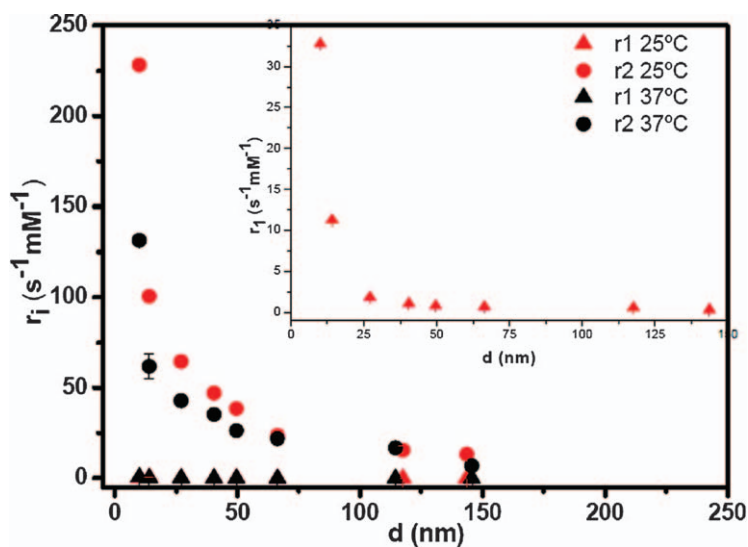


Figure 4.18 Evolution of r_1 and r_2 as a function of the diameter of silica-coated iron oxide nanoparticles at 25 and 37 °C at 500 MHz. Inset: evolution of r_1 at 25 °C at 20 MHz.¹⁵⁶

Adapted with permission from S. L. C. Pinho, G. A. Pereira, P. Voisin, J. Kassem, V. Bouchaud, L. Etienne, J. A. Peters, L. Carlos, S. Mornet, C. F. G. C. Geraldes, J. Rocha and M.-H. Delville, *ACS Nano*, 2010, 4, 5339. Copyright (2010) American Chemical Society.

relaxation caused by the inhomogeneity of the local magnetic field created by the nanoparticles. The thickness of silica shells determines the distance of closest approach of the diffusing water molecules to the superparamagnetic core of the particle. The authors suggested the existence of two regions in the silica coating: one fully impermeable to water, at the surface of the $\gamma\text{Fe}_2\text{O}_3$ core and one weakly permeable, located at the interface.

The introduction of mesopores within silica shells reduces the decrease of relaxivities observed with nonporous silica shells. Iron oxide nanoparticles coated with mesoporous silica shells of ~ 2 nm porosities were studied with respect to the evolutions of r_1 and r_2 with the thickness of the mesoporous silica shell.¹⁶¹ Iron oxide nanoparticles covered by the silica-free surfactant CTAB were compared with iron oxide nanoparticles with different thicknesses of mesoporous silica shell. As was the case with the nonporous silica coatings, r_1 decreased for nanoparticles coated with a mesoporous shell from $31.2 \text{ mM}^{-1} \text{ s}^{-1}$ at 20 MHz for nanoparticles without coating to $0.6 \text{ mM}^{-1} \text{ s}^{-1}$ for nanoparticles with a mesoporous coating that was 42 nm thick (core-shell diameter = 95 nm). A similar trend was observed at 60 MHz; the relaxivity decreased from 13.7 to $0.3 \text{ mM}^{-1} \text{ s}^{-1}$ (Table 4.6). Such a decrease in r_1 after coating with mesoporous silica can be explained by the limited diffusion of water molecules. The presence of a thick, mesoporous silica shell around the magnetic core can limit the diffusion of water near the magnetic core, thus decreasing r_1 . Where porous coatings differ from nonporous silica coatings is the effect on transverse relaxivities. Values of r_2 measured at 20 and 60 MHz (see Table 4.6) were barely affected by the coating of the mesoporous silica shell up to a core-shell diameter of 75 nm,

Table 4.6 Effect of the shell thickness of mesoporous silica on r_1 and r_2 of mesoporous-silica-coated iron oxide core-shell magnetic nanocomposites. Reproduced with permission from F. Ye, S. Laurent, A. Fornara, L. Astolfi, J. Qin, A. Roch, A. Martini, M. S. Toprak, R. N. Muller and M. Muhammed, *Contrast Media Mol. Imaging*, 2012, 7, 460. Copyright © 2012 John Wiley & Sons, Ltd.

Sample name (particle diameter by TEM)	Mean hydrodynamic diameter (nm) ^a	20 MHz			60 MHz		
		r_1	r_2	r_2/r_1	r_1	r_2	r_2/r_1
		($\text{s}^{-1} \text{ mM}^{-1}$)	($\text{s}^{-1} \text{ mM}^{-1}$)		($\text{s}^{-1} \text{ mM}^{-1}$)	($\text{s}^{-1} \text{ mM}^{-1}$)	
Fe_3O_4 -CTAB (11 nm)	67	31.25	81.37	2.61	13.69	82.18	6.01
Fe_3O_4 @mSiO ₂ (50 nm)	60	3.65	84.26	23.1	1.31	92.13	70.3
Fe_3O_4 @mSiO ₂ (75 nm)	77	2.13	79.93	37.5	0.97	87.54	90.3
Fe_3O_4 @mSiO ₂ (95 nm)	96	0.61	50.13	82.2	0.31	55.44	179
Feridex	72	40	160	4			
Resovist (38)	65	25	164	6.2			

^aMean hydrodynamic diameters and relaxivities of Fe_3O_4 -CTAB and different sized Fe_3O_4 @mSiO₂ nanoparticles measured at 20 MHz (0.47 T) and 60 MHz (1.41 T) in water (37 °C) and the reported relaxivity values for commercially available Feridex[®] and Resovist[®] contrast agents.

corresponding to a shell thickness of 32 nm. Beyond that thickness of coating, r_2 decreased from ~ 80 to $\sim 50 \text{ mM}^{-1} \text{ s}^{-1}$ at 20 MHz for a 95 nm core-shell diameter and from ~ 88 to $\sim 55 \text{ mM}^{-1} \text{ s}^{-1}$ at 60 MHz. These results indicate that the transverse (spin-spin) relaxation created by the local magnetic fields generated by the iron oxide cores has a long-range effect that is detectable up to a shell thickness of 40 nm, below which r_2 remains almost constant.

Biocompatibility of coatings for iron oxide nanoparticles is necessary to ensure the colloidal stability of the nanoparticles in physiological environments and to provide reactive groups on the surface of nanoparticles for conjugation of bioactive molecules such as targeting ligands, dyes, and drugs. For imaging by MRI, the coating can be designed to enhance the diffusion of water near the magnetic core. The mean hydrodynamic size (smaller than 100 nm) of coated nanoparticles is also a parameter that must be controlled to ensure good *in vivo* biodistribution, elimination, and targeting of specific organs.

The presence of anchoring groups in the coating ensures strong binding to the surface of the nanoparticles, which prevents their replacement by blood proteins and subsequent capture by the reticuloendothelial system. The use of anchoring groups with high affinity for the surface of iron oxide remains the methodology of choice when narrow size distributions and small hydrodynamic radii are required. However, the strength of anchoring is related to the nature of the surface complex that depends on the grafting strategy and method of synthesis of the nanoparticles. Characterization of coatings requires the combination of different characterization techniques that reveal the number of molecules and, therefore, the approximate number of functional groups on the surfaces of nanoparticles. Finally, the peripheral parts of the coating play important roles in regulating the interactions between the coated nanoparticles and biological molecules at the cellular and tissue levels.

4.4 Characterizing Functionalized Iron Oxide Nanoparticles

GEOFFREY COTIN, DAMIEN MERTZ, JEAN-MARC GRENECHE,
OVIDIU ERSEN, BENOIT PICHON, DELPHINE FELDER-FLESCH AND
SYLVIE BEGIN-COLIN*

Superparamagnetic iron oxide nanoparticles with surface coatings are widely used for biomedical applications, including as contrast agents for MRI. Most studies of these nanoparticles focus on improving biocompatibility and targeting through the design of organic coatings, and on enhancing the quality of the magnetic nanoparticles and their size distribution after functionalization.

To be useful *in vivo*, functionalized iron oxide nanoparticles should be stable in solutions that are biocompatible with respect to pH and osmolarity ($\sim 320 \text{ mmol L}^{-1}$ = osmolarity of blood plasma). The absence of aggregates is also mandatory for intravenous injection to avoid the risk of pulmonary embolisms caused by aggregates or coagulation disorders, which can result in animal death. Therefore, the coating and aggregation state (*i.e.* the size distribution) of iron oxide nanoparticles are important parameters to control for *in vivo* applications. Furthermore, upon entering the blood circulation, iron oxide nanoparticles are subjected to opsonization, the nonspecific fouling of the surfaces of nanoparticles by plasma proteins, and subsequent uptake by the reticuloendothelial system. Biodistribution must be favorable, with little nonspecific tissular uptake (mainly hepatic), and a quasi-complete elimination of the nanoparticles, with the most effective routes of elimination being the urinary and hepato-biliary pathways.^{13,202} To prevent opsonization of nanoparticles and to increase the ability to evade the reticuloendothelial system, organic coatings, including anchoring at the surface of nanoparticles, need to be tailored. Additionally, particle size distribution of functionalized nanoparticles must be optimized with respect to the desired properties. Long blood-circulation times increase the possibility of reaching target tissue: suspensions of particles with average hydrodynamic sizes of 10–100 nm are optimal for *in vivo* delivery because smaller sizes (<10 nm) are rapidly removed by renal clearance and larger sizes (>200 nm) are quickly sequestered by the reticuloendothelial system. Thus, the coating molecules of iron oxide nanoparticles bear several functions, including ensuring biocompatibility and targeting. These coatings need to be strongly anchored to the surface of nanoparticles to avoid their desorption *in vivo*. Consequently, grafting strategies are crucial and need to be optimized so that the particle size distributions stay below 100 nm and the properties of both nanoparticles and coating are preserved.

To design T_2 -shortening contrast agents for MRI, the saturation magnetization of the nanoparticles, the effective or aggregate size, and the water diffusion around the magnetic core are key parameters to control.²⁰⁰

Saturation magnetization depends on many factors, such as the size, composition, and shape of the iron-oxide-based nanoparticles. Research has demonstrated that the anisotropy of nanoparticles can be increased to enhance the magnetic properties by strategies such as tuning the morphology to promote shape anisotropy or synthesizing core-shell nanoparticles to induce exchange magnetic properties.^{203–206} These different aspects have been investigated to tune the contrast-enhancing effect of magnetic and superparamagnetic nanoparticles. However, the effect of the shape on the observed MRI-relevant properties is not well understood, and the composition of core-shell or doped ferrite is relatively complicated. For biomedical applications of iron oxide nanoparticles, it is thus important to characterize functionalized nanoparticles, both the nanoparticles and their coatings, to gain a better understanding of the key parameters in their design and to enable further improvements.

In that context, the main techniques for characterizing the shape, size, composition, and magnetic properties of nanoparticles, and in particular iron oxide nanoparticles, are described in this section. This includes the techniques used to characterize the organic coating, the type of surface complexes, and hydrodynamic size distributions.

4.4.1 Characterization of the Iron Oxide Core of Functionalized Nanoparticles

Characterization of the size and shape of nanoparticles is mainly performed by transmission electron microscopy (TEM). Classical TEM and energy dispersive spectroscopy (EDS), electron energy loss spectroscopy (EELS), high angle annular dark field in scanning TEM (HAADF-STEM), and electron tomography are modes that provide valuable information regarding the shape and composition of nanoparticles. Other techniques, such as X-ray diffraction (XRD), IR spectroscopy, and ⁵⁷Fe Mössbauer spectroscopy, and less-common techniques, such as Raman and photoemission (XPS) spectroscopies, enable investigation of the composition of iron oxide nanoparticles.

4.4.1.1 Characterization of the Size, Size Distribution, and Shape of Nanoparticles

4.4.1.1.1 Transmission Electron Microscopy and Electron Tomography. TEM enables analysis of nanoscale morphological features. This imaging technique is an essential characterization tool in the field of nanoparticles and contributes to the development of nanomaterials and the characterization of nanostructures.²⁰⁷ Because the properties of nanoparticles originate from their shape and size, systematic studies of such structural and morphological characteristics are required at the atomic scale. Given the strong interaction between accelerated electrons and matter, several types of signals result from the irradiation of the nanoparticles with electrons,

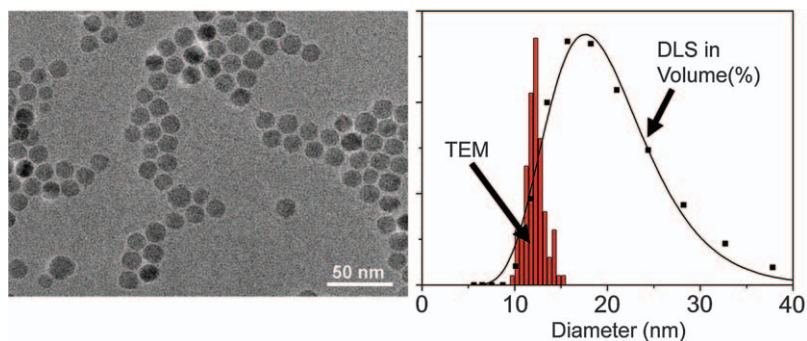


Figure 4.19 TEM image of iron oxide nanoparticles synthesized by thermal decomposition and coated with oleic acid (left) and size distributions from TEM images and dynamic-light-scattering measurements (right).

leading to various modes of analysis with specific selectivities. Thus, TEM is an authoritative characterization tool in the field of nanoparticles.

When applied in an existing imaging mode (for example, classical TEM or HAADF-STEM), TEM provides precise information regarding the size and shape of individual particles.²⁰⁸ Such analyses can be generalized to an assembly of nanoparticles using appropriate image treatment tools for obtaining statistical values representative of the whole specimen.²⁰⁹ The statistics of size can be calculated from the size measurements of nanoparticles in TEM images using the free ImageJ program (Figure 4.19).²¹⁰

In high-resolution TEM or STEM configurations, structural parameters such as the crystallographic structure and the type and density of atomic defects can be determined.²¹¹ In particular, the development of the incoherent HAADF-STEM imaging mode, in which image intensity is directly proportional to the mean atomic number of the nano-sized specimen, provided new capabilities of analysis enabling the spatial localization of phases with similar atomic numbers in the nanograin. A typical example is given in Figure 4.20 with the determination of the spatial distribution of two metallic phases within the same particle.²¹²

TEM holders that heat specimens enable dynamic *in situ* analyses of structural and morphological evolution of nanosystems and their reactivity in controlled environments.²¹³ By adapting experimental TEM conditions to minimize damage from irradiation, phase and reactivity diagrams can be obtained for oxide or metallic nanoparticles including direct information regarding their growth and formation. A typical example of such an *in situ* TEM study involved the analysis of the morphological and structural evolution of metallic nanoparticles confined inside carbon nanotubes as a function of temperature to observe in real time the evolution of the system at high temperatures (Figure 4.21).²¹⁴

In the case of nanoparticles with complex shapes or topographies or for particles with porous internal structures, classical two-dimensional analyses are often not sufficient for unraveling structural or morphological

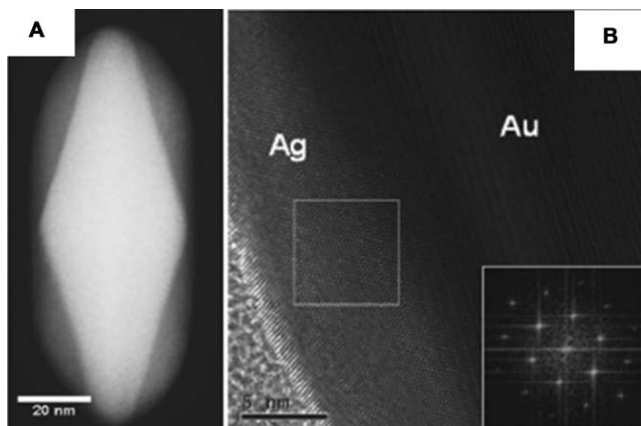


Figure 4.20 (A) Typical two-dimensional HAADF-STEM image of Au nanobipyramid coated with silver. (B) High-resolution TEM image of the silver shell at the interface on the lateral face with the corresponding fast-Fourier-transformation spectrum corresponding to the white region from the low silver loading.

Adapted from ref. 212 with permission from The Royal Society of Chemistry.

characteristics. To obtain a three-dimensional representation of the nano-object, a three-dimensional imaging method of electron tomography can be used. This tomography enables qualitative and quantitative three-dimensional analyses with nanometric (even atomic) spatial resolution.²¹⁵ Electron tomography involves recording a series of images of an object, tilted inside the electron microscope, along the widest possible angular range. The construction of a three-dimensional matrix describing the sample directly in the real space is performed by applying mathematical algorithms based on Radon's theorem. That process overcomes the limitations associated with two-dimensional image projections and provides more reliable insight into the three-dimensional shape and architecture of nanoparticles. To illustrate how this analysis is applied to nanoparticles, Figure 4.22 depicts a combined morphological and crystallographic study of Pt nanocrystals that are 5 nm in size.²¹⁶ Using HAADF-STEM tomography, their shape was shown to be close to a truncated octahedron, which is also the geometry that is energetically the most stable. Such three-dimensional detailed analyses enable quantification of the relative amounts of crystallographic facets and provide a model-based indication of the faceting of the nanocrystals.

4.4.1.1.2 X-ray Diffraction (XRD). The indexing of X-ray diffraction patterns enables identification of the crystalline phases of nanoparticles and determination of the mean crystallite size. The mean crystallite size, L , can be estimated using the Debye-Scherrer equation, $\Delta(2\theta) = K\lambda/(L \cos(\theta))$. In this equation, K is a dimensionless shape factor with a value close to unity (values of ~ 0.9 are often used), $\Delta(2\theta)$ is the line broadening at half the

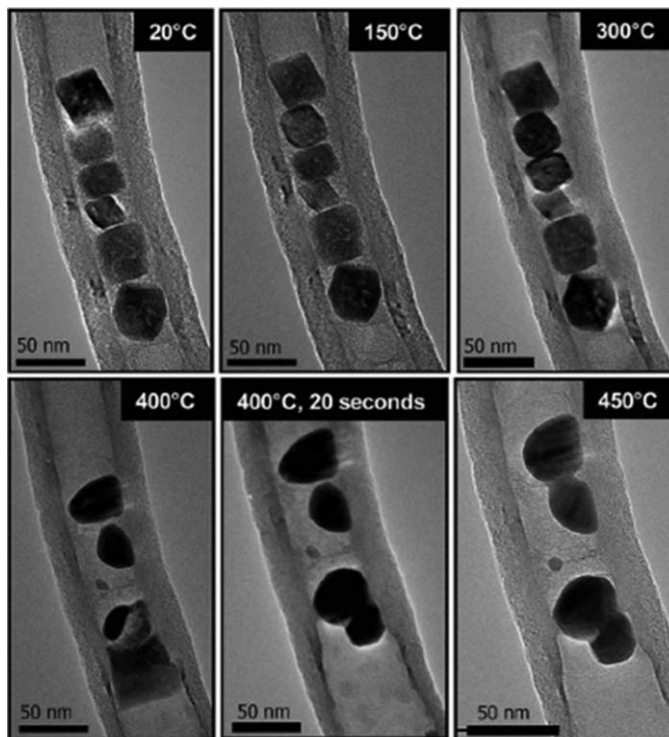


Figure 4.21 Thermal evolution of Co–CoO-based nanoparticles cast inside carbon nanotubes investigated by *in situ* TEM experiments under vacuum. The images reveal changes in the nanoparticle morphology and localization on the support.
Adapted from ref. 214 with permission from The Royal Society of Chemistry.

maximum intensity after subtracting the instrumental line broadening (in radians), λ is the X-ray wavelength, and θ is the Bragg angle (in degrees). The Debye–Scherrer equation is limited to nanoscale particles and is not applicable to grains larger than about 0.1 or 0.2 μm .

Mean crystallite size can be extracted from profile matching refinements that compare experimental and simulated XRD patterns. These comparisons are often performed using the Fullprof program²¹⁷ and LeBail’s method²¹⁸ with the modified Thompson–Cox–Hasting pseudo-Voigt profile function. Another approach involves deconvolution of the X-ray pattern using MAUD software based on the Rietveld method combined with a Fourier analysis. This type of analysis is particularly useful for describing the low part of the wings of Bragg peaks. This description can be applied to synchrotron, time-of-flight neutron, and electron patterns and is suitable for nanoparticles. This analysis enables refinement of microstructural parameters, including size of the coherent diffraction domain, microsize-strains, lattice parameters, and some instrumental parameters.^{219–221} This procedure gives rise

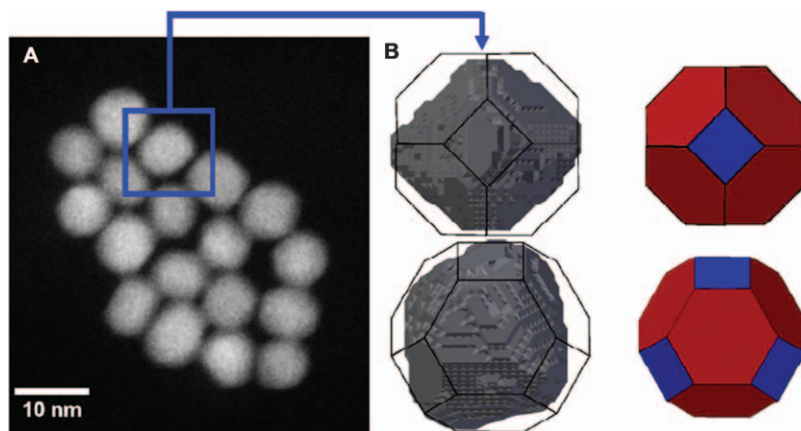


Figure 4.22 Electron tomography for the three-dimensional analysis of the crystallographic facets of Pt nanoparticles. (A) Initial two-dimensional image at a 0° tilt from the HAADF-STEM tilt series, illustrating the choice of the Pt nanoparticle used for a detailed morphological analysis. (B) Views of the particle model along two axes of symmetry compared to truncated-octahedron model crystals. This model is the outcome of the data segmentation procedure applied to the computed volume. Red facets depict $\{111\}$ crystallographic planes, and blue facets indicate $\{100\}$ planes. To illustrate similarities, the edges of the truncated octahedron are superimposed on the experimental model. Adapted from ref. 216 with permission from The Royal Society of Chemistry.

to estimates of the Rietveld texture and stress analysis in the case of thin films studied by X-ray diffraction. When the mean crystallite size from XRD is in agreement with the TEM-derived mean size, nanoparticles are considered as being monocrystalline or single crystal.

4.4.1.1.3 Granulometric Measurement by Dynamic Light Scattering (DLS). Particle size distributions in suspensions are generally determined using granulometric measurements that provide the mean hydrodynamic diameter of nanoparticles. Dynamic light scattering (DLS) (also referred to as photon correlation spectroscopy or quasi-elastic light scattering) is a technique that is used to determine the size-distribution profile of nanoparticles in suspension or polymers in solution. In this technique, suspensions of nanoparticles are illuminated by a laser and fluctuations of the scattered light are detected at known scattering angles by a fast photon detector.

Nanoparticles suspended within a liquid undergo Brownian motion, and this motion is inversely proportional to the size of the particles. DLS monitors the Brownian motion with light scattering. The speed at which nanoparticles are diffusing due to Brownian motion is measured by recording the rate at which the intensity of the scattered light fluctuates. Small

particles cause the intensity to fluctuate more rapidly than large particles. The dynamic information of the particles is derived from an autocorrelation of the intensity trace recorded during the experiment. Once the autocorrelation data have been generated, different mathematical analyses can be applied to determine particle size from the experimental data. DLS software associated with commercially available instruments typically displays the particle population at different diameters. If the system is monodisperse, there should only be one population (monomodal size distribution), whereas a polydisperse system shows multiple particle populations.

Particle size is reported in terms of hydrodynamic diameter, which is the diameter of a hard sphere that diffuses at the same speed as the nano-object being measured. Thus, hydrodynamic diameter depends on the size of the particle core and on the size of surface structures, particle concentration, and the type of ions in the medium. For example, the size distribution of oleic acid-coated nanoparticles determined from DLS is shifted by comparison with that determined by TEM because of the organic coating on the nanoparticles (thickness of 1–2 nm) suspended in tetrahydrofuran (Figure 4.19). For nonspherical particles, DLS provides the diameter of a sphere that has the same average translational diffusion coefficient as the particle being measured.

The primary size distribution acquired from a DLS measurement is the intensity-weighted distribution obtained from the chosen analysis. Volume or number-size distributions are derived from the intensity distribution using Mie theory; this conversion requires prior knowledge of the optical properties of the particles, including their refractive indices and absorptions. Conversion from intensity to volume or number of nanoparticles assumes that all particles are spherical, that all particles have a homogenous and equivalent density, and that the refractive indices and absorptions are known. Importantly, size distributions reported in number of nanoparticles do not accurately represent the suspension state of the nanoparticles. Size distributions in volume or intensity are more appropriate representations because they are directly proportional to the mass distribution.

Importantly, dynamic light scattering also enables the determination of the zeta potentials of nanoparticles in aqueous suspensions. The colloidal stability of nanoparticles is the result of an equilibrium between attractive forces and repulsive forces. In the case of iron oxide nanoparticles, the attractive forces are mainly due to van der Waals interactions and magnetic interactions between nanoparticles that are acting as magnetic dipoles. These interactions depend on the nature of the material and on the distance between nanoparticles. The energy of van der Waals interactions varies with $1/r^2$, whereas the energy of dipole–dipole interactions varies with $1/r^3$, where r is the distance between nanoparticles. Because iron oxide nanoparticles are superparamagnetic, magnetic interactions can be neglected, leaving van der Waals interactions as the main attractive force. Repulsive forces are needed to ensure the colloidal stability of nanoparticles in suspension; they are mainly induced by electrostatic interactions or steric repulsions.¹⁸⁴

At physiological pH, naked iron oxide nanoparticles are not stable in suspensions and flocculate. The surface of iron oxide is covered by amphoteric hydroxyl groups due to chemisorption of water. Depending on the pH of the solution, the surfaces of iron oxide nanoparticles can be positively or negatively charged. The isoelectric point is the pH at which the surface has equal numbers of positive and negative charges. For iron oxides, this pH value is roughly 6.8.²²² Iron oxide nanoparticles form stable suspensions by electrostatic interactions only at pH values far from their isoelectric point; therefore, they are not stable at physiological pH.

Thus, for applications in the biomedical field, iron oxide nanoparticles must be functionalized with molecules that provide repulsive steric or electrostatic interactions. The colloidal stability of nanoparticles provided by electrostatic interactions in water is broadly assessed by their zeta potential.¹⁸⁴ The zeta potential, ζ , is the electric potential in the interfacial double layer at the location of the slipping plane relative to a point in the bulk fluid away from the interface. In other words, the zeta potential is the potential difference between the dispersion medium and the stationary layer of fluid attached to the dispersed particles. A potential exists between the surface of particles and the dispersing liquids that varies according to the distance from the surface of the particles. The magnitude of the zeta potential indicates the degree of electrostatic repulsion between adjacent, similarly charged particles in an aqueous dispersion. Colloids with high absolute values of zeta potential (≥ 30) are electrically stabilized, and colloids with low zeta potentials tend to coagulate or flocculate (if no steric repulsion is provided).

4.4.1.2 Characterization of the Composition of Iron Oxide-based Nanoparticles

The most studied iron oxide phases are magnetite and maghemite (Section 4.1.1). Magnetite is an inverse spinel: $\text{Fe}^{3+}_A[\text{Fe}^{2+}\text{Fe}^{3+}]_B\text{O}_4^{2-}$. However, at the nanoscale, Fe^{II} ions in octahedral ($B = O_h$) sites are sensitive to oxidation. The oxidation of Fe^{II} to Fe^{III} is accompanied by the formation of a vacancy (\square), giving the general formula $\text{Fe}^{3+}_A[\text{Fe}^{2.5+}_{2-6\delta}\text{Fe}^{3+}_{5\delta}\square_\delta]_B\text{O}_4^{2-}$. Complete oxidation corresponds to $\delta = 1/3$, and leads to maghemite $\gamma\text{-Fe}_2\text{O}_3$. The XRD patterns of magnetite and maghemite are similar (Figure 4.23) and the lattice parameters are also similar, making it difficult to discriminate between magnetite and maghemite. Magnetite displays conductive properties and a saturation magnetization larger than that of maghemite. It is well-established that the Fe^{II} ions located at the surface of magnetite nanoparticles are sensitive to oxidation and that this sensitivity increases with decreasing sizes of nanoparticles.^{61,186,197,223-228}

To enhance the magnetic anisotropy or saturation magnetization of iron oxide nanoparticles beyond what is accessible by changing the shape of the nanoparticles, two strategies are commonly used: doping iron oxide with

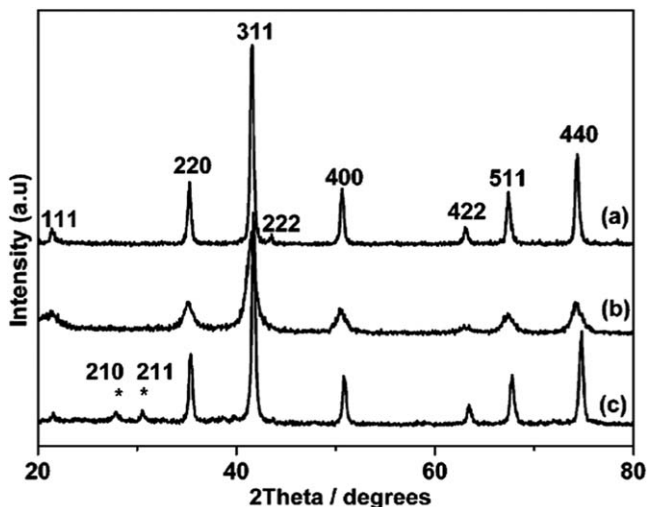


Figure 4.23 XRD patterns of $\text{Fe}_{3-x}\text{O}_4$ nanoparticles with mean diameters of (a) 40 nm or (b) 12 nm and of (c) maghemite $\gamma\text{-Fe}_2\text{O}_3$. The peaks marked with asterisks are additional peaks present in maghemite indicating the presence of vacancies.²²⁵

Adapted with permission from T. J. Daou, G. Pourroy, S. Bégin-Colin, J. M. Greneche, C. Ulhaq-Bouillet, P. Legaré, P. Bernhardt, C. Leuvrey and G. Rogez, *Chem. Mater.*, 2006, **18**, 4399. Copyright (2006) American Chemical Society.

elements such as Zn, Co, Ni, or Mn^{8,229–232} and synthesizing core-shell nanoparticles with two phases displaying different magnetic properties to induce exchange magnetic properties.^{208,231–233} For example, core-shell structures with antiferromagnetic and ferrimagnetic materials display exchange bias properties, which lead to large coercive fields and enable shifts of superparamagnetic limits towards room temperature.^{208,231,232} Another strategy is the synthesis of core-shell nanoparticles using mixed ferrites with hard and soft anisotropies, which induces exchange-coupled properties that are favorable to MRI.²³³ However, it is not easy to characterize the core-shell composition of nanoparticles or doping homogeneity and amount. Indeed, doped iron oxide nanoparticles generally display complex structures with chemical heterogeneities.^{231,232} The main characterization techniques that enable discrimination between magnetite and maghemite and that provide evidence of the composition of doped or core-shell nanoparticles are described in the following sections.

4.4.1.2.1 X-ray Diffraction (XRD). XRD patterns enable identification of crystalline phases present in powders. For core-shell nanoparticles, both types of phases can be indexed with XRD patterns if their weight is large enough ($\geq 5\%$). For doped iron oxide nanoparticles, the analysis of the XRD patterns enables confirmation that the nanoparticles have cubic

spinel structures (AB_2O_4) by comparing the lattice parameters to those of the Joint Committee on Powder Diffraction Standards (JCPDS) file for the expected ferrite. However, for both core-shell or doped iron oxide nanoparticles, XRD does not provide evidence of the presence of a composition gradient or of the presence of two types of ferrite. This is because in these situations, the lattice parameters are too similar to be distinguished. Other techniques such as ^{57}Fe -Mössbauer spectroscopy or X-ray magnetic circular dichroism experiments are needed to investigate such situations.

The magnetite phase and its corresponding oxidized phase, maghemite, have similar structures and, thus, display similar XRD patterns (Figure 4.23). The refinement of XRD patterns enables calculation of the mean values of lattice parameters and comparison to those of stoichiometric magnetite Fe_3O_4 (0.8396 nm, JCPDS file 19-629) and maghemite $\gamma\text{-Fe}_2\text{O}_3$ (0.8346 nm, JCPDS file 39-1346) phases. A lattice parameter between those of magnetite and maghemite indicates that the composition is intermediate between these two structures. The composition of iron oxide nanoparticles has been demonstrated to depend on the synthetic method and on the size of the nanoparticles.^{61,186,224} For nanoparticles synthesized by thermal decomposition,²³³ it has been reported that the small nanoparticles (<8 nm) are oxidized and have a composition closer to that of maghemite. Nanoparticles larger than 12 nm are composed of a magnetite core with an oxidized shell; the amount of magnetite in the nanoparticles increases with increasing nanoparticle size. For intermediate sizes (8–12 nm), the composition of nanoparticles is intermediate between those of magnetite and maghemite without a clear core-shell structure and with the occurrence of a perturbed oxidized state with defects. Similar results are obtained with nanoparticles synthesized by coprecipitation.²²⁴ The composition of nanoparticles smaller than 20 nm is closer to that of maghemite, whereas nanoparticles larger than 20 nm have core-shell structures with a core of stoichiometric magnetite surrounded by an oxidized layer. Such features are consistent with the disappearance of the Verwey transition in zero-field-cooled and field-cooled magnetic measurement curves (Section 4.5), when particles are smaller than 20 nm.²²⁴

4.4.1.2.2 IR Spectroscopy. Magnetite and maghemite phases can be differentiated based on symmetry. Wavenumbers assigned to spinel structures are in the range of 800 to 400 cm^{-1} . The IR spectrum of stoichiometric magnetite displays one peak near 570 cm^{-1} . The IR spectrum of maghemite, on the other hand, is more complicated due to the sensitivity of IR spectroscopy to vacancies (Figure 4.24). Indeed, maghemite differs from magnetite by the presence of vacancies within the O_h sites and the absence of Fe^{II} . Maghemite often displays superstructure forms that arise as a result of cationic and vacancy ordering (Figure 4.23). Vacancies can be randomly distributed (space group $Fd\bar{3}m$ as in magnetite) or partially ($P4332$) or totally ordered ($P43212$). Thus, maghemite phases display several bands between 800 and 400 cm^{-1} , and the number and

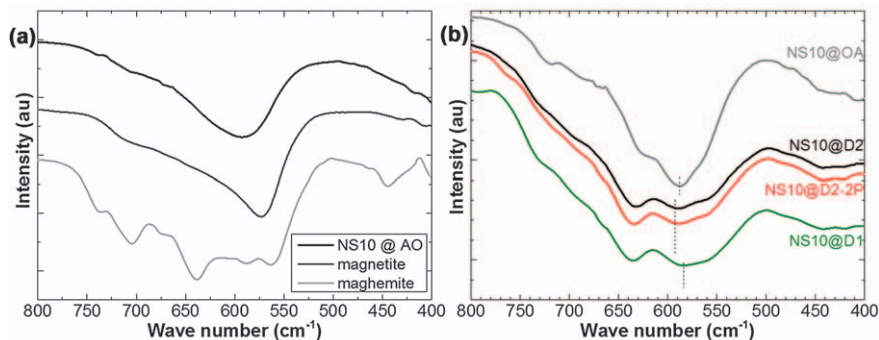


Figure 4.24 IR spectra between 800 and 400 cm^{-1} corresponding to the Fe–O bands of nanoparticles 10 nm in diameter synthesized by thermal decomposition compared to the IR spectra of maghemite (partially disordered vacancies) and magnetite.

Adapted with permission from A. Walter, A. Parat, A. Garofalo, S. Laurent, L. Vander Elst, R. N. Muller, T. Wu, E. Heuillard, E. Robinet, F. Meyer, D. Felder-Flesch and S. Begin-Colin, *Part. Part. Syst. Charact.*, 2015, 32, 552. Copyright © 2014 WILEY-VCH Verlag GmbH & Co. KGaA, Weinheim, Germany.

resolution of these bands depend on the structural order of the vacancies in maghemite.^{8,229,230,234,235} Higher order vacancies correspond to larger numbers of lattice absorption bands between 800 and 200 cm^{-1} (Figure 4.24). The IR spectrum of nanoparticles with a lattice parameter close to that of magnetite, that were identified as core-shell nanoparticles with a core of magnetite surrounded by an oxidized layer of composition close to that of disordered maghemite, displays an intense band at around 570 cm^{-1} with a large shoulder up to 750 cm^{-1} .

4.4.1.2.3 Raman Spectroscopy. Raman spectroscopy enables differentiation of iron-oxide phases.^{236–240} Magnetite exhibits characteristic bands at 668 and 535 cm^{-1} assigned to the A_{1g} and T_{2g} transitions that can be distinguished from maghemite transitions at 720, 500, and 350 cm^{-1} .^{236–238}

4.4.1.2.4 X-ray Photoelectron Spectroscopy. X-ray photoelectron spectroscopy (XPS) is a surface-sensitive quantitative spectroscopic technique that can be applied to a broad range of materials and provides quantitative and chemical information regarding the surface of the material being studied. The average depth of analysis for XPS is ~ 5 nm. XPS can confirm the presence and degree of oxidation of elements in nanoparticles.

The Fe2p doublet with binding energy values of 710 and 725 eV implies the presence of Fe–O bonds, typical for iron oxide. Furthermore, the Fe^{III} and Fe^{II} ions are distinguishable by XPS. When Fe^{II} ions are present at a surface, the satellites of the 2p_{3/2} peak around 719 eV characteristic of the Fe^{III} ions in γ -Fe₂O₃ become less resolved. This loss of resolution is due to the main 2p_{3/2} and 2p_{1/2} peaks broadening and to the rising intensity at about 716 eV

of the satellite for the Fe^{II} ions. Moreover, in this case, a shoulder is observed around 709 eV, the intensity of which decreases when the stoichiometric deviation in $\text{Fe}_{3-\delta}\text{O}_4$ increases.^{225,241-244} The presence of Fe^{II} at the probed surface of iron oxide is characterized by the absence of satellites around 719 eV between the main Fe 2p peaks. By contrast, this satellite is observed with a reduction of the contribution around 709 eV in the XPS spectra of nanoparticles that contain large amounts of magnetite.

4.4.1.2.5 ^{57}Fe -Mössbauer Spectroscopy. Mössbauer spectroscopy is the best method to evaluate the exact deviation from stoichiometry, δ , in $\text{Fe}_{3-\delta}\text{O}_4$. The discovery of “the recoilless nuclear resonance fluorescence of gamma radiation” by Rudolf Mössbauer in 1958²⁴⁵⁻²⁴⁹ gave rise to the development of Mössbauer spectroscopy, a resonance technique giving physical parameters that are relevant to and useful in materials science. The high sensitivity and nondestructive behavior make this technique of interest to physicists, chemists, geologists, metallurgists, biologists, and industrial scientists to better understand structural, chemical, magnetic, and electronic properties of Fe-containing materials. Many books and chapters have reported the fundamental aspects of the Mössbauer effect and the physical meaning of Mössbauer hyperfine parameters. They have also illustrated the wide range of interest and applications of transmission Mössbauer spectroscopy.²⁵⁰⁻²⁵⁷ This nuclear probing technique can be applied to materials including frozen solutions, but is not suitable for liquids and gases. This spectroscopic technique is sensitive to three hyperfine interactions that probe nuclei and can be simultaneously observed and quantified in a single Mössbauer spectrum. These interactions describe how nuclear moments interact with close electronic shells and atomic environments. One distinguishes electric-monopole interactions resulting in the isomer shift (IS, mm s^{-1}); the electric-quadrupole interaction causing the quadrupole splitting (QS, mm s^{-1}) of partially two-fold-degenerate nuclear levels; and the magnetic dipole interaction, which gives rise to magnetic splitting (hyperfine field B_{hf} in units of T) of completely six-fold-degenerate nuclear levels. The nuclear states and typical Mössbauer spectra (single line, quadrupolar doublet, and Zeeman sextets) are schematized in Figure 4.25 for ^{57}Fe (excited nuclear state $I_{\text{ex}} = 3/2$).

Specific attention needs to be paid to the preparation of samples for Mössbauer spectroscopy and to the instrumental conditions to optimize the registration time. Optimal experimental conditions use a thin powdered layer containing $5 \text{ mg of Fe cm}^{-2}$. This corresponds to the effective absorber thickness, which does not correspond to the real physical thickness but to the number of Mössbauer-active atoms per surface unit. This criterion must be satisfied to prevent thickness effects, which lead to nonhomogeneous broadening of lines, changes of intensities, and distortions of profiles. In the case of ferrofluids, attention must be paid to the quantity of Fe and the cooling conditions to obtain homogeneous distributions of nanoparticles in a sample. Special care should be applied to nanoparticles that are sensitive

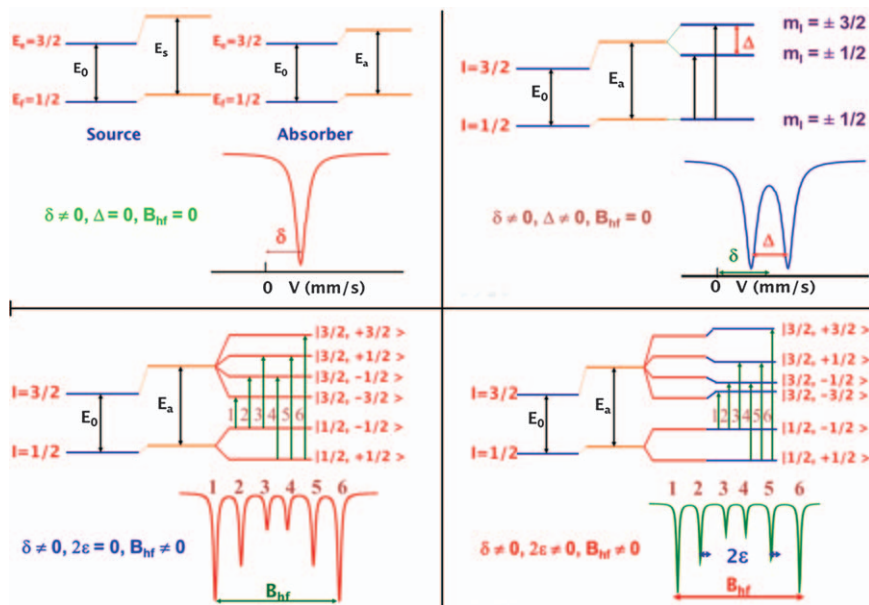


Figure 4.25 Nuclear-level ground and excited states and corresponding typical Mössbauer spectra for a random powdered sample: (top left) in the case of pure electric monopole interactions between electrons and protons that give rise to isomer shift δ ; (top right) in the case of a non-zero electric field gradient, electric quadrupole interactions result from the precession of the quadrupole moment and its neighbors giving rise to a partial degeneracy of excited levels and to a quadrupolar doublet characterized by quadrupolar splitting Δ ; (bottom left) in presence of magnetic dipolar interaction, a total degeneracy of ground and excited states is observed giving rise to Zeeman splitting into a sextet and the hyperfine field B_{hf} ; and (bottom right) in presence of combined magnetic-dipolar, electric-monopolar, and electric-quadrupolar interactions labeled as quadrupolar shift 2ϵ .

to atmosphere, in which case the sample holders need to be cleaned in a glove box and sealed before transfer to a Mössbauer spectrometer to prevent post-synthesis oxidation. Additionally, studies of ultra-fine nanoparticles might require insertion in a matrix. This step can improve registration times because of the recoil effect that is present due to the small size of the particles and to the interface between nanoparticles and matrix. These issues need to be considered when interpreting Mössbauer hyperfine structures.

Experimental spectra provide discrimination between the number of Fe species present in the sample, information relative to chemical bonding and structural properties, and estimation of respective proportions. The profile of Mössbauer lines (width and shape) enable conclusions to be made with respect to crystal quality, chemical composition, chemical disorder (including nonhomogeneities, defects, and vacancies), and the topological nature of the Fe network (for example, crystalline, amorphous, or

nanocrystalline states). The addition of temperature-dependent measurements facilitates monitoring *in situ* solid-state reactions, electron transfers and disproportionation mechanisms, spin transitions, structural phase transitions and transformations (crystallizations), magnetic ordering transitions, and some electron and magnetic relaxation phenomena.

The recoilless fraction, or Lamb-Mössbauer factor (f), and the second-order Doppler shift need to be taken into account in the estimation of each Fe species. These parameters are strongly dependent on the binding of the resonant nuclei in the lattice and vary with the chemical composition of the phases, the lattice structure, and environmental conditions such as temperature and pressure. Estimates of the f factor are extrapolated from the temperature evolution of absorption areas, but they are assumed to be similar within a single phase containing different Fe species or within different phases.

Furthermore, the application of an external magnetic field during spectroscopic measurements can aid in characterizing the orientation of the moments of Fe, the sign of hyperfine field (parallel or antiparallel to the magnetic moment),²⁵⁸ the sign of the quadrupolar splitting, and the magnetic structures. External magnetic fields can also be used to follow superparamagnetic relaxation phenomena from dynamic to blocked magnetic states in the case of magnetically confined nanostructures.²⁵⁹⁻²⁶² The intensities of the intermediate lines of the Zeeman sextet are correlated to the angle between the γ -beam and the magnetic Fe moment. The area ratios of the six lines are given by $3 : p : 1 : 1 : p : 3$, where $p = 4 \sin^2\theta / (2 - \sin^2\theta)$, where θ is the magnetic Fe moment. The area ratios of the six lines are given by the ratio of 3 to the propagation direction of the γ -beam. Consequently, theoretical in-field Mössbauer spectra can be modeled as a function of ideal magnetic collinear and noncollinear magnetic structures, as illustrated in Figure 4.26, assuming that the external magnetic field is oriented parallel to the γ -beam. Note that when the external field is applied perpendicular to the γ -beam, the respective relative ratios are inversed; the $3 : 4 : 1 : 1 : 4 : 3$ ratio becomes $3 : 0 : 1 : 1 : 0 : 3$ and *vice versa*. In addition, it is usually observed that the values of the intermediate intensities differ from 0 or 4 in the case of collinear magnetic structures because most magnetic structures are canted. Thus, it becomes possible to directly estimate this angle from in-field Mössbauer data: the total effective field at the nucleus results from the vectorial sum of the hyperfine field and the applied field leading to the following expression: $B_{\text{hf}}^2 = B_{\text{eff}}^2 + B_{\text{app}}^2 - 2B_{\text{eff}}B_{\text{app}}\cos\theta$, which enables the hyperfine field to be accurately estimated. It is thus possible to conclude whether the hyperfine field at Fe nuclei is parallel or antiparallel to the magnetic moment of Fe.

In the case of ferrimagnetic Fe-containing systems, the application of an external magnetic field enables discrimination of the Fe species located in octahedral and tetrahedral sites, contrary to zero-field measurements, which give rise to nonresolved or weakly resolved hyperfine structures. Proportions are discussed in terms of stoichiometry and cationic distribution, including

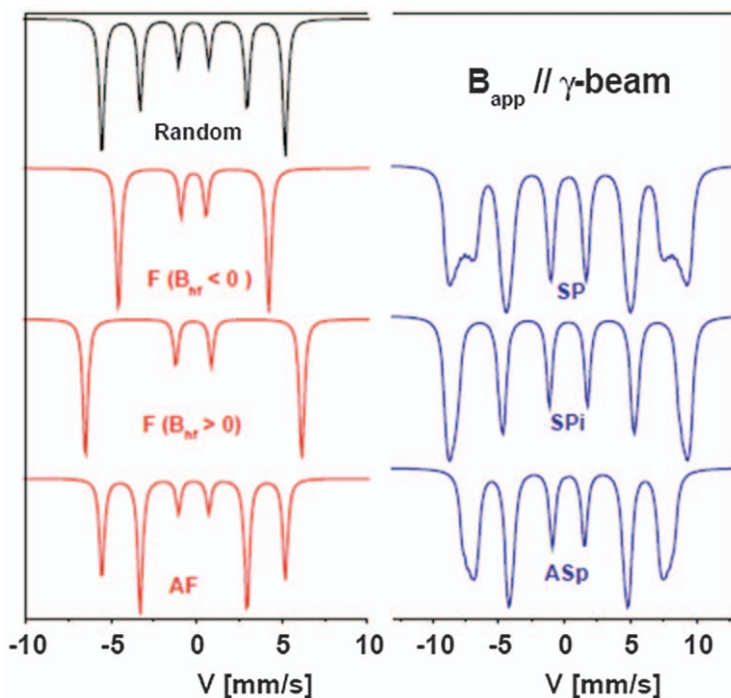


Figure 4.26 Theoretical Mössbauer spectra on linear and noncollinear magnetic structures in presence of an external field applied parallel to the γ -beam: random powder in zero-field (Random), ferromagnetic with magnetic moments antiparallel [$F (B_{hf} < 0)$] and parallel [$F (B_{hf} > 0)$] to the magnetic moment, and antiferromagnetic (AF) structures and noncollinear magnetic structures of speromagnet (SP), sperimagnet (SPi), and asperomagnet (ASp).

Adapted with permission from J.-M. Greneche, *The Contribution of ^{57}Fe Mössbauer Spectrometry to Investigate Magnetic Nanomaterials*, in *Mössbauer Spectroscopy*, ed. Y. Yoshida and G. Langouche, Springer, Heidelberg, 2013, p. 187. Copyright © 2013 Springer-Verlag Berlin Heidelberg. With permission of Springer.

inversion, and then compared to magnetic measurements, particularly in the presence of different paramagnetic species.

Elementary applications of Mössbauer spectroscopy in the case of Fe-containing materials consist of checking whether the sample under study contains Fe impurities (lower limit is $\sim 1\%$ Fe under optimal conditions). The modeling of spectra consists of describing the hyperfine structure from a superimposition of elementary quadrupolar or magnetic components composed of Lorentzian lines. In the case of crystalline samples, this modeling enables estimation of the number of Fe species, their respective proportions, and their valence and spin states. However, a first critical analysis of the linewidth enables conclusions to be drawn with respect to crystal quality: a broadening of lines is usually due to the presence of

chemical inhomogeneities in the form of vacancies, defects, or atomic disorder. Temperature-dependent studies under controlled atmosphere must be performed to establish the temperature-dependence of hyperfine parameters, which is needed to provide evidence of structural or spin-state transitions, electron transfers, and magnetic ordering of Fe moments. Results need to be compared to the predictions established from X-ray diffraction; any disagreement larger than the error bars on the proportions must be considered in terms of defective chemical compositions or stoichiometric effects. In the case of topologically disordered systems, the broadening and overlapping of lines needs to be described and modeled with discrete distributions of either quadrupolar splitting or hyperfine fields. When the profile of a spectrum is asymmetrical, a linear correlation should be performed with that of isomer shifts. The ratio $\langle\Delta^2\rangle/\langle\Delta\rangle^2$ is a parameter used to quantify topological disorder and enable conclusions to be made with respect to material behaving as amorphous.²⁶³

In addition to the usual applications of ^{57}Fe -Mössbauer spectroscopy, discrimination between surfaces and interiors and between static and dynamic magnetic effects is of interest for magnetic nanoparticles.^{262,264–274} The comparison of zero-field and in-field Mössbauer spectra provides models of the surface from structural and magnetic points of view; numerous such studies have been performed on maghemite and ferrite nanoparticles. Nevertheless, experiments at room temperature can be suitable to provide information regarding the nature of assemblies of nanoparticles. The presence of both quadrupolar and magnetic features with broadened or asymmetrical lines can be explained according to two main situations: (i) nanoparticles with different sizes, *i.e.* a mixture of nanoparticles exhibiting fast and slow superparamagnetic relaxation phenomena and static magnetic effects, or (ii) a mixture of noninteracting, weakly interacting, and strongly interacting nanoparticles resulting in well-dispersed, rather close, and aggregated nanoparticles, respectively. One way to identify the more realistic explanation of the two situations can be obtained from TEM by imaging hundreds of nanoparticles. A second method is to apply a small magnetic field (typically <0.5 T) to the sample to determine if the magnetic fraction is increased. Dynamic and static effects are influenced by external fields if the external magnetic fields are large enough.

Analysis of hyperfine structures resulting from zero-field and in-field Mössbauer spectra enabled characterization of the nonchemical homogeneity within monodisperse nanoparticles. An illustration of the usefulness of this characterization is found with some CoFe_2O_4 nanoparticles prepared by thermal decomposition.²⁷⁵ In this case, in-field Mössbauer hyperfine structures were modeled using joint distributions of canting angles and effective fields for both tetrahedral and octahedral Fe sites. This modeling enabled estimation of the respective hyperfine fields that were consistent with the zero-field Mössbauer spectrum obtained at the same temperature. Such a description gives rise to a nonhomogeneous cationic distribution with an excess of Co and Fe in the central and external part, respectively, of nanoparticles.

Because surface contributions are enhanced in confined systems, the occurrence of an Fe-oxide layer covering metallic nanoparticles, its chemical composition and its thickness can be evidenced by Mössbauer spectroscopy. Depending on the procedure by which they are synthesized, magnetite nanoparticles can rapidly undergo oxidation to yield nonstoichiometric magnetite ($\text{Fe}_3\text{O}_4\cdot\text{Fe}^{2+}\text{Fe}^{3+}_2\text{O}_4$) or maghemite ($\gamma\text{-Fe}_2\text{O}_3\cdot\text{Fe}^{3+}_2\text{O}_3$). X-ray diffraction is not suitable to distinguish between those two phases and to estimate their proportions because the lattice parameters are not different in the bulk state. The mean isomer shift value is a crucial parameter to determine the mean valence state and, consequently, the mean stoichiometry or the proportions of both magnetite and maghemite in a core-shell model. However, this naive description gives rise to an estimation of the thickness of maghemite shells (about 3 nm), which has been found to be rather independent of the size and morphology of nanoparticles and on the chemical route and is thus likely inaccurate.^{196,197,224,225}

A second fitting model considers two components corresponding to those of ideal magnetite and maghemite, as illustrated in Figure 4.27. Fitting experimental data with this model implies that Fe-oxide nanoparticles smaller than 6 nm consist only of maghemite except those synthesized under microoxic conditions; no magnetite is present in ultrasmall nanoparticles. This conclusion contradicts reports that concluded that the disappearance of the Verwey transition results from confined effects.

In addition, the mixed analysis of hyperfine structures characteristic of nonfunctionalized and functionalized nanoparticles provides information regarding the chemical bonds between the core and the grafted molecules that can be compared to some predictions established from *ab initio* calculations.^{197,276,277} Figure 4.28 illustrates the Mössbauer spectra of maghemite recorded at 77 K before and after grafting with dopamine: one new magnetic component suggests that the dopamine is linked to the octahedral Fe unit and that a partial electron transfer occurs. Those two features are consistent with *ab initio* predictions²⁷⁷ (see Figure 4.28).

The magnetic properties characteristic of the bulk and surface of nanoparticles can be obtained from analysis of in-field Mössbauer spectra assuming a core-shell magnetic structure. The external magnetic field must be strong enough to overcome superparamagnetic relaxation phenomena and to split the zero-field hyperfine structure into a well-resolved, in-field hyperfine structure (typically 8–10 T). Surfaces cause a breaking of symmetry and, thus, a loss of neighbors. Surfaces also lead to distortions of structural lattices, giving rise to changes of interatomic distances and contributing to changes of magnetic moments. Interactions between superficial magnetic moments are modified by surfaces, and topological frustration plays an important role in favoring noncollinear magnetic moments. The core-shell model assumes a shell with randomly oriented magnetic moments and a core with ideally oriented magnetic moments parallel or perpendicular to the external magnetic field. Thus, in-field hyperfine structures can be decomposed into two magnetic components: one reflecting a random

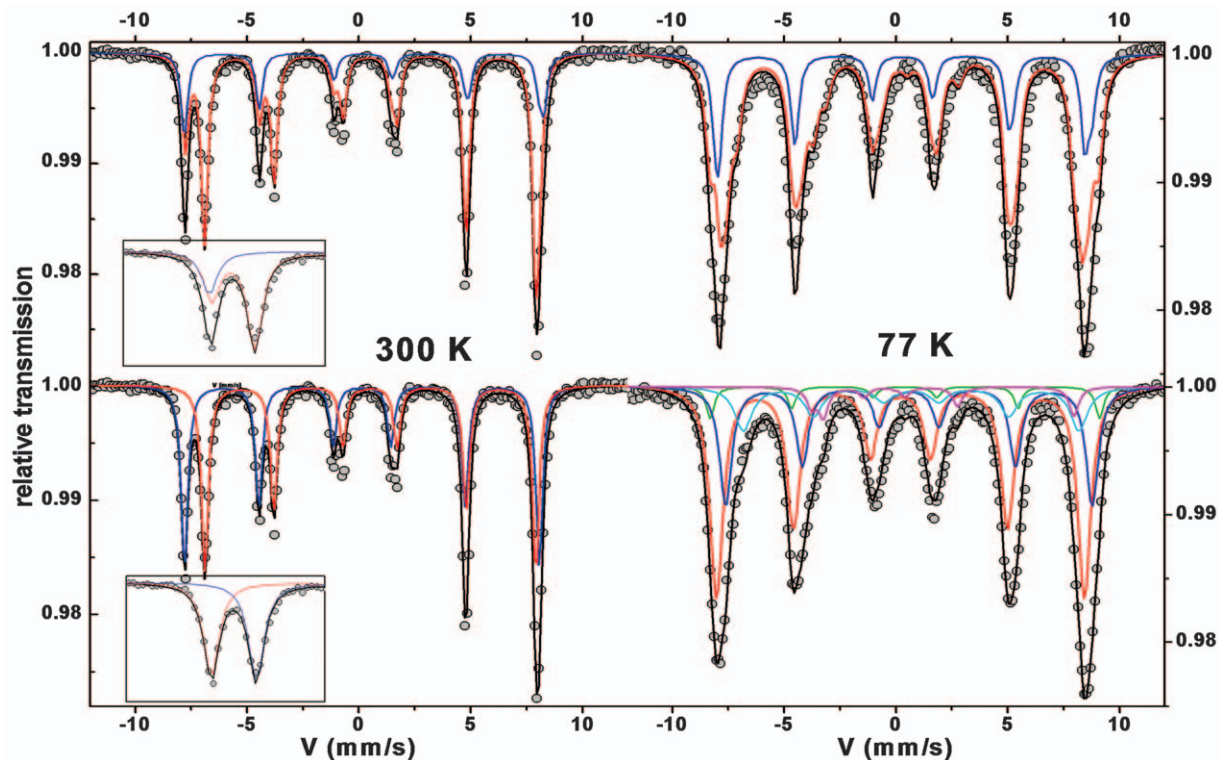


Figure 4.27 Examples of Mössbauer spectra at (left) 300 and (right) 77 K. The bottom spectra show decomposition into several components as generally done with a nonstoichiometric magnetite phase, and the top spectra were modeled assuming two stoichiometric phases as maghemite and magnetite. The insets show the differences of the left outermost lines and the hyperfine spectra for these two phases.

Adapted with permission from T. J. Daou, S. Begin-Colin, J. M. Greneche, F. Thomas, A. Derory, P. Bernhardt, P. Legaré and G. Pourroy, *Chem. Mater.* 2007, **19**, 4494. Copyright (2007) American Chemical Society.

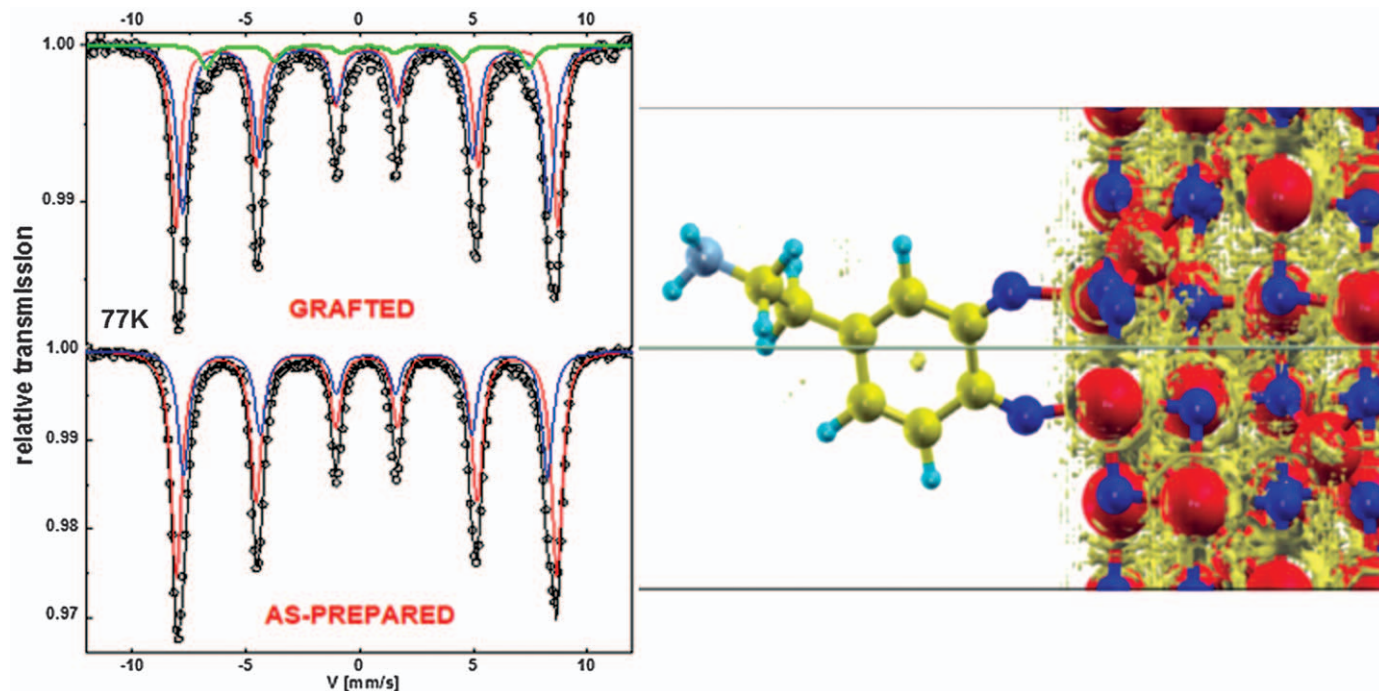


Figure 4.28 ^{57}Fe -Mössbauer spectra of maghemite particles (bottom) and their related nanohybrids resulting from dopamine grafting (top) recorded at 77 K. (right) Ionicity of the system, estimated by 0.5 isosurface of reduced density gradient (EPLF) in LDA + U.²⁷⁷
 Adapted with permission from J. Fouineau, K. Brymora, L. Ourry, F. Mammeri, N. Yaacoub, F. Calvayrac, S. Ammar-Merah and J.-M. Greneche, *J. Phys. Chem. C*, 2013, **117**, 14295. Copyright (2013) American Chemical Society.

distribution of magnetic moments with line area ratios of 3 : 2 : 1 : 1 : 2 : 3 and the second one typical of a saturated system as illustrated in Figure 4.29, which is attributed to the shell and core contributions. Such a model has been applied to nanoparticles of $\gamma\text{-Fe}_2\text{O}_3$ maghemite, which are ferri-magnetic.²⁷⁸⁻²⁸² The thickness of the canted magnetic superficial layer can be estimated from $e = r/2\sin^2\theta$ (assuming $e \ll r$), where r and θ represent the mean radius of the nanoparticles and the angle between the hyperfine field held by the nucleus probe and the propagation direction of the γ -beam, respectively. Figure 4.29 illustrates a series of in-field Mössbauer spectra obtained on dispersed nanoparticles of maghemite, *i.e.* noninteracting nanoparticles, with different sizes.²⁷⁹ The intensities of intermediate lines increase when the size decreases, suggesting that the canting of Fe magnetic moments increases: smaller sizes correlate to larger surface/volume ratios, suggesting that canting originates from the surface. It is important to

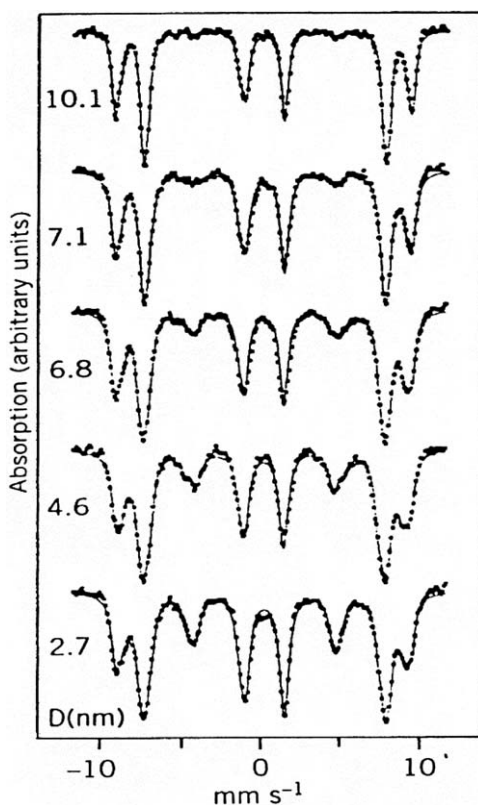


Figure 4.29 In a 6 T field, Mössbauer spectra of maghemite nanoparticles of different sizes. The sizes are mentioned on the left.

Adapted with permission from Hyperfine Interactions, Spin Canting in $\gamma\text{-Fe}_2\text{O}_3$ Nanoparticles, Volume 112, 1997, 97-100 E. Tronc, P. Prené, J. P. Jolivet, J. L. Dormann and G. M. Greneche. Copyright © 1998, Kluwer Academic Publishers. With permission of Springer.

emphasize that the zero intensity of intermediate lines does not mean that there is no canting but that the surface/volume ratio is too small to be observed.

The examples highlighted in this section illustrate how zero-field and in-field transmission Mössbauer spectroscopies provide information to understand the chemical, structural, and magnetic properties of individual and assemblies of magnetic nanoparticles. A particular application is the understanding of mixed magnetite and maghemite nanoparticles. Nevertheless, those results require improvement of experimental conditions and instrumental facilities, and special attention and particular strategy in modeling the hyperfine structures, which is a delicate task. In addition, complementary techniques, including field-cooled and zero-field-cooled magnetic measurements and X-ray magnetic circular dichroism, are necessary to compare Mössbauer results, requiring that the measured samples be previously characterized by X-ray diffraction and TEM. Finally, Monte Carlo, *ab initio*, and molecular dynamics computer modeling are also useful to study magnetic nanoparticles.

4.4.1.2.6 HAADF-STEM, EDX, and EELS. If analytical information is required to characterize nanoparticles, it can be obtained with the HAADF-STEM incoherent imaging mode due to the direct dependence of the image intensity on the atomic number.²⁸³ However, a large number of multiphase or heterogeneous particles are composed of elements with relatively close atomic numbers, which does not make HAADF-STEM tomography efficient. In these cases, the chemical composition of nanoparticles can be probed using energy dispersive X-ray spectroscopy (EDX) at the nanoscale and even at the atomic scale, depending on the spot size and intensity available in the STEM mode.²⁸⁴ High levels of chemically resolved spatial resolution and chemical sensitivity are possible using electron energy loss spectroscopy (EELS) and the related technique energy-filtered TEM (EFTEM). These techniques can be implemented on transmission electron microscopes equipped with electron spectrometers for the determination of the chemical composition of nanoparticles as well as their electronic and optical properties. For light elements such as oxygen for which the EDX analyses are not efficient, the acquisition of chemical maps by EELS is the best way to obtain spatially solved compositional information.²⁸⁵ As a representative example, EELS analysis of copper phosphide nanoparticles, synthesized by the reaction of preformed copper nanoparticles with P_4 , is shown in Figure 4.30.²⁰⁷ Two-dimensional analyses by EELS have been performed, using the EFTEM imaging mode. By superimposing the two-dimensional chemical maps of the three elements of interest (P, O, and Cu), visualization of their relative distribution is obtained that illustrates the core-shell structure of the nanoparticles, with a core composed of copper and a shell constituted by Cu_3P , which is partially oxidized on the surface due to air exposure.

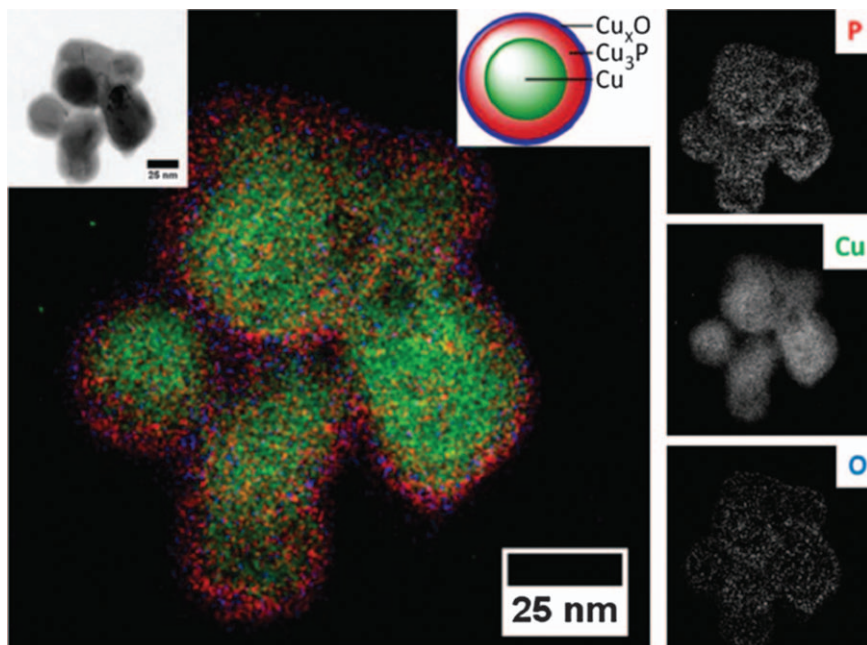


Figure 4.30 Core-shell structure of copper phosphide nanoparticles: Left: Two-dimensional relative map of the studied object with phosphorus in red, copper in green, and oxygen in blue. The left inset shows the TEM image of the nanoparticles. The right inset is a scheme of the particle structure. Right: elemental projections for each element obtained after background extraction from the total inelastic signal of the corresponding EELS.

Adapted from ref. 207 with permission from The Royal Society of Chemistry.

4.4.2 Characterization Techniques for Nanoparticle Coatings

It is important to characterize the coatings of nanoparticles and nature of the bonds formed between the coupling or anchoring groups and the surfaces of nanoparticles. Anchoring groups have different binding affinities that affect the final properties of nanoparticles (Sections 4.3.2 and 4.3.3). Strong anchoring groups tend to favor high densities of molecules at the surfaces of nanoparticles and, thus, promote stability, anti-biofouling ability, and high loading of bioactive molecules. For example, when the density of polyethylene glycol (PEG) reaches a threshold, nonspecific adsorption of protein to the nanoparticles is largely prevented.^{286,287}

In this section, the main characterization techniques used to confirm the grafting of molecules are detailed. These include IR spectroscopy, thermogravimetric analysis (TGA), dynamic light scattering (DLS), zeta potential measurements, transmission electron microscopy (TEM), photoemission spectroscopy (XPS), and elemental analysis. Elemental analysis brings valuable information regarding the presence of molecules and the grafting rate

when specific elements of molecules such as N, Si, and P are quantified with respect to iron. The combination of these techniques is useful for demonstrating the presence of the molecules at the surfaces of nanoparticles, but evaluation of the strength of anchoring remains a difficult challenge.

4.4.2.1 Fourier Transform Infrared Spectroscopy

IR spectroscopy is a suitable technique to characterize both iron oxide nanoparticles and their molecular and polymer coatings. Typically, the presence of iron oxide is confirmed by the presence of Fe–O bands in the range of 800–200 cm^{-1} that usually do not overlap with the vibration bands of organic or polymer coatings. Magnetite (Fe_3O_4) displays one broad band located at 580–590 cm^{-1} , whereas maghemite ($\gamma\text{-Fe}_2\text{O}_3$) displays several bands between 800 and 400 cm^{-1} that vary in number and resolution depending on the structural order of vacancies.^{85,234}

The first step in confirming the presence of a coating at the surface of nanoparticles is to compare the IR spectra of molecules to those of nanoparticles coated with the same molecules after purification. The characteristic bands of the molecules of the coating need to be identified in the IR spectra of purified, functionalized nanoparticles. The IR signatures of the coating depend on their structure, their functional groups, and on the types of bonds formed with the Fe–OH surfaces. Thus, the evolution of IR bands of the anchoring groups, with respect to shifts of position and changes in intensity, must be carefully investigated to determine the nature of surface complexes.

For silane coatings, IR spectroscopy is helpful to characterize the formation of Si–O–Fe bonds at the surfaces of iron oxide nanoparticles and Si–O bonds formed within polysiloxane shells. Usually, the appearance of bands between 1000 and 1150 cm^{-1} in the IR spectra after ligand exchange are attributed to Si–O–Si vibrations, confirming the presence of silane coatings. Alkyl chains of organosilanes display typical bands near 2920 and 2850 cm^{-1} , which are attributed to the asymmetric and symmetric, respectively, CH_2 stretching bands. For silica shells coated around inorganic cores, IR spectroscopy can be used to characterize the formation of Si–O–Si matrixes, which typically vibrate in the range of 1000 to 1100 cm^{-1} .^{156,159}

For molecules bearing carboxylate groups as anchoring agents, interactions of carboxylates with the surfaces of nanoparticles are confirmed by the appearance of asymmetric and symmetric COO^- stretching bands of metal carboxylates between 1700 and 1400 cm^{-1} . These asymmetric $\nu_{\text{as}}(\text{COO}^-)$ and symmetric $\nu_{\text{s}}(\text{COO}^-)$ bands are usually observed in the ranges of 1650–1500 cm^{-1} and 1440–1340 cm^{-1} , respectively. The wavenumber difference ($\Delta\nu$) between the $\nu_{\text{as}}(\text{COO}^-)$ and $\nu_{\text{s}}(\text{COO}^-)$ bands enables identification of the type of carboxylate surface complex, which can be monodentate ($\Delta\nu = 200\text{--}320 \text{ cm}^{-1}$) with one metal ion coordinated by one carboxylic oxygen atom, bidentate ($\Delta\nu = <110 \text{ cm}^{-1}$) with one metal ion coordinated by two oxygens of the same carboxylate, or bridging

($\Delta\nu = 140\text{--}190\text{ cm}^{-1}$) with two metal ions coordinated by two oxygens of the same carboxylate.²⁸⁸ The nature of the carboxylate complex depends on parameters such as the coating strategy and the synthetic method used to form the nanoparticles. Most reported surface complexes are either bridging or bidentate.²⁸⁹

Dopamine-based molecules are stable anchors for iron oxide nanoparticles.¹⁷² The mechanism of catecholate bonding has been studied for several years, and different interactions of catecholate groups with surfaces have been proposed: monodentate (one of the two catechol O^- groups binds to a metal cation with loss of a proton), bidentate (two oxygen atoms in catechol bind to a single metal ion), bridging (both O^- groups coordinate to two adjacent metal cations with loss of two protons), or hydrogen bonding.²⁹⁰ The type of complex depends on the pH. Bidentate interactions are favored at $\text{pH} > 5$ but promote dissolution of surface iron oxide. That observation might explain some problems reported with respect to the stability of this bond in water and biological fluids after long exposure periods.^{291–294} In IR spectra, the comparison between free molecules and grafted molecules at the surfaces of nanoparticles shows a strong characteristic band between 1650 and 1600 cm^{-1} attributed to the asymmetric $\nu(\text{C-O})$ stretching vibration of the catecholate function coupled with the $\nu(\text{C=C})$ vibration of the alkene function. These vibrations are related to the formation of a coordinate bond between atoms on the surfaces of nanoparticles and the catecholate aromatic ring.^{293,294} The vibration bands corresponding to C=C stretching between 1550 and 1650 cm^{-1} and vibration bands corresponding to C-O stretching and bending (between 950 and 1300 cm^{-1}) also appear modified upon surface binding.

P-OH and P=O bonds in phosphonate-containing molecules are characterized by the presence of bands at $900\text{--}1000$ and around $1200\text{--}1250\text{ cm}^{-1}$, respectively.^{85,197,295,296} However, clear identification of P-O bands is difficult because the bands overlap with bands from other groups, such as phenyl, C=C , C-C , and C-H bands. IR characterization of phosphonate-containing molecules at different synthetic steps might be possible *via* monitoring of the phosphonate bands in the $1250\text{--}800\text{ cm}^{-1}$ region. Comparison of phosphonate bands before and after grafting mostly reveals that phosphonate bands evolve, but unambiguous identification of the surface interactions is difficult. IR characterization of phosphonate-containing dendrons (named D1 in Figure 4.31) at different synthetic steps enabled identification of the P=O band around 1200 cm^{-1} and the P-OH bands at 1020 and 999 cm^{-1} .^{84,85} After dendronization of two types of iron oxide nanoparticles, the intensity of the P=O band decreased, the P-OH bands disappeared, and new bands appeared due to a modification of the electron density around the atoms with the formation of Fe-O-P bonds. For nanoparticles synthesized by thermal decomposition, two bands were clearly observed at 1047 and 985 cm^{-1} and were attributed to Fe-O-P bonds. For nanoparticles synthesized by coprecipitation, only one Fe-O-P band was identified at 975 cm^{-1} with the second Fe-O-P band likely contained within the shoulder (around 1050 cm^{-1}) of the band at 1109 cm^{-1} (attributed to the

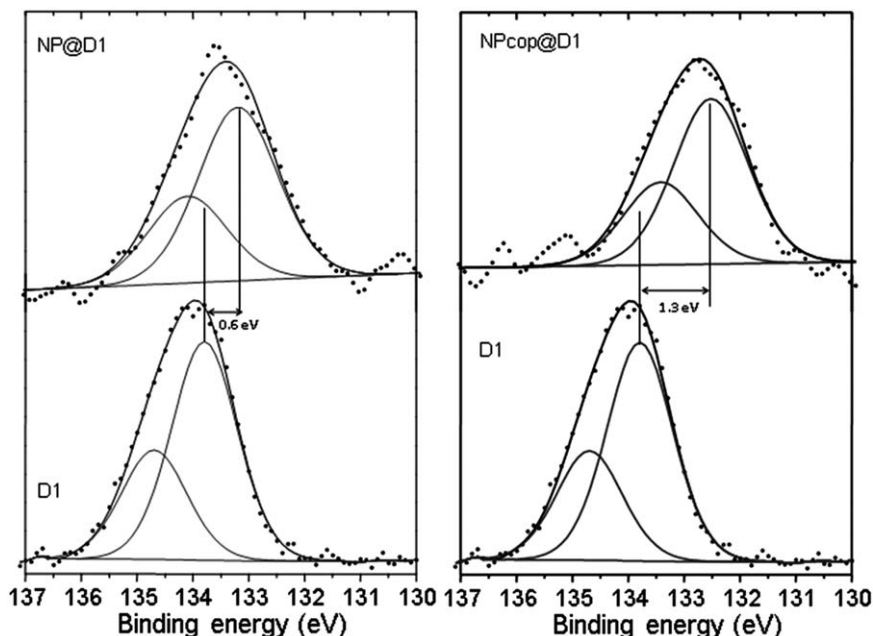


Figure 4.31 P2p XPS spectra of NP@D1 and D1 (left) and of NPcop@D1 and D1 (right) with D1 corresponding to a dendron-bearing phosphonate anchoring agent, NP to nanoparticles synthesized by thermal decomposition and NPcop to nanoparticles synthesized by co-precipitation. Adapted from ref. 83 with permission from The Royal Society of Chemistry.

aromatic C–C bonds). Based on the IR results, the phosphonate surfaces were possibly binuclear for both types of nanoparticles. However, hydrogen bonding might also be responsible for the shift or intensity decrease of the P–OH and P=O peaks. The combination of IR and XPS spectroscopies enables stronger conclusions to be drawn, as explained below.

4.4.2.2 X-ray Photoelectron Spectroscopy

X-ray photoelectron spectroscopy (XPS) is used to validate the successful coating of nanoparticles by considering C1s, O1s, N1s, P2p, and Fe2p spectra.⁸³ The C1s spectrum typically displays peaks at ~285, 286.5, 288.8, and 289.5 eV, attributed to atoms in C–C, C–H, C–O (ester bonds), O–C=O, and C=O (carbonyl) bonds.²⁹⁷ The C1s peak attributed to C–C and C–H bonds is generally used as reference and fixed at 285 eV. Carbonates at the surface of nanoparticles produce bands at ~290 eV. The appearance of C–N and N–C=O peaks at 285.8 and 287.3 eV, respectively, is due to the presence of amines and amides.

The consideration of O1s peaks is not the most suitable way to discriminate between the types of complex formed at the surfaces of

nanoparticles. The O1s peak of uncoated iron oxide nanoparticles synthesized by coprecipitation was deconvoluted into four spectral bands at 530.1, 531.0, 532.1, and 533.7 eV attributed to lattice oxygen (O^{2-}) (Fe–O–Fe) in the metal oxide, hydroxides (Fe–OH), water (Fe–OH₂), and carbonates, respectively, at the surface of iron oxide. Carbonates lead to an O1s band at 533.2 eV in correlation with the C1s band at 290 eV. After coating nanoparticles, the presence of supplementary peaks due to the coating molecules, such as the peak at 286.6 eV indicating the presence of C–O bonds mainly from PEG chains, confirms successful coating, even if the carboxylate anchoring is difficult to analyze by this technique. Apart from the presence of Si in the XPS spectrum, silane coatings lead to the appearance of two pronounced peaks in O1s spectra at \sim 531.5 and \sim 532.5 eV. These peaks are located at approximately +2 eV with respect to the principal Fe–O peak (\sim 530 eV) and can be assigned to Fe–O–Si and Si–O bonds, respectively.²⁹⁸ After grafting phosphonate-containing molecules, a peak located at a binding energy of \sim 531.5 eV is observed, corresponding to the contribution of P–O bonds (P=O, P–OH, and Fe–O–P). These observations are in agreement with bibliographic data that report the binding energies of M–O–P (M = metal), P=O, and P–OH to be in the range of 531.3 to 532.2 eV.^{85,197}

The P2p spectra of phosphonate-containing molecules exhibit two peaks at \sim 133.8 and 134.7 eV, corresponding to P2p_{3/2} and P2p_{1/2}, respectively.^{83,197,299,300} The P2p_{3/2} and P2p_{1/2} peaks present low binding energy differences between both 3/2 and 1/2 components due to a spin-orbit coupling of about 0.9 eV. When the molecules are grafted, a shift of the peaks towards lower binding energies is observed, and this shift is characteristic of the formation of P–O–Fe bonds. The value of the shift can be correlated to anchoring strength. For example, the P2p spectrum (Figure 4.31) of phosphonate-containing dendrons exhibits two components at \sim 133.8 and 134.7 eV, corresponding to P2p_{3/2} and P2p_{1/2}, respectively. When the dendrons with phosphonate anchoring agents were grafted onto iron oxide nanoparticles, a broadening and a shift of the peaks towards lower binding energies were observed. These changes were characteristic of the formation of P–O–Fe bonds.²⁹⁹ The observed shifts are consistent with oxygen atoms in a more shielded environment than for the single molecule (D1). The shielding likely arises because the oxygen atoms are linked not only to phosphorus but also to the iron ions in the nanoparticles. The environment of the phosphorus atoms is less electronegative; therefore, the energy required to remove an electron from 2p core levels of phosphorus atoms is reduced, decreasing the binding energy. However, the shift observed with nanoparticles synthesized by coprecipitation was higher than that observed with nanoparticles synthesized by thermal decomposition. This difference demonstrates that the phosphonate surfaces differed depending on the type of nanoparticle.¹⁹⁷ On the basis of the XPS and IR data, tri-nuclear complexes were suggested for nanoparticles synthesized by coprecipitation. In N1s spectra, peaks can appear at 400 and 406.08 eV, and these are attributed to tertiary nitrogen and amine bonds, respectively.

4.4.2.3 Thermogravimetric Analysis

Thermogravimetric analysis (TGA) enables estimations of the mass fraction between organic coatings and inorganic nanoparticles. In TGA, samples are heated from ambient temperature to ~ 1000 °C in the range of $5\text{--}20$ °C min^{-1} , and loss of mass due to degradation of organic components is recorded as a function of temperature. TGA is not relevant for iron oxide core-silica shell nanoparticles because silica is highly stable over the range of temperatures used with TGA. TGA is usually performed under an atmosphere of N_2 to limit oxidation.

Observed weight loss is evidence supporting the presence of organic coatings and can be used to evaluate grafting rates. For example, TGA was used to estimate the mass fraction of grafted silanes at the surface of cobalt ferrite nanoparticles.¹⁴⁴ Weight losses of the nanoferrite nanoparticles grafted with silanes containing PEG, amines, or carboxylates were in the range of 70–80%. The number of silane ligands per particle was calculated to be 2201, 6712, and 2495 silanes per particle for these three ligands. The authors reported that the surface coverage obtained after silane grafting was explained by the formation of a multilayered polysiloxane shell. It is important to compare experimental grafting rates with theoretical ones (using the molecular surface area) to distinguish between monolayer or multilayer coatings.

4.4.2.4 Dynamic Light Scattering and Zeta Potential

Dynamic light scattering (DLS) and zeta-potential measurements are usually used concomitantly to confirm the grafting of molecules and to establish the colloidal stability of nanoparticles dispersed in aqueous solutions (Section 4.4.1.1). In DLS, the light scattering by nanoparticles in solution is used to sense Brownian motion, which is used to provide information about diffusion coefficients and dynamic size distributions. When the size of grafting molecules is large enough, the particle size distribution of coated nanoparticles shifts towards larger sizes relative to nanoparticles before coating.

Zeta potential is defined as the electrical potential at the slipping plane of the double ionic layer of the coated nanoparticles (Section 4.4.1.1). In zeta potential measurements, by applying an alternative electric field, the electrophoretic mobility of the coated iron oxide-nanoparticles dispersed in aqueous solutions can be measured. Application of the Henry equation determines the zeta potential. In a first approximation, the zeta potential measurements give an indication of the surface charge of the coated nanoparticles. When zeta potential values are larger than 30 mV in absolute value, suspensions of nanoparticles bearing charged groups generally have high colloidal stability, which is ensured by electrostatic repulsions. Nevertheless, nanoparticles coated with non-charged polymers or molecules can have high colloidal stability that is ensured by steric repulsions, even with zeta potential values below 30 mV. Zeta potential measurements also enable

evaluation of the isoelectric point of the coated iron oxide nanoparticles, which correspond to the pH at which the zeta potential is equal to 0 mV. These studies are performed by measuring zeta potentials at different values of pH. The isoelectric point is an important parameter when evaluating the colloidal stability of coated iron oxide nanoparticles. After coating, the isoelectric point of iron oxide nanoparticles is generally shifted. This shift provides evidence of coating. It is because their isoelectric point is around 6.8–7 that naked iron oxide nanoparticles are not stable in suspensions at physiologically relevant pH.

Zeta potential measurements are well-suited to characterize the surface charge of different grafted silanes, including PEG silanes, aminosilanes, and carboxysilanes.¹⁴⁴ For carboxysilane-coated iron oxide nanoparticles, the isoelectric point is at pH 3.1 (Figure 4.32). This value is expected given the typical pK_a of carboxylic acids (~ 4.5). The constant value of the zeta potential of approximately -30 mV above pH 5 ensures the colloidal stability of carboxysilane-coated iron oxide nanoparticles. For aminosilane-modified iron oxide nanoparticles, the isoelectric point is close to 10.4. Zeta potential is close to $+40$ mV for $pH < 6$. These observations explain the colloidal stability of these nanoparticles in acidic aqueous media. Because PEG coatings are neutral, the isoelectric point of PEG-coated iron oxide nanoparticles (~ 8) is intermediate between the other two coatings in the study. The effect on zeta-potential values of a silica coating on the surface of iron oxide nanoparticles was also investigated.¹⁵⁶ The isoelectric point shifted from ~ 7 to 2 after coating with silica. The silica-coated iron oxide nanoparticles displayed a high colloidal stability in water in a wide range of pH values ≥ 3 .

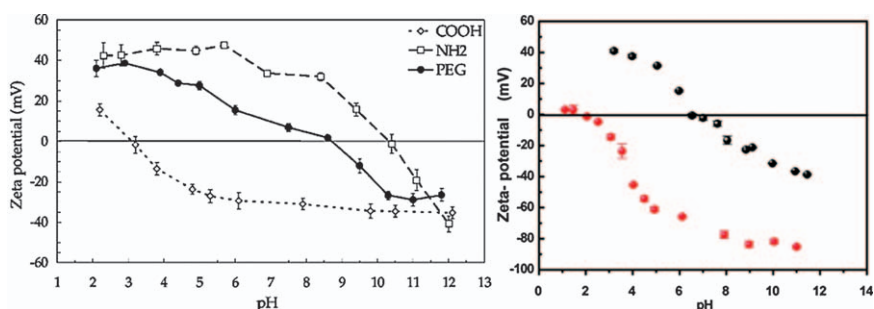


Figure 4.32 (Left) Evolution of zeta-potential measurements as a function of pH for three silanes modified with different end groups: carboxylate, PEG, and amine. (Right) Effect of a silica coating on the zeta potential of iron oxide nanoparticles measured as a function of pH.

Adapted with permission from (left) R. De Palma, S. Peeters, M. J. Van Bael, H. Van den Rul, K. Bonroy, W. Laureyn, J. Mullens, G. Borghs and G. Maes, *Chem. Mater.* 2007, **19**, 1821. Copyright (2007) American Chemical Society; and (right) S. L. C. Pinho, G. A. Pereira, P. Voisin, J. Kassem, V. Bouchaud, L. Etienne, J. A. Peters, L. Carlos, S. Mornet, C. F. G. C. Geraldés, J. Rocha and M.-H. Delville, *ACS Nano*, 2010, **4**, 5339. Copyright 2010 American Chemical Society.¹⁵⁶

4.4.2.5 Transmission Electron Microscopy

Transmission electron microscopy (TEM) is a choice method to image inorganic or dense coatings at the surfaces of iron oxide nanoparticles. Typically, nonporous-silica- or mesoporous-silica-coated iron oxide nanoparticles are well suited for TEM. TEM enables determination of the thickness of silica shells with resolution below the nm scale. For mesoporous silica coatings, TEM can also be used to visualize pore distributions. However, TEM of an organic coating is not useful because organic coatings are typically transparent to electron beams. Nevertheless, when a polymer shell is particularly dense, it can sometimes be imaged using TEM by adjusting the TEM parameters to limit the degradation of the organic shell.⁸⁶

The development of iron-oxide-based nanoparticles for biomedical applications faces several challenges with respect to the design of organic coatings and grafting onto the surface of nanoparticles. Indeed, molecules anchored at the surfaces of nanoparticles must provide functionalities for further grafting of dyes for optical imaging, targeting ligands to reach specific tissues or cells, or therapeutic agents for drug delivery. However, in addition to the design of bioactive molecules, grafting of these molecules must be controlled to ensure hydrodynamic sizes are kept below 100 nm to achieve favorable biodistribution. In addition, strong bonds between molecules and nanoparticles must be confirmed to avoid their desorption after *in vivo* injection. The mean hydrodynamic size (smaller than 100 nm) of coated nanoparticles depends on the nature of the grafted molecules and on the grafting strategy. To be used as a contrast agent for MRI, iron oxide nanoparticles must also display large values of saturation magnetization. All of these parameters (size distribution, mean size, shape, composition, hydrodynamic size, magnetic properties, and coating efficiency) are important to control and require the combination of different characterization techniques described in this chapter.

4.5 Magnetic Characterization

VLAD SOCOLIUC, VICTOR KUNCSEK,* RODICA TURCU AND
LADISLAU VÉKÁS*

4.5.1 Magnetic Parameters of Iron Oxide Nanoparticles of Interest to MRI

Superparamagnetic iron oxide nanoparticles have a diverse set of potential biomedical applications, including functional MRI, hyperthermia treatment for malignant cells, magnetic drug targeting, and manipulation of cell membranes.^{13,301,302} The unique advantages of iron oxide nanoparticles compared to other biomedical materials are related to the possibility of designing a large diversity of multifunctional magnetoresponsive nano-systems^{303–305} that could be able to satisfy both diagnostic and therapeutic purposes. These so-called nano-theranostic systems can contain both a drug and an imaging agent within a single formulation, and are potentially suitable for monitoring drug delivery, drug release, and drug efficacy. The choice of materials and structures for theranostic systems is constrained by biocompatibility, biodistribution, pharmacokinetics, toxicity, and clearance. For biomedical applications, iron oxide nanoparticles are coated and functionalized with organic molecules that can have therapeutic or targeting purposes or can aid with colloid stabilization, biocompatibility, or blood circulation time.^{302,304,306} Nevertheless, the magnetic core has a main actuation role. It is sensitive to static magnetic field distributions (for example, for magnetic separations or in magnetic-field-based drug targeting) and can be activated under AC magnetic fields (for instance, for locally induced drug release and hyperthermia treatments). The core also influences the fluctuation of the local magnetic fields, hence its ability to act as contrast agents for magnetic resonance imaging.

The majority of MRI is based on the idea that the nuclear magnetic moment of protons in different tissues, which all contain water and hence ^1H nuclides, relax differently after the absorption of an incident photon of radio-frequency.^{16,299,302,307,308} Magnetic relaxation, including nuclear relaxation, corresponds to the return to thermodynamic equilibrium of a spin system, nuclear spin in the case of nuclear relaxation, after being excited by an absorbed energy (see Chapter 2.1). For ^1H -MRI, signal intensity depends on the concentration of protons and nuclear relaxation times. A longitudinal, temperature-dependent spin-lattice relaxation time, T_1 , and a transversal, spin-spin relaxation time, T_2 , are defined for nuclear relaxation. Because each tissue has a unique water content with protons in different molecular environments, maps of signal intensities in MRI reflect the composition of the analyzed tissues. However, when imaging a single tissue, the contrast can be modulated only *via* the two relaxation times of the protons and the density of the proton nuclei. If an additional relaxation channel is available, as introduced by a contrast agent, the relaxation time

T_i is always decreased (according to the summation of transition probabilities *via* the two parallel channels). For a unitary report, independent of the concentration of the contrast agent, relaxivity is defined as the ratio between the transition probability $R = 1/T$ and the molar concentration of the contrast agent $[C]$ (Chapter 2.1). Accordingly, the proton relaxivity in the presence of the contrast agent is shown in eqn (4.14), where $i = 1$ or 2 for the longitudinal and transversal, respectively, relaxation times (R) and relaxivities (r).

$$r_i = r_i^0 + r_i^{\text{ad}} = \frac{1}{[C]} \frac{1}{T_i} = \frac{1}{[C]} \left(\frac{1}{T_i^0} + \frac{1}{T_i^{\text{ad}}} \right) \quad (4.14)$$

In eqn (4.14), r_i^0 is the usual proton relaxation channel (without the presence of the contrast agent), and r_i^{ad} is the additional relaxation channel due to the presence of the contrast agent. When looking to a contrast agent as surrounded by water molecules (protons) arranged in successive coordination spheres, the additional relaxation mechanism can be assumed to present two contributions, one coming from the first coordination sphere (inner sphere) and the other from the next coordination spheres (outer sphere). For molecular contrast agent such as the majority of Gd^{III} -based contrast agents, the inner-sphere contribution is the primary contribution to spin-lattice relaxation (Chapter 2.1). For large-sized iron oxide contrast agents, on the other hand, the outer-sphere contribution is the major contributor to relaxivity (Section 4.1.2).

An important component of T_1 - and T_2 -shortening contrast agents is the presence of uncompensated electron spins, or magnetic moments, that influence the relaxation of nearby protons. The inner-sphere relaxivity model is described by the Solomon–Bloembergen theory,^{309,310} and the outer-sphere relaxivity model is described by Freed theory.⁴⁹ In both models, the relaxivities are proportional to the square of the effective spin (magnetic moment) of the contrast agent and the square of its gyromagnetic factor, and hence its Landee factor g . Therefore, contrast agents with large spin values and high magnetic moments tend to be more efficient contrast agents. One of the ions with the highest spin value ($S = 7/2$) and reasonable g factor is Gd^{III} . However, Gd^{III} is toxic in the hydrated form $[\text{Gd}(\text{H}_2\text{O})_8]^{3+}$. Therefore, to minimize toxicity while maintaining magnetic properties, paramagnetic Gd^{III} complexes are widely used.³¹¹ These complexes are thermodynamically stable, inert complexes with the complexing ligand leaving a free coordination site such that water can interact with the metal ion. Relaxation mechanisms for different commercially available Gd^{III} -based paramagnetic complexes have been discussed elsewhere.³¹²

Superparamagnetic contrast agents, iron oxide nanoparticles in nanometer size regime, have higher magnetic moments than Gd^{III} complexes. In superparamagnetic nanoparticles, the superspin of the whole nanoparticle is a summation of the spins in each unit cell. The relaxivity of such nanoparticles is the result of the dipolar interactions between the many

proton spins in the outer-sphere water molecules and the superspin of the contrast agent. As discussed in Section 4.1.2, only the outer-sphere component of relaxivity has to be taken into account for iron oxide nanoparticles. The longitudinal relaxivity in the outer-sphere model is given by eqn (4.15).³¹²

$$r_1^{\text{ad}} \propto FS_{\text{eff}}^2 [7j(\omega_S \tau_D) + 3j(\omega_H \tau_D)] \quad (4.15)$$

In this equation, F is a factor that depends on the nuclear and electronic gyromagnetic factors as well as on the nuclear spin, S_{eff} is the effective spin of the contrast agent, which is proportional to its effective magnetic moment, ω_H is the angular frequency of the proton, which is equal to the nuclear Larmor frequency (in the MHz range for MRI), and ω_S is the angular frequency of the superspin. ω_S is directly related to the magnetic relaxation time of the superspin, τ , by $\omega_S = 1/\tau$. The translational correlation time, $\tau_D = d^2/4D$, takes into account the relative molecular diffusion constant of the contrast agent (D) with respect to the solvent and the distance between the relaxing water molecule and the contrast agent. For nanoparticles, this distance is approximated as $d/2$ where d is the diameter of the nanoparticle. The functions j in eqn (4.15) can be expressed by eqn (4.16):

$$j(\omega \tau_D) = \text{Re} \left[\frac{1 + \frac{1}{4} \left(i\omega \tau_D + \frac{\tau_D}{\tau} \right)^{1/2}}{1 + \left(i\omega \tau_D + \frac{\tau_D}{\tau} \right)^{1/2} + \frac{4}{9} \left(i\omega \tau_D + \frac{\tau_D}{\tau} \right) + \frac{1}{9} \left(i\omega \tau_D + \frac{\tau_D}{\tau} \right)^{3/2}} \right] \quad (4.16)$$

In this equation, ω is either ω_H or ω_S . According to eqn (4.15) and (4.16), the relaxivities of superparamagnetic contrast agents depend on two main magnetic parameters: (i) the effective magnetic moment and (ii) the specific magnetic relaxation time. A peculiar case of the static magnetic fields applied in MRI, which is on the order of 1 T, is observed with iron oxide nanoparticles with uniaxial anisotropy. For these nanoparticles, the superspins are usually kept only along the field direction, leading to quite long relaxation times ($\tau_D \ll \tau$). Hence, except for ultrasmall superparamagnetic iron oxide (USPIO) nanoparticles, which have high longitudinal relaxivity and can behave as positive contrast agents, larger superparamagnetic iron oxide nanoparticles are only effective as negative contrast agents because of their higher transversal relaxivity. This is because $r_2 \gg r_1$ in connection with eqn (4.15) providing $r_1^{\text{ad}} \rightarrow 0$.

Quantum mechanical treatment of magnetic dipolar interactions between nuclear and electronic spins indicates that transverse relaxivity can be expressed in two different regimes,^{13,313,314} namely the motional averaging regime and the static dephasing regime. An angular frequency shift experienced by a proton at the equator of the magnetic nanoparticle due to its induced additional stray field is equal to $\Delta\omega = \gamma_H \mu_0 M/3$, where μ_0 is the magnetic permeability of vacuum and M is the effective magnetization of the nanoparticle. In the case of the motional averaging regime

corresponding to the condition $\tau_D \Delta\omega < 1$, the additional transverse relaxivity is $r_2^{\text{ad}} \propto \tau_D (\Delta\omega)^2 \propto \tau_D S_{\text{eff}}^2$, whereas in the case of the static dephasing regime, which corresponds to the condition $\tau_D \Delta\omega > 1$, the additional transverse relaxivity is $\tau_D r_2^{\text{ad}} \Delta\omega \propto S_{\text{eff}}$.

Most applications of nanoparticulate systems in biomedicine and especially contrast agents in MRI depend on the magnetic response of the nanoparticle to an external field configuration and implicitly on its magnetic relaxation regime. As described in the remainder of this sub-chapter, the magnetic relaxation regime of a system of nanoparticles is sensitive to a large set of parameters, including anisotropy constants, distribution of particle sizes, magnetic couplings, and interactions among nanoparticles. Therefore, any characterization of a system of nanoparticles with respect to its magnetic relaxation behavior and its effective magnetic moment requires a multipronged approach including complex and complementary experimental tools. This is best complemented with comprehensive theoretical models that link different types of magnetic responses to as many as possible of the related parameters. Once the characterization of the magnetic relaxation behavior is completed, nanoparticles (single- or multi-core and simple or structured) better suited for a desired application can be more easily designed.³⁰⁴

4.5.2 Magnetism at the Nanoscale with Applications to Iron Oxide Nanoparticles

The least toxic of the iron oxides are the most stable: magnetite, which has a spinel structure, and hematite, which has a defected spinel structure with oxygen vacancies.³¹⁵ Therefore, some main notions of magnetism with the involved peculiarities related to the three-dimensional confinement at nanosized order (zero-dimensional systems) will be discussed for iron oxide nanoparticles with spinel-like structure.^{316,317} The spinel ferrite structure of general formula AB_2O_4 consists of a face centered cubic oxygen (O) array with eight formula units and with divalent or trivalent transition metal cations on the eight tetrahedral (A) and 16 octahedral (B) positions (Section 4.1.1). There are two structural limits: (i) the normal spinel ferrite, where Fe^{III} ions occupy all the 16 octahedral (B) positions with divalent transition metal cations, M^{II} , occupying the eight tetrahedral (A) positions and (ii) the inverse spinel ferrite, where Fe^{III} ions occupy all the eight tetrahedral (A) positions with the 16 octahedral (B) positions equally shared by Fe^{III} and M^{II} cations. Magnetite is typically an inverse spinel, with Fe^{II} ions in the B positions, with the general formula Fe_3O_4 . Maghemite, $\gamma\text{-Fe}_2\text{O}_3$, contains only Fe^{III} cations in insufficient number to fill all the A and B positions. In this case, the cation vacancies (absence of Fe^{II}) induce a trigonal local distortion although the crystal symmetry remains cubic.

The source of the magnetic moment at the atomic level is due to both orbital and spin kinetic moments of unpaired electrons specific to transition

metals with partially filled d-shells (in this case Fe^{II} or Fe^{III} ions) or to rare-earth metals with partially filled f-shells (such as for Gd^{III} ions). For isolated compounds such as oxides, the localized 3d or 4f electrons belong entirely to the central ion placed in a crystal field. Consequently, symmetry imposes splitting of electronic levels that influence the population of valence electrons. A quenching of orbital kinetic moment is also usually induced by the crystal field. The only contributions from this quenching come from the spin. Hence, Gd^{III} ions with a $4f^7$ electron configuration give rise in the high-spin configuration to a total spin $S = 7/2$ (seven uncoupled electrons) and consequently to a total magnetic moment of $7 \mu_{\text{B}}$ (μ_{B} = Bohr magneton). Similarly, Fe^{III} ($3d^5$) and Fe^{II} ($3d^6$) ions in the high-spin configuration of both the tetrahedral and octahedral positions in the spinel structure have spins of $5/2$ and $4/2$, respectively, and magnetic moments of 5 and $4 \mu_{\text{B}}$, respectively.

Once individual magnetic moments are estimated, the magnetic response of the system is determined by the way the spins are oriented relative to an applied magnetic field. This applied magnetic field is used as a quantization axis. The presence of an applied magnetic field gives rise to two possibilities: (1) either there is no effective magnetic interaction between neighboring spins—this leads to a rapid fluctuation of the spins along randomly oriented directions in such a way that their time-average spin value is always zero—or (2) there are interactions leading to a net internal spin structure per formula unit. The first situation corresponds to the paramagnetic state, and the second to a magnetically ordered state. Two types of magnetic interactions can exist between neighboring spins: a ferromagnetic type, which leads to a parallel coupling of the involved spins, and an antiferromagnetic one, which leads to an antiparallel coupling of the involved spins. These interactions are directly related to the superposition possibilities of electron orbitals. Antiferromagnetism involves coupling and interacting spins of equal absolute values whereas ferrimagnetism involves coupling and interacting spins of absolute values that are not equal.

For magnetite, which has an inverse spinel structure, the three Fe ions in the formula unit Fe_3O_4 are located as follows: one Fe^{III} occupies a tetrahedral position and one Fe^{II} and one Fe^{III} occupy two octahedral positions. In the spin structure, the coupling between ions of the same position is ferromagnetic and coupling between ions at different positions is antiferromagnetic, resulting in a total effective spin of $4/2$ per formula unit with an associated magnetic moment of $4 \mu_{\text{B}}$. For maghemite ($\gamma\text{-Fe}_2\text{O}_3$), the Fe^{III} ions are all located on the octahedral positions. Because these two positions are underpopulated by a ratio of $5/3$ instead, the total spin of maghemite is $(5/2)(2/3)$. This corresponds to a magnetic moment of $3.33 \mu_{\text{B}}$ per formula unit. Importantly, the effective magnetic moment per formula unit and its time average remain finite in magnetically ordered compounds. For single domains, they are thus equal to the above estimated maximum values at the lowest temperature and slightly decrease with increasing temperature due to thermally induced magnetic fluctuations. Only above a critical temperature, called the Curie temperature for ferromagnetic state and the Néel

temperature for antiferromagnetic or ferrimagnetic states, does the thermal energy surpass the exchange interaction energy. As a result, the system enters the paramagnetic state with randomly fluctuating spins leading to zero time average magnetic moments.

Below the critical temperature, specific laws govern the evolution of the effective magnetic moment with temperature and applied magnetic field. From an experimental point of view, an assembly of magnetic moments is measured for a sample of given mass or volume. The specific overall magnetic moment of the sample, which is defined as the projection along the field of the vectorial summation of the individual magnetic moments in the sample, is reported relative to the sample volume. This value is also called magnetization and is noted by M . When magnetization is given relative to the mass of the sample, M is called specific magnetization.

In a semi-quantic model, for paramagnetic states, the dependence of the magnetization on the applied field $\mathbf{B} = \mu_0 H$ and temperature T is given by a law of the type $M(B, T) = n\mu B_s(x)$ where n is the volume density of magnetic centers (for example, paramagnetic ions or formula units), μ is the maximum value of the magnetic moment per magnetic center, and $B_s(x)$ is the Brillouin function of argument where $x = \mu B/kT$.³¹⁷ For a ferrimagnetic or ferromagnetic state, $M(B, T)$ can be obtained only by an iterative or graphical solution of the implicit equation $M = n\mu B_s(x)$ with $x = \mu(B + \lambda M)/kT$ where λ is the molecular field constant, which is intimately connected to the exchange interaction.³¹⁷ Note that the Brillouin function increases with the applied field and reaches a saturation value of 1 for large values of the applied field.

Accordingly, for both magnetically ordered or paramagnetic states, the magnetic moments of all magnetic centers in the sample become parallel to the applied field for enough large values of the applied field. In this case, the saturation magnetization $M_s = n\mu$ can provide direct experimental information on the effective magnetic moment per magnetic center. On the other hand, taking into account the theoretical magnetic moments per formula unit of magnetite and maghemite as well as the involved structures with specific lattice parameters, the theoretical saturation magnetizations magnetite and maghemite at low temperature is 0.5×10^6 and $0.43 \times 10^6 \text{ A m}^{-1}$, respectively.

To minimize the magnetostatic energy, magnetic domains separated by domain walls can be formed in a magnetically ordered ferri- or ferromagnetic body, depending on its shape and intrinsic magnetic parameters.³¹⁷ However, when all sizes of a zero-dimensional magnetic entity of a nanoparticle decrease to the nanometer order, which is below the thickness of the domain wall, the entity behaves like a magnetic monodomain. In this case all spins of the formula units are oriented parallel to each other. The critical diameter for monodomain for iron oxide nanoparticles can be estimated at about 80–100 nm.³¹⁸ Hence, unless clusters of nanoparticles are used, nanoparticles for MRI are always of the magnetic monodomain type. For monodomains, the magnetic moment and effective spin of any

nanoparticle are provided by the number of formula units per nanoparticle times the effective magnetic moment or effective spin per formula unit, resulting in the so-called superspin associated with each nanoparticle. The superspin per nanoparticle behaves like an atomic spin. Hence, saturation magnetization can be expressed by $M_s = n\mu$ with n being the number of nanoparticles per unit volume and μ the magnetic moment of the nanoparticle. The dependence $M(B, T)$ follows the same laws as mentioned above with the extra consideration that the nanoparticle is the magnetic center or carrier. Taking into account that x is proportional to μ , and that for nanoparticles μ is thousands of times larger than the atomic moment, at the fields and temperatures typical of MRI experiments $x \gg 1$, and the Brillouin function reduces to the Langevin function $L(x) = \coth(x) - 1/x$.

Information about effective magnetic moments and superspins of nanoparticles can be obtained by following the field and temperature dependence of magnetization curves. Importantly, a complete analysis must consider that even the simplest real nanoparticle systems are characterized by three additional components, which also influence the effective magnetic moments. They are (i) the size distribution, (ii) the defect surface positions which can, at the extreme, result in a dead magnetic layer at the surface of the nanoparticle, and (iii) the inversion degree of the spinel structure.

It is worth noting that an applied magnetic field induces a magnetic anisotropy, which is a preferred orientation of the magnetic moments along the magnetic field. There are also different internal sources for magnetic anisotropy. For instance, the magneto-crystalline anisotropy depends on the different crystalline directions in a periodic structure and manifests itself in bulk systems. For magnetic entities of reduced dimensions and dimensionalities, a shape related anisotropy might be defined due to long-range dipolar interactions. This leads to a demagnetization energy that has a density (energy per unit volume) that can be expressed for a uniform magnetized body by $E_{\text{dmg}} = (\mu_0/2)NM^2$, with the coefficient N depending on the chosen direction inside the body. For ellipsoidal nanoparticles, the demagnetization energy along the longest c axis is minimum, and the demagnetization energies along the shortest a and b axes are maximum. Hence, spins always prefer to lie along the c axis, which is called the easy axis of magnetization, compared to the less preferable a and b axes, which are called hard axes of magnetization. The difference between the energies corresponding to the hard and easy axes is called the shape anisotropy, which is characterized by the shape anisotropy constant K_{shape} . This peculiar case of spins preferring a specific axis is called uniaxial anisotropy, and the corresponding expression of the anisotropy energy for spins oriented at the angle θ versus the direction of the easy axis is $E = KV\sin^2\theta$. For a shape with uniaxial anisotropy, $K = K_{\text{shape}}$. Notably, for aspect ratios $r = c/a$ even slightly larger than 1, the shape anisotropy constant might overpass the magneto-crystalline anisotropy constant.³¹⁸ One specific case of this overpassing is the case of bulk magnetite and maghemite where (in absolute value) $K = 1.2 \times 10^4$ and $2 \times 10^4 \text{ J m}^{-3}$, respectively.

In practice, nanoparticles present an enhanced number of defects and, hence, a structural disorder that is larger for smaller diameters. This results in magneto-crystalline anisotropy constants much lower for nanoparticles than the bulk values. Because transmission electron microscopy measurements have provided evidence that ellipsoidal shapes of aspect ratios larger than 1 are typical for nanoparticles with spinel structure,³¹⁹ a dominant uniaxial shape anisotropy is expected to be characteristic for such systems. Moreover, for nanoparticles with a relatively large surface-to-volume ratio, strain and surface anisotropies might also be present. Strain and surface anisotropy can be roughly taken into account by the overall anisotropy constant K in the above expression of uniaxial anisotropy. A representation of the anisotropy energy *versus* the angle θ of the magnetization (or magnetic moment of the nanoparticle) with the easy axis as a function of applied fields is given in Figure 4.33.³²⁰

For iron oxide nanoparticles in the nm size range, when the applied field is equal to zero, the anisotropy energy barrier KV is of the order of tenths of Kelvins. Therefore, the thermal energy, $k_B T$, can approach the anisotropy energy near ambient temperatures. Hence, the magnetic moment of the nanoparticle might be thermally activated, enabling it to pass over the energy barrier. Therefore, the effective magnetic moment of the nanoparticle, which is a time-averaged projection along the field direction is considered,

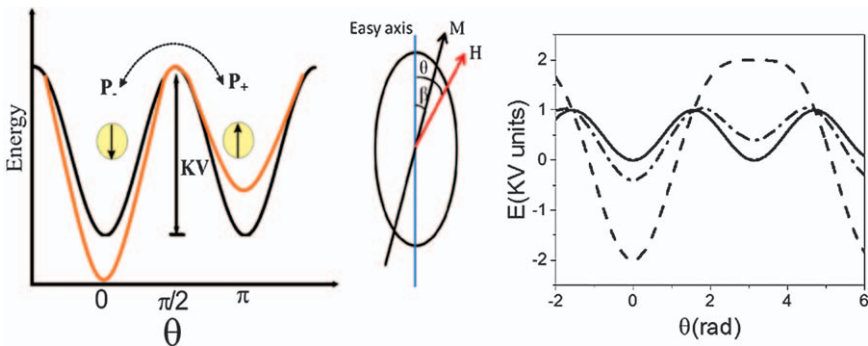


Figure 4.33 Anisotropy energy landscape (left) *versus* the angle θ made by the magnetic moment of the nanoparticle with the easy axis of magnetization (middle) for different values of the applied fields. Numerical evaluations of the anisotropy energy *versus* θ in a Stoner–Wohlfarth model, with the applied field along the easy axis, for field values of 0, 0.2, and 1 unit of the switching field.

Size Effects in Nanostructures: Basics and Applications, Engineering Magnetic Properties of Nanostructures via Size Effects and Interphase Interactions, V. Kuncser, P. Palade, A. Kuncser, S. Greculeasa and G. Schinteie, edited by V. Kuncser and L. Miu, Springer Series in Materials Science 205, Springer, Berlin, 2014, pp. 169–237. Copyright © 2014 Springer-Verlag Berlin Heidelberg. With permission of Springer.

becomes temperature dependent. It decreases from its maximal value, the spontaneous magnetic moment, in the magnetic frozen regime at low temperatures, to a value nearing 0 when $k_B T \gg KV$.

The theoretical treatment of the thermally induced fluctuations is usually divided in two regimes, depending on the ratio $r = k_B T / KV$: (i) the regime of the collective excitations, for $r < 0.1$, and (ii) the regime of the superparamagnetic relaxation, for $r > 0.1$.³²¹ In the regime of collective excitations, the local spins fluctuate by small angles θ around the equilibrium direction (e.g. the magnetic easy axis). These fluctuations lead to an almost linear decrease of the magnetization with temperature.³¹⁷ In the superparamagnetic relaxation regime, the superspin fluctuates by $\theta = 180^\circ$ along the easy-axis direction with a fluctuation time, τ_N , given in the simplest form by the Néel model:³²²

$$\tau_N = \tau_0 \exp(KV/k_B T) \quad (4.17)$$

where τ_0 is an attempt timescale in the range of 10^{-8} – 10^{-12} s.³¹⁷

Except for when the Néel relaxation time is due to the coherent rotation of the magnetic moments inside the nanocrystals, colloidal nanoparticles also have a second relaxation mechanism due to the Brownian movement of the nanoparticles inside the tissue. In this case, the anisotropy easy axis rotates together with the nanoparticle. This is described by a relaxation time τ_B that is proportional to the fluid viscosity and the hydrodynamic volume of the nanoparticle and is inversely proportional to the thermal energy. This overall relaxation time is given by $1/\tau = 1/\tau_B + 1/\tau_N$. However, according to Rosensweig's model,³²³ for magnetite nanoparticles of diameters smaller than 10 nm, the Néel relaxation mechanism prevails over the Brownian one, and $\tau = \tau_N$.

This relaxation time has to be compared to τ_D to determine whether longitudinal or transverse relaxivity is predominant, and to determine how to maximize relaxivity. For instance, water at 37 °C has a diffusion constant D in the order of $3 \times 10^{-9} \text{ m}^2 \text{ s}^{-1}$. For nanoparticles with a diameter $d = 5$ nm, $\tau_D = d^2/4D$ is in the order of 10^{-9} s. Note that this value is very sensitive to particle size and shape. According to eqn (4.16), the ratio τ_D/τ depends strongly on specific parameters related to the relaxation mechanism described by eqn (4.17), namely the time constant τ_0 and the anisotropy energy KV , which have to be determined using suitable characterization tools. Before describing such characterization methods, the analysis of the magnetic relaxation phenomena in applied magnetic fields will be briefly discussed as it relates to MRI contrast agents.

The direct effect of an applied field on a magnetic nanoparticle is that it modifies its energy landscape (Figure 4.33). This leads to a deeper energy minimum along the most convenient direction of the easy axis; the magnetic moment of the particle will prefer to orient along the direction of the magnetic field. The relaxation rates of the two minima of the easy axis and

field aligned magnetizations are different, which leads to specific time and temperature variations of magnetization. For low to moderate applied magnetic fields, an effective relaxation time τ^* is introduced as defined by eqn (4.18) and (4.19):³¹⁹

$$\frac{1}{\tau^*} = \frac{1}{\tau_+} + \frac{1}{\tau_-} \quad (4.18)$$

where:

$$\tau_{\pm} = \tau_0 \exp\left(\frac{KV \pm \Delta}{kT}\right) \quad (4.19)$$

In eqn (4.19), Δ is the energy asymmetry introduced by the field. For low applied fields, $\Delta = \mu_0 H \mu$. However, when the applied magnetic field overpasses the switching field in the Stoner–Wohlfarth model of a monodomain-like nanoparticle ($B_{sw} = 2K/M$), only one energy minimum is present, and the nanoparticle behaves like a system of noninteracting magnetic moments associated to individual nanoparticles. This superparamagnetic system is described by the classical Langevin law, which falls outside the above described relaxation mechanism. The switching field increases as the magnetization of the nanoparticle decreases. Therefore, specific tools for its determination that are comparable to the working applied magnetic fields in MRI are required.

The most important techniques that provide information on the above parameters that are specific to iron oxide nanoparticles of interest in MRI will be further described and exemplified in the remainder of this subchapter. Static magnetization curves can provide the average effective magnetic moment per nanoparticle as well as the nanoparticle size distribution. Hysteresis loops at low temperatures provide information about the Stoner–Wohlfarth switching field and spontaneous magnetic moment of nanoparticles. Zero-field-cooled–field-cooled (ZFC-FC) procedures along both DC and AC susceptibility provide information about both the anisotropy energy and the characteristic time of the Néel relaxation process. Dynamic light scattering provides information about particle size distribution and clustering and configurational effects influencing τ_D . X-ray photoelectron spectroscopy (XPS) provides information about the type of the magnetic ions and their inversion degree at the surface of nanoparticles (the most defected ones). Small angle neutron scattering (SANS) and Mössbauer spectroscopy offer microscopic information on the magnetic configuration inside nanoparticles, the magnetic and surrounding organic layers, clustering effects, average inversion degree over nanoparticles, type and orientation of the magnetic ions inside a nanoparticle, the iron phase composition of the sample, distributions of the anisotropy energy and its average value, relaxation time constant, and interparticle interactions.

4.5.3 Characterization Techniques of Iron Oxide Nanoparticles for MRI

4.5.3.1 DC Magnetometry

Under the influence of an external magnetic field, iron oxide nanoparticle dispersions acquire a macroscopic magnetization due to the thermally averaged magnetic moments oriented in the direction of the field. The magnetization of dispersions of iron oxide nanoparticles is determined by the magnetic relaxation properties of the particles. For particles with fast relaxation dynamics, a static or quasi-static external magnetic field, *i.e.* a direct current (DC) magnetization, will maintain the macroscopic magnetization in the superparamagnetic regime. The DC magnetization of iron oxide nanoparticle dispersions can be measured using vibrating sample magnetometry (VSM), alternating gradient magnetometry (AGM), or superconducting quantum interference device (SQUID) magnetometry as a function of the magnetic field intensity or temperature.

The dependence of the intensity on the magnetic field of the DC magnetization of diluted iron oxide nanoparticle dispersions for which the magnetic dipole–dipole interactions can be neglected is described by the Langevin model.^{324,325} For polydisperse iron oxide nanoparticle dispersions, the Langevin DC magnetization (M_L) is described by eqn (4.20).³²⁶

$$M_L(H) = n \int_{D_m=0}^{\infty} m(D_m) f(D_m) L\left(\frac{\mu_0 m(D_m) H}{k_B T}\right) dD_m \quad (4.20)$$

where H is the magnetic field intensity and D_m is the magnetic diameter of the iron oxide nanoparticles. The magnitude of the magnetic moment of the iron oxide nanoparticle is given by eqn (4.21):

$$m(D_m) = M_d \pi (D_m)^3 / 6 \quad (4.21)$$

where M_d is the domain magnetization of the material. In eqn (4.20), the Langevin function $L(x) = \coth(x) - 1/x$, μ_0 is the permeability of vacuum, k_B is Boltzmann's constant and T is the temperature. The distribution of the magnetic diameter is described by the probability density function $f(D_m)$ and the particle density n .

The DC magnetization of concentrated iron oxide nanoparticle dispersions is increased by the magnetic dipole–dipole interactions. The DC magnetization of concentrated iron oxide nanoparticle dispersions is given by eqn (4.22).

$$M(H) = M_L(H_e(H)) = n \int_{D_m=0}^{\infty} m(D_m) f(D_m) L\left(\frac{\mu_0 m(D_m) H_e(H)}{k_B T}\right) dD_m \quad (4.22)$$

This framework of a theoretical model of Ivanov and Kuznetsova^{327,328} is a generalization of the polydisperse Langevin model [eqn (4.19)], which

incorporates the magnetic dipole–dipole interactions in the effective field H_e [eqn (4.23)].

$$H_e(H) = H + \frac{M_L(H)}{3} \left(1 + \frac{1}{48} \frac{dM_L(H)}{dH} \right) \quad (4.23)$$

The effective field H_e formula can be improved for ultra-concentrated iron oxide nanoparticle dispersions as follows:³²⁹

$$H_e(H) = H + \frac{M_L(H)}{3} \left(1 + \frac{1}{48} M_L(H) \chi_L f(\rho) \right) \quad (4.24)$$

where $\chi_L = [dM_L/dH]_{H=0}$ is the Langevin initial susceptibility and ρ is the hydrodynamic volume fraction of the iron oxide nanoparticle dispersion.

Eqn (4.19) and (4.22) form the basis of magneto-granulometry. This is a method that enables the determination of the statistics of the size of iron oxide nanoparticle from the measured magnetization curves $M(H)$ of their dispersions. The nanoparticle size statistic is described by the probability density function of the iron oxide nanoparticle magnetic diameter $f(D_m)$, which is a parametric function of D_m . The magneto-granulometric determination of the probability density function parameters can be made either by algebraic means^{326,328} or by nonlinear regression.³³⁰ The choice of a particular probability density function class is usually based on the best fit of transmission electron microscopy granulometry histograms. The log-normal and gamma distributions are more common in the literature. A recently developed theoretical model for nanoparticle growth³³¹ shows that a log-normal size distribution stems from the growth rate equation based on the law of proportionate effect. The log-normal distribution function depends on two parameters: the median diameter, D_0 , and the standard deviation, S , of the diameter natural logarithm. These values can be determined by magneto-granulometry [eqn (4.25)].

$$f(D, \{D_0, S\}) = \left(DS\sqrt{2\pi} \right)^{-1} e^{-\frac{1}{2S^2} \left(\ln\left(\frac{D}{D_0}\right) \right)^2} \quad (4.25)$$

Special attention should be paid to experimentally measured magnetization curves of dispersions of iron oxide nanoparticles used in magneto-granulometry for which the nanoparticle volume fractions is above 5%. The field intensity measured experimentally is the field produced by the measuring instrument outside the sample holder. The theoretical models used in magneto-granulometry, however, assume that H is the field intensity acting on the sample. Because of demagnetization, the field acting on the sample is the measured field minus the demagnetizing field. The demagnetizing field is proportional to the sample magnetization. It is homogeneous only in spherical and rotation-ellipsoidal sample holders. In cylindrical sample holders, which are most widely used, the demagnetizing field is non-homogeneous, and thus the demagnetizing field correction is not trivial.³³²

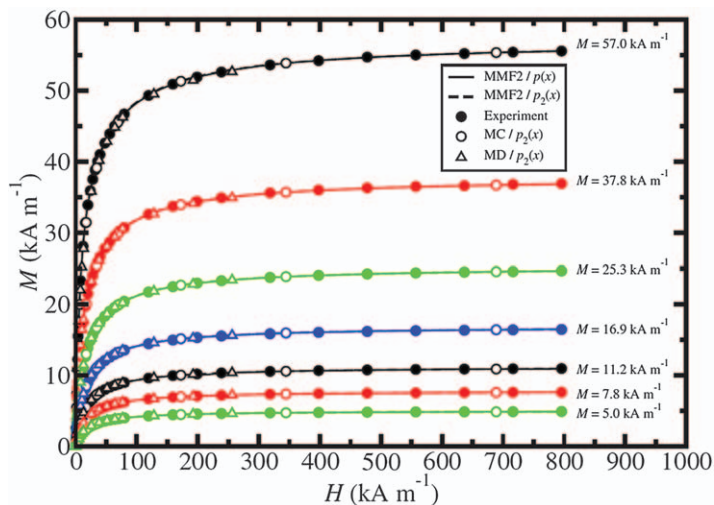


Figure 4.34 Magnetization curves for ferrofluid dilution series: experiment, theory, and numerical simulation.

Adapted with permission from A. O. Ivanov, S. S. Kantorovich, E. N. Reznikov, C. Holm, A. F. Pshenichnikov, A. V. Lebedev, A. Chremos and P. J. Camp, *Phys. Rev. E*, 2007, 75, 061405. Copyright © 2007 The American Physical Society.

The algebraic magneto-granulometry given by eqn (4.22) and (4.23) can be used to characterize a ferrofluid dilution series with saturation magnetization in the range 5–57 kA m^{-1} .³²⁸ As seen in Figure 4.34, the agreement between experimental data, theory, and numerical simulation is remarkably good. The variation of the average magnetic diameter (7.3 nm) across the entire ferrofluid concentration range is less than 0.1 nm.

Nonlinear regression magneto-granulometry [eqn (4.22) and (4.23)] was successfully used to characterize a ferrofluid dilution series with solid volume fraction in the range 0.8–21%³¹⁹ and an aqueous dispersion of multi-core magnetic nanogels.³³⁰ The first-order approximation of the Langevin polydisperse model [eqn (4.23)], which is suitable for magneto-granulometry of diluted samples, was also applied to characterize diluted ferrofluids synthesized *via* different methods.³³³

As shown in Figure 4.35, the regression magneto-granulometry method, like the algebraic method, provides consistent results across a wide range of sample concentrations.³¹⁹ Both the average and the standard deviation are within 0.3 nm. Eqn. (4.22) and (4.23) are particularly suitable for magnetic nanogels or multicore magnetic composites in which the nanoparticles are highly packed.³³¹ In Figure 4.36, the magnetization curve of a magnetic nanogel dispersion is presented. The theoretical fit R^2 is better than 0.999 and good agreement is observed between results obtained from transmission electron microscopy and magneto-granulometry-VSM.

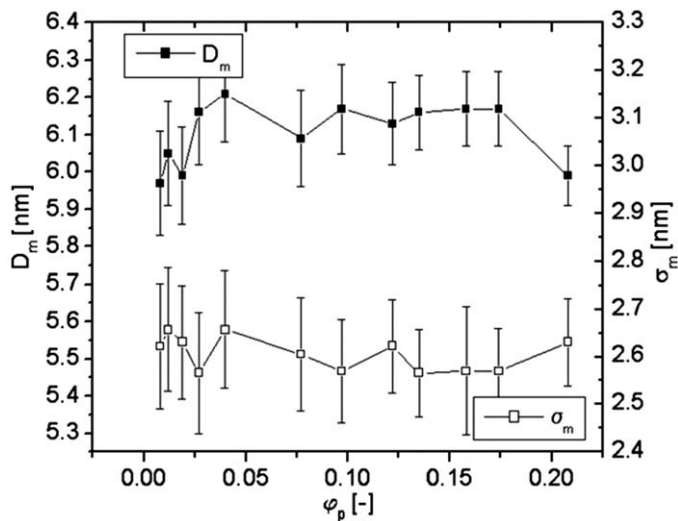


Figure 4.35 Volume fraction dependence of the magnetic diameter average and standard deviation as obtained by means of nonlinear regression magneto-granulometry.

Reprinted with permission from Journal of Colloid and Interface Science, Volume 373, D. Susan-Resiga, V. Socoliuc, T. Boros, T. Borbath, O. Marinica, A. Han and L. Vekas, The influence of particle clustering on the rheological properties of highly concentrated magnetic nano-fluids, 110–115, Copyright 2011, with permission from Elsevier.

In the right column of Figure 4.37, the black lines represent regression magneto-granulometry performed on diluted samples of nanoparticles synthesized by different protocols.³³³ Data corresponding to nanoparticles synthesized by chemical coprecipitation are shown in Figure 4.37b. The cubic shaped facets and round shaped twins particles shown in Figure 4.37a and Figure 4.37b, respectively, were obtained by thermal decomposition, as were the spherical monodisperse 8 nm sphere seeds and their subsequent 17 and 20 nm sphere-seeded growth shown in Figure 4.37a, b and c, respectively. As is apparent, there is good agreement between data obtained by TEM, XRD, and magneto-granulometry for nanoparticles obtained by coprecipitation as well as for the 8 nm sphere seeds. In these examples, the nanoparticles are magnetic monodomains and are mono-crystalline. The magnetic diameter is slightly smaller than the physical diameter due to the dead nonmagnetic layer. For the twins and seeded growth spheres, there is high discrepancy between the size distributions obtained from TEM, XRD, and magneto-granulometry. These nanoparticles have crystalline and magnetic disorder, due either to polycrystallinity, to defects or to amorphous phase content.

Information about the superparamagnetic state of the nanoparticles can be obtained from the ZFC-FC procedure. In the ZFC measurements, the system is cooled from an initially assumed superparamagnetic state down to

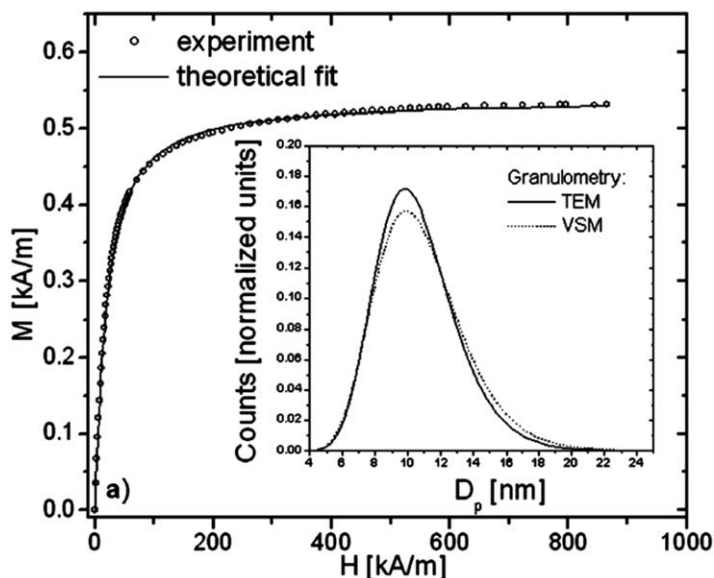


Figure 4.36 Magnetic nanogels magnetization curve: experiment and theoretical fit. Insert: nanoparticle size distributions from transmission electron microscopy and magneto-granulometry-VSM. Adapted from ref. 330 with permission from The Royal Society of Chemistry.

the lowest achievable state without any applied field. The magnetization is then measured at increasing temperatures using a weak measuring field in the mT range, which introduces a small asymmetry parameter $\Delta \ll KV$ [see Figure 4.38 and eqn (4.24)]. In the FC (field cooling) procedure, the magnetization is measured at decreasing temperatures from the superparamagnetic state to the lowest temperature in the measuring field. This curve is identical to that measured at increasing temperatures after cooling the system in the measuring field. By cooling the system in zero field, the initial magnetization at the lowest temperature is close to zero because both energy minima are equally populated. As can be seen from the corresponding asymmetrical anisotropy energy landscape in Figure 4.38, when measuring the magnetization at increasing temperature under a weak applied field, the jumping probabilities of the magnetic moments between the two minima are different [eqn (4.24)]. This initially leads to an overpopulation of the absolute minimum and thus an increase in magnetization. When the temperature is high enough, however, the two relaxation times become equal, $\tau_{\pm} \approx \tau_0$. This leads to equal populations of the two minima and hence to a net magnetization decreasing to zero.

Accordingly, the maximum in the ZFC experimental curve distinguishes between the magnetic frozen regime, which occurs at low temperature, and the superparamagnetic regime, which occurs at high temperature. The temperature corresponding to this maximum and which delimitates the two

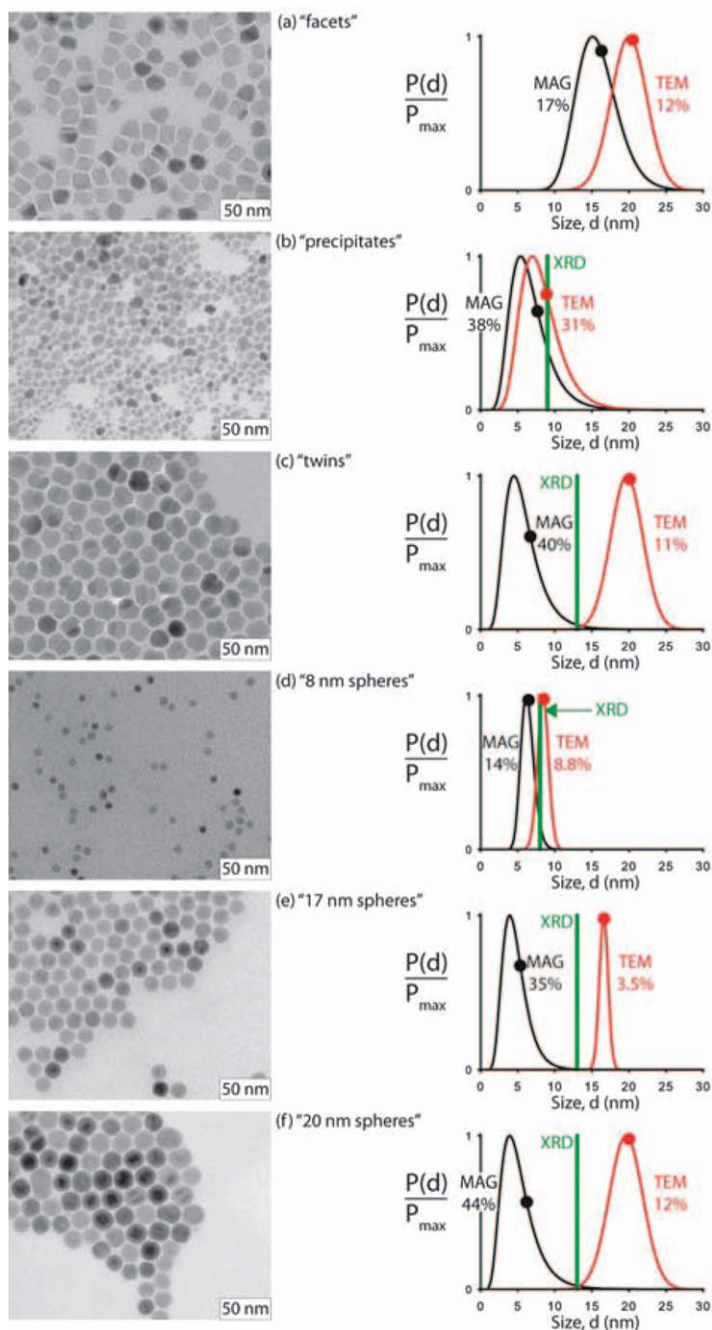


Figure 4.37 Transmission electron microscopy pictures and granulometry results from TEM, VSM, and XRD for particles synthesized by different methods.³³³ Adapted with permission from B. Luigjes, S. M. C. Woudenberg, R. de Groot, J. D. Meeldijk, H. M. T. Galvis, K. P. de Jong, A. P. Philipse and B. H. Ern e, *J. Phys. Chem. C*, 2011, **115**, 14598. Copyright (2011) American Chemical Society.

magnetic regimes is called the blocking temperature, T_B . The observed spin relaxation process actually depends on the value of τ^* and its comparison to the measurement time of the method, τ_m . If $\tau \ll \tau_m$, the magnetic relaxation is so fast that the particle system behaves as a paramagnet with a giant spin per particle. This is the super-paramagnetic regime. If $\tau \gg \tau_m$, however, the magnetic relaxation is so slow that quasi-static properties are observed. This is the spin blocked regime.

Quantitatively, the blocking temperature, T_B , is defined as the temperature where $\tau = \tau_m$; therefore, its value depends on the time window of the experimental method. The system behaves as a paramagnet above T_B with respect to the measurement technique used. However, the transition to the real paramagnetic state, which is associated with the bulk material of the nanoparticle, appears at the higher Curie or Néel temperature. Physically, the difference between the super-paramagnetic state and the real paramagnetic state resides in all of the spins inside the particles jumping coherently (altogether) along the easy axis of magnetization in the super-paramagnetic state. In the paramagnetic state, however, the spins jump independently and in random directions. Accordingly, in the case of zero or weak applied fields, the blocking temperature can be expressed by eqn (4.26).³¹⁷

$$T_B = \frac{KV}{k \ln(\tau_m/\tau_0)} \quad (4.26)$$

Once T_B has been determined experimentally by the maximum of the ZFC curve for a measurement technique of known τ_m , the anisotropy energy can be evaluated from the time constant τ_0 . Note that τ_0 can vary by four orders of magnitude.

In the FC experiment, the magnetization increases continuously as the temperature decreases. This increase follows a $1/T$ like paramagnetic law above T_B and is weaker at lower temperatures. This trend is expected and follows a continuous increasing population of the absolute energy minimum as shown in Figure 4.38. A characteristic of quasi-noninteracting magnetic nanoparticles is the superposition of the FC and the ZFC curves above T_B , and the larger magnetization values observed in the FC curve compared to the ZFC one below T_B . The position of the branching temperature with respect to T_B gives information on the distribution of magnetic volumes.³³⁴

ZFC-FC magnetization curves collected on two samples of iron oxide nanoparticles functionalized with polyethyleneimine are shown in Figure 4.38. The magnetization curves collected on the same samples at 2 K are shown in the insets. The two samples consist of 4 nm iron oxide nanoparticles (as measured by TEM) coated with a polyethyleneimine polymer at an iron oxide/polymer mass ratio of either (a) 1 or (b) 0.5. Both samples of iron oxide nanoparticles were synthesized in a single step according to a hydrothermal procedure at high pressure and low temperature.³³⁵ The characteristics of the ZFC-FC curves described above are observed in both

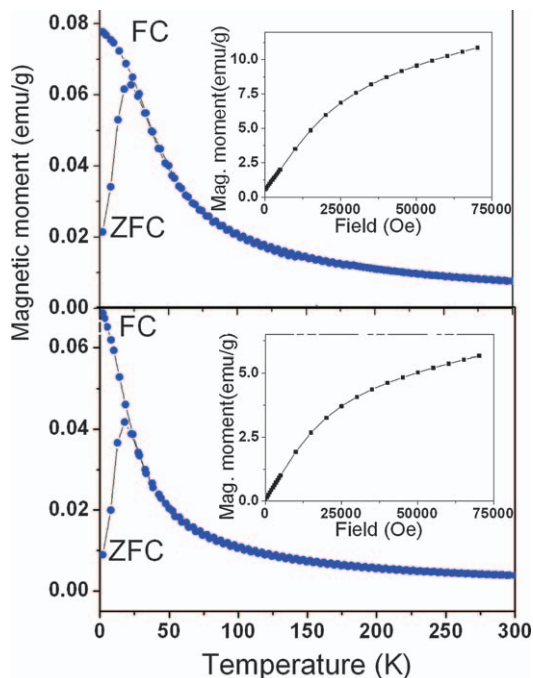


Figure 4.38 ZFC-FC curves taken under an applied field of 8 mT induction for two samples of iron oxide–polyethyleneimine nanoparticles. The sharp maximum in the ZFC curves provides the blocking temperature and the close-branching temperature (between ZFC and FC curves) providing evidence for narrow size distribution of the analyzed nanoparticles.

Adapted from *Materials Chemistry and Physics*, Volume 161, L. M. Popescu, R. M. Piticescu, M. Petriceanu, M. F. Ottaviani, M. Cangiotti, E. Vasile, M. M. Dîrtu, M. Wolff, Y. Garcia, G. Schinteie and V. Kuncser, Hydrothermal synthesis of nanostructured hybrids based on iron oxide and branched PEI polymers. Influence of high pressure on structure and morphology, 84–95, Copyright 2015, with permission from Elsevier.

samples. These magnetic nanoparticles have a T_B of about 30 K [27 K for (a) and 23 K for (b)]. The fact that the branching temperature is very close to T_B indicates that the nanoparticles have a narrow size distribution. The incomplete saturation of the magnetization shown in the insets, which is typical of ferrimagnetic structures, can provide information about the spontaneous magnetization of the nanoparticles, M_S , if the high field tail of the curve is suitably fitted by a law of approach.³¹⁸ In this case, the two samples have $M_S = 13(1)$ and $7(1)$ emu g^{-1} . The final specific spontaneous magnetizations of the magnetic phase of each sample are calculated to be $27(1)$ and $22(1)$ emu g^{-1} , respectively, based on their inorganic/organic weight ratio. In comparison, the M_S value of magnetite is 90emu g^{-1} . The lower M_S values for the two synthetic samples suggest that the nanoparticles have a disordered spin structure similar to a spin-glass.

Although the blocking temperature T_B can be determined precisely, both τ_m and τ_0 are imprecise. The time window in DC magnetometry ranges between 1 and 100 s. Therefore, the anisotropy energy calculated from eqn (4.26) is also imprecise. On the other hand, in the magnetic frozen regime (e.g. at 0 K), the magnetic monodomain of the nanoparticles behaves as an assembly of Stoner–Wohlfarth magnetic entities characterized by a coercive field $B_C^0 = B_{SW}/2$.³²⁰ In the superparamagnetic regime above T_B , the coercive field decreases to zero, as is typical for any paramagnetic system. The temperature dependence of the coercive field can be expressed as:³¹⁷

$$B_C = B_C^0 [1 - (T/T_B)^{1/2}] \quad (4.27)$$

Therefore, both T_B and the effective anisotropy constant K can be determined from the linear decrease of B_C versus $T^{1/2}$ observed in DC magnetic hysteresis loops collected at increasing temperatures.

The two hysteresis loops of the previous iron oxide/polyethyleneimine samples obtained in the magnetic frozen regime and in the superparamagnetic state are shown in Figure 4.39. A blocking temperature of about 10 K and a switching field B_{SW} of about 0.7 T were calculated for both samples from eqn (4.27). These numbers indicate that under the applied fields used in MRI, both transverse and longitudinal relaxivity mechanisms are contributing to the observed magnetic behavior. Effective anisotropy constants of about 40 and 30 kJ m^{-2} are calculated for these two samples based on their switching fields and spontaneous magnetizations. In this case, if the calculated switching fields and anisotropy constant are reliable, then the derived T_B is questionable due to the lack of the corresponding time window in a hysteresis loop measurement. A more reliable investigation of magnetic relaxation phenomena can be performed by magnetometry or alternating current (AC) magnetic susceptibility measurements.

4.5.3.2 AC Magnetic Susceptibility

This technique measures the magnetic response of a sample excited by a weak oscillatory (ac) magnetic field below 0.4 mT. Magnetic susceptibility is defined as the variation of magnetization relative to the field. The in-phase, χ' , and the out-of-phase, χ'' , part of the AC magnetic susceptibility can be expressed by eqn (4.28) and (4.29), respectively.³¹⁷

$$\chi' = \chi_0 / (1 + (\omega\tau^*)^2) \quad (4.28)$$

$$\chi'' = \chi_0 \omega\tau^* / (1 + (\omega\tau^*)^2) \quad (4.29)$$

where ω is the angular frequency of the applied ac magnetic field, τ^* is the effective relaxation time, and χ_0 is the real part of the susceptibility in the superparamagnetic regime which has a typical $1/T$ dependence. ZFC procedures can be applied for this technique. The advantage of this approach is that no static fields are required and that a measurement time window directly related to $1/\omega$ can be defined.

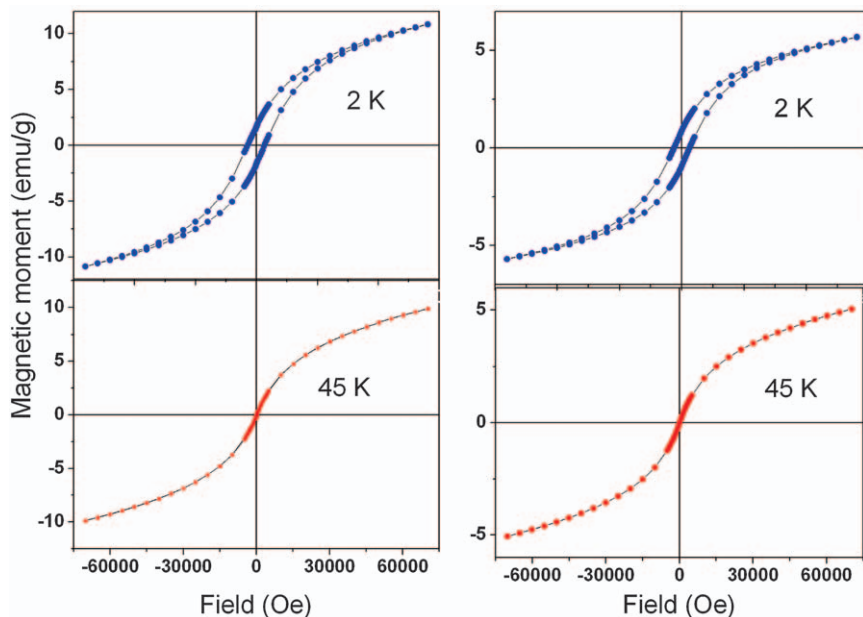


Figure 4.39 Magnetic hysteresis loops collected above and below the blocking temperature as shown in Figure 4.38 for the same iron oxide-poly(ethylene imine) samples. The coercive field in the low temperature curves can provide information about the switching field (above which relaxation is accessible by the classical Langevin treatment). Adapted from *Materials Chemistry and Physics*, Volume 161, L. M. Popescu, R. M. Piticescu, M. Petriceanu, M. F. Ottaviani, M. Cangiotti, E. Vasile, M. M. Dirtu, M. Wolff, Y. Garcia, G. Schinteie and V. Kuncser, *Hydrothermal synthesis of nanostructured hybrids based on iron oxide and branched PEI polymers. Influence of high pressure on structure and morphology*, 84–95, Copyright 2015, with permission from Elsevier.

Typically, the temperature dependence of the real part of the susceptibility has a maximum at a temperature that, conveniently, approaches the blocking temperature. This dependence is defined by eqn (4.26), which can be rewritten as:

$$\ln\tau_m = \ln\tau_0 + KV/k_B T_B \quad (4.30)$$

Therefore, both the time constant τ_0 and the average anisotropy energy KV can be obtained from a set of ZFC ac susceptibility measurements performed at different frequencies of the AC magnetic field according to the linear dependence $\ln\tau_m = f(1/T_B)$. Such data obtained for 6 nm iron oxide nanoparticles coated with a carbon shell is shown in Figure 4.40. Although in this case this procedure can determine both parameters of the relaxation process accurately, it can also lead to unreliable results for different materials. A main limitation of this technique is that AC magnetometers usually cover a

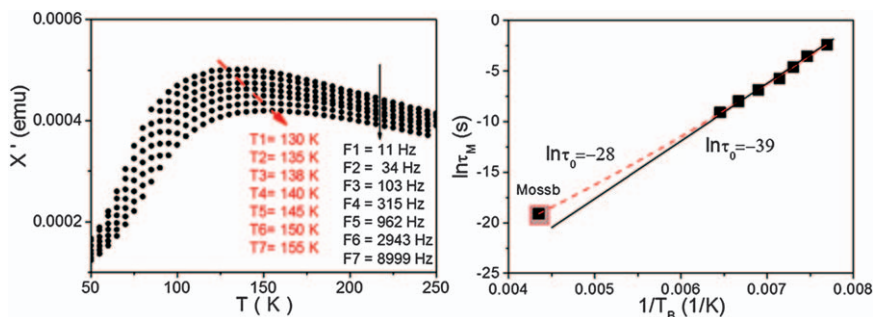


Figure 4.40 (Left side) In-phase AC susceptibility ZFC measurements at different excitation frequencies and (right side) the plot of the logarithm of the blocking time window *versus* the inverse of the blocking temperature, providing in principle both the anisotropy energy and the relaxation time constant. By completing this dependence *via* an additional blocking temperature obtained using a specific method of much shorter measuring time window (in this case Mössbauer spectroscopy), a more realistic value is obtained for τ_0 (verified also by alternative methods).

narrow range of frequencies for the excitation field (up to 10 kHz); whereas the associated range of magnetic fluctuations induced in iron oxide nanoparticles can reach the GHz range. Therefore, a reliable determination of the relaxation parameters obtained from the $\ln\tau_m = f(1/T_B)$ dependence of AC magnetometry should be complemented with data obtained from techniques with shorter time windows, such as Mössbauer spectroscopy (Section 4.5.3.6).

4.5.3.3 Granulometry by Light Scattering

For iron oxide nanoparticles to behave as MRI contrast agents, their specific surface must be preserved. A design value for the specific surface can be set using the diameter of nanoparticles or nanoparticle composites from transmission electron microscopy or other granulometry techniques, assuming a perfect colloidal stability of the liquid dispersion. However, a loss of specific surface in a dispersion of iron oxide nanoparticles can occur as a consequence of colloid aggregation due to various factors. Spontaneous aggregation can occur due to bridging interactions between layers of particles, van der Waals interactions between iron oxide cores of poorly stabilized particles, entropic interactions, loss of electrostatic repulsion due to pH or salinity imbalance, and magnetic dipole-dipole interactions between large monodomain magnetic nanoparticles. Spontaneous aggregation can be observed and characterized using dynamic light scattering or static light scattering using commercial instruments.

Magnetically induced aggregation is critical for dispersions of iron oxide nanoparticles used in MRI. As a result of the synergistic action of magnetic dipole-field and dipole-dipole interactions, iron oxide nanoparticles can

agglomerate on both the nano and micro scales. Nanoscale aggregation in single core iron oxide nanoparticles can lead to the formation of one-dimensional chains³³⁶ with small losses of specific surface. Magnetically induced dichroism and birefringence can be used to detect and characterize one-dimensional chains of iron oxide nanoparticles.³³⁷ Microscale aggregation, however, leads to the formation of large and highly packed aggregates of iron oxide nanoparticles either as condensed phase drops or zippered aggregates that are elongated in the direction of the magnetic field (Figure 4.41). Magnetically induced microscale aggregates with μm range diameters and 10–100s μm length have drastically reduced specific surface compared to colloidal iron oxide nanoparticles. This aggregation noticeably reduces MRI T_2 -weighted signal intensity.³³⁸ Magnetically induced μm aggregation can be detected and characterized by optical microscopy^{338,339} or static light scattering.^{330,339} Static light scattering enables the determination of the magnetic-field-intensity-dependence of iron oxide nanoparticle magnetic supersaturation, which is the percentage of iron oxide nanoparticles that will eventually become entrapped in the aggregates.³³⁰

Figure 4.41 shows the time evolution of the forward light scattering in an aqueous dispersion of magnetic nanogels at different values of magnetic field intensity.³³⁰ The field is turned on at $t=0$ and off at $t\approx 2-3$ min. Magnetically induced aggregates start to form and grow after the field is applied, leading to the forward scattered light decay. The scattered light

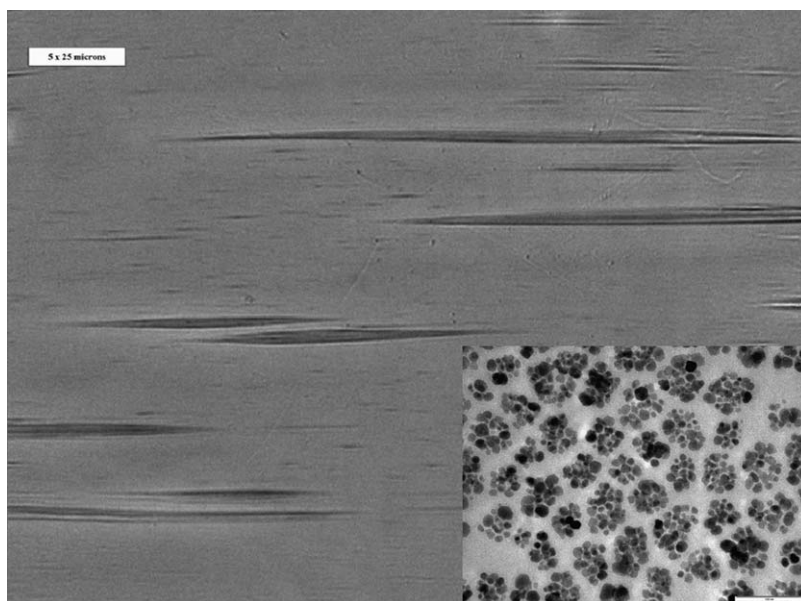


Figure 4.41 Optical microscopy of magnetically induced micron scale aggregates (the bar is $5\times 25\ \mu\text{m}$). Insert: $\sim 50\ \text{nm}$ multicore magnetic nanogels. Adapted from ref. 330 with permission from The Royal Society of Chemistry.

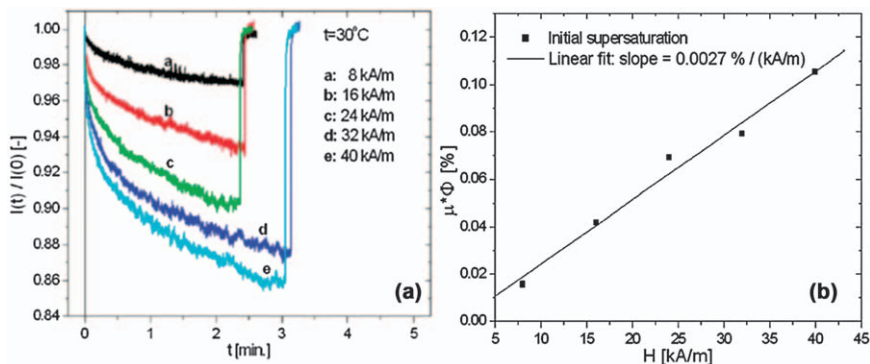


Figure 4.42 Left: kinetics of forward light scattering at different magnetic field intensities, and right: magnetic field intensity of the initial supersaturation. Adapted from ref. 330 with permission from The Royal Society of Chemistry.

increases with field intensity. After the field is removed, the aggregates dissolve rapidly. Socoliuc applied a theoretical model³³⁰ to the scattering data to determine the sample initial supersaturation as a function of the applied field intensity (Figure 4.42). The initial supersaturation grows linearly with field intensity in the range 0–40 kA m^{-1} , reaching a maximum of about 10% from the total volume of nanogel in the sample. The magnetic supersaturation of many types of magnetic colloids can be determined from this technique.

4.5.3.4 X-ray Photoelectron Spectroscopy

X-ray photoelectron spectroscopy (XPS) is a surface analysis method. It consists of irradiating a material by X-rays and determining the kinetic energies of the ejected photoelectrons, E_{kin} . This technique enables the determination of the binding energies of the electrons in the initial atomic states, E_b from $E_b = \hbar\nu - E_{\text{kin}}$, where $\hbar\nu$ is the energy of the incident X-ray photons. This technique provides the elemental composition of the surface, as well as the valence states, oxidation degree, and ligands of the emitting atoms. The valence and oxidation state of the metal is inferred from the areas of the photoelectron peaks. Information about the ligands can be obtained from the chemical shifts of the peaks compared to the elemental state. A chemical shift represents a change in E_b of a core electron of an element due to a change in the chemical bonding of that element. Core binding energies are determined by electrostatic interactions between electrons and the nucleus and are reduced by electrostatic shielding of the nuclear charge by other electrons in the atom. Removal or addition of electronic charge as a result of changes in bonding will alter shielding. Oxidation, which decreases valence electron charge, increases E_b whereas reduction, which increases valence electron charge, decreases E_b .

Chemical shifts in XPS provide information on the presence of functional groups, the nature of the chemical environment, and the oxidation state of the element. Depending on the chemical bonds and the neighboring atoms, the binding energy of a given element can be shifted from a fraction of an eV up to several eV. The presence of different chemical bonds types splits the spectral peaks into multiple peaks that can sometimes merge. Appropriate software can deconvolute these peaks into their components, each corresponding to a particular bond type.

XPS is one of the most powerful techniques to quantitatively analyze the chemical composition of the organic layer of magnetic nanoparticles coated with organic shells. XPS can determine the oxidation state of the metal in the magnetic core, differentiate between magnetite (Fe_3O_4) and maghemite ($\gamma\text{-Fe}_2\text{O}_3$), and identify possible additional phases that could alter the magnetic properties of the nanoparticles. Magnetic properties are affected by the distributions of cations and vacancies, nonstoichiometry, the nature of surface ligands, spin canting or surface contribution due to nanometric size, and oxidation effects. Understanding these contributions to magnetism require careful characterization techniques such as Mössbauer spectroscopy (Section 4.5.3.6).^{86,225,340–343}

For biomedical applications, iron oxide nanoparticles must have an organic coating that ensures electrostatic or steric stabilization of the nanoparticles at physiological pH.³⁰⁴ Various anchoring groups, such as carboxylates, phosphonates, catecholates, and silanes,¹⁸⁴ interact in different ways with the surface of nanoparticles and can influence their magnetic properties (Section 4.3).^{344,345} For example, carboxylate surface coatings induce spin canting in the oxidized layer, but no canted surface structure is observed with phosphonated ligands.⁸⁶ Optimizing the relaxivity of iron oxide nanoparticles requires identifying the surface complex formed and understanding how the surface chemistry affects the magnetic properties of the nanoparticles. XPS is the most appropriate method to evaluate the formation of surface complexes.

Stabilization of magnetic nanoparticles is often accomplished in such a way that the magnetic contribution of the particle surface layer is maintained with phosphate ligands.^{184,197} XPS, in concert with other characterization techniques such X-ray diffraction, Mössbauer and infrared spectroscopies, can be used to investigate the type of phosphate complex formed at the surface of the magnetite nanoparticles. For example,¹⁸⁴ XPS spectra indicate that the Fe2p bands in phosphate-coated magnetite nanoparticles are similar to those of magnetite. This similarity suggests that some Fe^{II} ions remain at the surface of phosphate-coated magnetite but also that the amount of Fe^{III} increases with increasing concentrations of phosphate ligand. The contribution of surface species has been analyzed from XPS spectra. This analysis indicates that the contribution of the Fe–OH bond was replaced by the contribution of an Fe–O–P bond and a P=O bond. XPS and Mössbauer techniques concluded that the phosphate-coated nanoparticles are magnetite with a small deviation from stoichiometry ($\text{Fe}_{2.90 \pm 0.02}\text{O}_4$).

The phosphates interact with Fe^{III} in octahedral sites *via* the formation of monoprotonated binuclear species.¹⁹⁷ XPS was also used to characterize magnetite nanoparticles coated with poly(glycidyl methacrylate) (pGMA), a precursor for further functionalization *via* nucleophilic ring opening of glycidyl-oxirane moieties.³⁴⁶

Core-shell magnetic nanoparticles can also be prepared by adsorption of monomers followed by their *in situ* surface polymerization. This approach combines the advantages of physicochemical surface modification and chemical binding.³⁴⁷ For instance, gallic acid was adsorbed onto magnetite nanoparticles and *in situ* surface polymerized resulting in a polygallate coating that protects the magnetic nanoparticles from aggregation at physiological pH and salt concentration. The polymer gives the nanoparticles the colloidal and chemical stability necessary for biomedical applications. XPS was used to elucidate the mechanism of surface-induced polymerization of gallic acid. The high-resolution XPS spectra of O, C, and Fe in a polygallate-coated magnetic nanoparticle sample are shown in Figure 4.43. The Fe^{III}/Fe^{II} atomic ratio at the surface of polygallate-coated magnetic nanoparticle as calculated from the Fe^{III} and Fe^{II} 2p peak areas decrease from 2 (bulk magnetite (Fe(III)₂Fe(II)O₄)) to 1.77. This decrease indicates that iron is reduced at the surface of the nanoparticle by gallic acid. The C1s peaks of polygallate-coated nanoparticles were assigned to aromatic carbons (C-C, 284.72 eV), phenolic OH groups (C-O, 285.6 eV, alcohols and ethers), carboxylic groups (O=C-O, 288.87 eV, carboxylic acids and esters) and carbonates (O-CO₂, 290.58 eV). The carbonate contamination in the polygallate-coated magnetic nanoparticle is due to the prolonged surface polymerization process under ambient conditions. The carbonate was successfully removed by acidifying the dispersions to pH of ~4 using HCl (Figure 4.43, bottom row). Iron reduction is accompanied by the oxidation of gallic acid as inferred from the doubling of the O=C-O/C-O ratio in the coating layer relative to its original value in gallic acid: 0.675 and 0.33, respectively. These XPS results elucidated the mechanism of chemical stabilization of iron oxide nanoparticles by polygallate.

4.5.3.5 Small Angle Neutron Scattering Techniques

Small angle neutron scattering (SANS) is one of the most efficient technique to investigate the structure of magnetic colloidal suspensions and magnetic fluids.³⁴⁸ The broadening of a beam of thermal neutrons with wavelengths of 0.1–1 nm passing through a sample is determined in terms of differential scattering cross-section per sample volume. The scattering intensity, $I(\vec{q})$, is a function of the scattering vector \vec{q} with the module $q = (4\pi/\lambda)\sin(\theta/2)$, where λ is the incident neutron wavelength and θ is the scattering angle.

The scattering intensity is sensitive to the structural features of magnetic nanoparticles ranging between 1–100 nm in size. Because the sizes of single magnetic nanoparticles and the characteristic correlation lengths between particles are most often in this dimensional range, SANS allows for in-depth

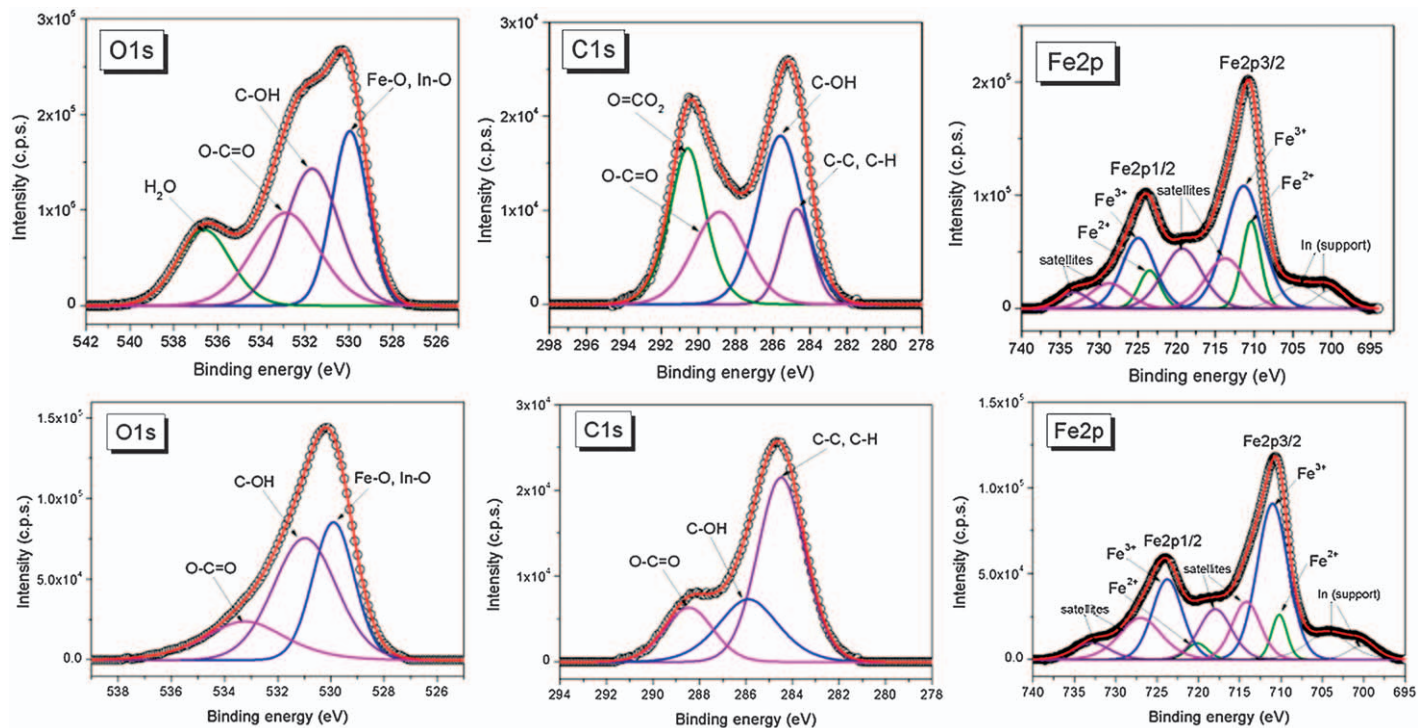


Figure 4.43 O 1s, C 1s, and Fe 2p spectra of the (top row) original and (bottom row) acidified polygallate-containing magnetic nanoparticles (bottom row) aged for 4 weeks at pH ~6.5 and 10 mM NaCl.³⁴⁷ Adapted with permission from I. Y. Tóth, M. Szekeres, R. Turcu, S. Sáringér, E. Illés, D. Nesztor and E. Tombáz, *Langmuir*, 2014, 30, 15451. Copyright (2014) American Chemical Society.

study of the structure of a wide range of magnetic nanoparticles of interest to biomedical applications. Using cold neutrons with wavelengths longer than 1 nm, it is possible to extend the range of correlations to more than 100 nm.

Unlike SANS, which uses neutron scattering on atomic nuclei, small angle X-ray scattering (SAXS) is based on radiation scattered on electron shells. Another significant difference between SANS and SAXS scattering techniques is that the intrinsic magnetic moment of neutrons give rise to an additional interaction between the neutrons and the electron shell of an atom. Consequently, in a SANS experiment, the differential cross section of the distribution of nuclear and magnetic scattering length densities (SLDs) inside inhomogeneities such as magnetic core, surfactant shells, or carrier liquid can be determined. The SLDs for a usual (H-based) carrier and the organic shell are quite similar. However, for a deuterated (D-based) carrier, the SLD is closer to the magnetic cores. This difference enables contrast variation by means of hydrogen–deuterium substitution, a powerful technique for structure investigation. The application of a magnetic field to a magnetic colloid in a SANS experiment gives rise to anisotropic magnetic scattering with respect to the radial angle in the plane of the detector.

The SANS technique can be modified with a neutron spin flipper device, which polarizes the neutron beam and orients the neutron magnetic moments in a direction collinear with the magnetic field. Together with contrast variation, this technique, known as small angle neutron scattering with polarization (SANSPOL),^{350–352} can elucidate structural processes in magnetic colloids.

The SANS technique and its derivatives, which use contrast variation and scattering of polarized neutrons, provide information about particle structure (including nanoparticle size, surfactant shell thickness, composition of core and shell, solvent rate penetration in surfactant layer), magnetic structure (size and composition of magnetic domains), particle interaction (interparticle potential, magnetic moment correlation, and phase separation) and cluster formation (aggregation and chain formation). Due to the high penetrability of neutrons, samples used in SANS investigations do not require any special preparation; unmodified (nondiluted) and bulk systems can be investigated. As opposed to other techniques such as TEM, clusters of magnetic nanoparticles detected by SANS are not artifacts due to the pre-treatment of samples.

SANSPOL can provide information on the magnetic moments of nanoparticles in a magnetic fluid because experimental magnetic scattering data are often different from those of model noninteracting polydisperse spheres, and because the corresponding magnetic correlation length is greater than the size of the nanoparticles. This technique is illustrated in two samples of synthetic highly stable colloidal magnetic fluids in deuterated cyclohexane that are almost free of aggregates. These samples of magnetite nanoparticles are coated either with a monolayer of oleic acid or myristic acid.

Because these samples are purely superparamagnetic and nonaggregated, the procedure described by Kohlbrecher and co-workers and Vekas and

co-workers for separating nuclear and magnetic scattering contributions can be applied.^{353,354} This procedure yields the form-factors of the nuclear and magnetic scattering, $F_N^2(q)$ and $F_M^2(q)$ (Figure 4.44). Because the nuclear scattering curves of both fluids fit well with the core-shell model, this model can provide the parameters of the log-normal size distribution function $D_N(R)$ for the magnetic nanoparticles. The thickness of the surfactant shell h (~ 1.4 nm) is the same for both samples. The magnetic scattering component reflects the correlation between the magnetic moments in the fluids, which is complex because their length exceeds the size of the magnetic nanoparticles. This correlation is demonstrated for both samples in Figure 4.44 by the radius gyration, the parameter obtained from the Guinier approximation to the initial parts of the curves. Note, however, that the polydispersity of the samples can influence the magnetic correlations.³⁵⁴

The same approach for the separation of the nuclear and magnetic scattering components was used by Perzynski and co-workers to characterize water-based magnetic fluids composed of charge-stabilized maghemite nanoparticles.³⁵⁵ The magnetic scattering signal shows that under a magnetic field, the fluid behaves as a purely superparamagnetic system of independent particles. The magnetic scattering length density indicates that the magnetization of the maghemite nanoparticles is approximately 25% lower than that of bulk maghemite. The citrate layer that stabilizes the nanoparticle is 0.5 nm thick, which is much smaller than the carboxylic acid monolayer of the sterically stabilized samples discussed above.

Krycka and co-workers expanded the capability of SANSPOLE to directly probe the three-dimensional magnetic morphology in any field of magnetite nanoparticles prepared by thermal decomposition (Figure 4.45a,b).^{356,357} The enhanced method indicated that under conditions of nominal saturation and at temperatures above 160 K, 9.0 nm magnetite nanoparticles have a uniformly canted magnetic shell 1.0 to 1.5 nm thick that is canted 90° to their ferrimagnetic cores (Figure 4.45c). The particles self-assemble, and the nanoparticle packing distance was determined to be an important parameter in the canting. Consequently, dipolar interparticle coupling might play a role in the magnetic core-shell morphology.

The microscopic internal magnetic (intracore) structures of three samples of magnetic iron oxide-dextran nanoparticles were investigated by polarization analyzed small angle neutron scattering (PASANS).³⁵⁸ The three samples were: (a) bionized nanoferrite (BNF) nanoparticles synthesized by a high temperature, high pressure homogenization process that leads to the formation of ordered iron oxide crystallites cores coated by a dextran shell; (b) JHU nanoparticles synthesized by a high gravity controlled precipitation method that also leads to the formation of iron oxide crystallites cores coated by dextran; and (c) commercially available nanomag-D-SPIO nanoparticles synthesized by coprecipitation of iron salts in the presence of dextran.

Unlike the BNF and JHU colloids, nanomag-D-SPIO particles have a diffuse core formed by multiple crystallites dispersed in a dextran matrix, similar to

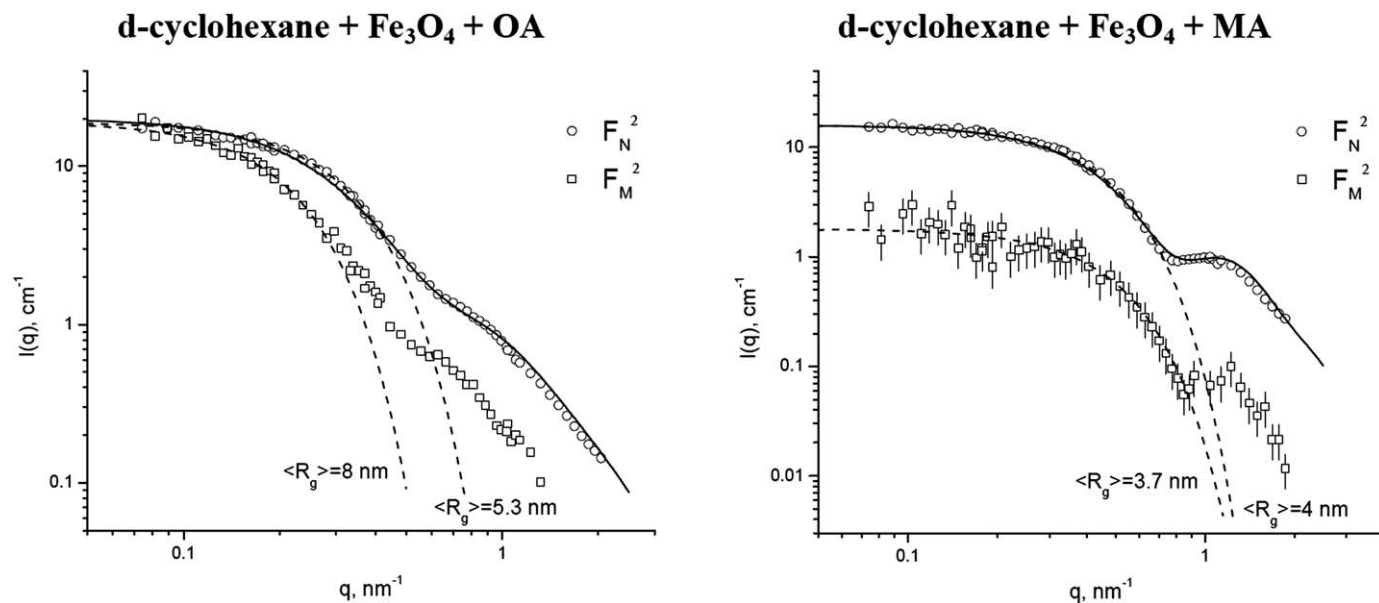


Figure 4.44 Separated nuclear and magnetic scattering components from SANSPOLE for magnetic fluids ($\varphi_m = 2.8\%$) based on deuterated cyclohexane and stabilized by (left) oleic and (right) myristic acids. Solid lines show fits of a core-shell model that takes into account particle size distribution function of log-normal type. Results of the fits are the following: **OA** - $R_0 = 3.4$ nm; $S = 0.38$; ($\langle R \rangle = 3.7$ nm; $\sigma = 1.4$ nm); $h = 1.38$ nm; **MA** - $R_0 = 2.3$ nm; $S = 0.28$; ($\langle R \rangle = 2.4$ nm; $\sigma = 0.7$ nm), $h = 1.35$ nm. Dashed lines show Guinier approximations; obtained radii of gyration are given (adapted from M. Balasoiu *et al. Rom. Rep. Phys.*, 2006, 58(3), 305–311; see also ref. 348a and ref. 349).

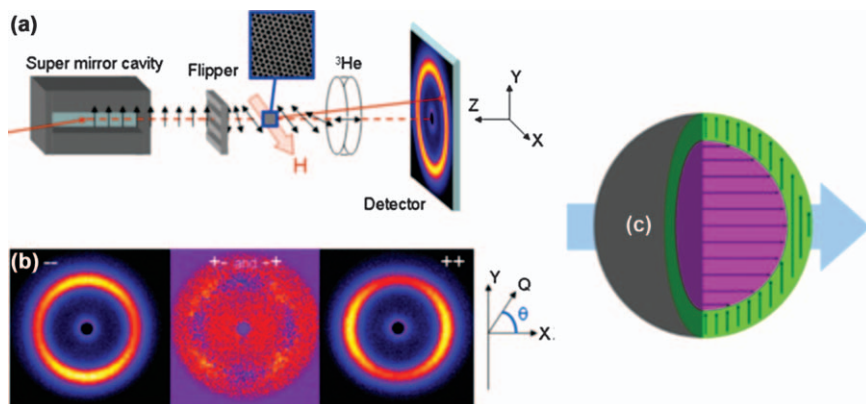


Figure 4.45 (a) Experimental setup includes a polarizing supermirror (FeSi multi-layer diffraction grating), an electromagnetic precession coil flipper, sample holder with cryostat and variable magnetic field, ^3He analyzer, and a position sensitive gas detector. Arrows indicate the neutron polarization direction. (b) Two-dimensional SANS images (shown here at 1.2 T, 200 K) are corrected for polarization efficiency. (c) Composite model involving a ferrimagnetic core of diameter $\approx 7:4$ nm with a 90° canted magnetic shell of thickness between 0.8 and 1.2 nm is depicted. Adapted with permission from K. L. Krycka, R. A. Booth, C. R. Hogg, Y. Ijiri, J. A. Borchers, W. C. Chen, S. M. Watson, M. Laver, T. R. Gentile, L. R. Dedon, S. Harris, J. J. Rhyne and S. A. Majetich, *Phys. Rev. Lett.* 2010, **104**, 207203. Copyright © The American Physical Society.

the most common magnetic iron oxide colloids used in medical imaging. Single magnetic nanoparticles (crystallites) can combine to form a magnetic core. This core can be formed of densely packed (as in the BNF and JHU samples) or loosely packed (as in the nanomag-D-SPIO sample) crystallites within the polymer matrix. Subtle variations among the crystallites and their spatial arrangements lead to complex micromagnetic structures that can be examined by SANS. The powerful polarization analyzed SANS technique can measure differences in magneto-structural properties among the nanoparticles, as evidenced by the magnetic interactions between crystallites within a core (intra-core) or between cores of neighboring nanoparticles (inter-core).

The resulting structural configurations of the composite particles are summarized in Figure 4.46.³⁵⁸ For BNF nanoparticles, analysis of the structure reveals that each dense core is comprised of stacked parallelepiped crystallites (roughly $8\text{ nm} \times 26\text{ nm} \times 66\text{ nm}$). Dipolar coupling between the crystallites favors alignment of the collinear components of the magnetic moments along the same direction, while the side-by-side components of the moments arrange antiparallel to one another. The magnetization components extracted from the PASANS results are consistent with the magnetic structure depicted in Figure 4.46D. Structural scattering measurements of the JHU nanoparticles (not shown here) suggest that each core is ~ 48 nm in

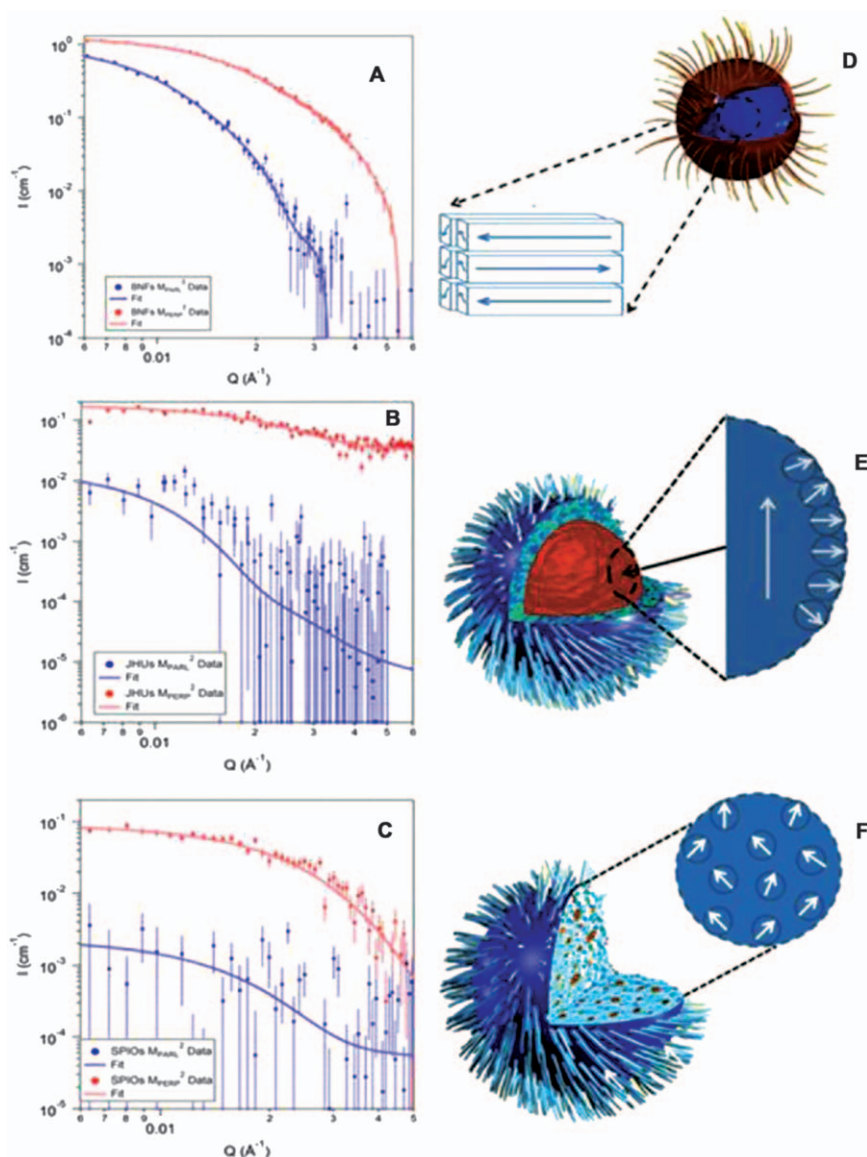


Figure 4.46 Magnetic scattering contributions, (blue) parallel and (red) perpendicular to the guide field with respect to the polarized beam SANS data of (A) BNF; (B) JHU; and (C) nanomag-D-spio (SPIO) nanoparticles in D_2O at room temperature. The fits use models illustrated in schematic diagrams D, E, and F. Domain structures of (D) BNF; (E) JHU; and (F) nanomag-D-spio particles obtained from analysis and modeling PASANS data. Error bars (1σ) might be smaller than the symbol. Scattered neutron intensity from JHU and nanomag-D-spio particles is lower than from BNF particles. Adapted with permission from C. L. Dennis, K. L., J. A. Borchers, R. D. Desautels, J. van Lierop, N. F. Huls, A. J. Jackson, C. Gruettner and R. Ivkov, *Adv. Funct. Mater.*, 2015, 25, 4300. Copyright © 2015 WILEY-VCH Verlag GmbH & Co. KGaA, Weinheim, Germany.

diameter and is comprised of many small, approximately spherical crystallites ~ 16 nm diameter. According to Dennis, Ivkov, and co-workers, the cores can be considered to have a magnetic core-shell-like structure with a magnetic core that is 36 nm in diameter and coherently magnetized parallel to the guide field. The magnetic shell has an average thickness of about 7 nm and is broken into smaller subdomains magnetized perpendicular to the guide field (Figure 4.46E). The nuclear scattering component measured for the nanomag-D-spio nanoparticles (not shown here) is accurately described by a collection of independent and approximately spherical crystallites of ~ 9 nm diameter that form aggregated diffuse cores in which the crystallites are dispersed throughout the polymer matrix (diameter ≈ 100 nm) (Figure 4.46F). The magnetic scattering perpendicular to the field is statistically significant (Figure 4.46C) and can be modeled as spherical domains of 14 nm in diameter, consistent with the average cluster size of 2–3 crystallites suggested by transmission electron microscopy analysis.

4.5.3.6 Mössbauer Spectroscopy

Mössbauer spectroscopy provides useful information regarding phase composition, local electronic configurations, and magnetic interactions, including relaxation phenomena in iron oxide nanoparticles.³⁵⁹ The best isotope for Mössbauer spectroscopy is ^{57}Fe both in terms of spectral resolution and appearance in magnetic phases. The natural abundance of ^{57}Fe is approximately 2%. Mössbauer spectroscopy is a nuclear resonance spectroscopy based on the resonant emission and absorption of γ radiation without loss of energy due to the recoil of the nucleus. The technique is specific to the solid state so only the solid part of a biomedical colloid can be investigated. A transmission spectrum records the intensity of the absorbed radiation following the Mössbauer events as a function of the relative velocity between an oscillatory moving radioactive source and the absorber.

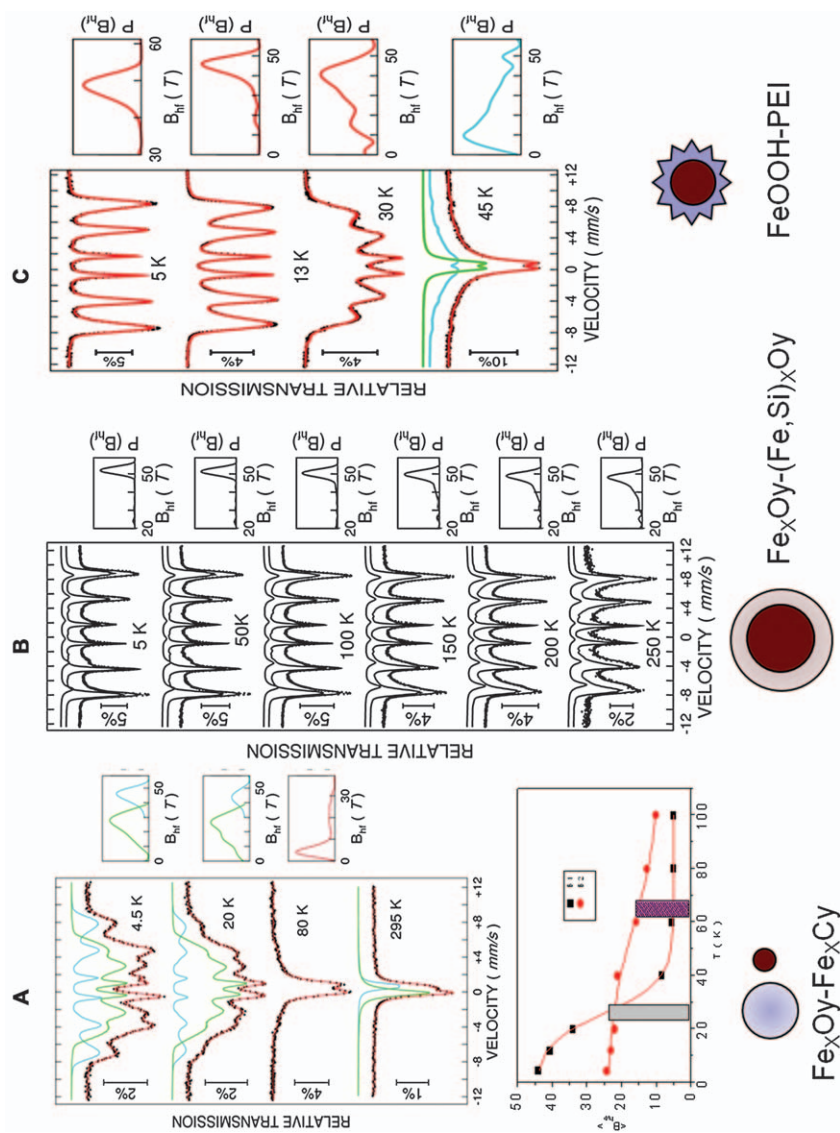
Local configurations of the iron within the nanoparticles give rise to small shifts or splittings of the nuclear levels due to the hyperfine interactions of the nucleus with the electron surrounding it. These hyperfine interactions are the same as in NMR spectroscopy, but are specific to ^{57}Fe . For ^{57}Fe , the range of these nuclear perturbations is tuned *via* the Doppler effect at a relative velocity in the order of 10 mm s^{-1} . One (singlet), two (doublet), or six (sextet) resonant absorption lines can appear for each configuration of the ^{57}Fe nuclide. These specific Mössbauer spectral patterns are described by the hyperfine parameters, including the isomer shift (δ), the quadrupole splitting (Δ), and the hyperfine magnetic field (B_{hf}). The first two parameters are electrostatic in nature and provide valuable information about the electron configuration of the central iron, including its valence and spin state, its coordination, its symmetry or asymmetry, the strength of the crystal field, and any electron delocalization phenomena. The hyperfine magnetic field is specific only to the sextet and can be uniquely determined from the nuclear magnetic splitting caused by the interaction between the nuclear spin and

the local magnetic field generated at the nucleus by the surrounding electrons. The hyperfine magnetic field is proportional to the net magnetic moment of the iron and is antiparallel to it when provided by spin-only contributions. This field gives information regarding the effective spin and magnetic moment. The averaged hyperfine magnetic field displays similar evolution as a function of temperature to the net magnetic moment. Reliable information describing magnetic relaxation phenomena can be obtained by following either the broadening of the sextet lines or the transition from the sextet, which characterizes a magnetically ordered state, to a doublet or singlet, characterizing a paramagnetic or superparamagnetic state.³²¹

Information about the direction of the atomic spin *versus* either the direction of the incoming radiation (laboratory axis) or the main direction of the electric field gradient (internal axis connected with crystalline directions) can be obtained *via* the intensity ratios or by comparing the quadrupole correction, which are specific to the magnetic state, to the quadrupolar splitting, which is specific to the paramagnetic state. Such local information is accessible for each Fe position and configuration in a sample, giving rise to a distinct spectral pattern. Hence, whereas magnetic measurements or macroscopic techniques provide average magnetic information about effective magnetic moments or relaxational mechanisms as if the sample is a homogeneous magnetic entity, Mössbauer spectroscopy provides this information for each Fe phase in a sample. In this regard, Mössbauer spectroscopy is more adequate for the study of iron oxide nanoparticles, where mixture of iron phases, bi-modal particle size distributions, or nanoparticles with core-shell structures are present.

A brief investigation of three samples demonstrates the capabilities of this technique in the investigation of iron-based nanoparticulate systems. Temperature-dependent Mössbauer spectra of iron oxide nanoparticles obtained *via* (A) laser pyrolysis, (B) chemical routes, and (C) hydrothermal synthesis are shown in Figure 4.47. In each case, the synthesis was expected to yield magnetite nanoparticles encapsulated in carbon, silica, or polyethyleneimine. XRD and TEM characterizations indicated that, in each sample, the nanoparticles had spinel-like structures and a broad size distribution with an average size of 4 nm (samples A and C) or 14 nm (sample B).

As expected, the Mössbauer spectra of these samples measured at the lowest temperature (4.5 to 5 K) consist of broad sextets. This is primarily due to the gradiental configuration of Fe ions along the particle diameter. At this temperature, the nanoparticles are in the magnetic frozen regime. In sample C, only one broad magnetic sextet is observed, suggesting that only one magnetic phase is present. Therefore, only one type of nanoparticle is present and a low number of Fe are involved in bonding with the polymer chains. The Mössbauer spectra of samples A and C, however, have two magnetic components. This observation suggests that two distinct Fe configurations are present. This can be explained either by the presence of two types of nanoparticles or by a core-shell structure. According to the



hyperfine parameters, the two Fe phases in sample A can be assigned to a defected spinel structure of the type $\text{Fe}_3\text{O}_{4-\gamma}\text{Fe}_2\text{O}_3$ and to Fe_3C . In sample B, however, the two phases belong to Fe_3O_4 and to the same spinel structure strongly penetrated by Si atoms. The type of phases formed provides evidence for two types of nanoparticles in sample A and for particles with a core-shell structure in sample B. The hyperfine parameters corresponding to the low-temperature spectrum of sample C provide evidence for goethite ($\alpha\text{-FeOOH}$) nanoparticles.

Information regarding the magnetic relaxation regime can be obtained by studying the temperature dependence of the hyperfine magnetic field, which is proportional to the atomic moment of Fe, following the same dynamics of the magnetic moment of a monodomain-like nanoparticle. Even though in the static regime the broad sextets impose a fitting with distributed hyperfine magnetic fields (the corresponding hyperfine field distributions are always shown on the right hand of the spectra), the relaxation regime follows the temperature evolution of the hyperfine magnetic field distribution and its characteristic parameters, including the average hyperfine magnetic field, $\langle B_{\text{hf}} \rangle$, and the distribution width, δB_{hf} . Both the collective excitation regime and the superparamagnetic regime can provide information describing τ_0 and the anisotropy energy of each type of nanoparticle. In the collective excitations regime,^{317,359} the hyperfine magnetic field decreases linearly according to eqn (4.31).

$$\langle B_{\text{hf}} \rangle / \langle B_{\text{hf}}^0 \rangle = 1 - \frac{k}{2KV} T \quad (4.31)$$

where $\langle B_{\text{hf}}^0 \rangle$ is the average hyperfine field in the magnetic frozen regime at the lowest temperature. The relationship for the blocking temperature [eqn (4.17)] can also be used if the Mössbauer time window, $\tau_{\text{m}} = 5 \times 10^{-9}$ s, is taken into account and if T_{B} can be determined from the temperature-dependent Mössbauer spectra. Kuncser proposed to define the blocking temperature in Mössbauer spectroscopy as the temperature where the

Figure 4.47 Mössbauer spectra of different temperatures as collected on three sets of nanoparticles: (A) iron oxide/C hybrids, (B) iron oxide/SiO₂ hybrids, and (C) iron oxohydroxide/polyethyleneimine hybrids (the evolution of the average hyperfine field *versus* temperature corresponding to both spectral components is shown only for the first case). The capability of Mössbauer spectroscopy is highlighted with respect to providing evidence of a particular phase composition and particle morphology in each case, as well as the power to analyze the magnetic relaxation mechanism for each phase.

Reprinted from *Materials Chemistry and Physics*, Volume 161, L. M. Popescu, R. M. Piticescu, M. Petriceanu, M. F. Ottaviani, M. Cangiotti, E. Vasile, M. M. Dirtu, M. Wolff, Y. Garcia, G. Schinteie and V. Kuncser, Hydrothermal synthesis of nanostructured hybrids based on iron oxide and branched PEI polymers. Influence of high pressure on structure and morphology, 84–95, Copyright 2015, with permission from Elsevier.

average hyperfine field decreases at half at its maximum value.³²¹ Two examples are shown in Figure 4.47. In these examples, blocking temperatures of 25 and 65 K were determined for the Fe oxide and Fe carbide nanoparticles, respectively. In these cases, the anisotropy energy KV can be obtained from eqn (4.31) from the linear decrease of the hyperfine magnetic field at temperatures much lower than T_B and the time constant τ_0 [eqn (4.17)] using the anisotropy energy and T_B determined from Mössbauer spectroscopy.

Alternatively, if τ_0 is determined by another method, such as using the power transferred to the ferrofluid by an induced AC magnetic field,³⁶⁰ both the anisotropy energy and the average size of the nanoparticles can be determined from eqn (4.17). For example, in Figure 4.47, in sample A, this approach determined that the average size of the Fe oxide nanoparticles is 2–3 nm, whereas that of the Fe carbide nanoparticles is 7–8 nm. Moreover, the relative spectral areas of the components determined that each type of nanoparticle is present in almost equal amounts. In comparison, transmission electron microscopy and magnetometry cannot provide evidence for the bimodal distribution of nanoparticles and their different relaxation mechanism.

For the SiO_2 -coated magnetite nanoparticles of sample B, the average particle size as determined by Mössbauer spectroscopy using the regime of collective excitations (valid up to the highest measuring temperatures) agrees well with the results obtained from transmission electron microscopy results. The thickness of the Si-penetrated layer, which is about 3 nm, was deduced from the relative spectral areas belonging to the core and to the shell Fe configurations. Finally, for sample C, a blocking temperature of 34 K was determined by Mössbauer spectroscopy, whereas a $\tau_0 = 10^{-10}$ s and an anisotropy constant K of 30 kJ m^{-3} were measured by DC magnetometry. From eqn (4.17), an average size of 4 nm was obtained for the goethite/polyethyleneimine nanoparticles, which is in excellent agreement with the results obtained from transmission electron microscopy,³³⁵ thereby confirming the relaxation time.

In spite of its numerous advantages, Mössbauer spectroscopy is rarely used to characterize iron oxide nanoparticles for MRI applications. Nonetheless, it is a powerful technique to evaluate scaling laws and to determine how the morpho-structural and magnetic parameters are connected to relaxivity.

4.5.4 Acknowledgements

This work was supported by the Research Program LLM-CCTFA 2016-2019 of the Romanian Academy. Financial support from the Romanian National Authority for Scientific Research and Innovation—ANCSI, Core Programme, Projects PN16-30 02 02 and PN16-48 01 02 are gratefully acknowledged. Valuable discussions in the framework of the COST Action TD1402 RADIO-MAG are highly appreciated.

4.6 Acquiring Phantom Images with Nanoparticles

PAULA FOSTER AND ROBERT BARTHA*

4.6.1 Contrast in T_2 - and T_2^* -weighted MRI

Several formulations of iron oxide nanoparticles have been tested for human use, including Feridex, Resovist, and Endorem (Section 4.1.1).¹⁶⁴ This subchapter contains information regarding the acquisition of phantom images using iron oxide nanoparticles. For articles summarizing the use of iron oxide nanoparticles in cancer, cell tracking, drug delivery, and as biosensors, interested readers are referred to other sources.^{40,361–367}

Iron oxide nanoparticles shorten the T_2 relaxation time constants of nearby hydrogen nuclei. This effect on relaxation is due to local magnetic field inhomogeneities induced by the agents that cause rapid loss of phase coherence (Section 4.1.2 and Figure 4.48).

In T_2 - and T_2^* -weighted images, this rapid dephasing of the magnetization results in a decrease in signal intensity observed in the material (for example, tissue or solvent) surrounding the agent. Because magnetic field distortions induced by the agents extend beyond the iron nanoparticles themselves, the region of signal loss observed in an image is greater than the dimension of the agent. This blooming artifact can be exploited to increase the detection sensitivity in some applications, including for the detection of single cells.³⁶⁸

The characterization of nanoparticles as contrast agents for magnetic resonance imaging is often achieved using specially prepared phantoms that attempt to replicate *in vivo* conditions. Observed image contrast is dependent on many factors including the concentration of the agent and the

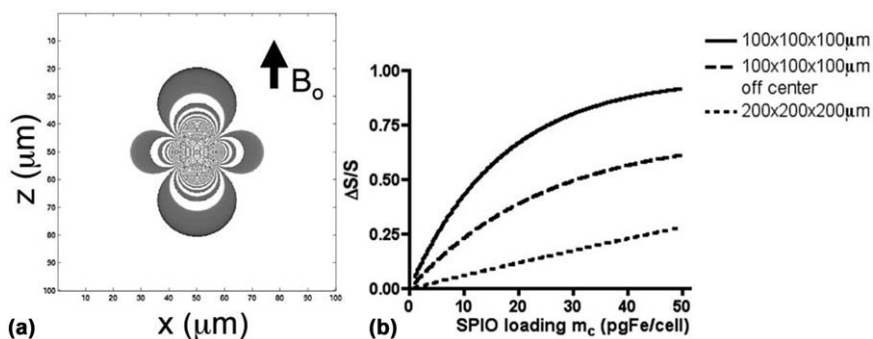


Figure 4.48 Numerical simulations of the phase and amplitude response of the fast imaging employing steady-state acquisition (FIESTA) pulse sequence for voxels containing a single, centered superparamagnetic-iron-oxide-labeled cell. The cross section through a 100 μm voxel shows the phase response surrounding a superparamagnetic-iron-oxide-loaded cell. Adapted with permission from C. Heyn, C. V. Bowen, B. K. Rutt and P. J. Foster, *Magn. Reson. Med.*, 2005, 53, 312. © 2005 Wiley-Liss, Inc.

magnetic field strength, which directly impact T_2 and T_2^* relaxation and imaging-relevant parameters, including pulse sequences, image resolution, and signal-to-noise ratios (SNR) of images. Superparamagnetic iron oxide nanoparticles achieve greatest sensitivity as contrast agents for MRI due to their ability to shorten T_2 relaxation time.^{369,370}

One example of the use of specially designed phantoms for iron oxide nanoparticles was the study of the detection threshold of single superparamagnetic-iron-oxide-labeled cells.³⁶⁸ In this work, the authors examined the effects of modifying image resolution and signal-to-noise ratio, and they derived an expression to predict the minimum amount of superparamagnetic iron oxide needed to observe a single cell in a homogeneous phantom. Phantoms compatible with magnetic resonance and optical imaging were created by placing iron-labeled cells on a single plane between two layers of gelatin (Figure 4.49).

A variety of imaging pulse sequences can be used to measure the presence of nanoparticles. Three-dimensional pulse sequences are most often used to provide optimal tissue coverage, tissue contrast, and image resolution.³⁷¹ The steady state balanced free precession sequence has been extensively investigated for the detection of iron oxide nanoparticles.

The steady state balanced free precession sequence is a type of gradient echo sequence³⁷² that produces images with large signal-to-noise ratios per unit time and is sensitive to flip angle and T_2/T_1 ratio, providing unique contrast relative to other sequences. Of particular interest for the detection of nanoparticles was the finding that images produced using the steady state balanced free precession sequence are insensitive to signal loss caused by

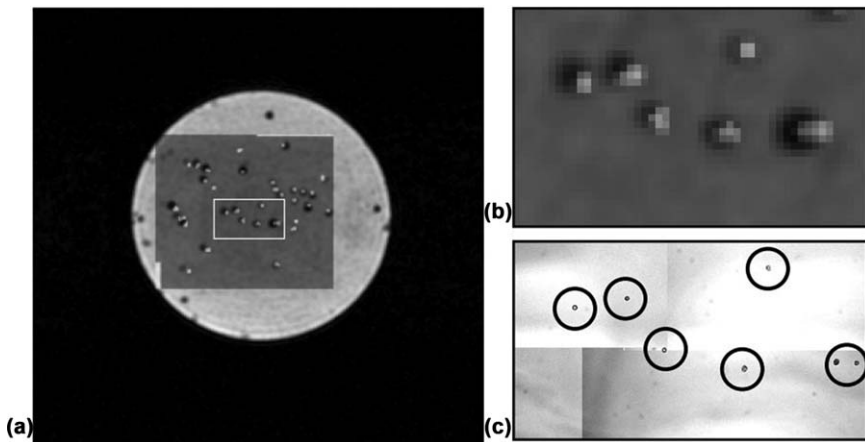


Figure 4.49 A three-dimensional-fast imaging employing steady-state acquisition image (100 μm isotropic pixel size) of a single plane of superparamagnetic-iron-oxide-labeled cells (10 pg per cell) (black holes) overlaid with a fluorescence microscopy image of cell distribution (white points). Adapted with permission from C. Heyn, C. V. Bowen, B. K. Rutt and P. J. Foster, *Magn. Reson. Med.*, 2005, 53, 312. © 2005 Wiley-Liss, Inc.

hemorrhage, which is not the case with T_2 - or T_2^* -weighted images. Under some conditions, steady state balanced free precession sequences can discriminate between iron associated with blood products in hemorrhage and the iron associated with cells labeled with superparamagnetic iron oxide.³⁷³

Although the majority of studies using iron oxide nanoparticles are based on detection using T_2 - or T_2^* -based imaging methods, the negative contrast induced in these images limits their interpretation. Voids in *in vivo* images could be due to the presence of iron nanoparticles or could be caused by other factors, including the presence of blood. In addition, quantification of the concentration of iron nanoparticles is only possible over a narrow range of low concentration values.

4.6.2 Contrast in T_1 -weighted MRI and Magnetic-field-strength Dependencies

Iron oxide nanoparticles also modulate T_1 relaxation in nuclei surrounding the nanoparticle, but the effect is usually less than the effect on T_2

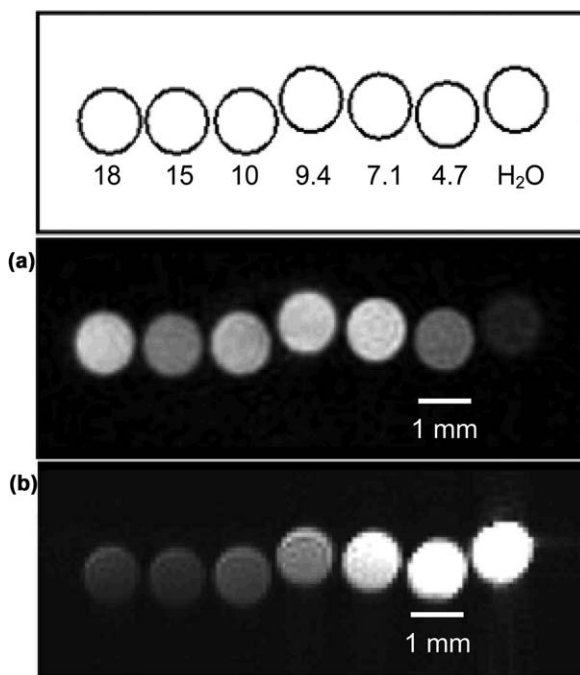


Figure 4.50 Magnetic resonance images of colloidal suspensions of cetrimonium-bromide-coated monocrystalline iron oxide nanocompounds of various sizes in water. In each case, $[\text{Fe}]_{\text{total}} = 4 \text{ mM}$. Top: average crystal size (nm) of nanocompounds imaged in each tube. (a) T_1 -weighted image acquired using sweep imaging with Fourier transform and (b) T_2^* -weighted gradient echo image. Adapted from ref. 379 with permission from The Royal Society of Chemistry.

relaxation.³⁷⁴ Nevertheless, T_1 -weighted imaging approaches can be used to detect iron-containing nanoparticles. Higher field strengths are expected to increase the contrast obtained from iron-containing nanoparticles. Generally signal-to-noise ratios increase in magnetic resonance images as a function of field strength. The additional signal-to-noise ratio available at higher fields can be used to increase the spatial resolution of the image, which alone improves the detection of iron-labeled cells.^{375–377} In addition, intra-voxel dephasing (T_2^*) increases with field strength, which increases contrast in images acquired with steady state balanced free precession sequences.³⁷⁸

Several studies have examined the effect of magnetic field strength on the potential contrast derived from iron oxide nanoparticles. Longitudinal relaxivity was found to be increased at lower magnetic field strengths with a plateau below ~ 0.02 T (~ 1 MHz for proton).³⁷⁹ In the same study, no change in transverse relaxivity was observed between 0.5 and 11.7 T (20–500 MHz for proton).³⁷⁹ This study went on to demonstrate the use of sweep imaging with Fourier transform (SWIFT) to produce a positive contrast for iron-containing nanoparticles (Figure 4.50a).³⁷⁹ The negative contrast observed for the same phantoms using T_2^* -weighted images is demonstrated in Figure 4.50b. Selective excitation of off-resonance water has also been used to generate positive contrast from iron-containing nanoparticles,³⁸⁰ as have methods that dephase background signal using gradients that are designed to maintain signals near nanoparticles.³⁸¹

Notes and References

1. J. U. Menon, P. Jadeja, P. Tambe, K. Vu, B. Yuan and K. T. Nguyen, *Theranostics*, 2013, **3**, 152.
2. A. Radomska, J. Leszczyszyn and M. W. Radomski, *Adv. Clin. Exp. Med.*, 2016, **25**, 151.
3. S.-F. Torabi and Y. Lu, *Curr. Opin. Biotechnol.*, 2014, **28**, 88.
4. M. Notarianni, J. Liu, K. Vernon and N. Motta, *Beilstein J. Nanotechnol.*, 2016, **7**, 149.
5. J. Wang and H. Gu, *Molecules*, 2015, **20**, 17070.
6. V. Nandwana, M. De, S. Chu, M. Jaiswal, M. Rotz, T. J. Meade and V. P. Dravid, *Cancer Treat. Res.*, 2015, **166**, 51.
7. D. Chen, C. A. Dougherty, K. Zhu and H. Hong, *J. Controlled Release*, 2015, **210**, 230.
8. C. S. S. R. Kumar and F. Mohammad, *Adv. Drug Delivery Rev.*, 2011, **63**, 789.
9. J.-H. Lee, J.-w. Kim and J. Cheon, *Mol. Cells*, 2013, **35**, 274.
10. S. K. Yen, P. Padmanabhan and S. T. Selvan, *Theranostics*, 2013, **3**, 986.
11. Y.-W. Li, Z.-G. Chen, J.-C. Wang and Z.-M. Zhang, *World J. Gastroenterol.*, 2015, **21**, 4334.
12. J. Estelrich, E. Escribano, J. Queralt and M. A. Busquets, *Int. J. Mol. Sci.*, 2015, **16**, 8070.

13. S. Laurent, D. Forge, M. Port, A. Roch, C. Robic, L. Vander Elst and R. N. Muller, *Chem. Rev.*, 2008, **108**, 2064.
14. D. Stanicki, L. V. Elst, R. N. Muller and S. Laurent, *Curr. Opin. Chem. Eng.*, 2015, **8**, 7.
15. W. H. Bragg, *Nature*, 1915, **95**, 344.
16. C. Ruemenapp, B. Gleich and A. Haase, *Pharm. Res.*, 2012, **29**, 1165.
17. A. Sundaresan and C. N. R. Rao, *Nano Today*, 2009, **4**, 96.
18. A. Fairweather, F. F. Roberts and A. J. E. Welch, *Rep. Prog. Phys.*, 1952, **15**, 142.
19. M. Modo, M. Hoehn and J. W. M. Bulte, *Mol. Imaging*, 2005, **4**, 143.
20. H.-J. Weinmann, W. Ebert, B. Misselwitz and H. Schmitt-Willich, *Eur. J. Radiol.*, 2003, **46**, 33.
21. Y. X. Wang, S. M. Hussain and G. P. Krestin, *Eur. Radiol.*, 2001, **11**, 2319.
22. L. L. Muldoon, M. Sandor, K. E. Pinkston and E. A. Neuwelt, *Neurosurgery*, 2005, **57**, 785.
23. G. H. Simon, J. von Vopelius-Feldt, Y. Fu, J. Schlegel, G. Pinotek, M. F. Wendland, M.-H. Chen and H. E. Daldrup-Link, *Invest. Radiol.*, 2006, **41**, 45.
24. R. Sun, J. Dittrich, M. Le-Huu, M. M. Mueller, J. Bedke, J. Kartenbeck, W. D. Lehmann, R. Krueger, M. Bock, R. Huss, C. Seliger, H.-J. Grone, B. Misselwitz, W. Semmler and F. Kiessling, *Invest. Radiol.*, 2005, **40**, 504.
25. L. Matuszewski, T. Persigehl, A. Wall, W. Schwindt, B. Tombach, M. Fobker, C. Poremba, W. Ebert, W. Heindel and C. Bremer, *Radiology*, 2005, **235**, 155.
26. F. K. Wacker, K. Reither, W. Ebert, M. Wendt, J. S. Lewin and K.-J. Wolf, *Radiology*, 2003, **226**, 459.
27. W. Li, S. Tutton, A. T. Vu, L. Pierchala, B. S. Y. Li, J. M. Lewis, P. V. Prasad and R. R. Edelman, *J. Magn. Reson. Imaging*, 2005, **21**, 46.
28. M. H. Schwenk, *Pharmacotherapy*, 2010, **30**, 70.
29. D. Artemov, *J. Cell. Biochem.*, 2003, **90**, 518.
30. D. Artemov, Z. M. Bhujwala and J. W. M. Bulte, *Curr. Pharm. Biotechnol.*, 2004, **5**, 485.
31. J. W. M. Bulte, S. C. Zhang, P. Van Gelderen, V. Herynek, E. K. Jordan, I. D. Duncan and J. A. Frank, *Proc. Natl. Acad. Sci. U. S. A.*, 1999, **96**, 15256.
32. L. G. Remsen, C. I. McCormick, S. Roman-Goldstein, G. Nilaver, R. Weissleder, A. Bogdanov, I. Hellstrom, R. A. Kroll and E. A. Neuwelt, *AJNR Am. J. Neuroradiol.*, 1996, **17**, 411.
33. R. Weissleder, A. Moore, U. Mahmood, R. Bhorade, H. Benveniste, E. A. Chiocca and J. P. Basilion, *Nat. Med.*, 2000, **6**, 351.
34. A. Moore, R. Weissleder and A. Bogdanov Jr., *J. Magn. Reson. Imaging*, 1997, **7**, 1140.
35. G. Fleige, F. Seeberger, D. Laux, M. Kresse, M. Taupitz, H. Pilgrim and C. Zimmer, *Invest. Radiol.*, 2002, **37**, 482.

36. A. Stroh, C. Zimmer, C. Gutzeit, M. Jakstadt, F. Marschinke, T. Jung, H. Pilgrimm and T. Grune, *Free Radic. Biol. Med.*, 2004, **36**, 976.
37. J. Schnorr, S. Wagner, C. Abramjuk, I. Wojner, T. Schink, T. J. Kroencke, E. Schellenberger, B. Hamm, H. Pilgrimm and M. Taupitz, *Invest. Radiol.*, 2004, **39**, 546.
38. J. Schnorr, S. Wagner, C. Abramjuk, R. Drees, T. Schink, E. A. Schellenberger, H. Pilgrimm, B. Hamm and M. Taupitz, *Radiology*, 2006, **240**, 90.
39. M. Taupitz, J. Schnorr, H. Pilgrimm, B. Hamm and S. Wagner, *Contrast Media Mol. Imaging*, 2006, **1**, 55.
40. S. Laurent, J.-L. Bridot, L. Vander Elst and R. N. Muller, *Future Med. Chem.*, 2010, **2**, 427.
41. J. W. Bulte, R. A. Brooks, B. M. Moskowitz, L. H. Bryant Jr. and J. A. Frank, *Magn. Reson. Med.*, 1999, **42**, 379.
42. A. Ouakssim, S. Fastrez, A. Roch, S. Laurent, Y. Gossuin, C. Pierart, L. Vander Elst and R. N. Muller, *J. Magn. Magn. Mater.*, 2004, **272–276**, E1711.
43. P. Gillis and S. H. Koenig, *Magn. Reson. Med.*, 1987, **5**, 323.
44. M. Gueron, *J. Magn. Reson.*, 1975, **19**, 58.
45. A. Roch and R. N. Muller, in *Proceeding of 11th Annual Meeting of the Society of Magnetic Resonance in Medicine*, ed. F. Welrli, 1992, p. 1447.
46. A. Roch, R. N. Muller and P. Gillis, *J. Chem. Phys.*, 1999, **110**, 5403.
47. A. Roch, P. Gillis, A. Ouakssim and R. N. Muller, *J. Magn. Magn. Mater.*, 1999, **201**, 77.
48. A. Roch, Y. Gossuin, R. N. Muller and P. Gillis, *J. Magn. Magn. Mater.*, 2005, **293**, 532.
49. J. H. Freed, *J. Chem. Phys.*, 1978, **68**, 4034.
50. Y. Ayant, E. Belorizky, J. Aluzon and J. Gallice, *J. Phys.*, 1975, **36**, 991.
51. V. K. LaMer and R. H. Dinegar, *J. Am. Chem. Soc.*, 1950, **72**, 4847.
52. *Nanobiotechnology: Inorganic Nanoparticles vs Organic Nanoparticles*, ed. J. M. de la Fuente and V. Grazu, Frontiers of Nanoscience Series, Elsevier, Oxford, 2012, vol. 4.
53. J.-P. Jolivet, E. Tronc and C. Chaneac, *C. R. Chim.*, 2002, **5**, 659.
54. C. Hui, C. Shen, T. Yang, L. Bao, J. Tian, H. Ding, C. Li and H. J. Gao, *J. Phys. Chem. C*, 2008, **112**, 11336.
55. C. Pereira, A. M. Pereira, C. Fernandes, M. Rocha, R. Mendes, M. P. Fernandez-Garcia, A. Guedes, P. B. Tavares, J.-M. Greneche, J. P. Araujo and C. Freire, *Chem. Mater.*, 2012, **24**, 1496.
56. M. Filippousi, M. Angelakeris, M. Katsikini, E. Paloura, I. Efthimiopoulos, Y. Wang, D. Zamboulis and G. Van Tendeloo, *J. Phys. Chem. C*, 2014, **118**, 16209.
57. H. Qu, D. Caruntu, H. Liu and C. J. O'Connor, *Langmuir*, 2011, **27**, 2271.
58. D. Stanicki, S. Boutry, S. Laurent, L. Wacheul, E. Nicolas, D. Crombez, L. Vander Elst, D. L. J. Lafontaine and R. N. Muller, *J. Mater. Chem. B*, 2014, **2**, 387.

59. B. H. Kim, K. Shin, S. G. Kwon, Y. Jang, H.-S. Lee, H. Lee, S. W. Jun, J. Lee, S. Y. Han, Y.-H. Yim, D.-H. Kim and T. Hyeon, *J. Am. Chem. Soc.*, 2013, **135**, 2407.
60. B. Qi, L. Ye, R. Stone, C. Dennis, T. M. Crawford and O. T. Mefford, *J. Phys. Chem. C*, 2013, **117**, 5429.
61. A. Demortiere, P. Panissod, B. P. Pichon, G. Pourroy, D. Guillon, B. Donnio and S. Begin-Colin, *Nanoscale*, 2011, **3**, 225.
62. C. de Montferrand, L. Hu, I. Milosevic, V. Russier, D. Bonnin, L. Motte, A. Brioude and Y. Lalatonne, *Acta Biomater.*, 2013, **9**, 6150.
63. G. Sharma and P. Jeevanandam, *RSC Adv.*, 2013, **3**, 189.
64. Z. Xu, C. Shen, Y. Tian, X. Shi and H. J. Gao, *Nanoscale*, 2010, **2**, 1027.
65. J. Park, K. An, Y. Hwang, J.-G. Park, H.-J. Noh, J.-Y. Kim, J.-H. Park, N.-M. Hwang and T. Hyeon, *Nat. Mater.*, 2004, **3**, 891.
66. N. Pimpha, S. Chaleawlerumpon and P. Sunintaboon, *Polymer*, 2012, **53**, 2015.
67. P. Guardia, N. Perez, A. Labarta and X. Batlle, *Langmuir*, 2010, **26**, 5843.
68. A. Louie, *Chem. Rev.*, 2010, **110**, 3146.
69. L. Chen, F. S. Razavi, A. Mumin, X. Guo, T.-K. Sham and J. Zhang, *RSC Adv.*, 2013, **3**, 2390.
70. A. Guerrero-Martinez, J. Perez-Juste and L. M. Liz-Marzan, *Adv. Mater.*, 2010, **22**, 1182.
71. J. Liu, S. Z. Qiao, Q. H. Hu and G. Q. Lu, *Small*, 2011, **7**, 425.
72. P. Yang, S. Gai and J. Lin, *Chem. Soc. Rev.*, 2012, **41**, 3679.
73. Y. Wang and H. Gu, *Adv. Mater.*, 2015, **27**, 576.
74. C.-M. Lee, S.-J. Cheong, E.-M. Kim, S. T. Lim, Y. Y. Jeong, M.-H. Sohn and H.-J. Jeong, *J. Nucl. Med.*, 2013, **54**, 1974.
75. E. Strable, J. W. M. Bulte, B. Moskowitz, K. Vivekanandan, M. Allen and T. Douglas, *Chem. Mater.*, 2001, **13**, 2201.
76. J. W. M. Bulte, T. Douglas, B. Witwer, S.-C. Zhang, E. Strable, B. K. Lewis, H. Zywicke, B. Miller, P. van Gelderen, B. M. Moskowitz, L. D. Duncan and J. A. Frank, *Nat. Biotechnol.*, 2001, **19**, 1141.
77. B. L. Frankamp, A. K. Boal, M. T. Tuominen and V. M. Rotello, *J. Am. Chem. Soc.*, 2005, **127**, 9731.
78. Z. Li, P. Huang, X. Zhang, J. Lin, S. Yang, B. Liu, F. Gao, P. Xi, Q. Ren and D. Cui, *Mol. Pharm.*, 2010, **7**, 94.
79. X. Shi, S. H. Wang, S. D. Swanson, S. Ge, Z. Cao, M. E. Van Antwerp, K. J. Landmark and J. R. Baker Jr., *Adv. Mater.*, 2008, **20**, 1671.
80. D. A. Tomalia, A. M. Naylor and W. A. Goddard, *Angew. Chem., Int. Ed. Engl.*, 1990, **29**, 138.
81. D. A. Tomalia, H. Baker, J. Dewald, M. Hall, G. Kallos, S. Martin, J. Roeck, J. Ryder and P. Smith, *Macromolecules*, 1986, **19**, 2466.
82. B. Pan, D. Cui, Y. Sheng, C. Ozkan, F. Gao, R. He, Q. Li, P. Xu and T. Huang, *Cancer Res.*, 2007, **67**, 8156.
83. B. Basly, G. Popa, S. Fleutot, B. P. Pichon, A. Garofalo, C. Ghobril, C. Billotey, A. Berniard, P. Bonazza, H. Martinez, D. Felder-Flesch and S. Begin-Colin, *Dalton Trans.*, 2013, **42**, 2146.

84. G. Lamanna, M. Kueny-Stotz, H. Mamlouk-Chaouachi, C. Ghobril, B. Basly, A. Bertin, I. Miladi, C. Billotey, G. Pourroy, S. Begin-Colin and D. Felder-Flesch, *Biomaterials*, 2011, **32**, 8562.
85. B. Basly, D. Felder-Flesch, P. Perriat, C. Billotey, J. Taleb, G. Pourroy and S. Begin-Colin, *Chem. Commun.*, 2010, **46**, 985.
86. T. J. Daou, J. M. Greneche, G. Pourroy, S. Buathong, A. Derory, C. Ulhaq-Bouillet, B. Donnio, D. Guillon and S. Begin-Colin, *Chem. Mater.*, 2008, **20**, 5869.
87. C. Boyer, V. Bulmus, P. Priyanto, W. Y. Teoh, R. Amal and T. P. Davis, *J. Mater. Chem.*, 2009, **19**, 111.
88. A. Bertin, J. Steibel, A.-I. Michou-Gallani, J.-L. Gallani and D. Felder-Flesch, *Bioconjugate Chem.*, 2009, **20**, 760.
89. A. Bertin, A.-I. Michou-Gallani, J. Steibel, J.-L. Gallani and D. Felder-Flesch, *New J. Chem.*, 2010, **34**, 267.
90. A. Bertin, A.-I. Michou-Gallani, J.-L. Gallani and D. Felder-Flesch, *Toxicol. In Vitro*, 2010, **24**, 1386.
91. A. J. L. Villaraza, A. Bumb and M. W. Brechbiel, *Chem. Rev.*, 2010, **110**, 2921.
92. J. Panyam and V. Labhasetwar, *Adv. Drug Delivery Rev.*, 2003, **55**, 329.
93. O. Pillai and R. Panchagnula, *Curr. Opin. Chem. Biol.*, 2001, **5**, 447.
94. S. M. Moghimi, A. C. Hunter and J. C. Murray, *Pharmacol. Rev.*, 2001, **53**, 283.
95. F. Alexis, E. Pridgen, L. K. Molnar and O. C. Farokhzad, *Mol. Pharm.*, 2008, **5**, 505.
96. C.-G. Gölander, J. N. Herron, K. Lim, P. Claesson, P. Stenius and J. D. Andrade, Properties of Immobilized PEG Films and the Interaction with Proteins: Experiments and Modeling, in *Poly(Ethylene Glycol) Chemistry: Biotechnical and Biomedical Applications*, ed. J. M. Harris, Plenum Press, New York, 1992, ch. 15, pp. 221–245.
97. M. Zhang and M. Ferrari, *Proc. SPIE*, 1998, **3258**, 15.
98. P. Caliceti, O. Schiavon, A. Mocali and F. M. Veronese, *Farmaco*, 1989, **44**, 711.
99. J. Cheng, B. A. Teply, I. Sherifi, J. Sung, G. Luther, F. X. Gu, E. Levy-Nissenbaum, A. F. Radovic-Moreno, R. Langer and O. C. Farokhzad, *Biomaterials*, 2007, **28**, 869.
100. W. Wang, X. Ji, H. B. Na, M. Safi, A. Smith, G. Palui, J. M. Perez and H. Mattoussi, *Langmuir*, 2014, **30**, 6197.
101. E. A. Osborne, T. M. Atkins, D. A. Gilbert, S. M. Kauzlarich, K. Liu and A. Y. Louie, *Nanotechnology*, 2012, **23**, 215602.
102. Y. Chao, P. P. Karmali and D. Simberg, *Adv. Exp. Med. Biol.*, 2012, **733**, 115.
103. S. M. Griffiths, N. Singh, G. J. S. Jenkins, P. M. Williams, A. W. Orbaek, A. R. Barron, C. J. Wright and S. H. Doak, *Anal. Chem.*, 2011, **83**, 3778.
104. Y. Wang, B. Li, F. Xu, D. Jia, Y. Feng and Y. Zhou, *J. Biomater. Sci., Polym. Ed.*, 2012, **23**, 843.

105. B. Stephen Inbaraj, T.-Y. Tsai and B.-H. Chen, *Sci. Technol. Adv. Mater.*, 2012, **13**, 015002.
106. X. Chen, H. Lv, M. Ye, S. Wang, E. Ni, F. Zeng, C. Cao, F. Luo and J. Yan, *Int. J. Pharm.*, 2012, **426**, 248.
107. H. L. Ma, Y. F. Xu, X. R. Qi, Y. Maitani and T. Nagai, *Int. J. Pharm.*, 2008, **354**, 217.
108. H.-L. Ma, X.-R. Qi, Y. Maitani and T. Nagai, *Int. J. Pharm.*, 2007, **333**, 177.
109. L. Zhou, B. He and F. Zhang, *ACS Appl. Mater. Interfaces*, 2012, **4**, 192.
110. M. Mahmoudi, A. Simchi, M. Imani, M. A. Shokrgozar, A. S. Milani, U. O. Haefeli and P. Stroeve, *Colloids Surf., B*, 2010, **75**, 300.
111. F. Cengelli, J. A. Grzyb, A. Montoro, H. Hofmann, S. Hanessian and L. Juillerat-Jeanneret, *ChemMedChem*, 2009, **4**, 988.
112. S. Hanessian, J. A. Grzyb, F. Cengelli and L. Juillerat-Jeanneret, *Bioorg. Med. Chem.*, 2008, **16**, 2921.
113. A. Petri-Fink, M. Chastellain, L. Juillerat-Jeanneret, A. Ferrari and H. Hofmann, *Biomaterials*, 2005, **26**, 2685.
114. H. Vu-Quang, M. Muthiah, Y.-K. Kim, C.-S. Cho, R. Namgung, W. J. Kim, J. H. Rhee, S. H. Kang, S. Y. Jun, Y.-J. Choi, Y. Y. Jeong and I.-K. Park, *Carbohydr. Polym.*, 2012, **88**, 780.
115. H. Vu-Quang, M.-K. Yoo, H.-J. Jeong, H.-J. Lee, M. Muthiah, J. H. Rhee, J.-H. Lee, C.-S. Cho, Y. Y. Jeong and I.-K. Park, *Acta Biomater.*, 2011, **7**, 3935.
116. X. He, X. Wu, X. Cai, S. Lin, M. Xie, X. Zhu and D. Yan, *Langmuir*, 2012, **28**, 11929.
117. Y. Chang, N. Liu, L. Chen, X. Meng, Y. Liu, Y. Li and J. Wang, *J. Mater. Chem.*, 2012, **22**, 9594.
118. X. Wu, X. He, L. Zhong, S. Lin, D. Wang, X. Zhu and D. Yan, *J. Mater. Chem.*, 2011, **21**, 13611.
119. W.-M. Liu, Y.-N. Xue, N. Peng, W.-T. He, R.-X. Zhuo and S.-W. Huang, *J. Mater. Chem.*, 2011, **21**, 13306.
120. Y.-L. Chang, X.-L. Meng, Y.-L. Zhao, K. Li, B. Zhao, M. Zhu, Y.-P. Li, X.-S. Chen and J.-Y. Wang, *J. Colloid Interface Sci.*, 2011, **363**, 403.
121. K. Uzun, E. Çevik, M. Şenel, H. Söezeri, A. Baykal, M. F. Abasiyanik and M. S. Toprak, *J. Nanopart. Res.*, 2010, **12**, 3057.
122. M. R. Saboktakin, A. Maharramov and M. A. Ramazanov, *Polym.-Plast. Technol. Eng.*, 2009, **48**, 834.
123. X. Shi, T. P. Thomas, L. A. Myc, A. Kotlyar and J. R. Baker Jr., *Phys. Chem. Chem. Phys.*, 2007, **9**, 5712.
124. K. J. Landmark, S. DiMaggio, J. Ward, C. Kelly, S. Vogt, S. Hong, A. Kotlyar, A. Myc, T. P. Thomas, J. E. Penner-Hahn, J. R. Baker, M. M. Banaszak Holl and B. G. Orr, *ACS Nano*, 2008, **2**, 773.
125. R. Zhu, W. Jiang, Y. Pu, K. Luo, Y. Wu, B. He and Z. Gu, *J. Mater. Chem.*, 2011, **21**, 5464.
126. A. L. Martin, L. M. Bernas, B. K. Rutt, P. J. Foster and E. R. Gillies, *Bioconjugate Chem.*, 2008, **19**, 2375.

127. N. Arsalani, H. Fattahi and M. Nazarpour, *eXPRESS Polym. Lett.*, 2010, **4**, 329.
128. H.-Y. Lee, S.-H. Lee, C. Xu, J. Xie, J.-H. Lee, B. Wu, A. L. Koh, X. Wang, R. Sinclair, S. X. Wang, D. G. Nishimura, S. Biswal, S. Sun, S. H. Cho and X. Chen, *Nanotechnology*, 2008, **19**, 165101.
129. X. L. Liu, H. M. Fan, J. B. Yi, Y. Yang, E. S. G. Choo, J. M. Xue, D. D. Fan and J. Ding, *J. Mater. Chem.*, 2012, **22**, 8235.
130. N. Miguel-Sancho, O. Bomati-Miguel, G. Colom, J. P. Salvador, M. P. Marco and J. Santamaria, *Chem. Mater.*, 2011, **23**, 2795.
131. C. Yue-Jian, T. Juan, X. Fei, Z. Jia-Bi, G. Ning, Z. Yi-Hua, D. Ye and G. Liang, *Drug Dev. Ind. Pharm.*, 2010, **36**, 1235.
132. J.-F. Lutz, S. Stiller, A. Hoth, L. Kaufner, U. Pison and R. Cartier, *Bio-macromolecules*, 2006, **7**, 3132.
133. D. Patel, J. Y. Moon, Y. Chang, T. J. Kim and G. H. Lee, *Colloids Surf., A*, 2008, **313 + 314**, 91.
134. C. Ravikumar and R. Bandyopadhyaya, *J. Phys. Chem. C*, 2011, **115**, 1380.
135. J. Sagiv, *J. Am. Chem. Soc.*, 1980, **102**, 92.
136. S. Onclin, B. J. Ravoo and D. N. Reinhoudt, *Angew. Chem., Int. Ed.*, 2005, **44**, 6282.
137. S. P. Pujari, L. Scheres, A. T. M. Marcelis and H. Zuilhof, *Angew. Chem., Int. Ed.*, 2014, **53**, 6322.
138. C. Haensch, S. Hoepfener and U. S. Schubert, *Chem. Soc. Rev.*, 2010, **39**, 2323.
139. A. V. Krasnoslobodtsev and S. N. Smirnov, *Langmuir*, 2002, **18**, 3181.
140. M. C. Pirrung, *Angew. Chem., Int. Ed.*, 2002, **41**, 1276.
141. R. G. Acres, A. V. Ellis, J. Alvino, C. E. Lenahan, D. A. Khodakov, G. F. Metha and G. G. Andersson, *J. Phys. Chem. C*, 2012, **116**, 6289.
142. Y. Liu, Y. Li, X.-M. Li and T. He, *Langmuir*, 2013, **29**, 15275.
143. N. Reinhardt, L. Adumeau, O. Lambert, S. Ravaine and S. Mornet, *J. Phys. Chem. B*, 2015, **119**, 6401.
144. R. De Palma, S. Peeters, M. J. Van Bael, H. Van den Rul, K. Bonroy, W. Laureyn, J. Mullens, G. Borghs and G. Maes, *Chem. Mater.*, 2007, **19**, 1821.
145. M. Ma, Y. Zhang, W. Yu, H.-y. Shen, H.-q. Zhang and N. Gu, *Colloids Surf., A*, 2003, **212**, 219.
146. E. K. U. Larsen, T. Nielsen, T. Wittenborn, H. Birkedal, T. Vorup-Jensen, M. H. Jakobsen, L. Oestergaard, M. R. Horsman, F. Besenbacher, K. A. Howard and J. Kjems, *ACS Nano*, 2009, **3**, 1947.
147. N. Arsalani, H. Fattahi, S. Laurent, C. Burtea, L. V. Elst and R. N. Muller, *Contrast Media Mol. Imaging*, 2012, **7**, 185.
148. M. Bloemen, W. Brullot, T. T. Luong, N. Geukens, A. Gils and T. Verbiest, *J. Nanopart. Res.*, 2012, **14**, 1100.
149. X.-Y. Wang, D. Mertz, C. Blanco-Andujar, A. Bora, M. Menard, F. Meyer, C. Giraudeau and S. Begin-Colin, *RSC Adv.*, 2016, **6**, 93784.
150. M. Ohmori and E. Matijevic, *J. Colloid Interface Sci.*, 1992, **150**, 594.

151. M. Klotz, A. Ayril, C. Guizard, C. Menager and V. Cabuil, *J. Colloid Interface Sci.*, 1999, **220**, 357.
152. A. P. Philipse, M. P. B. van Bruggen and C. Pathmamanoharan, *Langmuir*, 1994, **10**, 92.
153. L. M. Liz-Marzan, M. Giersig and P. Mulvaney, *Langmuir*, 1996, **12**, 4329.
154. Y. Kobayashi, M. Horie, M. Konno, B. Rodriguez-Gonzalez and L. M. Liz-Marzan, *J. Phys. Chem. B*, 2003, **107**, 7420.
155. T. Seeger, Th. Köhler, Th. Frauenheim, N. Grobert, M. Rühle, M. Terrones and G. Seifert, *Chem. Commun.*, 2002, 34.
156. S. L. C. Pinho, G. A. Pereira, P. Voisin, J. Kassem, V. Bouchaud, L. Etienne, J. A. Peters, L. Carlos, S. Mornet, C. F. G. C. Geraldés, J. Rocha and M.-H. Delville, *ACS Nano*, 2010, **4**, 5339.
157. Y. Lu, Y. Yin, B. T. Mayers and Y. Xia, *Nano Lett.*, 2002, **2**, 183.
158. D. K. Yi, S. S. Lee, G. C. Papaefthymiou and J. Y. Ying, *Chem. Mater.*, 2006, **18**, 614.
159. C. Cannas, A. Musinu, A. Ardu, F. Orru, D. Peddis, M. Casu, R. Sanna, F. Angius, G. Diaz and G. Piccaluga, *Chem. Mater.*, 2010, **22**, 3353.
160. J. Kim, J. E. Lee, J. Lee, J. H. Yu, B. C. Kim, K. An, Y. Hwang, C.-H. Shin, J.-G. Park, J. Kim and T. Hyeon, *J. Am. Chem. Soc.*, 2006, **128**, 688.
161. J. Kim, H. S. Kim, N. Lee, T. Kim, H. Kim, T. Yu, I. C. Song, W. K. Moon and T. Hyeon, *Angew. Chem., Int. Ed.*, 2008, **47**, 8438.
162. F. Ye, S. Laurent, A. Fornara, L. Astolfi, J. Qin, A. Roch, A. Martini, M. S. Toprak, R. N. Muller and M. Muhammed, *Contrast Media Mol. Imaging*, 2012, **7**, 460.
163. J. Liu, C. Detrembleur, M.-C. De Pauw-Gillet, S. Mornet, L. Vander Elst, S. Laurent, C. Jerome and E. Duguet, *J. Mater. Chem. B*, 2014, **2**, 59.
164. R. Qiao, C. Yang and M. Gao, *J. Mater. Chem.*, 2009, **19**, 9286.
165. N. Fauconnier, J. N. Pons, J. Roger and A. Bee, *J. Colloid Interface Sci.*, 1997, **194**, 427.
166. M. Lattuada and T. A. Hatton, *Langmuir*, 2007, **23**, 2158.
167. L. Maurizi, H. Bisht, F. Bouyer and N. Millot, *Langmuir*, 2009, **25**, 8857.
168. M. Racuciu, D. E. Creanga and A. Airinei, *Eur. Phys. J. E: Soft Matter Biol. Phys.*, 2006, **21**, 117.
169. T. J. Daou, S. Buathong, D. Ung, B. Donnio, G. Pourroy, D. Guillon and S. Begin, *Sens. Actuators, B*, 2007, **126**, 159.
170. B. Basly, D. Felder-Flesch, P. Perriat, G. Pourroy and S. Begin-Colin, *Contrast Media Mol. Imaging*, 2011, **6**, 132.
171. E. D. Smolensky, H.-Y. E. Park, T. S. Berquo and V. C. Pierre, *Contrast Media Mol. Imaging*, 2011, **6**, 189.
172. A. K. L. Yuen, G. A. Hutton, A. F. Masters and T. Maschmeyer, *Dalton Trans.*, 2012, **41**, 2545.
173. E. Amstad, S. Zurcher, A. Mashaghi, J. Y. Wong, M. Textor and E. Reimhult, *Small*, 2009, **5**, 1334.
174. N. A. Frey, S. Peng, K. Cheng and S. Sun, *Chem. Soc. Rev.*, 2009, **38**, 2532.
175. C. Fang and M. Zhang, *J. Mater. Chem.*, 2009, **19**, 6258.

176. H. B. Na, I. C. Song and T. Hyeon, *Adv. Mater.*, 2009, **21**, 2133.
177. A. G. Roca, R. Costo, A. F. Rebolledo, S. Veintemillas-Verdaguer, P. Tartaj, T. González-Carreño, M. P. Morales and C. J. Serna, *J. Phys. D: Appl. Phys.*, 2009, **42**, 224002.
178. S. Begin-Colin and D. Felder-Flesch, Functionalisation of Magnetic Iron Oxide Nanoparticles, in *Magnetic Nanoparticles: From Fabrication to Clinical Applications*, ed. N. T. K. Thanh, CRC Press, Boca Raton, 2012, ch. 6, pp. 151–191.
179. I. Milosevic, L. Motte, B. Aoun, T. Li, Y. Ren, C. Sun and M.-L. Saboungi, *Biochim. Biophys. Acta, Gen. Subj.*, 2017, **1861**, 3621.
180. G. Kataby, Y. Kolytyn, A. Ulman, I. Felner and A. Gedanken, *Appl. Surf. Sci.*, 2002, **201**, 191.
181. C. Boyer, M. R. Whittaker, V. Bulmus, J. Liu and T. P. Davis, *NPG Asia Mater.*, 2010, **2**, 23.
182. J. Zeng, L. Jing, Y. Hou, M. Jiao, R. Qiao, Q. Jia, C. Liu, F. Fang, H. Lei and M. Gao, *Adv. Mater.*, 2014, **26**, 2694.
183. C. Yee, G. Kataby, A. Ulman, T. Prozorov, H. White, A. King, M. Rafailovich, J. Sokolov and A. Gedanken, *Langmuir*, 1999, **15**, 7111.
184. A. Walter, A. Garofalo, A. Parat, H. Martinez, D. Felder-Flesch and S. Begin-Colin, *Nanotechnol. Rev.*, 2015, **4**, 581.
185. C. Vichery, I. Maurin, P. Bonville, J.-P. Boilot and T. Gacoin, *J. Phys. Chem. C*, 2012, **116**, 16311.
186. W. Baaziz, B. P. Pichon, S. Fleutot, Y. Liu, C. Lefevre, J.-M. Greneche, M. Toumi, T. Mhiri and S. Begin-Colin, *J. Phys. Chem. C*, 2014, **118**, 3795.
187. C. Sun, J. S. H. Lee and M. Zhang, *Adv. Drug Delivery Rev.*, 2008, **60**, 1252.
188. J. Cheon and J.-H. Lee, *Acc. Chem. Res.*, 2008, **41**, 1630.
189. P. Guardia, B. Batlle-Brugal, A. G. Roca, O. Iglesias, M. P. Morales, C. J. Serna, A. Labarta and X. Batlle, *J. Magn. Magn. Mater.*, 2007, **316**, e756.
190. D. K. Nagesha, B. D. Plouffe, M. Phan, L. H. Lewis, S. Sridhar and S. K. Murthy, *J. Appl. Phys.*, 2009, **105**, 07B317.
191. W. Wu, Q. He and C. Jiang, *Nanoscale Res. Lett.*, 2008, **3**, 397.
192. Y.-w. Jun, J.-H. Lee and J. Cheon, *Angew. Chem., Int. Ed.*, 2008, **47**, 5122.
193. J. Tian, Y. K. Feng and Y. S. Xu, *Macromol. Res.*, 2006, **14**, 209.
194. L. Wang, K. G. Neoh, E. T. Kang, B. Shuter and S.-C. Wang, *Adv. Funct. Mater.*, 2009, **19**, 2615.
195. A. Figuerola, R. Di Corato, L. Manna and T. Pellegrino, *Pharmacol. Res.*, 2010, **62**, 126.
196. T. J. Daou, G. Pourroy, J. M. Greneche, A. Bertin, D. Felder-Flesch and S. Begin-Colin, *Dalton Trans.*, 2009, 4442.
197. T. J. Daou, S. Begin-Colin, J. M. Greneche, F. Thomas, A. Derory, P. Bernhardt, P. Legare and G. Pourroy, *Chem. Mater.*, 2007, **19**, 4494.
198. M. Kumagai, M. R. Kano, Y. Morishita, M. Ota, Y. Imai, N. Nishiyama, M. Sekino, S. Ueno, K. Miyazono and K. Kataoka, *J. Controlled Release*, 2009, **140**, 306.

199. S. I. C. J. Palma, M. Marciello, A. Carvalho, S. Veintemillas-Verdaguer, M. d. P. Morales and A. C. A. Roque, *J. Colloid Interface Sci.*, 2015, **437**, 147.
200. C. Blanco-Andujar, A. Walter, G. Cotin, C. Bordeianu, D. Mertz, D. Felder-Flesch and S. Begin-Colin, *Nanomedicine*, 2016, **11**, 1889.
201. L. Pinho and M. J. Mosquera, *J. Phys. Chem. C*, 2011, **115**, 22851.
202. A. K. Gupta and M. Gupta, *Biomaterials*, 2005, **26**, 3995.
203. M. R. Jones, R. J. MacFarlane, A. E. Prigodich, P. C. Patel and C. A. Mirkin, *J. Am. Chem. Soc.*, 2011, **133**, 18865.
204. S. Nangia and R. Sureshkumar, *Langmuir*, 2012, **28**, 17666.
205. Q. Song and Z. J. Zhang, *J. Am. Chem. Soc.*, 2004, **126**, 6164.
206. D. Srikala, V. N. Singh, A. Banerjee and B. R. Mehta, *J. Nanosci. Nanotechnol.*, 2010, **10**, 8088.
207. S. Carencu, S. Moldovan, L. Roiban, I. Florea, D. Portehault, K. Valle, P. Belleville, C. Boissiere, L. Rozes, N. Mezailles, M. Drillon, C. Sanchez and O. Ersen, *Nanoscale*, 2016, **8**, 1260.
208. B. P. Pichon, O. Gerber, C. Lefevre, I. Florea, S. Fleutot, W. Baaziz, M. Pauly, M. Ohlmann, C. Ulhaq, O. Ersen, V. Pierron-Bohnes, P. Panissod, M. Drillon and S. Begin-Colin, *Chem. Mater.*, 2011, **23**, 2886.
209. W. D. Pyrz and D. J. Buttrey, *Langmuir*, 2008, **24**, 11350.
210. W. S. Rasband, *ImageJ* [Online], version 1.51n. U.S. National Institutes of Health, Bethesda, MD, 1997–2017. <https://imagej.nih.gov/ij/> (last accessed 2017).
211. A. Le Beulze, E. Duguet, S. Mornet, J. Majimel, M. Treguer-Delapierre, S. Ravaine, I. Florea and O. Ersen, *Langmuir*, 2014, **30**, 1424.
212. J. Burgin, I. Florea, J. Majimel, A. Dobri, O. Ersen and M. Treguer-Delapierre, *Nanoscale*, 2012, **4**, 1299.
213. S. Takeda and H. Yoshida, *Microscopy*, 2013, **62**, 193.
214. W. Baaziz, I. Florea, S. Moldovan, V. Papaefthimiou, S. Zafeiratos, S. Begin-Colin, D. Begin, O. Ersen and C. Pham-Huu, *J. Mater. Chem. A*, 2015, **3**, 11203.
215. O. Ersen, I. Florea, C. Hirlimann and C. Pham-Huu, *Mater. Today*, 2015, **18**, 395.
216. I. Florea, A. Demortiere, C. Petit, H. Bulou, C. Hirlimann and O. Ersen, *Nanoscale*, 2012, **4**, 5125.
217. J. Rodriguez-Carvajal, *Phys. B*, 1993, **192**, 55.
218. A. Le Bail, H. Duroy and J. L. Fourquet, *Mater. Res. Bull.*, 1988, **23**, 447.
219. L. Lutterotti and P. Scardi, *J. Appl. Crystallogr.*, 1990, **23**, 246.
220. L. Lutterotti, S. Matthies and H.-R. Wenk, MAUD (Material Analysis Using Diffraction): A User Friendly Java Program for Rietveld Texture Analysis and More, in *Proceedings of the Twelfth International Conference on Textures of Materials*, ed. J. A. Szipunar, NRC Research Press, Ottawa, 1999, vol. 1, pp. 1599–1604.
221. M. Ferrari and L. Lutterotti, *J. Appl. Phys.*, 1994, **76**, 7246.

222. J. C. Bacri, R. Perzynski, D. Salin, V. Cabuil and R. Massart, *J. Magn. Magn. Mater.*, 1990, **85**, 27.
223. T. Hyeon, S. S. Lee, J. Park, Y. Chung and H. B. Na, *J. Am. Chem. Soc.*, 2001, **123**, 12798.
224. J. Santoyo Salazar, L. Perez, O. de Abril, L. Truong Phuoc, D. Ihiawakrim, M. Vazquez, J.-M. Greneche, S. Begin-Colin and G. Pourroy, *Chem. Mater.*, 2011, **23**, 1379.
225. T. J. Daou, G. Pourroy, S. Begin-Colin, J. M. Greneche, C. Ulhaq-Bouillet, P. Legare, P. Bernhardt, C. Leuvrey and G. Rogez, *Chem. Mater.*, 2006, **18**, 4399.
226. T. Belin, N. Guigue-Millot, T. Caillot, D. Aymes and J. C. Niepce, *J. Solid State Chem.*, 2002, **163**, 459.
227. N. Guigue-Millot, Y. Champion, M. J. Hyetch, F. Bernard, S. Begin-Colin and P. Perriat, *J. Phys. Chem. B*, 2001, **105**, 7125.
228. J. P. Jolivet and E. Tronc, *J. Colloid Interface Sci.*, 1988, **125**, 688.
229. A. E. Deatsch and B. A. Evans, *J. Magn. Magn. Mater.*, 2014, **354**, 163.
230. R. Hergt, S. Dutz, R. Müller and M. Zeisberger, *J. Phys.: Condens. Matter*, 2006, **18**, S2919.
231. W. Baaziz, B. P. Pichon, C. Lefevre, C. Ulhaq-Bouillet, J.-M. Greneche, M. Toumi, T. Mhiri and S. Begin-Colin, *J. Phys. Chem. C*, 2013, **117**, 11436.
232. W. Baaziz, B. P. Pichon, Y. Liu, J.-M. Greneche, C. Ulhaq-Bouillet, E. Terrier, N. Bergéard, V. Halte, C. Boeglin, F. Choueikani, M. Toumi, T. Mhiri and S. Begin-Colin, *Chem. Mater.*, 2014, **26**, 5063.
233. J.-H. Lee, J.-t. Jang, J.-s. Choi, S. H. Moon, S.-h. Noh, J.-w. Kim, J.-G. Kim, I.-S. Kim, K. I. Park and J. Cheon, *Nat. Nanotechnol.*, 2011, **6**, 418.
234. P. Tartaj, M. del Puerto Morales, S. Veintemillas-Verdaguer, T. González-Carreño and C. J. Serna, *J. Phys. D: Appl. Phys.*, 2003, **36**, R182.
235. A. Walter, A. Parat, A. Garofalo, S. Laurent, L. Vander Elst, R. N. Muller, T. Wu, E. Heuillard, E. Robinet, F. Meyer, D. Felder-Flesch and S. Begin-Colin, *Part. Part. Syst. Charact.*, 2015, **32**, 552.
236. N. Pinna, S. Grancharov, P. Beato, P. Bonville, M. Antonietti and M. Niederberger, *Chem. Mater.*, 2005, **17**, 3044.
237. O. N. Shebanova and P. Lazor, *J. Solid State Chem.*, 2003, **174**, 424.
238. J. B. Yang, X. D. Zhou, W. B. Yelon, W. J. James, Q. Cai, K. V. Gopalakrishnan, S. K. Malik, X. C. Sun and D. E. Nikles, *J. Appl. Phys.*, 2004, **95**, 7540.
239. R. M. Cornell and U. Schwertmann, *The Iron Oxides: Structure, Properties, Reactions, Occurrences and Uses*, VCH, Weinheim, Germany, 1st edn, 1996, p. 135.
240. D. L. A. De Faria, S. V. Silva and M. T. De Oliveira, *J. Raman Spectrosc.*, 1997, **28**, 873.
241. M. Aronniemi, J. Sainio and J. Lahtinen, *Surf. Sci.*, 2005, **578**, 108.
242. C. W. Jung, *Magn. Reson. Imaging*, 1995, **13**, 675.

243. T. Fujii, F. M. F. de Groot, G. A. Sawatzky, F. C. Voogt, T. Hibma and K. Okada, *Phys. Rev. B: Condens. Matter Mater. Phys.*, 1999, **59**, 3195.
244. T. Kendelewicz, P. Liu, C. S. Doyle, G. E. Brown, E. J. Nelson and S. A. Chambers, *Surf. Sci.*, 2000, **453**, 32.
245. R. L. Mössbauer, *Z. Phys.*, 1958, **151**, 124.
246. R. L. Mössbauer, *Naturwissenschaften*, 1958, **45**, 538.
247. R. L. Mössbauer, *Z. Naturforsch.*, 1959, **14**, 211.
248. R. L. Mössbauer, *Science*, 1962, **137**, 731.
249. R. L. Mössbauer, Recoilless Nuclear Resonance Absorption of Gamma Radiation: Nobel Lecture, December 11, 1961, in *Nobel Lectures, Physics 1942–1962*, Elsevier, Amsterdam, 1964.
250. N. N. Greenwood and T. C. Gibb, *Mössbauer Spectroscopy*, Chapman and Hall, London, 1971.
251. P. Gütllich, R. Link and A. Trautwein, *Mössbauer Spectroscopy and Transition Metal Chemistry*, Inorganic Chemistry Concepts Series 3, Springer-Verlag, Berlin, 1978.
252. *Mössbauer Spectroscopy Applied to Inorganic Chemistry*, ed. G. J. Long, Modern Inorganic Chemistry Series, Plenum Press, New York, 1984, vol. 1.
253. *Mössbauer Spectroscopy Applied to Inorganic Chemistry*, ed. G. J. Long, Modern Inorganic Chemistry Series, Plenum Press, New York, 1987, vol. 2.
254. *Mössbauer Spectroscopy Applied to Inorganic Chemistry*, ed. G. J. Long and F. Grandjean, Modern Inorganic Chemistry Series, Plenum Press, New York, 1989, vol. 3.
255. *Mössbauer Spectroscopy Applied to Magnetism and Materials Science*, ed. G. J. Long and F. Grandjean, Modern Inorganic Chemistry Series, Plenum Press, New York, 1993, vol. 1.
256. *Mössbauer Spectroscopy Applied to Magnetism and Materials Science*, ed. G. J. Long and F. Grandjean, Modern Inorganic Chemistry Series, Plenum Press, New York, 1996, vol. 2.
257. P. Gütllich, E. Bill and A. X. Trautwein, *Mössbauer Spectroscopy and Transition Metal Chemistry: Fundamentals and Applications*, Springer, Heidelberg, Germany, 2011.
258. S. S. Hanna, J. Heberle, G. J. Perlow, R. S. Preston and D. H. Vincent, *Phys. Rev. Lett.*, 1960, **4**, 513.
259. J. Chappert, *J. Phys. Colloques*, 1974, **35**, C6–C71.
260. J. Chappert, J. Teillet and F. Varret, *J. Magn. Magn. Mater.*, 1979, **11**, 200.
261. J.-M. Greneche, *Acta Phys. Slovaca*, 1995, **45**, 45.
262. J.-M. Greneche, The Contribution of ^{57}Fe Mössbauer Spectroscopy to Investigate Magnetic Nanomaterials, in *Mössbauer Spectroscopy: Tutorial Book*, ed. Y. Yoshida and G. Langouche, Springer-Verlag, Berlin, 2013, ch. 4, pp. 187–241.
263. M. E. Lopez-Herrera, J. M. Greneche and F. Varret, *Phys. Rev. B: Condens. Matter Mater. Phys.*, 1983, **28**, 4944.

264. S. Mørup, J. A. Dumesic and H. Topsøe, Magnetic Microcrystals, in *Applications of Mössbauer Spectroscopy*, ed. R. L. Cohen, Academic Press, New York, 1980, ch. 1, vol. 2, pp. 1–53.
265. J. L. Dormann, *Rev. Phys. Appl.*, 1981, **16**, 275.
266. S. Mørup, Mössbauer Effect Studies of Microcrystalline Materials, in *Mössbauer Spectroscopy Applied to Inorganic Chemistry*, ed. G. J. Long, Modern Inorganic Chemistry Series, Plenum Press, New York, 1987, ch. 2, vol. 2, p. 89.
267. *Magnetic Properties of Fine Particles*, ed. J. L. Dormann and D. Fiorani, North-Holland, Amsterdam, 1992.
268. E. Tronc, *Nuovo Cimento Soc. Ital. Fis., D*, 1996, **18D**, 163.
269. J. L. Dormann, D. Fiorani and E. Tronc, *Adv. Chem. Phys.*, 1997, **98**, 283.
270. S. Mørup and M. F. Hansen, Superparamagnetic Particles, in *Handbook of Magnetism and Advanced Magnetic Materials*, ed. H. Krönmüller and S. Parkin, Wiley, Chichester, U.K., 2007, vol. 4, pp. 2159–2176.
271. G. C. Papaefthymiou, *Nano Today*, 2009, **4**, 438.
272. S. Mørup, C. Frandsen and M. F. Hansen, Magnetic Properties of Nanoparticles, in *The Oxford Handbook of Nanoscience and Technology: Volume 2: Materials: Structures, Properties and Characterization Techniques*, ed. A. V. Narlikar and Y. Y. Fu, Oxford University Press, Oxford, 2010, ch. 20.
273. S. Mørup, M. F. Hansen and C. Frandsen, *Beilstein J. Nanotechnol.*, 2010, **1**, 182.
274. S. Mørup, M. F. Hansen and C. Frandsen, Magnetic Nanoparticles, in *Comprehensive Nanoscience and Technology*, ed. D. L. Andrews, G. D. Scholes and G. P. Wiederrecht, Academic Press, London, 2011, vol. 1, ch. 1. 4, pp. 437–491.
275. D. Peddis, N. Yaacoub, M. Ferretti, A. Martinelli, G. Piccaluga, A. Musinu, C. Cannas, G. Navarra, J. M. Greneche and D. Fiorani, *J. Phys.: Condens. Matter*, 2011, **23**, 426004.
276. A. Karimi, B. Denizot, F. Hindré, R. Filmon, J.-M. Greneche, S. Laurent, T. J. Daou, S. Begin-Colin and J.-J. Le Jeune, *J. Nanopart. Res.*, 2010, **12**, 1239.
277. J. Fouineau, K. Brymora, L. Ourry, F. Mammeri, N. Yaacoub, F. Calvayrac, S. Ammar-Merah and J. M. Greneche, *J. Phys. Chem. C*, 2013, **117**, 14295.
278. J. M. D. Coey, *Phys. Rev. Lett.*, 1971, **27**, 1140.
279. E. Tronc, P. Prene, J. P. Jolivet, J. L. Dormann and J. M. Greneche, *Hyperfine Interact.*, 1997, **112**, 97.
280. E. Tronc, A. Ezzir, R. Cherkaoui, C. Chaneac, M. Nogues, H. Kachkachi, D. Fiorani, A. M. Testa, J. M. Greneche and J. P. Jolivet, *J. Magn. Magn. Mater.*, 2000, **221**, 63.
281. E. Tronc, D. Fiorani, M. Nogues, A. M. Testa, F. Lucari, F. D’Orazio, J. M. Greneche, W. Wernsdorfer, N. Galvez, C. Chaneac, D. Maily and J. P. Jolivet, *J. Magn. Magn. Mater.*, 2003, **262**, 6.

282. E. Tronc, M. Nogues, C. Chaneac, F. Lucari, F. D'Orazio, J. M. Greneche, J. P. Jolivet, D. Fiorani and A. M. Testa, *J. Magn. Magn. Mater.*, 2004, **272–276**, 1474.
283. T. Grieb, K. Mueller, R. Fritz, M. Schowalter, N. Neugebohrn, N. Knaub, K. Volz and A. Rosenauer, *Ultramicroscopy*, 2012, **117**, 15.
284. T. J. A. Slater, A. Janssen, P. H. C. Camargo, M. G. Burke, N. J. Zaluzec and S. J. Haigh, *Ultramicroscopy*, 2016, **162**, 61.
285. S. Carencio, X. F. Le Goff, J. Shi, L. Roiban, O. Ersen, C. Boissiere, C. Sanchez and N. Mezailles, *Chem. Mater.*, 2011, **23**, 2270.
286. D.-F. Liu, W. Wu, J.-J. Ling, S. Wen, N. Gu and X.-Z. Zhang, *Adv. Funct. Mater.*, 2011, **21**, 1498.
287. I. Szleifer, *Biophys. J.*, 1997, **72**, 595.
288. G. B. Deacon and R. J. Phillips, *Coord. Chem. Rev.*, 1980, **33**, 227.
289. A. Hofmann, S. Thierbach, A. Semisch, A. Hartwig, M. Taupitz, E. Ruehl and C. Graf, *J. Mater. Chem.*, 2010, **20**, 7842.
290. Q. Ye, F. Zhou and W. Liu, *Chem. Soc. Rev.*, 2011, **40**, 4244.
291. H. Gulley-Stahl, P. A. Hogan II, W. L. Schmidt, S. J. Wall, A. Buhlage and H. A. Bullen, *Environ. Sci. Technol.*, 2010, **44**, 4116.
292. E. Guénin, Y. Lalatonne, J. Bolley, I. Milosevic, C. Platas-Iglesias and L. Motte, *J. Nanopart. Res.*, 2014, **16**, 2596.
293. J. Bolley, Y. Lalatonne, O. Haddad, D. Letourneur, M. Soussan, J. Perard-Viret and L. Motte, *Nanoscale*, 2013, **5**, 11478.
294. M. D. Shultz, J. U. Reveles, S. N. Khanna and E. E. Carpenter, *J. Am. Chem. Soc.*, 2007, **129**, 2482.
295. L. Lartigue, K. Oumzil, Y. Guari, J. Larionova, C. Guerin, J.-L. Montero, V. Barragan-Montero, C. Sangregorio, A. Caneschi, C. Innocenti, T. Kalaivani, P. Arosio and A. Lascialfari, *Org. Lett.*, 2009, **11**, 2992.
296. O. K. Borggaard, B. Raben-Lange, A. L. Gimsing and B. W. Strobel, *Geoderma*, 2005, **127**, 270.
297. C. Huang, K. G. Neoh, L. Wang, E.-T. Kang and B. Shuter, *J. Mater. Chem.*, 2010, **20**, 8512.
298. M. R. Turner, E. Duguet and C. Labrugere, *Surf. Interface Anal.*, 1997, **25**, 917.
299. M. G. Nooney, T. S. Murrell, J. S. Corneille, E. I. Rusert, L. R. Hossner and D. W. Goodman, *J. Vac. Sci. Technol., A*, 1996, **14**, 1357.
300. M. Das, D. Mishra, P. Dhak, S. Gupta, T. K. Maiti, A. Basak and P. Pramanik, *Small*, 2009, **5**, 2883.
301. K. M. Krishnan, *IEEE Trans. Magn.*, 2010, **46**, 2523.
302. M. Colombo, S. Carregal-Romero, M. F. Casula, L. Gutierrez, M. P. Morales, I. B. Boehm, J. T. Heverhagen, D. Prospero and W. J. Parak, *Chem. Soc. Rev.*, 2012, **41**, 4306.
303. E. Amstad, M. Textor and E. Reimhult, *Nanoscale*, 2011, **3**, 2819.
304. E. Tombacz, R. Turcu, V. Socoliuc and L. Vekas, *Biochem. Biophys. Res. Commun.*, 2015, **468**, 442.
305. S. Behrens and I. Appel, *Curr. Opin. Biotechnol.*, 2016, **39**, 89.

306. S. Laurent, A. A. Saei, S. Behzadi, A. Panahifar and M. Mahmoudi, *Expert Opin. Drug Delivery*, 2014, **11**, 1449.
307. M.-A. Fortin, Nanoparticles for Magnetic Resonance Imaging (MRI) Applications in Medicine, in *Functional Materials: For Energy, Sustainable Development and Biomedical Sciences*, ed. M. Leclerc and R. Gauvin, De Gruyter, Berlin, 2014, ch. 13, pp. 332–374.
308. E. Peng, F. Wang and J. M. Xue, *J. Mater. Chem. B*, 2015, **3**, 2241.
309. I. Solomon, *Phys. Rev.*, 1955, **99**, 559.
310. N. Bloembergen, *J. Chem. Phys.*, 1957, **27**, 572.
311. V. C. Pierre, M. J. Allen and P. Caravan, *JBIC, J. Biol. Inorg. Chem.*, 2014, **19**, 127.
312. S. Laurent, L. V. Elst, A. Roch and R. N. Muller, Structure, Synthesis and Characterization of Contrast Agents for Magnetic Resonance Molecular Imaging, in *NMR-MRI, μ SR and Mössbauer Spectroscopies in Molecular Magnets*, ed. P. Carretta and A. Lasciafari, Springer, Milan, Milano, 2007, pp. 71–87.
313. M. R. J. Carroll, R. C. Woodward, M. J. House, W. Y. Teoh, R. Amal, T. L. Hanley and T. G. St Pierre, *Nanotechnology*, 2010, **21**, 035103.
314. Q. L. Vuong, J.-F. Berret, J. Fresnais, Y. Gossuin and O. Sandre, *Adv. Healthcare Mater.*, 2012, **1**, 502.
315. R. M. Cornell and U. Schwertmann, *The Iron Oxides: Structure, Properties, Reactions, Occurrences and Uses*, Wiley-VCH, Weinheim, Germany, 2nd edn, 2003.
316. S. Bedanta, O. Petravic and W. Kleemann, Supermagnetism, in *Handbook of Magnetic Materials*, ed. K. H. J. Buschow, North-Holland, Amsterdam, 2015, vol. 23, ch. 1.
317. V. Kuncser, P. Palade, A. Kuncser, S. Greculeasa and G. Schinteie, Engineering Magnetic Properties of Nanostructures via Size Effects and Interphase Interactions, in *Size Effects in Nanostructures: Basics and Applications*, ed. V. Kuncser and L. Miu, Springer Series in Materials Science 205, Springer, Heidelberg, Germany, 2014, ch. 7, pp. 169–237.
318. C. M. Sorensen, Magnetism, in *Nanoscale Materials in Chemistry*, ed. K. J. Klabunde, Wiley, New York, 2001, ch. 6, pp. 169–221.
319. D. Susan-Resiga, V. Socoliuc, T. Boros, T. Borbath, O. Marinica, A. Han and L. Vekas, *J. Colloid Interface Sci.*, 2012, **373**, 110.
320. A. Kuncser and V. Kuncser, *J. Magn. Magn. Mater.*, 2015, **395**, 34.
321. V. Kuncser, G. Schinteie, B. Sahoo, W. Keune, D. Bica, L. Vekas and G. Filoti, *J. Phys.: Condens. Matter*, 2007, **19**, 016205.
322. L. Neel, *Ann. Geophys.*, 1949, **5**, 99.
323. R. E. Rosensweig, *J. Magn. Magn. Mater.*, 2002, **252**, 370.
324. R. W. Chantrell, J. Popplewell and S. W. Charles, *IEEE Trans. Magn.*, 1978, **14**, 975.
325. *Ferrohydrodynamics*, ed. R. E. Rosensweig, Cambridge University Press, Cambridge U.K., 1985.
326. M. Rasa, *Eur. Phys. J. E: Soft Matter Biol. Phys.*, 2000, **2**, 265.

327. A. O. Ivanov and O. B. Kuznetsova, *Phys. Rev. E: Stat., Nonlinear, Soft Matter Phys.*, 2001, **64**, 041405.
328. A. O. Ivanov, S. S. Kantorovich, E. N. Reznikov, C. Holm, A. F. Pshenichnikov, A. V. Lebedev, A. Chremos and P. J. Camp, *Phys. Rev. E: Stat., Nonlinear, Soft Matter Phys.*, 2007, **75**, 061405.
329. I. Szalai, S. Nagy and S. Dietrich, *Phys. Rev. E: Stat., Nonlinear, Soft Matter Phys.*, 2015, **92**, 042314.
330. V. Socoliuc, L. Vekas and R. Turcu, *Soft Matter*, 2013, **9**, 3098.
331. G. Cogoni, M. Grosso, R. Baratti and J. A. Romagnoli, *AIChE J.*, 2012, **58**, 3731.
332. D. X. Chen, E. Pardo and A. Sanchez, *J. Magn. Magn. Mater.*, 2006, **306**, 135.
333. B. Luigjes, S. M. C. Woudenberg, R. de Groot, J. D. Meeldijk, H. M. Torres Galvis, K. P. de Jong, A. P. Philipse and B. H. Erne, *J. Phys. Chem. C*, 2011, **115**, 14598.
334. D. Predoi, V. Kuncser, M. Nogues, E. Tronc, J. P. Jolive, G. Filoti and G. Schinteie, *J. Optoelectron. Adv. Mater.*, 2003, **5**, 211.
335. L. M. Popescu, R. M. Piticescu, M. Petriceanu, M. F. Ottaviani, M. Cangiotti, E. Vasile, M. M. Dirtu, M. Wolff, Y. Garcia, G. Schinteie and V. Kuncser, *Mater. Chem. Phys.*, 2015, **161**, 84.
336. V. S. Mendeleev and A. O. Ivanov, *Phys. Rev. E: Stat., Nonlinear, Soft Matter Phys.*, 2004, **70**, 051502.
337. V. Socoliuc and L. B. Popescu, *J. Magn. Magn. Mater.*, 2012, **324**, 113.
338. S. L. Saville, R. C. Woodward, M. J. House, A. Tokarev, J. Hammers, B. Qi, J. Shaw, M. Saunders, R. R. Varsani, T. G. St Pierre and O. T. Mefford, *Nanoscale*, 2013, **5**, 2152.
339. V. Socoliuc and D. Bica, *Prog. Colloid Polym. Sci.*, 2001, **117**, 131.
340. A. L. Willis, N. J. Turro and S. O'Brien, *Chem. Mater.*, 2005, **17**, 5970.
341. D. Wilson and M. A. Langell, *Appl. Surf. Sci.*, 2014, **303**, 6.
342. R. Turcu, V. Socoliuc, I. Craciunescu, A. Petran, A. Paulus, M. Franzreb, E. Vasile and L. Vekas, *Soft Matter*, 2015, **11**, 1008.
343. H.-C. Roth, S. P. Schwaminger, M. Schindler, F. E. Wagner and S. Berensmeier, *J. Magn. Magn. Mater.*, 2015, **377**, 81.
344. J. Salafranca, J. Gazquez, N. Perez, A. Labarta, S. T. Pantelides, S. J. Pennycook, X. Batlle and M. Varela, *Nano Lett.*, 2012, **12**, 2499.
345. S. Sathish and S. Balakumar, *Mater. Chem. Phys.*, 2016, **173**, 364.
346. A. Nan, T. Radu and R. Turcu, *RSC Adv.*, 2016, **6**, 43330.
347. I. Y. Toth, M. Szekeres, R. Turcu, S. Saringer, E. Illes, D. Nesztor and E. Tombacz, *Langmuir*, 2014, **30**, 15451.
348. (a) L. Vékás, M. V. Avdeev and D. Bica, Magnetic Nanofluids: Synthesis and Structure, in *NanoScience in Biomedicine*, ed. D. Shi, Springer, Berlin, 2009, ch. 25, pp. 650–704; (b) M. V. Avdeev and V. L. Aksenov, *Phys.–Usp.*, 2010, **53**, 971.
349. M. V. Avdeev, D. Bica, L. Vékás, O. Marinica, M. Balasoiu, V. L. Aksenov, L. Rosta, V. M. Garamus and A. Schreyer, *J. Magn. Magn. Mater.*, 2007, **311**, 6.

350. A. Wiedenmann, *J. Appl. Crystallogr.*, 2000, **33**, 428.
351. A. Wiedenmann, *Phys. B*, 2005, **356**, 246.
352. M. Klokkenburg, B. H. Ern e, A. Wiedenmann, A. V. Petukhov and A. P. Philipse, *Phys. Rev. E: Stat., Nonlinear, Soft Matter Phys.*, 2007, **75**, 051408.
353. V. Aksenov, M. Avdeev, M. Balasoiu, L. Rosta, G. Torok, L. Vekas, D. Bica, V. Garamus and J. Kohlbrecher, *Appl. Phys. A: Mater. Sci. Process.*, 2002, **74**, S943.
354. M. V. Avdeev, M. Balasoiu, V. L. Aksenov, V. M. Garamus, J. Kohlbrecher, D. Bica and L. Vekas, *J. Magn. Magn. Mater.*, 2004, **270**, 371.
355. M. V. Avdeev, E. Dubois, G. Meriguet, E. Wandersman, V. M. Garamus, A. V. Feoktystov and R. Perzynski, *J. Appl. Crystallogr.*, 2009, **42**, 1009.
356. K. L. Krycka, R. A. Booth, C. R. Hogg, Y. Ijiri, J. A. Borchers, W. C. Chen, S. M. Watson, M. Laver, T. R. Gentile, L. R. Dedon, S. Harris, J. J. Rhyne and S. A. Majetich, *Phys. Rev. Lett.*, 2010, **104**, 207203.
357. S. Sun, H. Zeng, D. B. Robinson, S. Raoux, P. M. Rice, S. X. Wang and G. Li, *J. Am. Chem. Soc.*, 2004, **126**, 273.
358. C. L. Dennis, K. L. Krycka, J. A. Borchers, R. D. Desautels, J. van Lierop, N. F. Huls, A. J. Jackson, C. Gruettner and R. Ivkov, *Adv. Funct. Mater.*, 2015, **25**, 4300.
359. M. F. Thomas and C. E. Johnson, *Mossbauer Spectroscopy of Magnetic Solids*, in *Mossbauer Spectroscopy*, ed. D. P. E. Dickson and F. J. Berry, Cambridge University Press, Cambridge, U.K., 1986, ch. 4, pp. 143–197.
360. N. Iacob, G. Schinteie, C. Bartha, P. Palade, L. Vekas and V. Kuncser, *J. Phys. D: Appl. Phys.*, 2016, **49**, 295001.
361. Z. Bakhtiary, A. A. Saei, M. J. Hajipour, M. Raoufi, O. Vermesh and M. Mahmoudi, *Nanomedicine*, 2016, **12**, 287.
362. M. Iv, N. Telischak, D. Feng, S. J. Holdsworth, K. W. Yeom and H. E. Daldrup-Link, *Nanomedicine*, 2015, **10**, 993.
363. G. T. Jasmin, R. A. de Souza, P. H. Louzada, R. Rosado-de-Castro, Mendez-Otero and A. C. Campos de Carvalho, *Int. J. Nanomed.*, 2017, **12**, 779.
364. X.-H. Peng, X. Qian, H. Mao, A. Y. Wang, Z. Chen, S. Nie and D. M. Shin, *Int. J. Nanomed.*, 2008, **3**, 311.
365. V. Valdiglesias, N. Fernandez-Bertolez, G. Kilic, C. Costa, S. Costa, S. Fraga, M. J. Bessa, E. Pasaro, J. P. Teixeira and B. Laffon, *J. Trace Elem. Med. Biol.*, 2016, **38**, 53.
366. J. S. Weinstein, C. G. Varallyay, E. Dosa, S. Gahramanov, B. Hamilton, W. D. Rooney, L. L. Muldoon and E. A. Neuwelt, *J. Cereb. Blood Flow Metab.*, 2010, **30**, 15.
367. C. Zhang, Q. Zou, J. Chen, C. Li, Y. Yan and Y. Yan, *Asia Pac. J. Clin. Oncol.*, 2016, **12**, 13.
368. C. Heyn, C. V. Bowen, B. K. Rutt and P. J. Foster, *Magn. Reson. Med.*, 2005, **53**, 312.
369. Y.-X. J. Wang, *Quant. Imaging Med. Surg.*, 2011, **1**, 35.

370. J. R. Alger, J. H. Harreld, S. Chen, J. Mintorovitch and D. S. Lu, *J. Magn. Reson. Imaging*, 2001, **14**, 586.
371. S. H. Kim, S. N. Oh, H. S. Choi, H. S. Lee, J. Jun, Y. Nam, S. H. Lee, J. K. Lee and H. G. Lee, *Contrast Media Mol. Imaging*, 2016, **11**, 544.
372. O. Bieri and K. Scheffler, *J. Magn. Reson. Imaging*, 2013, **38**, 2.
373. E. A. Dunn, L. C. Weaver, G. A. Dekaban and P. J. Foster, *Mol. Imaging*, 2005, **4**, 53.
374. T. Ahmad, H. Bae, I. Rhee, Y. Chang, J. Lee and S. Hong, *Curr. Appl. Phys.*, 2012, **12**, 969.
375. C. Heyn, J. A. Ronald, L. T. Mackenzie, I. C. MacDonald, A. F. Chambers, B. K. Rutt and P. J. Foster, *Magn. Reson. Med.*, 2006, **55**, 23.
376. S. J. Dodd, M. Williams, J. P. Suhan, D. S. Williams, A. P. Koretsky and C. Ho, *Biophys. J.*, 1999, **76**, 103.
377. E. M. Shapiro, S. Skrtic, K. Sharer, J. M. Hill, C. E. Dunbar and A. P. Koretsky, *Proc. Natl. Acad. Sci. U. S. A.*, 2004, **101**, 10901.
378. S. S. Ramadan, C. Heyn, L. T. Mackenzie, A. F. Chambers, B. K. Rutt and P. J. Foster, *Magn. Reson. Mater. Phys., Biol. Med.*, 2008, **21**, 251.
379. E. D. Smolensky, H.-Y. E. Park, Y. Zhou, G. A. Rolla, M. Marjanska, M. Botta and V. C. Pierre, *J. Mater. Chem. B*, 2013, **1**, 2818.
380. C. H. Cunningham, T. Arai, P. C. Yang, M. V. McConnell, J. M. Pauly and S. M. Conolly, *Magn. Reson. Med.*, 2005, **53**, 999.
381. V. Mani, K. C. Briley-Saebo, V. V. Itskovich, D. D. Samber and Z. A. Fayad, *Magn. Reson. Med.*, 2006, **55**, 126.
382. P. H. Mutin, G. Guerrero and A. Vioux, *J. Mater. Chem.*, 2005, **15**, 3761.
383. A. Walter, A. Garofalo, A. Parat, J. Jouhannaud, G. Pourroy, E. Voirin, S. Laurent, P. Bonazza, J. Taleb, C. Billotey, L. Vander Elst, R. N. Muller, S. Begin-Colin and D. Felder-Flesch, *J. Mater. Chem. B*, 2015, **3**, 1484.

CHAPTER 5

Transition Metal-based T₁ Contrast Agents

ROSA PUJALES-PARADELA, MARTÍN REGUEIRO-FIGUEROA,
DAVID ESTEBAN-GÓMEZ AND CARLOS PLATAS-IGLESIAS*

Centro de Investigaciones Científicas Avanzadas (CICA) and Departamento de Química, Universidade da Coruña, 15008, Coruña, Spain

*Email: carlos.platas.iglesias@udc.es

5.1 Differences and Similarities Between Gd^{III} and Transition Metal Complexes

5.1.1 Historical Perspective

Transition metal ions such as Mn^{II} and Fe^{III} played a key role in the development of MRI. These metal ions were among the first to be studied as T₁-shortening agents by investigating their binding to DNA.¹ Pioneering MRI work by Lauterbur² and Goldman³ used an Mn^{II} salt to distinguish normal myocardial tissue and infarcted zones in dogs. Normal myocardial tissue accumulates Mn^{II}, and thus exhibits greater signal intensity than infarcted regions. Later, Young and co-workers used FeCl₃ to enhance the gastrointestinal track in humans.⁴ A few years later, the Gd^{III} complex of diethylenetriaminepentaacetate [Gd(DTPA)](H₂O)]²⁻ was demonstrated to be efficient in enhancing cerebral tumors in humans upon intravenous injection.⁵ This breakthrough triggered intense research into Gd^{III}-based contrast agents that led to the commercialization of several agents based on polyaminopolycarboxylate complexes of Gd^{III}.⁶ Shortly after the success

New Developments in NMR No. 13

Contrast Agents for MRI: Experimental Methods

Edited by Valérie C. Pierre and Matthew J. Allen

© The Royal Society of Chemistry 2018

Published by the Royal Society of Chemistry, www.rsc.org

of Gd^{III} -based contrast agents, research into transition-metal-based T_1 -shortening contrast agents almost vanished for about 20 years. During this period occasional reports were published, notably the work of Raymond, who developed the well-known hepatocyte-specific contrast agent mangafodipir trisodium ($Na_3[Mn(DPDP)]$, TELASCAN[®], Figure 5.1).⁷ However, *in vivo* contrast does not arise from this contrast agent but from the Mn^{II} released from the complex. More recently, a contrast agent denoted as CMC-001, composed of a mixture of $MnCl_2$, alanine, and vitamin D_3 , has been proposed for visualization of liver and bile and is currently in phase III clinical trials.⁸ It is also noteworthy that deoxyhemoglobin is used as an endogenous contrast agent providing a means to measure blood-oxygenation-level-dependent functions.⁹

Contrast agents based on Mn^{II} or Fe^{III} complexes present some advantages over Gd^{III} complexes. Both Mn^{II} and Fe^{III} are essential elements present in the human body, and thus humans have mechanisms to manage excesses of these free ions within limits. On the other hand, free Gd^{III} is toxic, and the release of the toxic metal ion after the administration of some Gd^{III} -based contrast agents to patients suffering from severe renal failure was shown to cause a disease called nephrogenic systemic fibrosis.^{10,11} Thus, Mn^{II} - and Fe^{III} -based contrast agents might have better toxicity profiles than some Gd^{III} complexes. This point has revitalized the research into transition-metal-based T_1 -shortening contrast agents over the last decade.^{12–16}

5.1.2 Similarities and Differences between the Coordination Chemistry of Gd^{III} , Mn^{II} , and Fe^{III}

The coordination chemistry of Mn^{II} and Fe^{III} is different than that of Gd^{III} in terms of the preferred coordination numbers and geometries. The large ionic radius of Gd^{III} (1.107 Å for CN 9)¹⁷ and the predominantly ionic bonding usually render complexes with high coordination numbers (8–10), and coordination geometries that are largely controlled by the nature of the ligands.¹⁸ Both Mn^{II} and Fe^{III} complexes in high-spin electronic configurations lack ligand field stabilization energy, and therefore coordination numbers and coordination geometries are substantially determined by the crowding of the coordination sphere. The smaller ionic radii of Mn^{II} and Fe^{III} (0.830 and 0.645 Å for CN 6, respectively)¹⁷ result in coordination numbers typically lower than those of Gd^{III} . Thus, the coordination number of Mn^{II} and Fe^{III} in aqueous solution is predominantly 6, although typical complexes with polyaminocarboxylate ligands, such as ethylenediaminetetraacetate (EDTA)—for example, $[Mn(EDTA)(H_2O)]^{2-}$ and $[Fe(EDTA)(H_2O)]^{2-}$ —present coordination numbers of seven.^{19–21} Concerning the nature of the ligand donor atoms, Mn^{II} , Fe^{III} , and Gd^{III} are relatively hard Lewis acids that have preferential affinity for hard donor atoms such as oxygen and, to a lesser extent, nitrogen. The design of ligands for the synthesis of Mn^{II} - or Fe^{III} -based contrast agents should take into account these

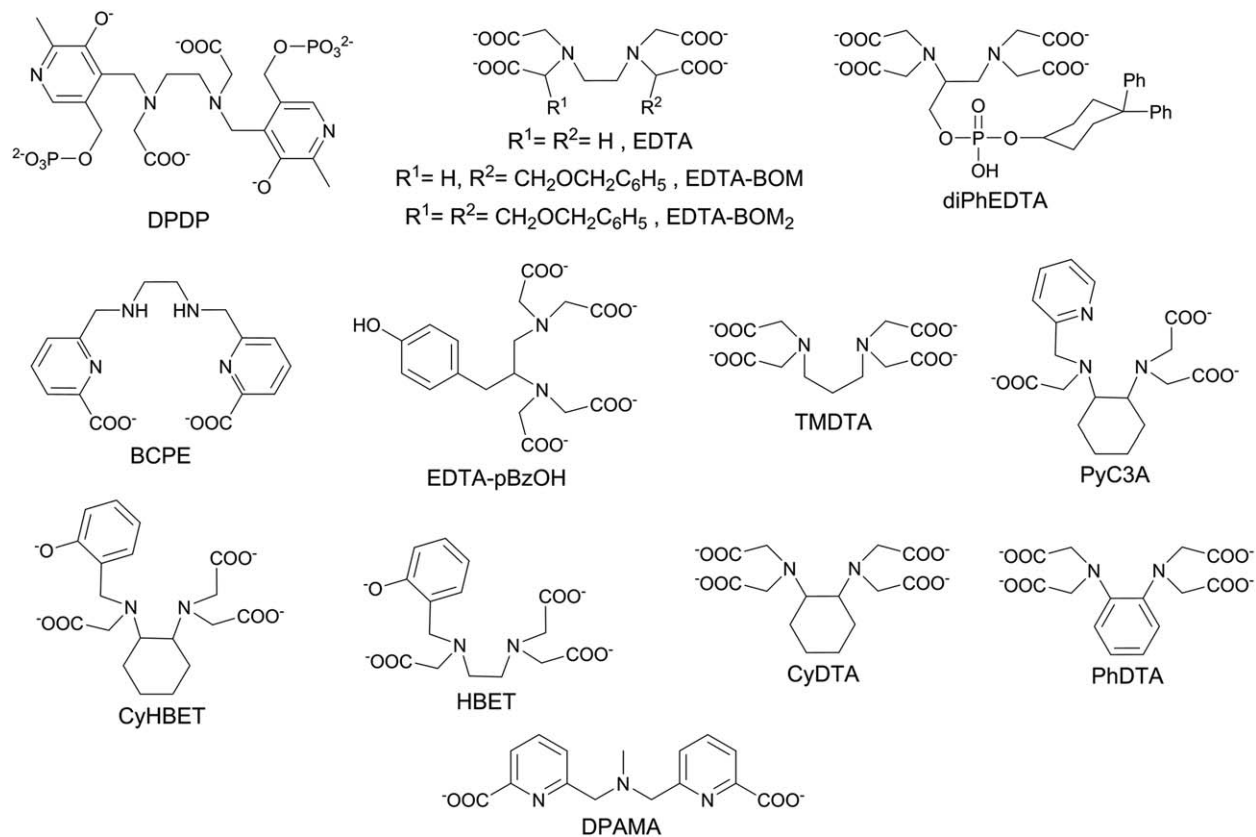


Figure 5.1 Non-macrocyclic ligands for transition-metal-based T_1 contrast agents.

basic coordination chemistry issues. An inspection of the non-macrocyclic (Figure 5.1) and macrocyclic (Figure 5.2) ligands investigated for Mn^{II} complexation in the context of contrast agents for MRI demonstrates the predominant role of polyaminopolycarboxylate ligands, which sometimes include other hard oxygen donor atoms from phosphonate or phenolate groups.

The spherical electronic distribution associated with the $[Ar]3d^5$ electronic configuration that is responsible for the slow electron spin relaxation times T_{1e} of Mn^{II} and Fe^{III} influences complex stability. Typically, thermodynamic stability constants of Mn^{II} and Fe^{III} complexes are determined using potentiometric or spectrophotometric pH titrations. The application of these techniques to transition metal complexes or Ln^{III} ions does not differ significantly. The lack of ligand field stabilization energy and the relatively low charge density of Mn^{II} generally results in complexes with rather low thermodynamic stability constants. For instance, the stability constant of $[Mn(EDTA)]^{2-}$ is $\log K_{MnL} = 13.88$,²² eleven orders of magnitude lower than

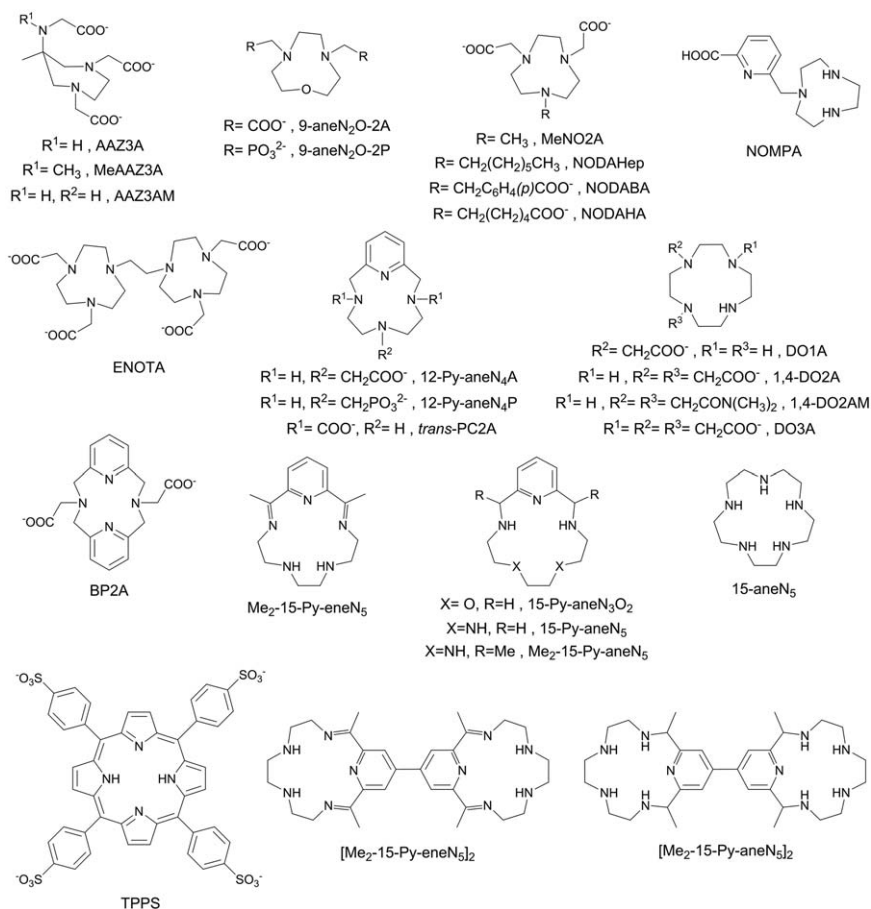


Figure 5.2 Macrocyclic ligands for transition-metal-based T_1 contrast agents.

that of the Fe^{III} analogue ($\log K_{\text{FeL}} = 24.95$).²³ In comparison, $[\text{Gd}(\text{EDTA})]^-$, which is too unstable for *in vivo* use, has a stability constant of $\log K_{\text{GdL}} = 17.3$,²⁴ whereas that of the benchmark $[\text{Gd}(\text{DTPA})]^{2-}$ is yet higher $\log K_{\text{GdL}} = 20.73$.²² The thermodynamic stability constants of Mn^{II} complexes with some macrocyclic ligands such as DO3A (Figure 5.2) are higher ($\log K_{\text{MnL}} = 19.40$)²⁵ than with EDTA, but the $[\text{Mn}(\text{DO3A})]^-$ complex lacks inner-sphere water molecules and therefore presents a rather low relaxivity ($1.3 \text{ mM}^{-1} \text{ s}^{-1}$ for the DO3A complex *versus* $3.3 \text{ mM}^{-1} \text{ s}^{-1}$ for the EDTA complex).²⁶ Removing one of the acetate pendant arms of DO3A to yield 1,4-DO2A leads to space for water to coordinate to the inner-sphere of Mn^{II} and, consequently, to an increase in the relaxivity of Mn^{II} ($[\text{Mn}(1,4\text{-DO2A})]^-$ relaxivity = $2.1 \text{ mM}^{-1} \text{ s}^{-1}$) due to the inner-sphere contribution.²⁶ However, this increase in relaxivity comes at the expense of complex stability ($\log K_{\text{MnL}} = 16.13$).²⁵

An important aspect that distinguishes the aqueous chemistry of Fe^{III} with respect to Mn^{II} and Gd^{III} is the high acidity of ferric complexes, which leads to the formation of hydroxide species at rather low pH values.²⁷ The formation of hydroxide and oxo species is observed above $\text{pH} \sim 5$ for $[\text{Fe}(\text{EDTA})]^-$,²³ but this effect is expected to occur at lower pH values if the positive charge of the complex increases. As a result, most Fe^{III} complexes investigated as potential contrast agents for MRI do not contain inner-sphere water molecules.²⁸ Consequently, the relatively low observed relaxivity values are the result of outer-sphere contributions. The species distribution diagrams shown in Figure 5.3 illustrate the speciation of Mn^{II}

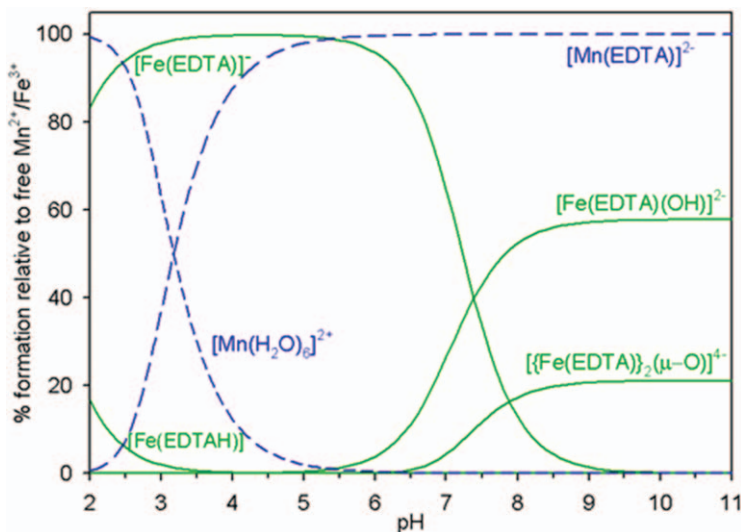


Figure 5.3 Species distribution diagrams of the $\text{Mn}^{\text{II}}:\text{EDTA}$ and $\text{Fe}^{\text{III}}:\text{EDTA}$ systems ($[\text{Mn}^{\text{II}}] = [\text{Fe}^{\text{III}}] = [\text{EDTA}] = 1 \text{ mM}$). Ligand protonation constants and stability constants were taken from ref. 22.

and Fe^{III} as a function of pH. The $[\text{Mn}(\text{EDTA})]^{2-}$ complex dissociates at a relatively low pH (<5.5), but no dissociation of $[\text{Fe}(\text{EDTA})]^-$ was observed in the pH range 2–11 as a result of the high thermodynamic stability of this complex. No hydroxide species were detected in solution for $[\text{Mn}(\text{EDTA})]^{2-}$, but $[\text{Fe}(\text{EDTA})]^-$ forms a mononuclear hydroxo complex $[\text{Fe}(\text{EDTA})(\text{OH})]^{2-}$ at $\text{pH} > 5.0$. This hydroxo complex dimerizes to give an oxo-bridged complex $[\{\text{Fe}(\text{EDTA})\}_2(\mu\text{-O})]^{4-}$ above $\text{pH} \sim 6.5$.²²

The mechanisms leading to the dissociation of Mn^{II} complexes do not differ significantly from those of Gd^{III} complexes. The main dissociation pathways that operate *in vivo* are spontaneous dissociation, acid-catalyzed dissociation, and dissociation promoted by endogenous metal ions (for example, Mg^{II} , Ca^{II} , Zn^{II} , or Cu^{II}) or endogenous ligands (for example, carbonate, citrate, or lactate).²⁹ However, although the dissociation mechanisms of Gd^{III} - and Mn^{II} -based contrast agents are the same, Mn^{II} complexes generally present much faster dissociation kinetics.³⁰ Thus, the design of thermodynamically stable and kinetically inert Mn^{II} -based contrast agents remains a challenge for coordination chemists. The number of studies reporting on the dissociation kinetics of Fe^{III} complexes with relevance to contrast agents for MRI is rather limited, and they focus mainly on the acid-catalyzed pathway.^{31–33} Nevertheless, Fe^{III} complexes are expected to be more inert than their Mn^{II} analogues.

Certain ligands possess the ability to stabilize both the divalent and trivalent oxidation states of Mn, thereby offering opportunities for the design of redox-responsive MRI probes.³⁴ Among the ligands that have been tested for this purpose are porphyrins such as TPPS (Figure 5.2)³⁵ and the non-macrocyclic derivative HBET (Figure 5.1)³⁶ and closely related derivatives.³⁷ Typically Mn^{II} complexes behave as potent T_1 -shortening relaxation agents compared to Mn^{III} analogues, resulting in an enhancement in relaxivity upon reduction.

5.1.3 Contributions to ^1H Relaxivity and Interpretation of NMRD Profiles

Early NMRD studies (Chapter 2.3.) performed by Koenig and co-workers showed that some transition metal complexes behave as efficient T_1 -shortening relaxation agents and could therefore be applied as contrast agents in MRI.^{38,39} Among the different transition metal ions, high-spin Mn^{II} and Fe^{III} complexes appeared to be the best candidates because their $[\text{Ar}]3d^5$ configuration results in slow electron spin relaxation times.^{40,41} As described in detail in Chapter 2, the observed longitudinal ^1H relaxivity (r_1) can be expressed as the sum of the inner-sphere (r_1^{IS}) and outer-sphere contributions (r_1^{OS}):

$$r_1 = r_1^{\text{IS}} + r_1^{\text{OS}} \quad (5.1)$$

The longitudinal relaxation time of a coordinated water molecule is, according to the Solomon–Bloembergen–Morgan (SBM) theory, proportional to $S(S+1)$, with S being the total spin of the paramagnetic ion.⁶ Furthermore, outer-sphere relaxivity is also proportional to $S(S+1)$, in addition to the diffusion coefficient d_{MH}^{298} and the distance of closest approach of an outer-sphere water molecule a_{MH} . These last two contributors are expected to be similar for Gd^{III} , Mn^{II} , and Fe^{III} complexes. Thus, one would expect somewhat higher relaxivities for complexes of Gd^{III} ($S=7/2$) with respect to Mn^{II} and Fe^{III} derivatives ($S=5/2$) containing the same number of coordinated water molecules. However, this relaxivity decrease is partially compensated by shorter $\text{Mn}^{\text{II}} \cdots \text{H}_{\text{water}}$ and $\text{Fe}^{\text{III}} \cdots \text{H}_{\text{water}}$ distances compared to $\text{Gd}^{\text{III}} \cdots \text{H}_{\text{water}}$.

Figure 5.4 shows ^1H -NMRD profiles simulated for typical complexes of these metal ions with one coordinated water molecule: $[\text{Gd}(\text{DTPA})]^{2-}$, $[\text{Mn}(\text{EDTA})]^{2-}$, and $[\text{Fe}(\text{EDTA})]^-$. The parameters used for the simulations are compiled in Table 5.1. The NMRD profiles of $[\text{Gd}(\text{DTPA})]^{2-}$ and $[\text{Mn}(\text{EDTA})]^{2-}$ show similar shapes, with a single dispersion in the range of 2–30 MHz, but the relaxivity of the Gd^{III} complex is higher than that of $[\text{Mn}(\text{EDTA})]^{2-}$. This difference is a direct consequence of the lower paramagnetism of the Mn^{II} complex, which is not compensated by the shorter $\text{Mn} \cdots \text{H}_{\text{water}}$ distance ($r_{\text{MnH}}=2.83 \text{ \AA}$ versus $r_{\text{GdH}}=3.1 \text{ \AA}$). In the case of $[\text{Fe}(\text{EDTA})]^-$, proton relaxivity is rather low in the proton Larmor frequency range 0.01–6.0 MHz, decreases from ~ 6 to 30 MHz, and increases at higher fields. Thus, compared to the NMRD profiles of the Gd^{III} - and Mn^{II} complexes, the dispersion for Fe^{III} is shifted to higher fields. Furthermore, while the relaxivity of $[\text{Fe}(\text{EDTA})]^-$ is low at low fields, it becomes comparable or even higher than that of $[\text{Mn}(\text{EDTA})]^{2-}$ above 100 MHz. Given the increasing magnetic fields used in modern MRI scanners,⁴² Fe^{III} complexes might offer

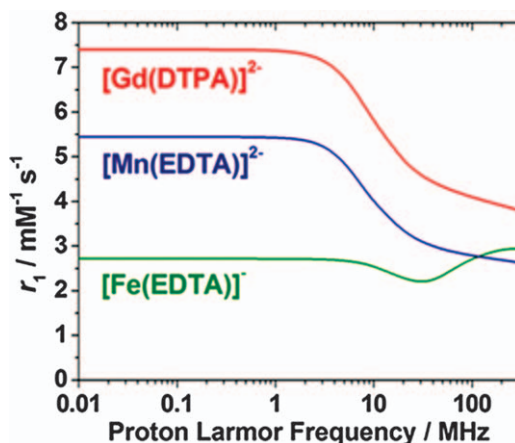


Figure 5.4 ^1H -NMRD profiles calculated with the parameters shown in Table 5.1 (25 °C).

Table 5.1 Parameters characterizing the relaxivities of [Gd(DTPA)]²⁻, [Mn(EDTA)]²⁻, and [Fe(EDTA)]⁻.^a

Parameter	[Gd(DTPA)] ²⁻ ^a	[Mn(EDTA)] ²⁻ ^b	[Fe(EDTA)] ⁻ ^c
$k_{\text{ex}}^{298}/10^6 \text{ s}^{-1}$	3.3	471	72
$\tau_{\text{R}}^{298}/\text{ps}$	58	57	57
$\tau_{\text{V}}^{298}/\text{ps}$	25	27.9	7.0
$d_{\text{MH}}^{298}/10^{-10} \text{ m}^2 \text{ s}^{-1}$	20	23	23
$\Delta^2/10^{19} \text{ s}^{-2}$	4.6	6.9	130
$r_{\text{MH}}/\text{\AA}$	3.1	2.83	2.75
$a_{\text{MH}}/\text{\AA}$	3.5	3.6	3.6

^aData from ref. 43.^bData from ref. 26.^cElectron spin relaxation parameters taken from ref. 44 and water exchange rate from ref. 45.

opportunities for the design of contrast agents that are alternatives to those based on Gd^{III}.

The different shapes of the NMRD profiles of Mn^{II}- and Fe^{III} complexes is related to the faster electron spin relaxation of Fe^{III} derivatives (Table 5.1). The parameters describing the electron spin relaxation of [Gd(DTPA)]²⁻ and [Mn(EDTA)]²⁻ (the electronic correlation time for the modulation of the zero-field-splitting interaction, τ_{v} , and the mean square zero-field-splitting energy, Δ^2) are similar. However, the value of Δ^2 obtained from the analysis of NMRD profiles of [Fe(EDTA)]⁻ is considerably higher, resulting in a shorter electron spin relaxation time. The longitudinal and transverse relaxation rates of the electron spin, $1/T_{1\text{e}}$ and $1/T_{2\text{e}}$, are often approximated using eqn (5.2)–(5.3).⁴⁶

$$\frac{1}{T_{1\text{e}}} = \frac{1}{25} \Delta^2 \tau \{4S(S+1) - 3\} \left(\frac{1}{1 + \omega_s^2 \tau^2} + \frac{4}{1 + \omega_s^2 \tau^2} \right) \quad (5.2)$$

$$\frac{1}{T_{2\text{e}}} = \frac{1}{50} \Delta^2 \tau \{4S(S+1) - 3\} \left(\frac{5}{1 + \omega_s^2 \tau^2} + \frac{2}{1 + 4\omega_s^2 \tau^2} + 3 \right) \quad (5.3)$$

Traditionally, the correlation time τ was assumed to be connected to the modulation of the zero field splitting due to distortions of the coordination geometry of the complex, τ_{v} . Simulations of $1/T_{1\text{e}}$ and $1/T_{2\text{e}}$ using eqn (5.2) and (5.3) and the parameters given in Table 5.1 (Figure 5.5) show that electron spin relaxation is considerably faster for [Fe(EDTA)]⁻ compared to [Mn(EDTA)]²⁻.

NMRD studies have been carried out for several Mn^{III} porphyrins.^{35,47–49} ¹H-relaxivity is generally constant for these complexes in the range 0.01–1 MHz, increases at faster frequencies to reach a maximum near 10–20 MHz, and decreases at higher fields. The different shapes of the NMRD profiles of the Mn^{II} and Mn^{III} derivatives are likely related to a relatively fast electron spin relaxation in the trivalent state, but quantitative analysis of the relaxivity data for these complexes needs to be performed.

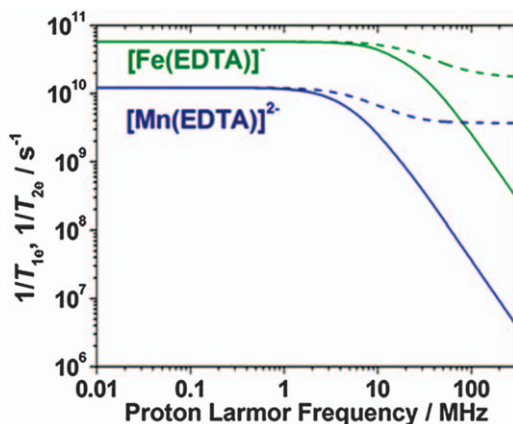


Figure 5.5 Electron spin relaxation rates calculated using the parameters in Table 5.1: $[\text{Mn}(\text{EDTA})]^{2-}$ blue; $[\text{Fe}(\text{EDTA})]^{-}$ green; $1/T_{1e}$: full lines, $1/T_{2e}$: dotted lines.

The NMRD profiles of a few Mn^{II} complexes, such as $[\text{Mn}(\text{H}_2\text{O})_6]^{2+}$, $[\text{Mn}_2(\text{ENOTA})(\text{H}_2\text{O})_2]$, and $[\text{Mn}(\text{trans-PC2A})]$, present a second dispersion at low fields. This second dispersion is associated with a scalar contribution to ^1H relaxivity that can be expressed with eqn (5.4).^{50–52}

$$\frac{1}{T_1^{\text{SC}}} = \frac{2S(S+1)}{3} \left(\frac{A_{\text{H}}}{\hbar} \right)^2 \left(\frac{\tau_{e2}}{1 + \omega_s^2 \tau_{e2}^2} \right) \quad (5.4)$$

In this equation, A_{H}/\hbar represents the ^1H hyperfine or scalar coupling constant, and $1/\tau_{e2}$ is the sum of the exchange rate constant and the transverse ($1/T_{2e}$) electron spin relaxation rate expressed by eqn (5.5).

$$\frac{1}{\tau_{e2}} = \frac{1}{T_{2e}} + k_{\text{ex}} \quad (5.5)$$

The values of the scalar coupling constants determined for $[\text{Mn}(\text{H}_2\text{O})_6]^{2+}$, $[\text{Mn}_2(\text{ENOTA})(\text{H}_2\text{O})_2]$, and $[\text{Mn}(\text{trans-PC2A})]$ amount to 5.43×10^6 , 2.9×10^6 , and $2.9 \times 10^6 \text{ rad s}^{-1}$, respectively. The important scalar contribution to proton relaxivity in these complexes is related to a slow electron spin relaxation and a rather low water-exchange rate of the inner-sphere water molecule.⁵³ Figure 5.6 shows simulations of ^1H -NMRD profiles obtained using different values of the mean square zero-field-splitting energy, Δ^2 . The NMRD curves show that the second dispersion at $\sim 0.3 \text{ MHz}$ is only visible for small Δ^2 values, which lead to slow electron spin relaxation rates [$1/T_{2e} < 5 \times 10^8 \text{ s}^{-1}$, eqn (5.3)].

An important parameter that influences proton relaxivities is the exchange rate of the coordinated water molecule (k_{ex}). Water-exchange rates can be measured using ^{17}O -NMR spectroscopy following the same methodology

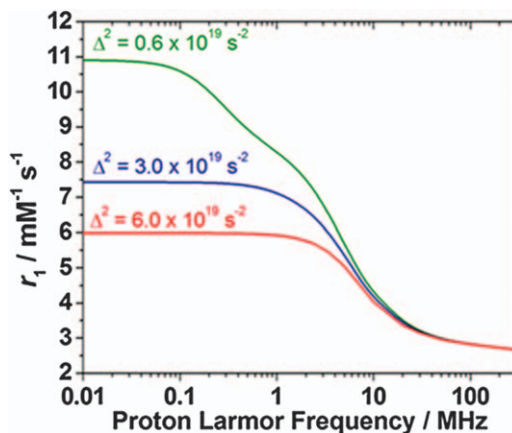


Figure 5.6 NMRD profiles calculated at 25 °C using the SBM equations for a hypothetical Mn^{II} complex using different values of Δ^2 . Other parameters are $\tau_v = 28$ ps; $\tau_R^{298} = 57$ ps; $d_{\text{MnH}}^{298} = 23 \times 10^{-10} \text{ m}^2 \text{ s}^{-1}$; $r_{\text{MnH}} = 2.83 \text{ \AA}$; $a_{\text{MnH}} = 3.6 \text{ \AA}$; $k_{\text{ex}} = 30 \times 10^6 \text{ s}^{-1}$; $A_{\text{H}}/\hbar = 5 \times 10^6 \text{ rad s}^{-1}$.

described for Gd^{III} complexes (Chapter 2). Generally, a simultaneous fitting of ^{17}O -NMR and ^1H -NMRD data provides more reliable fitted parameters than using only one technique, as discussed in detail for Gd^{III} complexes (Chapter 2.3).⁵⁴ This point is particularly important for the determination of τ_v and Δ^2 , which are strongly correlated in fittings that use only ^{17}O -NMR data.

The exchange rate of the inner-sphere water molecules in $[\text{Gd}(\text{H}_2\text{O})_8]^{3+}$ is very fast ($k_{\text{ex}}^{298} = 8.04 \times 10^8 \text{ s}^{-1}$), but complexation slows the water-exchange rate (Figure 5.7).⁴³ As a result, water-exchange rates of Gd^{III} expand over a range of about four orders of magnitude from the fastest determined for the aqua-ion to the slowest reported for DOTA-tetraamide derivatives ($k_{\text{ex}}^{298} = 5.0\text{--}12.5 \times 10^4 \text{ s}^{-1}$).⁵⁵ The water-exchange rate of $[\text{Mn}(\text{H}_2\text{O})_6]^{2+}$, $k_{\text{ex}}^{298} = 2.1\text{--}2.8 \times 10^7 \text{ s}^{-1}$,^{53,56} is slower than that of $[\text{Gd}(\text{H}_2\text{O})_8]^{3+}$, but often complexation of Mn^{II} accelerates the water-exchange rate. As a result, the ranges of water-exchange rates determined for Gd^{III} and Mn^{II} complexes present a wide overlap, although some six-coordinate Mn^{II} complexes present very fast water exchange rates ($[\text{Mn}(\text{DO1A})]^+$, $k_{\text{ex}}^{298} = 5.96 \times 10^9 \text{ s}^{-1}$;²⁶ $[\text{Mn}(12\text{-PyN4A})]^+$, $k_{\text{ex}}^{298} = 3.03 \times 10^9 \text{ s}^{-1}$;⁵⁷ $[\text{Mn}(\text{NOMPA})]^+$, $k_{\text{ex}}^{298} = 2.77 \times 10^9 \text{ s}^{-1}$).⁵⁸ On the lower side of the scale are Mn^{II} complexes with NO2A derivatives that contain bulky substituents in one of the nitrogen atoms of the macrocyclic unit (for example, $[\text{Mn}(\text{NODABA})]$, $k_{\text{ex}}^{298} = 1.3 \times 10^6 \text{ s}^{-1}$).⁵⁹ Nevertheless, the data reported to date for Mn^{II} and Gd^{III} complexes suggest that water-exchange rates of Mn^{II} chelates, which span four orders of magnitude, can be up to one order of magnitude faster than Gd^{III} complexes.

The water-exchange rates of several Mn^{III} porphyrins relevant as T_1 -shortening agents have also been determined using ^{17}O -NMR

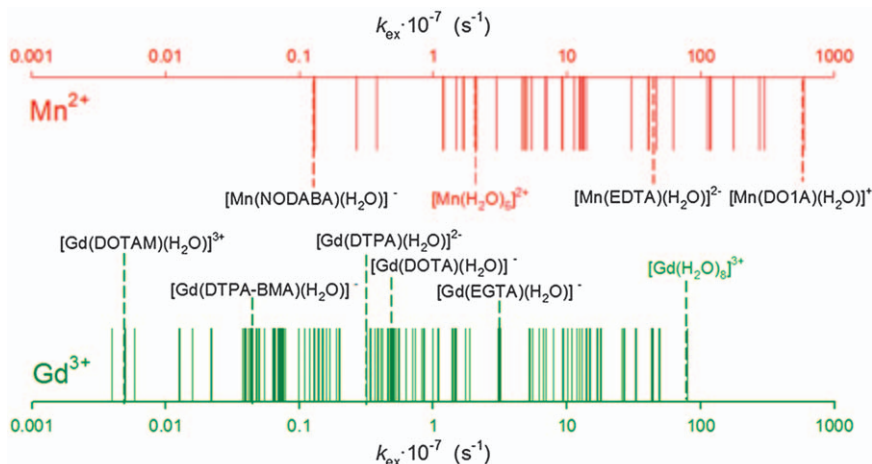


Figure 5.7 Water-exchange rates measured for Mn^{II} and Gd^{III} complexes at 298 K. The Mn^{II} data are compiled in Table 5.2, and the data for Gd^{III} were taken from ref. 60.

measurements.⁶¹ They were found to be in the range $k_{\text{ex}}^{298} = 4.1 \times 10^6 - 27.4 \times 10^6 \text{ s}^{-1}$, depending upon the charge density of the metal center and the steric compression around the coordinated water molecules. The parameters characterizing the electron spin relaxation (τ_v and Δ^2) determined for Mn^{II} complexes from ^{17}O -NMR and NMRD measurements should be taken with some caution for several reasons. First, eqn (5.2) and (5.3) are only valid within the motional narrowing condition or Redfield limit, while outside the extreme narrowing limit electron spin relaxation is expected to be a multi-exponential process.⁶² Second, both transient and static zero field splitting can contribute to electronic relaxation. Within the Redfield limit eqn (5.2) and (5.3) can be used to describe transient as well as static zero field splitting relaxation. In such a case, the correlation time τ in eqn (5.2) and (5.3) is expected to take values between the correlation time characterizing the transient zero field splitting ($\tau_v < 0.1 \text{ ps}$)⁶³ and the rotational correlation time τ_R that modulates the static zero field splitting.^{64,65} Therefore, the values of τ_v listed in Table 5.2 should be considered as effective correlation times, taking values in the range $\sim 1\text{--}70 \text{ ps}$. Third, the values of τ_v and Δ^2 determined using only ^{17}O -NMR data are strongly correlated. For instance, ^{17}O -NMR measurements provided $\tau_v = 1.4 \text{ ps}$ and $\Delta^2 \sim 1.4 \times 10^{19} \text{ s}^{-2}$ for $[\text{Mn}(\text{EDTA})]^{2-}$,^{19,41} while simultaneous analysis of NMRD and ^{17}O -NMR transverse relaxation rates and chemical shift data gave $\tau_v = 28 \text{ ps}$ and $\Delta^2 \sim 6.9 \times 10^{19} \text{ s}^{-2}$.²⁶ However, the k_{ex}^{298} values determined using the two approaches are identical within experimental error. The Δ^2 values listed in Table 5.2 suggest that zero-field-splitting energies of Mn^{II} may vary by up to 1 order of magnitude.

Table 5.2 Water exchange rates, ZFS parameters and scalar ^{17}O and ^1H hyperfine coupling constants of selected transition-metal-based T_1 contrast agents.

Parameter	$k_{\text{ex}}^{298}/10^7 \text{ s}^{-1}$	τ_v^{298}/ps	$\Delta^2/10^{19} \text{ s}^{-2}$	$-A_{\text{O}}/\hbar/10^6 \text{ rad s}^{-1}$	$A_{\text{H}}/\hbar/10^6 \text{ rad s}^{-1 a}$	Ref.
$[\text{Mn}(\text{H}_2\text{O})_6]^{II}$	2.8/2.1/15 ^b	10/3.3/1.5	0.60/0.56/0.39	34.6/33.3	5.43/4.3/	53/56/50
$[\text{Mn}(\text{EDTA})(\text{H}_2\text{O})]^{2-}$	41/44/47	1.4/1.4/28	1.3/1.4/6.9	40.2/42.5/40.5/40.7 ^d	2.0 ^d	19/41/26
$[\text{Mn}(\text{diPhEDTA})(\text{H}_2\text{O})]^{2-}$	23					66
$[\text{Mn}\{\text{EDTA}(\text{BOM})\}(\text{H}_2\text{O})]^{2-}$	9.3	24.7	7.3	37.9		67
$[\text{Mn}\{\text{EDTA}(\text{BOM})_2\}(\text{H}_2\text{O})]^{2-}$	13.0	35.3	5.3	37.9		67
$[\text{Mn}(\text{CyDTA})(\text{H}_2\text{O})]^{2-}$	14.0	1.8	1.36	31.4		20
$[\text{Mn}(\text{PhDTA})(\text{H}_2\text{O})]^{2-}$	35.0			38.0		68
$[\text{Mn}(\text{HBET})]^{2-}$	2.4			25.1		37
$[\text{Mn}(\text{CyHBET})]^{2-}$	6.7			25.3		37
$[\text{Mn}(\text{PyC3A})]^-$	5.4			28.7		69
$[\text{Mn}(\text{TMDTA})(\text{H}_2\text{O})]^{2-}$	13.2			75.4		19
$[\text{Mn}(\text{DPAMA})]$	30.6	39.2	2.38	45.8/50.3 ^d		70
MnAAZ3A	4.7	30	3.3	35.2 ^c		71
MnMeAAZ3A	12.6	32	3.5	27.6 ^c		71
MnAAZ3MA	13.3	36	4.5	26.4 ^c		71
$[\text{Mn}(9\text{-aneN}_2\text{O-2A})(\text{H}_2\text{O})_x]$	119	12.4	79	33.3		72
$[\text{Mn}(9\text{-aneN}_2\text{O-2P})(\text{H}_2\text{O})_x]$	1.2	30.7	60	33.3		72
$[\text{Mn}(\text{MeNO2A})]$	62.6	21.4	7.2	46/47.8 ^d		73
MnNODAHep	0.27	60	7	30		59
MnNODABA	0.13	60	7	33		59
MnNODAHA	0.27	69	7	30		59
$[\text{Mn}(\text{NOMPA})(\text{H}_2\text{O})]^+$	276.8	32.8	3.7	73.3/77.7 ^d		58
$[\text{Mn}(\text{ENOTA})(\text{H}_2\text{O})_2]$	5.5	7.7	0.47	32.7 ^c	2.9	51
$[\text{Mn}(\text{BP2A})(\text{H}_2\text{O})]$	18.1	1.6	26	46.2		52
$[\text{Mn}(12\text{-pyN}_4\text{A})(\text{H}_2\text{O})]^+$	303	8.7	4.0	36.6		57
$[\text{Mn}(12\text{-pyN}_4\text{P})(\text{H}_2\text{O})]$	177	14.3	30.2	39.9		57
$[\text{Mn}(\text{trans-PC2A})]$	15.2	1.3	27	47	2.1	52
$[\text{Mn}(\text{DO1A})(\text{H}_2\text{O})]$	595.7	13.9	12.8	39.4		26
$[\text{Mn}(1,4\text{-DO2A})(\text{H}_2\text{O})]^-$	113.4	4.4	48.1	43.0		26

Table 5.2 (Continued)

Parameter	$k_{\text{ex}}^{298}/10^7 \text{ s}^{-1}$	$\tau_{\text{v}}^{298}/\text{ps}$	$\Delta^2/10^{19} \text{ s}^{-2}$	$-A_{\text{O}}/\hbar/10^6 \text{ rad s}^{-1}$	$A_{\text{H}}/\hbar/10^6 \text{ rad s}^{-1} \text{ }^a$	Ref.
$[\text{Mn}(1,4\text{-DO2AM})(\text{H}_2\text{O})]^{II}$	11.5	5.5	51	37.1		74
$[\text{Mn}(\text{DO3A})]^{-}$		18.1	7.4			26
$[\text{Mn}(\text{Me}_2\text{-15-py-eneN}_5)(\text{H}_2\text{O})_2]^{II}$	2.0					75
$[\text{Mn}(15\text{-pyN}_3\text{O}_2)(\text{H}_2\text{O})_2]^{II}$	0.38	3.3	0.66	38.6		76
$[\text{Mn}(15\text{-pyN}_5)(\text{H}_2\text{O})_2]^{II}$	6.9	3.9	0.46	38.6		76
$[\text{Mn}(\text{Me}_2\text{-15-pyaneN}_5)(\text{H}_2\text{O})_2]^{II}$	5.3					75
$[\text{Mn}(15\text{-aneN}_5)(\text{H}_2\text{O})_2]^{II}$	≥ 10					75
$\{[\text{Mn}(15\text{-py-aneN}_5)(\text{H}_2\text{O})_2]_2\}^{4+}$	5.0	2.8	28.9	38.3		77
$\{[\text{Mn}(\text{Me}_2\text{-15-py-eneN}_5)(\text{H}_2\text{O})_2]_2\}^{4+}$	1.7	1.8	10	37.7		77
$[\text{Mn}(\text{EDTA-pBzOH})]^{2-}$	16.8			29.2		78

^aThe correct sign of the scalar ^{17}O coupling constant of coordinated water molecules is negative, corresponding to negative spin densities at the point nucleus that originate upfield shifts of the ^{17}O resonance.

^bValue at 308 K.

^cThe original papers report A_{O}/\hbar .

^dObtained with density functional theory calculations.

5.1.4 Characterizing Manganese and Iron Complexes

The techniques used for the characterization of Mn^{II} and Fe^{III} complexes do not differ much from those used for Gd^{III} -based analogues. From the perspective of structural characterization, X-ray diffraction plays a major role, although structures observed in the solid state might be different from those in solution. In the case of Gd^{III} , the analysis of high-resolution NMR spectra of complexes with other Ln^{III} ions represents a powerful tool to gain structural information in solution, as usually a given ligand forms an isostructural series of complexes with the whole or a part of the lanthanide series.^{79,80} Unfortunately this strategy is not applicable to Mn^{II} and Fe^{III} complexes. In terms of absorption and emission spectroscopy, $d-d$ transitions in high-spin Mn^{II} and Fe^{III} complexes are forbidden by the spin selection rule, and thus are extremely weak and usually not informative. Conversely, high-spin Mn^{III} complexes present considerably more intense $d-d$ transitions that can be used to monitor the oxidation of responsive probes based on the Mn^{II}/Mn^{III} pair.^{37,57}

Both Mn^{II} and Fe^{III} are active in electron paramagnetic resonance (EPR) spectroscopy, and thus this technique often provides structural insight. The EPR spectrum of $[Mn(H_2O)_6]^{2+}$ shows hyperfine splitting,⁸¹ which is often not observed for chelates as a result of line-broadening associated to a faster electronic relaxation.²⁶ Thus, EPR and electron nuclear double resonance (ENDOR) studies of high-spin metal ions is a challenge, especially at the conventional X-band frequencies.⁸² Nevertheless, ENDOR spectroscopy can in principle provide access to weak hyperfine couplings from ligand nuclei, thereby revealing structural details.^{83,84} EPR spectroscopy also allows determination of the zero field splitting parameters D and E that relate to the ZFS energy Δ [eqn (5.2) and (5.3)].^{85,86} Thus, EPR spectroscopy is a valuable tool to understand electron spin relaxation of transition metal-based T_1 -shortening contrast agents. Another technique that is specifically useful for the characterization of Fe^{III} complexes is ^{57}Fe -Mössbauer spectroscopy, which is normally applied to solid samples or frozen solutions at low temperatures.⁸⁷ Mössbauer spectroscopy provides structural information (for example, coordination numbers), but it has been scarcely exploited for the characterization of potential MRI contrast agents.⁸⁸

The relative stabilities of the M^{II} and M^{III} oxidation states of redox-sensitive probes can be conveniently assessed by using electrochemical techniques, notably cyclic voltammetry (CV) measurements. Cyclic voltammetry is an electrochemical experiment in which potential is changed over time in a reversible fashion. A typical set-up used for CV experiments is shown in Figure 5.8.⁸⁹ The electrochemical cell contains a working electrode, where the reaction of interest takes place; a counter electrode, which balances the Faraday process, and a reference electrode. The cell should be purged with an inert gas, typically N_2 or Ar, to exclude oxygen. The electrodes are connected to a potentiostat that controls the experiment by imposing on

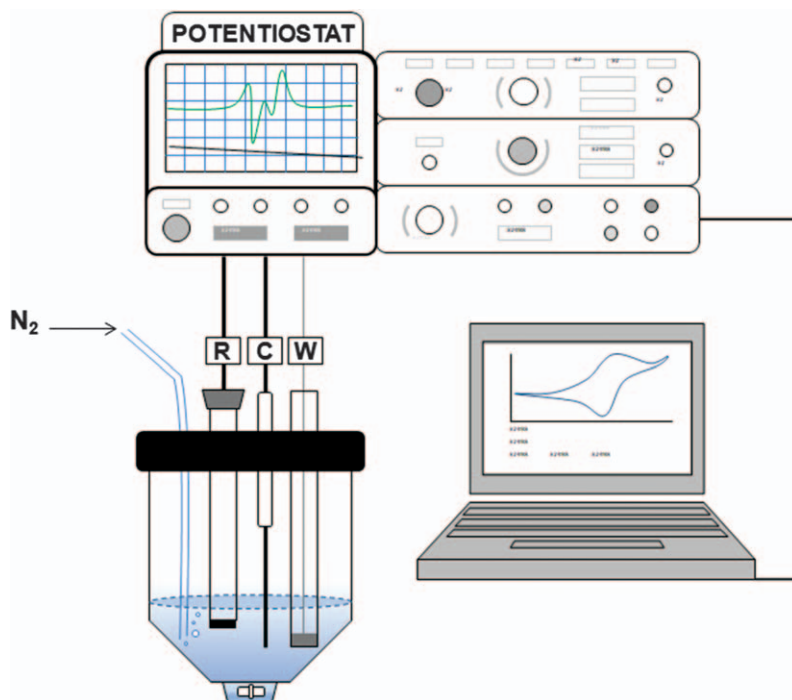


Figure 5.8 Typical setup used for cyclic voltammetry measurements. R, C, and W refer to the reference electrode, counter electrode, and working electrode, respectively.

the working electrode a back-and-forth linear potential sweep. A typical cyclic voltammogram is a current *versus* potential plot characterized by the initial (E_i), switching (E_s), and final (E_f) potentials.

A standard CV experiment typically requires a 1–5 mM solution of the electroactive species (*i.e.* the Mn^{II} or Fe^{III} complex) as well as a supporting electrolyte to enhance the conductivity of the solution (*i.e.* 0.15 M NaCl to mimic biological fluids). The working electrode is normally a solid disk electrode made of platinum, gold, or glassy carbon, and the counter electrode is typically a Pt rod. The mercury-drop electrode is useful for electrochemical measurements in aqueous solutions when large negative potentials need to be investigated; however, it is not generally required for the investigation of redox-responsive contrast agents for MRI because solid disk electrodes work well within the threshold for typical bioreductants (-0.4 V *versus* normal hydrogen electrode).⁹⁰ The most common reference electrodes used in aqueous solutions are Ag/AgCl and calomel electrodes. Care should be taken when comparing potentials obtained with different reference electrodes because potentials vary with the type of electrode used and with seemingly small changes to the same electrode, such as the concentration of the filling solution.⁹¹

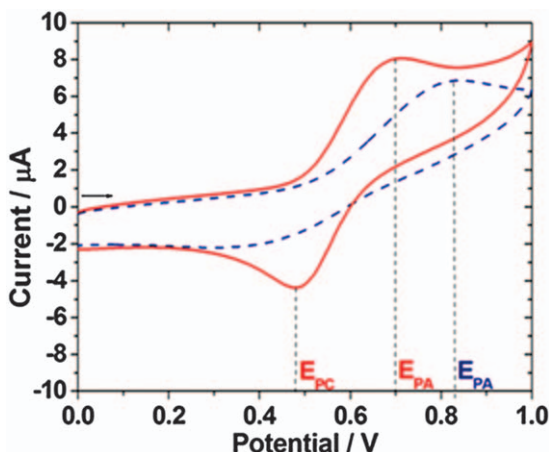


Figure 5.9 Cyclic voltammograms recorded from *ca.* 2 mM aqueous solutions (0.15 M NaCl, pH 7, scan rates 0.05 V s^{-1} , Ag/AgCl reference electrode) of [Mn(BCPE)] (solid line) and [Mn(PC2A)(H₂O)] (dashed line).^{52,70}

Figure 5.9 shows representative cyclic voltammograms recorded for Mn^{II} complexes showing a quasi-reversible system ([Mn(BCPE)]) and an irreversible system ([Mn(PC2A)(H₂O)]).^{52,70} The voltammogram recorded for [Mn(BCPE)] shows a well-defined anodic peak at $E_{PA} = +0.70 \text{ V}$ that corresponds to the oxidation of Mn^{II} to Mn^{III}. The Mn^{III} species deposited on the electrode surface is reduced in the reverse scan that shows a cathodic peak at $E_{PC} = +0.48 \text{ V}$. The difference in cathodic and anodic peak potentials is around $\sim 60 \text{ mV}$ for fully reversible electron transfer process ($60/n$ for multi-electron transfer processes, where n is the number of electrons in the process). Another feature of a reversible electron transfer process is that the ratio of the anodic to cathodic peak currents should be unity. An increase of irreversibility is reflected by an increased separation between anodic and cathodic peaks and a decrease in the peak current relative to the reversible case. Generally, the extent of irreversibility increases upon increasing the sweep rate. In the case of an irreversible system, no inverse peak is observed on inverting the scan direction. A typical irreversible voltammogram is shown in Figure 5.9 for [Mn(PC2A)(H₂O)]. The irreversibility of the oxidation process in this example has been attributed to the deprotonation of the coordinated water molecule, which may cause slow kinetics of the reverse reaction or precipitation on the electrode surface.⁵⁷

5.1.5 Computational Methods

The computational approaches available for the investigation of first-row transition metal complexes are essentially the same as those described for Gd^{III} complexes (Chapter 2.9). Density functional theory (DFT) methods are the most popular for the investigation of the electronic structure of

transition metal complexes.⁹² Relativistic effects can be generally neglected for the computation of molecular geometries, and thus common all-electron basis sets usually perform well. DFT studies of Mn^{II} and Fe^{III} complexes in aqueous solutions typically employ functionals based on the hybrid GGA (*i.e.* B3LYP),^{93,94} meta-GGA or hybrid meta-GGA approximations (for example, TPSSh)⁷³ in combination with polarized double- or triple- ξ basis sets (Chapter 2.9). Bulk solvent effects can be included by using the different polarized continuum approaches implemented in most of the program packages for electronic structure calculations. Because potential MRI contrast are often charged or neutral species with highly concentrated regions of charge density, the inclusion of bulk solvent effects often has an important impact on the calculation of geometries and energetics of the complexes.

DFT methods have been used to gain information on several parameters relevant to contrast agents for MRI. Among the structural parameters important for the interpretation of ¹H-NMRD and ¹⁷O-NMR data are the M–O_{water} and M···H_{water} distances and the scalar ¹H and ¹⁷O hyperfine coupling constants A_{H}/\hbar and A_{O}/\hbar . For Gd^{III} complexes, an accurate estimation of these parameters requires the explicit inclusion of a few second-sphere water molecules (typically two) involved in hydrogen bonds with the coordinated water molecule.⁷³ The presence of second-sphere water molecules provokes a remarkable shortening of the M–O_{water} distances and increases the absolute values of calculated A_{O}/\hbar values.⁷³ The hyperfine coupling constants obtained by using DFT methods are often in excellent agreement with the experimental values determined from ¹⁷O-NMR transverse relaxation rates and chemical shifts, with deviations typically <10% (Table 5.2).

The electronic ⁶S ground states of high-spin Mn^{II} and Fe^{III} ions are characterized by electronic spin states $S = 5/2$, which implies that the degeneracy of the magnetic sublevels $M_S = \pm 5/2, \pm 3/2$ and $\pm 1/2$ is broken in the absence of any applied magnetic field due to zero-field splitting effects.⁹⁵ Different computational studies calculated zero-field splitting parameters using DFT and multiconfigurational CASSCF calculations.^{63,96,97} The phenomenological zero-field splitting Hamiltonian can be expressed in terms of the symmetric tensor D [eqn (5.6)].⁹⁸

$$\hat{H}_{\text{ZFS}} = \hat{S}D\hat{S} \quad (5.6)$$

Taking a coordinate system that diagonalizes the D tensor allows writing the zero-field splitting Hamiltonian as in eqn (5.7), where D and E are the axial and rhombic zero-field splitting parameters given by eqn (5.8) and (5.9).

$$\hat{H}_{\text{ZFS}} = D\left(\hat{S}_z^2 - \frac{1}{3}\hat{S}^2\right) + E(\hat{S}_x^2 - \hat{S}_y^2) \quad (5.7)$$

$$D = D_{zz} - \frac{1}{2}(D_{xx} + D_{yy}) \quad (5.8)$$

$$E = \frac{1}{2}(D_{xx} - D_{yy}) \quad (5.9)$$

Zero-field splitting arises from a direct electron–electron magnetic dipole spin–spin interaction involving unpaired electrons and the spin-orbit coupling of excited states into the ground state. The zero-field splitting parameters calculated using DFT methods for different Mn^{II} complexes vary depending on the particular functional employed in the calculation, with accuracies of $\sim 0.1 \text{ cm}^{-1}$.^{63,96,97} On the other hand, *ab initio* CASSCF/NEVPT2 calculations were shown to provide zero-field splitting parameters in excellent agreement with experiments for both Mn^{II} and Mn^{III} complexes.^{63,98} The values of the axial and rhombic zero-field splitting parameters D and E relate to the zero-field splitting energy given in the McLachlan equations [eqn (5.2) and (5.3)] as described in eqn (5.10).

$$\Delta = \sqrt{\frac{2}{3}D^2 + 2E^2} \quad (5.10)$$

CASSCF/NEVPT2 calculations were found to provide values of Δ in good agreement with those obtained from the analysis of NMRD data for a small set of Mn^{II} complexes⁶³ and the aqua ion.⁹⁹

5.2 Determining Effective Magnetic Moment (μ_{eff})

Measurements of magnetic properties have been widely used to characterize a wide range of transition metal complexes having at least one oxidation state with an incomplete d subshell. Magnetic measurements provide information regarding electronic configuration, particularly for the first row transition ions for which electronic configuration is related to the oxidation state of the metal ion. The magnetic moment of a substance (μ_{eff}) cannot be determined using a direct measurement; it must be calculated from magnetic susceptibility values, which can be measured using different experimental techniques either in solution or in the solid state. Methods for solid-state samples include the use of Gouy and Faraday balances (force methods) or a vibrating sample magnetometer (VSM) or a superconducting quantum interference device (SQUID) magnetometer (induction methods).¹⁰⁰ In solution, the determination of magnetic susceptibility can be achieved using an NMR spectrometer (Evans' NMR method).¹⁰¹

The molar susceptibility of a paramagnetic compound expressed in SI units ($\text{m}^3 \text{ mol}^{-1}$) is given by Curie's law [eqn (5.11)], where N_A is Avogadro's number, μ_0 is the vacuum permeability ($4\pi \times 10^{-7} \text{ N A}^{-2}$), k_B is the Boltzmann constant ($1.380 \times 10^{-23} \text{ J K}^{-1}$) and T is the absolute temperature.

$$\chi_m = \frac{\mu_0 N_A \mu_{\text{eff}}^2 \mu_B^2}{3k_B T} \quad (5.11)$$

The experimental value of χ_m includes both paramagnetic and diamagnetic contributions. Because the paramagnetic contribution contains the relevant information, the diamagnetic contribution must be subtracted

from the experimental susceptibility to give the corrected value (sometimes called corrected magnetic susceptibility, is χ_m^{corr}):

$$\chi_m^{\text{corr}} = \chi_m - \chi_D \quad (5.12)$$

The diamagnetic contribution is often estimated using Pascal's constants according to eqn (5.13).¹⁰²

$$\chi_D = \sum_i \chi_{Di} + \sum_i \lambda_i \quad (5.13)$$

Here, χ_{Di} represents the diamagnetic contribution of atom i in the molecule and λ_i the contribution of bond i . The corrected magnetic susceptibility can be related to the effective magnetic moment by rearranging eqn (5.11) to give eqn (5.14), where μ_{eff} is expressed in Bohr magnetons per formula unit (BM) and χ_m^{corr} is normally given in $\text{cm}^3 \text{mol}^{-1}$ (SI units) or emu mol^{-1} (cgs units).

$$\mu_{\text{eff}} = \sqrt{\frac{3k_B}{\mu_0 N_A \mu_B^2} \chi_m^{\text{corr}} T} \quad (5.14)$$

Using SI units the first term in eqn (5.14) equals 797.8, so that $\mu_{\text{eff}} = 797.8 \sqrt{\chi_m^{\text{corr}} T}$, and the use of cgs units gives $\mu_{\text{eff}} = 2.827 \sqrt{\chi_m^{\text{corr}} T}$. Although the magnetic moment of a substance can be reported in electromagnetic units (emu) ($1 \text{ emu} = 1 \text{ erg G}^{-1} = 10^{-3} \text{ J T}^{-1}$), inorganic chemists commonly use of the Bohr magneton ($\mu_B = 9.274 \times 10^{-24} \text{ J T}^{-1}$), which corresponds to the magnetic moment of a 1s electron in a hydrogen atom.

The vast majority of Fe^{III} and Mn^{II} complexes investigated as potential contrast agents for MRI are mononuclear complexes with high-spin $[\text{Ar}]3d^5$ configurations. Thus, these systems present relatively simple magnetic properties due to the presence of a unique magnetic center without first-order orbital momentum. As a consequence, the magnetic susceptibility of these complexes often follows the Curie law, as plots of χ_m versus the inverse temperature (or $1/\chi_m$ versus T) give straight lines with slopes of $C = \mu_0 N_A \mu_{\text{eff}}^2 m_B^2 / k_B$ (or $1/C$, Figure 5.10). A convenient way of confirming that a given compound follows the Curie Law is to obtain a horizontal straight line in a plot of $\chi_m T$ versus T (Figure 5.10).¹⁰³ In the particular case of high-spin d^5 complexes, $\chi_m T$ is expected to be $4.37 \text{ cm}^3 \text{K mol}^{-1}$ using the spin-only formula $\mu_S = \sqrt{4S(S+1)}$.

Because magnetic measurements are normally recorded in the solid state, the magnetic species are rarely perfectly isolated from the environment, leading to deviations from Curie behavior. These deviations are often accounted for by the Curie-Weiss law, which can be written as $\chi_m = C(T - \Theta)$, where C is the Curie constant and Θ is the Weiss constant or Weiss temperature. Thus, plots of $1/\chi_m$ versus T for systems following the Curie-Weiss law give a straight line with slope $1/C$, while Θ is obtained from the intercept

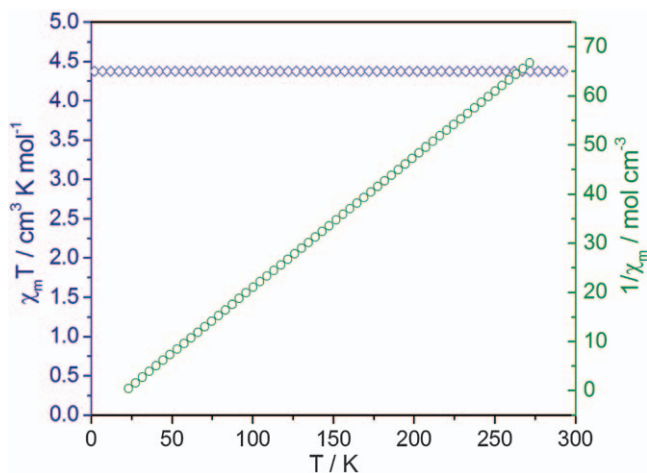


Figure 5.10 Plots of $\chi_m T$ and $1/\chi_m$ versus T simulated for a hypothetical high-spin d^5 metal complex that obeys the Curie law.

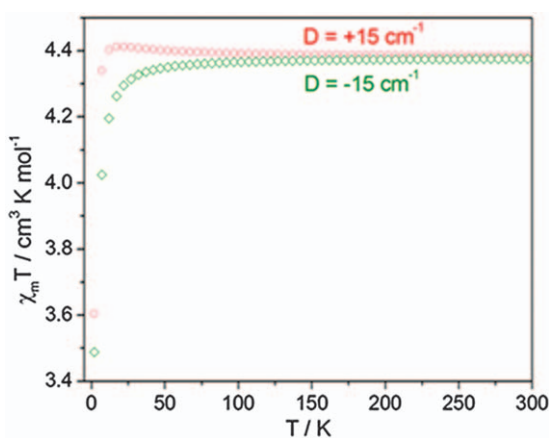


Figure 5.11 Plots of $\chi_m T$ versus T simulated for a hypothetical high-spin d^5 Fe^{III} complex with zero-field splitting energies of $D = +15 \text{ cm}^{-1}$ and $D = -15 \text{ cm}^{-1}$. The expressions used to simulate the curves were taken from ref. 104.

of the straight line with the T axis. A positive Θ value is indicative of ferromagnetic intermolecular interactions, and $\Theta < 0$ indicates antiferromagnetic intermolecular interactions.

The zero-field splitting operating on the electronic ^6S ground states of high-spin Mn^{II} and Fe^{III} ions can also have consequences for magnetic properties. Zero-field splitting is expected to be small for undistorted octahedral complexes ($\sim 0.01 \text{ cm}^{-1}$ for Fe^{III}) and increase upon symmetry lowering (Figure 5.11).¹⁰⁴ For instance, D values of $\sim 15 \text{ cm}^{-1}$ are rather

common for Fe^{III} porphyrins.¹⁰⁵ Simulations showing plots of $\chi_m T$ versus T for a hypothetical Fe^{III} complex with a $|D| = 15 \text{ cm}^{-1}$ provide support that $\chi_m T$ decreases upon cooling, with the shape of the curve varying slightly depending upon the sign of D . In the case of Mn^{II} complexes, the zero-field splitting energies are typically lower than $\sim 2 \text{ cm}^{-1}$, and thus the zero-field splitting has a negligible effect on magnetic properties. As a result, the product $\chi_m T$ remains constant with temperature, even at low temperatures.¹⁰³

The $\chi_m T$ product in Mn^{III} porphyrins at room temperature was found to be practically identical to that expected for one isolated high-spin d⁴ metal ion ($3.0 \text{ cm}^3 \text{ mol}^{-1} \text{ K}$), and lowering temperature provoked a decrease of the $\chi_m T$ values as a consequence of the zero-field splitting of the Mn^{III} ion.¹⁰⁶

5.2.1 Bulk Magnetic Susceptibility (BMS) Shifts

Evans' NMR method is a quite simple, reliable, and widely used method for determination of the magnetic susceptibility of paramagnetic molecules in solution. This method is based in the bulk magnetic susceptibility (BMS) shift that an inert compound (for example, *tert*-butyl alcohol or dioxane) experiences in the presence of a paramagnetic solute that influences nuclear spins, induces chemical shifts, and increases nuclear relaxation rates. There are several experimental procedures to measure BMS shifts. The most common one involves the use of a 5 mm co-axial NMR tube containing two separate solutions. Generally, the solution of the paramagnetic species and a known amount of the inert compound are placed in the inner coaxial tube, and the solvent containing an identical amount of the inert compound is placed in the outer coaxial tube (Figure 5.12). The difference between the chemical shifts obtained for the resonances of the inert compound in the inner and outer compartments are related to the BMS shift, $\Delta\delta^{\text{BMS}}$, by eqn (5.15), where c is the molar concentration of the paramagnetic substance and T is the absolute temperature.^{101,107}

$$\Delta\delta^{\text{BMS}} = \frac{4\pi c}{3T} \left(\frac{\mu_{\text{eff}}}{2.83} \right)^2 \times 10^3 \quad (5.15)$$

Thus, this expression allows determination of the concentration of the solution containing the paramagnetic compound knowing μ_{eff} , and *vice versa*. In the specific case of Mn^{II} and Fe^{III} complexes, the μ_{eff} values of mononuclear complexes at ambient temperature do not differ significantly from that predicted by the spin-only formula (5.9 BM). Octahedral high-spin Mn^{III} complexes have a ⁵E_g electronic ground state, and thus the orbital contribution to the magnetic moment is small. As a result, Evans' NMR method can be used to estimate the concentration of the paramagnetic complex in solution.¹⁰⁸ One should bear in mind, however, that for certain complexes such as high-spin Fe^{II} complexes with a ⁵T_{2g} electronic ground state, the observed magnetic moment likely presents a sizeable orbital contribution.

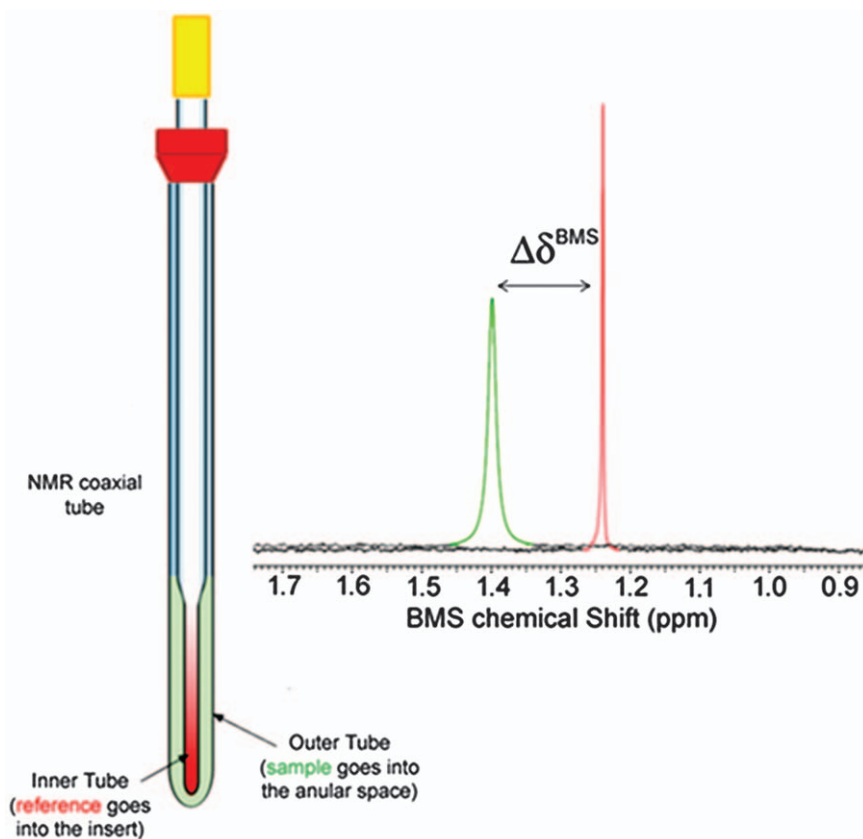


Figure 5.12 Schematic representation of the tubes and data used in the determination of bulk magnetic susceptibility shifts of paramagnetic solutions using Evans' NMR method.

5.2.2 Superconducting Quantum Interference Device (SQUID) Measurements

One of the most common ways of performing magnetic measurements in an effective and sensitive way is *via* the use of a superconducting quantum interference device (SQUID) magnetometer.¹⁰⁹ Functionally, it is a magnetic-flux-to-voltage converter with extremely low magnetic flux noise. The electrical device is shown schematically in Figure 5.13. It consists of a superconducting loop interrupted by two Josephson junctions (SQUID sensor) that is inductively coupled through an input coil to a suitable detection system (pick-up coil). The SQUID sensor is placed away from the sample in a liquid helium bath below a magnet and inside a superconducting shield, and the detection system is placed in the outside of the chamber at the center of the magnet.

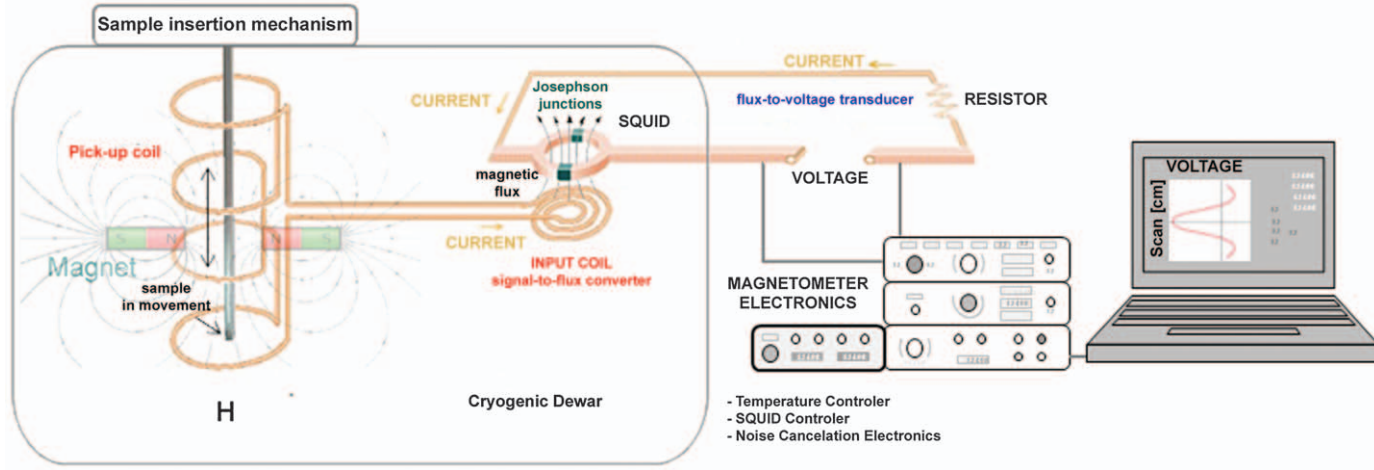


Figure 5.13 Schematic representation of a SQUID magnetometer.

The measurement is performed when the sample moves up and down through the pick-up coil. Due to the magnetic moment of the sample, the movement induces an electric current in the detection system that is inductively coupled with the SQUID sensor through the input coil. When properly configured, the SQUID electronics produces an output voltage that is proportional to the current flowing in the SQUID input coil. The output voltage is measured as a function of sample position in the pick-up coil, and based on the resulting voltage profile (and thus flux) *versus* position, the magnetic moment can be determined using different computer fits. Thus, the device is capable of amplifying small changes in the magnetic field of the detection system into measurable electrical signals that are proportional to the magnetic moment of the sample.

It is necessary to emphasize some aspects that ensure an accurate magnetic measurement: (1) The system must be accurately calibrated using a reference material with known mass and magnetic susceptibility. There are several calibration materials with magnetic susceptibilities that are known to a high degree of accuracy. Nevertheless, it is advisable to use a standard with a bulk susceptibility that is close in magnitude to that of the sample being studied. (2) It is critical to achieve as close to perfect a calibration as possible of the parameters that will be modified during the measurements, including the working temperature and applied magnetic field. (3) The purity of the sample must be high to prevent sources of magnetic response that do not arise from the sample. Single crystals or microcrystalline samples with known elemental analysis are preferable. (4) All experimental data must be corrected for magnetic signals that cannot be avoided (for example, sample holders). (5) When performing measurements with liquid helium, it is important to ensure that the instrument is vacuum-tight to prevent possible small leaks in the chamber that might introduce undesirable magnetic signals associated to condensation of gases over the sample.

5.3 Measuring q for Transition Metal Complexes

The determination of the number of water molecules coordinated to the metal ion (q) in transition metal complexes is not as straightforward as for Gd^{III} complexes. For instance, in the latter case luminescence lifetime measurements performed using solutions of the analogous Eu^{III} or Tb^{III} complexes in H_2O and D_2O provide access to hydration numbers (Chapter 2.4). These lanthanide ions possess ionic radii and coordination properties that are similar to those of Gd^{III} , and thus the q values obtained by these methods usually reflect accurately Gd^{III} hydration in solution. Furthermore, the presence of hydration equilibria in solution involving complex species with different q values can be assessed by analyzing the ${}^5D_0 \leftarrow {}^7F_0$ transition observed in the absorption spectra of the Eu^{III} analogues.^{110,111} Unfortunately, less progress has been achieved in developing methods to determine hydration numbers of transition metal complexes.

Caravan and co-workers developed a method to determine q of Mn^{II} complexes based on the analysis of transverse ^{17}O relaxivity that is defined analogously to proton relaxivity.¹¹²

$$r_2 = \frac{1/T_{2,\text{obs}} - 1/T_{2,\text{ref}}}{[\text{Mn}^{2+}]} = \frac{q}{1000 \times 55.5} \frac{1}{T_{2\text{m}} + \tau_{\text{m}}} \quad (5.16)$$

In eqn (5.16), concentration is given in units of mM, so that r_2 is expressed in $\text{mM}^{-1} \text{s}^{-1}$ units. The relaxation rate of the coordinated water molecule $T_{2\text{m}}$ is dominated by the scalar mechanism and can be approximated by eqn (5.17) and (5.18).

$$\frac{1}{T_{2\text{m}}} = \frac{S(S+1)}{3} \left(\frac{A_{\text{O}}}{\hbar} \right)^2 \tau_{\text{SC}} \quad (5.17)$$

$$\frac{1}{\tau_{\text{SC}}} = \frac{1}{T_{1\text{e}}} + \frac{1}{\tau_{\text{m}}} \quad (5.18)$$

Because τ_{m} decreases and $T_{2\text{m}}$ generally increases with increasing temperature, the sign of the temperature dependence of r_2 depends on which term dominates in the denominator of eqn (5.16). A change from the fast-exchange regime at high temperature [where $T_{2\text{m}}$ dominates the denominator of eqn (5.16)] to a slow exchange regime at low temperatures, where τ_{m} is the principal term, is characterized by a maximum in the temperature dependence of r_2 where $T_{2\text{m}} = \tau_{\text{m}}$. This is illustrated in Figure 5.14 for two Mn^{II} complexes with different hydration numbers. Caravan hypothesized that at sufficiently high magnetic fields the contribution of the $1/T_{1\text{e}}$ term in eqn (5.18) would be negligible, so that $\tau_{\text{SC}} \sim \tau_{\text{m}} = T_{2\text{m}}$. Combining eqn (5.16)

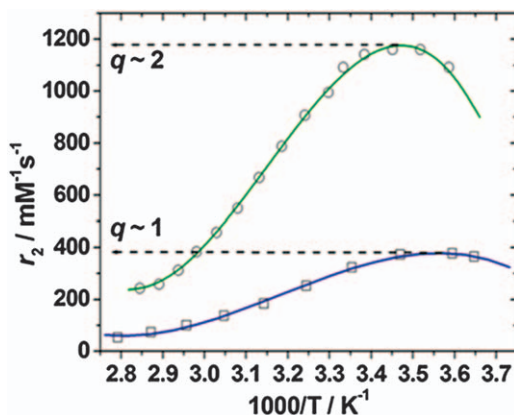


Figure 5.14 Transverse relaxivities determined for $[\text{Mn}(\text{DPAMA})(\text{H}_2\text{O})_2]$ (circles, 11.7 T)⁷⁰ and $[\text{Mn}(\text{BP2A})(\text{H}_2\text{O})]$ (squares, 9.4 T).⁵² The maxima of the r_2 versus the inverse temperature provide an estimate of the hydration number.

and (5.17) and solving for q this gives eqn (5.19) assuming a value of $33.3 \times 10^6 \text{ rad s}^{-1}$ for the scalar coupling constant A_O/\hbar :

$$q = r_{2 \text{ max}} \times 1000 \times 55.5 \left(\frac{2}{\sqrt{\frac{S(S+1)A_O}{3\hbar}}} \right) \approx \frac{r_{2 \text{ max}}}{510} \quad (5.19)$$

This method relies on several approximations, the most important ones being that the contribution of the $1/T_{1e}$ term in eqn (5.18) is negligible, and that the scalar hyperfine coupling constants of Mn^{II} complexes do not differ significantly from the value of $33.3 \times 10^6 \text{ rad s}^{-1}$ determined for the aqua ion. An inspection of the A_O/\hbar values reported in the literature reveals a typical range of 25×10^6 to $47 \times 10^6 \text{ rad s}^{-1}$, with only one case well out of the common interval (Table 5.2).⁵⁸ Thus, the variability of the A_O/\hbar values depending upon the ligand coordinated to Mn^{II} introduces an error in the calculated q values of $\pm 0.3 q$ units (for a $q = 1$ complex). The main limitation of this method is that it cannot be applied to systems in the fast exchange regime in the temperature range limited by the freezing and boiling points of the solution. In this situation, a simultaneous fit of NMRD data and ^{17}O -NMR relaxation rates and chemical shifts represents the best alternative to assess q and the remaining parameters that govern ^1H relaxivity.

5.4 Acknowledgements

The authors thank Ministerio de Economía y Competitividad (CTQ2013-43243-P and CTQ2015-71211-REDT) for generous financial support.

Notes and References

1. J. Eisinger, R. G. Shulman and W. E. Blumberg, *Nature*, 1961, **192**, 963.
2. P. C. Lauterbur, M. H. Mendonça Dias and A. M. Rudin, *Augmentation of Tissue Water Proton Spin-Lattice Relaxation Rates by In Vivo Addition of Paramagnetic Ions*, in *Frontiers of Biological Energetics: Electrons to Tissues*, ed. P. L. Dutton, J. S. Leigh and A. Scarpa, Academic Press, New York, 1978, vol. 1, pp. 752–759.
3. (a) T. J. Brady, M. C. Gebhardt, I. L. Pykett, F. S. Buonanno, J. H. Newhouse, C. T. Burt, R. J. Smith, H. J. Mankin, J. P. Kistler, M. R. Goldman, W. S. Hinshaw and G. M. Pohost, *Radiology*, 1982, **144**, 549; (b) M. R. Goldman, T. J. Brady, I. L. Pykett, C. T. Burt, F. S. Buonanno, J. P. Kistler, J. H. Newhouse, W. S. Hinshaw and G. M. Pohost, *Circulation*, 1982, **66**, 1012.
4. I. R. Young, G. J. Clarke, D. R. Bailes, J. M. Pennock, F. H. Doyle and G. M. Bydder, *J. Comput. Tomogr.*, 1981, **5**, 543.
5. D. H. Carr, J. Brown, G. M. Bydder, H.-J. Weinmann, U. Speck, D. J. Thomas and I. R. Young, *Lancet*, 1984, **323**, 484.

6. P. Caravan, J. J. Ellison, T. J. McMurry and R. B. Lauffer, *Chem. Rev.*, 1999, **99**, 2293.
7. S. M. Rocklage, W. P. Cacheris, S. C. Quay, F. E. Hahn and K. N. Raymond, *Inorg. Chem.*, 1989, **28**, 477.
8. (a) M. Rief, P. Asbach, T. Franiel, M. Taupitz, B. Hamm and M. Wagner, *Contrast Media Mol. Imaging*, 2009, **4**, 267; (b) N. Albiin, N. Kartalis, A. Bergquist, B. Sadigh and T. B. Brismar, *Magn. Reson. Mater. Phys., Biol. Med.*, 2012, **25**, 361.
9. F. Hyder and D. L. Rothman, *NeuroImage*, 2012, **62**, 985.
10. S. Cheng, L. Abramova, G. Saab, G. Turabelidze, P. Patel, M. Arduino, T. Hess, A. Kallen and M. Jhung, *J. Am. Med. Assoc.*, 2007, **297**, 1542.
11. T. H. Darrah, J. J. Prutsman-Pfeiffer, R. J. Poreda, M. E. Campbell, P. V. Hauschka and R. E. Hannigan, *Metallomics*, 2009, **1**, 479.
12. B. Drahoš, I. Lukeš and É. Tóth, *Eur. J. Inorg. Chem.*, 2012, **2012**, 1975.
13. M. Kueny-Stotz, A. Garofalo and D. Felder-Flesch, *Eur. J. Inorg. Chem.*, 2012, **2012**, 1987.
14. D. Pan, A. H. Schmieder, S. A. Wickline and G. M. Lanza, *Tetrahedron*, 2011, **67**, 8431.
15. D. D. Schwert, N. Richardson, G. Ji, B. Radüchel, W. Ebert, P. E. Heffner, R. Keck and J. A. Davies, *J. Med. Chem.*, 2005, **48**, 7482.
16. N. Kuźnik, G. Szafraniec-Gorol, L. Oczek, A. Grucela, P. Jewuła, A. Kuźnik, P. Zassowski and W. Domagala, *J. Organomet. Chem.*, 2014, **769**, 100.
17. R. D. Shannon, *Acta Crystallogr.*, 1976, **A32**, 751.
18. S. A. Cotton, *C. R. Chim.*, 2005, **8**, 129.
19. J. Maigut, R. Meier, A. Zahl and R. van Eldik, *J. Am. Chem. Soc.*, 2008, **130**, 14556.
20. J. Maigut, R. Meier, A. Zahl and R. van Eldik, *Inorg. Chem.*, 2008, **47**, 5702.
21. S. Richards, B. Pedersen, J. V. Silverton and J. L. Hoard, *Inorg. Chem.*, 1964, **3**, 27.
22. R. M. Smith, A. E. Martell and R. J. Motekaitis, *NIST Critically Selected Stability Constants of Metal Complexes Database, Version 8.0 for Windows*, National Institute of Standards and Technology, Gaithersburg, MD, 2004.
23. A. Brausam, J. Maigut, R. Meier, P. Á. Szilágyi, H.-J. Buschmann, W. Massa, Z. Homonnay and R. van Eldik, *Inorg. Chem.*, 2009, **48**, 7864.
24. R. G. Lacoste, G. V. Christoffers and A. E. Martell, *J. Am. Chem. Soc.*, 1965, **87**, 2385.
25. A. Bianchi, L. Calabi, C. Giorgi, P. Losi, P. Mariani, D. Palano, P. Paoli, P. Rossi and B. Valtancoli, *J. Chem. Soc., Dalton Trans.*, 2001, 917.
26. G. A. Rolla, C. Platas-Iglesias, M. Botta, L. Tei and L. Helm, *Inorg. Chem.*, 2013, **52**, 3268.
27. R. L. Gustafson and A. E. Martell, *J. Phys. Chem.*, 1963, **67**, 576.
28. N. Kuźnik and M. Wyskocka, *Eur. J. Inorg. Chem.*, 2016, **2016**, 445.
29. F. K. Kálmán and G. Tircsó, *Inorg. Chem.*, 2012, **51**, 10065.

30. B. Drahoš, V. Kubiček, C. S. Bonnet, P. Hermann, I. Lukeš and É. Tóth, *Dalton Trans.*, 2011, **40**, 1945.
31. H. Boukhalfa, T. J. Brickman, S. K. Armstrong and A. L. Crumbliss, *Inorg. Chem.*, 2000, **39**, 5591.
32. J. I. Wirgau, I. Spasojević, H. Boukhalfa, I. Batinić-Haberle and A. L. Crumbliss, *Inorg. Chem.*, 2002, **41**, 1464.
33. M. T. Caudle and A. L. Crumbliss, *Inorg. Chem.*, 1994, **33**, 4077.
34. P. B. Tsitovich, P. J. Burns, A. M. McKay and J. R. Morrow, *J. Inorg. Biochem.*, 2014, **133**, 143.
35. S. Aime, M. Botta, E. Gianolio and E. Terreno, *Angew. Chem., Int. Ed.*, 2000, **39**, 747.
36. G. S. Loving, S. Mukherjee and P. Caravan, *J. Am. Chem. Soc.*, 2013, **135**, 4620.
37. E. M. Gale, S. Mukherjee, C. Liu, G. S. Loving and P. Caravan, *Inorg. Chem.*, 2014, **53**, 10748.
38. C. F. G. C. Geraldes, A. D. Sherry, R. D. Brown III and S. H. Koenig, *Magn. Reson. Med.*, 1986, **3**, 242.
39. S. H. Koenig, C. M. Baglin and R. D. Brown III, *Magn. Reson. Med.*, 1985, **2**, 283.
40. I. Bertini, F. Capozzi, C. Luchinat and Z. Xia, *J. Phys. Chem.*, 1993, **97**, 1134.
41. M. S. Zetter, M. W. Grant, E. J. Wood, H. W. Dodgen and J. P. Hunt, *Inorg. Chem.*, 1972, **11**, 2701.
42. L. Helm, *Chimia*, 2011, **65**, 696.
43. D. H. Powell, O. M. Ni Dhubhghaill, D. Pubanz, L. Helm, Y. S. Lebedev, W. Schlaepfer and A. E. Merbach, *J. Am. Chem. Soc.*, 1996, **118**, 9333.
44. J. Bloch and G. Navon, *J. Inorg. Nucl. Chem.*, 1980, **42**, 693.
45. J. Maignut, R. Meier, A. Zahl and R. van Eldik, *J. Am. Chem. Soc.*, 2008, **130**, 14556.
46. A. D. McLachlan, *Proc. R. Soc. A*, 1964, **280**, 271.
47. G. Hernández and R. G. Bryant, *Bioconjugate Chem.*, 1991, **2**, 394.
48. W. Cheng, I. E. Haedicke, J. Nofiele, F. Martinez, K. Beera, T. J. Scholl, H.-L. M. Cheng and X.-A. Zhang, *J. Med. Chem.*, 2014, **57**, 516.
49. I. E. Haedicke, T. Li, Y. L. K. Zhu, F. Martinez, A. M. Hamilton, D. H. Murrell, J. T. Nofiele, H.-L. M. Cheng, T. J. Scholl, P. J. Foster and X.-A. Zhang, *Chem. Sci.*, 2016, **7**, 4308.
50. I. Bertini, F. Briganti, Z. Xia and C. Luchinat, *J. Magn. Reson., Ser. A*, 1993, **101**, 198.
51. E. Balogh, Z. He, W. Hsieh, S. Liu and É. Tóth, *Inorg. Chem.*, 2007, **46**, 238.
52. V. Nagy, K. Pota, Z. Garda, J. L. Barriada, R. Tripier, C. Platas-Iglesias, É. Tóth and G. Tircsó, *unpublished results*.
53. D. Esteban-Gómez, C. Cassino, M. Botta and C. Platas-Iglesias, *RSC Adv.*, 2014, **4**, 7094.
54. J. A. Peters, *Contrast Media Mol. Imaging*, 2016, **11**, 160.

55. S. Aime, A. Barge, J. I. Bruce, M. Botta, J. A. K. Howard, J. M. Moloney, D. Parker, A. S. de Sousa and M. Woods, *J. Am. Chem. Soc.*, 1999, **121**, 5762.
56. Y. Ducommun, K. E. Newman and A. E. Merbach, *Inorg. Chem.*, 1980, **19**, 3696.
57. B. Drahoš, J. Kotek, I. Císařová, P. Hermann, L. Helm, I. Lukeš and É. Tóth, *Inorg. Chem.*, 2011, **50**, 12785.
58. E. Molnár, N. Camus, V. Patinec, G. A. Rolla, M. Botta, G. Tircsó, F. K. Kálmán, T. Fodor, R. Tripier and C. Platas-Iglesias, *Inorg. Chem.*, 2014, **53**, 5136.
59. A. de Sá, C. S. Bonnet, C. F. G. C. Geraldés, É. Tóth, P. M. T. Ferreira and J. P. André, *Dalton Trans.*, 2013, **42**, 4522.
60. L. Helm and A. E. Merbach, *Chem. Rev.*, 2005, **105**, 1923.
61. A. Budimir, J. Kalmár, I. Fábrián, G. Lente, I. Bányai, I. Batinić-Haberle and M. Biruš, *Dalton Trans.*, 2010, **39**, 4405.
62. P.-O. Westlund, *Mol. Phys.*, 1995, **85**, 1165.
63. C. Platas-Iglesias, D. Esteban-Gómez, L. Helm and M. Regueiro-Figueroa, *J. Phys. Chem. A*, 2016, **120**, 6467.
64. P. H. Fries and E. Belorizky, *ChemPhysChem*, 2012, **13**, 2074.
65. E. Belorizky, P. H. Fries, L. Helm, J. Kowalewski, D. Kruk, R. D. Sharp and P.-O. Westlund, *J. Chem. Phys.*, 2008, **128**, 052315.
66. J. S. Troughton, M. T. Greenfield, J. M. Greenwood, S. Dumas, A. J. Wiethoff, J. Wang, M. Spiller, T. J. McMurry and P. Caravan, *Inorg. Chem.*, 2004, **43**, 6313.
67. S. Aime, P. L. Anelli, M. Botta, M. Brocchetta, S. Canton, F. Fedeli, E. Gianolio and E. Terreno, *J. Biol. Inorg. Chem.*, 2002, **7**, 58.
68. G. Liu, H. W. Dodgen and J. P. Hunt, *Inorg. Chem.*, 1977, **16**, 2652.
69. E. M. Gale, I. P. Atanasova, F. Blasi, I. Ay and P. Caravan, *J. Am. Chem. Soc.*, 2015, **137**, 15548.
70. A. Forgács, M. Regueiro-Figueroa, J. L. Barriada, D. Esteban-Gómez, A. de Blas, T. Rodríguez-Blas, M. Botta and C. Platas-Iglesias, *Inorg. Chem.*, 2015, **54**, 9576.
71. L. Tei, G. Gugliotta, M. Fekete, F. K. Kálmán and M. Botta, *Dalton Trans.*, 2011, **40**, 2025.
72. B. Drahoš, M. Pniok, J. Havlíčková, J. Kotek, I. Císařová, P. Hermann, I. Lukeš and É. Tóth, *Dalton Trans.*, 2011, **40**, 10131.
73. V. Patinec, G. A. Rolla, M. Botta, R. Tripier, D. Esteban-Gómez and C. Platas-Iglesias, *Inorg. Chem.*, 2013, **52**, 11173.
74. A. Forgács, L. Tei, Z. Baranyai, I. Tóth, L. Zékány and M. Botta, *Eur. J. Inorg. Chem.*, 2016, **2016**, 1165.
75. A. Dees, A. Zahl, R. Puchta, N. J. R. van Eikema Hommes, F. W. Heinemann and I. Ivanović-Burmazović, *Inorg. Chem.*, 2007, **46**, 2459.
76. B. Drahoš, J. Kotek, P. Hermann, I. Lukeš and É. Tóth, *Inorg. Chem.*, 2010, **49**, 3224.

77. D. Lieb, F. C. Friedel, M. Yawer, A. Zahl, M. M. Khusniyarov, F. W. Heinemann and I. Ivanović-Burmazović, *Inorg. Chem.*, 2013, **52**, 222.
78. J. Zhu, E. M. Gale, I. Atanasova, T. A. Rietz and P. Caravan, *Chem. – Eur. J.*, 2014, **20**, 14507.
79. J. A. Peters, J. Huskens and D. J. Raber, *Prog. Nucl. Magn. Reson. Spectrosc.*, 1996, **28**, 283.
80. C. Platas-Iglesias, *Eur. J. Inorg. Chem.*, 2012, **2012**, 2023.
81. A. W. Nolle and L. O. Morgan, *J. Chem. Phys.*, 1962, **36**, 378.
82. D. Baute and D. Goldfarb, *J. Phys. Chem. A*, 2005, **109**, 7865.
83. J. Dasgupta, A. M. Tyryshkin, Y. N. Kozlov, V. V. Klimov and G. C. Dismukes, *J. Phys. Chem. B*, 2006, **110**, 5099.
84. C. J. Walsby, J. Telser, R. E. Rigsby, R. N. Armstrong and B. M. Hoffman, *J. Am. Chem. Soc.*, 2005, **127**, 8310.
85. W. B. Lynch, R. S. Boorse and J. H. Freed, *J. Am. Chem. Soc.*, 1993, **115**, 10909.
86. J. N. Burstyn, J. A. Roe, A. R. Miksztal, B. A. Shaevitz, G. Lang and J. S. Valentine, *J. Am. Chem. Soc.*, 1988, **110**, 1382.
87. M.-E. Pandelia, N. D. Lanz, S. J. Booker and C. Krebs, *Biochim. Biophys. Acta, Mol. Cell Res.*, 2015, **1853**, 1395.
88. E. Rodríguez, R. V. Simoes, A. Roig, E. Molins, N. Nedelko, A. Ślawska-Waniewska, S. Aime, C. Arús, M. E. Cabañas, C. Sanfeliu, S. Cerdán and M. L. García-Martín, *Magn. Reson. Mater. Phys., Biol. Med.*, 2007, **20**, 27.
89. D. K. Gosser Jr., *Cyclic Voltammetry: Simulation and Analysis of Reaction Mechanisms*, VCH, New York, 1993, ch. 2, pp. 27–69.
90. M. Shokeen and C. J. Anderson, *Acc. Chem. Res.*, 2009, **42**, 832.
91. A. J. Bard and L. R. Faulkner, *Electrochemical Methods: Fundamentals and Applications*, Wiley, New York, 2nd edn, 2001, ch. 1, pp. 1–43.
92. A. C. Tsipis, *Coord. Chem. Rev.*, 2014, **272**, 1.
93. W. W. Rudolph and G. Irmer, *Dalton Trans.*, 2013, **42**, 14460.
94. M. Zhu, B. W. Puls, C. Frandsen, J. D. Kubicki, H. Zhang and G. A. Waychunas, *Inorg. Chem.*, 2013, **52**, 6788.
95. R. Boča, *Coord. Chem. Rev.*, 2004, **248**, 757.
96. S. Zein, C. Duboc, W. Lubitz and F. Neese, *Inorg. Chem.*, 2008, **47**, 134.
97. C. Duboc, M.-N. Collomb and F. Neese, *Appl. Magn. Reson.*, 2010, **37**, 229.
98. M. Retegan, N. Cox, D. A. Pantazis and F. Neese, *Inorg. Chem.*, 2014, **53**, 11785.
99. S. Khan, A. Kubica-Miształ, D. Kruk, J. Kowalewski and M. Odelius, *J. Chem. Phys.*, 2015, **142**, 034304.
100. C. J. O'Connor, Magnetic-Susceptibility Measurement Techniques, in *Molecule-Based Magnetic Materials*, ed. M. M. Turnbull, T. Sugimoto and L. K. Thompson, *ACS Symposium Series*, American Chemical Society, Washington, DC, 1996, vol. 644, ch. 4, pp. 44–66.
101. D. F. Evans, *J. Chem. Soc.*, 1959, 2003.
102. G. A. Bain and J. F. Berry, *J. Chem. Educ.*, 2008, **85**, 532.

103. C. Platas-Iglesias, L. Vaiana, D. Esteban-Gómez, F. Avecilla, J. A. Real, A. de Blas and T. Rodríguez-Blas, *Inorg. Chem.*, 2005, **44**, 9704.
104. O. Kahn, *Molecular Magnetism*, VCH, New York, 1993, p. 16.
105. D. V. Behere, R. Birdy and S. Mitra, *Inorg. Chem.*, 1981, **20**, 2786.
106. A. Pascual-Álvarez, J. Vallejo, E. Pardo, M. Julve, F. Lloret, J. Krystek, D. Armentano, W. Wernsdorfer and J. Cano, *Chem. – Eur. J.*, 2015, **21**, 17299.
107. D. M. Corsi, C. Platas-Iglesias, H. van Bekkum and J. A. Peters, *Magn. Reson. Chem.*, 2001, **39**, 723.
108. S. D. Springer and A. Butler, *J. Inorg. Biochem.*, 2015, **148**, 22.
109. R. L. Fagaly, *Rev. Sci. Instrum.*, 2006, **77**, 101101.
110. N. Graepi, D. H. Powell, G. Laurenczy, L. Zékány and A. E. Merbach, *Inorg. Chim. Acta*, 1995, **235**, 311.
111. E. Balogh, M. Mato-Iglesias, C. Platas-Iglesias, É. Tóth, K. Djanashvili, J. A. Peters, A. de Blas and T. Rodríguez-Blas, *Inorg. Chem.*, 2006, **45**, 8719.
112. E. M. Gale, J. Zhu and P. Caravan, *J. Am. Chem. Soc.*, 2013, **135**, 18600.

CHAPTER 6

Fluorine-based Contrast Agents

EMMA STARES,^a JUNSUNG RHO,^a ERIC T. AHRENS,^{*a}
PAULA FOSTER,^{b,c} ALEX LI^b AND ROBERT BARTHA^{*b,c,d}

^a Department of Radiology, University of California, San Diego, La Jolla, CA 92093, USA; ^b Robarts Research Institute, University of Western Ontario, London, Ontario N6A 3K7, Canada; ^c Department of Medical Biophysics, University of Western Ontario, London, Ontario N6A 3K7, Canada; ^d Departments of Medical Imaging and Psychiatry, University of Western Ontario, London, Ontario N6A 3K7, Canada
*Email: eahrens@ucsd.edu; rbartha@robarts.ca

6.1 Compositions for Fluorine-19 MRI Molecular Imaging Applications

EMMA STARES, JUNSUNG RHO AND ERIC T. AHRENS*

6.1.1 Fluorine-19 MRI Probes

Fluorine-19 (¹⁹F)-MRI is increasingly used in the field of *in vivo* cellular and molecular imaging. Imaging probes based on ¹⁹F potentially offer high detection specificity, quantitative imaging abilities, and an excellent safety profile. The renewed interest in ¹⁹F imaging probe development also coincides with the increased use of fluorine chemistry in biomedicine, where drug candidates are increasingly incorporating the fluorine atom. Fluorine can profoundly change the properties of compounds, including metabolic stability, binding interactions, and reactivities. A further motivator for ¹⁹F probe development stems from increased interest in alternatives to

traditional metal-ion-based contrast agents for MRI for cellular molecular imaging due to technological challenges associated with image specificity and quantification.

This chapter focuses on fluorine-based probes used for cell tracking with MRI and applications related to the detection of inflammation. These probes are mostly based on perfluorocarbon (PFC) molecules that are formulated as colloidal suspensions or emulsions in aqueous buffer. For cell tracking with MRI, which monitors the behavior of stem cells or immune cells *in vivo*, cells are intracellularly labeled in culture using a fluorine probe (Figure 6.1). Following transfer to the subject, cells are detected repeatedly *in vivo* using ^{19}F -MRI. Intracellular fluorine yields positive-signal 'hot-spot' images, with no background signal due to the absence of detectable fluorine atoms in host tissues. Images can be quantified to estimate cell numbers at sites of accumulation, thereby enabling '*in vivo* cytometry'.^{1,2} The sensitivity limits of detection are on the order of 10^5 cells voxel⁻¹.³ Alternatively, ^{19}F agents are formulated for direct intravenous injection. Often these injectable emulsion probes are scavenged by resident phagocytic cells, such as

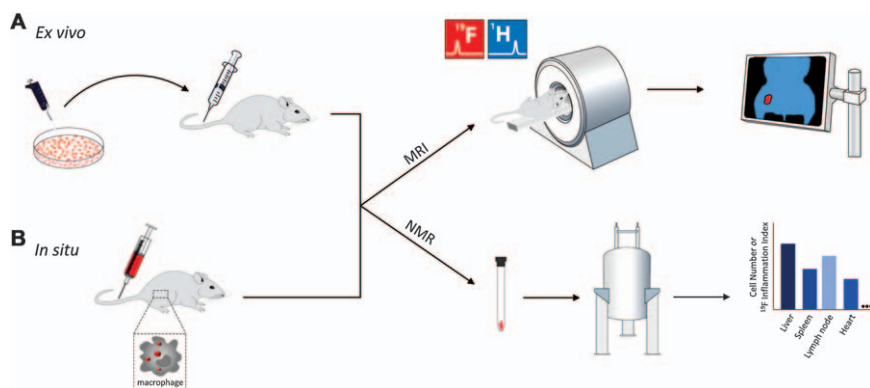


Figure 6.1 Schematic of the ^{19}F imaging schemes using PFC emulsions. (A) The '*in vivo* cytometry' approach, where cells of interest are co-cultured *ex vivo* with PFC emulsion, resulting in intracellular uptake. The labeled cells are then inoculated into a subject and imaged using MRI. Both ^{19}F -MRI (labeled cells) and ^1H -MRI (background anatomy) are acquired in the same imaging session. Spin-density-weighted ^{19}F -MRI yields a positive-contrast signal from labeled cells with no background. A $^{19}\text{F}/^1\text{H}$ -fusion image is constructed showing the regions containing labeled cells (red) in their anatomical context. Cell quantification is performed by integration of the total ^{19}F signal in a region of interest.¹ Alternatively, intact tissue samples excised from the subject are rapidly assayed using conventional ^{19}F NMR to determine cell number or cell density, thereby minimizing histological endpoints. (B) *In situ* cell labeling using an injectable PFC emulsion. PFC emulsion droplets are scavenged by phagocytic monocytes and macrophages that participate in sites of inflammation, or alternatively, accumulate at tissues of interest if a targeting moiety is used, yielding a ^{19}F hot-spot in MRI.

monocytes and macrophages, thereby labeling these cells. Since the cells' innate behavior is not disrupted, they can home to sites of inflammation, which are revealed as ^{19}F -MRI hot-spots.⁴⁻⁷ In other formulations of injectable ^{19}F probes, a targeting moiety (*e.g.*, peptide or antibody) is attached to the emulsion droplet surface, resulting in selective probe uptake in tissues harboring the receptor of interest.⁸⁻¹⁰ A detailed overview of the plethora of *in vivo* biological applications using ^{19}F -based MRI probes is provided elsewhere in several excellent review articles.^{3,11-17} This chapter focuses on ^{19}F imaging probe compositions using PFC molecules.

6.1.2 Perfluorocarbons (PFCs)

6.1.2.1 Basic Physiochemical Properties of PFCs

PFCs are aliphatic hydrocarbon derivatives, in which each hydrogen atom is replaced by a fluorine atom. Fluorine is a larger element than hydrogen, but its nine electrons occupy a proportionally smaller volume than the lone electron of hydrogen, giving fluorine a much greater electron density. The dense electron cloud of fluorine is not readily distorted: fluorine has a lower polarizability than every element except neon. In addition, fluorine has a very high ionization energy, and it is the most electronegative element on the periodic table.¹⁸

Perfluorocarbons display structural differences from their parent hydrocarbons. Due to the greater space required by fluorine atoms, PFCs are twisted into helical conformations, in contrast to the planar zigzag of hydrocarbons. PFCs are also bulkier and more rigid than the corresponding hydrocarbons.¹⁸ PFCs can be gaseous or liquid at room temperature, depending on the chain length.¹⁹ Liquid PFCs are of primary interest for cellular and molecular applications with MRI, although fluorinated gases are currently being explored for clinical lung-airway imaging.²⁰

The low polarizability of fluorine confers a set of interrelated physical properties upon PFCs. Because the fluorine electron cloud is not prone to fluctuation, few instantaneous dipoles occur. The resulting weak van der Waals forces cause liquid PFCs to exhibit low molecular cohesiveness. Thus, PFCs have an unusually high capacity for dissolving gases such as O_2 , N_2 , and CO_2 .¹⁸ Other physical properties common to PFCs include low boiling points, surface tensions, viscosities, dielectric constants, and refractive indices and high densities, compressibilities, spreading coefficients, and vapor pressures.^{18,21} Perhaps the most unusual feature of PFCs is their extreme hydrophobicity, in conjunction with usually substantial lipophobicity. Due to this phobic nature, PFCs tend toward aggregation and phase separation in mixtures.¹⁸

The chemical behavior of PFCs is characterized by great thermodynamic stability and chemical inertness, arising primarily from the strength of the intra-chain C-F covalent bonds. The enormous strength of the C-F bond is due to the energetic overlap of the carbon and fluorine atomic orbitals.¹⁸

In addition, the difference in electronegativity between the two atoms confers partial ionic character upon the bond. The strength of the C–C bonds in PFCs is enhanced by the inductive effect of the electronegative fluorine atoms. Furthermore, reactions such as oxidation are energetically prevented by the lack of low-lying molecular orbitals for interaction with molecules like O₂ and are hindered electrostatically by the densely repellent electron cloud surrounding the PFC chain.¹⁸

6.1.2.2 Biocompatibility

The biocompatibility of PFCs has been well-described over the investigation into their potential medicinal applications. Along with their chemical stability, perfluorocarbons exhibit immense biological inertness. PFCs do not undergo metabolism by enzymes or degradation within acidic lysosomes.²² They do not integrate with cellular membranes or structures, and they are excreted in vapor form by exhalation following uptake by the reticuloendothelial system.^{23,24} Due to the insolubility of PFCs in water, as well as their tendency not to interact with lipid membranes, *in vivo* applications generally require the formulation of PFCs into stable, biocompatible emulsions.

Early pre-clinical and clinical research into PFCs focused on their high capacity for O₂ dissolution.²⁵ PFCs were initially explored for the liquid ventilation of patients in respiratory distress.²⁶ The same property was harnessed for use in PFC-based oxygen-delivery systems (*i.e.*, ‘blood substitutes’), with some success.^{27–29}

6.1.2.3 Survey of Perfluorocarbons

Perfluorocarbons have several features that make them suitable tracers for ¹⁹F-MRI, including chemical and biological inactivity. In theory, an enormous array of perfluorocarbons is synthetically accessible, with varying chain lengths and branched structures. However, a relatively small number of PFCs have been considered for MRI. These may be divided into structural classes: linear perfluorocarbons, cyclic perfluorocarbons, perfluoroamines, and perfluoroethers. Representative molecules from each class are shown in Figure 6.2. Overall, the ideal ¹⁹F-MRI probe should have a simple ¹⁹F-NMR spectrum, preferably with a single, narrow resonance and a high concentration of equivalent fluorine atoms, for increased sensitivity. In addition, the molecule should ideally have a short spin-lattice (T_1) and long spin-spin (T_2) relaxation time to minimize image acquisition time. A given perfluorocarbon might possess some, or all, of these properties, depending upon its specific chemical structure.

Linear perfluorocarbons include the saturated straight-chain molecule perfluorooctyl bromide. Perfluorooctyl bromide was one of the first PFCs explored for ¹⁹F imaging³⁰ and has been used for oxygen-sensing,³¹ tumor imaging,³² and cellular tracking.³³ The terminal bromide confers slight

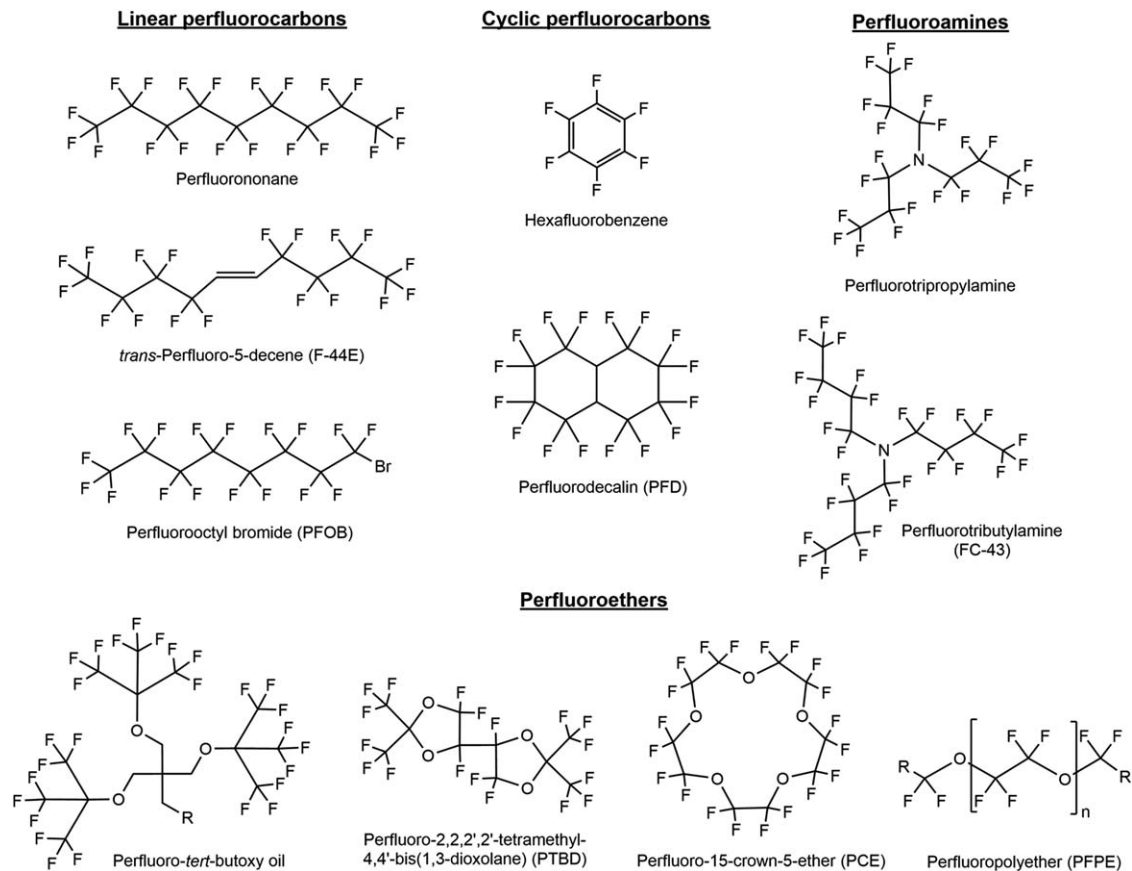


Figure 6.2 Representative perfluorocarbons considered as ^{19}F -MRI probes.

lipophilicity to the molecule and enhances its clearance rate from the body. However, perfluorooctyl bromide is less than an ideal tracer agent due to the unsymmetrical nature of perfluorooctyl bromide. Its NMR spectrum comprises eight peaks, corresponding to the eight distinct CF_n units. The presence of multiple peaks leads to unwanted chemical shift artifacts. In addition, the most intense peak results from only three equivalent fluorine atoms, yielding a low signal-to-noise ratio. Other linear PFCs include perfluorononane, which was briefly studied as a gastrointestinal imaging agent in its non-emulsified form,³⁴ and *trans*-perfluoro-5-decene, an unsaturated molecule with four unique fluorine environments, which was considered for inflammation imaging applications.³⁵

Cyclic perfluorocarbons are promising ^{19}F tracer agents due to the large number of equivalent fluorine atoms possible in ring structures. The six fluorine atoms of the aromatic compound hexafluorobenzene give rise to a single NMR resonance, which is desirable for imaging purposes. The molecule is sensitive to changes in oxygen pressure,³⁶ and has been used as a probe for tumor oxygenation.³⁷ The saturated polycyclic structure perfluorodecalin was investigated as a possible inflammation tracker because of its rapid clearance from the body. However, perfluorodecalin exists in two diastereomeric forms, resulting in a complex NMR spectrum and low sensitivity as a probe for MRI.³⁵

Tertiary *perfluoroamines* have nine equivalent fluorine atoms due to their three-fold symmetry. Examples include perfluorotripropylamine and perfluorotributylamine, which have been used for *in vivo* pO_2 sensing in animal models.^{38–40} However, both compounds display reduced sensitivity due to the presence of multiple ^{19}F resonances.

Perfluoroethers are a class of PFCs that are the most characterized ^{19}F tracer agents to date for preclinical and clinical applications. Perfluoro-*tert*-butyl groups [$\text{C}(\text{CF}_3)_3$, PF-*t*-Bu] each contain nine equivalent fluorine atoms. Molecules that incorporate multiples of this moiety in a symmetrical fashion have potential as sensitive ^{19}F probes. The *bis*(dioxolane) compound PTBD contains four equivalent PF-*t*-Bu groups. The simple two-peak spectrum of PTBD does not result in the chemical shift artifacts caused by the more complex perfluorooctyl bromide. PTBD is thus more sensitive than perfluorooctyl bromide, and does not require specialized MRI pulse sequences.⁴¹ A family of highly branched, symmetric perfluoro-*tert*-butoxy oils (Figure 6.2) was synthesized with a view toward potential ^{19}F -MRI applications.⁴² The 27 fluorine atoms of each compound give rise to one sharp peak. Perfluoro-15-crown-5-ether is a cyclic, highly symmetrical molecule with 20 equivalent fluorine atoms that give rise to a single narrow resonance. Perfluoro-15-crown-5-ether has been extensively used for preclinical *in vivo* cell tracking.^{3,33,43} Perfluoro-15-crown-5-ether has also been used for oxygen sensing in tumor tissue,^{44–47} and for the detection of atherosclerosis in mice.⁴⁸ Perfluoropolyethers are linear oligomeric molecules that are widely used for both preclinical and clinical cell tracking applications.^{1,2,49,50} Perfluoropolyethers have an inherently low T_1/T_2 ratio, a

desirable property for rapid MRI data acquisition, and one main resonance corresponding to the often >40 repeating $-\text{CF}_2\text{CF}_2\text{O}-$ units. A generalized perfluoropolyether is depicted in Figure 6.2.

6.1.2.4 Synthetic Modifications

6.1.2.4.1 End-group Chemistry. Perfluoropolyethers with reactive terminal groups can be chemically modified to introduce additional functionalities into the molecule. Primary and secondary amines, appended to useful moieties, react with di-ester perfluoropolyethers to form amide linkages. Unreacted reagents are readily removed by liquid–liquid extraction with an organic solvent, while the PFC-based components separate into a fluoruous phase.⁵¹ For example, the fluorescent dyes BODIPY-TR, FITC, and Alexa 647 were successfully conjugated to perfluoropolyethers in this manner (Scheme 6.1).⁴⁹ A mixture of mono- and di-functionalized perfluoropolyether molecules were synthesized, and the resulting fluorescent blended perfluoropolyethers amides were used to form dual-modality imaging agents.

In another approach, amine-functionalized poly(ethylene) glycol and perfluoropolyethers were combined to yield a poly(ethylene) glycol–perfluoropolyether block copolymer, *via* a reactive acyl chloride intermediate.⁵² This unique fluorosurfactant was formulated into a stable, bio-compatible PFC emulsion.

6.1.2.4.2 Incorporation of Metals. The incorporation of metal ions into a PFC emulsion can significantly enhance probe sensitivity. Certain paramagnetic metal ions can decrease T_1 ; a long T_1 increases the acquisition time and limits the amount of signal averaging and the signal-to-noise ratio that can be achieved for a fixed scan time. However, this synthetic modification is non-trivial. A suitable ligand must be soluble in the fluoruous phase, and the resulting complex should be neutral, coordinatively saturated, and thermodynamically stable. These conditions were satisfied by the synthesis of a PFC emulsion containing a stable Fe^{III} complex firmly bound within the fluoruous phase (Figure 6.3).⁵³ Perfluoropolyethers were conjugated to *p*-methoxyacetophenone, yielding the highly fluorinated β -diketone ligand *p*An-FDK (Figure 6.3A). Emulsions formulated from a blend of *p*An-FDK and other PFCs efficiently extracted and retained Fe^{III} from the aqueous phase. The presence of high spin, paramagnetic Fe^{III}



Scheme 6.1 General reaction of a perfluoropolyether methyl ester and a primary amino fluorescent dye to form a mono-amide.⁴⁹

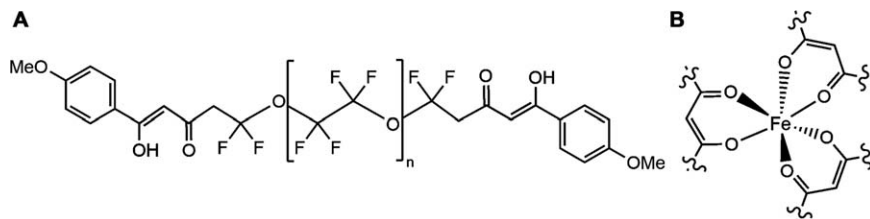


Figure 6.3 Representative approach for metallating PFC. (A) The fluorinated β -diketone ligand *pAn*-FDK and (B) the saturated coordination sphere of Fe(III) in a PFC emulsion.⁵³

within the emulsion resulted in an increase in probe sensitivity predicted to be 8-fold at a clinically relevant magnetic field strength (3 T).⁵³

6.1.2.5 Multimodal and Theranostic Agents

PFC-based emulsions are also an emerging platform for the development of agents for dual-modality imaging and theranostic potential. Dual-modality agents integrate ^{19}F -MRI with additional types of imaging moieties, such as fluorescence dyes. Fluorescent dyes have been covalently linked to perfluoropolyethers *via* end-group chemistry to yield combination MRI-fluorescence imaging agents (Scheme 6.1).⁴⁹ Near-IR dyes have also been encapsulated within PFC emulsions at the formulation stage. A near-IR PFC probe was successfully used to label tumor infiltrating macrophages in a rodent tumor model, enabling qualitative near-IR imaging as well as three-dimensional and quantitative ^{19}F -MRI.⁵⁴ PFC-based agents have also been used as dual-modality agents for ultrasound and MRI.¹⁹ In a tri-modal example, human pancreatic islet cells were labeled with a perfluorooctyl-bromide-based emulsion. The islets were successfully implanted below the renal capsule in mice and rabbits, and visualized by MRI, ultrasound, and X-ray computed tomography, where the cells became sufficiently brominated to provide a discernable X-ray cross section.⁵⁵

Theranostic agents include both therapeutic and diagnostic functionalities. Several examples of disease-targeted PFC probes with drug molecules linked to or contained within the emulsion have been reported. In an early example, perfluorooctyl bromide emulsions containing the anti-proliferation drugs doxorubicin or paclitaxel were targeted to vascular smooth muscle cells.⁵⁶ The proliferation and migration of vascular smooth muscle cells is a major complication following coronary angioplasty. The drug-carrying, vascular-smooth-muscle-cell-targeted emulsions effectively reduced cell proliferation and were readily quantified by ^{19}F -MRI.⁵⁶ A similar strategy was used for the targeted treatment of plaque angiogenesis, a characteristic feature of atherosclerosis.⁹ An $\alpha_v\beta_3$ integrin-targeted perfluorooctyl bromide emulsion was loaded with the anti-angiogenic compound fumagillin, enabling the delivery of the drug and quantification of its effect by ^1H -MRI.⁹ More recently, a fluorescent perfluorocarbon emulsion

loaded with the anti-inflammatory drug celecoxib was reported for the simultaneous visualization and treatment of inflammation in a murine model.⁵⁷ ¹⁹F-NMR confirmed that the theranostic emulsion was specifically taken up by CD68-positive macrophages expressing cyclooxygenase-2 at the inflammation site, while the therapeutic response (decrease in macrophage infiltration) was monitored by fluorescence. Importantly, these results and others provide proof-of-principle that targeted PFC emulsions allow visualization of the delivery and effectiveness of a therapeutic drug.¹⁰

6.1.3 Emulsion Formulations for Imaging

6.1.3.1 Background and Features

Using PFCs for cell labeling applications requires formulation into a biocompatible colloidal suspension in an aqueous buffer, *i.e.*, emulsion. Emulsification is typically achieved with lipids, non-ionic surfactants, or both to stabilize the emulsions by reducing the large interfacial tension from hydrophobicity of PFCs. Formulation of PFCs into emulsions has been extensively studied in the setting of developing PFCs as artificial blood substitutes.⁵⁸ These early efforts paved the way for developing PFCs as imaging probes. Moreover, emulsion formulation is not unique to PFCs but is rather widely used in the pharmaceutical industry, and advances in the field can be applied to PFCs.⁵⁹

In the context of ¹⁹F-MRI, cells can be labeled *ex vivo* or *in situ* depending on the experimental design. Depending on the route of cell labeling, optimal emulsion formulation will differ. For *ex vivo* labeling, a PFC emulsion needs to efficiently label the cells while in culture in a time-efficient and non-toxic manner. Furthermore, ideally these emulsions should have mean droplet sizes of less than ~200 nm so that unincorporated emulsion droplets can be easily separated from labeled cells *via* centrifugation after labeling because larger droplets can sediment with the cell pellet during centrifugation, causing unwanted contamination for subsequent applications. A small droplet size is also desirable for sterilization of the emulsion by filtration, *e.g.*, *via* passage through a 0.2 μm filter. For *in situ* labeling, emulsion stability in the bloodstream to promote vascular circulation for extended time periods is also desirable. For developing a clinical PFC probe for *in situ* labeling where large doses must be delivered, the clearance rate from the body is also an important factor; different PFCs have a wide range of retention times, in the order of days to greater than a month.³⁵

6.1.3.2 Emulsion Formulation

PFC emulsification should yield a non-toxic emulsion with physical and chemical stability, low polydispersity, and droplet surface properties appropriate for the desired biological application. Droplet size instability over time can be attributed to coalescence and molecular diffusion. Coalescence

is the formation of larger droplets by direct merging of smaller ones, facilitated by factors such as temperature.⁶⁰ Molecular diffusion, namely Ostwald ripening, is a process in which the larger particles gradually grow at the expense of smaller ones.⁶¹ Given these degradation mechanisms, the overall stability and size of a PFC emulsion depends on a number of factors, including the emulsification method, the chemical structure of the PFC, and the choice of surfactant.

To achieve an emulsion less than 200 nm in diameter (*i.e.*, loosely termed 'nanoemulsion') with low polydispersity (<0.2), high-energy processes such as sonication, high-shear homogenization, or high-pressure microfluidization are often employed.⁶² Sonication is often used in the research laboratory but tends to yield wide particle size distributions, suffers from poor reproducibility, and presents challenges with respect to manufacturing at large scale.⁵⁸ The process of sonication is also prone to unfavorable heat generation.⁶² Microfluidization, which uses high-pressure extrusion of the emulsion premix solution through a small orifice, is generally the preferred emulsification method because it delivers improved efficiency and produces emulsions with a narrow size distribution compared to sonication.⁵⁹

The properties of the PFC are the key factors affecting the degradation of emulsions.^{58,60,61,63} Because molecular diffusion (Ostwald ripening) is known to play a role in emulsion degradation, the solubility of PFCs in the aqueous phase effectively predicts emulsion stability.^{61,63,64} As a general rule, solubility decreases with increasing molecular weight. Therefore, a PFC of high molecular weight produces a more stable emulsion than a PFC of low molecular weight. Between PFCs of similar molecular weights, the presence of a cyclic structure increases solubility and compromises emulsion stability.⁶⁵ In terms of the molecular weight of the PFC, there is a trade-off between the resulting emulsion stability and the biological excretion rate.⁵⁸

Poloxamers and phospholipids (*e.g.*, Pluronic and egg yolk phospholipid, respectively) have historically been extensively used as surfactants for PFC emulsion formulation. Poloxamers are non-ionic triblock copolymers consisting of a central hydrophobic block and two flanking hydrophilic blocks. Emulsion formation does not require large amounts of surfactant and provides a steric barrier against coalescence.⁶⁶ Poloxamers are inexpensive and widely used in the cosmetic and pharmaceutical industries.⁶⁷ Indeed, one of the earliest reported PFC emulsions used Pluronic F68,⁶⁸ as did the first artificial blood substitute based on PFC (Fluosol). Fluosol was approved by the US Food and Drug Administration for use during angioplasty; however, side effects were reported.^{69–72} Fluosol was subsequently taken off the market due to difficulty in handling prior to use and short shelf life, not necessarily due to toxicity.⁷³ Poloxamers have other limitations. Their surface activity is relatively poor compared to egg yolk phospholipid and confers lower stability. Pluronic F68 also has a cloud point of 110–115 °C, below the 121 °C typical for terminal autoclave sterilization;⁵⁸ however, addition of soya oil can raise the threshold temperature for destabilization.^{74,75}

Egg yolk phospholipid was used for second-generation artificial blood substitutes. Egg yolk phospholipid has a long history of use in pharmaceuticals for delivering parenteral lipid nutrition,^{76,77} and it has an excellent safety profile and well-documented pharmacology.⁷⁸ Emulsions prepared with egg yolk phospholipid have shown longer intravascular half-lives compared to emulsions prepared with poloxamers.⁷⁹ This is especially beneficial for intravenous applications, such as *in situ* macrophage labeling for inflammation MRI, in which a long circulation time is desired. Importantly, egg yolk phospholipid delivers better stability compared to poloxamers,^{63,65,80} although some contradictory reports exist.^{74,75} The difference between poloxamers and egg yolk phospholipid in terms of emulsion stability is particularly remarkable with perfluorooctyl bromide,^{81–83} which is often used for ¹⁹F imaging. The stabilization effect is attributable to low interfacial tension. The slight lipophilic character of perfluorooctyl bromide owing to the presence of the bromine atom results in a better hydrophilic–lipophilic balance between egg yolk phospholipid and perfluorooctyl bromide compared to other PFCs. Factors including phospholipid composition, degree of unsaturation, and presence of trace metals can all affect hydrolysis and oxidation of egg yolk phospholipid, which in turn limit the stability of such emulsions.⁸⁴ To maximize shelf-life, addition of metal chelators and antioxidants can be beneficial.⁵⁸ Overall, chemical modification of both poloxamers and egg yolk phospholipid is an active area of research in molecular imaging, including, for example, molecularly targeted agents.

Other surfactants include fluorosurfactants and fluorocarbon–hydrocarbon diblocks. In principal, fluorosurfactants (*i.e.*, hydrophilic block combined with fluorocarbon block) can substantially lower PFC–water interfacial tension and have been effectively used to stabilize PFC emulsions.^{85–87} Some formulations using fluorosurfactants produced emulsions that remained stable for at least six years.⁸⁸ Fluorocarbon–hydrocarbon diblocks have been used to supplement egg yolk phospholipid for enhanced stabilization. Fluorocarbon–hydrocarbon diblocks anchor themselves at the interface of PFCs and egg yolk phospholipid⁸⁹ and, as a consequence, slow molecular diffusion of PFCs.⁹⁰ A potential limitation of using fluorous surfactants for MRI applications is that disparate ¹⁹F peaks from the surfactant can cause chemical shift artifacts in images.

6.1.3.3 Technical Considerations and Other Additives

In addition to the constitutive chemical components of the emulsion, there is considerable art in the optimization of formulation parameters for PFC nanoemulsions. For example, the amount of egg yolk phospholipid used largely determines the size of the emulsion droplet. With increasing egg yolk phospholipid/PFC ratio, the droplet size decreases and then levels off, and excess egg yolk phospholipid can form PFC-free vesicles that can negatively impact the stability of the emulsion.^{82,91} Similarly, energy applied to formulating the emulsion (*e.g.*, pressure, the number of passes through a

microfluidizer, or both) initially decreases the size of the emulsion droplet. However, excess energy can strip the phospholipid layers, resulting in less emulsion instability.⁸⁸ Therefore, the number of passes and pressure for microfluidization need to be optimized for each type of PFC formulation. For intravenous use of PFC emulsions, osmolarity and pH also need to be controlled. In the context of artificial blood substitute formulation, researchers have successfully used various combinations of sodium chloride, potassium chloride, magnesium chloride, calcium chloride, calcium bicarbonate, glycerol, dextrose, sodium bicarbonate, monosubstituted sodium phosphate, phosphate buffer, and alginate.⁶⁹ In addition, α -tocopherol and ethylenediaminetetraacetic acid have also been used to prevent oxidation of egg yolk phospholipid.⁶⁹

6.1.3.4 Characterization of PFC Emulsions

A thorough characterization of PFC emulsions is needed for optimization. The size distribution of the emulsion droplets can be measured by dynamic light scattering. Dynamic light scattering provides a reliable size estimate for single-peak populations of nanoparticles, which is usually the case for microfluidizer-prepared emulsions. Zeta potential can also be a predictor for colloidal stability. A large zeta potential (*e.g.*, $>|30|$ mV) implies electrostatic repulsion between the droplets and a relatively stable emulsion. However, this trend might not hold for poloxamer-based emulsions because poloxamers provide stabilization *via* hydrophilic steric hindrance rather than charge repulsion; thus, a stable poloxamer-based emulsion can have a relatively low zeta potential value.⁹²

Physical and biological stability of PFC emulsions can undergo further stress testing in settings that mimic *in vivo* environments. Specifically, a prepared emulsion can be subjected to proteinaceous cell culture media or incubated at 37 °C for both physiological and accelerated stability testing. Size measurements and quantitative ¹⁹F-NMR can be used to assess the stability of the emulsion in this condition, as discussed in detail elsewhere.⁹³

6.1.4 Acknowledgements

This work was funded by the National Institutes of Health grant R01-EB017271 and the California Institute for Regenerative Medicine grant LA1-C12-06919.

6.2 Acquiring Fluorine-19 Phantom Images

PAULA FOSTER, ALEX LI AND ROBERT BARTHA*

6.2.1 Fluorine-19 Imaging

The testing of ^{19}F -based contrast agents for MRI requires hardware that is not found on typical MRI scanners. Although the ^{19}F nucleus has a spin of $\frac{1}{2}$ similar to ^1H , the gyromagnetic ratio of the ^{19}F nucleus is slightly smaller than that of ^1H . As a result, the Larmor frequency of ^{19}F is slower than that of ^1H , requiring the use of broadband amplifiers and dedicated radiofrequency coils that are tuned to the ^{19}F resonance frequency for excitation and detection. At the low magnetic fields used for clinical imaging, it is sometimes possible to use existing amplifiers for excitation of the ^{19}F nuclei. The design of dual tuned radiofrequency coils for the detection of both ^1H and ^{19}F can simplify data acquisition. When using such coils, the ^1H coil is used for optimization of magnetic field homogeneity within the sample (shimming) and imaging of the phantom (solvent). ^{19}F images acquired with a ^{19}F coil can then be overlaid directly on ^1H images acquired during the same session to provide context. For example, Figure 6.4 shows a phantom composed of a hollow outer cylinder filled with water and an inner cylinder filled with ^{19}F perfluoropolyether. Images of both the ^1H and ^{19}F signal were obtained using a custom built dual tuned $^1\text{H}/^{19}\text{F}$ birdcage coil, tuned to 400.2 MHz for proton and 376.8 MHz for ^{19}F imaging. Images were acquired on a 9.4 T Agilent small animal MRI system using a balanced steady state free precession imaging sequence.

Several different types of pulse sequences can be used for imaging phantoms containing ^{19}F -based contrast agents that typically have short T_2 relaxation time constants and long T_1 relaxation time constants. The most common and widely available sequences used are the fast spin-echo



Figure 6.4 Cross-sectional phantom images acquired of a cylinder of ^{19}F surrounded by a concentric cylinder of water. Images were acquired using a three-dimensional balanced steady state free precession imaging sequence (field of view = 25.6 mm \times 25.6 mm \times 25.6 mm, matrix = 128 \times 128 \times 128, flip angle = 30°, T_R/T_E = 7.0/3.5 ms, 1 average, and 4 phase cycles, resulting in a scan time of \sim 8 minutes) with a dual tuned birdcage coil. The ^1H image of the water signal in A has significantly higher signal-to-noise ratio than the ^{19}F image in B. The overlay of the two images in (C) shows the spatial localization of the signals.

type,^{5,43,94–96} which reduce signal loss due to T_2^* relaxation effects. Balanced steady state free precession^{33,97,98} and ultra-short echo-time⁹⁹ types of sequences have been used to increase the signal-to-noise ratio per unit time. These sequences have short echo-times that decrease signal loss due to transverse relaxation, which has the added benefit of producing spin-density-weighted images suitable for quantification.

One application of ^{19}F imaging is the labeling of cells with perfluorocarbons (Section 6.1.1). Although the detection sensitivity of perfluorocarbon-labeled cells is much lower than that of superparamagnetic iron oxide agents, ^{19}F imaging can be used for the quantification of cell numbers. Such measurements are possible because there is a linear relationship between perfluorocarbon content within a voxel and signal-to-noise ratio. The sensitivity for detecting perfluorocarbon-labeled cells can be improved by increasing the number of ^{19}F spins per cell. Studies suggest that any cell type can be labeled with perfluorocarbons and that increased labeling efficiency depends on cell type and cell size.⁵⁰ Using higher field strengths, optimized pulse sequences, and cutting-edge radiofrequency coil technology all lead to higher signal-to-noise ratios and improved sensitivity.

For cells preloaded with perfluorocarbons, it is possible to quantify the number of cells from MR images.¹⁷ This type of quantification requires three measurements: the number of ^{19}F spins per cell as determined by NMR spectroscopy from a labeled cell sample, the signal-to-noise ratio obtained from a uniform reference phantom (typically the dilution of the original cell-labeling agent), and the signal-to-noise ratio obtained from the regions of interest containing the cells themselves in the MR image. Phantoms can be created from labeled cell pellets to verify the linear relationship between ^{19}F signal and number of labeled cells. An example calibration is shown in Figure 6.5, demonstrating the linear relationship between the number of cells calculated using ^{19}F MRI and the actual number of cells.

6.2.2 Complications of ^{19}F Imaging: Chemical Shift Dispersion and Multiple Peaks

Although many perfluorocarbon nanoparticle emulsions used as imaging agents have only a single peak in the ^{19}F spectrum, some agents, including perfluorooctyl bromide, have multiple peaks each with different relaxation time constants.¹⁰⁰ The presence of multiple peaks can complicate the acquisition of images using standard techniques, as can the short T_2 relaxation time constants that might be associated with each peak.⁴¹ Spectra with multiple peaks will lead to phase cancellation when imaging at non-zero echo times leading to complicated signal variation requiring careful optimization of pulse sequence parameters¹⁰¹ (also see Figure 1 in ref. 100). Refocusing of j -coupling modulation can also improve detection.¹⁰² A number of creative solutions have been proposed to optimize signal detection in ^{19}F -MRI,^{103,104}

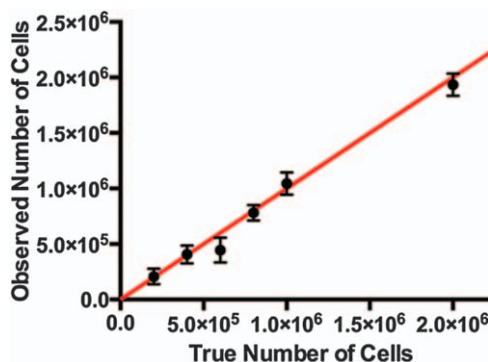


Figure 6.5 *In vitro* validation of ^{19}F -MRI quantification accuracy. Quantification was validated in a phantom study using cell pellets ranging from 2×10^5 to 2×10^6 mesenchymal stem cells. Pellets were imaged three times, with the error bars representing the standard deviation between scans. The ^{19}F -MRI quantification is in strong agreement with the true number of cells and has a Pearson correlation coefficient of 0.99. The red line represents the ideal result of a 1:1 correlation.

including the use of iterative decomposition of water and fat with echo asymmetry and least-squares estimation.¹⁰⁵ One of the most attractive methods to image ^{19}F is the application of ultra-short echo-time sequences that reduce phase modulation from multiple peaks and signal loss due to transverse relaxation.¹⁰⁶ For example, an ultra-short echo-time with a balanced steady state free precession sequence incorporating a three-dimensional radial readout was used for imaging of non-proton nuclei including ^{19}F .¹⁰⁰

Notes and References

1. M. Srinivas, P. A. Morel, L. A. Ernst, D. H. Laidlaw and E. T. Ahrens, *Magn. Reson. Med.*, 2007, **58**, 725.
2. M. Srinivas, M. S. Turner, J. M. Janjic, P. A. Morel, D. H. Laidlaw and E. T. Ahrens, *Magn. Reson. Med.*, 2009, **62**, 747.
3. E. T. Ahrens (inventor), Carnegie Mellon University (assignee), Cellular Labeling for Nuclear Magnetic Resonance Techniques, *U.S. Pat* 8,449,866 B2, May 28, 2013.
4. J. Zhong, K. Narsinh, P. A. Morel, H. Xu and E. T. Ahrens, *PLoS One*, 2015, **10**, e0140238.
5. A. Balducci, B. M. Helfer, E. T. Ahrens, C. F. O'Hanlon III and A. K. Wesa, *J. Inflammation*, 2012, **9**, 24.
6. U. Flögel, S. Su, I. Kreideweiß, Z. Ding, L. Galbarz, J. Fu, C. Jacoby, O. Witzke and J. Schrader, *Am. J. Transplant.*, 2011, **11**, 235.
7. B. Ebner, P. Behm, C. Jacoby, S. Burghoff, B. A. French, J. Schrader and U. Flögel, *Circ. Cardiovasc. Imaging*, 2010, **3**, 202.

8. S. Temme, C. Grapentin, C. Quast, C. Jacoby, M. Grandoch, Z. Ding, C. Owenier, F. Mayenfels, J. W. Fischer, R. Schubert, J. Schrader and U. Flögel, *Circulation*, 2015, **131**, 1405.
9. P. M. Winter, A. M. Neubauer, S. D. Caruthers, T. D. Harris, J. D. Robertson, T. A. Williams, A. H. Schmieder, G. Hu, J. S. Allen, E. K. Lacy, H. Zhang, S. A. Wickline and G. M. Lanza, *Arterioscler. Thromb. Vasc. Biol.*, 2006, **26**, 2103.
10. M. M. Kaneda, S. Caruthers, G. M. Lanza and S. A. Wickline, *Ann. Biomed. Eng.*, 2009, **37**, 1922.
11. G. M. Lanza, P. M. Winter, S. D. Caruthers, M. S. Hughes, G. Hu, D. Pan, A. H. Schmieder, C. Pham and S. A. Wickline, Perfluorocarbon Nanoparticles: A Theranostic Platform Technology, in *Nanopharmaceutics: The Potential Application of Nanomaterials*, ed. X.-J. Liang, World Scientific, Singapore, 2013, ch. 12, pp. 293–345.
12. J. Ruiz-Cabello, B. P. Barnett, P. A. Bottomley and J. W. M. Bulte, *NMR Biomed.*, 2011, **24**, 114.
13. C. Grapentin, F. Mayenfels, S. Barnert, R. Süß, R. Schubert, S. Temme, C. Jacoby, J. Schrader and U. Flögel, Optimization of Perfluorocarbon Nanoemulsions for Molecular Imaging by ^{19}F MRI, in *Nanomedicine* [Online], ed. A. Seifalian, A. de Mel and D. M. Kalaskar, One Central Press, 2014, ch. 10, pp. 268–286. <http://www.onecentralpress.com/optimization-of-perfluorocarbon-nanoemulsions-for-molecular-imaging-by-19f-mri/> (last accessed 2016).
14. A. H. Schmieder, S. D. Caruthers, J. Keupp, S. A. Wickline and G. M. Lanza, *Engineering*, 2015, **1**, 475.
15. G. Stoll, T. Basse-Lüsebrink, G. Weise and P. Jakob, *Wiley Interdiscip. Rev.: Nanomed. Nanobiotechnol.*, 2012, **4**, 438.
16. J. M. Janjic and E. T. Ahrens, *Wiley Interdiscip. Rev.: Nanomed. Nanobiotechnol.*, 2009, **1**, 492.
17. M. Srinivas, A. Heerschap, E. T. Ahrens, C. G. Figdor and I. J. M. de Vries, *Trends Biotechnol.*, 2010, **28**, 363.
18. J. G. Riess, *Artif. Cells, Blood Substitutes, Biotechnol.*, 2005, **33**, 47.
19. R. Díaz-López, N. Tsapis and E. Fattal, *Pharm. Res.*, 2010, **27**, 1.
20. M. J. Couch, I. K. Ball, T. Li, M. S. Fox, A. V. Ouriadov, B. Biman and M. S. Albert, *NMR Biomed.*, 2014, **27**, 1525.
21. M. P. Krafft and J. G. Riess, *J. Polym. Sci., Part A: Polym. Chem.*, 2007, **45**, 1185.
22. M. J. Patrick, J. M. Janjic, H. Teng, M. R. O'Hear, C. W. Brown, J. A. Stokum, B. F. Schmidt, E. T. Ahrens and A. S. Waggoner, *J. Am. Chem. Soc.*, 2013, **135**, 18445.
23. O. Castro, A. E. Nesbitt and D. Lyles, *Am. J. Hematol.*, 1984, **16**, 15.
24. M. P. Krafft, *Adv. Drug Delivery Rev.*, 2001, **47**, 209.
25. E. P. Wesseler, R. Iltis and L. C. Clark Jr., *J. Fluorine Chem.*, 1977, **9**, 137.
26. B. P. Fuhrman, *J. Pediatr.*, 1990, **117**, 73.
27. G. P. Biro, P. Blais and A. L. Rosen, *Crit. Rev. Oncol. Hematol.*, 1987, **6**, 311.

28. K. C. Lowe, *Blood Rev.*, 1999, **13**, 171.
29. K. C. Lowe, *Tissue Eng.*, 2003, **9**, 389.
30. A. V. Ratner, R. Hurd, H. H. Muller, B. Bradley-Simpson, W. Pitts, D. Shibata, C. Sotak and S. W. Young, *Magn. Reson. Med.*, 1987, **5**, 548.
31. S. Laukemper-Ostendorf, A. Scholz, K. Bürger, C. P. Heussel, M. Schmittner, N. Weiler, K. Markstaller, B. Eberle, H.-U. Kauczor, M. Quintel, M. Thelen and W. G. Schreiber, *Magn. Reson. Med.*, 2002, **47**, 82.
32. R. F. Mattrey, *AJR, Am. J. Roentgenol.*, 1989, **152**, 247.
33. K. C. Partlow, J. Chen, J. A. Brant, A. M. Neubauer, T. E. Meyerrose, M. H. Creer, J. A. Nolta, S. D. Caruthers, G. M. Lanza and S. A. Wickline, *FASEB J.*, 2007, **21**, 1647.
34. R. Schwarz, M. Schuurmans, J. Seelig and B. Künnecke, *Magn. Reson. Med.*, 1999, **41**, 80.
35. C. Jacoby, S. Temme, F. Mayenfels, N. Benoit, M. P. Krafft, R. Schubert, J. Schrader and U. Flögel, *NMR Biomed.*, 2014, **27**, 261.
36. D. Le, R. P. Mason, S. Hunjan, A. Constantinescu, B. R. Barker and P. P. Antich, *Magn. Reson. Imaging*, 1997, **15**, 971.
37. L. Mignon, J. Magat, O. Schakman, E. Marbaix, B. Gallez and B. F. Jordan, *Magn. Reson. Med.*, 2013, **69**, 248.
38. J. E. Fishman, P. M. Joseph, M. J. Carvlin, M. Saadi-Elmandjra, B. Mukherji and H. A. Sloviter, *Invest. Radiol.*, 1989, **24**, 65.
39. A. J. McGoron, R. Pratt, J. Zhang, Y. Shiferaw, S. Thomas and R. Millard, *Artif. Cells, Blood Substitutes, Biotechnol.*, 1994, **22**, 1243.
40. S. R. Thomas, R. G. Pratt, R. W. Millard, R. C. Samaratunga, Y. Shiferaw, A. J. McGoron and K. K. Tan, *Magn. Reson. Imaging*, 1996, **14**, 103.
41. C. H. Sotak, P. S. Hees, H.-N. Huang, M.-H. Hung, C. G. Krespan and S. Reynolds, *Magn. Reson. Med.*, 1993, **29**, 188.
42. Z.-X. Jiang and Y. B. Yu, *Tetrahedron*, 2007, **63**, 3982.
43. E. T. Ahrens, R. Flores, H. Xu and P. A. Morel, *Nat. Biotechnol.*, 2005, **23**, 983.
44. T. Q. Duong, C. Iadecola and S.-G. Kim, *Magn. Reson. Med.*, 2001, **45**, 61.
45. J. A. McNab, A. C. Yung and P. Kozlowski, *Magn. Reson. Mater. Phys., Biol. Med.*, 2004, **17**, 288.
46. D. K. K. Kadayakkara, J. M. Janjic, L. K. Pusateri, W.-B. Young and E. T. Ahrens, *Magn. Reson. Med.*, 2010, **64**, 1252.
47. J. Zhong, M. Sakaki, H. Okada and E. T. Ahrens, *PLoS One*, 2013, **8**, e59479.
48. A. M. Morawski, P. M. Winter, X. Yu, R. W. Fuhrhop, M. J. Scott, F. Hockett, J. D. Robertson, P. J. Gaffney, G. M. Lanza and S. A. Wickline, *Magn. Reson. Med.*, 2004, **52**, 1255.
49. J. M. Janjic, M. Srinivas, D. K. K. Kadayakkara and E. T. Ahrens, *J. Am. Chem. Soc.*, 2008, **130**, 2832.
50. E. T. Ahrens, B. M. Helfer, C. F. O'Hanlon and C. Schirda, *Magn. Reson. Med.*, 2014, **72**, 1696.

51. A. Studer, S. Hadida, R. Ferritto, S.-Y. Kim, P. Jeger, P. Wipf and D. P. Curran, *Science*, 1997, **275**, 823.
52. C.-A. Peng and F. Huang, *J. Dispersion Sci. Technol.*, 2008, **29**, 46.
53. A. A. Kislukhin, H. Xu, S. R. Adams, K. H. Narsinh, R. Y. Tsien and E. T. Ahrens, *Nat. Mat.*, 2016, **15**, 662.
54. A. Balducci, Y. Wen, Y. Zhang, B. M. Helfer, T. K. Hitchens, W. S. Meng, A. K. Wesa and J. M. Janjic, *OncoImmunology*, 2013, **2**, e23034.
55. B. P. Barnett, J. Ruiz-Cabello, P. Hota, R. Ouwerkerk, M. J. Shablott, C. Lauzon, P. Walczak, W. D. Gilson, V. P. Chacko, D. L. Kraitchman, A. Arepally and J. W. M. Bulte, *Contrast Media Mol. Imaging*, 2011, **6**, 251.
56. G. M. Lanza, X. Yu, P. M. Winter, D. R. Abendschein, K. K. Karukstis, M. J. Scott, L. K. Chinen, R. W. Fuhrhop, D. E. Scherrer and S. A. Wickline, *Circulation*, 2002, **106**, 2842.
57. S. K. Patel, W. Beaino, C. J. Anderson and J. M. Janjic, *Clin. Immunol.*, 2015, **160**, 59.
58. J. G. Riess, *Chem. Rev.*, 2001, **101**, 2797.
59. S. Mahdi Jafari, Y. He and B. Bhandari, *Int. J. Food Prop.*, 2006, **9**, 475.
60. M. G. Freire, A. M. A. Dias, M. A. Z. Coelho, J. A. P. Coutinho and I. M. Marrucho, *J. Colloid Interface Sci.*, 2005, **286**, 224.
61. A. S. Kabalnov and E. D. Shchukin, *Adv. Colloid Interface Sci.*, 1992, **38**, 69.
62. Y.-F. Maa and C. C. Hsu, *Pharm. Dev. Technol.*, 1999, **4**, 233.
63. M.-P. Krafft, M. Postel, J. G. Riess, Y. Ni, T. J. Pelura, G. K. Hanna and D. Song, *Biomater., Artif. Cells, Immobilization Biotechnol.*, 1992, **20**, 865.
64. M. Postel, J. G. Riess and J. G. Weers, *Artif. Cells, Blood Substitutes, Biotechnol.*, 1994, **22**, 991.
65. C. Varescon, C. Arlen, M. LeBlanc and J. G. Riess, *J. Chim. Phys. Phys.-Chim. Biol.*, 1989, **86**, 2111.
66. T. Tadros, P. Izquierdo, J. Esquena and C. Solans, *Adv. Colloid Interface Sci.*, 2004, **108-109**, 303.
67. S. Stolnik, L. Illum and S. S. Davis, *Adv. Drug Delivery Rev.*, 1995, **16**, 195.
68. C. M. Sharts, H. R. Reese, K. A. Ginsberg, F. K. Multer, M. D. Nielson, A. G. Greenburg, G. W. Peskin and D. M. Long, *J. Fluorine Chem.*, 1978, **11**, 637.
69. C. I. Castro and J. C. Briceno, *Artif. Organs*, 2010, **34**, 622.
70. P. K. Bentley, S. S. Davis, O. L. Johnson, K. C. Lowe and C. Washington, *J. Pharm. Pharmacol.*, 1989, **41**, 661.
71. L. C. Clark Jr., S. Kaplan and F. Becattini, *J. Thorac. Cardiovasc. Surg.*, 1970, **60**, 757.
72. T. A. Lane and V. Krukonis, *Transfusion*, 1988, **28**, 375.
73. J. S. Jahr, V. Walker and K. Manoochehri, *Curr. Opin. Anaesthesiol.*, 2007, **20**, 325.
74. O. L. Johnson, C. Washington and S. S. Davis, *Int. J. Pharm.*, 1990, **59**, 131.
75. O. L. Johnson, C. Washington and S. S. Davis, *Int. J. Pharm.*, 1990, **63**, 65.

76. M. Rotenberg, M. Rubin, A. Bor, D. Meyuhas, Y. Talmon and D. Lichtenberg, *Biochim. Biophys. Acta, Lipids Lipid Metab.*, 1991, **1086**, 265.
77. K. Westesen and T. Wehler, *Colloids Surf., A*, 1993, **78**, 115.
78. *Phospholipids: Characterization, Metabolism, and Novel Biological Applications: Proceedings of the 6th International Colloquium*, ed. G. Cevc and F. Paltauf, AOCS Press, Champaign, IL, 1995.
79. T. K. Putyatina, U. D. Aprosin and N. I. Afonin, *Artif. Cells, Blood Substitutes, Biotechnol.*, 1994, **22**, 1281.
80. B. Mukherji and H. A. Slovirer, *Transfusion*, 1991, **31**, 324.
81. D. C. Long, D. M. Long, J. Riess, R. Follana, A. Burgan and R. F. Mattrey, *Biomater. Artif. Cells, Artif. Organs*, 1988, **16**, 441.
82. J. G. Riess, J. L. Dalfors, G. K. Hanna, D. H. Klein, M.-P. Krafft, T. J. Pelura and E. G. Schutt, *Biomater., Artif. Cells, Immobilization Biotechnol.*, 1992, **20**, 839.
83. J. G. Weers, J. Liu, T. Fields, P. Resch, J. Cavin and R. A. Arlauskas, *Artif. Cells, Blood Substitutes, Biotechnol.*, 1994, **22**, 1175.
84. T. E. Tarara, S. H. Malinoff and T. J. Pelura, *Artif. Cells, Blood Substitutes, Biotechnol.*, 1994, **22**, 1287.
85. C. M. Edwards, K. C. Lowe, H. Trabelsi, P. Lucas and A. Cambon, *Artif. Cells, Blood Substitutes, Biotechnol.*, 1997, **25**, 327.
86. M. Gangoda, B. M. Fung and E. A. O'Rear, *J. Colloid Interface Sci.*, 1987, **116**, 230.
87. C. M. Sharts, A. A. Malik, J. C. Easdon, L. A. Khawli, D. M. Long, D. F. Shellhamer, V. L. Burton, M. K. Porter and L. F. Sprague, *J. Fluorine Chem.*, 1987, **34**, 365.
88. M. P. Krafft, J. G. Riess and J. G. Weers, The Design and Engineering of Oxygen-Delivering Fluorocarbon Emulsions, in *Submicron Emulsions in Drug Targeting and Delivery*, ed. S. Benita, Drug Targeting and Delivery Series, Harwood Academic, Amsterdam, 1998, ch. 10, pp. 235–333.
89. S. M. Bertilla, J.-L. Thomas, P. Marie and M. P. Krafft, *Langmuir*, 2004, **20**, 3920.
90. J. G. Riess, C. Cornelus, R. Follana, M. P. Krafft, A. M. Mahé, M. Postel and L. Zarif, Novel Fluorocarbon-Based Injectable Oxygen-Carrying Formulations with Long-Term Room-Temperature Storage Stability, in *Oxygen Transport to Tissue XV*, ed. P. Vaupel, R. Zander and D. F. Bruley, Advances in Experimental Medicine and Biology Series 345, Springer, New York, 1994, pp. 227–234.
91. M.-P. Krafft, J.-P. Rolland and J. G. Riess, *J. Phys. Chem.*, 1991, **95**, 5673.
92. S. K. Patel, J. Williams and J. M. Janjic, *Biosensors*, 2013, **3**, 341.
93. J. M. Janjic and S. K. Patel, Perfluorocarbon Theranostic Nanomedicines: Pharmaceutical Scientist's Perspective, in *Fluorine Magnetic Resonance Imaging*, ed. U. Flögel and E. Ahrens, Pan Stanford, Singapore, 2016, ch. 14, pp. 407–432.
94. U. Flögel, Z. Ding, H. Hardung, S. Jander, G. Reichmann, C. Jacoby, R. Schubert and J. Schrader, *Circulation*, 2008, **118**, 140.

95. P. Boehm-Sturm, L. Mengler, S. Wecker, M. Hoehn and T. Kallur, *PLoS One*, 2011, **6**, e29040.
96. T. K. Hitchens, Q. Ye, D. F. Eytan, J. M. Janjic, E. T. Ahrens and C. Ho, *Magn. Reson. Med.*, 2011, **65**, 1145.
97. E. J. Ribot, J. M. Gaudet, Y. Chen, K. M. Gilbert and P. J. Foster, *Int. J. Nanomed.*, 2014, **9**, 1731.
98. J. M. Gaudet, E. J. Ribot, Y. Chen, K. M. Gilbert and P. J. Foster, *PLoS One*, 2015, **10**, e0118544.
99. T. K. Hitchens, L. Liu, L. M. Foley, V. Simplaceanu, E. T. Ahrens and C. Ho, *Magn. Reson. Med.*, 2015, **73**, 367.
100. M. J. Goette, J. Keupp, J. Rahmer, G. M. Lanza, S. A. Wickline and S. D. Caruthers, *Magn. Reson. Med.*, 2015, **74**, 537.
101. A. Mastropietro, E. De Bernardi, G. L. Breschi, I. Zucca, M. Cametti, C. D. Soffientini, M. de Curtis, G. Terraneo, P. Metrangolo, R. Spreafico, G. Resnati and G. Baselli, *J. Magn. Reson. Imaging*, 2014, **40**, 162.
102. C. Giraudeau, J. Flament, B. Marty, F. Boumezbeur, S. Mériaux, C. Robic, M. Port, N. Tsapis, E. Fattal, E. Giacomini, F. Lethimonnier, D. Le Bihan and J. Valette, *Magn. Reson. Med.*, 2010, **63**, 1119.
103. F. Schmid, C. Höltnke, D. Parker and C. Faber, *Magn. Reson. Med.*, 2013, **69**, 1056.
104. H. K. Lee, O. Nalcioglu and R. B. Buxton, *Magn. Reson. Med.*, 1992, **23**, 254.
105. S. B. Reeder, Z. Wen, H. Yu, A. R. Pineda, G. E. Gold, M. Markl and N. J. Pelc, *Magn. Reson. Med.*, 2004, **51**, 35.
106. J. Rahmer, P. Börnert, J. Groen and C. Bos, *Magn. Reson. Med.*, 2006, **55**, 1075.

CHAPTER 7

Standard Biological and in vivo Methods

TANG TANG,^a ANGELIQUE Y. LOUIE,^{*a,b} ERIC M. GALE,^{*c}
PETER CARAVAN,^{*c} CHRISTIAN T. FARRAR^{*c} AND BORIS KEIL^c

^a Chemistry Graduate Group, University of California, Davis, CA 95616, USA; ^b Department of Biomedical Engineering, University of California, Davis, CA 95616, USA; ^c A. A. Martinos Center for Biomedical Imaging, Institute for Innovation in Imaging, Massachusetts General Hospital, Harvard Medical School, Charlestown, MA 02129, USA

*Email: aylouie@ucdavis.edu; pcaravan@partners.org; cfarrar@nmr.mgh.harvard.edu; egale@nmr.mgh.harvard.edu

7.1 Cell Toxicity, Binding, and Uptake

TANG TANG AND ANGELIQUE Y. LOUIE*

7.1.1 Introduction and Biological Characterization of Molecular Imaging Agents

MRI contrast agent development requires knowledge of organic and inorganic chemistry to produce probes of high signal generating capability. However, the chemistry alone is insufficient to create the most effective agents, and many promising candidates show properties in the test tube that never translate to *in vivo* applications. The effective development of contrast agents requires study and keen understanding of their effects on biological targets, including targeted cells or biomarkers, and bystander cells, such

as in clearance pathways. It is important to obtain detailed *in vitro* profiles of these contrast agents for optimization of biotolerance and image enhancement capabilities before further investigation *in vivo*. In this subchapter, a number of *in vitro* assessments of MRI contrast agent behavior for: (i) cytotoxicity; (ii) cell binding; and (iii) cell uptake will be discussed.

The design of molecular imaging agents requires an in-depth knowledge of the biological effect of the agents. For agents to be viable for future clinical use they ideally should be nontoxic and interact specifically with intended targets. Thus, common biological assays used for investigating imaging agents include toxicity studies and assays to characterize binding of imaging agents to, and uptake by, the intended targets. Binding studies can be performed on purified and isolated targets, using methods such as immobilization to membranes or phage display. However, the process of isolating biological targets can be nontrivial, especially if they are not commercially available. Moreover, purification and immobilization of the biological target can perturb its structure and affect its recognition, particularly in the case of transmembrane receptors. Thus, when possible, characterization studies are performed directly on intact cells expressing the targets. As an ethical consideration, lack of toxicity to cultured cells should be considered before proceeding to animal models.

What type of cells should be used for assays? Cell lines or primary cells selected for cytotoxicity studies should be reflective of the tissue type of interest in the imaging application. For example, for nanoparticle imaging agents, because these often are cleared through the liver, the retention of particles in the liver may give rise to concern about liver toxicity. Thus, selecting hepatocytes and other resident liver cells may be recommended to assess nanoparticle toxicity. Macrophages are involved in clearance of large particles, thus toxicity assessment of larger particles (*e.g.* >100 nm) might include studies of macrophages. Similarly, applications in the brain may consider assessing toxicity on glial cells, neurons, and microglia. For uptake and binding studies, care should be taken to select cell types that express the desired target at sufficient levels to be detected, and which recapitulate, as much as possible, the *in vivo* condition. For this reason, researchers sometimes prefer to work with primary culture cells, which are cells isolated from freshly harvested tissue, as opposed to immortal cell lines, which are cells that were harvested from tissue in the past and grown continuously in culture since then. Not all cells can be successfully grown in culture. If the desired cell type is not available, researchers must select the next closest representative, such as using a mouse cell if the human version is not available.

This chapter assumes a working knowledge of cell culture techniques. For the interested reader without this background there are many books, articles and videos available to aid in gaining familiarity with the topic.¹⁻⁴ The assays are presented with methods for adherent cells, but methods can be modified for cells in suspension by addition of centrifugation steps.

7.1.2 Cytotoxicity

7.1.2.1 Introduction to Cell Death and Assays for Cytotoxicity

Perhaps the most important assessment of any potential *in vivo* contrast agent is its lack of toxicity to tissues. *In vitro* assessment of potential toxicants is performed through cytotoxicity assays. Cytotoxicity is the quality of being toxic to cells. Cells that are treated with cytotoxic compounds may be perturbed to express markers of cell stress, stop proliferating, or, in the most extreme case, die. There are two major classes of toxicity assays: those that measure cell death and those that measure cell proliferation. This can be achieved by either counting the population of dead cells (*e.g.* trypan blue staining) or the population of viable cells [cell viability assays, such as adenosine triphosphate (ATP) assays] after treatment with a tested compound. Cell death assays, including both apoptotic and necrotic mechanisms of cell death, are widely used to assess cytotoxicity. Apoptosis is a controlled process of programmed cell death and an essential part of normal human development that continues into adulthood.⁵⁻⁷ It produces cell fragments that phagocytic cells are able to engulf and remove to avoid the contents of the cell spilling onto surrounding cells and causing damage. Apoptosis can be initiated by intrinsic (self-signaling) or extrinsic (signals from other cells) pathways and cannot be stopped once initiated.⁵ The apoptotic cell does not affect surrounding tissues, and this pathway is a nonpathogenic “pruning” mechanism for development of biological structures. On the contrary, necrosis is a form of traumatic cell death where the cell dies rapidly as a result of cell lysis, and is detrimental to surrounding tissues.⁸ Cells undergoing necrosis typically exhibit rapid swelling, lose membrane integrity, shut down metabolism, and release their contents into the environment.

In this chapter, the focus is primarily on assays for cell death that do not distinguish the mechanism of fatality. There are specific methods that distinguish apoptosis from necrosis, such as the Comet assay or TUNEL (terminal deoxynucleotidyl transferase dUTP nick end labeling) assays. The Comet assay is a sensitive technique that uses single cell gel electrophoresis to detect DNA strand breaks in eukaryotic cells.^{9,10} Cells are embedded in agarose suspension on a microscope slide and lysed in neutral or basic conditions. Electrophoresis of the lysed cells generates a pattern of DNA migration that resembles a comet due to the free extension of broken loops towards the anode. Further DNA staining offers visualization of the comet structure by fluorescence microscopy and the intensity of the comet tail relative to the head reflects the number of DNA breaks. On the other hand, the TUNEL assay detects DNA fragmentation from apoptotic signaling cascades by labeling the end of nicks, which are discontinuities in a double-stranded DNA molecule.^{11,12} Nicks can be identified with the use of terminal deoxynucleotidyl transferase, which catalyzes the addition of modified dUTPs (2'-deoxyuridine 5'-triphosphate) at the 3'-OH ends of fragmented

Table 7.1 Methods for apoptosis detection.

Category	Method
Caspase activation	Substrate cleavage or caspase processing ^{14,15}
DNA fragmentation	TUNEL (terminal dUTP nick end-labeling) ^{11,12,16} Comet assay ^{9,10}
Membrane alternation	Exposure of the phosphatidylserine to the outer cell membrane by Annexin-V binding ¹⁷
Mitochondrial damage	Cytochrome c release ¹⁸

DNA. dUTP modification can be detected either by direct fluorescent labeling (*e.g.* fluorescein-dUTP) or indirect labeling with streptavidin or antibodies. The most common methods to detect apoptosis are summarized in Table 7.1. Because these topics will not be covered in detail in this chapter, readers are referred to reviews of apoptosis.^{5,13}

In general, cytotoxicity can be measured by: (1) *in vitro* assays performed in multi-well plates where data are acquired using a plate reader or flow cytometer; (2) microscopic analysis of intracellular localization (electron microscopy and atomic force microscopy); and (3) gene expression analysis or genotoxicity. Here, widely accepted *in vitro* assays to measure cell death or cell proliferation will be reported, including: (a) membrane integrity assays, such as trypan blue exclusion or lactate dehydrogenase (LDH) leakage assays; (b) mitochondria and metabolic activity assays, *e.g.* tetrazolium reduction and ATP detection; and (c) proliferation assays, such as bromodeoxyuridine (BrdU) staining. Methods for high content microscopy imaging and gene expression analysis are beyond the scope of this chapter, and interested readers can refer to other literature.^{19,20} There are also many other assays that report on perturbations to normal cell function, such as oxidative stress and lipid peroxidation caused by reactive oxygen species (ROS); these methods are not provided here, but are discussed briefly at the end of Section 7.1.

7.1.2.1.1 Membrane Integrity Assays. Live cells have intact membranes that are selective with respect to which molecules can pass through the membrane. Damaged or dead cells with compromised membranes, however, cannot strictly control the traverse of molecules that should be excluded. This feature makes membrane integrity an excellent means to assess cell viability. Trypan blue is one of the most widely used and easiest methods to assess viability. It simply stains dead cells that are unable to stop the dye from traversing the compromised membrane.²¹ Similarly, propidium iodide (PI) and 7-aminoactinomycin D (7-AAD) are membrane impermeable and are generally excluded from viable cells. However, when a cell membrane is damaged, these fluorescent dyes freely cross the membrane and bind to nucleic acids, thus staining DNA in dead cells.^{22,23} There are now commercial LIVE/DEAD viability kits (*e.g.* LIVE/DEAD[®] Viability/Cytotoxicity Kit, Thermo Fisher Scientific) that use two different

dyes to stain live and dead cells, respectively. Alternatively, membrane integrity can also be evaluated by measuring the leakage of substances that are normally confined inside cells. Lactate dehydrogenase (LDH) is an enzyme that is found in nearly all living cells. A measurement of LDH leakage into the cell culture medium is a commonly used cytotoxicity assay.²⁴

7.1.2.1.2 Metabolic Activity Assays. Cells that are damaged lose the ability to maintain and provide energy for their metabolism and growth.¹³ Thus, measurement of metabolic activities that take place in mitochondria can reflect cell viability and can be an early sign of perturbation to the cell. 3-(4,5-Dimethylthiazol-2-yl)-2,5-diphenyltetrazolium bromide (MTT) and resazurin (also known as Alamar Blue) are molecules that can be reduced by oxidoreductase enzymes in the mitochondria and can thus provide information on metabolic level in colorimetric assays by indicating the redox potential of cells.^{25,26} ATP concentration can also be used as a marker of viability. For example, bioluminescent-based ATP assays such as the luciferase reaction can determine metabolic activity levels.²⁷

7.1.2.1.3 Cell Proliferation Assays. Cell proliferation can also be used to evaluate toxicity of compounds. Since DNA needs to be replicated before cell division, measurement of DNA synthesis is an effective way to assess cell proliferation. Bromodeoxyuridine (BrdU) is a dye that is used to monitor DNA replication and can thus indicate the ability of cells to synthesize DNA.²⁸ Detection of specific antigens present on proliferating cells allows quantification of cell growth as well. Examples of such antigens include the KI-67 antigen, proliferating cell nuclear antigen, and phosphohistone H3.²⁹⁻³¹ Non-endpoint metabolic activity assays, assays in which the measurement does not destroy the sample, can be used for continuous monitoring of cell proliferation as needed to follow dynamic changes in proliferation over time. Because there is a linear relationship between cell number and ATP concentration, ATP concentration determination, mentioned earlier in this chapter, also provides a sensitive readout for cell proliferation.³²

Contrast agents can affect cell morphology, membrane integrity, metabolic activity, proliferation, oxidative stress, and inflammatory reactions upon interaction with cell components, such as lipid membranes, proteins, and DNA. As mentioned previously, MTT (or other tetrazolium dyes) assays are the most commonly used method to evaluate the cytotoxicity of contrast agents with reduced metabolic activities. Unfortunately, due to the addition of dimethyl sulfoxide (DMSO), isopropanol or other solvents to dissolve formazan, this assay is considered to be an endpoint assay where the cells cannot be used for further monitoring. When compared to trypan blue staining, endpoint assays that measure cellular enzyme activity overestimate cell viability due to the frequent interaction between the enzymes and contrast agents.¹⁹ Contrast agents might also interfere with the assay readout by interacting with assay components.³³ For example, contrast

Table 7.2 Comparison of common cytotoxicity assays.

Category	Assay	Principles	Results	How to measure	Advantages	Limitations	
Membrane integrity	Trypan blue staining	Dyes can penetrate into cells with compromised membrane	Dead cells are stained blue	Count blue stained cells under microscopy or by automatic cell counter	Widely used, simple, inexpensive	Needs to be completed within 3–5 min	Underestimates the damage of intracellular cytotoxic compounds
	LDH leakage	Enzyme leaks into cell culture medium with compromised membrane	Presence of LDH in the medium from dead/damaged cells	Evaluate the amount of LDH with molecules that can be catalyzed by LDH to emit fluorescence	Widely used	Limited sensitivity (high background interference from FBS in culture medium)	
Metabolic activity	Tetrazolium salts (MTT, MTS, XTT, WST-1)	Dead and damaged cells have low levels of metabolism, thus have low concentrations of oxidoreductase or ATP	Low concentration of cellular oxidoreductase in mitochondria	Quantify the conversion of tetrazolium to formazan (absorbance at ~ 570 nm) in mitochondria	Widely used, inexpensive	Absorption methods have limited sensitivity; Sensitive to light and pH; MTT needs addition of solubilization solutions and is toxic (an endpoint assay)	Reflects cell metabolism but does not directly measure cell number (the reduction rate can change with culture conditions); cannot evaluate certain reducing agents

Cell proliferation	Resazurin			Measure the conversion of resazurin to resorufin (fluorescence at ~ 587 nm)	Inexpensive, sensitive	Fluorescence interference
	ATP		Low ATP concentration	Measure ATP concentration by luciferase reaction	Sensitive, fast, no fluorescence interference	Lytic protocol dictates sequence for multiplexing
	BrdU	Damaged cells have limited proliferation, thus have reduced DNA synthesis and concentration of ATP	BrdU is incorporated into newly synthesized DNA	Use BrdU specific antibody to assess DNA replication	Widely used, sensitive	Requires specific antibody and more steps, endpoint assay due to denature of the DNA for binding
	ATP		ATP concentration decreases with time	Measure ATP concentration by luciferase reaction and monitor over time	Sensitive, fast, no fluorescence interference	Lytic protocol dictates sequence for multiplexing

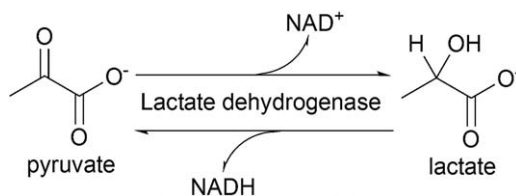
agents that bind LDH and impede its release into the extracellular medium. Combining assays from different categories—such as LDH-XTT-SRB (sulforhodamine B) that measures membrane integrity, metabolic activity, and protein content—can minimize false positive or false negative results from any one single assay. This is referred to as multiplexing, where multiple distinct signals from the same sample are obtained. Importantly, this approach requires compatibility of the different reagents used. Studying diverse cellular markers is a more rigorous approach to achieve a thorough understanding of cytotoxicity caused by contrast agents. Although short term *in vitro* results might not be a direct prognostic indicator of long-term *in vivo* physiological effects, the knowledge of cytotoxicity assists in assessment of the potential risks of materials *in vivo*.

In this subchapter, detailed methods are provided for widely applied assays for cytotoxicity, including the lactate dehydrogenase leakage (LDH) assay, the MTT and resazurin reduction assay, the ATP assay, and the bromodeoxyuridine (BrdU) assay. A summary of these methods is presented in Table 7.2. To choose the most appropriate assay for a contrast agent, readers need to decide first what they want to measure: whether it is the number of living cells, dead cells, apoptotic cells, or biomarkers for cell stress or perturbation. Understanding of the assay mechanism, as well as its limitations, compatibility, and potential artifacts is needed to correctly predict and interpret assay results.

7.1.2.2 Lactate Dehydrogenase (LDH) Assay for Membrane Integrity

Membrane integrity can be evaluated *via* dye exclusion or measurement of lactate dehydrogenase leakage. The concepts of LDH leakage and dye exclusion are similar. However, unlike for the trypan blue exclusion assay, the exact mechanism and molecular cut-off points for each molecule to pass the cell membrane are unknown with LDH leakage results, where the cytotoxic effect is concentration-independent.¹⁹ On the other hand, fluorescence-based protocols are more convenient, in general, than the trypan blue-based exclusion assay because they can be measured at longer time points after incubation with the fluorescent dye. The trypan blue assay must be ideally completed within 3–5 minutes because the number of blue-staining cells increases with time after addition of the dye.²²

Lactate dehydrogenase catalyzes the interconversion of pyruvate and lactate with concomitant interconversion of reduced nicotinamide adenine dinucleotide (NADH) and oxidized nicotinamide adenine dinucleotide (NAD⁺) (Scheme 7.1). Colorimetric or fluorescent assay reagents quantify the amount of LDH released into cell culture media through damaged membranes. These reagents either measure the absorbance of extracellular NADH produced or consumed directly by the reaction catalyzed by LDH (Scheme 7.1), or use reagents that react with NADH and are reduced to fluorescent products (*e.g.* resorufin or formazan).^{19,24} The amount of absorbance or fluorescence



Scheme 7.1 Reaction catalyzed by LDH.

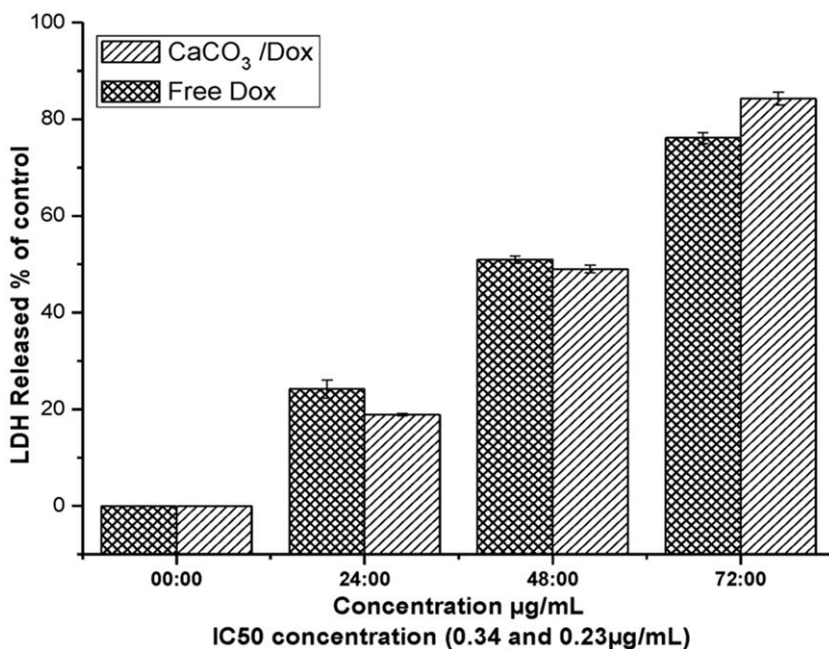


Figure 7.1 Example of LDH leakage assay to evaluate free doxorubicin (Dox) and Dox encapsulated in calcium carbonate on osteosarcoma bone cancer cell (MG 63).

Adapted with permission from ref. 34.

generated is proportional to LDH leakage and reflects the time-dependent membrane disruption caused by introduction of contrast agents and is a measure of the severity of membrane damage.

A typical example of an LDH leakage assay of free doxorubicin (Dox) and Dox encapsulated in calcium carbonate on osteosarcoma bone cancer cell (MG 63) is shown in Figure 7.1.³⁴ Positive control cells were lysed by lysis buffer and assumed to have 100% release of LDH. Release of LDH from cells incubated with free Dox or CaCO₃/Dox nanocrystals increased over time and was normalized against the positive control cells.

One limitation of membrane permeability assays is that they tend to underestimate the damage due to intracellular cytotoxic compounds. Cells

may be damaged and committed to die despite the plasma membrane being intact.

7.1.2.2.1 LDH Assay Protocol. Adapted from ref. 19 and 35. The type of cell used for a specific study is generally determined based on imaging purposes. For example, liver cells might be of particular interest for nanomaterial development because most nanoparticles eventually accumulate in the liver. The methods described in this section are designed for hepatocytes, but could be modified for any adherent cell type of interest. Readers can also adapt the assay for non-adherent cell lines. As for every assay described in this sub-chapter, all experiments should be performed in replicates so as to provide statistical significance. Culture cells in complete culture medium at 37 °C in a humidified 5% CO₂ atmosphere. Complete culture medium normally consists of culture medium, 10% fetal bovine serum, other supplements needed for specific cell lines, and sometimes antibiotics such as penicillin and streptomycin.

1. Seed cells into a 96-well plate (10^4 cells per well) in 100 μL of complete culture medium and incubate for 24 h at 37 °C in a humidified 5% CO₂ atmosphere.
2. Dissolve contrast agent in complete culture medium and prepare different concentrations samples ($5\text{--}100\ \mu\text{g mL}^{-1}$). Medium containing phenol red is compatible with the assay, unless mentioned in a specific commercial LDH kit. Pre-warm the medium at 37 °C.
3. Replace culture medium in the 96-well plate with the pre-warmed medium containing increasing concentrations of contrast agent from step 2.
4. Incubate cells for range of time points, *e.g.* 4, 24, and 48 h at 37 °C in humidified 5% CO₂.
5. Lyse cells using 10 μL of lysis buffers [*e.g.* HEPES (4-(2-hydroxyethyl)-1-piperazineethanesulfonic acid]-NaOH buffer, 1% Triton X-100) in the positive control wells, and let the plate sit for about 45 min to 1 h.
6. Centrifuge the plate at $250\times g$ for 3 min at 37 °C and place the supernatant (50 μL) into a new plate.
7. Add 20 μL of lactate solution ($36\ \text{mg mL}^{-1}$ of 10 mM Tris [Tris(hydroxymethyl)aminomethane] buffer, pH 8.5) to the supernatant, followed by 20 μL of 2-(4-iodophenyl)-3-(4-nitrophenyl)-5-phenyl-2*H*-tetrazolium (INT) solution [$2\ \text{mg mL}^{-1}$ of PBS (phosphate-buffered saline) prepared from a ten-fold concentrated stock solution in DMSO], and 20 μL of a mixture solution of NAD⁺ ($3\ \text{mg mL}^{-1}$), diaphorase ($13.5\ \text{U mL}^{-1}$), BSA (0.03%, w/v), and sucrose (1.2%, w/v) in PBS.
8. Allow the reactions to sit for 20–30 min at room temperature protected from light. LDH catalyzes the conversion of lactate to pyruvate *via* NAD⁺ reduction to NADH. Diaphorase then uses NADH to reduce INT to a red formazan product.

9. Add 20 μL of the LDH inhibitor oxamate solution (16.6 mg mL^{-1} of PBS) to the wells to terminate the reactions.
10. Measure the absorbance of the samples at 490 nm on a microplate reader.
11. Calculate the percentage of cytotoxicity in respect to the positive control wells whereby the lysed cells were assumed to have 100% LDH release. Percentage cytotoxicity = (fluorescence intensity of samples/ fluorescent intensity of positive control) \times 100.

7.1.2.3 Metabolic Activity Assays

MTT has been the most commonly used molecular probe in colorimetric assays for cell viability due to its simplicity and speed. It was first developed in the 1980s by Mosmann.³⁶ It is a yellow tetrazolium salt that is reduced to purple formazan after incubation for 1 to 4 h in the mitochondria of viable cells with active metabolism. Dead cells, however, lose the ability to convert tetrazolium to formazan. Due to the insolubility of formazan, a solubilization solution (such as dimethyl sulfoxide, acidified ethanol solution, or sodium dodecyl sulfate in diluted hydrochloric acid) is normally added to facilitate spectroscopic detection. Acidification of culture media to change the color of phenol red in the culture media to yellow minimizes interference with absorbance readings. The absorbance at 570 nm of the colored solution of dissolved formazan can be measured using a spectrophotometer. The cytotoxic nature of MTT makes this an endpoint assay, which limits its use in multiplexing.

An example of an MTT assay is shown in Figure 7.2.³⁷ Three types of superparamagnetic iron oxide nanoparticles (SPIONs) at different concentrations were assessed on various cell types and demonstrated distinct toxic effects. The absorbance of formazan from cells incubated with the blank ([SPIONs] = 0 mM) was set as 100% viability. The absorbance from other samples was then normalized against the blank. This MTT assay shows how the cytotoxic effect of SPIONs can be concentration-dependent. If needed, readers can also monitor cytotoxicity of a contrast agent over time.

There are several factors that can affect MTT assays, including whether cells are in the exponential phase of growth or if the pH of the medium is neutral. A pH < 5 will not enable the creation of formazan,³⁸ but higher pH values or long exposures to light might increase background absorbance. Thus, MTT assays are usually performed in the dark and at a neutral pH. It is also important to use consistent cell conditions (same cell cycle phases) when comparing MTT assay results.

Other tetrazolium dyes to study cell viability, including XTT (2,3-bis-(2-methoxy-4-nitro-5-sulfophenyl)-2H-tetrazolium-5-carboxanilide), MTS (3-(4,5-dimethylthiazol-2-yl)-5-(3-carboxymethoxyphenyl)-2-(4-sulfophenyl)-2H-tetrazolium), and WSTs (water-soluble tetrazolium salts, such as Cell Counting Kit-8 from Sigma Aldrich[®]), have been proposed as alternatives to MTT (Scheme 7.2).²⁵ One important difference among these dyes is their charge. MTT is positively

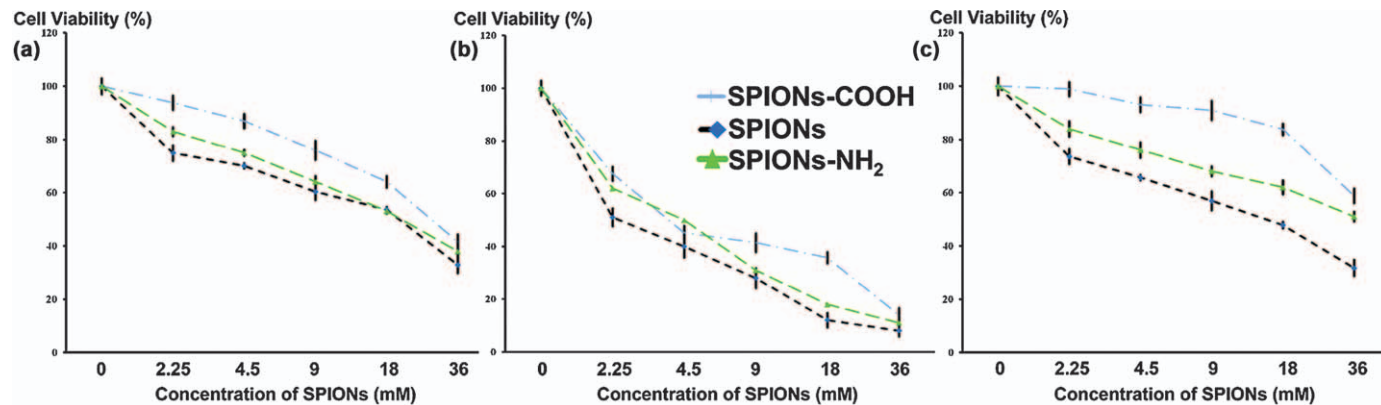
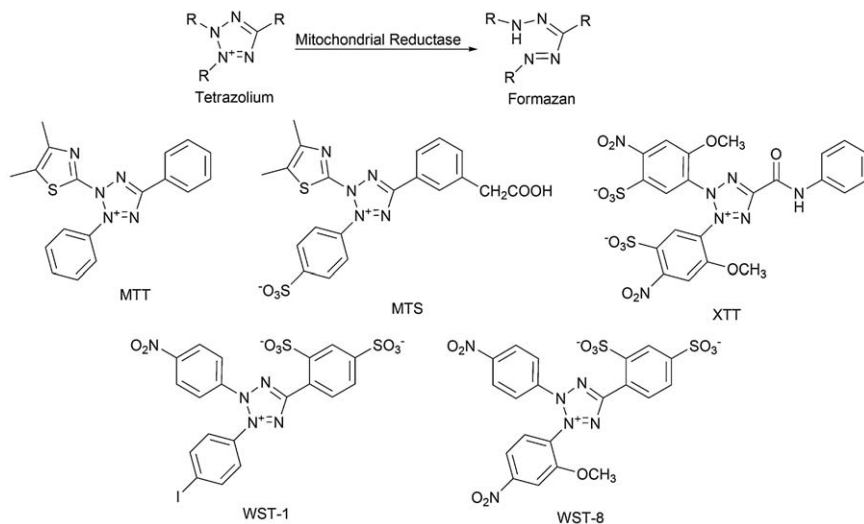


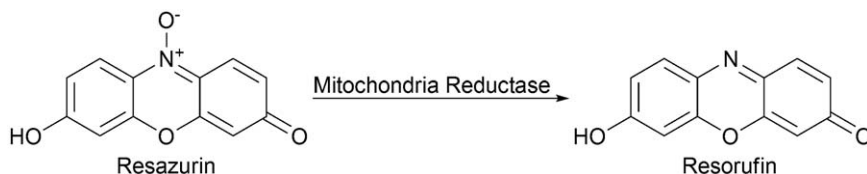
Figure 7.2 An example of MTT assay to evaluate (a) SPIONs-COOH, (b) SPIONs, and (c) SPIONs-NH₂ samples on human cardiac myocytes (HCM), human neuroblastoma (BE-2-C), and human embryonic kidney (293T) cell lines.³⁷ Adapted with permission from M. Mahmoudi, S. Laurent, M. A. Shokrgozar and M. Hosseinkhani, *ACS Nano*, 2011, 5, 7263. Copyright (2011) American Chemical Society.



Scheme 7.2 Reduction of tetrazolium to formazan and structures of common tetrazolium dyes for cell viability measurements.

charged and readily penetrates viable cells; MTS, XTT, and WST-1 are negatively charged and do not readily penetrate cells. The anionic dyes are typically used with an intermediate electron acceptor, such as phenazine methyl sulfate (PMS) or phenazine ethyl sulfate (PES), that transfers electrons from the cytoplasm or plasma membrane to facilitate the reduction of the tetrazolium into the colored formazan product.^{25,26} These newer dyes form water-soluble formazans, avoiding the need for the final solubilization step in the MTT assay.^{39,40} Note that XTT reduces less efficiently than MTT, whereas WST-1 is more sensitive, reduces more efficiently and shows faster color development compared to the other salts.²⁶

Resazurin is a cell-permeable, blue nonfluorescent molecule that can be irreversibly reduced by viable cells to the pink fluorescent dye resorufin (Scheme 7.3).⁴¹ Resazurin-based assays use similar protocols as tetrazolium salts, show excellent correlation with MTT assays, and are much easier and safer methods that do not require the addition of solubilization solutions or intermediate electron acceptors. Resazurin is nontoxic and enables continuous monitoring of proliferating cells. A derivative of resazurin, dodecylresazurin (C₁₂-resazurin), surpasses resazurin by being more lipophilic due to its C₁₂-carbon chain, which leads to better permeability and cellular retention (Vybrant™ Cell Metabolic Assay kit). Due to the higher sensitivity of fluorescence quantification compared to absorbance measurements, resazurin assays are more sensitive than tetrazolium salt assays.²⁵ They are also more stable and reliable than MTT assays. Users should be cautioned to look for potential interference with this assay if the contrast agent of interest carries a fluorophore. The fluorescence signal from the contrast agents can interfere with the emission from resorufin, thus providing false results for



Scheme 7.3 Reduction of resazurin to resorufin.

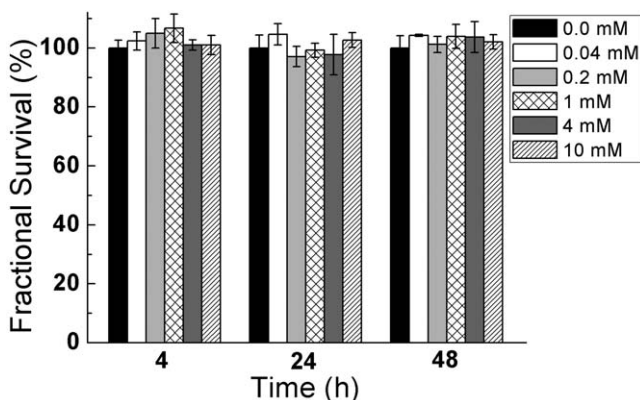


Figure 7.3 Cytotoxicity by C12-resazurin assay. HepG2 cells were incubated for 4, 24, and 48 h with different iron concentrations of sulfated dextran-coated iron oxide nanoparticles (SDIO – DO3A-10). Fluorescent intensities reflecting survival fractions were normalized against the signal from the untreated cells. All error bars present the standard error of the mean ($n = 3$).⁴²

Adapted with permission from T. Tang, C. Tu, S. Y. Chow, K. H. Leung, S. Du and A. Y. Louie, *Bioconjugate Chem.*, 2015, **26**, 1086. Copyright (2015) American Chemical Society.

the cell viability measured. Because the methods are similar, both methods are presented in this subsection. An example of data obtained using resazurin to evaluate dextran-coated superparamagnetic iron oxide contrast agents is shown in Figure 7.3.⁴² These data present a similar result format compared to the MTT assays in Figure 7.2 but demonstrates a biocompatible contrast agent that showed almost no toxic effect even at high concentrations and long incubation times.

Although tetrazolium and resazurin metabolic assays have been the most widely used assays for cytotoxicity, there are several general limitations with these assays. The reduction results reflect cell metabolism, but do not directly report cell number. The reduction rate can be affected by cell culture conditions, such as pH and glucose concentration. Additionally, tetrazolium or resazurin reduction can also be performed outside the mitochondria. Nicotinamide adenine dinucleotide (NADH) in cytoplasm or plasma membranes can also account for the observed reductions. Reducing agents that reduce tetrazolium salts or resazurin non-enzymatically can lead to

increased absorbance or fluorescence that interferes with assay results. Incubation with cells increases the possibility of artifacts as a function of time due to chemical interactions between the assay reagent, the contrast agents being tested, and the biochemistry of the cell. Because apoptosis is an active mode of cell death with metabolism continuing through the early stages, these assays underestimate cellular damage and cell death by only detecting the later stages of apoptosis when the metabolic activity of cells is reduced.

ATP is widely accepted as a marker of viable cells and is used to estimate cell viability in culture.²⁷ Damaged cells lose the ability to synthesize ATP, and endogenous ATPases rapidly deplete ATP from the cytoplasm.²⁵ Measurement of ATP is normally achieved through the luciferase reaction, where luciferase catalyzes the generation of bioluminescence from the substrate luciferin in the presence of ATP. The luminescent signal reaches a steady state and stabilizes within 10 minutes after addition of reagent and typically glows with a half-life longer than 5 hours. The luciferin–luciferase reaction is extremely sensitive, and most luminometers can detect picomoles of ATP. The sensitivity and speed make the ATP assay the fastest and the most sensitive method for measuring cell viability. This assay is also less prone to artifacts compared to other viability assays.²⁵ Typical result presentation is similar to that of the MTT and resazurin assays, as shown in Figures 7.2 and 7.3.

7.1.2.3.1 MTT and Resazurin Assay Protocols. Adapted from ref. 37 and 43–46. The methods below are designed for adherent cell types but can be modified for non-adherent cells.

1. Culture cells in appropriate complete cell culture medium at 37 °C in a humidified 5% CO₂ atmosphere.
2. Plate cells in 96-well plates at a concentration of 10⁴ cells per well in 100 μL of complete medium and incubate in a 5% CO₂ atmosphere at 37 °C overnight or 24 h.
3. Dissolve contrast agent in complete culture medium and prepare different concentrations.
4. Replace medium on cells with fresh medium containing varying concentrations of contrast agents and incubate for desired time (*e.g.* 24 h, 48 h, or even longer) at 37 °C in a humidified 5% CO₂ atmosphere.
5. Remove the contrast-agent-containing medium, and wash cells with pre-warmed PBS complete (with Ca²⁺ and Mg²⁺, to avoid detachment) three times.
6. After removal of the washing buffer, add 100 μL of medium containing MTT (0.5 mg mL⁻¹ to 5 mg mL⁻¹) or C₁₂-Resazurin (5 μM) to the wells and incubate at 37 °C in the humidified 5% CO₂ atmosphere for 15 min to 4 h (refer to the assay kit). For the MTT assay, remove the medium (if mentioned in the assay kit protocol) and solubilize formazan crystals by addition of about 150 μL of solubilization solution such as isopropyl alcohol (refer to the kit protocol) for 20 min at 37 °C in a humidified 5% CO₂ atmosphere.

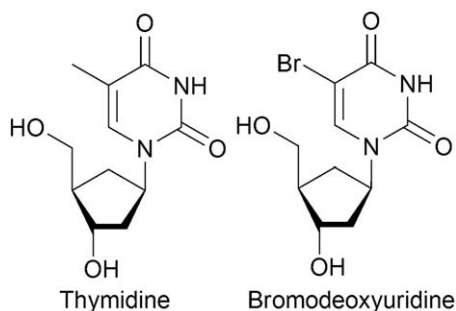
7. Measure the absorbance of formazan (normally between 500 to 600 nm) or the fluorescence of resorufin (excitation ~ 570 nm and emission ~ 587 nm) using a microplate reader.
8. Normalize absorbance or fluorescence intensity of different wells against a blank-medium-only well. Take the absorbance or fluorescence intensity of the blank well as 100%, and calculate the percentage of the experimental wells that represent the survival fraction and reflect cytotoxicity.

7.1.2.3.2 ATP Assay Protocol. Adapted from ref. 25, 47 and 48).

1. Culture cells in complete culture medium at 37 °C in a humidified 5% CO₂ atmosphere.
2. Seed cells into a 96-well plate (10^4 well⁻¹) in 100 μ L of complete culture medium and incubate for 24 h at 37 °C in a humidified 5% CO₂ atmosphere.
3. Dissolve contrast agent in complete culture medium and prepare different concentrations as needed.
4. After 24 h, replace culture medium in the 96-well plate with medium containing increasing contrast agent concentrations so that the final volume is 100 μ L in each well.
5. Incubate cells for range of time points (e.g. 4 h, 24 h, 48 h) at 37 °C in a humidified 5% CO₂ atmosphere.
6. Equilibrate plates to ambient temperature for 30 min to ensure uniform temperature across the plates during luminescent assays.
7. Add 20 μ L of 1% Triton-X 100 to all wells to lyse cells.
8. After 10 min, centrifuge the 96-well plate at 250 g for 2 min.
9. Transfer 50 μ L of the supernatant from each well to a new microplate.
10. Add 50 μ L buffer [25 mM Tricine buffer, pH 7.8, 5 mM MgSO₄, 0.1 mM ethylenediaminetetraacetic acid (EDTA) and 0.1 mM sodium azide] containing the reducing agent dithiothreitol (1 mM), D-luciferin (0.5 mM), and luciferase ($1.25 \mu\text{g mL}^{-1}$). Allow the plate to incubate at ambient temperature for 10 minutes to stabilize luminescence.
11. Record luminescence with a luminometer.
12. Normalize luminescence intensity of different wells against the control well. Take the luminescence intensity of the blank well as 100%, and calculate the percentage of the experimental wells, which is the survival fraction and reflects cytotoxicity.

7.1.2.4 Bromodeoxyuridine (BrdU) Assay for DNA Proliferation

Traditionally, proliferation assays use radiolabeled nucleosides such as ³H-thymidine to measure DNA synthesis.³⁶ The amount of ³H-thymidine incorporated into the cellular DNA can be assessed by a scintillation counter. Bromodeoxyuridine (5-bromo-2'-deoxyuridine, BrdU) is a synthetic nucleoside that is a halogenated derivative of thymidine (Scheme 7.4) and is commonly used to detect DNA proliferation, circumventing the limitations



Scheme 7.4 Structures of thymidine and bromodeoxyuridine.

associated with radioactive handling.^{28,49} The results of BrdU assays strongly correlate with those acquired by the ³H-thymidine methods, and BrdU assays can be almost as sensitive as the radioactive method. BrdU is incorporated into newly synthesized DNA during the S phase of the cell cycle and substitutes for thymidine during DNA replication.⁵⁰ Antibodies specific for BrdU can then be used to detect the incorporated BrdU under fluorescence microscopy, thus indicating that cells were actively replicating their DNA. Binding of the antibodies requires denaturation of DNA, usually by exposing the cells to acid or heat, making this an endpoint assay. The need for specific antibodies and extra steps makes this method less favored compared to MTT or other metabolic assays.

An example of a typical result from a BrdU assay is shown in Figure 7.4.²⁰ The number of stained/BrdU incorporated nuclei was counted as a percentage and compared to control cells cultured only in complete medium. In this case, the comparison suggested that contrast agents exert an influence on cell proliferation: the albumin-derivatized particles induced cell proliferation, whereas the plain and dextran-derivatized particles appeared to inhibit proliferation.

7.1.2.4.1 BrdU Assay Methods. Adapted from ref. 20, 51 and 52. The method below is designed for adherent cell types but can be modified for non-adherent cells.

1. Culture cells in appropriate cell culture medium at 37 °C in a humidified 5% CO₂ atmosphere.
2. Seed cells in 96-well plate at a density of 10⁴ cells per well in 100 μL of complete medium and incubate in a 5% CO₂ atmosphere at 37 °C for 24 h.
3. Dissolve contrast agent in complete culture medium supplemented with bromodeoxyuridin (10 μM).
4. Replace medium in the wells with 100 μL of fresh BrdU-supplemented medium containing varying concentrations of contrast agents and incubate for 24 h at 37 °C in humidified 5% CO₂ atmosphere.

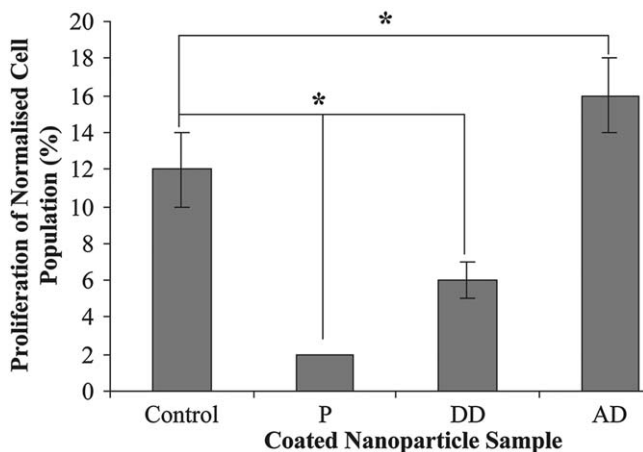


Figure 7.4 An example of the results of a BrdU assay for cell proliferation. Cell proliferation over a 24 h period as determined by BrdU incorporation of control cells, and cells incubated with plain (P), dextran derivatized (DD) or albumin derivatized (AD) nanoparticles. ($n = 3$, mean \pm standard error of the mean, $*p \leq 0.05$).

Reprinted from *Biomaterials*, Volume 24, C.C. Berry, S. Wells, S. Charles and A.S.G. Curtis, Dextran and albumin derivatised iron oxide nanoparticles: influence on fibroblasts *in vitro*, 4551, Copyright 2003, with permission from Elsevier.

5. Remove the contrast-agent-containing medium and wash cells with pre-warmed PBS complete (with Ca^{2+} and Mg^{2+} , the same as below) three times.
6. Fix cells in 100 μL 4% formaldehyde in PBS complete for 15 min at 37 $^{\circ}\text{C}$ or 70% ethanol for 20 min at ambient temperature.
7. Wash cells with pre-warmed PBS complete for three times.
8. Denature DNA with 100 μL of 2 M HCl for 10 min at 37 $^{\circ}\text{C}$.
9. Remove the HCl and add borate buffer (0.1 M, pH 9) to neutralize the residual acid and wash cells once with PBS.
10. Treat cells with 50 μL of a blocking buffer (PBS complete containing 0.1% Triton X-100 and 2% normal goat serum) for 15 min at 37 $^{\circ}\text{C}$.
11. Add 50 μL of anti-BrdU primary antibody (1 $\mu\text{g mL}^{-1}$, in blocking buffer), for 1 h at 37 $^{\circ}\text{C}$.
12. Remove antibody and wash samples with 100 μL pre-warmed 0.1% Triton in PBS complete three times.
13. Add 50 μL of a secondary, peroxidase-conjugated monoclonal goat anti-mouse IgG (2 $\mu\text{g mL}^{-1}$, in blocking buffer) for 30 min at 37 $^{\circ}\text{C}$.
14. Remove secondary antibody. Wash samples with 100 μL pre-warmed 0.1% Triton in PBS complete three times and then with only PBS once.
15. Add 100 μL of 50 mM phosphate in citrate buffer at pH 5 containing 0.05% of the soluble chromogen *o*-phenylenediamine (OPDA) and 0.02% H_2O_2 . Incubate for 15 min at 37 $^{\circ}\text{C}$.

16. Transfer 80 μL of supernatant from each well into a clean microplate containing 40 μL well⁻¹ of 2 N sulfuric acid to terminate the reaction.
17. Measure the absorbance at 490 nm using a microplate reader.
18. Wash the assay plate with the cell monolayer with PBS complete twice and stain for BrdU-DNA by adding 100 μL well⁻¹ of PBS complete containing 0.05% of the insoluble chromogen diaminobenzidine (DAB) and 0.02% H_2O_2 .
19. Observe the staining by light microscopy, determine the percentage of proliferating cells, those with stained nuclei, and compare to control cells cultured without contrast agent.

7.1.2.5 Cell Perturbation Assays

Because many safety concerns of contrast agents, especially superparamagnetic iron oxide (SPIO) nanoparticles, arise from their contribution to oxidative stress and the generation of reactive oxygen species (ROS), investigations of cell perturbation from ROS have attracted attention. The presence of ROS can lead to secondary products, such as hydrogen peroxide, that can cause lipid peroxidation on the cell membrane.¹⁹ This oxidative degradation of lipids can result in severe cell membrane damage. Thus, ROS levels and lipid peroxidation levels are strong indicators of cell perturbation and cytotoxicity.⁵³

ROS assays can determine oxidative stress levels caused by the generation of free radical oxygen species. Because ROS have extremely short half-lives and typically low concentrations, they are difficult to measure directly. Instead, they can be assessed by reactions with other molecules to yield more stable and long-lived analytes.⁵⁴ For example, 2',7'-dichlorodihydrofluorescein diacetate (H2DCFDA) is a cell-permeable chemically reduced form of fluorescein. Upon cleavage of an acetate groups by intracellular esterases and oxidation by the ROS in the cell, the non-fluorescent H2DCFDA is converted to a highly fluorescent 2',7'-dichlorofluorescein (DCF). The fluorescence can then be monitored by a microplate reader, fluorometer, or flow cytometer for sensitive and rapid detection of ROS. Other fluorescent probes are MitoSOXTM and Mito Tracker[®] red CM-H₂XRos (Molecular ProbesTM, Invitrogen). Compared to H2DCFDA, which is a suitable agent for both mitochondrial and non-mitochondrial (cytosolic) ROS detection, the other two are highly mitochondria-specific.⁵³

The end products of lipid peroxidation of polyunsaturated fatty acids are reactive aldehydes, such as malondialdehyde (MDA) or 4-hydroxynonenal, which are markers for oxidative stress. A quantification of the amount of MDA present in a cell can be used to estimate the degree of lipid peroxidation.⁵⁵ MDA is a thiobarbituric acid-reactive substance, and the interaction of MDA with thiobarbituric acid yields a fluorescent product that is rapidly and easily measured. We refer the interested reader to detailed examples of ROS and lipid peroxidation assays.¹⁹

7.1.3 Cell Binding

7.1.3.1 Introduction to Cell Binding

Many targeted contrast agents, including nanoparticles, have been reported. The efficiency of targeted nanoparticles has been described most often only qualitatively and primarily by observed relative increases in signal for the modality under consideration in cellular or animal studies. For example, fluorescent dyes or radiolabels that are attached to contrast agents are tracers to reflect the targeting ability of a contrast agent.^{56–58} Intensive biological assays or cytometric analysis are highly desirable for elucidating cell binding biology. Detailed binding studies provide an insight into how targeted materials bind to biomarkers and offer a possible standard to compare different imaging probes used for similar purposes. Optimization of probe efficiency is desirable to enable minimal doses to be administered to decrease side effects and toxicity, which is critical for clinical translation.

Detailed investigation of binding properties can take multiple forms, from evaluating the extent and affinity of binding to assessing the kinetics of interactions. Quantitative reporting of binding affinities offers an understanding of how targeting moieties attached to the contrast agents behave compared to their free counterparts. Without a means to characterize the binding affinities of contrast agents, it is difficult to understand what steps can be taken to optimize target recognition for clinical applications. Currently, there are a number of methods to quantify binding affinity: (1) radio-labeled ligand or fluorescent ligand binding assays;^{59,60} (2) surface plasmon resonance (SPR);⁶¹ (3) absorbance spectroscopy, *e.g.* O₂ binding to hemoglobin, based on red and infrared light absorption characteristics of oxygenated and deoxygenated hemoglobin; (4) circular dichroism, *e.g.* Ca²⁺ binding to thrombocyte fragments;⁶² (5) enzymatic activity, *e.g.* Ca²⁺-dependent enzyme activation;⁶³ and (6) calorimetry based on the thermodynamic properties of interactions between proteins and ligands.⁶⁴ Among those methods, fluorescence, radioactive, and SPR assays are widely used due to their high sensitivity and the generality of their applications. They are also commonly used for studying contrast agents as well as investigating protein–protein binding. Thus, this section focuses mainly on these methods.

SPR is one of the standard tools for measuring adsorption of material onto planar surfaces. It evaluates biomolecular events to elucidate kinetic constants from interactions such as the binding of a free-flowing conjugate.⁶⁵ However, it is a measurement based on the binding affinity and kinetics of molecules to isolated proteins or peptides immobilized on sensor chips.^{66,67} The need to purify and immobilize the target of interest onto chips presents a technical challenge and can also result in an unnatural presentation of the target. Thus, the measurement might not reflect interactions that take place when the target is in its native environment. This limitation is particularly an issue for membrane-localized receptors, which are difficult if not impossible to display full length in their natural membrane-spanning

conformation on chips. To address this issue, magnetic nanoparticles have been immobilized on sensor chips and cells were flowed over the chips to bind to the nanoparticles.⁶⁸ This method provided a better SPR technique to investigate interactions between nanoparticles and live cells but still required a great deal of method development.

Compared to the complicated system required by SPR, other *in vitro* binding assays overcome the limitation of the need for immobilization on sensor chips and are accessible to most researchers without specialized equipment or chemistry knowledge. There are three commonly used experimental protocols for fluorescent or radiolabeled binding assays: (1) Scatchard analysis with a saturation binding assay:^{69–71} The extent of binding is measured in the presence of different concentrations of the ligand. From an analysis of the relationship between binding and ligand concentration, the number of binding sites and dissociation constant— K_d —can be determined; (2) Competitive IC_{50} (the half maximal inhibitory concentration) binding assay:^{72,73} Competition between a ligand with a known binding affinity to the biological target enables the indirect measurement of the interaction between the targeted contrast agent and the biological target. (3) Kinetic experiments that measure the time course of association and dissociation to determine rate constants for ligand binding and dissociation. Scatchard analysis and competitive IC_{50} assays are described in this section. Interested readers are referred to related papers about kinetic experiments.^{59,74} A comparison of SPR, Scatchard analysis, and competitive IC_{50} is presented in Table 7.3.

Cell binding assays measure the process where a ligand molecule binds or associates to a receptor or antibody on cell surface. This interaction does not involve internalization of the molecule into the cell. Cell uptake, on the other hand, includes molecules that are transported into cells.

To accurately determine binding, cellular uptake processes must be blocked during the course of an assay. For cells with high phagocytosis activity, incubating cells with contrast agents at low temperatures such as 4 °C can reduce cellular uptake. Often, uptake is inhibited chemically by endocytosis inhibitors. Chlorpromazine and potassium depletion are used to inhibit the formation of clathrin-coated pits, thus hindering clathrin-mediated endocytosis.⁷⁵ Genistein, an inhibitor of tyrosine kinases, causes local disruption of the actin network at the site of endocytosis and prevents the recruitment of dynamin II, which leads to inhibition of caveolin-mediated endocytosis.^{75,76} Cytochalasin and nocodazole suppress the polymerization of actin and the microtubule cytoskeleton.⁷⁶ Potassium depletion is also an effective method to inhibit the formation of methyl- β -cyclodextrin (M β CD), which inhibits cholesterol-dependent endocytic processes by reversibly extracting the steroid from plasma membranes.⁷⁷ A brief description of these endocytic pathways is provided in Section 7.1.4. As the toxicity and efficacy of endocytosis inhibitors are cell-type-dependent, it is critical to choose the correct inhibitors for specific assays. The nonchemical inhibition by temperature is found to be effective and produce little interference for macrophages.

Table 7.3 Comparison of common cell binding assays.

Assay	Principles	What to measure	Advantages	Limitations
SPR	Association and dissociation of molecules on sensor chips changes the resonance angle with time	Association rate constant k_{on} , dissociation rate constant k_{off}	Widely accepted; provides not only the K_{d} value, but also kinetic information; real time quantitative analysis; can be performed in automated fashion	Need to isolate and immobilize the target of interest on sensor chips; cannot easily distinguish between specific and non-specific interactions; washing between steps does not completely dissociate the bound materials
Scatchard analysis	Using different concentrations of the ligand to saturate receptors	Maximum binding capacity (total concentration of the receptor) B_{max} ; dissociation constant K_{d}	Widely accepted; can be used for isolated targets or cell-based assays; suitable for multiple binding sites with different affinities	Amplifies the prominence of binding data at low ligand concentrations; linear fitting of $[\text{bound}]/[\text{free}]$ versus $[\text{bound}]$ introduces error
Competition/ IC_{50}	The ability of inhibition of another known ligand reflects the binding affinity of the molecule in interest	IC_{50} and inhibitory constant K_{i}	Simple experiment if labeled known ligand is available; can be used for isolated targets or cell-based assays	Requires fluorescent or radiolabeled known ligand; does not reveal cooperative binding

7.1.3.2 Surface Plasmon Resonance (SPR)

SPR is one of the standard tools for measuring adsorption of material onto planar surfaces.⁷⁸ When light is directed to a solid or liquid interface, it causes oscillations of the surface electromagnetic waves that propagate in a direction parallel to the interface and are sensitive to changes of surface properties. When the frequency of light photons matches the frequency of oscillatory surface electrons, resonance is established and results in the absorption of light. Adsorption of molecules on the surface causes changes of the refractive index, and thus a change in the resonance angle (the angle with the minimum reflected intensity), as shown in Figure 7.5.⁷⁹ Therefore, the reflected light provides information regarding surface molecular interactions in real-time. The resonance angle change is normally reported as resonance units (RU), where 1000 RU correspond to an angle change of $\sim 0.1^\circ$ or the binding of 1 ng of protein per square mm.

Normally, proteins are immobilized on a sensor chip using coupling chemistry, such as those between amines and carboxylic acids with the use of 1-ethyl-3-(3-dimethylaminopropyl)carbodiimide (EDC) or *N*-hydroxysuccinimide (NHS) coupling agents.⁸⁰ Through a microfluidic system, a solution with the analyte is injected over the protein layer. As analytes bind proteins, an increase in SPR signal is observed. Bound analyte is removed through the injection of a regeneration solution. Regeneration

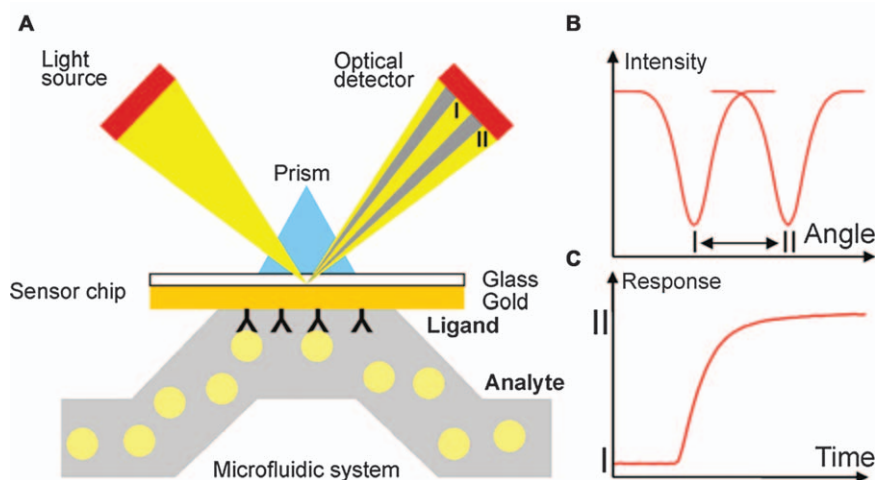


Figure 7.5 Principle of surface plasmon resonance. (A) Ligands (upside down black Ys) are immobilized on a chip, and analytes (yellow circles) flow by in a microfluidic system. When analytes bind to the ligands immobilized on the sensor chip, the resonance angle changes causing the reflected light to shift from I to II. (B) Binding of analytes results in a shift of the angle of the minimum reflected intensity (the resonance angle) from I to II. (C) The sensorgram is a plot of the change of the SPR angle *versus* time. It displays the real-time progress of interactions at the sensor surface. Adapted with permission from ref. 79.

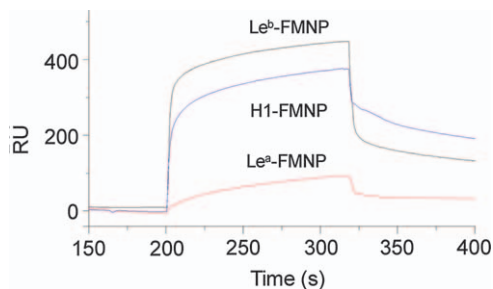


Figure 7.6 An example of association and dissociation of cells bound to blood group H type 1- and Lewis b-conjugated fluorescent magnetic nanoparticles (FMNP) detected by SPR. Amine-linked targeted nanoparticles were immobilized on the NHS-activated CM5 sensor chip through amine coupling. Cells (10^7 cells mL^{-1}) were injected for 3 min at a flow rate of 20 L min^{-1} through the modified CM5 sensor chip. Binding data were acquired using a Biacore 3000 (GE Healthcare). The sensor chip was regenerated by a 1 min pulse of 20 mM NaOH.⁶⁸ Adapted with permission from S. Park, G.-H. Kim, S.-H. Park, J. Pai, D. Rathwell, J.-Y. Park, Y.-S. Kang and I. Shin, *J. Am. Chem. Soc.*, 2015, 137, 5961. Copyright (2015) American Chemical Society.

buffers are usually low-pH buffers, such as 10 mM glycine at pH 1.5–2.5, or high-pH solutions, such as 10 mM NaOH, which break the interactions between ligands and analytes to regenerate sensor chip surfaces.⁸⁰ Values of K_d can be calculated using the association rate constant, k_{on} , and dissociation rate constant, k_{off} .⁸¹ SPR is a complicated system and detailed experimental protocols depend on the specific instruments and sensor chips, as well as the ligand and analyte of interest. We briefly introduce an example where amine-linked nanoparticles are immobilized on amine-reactive sensor chips to allow free cells flowing in solution to bind (Figure 7.6).⁶⁸ More information about SPR and coupling chemistry can be found in review articles.^{78,80} Readers are referred to several research articles using SPR to study binding (immobilized isolated protein or peptides, not *in vitro*).^{67,82}

7.1.3.3 Scatchard Analysis

Scatchard analysis is a well-known method adapted from Michaelis–Menten enzyme activity studies to describe binding between ligands and receptors as well as protein–protein interactions. In a typical assay, increasing amounts of ligand are added to a fixed concentration of isolated receptors or to fixed numbers of cells carrying the receptor. Eventually, the receptors become saturated. An example of a saturated binding curve is shown in Figure 7.7 for increasing concentrations of [^{125}I]-PD151242, a radiolabeled ligand for endothelin receptor A (ET_A), binding to ET_A on cryostat sections of human heart.⁵⁹ Non-specific binding (NSB) is determined by co-incubation of unlabeled ligand with a 1000-fold excess over the K_d and is subtracted from total binding to calculate specific binding. A Scatchard plot of the data is shown in Figure 7.7B. By plotting bound/free *versus* bound, the slope of the

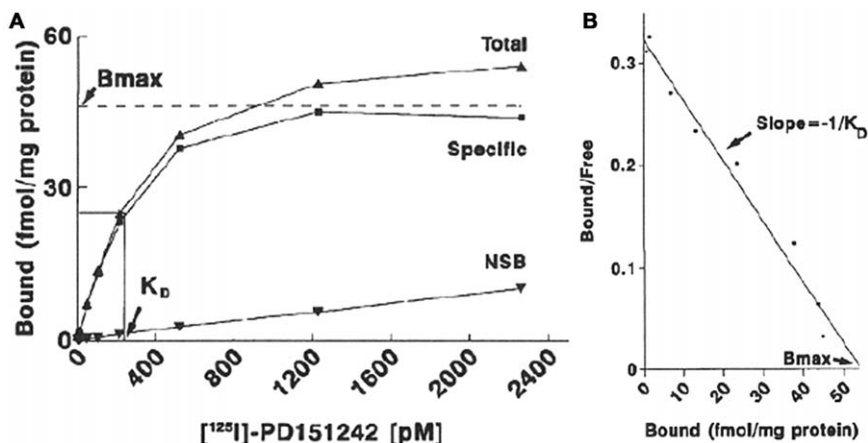


Figure 7.7 Example of saturation binding assay. (A) Plot of bound protein *versus* concentrations of the protein. The protein [¹²⁵I]-PD151242 is radiolabeled and binds to endothelin receptor A on cryostat sections of human heart. Radioactivity was measured using a gamma counter. (B) Scatchard plot of the data from (A). Current Directions in Radiopharmaceutical Research and Development, Radioligand Binding Assays: Theory and Practice, Developments in Nuclear Medicine Series 30, 1996, p. 173, A. P. Davenport and F. D. Russell, (©1996 Kluwer Academic Publishers) With permission of Springer.

line is equal to the negative reciprocal of K_d and the intercept of the line with the abscissa is an estimate of B_{max} , the total density or concentration of receptors and the maximum amount that can be bound.

Scatchard analysis is especially useful when the receptors or biological targets have multiple binding sites with different affinities or overlapping binding sites for multiple ligands. However, Scatchard analysis has been applied mainly to small molecules and macromolecules. Another method has been developed to quantify binding affinities for nanoparticles coated with macromolecule ligands (Figure 7.8).⁴² A linear plot indicated that there were no cooperativity effects. The biphasic plot also suggested that the nanoparticles interacted with more than one binding site on the receptor, with differing affinities. Competition studies demonstrated that the lower affinity binding site overlaps with the binding site for another ligand. The Scatchard analysis can thus be adapted for assessing particulate binders.

7.1.3.3.1 Binding Analysis Protocols. Adapted from ref. 42. The Scatchard method requires a number of data values, including total binding, nonspecific binding, and unbound material. The acquisition of each of these values is described below.

A. Total Binding Measurement Protocol

1. Culture cells in complete culture medium at 37 °C in a humidified 5% CO₂ atmosphere.

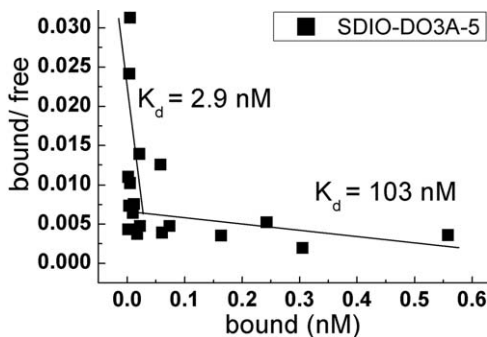


Figure 7.8 $^{111}\text{In}^{3+}$ radiolabeled nanoparticle binding studies at 4 °C. Scatchard Plot of sulfated dextran coated iron oxide nanoparticles binding to scavenger receptor class A on murine macrophages. The biphasic plot suggested two different binding sites on the receptors with different affinities.⁴² Adapted with permission from T. Tang, C. Tu, S. Y. Chow, K. H. Leung, S. Du and A. Y. Louie, *Bioconjugate Chem.*, 2015, 26, 1086. Copyright (2015) American Chemical Society.

- Distribute cells with appropriate culture medium into 24-well plates at a population of 1×10^5 (0.4 mL per well) and incubate for 24 h at 37 °C in a humidified 5% CO_2 atmosphere.
- Remove culture medium and replace with CO_2 -independent medium (pre-warmed to 37 °C). Because the binding assay is performed at 4 °C, not in a 37 °C incubator with supplemented CO_2 , CO_2 -independent medium is needed.
- Adapt cells to a cold environment (4 °C), to suppress endocytosis by placement over crushed ice for 15 min.
- Replace the medium with medium containing radiolabeled protein or contrast agents at different concentrations in cold CO_2 -independent medium and incubate for 1 hour at 4 °C in a refrigerator or cold room.
- Remove the contrast agent-containing medium and wash cells with 0.5 mL of cold PBS (with Ca^{2+} and Mg^{2+}) three times.
- If using adherent cell lines, detach or lyse cells using 0.5 mL of de-ionized water. Use freeze/thaw (−80 °C/ambient temperature, 30 min/20 min) cycles to expedite the process if needed.
- Transfer cell lysates into appropriate containers for radioactivity or fluorescence measurements. Radioactivity or fluorescence intensity represents the bound concentration of the targeted contrast agent. Obtain the free concentration of the contrast agent by subtracting the bound concentration from the total concentration added to each well. In most cases, the bound concentration is so low compared to the total concentration that the total concentration can be used as the free concentration.

B. Non-specific Binding Measurement Protocol

- 1–4. Follow the same instructions as above.
5. Replace the medium with radiolabeled contrast agents at different concentrations and a fixed high concentration of unlabeled, free counterpart (1000-fold excess) in cold CO₂-independent medium for a 1 hour incubation at 4 °C in a refrigerator or cold room.
- 6–8. Follow the same instructions as above.

C. Scatchard Analysis

1. Acquire specific binding by subtracting the contribution from non-specific binding (part B) from the total binding (part A).
2. Plot the ratio of bound/free ligand concentration *versus* bound ligand concentration.
3. Obtain the slope of the line, which is equal to the negative reciprocal of K_d .
4. Obtain the intercept of the line with the abscissa as an estimate of B_{max} .

7.1.3.4 Competition Assay/IC₅₀

Determination of IC₅₀ is simple if a radiolabeled competitor with known binding affinity to the same receptor is available. However, IC₅₀ determinations rely on a number of assumptions, including a lack of cooperative binding. Scatchard analysis, on the other hand, can reveal cooperative binding, which produces non-linear plots,^{83–85} and thus may be a more robust choice for assessment of binding properties of some contrast agents, notably nanomaterials.

An example of a competition binding assay is shown in Figure 7.9.⁷³ U87MG cells were incubated with targeted iron oxide nanoparticle contrast agent in the presence of a radiolabeled competitor ¹²⁵I-echistatin at a fixed concentration. Increasing concentrations of iron oxide nanoparticles with the cyclic peptide c(RGDyK) as the targeting moiety inhibits ¹²⁵I-echistatin binding to integrins on U87MG cells. The binding affinity of the targeted iron oxide nanoparticles can be calculated by eqn (7.1).

$$K_I = IC_{50}/(1 + [L]/K_d) \quad (7.1)$$

where IC₅₀ is the 50% inhibition concentration, *i.e.* the concentration of targeted iron oxide that produces radioligand binding half-way between the upper and lower plateaus of the semi-log plot, which can be determined from the competition plot. In this equation, [L] is the fixed concentration of radioligand/competitor and K_d is the known binding affinity of the radioligand, in this case ¹²⁵I-echistatin.

7.1.3.4.1 IC₅₀ Measurement Protocol. Adapted from ref. 86.

1. Culture cells in complete culture medium at 37 °C in a humidified 5% CO₂ atmosphere.

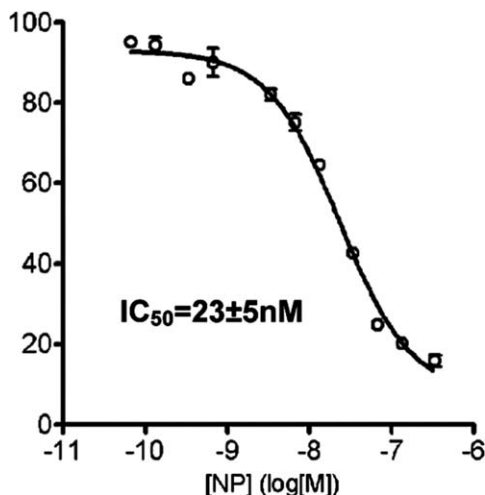


Figure 7.9 An example of a competition binding. The c(RGDyK)-MC-Fe₃O₄ concentration-dependent replacement of ¹²⁵I-echistatin on U87MG cells. The y-axis is the inhibition percentage.⁷³ Adapted with permission from J. Xie, K. Chen, H.-Y. Lee, C. Xu, A. R. Hsu, S. Peng, X. Chen and S. Sun, *J. Am. Chem. Soc.*, 2008, **130**, 7542. Copyright (2008) American Chemical Society.

2. Distribute cells with appropriate culture medium into 48-well plates at a population of 1×10^5 (0.2 mL per well) and incubate overnight at 37 °C in a humidified 5% CO₂ atmosphere.
3. Remove culture medium and replace with CO₂-independent medium (pre-warmed at 37 °C). Adapt cells to a cold environment (4 °C), to suppress endocytosis by placement over crushed ice for 15 min.
4. Premix radiolabeled competitor at a fixed concentration with the unlabeled targeted contrast agent at various concentrations (concentration range normally spans six orders of magnitude).
5. Replace CO₂-independent medium with 200 μL of mixed solutions of contrast agent and radiolabeled competitor. Incubate cells for 30 min or 1 h at 4 °C.
6. Remove the mixed solutions and wash cells with PBS complete (with Ca²⁺ and Mg²⁺, 200 μL, three times) to remove the unbound molecules.
7. Detach cells from the culture plates by incubation with 0.02% (w/v) EDTA (or EDTA-trypsin, depending on cell type) and concentrate cells by centrifugation for 5 min.
8. Disperse cells in 400 μL of PBS complete (with Ca²⁺ and Mg²⁺) in gamma counting tubes to measure the radioactivity.

Calculate the best-fit 50% inhibitory concentration (IC₅₀) values by fitting the data with nonlinear regression software.

7.1.4 Cell Uptake

7.1.4.1 Introduction to Cell Uptake

When incubated with cells, contrast agents interact with the lipids, proteins, and other components of the cell membrane. These interactions can be followed by the activation of an energy-dependent uptake mechanism. Several major endocytic pathways have been characterized, including the following four pathways: (1) Clathrin-mediated endocytosis, a pathway that involves specific receptors to recognize and internalize cargo into coated pits that are formed by cytosolic protein clathrin on the intracellular face of the plasma membrane.^{76,87} Mature clathrin-coated pits pinch off from membranes and form clathrin-coated vesicles (60–200 nm in diameter).^{88,89} This pathway is characteristic of receptor-mediated endocytosis.⁸⁷ (2) Caveolae-mediated endocytosis, the most common clathrin-independent endocytosis. It involves clustering of lipid raft components on the plasma membrane into the flask-shaped pits (~50 nm in diameter) called caveolae followed by the formation of caveolar vesicles.⁷⁶ Uptake of extracellular molecules is also mediated *via* receptors in caveolae. (3) Pinocytosis, a process in which the invagination of cell membranes form vesicles filled with large volumes of extracellular fluid and small molecules.⁹⁰ Because uncoated vesicles can be larger than coated ones, pinocytosis allows uptake of larger objects (>150 nm) and forms vesicles in the range of 0.5–5 μm in diameter.⁷⁶ Unlike receptor-mediated endocytosis, pinocytosis is non-specific and non-absorptive (molecules do not bind to the cell surface and concentrate before internalization). (4) Phagocytosis, the process in which a cell engulfs a solid particle to form an internal vesicle. It is normally restricted to specialized cells, such as leukocytes, and can internalize particulate matter larger than 0.75 μm in diameter, such as micro-organisms and apoptotic cells.⁸⁷

Contrast agents that are untargeted small molecules, such as Gd complexes, normally are internalized into the cell by nonspecific pinocytosis.^{91,92} Molecules are brought into cells within small vesicles or endosomes that subsequently fuse with lysosomes to degrade the molecules. Another method to artificially introduce Gd complexes into the cells is to use electroporation, which causes the formation of transient hydrophilic pores on the cell membrane upon the application of suitable electric pulses between two electrodes placed into a suspension of cells.⁹² Gd complexes in this case are delivered into cytoplasm instead of subcellular vesicles. Larger contrast agents, such as SPIO nanoparticles, can be taken up *via* endocytosis, or if large enough (>100 nm) by phagocytosis by phagocytic cells like macrophages, and further trafficked to different subcellular locations, typically ending in lysosomal accumulation.⁹³ Targeted contrast agents, such as functionalized Gd complexes or iron oxide nanoparticles, are internalized by receptor-mediated endocytosis. This uptake can be inhibited by competing ligands.

Chemical inhibitors are commonly used to differentiate endocytic pathways (see Section 7.1.3.1 for a description of agents that prevent cellular uptake in binding assays). For example, chlorpromazine, potassium-depletion,

monodansylcadaverine, phenylarsine oxide, cytosolic acidification, and hypertonic shock (sucrose) can be employed as inhibitors of clathrin-dependent endocytosis. Methyl- β -cyclodextrin and genistein can be employed as inhibitors of clathrin-independent endocytosis. By exploiting these chemical inhibitors or known ligands that are competitors to the contrast agents for the specific cell surface receptors of interest, researchers can determine the mechanism of cellular uptake.

As for their binding and biocompatibility properties, uptake efficiency of contrast agents is affected by their size, composition, surface chemistry, and the phase of the cell cycle.⁹⁴ Qualitative analysis of cellular uptake includes iron staining with Prussian blue, Berlin blue, or fluorescently labeled contrast agents that can be observed with a microscope.⁹⁵ Quantitative measurements of gadolinium or iron concentrations have been achieved with various methods in the past few decades. Details about these methods are described in the following sections and a comparison between those methods is presented in Table 7.4. Readers can choose the appropriate method based on specific needs.

7.1.4.2 Elemental Analysis

Elemental analysis is the most direct way to measure the amount of internalized contrast agents. This can usually be achieved with atomic absorption or emission spectroscopy to quantify gadolinium or iron concentrations. Techniques such as inductively coupled plasma-optical emission spectroscopy or mass spectrometry (ICP-OES or ICP-MS are sensitive methods that can reach parts-per-billion-level (ppb, e.g. $1 \mu\text{g L}^{-1}$) measurements, where conventional atomic absorption spectroscopy (AAS) provides results normally in the parts-per-million (ppm, e.g. 1 mg L^{-1}) range.

Trace levels of iron can also be measured by the ferrozine assay. Ferrozine (3-(2-pyridyl)-5,6-diphenyl-1,2,4-triazine-*p, p'*-disulfonic acid monosodium salt hydrate) is a colorimetric reagent that was reported in the 1970s to form a magenta complex upon reaction with ferrous ions.⁹⁶ It has been modified and improved to become a convenient commercial assay with detection range in sub-ppm levels. The ferrozine-iron complex is stable and soluble in water. For solutions that contain both ferrous and ferric ions, a reducing or oxidizing agent is added prior to ferrozine to ensure that all iron ions in a sample are in a single oxidation state. Measurement of the maximum absorbance of the solution near 570 nm determines the iron concentration, after calibration using a standard curve obtained from standard iron solutions.

7.1.4.2.1 Cell Uptake by Elemental Analysis Protocols.

(A) Atomic Absorption/Emission Spectroscopy for Determination of Concentrations of Gd, Fe, and Mn (Adapted From Ref. 97)

1. Culture cells in appropriate cell culture medium at 37°C in a humidified 5% CO_2 atmosphere.
2. Seed cells in 24-well culture plates, with approximately 10^5 cells in 1 mL of medium at 37°C for 24 h.

Table 7.4 Comparison of common cell uptake methods for MRI contrast agents.

Category	Assay	Principle	What to measure	Advantages	Limitations
Elemental analysis	Iron staining	Colorimetric reagents can stain iron ions	Iron concentration	Sensitive	Can only analyze iron-based contrast agents
	AAS/ICP-MS/ ICP-OES	Uses elemental absorption, optical emission, or MS to detect elements or molecules	Metal concentration (Fe, Gd, Mn)	Sensitive; can analyze Gd, Fe, Mn	Works best for elements without much biological background
Relaxation/MRI	Relaxation MR imaging	Contrast agents decrease the relaxation times of proton and generate enhanced contrast on MR images	T_1 or T_2 relaxation times of cell or cell lysates	Provides information on the ability of contrast enhancement	Not sensitive, no direct measurement of the uptake amount of contrast agents
Fluorescent/ Radioactive assays	Fluorescent	Uses fluorescent moiety in a multimodal imaging probe	Fluorescence intensity of cell or cell lysates	Sensitive	Need a fluorescent moiety; background issues with cell autofluorescence
	Radioactive	Use radioactive moiety in a multimodal imaging probe	Radioactivity of cell or cell lysates	Sensitive	Need a radioactive moiety; safety concerns with ionizing radiation; short half-life of radioactive isotopes

3. Remove culture medium and incubate cells with the contrast-agent-containing culture medium at different concentrations of contrast agent for 1 h. In control cultures, cells are placed in 1 mL of medium without contrast agent at the same cell density as the contrast agent samples.
 4. Remove medium and wash cells with PBS complete (with Ca^{2+} and Mg^{2+} , pre-warmed at $37\text{ }^\circ\text{C}$) three times.
 5. Detach cells, suspend cells in PBS complete, and centrifuge the cell suspension.
 6. Remove the supernatant, and dissolve the cell pellet in 37% HCl solution at $70\text{--}80\text{ }^\circ\text{C}$ for 30 min.
 7. Dilute the samples to a final iron (similar for Gd and Mn) concentration of approximately $1.0\text{--}4.0\text{ }\mu\text{g mL}^{-1}$.
 8. Measure the iron, gadolinium, or manganese concentration with atomic absorption or emission spectroscopy.
- (B) Ferrozine Assay for Determination of Iron Concentration Protocol (Adapted From Ref. 98, 99)
1. Culture cells in appropriate cell culture medium at $37\text{ }^\circ\text{C}$ in a humidified 5% CO_2 atmosphere.
 2. Distribute cells in 24-well plates at a concentration of 2.5×10^5 cells per well in 1 mL of medium and incubate in a 5% CO_2 atmosphere at $37\text{ }^\circ\text{C}$ for 18 to 24 h.
 3. Dissolve contrast agent in complete culture medium and prepare different concentrations (iron concentration range $40\text{--}800\text{ }\mu\text{g mL}^{-1}$).
 4. Remove culture medium and incubate the cells with the contrast agent-containing culture medium at different concentrations from 1 to 24 h. In control cultures, cells are placed in 1 mL of medium without contrast agent at the same cell density as the contrast agent samples.
 5. Remove contrast agent and wash cells thoroughly three times with PBS complete (with Ca^{2+} , Mg^{2+}).
 6. Mix samples with 250 μL of reagent A (4.5% KMnO_4 and 1.2 N HCl solutions mixed in equal volumes immediately before use) and incubate at $60\text{ }^\circ\text{C}$ for 2 h to lyse cells and oxidize all iron to Fe^{3+} .
 7. Allow the reaction mixture to cool to ambient temperature before addition of 50 μL of reagent B (6.5 mM ferrozine, 13.1 mM neocuproine, 2 M ascorbic acid, and 5 M ammonium acetate) for the colorimetric reaction.
 8. Measure the absorbance of samples at $\sim 570\text{ nm}$ using a microplate reader.
 9. Calculate concentrations using a standard curve prepared with ferrous ethylenediammonium sulfate in 0.01 N HCl, ranging from 0 to 6 mg Fe mL^{-1} . Treat the standard iron samples with steps 6–8.

7.1.4.3 Relaxation Assay and Magnetic Resonance Imaging

A qualitative measure of cell uptake can be acquired by monitoring changes in the magnetic properties of a cell suspension after incubation with a contrast agent. This monitoring can be realized with a bench-top relaxometer or an MRI scanner. Direct measurement in cells can also provide information about contrast agent effectiveness inside cells. For example, a study of Gd complexes showed that contrast agents internalized by pinocytosis or electroporation, resulting in contrast agents in endosomes or the cytoplasm, respectively, have different relaxivities.⁹² However, this method is not as sensitive as elemental analysis, does not differentiate internalization from adsorption to the cell surface, and does not directly report the exact amount of iron or gadolinium associated with cells. Therefore, it is best to use relaxation measurements in combination with another technique like elemental analysis. An example of the cellular uptake of Gd-SWCNTs (single-walled carbon nanotubes) by fibroblast (3T3 cells) was quantified by MRI and elemental analysis with ICP-OES (Figure 7.10).¹⁰⁰ While ICP-OES measured the average number of Gd³⁺ ions uptake per cell, MR images displayed positive contrast from the agent. Together, they characterized the uptake and labeling efficiency and the potential as contrast agents of the Gd-SWCNTs.

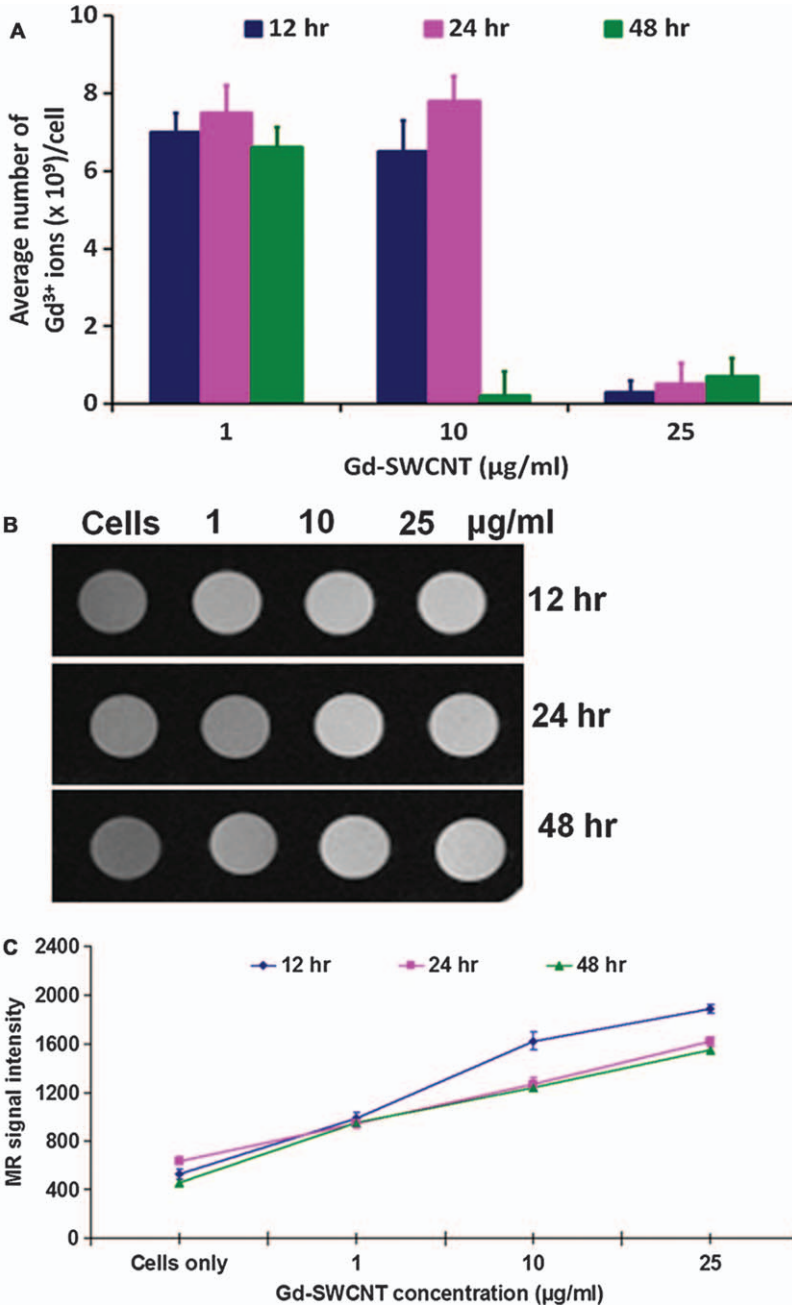
7.1.4.3.1 Cell Uptake by Magnetic Properties Protocols.

(A) Relaxation Assay (Adapted From Ref. 42)

1. Culture cells in appropriate cell culture medium at 37 °C in a humidified 5% CO₂ atmosphere.
2. Distribute cells into 6-well plates at a concentration of 1×10^6 cell mL⁻¹ in appropriate culture medium (2 mL per well). For adherent cell lines, incubate cells at 37 °C, 5% CO₂ for 18 to 24 h to allow adherence.
3. Prepare solutions of contrast agent at different concentrations by dissolving contrast agent in culture medium. Pre-warm the medium at 37 °C.
4. Replace cell medium in the plates with fresh medium containing contrast agents and incubate at 37 °C in humidified 5% CO₂ for 1 hour.
5. Remove the contrast agents and wash cells with 2 mL of pre-warmed PBS complete (with Ca²⁺, Mg²⁺) three times.
6. If using adherent cell lines, lyse cells in 1 mL of de-ionized water. Use freeze/thaw (-80 °C/ambient temperature, 30 min/20 min) cycles to expedite the process if needed.
7. Lyophilize cell lysates and add de-ionized water (0.3 mL) to the residue to prepare the solution for relaxation measurement by relaxometer. Compare the relaxation times of cell lysates that were incubated with contrast agents with the control (cells treated only with medium).

(B) Cell uptake Measured by MRI Protocol (Adapted From Ref. 95)

Cell lysates or cell pellets in PBS can also be measured by MRI. However, another method for MRI is to suspend the cells in an agarose gel as described below. Agarose gel (0.1%) can be prepared by



mixing 0.1 g of dry low melting agarose in 100 mL of distilled water. Heat this mixture to facilitate complete dissolution of the agarose, and then place the mixture in a warm water bath ($\sim 40^\circ\text{C}$) to a few degrees above the gelling temperature. The homogeneity and isotropy of agarose gel makes it an ideal test bed for MRI studies.¹⁰¹

1. Culture cells in appropriate cell culture medium at 37°C in a humidified 5% CO_2 atmosphere.
2. Place cells into 6-well plates at a concentration of 1×10^6 cell mL^{-1} in appropriate culture medium (2 mL per well). For adherent cell lines, incubate cells at 37°C , 5% CO_2 for 18 to 24 h to allow adherence.
3. Prepare solutions of contrast agents at different concentrations by dissolving contrast agent in culture medium. Pre-warm the medium to 37°C .
4. Replace cell medium in the plates with fresh medium containing contrast agents and incubate at 37°C in humidified 5% CO_2 atmosphere for 1 hour.
5. Remove the contrast agents and wash cells with 2 mL of pre-warmed PBS (with Ca^{2+} , Mg^{2+}) three times. Fix cells with formalin.
6. Adjust the concentration of cells to 4×10^6 cells mL^{-1} and dissolve the cells (0.5 mL) in 0.1% agarose gel (0.5 mL) to give a final concentration of 2.0×10^6 cells mL^{-1} . Care should be taken to avoid the introduction of bubbles into the agarose gels. Degassing the gel solution by putting it under vacuum for 10–15 min is sometimes helpful.
7. Maintain the sample at ambient temperature and image the cells suspended in agarose.
8. Measure T_1 or T_2 relaxation times from MR images. For example, for measurement of T_2 relaxation time, perform T_2 mapping using a multislice multiecho (MSME) spin-echo sequence (long repetition time such as 3000 ms; slice thickness = 1 mm; matrix = 128×128) with echo times ranging from 10 to 100 ms. Calculate T_2 maps from a single exponential fitting of MRI signal intensities at each echo time point. T_1 relaxation time can also be acquired by MSME spin-echo sequence with various repetition times.

Figure 7.10 Cellular uptake and MRI phantoms. (A) Histogram of Gd^{3+} ion uptake per 3T3 cell versus Gd-SWCNTs (1, 10, and 25 mg mL^{-1}) incubation concentrations at 12, 24, and 48 h time points. Data is presented as mean \pm standard deviation ($n = 3$ per group). (B) Representative T_1 -weighted MR images of untreated and Gd-SWCNT-treated 3T3 cells (4×10^6 cells) dispersed in 0.7% agar. (C) The signal intensity calculated from these images. Lines represent guides for the eyes.

Reprinted with permission from P. K. Avti, E. D. Caparelli and B. Sitharaman, *J. Biomed. Mater. Res., Part A*, 2013, **101**, 3580. Copyright © 2013 Wiley Periodicals, Inc., a Wiley Company.

7.1.4.4 Fluorescence and Radioactive Assays

For multimodal contrast agents, especially fluorescent or radiolabeled probes, measurement of fluorescence intensity or radioactivity is a sensitive method to quantify the efficiency of cellular uptake. These measurements are usually achieved with microplate readers for fluorescence or gamma counters for radioactivity. Due to autofluorescence, fluorescent assays are subject to background issues that radioactive assays are not. Thus, radioactive assays are generally more sensitive. However, some radioactive isotopes have a short half-life and decay quickly. Thus, the measurement must be performed within a short time period. Ionizing radiation also raises safety concerns and is only available for authorized users.

7.1.4.4.1 Fluorescence or Radioactive Assay For Cell Uptake Protocols.

- (A) Fluorescence Assay For Cell Uptake (Adapted From Ref. 102)
- (1) Culture cells in appropriate cell culture medium at 37 °C in a humidified 5% CO₂ atmosphere.
 - (2) Seed cells in 24-well plates at a density of 1×10^5 cells in 1 mL medium per well, and culture at 37 °C in a 5% CO₂ atmosphere for 24 h.
 - (3) Prepare solutions of contrast agent at different concentrations by dissolving contrast agent in culture medium. Pre-warm the medium at 37 °C.
 - (4) Replace cell medium in the plates with fresh medium containing fluorescent contrast agents and incubate at 37 °C in humidified 5% CO₂ for 1–2 hours.
 - (5) Remove the medium with contrast agent, and wash cells three times with pre-warmed PBS complete (with Ca²⁺, Mg²⁺). It is advised to include control samples for cell counting, to confirm that no cells were lost in the handling steps.
 - (6) Lyse cells with 0.2% (w/v) Triton X-100 and quantify the fluorescent intensity of cell lysates by fluorimetry.
- (B) Radioactive Assay for Cell Uptake Protocol (Adapted From Ref. 103)
- (1) Culture cells in appropriate cell culture medium at 37 °C in a humidified 5% CO₂ atmosphere.
 - (2) Distribute cells into 24-well plates at a concentration of 1×10^5 cell mL⁻¹ in 1 mL of appropriate culture medium. For adherent cell lines, incubate cells at 37 °C, 5% CO₂ for 18 to 24 h to allow adherence.
 - (3) Prepare solutions of contrast agent at different concentrations by dissolving contrast agent in culture medium. Pre-warm the medium at 37 °C.
 - (4) Replace cell medium in the plates with fresh medium containing radiolabeled contrast agents and incubate at 37 °C in humidified 5% CO₂ for 30 min to 1 hour.

IMPORTANT: Use of radioactive material must be approved by the university or employer radiation safety board. Ensure that you have appropriate training, shielding and other protection for use, storage, and disposal of radioactive materials. If shielding is not available in a cell incubator (37 °C, 5% CO₂), possible solutions include using CO₂-independent culture medium so that measurements can be performed on the benchtop behind a shielded area and using heating pads underneath culture plates.

- (5) After incubation, remove the radioactive contrast agents and wash cells with 1 mL of pre-warmed PBS (with Ca²⁺, Mg²⁺) three times.
- (6) Detach cells and resuspend cells with culture medium.
- (7) Transfer cell suspension into gamma counting tubes and measure the radioactivity of cells from each well in a well gamma counter.
- (8) Determine the protein content of each cell lysate sample (*e.g.* using Bradford assay) to normalize the data so that the radioactivity difference between samples are not from different numbers of cells.

The interactions between MRI contrast agents and cells are of key importance for the clinical translation of diagnostic agents. In this subchapter, a variety of methods were described to investigate cell toxicity, binding, and uptake properties, each having its own advantages and limitations. With the continual improvement in technology, these methods have become more sensitive and accurate, requiring minimal numbers of cells and reagents to produce results. Some radioactive methods, such as ³H-thymidine for monitoring cell proliferation, have been replaced by fluorescent assays with the same sensitivity and fewer safety concerns. Commercial assay kits also offer researchers easy, fast, and affordable access to most methods. It is important to choose the appropriate method based on the study needs, and give thoughtful consideration of what types of cells to assess. Equally important is the inclusion of appropriate control groups to account for experimental variation and sources of error. Careful assessment of biological effects on *in vitro* targets can help minimize unanticipated problems with *in vivo* testing and is a key step in the product development pathway.

7.2 Distribution, Metabolism, Pharmacokinetics, and Toxicity

ERIC M. GALE* AND PETER CARAVAN*

7.2.1 Rationale for Measuring Distribution, Metabolism, Pharmacokinetics, and Toxicity

The utility and safety of a contrast agent is largely dictated by its distribution, metabolism, and pharmacokinetics profile, as well as its toxicity. An understanding of distribution, metabolism, and pharmacokinetics is critical to interpreting *in vivo* imaging studies. For a targeted contrast agent, the signal generated will be a combination of signal arising from the compound in blood, unbound compound in the tissue of interest, and compound bound to the target in tissue. If the contrast agent has undergone metabolism, there might be more than one species present in blood and tissue. Knowledge of the distribution of the contrast agent, the presence of metabolites, and how the concentrations of all of these are changing with time is key to correct interpretation of imaging data. The pharmacokinetics of a contrast agent will dictate the timing of a contrast enhanced examination.

Figure 7.11 shows T_1 -weighted MR images of a patient with a breast cancer metastasis before and after administration of Gd-diethylenetetraminepentaacetic acetate (DTPA). The brain tumor is obvious on the

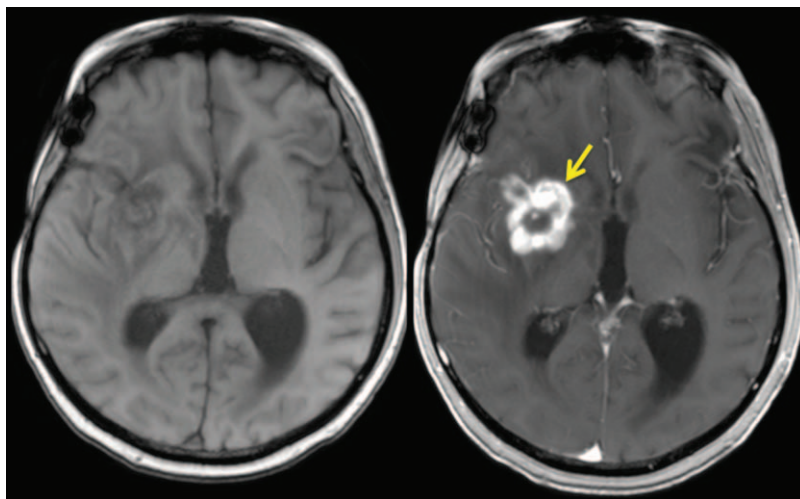


Figure 7.11 T_1 -weighted MR image of a patient with metastatic breast cancer before (left) and after (right) administration of Gd-DTPA. The brain metastasis is apparent in the contrast enhanced image. High contrast of the tumor is observed with an untargeted agent with the contrast arising because of the distribution of the agent. Image courtesy of Dr Gregory Sorensen.

contrast-enhanced image. These images illustrate the importance of distribution in contrast enhanced MRI. Gd-DTPA is not a targeted or activatable contrast agent, and yet it delivers extremely high contrast to this brain tumor. The mechanism of action is breakdown of the blood–brain barrier and leakage of the contrast agent into the extracellular space of the tumor. Other low molecular weight (<10 kDa) contrast agents would likely show similar enhancement of the tumor because of the same mechanism. For targeted or activatable agents, interpretation of the imaging data must take into account the potentially strong signal enhancement arising from distribution.

Distribution, metabolism, and pharmacokinetics studies also inform safety. For Gd^{III}-based compounds or other compounds using non-endogenous metal ions, it is imperative that the metal ion be eliminated from the body to reduce the risk of the delayed onset of toxicity. Distribution will guide the choice of toxicological studies to be performed. For instance, if a compound accumulates in the heart, then additional measures of cardiac toxicity might be required. Knowledge of compound metabolism will also inform toxicity. For instance, the metabolite might elicit a toxic response that is not observed with the parent compound. Subsequent chemical modifications might reduce or eliminate the degree of metabolism and improve the safety profile. The rate and route of elimination might also be used to stratify compounds for potential toxicity concerns. For metal complexes, a longer residency time in the body means more time available for metal ion dissociation. In subjects with renal or hepatic impairment, the rate of elimination might be even slower than in subjects without these conditions. Finally, local, acute, and sub-acute toxicity studies are needed to identify potential toxicities that might occur as a compound is transitioned to human clinical development.

7.2.2 Routes of Administration

There are a number of routes to administer a contrast agent depending on the question to be addressed.

Intravenous: Most commercial, clinical MRI contrast agent formulations are administered intravenously as a bolus injection. For angiographic (blood vessel) imaging applications, imaging is timed to the bolus injection. The contrast agent travels from the vein in the arm into the heart, through the right heart to the pulmonary veins, back to the left heart, and then to the systemic arteries. With careful timing, images are obtained that capture the contrast agent as it travels through the systemic arteries but before the contrast agent has returned to venous circulation, to produce an arteriogram. However, there are applications when slow infusions are advantageous. An infusion is performed with an injector pump and the rate of infusion can be matched to the rate of elimination from the blood. In this way, one can achieve a prolonged steady-state concentration of contrast agent that might be useful for quantitative imaging studies where one

desires a fixed and known concentration in the blood and extracellular space.

Intra-arterial: Direct administration into an artery is generally avoided because of increased bleeding risk, but there are applications where intra-arterial administration is warranted. For kinetic modeling studies of receptor binding, one requires an estimate of the arterial input function, *i.e.* the concentration of probe in the artery perfusing a tissue as a function of time. This input function can be calculated from the dose and rate of intra-arterial administration. Other reasons for intra-arterial injection are to enable the injection of a small amount of contrast agent or to avoid metabolism. These reasons are often associated with studies that might be performed early in development, when the goal is to establish an *in vivo* proof of concept. For instance, direct intra-arterial administration typically requires one tenth the dose of intravenous administration to deliver the same exposure to the organ of interest. For an intravenous injection, contrast agent is diluted in the heart and systemic circulation before reaching the organ of interest, and so a higher dose would be needed with a different injection method. Because contrast agents require large doses, an intra-arterial study might be valuable in a large-animal study when the amounts of contrast agent are limited early in development. In some cases, contrast agent metabolism is rapid in the kidneys and liver, such that the intact, active contrast agent might not reach an organ of interest with a different route of injection. An intra-arterial injection proximal to the organ of interest delivers intact compound before the compound is exposed to the liver and kidneys. Although generally not feasible for routine clinical use, such studies can be valuable to establish proof-of-concept and to justify the synthetic effort to identify new compounds that might be resistant to metabolism.

Oral: Oral formulations for MRI contrast have also been developed for gastrointestinal imaging. Some radiology practices use the high manganese content of blueberries by using blueberry juice as an oral contrast agent.¹⁰⁴ For applications outside the gastrointestinal tract, oral dosing is not practical. Contrast agents are given intravenously at high doses. For oral administration, one would require extremely high doses to deliver enough compound to the blood by intestinal absorption.

Direct administration: In some instances a local administration is used, for instance in MR arthrography a Gd^{III}-based contrast agent is injected directly into the shoulder joint at a low dose to enhance image contrast.¹⁰⁵

Subcutaneous: For lymph node imaging and lymphangiography, compounds have been administered subcutaneously, where the compound pools into lymphatic channels and then moves into the nearest lymph node and beyond.¹⁰⁶

Intrathecal (cisternography): Contrast agents have also been used clinically to look for leakage of cerebral spinal fluid.¹⁰⁷ Here, a low dose of Gd^{III}-based contrast agent is injected into the spinal canal and the cerebral spinal fluid signal is enhanced.

7.2.3 Dose and Exposure

The dose used should ultimately be the minimum dose that provides sufficient diagnostic power. For untargeted agents, an increased dose will typically provide an increased signal. For clinical extracellular fluid contrast agents like Gd-1,4,7,10-tetraazacyclododecane-1,4,7,10-tetraacetate (Gd-DOTA), the standard dose is 0.1 mmol kg^{-1} .¹⁰⁸ The albumin-binding contrast agent MS-325 exhibits a much higher relaxivity than extracellular fluid agents and was approved at a dose of $0.03 \text{ mmol kg}^{-1}$.¹⁰⁸ The liver-targeting agent Gd-EOB-DTPA accumulates in the liver to the extent that a dose of $0.025 \text{ mmol kg}^{-1}$ is sufficient for delayed-phase liver imaging.¹⁰⁸ Other indications might warrant different dosing. As noted above, MR arthrography involves diluting a contrast agent and injecting a small volume into the joint. For brain perfusion, Gd^{III}-based agents are often injected at double dose, 0.2 mmol kg^{-1} , to create a large magnetic susceptibility effect as the contrast agent travels through the brain.¹⁰⁹

Exposure is the cumulative amount of contrast agent that comes into contact with the body and is usually quantified by a measurement of area-under-the-curve for a graph of concentration *versus* time. For instance, with extracellular fluid agents that are excreted solely through the kidneys, exposure can increase if kidney function declines.^{110,111} In a renally impaired subject, the compound is in the body for a longer period of time, and thus the area-under-the-curve is increased relative to the area-under-the-curve measured in a subject with normal renal function administered with the same dose.

For untargeted agents, a higher dose equates to greater contrast. This correlation is not necessarily true of targeted agents. Increasing the dose will increase the signal at the target, but will also increase non-specific background signal. For instance, the collagen-targeted probe EP-3533 was used to assess liver fibrosis, where increased collagen is present in fibrotic liver.¹¹² In that study, four doses of EP-3533 (5, 10, 20, or $40 \text{ } \mu\text{mol kg}^{-1}$) were evaluated in fibrotic mice and control mice that had no fibrosis. Liver signal enhancement increased as the dose increased, but the ability to distinguish fibrotic animals from controls diminished as the dose increased from $10 \text{ } \mu\text{mol kg}^{-1}$ (Figure 7.12). On the other hand, at the lowest dose, there was good discrimination between fibrotic and control animals, but the signal enhancement was low, resulting in a larger relative error. This error was especially a problem in comparing animals with no disease and those with mild fibrosis. A dose of $10 \text{ } \mu\text{mol kg}^{-1}$ could reproducibly discriminate fibrotic animals from controls and was therefore chosen for all of the remaining studies.

7.2.4 Distribution in Tissue

The distribution of intravenously administered MRI contrast agents is largely dependent on the size and formal charge of the agents. Small molecule ($<10 \text{ kDa}$) agents undergo rapid extravasation from the intravascular

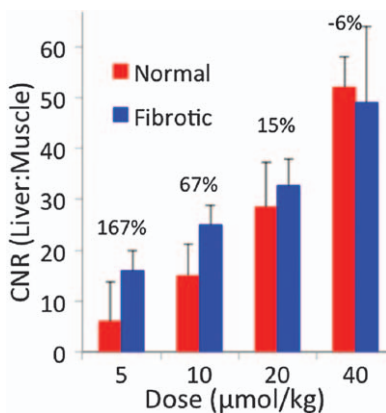


Figure 7.12 Effect of dose on targeted imaging agent. Collagen-targeted EP-3533 is expected to have increased uptake in collagen rich, fibrotic tissue. Cohorts of mice with normal or fibrotic livers were imaged with different doses of EP-3533. The signal observed, expressed as liver-to-muscle contrast-to-noise ratio, increases with increasing dose as expected. However the ability to discriminate normal from fibrotic tissue (expressed as percentage increase) decreases with increasing dose as the target becomes saturated and then increasing the dose increases non-specific signal. Although discrimination is best at the lowest dose, the noise in the data increases because the signal change becomes small. In this study, statistically significant differences were observed at the 10 $\mu\text{mol kg}^{-1}$ dose.

Adapted from *Journal of Hepatology*, Volume 59, B. C. Fuchs, H. Wang, Y. Yang, L. Wei, M. Polasek, D. T. Schühle, G. Y. Lauwers, A. Parkar, A. J. Sinskey, K. K. Tanabe and P. Caravan, Molecular MRI of collagen to diagnose and stage liver fibrosis, 992–998. Copyright (2013), with permission from Elsevier.

compartment into the peripheral tissues.¹¹³ Anionic and neutral agents usually confine to the extracellular spaces, but cationic species can passively diffuse into cells. A neutral small molecule contrast agent with mixed lipophilic and polar character was shown to be capable of crossing cell membranes *via* passive diffusion.¹¹⁴ Large nanoparticle-based agents that exceed 80 nm diameter are too large for extravasation but are rapidly accumulated by macrophages, mainly in the liver and spleen.^{115,116} Contrast agents that are >5 nm in diameter—whether macromolecules, agents bound to plasma proteins, or nanoparticles ranging 5–80 nm in diameter—are too large for extravasation from the blood pool but small enough to elude efficient macrophage uptake. As a result, these compounds tend to have long blood circulation half-lives.^{117,118} The varying distribution profiles of differently sized MRI contrast agents can be exploited for a diverse array of imaging applications.

Small-molecule agents that undergo rapid extravasation and clearance are optimal for the detection and characterization of tissue abnormalities such as lesions, infarcts, or perfusion defects. The pharmacokinetics of a contrast

agent are often altered in pathologic tissue, resulting in delayed washout and prolonged enhancement. For example, solid tumors are characterized by leaky vasculature and a diminished lymphatic drainage system. The practical consequence of this altered physiology is enhanced permeability and retention within the lesion. Small molecule contrast agents will retain in solid tumors for several minutes after the agent has cleared from the blood and adjacent tissue, thus rendering the lesion highly conspicuous in T_1 weighted scans. Higher molecular weight contrast agents that are otherwise too large for extravasation also distribute in tumors due to vascular leakage, albeit on a much slower timescale.

Commercially available MRI contrast agents are anionic or neutral Gd^{III} complexes of $MW < 800$ Da, *i.e.* small-molecule agents. Each agent has at least one indication for imaging lesions in the central nervous system or body.¹⁰⁸ Most clear predominantly *via* the kidneys into the urine. The contrast agent Gd-EOB-DTPA (gadoteric acid) is an anionic complex functionalized with a lipophilic side chain that results in hepatocyte accumulation by an active transport mechanism mediated by organic anion transporting polypeptides.^{119,120} The hepatocyte-accumulated portion of the injected dose is cleared into the bile by multidrug-resistant proteins and excreted in the feces. These hepatocyte-seeking agents are ideally suited for the detection of hepatomas. Organic anion transporting polypeptides are under-expressed on the surfaces of malignant cells compared to normal hepatocytes, and hepatomas are thus rendered hypo-intense relative to normal liver during the hepatocyte distribution phase of the contrast agent.¹²¹

The distribution profile of large (>80 nm) particles is useful for imaging tissues participating in the reticuloendothelial system, such as the lymph nodes and liver. For example, formulations of superparamagnetic iron oxide nanoparticles between 80 and 120 nm have been used to image liver lesions. The nanoparticles accumulate in Kupffer cells that are interspersed in the healthy liver parenchyma but absent from hepatomas.¹²² These particles generate negative contrast (signal loss) in the healthy liver, generating strong positive contrast to visualize the lesions. Similarly, nanoparticles in this size range have been used to identify lymph-node malignancies. Healthy, macrophage-rich lymph nodes accumulate the nanoparticles resulting in signal loss, whereas in tumor-invaded lymph nodes, macrophage content is low and malignant nodes retain MR signal.^{123,124}

The distribution of agents with $MW > 10$ kDa, agents bound to plasma proteins, and nanoparticle agents <80 nm is largely confined to the blood pool. The distribution behavior of these agents is ideally suited for MR angiography. Confinement to the intravascular compartment provides a prolonged time window for contrast-enhanced MR angiography.^{117,118,125} The prolonged imaging window obviates the need for a perfectly timed bolus, allows for multiple tries when imaging uncooperative patients, and enables practitioners to separately image disparate anatomical regions from a single contrast agent injection. The extended imaging window also enables acquisition of relatively high resolution scans. MS-325 (gadofosveset) is a

small-molecule Gd^{III}-based agent designed to bind serum albumin for confinement to the blood pool.^{118,126} MS-325 is highly effective in contrast-enhanced angiography and received an indication from the Food and Drug Administration for contrast-enhanced imaging of the abdominal aorta and iliac arteries. Ferumoxytol is an intravenous iron supplement comprised of superparamagnetic iron oxide nanoparticles sized 17–31 nm. Ferumoxytol has received off-label use in contrast-enhanced MR angiography.¹²⁵

Contrast agents can also be targeted to specific pathologies or tissues. For instance, EP-2104R is a peptide-gadolinium conjugate that targets the protein fibrin present in blood clots.¹²⁷ EP-2104R binds fibrin with greater than 200-fold selectivity over fibrinogen or other plasma proteins. It has been used to detect arterial and venous blood clots in animal models and in human clinical trials.^{128–130}

7.2.4.1 Methods of Quantification

The distribution and clearance of newly developed contrast agents can be tracked qualitatively through dynamic MR imaging after injection. However, it is challenging to quantify agent distribution from the MR data alone. The linear relationship between changes in water relaxation rate and the concentration of the contrast agent suggests that concentration can be estimated from measuring the T_1 or T_2 of the tissue and using relaxivity to convert to concentration. *In vivo*, the MR signal arises from water in vascular, intracellular, extravascular, and extracellular compartments. Contrast agents might not be distributed in all of these compartments, and thus, depending on the rate of water exchange between compartments, the relaxation times of water in a given voxel might be multiexponential.^{131,132} Relaxivity might also change *in vivo* due to protein binding, decreased water content, or increased microviscosity. For example, MS-325 exhibits >5-fold higher relaxivity when bound to albumin at 1.5 T compared to the unbound agent, but the fraction bound to albumin depends on the concentrations of both MS-325 and albumin in the tissue of interest.¹¹⁸

Elemental analysis of tissue is a commonly used method to quantify contrast agent biodistribution, although this method is labor intensive if multiple time points are required. The vast majority of MRI contrast agents use lanthanide or transition metal ions that are either not endogenously present or present at low concentrations, and can thus be detected directly by measuring tissue elemental content. Tissues of interest are harvested and digested for elemental quantitation by inductively coupled plasma mass spectrometry (ICP-MS) or ICP optical emission spectroscopy (ICP-OES). *Ex vivo* elemental analysis is routinely performed to determine the distribution profile of non-specific contrast agents but has also been used to confirm the binding and source of targeted signal enhancement in studies using target-specific contrast agents. For example, the collagen-targeted agent EP-3533 was shown to have increased accumulation in the lungs of mice with pulmonary fibrosis and the *ex vivo* Gd measurement

correlated linearly with the concentration of collagen determined biochemically.¹³³

Ex vivo distribution can be measured with a much higher degree of spatial resolution with laser ablation ICP-MS (LA-ICP-MS) or X-ray fluorescence microscopy. In the LA-ICP-MS experiment, a high-powered laser is raster scanned across a tissue slice releasing a laser-induced aerosol. Sub-micrometer-resolution element mapping is achieved through elemental sampling of the aerosolized tissue. *Ex vivo* LA-ICP-MS was recorded on slices of human ovarian cancer xenografts harvested from a mouse model following intravenous injection of a Gd^{III}-containing liposomal contrast formulation.¹³⁴ LA-ICP-MS quantification of Gd distribution within the lesion revealed higher Gd accumulation in regions histologically identified as highly vascular. In another study, it was shown that T_1 -distribution correlated closely with LA-ICP-MS measurements of local Gd content in samples of articular cartilage incubated with Gd-DTPA *ex vivo*.¹³⁵ X-ray fluorescence microscopy can map elemental content with subcellular resolution and can also provide information regarding elemental speciation. There are a few reports pertaining to the fate and distribution of the metal ions present in MRI contrast formulations. X-ray fluorescence microscopy has been used to map Gd distribution across sections of liver tissue from mice receiving the Gd^{III}-based agent B22956/1.¹³⁶ In another study, X-ray fluorescence microscopy measurements were used to quantify the distribution of gadodiamide, an extracellular agent, and VO(acac)₂, which accumulates in proliferating cells, in a colonic adenoma and in the adjacent tissue excised from a mouse model.¹³⁷

Labeling an MRI contrast agent with a radionuclide is another way to quantify biodistribution. *Ex vivo* distribution can be obtained by gamma counting experiments. In some cases, dynamic *in vivo* biodistribution can be obtained if the radionuclide is suitable for positron emission tomography or single photon emission computed tomography imaging. Radiolabelling can be achieved *via* synthetic manipulation of the ligand to incorporate tracers such as ¹⁴C or ¹⁸F, or often more simply by substituting the metal ion with an appropriate metallo-radionuclide. Radiolabeling with metal ions is often quantitative and circumvents many of the difficulties associated with radiotracer synthesis, such as multistep synthesis and purification using high-performance liquid chromatography.

For Gd^{III}-based compounds, the gamma-emitting isotope ¹⁵³Gd is available, but it has a 240 day half-life. Other lanthanide ions with shorter half-lives like ¹⁷⁷Lu ($t_{1/2}$ = 6.6 days) could be used, but using a surrogate metal ion might result in a different biodistribution. A challenge with using a metallic radionuclide to track distribution is that small impurities of free, unchelated isotope can profoundly alter distribution data. Simple salts of lanthanide ions are strongly retained in the liver, kidneys, and bone after intravenous injection, *e.g.* Gd administered as Gd₂(OAc)₃ is >60% retained over 7 days in rats whereas Gd-DTPA is almost entirely eliminated within 24 h.¹³⁸ Thus, small amounts of unlabeled impurities can have a disproportionate

effect when studying the metal ion retention of rapidly eliminated contrast agents.

Dual label experiments can be performed to determine if the metal is still associated with its ligand. For instance, in the case of the liver-targeting agent Mn-dipyridoxal diphosphate (DPDP), which is largely dissociated *in vivo*, the distribution patterns of the DPDP ligand and Mn^{II} ion were determined through separate analyses following injection of ¹⁴C-labeled ligand and ⁵⁴Mn-labeled complex, respectively.¹³⁹

In vivo biodistribution can be dynamically and quantitatively tracked with positron emission tomography or single photon emission computed tomography imaging. Positron emission tomography offers better temporal resolution (seconds) than single photon emission computed tomography, while for rodent imaging higher spatial resolution can be achieved with single photon emission computed tomography (~0.5 mm for single photon emission computed tomography *versus* ~1 mm for micro-positron emission tomography) if sufficiently high radiochemical doses are used. Manganese has two positron-emitting isotopes, ⁵¹Mn and ⁵²Mn. ¹⁷⁷Lu has been used for single photon emission computed tomography imaging. The most widely available positron emission tomography and single photon emission computed tomography metalloradionuclides are ⁶⁸Ga, ⁶⁴Cu, ¹¹¹In, and ^{99m}Tc. Although ions of these elements form complexes with the same ligands used for Mn^{II}- and Ln^{III}-based contrast agents, assumptions about their *in vivo* stability and equivalent biodistribution might not be valid. For instance, the biodistribution of EP-2104R was assessed by ICP-MS of Gd and compared with ⁶⁴Cu-labeled EP-2104R.¹⁴⁰ To a first approximation, the distributions of Gd and ⁶⁴Cu were similar, but in the liver, there was $1.1 \pm 0.3\%$ of the injected dose of ⁶⁴Cu per gram of liver (%ID g⁻¹) at 2 hours post injection in rats compared with only $0.036 \pm 0.005\%$ for Gd. The liver is a target organ for free copper, and the higher liver uptake with ⁶⁴Cu compared to Gd reflects dissociation of ⁶⁴Cu from EP-2104R and not the distribution of the intact contrast agent.

7.2.5 Pharmacokinetics and Elimination

The MR signal change from a targeted contrast agent in a given voxel will have a contribution from the agent in the blood vessels, the agent bound to its target, and unbound agent in the extracellular space. Similarly, signal arising from an activatable contrast agent will have contributions from the active and inactive forms of the agent and their relative distributions. Therefore, correct interpretation of imaging data requires an understanding of pharmacokinetics.

For example, Figure 7.13 shows long-axis and short-axis images of the heart with a region of hyper-enhancement in the myocardium as denoted by the arrows. The area of enhancement corresponds to myocarditis or infection of the heart muscle. However, these images were not obtained with an infection-specific contrast agent. Rather Gd-DTPA was used. This

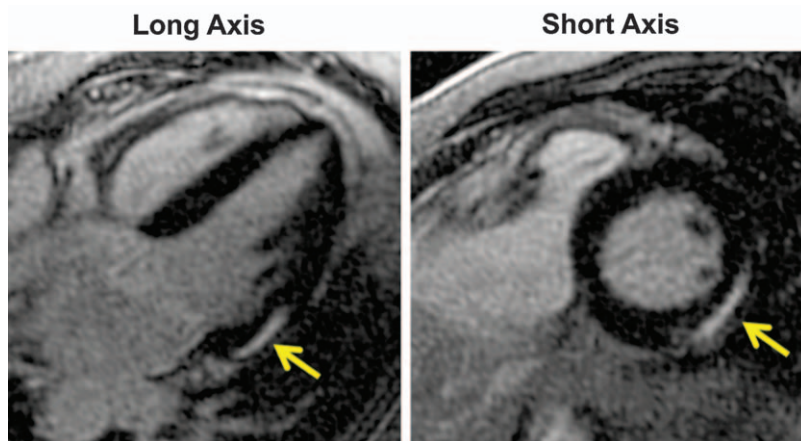


Figure 7.13 Delayed, T_1 -weighted image of the heart after injection of Gd-DTPA. The area of signal enhancement in myocardial wall is due to myocarditis or an infection of the heart. Infection causes necrosis and an increase in extracellular volume. The increased extracellular volume results in an effectively higher concentration of Gd-DTPA in the lesion, while cell death leads to a poorly perfused tissue resulting in a delayed uptake of Gd-DTPA relative to the remote, healthy myocardium. Image courtesy of Dr David Sosnovik, Massachusetts General Hospital.

example highlights the enhanced permeability and retention effect as shown schematically in Figure 7.14. The concentrations of Gd-DTPA in the blood and remote myocardium exhibit an exponential decay. In the infection site, there is some tissue necrosis and slower delivery into this poorly perfused tissue. The poor perfusion also results in slower washout. The infected tissue also has a larger extracellular volume because of tissue necrosis, and this volume results in a higher concentration of an extracellular contrast agent compared to normal myocardium. The image acquisition in Figure 7.13 takes advantage of this difference in tissue pharmacokinetics. An inversion pre-pulse is used that nulls the signal in the normal, remote myocardium. This inversion-prepared T_1 -weighted image serves to amplify contrast between the pathology and normal tissue.

As shown in Figures 7.11 and 7.13, extracellular fluid agents can be used to highlight pathology in cancer and cardiovascular applications by exploiting differences in tissue pharmacokinetics in the presence of pathology. This same phenomenon can be applied to other pathologies, where the disease results in increased endothelial permeability, increased extracellular volume fraction, or both. The behavior of Gd-DTPA was described in these examples in the context of the enhanced permeability and retention effect. The enhanced permeability and retention effect is often attributed to the retention of macromolecules and nanoparticles in tumors. It is the same phenomenon as described in Figure 7.14, except that for nanoparticles the timescale might be hours and for smaller compounds like Gd-DTPA the time scale is minutes.

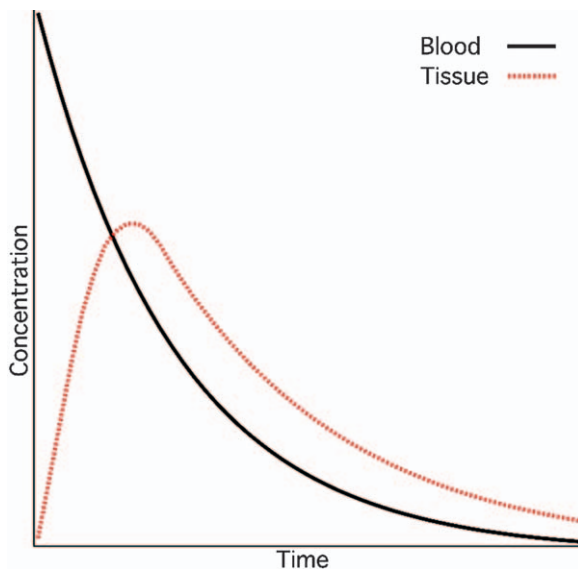


Figure 7.14 Idealized pharmacokinetic curves of an untargeted contrast agent in the blood and in a lesion (tissue) as a function of time. After intravenous injection, the agent is eliminated from the blood with an exponential decay. Uptake in the lesion can be slow if the tissue is poorly perfused, like in tumors and infarcts. After reaching a maximum concentration in the lesion, the agent begins to wash out. If imaging is performed at a delayed time point, positive contrast between the lesion and surrounding tissue can be obtained. This behavior is general: for small molecules like Gd-DTPA, the time scale is in the order of minutes, and for iron oxide nanoparticles, the rates of uptake and clearance are typically hours.

Pharmacokinetics are important in designing experiments with appropriate controls. There are many papers that describe nanoparticles for tumor imaging and compare them to an extracellular fluid agent like Gd-DTPA, using the same imaging time point for the comparison. By imaging hours after injection, there might be accumulation of the nanoparticle, but the small molecule has long since cleared the tumor and the body. This is not an appropriate comparison because if the same tumor was imaged immediately after injection, it would be strongly enhanced by Gd-DTPA with little enhancement by the particle. To compare two compounds at a fixed time point, both compounds should exhibit similar pharmacokinetics. For nanoparticles, it cannot be assumed that the pharmacokinetic behavior is the same just because the size is the same. Different coatings, the presence or absence of targeting groups, and differences in surface charge can change the rate of clearance because of differences in how these particles are recognized by the reticuloendothelial system.¹⁴¹ Therefore, it is imperative to measure pharmacokinetics and confirm that any comparisons in uptake are appropriate.

An appropriate imaging control compound should also be relaxivity-matched. Consider two compounds with similar pharmacokinetics, but one has a 2-fold higher relaxivity than the other. The compound with the higher relaxivity would be expected to provide greater lesion enhancement if the chemical dose is the same. In these situations it is more appropriate to dose these compounds at a ratio where the relaxation effect would be equivalent, *i.e.* the high relaxivity compound would be dosed at half the chemical dose as the low relaxivity compound.

Because most pathologies can be enhanced by a non-specific contrast agent with the appropriate choice of dose, image timing, and image acquisition, a detailed understanding of pharmacokinetics is critical to understanding the *in vivo* behavior of targeted or activatable agents and in designing effective experiments. Targeted or activatable agents might offer the benefit of enhanced signal detection or in specifically quantifying a protein or environmental factor such as pH.^{142,143} In general, a targeted agent is expected to show an initial signal enhancement similar to a relaxivity-matched untargeted agent because the signal change immediately after injection will be due primarily to distribution. As the unbound agent (targeted or untargeted) is washed out of the lesion, some bound targeted agent remains. This retention is illustrated in Figure 7.15. By performing dynamic imaging, it is possible to model the signal in the lesion as a combination of the signal from the agent in the blood, the unbound agent in the lesion, and the bound lesion. Alternatively, it might be possible to wait a period of time

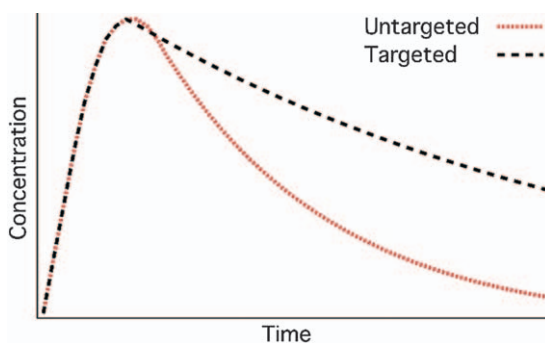


Figure 7.15 Idealized pharmacokinetic curves of an untargeted contrast agent and a targeted contrast agent in a lesion as a function of time. The agents have similar size and blood clearance properties. After intravenous injection, both agents are taken up by the lesion due to distribution. With time, the untargeted agent is washed out of the lesion. Because of specific binding, the targeted agent washes out more slowly. This data can be modeled to estimate lesion permeability, and in the case of the targeted agent, target (receptor) concentration. Alternately, the data can be used to identify a suitable delayed imaging time point where the signal mainly arises from the bound, targeted agent.

where the signal in the lesion is dominated by the bound component and take an image that is largely reflective of the bound agent.

For targeted agents, structurally similar compounds have been used as negative controls to confirm the mechanism of action and quantify the bound agent. For instance, using the collagen-targeted compound EP-3533, an isomer was employed where one of the cysteine groups was changed from L- to D-chirality. This compound had the same relaxivity and pharmacokinetics as EP-3533, but it showed no binding to collagen. These compounds were used to demonstrate the specificity of EP-3533 for cardiac and pulmonary fibrosis.^{133,144} Similarly, the fibrin-targeted agent EP-2104R was used to detect fibrin associated with cancers. EP-2104R employs a cyclic peptide for fibrin recognition. In this study, a linear version of the peptide was made to yield a compound of similar structure and relaxivity but no fibrin affinity.¹⁴⁵ The half-life of EP-2104R was 2.5 times longer in the tumor than its negative control compound. Based on this pharmacokinetic data, a time point of 85 minutes post injection was chosen where non-specific enhancement of the tumor was negligible.

The pharmacokinetic behavior of a contrast agent can depend on a number of factors including molecular weight, interactions with biomolecules or cells, whether the agent undergoes biotransformation, and route of excretion. MRI contrast agents can be cleared through the kidneys into the urine, cleared through the liver into the bile and feces, or cleared *via* both paths. Most contrast agents are designed to distribute and clear rapidly without undergoing biotransformation and thus exhibit relatively uncomplicated pharmacokinetics and clearance profiles.

7.2.5.1 Methods of Quantification

To quantify pharmacokinetics, agent concentration in the blood or tissue of interest is measured as a function of time and an appropriate pharmacokinetic model is fit to the data (see below). Quantification of agent concentration can be performed using high-performance liquid chromatography, elemental analysis, gamma counting, or with imaging techniques like MRI or positron emission tomography. Methods to detect and quantify metabolites are described in Section 7.2.6.

7.2.5.2 Pharmacokinetic Models

Intravenous: Pharmacokinetics of intravenously injected contrast agents are most frequently described by a two-compartment model. The intravenously injected contrast agent moves through a central compartment comprising the blood pool and highly perfused tissues and a peripheral compartment comprising the tissues that are not as strongly perfused. Excretion occurs through the central compartment, as the kidney and liver are highly perfused organs. Clearance from the central compartment generally occurs with

a bi-exponential profile including a distribution phase and an elimination phase as described by eqn (7.2).

$$C(t) = Ae^{-\alpha t} + Be^{-\beta t} \quad (7.2)$$

where $C(t)$ is the concentration of the contrast agent as a function of time; α and β describe the rate of equilibration between the central and peripheral compartments (distribution) and the rate of clearance from the central compartment due to excretion and metabolism (elimination), respectively; and A and B are the corresponding distribution and elimination coefficients. This model is a simplification in that the blood and well-perfused tissues and the entirety of peripheral tissues are combined into two neat compartments. Nonetheless, the two-compartment model is effective and is widely used to describe contrast agent pharmacokinetics. Because intravenous contrast agents are eliminated directly from the central compartment and are generally resistant to biotransformation, detailed pharmacokinetic information can be extrapolated by recording plasma concentration of the relaxor metal ion as a function of time.¹⁴⁶

Higher order compartment models have also been applied to describe contrast agent pharmacokinetics. The agent plasma concentration *versus* time data of intravenous gadopentetic acid in rats was best fit with a three-compartment model comprising central, rapidly equilibrating peripheral, and slowly equilibrating peripheral compartments.¹⁴⁷ The pharmacokinetics of some agents can also be described by a one-compartment model. Intravascular contrast agents exhibit a negligible distribution phase and changing agent concentration in the central compartment can be solely accounted for by elimination. For example, the time-dependence of plasma Fe content following injection of the intravascular agent ferumoxytol is best fit with a monoexponential function describing elimination.¹⁴⁸

The pharmacokinetics of intravenously administered contrast agents can also exhibit a dependence on the magnitude of the injected dose. This occurs in instances when the mechanism responsible for clearance or metabolism of the agent becomes saturated. Dose-dependent pharmacokinetics are more commonly observed in agents that clear *via* transporter-mediated mechanisms or metabolic processing. For example, the pharmacokinetics of ferumoxytol, which is cleared *via* hepatocyte accumulation and metabolic degradation to labile iron, exhibits a strong dependence on injected dose. Similarly, agents such as gadoxetic acid, which accumulates in hepatocytes *via* organic-anion-transporting-polypeptide-mediated transport and is transported into the bile *via* multidrug resistant proteins, also exhibit dose-dependent pharmacokinetics because membrane-transport-protein-mediated transport from the liver to bile is saturable.¹⁴⁹ The effect is less common in agents excreted predominantly by glomerular filtration. Gd-DTPA, which is cleared predominantly *via* glomerular filtration, exhibits dose-independent pharmacokinetics in rats between 0.001 and 1.0 mmol kg⁻¹ injected dose.¹⁴⁷

Protein binding and cellular accumulation can also complicate the pharmacokinetics of contrast agents. The albumin-binding agent MS-325 is cleared from higher mammals (for example, primates and humans) predominantly *via* glomerular filtration, but the elimination half-life decreases with increasing dose because albumin binding becomes saturated. Similarly, MS-325 exhibits a high degree of extravasation when albumin binding saturates; this extravasation is reflected by an increase in experimentally determined apparent volume of distribution (the volume required to dilute the injected dose to the concentration determined in blood plasma) with increasing dose; an ideal blood pool contrast agent would have an apparent volume of distribution equal to the blood volume.¹⁵⁰

Experimentally determined pharmacokinetic parameters can exhibit a dependence on injection rate. Equilibration of extracellular contrast agents between the central and peripheral spaces can occur rapidly with half-lives in the order of seconds. A contrast bolus injected over the course of 3 or 15 s can exhibit profoundly different kinetics. Variance in injection rate can drastically influence the efficacy of MRI examinations to quantify the kinetics of tissue perfusion. Perfusion MRI scans such as dynamic contrast enhanced MRI and dynamic-susceptibility contrast are routinely used to characterize lesions in the central nervous system and cerebrovascular injuries. Dynamic contrast enhanced scans track the pharmacokinetics of contrast agent exchange between the intravascular and lesion extracellular spaces. Physiological parameters that are useful in characterizing lesions can be extrapolated from a properly performed dynamic contrast enhanced examination, including the volume transfer coefficient, lesion extracellular volume, capillary permeability, and the rate of fluid exchange between the plasma and lesion extracellular space. Delivery of a compact bolus provides a dramatic signal change as the agent distributes from arterial blood into the lesion periphery and then clears into venous blood. Dynamic-susceptibility contrast scans utilize the T_2^* effect of a bolus during first passage through cerebral microvasculature. An elongated injection rate results in a diffuse bolus and weakened susceptibility contrast. Figure 7.16 shows the effect of bolus timing on MR signal in the brain. In this study,¹⁵¹ two formulations of gadobutrol were compared: 0.5 and 1 M. The contrast agent was injected at the same rate and dose, but the 1 M formulation was injected in half the volume and thus in half the time. Figure 7.16 shows that the 1 M formulation produced a sharper and deeper signal drop compared to the 0.5 M formulation. The signal drop from the second pass of the contrast agent can also be readily observed with the more compact bolus. The authors concluded that brain perfusion images were superior with the higher concentration formulation that resulted in a significantly larger signal change.

If intravenous delivery of the contrast agent is fast relative to the observed pharmacokinetic parameter, variances in injection rate will manifest more negligibly. For example, an intravenous injection dose of 4 mg Fe per kg of ferumoxytol exhibits a half-life of 14.5 h. The half-life is unchanged across a series of varying injection rates between 90 and 1800 mg Fe per min.¹⁴⁸

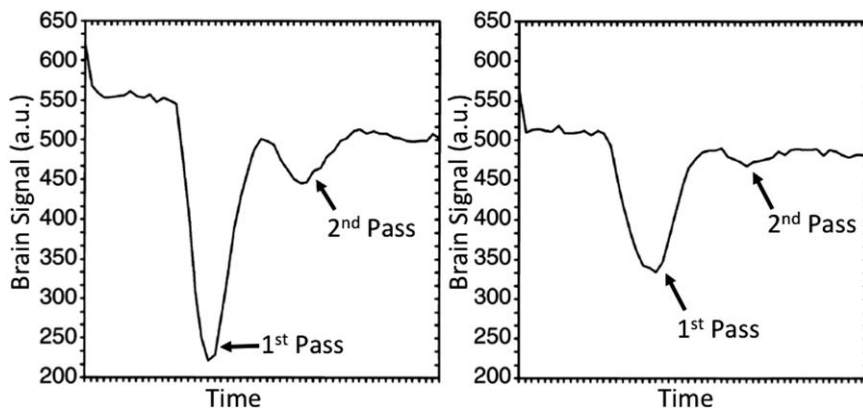


Figure 7.16 Effect of formulation and injection rate on brain signal. Brain signal *versus* time curves for 0.3 mmol kg^{-1} injection of gadobutrol injected at 5 mL per second . Left panel is 28 mL of a 1 M formulation, right panel is 56 mL of a 0.5 M formulation injected into the same human. Although the dose is the same, the smaller volume injection of the higher concentration formulation results in a narrower bolus and a significantly larger signal drop upon first pass of the agent through the brain.

Adapted with permission from Figure 1, B. Tombach, T. Benner, P. Reimer, G. Schuierer, E.-M. Fallenberg, V. Geens, T. Wels and A. G. Sorenson. Do highly concentrated gadolinium chelates improve MR brain perfusion imaging? Intraindividually controlled randomized crossover concentration comparison study of 0.5 versus 1.0 mol/L gadobutrol. *Radiology*, 2003; 226; 880–888. Copyright © RSNA, 2003.

Often, when a pharmacokinetic parameter such as elimination half-life, which is typically in the order of minutes to hours, is experimentally determined from a bolus injection of contrast agent, then the bolus injection can be treated as infinitely fast. However, treatments do exist that factor in the rate of input of injected material into the central compartment.¹⁵²

Intra-arterial: Like intravenous injection, intra-arterial injection provides direct delivery of the contrast agent to the central compartment. Thus, the pharmacokinetics of intra-arterial injected agents can be quantified *via* serial blood sampling and application of the same models discussed above. However, tissue uptake of an agent administered intra-arterially can occur before dilution into the systemic circulation. As a result, the rate of input to venous blood can be dictated largely by the rate at which the agent drains from a given tissue. Generally, intra-arterial injections are best suited for studies aimed at determining the pharmacokinetics of agent uptake and elimination within a specific tissue of interest, rather than systemic distribution and elimination. For example, organ clearance per unit time can be quantified from the difference in plasma concentration of an agent in an artery and veins leading directly to and away from, respectively, the organ.

Oral. Orally administered contrast agents are either passed directly through the digestive tracts and excreted in the feces or absorbed into the

central compartment where clearance occurs as with intravascularly administered agents. Models to describe the pharmacokinetics and clearance of oral contrast agents must include an additional exponential term to describe the absorption of the agent into the central compartment.

Direct, subcutaneous, and intrathecal injection. Contrast agents administered by direct, subcutaneous, or intrathecal injections are eventually carried to the central compartment *via* lymphatic drainage where the agent can be distributed to peripheral tissues or eliminated. An additional term must be modeled to account for input of the locally administered agent to the central compartment.

7.2.6 Metabolism

Contrast agents for MRI are generally comprised of metal complexes and ligand–metal dissociation is an important mode of metabolism in contrast agent development. Dissociated metal ions and ligand components of a contrast agent can pose severe toxicity risk, even if the complex itself is well-tolerated. Contrast agents are of course also subject to the same metabolism (for example, oxidation and enzymatic degradation) as other oral and intravenous pharmaceutical formulations. Therefore, metabolism also must be considered in the design of contrast agents because metabolites can alter relaxivity or pose unforeseen toxicity.

7.2.6.1 Methods of Analysis

Ligand–metal dissociation metabolism is usually the result of transchelation with endogenous metals such as Zn^{II} or Fe^{III} (see Chapters 1.3 and 1.4). One *in vitro* assay to estimate the susceptibility of Gd^{III} -based contrast agents to metal–ligand dissociation involves relaxation rate.^{153,154} In this assay, a contrast agent (2.5 mM) is incubated with ZnCl_2 (2.5 mM), and the relaxation rate is measured as a function of time. Displaced Gd^{III} ions precipitate as insoluble $\text{Gd}_2(\text{PO}_4)_3$, which has a negligible contribution to the water proton relaxation rate. The relaxation rate therefore decreases with precipitation, thus corresponding to the displacement of Gd^{III} . Rate constants are not quantified from this assay due to the heterogeneous nature of the reaction conditions. Rather, the time required to achieve a decrease in relaxation rate of 20% is used as a kinetic index. The kinetic indices of commercially available contrast agents correlate well with the incidences of Gd^{III} -related toxicity.^{155,156} A higher rate of toxicity is reported for more kinetically labile agents.

Although less frequently discussed in the contrast agent literature, contrast agents for MRI that are in development for clinical use must undergo the same metabolic evaluation as other pharmaceuticals. Reaction phenotyping can be performed by *in vitro* enzymatic challenges. For example, reactions against expressed cytochrome P450 enzymes and microsomal preparations are evaluated for pharmaceuticals that display partial or whole

hepatobiliary clearance. The liver microsomal preparations encompass enzymes directly responsible for the metabolism of 90% of marketed pharmaceuticals. Screening for metabolism against cytosolic preparations can also be performed, but this screening is usually not relevant to contrast agents that are generally confined to interstitial tissue spaces.

Stability in blood plasma can be evaluated by analysis of plasma solutions incubated with a contrast agent. Interactions between small-molecule contrast agents and blood proteins can be identified by filtration of plasma solutions of the agent through a low molecular weight cutoff filter.¹⁵⁷ The concentration difference between the unfiltered plasma and the plasma filtrate reflects protein binding.

Contrast agents can also be incubated with live cells, and metabolism can be evaluated in culture medium, lysed cells, or both. Screening against proteolytic degradation is relevant for peptide-based contrast agents or agents that contain amides or esters. *In vitro* metabolism is most commonly detected using high-performance liquid chromatography with UV-visible absorption, fluorescence, mass spectrometric, elemental, or gamma ray detection.

In vivo metabolism is examined by analyzing blood plasma and excreta collected after injection of an agent and by *ex vivo* digestion of tissues. High-performance liquid chromatography methods are commonly used to detect and quantify metabolites. Tandem high-performance-liquid-chromatography-ICP-MS is a particularly valuable method to monitor metabolic stability of contrast agents because of the sensitivity of ICP-MS (~parts per billion). For instance, high-performance-liquid-chromatography-ICP-MS was used to monitor the metabolic degradation of a fibrin-seeking Mn-based contrast agent following injection.¹⁵⁸ Total plasma Mn content was quantified by elemental analysis, and the plasma concentration of the unmetabolized contrast agent was estimated from a calibration curve generated from the injected material. This method detected the presence of both intact agents and a newly formed Mn-containing metabolite that grew in relative abundance throughout the agent's circulatory lifetime (Figure 7.17).

7.2.7 Toxicity

Toxicity can arise from the complex itself, from the metal ion if dissociation occurs, from the ligand if dissociation occurs, or from other metabolites. Before administration to humans, contrast agents must undergo a battery of toxicological tests. Toxicology usually comes later in preclinical development after *in vivo* efficacy has been established. Unless there is a reason to suspect a toxic mechanism, it is generally not advisable to perform toxicity studies early. This is because compounds might fail for other reasons, such as insufficient image enhancement, unfavorable pharmacokinetics, or poor or incomplete elimination of the contrast agent. Once a development candidate has been identified that meets the criteria for efficacy, then toxicology studies begin.

Toxicity studies are performed at high doses of contrast agent. One goal of toxicity testing is to elicit a toxic response in animals such that patients in

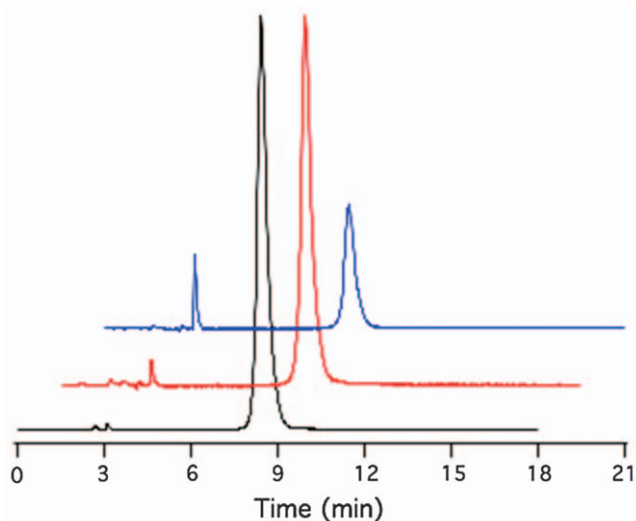


Figure 7.17 High-performance-liquid-chromatography-ICP-MS Mn detection traces depicting *in vivo* metabolism of an Mn-based fibrin-targeted contrast agent. The high-performance liquid chromatography trace of the injected solution is shown in black where the agent elutes at 8.5 min. High-performance liquid chromatography traces of blood plasma drawn 2 and 30 min post-injection are shown in red and blue, respectively. The high-performance liquid chromatography traces reveal formation of an Mn-containing metabolite that elutes at 3.1 min.¹⁵⁸ The relative abundance of the metabolite *versus* intact agent increases between 2 and 30 min. Adapted with permission from E. M. Gale, I. P. Atanasova, F. Blasi, I. Ay and P. Caravan, *J. Am. Chem. Soc.*, 2015, **137**, 15548. Copyright (2015) American Chemical Society.

clinical trials can be carefully monitored to see if there is any clinical manifestation of that toxicity. A second goal is to establish a no observable adverse effects limit. The no observable adverse effects limit should be much higher than the anticipated human dose to provide a high margin of safety.

Compound purity is another consideration in toxicity testing. Because contrast agents are given at relatively high doses and toxicity studies are performed at high multiples of those doses, the amount of impurities administered can be quite high. Toxicity testing should ultimately be performed on the same material that will be used for human studies, or at least have the same impurity profile, such that any toxicity observed is representative.

7.2.7.1 Complex-related Toxicity

Contrast agents are administered at quite high doses. The standard 0.1 mmol kg^{-1} dose equates to about 3.5 grams of the metal chelate administered to an adult patient. However, the clinically approved gadolinium-based contrast agents are well-tolerated. Apart from risk of nephrogenic

systemic fibrosis in renally impaired patients (see below), approved Gd^{III}-based agents have similar safety profiles. The most common adverse events were headache, nausea, taste perversion, and urticaria (hives). Nearly all adverse events with these agents were transient, mild, and self-limiting. Nevertheless, there are reports of serious adverse reactions, including life-threatening anaphylactoid reactions and death. The rate of severe, potentially lethal adverse drug reactions (not including nephrogenic systemic fibrosis) is estimated to lie between in the range of 1 in 200 000 and 1 in 400 000 patient administrations.¹⁵⁹

Although the approved agents show low toxicity, it is important to note that other metal complexes might behave quite differently. For instance, a series of lanthanide-DOTA-tetraamide complexes was studied and it was found that some complexes were well-tolerated, but others were lethal at doses used for MRI. In that series of compounds, the complexes with overall positive charge exhibited acute toxicity, which was subsequently traced to an acute cardiac toxicity.¹⁶⁰

Clinically approved nanoparticle formulations have been used in fewer patients than Gd^{III}-based small molecules. However, nanoparticles are thought to exhibit a higher adverse event rate than approved Gd^{III}-based chelates. For the iron oxide particle ferumoxytol, which is approved as an iron replacement therapy but has been used for MRI applications, serious adverse events occur with higher incidence than with Gd^{III}-based contrast agents.¹⁶¹ Severe hypersensitivity reactions were observed in 0.2% of patients during clinical trials. The US Food and Drug Administration received 79 reports of severe anaphylaxis resulting from intravenous administration of ferumoxytol between 2009 and 2014, including 18 fatal cases. Consequently, the US Food and Drug Administration assigned a boxed warning to ferumoxytol in 2015.¹⁶²

7.2.7.2 Metal-related Toxicity

Metal-related toxicity is a primary toxicity concern in contrast agent design. Any metal ion capable of generating contrast poses a risk for potential toxicity. Although Gd^{III} is not as toxic as heavy metals like lead and mercury, it can be quite toxic at the doses required for MRI. The release of large amounts of Gd^{III} is associated with acute cardiotoxicity. Accumulation of Gd^{III} can result in a delayed onset toxicity termed nephrogenic systemic fibrosis. Nephrogenic systemic fibrosis is a debilitating and potentially lethal disease that is associated with Gd^{III}.^{163,164} In patients with renal impairment, the plasma elimination half-life can increase to days compared to the ~90 minute half-life observed in patients with normal kidney function.^{110,111} This much greater exposure increases the risk of Gd^{III} demetallation. The incidence of nephrogenic systemic fibrosis appears to correlate with decreasing kinetic inertness among the approved contrast agents.^{155,156} Long-term retention of Gd^{III} in the central nervous system of patients receiving multiple contrast-enhanced examinations was recently

discovered, but the safety implications of these findings are unknown at this time.^{165,166}

Divalent manganese is well tolerated and more readily cleared compared to Gd^{III}. The first contrast-enhanced MRI examinations in animals were performed with MnCl₂, and an intravenous contrast agent formulation that released Mn^{II} from its chelator has an indication from the US Food and Drug Administration for liver imaging.^{167,168} However, manganese overexposure also poses substantial risk. Mn^{II} is a Ca^{II} transporter antagonist, and acute Mn^{II} exposure is cardio-depressive.¹⁶⁹ Sub-chronic and chronic overexposure can lead to a neurodegenerative disorder named manganism, which presents similarly to Parkinson's disease.^{169,170}

Intravenous, non-transferrin-bound iron induces oxidative stress and contributes to the pathogenesis of cardiovascular disease and diabetes. However, superparamagnetic iron oxide nanoparticle formulations are robust to the release of intravenous iron. Superparamagnetic iron oxide nanoparticles are metabolized in the liver, liberating labile iron.¹⁷¹ Iron liberated from intravenous formulation can contribute to virulence and hepatotoxicity in liver disease patients. However, the toxicity of superparamagnetic iron oxide nanoparticle is most frequently associated with the intact particles, which can trigger severe anaphylaxis.¹⁶¹

7.2.7.3 Ligand-related Toxicity

Dissociated ligands also pose a toxicity risk. Ligand-related toxicity is generally due to ligand sequestration of essential nutrients. For example, the Food and Drug Administration package insert for a pharmaceutical formulation of DTPA indicated for treatment of heavy metal exposure warns of endogenous metal depletion.¹⁷² Sub-chronic exposures to DTPA are associated with the deterioration of metal-mediated biological functions, including mitosis and hematopoiesis.¹⁷²

Exposure to free ligand also poses the risk of redistribution of previously deposited and settled exogenous metals. It has been shown that a pharmaceutical formulation of ethylenediaminetetraacetic acid (EDTA), which has a US Food and Drug Administration indication for lead remediation, simultaneously leads to increased lead excretion but also lead mobility and redistribution to brain tissue.¹⁷³

7.2.7.4 Toxicity Testing

Toxicity testing is classified as acute (single administration), sub-chronic (repeated administration for a period of 2–4 weeks), or chronic (daily dosing for a period of months). For contrast agents that are typically administered once, only acute and sub-chronic toxicity studies are required to initiate human studies. These toxicity studies are performed in two species: one rodent and one non-rodent. Acute toxicity is assessed in a single ascending dose study, *i.e.* a single dose is administered and different groups of animals

receive an increasing dose up to hundreds of times the intended dose. Acute toxicity testing is performed to identify the no observable adverse effects limit. The no observable adverse effects limit is identified by administering an escalating dose of a pharmaceutical until a toxic effect is observed. Sub-chronic toxicity testing is performed to generate a large exposure to the contrast agent. A high dose, *e.g.* 5–10 times the intended dose, is administered daily for 14 or 28 days.

Toxicity is evaluated by monitoring for mortality, abnormalities, and signs of pain and distress daily. Body weights are recorded as well as food intake. At times of sacrifice, blood and urine are taken and analyzed using standard hematology, coagulation, and clinical chemistry panels. At sacrifice, organs are weighed and tissue samples taken, fixed, and stained for histopathology. A typical design for an acute dose study has three or more groups of animals dosed with a high dose of agent, a control group that is dosed with the injection vehicle (*e.g.* water or saline), and other animals dosed with lower doses of agent. Some of the animals are sacrificed 24 hours after the dose, and the remaining animals have some recovery period, *e.g.* two weeks, before being sacrificed. At the end of the study, the findings from the dose groups are compared to the control group. The sub-chronic toxicity study design is similar except that there is usually only one dose level of agent evaluated.

The excretory organs experience high and prolonged agent exposure and are among the most likely tissues to suffer from agent-induced toxicity. There are a number of clinical chemistry tests to identify toxicity to the kidneys or liver. Elevated blood levels of blood urea nitrogen, creatinine, or inorganic phosphate following agent exposure are ancillary indicators of renal damage. Elevated serum concentrations of alanine aminotransferase, aspartate transaminase, γ -glutamyl transferase, and bilirubin correlate with hepatotoxicity, as does a decrease in serum albumin levels. Sometimes in acute and sub-chronic toxicity studies, blood and tissue are analyzed for the presence of contrast agent. These analyses are similar to those performed in a pharmacokinetic study, but when performed as part of a toxicology study are referred to as toxicokinetics.

7.2.7.5 Other Toxicity Studies

Contrast agents must undergo a number of toxicity screens before clinical use.

Cell toxicity: Cell toxicity studies are usually performed on cells expected to have the greatest exposure to the contrast agent. These are typically kidney cells and hepatocytes. However, targeted agents might accumulate in a specific organ, *e.g.* the heart, and then additional cell toxicity studies would be required. Testing of cell toxicity can provide a time- and cost-effective go or no go screen before carrying an agent to *in vivo* use. This aid in decision making is especially true if the contrast agent is designed to target a specific cell or organ, or if there are chemical reasons to suspect a specific toxicity. Cell-toxicity assays are also useful in determining the underlying source of

unexpected *in vivo* toxicity. For example, if renal toxicity is identified from *in vivo* testing, an agent might undergo *in vitro* toxicity screening against various renal cell types to home in on an underlying toxic effect. See Section 7.1.2. for a discussion of cytotoxicity and methods to measure it.

Local site toxicity: Local site toxicity is generally not severe, and is generally characterized by irritation or swelling. Local site toxicity is assessed *in vivo* via observation of the injection site for several hours after injection.

Allergic reaction or immunogenicity: Allergic reaction is one of the more typical adverse drug reactions associated with MRI contrast agents. Allergenicity can be assayed *in vitro* by monitoring histamine release from mast cells as a function of agent concentration. Animals can be sensitized with contrast agent to determine whether the organism can produce agent-specific antibodies.

Genotoxicity: Genotoxicity testing is another requirement before a contrast agent can be used in humans. It can be identified by screening for clastogenicity (capacity to generate chromosomal aberrations) and mutagenicity.

Blood compatibility: Because contrast agents are directly administered to the blood, it is important to test for compatibility with blood. Typical blood compatibility screens include hemolytic potential (does the compound cause lysis of the red cells?) and coagulation tests (does the compound make the blood more or less prone to clotting?). Contrast agents are often administered at high doses that are hyperosmotic compared to blood. Some hyperosmotic contrast formulations have been known to induce erythrocyte deformations.¹⁷⁴

In this sub-chapter, distribution, metabolism, pharmacokinetics and toxicology were described in the context of why they are important for the development of contrast agents. Methods for measuring distribution, metabolism, pharmacokinetics and toxicity were also described. Understanding of distribution, metabolism, and pharmacokinetics is fundamental to understanding the *in vivo* mechanism of action of a contrast agent, and these properties serve as quantitative metrics that can be used to develop optimized and new contrast agents. Some preliminary measure of distribution, metabolism, and pharmacokinetics should be performed before embarking on *in vivo* imaging efficacy studies. The distribution, metabolism, and pharmacokinetics studies will guide dosing and the timing of imaging. On the other hand, with the exception of cell toxicity, *in vivo* toxicity studies are usually best performed once an optimized contrast agent has been identified and is ready for the next stage of development. *In vitro* toxicity can be used as a relatively low-cost screen, especially if there is existing evidence that a class of compounds might show a toxic effect.

7.3 Practical Aspects of Contrast-enhanced Preclinical MRI

CHRISTIAN T. FARRAR* AND BORIS KEIL

7.3.1 When to Image: Molecular Probe Clearance

For accurate quantification of a bound molecular probe, one needs to wait sufficient time following contrast agent delivery for MRI signal enhancement to be dominated by the bound probe and not the unbound probe. This typically means waiting sufficient time for the unbound probe to largely clear from the blood pool and the MRI signal intensity in the tissue of interest to reach a steady state. For example, shown in Figure 7.18 are probe liver clearance data for EP-3533¹⁴⁴ and CM-101,¹⁷⁵ both collagen-targeted probes used for imaging fibrosis, acquired in Sprague-Dawley rats. CM-101 is cleared from the liver rapidly with a half-life of 5.8 minutes, and steady-state signal intensity on T_1 -weighted images is obtained at approximately 20 minutes post probe injection. In contrast, EP-3533 has a significantly longer liver half-life of 40.9 minutes, and steady-state signal intensity is only achieved after approximately 60 minutes. The time point at which one quantifies the contrast-to-noise ratio, signal-to-noise ratio, or longitudinal relaxation time (T_1) for these two molecular probes will therefore be different.

In addition, the rapid clearance of CM-101 make it difficult to quantify the probe concentration from T_1 relaxation measurements, which can take 10 minutes or more to acquire. This acquisition time is too long relative to the probe clearance rate and therefore the probe is best quantified from the contrast-to-noise ratio of a T_1 -weighted image that can be acquired rapidly. The probe clearance time will therefore not only dictate when to acquire post

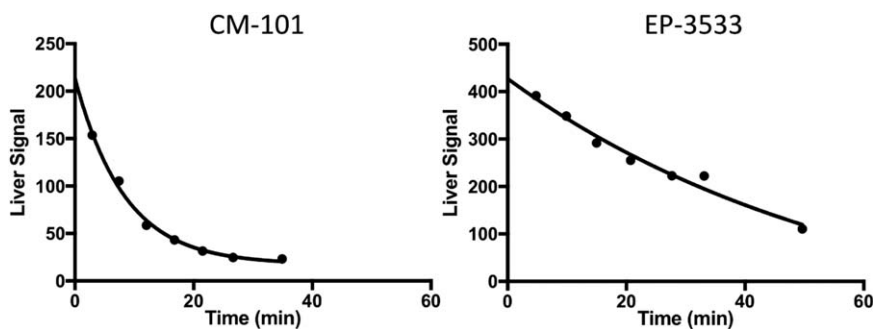


Figure 7.18 Time dependence of the liver signal intensity in bile duct ligated (day 10 post bile duct ligation) Sprague-Dawley rat models of liver fibrosis, acquired at 1.5 Tesla with an inversion-recovery ($TI = 250$ ms) 3D-FLASH MRI sequence, following injection of (left) CM-101 ($t_{1/2} = 5.8$ min) or (right) EP-3533 ($t_{1/2} = 40.9$ min).

contrast images, but also how to quantify the probes. The different methods for probe quantification are discussed in more detail below (Section 7.3.2).

7.3.1.1 *Dependence of Probe Clearance on Temperature and Anesthesia*

Both body temperature and anesthesia will effect cardiac output and hence probe clearance. Therefore, care must be taken to maintain a constant body temperature and a constant depth of anesthesia. For example, the longitudinal relaxation rate changes (ΔR_1) observed 60 minutes after injection of EP-3533 for two different rat liver fibrosis studies that were performed with different anesthesia depth as quantified by respiration rate are shown in Table 7.5. The studies were performed on the same MRI scanner with the same radio-frequency coil and EP-3533 dose. However, the two studies reported different ΔR_1 values for both control and severely fibrotic animals. Inductively coupled plasma mass spectrometry verified this difference upon *ex vivo* quantification of the liver tissue Gd content, where higher Gd content was observed consistently in one of the two studies even in the control animals of the study. The only differences between the studies were the depth of anesthesia and the rat strain used: the two studies maintained average respiration rates of 60 ± 5 breaths per minute in CD rats and 45 ± 5 breaths per minute in Wistar rats. This example points to the importance of respiratory monitoring for maintaining a consistent depth of anesthesia and hence probe clearance. Body temperature can have a similar effect on agent clearance and hence image contrast. Temperature and anesthesia affect not only probe clearance but also measured relaxation rates.¹⁷⁶ The R_1 longitudinal relaxation rate is sensitive to molecular motion^{177,178} and is hence sensitive to temperature.

7.3.1.2 *Effect of Vascular Perfusion and Permeability on Probe Delivery and Retention*

Vascular perfusion and permeability also affect quantification of molecular targets. For example, tumors typically exhibit elevated vascular permeability and extravascular-extracellular space leading to leakage and non-specific retention of probe in the extravascular-extracellular space for long periods of time. Elevated R_1 relaxation rates and Gd concentrations have been

Table 7.5 Liver Gd content and ΔR_1 measured in control and severely fibrotic rat liver models.

Liver model	Respiration rate = 60 ± 5 bpm ¹⁷⁵		Respiration rate = 45 ± 5 bpm ¹⁸⁸	
	[Gd] (nmol g ⁻¹)	ΔR_1 (s ⁻¹)	[Gd] (nmol g ⁻¹)	ΔR_1 (s ⁻¹)
Control	33.3 ± 4.7	0.44 ± 0.15	40.1 ± 3.2	0.73 ± 0.04
Fibrotic	44.6 ± 7.4	0.89 ± 0.27	51.3 ± 7.1	1.24 ± 0.22

measured in brain tumors long (>2 hours) after receiving non-targeted Gd^{III}-based contrast agents, indicating that even non-targeted probes can remain trapped in the extravascular-extracellular space of tumors for long periods of time.^{179,180} It is therefore critical to validate the specificity of targeted probes with non-targeted control probes. Conversely, diseases in which the tissue might be poorly perfused will lead to relatively low amounts of probe reaching target sites. For example, tumors with highly necrotic, avascular cores can demonstrate little enhancement following targeted contrast agent injection despite an abundant amount of molecular target being present.

7.3.2 How to Image: MRI Methods for Probe Quantification

7.3.2.1 T_1 -shortening Contrast Agents

For T_1 -shortening contrast agents, the change in longitudinal relaxation rate ($R_1 = 1/T_1$) after contrast agent injection is linearly proportional to the contrast agent concentration [eqn (7.3)].

$$\Delta R_1 = r_1[CA] \quad (7.3)$$

Measurement of R_1 pre- and post-contrast agent, therefore, enables direct quantification of probe concentration. Eqn (7.3) is valid under conditions of fast water exchange between different tissue compartments, so that the tissue can be described as a single compartment characterized by a single R_1 . However, in some situations, slow exchange of water between the extracellular and cellular compartments leads to a non-linear dependence of R_1 on contrast agent concentration, where the tissue can no longer be treated as a single compartment with a single R_1 .^{181,182} Therefore, if R_1 data are not well-fit by a single exponential, it is likely that a more complicated modeling of the relaxation data, including exchange kinetics, will be required to obtain accurate measurements of the concentration of the contrast agent.^{181,182}

Relaxation rate can be quantified using a variety of MRI methods. The three most commonly used methods are the inversion-recovery, variable repetition time (TR), and variable flip-angle methods, which are discussed in more detail below. The inversion-recovery method for R_1 mapping tends to be more accurate, but takes longer (many minutes) to acquire. The variable flip-angle method is faster, but less accurate. Finally, a simple analysis of the change in contrast-to-noise ratio or signal intensity ratio pre- and post-probe injection can provide a relative measurement of the probe concentration.

7.3.2.1.1 Quantification of R_1 Relaxation Rate with Inversion-recovery MRI.

In an inversion-recovery sequence, a 180° radio-frequency pulse inverts the magnetization and the MRI signal is sampled at various inversion-recovery delay times (TI) after the inversion pulse (Figure 7.19, left). The MRI signal intensity will recover exponentially back to equilibrium following the inversion pulse with time constant T_1 (Figure 7.19, right). The signal intensity (S) as a function of inversion-recovery time (TI)

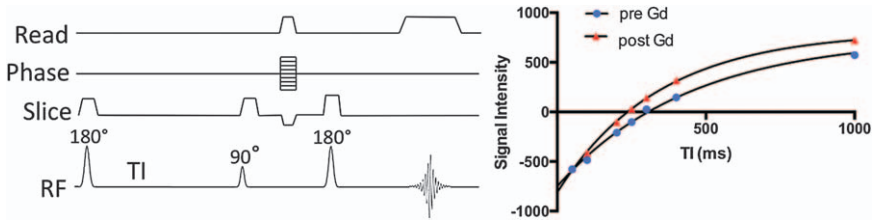


Figure 7.19 (Left) Generic inversion-recovery pulse sequence. (Right) Pre- and post-contrast liver signal intensity in a Sprague-Dawley rat injected with EP-3533 as a function of the inversion-recovery time (T_I). The post contrast images were acquired ~ 60 minutes following the injection of contrast agent.

can be fit by eqn (7.4), where T_I = inversion-recovery time, T_R = repetition time, T_1 = spin-lattice relaxation time, α = flip angle of the inversion pulse (ideally 180°), and S_0 = equilibrium magnetization signal.

$$S = S_0[1 - \cos(\alpha)e^{-T_R/T_1} + (1 - \cos(\alpha))e^{-T_I/T_1}] \quad (7.4)$$

The advantage of the inversion-recovery method is that it is not sensitive to errors in the inversion flip angle and provides accurate R_1 measurement for even arbitrary inversion pulse flip angles. However, the inversion-recovery method is typically slow and acquisition times of 10 minutes or more are common.

7.3.2.1.2 Quantification of R_1 Relaxation Rate with Variable Repetition Time (T_R). The R_1 relaxation rate can also be determined using a partial saturation recovery method in which a series of images is acquired with different repetition times (T_R). The signal intensity (S) as a function of repetition time can be fit using eqn (7.5), where T_R = repetition time, T_1 = spin-lattice relaxation time, and S_0 = equilibrium magnetization.

$$S = S_0(1 - e^{-T_R/T_1}) \quad (7.5)$$

Optimal T_R values should range between a T_1 -weighted image with $T_R \leq T_1$ and a proton-density-weighted image with $T_R > 3T_1$. While somewhat faster than the inversion-recovery method, the accuracy is more sensitive to errors in the 90° excitation pulse flip angle. The homogeneity of the B_1 magnetic field generated by the radio-frequency coil for exciting the nuclear spins can vary greatly over a subject and depends on the type and design of the radio-frequency coil used (Section 7.3.6). Different parts of the sample might therefore see different actual flip angles than the nominal value set in the sequence protocol.

7.3.2.1.3 Quantification of R_1 Relaxation Rate with Variable Flip Angle MRI. The R_1 relaxation rate can be quantified from images acquired with different radio-frequency flip angles.¹⁸³ The signal intensity (S) as a function of repetition time (T_R), longitudinal relaxation time (T_1) and

radio-frequency flip angle (α) is given by eqn (7.6), which can be rearranged into a linear equation of the form $Y = mX + C$ [eqn (7.7)], with $Y = S/\sin(\alpha_n)$, $X = S/\tan(\alpha_n)$, and the slope given by $m = e^{-T_R/T_1}$. T_1 can therefore be determined from the slope of a plot of $S/\sin(\alpha_n)$ versus $S/\tan(\alpha_n)$ for images acquired with two different flip angles (α_n) as given by eqn (7.8).

$$S = S_0 \frac{1 - e^{-T_R/T_1}}{1 - \cos(\alpha)e^{-T_R/T_1}} \quad (7.6)$$

$$\frac{S}{\sin(\alpha_n)} = m \frac{S}{\tan(\alpha_n)} + S_0(1 - m) \quad (7.7)$$

$$T_1 = \frac{-T_R}{\ln(m)} \quad (7.8)$$

The variable flip angle method has the advantage that R_1 maps can be generated quickly because only two images with different flip angles are required. However, the accuracy of the method depends on having accurate flip angles and hence is sensitive to errors in the B_1 field.¹⁸⁴ The variable-flip-angle method, while faster, is therefore typically not as accurate as the inversion-recovery method.

7.3.2.1.4 Quantification of Contrast-to-noise Ratio and Signal Intensity Ratio. Finally, the change in contrast-to-noise ratio, signal intensity ratio, and signal-to-noise ratio pre- and post-injection of contrast agent can be used to provide a relative measure of probe concentration. While not an absolute measure of probe concentration, these metrics have the advantage that only a single image is required and the dynamic signal intensity changes induced by the contrast agent can be sampled rapidly providing information on probe clearance (Figure 7.18). While the signal-to-noise ratio is useful for quantifying probe clearance, it does not provide information regarding the specificity of the targeted probe because initially many tissues enhance following probe injection due to non-specific circulation of the probe. In contrast, the contrast-to-noise ratio between the tissue of interest and a reference tissue such as a muscle can provide information on target specificity, with increased enhancement of the target tissue relative to the reference tissue. Similarly, the signal intensity ratio between a target and reference tissue can provide information regarding specificity, where potential differences in noise are accounted for by normalizing with the reference tissue signal intensity.

When quantifying changes in signal-to-noise ratio, contrast-to-noise ratio, and signal intensity ratio, it is important to ensure that the receiver gain is the same for all pre- and post-contrast images. Typically, the first pre-contrast image is acquired with automated receiver gain adjustment. All following images are then acquired without automated receiver gain

adjustment, and the receiver gain is instead set manually to the same value as the pre-contrast images.

7.3.2.2 T_2 - and T_2^* -based Contrast Agents

For T_2 - and T_2^* -based contrast agents, such as iron-oxide nanoparticles, the change in transverse relaxation rate measured with a spin-echo sequence ($R_2 = 1/T_2$) or gradient echo sequence ($R_2^* = 1/T_2^*$) after contrast agent injection also scales linearly with the concentration of contrast agent [eqn (7.9)].

$$\Delta R_2 = r_2[CA] \quad (7.9)$$

For iron-oxide contrast agents, eqn (7.9) should be valid even for cases where water exchange between tissue compartments is not in the fast exchange limit because the spatial extent of the susceptibility field gradients generated by iron-oxide nanoparticles is typically much larger than the size of the tissue compartments.

The T_2 or T_2^* relaxation times can be quantified from a series of spin-echo or gradient echo images, respectively, acquired with different echo times (T_E), where the signal intensity (S) decreases exponentially as a function of T_E , as given by eqn (7.10).

$$S = S_0(1 - e^{-T_R/T_1})e^{-T_E/T_2} = Ae^{-T_E/T_2} \quad (7.10)$$

A minimum of three echo times is required for T_2 or T_2^* fitting, but typically 10–20 echo times are acquired. The first echo time (T_{E1}) should be short relative to the expected T_2 relaxation time ($T_{E1} \ll T_2$), and the final echo time (T_{Ef}) should be at least 1–2 times the T_2 relaxation time ($T_{Ef} \geq T_2$). Because a series of images is acquired with different echo times, the magnetization recovery time after a 180° refocusing pulse will be variable ($T_{rec} = T_R - T_E/2$). Therefore, for accurate T_2 measurements, the difference between the repetition time (T_R) and the maximal echo time (T_E^{\max}) should be kept long relative to the T_1 relaxation time, typically $(T_R - T_E^{\max}) > 3T_1$. If T_R is not long enough, images acquired with longer echo times will have artificially decreased signal intensity due to the decreased magnetization recovery time and the measured T_2 will be artificially short.

To speed up the acquisition of the T_2 or T_2^* relaxation data, a multi-echo spin-echo or a multi-echo gradient-echo sequence, respectively, are typically used with a train of 180° refocusing radio-frequency or gradient pulses to enable multiple echo times to be sampled in a single acquisition. However, multi-echo methods have relatively low accuracy due to the signal loss that can occur due to imperfections in 180° refocusing pulses. In addition, stimulated echoes generated in a multi-echo spin-echo sequence (by different combinations of the radio-frequency pulses and spin echoes) will also influence signal decay. In particular, the stimulated echo contribution to the second spin-echo frequently results in signal intensity greater than that observed for the first spin-echo, which contains no stimulated echo

contributions. Therefore the first echo from a multi-echo spin-echo sequence is usually not used for the T_2 fitting.

Quantifying the concentration of a probe from changes in T_2 relaxation time can be complicated by other factors that influence T_2 . First, it can be difficult to distinguish decreased T_2 relaxation times induced by the contrast agent from those induced by magnetic susceptibility artifacts, such as those that occur at air–tissue interfaces. This difficulty can be especially problematic for slowly clearing contrast agents where the pre- and post-contrast images are acquired hours apart from each other, providing time during which scanner drift, subject motion, and other $1/f$ biological noise can complicate image analysis (Section 7.3.6.2). Second, nanoparticle aggregation or compartmentalization in cells can lead to changes in T_2 without changes in actual probe concentration. The dependence of T_2 relaxation time on iron-oxide cluster size and compartmentalization has even been exploited by several groups to generate activatable magnetic switches.^{185,186}

7.3.3 Where to Image: Magnetic Field Strength and Contrast Agent Relaxivity

The longitudinal R_1 relaxation rate of blood and tissue decreases (T_1 increases) with increasing magnetic field strength. Therefore, for a contrast agent with similar relaxivity at different field strengths, the fractional change in relaxation rate ($\Delta R_1/R_1^0$) induced by the probe will be greater at higher fields due to the slower baseline R_1 relaxation rate (R_1^0) at the higher field strength. This situation holds mostly for small, rapidly tumbling, extracellular contrast agents such as Gd-DTPA.¹⁸⁷ However, the relaxivity of contrast agents is not necessarily constant and, in general, depends on field strength, temperature, hydration state, and molecular size.¹⁷⁸ The longitudinal relaxivity (r_1) of targeted contrast agents generally decreases with increasing magnetic field strength.¹⁷⁸ Although this might suggest that MR molecular imaging studies are best performed at lower magnetic fields, this is not always the case. In particular, the advantages of higher signal-to-noise ratio, and hence the ability to acquire higher resolution images, at high field strength can outweigh the limitations of decreased relaxivity of a contrast agent. In addition, the fractional change in relaxation rate, $\Delta R_1/R_1^0$, in some cases is not different at higher fields because both the change in relaxation rate (ΔR_1) and the baseline relaxation rate (R_1^0) decrease with increasing field.

7.3.4 Physiological Monitoring and Image Gating

7.3.4.1 Respiratory Gating and Probe Quantification from Contrast-to-noise Ratio

Body imaging provides several challenges for quantitative imaging of targeted probes. Respiratory-gated images are frequently required to obtain good image quality. The gating of image acquisition, however, results in an

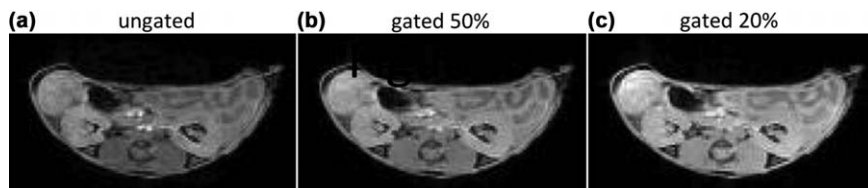


Figure 7.20 2D-FLASH images acquired at 9.4 T of a mouse abdomen with (a) no respiratory gating ($T_R = 11$ ms), (b) respiratory gating and a 50% gating window, and (c) respiratory gating and a 20% gating window.

Table 7.6 Liver, kidney and muscle signal-to-noise ratios (SNR) and liver:muscle and kidney:muscle contrast-to-noise ratios (CNR) for 2D-FLASH images acquired with no respiratory gating or respiratory gated with either a 50 or 20% acquisition gating window.

Acquisition gating	Liver SNR	Kidney SNR	Muscle SNR	Liver: Muscle CNR	Kidney: Muscle CNR
Gated	52.8	113.2	74.6	24.5	38.6
50% gating window	61.9	147.8	116.0	48.5	31.9
20% gating window	62.7	163.6	140.1	54.4	23.5

effective repetition time that can be longer than the ungated sequence repetition time and that will depend on the respiration rate and the length of the gating window. For example, 2D-FLASH images of a mouse abdomen acquired with no gating, a gated acquisition with the gating window constituting 50% of the respiratory period, and a gated acquisition acquired with a 20% gating window are shown in Figure 7.20. The gated acquisitions display progressively higher signal-to-noise ratios for the smaller gating windows as the effective repetition time is increased (Table 7.6).

The contrast-to-noise ratio in different tissues can either decrease or increase depending on the T_1 of the tissues being compared. Tissues with long T_1 relaxation times have larger increases in signal intensity with increasing effective TR than tissues with shorter T_1 relaxation times. This difference is demonstrated in Table 7.6, where the liver:muscle contrast-to-noise ratio increased with increased effective T_R , and the kidney:muscle contrast-to-noise ratio decreased with increased effective T_R . It is therefore crucial to maintain the same respiration rate and acquisition-gating window when acquiring gated images to accurately quantify dynamic changes in signal intensity induced by contrast agents.

7.3.4.2 Respiratory Gating and Probe Quantification from R_1

Maintaining a constant respiratory rate for long periods of time can be challenging. This is especially problematic when trying to quantify the R_1

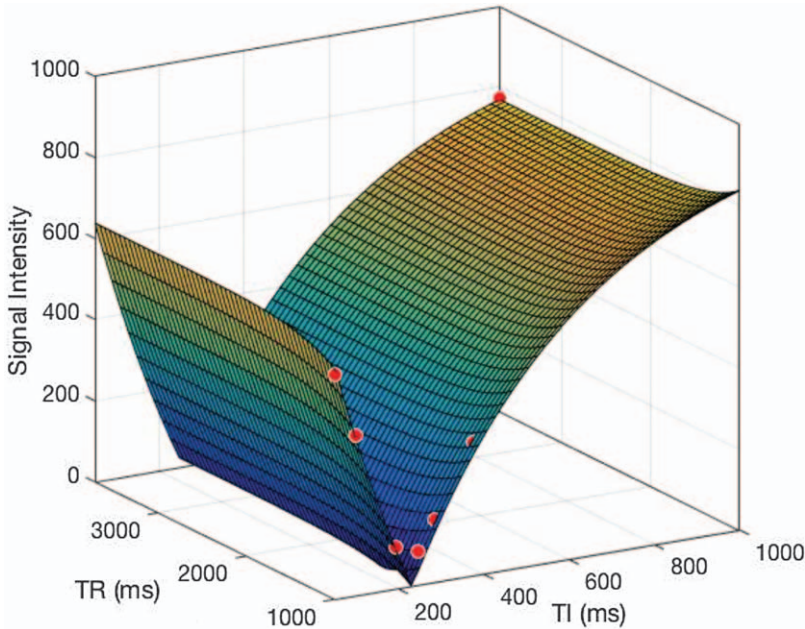


Figure 7.21 Three-dimensional surface fit of the signal intensity (red dots) from a series of inversion-recovery images acquired with different inversion-recovery times (T_I) and repetition times (T_R).

relaxation rate from a series of inversion-recovery images acquired with different inversion-recovery times (T_I), where different images might have been acquired with different respiration rates and, hence, repetition times (T_R). This problem can be overcome by fitting signal intensity as a function of both T_I and T_R ,¹⁸⁸ where instead of fitting a two dimensional curve to the signal intensity as a function of T_I , a three-dimensional surface is fit to signal intensity in which both T_I and T_R can vary (Figure 7.21).

7.3.5 Image Reconstruction and Probe Quantification

The dynamic changes in signal-to-noise ratio following the injection of a contrast agent can be influenced by the type of image reconstruction performed. For example, on a Bruker MRI scanner, the default image reconstruction method uses “absolute” mapping. However, the raw (2dseq) image file reconstructed using absolute mapping (with 16-bit signed integer data format) scales the maximum signal intensity to 32 768 for any given image. Therefore, dynamic changes in signal intensity for a series of images will not be accurately quantified because signal intensity will be scaled differently for each image with the maximum always being 32 768. This issue is demonstrated in Figure 7.22, where images of a phantom acquired with either a 30 or 60° flip angle and a long T_R result in essentially identical signal intensity (Table 7.7) when absolute mapping is used in the image

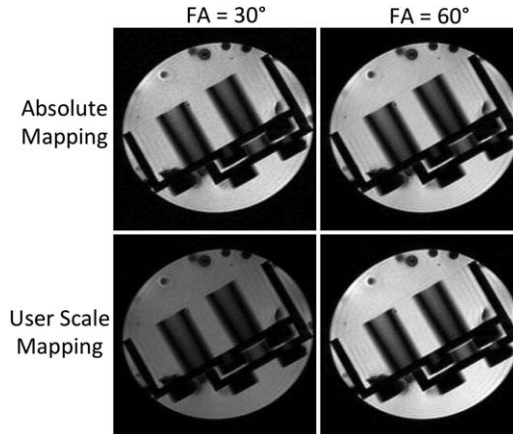


Figure 7.22 2D-FLASH images of a phantom acquired with a T_R of 2 seconds and a radio-frequency flip angle of either 30 or 60° reconstructed using either “absolute” or “user scale” signal intensity mapping. For the user scale image reconstruction, an offset of 0 and a slope of 300 were used.

Table 7.7 2D-FLASH image signal intensity from a region of interest in a phantom acquired with a flip angle (FA) of 30 or 60° and reconstructed with either absolute or user scale signal intensity mapping.

Image reconstruction mapping	Signal intensity (arbitrary units)	
	FA = 30°	FA = 60°
Absolute	23 016	23 698
User scale	4767	8512

reconstruction. In contrast, when the image reconstruction is performed with the same user-defined scale for both images, the signal intensity of the 60° flip angle image is almost twice as large as the 30 flip angle image (Table 7.7), as expected for these radio-frequency flip angles. It is therefore critical to either quantify the contrast-to-noise ratio or signal intensity ratio, where a reference tissue such as muscle normalizes the signal-to-noise ratio, or it is critical to use the same user-defined scaling or user-defined range in the image reconstruction for all images.

7.3.6 MRI Radio-frequency Coils

7.3.6.1 Radio-frequency Coil Design: Signal-to-noise Ratio and B_1 Field Homogeneity

The design of the radio-frequency coil impacts both the image signal-to-noise ratio, in particular the coil filling factor ($\eta = V_{\text{voxel}}/V_{\text{coil}}$), and the B_1 field homogeneity. The three most commonly used MRI coils are the surface, solenoid, and birdcage coils (Figure 7.23). Surface coils have the best

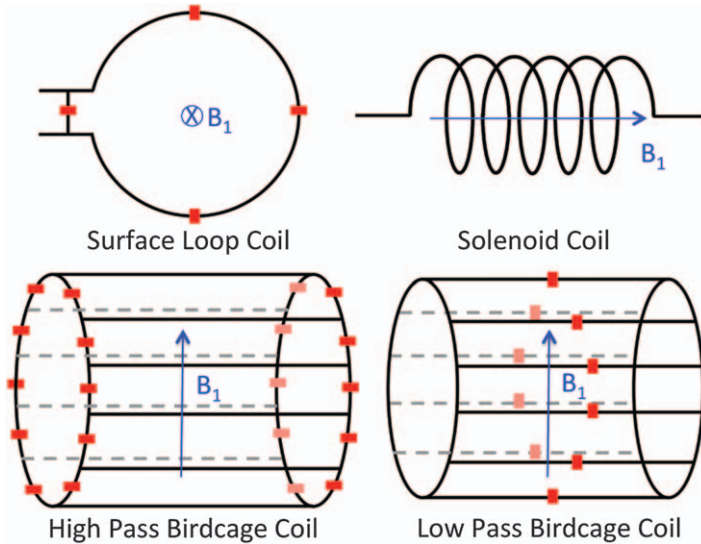


Figure 7.23 Depiction of surface, solenoid, and birdcage radio-frequency coils commonly used in MRI. The red rectangles represent capacitors used for tuning and matching the coils. For MRI, the direction of the radio-frequency coil B_1 field (shown in blue) must be perpendicular to the static B_0 magnetic field.

sensitivity close to the surface of the coil due to the favorable filling factor, but the worst B_1 field homogeneity – the field strength along the axis of a surface coil with radius r is given by eqn (7.11) and drops off with distance d from the surface of the coil as $\sim 1/d^3$.

$$B_1(d) \propto \frac{1}{(r^2 + d^2)^{3/2}} \quad (7.11)$$

Relative to a surface coil, large volume coils (birdcage or solenoid) have relatively good B_1 uniformity over large volumes, but worse filling factors and, hence, sensitivities. The development of phased-array receiver coils is helping overcome these challenges where large volume coils are used for radio-frequency transmission, but an array of surface coils is used for signal detection. The large volume transmit coil provides a uniform B_1 field, and hence radio-frequency flip angle, over the imaging volume. For signal detection, an array of surface coils is used that individually only have localized high sensitivity, but when combined, provide high detection sensitivity over a large volume.

7.3.6.2 Parameters Governing MRI Signal-to-noise Ratio

The signal-to-noise ratio in an MR image is governed by several factors including: (1) subject properties, (2) subject-radio-frequency coil properties,

(3) radio-frequency coil properties, and (4) MR system properties [eqn (7.12)]. Subject properties include the gyromagnetic ratio (γ) and spin quantum number (I) of the nucleus being imaged (typically ^1H), the nuclear spin density (d), the spin-lattice relaxation time (T_1), the spin-spin relaxation time (T_2), and the subject temperature (T). The subject-radio-frequency coil properties include the voxel volume (V_{voxel}), coil volume (V_{coil}), filling factor ($\eta = V_{\text{voxel}}/V_{\text{coil}}$), and the coil ($\rho =$ coil wire electrical resistivity, $r_w =$ radius of radio-frequency coil wire, $\omega_0 =$ proton Larmor frequency, $a =$ constant) and subject ($\sigma =$ subject electrical conductivity, $r_s =$ subject radius, $r_c =$ coil radius, $b =$ constant) resistances. Coil properties include the coil quality factor (Q , coil resonance sharpness) and the radio-frequency coil radius (r_c). MR system properties include the magnetic field strength (B_0), number of signal averages (N), and the system noise figure (F).

$$\text{SNR} = \left[\gamma^2 I(I+1) d \left(\frac{T_2}{T_1} \right)^{1/2} \frac{1}{T} \right] \times \left[V_{\text{voxel}} \eta \left(\frac{a \rho \omega_0^{1/2}}{r_w} + b \sigma \omega_0^2 \frac{r_s^5}{r_c^2} \right)^{-1/2} \right] \\ \times \left[\frac{Q}{r_c} \right] \times \left[\frac{B_0^2 N^{1/2}}{F^{1/2}} \right] \quad (7.12)$$

Significant changes in signal-to-noise ratio can occur over long periods of time (hours) due to scanner drift, subject motion, and other $1/f$ biological noise. Biological $1/f$ noise arises due to fluctuations, or noise, in biological processes. The “noise” in many of these biological processes, such as heart rate and neural processes, has been shown to have a power spectrum (energy or power per frequency interval) given by $1/f$, where f is the frequency of the fluctuation. Such changes in magnetic field, subject motion, and $1/f$ noise can lead to changes in signal-to-noise ratio that are unrelated to the contrast-agent-induced changes in signal-to-noise ratio. This effect can be particularly problematic for slowly clearing contrast agents where pre- and post-contrast images might be acquired as long as 24 hours apart. In these cases, it is important to normalize the signal-to-noise ratio using a reference tissue (such as muscle) and report the contrast-to-noise ratio or signal intensity ratio. In addition, quantification of the relaxation rate is relatively insensitive to changes in signal-to-noise ratio over time and may provide a more robust quantitative probe metric than contrast-to-noise ratio or signal intensity ratio.

7.3.6.3 Estimating Signal-to-noise Ratio

The signal voltage (S) is determined by the rate of change of the magnetic flux (Φ) that passes through the receiver coil as $S = -d\Phi/dt$. Thus, flux is proportional to the magnetization that generates it and is dependent on the relative geometry between the coil and sample. The time-dependence of flux

is a simple sinusoidal function oscillating at the Larmor frequency, $\omega_0 = \gamma B_0$. Because the temporal derivative of $\sin(\omega_0 t)$ is $-\omega_0 \cos(\omega_0 t)$, signal voltage is proportional to $M_0 \omega_0$, where M_0 is the equilibrium magnetization. Because both M_0 and ω_0 are proportional to B_0 , signal intensity increases quadratically with field strength as $S \propto B_0^2$. However, the sensitivity in a given MRI experiment is also determined by its noise power. Noise is induced by the thermal fluctuations in the electrically lossy sample and the electric noise of the coil (cause by coil components, preamplifiers, and receiver chain), as given in eqn (7.13). An MRI coil should be designed such that the body resistance dominates over the coil noise. In this scenario, the body noise voltage follows the fluctuation dissipation theorem¹⁸⁹ and scales linearly with the Larmor frequency ω_0 .¹⁹⁰ Thus, the noise power N has a linear dependence on the field strength, $N \propto B_0$. Dividing the signal by the noise power, the total signal-to-noise performance of a system is therefore proportional to the field strength B_0 , in the case of sample noise dominance:

$$\frac{S}{N} \propto \frac{B_0^2}{B_0} = B_0 \quad (7.13)$$

The signal-to-noise ratio of an MRI image is a fundamental quantitative metric regarding image quality and system performance. The signal is commonly quantified as the average pixel value in a small region-of-interest of the image. However, full characterization of the noise can be difficult and needs some knowledge of the coil design (single channel or array coil) and the image reconstruction method used (for example, image combination methods or parallel imaging). The estimation of signal-to-noise ratios in conventional single channel images assumes that the noise is evenly distributed across the image and that the noise is thermal noise generated by the object. The sources of noise within an object are assumed to be independent and spatially identically distributed. Thus, the noise follows a Gaussian distribution with a zero mean. Because the root-mean-square amplitude of a Gaussian distribution equals its standard deviation, the signal-to-noise ratio of an image can be measured as the ratio of the mean signal from a region of interest located in the object (S_{ROI}) to the standard deviation of the noise (σ_{noise}) measured from a region of interest located outside the object (image background) as given by eqn (7.14).

$$\text{SNR} = \frac{S_{\text{ROI}}}{\sigma_{\text{noise}}} \quad (7.14)$$

7.3.6.3.1 Signal-to-noise Ratios for Magnitude Images. Although the above procedure holds true for complex valued images, it does not tell the whole story because MR images are usually presented as magnitude images. The magnitude operation transforms the Gaussian noise distribution of a complex image into a Rician noise distribution, where the measured

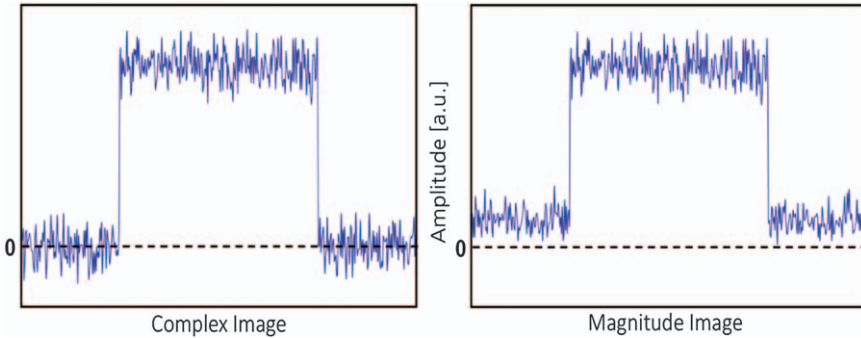


Figure 7.24 Signal amplitude profile along a cross section of a phantom. (Left) The noise in the complex image follows a Gaussian distribution with zero mean. (Right) After the magnitude transformation, the noise in the background (low signal amplitude) has a Rician distribution with a smaller standard deviation than for the complex image. However, the noise in the sample (high signal amplitude) remains unaffected if the signal-to-noise ratio is high enough.

standard deviation of the noise of the magnitude image is smaller than the true standard deviation by a factor of 0.655 (Figure 7.24).¹⁹¹ Therefore, measuring the standard deviation of the background noise of a magnitude image will greatly overestimate the signal-to-noise ratio if the correction factor is not considered.

7.3.6.3.2 Signal-to-noise Ratios for Phased Array Coils. For multi-channel coil applications, unfortunately, the commonly used region-of-interest method for signal-to-noise ratio estimation is not valid. Furthermore, great caution must be used when measuring signal-to-noise ratios in images obtained from array coils. Image noise cannot reliably be acquired from a region of interest in the background of an image formed after the array elements have been combined. This problem arises because the noise amplitude depends on the weightings used to combine the array elements (Figure 7.25). The weights are chosen to maximize the signal-to-noise ratio of the combined pixel. Therefore, the pixel intensity, I , is the weighted sum of the pixel intensities seen by each array element, as given by eqn (7.15):

$$I = \lambda \mathbf{w}^H \mathbf{S} \quad (7.15)$$

where λ is a normalization constant that might vary as a function of location but does not affect the pixel signal-to-noise ratios. The matrix is the complex weighting function, and \mathbf{S} is the measured signal level. If the noise covariance, usually called Ψ , is equal and uncorrelated (Ψ is proportional to the identity matrix) for the different array coils, then $\mathbf{w} = \mathbf{C}$, where \mathbf{C} is the coil sensitivity vector and $I = \lambda \mathbf{C}^H \mathbf{S}$.¹⁹² To create an image with spatially uniform noise levels, λ is chosen as defined by eqn (7.16).

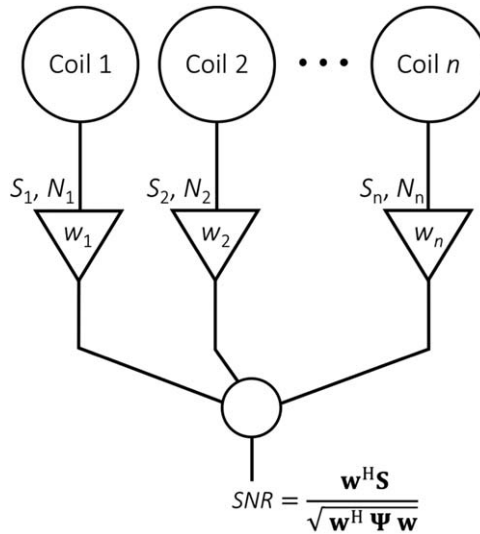


Figure 7.25 Complex-valued weights are chosen to maximize the image signal-to-noise ratio using coil sensitivity profiles and the noise covariance matrix ($\Psi_{ij} = \langle \mathbf{N}_i \mathbf{N}_j^* \rangle$). The problem with calculating the signal-to-noise ratio from a simple noise region of interest in the “black” background area of an image is that usually there is no estimate of the coil sensitivities in this region. This results in a sub-optimum combination of the array elements in this region and noise that is biased by unknown factors.

$$\lambda = (\mathbf{C}^H \mathbf{C})^{-1/2} \quad (7.16)$$

In coil arrays, noise correlations always occur between channels. Taking those coupling effects into account, image combinations are further weighted by the inverse of the noise covariance Ψ and are therefore fully optimized when $\mathbf{w} = \Psi^{-1} \mathbf{C}$. This relationship results in signal intensity with optimal signal-to-noise ratio (SNR) given by eqn (7.17):

$$I^{\text{optSNR}} = \lambda \mathbf{C}^H \Psi^{-1} \mathbf{S} \quad (7.17)$$

where λ is

$$\lambda = (\mathbf{C}^H \Psi^{-1} \mathbf{C})^{-1/2} \quad (7.18)$$

This mathematical treatment can be thought of as “pre-whitening” the signal vector \mathbf{S} prior to the combination (replacing \mathbf{S} with $\Psi^{-1} \mathbf{S}$). If the signal-to-noise ratio is high in each channel, then the coil sensitivity vector \mathbf{C} is well approximated by the signal vector \mathbf{S} and does not need to be measured. Thus, a simple expression can be applied:

$$I^{\text{cov-rSoS}} = \sqrt{\mathbf{S}^H \Psi^{-1} \mathbf{S}} \quad (7.19)$$

which is called the “covariance-weighted root-sum-of-squares” image combination. Given the choice of weights, w_i , the image signal-to-noise ratio (SNR) is given by eqn (7.20).¹⁹²

$$\text{SNR} = \frac{\mathbf{w}^H \mathbf{S}}{\sqrt{\mathbf{w}^H \boldsymbol{\Psi} \mathbf{w}}} \quad (7.20)$$

Following the same substitution process using $\mathbf{w} = \boldsymbol{\Psi}^{-1} \mathbf{S}$ for the combination method, the resulting “covariance-weighted root-sum-of-squares” signal-to-noise ratio is given by eqn (7.21).

$$\text{SNR}^{\text{cov-rSoS}} = \sqrt{\mathbf{S}^H \boldsymbol{\Psi}^{-1} \mathbf{S}} \quad (7.21)$$

Interestingly, the signal-to-noise ratio for the covariance-weighted sum-of-squares image is the same as the image itself when optimally combined. However, the obtained signal-to-noise ratio is still a relative metric and cannot be compared across array coils with different channel counts or across scanners at this point. Assessing the signal-to-noise ratio of an MR image acquired with array coils in a sense of absolute units requires further considerations.

First, the digital filters that define the field of view in the readout direction are typically set slightly broader than the hardware-implemented anti-aliasing filter of the receiver. This setting is done to prevent noise from aliasing into the field of view. Unfortunately, this design choice “colors” the image noise and alters the effective bandwidth of the noise measurement. To de-color the image noise, a “noise equivalent bandwidth” of the receiver needs to be estimated. This is the filter bandwidth of a perfect rectangular filter that would produce the same output noise power.

The second factor accounts for noise averaging by the Fourier transform by normalizing the noise covariance matrix by the number of samples contributing to the image. The final number of image pixels can differ from the number of the acquired k -space samples (*e.g.* oversampling or partial-Fourier acquisition). Thus, the noise covariance matrix must be normalized by the number of k -space samples contributing to each image pixel.

The noise covariance matrix must be normalized by an additional third correction factor of $\sqrt{2}$ that arises because the observation model assumes the noise is real-valued, but the noise is actually complex-valued with independent and identically distributed real and imaginary parts.

A fourth correction factor needs to be applied to account for the incorrect assumption of Gaussian-distributed noise statistics in magnitude images.^{191,193} This correction is the generalization of the Rician-distribution correction applied to array coils.¹⁹⁴ The noise statistics for the final magnitude image from an array follows a non-central chi distribution, with $2n$ degrees of freedom, where n is the number of coils.¹⁹³ Although often considered unimportant for images with signal-to-noise ratios above 10, this

correction factor can be significant for low signal-to-noise ratio images (e.g. diffusion) or highly parallel arrays for typical signal-to-noise ratio levels.

Finally, the use of accelerated parallel image reconstructions further complicates the characterization of image noise. Parallel reconstructions introduce spatially variant noise-enhancement in the image domain, leading to degradation of image signal-to-noise ratios associated with the acceleration factor and the geometry factor (*g*-factor) of the coil.¹⁹⁵ Local noise enhancement occurs from an ill-conditioned linear equation set that lacks orthogonality for a given acceleration scenario.

Notes and References

1. R. I. Freshney, *Culture of Animal Cells: A Manual of Basic Technique and Specialized Applications*, Wiley, Hoboken, NJ, 6th edn, 2010.
2. *Animal Cell Culture Techniques*, ed. M. Clynes, Springer, Berlin, 1998.
3. R. J. Coté, *Aseptic Technique for Cell Culture*, in *Current Protocols in Cell Biology[Online]*, ed. J. S. Bonifacino, M. Dasso, J. B. Harford, J. Lippincott-Schwartz and K. M. Yamada, 2001, ch. 1, Unit 1.3, pp. 1.3.1–1.3.10. <http://onlinelibrary.wiley.com/doi/10.1002/0471143030.cb0103s00/abstract> (last accessed 2016).
4. C. Philippeos, R. D. Hughes, A. Dhawan and R. R. Mitry, *Introduction to Cell Culture*, in *Human Cell Culture Protocols*, ed. R. R. Mitry and R. D. Hughes, Methods in Molecular Biology Series 806, Humana Press, New York, 3rd edn, 2012, ch. 1, pp. 1–13.
5. S. Elmore, *Toxicol. Pathol.*, 2007, **35**, 495.
6. D. Kanduc, A. Mittelman, R. Serpico, E. Sinigaglia, A. A. Sinha, C. Natale, R. Santacroce, M. G. Di Corcia, A. Lucchese, L. Dini, P. Pani, S. Santacroce, S. Simone, R. Bucci and E. Farber, *Int. J. Oncol.*, 2002, **21**, 165.
7. M. O. Hengartner, *Nature*, 2000, **407**, 770.
8. L. Ouyang, Z. Shi, S. Zhao, F.-T. Wang, T.-T. Zhou, B. Liu and J.-K. Bao, *Cell Proliferation*, 2012, **45**, 487.
9. A. R. Collins, *Mol. Biotechnol.*, 2004, **26**, 249.
10. P. Choucroun, D. Gillet, G. Dorange, B. Sawicki and J. D. Dewitte, *Mutat. Res., Fundam. Mol. Mech. Mutagen.*, 2001, **478**, 89.
11. D. T. Loo, *In Situ Detection of Apoptosis by the TUNEL Assay: An Overview of Techniques*, in *DNA Damage Detection In Situ, Ex Vivo, and In Vivo: Methods and Protocols*, ed. V. V. Didenko, Methods in Molecular Biology Series 682, Humana Press, New York, 2011, ch. 1, pp. 3–13.
12. V. M. Heatwole, *TUNEL Assay for Apoptotic Cells*, in *Immunocytochemical Methods and Protocols*, ed. L. C. Javois, Methods in Molecular Biology Series 115, Humana Press, Totowa, NJ, 2nd edn, 1999, ch. 19, pp. 141–148.
13. Apoptosis, Cytotoxicity, and Cell Proliferation [Online], ed. H.-J. Rode, Roche Diagnostics GmbH, Mannheim, Germany, 4th edn, 2008. https://shop.roche.com/wcsstore/RASCatalogAssetStore/Articles/05242134001_05.08.pdf (last accessed 2016).

14. T. Nakagawa, H. Zhu, N. Morishima, E. Li, J. Xu, B. A. Yankner and J. Yuan, *Nature*, 2000, **403**, 98.
15. V. Gurtu, S. R. Kain and G. Zhang, *Anal. Biochem.*, 1997, **251**, 98.
16. Z. Darzynkiewicz, D. Galkowski and H. Zhao, *Methods*, 2008, **44**, 250.
17. E. Bossy-Wetzel and D. R. Green, *Methods Enzymol*, 2000, **322**, 15.
18. L. Scorrano, M. Ashiya, K. Buttle, S. Weiler, S. A. Oakes, C. A. Mannella and S. J. Korsmeyer, *Dev. Cell*, 2002, **2**, 55.
19. C. Hoskins, A. Cuschieri and L. Wang, *J. Nanobiotechnol.*, 2012, **10**, 15.
20. C. C. Berry, S. Wells, S. Charles and A. S. G. Curtis, *Biomaterials*, 2003, **24**, 4551.
21. W. Strober, Trypan Blue Exclusion Test of Cell Viability, in *Current Protocols in Immunology* [Online], ed. J. E. Coligan, B. E. Bierer, P. Brown, J. C. Donovan, A. M. Kruisbeek, D. H. Margulies, E. M. Shevach and W. Strober, 2015, Appendix 3, Unit 3B, A3.B.1–A3.B.3. <http://onlinelibrary.wiley.com/doi/10.1002/0471142735.ima03bs111/abstract> (last accessed 2016).
22. K. H. Jones and J. A. Senft, *J. Histochem. Cytochem.*, 1985, **33**, 77.
23. N. C. L. Zembruski, V. Stache, W. E. Haefeli and J. Weiss, *Anal. Biochem.*, 2012, **429**, 79.
24. G. Fotakis and J. A. Timbrell, *Toxicol. Lett.*, 2006, **160**, 171.
25. T. L. Riss, R. A. Moravec, A. L. Niles, S. Duellman, H. A. Benink, T. J. Worzella and L. Minor, Cell Viability Assays, in *Assay Guidance Manual* [Online], ed. G. S. Sittampalam, N. P. Coussens, K. Brimacombe, A. Grossman, M. Arkin, D. Auld, C. Austin, B. Bejcek, M. Glicksman, J. Inglese, P. W. Inversen, Z. Li, J. McGee, O. McManus, L. Minor, A. Napper, J. M. Peltier, T. Riss, O. J. Trask Jr. and J. Weidner, Eli Lilly & Company and the National Center for Advancing Translational Sciences, Bethesda, MD, 2004, pp. 305–335. <https://www.ncbi.nlm.nih.gov/books/NBK53196/> (last accessed 2016).
26. M. V. Berridge, P. M. Herst and A. S. Tan, Tetrazolium Dyes as Tools in Cell Biology: New Insights into their Cellular Reduction, in *Biotechnology Annual Review*, ed. M. R. El-Gewely, 2005, vol. 11, pp. 127–152.
27. R. D. Petty, L. A. Sutherland, E. M. Hunter and I. A. Cree, *J. Biolumin. Chemilumin.*, 1995, **10**, 29.
28. G. Morstyn, K. Pyke, J. Gardner, R. Ashcroft, A. de Fazio and P. Bhathal, *J. Histochem. Cytochem.*, 1986, **34**, 697.
29. N. Kee, S. Sivalingam, R. Boonstra and J. M. Wojtowicz, *J. Neurosci. Methods*, 2002, **115**, 97.
30. G. Aune, A. K. Stunes, S. Tingulstad, Ø. Salvesen, U. Syversen and S. H. Torp, *Int. J. Clin. Exp. Pathol.*, 2011, **4**, 444.
31. P. A. Hall, D. A. Levison, A. L. Woods, C. C.-W. Yu, D. B. Kellock, J. A. Watkins, D. M. Barnes, C. E. Gillett, R. Camplejohn, R. Dover, N. H. Waseem and D. P. Lane, *J. Pathol.*, 1990, **162**, 285.
32. S. P. M. Crouch, R. Kozlowski, K. J. Slater and J. Fletcher, *J. Immunol. Methods*, 1993, **160**, 81.
33. G. Liu, J. Gao, H. Ai and X. Chen, *Small*, 2013, **9**, 1533.

34. S. A. Kamba, M. Ismail, S. H. Hussein-Al-Ali, T. A. T. Ibrahim and Z. A. B. Zakaria, *Molecules*, 2013, **18**, 10580.
35. T. Decker and M.-L. Lohmann-Matthes, *J. Immunol. Methods*, 1988, **115**, 61.
36. T. Mosmann, *J. Immunol. Methods*, 1983, **65**, 55.
37. M. Mahmoudi, S. Laurent, M. A. Shokrgozar and M. Hosseinkhani, *ACS Nano*, 2011, **5**, 7263.
38. D. Sgouras and R. Duncan, *J. Mater. Sci.: Mater. Med.*, 1990, **1**, 61.
39. N. W. Roehm, G. H. Rodgers, S. M. Hatfield and A. L. Glasebrook, *J. Immunol. Methods*, 1991, **142**, 257.
40. M. G. Stevens and S. C. Olsen, *J. Immunol. Methods*, 1993, **157**, 225.
41. J. O'Brien, I. Wilson, T. Orton and F. Pognan, *Eur. J. Biochem.*, 2000, **267**, 5421.
42. T. Tang, C. Tu, S. Y. Chow, K. H. Leung, S. Du and A. Y. Louie, *Bioconjugate Chem.*, 2015, **26**, 1086.
43. P.-P. Lv, Y.-F. Ma, R. Yu, H. Yue, D.-Z. Ni, W. Wei and G.-H. Ma, *Mol. Pharm.*, 2012, **9**, 1736.
44. J.-B. Qu, H.-H. Shao, G.-L. Jing and F. Huang, *Colloids Surf., B*, 2013, **102**, 37.
45. Z. Chen, J.-J. Yin, Y.-T. Zhou, Y. Zhang, L. Song, M. Song, S. Hu and N. Gu, *ACS Nano*, 2012, **6**, 4001.
46. Z. Sun, V. Yathindranath, M. Worden, J. A. Thliveris, S. Chu, F. E. Parkinson, T. Hegmann and D. W. Miller, *Int. J. Nanomed.*, 2013, **8**, 961.
47. H. Mueller, M. U. Kassack and M. Wiese, *J. Biomol. Screening*, 2004, **9**, 506.
48. E. Ulukaya, F. Ozdikicioglu, A. Y. Oral and M. Demirci, *Toxicol. In Vitro*, 2008, **22**, 232.
49. L. Muskhelishvili, J. R. Latendresse, R. L. Kodell and E. B. Henderson, *J. Histochem. Cytochem.*, 2003, **51**, 1681.
50. S. B. Buck, J. Bradford, K. R. Gee, B. J. Agnew, S. T. Clarke and A. Salic, *BioTechniques*, 2008, **44**, 927.
51. E. Pawelczyk, A. S. Arbab, A. Chaudhry, A. Balakumaran, P. G. Robey and J. A. Frank, *Stem Cells*, 2008, **26**, 1366.
52. D. Muir, S. Varon and M. Manthorpe, *Anal. Biochem.*, 1990, **185**, 377.
53. A. V. Kuznetsov, I. Kehrer, A. V. Kozlov, M. Haller, H. Redl, M. Hermann, M. Grimm and J. Troppmair, *Anal. Bioanal. Chem.*, 2011, **400**, 2383.
54. J. M. Burns, W. J. Cooper, J. L. Ferry, D. W. King, B. P. DiMento, K. McNeill, C. J. Miller, W. L. Miller, B. M. Peake, S. A. Rusak, A. L. Rose and T. D. Waite, *Aquat. Sci.*, 2012, **74**, 683.
55. H. H. Draper and M. Hadley, *Methods Enzymol.*, 1990, **186**, 421.
56. E. T. Ahrens, M. Feili-Hariri, H. Xu, G. Genove and P. A. Morel, *Magn. Reson. Med.*, 2003, **49**, 1006.
57. M. M. Ali, B. Yoo and M. D. Pagel, *Mol. Pharmaceutics*, 2009, **6**, 1409.

58. X. Gao, Y. Cui, R. M. Levenson, L. W. K. Chung and S. Nie, *Nat. Biotechnol.*, 2004, **22**, 969.
59. A. P. Davenport and F. D. Russell, Radioligand Binding Assays: Theory and Practice, in *Current Directions in Radiopharmaceutical Research and Development*, ed. S. J. Mather, Developments in Nuclear Medicine Series 30, Kluwer Academic Publishers, Dordrecht, The Netherlands, 1996, ch. 11, pp. 169–179.
60. P. Chenprakhon, J. Sucharitakul, B. Panijpan and P. Chaiyen, *J. Chem. Educ.*, 2010, **87**, 829.
61. R. De Santis, A. M. Anastasi, V. D'Alessio, A. Pelliccia, C. Albertoni, A. Rosi, B. Leoni, R. Lindstedt, F. Petronzelli, M. Dani, A. Verdoliva, A. Ippolito, N. Campanile, V. Manfredi, A. Esposito, G. Cassani, M. Chinol, G. Paganelli and P. Carminati, *Br. J. Cancer*, 2003, **88**, 996.
62. N. J. Greenfield, *Nat. Protoc.*, 2006, **1**, 2876.
63. Y. Shen, Y.-S. Lee, S. Soelaiman, P. Bergson, D. Lu, A. Chen, K. Beckingham, Z. Grabarek, M. Mrksich and W.-J. Tang, *EMBO J*, 2002, **21**, 6721.
64. A. Schuetz, A. Allali-Hassani, F. Martín, P. Loppnau, M. Vedadi, A. Bochkarev, A. N. Plotnikov, C. H. Arrowsmith and J. Min, *EMBO J.*, 2006, **25**, 4245.
65. J. E. Silpe, M. Sumit, T. P. Thomas, B. Huang, A. Kotlyar, M. A. van Dongen, M. M. Banaszak Holl, B. G. Orr and S. K. Choi, *ACS Chem. Biol.*, 2013, **8**, 2063.
66. C. Tassa, J. L. Duffner, T. A. Lewis, R. Weissleder, S. L. Schreiber, A. N. Koehler and S. Y. Shaw, *Bioconjugate Chem.*, 2010, **21**, 14.
67. E. Amstad, S. Zurcher, A. Mashaghi, J. Y. Wong, M. Textor and E. Reimhult, *Small*, 2009, **5**, 1334.
68. S. Park, G.-H. Kim, S.-H. Park, J. Pai, D. Rathwell, J.-Y. Park, Y.-S. Kang and I. Shin, *J. Am. Chem. Soc.*, 2015, **137**, 5961.
69. G. Scatchard, J. S. Coleman and A. L. Shen, *J. Am. Chem. Soc.*, 1957, **79**, 12.
70. X.-Y. Zhao, P. J. Malloy, A. V. Krishnan, S. Swami, N. M. Navone, D. M. Peehl and D. Feldman, *Nat. Med.*, 2000, **6**, 703.
71. P. Kanakaraj, T.-S. Migone, B. Nardelli, S. Ullrich, Y. Li, H. S. Olsen, T. W. Salcedo, T. Kaufman, E. Cochrane, Y. Gan, D. M. Hilbert and J. Giri, *Cytokine*, 2001, **13**, 25.
72. Z. Liu, W. Cai, L. He, N. Nakayama, K. Chen, X. Sun, X. Chen and H. Dai, *Nat. Nanotechnol.*, 2007, **2**, 47.
73. J. Xie, K. Chen, H.-Y. Lee, C. Xu, A. R. Hsu, S. Peng, X. Chen and S. Sun, *J. Am. Chem. Soc.*, 2008, **130**, 7542.
74. S. A. Mousavi, K. E. Berge, T. Berg and T. P. Leren, *FEBS J*, 2011, **278**, 2938.
75. D. Vercauteren, R. E. Vandenbroucke, A. T. Jones, J. Rejman, J. Demeester, S. C. De Smedt, N. N. Sanders and K. Braeckmans, *Mol. Ther.*, 2010, **18**, 561.

76. T. dos Santos, J. Varela, I. Lynch, A. Salvati and K. A. Dawson, *PLoS One*, 2011, **6**, e24438.
77. S. K. Rodal, G. Skretting, Ø. Garred, F. Vilhardt, B. van Deurs and K. Sandvig, *Mol. Biol. Cell*, 1999, **10**, 961.
78. P. Pattnaik, *Appl. Biochem. Biotechnol.*, 2005, **126**, 79.
79. V. Hodnik and G. Anderluh, *Sensors*, 2009, **9**, 1339.
80. M. J. E. Fischer, Amine Coupling Through EDC/NHS: A Practical Approach, in *Surface Plasmon Resonance: Methods and Protocols*, ed. N. J. de Mol and M. J. E. Fischer, Methods in Molecular Biology Series 627, Humana Press, New York, 2010, ch. 3, pp. 55–73.
81. G. Mikhaylov, U. Mikac, A. A. Magaeva, V. I. Itin, E. P. Naiden, I. Psakhye, L. Babes, T. Reinheckel, C. Peters, R. Zeiser, M. Bogyo, V. Turk, S. G. Psakhye, B. Turk and O. Vasiljeva, *Nat. Nanotechnol.*, 2011, **6**, 594.
82. G. B. Sigal, C. Bamdad, A. Barberis, J. Strominger and G. M. Whitesides, *Anal. Chem.*, 1996, **68**, 490.
83. D. Alvarado, D. E. Klein and M. A. Lemmon, *Cell*, 2010, **142**, 568.
84. B. Segerman, N. Larsson, P. Holmfeldt and M. Gullberg, *J. Biol. Chem.*, 2000, **275**, 35759.
85. J. C. Byrd and R. G. MacDonald, *J. Biol. Chem.*, 2000, **275**, 18638.
86. J. Wang, D. Liu and Z. Wang, *Anal. Methods*, 2011, **3**, 1745.
87. A. I. Ivanov, Pharmacological Inhibition of Endocytic Pathways: Is It Specific Enough to Be Useful? in *Exocytosis and Endocytosis*, ed. A. I. Ivanov, Methods in Molecular Biology Series 440, Humana Press, Totowa, NJ, 1st edn, 2008, ch. 2, pp. 15–33.
88. J. Rejman, V. Oberle, I. S. Zuhorn and D. Hoekstra, *Biochem. J.*, 2004, **377**, 159.
89. T. Kirchhausen, *Annu. Rev. Biochem.*, 2000, **69**, 699.
90. J. A. Swanson and C. Watts, *Trends Cell Biol.*, 1995, **5**, 424.
91. S. G. Crich, L. Biancone, V. Cantaluppi, D. Duò, G. Esposito, S. Russo, G. Camussi and S. Aime, *Magn. Reson. Med.*, 2004, **51**, 938.
92. E. Terreno, S. G. Crich, S. Belfiore, L. Biancone, C. Cabella, G. Esposito, A. D. Manazza and S. Aime, *Magn. Reson. Med.*, 2006, **55**, 491.
93. A. Lesniak, A. Salvati, M. J. Santos-Martinez, M. W. Radomski, K. A. Dawson and C. Åberg, *J. Am. Chem. Soc.*, 2013, **135**, 1438.
94. J. A. Kim, C. Åberg, A. Salvati and K. A. Dawson, *Nat. Nanotechnol.*, 2012, **7**, 62.
95. S. Saito, M. Tsugeno, D. Koto, Y. Mori, Y. Yoshioka, S. Nohara and K. Murase, *Int. J. Nanomed.*, 2012, **7**, 5415.
96. L. L. Stookey, *Anal. Chem.*, 1970, **42**, 779.
97. Y. Zhang, N. Kohler and M. Zhang, *Biomaterials*, 2002, **23**, 1553.
98. K. Müller, J. N. Skepper, M. Posfai, R. Trivedi, S. Howarth, C. Corot, E. Lancelot, P. W. Thompson, A. P. Brown and J. H. Gillard, *Biomaterials*, 2007, **28**, 1629.
99. C. Fan, W. Gao, Z. Chen, H. Fan, M. Li, F. Deng and Z. Chen, *Int. J. Pharm.*, 2011, **404**, 180.

100. P. K. Avti, E. D. Caparelli and B. Sitharaman, *J. Biomed. Mater. Res., Part A*, 2013, **101**, 3580.
101. B. Dawe and T. Erickson, *J. Young Investig.* [Online], 2008, May. <http://www.jyi.org/issue/convection-enhanced-delivery-into-agarose-gel-brain-tissue-phantoms/> (last accessed 2016).
102. C. He, Y. Hu, L. Yin, C. Tang and C. Yin, *Biomaterials*, 2010, **31**, 3657.
103. M. Shokeen, E. D. Pressly, A. Hagooly, A. Zheleznyak, N. Ramos, A. L. Fiamengo, M. J. Welch, C. J. Hawker and C. J. Anderson, *ACS Nano*, 2011, **5**, 738.
104. K. Hiraishi, I. Narabayashi, O. Fujita, K. Yamamoto, A. Sagami, Y. Hisada, Y. Saika, I. Adachi and H. Hasegawa, *Radiology*, 1995, **194**, 119.
105. G. Andreisek, S. R. Duc, J. M. Froehlich, J. Hodler and D. Weishaupt, *AJR, Am. J. Roentgenol.*, 2007, **188**, 1081.
106. M. Notohamiprodjo, R. G. H. Baumeister, T. F. Jakobs, K. U. Bauner, H. F. Boehm, A. Horng, M. F. Reiser, C. Glaser and K. A. Herrmann, *Eur. Radiol.*, 2009, **19**, 2771.
107. O. Algin and B. Turkbey, *AJNR, Am. J. Neuroradiol.*, 2013, **34**, 14.
108. E. M. Gale, P. Caravan, A. G. Rao, R. J. McDonald, M. Winfield, R. J. Fleck and M. S. Gee, *Pediatr. Radiol.*, in press.
109. C. Warmuth, M. Günther and C. Zimmer, *Radiology*, 2003, **228**, 523.
110. S. K. Swan, J. F. Baker, R. Free, R. M. Tucker, B. Barron, R. Barr, S. Seltzer, G. S. Gazelle, K. R. Maravilla, W. Barr, G. R. Stevens, L. J. Lambrecht and J. A. Pierro, *J. Magn. Reson. Imaging*, 1999, **9**, 317.
111. G. Schuhmann-Giampieri and G. Krestin, *Invest. Radiol.*, 1991, **26**, 975.
112. B. C. Fuchs, H. Wang, Y. Yang, L. Wei, M. Polasek, D. T. Schühle, G. Y. Lauwers, A. Parkar, A. J. Sinskey, K. K. Tanabe and P. Caravan, *J. Hepatol.*, 2013, **59**, 992.
113. S. Aime and P. Caravan, *J. Magn. Reson. Imaging*, 2009, **30**, 1259.
114. A. Barandov, B. B. Bartelle, B. A. Gonzalez, W. L. White, S. J. Lippard and A. Jasanoff, *J. Am. Chem. Soc.*, 2016, **138**, 5483.
115. S.-D. Li and L. Huang, *Mol. Pharmaceutics*, 2008, **5**, 496.
116. H. Arami, A. Khandhar, D. Liggitt and K. M. Krishnan, *Chem. Soc. Rev.*, 2015, **44**, 8576.
117. M. D. Hope, T. A. Hope, C. Zhu, F. Faraji, H. Haraldsson, K. G. Ordovas and D. Saloner, *AJR, Am. J. Roentgenol.*, 2015, **205**, W366.
118. P. Caravan, *Acc. Chem. Res.*, 2009, **42**, 851.
119. V. T. Tran and S. Vasanaawala, *Radiol. Clin. North Am.*, 2013, **51**, 599.
120. B. E. Van Beers, C. M. Pastor and H. K. Hussain, *J. Hepatol.*, 2012, **57**, 421.
121. M. K. Seale, O. A. Catalano, S. Saini, P. F. Hahn and D. V. Sahani, *Radiographics*, 2009, **29**, 1725.
122. Y.-X. J. Wang, S. M. Hussain and G. P. Krestin, *Eur. Radiol.*, 2001, **11**, 2319.
123. M. G. Harisinghani, J. Barentsz, P. F. Hahn, W. M. Deserno, S. Tabatabaei, C. H. van de Kaa, J. de la Rosette and R. Weissleder, *N. Engl. J. Med.*, 2003, **348**, 2491.

124. R. A. M. Heesakkers, G. J. Jager, A. M. Hövels, B. de Hoop, H. C. M. van den Bosch, F. Raat, J. A. Witjes, P. F. A. Mulders, C. H. van der Kaa and J. O. Barentsz, *Radiology*, 2009, **251**, 408.
125. N. Ruangwattanapaisarn, A. Hsiao and S. S. Vasanawala, *Pediatr. Radiol.*, 2015, **45**, 831.
126. R. B. Lauffer, D. J. Parmelee, S. U. Dunham, H. S. Ouellet, R. P. Dolan, S. Witte, T. J. McMurry and R. C. Walovitch, *Radiology*, 1998, **207**, 529.
127. K. Overoye-Chan, S. Koerner, R. J. Looby, A. F. Kolodziej, S. G. Zech, Q. Deng, J. M. Chasse, T. J. McMurry and P. Caravan, *J. Am. Chem. Soc.*, 2008, **130**, 6025.
128. E. Spuentrup, M. Katoh, A. J. Wiethoff, E. C. Parsons, Jr., R. M. Botnar, A. H. Mahnken, R. W. Günther and A. Buecker, *Am. J. Respir. Crit. Care Med.*, 2005, **172**, 494.
129. E. Spuentrup, M. Katoh, A. Buecker, B. Fausten, A. J. Wiethoff, J. E. Wildberger, P. Haage, E. C. Parsons, Jr., R. M. Botnar, P. B. Graham, M. Vettelschoss and R. W. Günther, *Invest. Radiol.*, 2007, **42**, 586.
130. E. Spuentrup, R. M. Botnar, A. J. Wiethoff, T. Ibrahim, S. Kelle, M. Katoh, M. Özgun, E. Nagel, J. Vymazal, P. B. Graham, R. W. Günther and D. Maintz, *Eur. Radiol.*, 2008, **18**, 1995.
131. X. Li, W. D. Rooney and C. S. Springer, Jr., *Magn. Reson. Med.*, 2005, **54**, 1351.
132. C. F. Hazlewood, D. C. Chang, B. L. Nichols and D. E. Woessner, *Biophys. J.*, 1974, **14**, 583.
133. P. Caravan, Y. Yang, R. Zachariah, A. Schmitt, M. Mino-Kenudson, H. H. Chen, D. E. Sosnovik, G. Dai, B. C. Fuchs and M. Lanuti, *Am. J. Respir. Cell Mol. Biol.*, 2013, **49**, 1120.
134. N. Kamaly, J. A. Pugh, T. L. Kalber, J. Bunch, A. D. Miller, C. W. McLeod and J. D. Bell, *Mol. Imaging Biol.*, 2010, **12**, 361.
135. A. Sussulini, E. Wiener, T. Marnitz, B. Wu, B. Müller, B. Hamm and J. S. Becker, *Contrast Media Mol. Imaging*, 2013, **8**, 204.
136. R. Delfino, M. Altissimo, R. H. Menk, R. Alberti, T. Klatka, T. Frizzi, A. Longoni, M. Salomè, G. Tromba, F. Arfelli, M. Clai, L. Vaccari, V. Lorusso, C. Tiribelli and L. Pascolo, *Clin. Exp. Pharmacol. Physiol.*, 2011, **38**, 834.
137. D. Mustafi, J. Ward, U. Dougherty, M. Bissonnette, J. Hart, S. Vogt and G. S. Karczmar, *Mol. Imaging*, 2015, **14**, 5.
138. P. Wedeking, K. Kumar and M. F. Tweedle, *Nucl. Med. Biol.*, 1993, **20**, 679.
139. S. O. Hustvedt, D. Grant, T. E. Southon and K. Zech, *Acta Radiol.*, 1997, **38**, 690.
140. R. Uppal, C. Catana, I. Ay, T. Benner, A. G. Sorenson and P. Caravan, *Radiology*, 2011, **258**, 812.
141. E. Ruoslahti, S. N. Bhatia and M. J. Sailor, *J. Cell Biol.*, 2010, **188**, 759.
142. C. Tu, E. A. Osborne and A. Y. Louie, *Ann. Biomed. Eng.*, 2011, **39**, 1335.
143. D. V. Hingorani, A. S. Bernstein and M. D. Pagel, *Contrast Media Mol. Imaging*, 2015, **10**, 245.

144. P. Caravan, B. Das, S. Dumas, F. H. Epstein, P. A. Helm, V. Jacques, S. Koerner, A. Kolodziej, L. Shen, W.-C. Sun and Z. Zhang, *Angew. Chem., Int. Ed.*, 2007, **46**, 8171.
145. R. Uppal, Z. Medarova, C. T. Farrar, G. Dai, A. Moore and P. Caravan, *Invest. Radiol.*, 2012, **47**, 553.
146. S. Gschwend, W. Ebert, M. Schultze-Mosgau and J. Breuer, *Invest. Radiol.*, 2011, **46**, 556.
147. P. Wedeking, S. Eaton, D. G. Covell, S. Nair, M. F. Tweedle and W. C. Eckelman, *Magn. Reson. Imaging*, 1990, **8**, 567.
148. R. Landry, P. M. Jacobs, R. Davis, M. Shenouda and W. K. Bolton, *Am. J. Nephrol.*, 2005, **25**, 400.
149. G. Benness, M. Khangure, I. Morris, A. Warwick, P. Burrows, H. Vogler and H.-J. Weinmann, *Invest. Radiol.*, 1996, **31**, 211.
150. D. J. Parmelee, R. C. Walovitch, H. S. Ouellet and R. B. Lauffer, *Invest. Radiol.*, 1997, **32**, 741.
151. B. Tombach, T. Benner, P. Reimer, G. Schuierer, E.-M. Fallenberg, V. Geens, T. Wels and A. G. Sorenson, *Radiology*, 2003, **226**, 880.
152. R. Lawaczek, G. Jost and H. Pietsch, *Invest. Radiol.*, 2011, **46**, 576.
153. S. Laurent, L. Vander Elst, C. Henoumont and R. N. Muller, *Contrast Media Mol. Imaging*, 2010, **5**, 305.
154. S. Laurent, L. Vander Elst, F. Copoix and R. N. Muller, *Invest. Radiol.*, 2001, **36**, 115.
155. U.S. Food and Drug Administration and Joint Meeting of the Cardiovascular and Renal Drugs and Drug Safety and Risk Management Advisory Committee, *Gadolinium-Based Contrast Agents & Nephrogenic Systemic Fibrosis: FDA Briefing Document*, ucm190850, Washington, DC, 2009. <http://www.fda.gov/downloads/advisorycommittees/committees-meetingmaterials/drugs/drugsafetyandriskmanagementadvisor-ycommittee/ucm190850.pdf> (last accessed 2016).
156. Assessment Report for Gadolinium-Containing Contrast Agents, H-A-31-1097 and European Medicines Agency, London, 2010. http://www.ema.europa.eu/docs/en_GB/document_library/Referrals_document/gadolinium_31/WC500099538.pdf (last accessed 2016).
157. P. Caravan, N. J. Cloutier, M. T. Greenfield, S. A. McDermid, S. U. Dunham, J. W. M. Bulte, J. C. Amedio Jr., R. J. Looby, R. M. Supkowski, W. D. Horrocks Jr., T. J. McMurry and R. B. Lauffer, *J. Am. Chem. Soc.*, 2002, **124**, 3152.
158. E. M. Gale, I. P. Atanasova, F. Blasi, I. Ay and P. Caravan, *J. Am. Chem. Soc.*, 2015, **137**, 15548.
159. J. J. Carr, *Neuroimaging Clin. N. Am.*, 1994, **4**, 43.
160. M. Woods, P. Caravan, C. F. G. C. Galdes, M. T. Greenfield, G. E. Kiefer, M. Lin, K. McMillan, M. I. M. Prata, A. C. Santos, X. Sun, J. Wang, S. Zhang, P. Zhao and A. D. Sherry, *Invest. Radiol.*, 2008, **43**, 861.
161. B. Schiller, P. Bhat and A. Sharma, *Clin. Ther.*, 2014, **36**, 70.
162. (a) M. Crane, New Safety Recommendations for Ferumoxytol, EMA says, *Medscape* [Online], 2014. <http://www.medscape.com/viewarticle/828151>

- (last accessed 2016); (b) A. Ault, FDA Orders Stricter Warnings for Ferumoxoytol (Feraheme), *Medscape* [Online], 2015. <http://www.medscape.com/viewarticle/842309> (last accessed 2016).
163. T. Grobner and F. C. Prischl, *Kidney Int.*, 2007, **72**, 260.
 164. J. L. Abraham, C. Thakral, L. Skov, K. Rossen and P. Marckmann, *Br. J. Dermatol.*, 2008, **158**, 273.
 165. T. Kanda, K. Ishii, H. Kawaguchi, K. Kitajima and D. Takenaka, *Radiology*, 2014, **270**, 834.
 166. T. Kanda, T. Fukusato, M. Matsuda, K. Toyoda, H. Oba, J. Kotoku, T. Haruyama, K. Kitajima and S. Furui, *Radiology*, 2015, **276**, 228.
 167. T. J. Vogl, B. Hamm, B. Schnell, C. McMahon, G. Branding, J. Lissner and K.-J. Wolf, *J. Magn. Reson. Imaging*, 1993, **3**, 51.
 168. G. Jung, W. Heindel, T. Krahe, H. Kugel, C. Walter, R. Fischbach, H. Klaus and K. Lackner, *Magn. Reson. Imaging*, 1998, **16**, 925.
 169. S. L. O'Neal and W. Zheng, *Curr. Environ. Health Rep.*, 2015, **2**, 315.
 170. L. Normandin and A. S. Hazell, *Metab. Brain Dis.*, 2002, **17**, 375.
 171. N. Singh, G. J. S. Jenkins, R. Asadi and S. H. Doak, *Nano Rev.* [Online], 2010, **1**, 5358. <http://www.tandfonline.com/doi/full/10.3402/nano.v1i0.5358> (last accessed 2016).
 172. Pentetate Calcium Trisodium Prescribing Information, FDA Reference ID 3279941, Hameln Pharmaceuticals Ltd, Gloucester, U.K., 2013. http://www.accessdata.fda.gov/drugsatfda_docs/label/2013/021749s008lbl.pdf (last accessed 2016).
 173. D. A. Cory-Slechta, B. Weiss and C. Cox, *J. Pharmacol. Exp. Ther.*, 1987, **243**, 804.
 174. T. Miyazawa, H. Nakagawa and N. Oshino, *Invest. Radiol.*, 1989 **24**, 383.
 175. C. T. Farrar, R. Kennan, E. Gale, I. Ramsay, R. Masia, G. Arora, K. Looby, L. Wei, M. M. Bunzel, C. Zhang, Y. Zhu, T. Akiyama, M. Klimas, S. Pinto, H. Diyabalanage, K. K. Tanabe, V. Humblet, B. C. Fuchs and P. Caravan, CM-101: a MR probe optimized for clinical translation that targets type I collagen for fibrosis detection, *Radiology*, submitted for publication.
 176. S. J. Karlik, J. Fuller and A. W. Gelb, *Acta Radiol., Suppl.*, 1986, **369**, 500.
 177. A. G. Redfield, *Adv. Magn. Reson.*, 1965, **1**, 1.
 178. P. Caravan, C. T. Farrar, L. Frullano and R. Uppal, *Contrast Media Mol. Imaging*, 2009, **4**, 89.
 179. T. Zhang, A. Matsumura, T. Yamamoto, F. Yoshida, T. Nose and N. Shimojo, *AJNR, Am. J. Neuroradiol.*, 2002, **23**, 15.
 180. R. L. Xia, J. A. Davis, Crawford and J. L. Abraham, *Acta Radiol.*, 2010, **51**, 1126.
 181. C. S. Landis, X. Li, F. W. Telang, J. A. Coderre, P. L. Micca, W. D. Rooney, L. L. Latour, G. Véték, I. Pályka and C. S. Springer Jr., *Magn. Reson. Med.*, 2000, **44**, 563.
 182. C. S. Landis, X. Li, F. W. Telang, P. E. Molina, I. Palyka, G. Vetek and C. S. Springer Jr., *Magn. Reson. Med.*, 1999, **42**, 467.

183. E. K. Fram, R. J. Herfkens, G. A. Johnson, G. H. Glover, J. P. Karis, A. Shimakawa, T. G. Perkins and N. J. Pelc, *Magn. Reson. Imaging*, 1987, **5**, 201.
184. M. C. Schabel and G. R. Morrell, *Phys. Med. Biol.*, 2009, **54**, N1.
185. M. Zhao, L. Josephson, Y. Tang and R. Weissleder, *Angew. Chem., Int. Ed.*, 2003, **42**, 1375.
186. J. M. Perez, F. J. Simeone, Y. Saeki, L. Josephson and R. Weissleder, *J. Am. Chem. Soc.*, 2003, **125**, 10192.
187. M. Rohrer, H. Bauer, J. Mintorovitch, M. Requardt and H.-J. Weinmann, *Invest. Radiol.*, 2005, **40**, 715.
188. B. Zhu, L. Wei, N. Rotile, H. Day, T. Rietz, C. T. Farrar, G. Y. Lauwers, K. K. Tanabe, B. Rosen, B. C. Fuchs and P. Caravan, *Hepatology*, 2017, **65**, 1015.
189. H. Nyquist, *Phys. Rev.*, 1928, **32**, 110.
190. A. Macovski, *Magn. Reson. Med.*, 1996, **36**, 494.
191. R. M. Henkelman, *Med. Phys.*, 1985, **12**, 232.
192. P. B. Roemer, W. A. Edelstein, C. E. Hayes, S. P. Souza and O. M. Mueller, *Magn. Reson. Med.*, 1990, **16**, 192.
193. C. D. Constantinides, E. Atalar and E. R. McVeigh, *Magn. Reson. Med.*, 1997, **38**, 852.
194. H. Gudbjartsson and S. Patz, *Magn. Reson. Med.*, 1995, **34**, 910.
195. K. P. Pruessmann, M. Weiger, M. B. Scheidegger and P. Boesiger, *Magn. Reson. Med.*, 1999, **42**, 952.

Subject Index

- 1,4,7,10-tetraazacyclododecane-
 - 1,4,7,10-tetraacetic acid (DOTA), 19–26
- 3,6,9,15-tetra-azabicyclo[9.3.1]pentadeca-1(15),11,13-triene-3,6,9-triacetic acid (PCTA), 26–27
- 6-amino-6-methylperhydro-1,4-diazepinetetraacetic acid (AAZTA), 26–27

- AAZTA. *see* 6-amino-6-methylperhydro-1,4-diazepinetetraacetic acid (AAZTA)
- ab initio* methods, 198–203
- AC magnetic susceptibility, 409–411
- adenosine triphosphate (ATP), 340–341, 514
- anchoring groups, 353–356
- ATP. *see* adenosine triphosphate (ATP)

- B_0 field correction, 304–306
- B_1 field correction, 306
- B_1 field homogeneity, 568–569
- binding interactions, 302–303
- biocompatibility, 482
- biological and *in vivo* methods
 - cell binding
 - competition assay, 525–526
 - overview, 518–520
 - Scatchard analysis, 522–525
 - surface plasmon resonance (SPR), 521–522
 - cell uptake
 - complex-related toxicity, 554–555
 - distribution, metabolism, pharmacokinetics, and toxicity, 536–537
 - distribution in tissue, 539–544
 - dose and exposure, 539
 - elemental analysis, 528–530
 - fluorescence and radioactive assays, 534–535
 - ligand-related toxicity, 556
 - metabolism, 552–553
 - metal-related toxicity, 555–556
 - overview, 527–528
 - pharmacokinetics and elimination, 544–552
 - relaxation assay and magnetic resonance imaging (MRI), 531–533
 - routes of administration, 537–538
 - toxicity, 553–558
 - toxicity testing, 556–557
 - cytotoxicity, 501–517
 - ATP assay, 514
 - bromodeoxyuridine (BrdU) assay, 514–517
 - and cell death, 501–506

biological and *in vivo* methods*(continued)*

- cell perturbation
 - assays, 517
- cell proliferation assays, 503–506
- lactate dehydrogenase (LDH), 506–509
- membrane integrity
 - assays, 502–503
- metabolic activity assays, 503, 509–514
- MTT and resazurin assay, 513–514
- image reconstruction and probe quantification, 567–568
- magnetic field strength and contrast agent relaxivity, 565
- molecular probe clearance, 559–561
- MRI radio-frequency coils, 568–575
 - estimating signal-to-noise ratio, 570–575
 - parameters, 569–570
 - signal-to-noise ratio and B_1 field homogeneity, 568–569
- overview, 499–500
- physiological monitoring and image gating, 565–567
- T_2 - and T_2^* -based contrast agents, 564–565
- T_1 -shortening contrast agents, 561–564
- BrdU. *see* bromodeoxyuridine (BrdU) assay
- bromodeoxyuridine (BrdU) assay, 514–517
- bulk magnetic susceptibility (BMS), 180–182, 468–469
- calorimetry, 63
- capillary electrophoresis (CE), 86
- carbon-13-NMR spectroscopy, 158–161
- CE. *see* capillary electrophoresis (CE)
- cell-based paramagnetic CEST agents, 296–302
- cell binding
 - competition assay, 525–526
 - overview, 518–520
 - Scatchard analysis, 522–525
 - surface plasmon resonance (SPR), 521–522
- cell death, and cytotoxicity, 501–506
- cell perturbation assays, 517
- cell proliferation assays, 503–506
- cell uptake
 - distribution, metabolism, pharmacokinetics, and toxicity, 536–537
 - distribution in tissue, 539–544
 - dose and exposure, 539
 - elemental analysis, 528–530
 - fluorescence and radioactive assays, 534–535
 - metabolism, 552–553
 - overview, 527–528
 - pharmacokinetics and elimination, 544–552
 - relaxation assay and magnetic resonance imaging (MRI), 531–533
 - routes of administration, 537–538
 - toxicity, 553–558
 - complex-related, 554–555
 - ligand-related, 556
 - metal-related, 555–556
 - testing, 556–557
- CEST. *see* chemical exchange saturation transfer (CEST) agents
- characterization
 - of iron-oxide nanoparticles
 - by dynamic light scattering (DLS), 367–369, 388–389
 - electron energy loss spectroscopy (EELS), 382–383

- by electron tomography, 363–365
- energy dispersive X-ray spectroscopy (EDX), 382–383
- Fourier transform infrared spectroscopy, 384–386
- high angle annular dark field in scanning TEM (HAADF-STEM), 382–383
- IR spectroscopy, 371–372
- Mössbauer spectroscopy, 373–382
- for nanoparticle coatings, 383–390
- Raman spectroscopy, 372
- thermogravimetric analysis (TGA), 388
- by transmission electron microscopy (TEM), 363–365, 390
- by X-ray diffraction (XRD), 365–367, 370–371
- X-ray photoelectron spectroscopy (XPS), 372–373, 386–387
- magnetic
 - AC magnetic susceptibility, 409–411
 - DC magnetometry, 401–409
 - granulometry by light scattering, 411–413
 - magnetic parameters, 391–394
 - magnetism at nanoscale, 394–400
 - Mössbauer spectroscopy, 422–426
 - small angle neutron scattering (SANS), 415–422
 - X-ray photoelectron spectroscopy (XPS), 413–415
- manganese and iron complexes, 461–463
- chemical exchange saturation transfer (CEST) agents
 - binding interactions, 302–303
 - cell-based paramagnetic, 296–302
 - classification of, 253–257
 - data post-processing and analysis, 265–266
 - enhancing sensitivity, 280–281
 - field-strength dependencies, 309
 - iodinated CT-contrast agents as, 262
 - Ln-HPDO3A probes as, 258–262
 - luminescence spectroscopy, 269–273
 - overview, 244–247
 - oxygen-17 NMR spectroscopy, 267–269
 - paramagnetic liposomes, 286–293
 - paramagnetic micelles, 281–286
 - paramagnetic nanosystems, 293–296
 - parameters affecting, 251–253
 - phantom image formation
 - B_0 field correction, 304–306
 - B_1 field correction, 306
 - continuous wave saturation, 306
 - and proton exchange linewidth measurement
 - for assessing, 274
 - overview, 274
 - QUEST and QUESP experiments, 275–279
 - water-exchange (WEX), 275
 - theoretical and practical considerations, 247–251, 306–309
 - and Z-spectra
 - instrumentation and sample conditions for, 263
 - pulse sequences utilized for, 263–265

- coatings, for iron-oxide nanoparticles
- adenosine triphosphate (ATP), 340–341
 - and anchoring groups, 353–356
 - dendrimers, 341–342
 - functionalization
 - by nonporous and porous silica shells, 359–361
 - by polymers and dendrons, 357–359
 - mesoporous silica coatings, 351–353
 - nonporous silica coatings, 348–350
 - overview, 339
 - polymers, 342–344
 - relaxivity, 356–361
 - silane coatings, 344–348
- competition assay, 525–526
- complexometry, 182–186
- complex-related toxicity, 554–555
- complicated equilibrium calculations, 67
- computational methods
- basis sets and relativistic effects, 203–205
 - density functional theory and *ab initio* methods, 198–203
 - molecular mechanics and molecular dynamics simulations, 196–198
 - overview, 196
 - practical aspects and selected examples, 207–214
 - semi-empirical calculations, 198
 - software and hardware, 214
 - solvent effects, 205–207
 - transition metal-based T_1 contrast agents, 463–465
- concentration, of gadolinium-based contrast agents
- bulk magnetic susceptibility, 180–182
 - complexometry, 182–186
 - importance of accurate measurements, 174–175
 - metal analysis with plasma techniques, 177–180
 - NMR relaxometry, 175–177
- continuous wave saturation, 306
- coordination chemistry, 449–453
- coprecipitation method, 332–334
- cyclic perfluorocarbons, 484–485, 501–517
- adenosine triphosphate (ATP) assay, 514
 - bromodeoxyuridine (BrdU) assay, 514–517
 - and cell death, 501–506
 - cell perturbation assays, 517
 - cell proliferation assays, 503–506
 - lactate dehydrogenase (LDH), 506–509
 - membrane integrity assays, 502–503
 - metabolic activity assays, 503, 509–514
 - MTT and resazurin assay, 513–514
- data post-processing and analysis, 265–266
- DC magnetometry, 401–409
- Debye–Stokes equation, 156
- decomplexation reactions, 82–88
- dendrimers, 341–342
- dendrons, and polymers, 357–359
- density functional theory, 198–203
- deuterium-NMR spectroscopy, 157–158
- diethylenetriaminepentaacetic acid (DTPA), 15–18
- dissociation kinetics, of metal chelates, 76–81
- DLS. *see* dynamic light scattering (DLS)
- DOTA. *see* 1,4,7,10-tetra-azacyclododecane-1,4,7,10-tetraacetic acid (DOTA)

- DTPA. *see* diethylene-triaminepentaacetic acid (DTPA)
- dynamic light scattering (DLS), 367–369, 388–389
- EDX. *see* energy dispersive X-ray spectroscopy (EDX)
- EELS. *see* electron energy loss spectroscopy (EELS)
- effective magnetic moment, 465–468
- electron energy loss spectroscopy (EELS), 382–383
- electron nuclear double resonance (ENDOR), 149–151
- electron tomography, 363–365
- elemental analysis, 528–530
- emulsion formulations, 487–490
- end-group chemistry, 485
- ENDOR. *see* electron nuclear double resonance (ENDOR)
- energy dispersive X-ray spectroscopy (EDX), 382–383
- enhancement factor, 192–194
- equilibrium constants, for metal–ligand interactions, 41–46
- equilibrium distribution curves, 63–67
- equilibrium models, 46–51
- E-relaxometric titrations, 188–192
- EXAFS. *see* extended X-ray absorbance fine structure (EXAFS) spectroscopy
- extended X-ray absorbance fine structure (EXAFS) spectroscopy, 151–152
- field-strength dependencies, 228–229, 309
- fluorescence and radioactive assays, 534–535
- fluorine-based contrast agents
 - fluorine-19 MRI probes, 479–481
 - perfluorocarbons (PFCs)
 - biocompatibility, 482
 - cyclic perfluorocarbons, 484–485
 - emulsion formulations, 487–490
 - end-group chemistry, 485
 - linear perfluorocarbons, 482–483
 - multimodal and theranostic agents, 486–487
 - physiochemical properties of, 481–482
 - survey of, 482–485
 - synthetic modifications, 485–486
 - phantom image formation
 - chemical shift dispersion and multiple peaks, 492–493
 - fluorine-19 imaging, 491–492
 - fluorine-19 MRI probes, 479–481
- functionalization, for iron-oxide nanoparticles
 - by nonporous and porous silica shells, 359–361
 - by polymers and dendrons, 357–359
- gadolinium-based contrast agents
 - computational methods
 - basis sets and relativistic effects, 203–205
 - density functional theory and *ab initio* methods, 198–203
 - molecular mechanics and molecular dynamics simulations, 196–198
 - overview, 196
 - practical aspects and selected examples, 207–214
 - semi-empirical calculations, 198
 - software and hardware, 214
 - solvent effects, 205–207

gadolinium-based contrast agents

(continued)

- concentration of
 - bulk magnetic susceptibility, 180–182
 - complexometry, 182–186
 - importance of accurate measurements, 174–175
 - metal analysis with plasma techniques, 177–180
 - NMR relaxometry, 175–177
- field-strength dependencies, 228–229
- image formation in MRI
 - gradients and *k*-space, 216–219
 - image formation, 219
 - magnetization and relaxation, 215–216
 - slice selection, 219–220
 - spatial encoding, 220–221
- longitudinal and transverse relaxation times
 - choice of delays, 131
 - description, 128–130, 132–134
 - FID *versus* spectrum, 131
 - O-longitudinal relaxation, 131
 - radiation damping, 130–131
- measurement of time
 - constants by MRI, 225–228
- MRI pulse sequences
 - gradient-recalled-echo sequences, 222–224
 - image contrast, 224–225
 - spin-echo sequences, 222
- nuclear magnetic relaxation dispersion (NMRD)
 - acquisition of, 135–136
 - interpretation of, 136–138

relaxivity

- definition, 122–123
- inner-sphere, 124–126
- outer-sphere, 127

relaxometric titrations

- E- and M-titrations, 188–192
- enhancement factor, 192–194
- experimental procedure, 194–195
- overview, 187

rotational correlation times

- carbon-13-NMR spectroscopy, 158–161
- Debye–Stokes equation, 156
- deuterium-NMR spectroscopy, 157–158
- hydrogen-NMR longitudinal relaxation rates, 161–163
- and NMRD, 154–156
- overview, 153–154
- oxygen-17 $1/T_1$ NMR spectroscopy, 156–157

water coordination numbers

- electron nuclear double resonance (ENDOR), 149–151

extended X-ray

- absorbance fine structure (EXAFS) spectroscopy, 151–152

inner- *versus* outer-sphere water ligands, 139

luminescence

- spectroscopy, 142–149
- oxygen-17 NMR spectroscopy, 139–142

single crystal X-ray diffraction, 151

water residence times

- hydrogen-NMRD profiles, 170–171
- overview, 164

- temperature dependence
 - of proton relaxivity, 171–173
 - variable temperature
 - hydrogen-NMR spectroscopy, 169–170
 - variable temperature
 - oxygen-17-NMR spectroscopy, 164–168
- gadolinium complexes, 88–95
 - lability of, 88–95
 - stability of, 69–74
- gradient-recalled-echo sequences, 222–224
- gradients and *k*-space, 216–219
- granulometry, by light scattering, 411–413
- HAADF-STEM. *see* high angle annular dark field in scanning TEM (HAADF-STEM)
- high angle annular dark field in scanning TEM (HAADF-STEM), 382–383
- high-performance liquid chromatography (HPLC), 86
- HPLC. *see* high-performance liquid chromatography (HPLC)
- hydrogen-NMRD profiles, 170–171
- hydrogen-NMR longitudinal relaxation rates, 161–163
- hydrogen-NMR spectroscopy, 169–170
- ICP-AES. *see* inductively coupled plasma atomic emission spectroscopy (ICP-AES)
- ICP-MS. *see* inductively coupled plasma mass spectrometry (ICP-MS)
- image contrast, 224–225
- image formation
 - of CEST agents
 - B_0 field correction, 304–306
 - B_1 field correction, 306
 - continuous wave
 - saturation, 306
- fluorine-based contrast agents
 - chemical shift dispersion and multiple peaks, 492–493
 - fluorine-19 imaging, 491–492
- gadolinium-based contrast agents
 - description, 219
 - gradients and *k*-space, 216–219
 - magnetization and relaxation, 215–216
 - slice selection, 219–220
 - spatial encoding, 220–221
- iron-oxide nanoparticle-based contrast agents
 - magnetic-field strength dependencies, 429–430
 - T_2 - and T_2^* -weighted MRI, 427–429
- inductively coupled plasma atomic emission spectroscopy (ICP-AES), 86
- inductively coupled plasma mass spectrometry (ICP-MS), 86
- inner-sphere relaxivity, 124–126
- inner-sphere water ligands, 139
- iodinated CT-contrast agents, 262
- iron and manganese complexes, 461–463
- iron-oxide nanoparticle-based contrast agents
 - characterization
 - by dynamic light scattering (DLS), 367–369, 388–389
 - electron energy loss spectroscopy (EELS), 382–383
 - by electron tomography, 363–365
 - energy dispersive X-ray spectroscopy (EDX), 382–383
 - Fourier transform infrared spectroscopy, 384–386

- iron-oxide nanoparticle-based
 contrast agents (*continued*)
 high angle annular dark field in scanning TEM (HAADF-STEM), 382–383
 IR spectroscopy, 371–372
 Mössbauer spectroscopy, 373–382
 for nanoparticle coatings, 383–390
 Raman spectroscopy, 372
 thermogravimetric analysis (TGA), 388
 by transmission electron microscopy (TEM), 363–365, 390
 by X-ray diffraction (XRD), 365–367, 370–371
 X-ray photoelectron spectroscopy (XPS), 372–373, 386–387
 coatings for
 adenosine triphosphate (ATP), 340–341
 and anchoring groups, 353–356
 dendrimers, 341–342
 functionalization by nonporous and porous silica shells, 359–361
 functionalization by polymers and dendrons, 357–359
 mesoporous silica coatings, 351–353
 nonporous silica coatings, 348–350
 overview, 339
 polymers, 342–344
 relaxivity, 356–361
 silane coatings, 344–348
 magnetic characterization
 AC magnetic susceptibility, 409–411
 DC magnetometry, 401–409
 granulometry by light scattering, 411–413
 magnetic parameters, 391–394
 magnetism at nanoscale, 394–400
 Mössbauer spectroscopy, 422–426
 small angle neutron scattering (SANS), 415–422
 X-ray photoelectron spectroscopy (XPS), 413–415
 overview, 319–322
 phantom image formation
 magnetic-field strength dependencies, 429–430
 T_2 - and T_2^* -weighted MRI, 427–429
 relaxation of, 322–330
 synthesis of, 331–332
 coprecipitation method, 332–334
 mechanism of formation, 331–332
 thermal decomposition, 334–338
 IR spectroscopy, 371–372
 isolation and purification, 27–28
 kinetic studies, 81–82
 k -space, and gradients, 216–219
 lability, of metal complexes
 decomplexation reactions, 82–88
 dissociation kinetics of metal chelates, 76–81
 gadolinium complexes, 88–95
 kinetic studies, 81–82
 model calculations, 86–88
 overview, 75–76
 relaxometric measurements, 83–84
 spectrophotometric measurements, 84–86

- lactate dehydrogenase (LDH),
506–509
- LDH. *see* lactate dehydrogenase (LDH)
- ligand design, for MRI contrast agents, 5–15
- ligand-related toxicity, 556
- ligand synthesis and characterization
description, 29–31
isolation and purification, 27–28
ligand design for MRI contrast agents, 5–15
structure and properties, 1–5
synthetic methods
DOTA and its derivatives, 19–26
DTPA and its derivatives, 15–18
PCTA and AAZTA, 26–27
- light scattering, granulometry by, 411–413
- linear perfluorocarbons, 482–483
- linewidth measurement, for CEST, 274
- Ln-HPDO3A probes, 258–262
- longitudinal and transverse relaxation times
choice of delays, 131
description, 128–130, 132–134
FID *versus* spectrum, 131
O-longitudinal relaxation, 131
radiation damping, 130–131
- luminescence spectroscopy, 142–149, 269–273
- magnetic characterization
AC magnetic susceptibility, 409–411
DC magnetometry, 401–409
granulometry by light scattering, 411–413
parameters, 391–394
magnetism at nanoscale, 394–400
Mössbauer spectroscopy, 422–426
small angle neutron scattering (SANS), 415–422
X-ray photoelectron spectroscopy (XPS), 413–415
- magnetic-field strength dependencies, 429–430
- magnetic parameters, 391–394
- magnetic resonance imaging (MRI)
contrast agents, ligand design for, 5–15
fluorine-19 probes, 479–481
and gadolinium-based contrast agents
gradients and k -space, 216–219
image formation, 219
magnetization and relaxation, 215–216
slice selection, 219–220
spatial encoding, 220–221
measurement of time constants, 225–228
pulse sequences
gradient-recalled-echo sequences, 222–224
image contrast, 224–225
spin-echo sequences, 222
radio-frequency coils, 568–575
estimating signal-to-noise ratio, 570–575
parameters, 569–570
signal-to-noise ratio and B_1 field homogeneity, 568–569
relaxation assay and, 531–533
 T_1 - and T_2 -weighted, 427–429
- magnetism, at nanoscale, 394–400
- magnetization, and relaxation, 215–216
- manganese and iron complexes, 461–463
- membrane integrity assays, 502–503
- mesoporous silica coatings, 351–353

- metabolic activity assays, 503, 509–514
- metal analysis, with plasma techniques, 177–180
- metal chelates, dissociation kinetics of, 76–81
- metal complexes
- characterization of, 34–39
 - lability of
 - decomplexation reactions, 82–88
 - dissociation kinetics of metal chelates, 76–81
 - gadolinium complexes, 88–95
 - kinetic studies, 81–82
 - model calculations, 86–88
 - overview, 75–76
 - relaxometric measurements, 83–84
 - spectrophotometric measurements, 84–86
 - metal–ligand interactions
 - equilibrium constants for, 41–46
 - physicochemical methods for, 51–69
 - preparation of, 32–34
 - stability of
 - and calorimetry, 63
 - complicated equilibrium calculations, 67
 - equilibrium distribution curves, 63–67
 - equilibrium models, 46–51
 - experimental methods, 52–60
 - gadolinium complexes, 69–74
 - limitations, 67–69
 - methods relying on separation, 60–63
 - overview, 40–41
 - speciation diagrams, 63–67
- metal ion, and transition metal-based T_1 contrast agents, 471–473
- metal–ligand interactions
- equilibrium constants for, 41–46
 - physicochemical methods for, 51–69
- metal-related toxicity, 555–556
- model calculations, of metal complexes, 86–88
- molecular dynamics imulations, 196–198
- molecular mechanics, 196–198
- molecular probe clearance, 559–561
- Mössbauer spectroscopy, 373–382, 422–426
- M-relaxometric titrations, 188–192
- MRI. *see* magnetic resonance imaging (MRI)
- multimodal and theranostic agents, 486–487
- nanoparticle coatings, 383–390
- NMRD. *see* nuclear magnetic relaxation dispersion (NMRD)
- NMR relaxometry, 175–177
- nonporous silica coatings, 348–350
- nonporous silica shells, 359–361
- nuclear magnetic relaxation dispersion (NMRD)
- acquisition of, 135–136
 - interpretation of, 136–138
 - and rotational correlation times, 154–156
 - transition metal-based T_1 contrast agents, 453–460
- O-longitudinal relaxation, 131
- outer-sphere relaxivity, 127
- outer-sphere water ligands, 139
- oxygen-17-NMR spectroscopy
- chemical exchange saturation transfer (CEST) agents, 267–269
 - rotational correlation times, 156–157
 - water coordination numbers, 139–142
 - water residence times, 164–168

- paramagnetic liposomes, 286–293
- paramagnetic micelles, 281–286
- paramagnetic nanosystems, 293–296
- PCTA. *see* 3,6,9,15-tetra-azabicyclo[9.3.1]pentadeca-1(15),11,13-triene-3,6,9-triacetic acid (PCTA)
- perfluorocarbons (PFCs)
- biocompatibility, 482
 - cyclic perfluorocarbons, 484–485
 - emulsion formulations, 487–490
 - end-group chemistry, 485
 - linear perfluorocarbons, 482–483
 - multimodal and theranostic agents, 486–487
 - physiochemical properties of, 481–482
 - survey of, 482–485
 - synthetic modifications, 485–486
- PFCs. *see* perfluorocarbons (PFCs)
- phantom image formation
- of CEST agents
 - B_0 field correction, 304–306
 - B_1 field correction, 306
 - continuous wave saturation, 306
 - fluorine-based contrast agents
 - chemical shift dispersion and multiple peaks, 492–493
 - fluorine-19 imaging, 491–492
 - gadolinium-based contrast agents
 - description, 219
 - gradients and k -space, 216–219
 - magnetization and relaxation, 215–216
 - slice selection, 219–220
 - spatial encoding, 220–221
 - iron-oxide nanoparticle-based contrast agents
 - magnetic-field strength dependencies, 429–430
 - T_2 - and T_2^* -weighted MRI, 427–429
- physicochemical methods, for metal complexes, 51–69
- physiochemical properties, PFCs, 481–482
- plasma techniques, metal analysis with, 177–180
- polymers, 342–344
- and dendrons, 357–359
- porous silica shells, 359–361
- proton exchange, and CEST
- linewidth measurement for assessing, 274
 - overview, 274
 - QUEST and QUESP experiments, 275–279
 - water-exchange (WEX), 275
- proton relaxivity, temperature dependence of, 171–173
- Pulse sequences, for CEST, 263–265
- purification and isolation, 27–28
- QUEST and QUESP experiments, 275–279
- radiation damping, 130–131
- radioactive and fluorescence assays, 534–535
- radio-frequency coils, MRI, 568–575
- parameters, 569–570
 - signal-to-noise ratio and B_1 field homogeneity, 568–569
 - estimating, 570–575
- Raman spectroscopy, 372
- relativistic effects, 203–205
- relaxation assay, and MRI, 531–533
- relaxivity
- definition, 122–123
 - inner-sphere, 124–126

- relaxivity (*continued*)
 for iron-oxide nanoparticles, 356–361
 outer-sphere, 127
 and transition metal-based T_1 contrast agents, 453–460
- relaxometric measurements, 83–84
- relaxometric titrations
 E- and M-titrations, 188–192
 enhancement factor, 192–194
 experimental procedure, 194–195
 overview, 187
- resazurin assay, 513–514
- rotational correlation times
 carbon-13-NMR spectroscopy, 158–161
 Debye–Stokes equation, 156
 deuterium-NMR spectroscopy, 157–158
 hydrogen-NMR longitudinal relaxation rates, 161–163
 and NMRD, 154–156
 overview, 153–154
 oxygen-17 $1/T_1$ NMR spectroscopy, 156–157
- SANS. *see* small angle neutron scattering (SANS)
- Scatchard analysis, 522–525
- semi-empirical calculations, 198
- separation methods, and metal complexes, 60–63
- signal-to-noise ratio
 and B_1 field homogeneity, 568–569
 estimating, 570–575
- silane coatings, 344–348
- single crystal X-ray diffraction, 151
- slice selection, 219–220
- small angle neutron scattering (SANS), 415–422
- solvent effects, 205–207
- spatial encoding, 220–221
- speciation diagrams, 63–67
- spectrophotometric measurements, 84–86
- spin-echo sequences, 222
- SPR. *see* surface plasmon resonance (SPR)
- SQUID. *see* superconducting quantum interference device (SQUID)
- stability, of metal complexes
 and calorimetry, 63
 complicated equilibrium calculations, 67
 equilibrium distribution curves, 63–67
 equilibrium models, 46–51
 experimental methods, 52–60
 gadolinium complexes, 69–74
 limitations, 67–69
 overview, 40–41
 physicochemical methods for, 51–69
 and separation methods, 60–63
 speciation diagrams, 63–67
- superconducting quantum interference device (SQUID), 469–471
- surface plasmon resonance (SPR), 521–522
- synthesis
 of iron-oxide nanoparticles, 331–332
 coprecipitation method, 332–334
 mechanism of formation, 331–332
 thermal decomposition, 334–338
- ligand
 DOTA and its derivatives, 19–26
 DTPA and its derivatives, 15–18
 PCTA and AAZTA, 26–27
- synthetic modifications, 485–486

- T_1 -shortening contrast agents, 561–564
- T_2 - and T_2^* -based contrast agents, 564–565
- T_2 - and T_2^* -weighted MRI, 427–429
- TEM. *see* transmission electron microscopy (TEM)
- temperature dependence, of proton relaxivity, 171–173
- TGA. *see* thermogravimetric analysis (TGA)
- theranostic and multimodal agents, 486–487
- thermal decomposition, 334–338
- thermogravimetric analysis (TGA), 388
- toxicity, cell uptake, 553–558
 - complex-related, 554–555
 - ligand-related, 556
 - metal-related, 555–556
 - testing, 556–557
- transition metal-based T_1 contrast agents
 - bulk magnetic susceptibility (BMS), 468–469
 - characterizing manganese and iron complexes, 461–463
 - computational methods, 463–465
 - coordination chemistry, 449–453
 - effective magnetic moment, 465–468
 - and metal ion, 471–473
 - and NMRD, 453–460
 - overview, 448–449
 - and relaxivity, 453–460
 - superconducting quantum interference device (SQUID), 469–471
- transmission electron microscopy (TEM), 363–365, 390
- transverse relaxation times
 - choice of delays, 131
 - description, 128–130, 132–134
 - FID *versus* spectrum, 131
 - O-longitudinal relaxation, 131
 - radiation damping, 130–131
- T_1 -shortening contrast agents, 561–564
- water coordination numbers
 - electron nuclear double resonance (ENDOR), 149–151
 - extended X-ray absorbance fine structure (EXAFS) spectroscopy, 151–152
 - luminescence spectroscopy, 142–149
 - oxygen-17 NMR spectroscopy, 139–142
 - single crystal X-ray diffraction, 151
- water-exchange (WEX), 275
- water residence times
 - hydrogen-NMRD profiles, 170–171
 - overview, 164
 - temperature dependence of proton relaxivity, 171–173
 - variable temperature hydrogen-NMR spectroscopy, 169–170
 - variable temperature oxygen-17-NMR spectroscopy, 164–168
- WEX. *see* water-exchange (WEX)
- XPS. *see* X-ray photoelectron spectroscopy (XPS)
- X-ray diffraction (XRD), 365–367, 370–371
- X-ray photoelectron spectroscopy (XPS), 372–373, 386–387, 413–415
- XRD. *see* X-ray diffraction (XRD)
- Z-spectra, and CEST
 - instrumentation and sample conditions for, 263
 - pulse sequences utilized for, 263–265

